CONVECTION HEAT TRANSFER

Other books by Adrian Bejan:

Entropy Generation Through Heat and Fluid Flow, Wiley, 1982.

Advanced Engineering Thermodynamics, Third Edition, Wiley, 2006.

Thermal Design and Optimization, with G. Tsatsaronis and M. Moran, Wiley, 1996.

Entropy Generation Minimization, CRC Press, 1996.

Shape and Structure, from Engineering to Nature, Cambridge, 2000.

Heat Transfer Handbook, with A. D. Kraus, eds., Wiley, 2003.

Design with Constructal Theory, with S. Lorente, Wiley, 2008.

Design in Nature, with J. P. Zane, Doubleday, 2012.

Convection in Porous Media, with D. A. Nield, Fourth Edition, Springer, 2013.

CONVECTION HEAT TRANSFER

FOURTH EDITION

Adrian Bejan

J.A. Jones Distinguished Professor
Duke University
Durham, North Carolina

WILEY

The entrepreneur, as a creator of the new and a destroyer of the old, is constantly in conflict with convention. He inhabits a world where belief precedes results, and where the best possibilities are usually invisible to others. His world is dominated by denial, rejection, difficulty, and doubt. And although as an innovator, he is unceasingly imitated when successful, he always remains an outsider to the ''establishment.''

Theodore Forstmann, 2003.

In science, the ''entrepreneur'' is the one who gets the unusual idea, climbs out on a limb, jumps, and runs with it on the landscape. His fate at the feet of the establishment is the same.

CONTENTS

PREFACE

An author is fortunate if his book is popular enough to merit a second edition somewhere down the line, yet the flow of ideas that grew around this book since the first edition (1988) has been beyond expectations. I will let others comment on this flow. In this brief Preface, I comment on just one feature of the flow of ideas and one bit of history.

The flow of ideas is illustrated by the changes made in this new edition. Good ideas (in this or any other field) attract interesting minds—researchers, educators, and authors with ideas. These minds grow the field the way that the yeast grows the cake. While revising this edition, it was not possible to keep up with this growth, but I tried, even though this meant abandoning some of the material from earlier editions. The new growth is represented by the impact of the science of discovering effective flow configurations (constructal theory and design), the streamlining of the discipline along methods that are direct, muscular, and at the same time lean (scale analysis, intersection of asymptotes, heatlines), the oneness with thermodynamics through the irreversibility (entropy generation) phenomenon, and new references and problems at the end of chapters.

Because we know where convection and thermodynamics come from, this growth illustrates that science (education, knowledge, information) is an evolutionary design [1–4], a flow system that constantly morphs and improves so that our own movement and life are facilitated and extended on the landscape. This is nature, the animate and the inanimate alike.

Because research is autobiographical, good research is a book of wonderful memories. I close this preface with the story of how the first edition of this book was born. It was an accident, literally. At age 33, I was behaving as if I was meant to play basketball forever, and I was wrong. During a game in January 1982, one of my Achilles' tendons was severed, and I ended up in a wheelchair for the entire semester. I had to teach my convection course, for which I had written notes, but this time I was forced to write each lecture on transparencies, for the screen. My first graduate student, Shigeo Kimura, now professor at Kanazawa University, Japan, was my teaching assistant. He would wheel me into the classroom every morning, and my convection book would come to life, one original drawing at

a time, one original (solved) problem after another. One such problem was the method of intersecting the asymptotes and the back-of-the-envelope prediction of optimal spacings (Problem 11, Chapter 4, p. 157, in the first edition).

There was so much richness during the spring of 1982 that the accident was a blessing.

ADRIAN BEJAN

Duke University

REFERENCES

1. A. Bejan and J. P. Zane, *Design in Nature*, Doubleday, New York, 2012.
2. A. Bejan, Science and technology as evolving flow architectures, *Int. J. Energy Res.*, Vol. 33, 2009, pp. 112–125.
3. A. Bejan and S. Lorente. The physics of spreading of ideas, *Int. J. Heat Mass Transfer*, Vol. 55, 2012, pp. 802–807.
4. A. Bejan, Two hierarchies in science: The free flow of ideas and the academy, *Int. J. Design Nature Ecodynam.*, Vol. 4, No. 4, 2009, pp. 386–394.

PREFACE TO THE THIRD EDITION

Research is autobiographical. I often say this when I lecture, and I find it true as I look at this new edition of *Convection Heat Transfer*. It is even more true as I look at all three editions together. This book is a chronicle of the heat transfer side of my career, the methods I developed and taught along the way, and the great fortune I had to work with extremely gifted colleagues. The three editions are also a story of how the field has grown and prospered. It has done so based on new challenges and especially, new ideas.

One trend that is made visible (and useful, I hope) in this edition is the new emphasis on *design as science*—the generation of flow configuration based on principle. For many years, the field of convection was preoccupied with documenting the transport characteristics of various but simple flow configurations—relationships between temperature differences and heat transfer rates. This information is essential in the modeling and simulations that are necessary in design. The reality, however, is harsh: Constraints exist, and one overriding constraint is space (size, volume, weight). Putting more and more heat transfer into a given volume has been the objective, from the compact heat exchangers of my MIT years to the heat transfer augmentation techniques and the cooling of electronics packages of today. Doing more with limited resources has been the driving force.

Miniaturization marches forward, but this is not even half of the story. The reason is that the devices we touch must be made at our scale—they must be macroscopic, no matter how small the smallest components. The more successful we are in making smaller components, the greater the challenge to install larger numbers of such components and to connect them with currents (heat, fluid, electricity), to keep them *alive*. The challenge is to ''construct,'' to assemble and design while assembling (i.e., to design complexity and to *deduce* the flow configuration of the macroscopic device).

Construction must be shouted from the rooftops, especially today as the crowd marches toward smaller scales. To construct is to proceed in the opposite

direction, from small to large, because only in this direction can the small scales be made useful. Only after the achievement of constructal assembly can small-scale components deliver high densities of heat transfer.

In this new edition, the first steps toward constructs with high heat transfer density are used as an introduction to *constructal theory and design**: the generation of flow architecture in the pursuit of maximal global performance subject to global constraints, when the flow architecture is free to morph. The focus is on method, on design as science, on the generation of optimal and complex architectures based on the constructal law. To emphasize this facet of the third edition is appropriate not only because of its importance today, but also because it had its start in the 1984 edition [see the optimization of spacings with natural convection (p. 157, Problem 11, Chapter 4).

The focus on methodology is why in this new edition I chart the progress made by three other methods that were pioneered in the 1984 edition. These methods have become recognized and now occupy growing sections of the literature:

The intersection of asymptotes method, which delivered in amazingly direct fashion the optimal spacing for natural convection (see above), has since been extended to spacings for forced convection and the constructal theory prediction of all the basic features of Bénard convection. The intersection of asymptotes is also useful pedagogically, in the teaching of the concept of *transition* (e.g., laminar–turbulent flow, natural–forced convection).

Heatlines are now being used to visualize the true paths followed by convection: the paths of energy flow, not fluid flow. They were introduced in the 1984 edition, with an example of natural convection in an enclosure. The concept has since been extended to mass transfer and a variety of basic and applied configurations with natural and forced convection in fluids and fluid-saturated porous media. This method of visualization is particularly well suited for computational heat transfer and should be included in commercial computational packages.

Scale analysis continues to be the main method for teaching the basics of convection in this new edition. The rules and promise of scale analysis as a problem-solving method were first formulated in the 1984 edition. Today the method is used widely, and this makes it even more essential in a basic course of convection. The increased importance of scale analysis is also due to the proliferation of computational heat transfer. If done correctly, scale analysis can shed light on what the deluge of numerical results is trying to tell us. Even more, to teach scale analysis is to remind the student not to give up on pencil and paper. Not everything must be done on the computer.

Porous media were brought into a heat transfer course for the first time by the 1984 edition of this book. Since then, convection in porous media has developed into a field of its own. In this edition we continue to emphasize the basic method and the most basic results. A connection is also made between porous media and

*A. Bejan, *Shape and Structure, from Engineering to Nature*, Cambridge University Press, Cambridge, 2000.

designed complex flow structures,* and this serves as one more bridge to the constructal design method.

Interdisciplinary teaching and research is one of the missions of this course, but with this warning: Learn your disciplines first; only then you will be strong on the interdisciplinary frontiers. The teaching of convection in porous media is a good example. This is presented not as a self-standing subject but as an interaction between principles of convection in pure fluids, which we all learn, and newly emerging technological applications that employ porous flow structures.

In my work on this new edition I benefited from the help and ideas offered by Professors C. Biserni, J. Bonjour, I. Dincer, M. Feidt, D. Gobin, Y. Fautrelle, S. J. Kim, A. D. Kraus, S. Lorente, E. Lorenzini, G. Lorenzini, N. Mazet, F. Meunier, A. F. Miguel, W. J. Minkowycz, P. Neveu, D. A. Nield, A. H. Reis, E. Sciubba, B. Spinner, F. B. Tehrani, J. V. C. Vargas, M. E. Weber, and C. Zamfirescu. In particular, I wish to thank my doctoral students Y. Azoumah, T. Bello-Ochende, A. K. da Silva, L. Gosselin, J. C. Ordonez, Luiz A. O. Rocha, and W. Wechsatol.

ADRIAN BEJAN

Durham, North Carolina
April 2004

---

*A. Bejan, I. Dincer, S. Lorente, A. F. Miguel, and A. H. Reis, *Porous and Complex Flow Structures in Modern Technologies*, Springer-Verlag, New York, 2004.

PREFACE TO THE SECOND EDITION

I want to thank John Wiley & Sons, Inc. and the users of my *Convection Heat Transfer* for giving me this opportunity to prepare a second edition. The changes and additions that I made are due to the suggestions received from many colleagues and students, and to the evolution of my own research activity.

I made changes in both format and content. The format is now based on numbered sections and equations, to make it easier for the first-time user to use this book as a reference. I assembled all the symbols in a list that precedes the text. The Author Index acknowledges one more time the individuals whose work is quoted in the text. The Solutions Manual is now produced on the word processor, and has the appearance of a companion book.

The changes in content are more significant and at more than one level. New topics covered in the second edition are convection with change of phase (condensation, boiling, melting), the cooling of electronic packages by forced and natural convection, lubrication by contact melting, and several examples of conjugate heat transfer, i.e., convection coupled with conduction or radiation. I augmented most chapters with results, namely, formulas, tables, charts, and appendixes that are recommended for use in engineering design work. And, speaking of design, many of the new problems at the end of chapters refer to basic principles of thermal design.

Relative to the first edition, the chapters dealing with laminar and, especially, turbulent forced convection have been expanded. To make room for the new material and still respect the prescribed space limits, I had to eliminate the chapter on numerical methods, and to condense the treatment of convection in porous media. Numerical methods are now covered in courses devoted entirely to computational fluid dynamics and heat transfer. For porous media, I recently completed with Professor D. A. Nield a separate textbook, *Convection in Porous Media* (Springer, 1992; now in 4th edition, 2013).

As in the first edition, the most important feature of this book is that many of the topics and problems came from my own research. These problems recommended themselves as interesting and beautiful, i.e., worthy of study. They represent my argument in favor of practicing *laissez faire* in engineering research, and against the *dirigiste* policy advocated by others.

ADRIAN BEJAN

Durham, North Carolina
June 1994

PREFACE TO THE FIRST EDITION

My main reason for writing a convection textbook is to place the field's past 100 years of growth in perspective. This book is intended for the educator who wants to present his students with more than a review of the generally accepted ''classical'' methods and conclusions. Through this book I hope to encourage the convection student to question what is known and to think freely and creatively about what is unknown.

There is no such thing as ''unanimous agreement'' on any topic. The history of scientific progress shows clearly that our present knowledge and understanding—contents of today's textbooks—are the direct result of conflict and controversy. By encouraging our students to question authority, we encourage them to make discoveries on their own. We can all only benefit from the scientific progress that results.

In writing this book, I sought to make available a textbook alternative that offers something new on two other fronts: (1) content, or the selection of topics, and (2) method, or the approach to solving problems in convection heat transfer.

Regarding content, this textbook reflects the relative change in the priorities set by our technological society over the past two decades. Historically, the field of convective heat transfer grew out of great engineering pursuits such as energy conversion (power plant technology), the aircraft, and the exploration of extraterrestrial space. Today, we are forced to face additional challenges, primarily in the areas of ''energy'' and ''ecology.'' Briefly stated, engineering education today places a strong emphasis on man's need to coexist with the environment. This new emphasis is reflected in the topics assembled in this book. Important areas covered for the first time in a convection textbook are: (1) natural convection on *an equal footing* with forced convection, with application to energy conservation in buildings and to geophysical dynamics, (2) convection through porous media saturated with fluid, with application to geothermal and thermal insulation engineering, and (3) turbulent mixing in free-stream flow, with application to the dispersion of pollutants in the atmosphere and the hydrosphere.

Regarding method, in this book I made a consistent effort to teach problem solving (a *Solutions Manual* is available from the publisher or from me). This book is a textbook to be used for teaching a course, not a handbook. Of course, important engineering results are listed; however, the emphasis is placed on the thinking that leads to these results. A unique feature of this book is that it stresses the importance of correct scale analysis as an eligible and cost-effective method of solution, and as a precondition for more refined methods of solution. It also stresses the need for correct scaling in the graphic reporting of more refined analytical results and of experimental and numerical data. The cost and the ''return on investment'' associated with a possible method of solution are issues that each student-researcher should examine critically: these issues are stressed throughout the text.

I wrote this book during the academic year 1982–1983, in our mountain-side house on the greenbelt of North Boulder. This project turned out to be a highly rewarding intellectual experience for me, because it forced upon me the rare opportunity to think about an entire field, while continuing my own research on special topics in convection and other areas (specialization usually inhibits the ability to enjoy a bird's-eye-view of anything). It is a cliché in education and research for the author of a new book to end the preface by thanking his family for the ''sacrifice'' that allowed completion of the work. My experience with writing *Convection Heat Transfer* has been totally different (i.e., much more enjoyable!), to the point that I must thank this book for making me work at home and for triggering so many inspiring conversations with Mary. Convection can be entertaining.

ADRIAN BEJAN

Boulder, Colorado
July 1984

LIST OF SYMBOLS

a, b	dimensions of rectangular duct cross section (Fig. 3.5)
A	area
A_c	cross-sectional area
A, B	constants in the logarithmic law of the wall [eqs. (7.41) and (7.42)]
Ar	Archimedes number [eq. (10.80)]
b	empirical constant, Forchheimer flow [eq. (12.15)]
b	natural convection parameter [eq. (5.117)]
b	radial length scale of round velocity jet [eq. (9.40)]
b	stratification parameter [eq. (12.116)]
b	taper parameter [eq. (2.140)]
b	thermal stratification number [eq. (4.81)]
b_T	radial length scale of round thermal jet [eq. (9.43)]
$\tilde{b}_{1,2}$	empirical factors (Table 11.6)
B	condensation driving parameter [eq. (10.26)]
B	cross-sectional shape number (Fig. 3.7)
B	dimensionless group [eq. (2.147)]
B	dimensionless group [eq. (12.107)]
Be_L	Bejan number, pressure drop number [eq. (3.120′)]
Be_p	Bejan number for a porous medium [eq. (12.113)]
Bo_H	Boussinesq number [eq. (4.35)]
c	specific heat of incompressible substance
c_v	specific heat at constant volume
c_P	specific heat at constant pressure
$c_{1,2}$	constants
C	compressive impulse or reaction [eq. (6.7)]
C	concentration [eq. (11.1)]
C	constant
$C_{f,x}$	local skin friction coefficient [eqs. (2.57) and (7.52)]
C_n	factor (Fig. 7.11)
C_1, C_2, C_μ	constants [eq. (8.61)]
C_D	drag coefficient [eq. (7.103)]
C_{sf}	constant (Table 10.1)
d, D	diameter
D	mass diffusivity [eq. (11.24), Tables 11.1 and 11.2]
D	plate-to-plate spacing (Fig. 3.1)
D	stream transversal length scale
D_h	hydraulic diameter [eq. (3.26)]
D_{k-k}	knee-to-knee thickness of time-averaged turbulent shear layer (Fig. 9.3)

D_T	distance of maximum thermal penetration in the y direction, in the vicinity of a direct contact spot [eq. (7.94)]
e	specific energy (labeled u in Table 1.1)
f	Blasius streamfunction similarity profile [eq. (2.80)]
f	factor [eq. (7.113)]
f	friction factor [eq. (3.24)]
f	porous medium friction factor [eq. (12.12)]
f	roll thickness [eq. (5.92)]
f_u	curve fit for the velocity profile [eq. (7.53)]
f_v	frequency of vortex shedding [eq. (7.102)]
F	force
F	streamfunction similarity profile [eqs. (4.60) and (12.139)]
Fo	Fourier number [eq. (10.104)]
F_D	drag force
F_n	normal force
F_t	tangential force
g	gravitational acceleration
Gr_H	Grashof number [eq. (4.38)]
Gr_*	Grashof number based on heat flux (Table 6.1)
Gz	Graetz number [eq. (3.107)]
$G_\pounds$	constant (Table 4.3)
h	heat transfer coefficient [eq. (2.4)]; local heat transfer coefficient [eq. (2.100)]
h	specific enthalpy
h_{fg}	latent heat of condensation or evaporation (Table 10.2)
h'_{fg}	augmented latent heat [eq. (10.10)]
h''_{fg}	augmented latent heat [eq. (10.41)]
h_m	mass transfer coefficient [eq. (11.46)]
h_{sf}	latent heat of melting
H	enthalpy flow rate [eq. (10.5)]
H	heatfunction [defined via eqs. (1.68) and (1.69)]
H	height
H	Henry's constant [eq. (11.35) and Table 11.3]
I	area moment of inertia
I	integral [eq. (3.135)]
j	diffusion flux [eq. (11.20)]
j_{app}	apparent mass flux [eq. (11.102)]
J	dimensionless thickness parameter [eq. (2.139)]
Ja	Jakob number [eq. (10.19)]
k	thermal conductivity
k	wave number
$k''_n,\ k'''_n$	reaction rates [eqs. (11.135) and (11.136)]
k_s	sand grain size [eq. (8.16)]

K	jet strength [eq. (9.33)]
K	permeability [eq. (12.9)]
$K_{1,2}$	constants
l	effective length [eq. (4.127)]
l	mixing length [eq. (7.27)]
L	length
L	length of direct viscous contact [eq. (7.92)]
L_c	characteristic length
ℓ	equivalent length [eq. (10.86)]
L_m	length of direct thermal contact [eq. (7.95)]
£	effective length [eq. (4.128)]
Le	Lewis number [eq. (11.93)]
m	exponent in flow over a wedge [eq. (2.124)]
m	function [eq. (6.27)]
m	profile shape function for integral analysis [eq. (2.54)]
$\dot{m}$	mass flow rate
$\dot{m}'$	mass transfer rate per unit length [eq. (11.52)]
$\dot{m}'''$	volumetric mass generation rate [eq. (11.15)]
M	bending moment [eq. (6.8)]
M	function [eq. (8.22)]
M	impulse or reaction force due to fluid flow into or out of a control volume (Fig. 2.3)
M	mass
M	massfunction [eqs. (11.133)–(11.134)]
M	material constraint [eq. (3.132)]
M	molar mass [eq. (11.4)]
n	dimensionless coordinate across the velocity boundary layer (y/δ) [eq. (2.54)]
n	number of cylinders
n	number of heat-generating boards
n	number of moles [eq. (11.4)]
n_l	number of rows
N_B	buckling number [eq. (6.14)]
N_{tu}	number of heat transfer units [eq. (8.56)]
Nu	local Nusselt number [eq. (2.101)]
Nu	Nusselt number in the fully developed region [eq. (3.52)]
$\overline{\text{Nu}}$	overall Nusselt number
$\overline{\text{Nu}}_L^{\,0}$	constant (Table 4.3)
Nu_{0-x}	overall Nusselt number [eq. (3.91)]
Nu_x	local Nusselt number in the developing (entrance) region [eq. (3.90)]
p	dimensionless coordinate across the thermal boundary layer (y/δ_T) [eq. (2.58)]
p	even function (eq. (5.37))

p	wetted perimeter
P	pressure
P_∞	pressure in the free stream
Pe_D	Péclet number (UD/α)
Pe_L	Péclet number ($U_\infty L/\alpha$)
Po	Poiseuille number ($f\,\text{Re}_{Dh}$)
Pr	Prandtl number (ν/α)
Pr_p	porous medium Prandtl number [eq. (12.215)]
Pr_t	turbulent Prandtl number [eq. (7.66)]
q	heat transfer rate (W)
q	odd function [eq. (5.37)]
q'	heat transfer rate per unit length (W/m)
q''	heat flux (W/m^2)
q''_{app}	apparent heat flux [eq. (7.24)]
$q''_{0,\text{max}}$	maximum heat flux, under a direct thermal contact spot [eq. (7.86)]
q'''	rate of internal heat generation (W/m^3)
$\dot{Q}$	heat transfer rate (W)
Q	flow rate (m^2/s) [eq. (10.69)]
r	radial coordinate
r_0	tube radius
r_h	hydraulic radius [eq. (3.26)]
r, θ, z	cylindrical coordinates (Fig. 1.1)
r, ϕ, θ	spherical coordinates (Fig. 1.1)
R	ideal gas constant
$\overline{R}$	universal gas constant
R	radius
R	thermal resistance
Ra_H	Rayleigh number [eq. (4.25)]
Ra_y	Darcy modified Rayleigh number [eq. (12.89)]
$\text{Ra}_{m,y}$	mass transfer Rayleigh number [eq. (11.86)]
Ra_q	Rayleigh number based on source strength [eq. (6.6)]
Ra_{*H}	Rayleigh number based on heat flux [eq. (4.70)]
Ra_{*y}	Darcy modified Rayleigh number based on heat flux [eq. (12.99)]
Re_D	Reynolds number (UD/ν)
Re_{Dh}	Reynolds number based on hydraulic diameter (UD_h/ν)
Re_l	local Reynolds number [eq. (6.15)]
Re_L	Reynolds number ($U_\infty L/\nu$)
Re_t	terminal Reynolds number [eq. (10.37)]
s	constant (Table 10.1)
s	specific entropy
s	thickness of liquid zone (Fig. 10.24)
S	entropy (J/K)

S_{gen}	entropy generation rate (W/K)
Sc	Schmidt number [eq. (11.40)]
Sc_t	turbulent Schmidt number [eq. (11.116)]
Sh	Sherwood number [eq. (11.42)]
St_x	local Stanton number [eq. (7.76)]
Ste	Stefan number [eq. (10.80)]
Ste_μ	Stefan number for viscous heating [eq. (10.98)]
t	thickness
t	time
t_B	buckling time or time of eddy formation [eq. (6.13)]
t_f	time of convective boundary layer development [eq. (5.13′)]
t_v	transversal viscous communication time [eq. (6.12)]
T	absolute temperature
T'_A	Oseen-linearization function [eq. (5.25″)]
T_0	absolute temperature of the ambient
T_0	reference temperature
T_0	temperature of nozzle fluid
T_0	wall temperature
T_m	bulk temperature [eq. (3.42)]
T_m	melting point
T_{IN}	inlet temperature
T_∞	free-stream temperature
$T_{\infty,0}$	bottom temperature of a thermally stratified fluid reservoir (Fig. 4.8)
$T_{*\infty}$	core temperature in the high-Ra_H regime
u_A	Oseen-linearization function
u_*	friction velocity [eq. (7.34)]
$u_{*\infty}$	core velocity in the high-Ra_H regime
u_0	centerline velocity
u, v, w	velocity components in the (x, y, z) system of coordinates (Fig. 1.1)
u', v'	velocity disturbances [eq. (6.19)]
$\hat{u}, \hat{v}$	disturbance amplitudes [eq. (6.21)]
U	duct-averaged velocity
U	longitudinal base flow [eq. (6.19)]
U	slider velocity [eq. (10.55)]
U_c	centerline velocity
U_{max}	maximum average velocity [eq. (7.111)]
U_0	velocity of nozzle fluid
U_∞	free-stream velocity
v_0	blowing or suction velocity
V	stream velocity scale [eq. (6.7)]
V	velocity

V	volume [eq. (11.2)]
V	volume constraint [eq. (3.131)]
W	width
$\dot{W}$	work transfer rate, power
x, y, z	Cartesian coordinates (Fig. 1.1)
x_i	mole fraction [eq. (11.7)]
x_1	dimensionless horizontal coordinate in the end-turn region [eq. (5.58)]
x_*	thermal entrance coordinate [eq. (3.84)]
x_+	hydraulic entrance coordinate [eq. (3.105)]
x_0	starting length [defined in eqs. (9.22) and (9.28)]
x_0	unheated starting length (Fig. 2.8)
X	hydrodynamic entrance length
X	transversal coordinate of a point situated outside the boundary layer
X_C	concentration entrance length [eq. (11.73)]
X_l	longitudinal pitch
X_t	transversal pitch
X_T	thermal entrance length
X, Y, Z	body force terms in eqs. (1.19)
X_l^*	dimensionless longitudinal pitch [eq. (7.114)]
X_t^*	transversal longitudinal pitch [eq. (7.114)]
y	function [eg. (8.56)]
Y	equilibrium shape of a nearly straight stream [eq. (6.8)]
Y	y coordinate of a point situated in the free stream
Y_T	thermal entrance length
z	altitude (Fig. 10.24)

Greek Letters

α	thermal diffusivity
α	porous medium thermal diffusivity [eq. (12.35)]
$\hat{\alpha}$	empirical constant [eq. (9.73)]
α_{k-k}	knee-to-knee angle of time-averaged turbulent shear layer (Fig. 9.3)
β	coefficient of thermal expansion
β_c	concentration expansion coefficient [eq. (11.80)]
β	wedge angle (Fig. 2.10)
Γ	condensate mass flow rate [Table 6.1, eq. (10.4)]
γ	empirical constant [eq. (9.19)]
γ	function [eq. (6.27)]
γ	vertical temperature gradient (K/m) [eqs. (4.77) and (12.110)]
γ_0	empirical constant [eq. (9.37)]
Δ	discriminant [eq. (6.28)]

Δ	ratio [eq. (11.143)]
ΔP	pressure drop
ΔT	temperature difference
ΔT_{avg}	average temperature difference [eq. (3.97)]
ΔT_{lm}	log-mean temperature difference [eq. (3.92)]
δ	dimensionless thickness of the end region in a shallow enclosure
δ	film thickness
δ	outer thickness of a Pr > 1 natural convection boundary layer (Fig. 4.2)
δ	velocity boundary layer thickness
δ_c	concentration boundary layer thickness [eq. (11.87)]
δ_T	thermal boundary layer thickness
$\delta_{T,f}$	thermal boundary layer thickness at the end of its development [eq. (5.14)]
δ_v	inner viscous layer thickness of a Pr < 1 natural convection boundary layer (Fig. 4.2)
δ_v	velocity boundary layer thickness [eq. (5.17)]
δ^*	displacement thickness [eq. (2.86)]
ϵ	small parameter $(H/L)^2$ for shallow enclosures
ϵ	turbulence dissipation function [eq. (8.57)]
ϵ_H	thermal eddy diffusivity [eq. (7.23)]
ϵ_m	mass eddy diffusivity [eq. (11.103)]
ϵ_M	momentum eddy diffusivity [eq. (7.23)]
ϵ_w	emissivity [eq. (10.51)]
ζ	similarity variable [eq. (12.58)]
ζ	vorticity function [eq. (6.18)]
η	density of contact spots [eq. (7.85)]
η	similarity variable [eqs. (2.71), (4.55), (12.48), and (12.90)]
η_d	ventilation or displacement efficiency [eq. (11.121)]
θ	angle (Fig. 12.12a)
θ	dimensionless temperature function [eq. (2.93)]
θ	dimensionless time [eqs. (8.55) and (10.103)]
θ	momentum thickness [eq. (2.87)]
θ	similarity temperature profile [eqs. (4.58) and (9.90)]
θ	temperature difference
κ	von Kármán's constant [eq. (7.31)]
λ	Lagrange multiplier [eq. (3.135)]
λ	wavelength
λ_B	buckling wavelength
$\lambda_{1,2}$	functions of altitude [eq. (5.31)]
μ	viscosity
μ_f	friction coefficient [eq. (10.78)]
ν	kinematic viscosity
ρ	density (labeled $1/v$ in Table 1.1, where v is the specific volume)
σ	capacity ratio [eq. (12.30)]

σ	disturbance growth rate [eq. (6.21)]
σ	empirical constant [eq. (9.8)]
σ	normal stress
σ	surface tension (Table 10.2)
$\sigma_k, \sigma_\epsilon$	constants [eq. (8.61)]
τ	angle of tilt (Fig. 5.24)
τ	shear stress
$\tau*$	dimensionless time [eq. (11.122)]
τ_{app}	apparent shear stress [eq. (7.24)]
$\tau_{0, max}$	maximum shear stress, under a direct viscous constant spot [eq. (7.86)]
ϕ	angle
ϕ	fully developed temperature profile function [eq. (3.51)]
ϕ	function [eq. (12.19)]
ϕ	porosity [eq. (12.22)]
ϕ	volume fraction [eq. (5.103)]
ϕ_r	ratio [eq. (11.149)]
Φ	mass fraction [eq. (11.6)]
Φ	viscous dissipation function
χ	factor [eq. (7.113)]
ψ	streamfunction
ω	wall parameter [eq. (4.85)]
ω	wall parameter [eq. (12.106)]

Subscripts

$(\cdot)_a$	air
$(\cdot)_{app}$	apparent
$(\cdot)_{av}$	average
$(\cdot)_{avg}$	average
$(\cdot)_b$	base solution
$(\cdot)_b$	bulk
$(\cdot)_c$	cold
$(\cdot)_c$	constant, uniform
$(\cdot)_c$	convection
$(\cdot)_c$	dimensionless variables for the shallow core solution [eq. (5.47)]
$(\cdot)_c$	properties where the wall condition is imposed on the $k-\epsilon$ model [eqs. (8.64)–(8.65)]
$(\cdot)_c$	property measured along the stream centerline
$(\cdot)_{cv}$	property of the control volume
$(\cdot)_{CSL}$	conduction sublayer
$(\cdot)_e$	end
$(\cdot)_e$	expressions for the integral analysis of the end region [eq. (5.61)]

$(\cdot)_f$	final
$(\cdot)_f$	fluid
$(\cdot)_f$	saturated liquid
$(\cdot)_{FC}$	forced convection
$(\cdot)_g$	saturated vapor
$(\cdot)_h$	hot
$(\cdot)_{HT}$	heat transfer
$(\cdot)_i$	component i
$(\cdot)_i$	inner
$(\cdot)_{in}$	inlet
$(\cdot)_l$	liquid
$(\cdot)_m$	mean
$(\cdot)_{max}$	maximum
$(\cdot)_{min}$	minimum
$(\cdot)_{MT}$	mass transfer
$(\cdot)_{NC}$	natural convection
$(\cdot)_o$	outer
$(\cdot)_{opt}$	optimal
$(\cdot)_p$	pore
$(\cdot)_{rad}$	radiation
$(\cdot)_{ref}$	reference
$(\cdot)_{r,\theta,z}$	components of a vector in cylindrical coordinates
$(\cdot)_{r,\phi,\theta}$	components of a vector in spherical coordinates
$(\cdot)_s$	solid
$(\cdot)_{sat}$	saturation
$(\cdot)_{tr}$	transition
$(\cdot)_v$	vapor
$(\cdot)_{VSL}$	viscous sublayer
$(\cdot)_w$	wall
$(\cdot)_w$	water
$(\cdot)_0$	wall
$(\cdot)_{0-L}$	quantity averaged from $x = 0$ to $x = L$
$(\cdot)_*$	dimensionless variables for the high-Ra_H solution [eq. (5.23)]
$(\cdot)_\infty$	property of reservoir fluid

Superscripts

$(\bar{\cdot})$	average
$(\bar{\cdot})$	time-averaged part
$(\cdot)'$	fluctuating part
$(\cdot)^+$	wall coordinates and wall variables [eq. (7.35)]

FUNDAMENTAL PRINCIPLES

Convective heat transfer, or simply, *convection*, is the study of heat transport processes effected by the flow of fluids. The very word *convection* has its roots in the Latin verbs *convecto-are* and *convĕho-vĕhĕre* [1],* which mean to bring together or to carry into one place. Convective heat transfer has grown to the status of a contemporary science because of our need to understand and predict how a fluid flow acts as a ''carrier'' or ''conveyor belt'' for energy and matter.

Convective heat transfer is clearly a field at the interface between two older fields: heat transfer and fluid mechanics. To study the *interdisciplinary* is valuable, but it must come after one possesses the *disciplines*, not the other way around. For this reason, the study of any convective heat transfer problem must rest on a solid understanding of basic heat transfer and fluid mechanics principles. The objective in this chapter is to review these principles in order to establish a common language for the more specific issues addressed in later chapters.

Before reviewing the foundation of convective heat transfer methodology, it is worth reexamining the historic relationship between fluid mechanics and heat transfer. Especially during the past 100 years, heat transfer and fluid mechanics have enjoyed a symbiotic relationship in their development, a relationship where one field was stimulated by the curiosity and advance in the other field. Examples of this symbiosis abound in the history of boundary layer theory and natural convection. The field of convection grew out of this symbiosis, and if we are to learn anything from history, important advances in convection will continue to result from this symbiosis. Thus, the student and the future researcher would be well advised to devote equal attention to fluid mechanics and heat transfer literature.

---

*Numbers in brackets indicate references at the end of each chapter.

1.1 MASS CONSERVATION

The first principle to review is undoubtedly the oldest: It is the conservation of mass in a closed system or the ''continuity'' of mass through a flow (open) system. From engineering thermodynamics, we recall the mass conservation statement for a control volume [2]:

$$\frac{\partial M_{cv}}{\partial t} = \sum_{\substack{\text{inlet} \\ \text{ports}}} \dot{m} - \sum_{\substack{\text{outlet} \\ \text{ports}}} \dot{m} \tag{1.1}$$

where M_{cv} is the mass that is trapped instantaneously inside the control volume (cv), while the $\dot{m}$'s are the mass flow rates associated with flow into and out of the control volume. In convective heat transfer, we are usually interested in the velocity and temperature distribution in a flow region near a solid wall; hence, the control volume to consider is the infinitesimally small $\Delta x \, \Delta y$ box drawn around a fixed location (x, y) in a flow field. In Fig. 1.1, as in most of the problems analyzed in this book, the flow field is two-dimensional (i.e., the same in any plane parallel to the plane of Fig. 1.1). In a three-dimensional flow field, the control volume would be the parallelepiped $\Delta x \, \Delta y \, \Delta z$. Taking u and v as the local velocity components at point (x, y), the mass conservation equation (1.1) requires that

$$\frac{\partial}{\partial t}(\rho \, \Delta x \, \Delta y) = \rho u \, \Delta y + \rho v \, \Delta x - \left[\rho u + \frac{\partial (\rho u)}{\partial x} \Delta x\right] \Delta y$$
$$- \left[\rho v + \frac{\partial (\rho v)}{\partial y} \Delta y\right] \Delta x \tag{1.2}$$

or, dividing through by the constant size of the control volume $(\Delta x \, \Delta y)$,

$$\frac{\partial \rho}{\partial t} + \frac{\partial(\rho u)}{\partial x} + \frac{\partial(\rho v)}{\partial y} = 0 \tag{1.3}$$

In a three-dimensional flow, an analogous argument yields

$$\frac{\partial \rho}{\partial t} + \frac{\partial(\rho u)}{\partial x} + \frac{\partial(\rho v)}{\partial y} + \frac{\partial(\rho w)}{\partial z} = 0 \tag{1.4}$$

where w is the velocity component in the z direction. The local mass conservation statement (1.4) can also be written as

$$\frac{\partial \rho}{\partial t} + u\frac{\partial \rho}{\partial x} + v\frac{\partial \rho}{\partial y} + w\frac{\partial \rho}{\partial z} + \rho\left(\frac{\partial u}{\partial x} + \frac{\partial v}{\partial y} + \frac{\partial w}{\partial z}\right) = 0 \tag{1.5}$$

(a) Cartesian coordinates

(b) Cylindrical coordinates

(c) Spherical coordinates
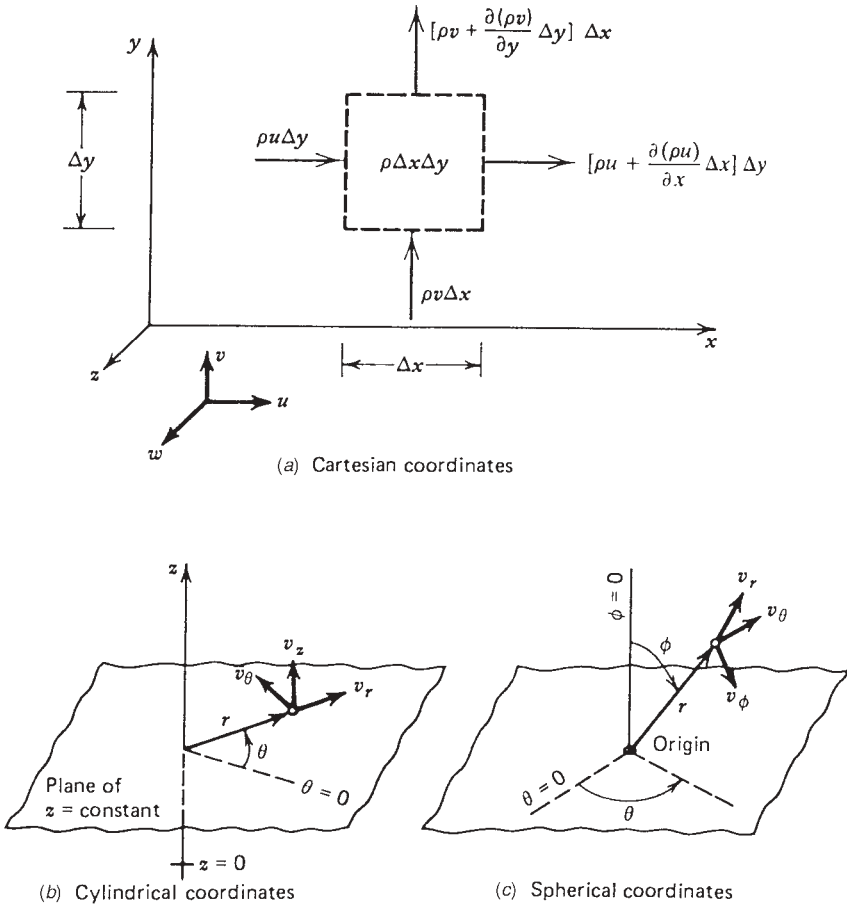
Figure 1.1 Mass conservation and systems of coordinates.

or

$$\frac{D\rho}{Dt} + \rho \nabla \cdot \mathbf{v} = 0 \tag{1.6}$$

In expression (1.6), $\mathbf{v}$ is the velocity vector (u, v, w), and D/Dt represents the "material derivative" operator,

$$\frac{D}{Dt} = \frac{\partial}{\partial t} + u\frac{\partial}{\partial x} + v\frac{\partial}{\partial y} + w\frac{\partial}{\partial z} \tag{1.7}$$

Of particular interest to *classroom* and *fundamental* treatment of the convection problem is the wide class of flows in which temporal and spatial variations

in density are negligible relative to the local variations in velocity. For this class, the mass conservation statement reads

$$\frac{\partial u}{\partial x} + \frac{\partial v}{\partial y} + \frac{\partial w}{\partial z} = 0 \tag{1.8}$$

The equivalent forms of eq. (1.8) in cylindrical and spherical coordinates are (Fig. 1.1)

$$\frac{\partial v_r}{\partial r} + \frac{v_r}{r} + \frac{1}{r}\frac{\partial v_\theta}{\partial \theta} + \frac{\partial v_z}{\partial z} = 0 \tag{1.9}$$

and

$$\frac{1}{r}\frac{\partial}{\partial r}(r^2 v_r) + \frac{1}{\sin\phi}\frac{\partial}{\partial\phi}(v_\phi \sin\phi) + \frac{1}{\sin\phi}\frac{\partial v_\theta}{\partial\theta} = 0 \tag{1.10}$$

It is tempting to think that eqs. (1.8)–(1.10) are valid only for incompressible fluids; in fact, their derivation shows that they apply to *flows* (not fluids) where the density and velocity gradients are such that the $D\rho/Dt$ terms are negligible relative to the $\rho \nabla \cdot \mathbf{v}$ terms in eq. (1.6). Most of the gas flows encountered in heat exchangers, heated enclosures, and porous media obey the simplified version of the mass conservation principle [eqs. (1.8)–(1.10)].

1.2 FORCE BALANCES (MOMENTUM EQUATIONS)

From the dynamics of thrust or propulsion systems, we recall that the instantaneous force balance on a control volume requires that (see Ref. 3, p. 15)

$$\frac{\partial}{\partial t}(Mv_n)_{cv} = \sum F_n + \sum_{\substack{\text{inlet}\\\text{ports}}} \dot{m}v_n - \sum_{\substack{\text{outlet}\\\text{ports}}} \dot{m}v_n \tag{1.11}$$

where n is the direction chosen for analysis and v_n and F_n are the projections of fluid velocity and forces in the n direction. Equation (1.11) is recognized in the literature as the *momentum principle* or *momentum theorem*. In essence, eq. (1.11) is the control volume formulation of Newton's second law of motion, where in addition to terms accounting for *forces* and *mass × acceleration*, we now have the *impact* due to the flow of momentum into the control volume, plus the *reaction* associated with the flow of momentum out of the control volume. In the two-dimensional flow situation of Fig. 1.2, we can write two force balances of type (1.11), one for the x direction and the other for the y direction.

Consider now the special form taken by eq. (1.11) when applied to the finitesize control volume $\Delta x \, \Delta y$ drawn around point (x, y) in Fig. 1.2. Consider first the balance of forces in the x direction. In Fig. 1.2a, showing the $\Delta x \, \Delta y$ control volume, we see the sense of the impact and reaction forces associated with the flow of momentum through the control volume. In Fig. 1.2b, we see the more classical forces represented by the normal stress (σ_x), tangential stress

$$[\rho uv + \frac{\partial}{\partial y}(\rho uv)\,\Delta y]\,\Delta x$$

$$\rho u^2\,\Delta y$$

$$[\rho u^2 + \frac{\partial(\rho u^2)}{\partial x}\,\Delta x]\,\Delta y$$

$$\frac{\partial}{\partial t}(\rho u)\,\Delta x\Delta y$$

$$\rho uv\Delta x$$

(a)

$$(\tau_{xy} + \frac{\partial \tau_{xy}}{\partial y}\,\Delta y)\,\Delta x$$

$$\sigma_x\Delta y$$

$$X\,\Delta x\Delta y$$

$$(\sigma_x + \frac{\partial \sigma_x}{\partial x}\,\Delta x)\,\Delta y$$

$$\tau_{xy}\,\Delta x$$

(b)
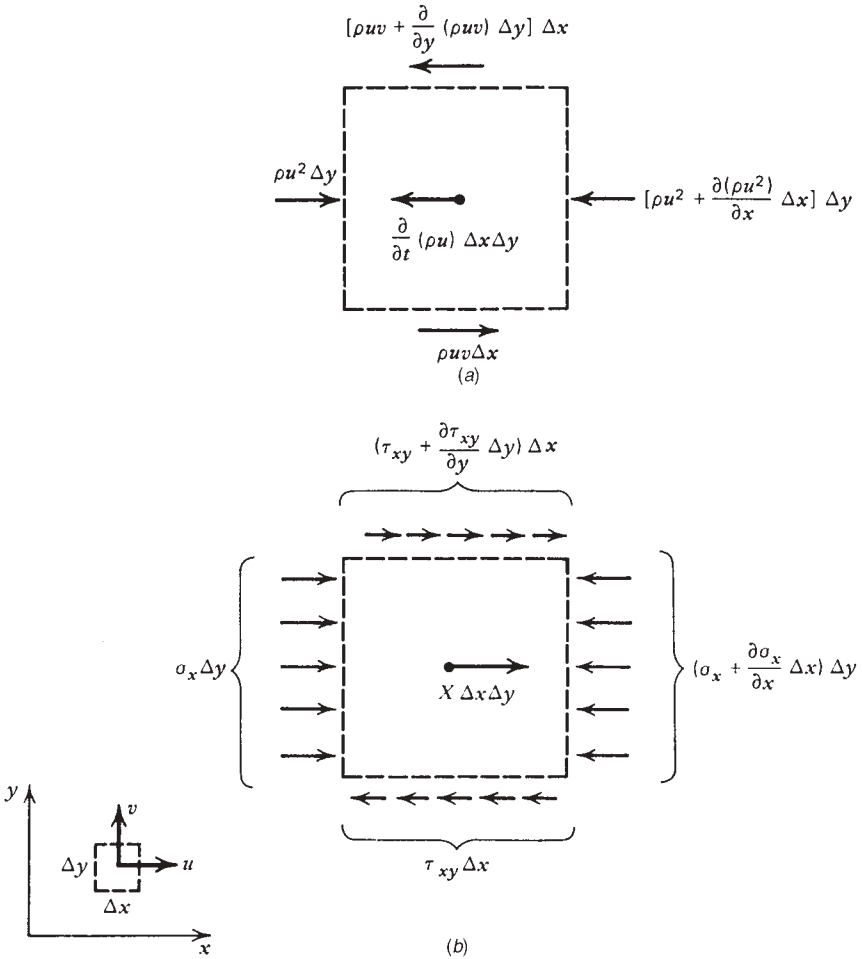
Figure 1.2 Force balance in the *x* direction on a control volume in two-dimensional flow.

(τ_{xy}), and the *x*-direction body force per unit volume (*X*). Projecting all these forces on the *x* axis, we obtain

$$-\frac{\partial}{\partial t}(\rho u\,\Delta x\,\Delta y) + \rho u^2\,\Delta y - \left[\rho u^2 + \frac{\partial}{\partial x}(\rho u^2)\,\Delta x\right]\Delta y$$

$$+ \rho uv\,\Delta x - \left[\rho uv + \frac{\partial}{\partial y}(\rho uv)\,\Delta y\right]\Delta x$$

$$+ \sigma_x\,\Delta y - \left(\sigma_x + \frac{\partial \sigma_x}{\partial x}\Delta x\right)\Delta y - \tau_{xy}\,\Delta x$$

$$+ \left(\tau_{xy} + \frac{\partial \tau_{xy}}{\partial y}\Delta y\right)\Delta x + X\,\Delta x\,\Delta y = 0 \qquad (1.12)$$

or, dividing by $\Delta x\, \Delta y$ in the limit $(\Delta x, \Delta y) \to 0$,

$$\rho\frac{Du}{Dt} + u\left[\frac{D\rho}{Dt} + \rho\left(\frac{\partial u}{\partial x} + \frac{\partial v}{\partial y}\right)\right] = -\frac{\partial \sigma_x}{\partial x} + \frac{\partial \tau_{xy}}{\partial y} + X \tag{1.13}$$

According to the mass conservation equation (1.6), the quantity in brackets is equal to zero; hence,

$$\rho\frac{Du}{Dt} = -\frac{\partial \sigma_x}{\partial x} + \frac{\partial \tau_{xy}}{\partial y} + X \tag{1.14}$$

Next, we relate the stresses σ_x and τ_{xy} to the local flow field by recalling the constitutive relations

$$\sigma_x = P - 2\mu\frac{\partial u}{\partial x} + \frac{2}{3}\mu\left(\frac{\partial u}{\partial x} + \frac{\partial v}{\partial y}\right) \tag{1.15}$$

$$\tau_{xy} = \mu\left(\frac{\partial u}{\partial y} + \frac{\partial v}{\partial x}\right) \tag{1.16}$$

These relations are of empirical origin: They summarize the experimental observation that a fluid packet offers no resistance to a change of shape but resists the time rate of a change of shape. Equations (1.15) and (1.16) serve as definition for the measurable coefficient of *viscosity* μ. Combining eqs. (1.14)–(1.16) yields the *Navier—Stokes equation*,

$$\rho\frac{Du}{Dt} = -\frac{\partial P}{\partial x} + \frac{\partial}{\partial x}\left[2\mu\frac{\partial u}{\partial x} - \frac{2\mu}{3}\left(\frac{\partial u}{\partial x} + \frac{\partial v}{\partial y}\right)\right]$$

$$+ \frac{\partial}{\partial y}\left[\mu\left(\frac{\partial u}{\partial y} + \frac{\partial v}{\partial x}\right)\right] + X \tag{1.17}$$

Of particular interest is the case when the *flow* may be treated as *incompressible* and the viscosity μ may be regarded as constant. Then the *x momentum equation* reduces to

$$\rho\left(\frac{\partial u}{\partial t} + u\frac{\partial u}{\partial x} + v\frac{\partial u}{\partial y}\right) = -\frac{\partial P}{\partial x} + \mu\left(\frac{\partial^2 u}{\partial x^2} + \frac{\partial^2 u}{\partial y^2}\right) + X \tag{1.18}$$

A similar equation can be derived from the force balance in the y direction. For a three-dimensional flow in the (x, y, z), (u, v, w) Cartesian system, the three momentum equations for $(\rho, \mu) \cong$ constant flows are

$$\rho\left(\frac{\partial u}{\partial t} + u\frac{\partial u}{\partial x} + v\frac{\partial u}{\partial y} + w\frac{\partial u}{\partial z}\right)$$

$$= -\frac{\partial P}{\partial x} + \mu\left(\frac{\partial^2 u}{\partial x^2} + \frac{\partial^2 u}{\partial y^2} + \frac{\partial^2 u}{\partial z^2}\right) + X \tag{1.19a}$$

$$\rho \left(\frac{\partial v}{\partial t} + u\frac{\partial v}{\partial x} + v\frac{\partial v}{\partial y} + w\frac{\partial v}{\partial z} \right)$$

$$= -\frac{\partial P}{\partial y} + \mu \left(\frac{\partial^2 v}{\partial x^2} + \frac{\partial^2 v}{\partial y^2} + \frac{\partial^2 v}{\partial z^2} \right) + Y \qquad (1.19b)$$

$$\rho \left(\frac{\partial w}{\partial t} + u\frac{\partial w}{\partial x} + v\frac{\partial w}{\partial y} + w\frac{\partial w}{\partial z} \right)$$

$$= -\frac{\partial P}{\partial z} + \mu \left(\frac{\partial^2 w}{\partial x^2} + \frac{\partial^2 w}{\partial y^2} + \frac{\partial^2 w}{\partial z^2} \right) + Z \qquad (1.19c)$$

Alternative forms of eqs. (1.19) are:

Vectorial notation:

$$\rho \frac{D\mathbf{v}}{Dt} = -\nabla P + \mu \nabla^2 \mathbf{v} + \mathbf{F} \qquad (1.20)$$

where **F** is the body force vector per unit volume (*X, Y, Z*).

Cylindrical coordinates (Fig. 1.1b):

$$\rho \left(\frac{\partial v_r}{\partial t} + v_r\frac{\partial v_r}{\partial r} + \frac{v_\theta}{r}\frac{\partial v_r}{\partial \theta} - \frac{v_\theta^2}{r} + v_z\frac{\partial v_r}{\partial z} \right)$$

$$= -\frac{\partial P}{\partial r} + \mu \left(\frac{\partial^2 v_r}{\partial r^2} + \frac{1}{r}\frac{\partial v_r}{\partial r} - \frac{v_r}{r^2} + \frac{1}{r^2}\frac{\partial^2 v_r}{\partial \theta^2} - \frac{2}{r^2}\frac{\partial v_\theta}{\partial \theta} + \frac{\partial^2 v_r}{\partial z^2} \right) + F_r$$

$$(1.21a)$$

$$\rho \left(\frac{\partial v_\theta}{\partial t} + v_r\frac{\partial v_\theta}{\partial r} + \frac{v_\theta}{r}\frac{\partial v_\theta}{\partial \theta} + \frac{v_r v_\theta}{r} + v_z\frac{\partial v_\theta}{\partial z} \right)$$

$$= -\frac{1}{r}\frac{\partial P}{\partial \theta} + \mu \left(\frac{\partial^2 v_\theta}{\partial r^2} + \frac{1}{r}\frac{\partial v_\theta}{\partial r} - \frac{v_\theta}{r^2} + \frac{1}{r^2}\frac{\partial^2 v_\theta}{\partial \theta^2} + \frac{2}{r^2}\frac{\partial v_r}{\partial \theta} + \frac{\partial^2 v_\theta}{\partial z^2} \right) + F_\theta$$

$$(1.21b)$$

$$\rho \left(\frac{\partial v_z}{\partial t} + v_r\frac{\partial v_z}{\partial r} + \frac{v_\theta}{r}\frac{\partial v_z}{\partial \theta} + v_z\frac{\partial v_z}{\partial z} \right)$$

$$= -\frac{\partial P}{\partial z} + \mu \left(\frac{\partial^2 v_z}{\partial r^2} + \frac{1}{r}\frac{\partial v_z}{\partial r} + \frac{1}{r^2}\frac{\partial^2 v_z}{\partial \theta^2} + \frac{\partial^2 v_z}{\partial z^2} \right) + F_z \qquad (1.21c)$$

where (v_r, v_θ, v_z) and (F_r, F_θ, F_z) are the velocity and body force vectors.

Spherical coordinates (Fig. 1.1c):

$$\rho \left(\frac{Dv_r}{Dt} - \frac{v_\phi^2 + v_\theta^2}{r} \right)$$

$$= -\frac{\partial P}{\partial r} + \mu \left(\nabla^2 v_r - \frac{2v_r}{r^2} - \frac{2}{r^2}\frac{\partial v_\phi}{\partial \phi} - \frac{2v_\phi \cot \phi}{r^2} - \frac{2}{r^2 \sin \phi}\frac{\partial v_\theta}{\partial \theta} \right) + F_r$$

$$(1.22a)$$

$$\rho \left(\frac{Dv_\phi}{Dt} + \frac{v_r v_\phi}{r} - \frac{v_\theta^2 \cot \phi}{r} \right)$$

$$= -\frac{1}{r} \frac{\partial P}{\partial \phi} + \mu \left(\nabla^2 v_\phi + \frac{2}{r^2} \frac{\partial v_r}{\partial \phi} - \frac{v_\phi}{r^2 \sin^2 \phi} - \frac{2 \cos \phi}{r^2 \sin^2 \phi} \frac{\partial v_\theta}{\partial \theta} \right) + F_\phi$$

$$(1.22b)$$

$$\rho \left(\frac{Dv_\theta}{Dt} + \frac{v_\theta v_r}{r} + \frac{v_\phi v_\theta \cot \phi}{r} \right)$$

$$= -\frac{1}{r \sin \phi} \frac{\partial P}{\partial \theta} + \mu \left(\nabla^2 v_\theta - \frac{v_\theta}{r^2 \sin^2 \phi} + \frac{2}{r^2 \sin \phi} \frac{\partial v_r}{\partial \theta} \right.$$

$$\left. + \frac{2 \cos \phi}{r^2 \sin^2 \phi} \frac{\partial v_\phi}{\partial \theta} \right) + F_\theta$$

$$(1.22c)$$

where (v_r, v_ϕ, v_θ) and (F_r, F_ϕ, F_θ) are the velocity and body force vectors, and

$$\frac{D}{Dt} = \frac{\partial}{\partial t} + v_r \frac{\partial}{\partial r} + \frac{v_\phi}{r} \frac{\partial}{\partial \phi} + \frac{v_\theta}{r \sin \phi} \frac{\partial}{\partial \theta} \tag{1.23}$$

$$\nabla^2 = \frac{1}{r^2} \frac{\partial}{\partial r} \left(r^2 \frac{\partial}{\partial r} \right) + \frac{1}{r^2 \sin \phi} \frac{\partial}{\partial \phi} \left(\sin \phi \frac{\partial}{\partial \phi} \right) + \frac{1}{r^2 \sin^2 \phi} \frac{\partial^2}{\partial \theta^2} \tag{1.24}$$

are the material derivative and Laplacian operators in spherical coordinates.

1.3 FIRST LAW OF THERMODYNAMICS

The preceding two principles—mass conservation and force balances—are in many cases sufficient for solving the *flow part* of the convective heat transfer problem. Note at this juncture the availability of four equations (mass conservation plus three force balances) for determining four unknowns (three velocity components plus pressure). The exception to this statement is the subject of Chapter 4, where the natural flow is driven by the heat administered to the flowing fluid. In all cases, however, the *heat transfer part* of the convection problem requires a solution for the temperature distribution through the flow, especially in the close vicinity of the solid walls bathed by the heat-carrying fluid stream (Chapter 2). The additional equation for accomplishing this ultimate objective is the first law of thermodynamics or the *energy equation*.

For the control volume of finite size $\Delta x \, \Delta y$ in Fig. 1.3, the first law of thermodynamics requires that (see Ref. 2, p. 22)

$$\begin{pmatrix} \text{rate of energy} \\ \text{accumulation in the} \\ \text{control volume} \end{pmatrix}_1$$

$$= \begin{pmatrix} \text{net transfer of} \\ \text{energy by fluid flow} \end{pmatrix}_2 + \begin{pmatrix} \text{net heat transfer} \\ \text{by conduction} \end{pmatrix}_3$$

$$+ \begin{pmatrix} \text{rate of internal} \\ \text{heat generation (e.g.,} \\ \text{electrical power} \\ \text{dissipation)} \end{pmatrix}_4 - \begin{pmatrix} \text{net work transfer} \\ \text{from the control} \\ \text{volume to its} \\ \text{environment} \end{pmatrix}_5 \qquad (1.25)$$
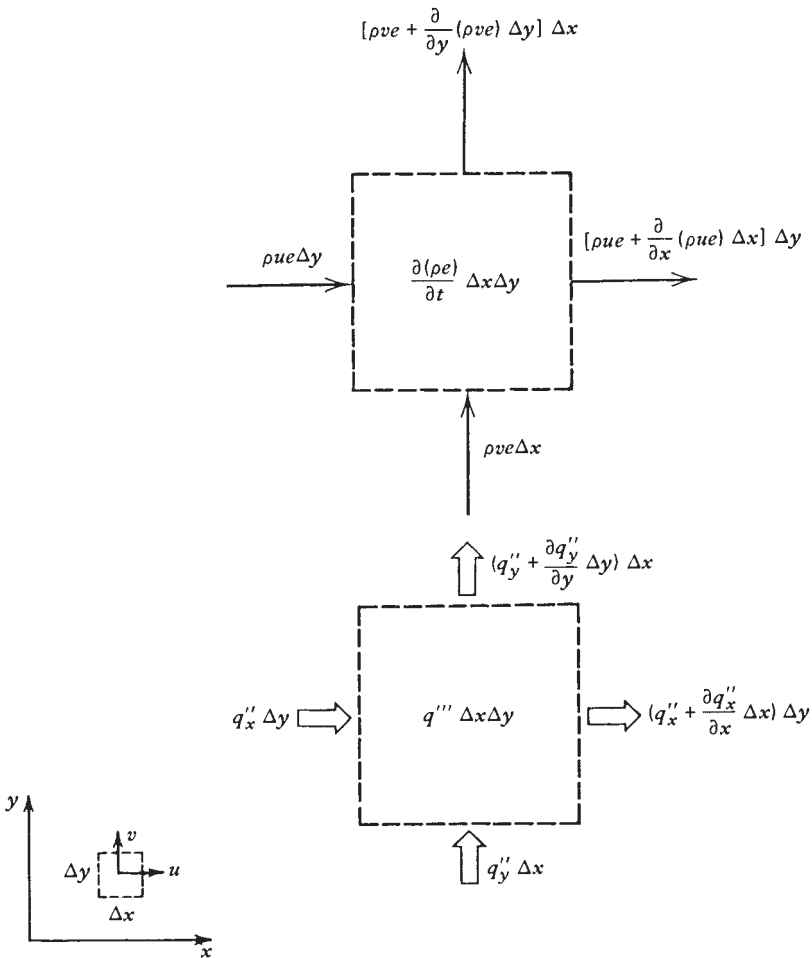
Figure 1.3 First law of thermodynamics applied to a control volume in two-dimensional flow (for work transfer, see Fig. 1.2).

According to the energy flows sketched in Fig. 1.3, the groups of terms above are

$$\{\cdot\}_1 = \Delta x \, \Delta y \, \frac{\partial}{\partial t} \, (\rho e)$$

$$\{\cdot\}_2 = -(\Delta x \, \Delta y) \left[\frac{\partial}{\partial x} \, (\rho u e) + \frac{\partial}{\partial y}(\rho v e) \right]$$

$$\{\cdot\}_3 = -(\Delta x \, \Delta y) \left(\frac{\partial q_x''}{\partial x} + \frac{\partial q_y''}{\partial y} \right)$$

$$\{\cdot\}_4 = (\Delta x \, \Delta y) q'''$$

$$\{\cdot\}_5 = (\Delta x \, \Delta y) \left(\sigma_x \frac{\partial u}{\partial x} - \tau_{xy} \frac{\partial u}{\partial y} + \sigma_y \frac{\partial v}{\partial y} - \tau_{yx} \frac{\partial v}{\partial x} \right)$$

$$\qquad + (\Delta x \, \Delta y) \left(u \frac{\partial \sigma_x}{\partial x} - u \frac{\partial \tau_{xy}}{\partial y} + v \frac{\partial \sigma_y}{\partial y} - v \frac{\partial \tau_{yx}}{\partial x} \right)_*$$

$$(1.25')$$

where e, q_x'', q_y'', and q''' are the specific internal energy, heat flux in the x direction, heat flux in the y direction, and dissipation rate or rate of internal heat generation.

The origin of the dissipation rate term $\{\cdot\}_5$ lies in the work transfer effected by the normal and tangential stresses sketched in Fig. 1.2b. For example, the work done per unit time by the normal stresses σ_x on the left side of the $\Delta x \, \Delta y$ element is negative and equal to the force acting on the boundary ($\sigma_x \, \Delta y$) times the boundary displacement per unit time (u), which yields $-u\sigma_x \, \Delta y$. Similarly, the work transfer rate associated with normal stresses acting on the right side of the element is positive and equal to $[\sigma_x + (\partial \sigma_x/\partial x) \, \Delta x][u + (\partial u/\partial x) \, \Delta x] \, \Delta y$. The net work transfer rate due to these two contributions is $[\sigma_x(\partial u/\partial x) + u(\partial \sigma_x/\partial x)]$ $(\Delta x \, \Delta y)$, as shown in the $\{\cdot\}_5$ term of eq. (1.25′).

Three more work transfer rates can be calculated in the same manner by examining the effect of the remaining three stresses, τ_{xy} in the x direction and σ_y and τ_{yx} in the y direction. In the $\{\cdot\}_5$ expression above, the eight terms have been separated into two groups. It can be shown that the group denoted as $(\cdot)_*$ reduces to $-\rho(D/Dt)(u^2 + v^2)/2$, which represents the change in kinetic energy of the fluid packet; in the present treatment, this change is considered negligible relative to the internal energy change $\partial(\rho e)/\partial t$ appearing in $\{\cdot\}_1$.

Assembling expressions (1.25′) into the energy conservation statement that preceded them, and using constitutive relations (1.15) and (1.16), we obtain

$$\rho \frac{De}{Dt} + e \left(\frac{D\rho}{Dt} + \rho \, \nabla \cdot \mathbf{v} \right) = -\nabla \cdot \mathbf{q}'' + q''' - P \, \nabla \cdot \mathbf{v} + \mu \Phi \qquad (1.26)$$

where $\mathbf{q}''$ is the heat flux vector (q_x'', q_y'') and Φ is the *viscous dissipation function*, shown later in eq. (1.45a). The quantity between parentheses on the left-hand side of eq. (1.26) is equal to zero [cf. eq. (1.6)]. In the special case where the flow

can be modeled as incompressible and two-dimensional, the viscous dissipation function reduces to

$$\Phi = 2\left[\left(\frac{\partial u}{\partial x}\right)^2 + \left(\frac{\partial v}{\partial y}\right)^2\right] + \left(\frac{\partial u}{\partial y} + \frac{\partial v}{\partial x}\right)^2 \qquad (1.27)$$

To express eq. (1.26) in terms of enthalpy, we use the thermodynamics definition $h = e + (1/\rho)P$; hence,

$$\frac{Dh}{Dt} = \frac{De}{Dt} + \frac{1}{\rho}\frac{DP}{Dt} - \frac{P}{\rho^2}\frac{D\rho}{Dt} \qquad (1.28)$$

In addition, we can express the directional heat fluxes q_x'' and q_y'' in terms of the local temperature gradients, by invoking the *Fourier law of heat conduction*,

$$\mathbf{q''} = -k\,\nabla T \qquad (1.29)$$

Then, combining eqs. (1.26), (1.28), and (1.29) we obtain

$$\rho\frac{Dh}{Dt} = \nabla \cdot (k\,\nabla T) + q''' + \frac{DP}{Dt} + \mu\,\Phi - \frac{P}{\rho}\left(\frac{D\rho}{Dt} + \rho\,\nabla \cdot \mathbf{v}\right) \qquad (1.30)$$

Finally, the mass conservation equation (1.6) shows that the last terms in parentheses in eq. (1.30) add up to zero, and the first law of thermodynamics reduces to

$$\rho\frac{Dh}{Dt} = \nabla \cdot (k\,\nabla T) + q''' + \frac{DP}{Dt} + \mu\,\Phi \qquad (1.31)$$

In order to express the energy equation (1.31) in terms of temperature, it is tempting to replace the specific enthalpy on the left-hand side by the product of specific heat × temperature. This move is correct only in cases where the fluid behaves like an ideal gas (see the ideal gas model, Table 1.1). In general, the change in specific enthalpy for a single-phase substance is expressed by the canonical relation for enthalpy [2],

$$dh = T\,ds + \frac{1}{\rho}\,dP \qquad (1.32)$$

where T is the absolute temperature and ds the specific entropy change,

$$ds = \left(\frac{\partial s}{\partial T}\right)_P dT + \left(\frac{\partial s}{\partial P}\right)_T dP \qquad (1.33)$$

From the last of Maxwell's relations (see Ref. 2, p. 172), we have

$$\left(\frac{\partial s}{\partial P}\right)_T = -\left[\frac{\partial\,(1/\rho)}{\partial T}\right]_P = \frac{1}{\rho^2}\left(\frac{\partial\rho}{\partial T}\right)_P = -\frac{\beta}{\rho} \qquad (1.34)$$

Table 1.1   Summary of thermodynamic relations[a] and models

	Internal Energy $du = T\,ds - P\,dv$	Enthalpy $dh = T\,ds + v\,dP$	Entropy $ds = \dfrac{1}{T}du + \dfrac{P}{T}dv$
Pure substance	$du = c_v\,dT$ $+\left[T\left(\dfrac{\partial P}{\partial T}\right)_v - P\right]dv$	$dh = c_p\,dT$ $+\left[-T\left(\dfrac{\partial v}{\partial T}\right)_p + v\right]dP$	$ds = \dfrac{c_p}{T}dT - \left(\dfrac{\partial v}{\partial T}\right)_P dP$ $= \dfrac{c_v}{T}dT + \left(\dfrac{\partial P}{\partial T}\right)_v dv$
Ideal gas	$du = c_v\,dT$	$dh = c_P\,dT$	$ds = c_P\dfrac{dT}{T} - R\dfrac{dP}{P}$ $= c_v\dfrac{dT}{T} + R\dfrac{dv}{v}$ $= c_v\dfrac{dP}{P} + c_P\dfrac{dv}{v}$
Incompressible liquid	$du = c\,dT$	$dh = c\,dT + v\,dP$	$ds = c\dfrac{dT}{T}$

Source: Ref. 2.

[a]According to the classical thermodynamics notation, v is the specific volume, $v = 1/\rho$, and u is the internal energy (e in the text).

where β is the coefficient of thermal expansion,

$$\beta = -\frac{1}{\rho}\left(\frac{\partial \rho}{\partial T}\right)_P \tag{1.35}$$

Table 1.1 also shows that

$$\left(\frac{\partial s}{\partial T}\right)_P = \frac{c_P}{T} \tag{1.36}$$

Together, eqs. (1.32)–(1.36) state that

$$dh = c_P\,dT + \frac{1}{\rho}(1 - \beta T)\,dP \tag{1.37}$$

in other words, the left-hand side of the energy equation (1.31) is

$$\rho\frac{Dh}{Dt} = \rho c_P\frac{DT}{Dt} + (1 - \beta T)\frac{DP}{Dt} \tag{1.38}$$

The ''temperature'' formulation of the first law of thermodynamics is therefore

$$\rho c_P\frac{DT}{Dt} = \nabla \cdot (k\,\nabla T) + q''' + \beta T\frac{DP}{Dt} + \mu\,\Phi \tag{1.39}$$

with the following special forms:

Ideal gas ($\beta = 1/T$):

$$\rho c_P \frac{DT}{Dt} = \nabla \cdot (k \nabla T) + q''' + \frac{DP}{Dt} + \mu \, \Phi \tag{1.40}$$

Incompressible liquid ($\beta = 0$):

$$\rho c \frac{DT}{Dt} = \nabla \cdot (k \nabla T) + q''' + \mu \, \Phi \tag{1.41}$$

Most of the convection problems addressed in this book obey an even simpler model: namely, constant fluid conductivity k, zero internal heat generation q''', negligible viscous dissipation $\mu \Phi$, and negligible compressibility effect βT DP/Dt. The energy equation for this model is

$$\rho c_P \frac{DT}{Dt} = k \nabla^2 T \tag{1.42}$$

or, in terms of specific coordinate systems (Fig. 1.1):

Cartesian (x, y, z):

$$\rho c_P \left(\frac{\partial T}{\partial t} + u \frac{\partial T}{\partial x} + v \frac{\partial T}{\partial y} + w \frac{\partial T}{\partial z} \right) = k \left(\frac{\partial^2 T}{\partial x^2} + \frac{\partial^2 T}{\partial y^2} + \frac{\partial^2 T}{\partial z^2} \right) \tag{1.43a}$$

Cylindrical (r, θ, z):

$$\rho c_P \left(\frac{\partial T}{\partial t} + v_r \frac{\partial T}{\partial r} + \frac{v_\theta}{r} \frac{\partial T}{\partial \theta} + v_z \frac{\partial T}{\partial z} \right)$$
$$= k \left[\frac{1}{r} \frac{\partial}{\partial r} \left(r \frac{\partial T}{\partial r} \right) + \frac{1}{r^2} \frac{\partial^2 T}{\partial \theta^2} + \frac{\partial^2 T}{\partial z^2} \right] \tag{1.43b}$$

Spherical (r, ϕ, θ):

$$\rho c_P \left(\frac{\partial T}{\partial t} + v_r \frac{\partial T}{\partial r} + \frac{v_\phi}{r} \frac{\partial T}{\partial \phi} + \frac{v_\theta}{r \sin \phi} \frac{\partial T}{\partial \theta} \right)$$
$$= k \left[\frac{1}{r^2} \frac{\partial}{\partial r} \left(r^2 \frac{\partial T}{\partial r} \right) + \frac{1}{r^2 \sin \phi} \frac{\partial}{\partial \phi} \left(\sin \phi \frac{\partial T}{\partial \phi} \right) + \frac{1}{r^2 \sin^2 \phi} \frac{\partial^2 T}{\partial \theta^2} \right]$$
$$\tag{1.43c}$$

If the fluid can be modeled as an incompressible liquid, then, as in eq. (1.41), the specific heat at constant pressure c_P is replaced by the lone specific heat of the incompressible liquid, c (Table 1.1).

When dealing with extremely viscous flows of the type encountered in lubrication problems or the piping of crude oil, the model above is improved by taking into account the internal heating due to viscous dissipation,

$$\rho c_P \frac{DT}{Dt} = k \ \nabla^2 T + \mu \ \Phi \tag{1.44}$$

In three dimensions, the viscous dissipation function is expressed as follows:

Cartesian (x, y, z):

$$
\begin{aligned}
\Phi = 2 &\left[\left(\frac{\partial u}{\partial x} \right)^2 + \left(\frac{\partial v}{\partial y} \right)^2 + \left(\frac{\partial w}{\partial z} \right)^2 \right] \\
&+ \left[\left(\frac{\partial u}{\partial y} + \frac{\partial v}{\partial x} \right)^2 + \left(\frac{\partial v}{\partial z} + \frac{\partial w}{\partial y} \right)^2 + \left(\frac{\partial w}{\partial x} + \frac{\partial u}{\partial z} \right)^2 \right] \\
&- \frac{2}{3} \left(\frac{\partial u}{\partial x} + \frac{\partial v}{\partial y} + \frac{\partial w}{\partial z} \right)^2
\end{aligned}
\tag{1.45a}
$$

Cylindrical (r, θ, z):

$$
\begin{aligned}
\Phi = 2 &\left[\left(\frac{\partial v_r}{\partial r} \right)^2 + \left(\frac{1}{r} \frac{\partial v_\theta}{\partial \theta} + \frac{v_r}{r} \right)^2 + \left(\frac{\partial v_z}{\partial z} \right)^2 \right. \\
&+ \frac{1}{2} \left(\frac{\partial v_\theta}{\partial r} - \frac{v_\theta}{r} + \frac{1}{r} \frac{\partial v_r}{\partial \theta} \right)^2 + \frac{1}{2} \left(\frac{1}{r} \frac{\partial v_z}{\partial \theta} + \frac{\partial v_\theta}{\partial z} \right)^2 \\
&\left. + \frac{1}{2} \left(\frac{\partial v_r}{\partial z} + \frac{\partial v_z}{\partial r} \right)^2 - \frac{1}{3} (\nabla \cdot \mathbf{v})^2 \right]
\end{aligned}
\tag{1.45b}
$$

Spherical (r, φ, θ):

$$
\begin{aligned}
\Phi = 2 &\left\{ \left[\left(\frac{\partial v_r}{\partial r} \right)^2 + \left(\frac{1}{r} \frac{\partial v_\phi}{\partial \phi} + \frac{v_r}{r} \right)^2 + \left(\frac{1}{r \sin \phi} \frac{\partial v_\theta}{\partial \theta} + \frac{v_r}{r} + \frac{v_\phi \cot \phi}{r} \right)^2 \right] \right. \\
&+ \frac{1}{2} \left[r \frac{\partial}{\partial r} \left(\frac{v_\phi}{r} \right) + \frac{1}{r} \frac{\partial v_r}{\partial \phi} \right]^2 + \frac{1}{2} \left[\frac{\sin \phi}{r} \frac{\partial}{\partial \phi} \left(\frac{v_\theta}{r \sin \phi} \right) + \frac{1}{r \sin \phi} \frac{\partial v_\theta}{\partial \theta} \right]^2 \\
&\left. + \frac{1}{2} \left[\frac{1}{r \sin \phi} \frac{\partial v_r}{\partial \theta} + r \frac{\partial}{\partial r} \left(\frac{v_\theta}{r} \right) \right]^2 \right\} - \frac{2}{3} (\nabla \cdot \mathbf{v})^2
\end{aligned}
\tag{1.45c}
$$

If the density does not vary significantly through the flow field, $\nabla \cdot \mathbf{v} = 0$ [eq. (1.6)] and the last term in each of expressions (1.45) vanishes.

It is worth reviewing the constant-ρ approximation that led to eq. (1.8) and recognizing that it differs conceptually from the ''incompressible substance model'' of thermodynamics. The latter is considerably more restrictive than the ''nearly constant'' density model, eq. (1.8). For example, a compressible substance such as air can flow in such a way that eq. (1.8) is a very good approximation of eq. (1.6).

For the restrictive class of fluids that are ''incompressible'' from the thermodynamic point of view, the specific heat at constant pressure c_P can be replaced by the lone specific heat of the fluid, c, on the left side of eq. (1.39). Water, liquid mercury, and engine oil are examples of fluids for which this substitution is justified. There are even convection problems in which the moving materials are actually solid (e.g., a roller and its substrate, in the zone of elastic contact). In such cases the $c_P = c$ substitution is permissible also.

Note that the specific heat at constant volume c_v does not belong on the left side of eq. (1.39). This observation is important because Fourier [4, 5], and later Poisson [6], who were the first to derive the energy equation for a convective flow, wrote c on the left side of eq. (1.39). They made this choice because their analyses were aimed specifically at *incompressible fluids* (liquids), for which c happens to have nearly the same value as c_P. Because of this choice, they did not have to account for the $P\,dV$ type of work done by the fluid packet as it expands or contracts in the flow field. In the modern era, however, the use of c_v instead of c_P is an error.

The prethermodynamics (caloric conservation) origins of the science of convection are also responsible for the ''thermal energy equation'' label that some prefer to attach to eq. (1.39) without the $\beta T\,DP/Dt$ term. This terminology is sometimes used to stress (incorrectly) the conservation of ''thermal'' energy as something distinct from ''mechanical and thermal'' energy. In classical thermodynamics, however, this distinction disappeared when the first law of thermodynamics was enunciated, that is, when the thermodynamic property ''energy'' was defined, which happened in the years 1850–1851 (see Ref. 2, pp. 28–29).

Equation (1.39) represents the first law of thermodynamics. This law proclaims the conservation of the sum of energy change (the property) and energy interactions (heat transfer *and* work transfer). The suggestion that mechanical effects (e.g., work transfer) are absent from eq. (1.39) when the $\beta T\,DP/Dt$ term is absent is wrong. The presence of c_P on the left side of the equation is the sign that each fluid packet expands or contracts (i.e., it does $P\,dV$-type work) as it rides on the flow. The terms q''' and $\mu\Phi$ are work transfer rate terms also.

1.4   SECOND LAW OF THERMODYNAMICS

Any discussion of the basic principles of convective heat transfer must include the second law of thermodynamics, not because the second law is necessary for determining the flow and temperature field (it is not, because it is not an

equation), but because the second law is the basis for much of the engineering *motive* (objective, purpose) for formulating and solving convection problems. For example, in the development of knowhow for the heat exchanger industry, we strive for improved thermal contact (enhanced heat transfer) *and* reduced pump power loss in order to improve the *thermodynamic* efficiency of the heat exchanger. Good heat exchanger design means, ultimately, efficient thermodynamic performance, that is, *minimum generation of entropy* or minimum destruction of exergy in the power/refrigeration system incorporating the heat exchanger [7, 8].

The second law of thermodynamics states that all real-life processes are irreversible: In the case of a control volume, as in Fig. 1.1, this statement is

$$\frac{\partial S_{cv}}{\partial t} \geq \sum \frac{q_i}{T_i} + \underbrace{\sum \dot{m}s}_{\substack{\text{inlet} \\ \text{ports}}} - \underbrace{\sum \dot{m}s}_{\substack{\text{outlet} \\ \text{ports}}} \tag{1.46}$$

where S_{cv} is the instantaneous entropy inventory of the control volume, $\dot{m}s$ represents the entropy flows (streams) into and out of the control volume, and T_i is the absolute temperature of the boundary crossed by the heat transfer q_i.* The irreversibility of the process is measured by the strength of the inequality sign in eq. (1.46), or by the entropy generation rate S_{gen}, defined as

$$S_{\text{gen}} = \frac{\partial S_{cv}}{\partial t} - \sum \frac{q_i}{T_i} - \underbrace{\sum \dot{m}s}_{\substack{\text{inlet} \\ \text{ports}}} + \underbrace{\sum \dot{m}s}_{\substack{\text{outlet} \\ \text{ports}}} \geq 0 \tag{1.47}$$

One can show that the rate of destruction of useful work in an engineering system, W_{lost}, is directly proportional to the rate of entropy generation [2, 3, 7],

$$W_{\text{lost}} = T_0 S_{\text{gen}} \tag{1.48}$$

where T_0 is the absolute temperature of the ambient temperature reservoir (T_0 = constant). Equation (1.48) stresses the engineering importance of estimating the irreversibility or entropy generation rate of convective heat transfer processes: If not used wisely, these processes contribute to the waste of precious fuel resources.

Based on an analysis similar to the analyses presented for mass conservation, force balances, and the first law of thermodynamics, the second law (1.47) may be applied to a finite-size control volume $\Delta x \, \Delta y \, \Delta z$ at an arbitrary point (x, y, z) in a flow field. Thus, the rate of entropy generation per unit time and per unit volume S'''_{gen} is [2, 3, 7]

$$S'''_{\text{gen}} = \underbrace{\frac{k}{T^2}(\nabla T)^2}_{\geq 0} + \underbrace{\frac{\mu}{T}\Phi}_{\geq 0} \geq 0 \tag{1.49}$$

*Defined as positive *into* the control volume.

where k and μ are assumed constant. In a two-dimensional convection situation such as in Figs. 1.1–1.3, the local entropy generation rate (1.49) yields

$$S_{\text{gen}}''' = \frac{k}{T^2}\left[\left(\frac{\partial T}{\partial x}\right)^2 + \left(\frac{\partial T}{\partial y}\right)^2\right]$$

$$+ \frac{\mu}{T}\left\{2\left[\left(\frac{\partial u}{\partial x}\right)^2 + \left(\frac{\partial v}{\partial y}\right)^2\right] + \left(\frac{\partial u}{\partial y} + \frac{\partial v}{\partial x}\right)^2\right\} \geq 0 \qquad (1.50)$$

In the last two equations, T represents the *absolute* temperature of the point where S_{gen}''' is being evaluated. The two-dimensional expression (1.50) illustrates the competition between viscous dissipation and imperfect thermal contact (finite-temperature gradients) in the generation of entropy via convective heat transfer.

Equations (1.48) and (1.50) constitute the bridge between two research activities: fundamental convection heat transfer and thermodynamics (entropy generation minimization). Beginning with Chapter 2, we focus on the fundamental problems of determining the flow and temperature fields in a given convection heat transfer configuration. However, through eq. (1.50), we are invited to keep in mind that these fields contribute hand-in-hand to downgrading the thermodynamic merit of the engineering device that ultimately employs the convection process under consideration. The science of adjusting the convection process so that it destroys the least exergy (subject to various system constraints) is the focus of *entropy generation minimization;* this activity has been reviewed in Refs. 2, 3, and 7. The generation of flow configuration (geometry, architecture) for maximal performance under constraints is *constructal theory and design* [2, 9–14].

1.5   RULES OF SCALE ANALYSIS

This section is designed to introduce the student to the problem-solving method of *scale analysis* or *scaling*. This is necessary because scale analysis is used extensively throughout the book; in fact, scale analysis is recommended as the premier method for obtaining the most information per unit of intellectual effort. This section is also necessary because scale analysis is not discussed in the heat transfer and fluid mechanics textbooks of our time, despite the fact that it is a precondition for good analysis in dimensionless form. Scale analysis is often confused with dimensional analysis or the often arbitrary nondimensionalization of the governing equations before performing a perturbation analysis or a numerical simulation on the computer.

The object of scale analysis is to use the basic principles of convective heat transfer to produce order-of-magnitude estimates for the quantities of interest. This means that if one of the quantities of interest is the thickness of the boundary layer in forced convection, the object of scale analysis is to determine whether the boundary layer thickness is measured in millimeters or meters. Note that scale

analysis goes beyond dimensional analysis (whose objective is to determine the dimension of boundary layer thickness, namely, length). When done properly, scale analysis anticipates within a factor of order one (or within percentage points) the expensive results produced by ''exact'' analyses. The value of scale analysis is remarkable, particularly when we realize that the notion of ''exact analysis'' is as false and ephemeral as the notion of ''experimental fact.''

As the first example of scale analysis, consider a problem from the field of conduction heat transfer [15]. In Fig. 1.4 we see a plate plunged at $t = 0$ into a highly conducting fluid, such that the surfaces of the plate instantaneously assume the fluid temperature $T_\infty = T_0 + \Delta T$. Suppose that we are interested in estimating the time needed by the thermal front to penetrate the plate, that is, the time until the center plane of the plate ''feels'' the heating imposed on the outer surfaces.

To answer the question above, we focus on a half-plate of thickness $D/2$ and the energy equation for pure conduction in one direction:

$$\rho c_P \frac{\partial T}{\partial t} = k \frac{\partial^2 T}{\partial x^2} \tag{1.51}$$

Next, we estimate the order of magnitude of each of the terms appearing in eq. (1.51). On the left-hand side we have

$$\rho c_P \frac{\partial T}{\partial t} \sim \rho c_P \frac{\Delta T}{t} \tag{1.52}$$
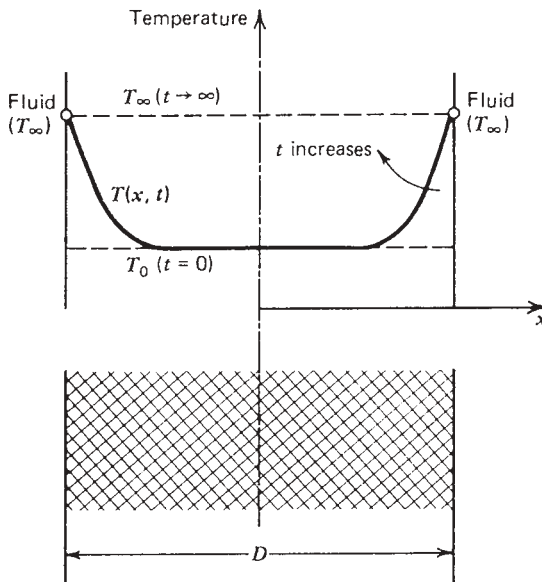
Figure 1.4 Transient heat conduction in a slab with sudden temperature change on the boundaries.

In other words, the scale of the temperature change (in the chosen space and in a time of order t) is ΔT. On the right-hand side we obtain

$$k\frac{\partial^2 T}{\partial x^2} = k\frac{\partial}{\partial x}\left(\frac{\partial T}{\partial x}\right) \sim \frac{k}{D/2}\frac{\Delta T}{D/2} = \frac{k\,\Delta T}{(D/2)^2} \tag{1.53}$$

Equating the two orders of magnitude (1.52) and (1.53), as required by the energy equation (1.51), we find the answer

$$t \sim \frac{(D/2)^2}{\alpha} \tag{1.54}$$

where α is the thermal diffusivity of the medium, $k/\rho c_P$. The penetration time (1.54) compares well with any order-of-magnitude interpretation of the exact solution to this classical problem [15]. However, the time and effort associated with deriving eq. (1.54) do not compare with the labor required by Fourier analysis and the graphical presentation of Fourier series.

Based on this introductory example, the following rules of scale analysis are worth teaching:

- *Rule 1*. Always define the spatial extent of the region in which you perform the scale analysis. In the example of Fig. 1.4, the size of the region of interest is $D/2$. In other problems, such as boundary layer flow, the size of the region of interest is unknown; as shown in Chapter 2, the scale analysis begins by selecting the region and by labeling the unknown thickness of this region δ. Any scale analysis of a flow or a flow region that is not uniquely defined is nonsense.
- *Rule 2*. One equation constitutes an equivalence between the scales of two dominant terms appearing in the equation. In the transient conduction example of Fig. 1.4, the left-hand side of eq. (1.51) could only be of the same order of magnitude as the right-hand side. The two terms appearing in eq. (1.51) are the dominant terms (considering that the discussion referred to pure conduction); in general, the energy equation can contain many more terms [eq. (1.39)], not all of them important. The reasoning for selecting the dominant scales from many scales is condensed in rules $3-5$.
- *Rule 3*. If in the sum of two terms,

$$c = a + b \tag{1.55}$$

the order of magnitude of one term is greater than the order of magnitude of the other term,

$$O(a) > O(b) \tag{1.56}$$

then the order of magnitude of the sum is dictated by the dominant term:

$$O(c) = O(a) \tag{1.57}$$

The same conclusion holds if instead of eq. (1.55), we have the difference $c = a - b$ or $c = -a + b$.

- *Rule 4*. If in the sum of two terms, eq. (1.55), the two terms are of the same order of magnitude,

$$O(a) = O(b) \tag{1.58}$$

then the sum is also of the same order of magnitude:

$$O(c) \sim O(a) \sim O(b) \tag{1.59}$$

- *Rule 5*. In any product

$$p = ab \tag{1.60}$$

the order of magnitude of the product is equal to the product of the orders of magnitude of the two factors

$$O(p) = O(a)O(b) \tag{1.61}$$

If, instead of eq. (1.60), we have the ratio

$$r = \frac{a}{b} \tag{1.62}$$

then

$$O(r) = \frac{O(a)}{O(b)} \tag{1.63}$$

In addition to having its own set of rules, scale analysis requires special care with regard to notation. In rules 1–5, we used the following symbols:

$\sim$ is of the same order of magnitude as

$O(a)$ the order of magnitude of a

$>$ greater than, in an order-of-magnitude sense

For brevity, the scale analyses included in this book employ the language of expressions (1.56), (1.57), (1.61), and (1.63) without the repetitive potentially confusing notation $O(\cdot)$ for "order of magnitude."

Scale analysis is now employed widely in heat transfer, and the fundamental scaling results that have been developed go beyond the first steps presented in this book. For example, Bhattacharjee and Grosshandler [16] have reported the scale analysis of a pressure-driven wall jet. Li and Djilali [17] have used scale analysis to describe the behavior of separating flows behind backward-facing steps (separation bubbles). Li [18] has reported the scaling results for jet diffusion flames. Dowell [19] applied the method of scale analysis to the study of linear and nonlinear dynamics and aerodynamics.

1.6 HEATLINES FOR VISUALIZING CONVECTION

The opportunity to actually ''see'' the solution to a problem is essential to a problem solver's ability to learn from experience and in this way to improve his or her technique. In convection problems it is important to visualize the flow of fluid and, riding on this, the flow of energy. For example, in the two-dimensional Cartesian configuration of Fig. 1.1, it has been common practice to define a streamfunction $\psi(x, y)$ as

$$u = \frac{\partial \psi}{\partial y}, \qquad v = -\frac{\partial \psi}{\partial x} \tag{1.64}$$

such that the mass continuity equation for incompressible flow,

$$\frac{\partial u}{\partial x} + \frac{\partial v}{\partial y} = 0 \tag{1.65}$$

is satisfied identically. It is easy to verify that the actual flow is locally parallel to the ψ = constant line passing through the point of interest. Therefore, although there are no substitutes for u and v as bearers of information regarding the local flow, the family of ψ = constant streamlines provides a bird's-eye view of the entire flow field and its main characteristics.

In convection, the transport of energy through the flow field is a combination of both thermal diffusion and enthalpy flow [cf. eq. (1.42)]. For any such field, Kimura and Bejan [20] and the 1984 edition of this book defined a new function $H(x, y)$ such that the net flow of energy (thermal diffusion and enthalpy flow) is zero across each H = constant line. The mathematical definition of the *heatfunction H* follows in the steps of eqs. (1.64) with the aim of satisfying the energy equation. For steady-state two-dimensional convection through a constant-property homogeneous fluid, eq. (1.42) becomes

$$u\frac{\partial T}{\partial x} + v\frac{\partial T}{\partial y} = \alpha \left(\frac{\partial^2 T}{\partial x^2} + \frac{\partial^2 T}{\partial y^2} \right) \tag{1.66}$$

or

$$\frac{\partial}{\partial x} \left(\rho c_p u T - k\frac{\partial T}{\partial x} \right) + \frac{\partial}{\partial y} \left(\rho c_p v T - k\frac{\partial T}{\partial y} \right) = 0 \tag{1.67}$$

The heatfunction is defined as follows:

Net energy flow in the x direction:

$$\frac{\partial H}{\partial y} = \rho c_p u(T - T_{\text{ref}}) - k\frac{\partial T}{\partial x} \tag{1.68}$$

Net energy flow in the y direction:

$$-\frac{\partial H}{\partial x} = \rho c_p v(T - T_{\text{ref}}) - k\frac{\partial T}{\partial y} \tag{1.69}$$

so that the heatfunction $H(x, y)$ satisfies eq. (1.66) identically. Note that the definition above also applies to convection through a fluid-saturated porous medium, where eq. (1.66) accounts for energy conservation (Chapter 12).

The reference temperature T_{ref} is, in principle, an arbitrary constant that can be selected based on convention. Patterns of $H =$ constant *heatlines* are instructive when T_{ref} is the lowest temperature that occurs in the heat transfer configuration. For example, if the wall shown in Fig. 2.1 is warmer than the free stream, $T_0 > T_{\infty}$, the choice of reference temperature is $T_{ref} = T_{\infty}$. For a meaningful comparison of the heatlines of one flow with the heatlines of another flow, I proposed that T_{ref} always be set equal to the lowest temperature of the flow field.

If the fluid flow subsides ($u = v = 0$), the heatlines become identical to the *heat flux lines* employed frequently in the study of conduction phenomena. Therefore, as a heat transfer visualization technique, the use of heatlines is the convection counterpart or generalization of a standard technique (heat flux lines) used in conduction. Note that the contemporary use of $T =$ constant lines is not a proper way to visualize heat transfer in the field of convection; isotherms are a proper heat transfer visualization tool only in the field of conduction (where, in fact, they have been invented) because only there are they locally orthogonal to the true direction of energy flow. The use of $T =$ constant lines to visualize convection heat transfer makes as much sense as using $P =$ constant lines to visualize fluid flow.

The heatline method for the visualization of convective heat transfer was proposed in the first edition of this book (1984), along with a first application to natural convection in an enclosure heated from the side [20]. The method has since been adopted and extended in many ways in the post-1984 heat transfer literature [21–55].

REFERENCES

1. D. P. Simpson, *Cassell's Latin Dictionary*, Macmillan, New York, 1978, p. 150.
2. A. Bejan, *Advanced Engineering Thermodynamics*, 3rd ed., Wiley, Hoboken, 2006, p. 23.
3. A. Bejan, *Entropy Generation through Heat and Fluid Flow*, Wiley, New York, 1982.
4. J. B. J. Fourier, Mémoire d'analyse sur le mouvement de la chaleur dans les fluides, in *Mémoires de l'Académie Royale des Sciences de l'Institut de France*, Didot, Paris, 1833, pp. 507–530 (presented on Sept. 4, 1820).
5. J. B. J. Fourier, *Oeuvres de Fourier*, G. Darboux, ed., Vol. 2, Gauthier-Villars, Paris, 1890, pp. 595–614.
6. S. D. Poisson, *Théorie Mathématique de la Chaleur*, Paris, 1835, Chapter 4, p. 86.
7. A. Bejan, *Entropy Generation Minimization*, CRC Press, Boca Raton, FL, 1996.
8. A. Bejan, G. Tsatsaronis, and M. Moran, *Thermal Design and Optimization*, Wiley, New York, 1996.

9. A. Bejan, *Shape and Structure, from Engineering to Nature*, Cambridge University Press, Cambridge, 2000.

10. R. N. Rosa, A. H. Reis, and A. F. Miguel, eds., *Bejan's Constructal Theory of Shape and Structure*, Évora Geophysics Center, University of Évora, Portugal, 2004.

11. H. Poirier, Une théorie explique l'intelligence de la nature, *Science & Vie*, *No.* 1034, November 2003, pp. 44–63.

12. A. Bejan and S. Lorente, Constructal theory of generation of configuration in nature and engineering, *J. Appl. Phys.*, Vol. 100, 2006, 041301.

13. A. Bejan and S. Lorente, The constructal law of design and evolution in nature, *Phil. Trans. R. Soc. B*, Vol. 365, 2010, pp. 1335–1347.

14. A. Bejan and S. Lorente, *Design with Constructal Theory*, Wiley, Hoboken, 2008.

15. A. Bejan, *Heat Transfer*, Wiley, New York, 1993, Chapter 4.

16. S. Bhattacharjee and W. L. Grosshandler, The formation of a wall jet near a high temperature wall under microgravity environment, *ASME HTD*, Vol. 96, 1988, pp. 711–716.

17. X. Li and N. Djilali, On the scaling of separation bubbles, *JSME Int. J., Ser. B*, Vol. 38, No. 4, 1995, pp. 541–548.

18. X. Li, On the scaling of the visible lengths of jet diffusion flames, *J. Energy Resour. Technol.*, Vol. 118, 1996, pp. 128–133.

19. E. H. Dowell, Transonic unsteady potential flow: Scaling analysis of linear and nonlinear dynamics, *AIAA J.*, Vol. 48, 2010, pp. 1017–1019.

20. S. Kimura and A. Bejan, The ''heatline'' visualization of convective heat transfer, *J. Heat Transfer*, Vol. 105, 1983, pp. 916–919.

21. D. Littlefield and P. Desai, Buoyant laminar convection in a vertical cylindrical annulus, *J. Heat Transfer*, Vol. 108, 1986, pp. 814–821.

22. O. V. Trevisan and A. Bejan, Combined heat and mass transfer by natural convection in a vertical enclosure, *J. Heat Transfer*, Vol. 109, 1987, pp. 104–109.

23. F. L. Bello-Ochende, Analysis of heat transfer by free convection in tilted rectangular cavities using the energy analogue of the stream function, *Int. J. Mech. Eng. Ed.*, Vol. 15, 1987, pp. 91–98.

24. F. L. Bello-Ochende, A heat function formulation for thermal convection in a square cavity, *Int. Comm. Heat Mass Transfer*, Vol. 15, 1988, pp. 193–202.

25. A. M. Morega, The heat function approach to the thermo-magnetic convection of electroconductive melts, *Rev. Roum. Sci. Tech. Ser. Electrotech. Energ.*, Vol. 33, 1988, pp. 33–39.

26. S. K. Aggarwal and A. Manhapra, Use of heatlines for unsteady buoyancy-driven flow in a cylindrical enclosure, *J. Heat Transfer*, Vol. 111, 1989, pp. 576–578.

27. S. K. Aggarwal and A. Manhapra, Transient natural convection in a cylindrical enclosure nonuniformly heated at the top wall, *Numer. Heat Transfer, Part A*, Vol. 15, 1989, pp. 341–356.

28. C. J. Ho, Y. H. Lin, and T. C. Chen, A numerical study of natural convection in concentric and eccentric horizontal cylindrical annuli with mixed boundary conditions, *Int. J. Heat Fluid Flow*, Vol. 10, 1989, pp. 40–47.

29. C. J. Ho and Y. H. Lin, Thermal convection heat transfer of air/water layers enclosed in horizontal annuli with mixed boundary conditions, *Wärme Stoffübertrag.*, Vol. 24, 1989, pp. 211–224.

30. C. J. Ho and Y. H. Lin, Natural convection of cold water in a vertical annulus with constant heat flux on the inner wall, *J. Heat Transfer*, Vol. 112, 1990, pp. 117–123.

31. A. M. Morega and A. Bejan, Heatline visualization of forced convection boundary layers, *Int. J. Heat Mass Transfer*, Vol. 36, 1993, pp. 3957–3966.

32. A. M. Morega and A. Bejan, Heatline visualization of forced convection in porous media, *Int. J. Heat Fluid Flow*, Vol. 15, 1994, pp. 42–47.

33. V. A. F. Costa, Double diffusive natural convection in a square enclosure with heat and mass diffusive walls, *Int. J. Heat Mass Transfer*, Vol. 40, 1997, pp. 4061–4071.

34. V. A. F. Costa, Double diffusive natural convection in enclosures with heat and mass diffusive walls, in G. De Vahl Davis and E. Leonardi., eds., *Proceedings of the International Symposium on Advances in Computational Heat Transfer (CHT'97)*, Begell House, New York, 1998, pp. 338–344.

35. H. Y. Wang, F. Penot, and J. B. Saulnier, Numerical study of a buoyancy-induced flow along a vertical plate with discretely heated integrated circuit packages, *Int. J. Heat Mass Transfer*, Vol. 40, 1997, pp. 1509–1520.

36. V. A. F. Costa, Unification of the streamline, heatline and massline methods for the visualization of two-dimensional transport phenomena, *Int. J. Heat Mass Transfer*, Vol. 42, 1999, pp. 27–33.

37. S. J. Kim and S. P. Jang, Experimental and numerical analysis of heat transfer phenomena in a sensor tube of a mass flow controller, *Int. J. Heat Mass Transfer*, Vol. 44, 2001, pp. 1711–1724.

38. Q.-H. Deng and G.-F. Tang, Numerical visualization of mass and heat transport for conjugate natural convection/heat conduction by streamline and heatline, *Int. J. Heat Mass Transfer*, Vol. 45, 2002, pp. 2375–2385.

39. Q.-H. Deng and G.-F. Tang, Numerical visualization of mass and heat transport for mixed convective heat transfer by streamline and heatline, *Int. J. Heat Mass Transfer*, Vol. 45, 2002, pp. 2387–2396.

40. A. Mukhopadhyay, X. Qin, S. K. Aggarwal, and I. K. Puri, On extension of ''heatline'' and ''massline'' concepts to reacting flows through the use of conserved scalars, *J. Heat Transfer*, Vol. 124, 2002, pp. 791–799.

41. V. A. F. Costa, Comment on the paper by Qi-Hong Deng and Guang-Fa Tang, Numerical visualization of mass and heat transport for conjugate natural convection/ heat conduction by streamline and heatline, *Int. J. Heat Mass Transfer*, Vol. 46, 2003, pp. 185–187.

42. V. A. F. Costa, Unified streamline, heatline and massline methods for the visualization of two-dimensional heat and mass transfer in anisotropic media, *Int. J. Heat Mass Transfer*, Vol. 46, 2003, pp. 1309–1320.

43. A. Mukhopadhyay, X. Qin, I. K. Puri, and S. K. Aggarwal, Visualization of scalar transport in nonreacting and reacting jets through a unified ''heatline'' and ''massline'' formulation, *Numerical Heat Transfer, Part A*, Vol. 44, 2003, pp. 683–704.

44. A. Dalal and M. K. Das, Heatline method for the visualization of natural convection in a complicated cavity, *Int. J. Heat Mass Transfer*, Vol. 51, 2008, pp. 263–272.

45. F.-Y. Zhao, D. Liu, and G.-F. Tang, Application issues of the streamline, heatline and massline for conjugate heat and mass transfer, *Int. J. Heat Mass Transfer*, Vol. 50, 2007, pp. 320–334.
46. T. Basak and S. Roy, Role of ''Bejan's heatlines'' in heat flow visualization and optimal thermal mixing for differentially heated square enclosures, *Int. J. Heat Mass Transfer*, Vol. 51, 2008, pp. 3486–3503.
47. E. Hakyemez, M. Mobedi, and H. F. Oztop, Effects of wall-located heat barrier on conjugate conduction/natural-convection heat transfer and fluid flow in enclosures, *Numer. Heat Transfer Part A*, Vol. 54, 2008, pp. 197–220.
48. S. Mahmud and R. A. Fraser, Visualizing energy flows through energy streamlines and pathlines, *Int. J. Heat Mass Transfer*, Vol. 50, 2007, pp. 3990–4002.
49. T. Basak, S. Roy, and I. Pop, Heat flow analysis for natural convection within trapezoidal enclosures based on heatline concept, *Int. J. Heat Mass Transfer*, Vol. 52, 2009, pp. 2471–2483.
50. T. Basak, G. Aravind, and S. Roy, Visualization of heat flow due to natural convection within triangular cavities using Bejan's heatline concept, *Int. J. Heat Mass Transfer*, Vol. 52, 2009, pp. 2824–2833.
51. R. S. Kaluri, T. Basak, and S. Roy, Bejan's heatlines and numerical visualization of heat flow and thermal mixing in various differentially heated porous square cavities, *Numer. Heat Transfer Part A*, Vol. 55, 2009, pp. 487–516.
52. M. A. Waheed, Heatfunction formulation of thermal convection in rectangular enclosures filled with porous media, *Numer. Heat Transfer Part A*, Vol. 55, 2009, pp. 185–204.
53. Y. Varol, H. F. Oztop, M. Mobedi, and I. Pop, Visualization of natural convection heat transport using heatline method in porous non-isothermally heated triangular cavity, *Int. J. Heat Mass Transfer*, Vol. 51, 2008, pp. 5040–5051.
54. T. Basak, S. Roy, and G. Aravind, Analysis of heat recovery and thermal transport within entrapped fluid based on heatline approach, *Chem. Eng. Sci.*, Vol. 64, 2009, pp. 1673–1686.
55. R. S. Kaluri, T. Basak, and S. Roy, Heatline approach for visualization of heat flow and efficient thermal mixing with discrete heat sources, *Int. J. Heat Mass Transfer*, Vol. 53, 2010, pp. 3241–3261.

PROBLEMS

1.1. Consider the unsteady mass conservation equation (1.5) as it might describe the flow accelerating through a duct with a variable cross section. If the largest velocity gradient measured locally is du/dx and the largest density gradient is $d\rho/dx$, what order-of-magnitude relationship must exist between du/dx and $d\rho/dx$ for the simplified equation (1.8) to be applicable?

1.2. Derive the mass conservation equation in cylindrical coordinates [eq. (1.9)] by applying the general principle (1.1) to an elementary control volume of size $\Delta r(r\,\Delta\theta)\,\Delta z$ in Fig. 1.1b (assume that ρ = constant).

1.3. Derive the mass conservation statement for spherical coordinates [eq. (1.10)] by writing eq. (1.1) for the elementary control volume $(\Delta r)(r \sin \phi \, \Delta\theta)(r \, \Delta\phi)$ around point (r, θ, ϕ) in Fig. 1.1c (assume that $\rho = $ constant).

1.4. Consider a flow in which ρ and μ may be regarded as constant. Show that the x momentum equation (1.18) follows from eq. (1.17) through proper use of the mass conservation principle.

1.5. Imagine a flow described by eqs. (1.9) and (1.21) in cylindrical coordinates. If the flow is situated on one side of and infinitely far from the $r = 0$ origin of the coordinate system, the local three-directional increments Δr, $r \, \Delta\theta$, Δz become analogous to three Cartesian increments Δx, Δy, Δz measured away from the local point (r, θ, z) in the flow field. Show that in the limit $r \rightarrow \infty$, the transformation $\Delta r \rightarrow \Delta x$, $r \, \Delta\theta \rightarrow \Delta y$, $\Delta z \rightarrow \Delta z$ leads to the collapse of eqs. (1.9) and (1.21) into their (x, y, z) Cartesian equivalents [eqs. (1.8) and (1.19)].

1.6. Consider the conservation of mass and the three force balances in spherical coordinates [eqs. (1.10) and (1.22)]. If the flow described by these equations is situated infinitely far from the $r = 0$ origin of the spherical system, the following transformation is applicable (Fig. 1.1): $\Delta r \rightarrow \Delta x$, $r \sin \phi \, \Delta\theta \rightarrow \Delta y$, $r \, \Delta\phi \rightarrow \Delta z$. Show that through this transformation, in the limit $r \rightarrow \infty$, eqs. (1.10) and (1.22) become the same as eqs. (1.8) and (1.19).

1.7. Implicit in the derivation of the energy equation (1.39) is the assumption that changes in kinetic energy $V^2/2$ are negligible relative to changes in internal energy e [see expressions (1.25), where e should, in general, be replaced by $e + V^2/2$]. Retrace the path leading to eq. (1.39) by taking into account changes in kinetic energy; show that the result of this more rigorous analysis is identical to eq. (1.39).

1.8. Demonstrate that lost work is always proportional to entropy generation [eq. (1.48)], where $W_{\text{lost}} = W_{\text{maximum}} - W_{\text{actual}}$, and where W_{maximum} corresponds to the reversible limit ($S_{\text{gen}} = 0$). Write the first law of thermodynamics for a control volume, first for the actual (real) process and then for the reversible process. Then use the definition of W_{lost} and S_{gen} to prove eq. (1.48).

1.9. Derive the formula for the local rate of entropy generation [eq. (1.49)]. Begin with translating the general statement (1.47) into the language of the two-dimensional control volume $\Delta x \, \Delta y$. Combine the resulting expression with the first law of thermodynamics as given by eq. (1.26), plus the canonical relation for internal energy (Table 1.1).

1.10. Consider the Couette flow between two parallel plates separated by a gap of width D and moving relative to one another with a speed U. The temperature difference ΔT is imposed between the two plates. Estimate the rate of entropy generation per unit volume in this flow. What relationship

must exist between D, U, ΔT and the fluid properties μ and k for S'''_{gen} to be dominated by the irreversibility due to fluid friction?

1.11. According to the one-dimensional (longitudinal) conduction model of a fin, the temperature distribution along the fin, $T(x)$, obeys the energy equation [15]

$$\underbrace{kA\frac{d^2T}{dx^2}}_{\substack{\text{Longitudinal} \\ \text{conduction}}} - \underbrace{hP(T - T_0)}_{\substack{\text{Lateral} \\ \text{convection}}} + \underbrace{q'''A}_{\substack{\text{Internal} \\ \text{heat} \\ \text{generation}}} = 0$$

where A, h, P, and q''' are the fin cross-sectional area, fin-fluid heat transfer coefficient, perimeter of the fin cross section (called the *wetted perimeter*), and volumetric rate of heat generation. Consider the semi-infinite fin that, as shown in Fig. P1.11, is bathed by a fluid of temperature T_0 and is attached to a solid wall of temperature T_0. The heat generated by the fin is absorbed by either the fluid or the solid wall.
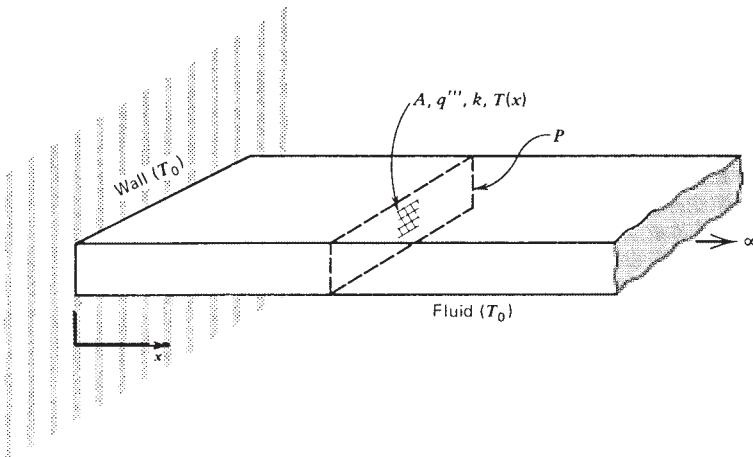
Figure P1.11

(a) As a system for scale analysis, select the fin section of length x, where x is measured away from the wall. Let T_∞ be the fin temperature sufficiently far from the wall. Show that if x is large enough, the longitudinal conduction term becomes negligible in the energy equation.

(b) Invoking the balance between lateral convection and internal heat generation, determine the fin temperature sufficiently far from the wall, T_∞.

(c) Determine the fin section of length δ near the wall where the heat transfer is ruled by the balance between longitudinal conduction and internal heat generation.

(d) Determine the heat transfer rate into the wall through the base of the fin.

1.12. Consider the laminar flow near a flat, solid wall, as illustrated in Fig. 2.1. The momentum equation for this flow involves the competition among three effects: inertia, pressure gradient, and friction [see eq. (2.26)]. For the purpose of scale analysis, consider a flow region of length L and thickness L. Show that in this region, the ratio of inertia to friction is of order Re_L, where Re_L is the Reynolds number based on wall length. Note that the region selected for analysis is not the boundary layer region discussed in Chapter 2. In a certain flow, the value of Re_L is 10^3. What force balance rules the $L \times L$ region: inertia $\sim$ pressure, inertia $\sim$ friction, or pressure $\sim$ friction?

1.13. The hot components of a power plant must be fitted with thermal insulation so that they do not leak heat excessively to the ambient (T_0). The thermal conductivity of the insulation is known (k). The total volume of the insulation (V) is fixed.

A simple model of the hot components is the two-chamber model shown in Fig. P1.13. The hottest is the furnace, which is enclosed by a surface of area A_H and high temperature T_H. The thickness of the insulation mounted on A_H is t_H. This thickness is sufficiently small so that the volume of the insulation on A_H is $A_H t_H$.
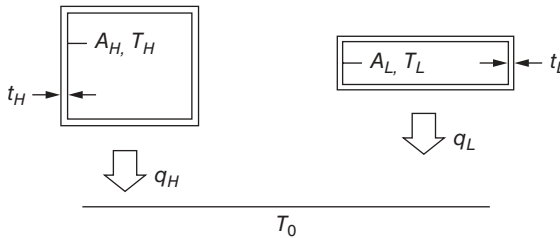
Figure P1.13

The rest of the hot components (pipes, feed water heaters, turbines) are not as hot as the furnace. They are inside an enclosure with area A_L, temperature T_L, insulation thickness t_L, and insulation volume $A_L t_L$.

The heat leaks q_H and q_L are by pure conduction and are driven by the temperature differences $\Delta T_H = T_H - T_0$ and $\Delta T_L = T_L - T_0$, respectively. These temperature differences are known. The problem is to determine t_H/t_L, that is, how to distribute the available insulation on A_H and A_L.

1. Minimize the total heat leak from A_H and A_L to the ambient, namely $q_H + q_L$, and determine the optimal ratio t_H/t_L as a function of other parameters of the two-chamber model. Does t_H/t_L depend on A_H/A_L?

2. Explain why 1 W of heat leak from T_H is not the same as 1 W of heat leak from T_L. Which do you think is more damaging to the performance of the power plant?

3. Imagine that q_H can be intercepted outside A_H and used to run a Carnot engine between T_H and T_0. The power producible in this way (W_H) is lost because q_H is dumped straight into the ambient. Imagine the equivalent scenario for q_L, and derive a formula for the Carnot power W_L that is lost because of this second heat leak.

4. Minimize the total loss of power ($W_H + W_L$) and determine the optimal ratio t_H/t_L.

5. Compare the t_H/t_L results obtained at sections 1 and 4. Which ratio is larger? Which is more relevant for actual implementation?

2

LAMINAR BOUNDARY LAYER FLOW

To begin a course in convective heat transfer with a chapter on boundary layers is to recognize the origins of the field. In this chapter we take a close look at the meaning of boundary layer theory and at the revolution that this theory triggered, not only in convective heat transfer but especially in fluid mechanics. What today is a universally accepted viewpoint and language was, at the beginning of the twentieth century, simply one man's revolutionary idea.

Boundary layer theory was proposed by Prandtl shortly after the completion of his doctoral dissertation in 1904 [1]. This idea was not accepted immediately by his contemporaries. To appreciate Prandtl's enormous accomplishment in converting the establishment, the reader has only to examine the 1932 edition of Lamb's *Hydrodynamics* [2]. This treatise of 385 articles devotes only one article to boundary layer theory and its pre-1932 results. It took three or four decades of persistent exposition by Prandtl for his theory to become the common language we speak today.

It would be inaccurate to present boundary layer theory as dogma to be applied unreflectively to solve a very long list of fluid mechanics and heat transfer problems. A theory is never perfect [3], and there is little that is ''exact'' about the similarity solutions to Prandtl's *approximate* boundary layer equations. As students and researchers, we can learn important lessons from the history of boundary layer theory. For example:

1. No theory is perfect and forever, not even boundary layer theory.
2. It is legal and, indeed, desirable to question any accepted theory.
3. Any theory is better than no theory at all.
4. It is legal to propose a new theory or a new idea in place of any accepted theory.

5. Lack of immediate acceptance of a new theory does not mean that the new theory is not better.
6. It is crucial to persevere to prove the worth of a new theory.

The history of scientific progress is a string of episodes of the type exemplified by Prandtl's boundary layer theory [4]. Knowledge of history is good for the intellectual happiness of the researcher. Theory is also good, and it should not be forgotten under the growing deluge of empiricism. On the rightful place of theory in engineering science, I draw attention to the preface to my second constructal theory book [3].

2.1   FUNDAMENTAL PROBLEM IN CONVECTIVE HEAT TRANSFER

Consider the fundamental questions that arise in connection with heat transfer from a solid object to a fluid stream in external flow. Think, for example, of a flat plate of temperature T_0 suspended in a uniform stream of velocity U_∞ and temperature T_∞, as shown in Fig. 2.1. If this flat plate is the plate fin protruding from a heat exchanger surface into the stream that bathes it, we want to know:

1. The net force exerted by the stream on the plate
2. The resistance to the transfer of heat from the plate to the stream

We must answer question 1 in order to predict the total drag force exerted by the stream on the heat exchanger surface. From a simple force balance around the duct through which the stream flows (Chapter 3), we learn that the drag force felt by the solid surface translates into the pressure drop—hence, the pumping power or exergy payment [5] required to keep the stream flowing. Question 2 must
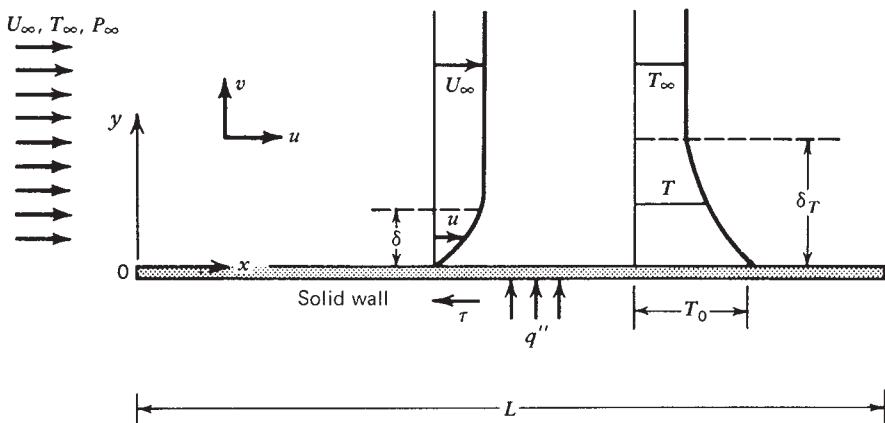
Figure 2.1   Velocity and temperature boundary layers near a plate parallel to a uniform flow.

be answered in order to predict the heat transfer rate between solid and fluid. Question 2 is the fundamental question in the field of heat transfer, while question 1 is the key question in fluid mechanics as it applies to heat transfer science.

Referring to Fig. 2.1, we are interested in calculating the total force

$$F = \int_0^L \tau W \, dx \tag{2.1}$$

and the total heat transfer rate

$$q = \int_0^L q'' W \, dx \tag{2.2}$$

Symbols τ, q'', and W stand for skin friction (shear stress experienced by the wall)

$$\tau = \mu \left(\frac{\partial u}{\partial y} \right)_{y=0} \tag{2.3}$$

wall heat flux

$$q'' = h(T_0 - T_\infty) \tag{2.4}$$

and the width of the flat plate in the direction perpendicular to the plane of Fig. 2.1, respectively. Equations (2.3) and (2.4) serve as definitions for the concepts of viscosity μ and heat transfer coefficient h.

Historically, eq. (2.4) was first written by Fourier [6], who in this way introduced the concept of heat transfer coefficient (*external conductivity* in his terminology), to which he gave the symbol h. Fourier also emphasized the fundamental difference between h and the ''proper'' thermal conductivity k. More than 100 years earlier, Newton [7] had published an essay in which he reported temperature measurements showing that the rate of temperature decrease (dT/dt) of a body immersed in a fluid is at all times proportional to the body—fluid temperature difference ($T - T_\infty$). This is why beginning with Fourier's contemporaries (e.g., Péclet [8]), eq. (2.4) acquired the incorrect name ''Newton's law of cooling.'' Newton wrote no such thing. Fourier wrote eq. (2.4). In today's terminology, Newton's observation can be written [9] as $dT/dt = b(T - T_\infty)$, in which the b coefficient (assumed constant) accounts for the ratio h/c, that is, the heat transfer coefficient divided by the specific heat of the immersed body. The concepts of heat transfer coefficient and specific heat were unknown in Newton's time. Convection currents in liquids were first discovered experimentally by Count Rumford [10, 11], who also visualized the flow by suspending neutrally buoyant particles in the liquid. The heat transfer effect of such currents was named *convection* by Prout in 1834 [12].

In sum, convection was born at the same time as conduction. The creator of both was Fourier, who also wrote the first energy equation for a convective flow (see Section 1.3).

In this treatment, we accept empirically (i.e., as a matter of repeated physical observation) that the fluid layer situated at $y = 0^+$ is, in fact, stuck to the solid wall. This is the *no-slip hypothesis*, on which the bulk of convective heat transfer research is based; it acknowledges the observation that from heat exchangers to the honey in a jar, a fluid *wets* the solid surface with which it makes contact. The no-slip condition implies that since the $0 < y < 0^+$ fluid layer is motionless, the transfer of heat from the wall to the fluid is first by pure conduction. Therefore, in place of eq. (2.4), we can write the statement for *pure conduction* through the fluid layer immediately adjacent to the wall,

$$q'' = -k \left(\frac{\partial T}{\partial y} \right)_{y=0} \tag{2.5}$$

Note the sign convention defined in Fig. 2.1: The heat flux q'' is positive when the wall releases energy into the stream. Combining eqs. (2.4) and (2.5), we calculate the heat transfer coefficient when the temperature distribution in the fluid near the wall is known:

$$h = \frac{-k(\partial T/\partial y)_{y=0}}{T_0 - T_\infty} \tag{2.6}$$

To summarize, the two key questions in the field of convective heat transfer, the questions of friction and thermal resistance, boil down to carrying out the calculations dictated by eqs. (2.1) and (2.2). However, eqs. (2.3) and (2.5) demonstrate that to be able to calculate F and q, we must first determine the flow and temperature fields in the vicinity of the solid wall. Thus, it is the demand for F and q that leads to the mathematical problem of solving for the flow (u, v) and temperature (T) in the fluid space outlined in Fig. 2.1.

Modeling the flow as incompressible and of constant property (Chapter 1), the complete mathematical statement of this problem consists of the following. Solve four equations:

$$\frac{\partial u}{\partial x} + \frac{\partial v}{\partial y} = 0 \tag{2.7}$$

$$u \frac{\partial u}{\partial x} + v \frac{\partial u}{\partial y} = -\frac{1}{\rho} \frac{\partial P}{\partial x} + v \left(\frac{\partial^2 u}{\partial x^2} + \frac{\partial^2 u}{\partial y^2} \right) \tag{2.8}$$

$$u \frac{\partial v}{\partial x} + v \frac{\partial v}{\partial y} = -\frac{1}{\rho} \frac{\partial P}{\partial y} + v \left(\frac{\partial^2 v}{\partial x^2} + \frac{\partial^2 v}{\partial y^2} \right) \tag{2.9}$$

$$u \frac{\partial T}{\partial x} + v \frac{\partial T}{\partial y} = \alpha \left(\frac{\partial^2 T}{\partial x^2} + \frac{\partial^2 T}{\partial y^2} \right) \tag{2.10}$$

for four unknowns (u, v, P, T), subject to the following boundary conditions:

$$
\left.
\begin{array}{lll}
\text{(i)} & \text{No slip} & u = 0 \\
\text{(ii)} & \text{Impermeability} & v = 0 \\
\text{(iii)} & \text{Wall temperature} & T = T_0
\end{array}
\right\} \quad \text{at the solid wall}
$$

$$\tag{2.11}$$

$$
\left.
\begin{array}{lll}
\text{(iv)} & \text{Uniform flow} & u = U_\infty \\
\text{(v)} & \text{Uniform flow} & v = 0 \\
\text{(vi)} & \text{Uniform temperature} & T = T_\infty
\end{array}
\right\}
\begin{array}{l}
\text{infinitely far from the solid,} \\
\text{in both the } y \text{ and } x \text{ directions}
\end{array}
$$

In eqs. (2.7)–(2.10), we recognize, in order, statements accounting for the steady-state conservation of mass, momentum, and energy at every point in the two-dimensional flow field. Conditions (i) and (ii) apply to the horizontal surfaces in Fig. 2.1. Along the short leading and trailing surfaces of the flat plate $(x = 0, L)$, the no-slip condition reads $u = 0$ and the impermeable wall condition reads $v = 0$.

2.2 CONCEPT OF BOUNDARY LAYER

The nonlinear partial differential problem stated as eqs. (2.7)–(2.11) has served as one of the central stimuli in the development of the field of applied mathematics during the past 200 years. The most remarkable feature of this problem is that despite all this time and effort, it has not been solved. It is this feature that makes the boundary layer idea so special: It is a clever way to think and a way to solve many historically unsolvable problems. As with any great theory, it is a way to see simplicity.

Referring to Fig. 2.1 and the complete problem statement (2.7)–(2.11), we have the freedom to think that the velocity change from $u = 0$ to $u = U_\infty$ and the temperature change from $T = T_0$ to $T = T_\infty$ occur in a *space* situated relatively close to the solid wall. How close is "close" is the object of the scale analysis presented later in this section. The important thing to understand at this stage is the revolutionary step taken by Prandtl in thinking of the region close to the wall (the boundary layer) as a region *distinct* from the immense domain in which the unsolvable mathematical problem (2.7)–(2.11) was formulated by his contemporaries.

Prandtl's decision is equivalent to carving out of the entire flow field only that region that is truly relevant to answering the questions formulated in the preceding section. Outside the boundary layer, he imagines a *free stream*, that is, a flow region not affected by the obstruction and heating effect introduced by the solid object. The free stream is characterized by

$$
u = U_\infty, \qquad v = 0, \qquad P = P_\infty, \qquad T = T_\infty \tag{2.12}
$$

Let δ be the order of magnitude of the distance in which u changes from 0 at the wall to roughly U_∞ in the free stream. Thus, in the space of height δ and length L in Fig. 2.1, we identify the following scales for changes in x, y, and u:

$$x \sim L, \qquad y \sim \delta, \qquad u \sim U_\infty \tag{2.13}$$

In the $\delta \times L$ region, then, the longitudinal momentum equation (2.8) accounts for the competition between three types of forces:

$$
\begin{array}{ccc}
\text{Inertia} & \text{Pressure} & \text{Friction} \\
U_\infty \dfrac{U_\infty}{L}, \quad v \dfrac{U_\infty}{\delta} & \dfrac{P}{\rho L} & v \dfrac{U_\infty}{L^2}, \quad v \dfrac{U_\infty}{\delta^2}
\end{array}
\tag{2.14}
$$

In (2.14) each term represents the scale of each of the five terms appearing in eq. (2.8). Since the mass continuity equation (2.7) requires that

$$\frac{U_\infty}{L} \sim \frac{v}{\delta} \tag{2.15}$$

we learn that the inertia terms in eq. (2.14) are *both* of order U_∞^2/L; hence, neither can be neglected at the expense of the other. Next, if the boundary layer region $\delta \times L$ is *slender*, such that

$$\delta \ll L \tag{2.16}$$

then the last scale in eq. (2.14) is the scale most representative of the friction force in that region. Thus, neglecting the $\partial^2 u/\partial x^2$ term at the expense of the $\partial^2 u/\partial y^2$ term in the x momentum equation (2.8) yields

$$u \frac{\partial u}{\partial x} + v \frac{\partial u}{\partial y} = -\frac{1}{\rho} \frac{\partial P}{\partial x} + v \frac{\partial^2 u}{\partial y^2} \tag{2.17}$$

Invoking the same scaling argument—the *slenderness* of the boundary layer region—the y momentum equation reduces to

$$u \frac{\partial v}{\partial x} + v \frac{\partial v}{\partial y} = -\frac{1}{\rho} \frac{\partial P}{\partial y} + v \frac{\partial^2 v}{\partial y^2} \tag{2.18}$$

Equation (2.18) is not usually discussed in connection with the boundary layer analysis of specific laminar flow problems. However, it is the basis for another important result: the replacement of $\partial P/\partial x$ by a known quantity (dP_∞/dx) in eq. (2.17). To show how this is done, consider answering the following question: In a slender region $\delta \times L$, is the pressure variation in the y direction negligible compared with the pressure variation in the x direction? Intuitively, we suspect that the answer must be ''yes'' because the region of interest $(\delta \times L)$ is by definition slender.

In general, the pressure at any point in the fluid of Fig. 2.1 is a function of both x and y; hence, the total derivative

$$dP = \frac{\partial P}{\partial x}\, dx + \frac{\partial P}{\partial y}\, dy \qquad (2.19)$$

Dividing by dx, the question formulated in the preceding paragraph amounts to whether the last term is negligible in the expression

$$\frac{dP}{dx} = \frac{\partial P}{\partial x} + \frac{\partial P}{\partial y}\frac{dy}{dx} \qquad (2.20)$$

The orders of magnitude of the two pressure gradients can be deduced from eqs. (2.17) and (2.18) by recognizing a balance between pressure forces and *either* friction or inertia [eq. (2.14)]. For the present argument, it is not crucial which balance we invoke as long as the same balance is invoked in both eqs. (2.17) and (2.18). For instance, the pressure $\sim$ friction balance in eq. (2.17) suggests that

$$\frac{\partial P}{\partial x} \sim \frac{\mu U_\infty}{\delta^2} \qquad (2.21)$$

whereas the same balance in eq. (2.18) yields

$$\frac{\partial P}{\partial y} \sim \frac{\mu v}{\delta^2} \qquad (2.22)$$

Now, turning our attention to the right-hand side of eq. (2.20), the ratio of the second term divided by the first term is of order

$$\frac{(\partial P/\partial y)(dy/dx)}{\partial P/\partial x} \sim \frac{v\delta}{U_\infty L} \sim \left(\frac{\delta}{L}\right)^2 \ll 1 \qquad (2.23)$$

Note that to complete this last statement, we had to use the mass continuity scaling [eq. (2.15)] and the slenderness postulate [eq. (2.16)]. In conclusion, the last term in eq. (2.20) is less significant as the $\delta \times L$ region becomes more slender,

$$\frac{dP}{dx} = \frac{\partial P}{\partial x} \qquad (2.24)$$

This means that inside the boundary layer, the pressure varies chiefly in the longitudinal direction; in other words, at any x, the pressure inside the boundary layer region is practically the same as the pressure immediately outside it,

$$\frac{\partial P}{\partial x} = \frac{dP_\infty}{dx} \qquad (2.25)$$

Making this last substitution in the x momentum equation (2.17), we finally obtain

$$u \frac{\partial u}{\partial x} + v \frac{\partial u}{\partial y} = -\frac{1}{\rho} \frac{dP_\infty}{dx} + v \frac{\partial^2 u}{\partial y^2} \tag{2.26}$$

This is the *boundary layer equation* for momentum, and keeping in mind how it was derived, it is a statement of momentum conservation in *both* the x and y directions.

The boundary layer equation for energy follows from eq. (2.10), where we neglect the term accounting for thermal diffusion in the x direction,

$$u \frac{\partial T}{\partial x} + v \frac{\partial T}{\partial y} = \alpha \frac{\partial^2 T}{\partial y^2} \tag{2.27}$$

With this statement, we finish rewriting the original flow and heat transfer problem [eqs. (2.7)–(2.11)] in the language of boundary layer theory. We now have only three equations to solve [eqs. (2.7), (2.26), and (2.27)] for three unknowns (u,v,T). Compare this with the ''four equations and four unknowns'' problem contemplated originally. In addition, the disappearance of the $\partial^2/\partial x^2$ diffusion terms from the momentum and energy equations makes this new problem solvable in a variety of ways. In the next section we begin with the most cost-effective method of solution: scale analysis.

2.3 SCALE ANALYSIS

The boundary layer equations (2.26) and (2.27) are based on the thought that the significant variations in velocity and temperature occur in a slender region near the solid wall. This does not mean that u and T reach their free-stream values within the same distance δ. Indeed, we have the freedom to think not of one but of an infinity of slender flow regions adjacent to the wall. Let δ be the thickness of the region in which u varies from 0 at the wall to U_∞ in the free stream. Let δ_T be the thickness of another slender region super imposed on the first in which T varies from T_0 at the wall to T_∞ in the free stream. Keeping up with tradition, we refer to δ and δ_T as the velocity boundary layer thickness and the thermal boundary layer thickness, respectively. These scales are shown schematically in Fig. 2.1; in general, $\delta \neq \delta_T$.

In scaling terms, the flow friction question (2.3) becomes

$$\tau \sim \mu \frac{U_\infty}{\delta} \tag{2.28}$$

Thus, to estimate the wall frictional shear stress, we must evaluate the extent δ of this imaginary slender wall region. Consider the simplest free stream possible, a free stream with uniform pressure P_∞. (This is a very good approximation for

the flow around a plate fin in a heat exchanger passage because the pressure drop in the direction of flow is not significant over the longitudinal length L dictated by the plate fin.) With $dP_\infty/dx = 0$ in eq. (2.26), the boundary layer momentum equation implies that

$$\text{inertia} \sim \text{friction}$$

$$\frac{U_\infty^2}{L}, \frac{vU_\infty}{\delta} \sim v\frac{U_\infty}{\delta^2} \tag{2.29}$$

Referring once again to the mass continuity scaling (2.15), we conclude that the two inertia terms are of the same order of magnitude. Therefore, eq. (2.29) requires that

$$\delta \sim \left(\frac{vL}{U_\infty}\right)^{1/2} \tag{2.30}$$

In other words,

$$\frac{\delta}{L} \sim \text{Re}_L^{-1/2} \tag{2.31}$$

where Re_L is the Reynolds number based on the longitudinal dimension of the boundary layer region, $Re_L = U_\infty L/v$.

The boundary layer thickness δ is the transversal distance to which viscous diffusion spreads while the flow sweeps the wall longitudinally. The time of transversal viscous diffusion is $t_\delta \sim \delta^2/v$. The time of longitudinal convection is $t_L \sim L/U_\infty$. Recognizing that at the trailing end of the wall these two times are in fact the same time scale, $t_\delta \sim t_L$, we arrive at the δ scale shown in eqs. (2.30) and (2.31).

Equation (2.31) is an important result: It states that the slenderness postulate on which the boundary layer theory is based ($\delta \ll L$) is valid provided that $\text{Re}_L^{1/2} \gg 1$. Thus, eq. (2.31) is a test of whether a given external flow situation lends itself to boundary layer analysis, as Re_L can easily be calculated beforehand. Furthermore, even when $\text{Re}_L^{1/2} \gg 1$, eq. (2.31) can be used to assess the limitations of the boundary layer analysis: For example, the boundary layer solution will fail in the tip region of length l, short enough so that $\text{Re}_l^{1/2}$ is not considerably greater than unity.

Returning to the friction question [eq. (2.28)], the wall shear stress scales as

$$\tau \sim \mu\frac{U_\infty}{L}\text{Re}_L^{1/2} \sim \rho U_\infty^2\text{Re}_L^{-1/2} \tag{2.32}$$

Therefore, the dimensionless *skin friction coefficient* $C_f = \tau/\left(\frac{1}{2}\rho U_\infty^2\right)$ depends on the Reynolds number,

$$C_f \sim \text{Re}_L^{-1/2} \tag{2.33}$$

At this point, the question of wall friction has been answered in an order-of-magnitude sense. The scaling analysis on which eq. (2.32) is based assures us

that the real (measured or calculated) value of τ will differ from $\rho U_\infty^2 \, \mathrm{Re}_L^{-1/2}$ by only a factor of order unity. This prediction is amply verified by more exact analyses, as is shown later in this chapter.

The heat transfer question [eq. (2.6)] is answered by focusing on the thermal boundary layer of thickness δ_T,

$$h \sim \frac{k(\Delta T/\delta_T)}{\Delta T} \sim \frac{k}{\delta_T} \tag{2.34}$$

where $\Delta T = T_0 - T_\infty$ is the temperature variation in the region $\delta_T \times L$. The boundary layer energy equation (2.27) states that there is always a balance between conduction from the wall into the stream and convection (enthalpy flow) parallel to the wall:

$$\text{convection} \sim \text{conduction}$$

$$u \frac{\Delta T}{L}, v \frac{\Delta T}{\delta_T} \sim \alpha \frac{\Delta T}{\delta_T^2} \tag{2.35}$$

The δ_T scale needed for estimating $h \sim k/\delta_T$ can be determined analytically in the following two limits:

1. *Thick thermal boundary layer, $\delta_T \gg \delta$.* In this limit, the δ_T layer is thick relative to the velocity boundary layer thickness measured at the same L. The u scale outside the velocity boundary layer (and inside the δ_T layer) is U_∞. According to eq. (2.15), the v scale in the same region is $v \sim U_\infty \delta/L$. This means that the second term on the left side of eq. (2.35) is of order

$$v \frac{\Delta T}{\delta_T} \sim U_\infty \frac{\Delta T}{L} \frac{\delta}{\delta_T} \tag{2.36}$$

in which $\delta/\delta_T \ll 1$. The second term, $(v \, \Delta T)/\delta_T$, is therefore δ/δ_T times smaller than the first, $(u \, \Delta T)/L$, and the entire left side of eq. (2.35) is dominated by the scale $U_\infty \, \Delta T/L$.

In conclusion, the convection $\sim$ conduction balance expressed by the energy equation (2.35) is simply $(U_\infty \, \Delta T)/L \sim (\alpha \, \Delta T)/\delta_T^2$, which yields

$$\frac{\delta_T}{L} \sim \mathrm{Pe}_L^{-1/2} \sim \mathrm{Pr}^{-1/2} \mathrm{Re}_L^{-1/2} \tag{2.37}$$

where $\mathrm{Pe}_L = U_\infty L/\alpha$ is the Péclet number. Comparing eq. (2.37) with eq. (2.31), we find the interesting result that the relative size of δ_T and δ depends on the Prandtl number $\mathrm{Pr} = \nu/\alpha$,

$$\frac{\delta_T}{\delta} \sim \mathrm{Pr}^{-1/2} \gg 1 \tag{2.38}$$

The first assumption, $\delta_T \gg \delta$, is therefore valid in the limit $\mathrm{Pr}^{1/2} \ll 1$, which represents the range occupied by liquid metals. The heat transfer coefficient corresponding to the low-Prandtl number limit is

$$h \sim \frac{k}{L} \mathrm{Pr}^{1/2} \mathrm{Re}_L^{1/2} \qquad (\mathrm{Pr} \ll 1) \qquad (2.39)$$

or, expressed as a Nusselt number $\mathrm{Nu} = hL/k$,

$$\mathrm{Nu} \sim \mathrm{Pr}^{1/2} \mathrm{Re}_L^{1/2} \qquad (2.40)$$

2.   *Thin thermal boundary layer, $\delta_T \ll \delta$.* Of considerably greater interest is the class of fluids with Prandtl numbers of order 1 (e.g., air) or greater than 1 (e.g., water or oils). As shown in Fig. 2.2b, the thermal thickness is assumed smaller than the velocity thickness. Geometrically, it is clear that the scale of u in the δ_T layer is not U_∞ but

$$u \sim U_\infty \frac{\delta_T}{\delta} \qquad (2.41)$$
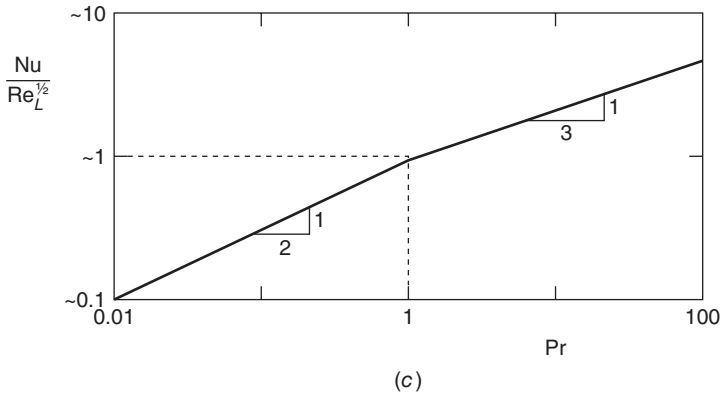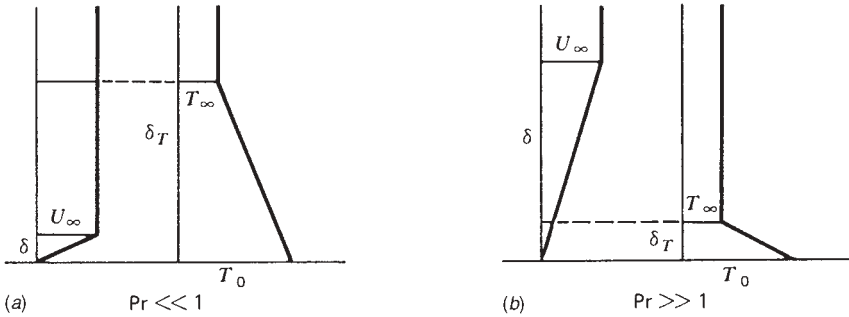
Figure 2.2   Prandtl number effect on the relative thickness of the velocity and temperature boundary layers and on heat transfer.

Next, in eq. (2.35) we note that $u/L \sim v/\delta_T$ because of mass conservation, and therefore $u/L \sim \alpha/\delta_T^2$. Combining this scale relation with eq. (2.41), after using eq. (2.31) we obtain

$$\frac{\delta_T}{L} \sim \mathrm{Pr}^{-1/3}\,\mathrm{Re}_L^{-1/2} \tag{2.42}$$

which means that

$$\frac{\delta_T}{\delta} \sim \mathrm{Pr}^{-1/3} \ll 1 \tag{2.43}$$

Thus, the assumption $\delta_T \ll \delta$ is valid in the case of $\mathrm{Pr}^{1/3} \gg 1$ fluids. The heat transfer coefficient and Nusselt number vary as

$$h \sim \frac{k}{L}\,\mathrm{Pr}^{1/3}\,\mathrm{Re}_L^{1/2} \qquad (\mathrm{Pr} \gg 1) \tag{2.44}$$

$$\mathrm{Nu} \sim \mathrm{Pr}^{1/3}\,\mathrm{Re}_L^{1/2} \qquad (\mathrm{Pr} \gg 1) \tag{2.45}$$

where $\mathrm{Nu} = hL/k$. These scaling results agree within a factor of order unity with the classical analytical results discussed next.

The thermal boundary layer thickness δ_T is the transversal distance to which thermal diffusion spreads, which happens during the time $t_{\delta_T} \sim \delta_T^2/\alpha$. When $\mathrm{Pr} < 1$, the longitudinal speed inside the δ_T layer is U_∞, and the time of longitudinal sweep is $t_L \sim L/U_\infty$. From the observation that t_{δ_T} and t_L represent the same time scale follows the δ_T scale derived in eq. (2.37). When $\mathrm{Pr} > 1$, the scale of the longitudinal speed inside the δ_T layer is $(\delta_T/\delta)U_\infty$ (cf. Fig. 2.2b), and the time of longitudinal sweep is $L/[(\delta_T/\delta)U_\infty]$. Setting this time scale equal to the transversal diffusion time δ_T^2/α and using eq. (2.30), we arrive at eq. (2.43). In summary, the boundary layer thickness is the thickness of the slender space covered by transversal diffusion while the moving material sweeps the wall longitudinally.

The meaning of Reynolds number. An important observation concerns eq. (2.31), which is the first place we encounter the Reynolds number in external flow, $\mathrm{Re}_L = U_\infty L/\nu$. In most treatments of fluid mechanics, the Reynolds number is described as the order of magnitude of the inertia/friction ratio in a particular flow (see Problem 1.12). This interpretation is not correct because in the boundary layer region examined above, there is always *a balance* between inertia and friction, whereas Re_L can reach as high as 10^5 before the transition to turbulent flow (Table 6.1). The only physical interpretation of the Reynolds number in boundary layer flow is geometric

$$\mathrm{Re}_L^{1/2} = \frac{\text{wall length}}{\text{boundary layer thickness}}$$

In other words, it is not Re_L, but the square root of Re_L, that means something: $\mathrm{Re}_L^{1/2}$ is *a geometric parameter of the flow region*—the *slenderness ratio*.

It is also worth noting that according to eq. (2.30), δ must be proportional to $L^{1/2}$. More refined analyses described later in this chapter confirm that along the wall ($0 < x < L$), the boundary layer thickness increases as $x^{1/2}$. Now, one particular property of the $x^{1/2}$ function is that its slope is infinite at $x = 0$, as shown in Fig. 2.8. This geometric feature of the boundary layer is inexplicably absent from the graphics employed by most texts that teach boundary layer theory. Most texts show sketches of boundary layers with sharp tips (finite slope at the tip), which are incorrect from the point of view of boundary layer theory.

Scale analysis was formulated and recommended as a problem-solving method in the first edition of this book [13] and elsewhere during that period [14, 15]. The method has been used widely in the intervening years in both research and education. One example is Bhattacharjee and Grosshandler's [16] original analysis of the pressure-driven jet near a hot wall. Costa [17] formulated a unified treatment of convection by identifying first the time scales of the respective growth processes. Weyburne [18] developed a new mathematical formulation of the fluid boundary layer.

2.4   INTEGRAL SOLUTIONS

The next step toward refining the answers to the friction and heat transfer questions (2.3) and (2.6) amounts to determining the numerical factors missing from the scaling laws (2.32), (2.39), and (2.44). So far, the scaling laws tell us the *manner* in which various flow and geometric parameters affect τ and h. For example, we now know that both τ and h are proportional to $L^{-1/2}$, meaning that the skin friction and heat flux are more intense near the leading edge of the flat plate. In scale analysis, we made no distinction between the *local* values of τ and h (the values right at $x = L$) and the *average* values τ_{0-L} and h_{0-L}, defined as (these average values are also abbreviated as $\overline{\tau}$ and $\overline{h}$)

$$\tau_{0-L} = \frac{1}{L} \int_0^L \tau \, dx, \qquad h_{0-L} = \frac{1}{L} \int_0^L h \, dx \qquad (2.46)$$

The reason for such treatment is that average quantities $(\tau,h)_{0-L}$ have the same scale as the τ and h evaluated at $x = L$; this scaling conclusion is easily drawn from eqs. (2.46) and the specific (more exact) results developed in the remainder of this chapter.

The *integral* approach to solving the boundary layer equations is an important piece of analysis developed by Prandtl's disciples Pohlhausen (doctoral student) and von Kármán (postdoc) in the first decades of this century. The philosophy on which this approach is based is the same philosophy that allowed Prandtl to separate from an immense and complicated flow field only the region *most relevant* to answering the practical question at hand.

In the integral method, we look at the definitions of τ and h [eqs. (2.3) and (2.6)] and recognize that what we need is not a complete solution for the velocity
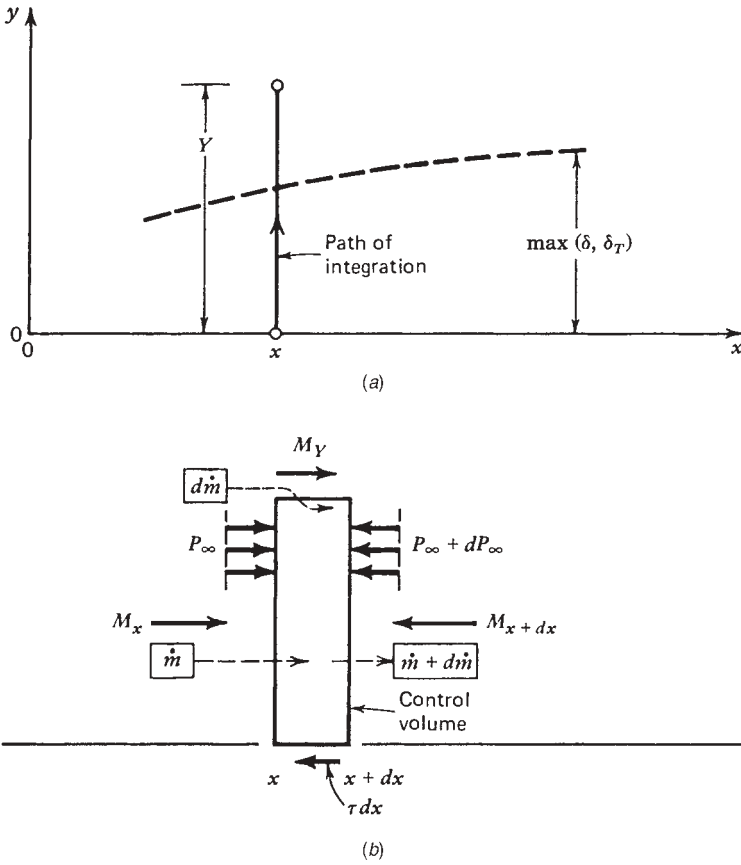
Figure 2.3 Derivation of the integral boundary layer equations: force balance on a control volume of height Y and thickness dx.

$u(x,y)$ and temperature $T(x,y)$ near the wall, but only the gradients $\partial(u,T)/\partial y$ evaluated at $y = 0$. Because the $y > 0$ variation of u and T is not the most relevant to evaluating τ and h, we have the opportunity to simplify the boundary layer equations (2.26) and (2.27) by eliminating y as a variable. As shown in Fig. 2.3, this is accomplished by integrating each equation term by term from $y = 0$ to $y = Y$, where $Y > \max(\delta, \delta_T)$ is situated in the free stream.

Before integrating, it is useful to rewrite eqs. (2.26) and (2.27) as

$$\frac{\partial}{\partial x}(u^2) + \frac{\partial}{\partial y}(uv) = -\frac{1}{\rho}\frac{dP_\infty}{dx} + \nu\frac{\partial^2 u}{\partial y^2} \qquad (2.47)$$

$$\frac{\partial}{\partial x}(uT) + \frac{\partial}{\partial y}(vT) = \alpha\frac{\partial^2 T}{\partial y^2} \qquad (2.48)$$

Form (2.47) is obtained by multiplying the left-hand side of the mass conservation equation (2.7) by u and adding it to the left-hand side of eq. (2.26); form (2.48) is

obtained in a similar fashion, by multiplying eq. (2.7) by T. Integrating eqs. (2.47) and (2.48) from $y = 0$ to $y = Y$ and using Leibnitz's integral formula yields

$$\frac{d}{dx} \int_0^Y u^2 \, dy + u_Y v_Y - u_0 v_0 = -\frac{1}{\rho} Y \frac{dP_\infty}{dx} + v \left(\frac{\partial u}{\partial y} \right)_Y - v \left(\frac{\partial u}{\partial y} \right)_0 \quad (2.49)$$

$$\frac{d}{dx} \int_0^Y uT \, dy + v_Y T_Y - v_0 T_0 = \alpha \left(\frac{\partial T}{\partial y} \right)_Y - \alpha \left(\frac{\partial T}{\partial y} \right)_0 \quad (2.50)$$

in which the indexes Y and 0 indicate the level y where the respective quantities are to be evaluated. Because the free stream is uniform, we note that $(\partial/\partial y)_Y = 0$, $u_Y = U_\infty$, and $T_Y = T_\infty$. Also, since the wall is impermeable, $v_0 = 0$, and we evaluate v_Y by performing the same integral on the continuity equation (2.7),

$$\frac{d}{dx} \int_0^Y u \, dy + v_Y - v_0 = 0 \quad (2.51)$$

Substituting v_Y into eqs. (2.49) and (2.50), assuming that T_∞ is, in general, a function of x, and rearranging the resulting expression, we obtain, finally,

$$\frac{d}{dx} \int_0^Y u(U_\infty - u) \, dy = \frac{1}{\rho} Y \frac{dP_\infty}{dx} + \frac{dU_\infty}{dx} \int_0^Y u \, dy + v \left(\frac{\partial u}{\partial y} \right)_0 \quad (2.52)$$

$$\frac{d}{dx} \int_0^Y u(T_\infty - T) \, dy = \frac{dT_\infty}{dx} \int_0^Y u \, dy + \alpha \left(\frac{\partial T}{\partial y} \right)_0 \quad (2.53)$$

These are the integral boundary layer equations for momentum and energy. They account for the conservation of momentum and energy not at every point (x,y) as eqs. (2.26) and (2.27), but in every *slice* of thickness dx and height Y (see Fig. 2.3b). Note that eqs. (2.52) and (2.53) can also be derived by invoking the x momentum theorem and the first law of thermodynamics (Chapter 1) for the control volume of size $Y \times dx$ shown in Fig. 2.3b. For example, the momentum equation (2.52) represents the following force balance:

1. Forces acting from left to right on the control volume (Fig. 2.3b):

$$M_x = \int_0^Y \rho u^2 \, dy \quad \text{Impulse due to the flow of a stream } into \text{ the control volume}$$

$$M_Y = U_\infty \, \dot{m} \quad \text{Impulse due to the flow of fast fluid } (U_\infty) \text{ into the control volume, at a rate } \dot{m},$$

$$\text{where } \dot{m} = \int_0^Y \rho u \, dy \text{ is the mass flow rate through the slice of height } Y$$

$$P_\infty Y \quad \text{Force due to pressure}$$

2. Forces acting from right to left on the control volume (Fig. 2.3*b*):

$$M_{x+dx} = M_x + (dM_x/dx)\, dx$$ Reaction force due to flow of a stream *out* of the control volume

$$\tau\, dx$$ Tangential force due to friction

$$Y[P_\infty + (dP_\infty/dx)\, dx]$$ Force due to pressure

Setting the resultant of all these forces equal to zero, we arrive at eq. (2.52). The integral energy equation (2.53) can be obtained similarly by summing up all the heat transfer and enthalpy flow rates around the control surface.

Consider next the simplest laminar boundary layer problem—the uniform flow (U_∞, P_∞ = constants) analyzed in the preceding section. To solve for the wall shear stress now appearing explicitly in eq. (2.52), we must make an assumption as a substitute for the information we gave up when we integrated the original boundary layer equation (2.26): the *y* variation of the flow. Let us assume that the *shape* of the longitudinal velocity profile is described by

$$u = \begin{cases} U_\infty m\,(n), & 0 \le n \le 1 \\ U_\infty, & 1 \le n \end{cases} \tag{2.54}$$

where *m* is an unspecified shape function that varies from 0 to 1, and where $n = y/\delta$ (see Fig. 2.4). Substituting this assumption into eq. (2.52) and noting that $dP_\infty/dx = 0$ and $dU_\infty/dx = 0$ yields a first-order ordinary differential equation for the velocity boundary layer thickness $\delta(x)$,

$$\delta\, \frac{d\delta}{dx}\left[\int_0^1 m\,(1-m)\, dn\right] = \frac{\nu}{U_\infty}\left(\frac{dm}{dn}\right)_{n=0} \tag{2.55}$$

The resulting expressions for *local* boundary layer thickness and skin friction coefficient are

$$\frac{\delta}{x} = a_1\, \mathrm{Re}_x^{-1/2} \tag{2.56}$$

$$C_{f,x} = \frac{\tau}{\frac{1}{2}\rho U_\infty^2} = a_2\, \mathrm{Re}_x^{-1/2} \tag{2.57}$$

with the following notation:

$$a_1 = \left[\frac{2(dm/dn)_{n=0}}{\int_0^1 m(1-m)\, dn}\right]^{1/2} \tag{2.56'}$$

$$a_2 = \left[2\left(\frac{dm}{dn}\right)_{n=0}\int_0^1 m(1-m)\, dn\right]^{1/2} \tag{2.57'}$$
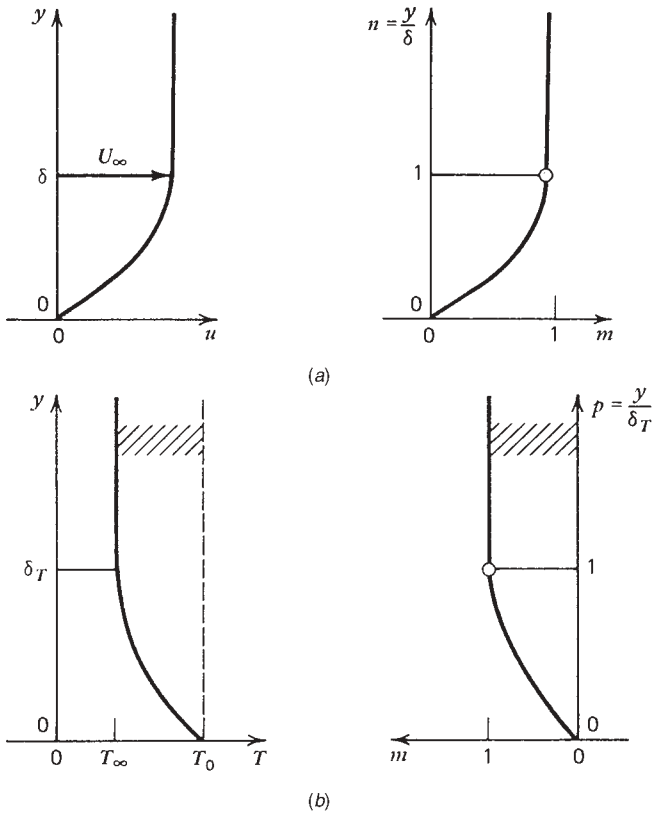
Figure 2.4 Selection of (a) velocity profile and (b) temperature profile for integral boundary layer analysis.

Results (2.56) and (2.57) agree in an order-of-magnitude sense with the earlier conclusions [eqs. (2.31) and (2.33)]. The numerical coefficients a_1 and a_2 are of order 1 and depend on the assumption made for the profile shape function m: Table 2.1 shows that as long as this shape is reasonable,[*] the choice of $m(n)$ does not influence the skin friction result appreciably.

Heat transfer coefficient information is extracted in a similar fashion from eq. (2.53) with $dT_\infty/dx = 0$. Thus, we assume the temperature profile shapes

$$T_0 - T = (T_0 - T_\infty)m(p), \qquad\qquad 0 \le p \le 1$$

$$T = T_\infty, \qquad\qquad 1 \le p \qquad (2.58)$$

with $p = y/\delta_T$. Educated by the scale analysis discussed earlier [see eqs. (2.38) and (2.43)], we assume that

$$\frac{\delta_T}{\delta} = \Delta \qquad\qquad (2.59)$$

---

[*]A function that increases from $n = 0$ to $n = 1$ monotonically and smoothly and that has a finite slope at $n = 0$.

Table 2.1 Impact of the assumed profile shape on the integral solution to the laminar boundary layer friction and heat transfer problem

Profile Shape $m(n)$ or $m(p)$ (Fig. 2.4)	$\dfrac{\delta}{x}\mathrm{Re}_x^{1/2}$	$C_{f,x}\,\mathrm{Re}_x^{1/2}$	Nu $\mathrm{Re}_x^{-1/2}\,\mathrm{Pr}^{-1/3}$ Uniform Temperature (Pr > 1)	Uniform Heat Flux (Pr > 1)
$m = n$	3.46	0.577	0.289	0.364
$m = (n/2)\,(3 - n^2)$	4.64	0.646	0.331	0.417
$m = \sin\,(\pi n/2)$	4.8	0.654	0.337	0.424
Similarity solution	4.92[a]	0.664	0.332	0.453

Source: After Ref. 19.
[a]Thickness defined as the y value corresponding to $u/U_\infty = 0.99$.

where Δ is a function of Prandtl number only and δ is given by eq. (2.56). Based on these assumptions and $\delta_T < \delta$ (high-Pr fluids), the integral energy equation (2.53) reduces to

$$\mathrm{Pr} = \frac{2(dm/dp)_{p=0}}{(a_1\Delta)^2}\left[\int_0^1 m\,(p\Delta)\,[1 - m(p)]\,dp\right]^{-1} \tag{2.60}$$

This result is an implicit expression for thickness ratio $\Delta(\mathrm{Pr})$, thus confirming the validity of the scaling arguments on which eq. (2.59) was based.

Assuming the simplest temperature profile, $m = p$, expression (2.60) becomes

$$\Delta = \mathrm{Pr}^{-1/3} \tag{2.61}$$

which is numerically identical to the scaling law for $\mathrm{Pr} \gg 1$ fluids [eq. (2.43)]. As shown by Table 2.1, other choices of profile shape $m(p)$ change the proportionality factor in eq. (2.61) by only percentage points. The results usually listed in the literature correspond to the cubic profile $m = (p/2)(3 - p^2)$:

$$\Delta = \frac{\delta_T}{\delta} = 0.976\mathrm{Pr}^{-1/3} \tag{2.62}$$

$$h = 0.331\frac{k}{x}\mathrm{Pr}^{1/3}\,\mathrm{Re}_x^{1/2} \tag{2.63}$$

$$\mathrm{Nu} = \frac{hx}{k}$$

$$= 0.331\mathrm{Pr}^{1/3}\,\mathrm{Re}_x^{1/2} \tag{2.64}$$

Again, the local heat transfer results listed above are anticipated correctly by the scale analysis [eqs. (2.44) and (2.45)].

In the case of liquid metals ($\Delta \gg 1$), instead of eq. (2.60), we obtain

$$\mathrm{Pr} = \frac{2(dm/dp)_{p=0}}{(a_1 \Delta)^2} \left[\int_0^{1/\Delta} m\,(p\Delta)\,[1 - m(p)]\,dp + \int_{1/\Delta}^1 [1 - m(p)]\,dp \right]^{-1}$$

(2.65)

The sum of two integrals stems from the fact that when $\delta_T \gg \delta$, immediately next to the wall ($0 < y < \delta$), the velocity is described by the assumed shape $U_\infty m$, whereas for $\delta < y < \delta_T$, the velocity is uniform, $u = U_\infty$ [eq. (2.54)]. Since Δ is much greater than unity, the second integral dominates in eq. (2.65). Taking the simplest profile $m = p$, we obtain

$$\Delta = \frac{\delta_T}{\delta} = (3\mathrm{Pr})^{-1/2} \qquad (\mathrm{Pr} \ll 1) \tag{2.66}$$

In other words,

$$\frac{\delta_T}{x} = 2\mathrm{Pr}^{-1/2}\,\mathrm{Re}_x^{-1/2} \qquad (\mathrm{Pr} \ll 1) \tag{2.67}$$

From eq. (2.6), we derive the local heat transfer coefficient

$$h = \frac{k}{\delta_T} = \frac{1}{2}\frac{k}{x}\mathrm{Pr}^{1/2}\,\mathrm{Re}_x^{1/2} \qquad (\mathrm{Pr} \ll 1) \tag{2.68}$$

or the local Nusselt number

$$\mathrm{Nu} = \frac{hx}{k} = \frac{1}{2}\mathrm{Pr}^{1/2}\,\mathrm{Re}_x^{1/2} \qquad (\mathrm{Pr} \ll 1) \tag{2.69}$$

These results compare favorably with the scaling laws [eqs. (2.37)–(2.40)]. As shown in Section 2.5, they also compare favorably with more exact (and expensive) solutions.

2.5   SIMILARITY SOLUTIONS

2.5.1   Method

In this section we review the exact solutions to the boundary layer problem of Fig. 2.1, solutions due to two of Prandtl's doctoral students: Blasius [20] for the flow problem and Pohlhausen [21] for the heat transfer problem. Relative to the integral solutions presented in Section 2.4, the Blasius–Pohlhausen solutions have the added benefit that they describe the y variation of the flow and temperature fields in the boundary layer regions.

The basic idea in the construction of these solutions is the observation that from one location x to another, the u and T profiles look *similar* (hence, the name *similarity solutions*). Geometry, similarity, pattern and design (drawing) are at
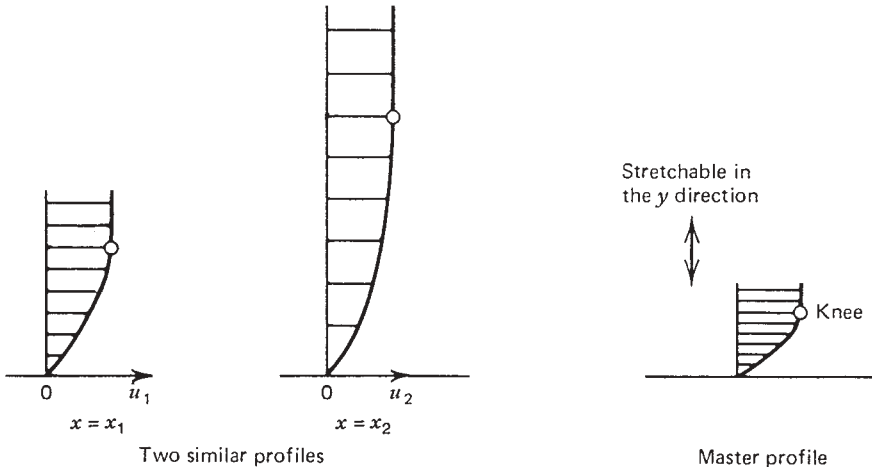
Figure 2.5   Construction of similar profiles in the analysis of velocity boundary layers.

the core of science [3]. Figure 2.5 shows that although more and more fluid slows down near the wall as x increases, the longitudinal velocity is always $u = 0$ at the wall and $u = U_\infty$ sufficiently far from the wall.

Imagine that the two profiles $u_1(y)$ and $u_2(y)$ were drawn by an artist who used the master profile shown in Fig. 2.5; like the elastic metal band of a wristwatch, this master profile can be stretched appropriately at x_1 and x_2 so as to fit the actual velocity profiles. Mathematically, the stretching of a master profile amounts to writing

$$\frac{u}{U_\infty} = \text{function}(\eta) \tag{2.70}$$

where the *similarity variable* η is proportional to y and the proportionality factor depends on x. Based on the scaling laws we already know, it is fairly obvious that η must be proportional to $y/\delta(x)$, with $\delta \sim x\,\text{Re}_x^{-1/2}$. We assume, therefore, that

$$\frac{u}{U_\infty} = f'(\eta), \quad \eta = \frac{y}{x}\text{Re}_x^{1/2} \tag{2.71}$$

Function $f' = df/d\eta$ is presently unknown and accounts for the shape of the master profile; this function is the object of the following analysis. The flow problem can be restated as the conservation of mass and momentum at every point in a $P_\infty = \text{constant}$ boundary layer:

$$\frac{\partial u}{\partial x} + \frac{\partial v}{\partial y} = 0 \tag{2.72}$$

$$u\frac{\partial u}{\partial x} + v\frac{\partial u}{\partial y} = \nu\frac{\partial^2 u}{\partial y^2} \tag{2.73}$$

subject only to three boundary conditions

$$u = v = 0 \qquad \text{at } y = 0 \tag{2.74}$$

$$u \to U_\infty \qquad \text{as } y \to \infty \tag{2.75}$$

A useful bit of shorthand is the streamfunction $\psi(x,y)$, defined as

$$u = \frac{\partial \psi}{\partial y}, \qquad v = -\frac{\partial \psi}{\partial x} \tag{2.76}$$

so that the continuity equation (2.72) is satisfied identically (see Section 1.6). In terms of the streamfunction, the problem (2.72)–(2.75) consists of solving

$$\frac{\partial \psi}{\partial y} \frac{\partial^2 \psi}{\partial x \partial y} - \frac{\partial \psi}{\partial x} \frac{\partial^2 \psi}{\partial y^2} = \nu \frac{\partial^3 \psi}{\partial y^3} \tag{2.77}$$

subject to

$$\frac{\partial \psi}{\partial y} = 0, \quad \psi = 0 \text{ at } y = 0 \tag{2.78}$$

$$\frac{\partial \psi}{\partial y} \to U_\infty \quad \text{as } y \to \infty \tag{2.79}$$

This problem is finally placed in the language of the similarity transformation (2.70) and (2.71) by evaluating ψ and its derivatives. For example, from the first of eqs. (2.76), we obtain

$$\psi = (U_\infty \nu x)^{1/2} f(\eta) \tag{2.80}$$

and from the second of eqs. (2.76),

$$v = \frac{1}{2} \left(\frac{\nu U_\infty}{x} \right)^{1/2} (\eta f' - f) \tag{2.81}$$

Expressions for the partial derivatives of ψ appearing in eq. (2.77) are obtained by keeping in mind that according to eq. (2.80), ψ depends on x directly and via $\eta(x,y)$. The similarity statement of the problem (2.77)–(2.79) reduces to

$$2f''' + ff'' = 0 \tag{2.82}$$

with the following boundary conditions:

$$f' = f = 0 \quad \text{at } \eta = 0 \tag{2.83}$$

$$f' \to 1 \quad \text{as } \eta \to \infty \tag{2.84}$$

2.5.2 Flow Solution

Equation (2.82) is nonlinear; Blasius solved it approximately by the method of matched asymptotic expansions (see Problem 2.2). Blasius's method as well as a number of more recent solutions are reviewed in Schlichting and Gersten [22]. The numerical shooting method, in which shooting is required only once, is described in Problem 2.3.

The resulting velocity profile f' is shown in Fig. 2.6: u reaches U_∞ asymptotically as η tends to infinity. Unlike in the integral solution based on linear profiles, there is no clear *knee* in the u/U_∞ curve to mark the boundary layer thickness δ. For this reason, in the Blasius profile, δ is defined based on *convention*. Numerically, it is found that $u = 0.99U_\infty$ at $\eta = 4.92$; the boundary layer thickness is taken as equal to the value of y corresponding to 99 percent of U_∞:

$$\frac{\delta}{x} = 4.92 \mathrm{Re}_x^{-1/2} \tag{2.85}$$
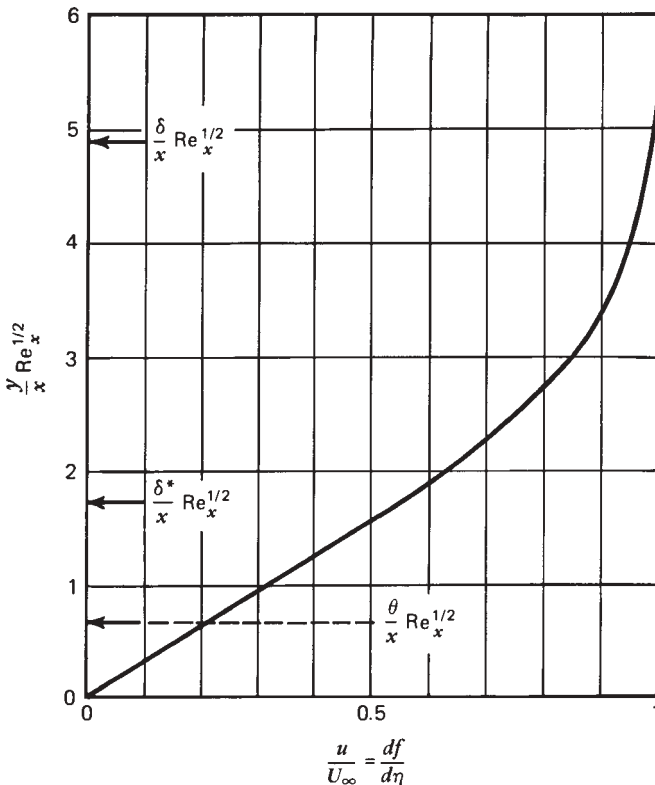
Figure 2.6 Similarity velocity profile for laminar boundary layer flow on a plate aligned with a free stream.

To get around the need for convention in defining δ, two other thicknesses have been in use in the field of boundary layer theory:

Displacement thickness:

$$\delta^* = \int_0^\infty \left(1 - \frac{u}{U_\infty}\right) dy \tag{2.86}$$

Momentum thickness:

$$\theta = \int_0^\infty \frac{u}{U_\infty} \left(1 - \frac{u}{U_\infty}\right) dy \tag{2.87}$$

As shown in Fig. 2.7, the displacement thickness is a measure of the fraction of the original free stream slowed down viscously by the wall

$$\delta^* U_\infty = \int_0^\infty U_\infty \, dy - \int_0^\infty u \, dy \tag{2.88}$$

The dotted line in Fig. 2.7 shows that at any x, the free stream appears to be displaced away from the wall so that it can avoid and flow past the fluid viscously stuck to the wall.

The momentum thickness θ is based on a similar argument: It is a measure of the longitudinal momentum missing at any x relative to the original ($x = 0$) amount

$$\theta U_\infty^2 = \underbrace{\int_0^\infty U_\infty^2 \, dy}_{\substack{x \text{ momentum} \\ \text{at } x = 0}} - \underbrace{\int_0^\infty U^2 \, dy}_{\substack{x \text{ momentum} \\ \text{at any } x}} - \underbrace{U_\infty \int_0^\infty (U_\infty - u) \, dy}_{\substack{x \text{ momentum of the} \\ \text{fluid displaced out of the} \\ \text{boundary layer region}}} \tag{2.89}$$
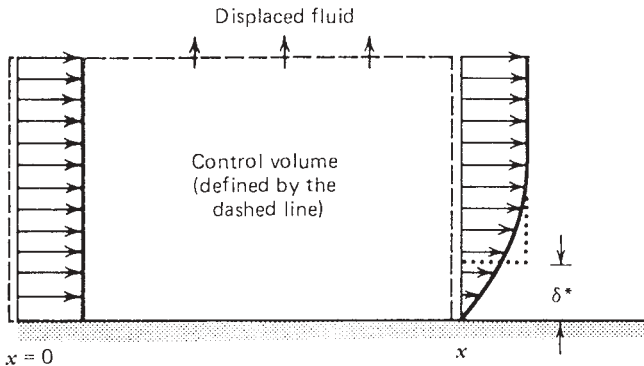
Figure 2.7 Displacement thickness δ^* and its physical interpretation.

Note that expression (2.87) is a restatement of the left-hand side of the integral momentum equation (2.52). The displacement and momentum thicknesses for the Blasius similarity solution (Fig. 2.6) are

$$\frac{\delta^*}{x} = 1.73 \text{Re}_x^{-1/2}, \qquad \frac{\theta}{x} = 0.664 \text{Re}_x^{-1/2} \tag{2.90}$$

Finally, the local skin friction coefficient predicted from the similarity solution is

$$C_{f,x} = \frac{\mu(\partial u/\partial y)_0}{\frac{1}{2}\rho U_\infty^2} = 2(f'')_{\eta=0} \text{ Re}_x^{-1/2} \tag{2.91}$$

Numerically, it is found that $(f'')_{y=0} = 0.332$ [23]; hence,

$$C_{f,x} = 0.664 \text{Re}_x^{-1/2} \tag{2.92}$$

This result is not far from any of the considerably less laborious predictions based on the integral method (Table 2.1). The average skin friction coefficient that corresponds to the local result (2.92) is

$$C_{f,0-x} = \frac{\tau_{0-x}}{\frac{1}{2}\rho U_\infty^2} = 1.328 \text{Re}_x^{-1/2} \tag{2.92'}$$

In other words, the value averaged from $x = 0$ to any x is twice as large as the local value calculated at x. The laminar skin friction results (2.92) and (2.92′) are valid when $\text{Re}_x \lesssim 5 \times 10^5$ (see Table 6.1).

2.5.3 Heat Transfer Solution

The heat transfer part of the problem was solved along similar lines [21]. Introducing the dimensionless similarity temperature profile

$$\theta(\eta) = \frac{T - T_0}{T_\infty - T_0} \tag{2.93}$$

the boundary layer energy equation (2.27) assumes the form

$$\theta'' + \frac{\text{Pr}}{2} f \theta' = 0 \tag{2.94}$$

This equation must be solved subject to the known wall and free-stream temperature conditions:

$$\theta = 0 \qquad \text{at } \eta = 0 \tag{2.95}$$

$$\theta \to 1 \qquad \text{as } \eta \to \infty \tag{2.96}$$

Note that if $\mathrm{Pr} = 1$ and $\theta = f'$, the heat transfer problem (2.94)–(2.96) becomes identical to the flow problem (2.82)–(2.84). This means that for $\mathrm{Pr} = 1$ fluids, the similarity temperature profile is already known and plotted in Fig. 2.6. In general (for any Pr), eq. (2.94) can be integrated, keeping in mind that $f(\eta)$ is a known function available in tabular form [23]. Via separation of variables, we integrate eq. (2.94) and obtain

$$\theta'(\eta) = \theta'(0) \exp\left[-\frac{\mathrm{Pr}}{2} \int_0^\eta f(\beta)\, d\beta\right] \tag{2.97}$$

Integrating again from 0 to η and using the wall condition (2.95) yields

$$\theta(\eta) = \theta'(0) \int_0^\eta \exp\left[-\frac{\mathrm{Pr}}{2} \int_0^\gamma f(\beta)\, d\beta\right] d\gamma \tag{2.98}$$

where β and γ are two dummy variables. The solution for $\theta(\eta)$ above depends on an unknown constant of integration, $\theta'(0)$, because the free-stream condition (2.96) has not been used yet; using it, we find that

$$\theta'(0) = \left\{\int_0^\infty \exp\left[-\frac{\mathrm{Pr}}{2} \int_0^\gamma f(\beta)\, d\beta\right] d\gamma\right\}^{-1} \tag{2.99}$$

The solution is now complete. The value of $\theta'(0)$ is all important in calculating the heat transfer coefficient: From eq. (2.6), we learn that

$$h = \frac{k}{x} \mathrm{Re}_x^{1/2}\ \theta'(0) \tag{2.100}$$

Hence,

$$\mathrm{Nu} = \frac{hx}{k} = \theta'(0)\,\mathrm{Re}_x^{1/2} \tag{2.101}$$

As shown by eq. (2.99), $\theta'(0)$ is a function of the Prandtl number that accounts for the relationship between Nu and Pr predicted on scaling grounds early in this chapter. Pohlhausen [21] calculated several $\theta'(0)$ values that for $\mathrm{Pr} > 0.5$ are correlated accurately by

$$\theta'(0) = 0.332\mathrm{Pr}^{1/3} \tag{2.102}$$

The theoretical basis for this correlation is contained in the discussion leading to eq. (2.45). The similarity solution for the local heat transfer coefficient (local Nusselt number) is therefore

$$\mathrm{Nu} = 0.332\mathrm{Pr}^{1/3}\,\mathrm{Re}_x^{1/2} \qquad (\mathrm{Pr} > 0.5) \tag{2.103}$$

Another correlation must be used below $\mathrm{Pr} < 0.5$, or if the Prandtl number of a particular liquid metal is given, eq. (2.99) should be solved once for that

particular Pr. It is even better to develop an analytical replacement for the Nu formula (2.103) in the limit Pr $\to$ 0. According to Fig. 2.2a, in highly conductive fluids the velocity boundary layer is much thinner than the thermal layer. Therefore, in this limit it is permissible to set $f' = 1$ in the region occupied by the thermal boundary layer $\theta(\eta)$. Differentiating eq. (2.94) once, we obtain

$$\frac{d}{d\eta}\left(\frac{\theta''}{\theta'}\right) = -\frac{\Pr}{2}f' \tag{2.104}$$

This equation leads to an explicit solution for $\theta(\eta)$ in the limit Pr $\to$ 0. The ensuing analysis is proposed as an exercise; its chief results are

$$\theta(\eta) = \operatorname{erf}\left(\frac{\eta}{2}\Pr^{1/2}\right) \tag{2.105}$$

$$\theta'(0) = \left(\frac{\Pr}{\pi}\right)^{1/2} \tag{2.106}$$

$$\mathrm{Nu} = \frac{hx}{k} = 0.564 \Pr^{1/2}\mathrm{Re}_x^{1/2} \qquad (\Pr \to 0) \tag{2.107}$$

This limiting heat transfer result actually holds for Pr < 0.5 and compares favorably with the scaling law (2.40).

The total heat transfer rate between the x-long wall and the adjacent flow, per unit length in the direction normal to the plane of Fig. 2.1, is

$$\int_0^x q'' \, dx = xq''_{0-x} \tag{2.108}$$

Equation (2.108) is the definition of the x-averaged wall heat flux q''_{0-x}; this can be calculated by substituting eqs. (2.103) and (2.107) into Nu $= hx/k$, with $h = q''/(T_0 - T_\infty)$. The average heat flux obtained in this manner can be non-dimensionalized as the *overall* Nusselt number:

$$\mathrm{Nu}_{0-x} = \frac{q''_{0-x}}{T_0 - T_\infty}\frac{x}{k} = \frac{h_{0-x}x}{k} \tag{2.109}$$

where h_{0-x} is the average heat transfer coefficient. The overall Nusselt number formulas that correspond* to the local Nusselt number asymptotes (2.103) and (2.107) are

$$\mathrm{Nu}_{0-x} = \begin{cases} 0.664 \Pr^{1/3}\mathrm{Re}_x^{1/2} & (\Pr > 0.5) & (2.110) \\ 1.128 \Pr^{1/2}\mathrm{Re}_x^{1/2} & (\Pr < 0.5) & (2.111) \end{cases}$$

---

*The average heat transfer coefficient that corresponds to a local heat transfer coefficient expression can be estimated rapidly by invoking the following theorem. If the local quantity h has a power law dependence on x,

$$h = Cx^n \tag{a}$$

where C is a constant, the quantity averaged from $x = 0$ to x is simply

$$h_{0-x} = \frac{h}{1+n} \tag{b}$$

in which—it is worth noting—the numerical coefficients are twice as large as the coefficients of eqs. (2.103) and (2.107). An overall Nusselt number expression that covers the entire Prandtl number range was recommended by Churchill and Ozoe [24]:

$$Nu_{0-x} = \frac{0.928 Pr^{1/3} Re_x^{1/2}}{[1 + (0.0207/Pr)^{2/3}]^{1/4}} \tag{2.112}$$

It is valid when the Péclet number $Pe_x = U_\infty x/\alpha = Re_x Pr$ is greater than approximately 100. The laminar heat transfer results developed in this section are valid when $Re_x \lesssim 5 \times 10^5$ (see Table 6.1).

In concluding this section, it is worth noting the imperfect character of boundary layer theory and the approximation built into the *exact similarity solution*. Examination of the Blasius solution for the velocity normal to the wall shows that v tends to a finite value, $0.86 U_\infty Re_x^{-1/2}$, as η tends to infinity. This feature distinguishes the boundary layer problem from the complete problem stated in eqs. (2.7)–(2.11), where v must vanish sufficiently far from the wall [condition (v), eq. (2.11)]. Because in boundary layer theory $v/U_\infty \sim Re_x^{-1/2}$ as $\eta \to \infty$, this theory becomes ''better'' as $Re_x^{1/2}$ increases, that is, as the boundary layer region becomes more slender. Other limitations of the theory were discussed earlier in connection with the breakdown of the *slenderness* feature in the region near the tip [see the discussion following eq. (2.31)].

2.6   OTHER WALL HEATING CONDITIONS

What we have seen so far is the competition between three methodologies (scaling, integral, similarity) in the search for answers to the basic questions of convective heat transfer. The laminar boundary layer near an isothermal flat plate was the simplest and, historically, oldest setting in which to witness this competition. Despite what the pure scientists among us may want us to believe, there can be no official winner in such a competition. The individual researcher with personal mathematics background and, most important, personal supply of curiosity and time can and should judiciously evaluate the worthiness of any of these methodologies relative to his ability and taste. And he or she is free to choose.

The problems we encounter in practice are diverse and, quite often, demand models that differ from the isothermal flat plate problem of Fig. 2.1. Although in each case the model and answers (C_f, Nu) are different, the conceptual basis is the same, as defined by Prandtl's boundary layer theory. Numerous advances have been made along the lines of this theory, and the most important of these are reviewed in the most recent handbook [25]. In this section we review only a few examples.

(a)

(b)
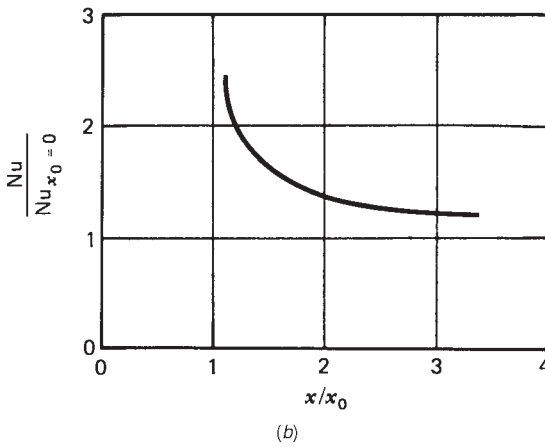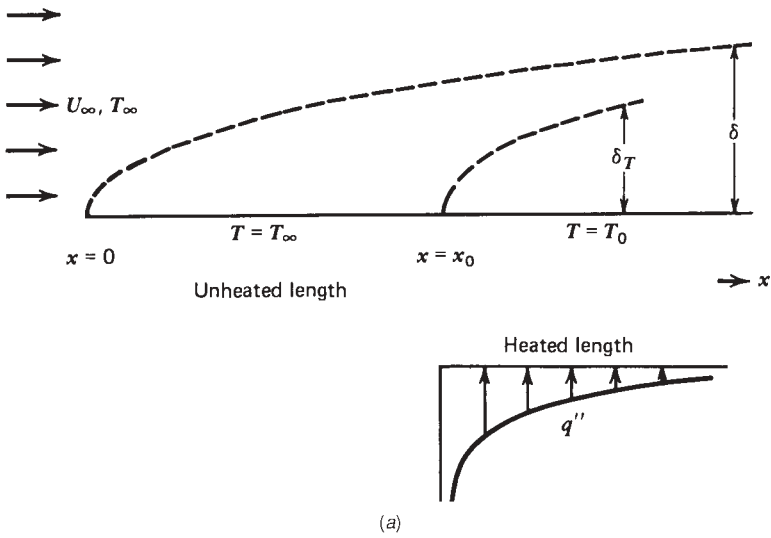
Figure 2.8   Boundary layer with unheated starting length.

2.6.1   Unheated Starting Length

In cases such as the forced convection cooling of an electric circuit board, the heating effect is distributed discretely along the flat plate. The simplest question is sketched in Fig. 2.8: What is the heat transfer rate from the wall to the fluid stream if the leading segment $0 < x < x_0$ is unheated $(T = T_\infty)$? An answer is possible based on the integral method. Assuming the temperature profile shape

$m = (p/2)(3 - p^2)$ and the velocity cubic profile shape $m = (n/2)(3 - n^2)$, the integral energy equation (2.53) yields

$$\Delta^3 + 4\Delta^2 x \frac{d\Delta}{dx} = \frac{0.929}{\text{Pr}} \tag{2.113}$$

with the general solution

$$\Delta^3 = \frac{0.929}{\text{Pr}} + Cx^{-3/4} \tag{2.114}$$

Constant C follows from the condition that heating (that is, a thermal boundary layer,) starts at $x = x_0$; hence,

$$\Delta = 0.976 \text{Pr}^{-1/3} \left[1 - \left(\frac{x_0}{x} \right)^{3/4} \right]^{1/3} \tag{2.115}$$

which is the same as eq. (2.62) if $x_0 = 0$. The local Nusselt number is

$$\text{Nu} = \frac{hx}{k} = 0.332 \text{Pr}^{1/3} \text{Re}_x^{1/2} \left[1 - \left(\frac{x_0}{x} \right)^{3/4} \right]^{-1/3} \tag{2.116}$$

As is shown in Fig. 2.8b, the effect of the unheated length x_0 on the local Nusselt number drops below 20 percent if x is beyond $3x_0$ from the leading edge of the flat plate.

2.6.2 Arbitrary Wall Temperature

The integral solution for heat transfer with an unheated starting length is the building block for the construction of heat transfer results for more complicated situations. Consider, for example, heat transfer from the heated spot $x_1 < x < x_2$, shown in Fig. 2.9c: The wall temperature upstream and downstream from the heated spot is equal to the constant free-stream value, T_∞, while the spot temperature is T_0. Since the integral energy equation (2.53) is linear in temperature, the thermal boundary layer generated by the T_0 spot can be reconstructed as the superposition of two thermal boundary layers of type (2.116). The first thermal boundary layer, $\delta_{T,1}$ (Fig. 2.9a), is the fingerprint of wall heating ($T_\infty + \Delta T$) downstream from $x = x_1$. The second thermal boundary layer (Fig. 2.9b) is the result of wall cooling ($T_\infty - \Delta T$) downstream from $x = x_2$. The superposition of the two thermal layers (Fig. 2.9c) constitutes the thermal boundary layer due to spot heating. Of interest is the heat flux q'' from the wall to the fluid. To calculate q'', we identify three distinct wall regions:

1. $0 < x < x_1$, the unheated started length, where $q'' = 0$ because the wall is in thermal equilibrium with the free stream
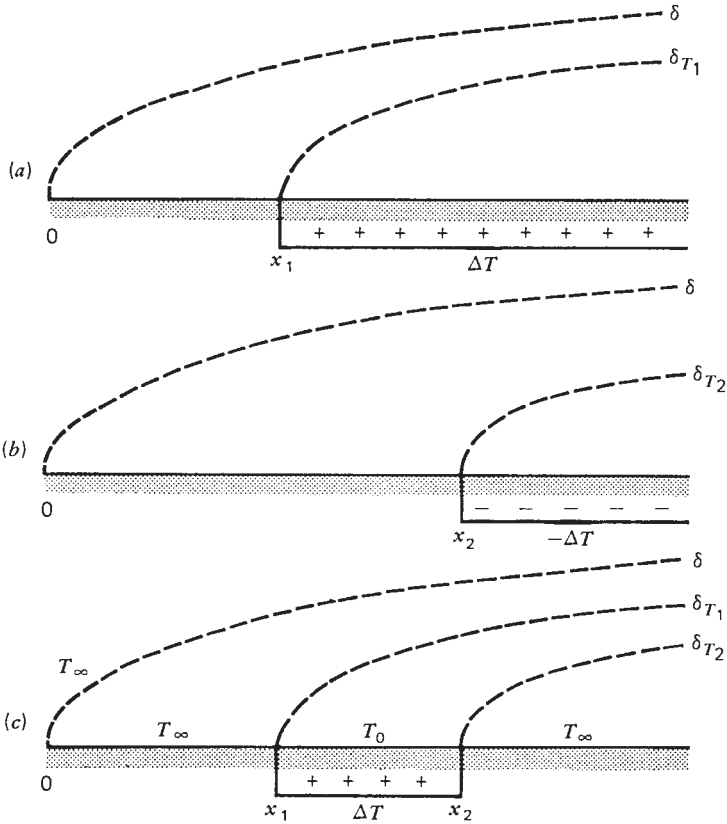
Figure 2.9 Principle of superposition in the construction of integral solutions for boundary layers with finite heated length.

2. $x_1 < x < x_2$, the heated spot, where eq. (2.116) applies unchanged:

$$q'' = 0.332 \frac{k}{x} \Pr^{1/3} \operatorname{Re}_x^{1/2} \left\{ \frac{\Delta T}{\left[1 - (x_1/x)^{3/4}\right]^{1/3}} \right\} \qquad (2.117)$$

3. $x > x_2$, the trailing section, where q'' is the superposition of two effects of type (2.117):

$$q'' = 0.332 \frac{k}{x} \Pr^{1/3} \operatorname{Re}_x^{1/2} \left\{ \frac{\Delta T}{\left[1 - (x_1/x)^{3/4}\right]^{1/3}} + \frac{-\Delta T}{[1 - (x_2/x)^{3/4}]^{1/3}} \right\} \qquad (2.118)$$

Note that since $x_2 > x_1$, the heat flux q'' in region 3 is negative. This means that in the trailing section, the wall reabsorbs part of the heat released earlier in

region 2. Result (2.118) can be generalized (e.g., Ref. 26). The heat flux from the wall to the fluid, downstream from N step changes ΔT_i in wall temperature, is given by

$$q'' = 0.332 \frac{k}{x} \mathrm{Pr}^{1/3} \mathrm{Re}_x^{1/2} \sum_{i=1}^{N} \frac{\Delta T_i}{[1 - (x_i/x)^{3/4}]^{1/3}} \qquad (2.119)$$

where x_i is the longitudinal position of each temperature step change ΔT_i. If the wall temperature varies smoothly, $T_0(x)$, formula (2.119) is replaced by its integral limit (the limit of infinitesimally small steps):

$$q'' = 0.332 \frac{k}{x} \mathrm{Pr}^{1/3} \mathrm{Re}_x^{1/2} \int_0^x \frac{(dT_0/d\xi)\, d\xi}{[1 - (\xi/x)^{3/4}]^{1/3}} \qquad (2.120)$$

The heat flux q'' in eqs. (2.117)–(2.120) is the *local* value (i.e., the heat flux at the position x along the wall). The factor 0.332, which appears on the right-hand side of eqs. (2.116)–(2.120), was borrowed from the similarity solution (2.103). The actual factor generated by the integral solution with cubic profile described in eqs. (2.113)–(2.115) is 0.331 (see Table 2.1).

2.6.3 Uniform Heat Flux

In many problems, particularly those involving the cooling of electrical and nuclear systems, the wall heat flux q'' is known. In such problems, overheating, burnout, and meltdown are very important issues; therefore, the object of heat transfer analysis is the prediction of the wall temperature variation $T_0(x)$. The design objective is to control this temperature and to keep it under an allowable limit. The heat transfer problem continues to be the calculation of heat transfer coefficient $h = q''/[T_0(x) - T_\infty]$ when the heat flux q'' is known.

The integral method and profile shapes used to generate eqs. (2.62)–(2.64) can be applied to the calculation of $T_0(x) - T_\infty$ when $q'' = $ constant is specified. One such result is (see Table 2.1)

$$\mathrm{Nu} = \frac{q''}{T_0(x) - T_\infty} \frac{x}{k} = 0.453 \mathrm{Pr}^{1/3} \mathrm{Re}_x^{1/2} \qquad (0.5 < \mathrm{Pr} < 10) \qquad (2.121)$$

The similarity solution is reported in Problems 2.7 and 2.27 and in Ref. 27. The more general result corresponding to the case of nonuniform wall heat flux $q''(x)$ is [28]

$$T_0(x) - T_\infty = \frac{0.623}{k} \mathrm{Pr}^{-1/3} \mathrm{Re}_x^{-1/2} \int_{\xi=0}^{x} \left[1 - \left(\frac{\xi}{x} \right)^{3/4} \right]^{-2/3} q''(\xi)\, d\xi$$

$$(\mathrm{Pr} > 0.5) \qquad (2.122)$$

Equations (2.116)–(2.122) are valid for fluids with Prandtl numbers of the order of 1 or greater than 1. The flow regime must be laminar, $\mathrm{Re}_x \lesssim 5 \times 10^5$.

2.6.4   Film Temperature

The wall friction and heat transfer results developed so far are based on the constant-property model, Chapter 1. In real situations, fluid properties such as k, ν, μ, and α are not constant, as they depend primarily on the local temperature in the flow field. It turns out that the constant-property formulas describe sufficiently accurately the actual convective flows encountered in applications, provided that the maximum temperature variation experienced by the fluid $(T_0 - T_\infty)$ is small relative to the *absolute* temperature level of the fluid (T_0 or T_∞, expressed in kelvin). In such cases, the properties needed for calculating the various dimensionless groups (Re, Pe, Pr, C_f, Nu) can be evaluated at the average temperature of the fluid in the thermal boundary layer,

$$T = \tfrac{1}{2}(T_0 + T_\infty) \tag{2.123}$$

This average is commonly recognized as the *film temperature* of the fluid and is generally recommended for use in formulas of the constant-property type. Worth keeping in mind is that there are special correlations in which the effect of temperature-dependent properties is taken into account by means of explicit correction factors.

2.7   LONGITUDINAL PRESSURE GRADIENT: FLOW PAST A WEDGE AND STAGNATION FLOW

The preceding results are based on the assumption that the pressure gradient term is negligible relative to inertia and friction in the boundary layer momentum equation (2.26). This assumption applies to the case of a flat wall parallel to a uniform stream. If, as shown in the sketch at the bottom of Fig. 2.10, the wall makes a positive angle $\beta/2$ with the free stream, the free stream is accelerated in the x direction along the wall (x is measured away from the tip of the wedge). Graphically, the acceleration of the flow is indicated by the gradual increase in the density of streamlines.

Neglecting the laminar boundary layer in which viscosity balances inertia, the flow engulfing the wedge of total angle β may be treated as inviscid and may be determined analytically based on potential flow theory. The inviscid flow residing outside the laminar boundary layer is governed by the balance between inertia and pressure gradients. The potential flow solution for the velocity variation along the wedge-shaped wall (i.e., along the boundary layer that coats the wall) is

$$U_\infty(x) = Cx^m \tag{2.124}$$

where C is a constant and m is related to the β angle of Fig. 2.10,

$$m = \frac{\beta}{2\pi - \beta} \tag{2.125}$$
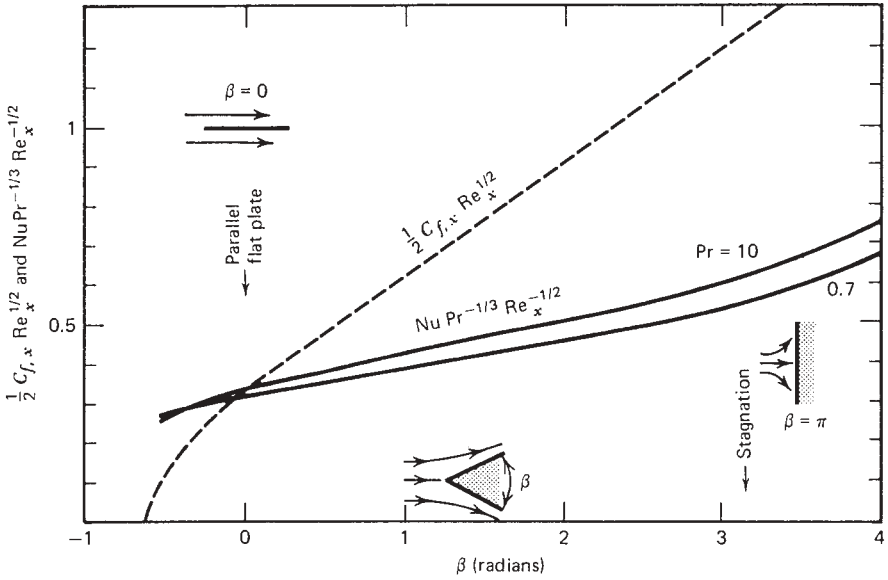
Figure 2.10   Local heat transfer and friction results for laminar boundary layer flow over an isothermal wedge-shaped body.

Invoking the Bernoulli equation along the streamline that coincides with the wall,

$$\frac{1}{\rho}\frac{dP_\infty}{dx} = -U_\infty\frac{dU_\infty}{dx} \tag{2.126}$$

and using formula (2.124), the boundary layer equation for momentum becomes

$$u\frac{\partial u}{\partial x} + v\frac{\partial u}{\partial y} = \frac{m}{x}U_\infty^2 + \nu\frac{\partial^2 u}{\partial y^2} \tag{2.127}$$

Falkner and Skan [29] showed that eq. (2.127) admits a similarity solution with m as an additional parameter (note that the Blasius solution is the special case $m = 0$). The development of the similarity equation is proposed in Problem 2.8:

$$2f''' + (m+1)ff'' + 2m[1 - (f')^2] = 0 \tag{2.128}$$

In this equation, $(\cdot)'$ is shorthand for $d(\cdot)/d\eta$, where $\eta = y(U_\infty/\nu x)^{1/2}$ and $U_\infty = Cx^m$. The longitudinal velocity is $u = U_\infty f'$. The function $f(\eta)$ can be obtained numerically by solving eq. (2.128) subject to $f(0) = 0, f'(0) = 0$, and $f'(\infty) = 1$. The resulting expression for the local skin friction coefficient is the same as in eq. (2.91),

$$C_{f,x} = 2f''(0)\,\mathrm{Re}_x^{-1/2} \tag{2.129}$$

Table 2.2   The local skin friction coefficient for laminar boundary layer flow over a wedge

β	m	$f''(0) = \frac{1}{2}C_{f,x}\mathrm{Re}_x^{1/2}$
$2\pi = 6.28$	∞	∞
$\pi = 3.14$	1	1.233 (two-dimensional stagnation)
$\pi/2 = 1.57$	$\frac{1}{3}$	0.757
$\pi/5 = 0.627$	$\frac{1}{9}$	0.512
0	0	0.332
-0.14	-0.0654	0.164
-0.199	-0.0904	0 (separation)

Source: Ref. 30.

except that now $\mathrm{Re}_x = U_\infty x/\nu = Cx^{m+1}/\nu$. Representative values of the $f''(0)$ constant are shown in Table 2.2, while Fig. 2.10 provides a bird's-eye view of the effect of the wedge angle. Relative to the case of the plate parallel to the flow ($\beta = 0$), the acceleration of the free stream brings about a substantial increase in the numerical coefficient appearing in the $C_{f,x} \sim \mathrm{Re}_x^{-1/2}$ scaling law.

The heat transfer similarity solution can be developed in the same way as Pohlhausen's solution, this time by substituting the Falkner–Skan similarity flow into the boundary layer energy equation (2.27). The wedge surface is isothermal at T_0, while the free-stream temperature is T_∞. The resulting equation for the similarity temperature profile $\theta(\eta) = (T - T_0)/(T_\infty - T_0)$ is

$$\theta'' + \frac{1}{2}\ \mathrm{Pr}(m+1)f\theta' = 0 \qquad (2.130)$$

which can be compared with eq. (2.94) to see that Pr is now replaced by $\mathrm{Pr}(m+1)$. Eckert [31] integrated eq. (2.130) subject to $\theta(0) = 0$ and $\theta(\infty) = 1$; some of his results for the local Nusselt number $\mathrm{Nu} = hx/k$ are shown in Table 2.3.

Table 2.3   Local Nusselt number $\mathrm{Nu}/\mathrm{Re}_x^{1/2}$ for laminar boundary layer flow over a wedge

		Pr				
β	m	0.7	0.8	1	5	10
-0.512	-0.0753	0.242	0.253	0.272	0.457	0.570
0	0	0.292	0.307	0.332	0.585	0.730
$\pi/5$	$\frac{1}{9}$	0.331	0.348	0.378	0.669	0.851
$\pi/2$	$\frac{1}{3}$	0.384	0.403	0.440	0.792	1.013
π	1	0.496	0.523	0.570	1.043	1.344
$8\pi/5$	4	0.813	0.858	0.938	1.736	2.236

Source: Ref. 31.

The solid curves in Fig. 2.10 show that when the proper heat transfer scaling law (2.45) is used, the group $\mathrm{Nu}/\mathrm{Pr}^{1/3}\,\mathrm{Re}_x^{1/2}$ depends mainly on the wedge angle β. The local heat transfer coefficient h varies as $x^{-1}\,\mathrm{Re}_x^{1/2}$ as x increases away from the tip. In view of eq. (2.124), this means that h varies as $x^{(m-1)/2}$. The relation between the local heat transfer coefficient at x and the heat transfer coefficient averaged from $x = 0$ to x is

$$h_{0-x} = \frac{h}{1 + (m-1)/2} = \frac{2}{1+m}\,h \qquad (2.131)$$

A special case of the general wedge geometry is the two-dimensional stagnation flow $\beta = \pi$ (or $m = 1$) sketched in Fig. 2.10. In this case, U_∞ increases as Cx away from the stagnation point, and since h varies generally as $x^{(m-1)/2}$, the local heat transfer coefficient delivered by Table 2.3 is a constant. The two-dimensional stagnation flow is a good approximation for the flow near the stagnation line on a cylinder of diameter D suspended in a cross flow with far-field velocity V. The free-stream velocity in the immediate vicinity ($x \ll D$) of the stagnation line is $U_\infty = (4V/D)x$, where x is measured along the circular perimeter away from the stagnation point. This description also holds for a two-dimensional blunt body whose cross section has a nose with the radius of curvature $D/2$.

The similarity solution for the three-dimensional stagnation flow against the nose of an axisymmetric body can be derived through the Mangler coordinate transformation [32] from a two-dimensional flow past a wedge. For fluids with constant properties and Prandtl numbers in the range covered by Table 2.3, the local heat transfer coefficient near the axisymmetric stagnation point is correlated by [33]

$$\mathrm{Nu} = 0.77\mathrm{Pr}^{0.4}\,\mathrm{Re}_x^{1/2} \qquad (2.132)$$

If the velocity of the far-field fluid is V and the radius of curvature of the axisymmetric nose is $D/2$, the free-stream velocity in the vicinity of the stagnation point ($x \ll D$) is $U_\infty = (3V/D)x$. Substituting $\mathrm{Re}_x = U_\infty x/\nu$ and $\mathrm{Nu} = hx/k$ in eq. (2.132), we find that x drops out and h is a constant. This result also applies to the near-stagnation region on a sphere of diameter D. Additional results for boundary layers with longitudinal pressure gradient are summarized by Pletcher [34]. This class of results is pivotal in the fast-developing field of electronics cooling by impinging jets (see, e.g., Ref. 35).

2.8 FLOW THROUGH THE WALL: BLOWING AND SUCTION

If the fluid can flow into or out of the wall surface, the skin friction and heat transfer coefficients can differ substantially from the results presented so far. Recall that until now the wall surface was assumed impermeable, as done in the development of the Blasius similarity solution [see eq. (2.74)]. In this section we

relax this assumption and consider the general case where the boundary layer fluid crosses the wall surface with the normal velocity $v_0(x)$, which may vary with the distance x from the leading edge of the wall. Positive v_0 values indicate *blowing*, that is, the injection of fluid (the same fluid type as in the free stream) from the wall into the boundary layer. Negative v_0 values represent *suction*, the removal of some of the boundary layer fluid by forcing it to flow through the porous surface of the wall.

To see this effect on $C_{f,x}$ and Nu_x, consider again the free stream $U_\infty = Cx^m$ that flows outside the boundary layer that coats the wedge of angle β (see Fig. 2.10). The surface is isothermal (T_0), and the fluid that crosses this surface with normal velocity v_0 has temperature T_0. Let y be the direction perpendicular to the wall. Similarity solutions for the boundary layer velocity and temperature fields can be developed only if v_0 varies as $x^{(m-1)/2}$ along the wall. The reason is that if we combine $v = -\partial\psi/\partial\xi$ with $\psi = (U_\infty vx)^{1/2}f(\eta)$, $\eta = y(U_\infty/vx)^{1/2}$, and $U_\infty = Cx^m$, we obtain

$$\psi = (Cvx^{m+1})^{1/2}f[y(C/v)^{1/2}x^{(m-1)/2}] \tag{2.133}$$

and

$$v = -\frac{\partial\psi}{\partial x} = -\frac{m+1}{2}x^{(m-1)/2}(Cv)^{1/2}f(\eta)$$
$$- (Cvx^{m+1})^{1/2}\frac{df}{d\eta}y(C/v)^{1/2}\frac{m-1}{2}x^{(m-3)/2} \tag{2.134}$$

At the wall, the normal velocity $v_0 = v(y = 0)$ reduces to

$$v_0 = -\frac{m+1}{2}x^{(m-1)/2}(Cv)^{1/2}f(0) \tag{2.135}$$

This expression shows that if $f(0) = $ constant is to be used [next to $f'(0) = 0$ and $f'(\infty) = 1$] as a boundary condition to solve eq. (2.128), v_0 must vary as $x^{(m-1)/2}$ so that x drops from both sides of eq. (2.135). For example, if the free stream is parallel to the flat wall ($m = 0$), v_0 must decrease as $x^{-1/2}$. In two-dimensional stagnation flow ($m = 1$), the blowing velocity that leads to a similarity solution is uniform (x-independent). The constant $f(0)$ that accounts for the $v = v_0$ boundary condition at $y = 0$ can be rewritten [cf. eq. (2.135)] as

$$f(0) = -\frac{2}{m+1}\frac{v_0}{U_\infty}Re_x^{1/2} \qquad \text{(constant)} \tag{2.136}$$

in which $Re_x = U_\infty x/v$. The dimensionless constant represented by the group $(v_0/U_\infty)\,Re_x^{1/2}$ is the *blowing parameter* and accounts for the effect of a finite v_0 in the flow similarity solution. The temperature profile $\theta(\eta)$ is obtained subsequently by substituting $f(\eta)$ in eq. (2.130) and using the boundary conditions $\theta(0) = 0$ and $\theta(\infty) = 1$.

Table 2.4 Effect of flow through the wall: local skin friction coefficient and Nusselt number for laminar boundary layer flow over a permeable isothermal wall parallel to the stream

$\dfrac{v_0}{U_\infty}\mathrm{Re}_x^{1/2}$	$f''(0) = \tfrac{1}{2}C_{f,x}\ \mathrm{Re}_x^{1/2}$	$\mathrm{Nu}/\mathrm{Re}_x^{1/2}$			
		Pr = 0.7	Pr = 0.8	Pr = 0.9	
−2.5	2.59	1.85	2.097	2.59	⎫
−0.75	0.945	0.722	0.797	0.945	⎬ Suction
−0.25	0.523	0.429	0.461	0.523	⎭
0	0.332	0.292	0.307	0.332	Impermeable wall
+0.25	0.165	0.166	0.166	0.165	⎫
+0.375	0.094	0.107	0.103	0.0937	⎬ Blowing
+0.5	0.036	0.0517	0.0458	0.0356	⎭
+0.619	0	0	0	0	Separation

Source: Ref. 28.

Table 2.4 shows the effect of the blowing parameter $(v_0/U_\infty)\,\mathrm{Re}_x^{1/2}$ on the local skin friction coefficient and the local Nusselt number when the wall is parallel to the free stream ($m = 0$). The table is based on two compilations of data made by Kays and Crawford [28]. The middle line of the table serves as reference and corresponds to the impermeable wall, which is covered by the Blasius and Pohlhausen solutions of Section 2.5. Worth noting is that in the range covered by Table 2.4, the blowing parameter is on the order of 1. This means that the blowing or suction velocity is of order $U_\infty\mathrm{Re}_x^{-1/2}$ [i.e., of the same order as the scale of the transversal velocity v inside the boundary layer, eq. (2.81)]. Indeed, if the scale of v_0 is small relative to the natural scale v of the boundary layer fluid, the effect of v_0 on $C_{f,x}$ and Nu is insignificant: In such cases, the flow through the porous wall is too weak to influence the thickness of the boundary layer.

The local skin friction coefficient $C_{f,x}$ is related to $f''(0)$ through eq. (2.129). The tabulated values show that one effect of suction ($v_0 < 0$) is to increase $C_{f,x}$ above the impermeable-wall limit of eq. (2.92). This effect is due to the fact that as some of the fluid is drawn across the wall surface, the boundary layer becomes thinner. The opposite effect—a lower $C_{f,x}$ caused by a thicker boundary layer—occurs in a boundary layer with blowing ($v_0 > 0$). Similarity results of this type expire when $f''(0)$, or the velocity gradient $(\partial u/\partial y)_{y=0}$, becomes zero (i.e., when the boundary layer separates from the wall).

The local Nusselt number Nu $= hx/k$ exhibits similar behavior: higher values for thinner boundary layers on walls with suction, and lower values for thicker boundary layers on walls with blowing. In the range covered by the blowing parameter in Table 2.4, the Prandtl number effect cannot be correlated by using the factor $\mathrm{Pr}^{1/3}$, that is, by seeking a formula of the type $\mathrm{Nu}/\mathrm{Pr}^{1/3}\ \mathrm{Re}_x^{1/2} = \text{function}[(v_0/U_\infty)\ \mathrm{Re}_x^{1/2}]$. The reason is that for suction, Nu increases

Table 2.5 Local Nusselt number $Nu/Re_x^{1/2}$ for laminar boundary layer flow over an isothermal wedge with blowing (Pr = 0.7)

$\dfrac{v_0}{U_\infty}Re_x^{1/2}$	m							
	−0.0418 ($\beta/\pi = -0.08$)	−0.0036 (−0.0072)	0 (0)	0.0257 (0.05)	0.0811 (0.15)	0.333 (1/2)	0.500 (2/3)	1 (1)
0			0.292			0.384		0.496
0.0239	0.103							
0.25			0.166					
0.333						0.242		
0.375			0.107				0.259	
0.5		0.0251	0.0517					0.293
0.518				0.087				
0.558					0.109			
0.667						0.131		
1								0.146

Source: Ref. 28.

with Pr, while in the case of blowing Nu decreases as Pr increases. Since the wall is parallel to the free stream ($m = 0$), the heat transfer coefficient averaged from $x = 0$ to x is twice the local heat transfer coefficient at x; in other words, $h_{0-x} = 2h$.

The effect of the wedge angle on the local Nusselt number is documented in Table 2.5, which is a compilation based on data from the literature. The relation between m and the wedge angle β (Fig. 2.10) is given in eq. (2.125), while $U_\infty = Cx^m$ and $Re_x = U_\infty x/\nu$. The Nu data show once again the β effect seen in Fig. 2.10 and Table 2.3 and the blowing parameter effect revealed by Table 2.4. The average heat transfer coefficient h_{0-x} can be calculated with eq. (2.131).

Similarity results for the stagnation flow against an axisymmetric body have been obtained [36] by using the Mangler coordinate transformation [22, 32]. Table 2.6 shows the effect of the blowing parameter when v_0 is positive. Once again, the local heat transfer coefficient decreases as the blowing velocity increases. While using the data of Table 2.6, it is worth recalling that $U_\infty = (3V/D)x$ in the vicinity ($x \ll D$) of the stagnation point, where V is the approach velocity of the far-field fluid and $D/2$ is the radius of curvature of

Table 2.6 Effect of blowing on the local Nusselt number in laminar stagnation flow on an isothermal axisymmetric body (Pr = 0.7)

$\dfrac{v_0}{U_\infty}Re_x^{1/2}$	0	0.567	1.154
$Nu/Re_x^{1/2}$	0.664	0.419	0.227

Source: Ref. 36.

the nose of the axisymmetric body (e.g., sphere). The approaching fluid flows parallel to the axis of symmetry of the blunt body.

2.9 CONDUCTION ACROSS A SOLID COATING DEPOSITED ON A WALL

The Pohlhausen solution (2.101)–(2.107) for heat transfer across the laminar boundary layer on a flat impermeable wall is based on a model in which the wall surface is assumed isothermal at T_0. Consider now the more general situation [37] sketched in Fig. 2.11, in which an isothermal wall T_0 is coated with a layer of solid material of thermal conductivity k_w. The layer thickness may be nonuniform, $t(x)$; however, it is sufficiently smaller than the wall length L so that the effect of *longitudinal* conduction through this layer can be neglected.

The thickness $t(x)$ has been exaggerated in Fig. 2.11 for clarity. The heat transfer between the wall T_0 and the free stream T_∞ is impeded by two thermal resistances in series, conduction across the $t(x)$ layer and convection across the laminar boundary layer. The heat transfer process is one of *conjugate* conduction and convection, in which the surface touched by the flow acquires a non-uniform temperature that floats to a steady position situated between T_0 and T_∞.

The relation between the temperature difference $(T_\infty - T_0)$ and the total heat transfer rate into the wall $(q' = Lq_{0-L}'')$ can be obtained by integrating the energy equation (2.94) with the Blasius solution for $f(\eta)$, subject to the free-stream condition (2.96) and the new surface condition

$$k \frac{\partial T}{\partial y} = k_w \frac{T - T_0}{t} \qquad (y = 0) \qquad (2.137)$$

This equation states that the heat flux that enters the wall surface from the fluid side continues as a pure conduction heat flux across the coating of thickness t.
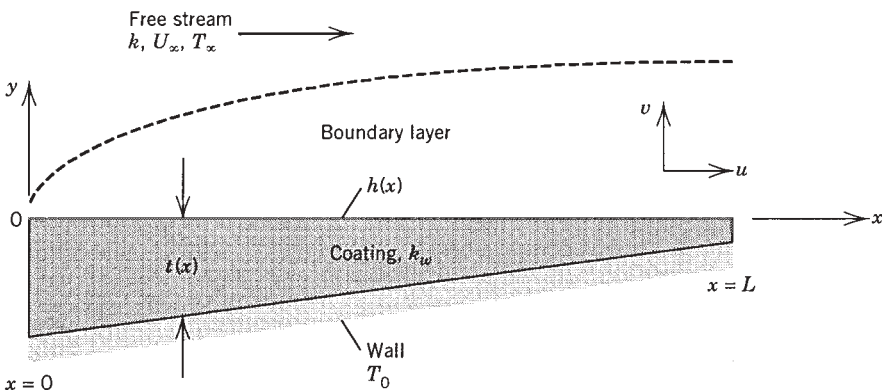
Figure 2.11 Laminar boundary layer flow over an isothermal wall coated with a solid of variable thickness. (From Ref. 37.)

The nondimensional version of eq. (2.137), which replaces eq. (2.95) of the original Pohlhausen problem, is

$$J \frac{\partial \theta}{\partial \eta} = \theta \qquad (\eta = 0) \tag{2.138}$$

where $\theta = (T - T_0)/(T_\infty - T_0)$, $\eta = y(U_\infty/\nu x)^{1/2}$, and

$$J = \frac{k}{k_w} \left(\frac{U_\infty t^2}{\nu x} \right)^{1/2} \tag{2.139}$$

The dimensionless number J is generally a function of x. The limiting value $J = 0$ corresponds to the Pohlhausen problem: an isothermal wall without coating or a wall coated with a sufficiently thin and thermally conductive solid layer. A similarity solution $\theta(\eta, \mathrm{Pr}, J)$ can be found for cases in which J is a constant [i.e., when $t(x)$ varies as $x^{1/2}$] (see Problem 2.6).

Lim et al. [37] solved the problem for the more realistic situation in which the coating thickness is uniform or varies linearly along a wall,

$$t(x) = \bar{t} \left[1 + b \left(\frac{1}{2} - \frac{x}{L} \right) \right] \tag{2.140}$$

In this expression, $\bar{t}$ is the coating thickness averaged from $x = 0$ to $x = L$, and b is a dimensionless taper parameter. Note that the coating thickness varies linearly from $(1 + b/2)$ at the leading edge to $(1 - b/2)$ at the trailing edge. The J parameter that corresponds to the thickness function (2.140) is

$$J = \bar{J} \left(\frac{x}{L} \right)^{-1/2} \left[1 + b \left(\frac{1}{2} - \frac{x}{L} \right) \right] \tag{2.141}$$

in which $\bar{J}$ is the J value based on the L-averaged thickness $\bar{t}$,

$$\bar{J} = \frac{k}{k_w} \frac{\bar{t}}{L} \mathrm{Re}_L^{1/2} \tag{2.142}$$

Since a single similarity solution for θ does not exist in this case, Lim et al. [37] integrated eq. (2.94) for a given x/L and obtained numerically the $\theta'(0)$ coefficient of eq. (2.101) as a function of x/L, $\bar{J}$, and Pr. The total heat transfer rate that emerges from this calculation is

$$q' = \int_0^L k \left(\frac{\partial T}{\partial y} \right)_{y=0} dx$$

$$= k(T_\infty - T_0) \mathrm{Re}_L^{1/2} \int_0^1 \theta'(0) \left(\frac{x}{L} \right)^{-1/2} d \left(\frac{x}{L} \right) \tag{2.143}$$
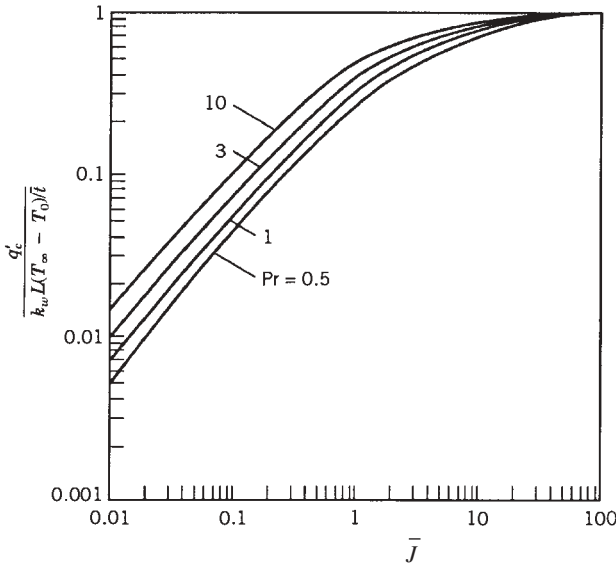
Figure 2.12 Total heat transfer rate when the wall of Fig. 12.11 is coated with a layer of uniform thickness ($b = 0$). (From Ref. 37.)

Figure 2.12 shows the effect of the coating on the total heat transfer rate when the coating has uniform thickness, $q_c' = q'(b = 0)$. The $\overline{J}$ constant differentiates between situations in which the overall thermal resistance is dominated by the coating $(\overline{J} \gg 1)$ and by situations where the boundary layer poses the greater resistance $(\overline{J} \ll 1)$. On the ordinate, q_c' was nondimensionalized by using as the denominator the conduction heat transfer rate in the $\overline{J} \gg 1$ limit in which the coating is an effective insulator, $k_w L(T_\infty - T_0)/\bar{t}$. It can be verified numerically that in the $\overline{J} \ll 1$ limit, the group $q_c'/[k_w L(T_\infty - T_0)/\bar{t}]$ approaches the Pohlhausen solution, which for $\mathrm{Pr} \gtrsim 1$ is $0.664 \mathrm{Pr}^{1/3} \ \overline{J}$.

We should not be surprised that $\overline{J} \sim 1$ marks the transition between an overall resistance dominated by the boundary layer and one dominated by the solid coating. If, for the sake of the argument, in eq. (2.142) we assume that the fluid and the coating have similar thermal conductivities, $\overline{J}$ emerges as the ratio of two thicknesses: the coating thickness $\bar{t}$ divided by the thickness of the thermal boundary layer when $\mathrm{Pr} \sim 1$, namely, $L \, \mathrm{Re}_L^{-1/2}$.

The effect of the taper parameter b is shown in Fig. 2.13, which was drawn only for $\mathrm{Pr} = 1$ and $\overline{J} = 1$. Plotted on the ordinate is the ratio between the total heat transfer when the coating has uniform thickness $(q_c'; b = 0)$ and the heat transfer when the coating is tapered $(q'; b \neq 0)$, but has the same average thickness. The abscissa shows the taper parameter b. Although the quantitative effect of b is small, we note that when the coating is tapered as in Fig. 2.11 $(b > 0)$, it provides more of an insulation effect than when it is spread uniformly
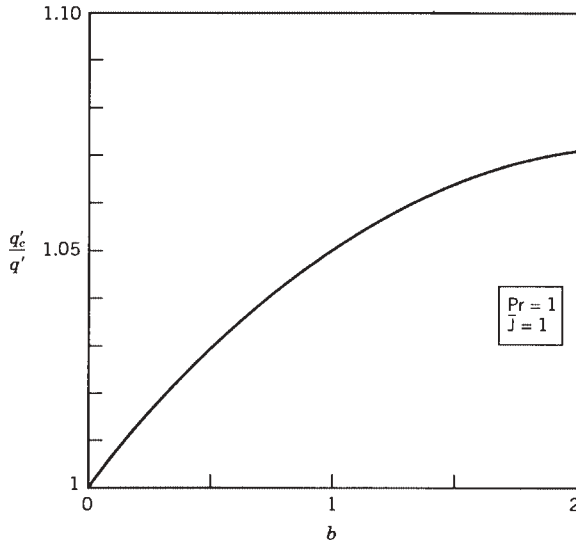
Figure 2.13   Effect of taper (b) on the total heat transfer rate through the wall of Fig. 2.11 when Pr = 1 and J = 1. (From Ref. 37.)

over the isothermal wall, $q'_c > q'$. The effect of changing the coating thickness $\overline{J}$ in addition to b is documented in Ref. 37.

The constructal design aspects of distributing a solid coating on a wall form an active subfield in the current literature [3, 38, 39].

2.10   ENTROPY GENERATION MINIMIZATION IN LAMINAR BOUNDARY LAYER FLOW

Once we have understood the mechanism of friction and heat transfer of a certain convective flow, we are equipped to ask the thermodynamic design question—of how much useful work (exergy) is being destroyed by convection and how the geometry should be modified to minimize this destruction.* Consider this question in the context of forced convection in laminar boundary layer flow. Figure 2.14 shows the simplest two-dimensional geometry: The plate is sufficiently thin, the heat flux q'' is assumed uniform on both sides, and the free stream is parallel to the plate.

Calculating the rate of destruction of useful energy in the convective arrangement of Fig. 2.14 is analogous to calculating the rate of entropy generation in

---

*This method is known as *entropy generation minimization*, renamed more recently as *finite-time thermodynamics*, first recognized in book form in 1982 [40].
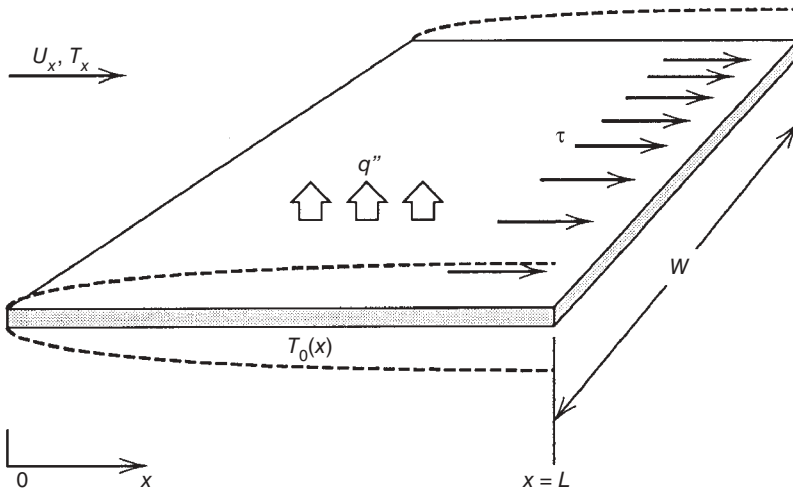
Figure 2.14   Laminar boundary layer flow on a plate with uniform heat flux on both sides. (From Ref. 40.)

the surrounding flow [cf. eq. (1.48)]. A fundamental result in thermodynamics is that the total rate of entropy generation due to heat transfer between a body and a flow (U_∞, T_∞) that surrounds the body is [5, 40–42]

$$S_{\text{gen}} = \frac{1}{T_\infty^2} \int_A q''(T_0 - T_\infty)\, dA + \frac{F_D U_\infty}{T_\infty} \qquad (2.144)$$

In this expression, A is the body surface area, T_0 is the surface temperature, and F_D is the drag force experienced by the body. It is assumed that the temperature difference $T_0 - T_\infty$ is small relative to the absolute temperature T_∞. Note that in Fig. 2.14, the heat flux was drawn such that it points toward the fluid (i.e., as if $T_0 > T_\infty$). The product $q''(T_0 - T_\infty)$ is always positive, regardless of whether the body is warmer or colder than the surrounding fluid.

The entropy generation formula (2.144) has two terms because it is the integral of the volumetric rate of eq. (1.49) over the space occupied by the fluid. The first term accounts for the irreversibility of heat transfer, and the second represents the irreversibility of fluid flow. These two contributions are coupled through the geometry of the body, as we demonstrate next.

We evaluate the two terms of eq. (2.144) by using the heat transfer and skin friction results developed in Section 2.5. We replace the integral with $q''(\overline{T}_0 - T_\infty)(2LW)$, in which $\overline{T}_0 - T_\infty$ is the wall–fluid temperature difference averaged from $x = 0$ to $x = L$. This average can be obtained by using the local temperature difference $[T_0(x) - T_\infty]$ furnished by eq. (2.121), which holds for $\text{Pr} > 0.5$.

The second term on the right side of eq. (2.144) is evaluated by noting that the drag force experienced by the thin plate is $F_D = 2LW\tau_{0-L}$. The average wall shear stress is furnished by eq. (2.92′), which yields $\tau_{0-L} = 0.664\rho U_\infty^2 \mathrm{Re}_L^{-1/2}$. Substituting these estimates in eq. (2.144), we obtain

$$\frac{S_{\text{gen}}}{W} = \frac{0.736(q')^2}{T_\infty^2 k \ \mathrm{Pr}^{1/3} \mathrm{Re}_L^{1/2}} + 1.328 \frac{\mu}{T_\infty} U_\infty^2 \mathrm{Re}_L^{1/2} \tag{2.145}$$

where q' is the total rate of heat transfer between the plate and the fluid, per unit transversal length, $q' = 2Lq''$.

The swept length L appears as $\mathrm{Re}_L = U_\infty L/\nu$ in both terms on the right side of eq. (2.145). The irreversibility due to heat transfer decreases as the plate is made longer, while the fluid flow irreversibility increases. This behavior means that S_{gen} is minimum when L has a certain value that is neither too small nor too large. That value is obtained by solving $\partial S_{\text{gen}}/\partial \mathrm{Re}_L = 0$,

$$\mathrm{Re}_{L,\text{opt}} = 0.554B^2 \tag{2.146}$$

where $\mathrm{Re}_{L,\text{opt}} = U_\infty L_{\text{opt}}/\nu$. The number B is the dimensionless version of the ratio of the heat transfer rate divided by the flow speed,

$$B = \frac{q'/U_\infty}{(k\mu T_\infty \ \mathrm{Pr}^{1/3})^{1/2}} \tag{2.147}$$

The B number identified above governs the entropy generation characteristics of forced convection by laminar boundary layer flow. If the flow and the plate are such that $\mathrm{Re}_L \ll B^2$, the entropy generation rate is due mainly to heat transfer and is considerably greater than when the swept length is optimal [eq. (2.146)]. In the other extreme, $\mathrm{Re}_L \gg B^2$, the plate is so long that most of its work destruction is due to fluid friction.

In conclusion, if a plate (e.g., fin) is to transfer heat at a given rate (q') to a stream with specified velocity (U_∞), its swept length for minimum irreversibility is

$$L_{\text{opt}} = 0.554 \frac{(q')^2}{kT_\infty \rho U_\infty^3 \ \mathrm{Pr}^{1/3}} \tag{2.148}$$

The corresponding minimum rate of exergy destruction is $T_\infty S_{\text{gen,min}}$, where

$$S_{\text{gen,min}} = 1.98 \frac{qU_\infty}{(k/\mu)^{1/2}T_\infty^{3/2} \ \mathrm{Pr}^{1/6}} \tag{2.149}$$

The minimization of entropy generation in other fundamental configurations of external and internal convective heat transfer is presented in Refs. 40–42.

2.11   HEATLINES IN LAMINAR BOUNDARY LAYER FLOW

The heatfunction $H(x, y)$ for two-dimensional flow in Cartesian coordinates was defined in eqs. (1.68)–(1.69) for the more general case in which the longitudinal thermal diffusion term $k\,\partial^2 T/\partial x^2$ is not negligible in the energy equation. The special feature of the boundary layer simplified equation (2.27) is that the $k\,\partial^2 T/\partial x^2$ term is missing. This feature demands a special definition for the heat-function $H(x, y)$ that is valid inside the boundary layer region [27]:

$$\frac{\partial H}{\partial y} = \rho c_P u (T - T_{\text{ref}}) \tag{2.150}$$

$$-\frac{\partial H}{\partial x} = \rho c_P v (T - T_{\text{ref}}) - k\frac{\partial T}{\partial y} \tag{2.151}$$

Assume that the wall is isothermal at T_0. We begin with the case where the free stream is warm and the wall is cold, $T_\infty > T_0$, which means that $T_{\text{ref}} = T_0$. Later, we consider the reverse situation in which the wall is warmer than the stream.

It is easy to verify that the function $H(x, y)$ defined by eqs. (2.150)–(2.151) satisfies the energy equation (2.27) identically. The challenge is to find this function by using eqs. (2.150)–(2.151). The boundary layer flow field is described by the Blasius solution, eqs. (2.71) and (2.81). The boundary layer temperature field is furnished by the Pohlhausen solution, eq. (2.98). Next, we state the heatfunction problem in terms of the scale analysis-based dimensionless variables:

$$\tilde{x} = \frac{x}{L}, \quad \tilde{y} = \frac{y}{L\,\text{Re}_L^{-1/2}} = \eta\tilde{x}^{1/2} \tag{2.152}$$

$$\theta = \frac{T - T_0}{T_\infty - T_0}, \quad \tilde{H} = \frac{H}{\rho c_P U_\infty (T_\infty - T_0) L\,\text{Re}_L^{-1/2}} \tag{2.153}$$

in which $\text{Re}_L = U_\infty L/\nu$. By using these definitions, we can rewrite the heatfunction gradients (2.150)–(2.151) as

$$\frac{\partial \tilde{H}}{\partial \tilde{y}} = f'\theta \tag{2.154}$$

$$-\frac{\partial \tilde{H}}{\partial \tilde{x}} = \frac{1}{2}\tilde{x}^{-1/2}(\eta f' - f)\theta - \frac{1}{\text{Pr}}\frac{\partial \theta}{\partial \tilde{y}} \tag{2.155}$$

Like the temperature field of the Pohlhausen solution, the heatfunction field depends on the Prandtl number. The derivation of the analytical form of the dimensionless heatfunction $\tilde{H}(\tilde{x}, \tilde{y})$ begins by assuming that [27]

$$\tilde{H}(\tilde{x}, \tilde{y}) = \tilde{x}^{1/2} g[\eta(\tilde{x}, \tilde{y})] \tag{2.156}$$

and rewriting eqs. (2.154)–(2.155) in terms of the unknown function $g(\eta)$:

$$g' = f'\theta \tag{2.157}$$

$$\eta g' - g = (\eta f' - f)\theta - \frac{2}{\mathrm{Pr}}\theta' \tag{2.158}$$

where $g' = dg/d\eta$. By eliminating g' between eqs. (2.157) and (2.158), we obtain $g(\eta) = f\theta + (2/\mathrm{Pr})\theta'$. In conclusion, the analytical form of the boundary layer–approximated heatfunction for a cold isothermal wall is

$$\tilde{H}(\tilde{x},\tilde{y}) = \tilde{x}^{1/2}\left[f(\eta)\,\theta(\eta) + \frac{2}{\mathrm{Pr}}\theta'(\eta)\right] \tag{2.159}$$

The similarity heatfunction $g(\eta)$ accounts simultaneously for the two heat transfer mechanisms that are present in the boundary layer, convection ($f\theta$) and transversal conduction ($2\theta'/\mathrm{Pr}$). The $g(\eta)$ function is the *similarity H profile* of the boundary layer: g is as basic a feature of the similarity boundary layer as are f and θ.

Equation (2.159) shows that $\tilde{H}$ increases as $\tilde{x}^{1/2}$ along the wall because $f(0) = 0$ and $\theta'(0)$ is only a function of Pr [eq. (2.99)]. The wall heatfunction is zero at the tip. At the downstream end of the wall ($\tilde{x} = 1$), the heatfunction reaches its highest value, which is $2\theta'(0)/\mathrm{Pr}$. This value is proportional to the total heat transfer rate absorbed by the wall. Note the factor of 2 in front of $\theta'(0)$ and the limiting values $\tilde{H}(1,0) = 0.664\mathrm{Pr}^{-2/3}$ for $\mathrm{Pr} > 0.5$, and $\tilde{H}(1,0) = 1.128\mathrm{Pr}^{-1/2}$ for $\mathrm{Pr} \ll 0.5$. The factors 0.664 and 1.128 are the same as in the expressions for the overall Nusselt number $\mathrm{Nu}_{0-L} = q''_{0-L}L/k(T_\infty - T_0)$, which can be obtained based on eqs. (2.103) and (2.107). Over the entire Pr range, the relationship between Nu_{0-L} and the $\tilde{H}$ value at the trailing edge is $\mathrm{Nu}_{0-L} = \tilde{H}(1,0)\mathrm{Pr}\,\mathrm{Re}_L^{1/2}$, which is equivalent to

$$H(x = L, y = 0) = q''_{0-L}L \tag{2.160}$$

In conclusion, the physical (dimensional) value of the trailing-edge heatfunction is equal to the total heat transfer rate through the wall.

Figure 2.15 shows the pattern of heatlines in the laminar boundary layer of a $\mathrm{Pr} = 0.72$ fluid such as air. The heatlines are plotted only in the boundary layer region, which corresponds to $\tilde{y}$ values where $\eta < 5$. The $\eta = 5$ curve (or $\tilde{y} = 5\tilde{x}^{1/2}$) is shown by the dotted line. The heatlines show the actual path of the energy absorbed by the wall. They are perpendicular to the wall because at $\tilde{y} = 0^+$ the heat transfer is by pure conduction (remember: $u = 0$ at $y = 0$). The heatlines that cross the wall ($0 < \tilde{H}\,\mathrm{Pr}^{2/3} < 0.664$) originate from the flow region situated immediately upstream of the tip.

The heatlines that cross the wall are more crowded near the tip than farther downstream. This feature of the heatline pattern makes visible the nonuniform distribution of the heat flux over the isothermal wall, namely, a heat flux q'' that is proportional to $x^{-1/2}$.
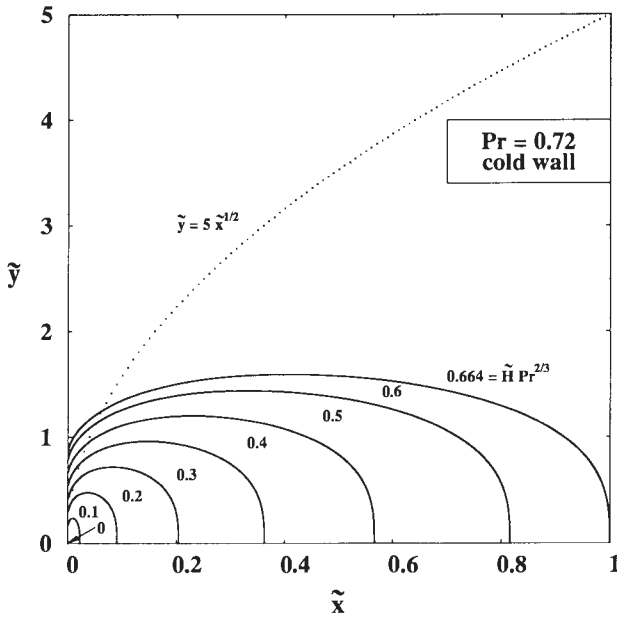
Figure 2.15   Heatlines in the boundary layer of a wall that is colder than the free stream. (From Ref. 27.)

Consider now the reverse situation in which T_0 is greater than T_∞, and the wall heats the stream. The temperature field (the pattern of isotherms) is insensitive to this change; however, the pattern of heatlines is markedly different. The analytical construction of the $\tilde{H}$ function begins with setting $T_{\mathrm{ref}} = T_\infty$ in eqs. (2.150)–(2.151) and follows the steps that led to eq. (2.159). The expression for the dimensionless heatfunction is [27]

$$\frac{H}{\rho c_P\, U_\infty (T_0 - T_\infty) L\,\mathrm{Re}_L^{-1/2}} = \tilde{H}(\tilde{x}, \tilde{y}) = -\tilde{x}^{1/2}\left\{ f(\eta)\,[\theta(\eta) - 1] + \frac{2}{\mathrm{Pr}}\theta'(\eta)\right\}$$
(2.161)

Figure 2.16 shows the pattern of heatlines near the hot wall when the Prandtl number is 0.72. This figure can be compared with Fig. 2.15 to see the difference between a wall that releases heat and one that absorbs heat. The heatlines point in the $\tilde{y}$ direction as they emerge from the wall; later, they are swept downstream by the flow. Their higher density near the tip indicates higher heat fluxes. They occupy the same region as the velocity boundary layer (the dotted line), and in this way they visualize the meaning of a Prandtl number that is on the order of 1.

The effect of the Prandtl number on the heatline pattern is illustrated further in Ref. 27. The same study reports in closed form the heatfunction for the boundary layer on a wall with uniform heat flux. The growing literature on the use of heatlines and masslines is reviewed at the end of Chapter 1.
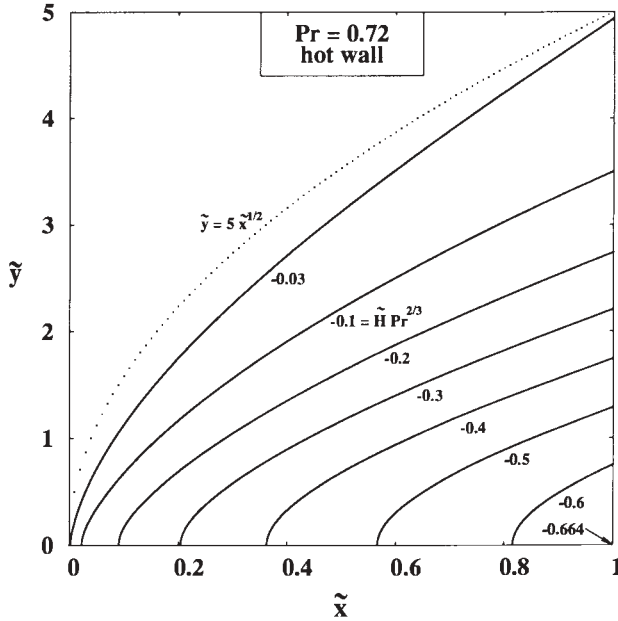
Figure 2.16   Heatlines in the boundary layer of a wall that is warmer than the free stream. (From Ref. 27.)

2.12   DISTRIBUTION OF HEAT SOURCES ON A WALL COOLED BY FORCED CONVECTION

Consider a horizontal plate of length L which is in contact with a free stream of velocity U_∞ and temperature T_∞. The plate is heated by line heat sources of fixed strength q' (W/m). The heat sources appear as points on the plate sketched in Fig. 2.17. Each line heat source extends in the direction perpendicular to the figure. The flow is two-dimensional and in the laminar boundary layer regime. The number of heat sources per unit of plate length (N') is unknown.

In accordance with the method of constructal design, if T_{max} is the maximal temperature that must not be exceeded at the hot spots that occur on the plate, then the entire plate should operate at T_{max}. The problem is to determine the
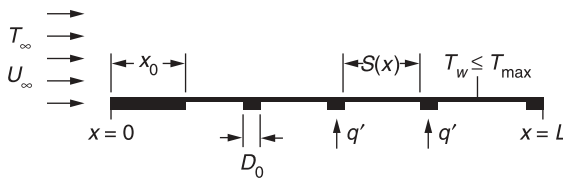
Figure 2.17   The multiple length scales of the distribution of finite-size heat sources on a wall [43].

distribution of heat sources on the plate, $N(y)$, such that the wall temperature is near the allowed limit $T_w(x) = T_{max}$, constant. First, we assume that the density of line sources is sufficiently high so that we may express the distribution of discrete q' sources as a nearly continuous distribution of heat flux:

$$q''(x) = q'N' \tag{2.162}$$

The heat flux distribution that corresponds to eq. (2.162) and $\mathrm{Pr} \gtrsim 1$ is given by eq. (2.103), $\mathrm{Nu} = 0.332\,\mathrm{Pr}^{1/3}\,\mathrm{Re}_x^{1/2}$, or

$$\frac{q''x}{k\,(T_{max} - T_\infty)} = 0.332\,\mathrm{Pr}^{1/3} \left(\frac{U_\infty x}{\nu}\right)^{1/2} \tag{2.163}$$

By eliminating q' between eqs. (2.162) and (2.163) we obtain the required distribution of heat sources,

$$N'(x) = 0.332\,\frac{k}{q'}\,(T_{max} - T_\infty)\,\mathrm{Pr}^{1/3} \left(\frac{U_\infty}{\nu}\right)^{1/2} x^{-1/2} \tag{2.164}$$

The function $N'(x)$ represents the optimal configuration of heat sources. It shows that the sources must be positioned closer when they are near the start of the boundary layer. The total number of heat sources is

$$N = \int_0^L N'\,dx = 0.664\,\frac{k}{q'}\,(T_{max} - T_\infty)\,\mathrm{Pr}^{1/3}\,\mathrm{Re}^{1/2} \tag{2.165}$$

where $\mathrm{Re} = U_\infty L/\nu$. The rate of heat transfer from all the heat sources to the T_∞ fluid is

$$Q'_{max} = q'N = 0.664\,k(T_{max} - T_\infty)\,\mathrm{Pr}^{1/3}\,\mathrm{Re}^{1/2} \tag{2.166}$$

This Q'_{max} expression is the same as the total heat transfer rate from an isothermal wall at T_{max}. Equation (2.166) represents the maximized global performance of the wall with discretely distributed heat transfer.

The physical implementation of the optimal distribution is limited by an important manufacturing constraint: There exists a smallest scale in the design—the D_0 thickness of the line heat source. Features smaller than D_0 cannot be made. This constraint endows the design with structure, graininess (coarseness), and visibility.

The local spacing between two adjacent heatlines is $S(x)$. This spacing varies with x in accordance with the optimal N' distribution function, eq. (2.164). The plate length interval that corresponds to a single line heat source q' is $D_0 + S(x)$. This means that the local number of heat sources per unit of wall height is

$$N'(x) = \frac{1}{D_0 + S(x)} \tag{2.167}$$

The strength of one source (q') is spread uniformly over the finite thickness of the source ($q_0'' = q'/D_0$). The heat flux q_0'' is a known constant, unlike the function $q'(x)$ of eq. (2.163), which is the result of design. By eliminating $N'(x)$ between eqs. (2.164) and (2.167), we obtain the rule for how the wall heating design should be constructed:

$$\frac{S(x)}{L} \cong \frac{3q' \, \mathrm{Pr}^{-1/3} \, \mathrm{Re}^{-1/2}}{k \, (T_{\max} - T_{\infty})} \left(\frac{x}{L}\right)^{1/2} - \frac{D_0}{L} \qquad (2.168)$$

The spacing S increases as x increases. Near the start of the boundary layer, the $S(x)$ function of eq. (2.168) has negative values. This means that the above description breaks down in a region ($0 \le x \le x_0$) near the start of the boundary layer. Because D_0 is the smallest length scale of the structure, the spacings S cannot be smaller than D_0. We define x_0 as the longitudinal scale where S is as small as D_0 in an order-of-magnitude sense,

$$S \sim D_0 \qquad \text{when} \qquad x \sim x_0 \qquad (2.169)$$

By substituting this into eq. (2.168), we determine the starting length scale over which eq. (2.168) is not valid,

$$\left(\frac{x_0}{L}\right)^{1/2} \sim 0.664 \, \frac{D_0}{L} \frac{k}{q'} \, (T_{\max} - T_0) \, \mathrm{Pr}^{1/3} \, \mathrm{Re}^{1/2} \qquad (2.170)$$

In summary, the wall structure has two distinct sections. Downstream of $x \sim x_0$, the wall is heated on discrete patches of length D_0 which are spaced according to eq. (2.168). Upstream of $x \sim x_0$, the heat sources are mounted flush against each other. We model this starting section as one with uniform heat flux in such a way that at the end of this section (at $x \sim x_0$) the wall temperature reaches the same maximum level ($T_{\max}$) that the optimized spacings (2.168) are designed to maintain downstream of $x \sim x_0$. The wall temperature is T_0 at $x = 0$. It reaches $T_{\max}$ at the transition distance x_0 and continues undulating at $T_{\max}$ (and slightly under) from x_0 until L.

These basic features of the optimal design are illustrated in Fig. 2.17. The design has multiple length scales: L, D_0, x_0, and $S(x)$. The first two length scales are constraints. The last two are results of global maximization of performance in a morphing architecture subjected to the constraints. Taken together, the lengths represent multiscale constructal design—the flow architecture that brings the entire wall to the highest performance level possible. The performance of this constructal design is described further in Ref. 43.

2.13   THE FLOW OF STRESSES

As a good-bye to boundary layer theory, I draw attention to its most recent extension to the shaping of thin structures for the *flow of stresses* without

strangulations [44]. To look at stresses as flow is quite unusual but it is effective when the objective is to discover the best configuration of the stressed volume. In Ref. 44 we illustrated the ''flow-of-stresses'' concept by using the simplest possible examples that have analogs to fluid flow and convective heat transfer: single ducts, bifurcated ducts, fins with heat tubes, and single and conjugate boundary layers.

High density is the design value of the flow of stresses image, and it is analogous to the maximum heat transfer density that packages of electronics and compact heat exchangers achieve when their internal pathways for heat and fluid flow are configured such that strangulations are minimized. To facilitate the flow of stresses, fluid, and heat is to generate the configuration of the flow system.

REFERENCES

1. L. Prandtl, Über Flussigkeitsbewegung bei sehr kleiner Reibung, *Proceedings of the 3rd International Mathematics Congress*, Heidelberg, Germany, 1904; also NACA TM 452, 1928.

2. H. Lamb, *Hydrodynamics*, Dover, New York, 1945.

3. A. Bejan, *Shape and Structure, from Engineering to Nature*, Cambridge University Press, Cambridge, 2000.

4. A. Bejan, Science and technology as evolving flow architectures, *Int. J. Energy Res.*, Vol. 33, 2009, pp. 112–125.

5. A. Bejan, *Advanced Engineering Thermodynamics*, 3rd ed., Wiley, Hoboken, 2006.

6. J. Fourier, *Analytical Theory of Heat*, translated, with notes, by A. Freeman, G. E. Stechert & Co., New York, 1878.

7. I. Newton, Scala Graduum Caloris, Calorum Descriptiones & Signa, *Philos. Trans. Roy. Soc. London*, Vol. 8, 1701, pp. 824–829; translated from Latin in *Philos. Trans. Roy. Soc. London*, Abridged, Vol. IV (1694–1702), 1809, pp. 572–575.

8. E. Péclet, *Traité de la chaleur considérée dans ses applications*, Vol. 1, 3rd ed., Victor Masson, Paris, 1860, p. 364.

9. A. E. Bergles, Enhancement of convective heat transfer: Newton's legacy pursued, in E. T. Layton, Jr. and J. H. Lienhard, eds., *History of Heat Transfer*, American Society of Mechanical Engineers, New York, 1988, pp. 53–64.

10. Count of Rumford, *Essays, Political, Economical and Philosophical*, Vol. II, T. Cadell and W. Davis, London, 1798, Essay VII.

11. S. C. Brown, The discovery of convection currents by Benjamin Thompson, Count of Rumford, *Am. J. Phys.*, Vol. 15, 1947, pp. 273–274.

12. W. Prout, *Bridgewater Treatises*, Vol. 8, Carey, Lea & Blanchard, Philadelphia, 1834, p. 65.

13. A. Bejan, *Convection Heat Transfer*, Wiley, New York, 1984.

14. A. Bejan, The method of scale analysis: natural convection in fluids, in S. Kakac, W. Aung, and R. Viskanta, eds., *Natural Convection: Fundamentals and Applications*, Hemisphere, Washington, DC, 1985, pp. 75–94.

15. A. Bejan, The method of scale analysis: natural convection in porous media, in S. Kakac, W. Aung, and R. Viskanta, eds., *Natural Convection: Fundamentals and Applications*, Hemisphere, Washington, DC, 1985, pp. 548–572.

16. S. Bhattacharjee and W. L. Grosshandler, The formation of a wall jet near a high temperature wall under microgravity environment, ASME HTD-Vol. 96, 1988, pp. 711–716.

17. V. A. F. Costa, A time scale-based analysis of the laminar convective phenomena, *Int. J. Therm. Sci.*, Vol. 41, 2002, pp. 1131–1140.

18. D. W. Weyburn, A mathematical description of the fluid boundary layer, *Appl. Math. Comput.*, Vol. 175, 2009, pp. 1675–1684.

19. W. M. Rohsenow and H. Y. Choi, *Heat, Mass and Momentum Transfer*, Prentice-Hall, Englewood Cliffs, NJ, 1961, p. 149.

20. H. Blasius, Grenzschichten in Flüssigkeiten mit kleiner Reibung, *Z. Math. Phys.*, Vol. 56, 1908, p. 1; also NACA TM 1256.

21. E. Pohlhausen, Der Wärmeaustausch zwischen festen Körpern und Flüssigkeiten mit kleiner Reibung and kleiner Wärmeleitung, *Z. Angew. Math. Mech.*, Vol. 1, 1921, pp. 115–121.

22. H. Schlichting and K. Gersten, *Boundary Layer Theory, 8th* enlarged and revised ed., Springer-Verlag, New York, 2000.

23. L. Howarth, On the solution to the laminar boundary layer equations, *Proc. R. Soc. London*, *Ser. A*, Vol. 164, 1938, p. 547.

24. S. W. Churchill and H. Ozoe, Correlations for laminar forced convection with uniform heating in flow over a plate and in developing and fully developed flow in a tube, *J. Heat Transfer*, Vol. 95, 1973, pp. 78–84.

25. Y. Joshi and W. Nakayama, Forced convection: external flows, in A. Bejan and A. D. Kraus, eds., *Heat Transfer Handbook*, Wiley, New York, 2003.

26. E. R. G. Eckert, *Introduction to the Transfer of Heat and Mass*, McGraw-Hill, New York, 1959.

27. A. M. Morega and A. Bejan, Heatline visualization of forced convection boundary layers, *Int. J. Heat Mass Transfer*, Vol. 36, 1993, pp. 3957–3966.

28. W. M. Kays and M. E. Crawford, *Convective Heat and Mass Transfer*, McGraw-Hill, New York, 1980, pp. 51–54.

29. V. M. Falkner and S. W. Skan, Some approximate solutions of the boundary layer equations, *Philos. Mag.*, Vol. 12, 1931, pp. 865–896.

30. D. R. Hartree, On an equation occurring in Falkner and Skan's approximate treatment of the equations of the boundary layer, *Proc. Cambridge Philos. Soc.*, Vol. 33, Part II, 1937, pp. 223–239.

31. E. R. G. Eckert, Die Berechnung des Wärmeüberganges in der Laminaren Grenzschicht um strömter Körper, *VDI-Forschungsheft*, Vol. 416, 1942, pp. 1–24.

32. W. Mangler, Zusammenhang zwischen eben und rotationssymmetrischen Grenzschichten in kompressiblen Flüssigkeiten, *ZAMM*, Vol. 28, 1948, pp. 97–103.

33. N. B. Cohen, Boundary-layer similar solutions and correlation equations for laminar heat transfer distribution in equilibrium air at velocities up to 41,000 feet per second, NASA Tech. Rep. R-118, 1961.

34. R. H. Pletcher, External flow forced convection, in S. Kakac, R. K. Shah, and W. Aung, eds., *Handbook of Single-Phase Convective Heat Transfer*, Wiley, New York, 1987, Chapter 2.

35. V. A. Chiriac and A. Ortega, A numerical study of the unsteady flow and heat transfer in a transitional confined slot jet impinging on an isothermal surface, *Int. J. Heat Mass Transfer*, Vol. 45, 2002, pp. 1237–1248.

36. J. T. Howe and W. A. Mersman, Solutions of the laminar compressible boundary-layer-equations with transpiration which are applicable to the stagnation regions of axisymmetric blunt bodies, NASA TN D-12, Washington, DC, 1959.

37. J. S. Lim, A. Bejan, and J. H. Kim, The optimal thickness of a wall with convection on one side, *Int. J. Heat Mass Transfer*, Vol. 35, 1992, pp. 1673–1679.

38. A. Bejan, How to distribute a finite amount of insulation on a wall with nonuniform temperature, *Int. J. Heat Mass Transfer*, Vol. 36, 1993, pp. 49–56.

39. M. Kalyon and A. Z. Sahin, Application of optimal control theory in pipe insulation, *Numer. Heat Transfer, Part A*, Vol. 41, 2002, pp. 391–402.

40. A. Bejan, *Entropy Generation through Heat and Fluid Flow*, Wiley, New York, 1982.

41. A. Bejan, Entropy generation minimization: the new thermodynamics of finite-size devices and finite-time processes, *J. Appl. Phys.*, Vol. 79, Feb. 1, 1996, pp. 1191–1218.

42. A. Bejan, *Entropy Generation Minimization*, CRC Press, Boca Raton, FL, 1996.

43. A. K. da Silva, S. Lorente, and A. Bejan, Optimal distribution of discrete heat sources on a plate with laminar forced convection, *Int. J. Heat Mass Transfer*, Vol. 47, 2004, pp. 2139–2148.

44. S. Lorente, J. Lee, and A. Bejan, The ''flow of stresses'' concept: The analogy between mechanical strength and heat convection, *Int. J. Heat Mass Transfer*, Vol. 53, 2010, pp. 2963–2968.

45. S. Goldstein, ed., *Modern Developments in Fluid Dynamics*, Oxford University Press, London, 1938, p. 135.

46. E. M. Sparrow and S. H. Lin, Boundary layers with prescribed heat flux: application to simultaneous convection and radiation, *Int. J. Heat Mass Transfer*, Vol. 8, 1965, pp. 437–448.

47. A. Bejan, Theory of rolling contact heat transfer, *J. Heat Transfer*, Vol. 111, 1989, pp. 257–263.

PROBLEMS

2.1. Derive eq. (2.53) by invoking the first law of thermodynamics in the open system defined by the control volume in Fig. 2.3*b*.

2.2. Develop a power series expression for the Blasius profile (Fig. 2.6) as a solution of eq. (2.82) subject to conditions (2.83) and (2.84). Assume that $f = \sum_{i=0}^{\infty} a_i \eta^i$. Show that for small η, the expression

$$f = \frac{\alpha \eta^2}{2!} - \frac{\alpha^2 \eta^5}{(2)(5!)} + \frac{11\alpha^3 \eta^8}{(4)(8!)} - \frac{375\alpha^4 \eta^{11}}{(8)(11!)} + \cdots$$

satisfies the Blasius equation and the boundary conditions at $\eta = 0$. The curvature at the wall, $\alpha = f''(0)$, is unknown and would have to be determined from the condition (2.84) at $\eta = \infty$, where the series expression above does not hold. To complete the solution, develop an asymptotic expansion valid for large values of η,

$$f = f_1 + f_2 + \cdots$$

where the higher-order approximations must be small compared with the lower-order approximations (e.g., $f_2 \ll f_1$). Using Ref. 22 as a guide, show that for large values of η,

$$f = \eta - \beta + \gamma \int_\infty^\eta d\eta \int_\infty^\eta \exp\left[-\tfrac{1}{4}(\eta - \beta)^2\right] d\eta + \cdots$$

where β and γ are two additional unknown constants. The three unknowns (α, β, γ) can be determined by *matching* the two expansions, that is, by making f, f', and f'' equal at some $\eta = \eta_1 = O(1)$. This is how Blasius found that $\alpha = 0.332$, which is extremely close to the correct numerical result [23].

2.3. Determine the Blasius profile (Fig. 2.6) by solving eq. (2.82) numerically using a shooting scheme. First, divide the η domain into small intervals $\Delta\eta$ of size 0.01 or smaller. Write finite-difference approximations for the derivatives f'' and f''' [e.g., $f_i'' = (f_{i+1} + f_{i-1} - 2f_i)/(\Delta\eta)^2$, where i indicates the position of the ith node, defined as $\eta_i = i\Delta\eta$], and substitute these expressions into eq. (2.82). The result of this operation is a formula for calculating the value of f at any node, based on the f values at the *three* preceding nodes. The numerical integration starts from the wall, by first calculating f_3 based on $f_0 = f_1 = 0$ [eq. (2.83)] and a guess for the value of f_2. The calculation is repeated for $f_4, f_5, \ldots$, until η becomes large, $O(10)$: in this range, the third boundary condition [eq. (2.84)] must be used as the test for how good the initial f_2 guess was. If eq. (2.84) is not satisfied, the integration sequence is repeated using an updated guess for the value of f_2 [synonymous with guessing $f''(0)$].

　　The need for performing the integration more than once is eliminated based on the observation that the Blasius equation (2.82) and the initial conditions (2.83) are invariant under the transformation [45]

$$f \to bf, \qquad \eta \to \frac{\eta}{b}$$

　　If eq. (2.82) is integrated to $\eta \sim 10$ using a certain initial curvature, say, $f''(0) = 1$, the numerically calculated outer slope $a = f'(10)$ and eq. (2.84) imply that the correct guess for initial curvature $f''(0)$ must be $a^{-3/2}$.

2.4. Derive the expression for the local Nusselt number along a flat wall with uniform heat flux using the integral method. Assume one of the temperature profiles listed in Table 2.1 and you will take advantage of the fact that the flow part of the problem has already been solved [i.e., $\delta(x)$ is known]. Keep in mind that in this problem $T_0(x)$ is an additional unknown; the necessary additional equation is the definition of q'' (known) [eq. (2.5)].

2.5. Consider the laminar boundary layer flow of an isothermal fluid (U_∞, T_∞) over a flat isothermal wall (T_0). At a certain distance x from the leading edge, the local skin friction coefficient is $C_{f,x} = 0.0066$. What is the value of the local Nusselt number at the same location if the Prandtl number is $\mathrm{Pr} = 7$?

2.6. Assume that the solid layer that coats the isothermal wall shown in Fig. 2.11 has the thickness $t = Cx^{1/2}$, in which C is a constant. Show that a similarity solution exists for the temperature profile across the thermal boundary layer. Let $q'(J)$ be the total heat transfer rate through the coated wall of length L, and $q'(0)$ be the heat transfer when the coating is absent. Show that when $\mathrm{Pr} > 0.5$, the relative effect of the coating is described by

$$\frac{q'(J)}{q'(0)} = (1 + 0.332\mathrm{Pr}^{1/3}\mathrm{J})^{-1}$$

2.7. It has been claimed that a similarity solution does not exist for the laminar thermal boundary layer over a flat plate with *uniform heat flux* [28, p. 151]. Develop this similarity solution for the geometry of Fig. 2.1, in which $q'' = \text{constant}$ (see Ref. 27). As a similarity temperature variable, choose $\theta(\eta, \mathrm{Pr})$, where

$$\theta = \frac{T(x,y) - T_\infty}{(q''/k)(vx/U_\infty)^{1/2}}$$

Show that the energy equation in the boundary layer reduces to [46]

$$\theta'' + \frac{\mathrm{Pr}}{2}(f\theta' - f'\theta) = 0$$

Solve this equation numerically for several Pr values subject to appropriate boundary conditions. Report your conclusions in the style of eqs. (2.103) and (2.107), that is, as asymptotic formulas for the local Nusselt number $\mathrm{Nu} = q''x/k[T_0(x) - T_\infty]$.

2.8. Consider the laminar boundary layer formed by the flow of $10°C$ water over a $10°C$ flat wall of length L. Show that the total shear force experienced by the wall and the mechanical power P spent on dragging the wall through the fluid is proportional to $v^{1/2}$.

  (a) The dissipated drag power described above refers to the case in which the wall is as cold as the free-stream water. Show that if the wall is

heated isothermally so that its temperature rises to 90°C, the dissipated power decreases by 35 percent. In other words, show that $P_h/P_c = 0.65$, where h and c refer to the hot- and cold-wall conditions.

(b) Compare the power savings due to heating the wall $(P_c - P_h)$ with the electrical power needed to heat the wall to 90°C. How fast must the water flow be so that the savings in fluid-friction power dissipation become greater than the electrical power invested in heating the wall? How short must the swept length L be so that the boundary layer remains laminar while the power savings $P_c - P_h$ exceed the heat input to the wall?

2.9. The wind blows at 0.5 m/s parallel to the short side of a flat roof with rectangular area 10 m × 20 m. The roof temperature is 40°C, and the temperature of the air free stream is 20°C. Calculate the total force experienced by the roof. Estimate also the total heat transfer rate by laminar forced convection from the roof to the atmosphere.

2.10. Make a qualitative sketch of how the local heat flux q''_x varies along an isothermal wall bathed by a laminar boundary layer of total length L. Use q''_x on the ordinate and x on the abscissa. On the same sketch, draw a horizontal line at the level that would correspond to the heat flux averaged over the entire length of the plate, $\overline{q}''_L$. Determine analytically **(a)** the position x where the local heat flux matches the value of the L-averaged heat flux, and **(b)** the relationship between the midpoint local flux and the L-averaged value, that is, the ratio $q''_{L/2}/\overline{q}''_L$.

2.11. Consider the sharp-edged entrance to a round duct of diameter D (Fig. P2.11). The laminar boundary layer that forms over the duct length L is much thinner than the duct diameter. The temperature difference between the duct wall (isothermal) and the inflowing stream is ΔT. The longitudinal inlet velocity of the stream is U_∞. Derive expressions for the total force F experienced by the duct section of length L and the total heat transfer rate from the duct wall to the stream, q. In the end, show that q and F are proportional:

$$\frac{q}{F} = \mathrm{Pr}^{-2/3} \frac{c_P \Delta T}{U_\infty} \qquad (\mathrm{Pr} \gtrsim 0.5)$$
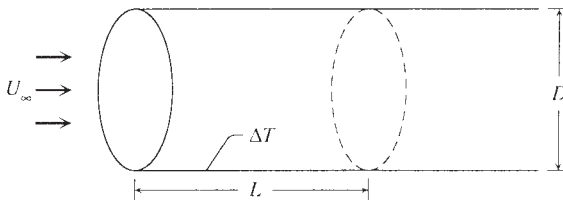
Figure P2.11

2.12. A stream of $20°C$ water enters a duct, the wall temperature of which is uniform and equal to $50°C$. The inlet velocity is 5 cm/s. The duct cross section is a 20 cm $\times$ 20 cm square. Assume that the thickness of the boundary layer that lines the inner surface of the duct is much smaller than 20 cm, and calculate **(a)** the local heat transfer coefficient at $x = 1$m downstream from the mouth, **(b)** the total heat transfer rate between the duct section of length $x = 1$ m and the water stream, and **(c)** the velocity boundary layer thickness (δ) at $x = 1$ m. Verify in this way the validity of the assumption that δ is much smaller than the duct width.
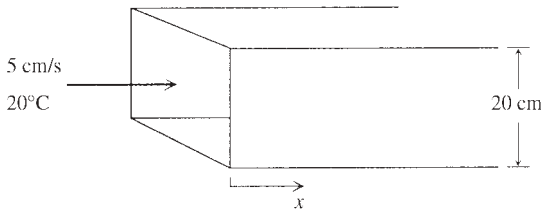
Figure P2.12

2.13. The plane wall shown in Fig. P2.13 is swept by the laminar boundary layer flow of an isothermal fluid (T_∞, U_∞) with Prandtl number greater than 0.5. Deposited on the surface of this wall is a narrow strip of metallic film that runs parallel to the leading edge of the wall, that is, in the direction normal to the plane of the figure. As part of an electrical circuit, the strip generates Joule heating at the rate q'_w (W/m), or as the heat flux $q''_w = q'_w/\Delta x = $ constant. The width of the strip is much smaller than the distance to the leading edge, $\Delta x \ll x_1$.

Determine analytically the wall temperature distribution over the unheated downstream portion $x > x_1$. In other words, determine the "thermal wake" effect of the strip conductor. Assume that the entire Joule heating effect q'_w can only escape through the fluid side of the metallic strip. In other words, assume that the wall side of the strip is adiabatic.
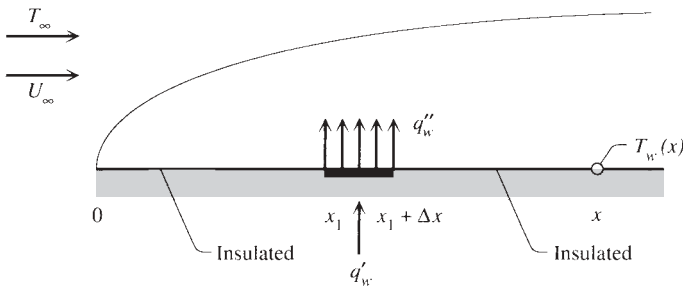
Figure P2.13

2.14. **(a)** A plane wall of length L is cooled by the laminar boundary layer flow of a fluid with $\mathrm{Pr} \gtrsim 0.5$. The wall is heated electrically so that it releases the uniform heat flux q'' over the front half of its swept length, $0 < x < L/2$. The trailing half $L/2 < x < L$ is without heat transfer. Determine analytically the wall–fluid temperature difference at the trailing edge, $T_w(L) - T_\infty$.
(b) A simpler (approximate) approach would be to assume that the total heat transfer rate described above $(q''L/2)$ is distributed uniformly over the entire length L. Determine the trailing-edge temperature difference, compare it with the estimate of part (a), and comment on the accuracy of this approximate approach.

2.15. An isothermal flat strip is swept by a parallel stream of water with a temperature of $20°\mathrm{C}$ and a free-stream velocity of $0.5\,\mathrm{m/s}$. The width of the strip, $L = 1\,\mathrm{cm}$, is parallel to the flow. The temperature difference between the strip and the free stream is $\Delta T = 1°\mathrm{C}$. Calculate the L-averaged shear stress $\overline{\tau}$ and the L-averaged heat flux $\overline{q}''$ between the strip and the water flow.

2.16. It is proposed to estimate the uniform velocity U_∞ of a stream of air of temperature $20°\mathrm{C}$ by measuring the temperature of a thin metallic blade that is heated and inserted parallel to U_∞ in the airstream (Fig. P2.16). The width of the blade (i.e., the dimension aligned with U_∞) is $L = 2\,\mathrm{cm}$. The blade is considerably longer in the direction normal to the figure; therefore, the boundary layer flow that develops is two-dimensional. The blade is heated volumetrically by an electric current so that 0.03 W electrical power is dissipated in each square centimeter of metallic blade. It is assumed that the blade is so thin that the effect of heat conduction through the blade (in the x direction) is negligible. A temperature sensor mounted on the trailing edge of the blade reads $T_w = 30°\mathrm{C}$. Calculate the free-stream velocity U_∞ that corresponds to this reading.

$U_\infty, T_\infty = 20°\mathrm{C}$

$T_w = 30°\mathrm{C}$

L

$0 \quad x$
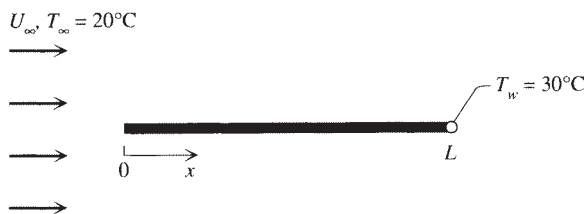
Figure P2.16

2.17. When two elastic cylinders are pressed against one another, they make contact over a strip of width L (Fig. P2.17). This width is assumed known. In general, it depends on the elastic properties and radii of the two cylinders and on the force with which one cylinder is pressed against the other. The radii of the cylinders are much larger than the contact width L.

Two cylindrical bodies have different temperatures, T_1 and T_2, and roll past one another without slip. The peripheral velocity U with which both bodies pass through the frame of reference attached to the contact region is known. The objective of this exercise is to show how the ''fluid'' boundary layer method of this chapter can be used to calculate the heat transfer rate between two *solids* [47].
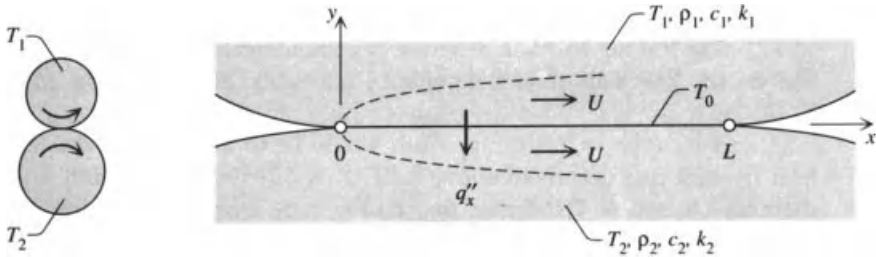
Figure P2.17

(a) Assume that the interface temperature T_0 (unknown) is uniform, that is, independent of x. Write the expression for the local heat flux q_x'' by noting that the ''flow'' of each solid through its respective thermal boundary layer region (with constant U) is similar to that of a fluid with extremely low Prandtl number.

(b) Show that the interface temperature depends on the physical properties of the two solids in the following manner:

$$T_0 = \frac{r}{1+r}T_1 + \frac{1}{1+r}T_2 \quad \text{with} \quad r = \frac{(\rho c k)_1^{1/2}}{(\rho c k)_2^{1/2}}$$

(c) Derive the expression for the L-averaged heat flux between the two bodies:

$$\overline{q}'' = \frac{1.128}{1+r}k_1(T_1 - T_2)\left(\frac{U}{\alpha_1 L}\right)^{1/2}$$

(d) How fast must the cylinders roll for these analytical results to be valid?

2.18. Design a plate fin for maximum heat transfer rate q_B subject to fixed volume ($V = bLt = $ constant). If the heat transfer through the fin can be described as one-dimensional, the total heat transfer rate pulled by the fin from the wall T_B is

$$q_B = (T_B - T_\infty)(hpkA)^{1/2} \ \tanh\left[L\left(\frac{hp}{kA}\right)^{1/2}\right]$$

where h, p, k, and A are the average heat transfer coefficient at location x along the fin (away from the wall; Fig. P2.18), the wetted perimeter at

$x = $ constant, the thermal conductivity of the fin, and the fin cross-sectional area at $x = $ constant. It is assumed that $L \gg b \gg t$, where L, b, and t are the dimensions of the plate fin. The fin is in contact with a uniform stream (U_∞, T_∞) in laminar boundary layer flow parallel to the b dimension of the fin; hence, the heat transfer coefficient at any location x along the fin is

$$\frac{hb}{k_f} = 0.664 \mathrm{Pr}^{1/3} \left(\frac{U_\infty b}{\nu} \right)^{1/2}.$$

where k_f, Pr, and ν are the fluid conductivity, the Prandtl number, and the kinematic viscosity, respectively. Assuming that all other design variables are given (including the plate thickness t), determine the optimal dimension b for maximum q_B and fixed V. Express your result in dimensionless form as

$$\frac{b_{\mathrm{opt}}}{t} = \text{function} \left(\frac{V}{t^3}, \frac{k_f}{k}, \mathrm{Pr}, \frac{U_\infty t}{\nu} \right)$$
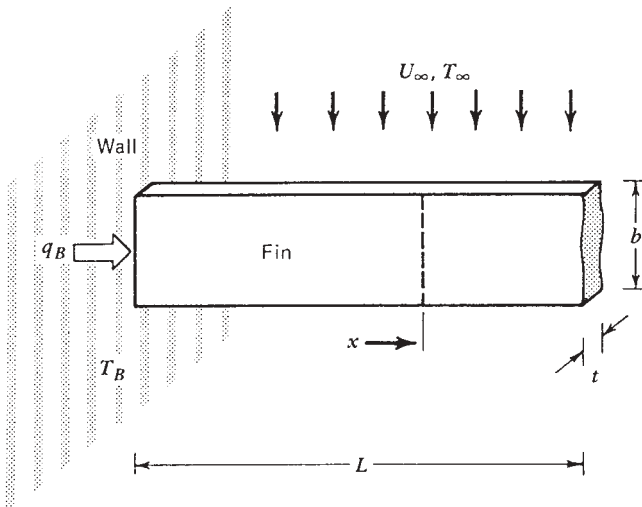
Figure P2.18

2.19. Consider the plate fin discussed in Problem 2.18, and think of the limit where the fin length L is large enough so that the base heat transfer rate q_B is no longer influenced by L. **(a)** If all design variables except b are fixed, and if b increased by a factor of 2, by what factor will the total base heat transfer rate q_B increase? **(b)** When in contact with air, the fin shown in Fig. P2.18 experiences the heat transfer rate $q_{B,a}$. Immersed in a water stream with the same velocity and temperature as those of the original airstream (U_∞, T_∞), the same fin experiences a new heat transfer rate,

$q_{B,w}$. Calculate the ratio $q_{B,w}/q_{B,a}$, keeping in mind the following property ratios:

$$\frac{k_w}{k_a} = 23, \qquad \frac{v_w}{v_a} = 0.07, \qquad \frac{Pr_w}{Pr_a} = \frac{7}{0.72}$$

where subscripts w and a indicate water and air, respectively.

2.20. Develop the similarity forms of the boundary layer momentum and energy equations for uniform flow past an inclined wall, as shown in the bottom sketch of Fig. 2.10. For the momentum equation, begin with eq. (2.127) and apply the similarity transformation contained in eqs. (2.71) and (2.80). Show that Blasius's equation (2.82) is now replaced by

$$2f''' + (m + 1)ff'' + 2m[1 - (f')^2] = 0$$

Apply the same transformation to the energy equation and show that Pohlhausen's equation (2.94) is replaced by the more general form

$$2\theta'' + Pr(m + 1)f\theta' = 0$$

Establish whether the angle of inclination has any effect on the boundary conditions to be used in conjunction with the equations above.

2.21. Consider the laminar boundary layer *frictional heating* of an adiabatic wall parallel to a free stream (U_∞, T_∞; Fig. 2.1). Modeling the flow as one with temperature-independent properties and assuming that the Blasius velocity solution holds, use scaling arguments to show that the relevant boundary layer energy equation for this problem is

$$\rho c_P \left(u \frac{\partial T}{\partial x} + v \frac{\partial T}{\partial y} \right) = k \frac{\partial^2 T}{\partial y^2} + \mu \left(\frac{\partial u}{\partial y} \right)^2$$

and that the wall temperature rise scales as U_∞^2/c_P when $Pr > 1$. Determine the wall temperature ($T_0 > T_\infty$), assuming that the wall is insulated ($\partial T/\partial y = 0$ at $y = 0$) and that $T \to T_\infty$ as $y \to \infty$. The path suggested is to develop the similarity solution for the dimensionless temperature profile

$$\theta_r(\eta) = \frac{T - T_\infty}{U_\infty^2/(2c_P)}$$

where the similarity transformation is the same as in eqs. (2.71) and (2.80). Show that the energy equation reduces to

$$\theta_r'' + \frac{Pr}{2}f\theta_r' + 2Pr(f'')^2 = 0$$

where $f(\eta)$ is the Blasius solution. Solving this equation subject to θ'_r $(0) = 0$ and $\theta'_r (\infty) = 0$, prove that the temperature rise in the boundary layer is

$$\theta_r(\eta) = 2\mathrm{Pr} \int_\eta^\infty \left\{ \left[\int_0^p [f''(\beta)]^2 \exp\left(\frac{\mathrm{Pr}}{2} \int_0^\beta f(\gamma)\, d\gamma \right) d\beta \right] \right.$$

$$\left. \times \exp\left(-\frac{\mathrm{Pr}}{2} \int_0^p f(m)\, dm \right) dp \right.$$

Calculate the wall temperature rise $\theta_r(0)$ as a function of Prandtl number using the formula above. Evaluate the nested integrals numerically using an appropriate analytical approximation for the streamfunction profile $f(\eta)$. Based on scale analysis, show that $\theta_r(0)$ is of order $O(\mathrm{Pr})$ and $O(1)$ in the two limits $\mathrm{Pr} \to 0$ and $\mathrm{Pr} \to \infty$, respectively.

2.22. Consider the development of a two-dimensional laminar jet discharging in the x direction into a fluid reservoir that contains the same fluid as the jet (Fig. P2.22). The reservoir pressure P_∞ is uniform. The jet is generated by a narrow slit of width D_0; the average fluid velocity through the slit is U_0.
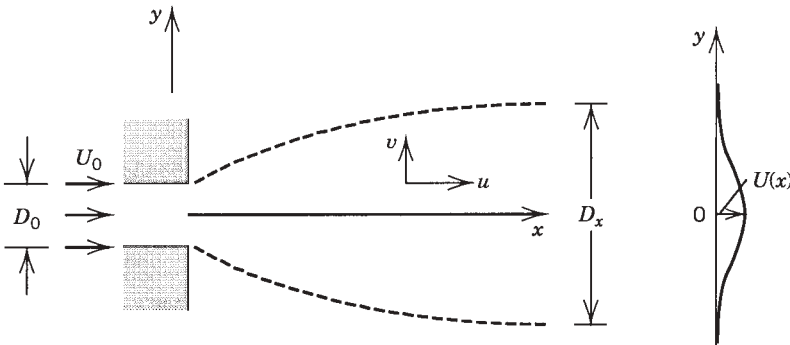
Figure P2.22

Let $D(x)$ and $U(x)$ be the jet thickness scale and the centerline velocity scale at a sufficiently long distance x away from the nozzle (the slit). Relying on the mass and momentum conservation equations, on boundary layer theory ($D \ll x$), and on scale analysis in a flow region of length x and thickness D, determine the order of magnitude of D and U in terms of D_0, U_0, x, and ν:

$$\frac{D(x)}{D_0} \sim \left(\frac{x/D_0}{U_0 D_0/\nu} \right)^{2/3}$$

$$\frac{U(x)}{U_0} \sim \left(\frac{x/D_0}{U_0 D_0/\nu} \right)^{-1/3}$$

Hint: Integrate the momentum equation over an $x = $ constant plane (i.e., from $y = -\infty$ to $y = +\infty$) and show that the integral $\int_{-\infty}^{+\infty} u^2 \, dy$ is independent of x. This result is the basis for an additional scaling law necessary for determining the D and U scales uniquely.

2.23. Consider the development of a two-dimensional thermal jet if the velocity jet (D, U) determined in Problem 2.22 has an original temperature T_0 as it comes out through the slit (Fig. P2.23). The reservoir temperature is uniform, T_∞, and buoyancy effects are negligible.
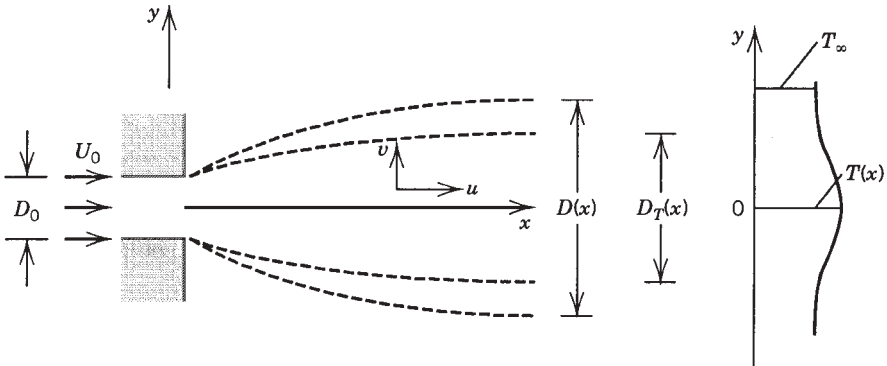
Figure P2.23

Let $D_T(x)$ and $T(x)$ be the thermal jet thickness scale and the centerline temperature scale at a sufficiently long distance x away from the slit. Again, based on boundary layer scale analysis, determine the order of magnitude of D_T and T in terms of D_0, U_0, x, ν, T_0, and α:

$$\frac{D_T(x)}{D(x)} \sim \mathrm{Pr}^{-1/2}$$

$$\frac{T(x) - T_\infty}{T_0 - T_\infty} \sim \begin{cases} \left(\dfrac{U_0 D_0/\nu}{x/D_0}\right)^{1/3} \mathrm{Pr}^{1/2} & (\mathrm{Pr} \gg 1) \\[3mm] \left(\dfrac{U_0 D_0/\nu}{x/D_0}\right)^{1/3} & (\mathrm{Pr} \ll 1) \end{cases}$$

Hint: Integrate the energy equation over an $x = $ constant plane and show that the integral $\int_{-\infty}^{\infty} uT \, dy$ is independent of x. Consider the two possibilities ($D_T < D$ and $D_T > D$) separately as you interpret the scaling law implied by the x independent longitudinal enthalpy flow integral.

2.24. Consider the laminar flow of a two-dimensional liquid film on a flat wall inclined at an angle α relative to the horizontal direction. The film flow is driven by the gravitational acceleration component ($g \sin\alpha$) acting parallel

to the wall. Attach the Cartesian system of coordinates (x, y) and (u, v) to the wall, such that x and u point in the flow direction. In this notation, derive the *terminal* velocity distribution in the liquid film $u(y)$; in other words, determine the flow in the limit where the film inertia is negligible and the x momentum equation expresses a balance between film weight and wall friction. Let U be the undetermined free surface velocity at $y = \delta$, where δ is the film thickness. Note that U is undetermined because the film flow rate can be varied at will by the person who pours liquid on the incline.

Consider next the heat transfer from the wall to the liquid film in the case where the film and wall temperature is T_0 everywhere upstream of $x = 0$ and where the wall temperature alone is raised to $(T_0 + \Delta T)$ downstream of $x = 0$. Let δ_T be the thermal boundary layer thickness of the thin liquid region in which the wall heating effect is felt. Using scale analysis, demonstrate that immediately downstream from $x = 0$ (where δ_T is much smaller than δ), the thermal boundary layer thickness δ_T scales as $[(\alpha \, \delta \, x)/U]^{1/3}$.

Determine the temperature distribution in the film based on an *integral* analysis, assuming the following temperature profile:

$$\frac{T(x, y) - T_0}{\Delta T} = 1 - 2\frac{y}{\delta_T} + \left(\frac{y}{\delta_T}\right)^2, \quad 0 \le y \le \delta_T$$

$$T(x, y) = T_0, \quad \delta_T < y \le \delta$$

Note that this integral analysis is valid as long as $\delta_T(x) \le \delta$. At what distance $x = x_1$ will the free surface feel the heating effect of the wall (i.e., at what x will δ_T equal δ)? Devise an integral analysis to determine the film temperature field $T(x, y)$ downstream from the point $x = x_1$.

2.25. An infinitely long flat plate is initially at rest immersed in a liquid pool with properties ν, α, and T_∞. The plate is also in thermal equilibrium with the pool. At a certain instant, $t = 0$, the plate starts moving at constant velocity U along itself. Determine the time-dependent velocity distribution in the fluid for times $t > 0$ in the immediate vicinity of the solid wall.

At another point in time, $t = t_1$, the plate temperature is changed to a new temperature $T = T_0$. Determine the time-dependent temperature distribution in the fluid in the immediate vicinity of the wall and for times $t > t_1$. Based on the expressions obtained for the velocity and temperature fields, decide whether the solid plate is lined by boundary layer regions. Does the temperature field depend on the velocity distribution [as in Pohlhausen's problem, eq. (2.98)]?

2.26. The flat plate shown in Fig. P2.26 is isothermal (T_w) and parallel to the flow of a fluid (k, U_∞, T_∞) with Prandtl number greater than 0.5. The boundary layer flow is laminar. The plate is coated with a thin layer

of low-thermal-conductivity material (k_w). The thickness of this coating, $t(x)$, varies in such a way that the heat flux q'' removed by the fluid is independent of x. The L-averaged thickness of the coating, $\bar{t}$, is known. Determine the coating profile $t(x)$ as a function of $x, \bar{t}, L, k/k_w$, Pr, and Re_L. Sketch $t(x)$ qualitatively. Derive an expression for the overall thermal resistance $(T_w - T_\infty)k/q''L$, and comment on why this expression has two terms.
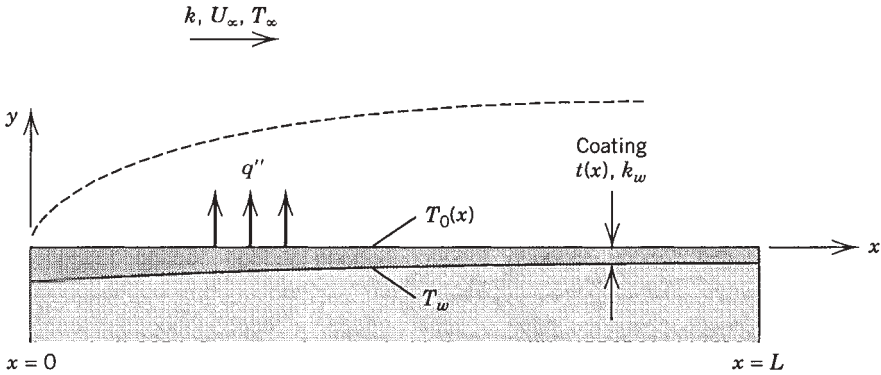
Figure P2.26

2.27. Assume that the laminar boundary layer of Fig. 2.1 sweeps a wall with uniform heat flux and that $\mathrm{Pr} = 0$. Note that $\mathrm{Pr} = 0$ means that $u = U_\infty$ in the entire thermal boundary layer region. Show that in this case the temperature distribution in the fluid and the local Nusselt number can be determined analytically in closed form [27]:

$$T(x, y) = T_\infty + \frac{q''}{k}\left(\frac{\alpha x}{U_\infty}\right)^{1/2}\tau(\zeta)$$

$$\mathrm{Nu} = \frac{\pi^{1/2}}{2}\mathrm{Pr}^{1/2}\mathrm{Re}_x^{1/2}$$

where $\zeta = y(U_\infty/\alpha x)^{1/2}$ and

$$\tau(\zeta) = \frac{2}{\pi^{1/2}}\exp\left(-\frac{\zeta^2}{4}\right) - \zeta\ \mathrm{erfc}\left(\frac{\zeta}{2}\right)$$

2.28. Use the same statement as in Problem 2.4. Assume the linear profile, but instead of $\mathrm{Pr} \gg 1$, derive the local Nu solution for $\mathrm{Pr} \ll 1$.

2.29. The nondimensionalization of wall shear stress as a skin friction coefficient is not appropriate because the stagnation pressure rise $\frac{1}{2}\rho U_\infty^2$ is not present

in the boundary layer flow field. Use eq. (2.29) and arrive at a new nondimensionalization of $\overline{\tau}$,

$$\frac{\overline{\tau}L^2}{\mu\nu} = 0.664\left(\frac{U_\infty L}{\nu}\right)^{3/2}$$

This shows that the wall shear stress increases monotonically with the Reynolds number. Note also the similarity between the group $\overline{\tau}L^2/\mu\nu$ and the pressure drop number defined in eq. (3.120′), hence the notation

$$\frac{\overline{\tau}L^2}{\mu\nu} = \mathrm{Be}_\tau \mathrm{Pr}^{-1}$$

where $\mathrm{Be}_\tau = \overline{\tau}L^2/\mu\alpha$. Use the Pohlhausen solution for $\mathrm{Pr} > 1$ to show that the overall Nusselt number is essentially the same as $\mathrm{Be}_\tau^{1/3}$:

$$\mathrm{Nu}_{0-L} = 0.664^{2/3}\mathrm{Be}_\tau^{1/3}$$

3

LAMINAR DUCT FLOW

In this chapter we study the fluid friction and heat transfer between a stream and a solid object in internal flow, that is, when the solid surface is the duct that guides the stream. This is a vast field [1] in which the fundamental questions are the same as in external flow (Chapter 2):

1. What is the friction force (or pressure drop) in the flow direction?
2. What is the heat transfer coefficient, or the resistance to heat transfer in the direction normal to the flow?

We will see that the theoretical view that makes the answers to these questions most accessible to the analyst is the concept of *fully developed* flow and temperature fields. This is a powerful concept that like Prandtl's boundary layer in external convective heat transfer is responsible for much of the language and results presently known in connection with laminar duct flow and heat transfer.

Traditionally, the concept of fully developed flow is taught as a self-standing topic, as a useful approximation when confronted by the Navier–Stokes equations. This traditional approach is not incorrect, provided that the theoretical basis for the approximation is well understood. I find it more appropriate to introduce the concept of fully developed flow as a direct consequence of the concept of boundary layer encountered in external flow. Both concepts are expressions of the view that certain *finite-size regions* of a flow field possess special properties. With the concept of boundary layer, we divide a flow into two regions: a free stream and a boundary layer. Similarly, the concept of *fully developed* divides a duct flow into a *developing* length succeeded by a fully developed length. The same view is used in Chapters 6–9, where the longitudinal buckling wavelength λ_B is a property of a flow region of *finite thickness*.

3.1   HYDRODYNAMIC ENTRANCE LENGTH

Consider the flow configuration sketched in Fig. 3.1: Two parallel plates form a two-dimensional duct intaking the uniform stream U. We are interested in the friction force exerted by the flow on the two walls and the dependence of the velocity profile $u(x, y)$ on the longitudinal position x along the duct. The integral solution outlined below was constructed by Sparrow [2].

Based on what we learned in Chapter 2, we expect the formation of velocity boundary layers along the two walls in the region x ''close enough'' to the mouth of the channel, where the tip of each plate is surrounded by the U stream in the same manner as in Fig. 2.1. Since the thickness δ of each layer grows in the x direction, and since one layer can grow only to a thickness $D/2$ before merging with the other layer, the channel flow can be thought of as the succession of two distinct flow regions. In the first (called the *entrance* or *developing section*), distinct boundary layers coexist with *core* fluid that has not yet felt viscously the presence of the walls. In the second region, the core has disappeared and the boundary layers are no longer distinct.

We obtain a scaling estimate of the entrance length X by writing $\delta(X) = D/2$ in Blasius's boundary layer thickness [eq. (2.85)],

$$\frac{X/D}{\mathrm{Re}_D} = 0.01 \tag{3.1}$$

Relative to this simple result, the integral solution to the entrance length problem accounts for the fact that the core fluid is squeezed, hence accelerated in the x direction. This effect is illustrated in Fig. 3.1: Since more fluid stagnates near the walls as the boundary layers thicken, the core velocity U_c must increase so that the mass flow rate in each cross section x is constant and equal to $\rho U D$.

We start with the integral momentum equation (2.52), where $U_\infty = U_c$ and $Y = \delta(x)$. The free-stream pressure gradient dP_∞/dx appearing in eq. (2.52) is
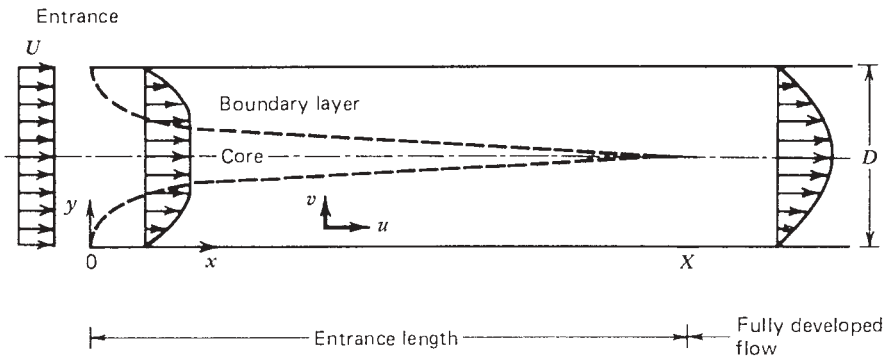
Figure 3.1   Developing flow in the entrance region of a duct formed between two parallel plates.

now the core pressure gradient dP/dx. Since the core flow is inviscid, dP/dx is related to $U_c(x)$ through the Bernoulli equation $\rho U_c^2/2 + P = \text{constant}$; hence,

$$U_c \frac{dU_c}{dx} + \frac{1}{\rho} \frac{dP}{dx} = 0 \tag{3.2}$$

Eliminating dP/dx between eqs. (3.2) and (2.52) yields

$$\frac{d}{dx}\left[\int_0^\delta (U_c - u) u \, dy\right] + \frac{dU_c}{dx} \int_0^\delta (U_c - u) \, dy = v\left(\frac{\partial u}{\partial y}\right)_0 \tag{3.3}$$

In addition, mass conservation in the channel of half-width (from $y = 0$ to $y = D/2$) requires that

$$\int_0^\delta \rho u \, dy \; + \; \int_\delta^{D/2} \rho U_c \, dy = \rho U \frac{D}{2} \tag{3.4}$$

Equations (3.3) and (3.4) are solved for $\delta(x)$ and $U_c(x)$ by first assuming a boundary layer profile shape. Taking $u/U_c = 2y/\delta - (y/\delta)^2$, we obtain

$$\frac{x/D}{\text{Re}_D} = \frac{3}{40}\left(9\frac{U_c}{U} - 2 - 7\frac{U}{U_c} - 16 \ln \frac{U_c}{U}\right) \tag{3.5}$$

$$\frac{\delta(x)}{D/2} = 3\left[1 - \frac{U}{U_c(x)}\right] \tag{3.6}$$

At the location X where the two boundary layers merge we set $\delta(X) = D/2$, and eqs. (3.5) and (3.6) yield $U_c(X) = \frac{3}{2}U$ and

$$\frac{X/D}{\text{Re}_D} = 0.026 \tag{3.7}$$

In conclusion, the laminar entrance length predicted by the integral solution is of the same order of magnitude as the scaling estimate [eq. (3.1)]. The contribution of both methods is that they show analytically the extent of the laminar developing region: X scales with $D \text{Re}_D$, and the proportionality factor is a number on the order of 10^{-2}. Schlichting [3] solved the same problem by obtaining a series solution for the accelerated boundary layer flow in the beginning of the entrance length and by matching this series to a second-series solution valid near the end of the laminar entrance length. Although in his solution the velocity profile varies smoothly as it asymptotically reaches the fully developed shape, the entrance region has a characteristic length perceived approximately as [3]

$$\frac{X/D}{\text{Re}_D} \cong 0.04 \tag{3.8}$$
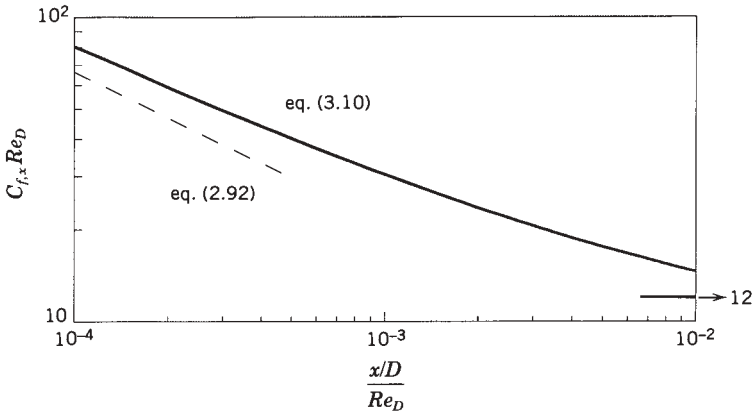
Figure 3.2 Local skin friction coefficient in the entrance region of a duct formed between two parallel plates.

The fundamental difference between the entrance length and the fully developed region is illustrated further by the variation of wall frictional shear stress as x increases. Figure 3.2 shows the skin friction coefficient defined by

$$C_{f,x} = \frac{\tau_{\text{wall}}(x)}{\frac{1}{2}\rho U^2} \tag{3.9}$$

with $\tau_{\text{wall}} = \mu(\partial u/\partial y)_0$. For the integral solution (3.5)–(3.7), the $C_{f,x}$ formula is

$$C_{f,x} \text{ Re}_D = \frac{8}{3}\frac{U_c}{U}\left(1 - \frac{U}{U_c}\right)^{-1} \tag{3.10}$$

Figure 3.2 also shows the $C_{f,x}$ calculation based on the Blasius result [eq. (2.92)] with U_∞ replaced by U in the definition of $C_{f,x}$ and Re_x. In the entrance region, $C_{f,x}$ behaves in a manner that suggests the presence of distinct boundary layers. In the fully developed region, on the other hand, τ_{wall} and $C_{f,x}$ are no longer functions of x because the velocity profile $u(x, y)$ has become practically independent of x. We focus more closely on this effect in the next section.

The hydrodynamic entrance length in a round tube can be predicted along similar lines. Figure 3.3 shows the variation of $C_{f,x}$ in the entrance region. Note that in most textbooks and handbooks, the same information appears with $\text{Re}_D/(x/D)$ plotted on the abscissa, which is a strange way of plotting a quantity $(C_{f,x})$ that varies along x. The dimensionless coordinate plotted on the abscissas of Figs. 3.2 and 3.3 is $(x/D)/\text{Re}_D$, which increases proportionally with x as the flow travels deeper into the duct. Figure 3.3 also shows the average skin friction coefficient, that is, the value of $C_{f,x}$ averaged from $x = 0$ to x. An analytical expression for $(C_f)_{0-x}$ is given later in eqs. (3.117)–(3.119).
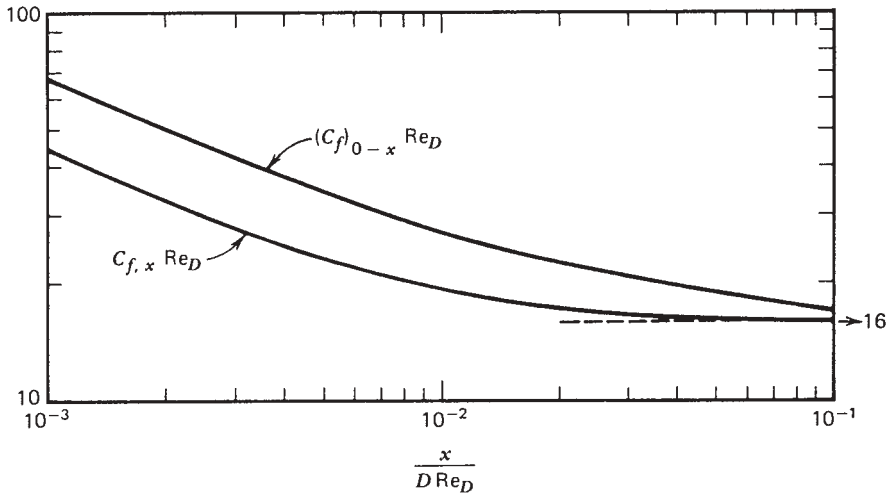
Figure 3.3   Local and average skin friction coefficients in the entrance region of a round tube. (After Ref. 4.)

3.2   FULLY DEVELOPED FLOW

The statements for steady-state mass and momentum conservation at any point (x, y) inside the two-dimensional channel of Fig. 3.1 are

$$\frac{\partial u}{\partial x} + \frac{\partial v}{\partial y} = 0 \tag{3.11}$$

$$u\frac{\partial u}{\partial x} + v\frac{\partial u}{\partial y} = -\frac{1}{\rho}\frac{\partial P}{\partial x} + \nu\left(\frac{\partial^2 u}{\partial x^2} + \frac{\partial^2 u}{\partial y^2}\right) \tag{3.12}$$

$$u\frac{\partial v}{\partial x} + v\frac{\partial v}{\partial y} = -\frac{1}{\rho}\frac{\partial P}{\partial y} + \nu\left(\frac{\partial^2 v}{\partial x^2} + \frac{\partial^2 v}{\partial y^2}\right) \tag{3.13}$$

These equations can be simplified based on the following scaling argument. At any location $x \sim L$ in the fully developed region, we have $y \sim D$ and $u \sim U$. Therefore, using eq. (3.11), the transversal velocity in the fully developed region must scale as

$$v \sim \frac{DU}{L} \tag{3.14}$$

We can then think of the *fully developed* region as being that section of the duct flow that is situated far enough from the entrance such that the scale of v is

negligible. Based on this definition, the mass continuity equation (3.11) requires in the fully developed flow limit

$$v = 0 \quad \text{and} \quad \frac{\partial u}{\partial x} = 0 \tag{3.15}$$

In most treatises of fluid mechanics, eqs. (3.15) are taken as *definitions* and a starting point in the analysis of the fully developed regime. More important, I think, are the scaling foundations of eqs. (3.15). We can think of a fully developed region only because we can think of a flow region where the scale of y is D (fixed). This corresponds to a velocity variation that spreads over the entire cross section. In the entrance region, on the other hand, the scale of y is δ (not fixed), and as a consequence, neither v nor $\partial u/\partial x$ is negligible.

Based on eqs. (3.15), the y momentum equation (3.13) reduces to

$$\frac{\partial P}{\partial y} = 0 \tag{3.16}$$

which indicates that P is a function of x only. This conclusion is similar to the one reached previously in the study of the laminar boundary layer (Chapter 2): The pressure is only a function of x in the two entrance boundary layers merging to create the fully developed region.

Finally, the x momentum equation (3.12) leads to two equations

$$\frac{dP}{dx} = \mu \frac{d^2 u}{dy^2} = \text{constant} \tag{3.17}$$

Each term must be equal to the same *constant* because P is a function of x and u is a function of y [cf. eq. (3.15)]. Solving eq. (3.17) subject to the no-slip conditions

$$u = 0 \qquad \text{at} \quad y = \pm D/2 \tag{3.18}$$

yields the solution for fully developed flow between parallel plates,

$$u = \frac{3}{2} U \left[1 - \left(\frac{y}{D/2} \right)^2 \right]$$

$$U = \frac{D^2}{12\mu} \left(-\frac{dP}{dx} \right) \tag{3.19}$$

where y is measured away from the centerline of the channel. The velocity profile is parabolic and the velocity is proportional to the pressure drop per unit duct length in the direction of flow.

In general, for a duct of arbitrary cross section, eq. (3.17) is replaced by

$$\frac{dP}{dx} = \mu \nabla^2 u = \text{constant} \tag{3.20}$$

where in the Laplacian operator ∇^2, $\partial^2 u/\partial x^2 = 0$. For example, the fully developed laminar flow in a round tube of radius r_0 is governed by

$$\frac{dP}{dx} = \mu \left(\frac{d^2 u}{dr^2} + \frac{1}{r} \frac{du}{dr} \right) \tag{3.21}$$

Solving this equation subject to $u = 0$ on the periphery of the cross section ($r = r_0$) yields

$$u = 2U \left[1 - \left(\frac{r}{r_0} \right)^2 \right]$$

$$U = \frac{r_0^2}{8\mu} \left(-\frac{dP}{dx} \right) \tag{3.22}$$

$$\dot{m} = \frac{\pi r_0^4}{8\nu} \left(-\frac{dP}{dx} \right)$$

where $\dot{m} = \rho U \pi r_0^2$ is the mass flow rate. This flow solution was first reported by Hagen [5] in 1839 and Poiseuille [6] in 1840.

In eqs. (3.19) and (3.22) we see the simplest solutions available for laminar fully developed flow in the rectilinear duct. In general, as shown in the next section, the solution to the Poisson-type equation (3.20) is considerably more difficult.

It is common practice to assign to a Hagen–Poiseuille flow a *Reynolds number* defined for a round tube as $\mathrm{Re}_D = UD/\nu$. Fluid mechanics textbooks teach the seemingly obvious explanation that the Reynolds number is the ratio of two forces, the inertia divided by the friction force. This explanation is wrong.

Although there are certain *flow regions* in which one could envision a Reynolds number as the inertia/friction ratio (e.g., Problem 1.12), it is not true that the Reynolds number means the same thing for all flows. In Chapter 2 we saw that in laminar boundary layer flow the inertia effect always balances the friction effect (i.e., the ratio inertia/friction is 1) and that the only physical meaning attached to the Reynolds number is the geometric feature represented by the boundary layer slenderness ratio squared [eq. (2.31)]. In Hagen–Poiseuille flow through a straight duct, the inertia/friction interpretation of the Reynolds number is nonsense. Hagen–Poiseuille flows are flows in which the fluid inertia is *zero* everywhere; these flows are governed by a permanent and perfect balance between the imposed (driving) longitudinal pressure gradient ($-dP/dx$) and the opposing effect of friction exerted by the wall on the flow. So if we must define a dimensionless group for fully developed laminar flow through a straight duct, this group can only be the ratio

$$\frac{\text{longitudinal pressure force}}{\text{friction force}}$$

According to the momentum equation for Hagen–Poiseuille flow and all subsequent solutions available for such flows, the order of magnitude of this ratio is unity:

$$\frac{-dP/dx}{\mu\,\partial^2 u/\partial r^2} \sim \frac{\Delta P/L}{\mu U/D^2} = O(1)$$

This is the force balance that *means* Hagen–Poiseuille flow. The dimensionless group that just appeared above is discussed later in this section (see also the description of the group of $f\,\mathrm{Re}_{D_h}$).

There are other signs that Re_D has no meaning in fully developed laminar duct flow. First, it is well known that the Re_D calculated in such flows can reach as high as 2300, which is a number considerably greater than unity. Such a large number, coupled with the inertia/friction interpretation of the Reynolds number, would suggest that inertia overwhelms friction in Hagen–Poiseuille flow—an absurd conclusion, because inertia is zero.

Another sign is the friction factor f defined in eq. (3.24): In laminar flow, both f and τ_w are very sensitive to changes in Re_D, demonstrating that the Reynolds number is an inappropriate ratio of scales and that the dynamic pressure difference $\frac{1}{2}\rho U^2$ is an inappropriate pressure unit for Hagen–Poiseuille flow. The group $\frac{1}{2}\rho U^2$ is inappropriate as a pressure unit here and in Chapter 2 because it is a Bernoulli equation concept, that is, a *reversible flow concept* [7]. Laminar boundary layers and fully developed flows through ducts are flows governed by friction (thermodynamic irreversibility); hence, the use of a reversible flow concept to scale such flows is a conceptual inconsistency. Furthermore, the dynamic pressure does not occur anywhere in the flow field; the flow is parallel to the walls, not perpendicular.

The fact that the Reynolds number is not conceptually justified in a discussion of fully developed laminar flow does not mean that it is not a *useful* dimensionless group for convective heat transfer engineering. The Reynolds number is useful, particularly in the presentation of duct friction data on a *single* plot for both the turbulent and laminar regimes (as in the Moody chart of Fig. 8.2). For this reason, the classical Reynolds number nomenclature is retained in the present treatment. But at the same time, the reader should be aware of the fact that the classical meaning of the Reynolds number is questionable. A proposal in this direction is advanced in Chapter 6 and in constructal theory [8], where the concept of Reynolds number is linked to the equality of two characteristic time scales that collaborate to facilitate the transport of momentum perpendicularly to the shear flow (the constructal law).

3.3 HYDRAULIC DIAMETER AND PRESSURE DROP

The objective of the preceding analysis is the calculation of the pressure drop in a duct with prescribed flow rate or the calculation of the flow rate in a duct with prescribed pressure drop. In fully developed laminar flow, $\dot{m}$ and ΔP are
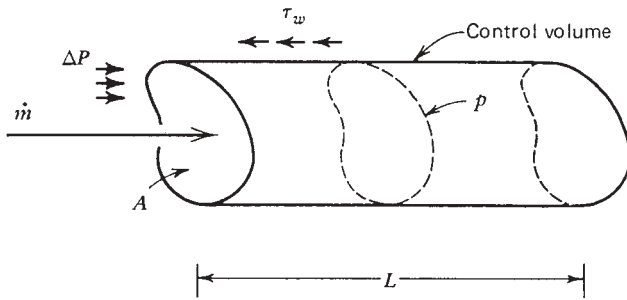
Figure 3.4   Control volume showing the force balance expressed by eq. (3.23).

proportional to one another. In general (especially in turbulent flow), the $\dot{m}(\Delta P)$ relationship is not as simple and is usually the object of laboratory measurements. The historically empirical approach to determining the $\dot{m}(\Delta P)$ relationship* is responsible for the terminology in use today.

Consider the duct with *arbitrary* flow cross section A and length L shown in Fig. 3.4. Treating the AL control volume as a black box, that is, without looking inside to see the actual flow, the momentum theorem in the longitudinal direction (Chapter 1) requires

$$A \, \Delta P = \tau_w pL \tag{3.23}$$

where p is the perimeter of the cross section (the wetted perimeter). The unknown wall shear stress τ_w is replaced by a dimensionless unknown, the *friction factor*, defined as

$$f = \frac{\tau_w}{\frac{1}{2}\rho U^2} \tag{3.24}$$

This definition is essentially the same as eq. (3.9) for the skin friction coefficient in the entrance region. One important difference between f and $C_{f,x}$ is that the friction factor f is x independent because it is a *fully developed regime* concept.

---

*This approach was the trademark of hydraulics, the precursor of modern fluid mechanics. About the hydraulics of the nineteenth century, Tietjens [9] wrote in 1934: "The hydraulics, which tried to answer the multitudinous problems of practice, disintegrated into a collection of unrelated problems. Each individual question was solved by assuming a formula containing some undetermined coefficients and then determining these by experiments. Each problem was treated as a separate case and there was lacking an underlying theory by which the various problems could be correlated." In contemporary fluid mechanics research, we like to think that the classical mechanics embodied in the Navier–Stokes equations offers a common theoretical basis for all fluid flow phenomena. Yet, the study of turbulence has retraced the empirical course chosen by hydraulics; in fact, replace *hydraulics* with *turbulence* in the quotation from Tietjens and you will obtain a fairly close description of turbulence research. Granted, the empirical constants of hydraulics have been replaced by shady (however, equally empirical) concepts such as eddy diffusivity, numerical models, and many "universal" constants. It is on this background of empiricism that the scaling laws of Chapter 6 and constructal theory [8] show how a single idea accounts for turbulent flows as designs in nature.

Definition (3.24) is not unique; the heat transfer literature also uses $4f$ as the friction factor since the product $4f$ appears explicitly in eq. (3.27). The reader can tell which f definition is used (if the f definition is missing) by checking the f formula for a round tube. Thus, if $f = 16/\text{Re}_D$, the present definition [eq. (3.24)] was used.

After these definitions, the pressure drop ΔP across the duct is

$$\Delta P = f \frac{pL}{A}\left(\frac{1}{2}\rho U^2\right)$$ (3.25)

Finally, note that A/p is the linear dimension of the cross section:

$$r_h = \frac{A}{p} \qquad \text{hydraulic radius}$$ (3.26)

or

$$D_h = 4r_h = \frac{4A}{p} \qquad \text{hydraulic diameter}$$ (3.26′)

Table 3.1 shows a vertically aligned column of five different cross-sectional shapes and sizes, all having the same hydraulic diameter D_h. This arrangement shows the meaning of hydraulic diameter; it is a conventional length that accounts for "how close" the wall and its resistive effect are positioned relative to the stream. Thus, in the case of highly asymmetric cross sections such as the gap between two infinite parallel plates, the hydraulic diameter scales with the *smallest* of the two dimensions of the cross section. The D_h value of a regular polygon is equal to the diameter of the inscribed circle.

The pressure drop formula (3.25) can be written as

$$\Delta P = f \frac{4L}{D_h}\left(\frac{1}{2}\rho U^2\right)$$ (3.27)

The calculation of ΔP is possible provided that we know the friction factor f. The friction factors derived from the Hagen–Poiseuille solutions (3.19) and (3.22) are, respectively:
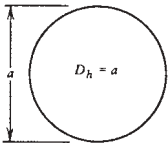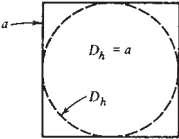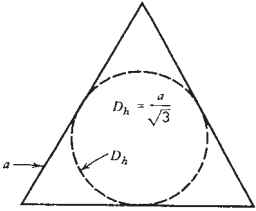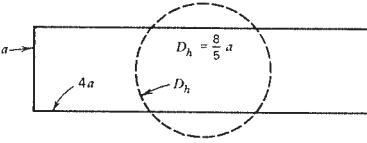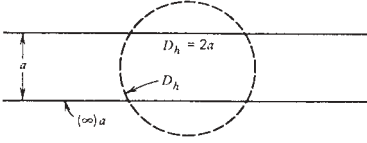
$$f = \frac{24}{\text{Re}_{D_h}}, \qquad D_h = 2D \qquad \text{parallel plates } (D = \text{gap thickness})$$ (3.28)

$$f = \frac{16}{\text{Re}_{D_h}}, \qquad D_h = D \qquad \text{round tube } (D = \text{tube diameter})$$ (3.29)

These formulas hold as long as the flow is in the laminar regime ($\text{Re}_{D_h} < 2000$).

The literature is rich in results that are equivalent to eqs. (3.28) and (3.29) for other duct cross sections. Most of these numbers (the numerical values of

Table 3.1   Scale drawings of five ducts that have the same hydraulic diameter
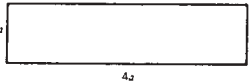
Cross Section

Circular	$D_h = a$

Square	$D_h = a$

Equilateral triangle	$D_h = \dfrac{a}{\sqrt{3}}$

Rectangular (4:1)	$D_h = \dfrac{8}{5} a$

Infinite parallel plates	$D_h = 2a$

the product $f\,\mathrm{Re}_{D_h}$) have been compiled in Ref. 10 and some are shown here in Table 3.2. The product $f\,\mathrm{Re}_{D_h}$ is a number that depends only on the shape of the cross section. This number has been named the *Poiseuille number* [11], $\mathrm{Po} = f\,\mathrm{Re}_{D_h}$. Furthermore, the reader may verify that $f\,\mathrm{Re}_{D_h}$ is the same as the dimensionless group identified in the force balance shown under eq. (3.22),

$$\frac{\Delta P/L}{\mu U/D_h^2} \sim f\,\mathrm{Re}_{D_h}$$

The fact that $f\,\mathrm{Re}_{D_h}$ is a constant (of order close to 1) expresses the balance between the only two forces that are present, imposed pressure difference and fluid friction.

Table 3.2   Effect of cross-sectional shape on f and Nu in fully developed duct flow

Cross-sectional geometry	$f\,\mathrm{Re}_{D_h}$	$B = \dfrac{\pi D_h^2/4}{A_{\text{duct}}}$	Nu = hD_h/k	
			Uniform q''	Uniform T_0
(triangle, 60°)	13.3	0.605	3	2.35
(square)	14.2	0.785	3.63	2.89
(circle)	16	1	4.364	3.66
(rectangle, a, $4a$)	18.3	1.26	5.35	4.65
(parallel plates)	24	1.57	8.235	7.54
(parallel plates, One side insulated)	24	1.57	5.385	4.86

In general, the friction factor f is obtained by solving the Poisson equation (3.20) in the duct cross section of interest. To illustrate this procedure beyond the two simple examples given in Section 3.2, consider the fully developed laminar flow through a duct of rectangular cross section (Fig. 3.5). We solve

$$\frac{dP}{dx} = \mu \left(\frac{\partial^2 u}{\partial y^2} + \frac{\partial^2 u}{\partial z^2} \right) = \text{constant} \tag{3.30}$$

in the $y - z$ plane in which the cross-sectional dimensions are a and b, respectively. Equation (3.30) can be solved for $u(y, z)$ by Fourier series (see Problem 3.4). In this section we outline a more direct, approximate approach to the answer needed. To calculate f or τ_w, we need the velocity distribution $u(y, z)$: From the parallel-plate and round-tube solutions discussed previously, we expect $u(y, z)$ to be adequately represented by the expression

$$u(y, z) = u_0 \left[1 - \left(\frac{y}{a/2} \right)^2 \right] \left[1 - \left(\frac{z}{b/2} \right)^2 \right] \tag{3.31}$$

where u_0 is the centerline (peak) velocity. The problem reduces to calculating u_0 from eq. (3.30): Since $u(y, z)$ of eq. (3.31) will not satisfy eq. (3.30) at every point
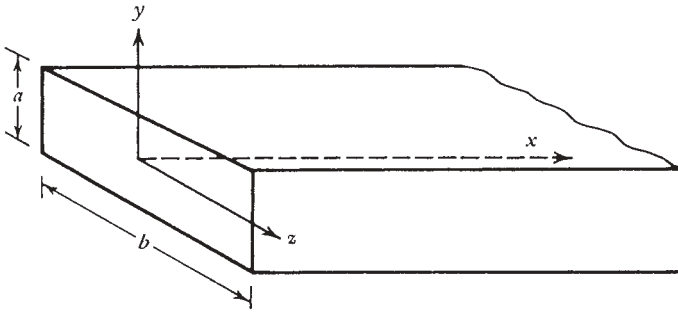
Figure 3.5   Straight duct with rectangular cross section.

(y, z), we can select u_0 such that expression (3.31) satisfies eq. (3.30) *integrated* over the entire cross section:

$$ab\frac{dP}{dx} = \mu \int_{-a/2}^{a/2} \int_{-b/2}^{b/2} \left(\frac{\partial^2 u}{\partial y^2} + \frac{\partial^2 u}{\partial z^2} \right) dz \, dy \qquad (3.32)$$

The result is

$$ab\frac{dP}{dx} = -\frac{16}{3}\mu u_0 \left(\frac{b}{a} + \frac{a}{b} \right) \qquad (3.33)$$

From the definition of average velocity U,

$$abU = \int_{-a/2}^{a/2} \int_{-b/2}^{b/2} u \, dz \, dy \qquad (3.34)$$

we also obtain

$$u_0 = \tfrac{9}{4}U \qquad (3.35)$$

Substituting eqs. (3.33) and (3.35) into the pressure drop [eq. (3.27)] yields

$$f = \frac{a^2 + b^2}{(a + b)^2} \frac{24}{\mathrm{Re}_{D_h}} \qquad (3.36)$$

where

$$D_h = \frac{4ab}{2(a + b)} \qquad (3.37)$$

The friction factor f [eq. (3.36)] is invariant to the transformation $a \to b$, $b \to a$ because the cross-sectional geometry is invariant (rectangular) to the
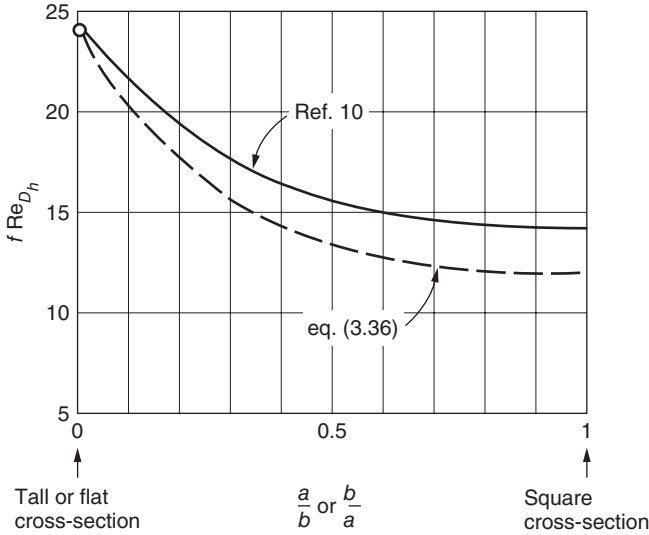
Figure 3.6 Friction factor for fully developed flow in a duct with rectangular cross section.

transformation $y \to z$, $z \to y$ (Fig. 3.5). Figure 3.6 shows this relatively simple result next to the numerical calculation of $f \, \mathrm{Re}_{D_h}$ [10]. The present $f \, \mathrm{Re}_{D_h}$ result coincides with the numerical result in the tall and flat cross-sectional shape limits because in those limits the profile shape assumption (3.31) is exactly the Hagen–Poiseuille profile shape. Overall, the agreement between eq. (3.36) and numerically derived results is better than 15 percent.

Table 3.2 shows a compilation of friction factors for laminar fully developed flow in the most common duct geometries. Regardless of cross-sectional shape, the value of $f \, \mathrm{Re}_{D_h}$ is consistently on the order of 20, thus stressing the usefulness of the hydrodynamic diameter scaling discussed immediately following eqs. (3.26). The length scale D_h accounts for the effective distance between the walls ''squeezing'' the flow. In equilateral triangles, D_h underestimates this distance, whereas in parallel-plate channels, the wall-to-wall distance is overestimated by D_h.

This mismatch between D_h and the wall-to-wall distance explains why $f \, \mathrm{Re}_{D_h}$ *increases* in Table 3.2, from the equilateral triangle to the parallel-plate channel. Indeed, as shown in Fig. 3.7, there is an approximate proportionality between $f \, \mathrm{Re}_{D_h}$ and the degree to which D_h misjudges the wall-to-wall distance. In the first edition of this book it was proposed to measure the mismatch between D_h and the average wall-to-wall distance by using the geometric ratio $B = (\pi D_h^2/4)/A_{\mathrm{duct}}$ [in the case of extremely flat cross sections, A_{duct} is equal to aD_h, where a is the actual plate-to-plate distance (see Table 3.1)]. The usefulness
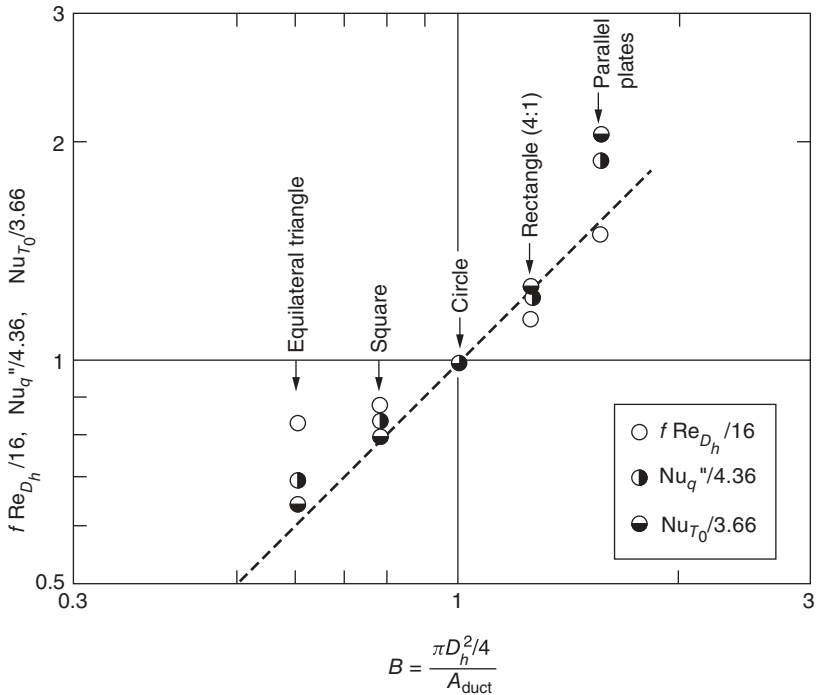
Figure 3.7   Cross-sectional shape number B and fully developed friction and heat transfer in straight ducts.

of the new dimensionless group $B = (\pi D_h^2/4)/A_{duct}$ is illustrated further in Problem 3.6.

3.4   HEAT TRANSFER TO FULLY DEVELOPED DUCT FLOW

3.4.1   Mean Temperature

The key question about the heat transfer to duct flow is the relationship between the wall–stream temperature difference and the wall–stream heat transfer rate (or the longitudinal temperature variation of the stream). Without loss of generality, consider a tube of radius r_0, average axial velocity U, and mass flow rate $\dot{m} = \rho \pi r_0^2 U$ (Fig. 3.8). From the thermodynamics of flow systems (Chapter 1), we know that the heat transferred from the wall to the stream ($q'' 2\pi r_0 \, dx$) equals the enthalpy gain experienced by the stream; for the control volume of length dx in Fig. 3.8, the first law of thermodynamics requires

$$q'' \cdot 2\pi r_0 \, dx = \dot{m}(h_{x+dx} - h_x) \tag{3.38}$$
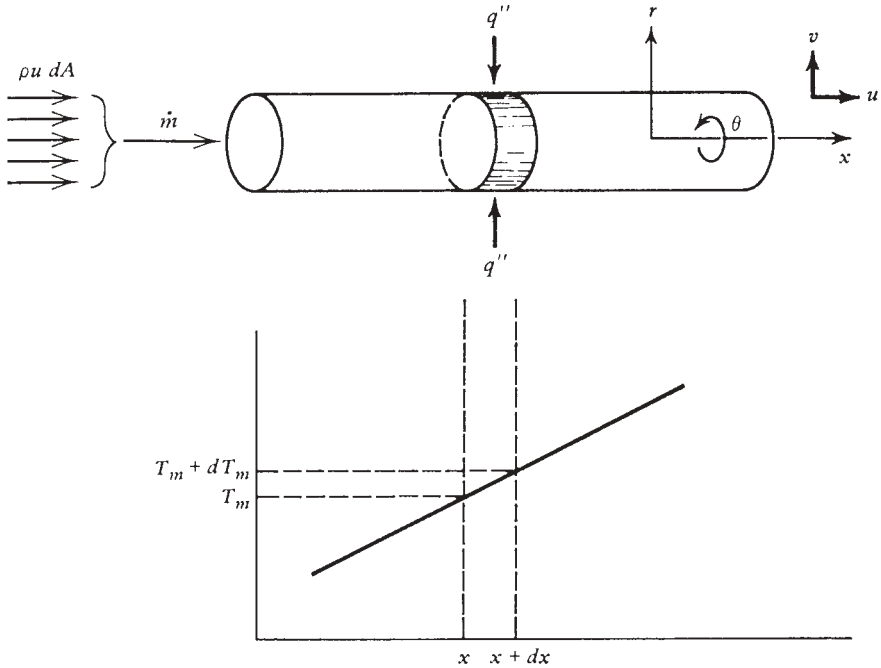
Figure 3.8   Energy conservation in a duct segment of length dx.

Modeling the fluid as an ideal gas ($dh = c_P dT_m$) or an incompressible liquid with negligible pressure changes ($dh \cong c\,dT_m$)* eq. (3.38) yields

$$\frac{dT_m}{dx} = \frac{2}{r_0}\frac{q''}{\rho c_P U} \tag{3.39}$$

where c_P is replaced by c for incompressible liquids.

The temperature T_m appearing in the first law analysis of the duct ''control volume'' is the *bulk temperature* of the stream. In heat transfer—an activity that developed in parallel with modern thermodynamics [7]—T_m is the *mean temperature* of the stream. Implicit in this name is the fact that the fluid temperature cannot be uniform over the duct cross section at $x =$ fixed; for example, if the stream is heated by the wall, the fluid layer or *lamina* situated closer to the wall is warmer than a layer situated farther from the wall. Of course, a relationship must exist between the temperature at every point in the cross section $T(x, r)$ and the mean temperature $T_m(x)$. However, T_m is not just any average; it is the mean temperature the definition of which is the first law for

*This approximation is correct only if over the duct length of interest $c\,\Delta T_m$ is considerably greater than $\Delta P/\rho$ (see Table 1.1).

bulk flow [eq. (3.38)]. We write the first law for the bundle of ministreams ρu dA piercing the tube cross section,

$$q'' \cdot 2\pi r_0 \, dx = d \iint_A \rho u c_P T \, dA \tag{3.40}$$

Combining eq. (3.40) with eq. (3.39), we obtain the formula for T_m:

$$T_m \rho c_P U A = \iint_A \rho c_p u T \, dA \tag{3.41}$$

For constant-property tube flow, eq. (3.41) reduces to

$$T_m = \frac{1}{\pi r_0^2 U} \int_0^{2\pi} \int_0^{r_0} u T r \, dr \, d\theta \tag{3.42}$$

Returning to the basic heat transfer question for duct flow, we want to know the relationship between q'' and the wall–fluid temperature difference. Since the fluid temperature varies over the duct cross section, $\Delta T = T_0 - T_m$ is *conventionally* selected as the representative wall–fluid temperature difference. The heat transfer coefficient is defined as

$$h = \frac{q''}{T_0 - T_m} = \frac{k(\partial T / \partial r)_{r=r_0}}{T_0 - T_m} \tag{3.43}$$

where, as in Chapter 2, q'' is defined as positive when proceeding from the wall into the fluid [compare eq. (3.43) with eq. (2.6)].

3.4.2   Fully Developed Temperature Profile

Equation (3.43) outlines the analytical path to follow: We must first determine the temperature field in the fluid $T(x, r)$ by solving the energy equation subject to appropriate wall–temperature boundary conditions. For steady, θ-symmetric flow through a round tube, the energy equation (1.43b) reduces to

$$\frac{1}{\alpha} \left(u \frac{\partial T}{\partial x} + v \frac{\partial T}{\partial r} \right) = \frac{\partial^2 T}{\partial r^2} + \frac{1}{r} \frac{\partial T}{\partial r} + \frac{\partial^2 T}{\partial x^2} \tag{3.44}$$

In the *hydrodynamic* fully developed region, we have $v = 0$ and $u = u(r)$; hence,

$$\frac{u(r)}{\alpha} \frac{\partial T}{\partial x} = \frac{\partial^2 T}{\partial r^2} + \frac{1}{r} \frac{\partial T}{\partial r} + \frac{\partial^2 T}{\partial x^2} \tag{3.45}$$

The energy equation (3.45) expresses a balance among a maximum of three possible energy flows: axial convection, radial conduction, and axial conduction. Their respective scales are

$$\overbrace{\frac{U}{\alpha}\left(\frac{q''}{D\rho c_P U}\right)}^{\text{Convection}}, \qquad \overbrace{\underbrace{\frac{\Delta T}{D^2}}_{\text{radial}}, \quad \underbrace{\frac{1}{x}\left(\frac{q''}{D\rho c_P U}\right)}_{\text{longitudinal}}}^{\text{Conduction}} \tag{3.46}$$

where we used eq. (3.39) to recognize that $\partial T/\partial x \sim q''/(D\rho c_P U)$. Of the three scales in (3.46), the radial conduction effect will always be present because, without it, the heat transfer problem of this chapter vanishes. Multiplying scales (3.46) by $D^2/\Delta T$ and using the definition of heat transfer coefficient $h = q''/\Delta T$, we obtain

$$\overbrace{\frac{hD}{k}}^{\text{Convection}}, \qquad \overbrace{\underbrace{1}_{\text{radial}}, \quad \underbrace{\left(\frac{hD}{k}\right)^2\left(\frac{\alpha}{UD}\right)^2}_{\text{longitudinal}}}^{\text{Conduction}} \tag{3.47}$$

By comparing the first and third scales, we conclude that in the limit

$$\text{Pe}_D = \frac{UD}{\alpha} \gg 1 \tag{3.48}$$

the longitudinal conduction effect is negligible. Next, from the convection–radial conduction balance, we learn that the Nusselt number is a constant of order 1:

$$\text{Nu} = \frac{hD}{k} \sim 1 \tag{3.49}$$

This Nu scaling is confirmed by many (and much more accurate) solutions. In the same domain ($\text{Pe}_D \gg 1$), the energy equation to solve for $T(x, r)$ is therefore

$$\frac{u(r)}{\alpha}\frac{\partial T}{\partial x} = \frac{\partial^2 T}{\partial r^2} + \frac{1}{r}\frac{\partial T}{\partial r} \tag{3.50}$$

It is instructive to summarize the assumptions on which the simplified energy equation (3.50) is based. First, we assumed that the flow is hydrodynamically fully developed; hence, the velocity profile $u(r)$ is the same at any x along the duct. Second, we assumed that the scale of $\partial^2 T/\partial r^2$ is $\Delta T/D^2$ [eq. (3.46)]; in other words, the effect of thermal diffusion has had time to reach the centerline of the stream. This last assumption is not valid in a *thermal entrance region* X_T near the duct entrance, where the proper scale of $\partial^2 T/\partial r^2$ is $\Delta T/\delta_T^2$, with $\delta_T \ll D$. The extent of X_T and the heat transfer coefficient in the thermal entrance region are determined later in this chapter.

On theoretical scaling grounds, the two assumptions listed above should be sufficient for regarding the temperature profile $T(x, r)$ as *fully developed*: This is the profile in the region situated sufficiently downstream from the two entrance regions (X, X_T) such that both u and T are developed.

The scaling feature of the thermally developed region is Nu = constant = $O(1)$ [eq. (3.49)]. Instead, many authors define the fully developed temperature by writing

$$\frac{T_0 - T}{T_0 - T_m} = \phi \left(\frac{r}{r_0} \right) \tag{3.51}$$

where, in general, T, T_0, and T_m can be functions of x. It is important to note that this special expression for $T(x, r)$ is purely the result of the scaling law Nu ~ 1; to see the relationship between eqs. (3.51) and (3.49), recall that

$$\text{Nu} = \frac{hD}{k} = \frac{D}{k} \frac{q''}{T_0 - T_m} \tag{3.52}$$

Hence,

$$\text{Nu} = D \frac{(\partial T / \partial r)_{r=r_0}}{T_0 - T_m} \sim 1 \tag{3.53}$$

Thus, the x variation of $(\partial T / \partial r)_{r=r_0}$ must be the same as that of $T_0(x) - T_m(x)$. Since $\partial T / \partial r$ is a function of both x and r, then, according to eq. (3.53),

$$\frac{\partial T / \partial (r/r_0)}{T_0(x) - T_m(x)} = f_1 \left(\frac{r}{r_0} \right) = O(1) \tag{3.54}$$

Integrating this expression with respect to r/r_0 yields

$$T \left(x, \frac{r}{r_0} \right) = (T_0 - T_m) f_2 \left(\frac{r}{r_0} \right) + f_3(x) \tag{3.55}$$

where f_2 and f_3 are arbitrary functions of r/r_0 and x, respectively. Expression (3.55) is the same as eq. (3.51), which is used routinely as a definition of full thermal development.

3.4.3 Uniform Wall Heat Flux

If q'' is not a function of x, eq. (3.50) can be solved analytically because the gradient $\partial T / \partial x$ is a constant proportional to q''. To see this, we rewrite the fully developed temperature profile as

$$T(x, r) = T_0(x) - \frac{q''}{h} \phi \left(\frac{r}{r_0} \right) \tag{3.56}$$

Hence,

$$\frac{\partial T}{\partial x} = \frac{dT_0}{dx} \tag{3.57}$$

Next, we rewrite eq. (3.49) as $q'' D/k[T_0(x) - T_m(x)] \sim 1$, differentiate it with respect to x, and find that

$$\frac{dT_0}{dx} = \frac{dT_m}{dx} \tag{3.58}$$

Finally, combining eqs. (3.57) and (3.58) and using the first law (3.39), we obtain

$$\frac{\partial T}{\partial x} = \frac{2}{r_0} \frac{q''}{\rho c_P U} = \text{constant} \tag{3.59}$$

This means that the temperature everywhere in the cross section varies linearly in x, the slope of the line being proportional to q''. The main features of this temperature field are summarized in Fig. 3.9.

The radial variation of T, namely, the dimensionless profile $\phi(r/r_0)$, is obtained by solving the energy equation for thermally developed flow [eq. (3.50)]. Substituting the temperature profile (3.56) and the Hagen–Poiseuille velocity profile (3.22) into eq. (3.50) leads to the following dimensionless equation for $\phi(r_*)$, where $r_* = r/r_0$:

$$-2 \frac{hD}{k}(1 - r_*^2) = \frac{d^2\phi}{dr_*^2} + \frac{1}{r_*}\frac{d\phi}{dr_*} \tag{3.60}$$

The object of this analysis, $hD/k = \text{Nu}$, appears explicitly in eq. (3.60). Integrating this equation twice and invoking one boundary condition (finite ϕ' at $r_* = 0$) yields

$$\phi = C_2 - 2\text{Nu}\left(\frac{r_*^2}{4} - \frac{r_*^4}{16}\right) \tag{3.61}$$

where C_2 is the second, undetermined constant of integration. Combining eqs. (3.61) and (3.56) and setting $T = T_0$ at $r_* = 1$ to determine C_2, we obtain

$$T = T_0 - (T_0 - T_m)\,\text{Nu}\left(\frac{3}{8} - \frac{r_*^2}{2} + \frac{r_*^4}{8}\right) \tag{3.62}$$

The mean temperature difference $T_0 - T_m$ follows from the definition of bulk (mean) temperature [eq. (3.42)],

$$T_0 - T_m = \frac{1}{\pi r_0^2 U}\int_0^{2\pi}\int_0^{r_0}(T_0 - T)ur\,dr\,d\theta$$

$$= 4\int_0^1 (T_0 - T)(1 - r_*^2)r_*\,dr_* \tag{3.63}$$
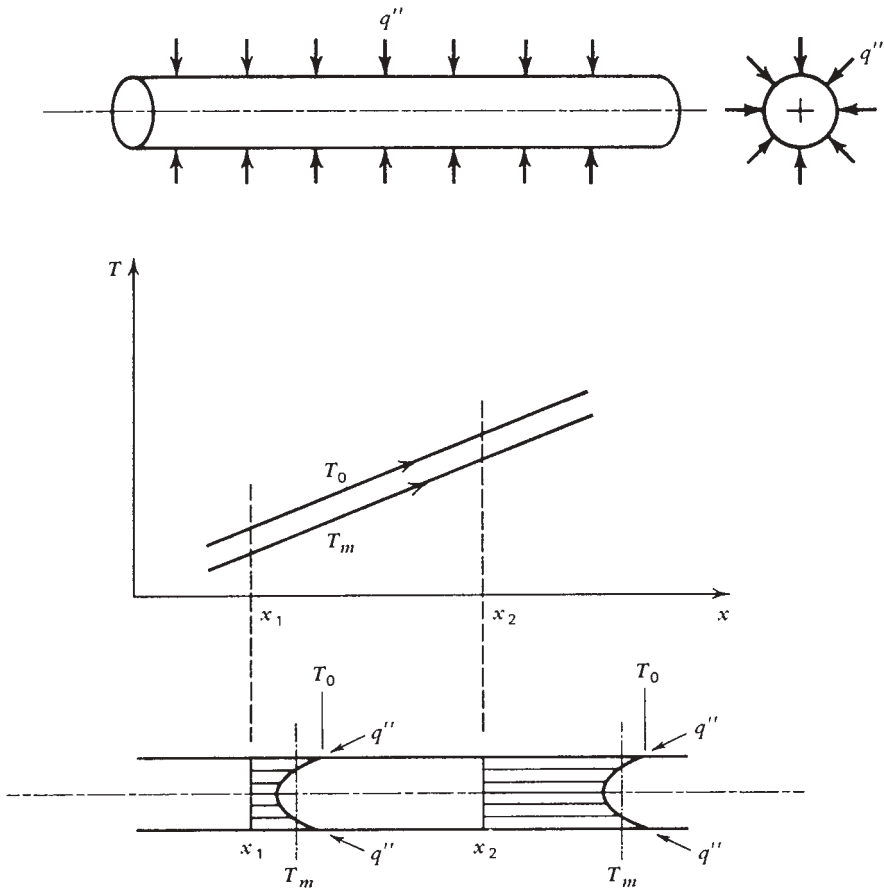
Figure 3.9   Fully developed temperature profile in a round tube with uniform heat flux.

Using expression (3.62) for $T_0 - T$ under the integral sign, the mean temperature difference drops out from both sides of the equal sign, leaving an equation for Nu:

$$1 = 4\text{Nu} \int_0^1 \left(\frac{3}{8} - \frac{r_*^2}{2} + \frac{r_*^4}{8} \right)(1 - r_*^2)r_* \, dr_* = \frac{11}{48} \text{Nu} \qquad (3.64)$$

The Nusselt number for thermally fully developed Hagen–Poiseuille flow with uniform heat flux is therefore

$$\text{Nu} = \frac{48}{11} = 4.36 \qquad (3.65)$$

which agrees in an order-of-magnitude sense with the scaling law (3.49). The Nu values corresponding to other duct cross-sectional shapes are listed in Table 3.2.

For noncircular cross sections, the Nusselt number is based on the hydraulic diameter

$$\text{Nu} = \frac{hD_h}{k} \tag{3.66}$$

and for this reason, the Nu values of Table 3.2 vary in the same manner as the area ratio $B = (\pi D_h^2/4)/A_{\text{duct}}$ (see Section 3.3 and Problem 3.6).

For noncircular cross sections, the problem is solved numerically, starting with the equation

$$\frac{u}{\alpha}\frac{\partial T}{\partial x} = \nabla^2 T \tag{3.67}$$

and replacing $\partial T/\partial x$ by a first law balance of type (3.39), namely,

$$\frac{dT_m}{dx} = \frac{q'}{\rho c_P A U} = \text{constant} \tag{3.68}$$

Here, q' is the heat transfer rate per unit duct length, regarded as independent of x. The wall temperature T_0 at a given x is usually assumed uniform around the noncircular periphery of the duct; consequently, the local heat flux around the periphery is nonuniform, varying from a maximum in wall regions close to the stream to a minimum in wall regions close to other wall regions (q'' drops to zero in the sharp corners of the cross section). Thus, q' is the perimeter (line) integral of q''. Also, since q'' varies along the perimeter, the heat transfer coefficient varies, too; the Nusselt numbers listed in Table 3.2 refer to the heat transfer coefficient averaged over the duct perimeter.

3.4.4   Uniform Wall Temperature

In a round tube with wall temperature T_0 independent of x, we expect a temperature field of the type sketched in Fig. 3.10. Suppose that the stream bulk temperature is T_1 at some place $x = x_1$ in the fully developed region. Given the temperature difference $T_0 - T_1$, heat will be transferred from the wall to the stream and, as a result, the stream temperature will rise monotonically in the direction of flow. This also means that $T_0 - T_m$ (and q'') will decrease monotonically in the x direction.

This discussion can easily be translated into analysis by combining the first law of thermodynamics [eq. (3.39)] with the only other thing we know at this point ($T_0 = $ constant); thus,

$$q''(x) = h[T_0 - T_m(x)] \tag{3.69}$$

where, on scaling grounds, h is also a constant [see eq. (3.49)]. Eliminating $q''(x)$ between eqs. (3.69) and (3.39) and integrating the result from $T_m = T_1$ at $x = x_1$ yields

$$T_0 - T_m(x) = (T_0 - T_1)\exp\left[-\frac{\alpha\,\text{Nu}}{r_0^2 U}(x - x_1)\right] \tag{3.70}$$
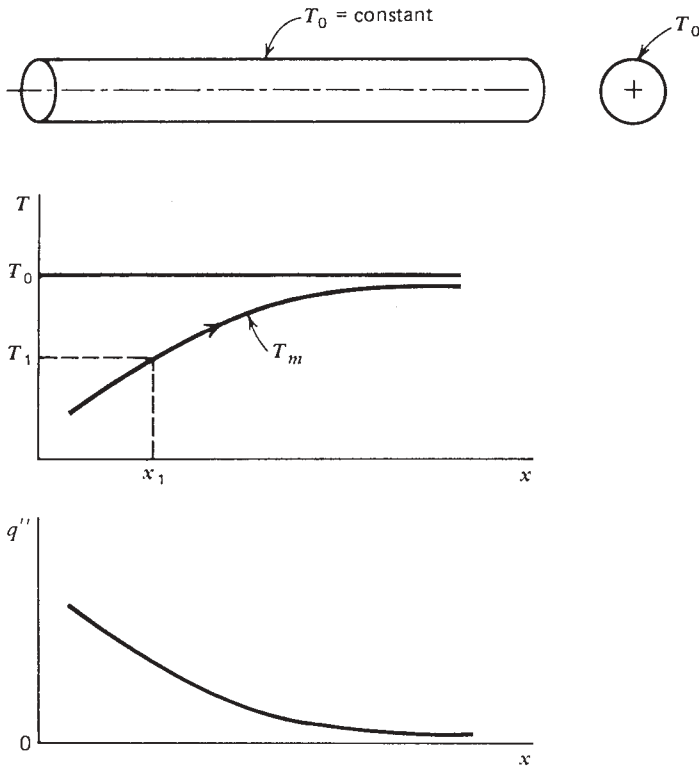
Figure 3.10   Exponential longitudinal variation of the mean temperature and wall heat flux in thermally fully developed flow through a tube with isothermal wall.

The mean temperature difference decreases exponentially in the flow direction and so does the heat flux [eq. (3.69)]. See Fig. 3.10.

The Nusselt number appearing in eq. (3.70) can be calculated by again solving the energy equation (3.50). This time, $\partial T/\partial x$ is replaced by

$$\frac{\partial T}{\partial x} = \frac{\partial}{\partial x}[T_0 - \phi(T_0 - T_m)] = \phi\frac{dT_m}{dx} \tag{3.71}$$

Substituting this expression, the Hagen–Poiseuille profile, and $T = T_0 - \phi(T_0 - T_m)$ into the energy equation (3.50) yields the following dimensionless equation for the unknown $\phi(r_*)$:

$$-2\mathrm{Nu}(1 - r_*^2)\phi = \frac{d^2\phi}{dr_*^2} + \frac{1}{r_*}\frac{d\phi}{dr_*} \tag{3.72}$$

This equation is similar to eq. (3.60) for uniform heat flux, except that the unknown $\phi(r_*)$ is present on the left-hand side. Furthermore, we now have two

boundary conditions to impose on ϕ:

$$d\phi/dr_* = 0 \quad \text{at} \ r_* = 0 \qquad\qquad \text{radial symmetry}$$

$$\phi = 0 \quad \text{at} \ r_* = 1 \qquad\qquad \text{isothermal wall} \qquad (3.73)$$

In principle, eq. (3.72) and conditions (3.73) are sufficient for determining the unknown function ϕ. However, in view of the makeup of eq. (3.72), the radial profile ϕ will be a function of both r_* and Nu, where Nu is the unknown in this problem. The additional condition for determining Nu uniquely is the definition of the heat transfer coefficient (i.e., Nu) [eq. (3.43)]; this condition can be written as

$$\text{Nu} = -2 \left(\frac{d\phi}{dr_*} \right)_{r_*=1} \qquad (3.74)$$

The problem statement is now complete: The value of Nu must be such that the $\phi(r_*, \text{Nu})$ solution of eqs. (3.72) and (3.73) satisfies the Nu definition (3.74). The actual solution may be pursued in a number of ways, for example, by successively approximating (guessing) and improving the ϕ solution (see Problem 3.7). Today, it is more convenient to solve the problem numerically: the differential equation (3.72) is first approximated by finite differences and integrated from $r_* = 1$ to $r_* = 0$. To perform the integration at all, we must first guess the value of Nu, which also gives us a guess for the initial slope of the ensuing $\phi(r_*)$ curve [see eq. (3.74)]. The success of the Nu guess is judged by means of the first of conditions (3.73); the refined result is ultimately

$$\text{Nu} = 3.66 \qquad (3.75)$$

which, again, agrees with the scaling law (3.49).

Table 3.2 lists other Nu values for noncircular cross sections. The slight variation in these values mimics that of $B = (\pi D_h^2/4)/A_{\text{duct}}$, implying that it is caused by hydraulic diameter nondimensionalization, that is, by the mismatch between hydraulic diameter and effective wall–stream distance (Fig. 3.7). This behavior again stresses the importance of the new dimensionless group $B = (\pi D_h^2/4)/A_{\text{duct}}$.

Table 3.3 shows the fully developed values of the friction factor and the Nusselt number in a duct with regular polygonal cross section. Some of the cases covered by this table are also covered by Table 3.2. The less than 1 percent discrepancies that exist between the data covered by both tables (e.g., the square cross section) are representative of the discrepancies found between results reported by different investigators. Note again that in noncircular cases with uniform heat flux, the wall temperature changes along the perimeter. In these cases, the heat transfer coefficient is based on the perimeter averaged wall temperature.

Table 3.3   Friction factors and Nusselt numbers for heat transfer to laminar flow through ducts with regular polygonal cross sections

	$f\,Re_{D_h}$	Nu = hD_h/k			
		Uniform Heat Flux		Isothermal Wall	
Cross Section	Fully Developed Flow	Fully Developed Flow	Slug Flow	Fully Developed Flow	Slug Flow
Square	14.167	3.614	7.083	2.980	4.926
Hexagon	15.065	4.021	7.533	3.353	5.380
Octagon	15.381	4.207	7.690	3.467	5.526
Circle	16	4.364	7.962	3.66	5.769

Source: Data from Ref. 12.

Table 3.3 shows that the thermally developed Nu value is considerably smaller in fully developed flow than in *slug flow*. The latter refers to the flow of a solid material (slug, rod), or a fluid with an extremely small Prandtl number (Pr → 0), where the viscosity is so much smaller than the thermal diffusivity that the longitudinal velocity profile remains uniform over the cross section, $u = U$, like the velocity distribution of a solid slug.

The presentation so far has been based on the assumption of large Péclet numbers, eq. (3.48), which led to Nusselt numbers that are constant (x independent) when the flow is thermally and hydrodynamically fully developed. The existence of a fully developed temperature profile does not require the assumption of a large Péclet number (i.e., negligible longitudinal conduction). This has been demonstrated by Nield and Lage [13] for slug flow.

3.5   HEAT TRANSFER TO DEVELOPING FLOW

The heat transfer results listed in Table 3.2 apply to laminar duct flow regions where both the velocity and temperature profiles are fully developed. Measuring x from the actual entrance of the duct (Fig. 3.11), these results are valid in the downstream section delineated by

$$x > \max(X, X_T) \tag{3.76}$$

where X and X_T are the hydrodynamic and thermal entrance lengths, respectively. We know from the discussion of hydrodynamic entrance length earlier in this chapter that the extent of X_T is determined by the point where the entrance thermal boundary layer thickness δ_T becomes of the same order as the hydraulic diameter of the duct.
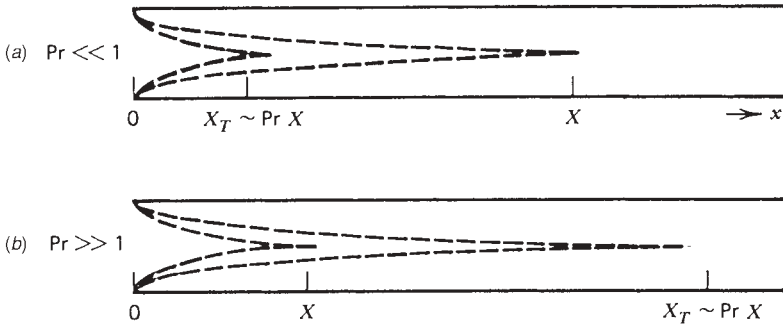
Figure 3.11   Prandtl number effect on the size of the hydrodynamic entrance length X relative to the size of the thermal entrance length X_T.

3.5.1   Scale Analysis

Figure 3.11 shows qualitatively the $\delta_T(X_T) \sim D_h$ scaling, namely, the relative size of X and X_T as influenced by the Prandtl number. Since, according to Chapter 2, the ratio δ/δ_T increases monotonically with Pr, the ratio X/X_T must decrease monotonically as Pr increases. To determine the X_T scale, hence the ratio X/X_T, first consider the limit of low–Prandtl number fluids.

Pr $\ll$ 1.   According to eq. (2.37), δ_T develops faster than δ,

$$\delta_T(x) \sim x \ \mathrm{Pr}^{-1/2} \ \mathrm{Re}_x^{-1/2} \tag{3.77}$$

Because at the end of thermal development $x \sim X_T$ and $\delta_T \sim D_h$, we have

$$X_T \ \mathrm{Pr}^{-1/2} \ \mathrm{Re}_{X_T}^{-1/2} \sim D_h \tag{3.78}$$

or

$$\left(\frac{X_T/D_h}{\mathrm{Re}_{D_h} \ \mathrm{Pr}} \right)^{1/2} \sim 1 \tag{3.79}$$

This is a well-known X_T result listed in other publications as

$$\frac{X_T/D_h}{\mathrm{Re}_{D_h} \ \mathrm{Pr}} \sim 0.1 \tag{3.80}$$

Note that eq. (3.80) is of the same type as eq. (3.1) where the constant is also less than unity. In view of the apparent discrepancy between eqs. (3.79) and (3.80), the reader should keep in mind that eq. (3.79) is the correct way of writing $\delta_T \sim D_h$. Squaring any proportionality in which the coefficient is $O(1)$ but less than 1 leads to a proportionality of type (3.80) where the coefficient is no longer $O(1)$; this coefficient later assumes the role of *transition constant*, adding to the long list of empirical constants the handbooks ask us to memorize.

In conclusion, the correct scaling for the transition from the developing to the thermally developed temperature profile is $\delta_T \sim D_h$, which means that the proper dimensionless group governing this transition is $[(X_T/D_h)/(\mathrm{Re}_{Dh}\,\mathrm{Pr})]^{1/2}$ [cf. eq. (3.79)]. Similarly, the proper dimensionless group governing the transition from the developing to the fully developed velocity profile is

$$\left(\frac{X/D_h}{\mathrm{Re}_{D_h}}\right)^{1/2} \sim 1 \tag{3.81}$$

The reason these groups govern transition phenomena is that they become of order 1 during transition. They become of order 1 because they represent the competition between the *correct scales*, which, after all, make the concept of *transition* meaningful. This point is discussed further in Chapter 6.

Pr ≫ 1. In the case of fluids such as water and oils (Fig. 3.11b), it is tempting to compare D_h with the δ_T given by eq. (2.42). Such a comparison is incorrect because the δ_T scale (2.42) is valid in boundary layers where the velocity thickness is consistently much greater than δ_T [so that the u scale is $(\delta_T/\delta)U_\infty$ inside a layer of thickness δ_T]. In a duct, unlike in external flow (Chapter 2), the velocity profile spreads over D_h; hence, the u scale inside the δ_T layer is U itself. Thus, it is easy to show that $\delta_T(x) \sim x\mathrm{Pr}^{-1/2}\mathrm{Re}_x^{-1/2}$, which is identical to the scaling encountered in Pr ≪ 1 cases.

In conclusion, criterion (3.79) is general and also applies in the case of Pr ≫ 1 fluids. Dividing eqs. (3.79) and (3.81), we learn that

$$\frac{X_T}{X} \sim \mathrm{Pr} \tag{3.81'}$$

This scaling is valid for all values of Pr (Fig. 3.11). The local Nusselt number in the thermally developing section ($x \ll X_T$) scales as follows:

$$\mathrm{Nu} = \frac{hD_h}{k} \sim \frac{q''}{\Delta T}\frac{D_h}{k} \sim \frac{D_h}{\delta_T} \sim \left(\frac{x/D_h}{\mathrm{Re}_{D_h}\mathrm{Pr}}\right)^{-1/2} \tag{3.82}$$

Since the δ_T scale is $x\,\mathrm{Pr}^{-1/2}\,\mathrm{Re}_x^{-1/2}$ over the entire Pr range, the Nu scale (3.82) is valid for all values of Pr. As is shown later in this section (Figs. 3.12–3.14), this conclusion is supported by numerical analysis.

3.5.2 Thermally Developing Hagen–Poiseuille Flow

Consider the high-Pr limit (Fig. 3.11b) and focus on the tube section described by $X < x < X_T$. Here the velocity profile is fully developed while the temperature profile is just being developed. Neglecting the effect of axial conduction ($\mathrm{Pe}_x \gg 1$), we must solve eq. (3.50) subject to these conditions:

Uniform wall temperature, $T_0 =$ constant
Symmetry about the centerline, $\partial T/\partial r = 0$ at $r = 0$

Isothermal entering fluid, $T = T_{IN}$ for $x < 0$, where x is measured (positive) downstream from the location X in Fig. 3.11*b*

This problem was treated for the first time by Graetz [15] in 1883 and is known as the *Graetz problem*. The problem statement is

$$\frac{1}{2}(1 - r_*^2)\frac{\partial \theta_*}{\partial x_*} = \frac{\partial^2 \theta_*}{\partial r_*^2} + \frac{1}{r_*}\frac{\partial \theta_*}{\partial r_*}$$

$$\theta_* = 0 \quad \text{at } r_* = 1 \tag{3.83}$$

$$\frac{\partial \theta_*}{\partial r_*} = 0 \quad \text{at } r_* = 0$$

$$\theta_* = 1 \quad \text{at } x_* = 0$$

with the following notation:

$$\theta_* = \frac{T - T_0}{T_{IN} - T_0}, \qquad r_* = \frac{r}{r_0}, \qquad x_* = \frac{x/D}{\text{Re}_D \ \text{Pr}} \tag{3.84}$$
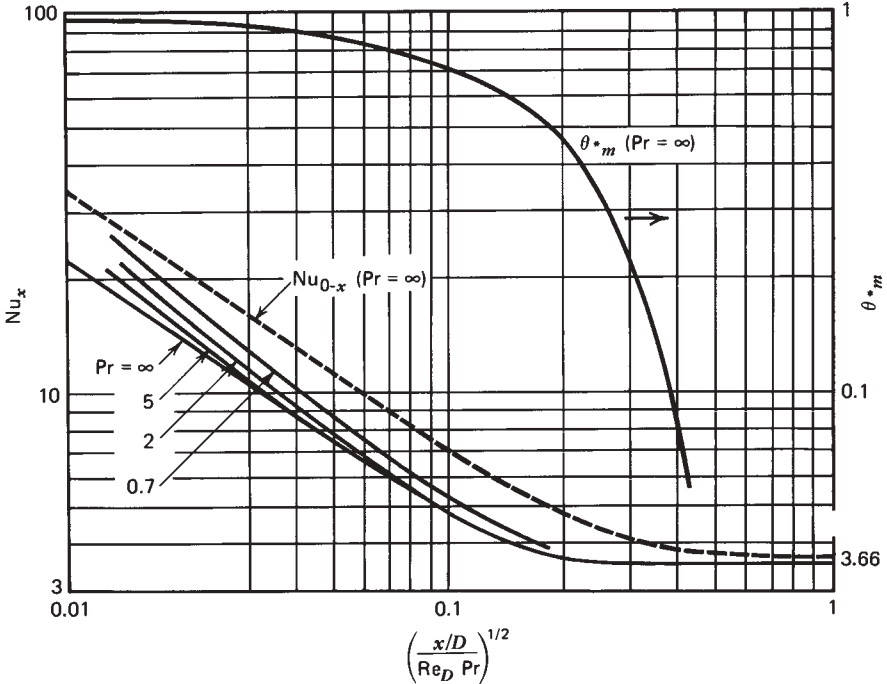
Figure 3.12 Heat transfer in the entrance region of a round tube with isothermal wall. (Based on data from Refs. 10 and 14.)
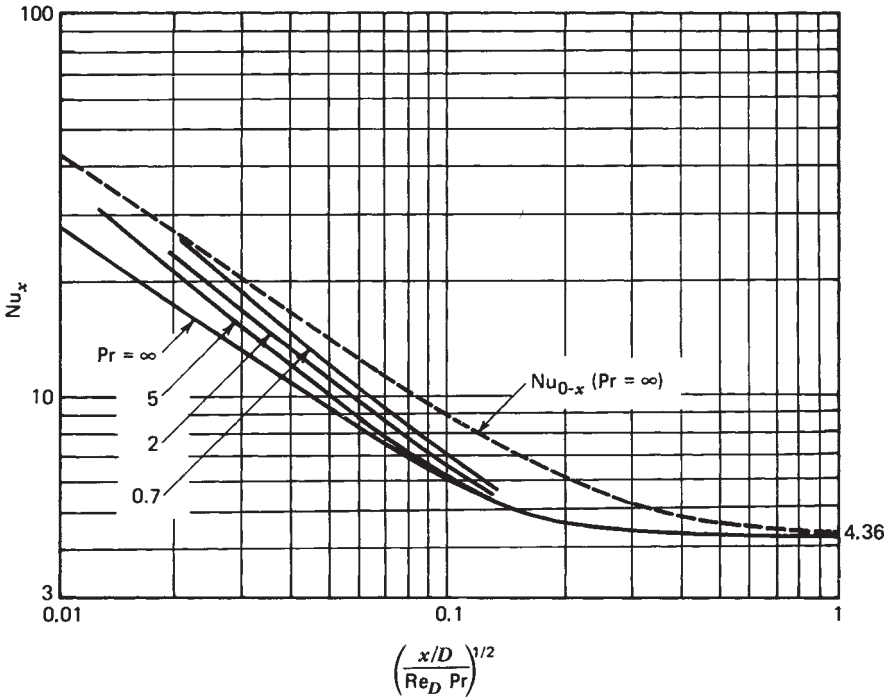
Figure 3.13   Heat transfer in the entrance region of a round tube with uniform heat flux. (Based on data from Refs. 10 and 14.)

The energy equation is linear and homogeneous. Separation of variables is achieved by assuming a product solution for $\theta_*(r_*, x_*)$,

$$\theta_* = R(r_*)\ \Xi(x_*) \tag{3.85}$$

that yields two linear and homogeneous equations for R and Ξ,

$$R'' + \frac{1}{r_*}R' + \lambda^2(1 - r_*^2)R = 0 \tag{3.86}$$

$$\Xi' + 2\lambda^2\Xi = 0 \tag{3.87}$$

The Ξ equation admits solutions of the type $\Xi = C \exp(-2\lambda^2 x_*)$, where both C and λ^2 are arbitrary constants. The R equation is of the Sturm–Liouville type and its solution is obtainable as infinite series; the θ_* solution satisfying the $r_* = 0,1$ boundary conditions in (3.83) becomes the *Graetz series*

$$\theta_* = \sum_{n=0}^{\infty} C_n R_n(r_*) \exp(-2\lambda_n^2 x_*) \tag{3.88}$$
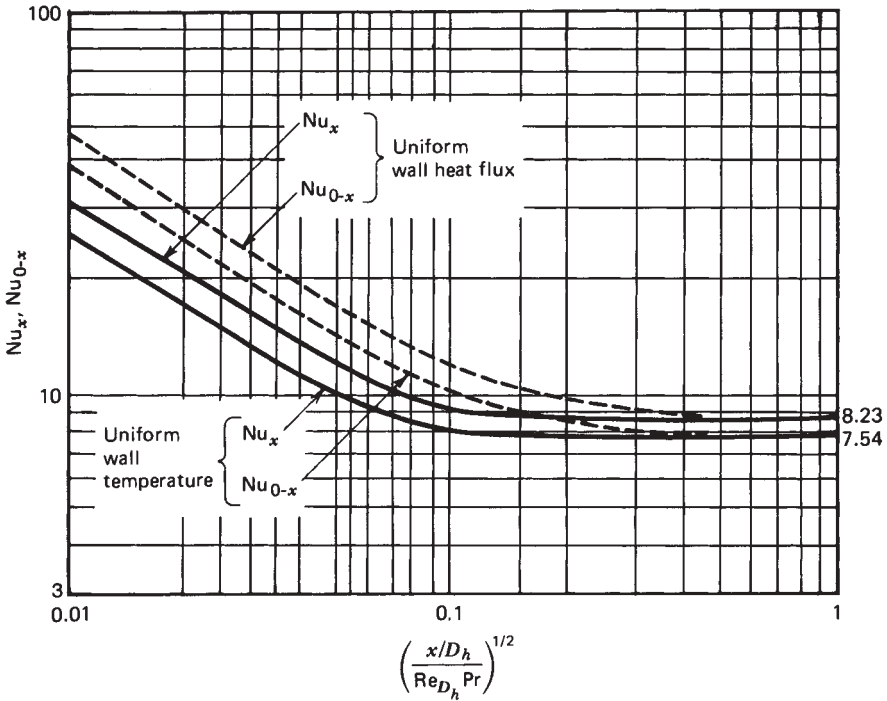
Figure 3.14 Heat transfer in the thermal entrance region of a parallel-plate duct with Hagen–Poiseuille flow. (Based on data from Ref. 10.)

where R_n and λ_n are eigenfunctions and eigenvalues, and the C_n are constants determined by the $x_* = 0$ condition in the problem statement (3.83). The heat transfer results of interest are

$$\theta_{*m} = \frac{T_m - T_0}{T_{\mathrm{IN}} - T_0} = 8 \sum_{n=0}^{\infty} \frac{G_n}{\lambda_n^2} \exp(-2\lambda_n^2 x_*) \tag{3.89}$$

$$\mathrm{Nu}_x = \frac{\displaystyle\sum_{n=0}^{\infty} G_n \, \exp(-2\lambda_n^2 x_*)}{2 \displaystyle\sum_{n=0}^{\infty} (G_n/\lambda_n^2) \, \exp(-2\lambda_n^2 x_*)} \tag{3.90}$$

$$\mathrm{Nu}_{0-x} = \frac{1}{4x_*} \, \ln \, \frac{1}{\theta_{*m}} \tag{3.91}$$

where θ_{*m}, Nu_x, and Nu_{0-x} are the bulk dimensionless temperature, the local Nusselt number, and the overall Nusselt number for the entrance section of

Table 3.4   Graetz series eigenvalues and constants (round tube, isothermal wall, Hagen–Poiseuille flow)

n	λ_n	G_n
0	2.704	0.7488
1	6.679	0.5438
2	10.673	0.4629
3	14.671	0.4154
4	18.67	0.3829
5	22.67	0.3587

Source: Ref. 10.

length x. The eigenvalues λ_n and the constants $G_n = -(C_n/2) R'_n (1)$ for the first five terms of the infinite series are tabulated in Table 3.4. The overall Nusselt number for the thermal entrance region of a tube with isothermal wall is defined as $\mathrm{Nu}_{0-x} = q''_{0-x}D/k\,\Delta T_{lm}$, where ΔT_{lm} is the log-mean temperature difference, and $T_{IN} = T_m(0)$,

$$\Delta T_{lm} = \frac{[T_0 - T_{IN}(x)] - (T_0 - T_m)}{\ln\{[T_0 - T_m(x)]/(T_0 - T_{IN})\}} \tag{3.92}$$

Figure 3.12 shows expressions (3.89)–(3.91) as the curves labeled $\mathrm{Pr} = \infty$ for θ_{*_m}, Nu_x, and Nu_{0-x}. The group $x_*^{1/2} = [(x/D)/(\mathrm{Re}_D\mathrm{Pr})]^{1/2}$ is used on the abscissa to illustrate the scaling law (3.79) that rules the transition from thermally developing to thermally fully developed duct flow. The Nusselt number curves show a knee at $x_*^{1/2} = O(1)$, in very good agreement with eq. (3.79): The validity of this transition criterion is dramatized further by the sudden drop of the bulk temperature from the inlet value ($\theta_{*_m} = 1$) to the wall value ($\theta_{*_m} = 0$).

The following expressions are recommended by a simpler alternative to the Graetz series solution, which is known as the *Lévêque solution* [16]. Analytical alternatives [10, 17] to the $\mathrm{Pr} = \infty$ curves shown in Fig. 3.12 are

$$\mathrm{Nu}_x = \begin{cases} 1.077x_*^{-1/3} - 0.7, & x_* \leq 0.01 \\ 3.657 + 6.874(10^3 x_*)^{-0.488} \exp(-57.2x_*), & x_* > 0.01 \end{cases} \tag{3.93}$$

$$\mathrm{Nu}_{0-x} = \begin{cases} 1.615x_*^{-1/3} - 0.7, & x_* \leq 0.005 \\ 1.615x_*^{-1/3} - 0.2, & 0.005 < x_* < 0.03 \\ 3.657 + 0.0499/x_*, & x_* \geq 0.03 \end{cases} \tag{3.94}$$

The thermally developing Hagen–Poiseuille flow in a round tube with uniform heat flux q'' can be analyzed by applying the same method (Fig. 3.13, the $\mathrm{Pr} = \infty$

curve). The results for the local and overall Nusselt numbers are represented within 3 percent by the formulas [10, 17]

$$\mathrm{Nu}_x = \begin{cases} 1.302x_*^{-1/3} - 1, \\ \qquad x_* \leq 0.00005 \\ 1.302x_*^{-1/3} - 0.5, \\ \qquad 0.00005 \leq x_* \leq 0.0015 \\ 4.364 + 8.68(10^3 x_*)^{-0.506} \exp(-41x_*), \\ \qquad x_* \geq 0.001 \end{cases} \tag{3.95}$$

$$\mathrm{Nu}_{0-x} = \begin{cases} 1.953x_*^{-1/3}, & x_* \leq 0.03 \\ 4.364 + 0.0722/x_*, & x_* > 0.03 \end{cases} \tag{3.96}$$

where $\mathrm{Nu}_x = q'' D/k[T_0(x) - T_m(x)]$ and $\mathrm{Nu}_{0-x} = q'' D/(k \Delta T_{\mathrm{avg}})$ with

$$\Delta T_{\mathrm{avg}} = \left[\frac{1}{x} \int_0^x \frac{dx}{T_0(x) - T_m(x)} \right]^{-1} \tag{3.97}$$

Analogous results are available for the heat transfer to thermally developing Hagen–Poiseuille flow in ducts with other cross-sectional shapes. The Nusselt numbers for a parallel-plate channel are shown in Fig. 3.14. The curves for a channel with isothermal surfaces are approximated by [10, 17]

$$\mathrm{Nu}_x = \begin{cases} 1.233x_*^{-1/3} + 0.4, & x_* \leq 0.001 \\ 7.541 + 6.874(10^3 x_*)^{-0.488} \exp(-245x_*), & x_* > 0.001 \end{cases} \tag{3.98}$$

$$\mathrm{Nu}_{0-x} = \begin{cases} 1.849x_*^{-1/3}, & x_* \leq 0.0005 \\ 1.849x_*^{-1/3} + 0.6, & 0.0005 < x_* \leq 0.006 \\ 7.541 + 0.0235/x_*, & x_* > 0.006 \end{cases} \tag{3.99}$$

If the plate-to-plate spacing is D, the Nusselt numbers are defined as $\mathrm{Nu}_x = q''(x)D_h/k[T_0 - T_m(x)]$ and $\mathrm{Nu}_{0-x} = q''_{0-x}D_h/(k \Delta T_{lm})$, where $D_h = 2D$ and ΔT_{lm} is given by eq. (3.92).

The thermal entrance region of the parallel-plate channel with uniform heat flux and Hagen–Poiseuille flow is characterized by [10, 17]

$$\mathrm{Nu}_x = \begin{cases} 1.490x_*^{-1/3}, & x_* \leq 0.0002 \\ 1.490x_*^{-1/3} - 0.4, & 0.0002 < x_* \leq 0.001 \\ 8.235 + 8.68(10^3 x_*)^{-0.506} \exp(-164x_*), & x_* > 0.001 \end{cases} \tag{3.100}$$

$$\text{Nu}_{0-x} = \begin{cases} 2.236x_*^{-1/3}, & x_* \le 0.001 \\ 2.236x_*^{-1/3} + 0.9, & 0.001 < x_* \le 0.01 \\ 8.235 + 0.0364/x_*, & x_* \ge 0.01 \end{cases} \qquad (3.101)$$

The definitions are $\text{Nu}_x = q''D_h/k[T_0(x) - T_m(x)]$ and $\text{Nu}_{0-x} = q''D_h/(k \, \Delta T_{\text{avg}})$, where ΔT_{avg} is furnished by eq. (3.97). It is worth repeating that x_* represents the dimensionless longitudinal coordinate in the thermal entrance region, eq. (3.84), which in the case of the parallel-plate channel becomes $x_* = (x/D_h)/\text{Re}_{D_h} \text{Pr}$. All the results compiled in the section apply in the limit $\text{Pr} \to \infty$.

3.5.3 Thermally and Hydraulically Developing Flow

The most realistic (and most difficult) version of the tube flow problem consists of solving eqs. (3.83) with the Hagen–Poiseuille profile $2(1 - r_*^2)$ replaced by the actual x-dependent velocity profile present in the hydrodynamic entry region. This, the finite-Pr problem, has been solved numerically by a number of investigators: The history of this numerical work is recounted in Ref. 10.

Figure 3.12 shows a sample of the finite-Pr data available for a round tube with isothermal wall. The analytical expressions recommended for the local [17] and overall [18] Nusselt numbers in the range $0.1 < \text{Pr} < 1000$ in parallel-plate channels are

$$\text{Nu}_x = 7.55 + \frac{0.024x_*^{-1.14}(0.0179\text{Pr}^{0.17}x_*^{-0.64} - 0.14)}{(1 + 0.0358\text{Pr}^{0.17}x_*^{-0.64})^2} \qquad (3.102)$$

$$\text{Nu}_{0-x} = 7.55 + \frac{0.024x_*^{-1.14}}{1 + 0.0358\text{Pr}^{0.17}x_*^{-0.64}} \qquad (3.103)$$

The pressure drop over the hydrodynamically developing length x, or $\Delta P = P(0) - P(x)$, can be calculated with [10]

$$\frac{\Delta P}{\frac{1}{2}\rho U^2} = 13.74(x_+)^{1/2} + \frac{1.25 + 64x_x - 13.74(x_+)^{1/2}}{1 + 0.00021(x_+)^{-2}} \qquad (3.104)$$

Here, x_+ is the dimensionless coordinate for the hydrodynamic entrance region,

$$x_+ = \frac{x/D}{\text{Re}_D} \qquad (3.105)$$

which also appears on the abscissa of Fig. 3.3. Equation (3.104) can be used instead of the $(C_f)_{0-x} \text{Re}_D$ curve shown in Fig. 3.3 by nothing the force balance $\Delta P(\pi D^2/4) = \tau_{0-x}\pi Dx$, or

$$\frac{\Delta P}{\frac{1}{2}\rho U^2} = 4x_+(C_f)_{0-x} \, \text{Re}_D \qquad (3.106)$$

Figure 3.13 shows several finite-Pr solutions for the local Nusselt number in the entrance region of a tube with uniform heat flux. A closed-form expression that covers both the entrance and fully developed regions is [19]

$$\frac{\mathrm{Nu}_x}{4.364[1 + (\mathrm{Gz}/29.6)^2]^{1/6}}$$

$$= \left[1 + \left(\frac{\mathrm{Gz}/19.04}{[1 + (\mathrm{Pr}/0.0207)^{2/3}]^{1/2}[1 + (\mathrm{Gz}/29.6)^2]^{1/3}} \right)^{3/2} \right]^{1/3} \tag{3.107}$$

where $\mathrm{Nu}_x = q'' D/k[T_0(x) - T_m(x)]$ and $\mathrm{Gz} = \pi/(4x_*)$ is the Graetz number. Equation (3.107) agrees within 5 percent with numerical data for $\mathrm{Pr} = 0.7$ and $\mathrm{Pr} = 10$ and has the correct asymptotic behavior for large and small Gz and Pr.

The heat transfer and pressure drop results for thermally and hydrodynamically developing flow in ducts with other cross-sectional shapes have been cataloged in Refs. 10 and 17. In general, the results show that in the entrance region $(x_*^{1/2} \ll 1)$, the Nusselt number obeys a relationship of the type

$$\mathrm{Nu}_x = (\text{constant}) \left(\frac{x/D_h}{\mathrm{Re}_{D_h}\,\mathrm{Pr}} \right)^{-1/2} \tag{3.108}$$

where (constant) $= O(1)$. This proves the validity of the scaling law (3.82) and, considering the century-long effort of obtaining and perfecting the curves of Figs. 3.12–3.14, illustrates the power of proper scale analysis. The log–log presentation of Figs. 3.12–3.14 is intentional, to illustrate the existence of the scaling law (3.82) as lines of slope −1.

Thermally developing flow is a fundamental topic with applications throughout thermal engineering [1]. One important application is the maximization of heat transfer rate density (heat transfer per unit volume) in the miniaturization of heat exchanger structures [20], the theoretical basis of which is presented in the next section. Another application is in bioengineering, in the detection of vocal fold pathology [21]. Developing flows in noncircular ducts are presented in Ref. 22.

3.6   STACK OF HEAT-GENERATING PLATES

In this section we determine the spacing for maximum heat transfer density in a package (stack) of parallel plates that are cooled by forced convection [23, 24]. An application of this arrangement is the forced-air cooling of a stack of electronic circuit boards. Of principal interest is the maximum heat transfer, rate, that is, the maximum density of heat-generating electronics that can be fitted in a package of specified volume.

Consider the geometry of Fig. 3.15, in which the coolant inlet temperature T_∞ and the pressure head established by the compressor (fan or pump) ΔP are
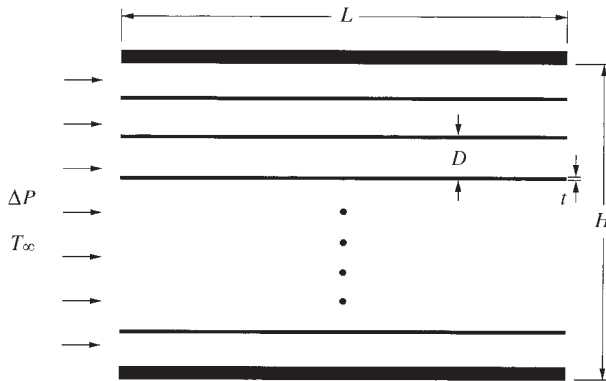
Figure 3.15   Stack of parallel heat-generating plates cooled by forced convection.

fixed. The solution was first proposed for optimal natural convection spacings in the 1984 edition of this book [25]. The analysis was based on the *intersection-of-asymptotes method*. It has since been generalized to other domains, including electrical engineering [26]. The flow is assumed laminar, and the board temperature is assumed uniform at the safe level T_w. Each board has a thickness t that is sufficiently smaller than D. To determine the optimal board-to-board spacing D is the same as determining the optimal number of boards ($n \gg 1$) that fill a space of thickness H,

$$n \simeq \frac{H}{D} \tag{3.109}$$

Small Spacings Limit. Consider first the limit $D \to 0$ when each channel is slender enough so that the flow is fully developed all along L, and the fluid outlet temperature approaches the board temperature T_w. The average fluid velocity in each channel is given by eq. (3.19),

$$U = \frac{D^2}{12\mu} \frac{\Delta P}{L} \tag{3.110}$$

and the total mass flow rate $\dot{m}'$ through the stack of thickness H is

$$\dot{m}' = \rho U H = \rho H \frac{D^2}{12\mu} \frac{\Delta P}{L} \tag{3.111}$$

The mass flow rate $\dot{m}'$ is expressed per unit length in the direction perpendicular to Fig. 3.15. The total heat transfer rate removed from the stack by the $\dot{m}'$ stream is

$$q_a' \simeq \dot{m}' c_P (T_w - T_\infty) = \rho H \frac{D^2}{12\mu} \frac{\Delta P}{L} c_P (T_w - T_\infty) \tag{3.112}$$

In conclusion, in the limit $D \rightarrow 0$, the total cooling rate (or total rate of allowable Joule heating in the package) decreases as D^2. This trend is illustrated qualitatively as curve (a) in Fig. 3.16. The direction toward small D values is not good for design performance.

Large Spacings Limit. In the opposite extreme, $D \rightarrow \infty$, the boundary layer that lines one surface becomes ''distinct.'' In other words, each channel looks like the entrance region to a parallel-plate duct. The overall pressure drop is fixed at ΔP; therefore, we ask: What is the free-stream velocity U_∞ that sweeps these boundary layers? The overall force balance on the control volume $H \times L$ requires that

$$\Delta P \, H = n \cdot 2\overline{\tau_w}L \tag{3.113}$$

in which n is the number of channels and $\overline{\tau_w}$ is the L-averaged wall shear stress [cf. eq. (2.92')],

$$\overline{\tau_w} = 1.328 \mathrm{Re}_L^{-1/2} \cdot \tfrac{1}{2}\rho U_\infty^2 \tag{3.114}$$

Combined, eqs. (3.113) and (3.114) yield

$$U_\infty = \left(\frac{1}{1.328} \, \frac{\Delta P}{nL^{1/2}} \, \frac{H}{\rho v^{1/2}} \right)^{2/3} \tag{3.115}$$

The total heat transfer rate from one of the L-long surfaces (q_1') is calculated from the overall Nusselt number for $\mathrm{Pr} > 0.5$ [cf. eq. (2.110)],

$$\frac{\overline{h}L}{k} = \frac{\overline{q}''}{T_w - T_\infty} \frac{L}{k} = 0.664 \mathrm{Pr}^{1/3} \left(\frac{U_\infty L}{v} \right)^{1/2} \tag{3.116}$$

which leads to

$$q_1' = \overline{q}''L = k(T_w - T_\infty)0.664 \mathrm{Pr}^{1/3} \left(\frac{U_\infty L}{v} \right)^{1/2} \tag{3.117}$$

The total heat transfer rate released by the stack is $2n$ times larger than q_1' (we are assuming that both surfaces of one board are Joule-heated to T_w):

$$q_b' = 2nq_1' = 2nk(T_w - T_\infty)0.664 \mathrm{Pr}^{1/3} \left(\frac{U_\infty L}{v} \right)^{1/2} \tag{3.118}$$

In view of the n and U_∞ expressions in eqs. (3.109) and (3.115), the total heat transfer rate becomes

$$q_b' = 1.208k(T_w - T_\infty)H \, \frac{\mathrm{Pr}^{1/3} \, L^{1/3} \, \Delta P^{1/3}}{\rho^{1/3} v^{2/3} D^{2/3}} \tag{3.119}$$

Intersection of Asymptotes. The second conclusion we reach is that in the large-D limit, the total heat transfer rate decreases as $D^{-2/3}$. This second trend has been added as curve (*b*) in Fig. 3.16, to suggest that the maximum of the actual (unknown) curve $q'(D)$ can occur only at a spacing D_{opt} that is of the same order as the D value obtained by intersecting the asymptotes (3.112) and (3.119). The order-of-magnitude statement $q'_a \sim q'_b$ yields the optimal spacing:

$$D_{opt} \simeq 2.73L \; Be_L^{-1/4} \tag{3.120}$$

where

$$Be_L = \frac{\Delta P \; L^2}{\mu\alpha} \tag{3.120'}$$

is the dimensionless pressure drop that in 1988 Bhattacharjee and Grosshandler [27] termed the *Bejan number*. The role of this dimensionless group in forced convection is discussed by Petrescu [28]. Equation (3.120) agrees very well with the more exact result obtained by locating the maximum of the actual $q'(D)$ sketched in Fig. 3.16. Reference 23 showed numerically that in the Pr range $0.7-10^3$, the optimal spacing is correlated by an expression like eq. (3.120) in which the coefficient 2.73 is replaced by 3.05. The existence of the optimal spacing (3.120) was also confirmed by experiments with microchannels [29].

The numerical maximization [23] of the actual $q'(D)$ relation demonstrated that in the entire range $0.7 < Pr < 10^3$, the dimensionless length $x_* = (L/D_h)/(UD_h/\alpha)$ was consistently equal to 0.04 when $D = D_{opt}$. In view of eq. (3.80), this means that the optimal board-to-board spacing must be such that the board length is of the same order of magnitude as the *thermal entrance length* of the parallel-plate channel. This feature is the key to the design of compact heat exchanger structures with maximal heat transfer rate density [20]. This idea
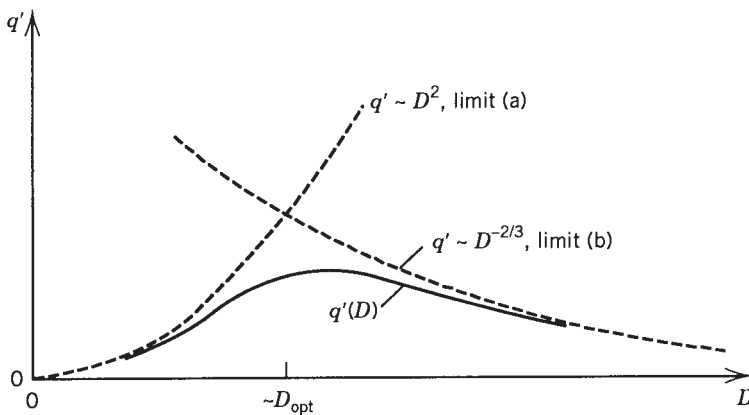
Figure 3.16   Intersection-of-asymptotes method: the optimal spacing as the intersection of the small-D asymptote with the large-D asymptote.

has been taken to higher performance levels in two ways, by optimally shaping the channel with optimized spacing (i.e., by fitting the duct to the convective flow [30]) and by packing a series of smaller plates and channels in the entrance regions of the stack of Fig. 3.15. The latter is a generally valid strategy for achieving maximal heat transfer density by constructing a flow structure with multiple length scales [31]. The smallest length scale in such a structure (the ''alveolus'' of this ''lung'') is the cutoff below which convection ceases to be effective (cf. constructal theory [8]). Along this conceptual route, the multiscale flow structure with large-scale convection and small-scale diffusion becomes a *designed porous medium* [32]. We return to this concept in more detail in Section 12.10.

The order of magnitude of the maximum package heat transfer rate that corresponds to $D = D_{opt}$ is obtained by combining eqs. (3.112) and (3.120):

$$q'_{\max} \lesssim 0.62 \left(\frac{\rho \ \Delta P}{\Pr} \right)^{1/2} H c_P (T_w - T_\infty) \qquad (3.121)$$

The inequality sign is a reminder that the actual q' maximum is lower than the q' value obtained by intersecting asymptotes (*a*) and (*b*) in Fig. 3.16. The group of properties and dimensions that emerged on the right side of eq. (3.121) represents the correct scale of $q'_{\max}$. Indeed, the numerical maximization of the actual $q'(D)$ relation [23] for $0.7 < \Pr < 10^3$ proved that $q'_{\max}$ is correlated by an expression of type (3.121) where 0.62 is replaced by 0.52.

The intersection-of-asymptotes analysis presented in this section can be repeated for the situation in which only one surface of the board is Joule-heated to T_w, and the other surface can be modeled as adiabatic. The only change is that $2n$ is replaced by n in eq. (3.118), so that the results become

$$D_{opt} \cong 2.10 L \ \mathrm{Be}_L^{-1/4} \qquad (3.122)$$

$$q'_{\max} \lesssim 0.37 \left(\frac{\rho \ \Delta P}{\Pr} \right)^{1/2} H c_p (T_w - T_\infty) \qquad (3.123)$$

Comparing eqs. (3.122)–(3.123) with eqs. (3.120)–(3.121) we see the preservation of the scales derived for D_{opt} and $q'_{\max}$. In other words, the change in the thermal boundary conditions of one board-to-board channel influences (by a factor of order 1) only the value of the numerical coefficient in the expressions for D_{opt} and $q'_{\max}$.

The stack in which both surfaces of each board release *uniform heat flux* was optimized in Ref. 23, in which the peak of the $q'(D)$ curve was determined numerically. The results showed that in the Pr range 0.7–10, the optimal board-to-board spacing is correlated by eq. (3.120) with 3.2 in place of 2.73. In the same Pr range, the maximum thermal conductance of the stack $q'/(T_{w,L} - T_\infty)$ is

once again correlated by eq. (3.121), with $\cong 0.4$ in place of $\lesssim 0.62$ and $(T_{w,L} - T_\infty)$ in place of $(T_w - T_\infty)$. Note that when the boards release uniform heat flux, the hot spot occurs at the trailing edge of the board, where the temperature is $T_{w,L}$.

The optimization of spacings for structures with *maximal heat transfer density* has developed into a field of its own, which is growing [33–54]. Optimal spacings have been identified for packages filled with staggered parallel plates, round and elliptical cylinders in cross flow, natural convection (see Section 4.12), and pin-fin arrays with impinging flow. This work is reviewed in a new book [8].

3.7 HEATLINES IN FULLY DEVELOPED DUCT FLOW

In this section we develop for duct flow the heatline visualization method introduced in Section 1.6. Consider a parallel-plate channel of spacing D and flow length L, and assume that the two walls release the heat flux q'' uniformly into the stream (Fig. 3.17). The channel is long enough so that the flow is hydrodynamically and thermally fully developed over most of the length L. The velocity distribution $u(y)$ was derived in eq. (3.19). By repeating the steps that led to eq. (3.62) for the round tube, it is possible to show that the temperature distribution in the fluid is (see Problem 3.8 and Ref. 55)

$$T(x,y) = T_0(x) - (T_0 - T_m) \, \frac{105}{68} \left[\frac{5}{6} - \left(\frac{y}{D/2} \right)^2 + \frac{1}{6} \left(\frac{y}{D/2} \right)^4 \right] \quad (3.124)$$

in which $q''D/k(T_0 - T_m) = 70/17$. This Nusselt number can be rewritten based on the hydraulic diameter $D_h = 2D$, namely, $q''D_h/k(T_0 - T_m) = 140/17 = 8.235$, to see that it is the same as the Nu value listed in Table 3.2.

The heatfunction $H(x, y)$ is obtained by integrating eqs. (1.68) and (1.69), in which we note two simplifications. First, the transversal velocity v is zero in eq. (1.69) because the flow is hydrodynamically fully developed. Second, the longitudinal conduction term $k \, \partial T/\partial x$ must be left out of eq. (1.68) because the same effect was neglected in the development of the energy equation for thermally fully developed flow [cf. eq. (3.48)]. With these simplifications, eqs. (1.68) and (1.69) reduce to

$$\frac{\partial H}{\partial y} = \rho c_P u(T - T_{\text{ref}}) \quad (3.125)$$

$$\frac{\partial H}{\partial x} = k \frac{\partial T}{\partial y} \quad (3.126)$$

We note that if q'' is assumed positive in the direction shown in Fig. 3.17, the wall is warmer than the fluid. The lowest temperature in the entire duct occurs
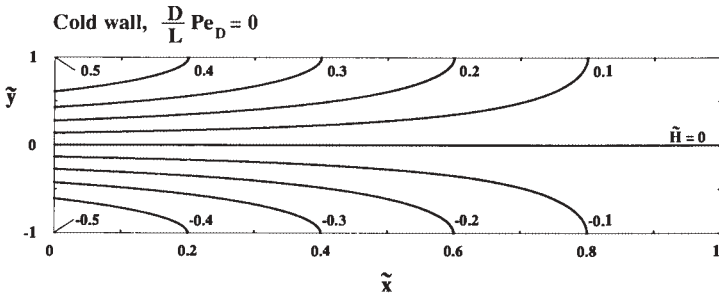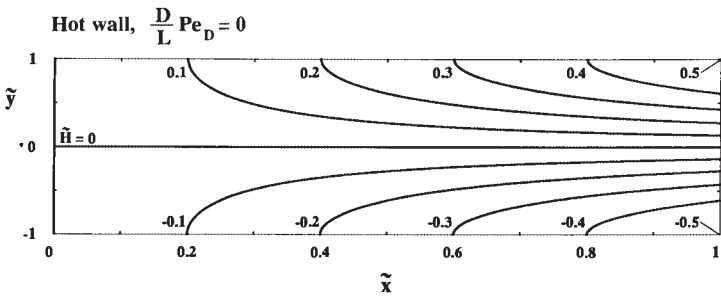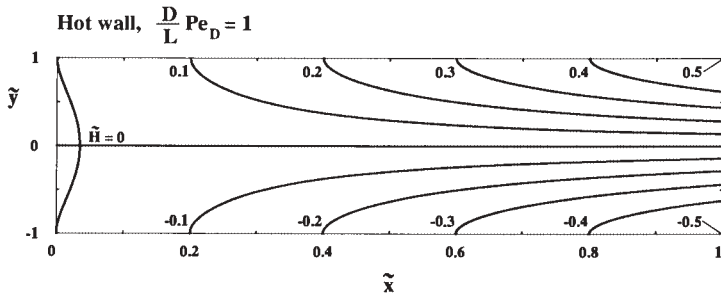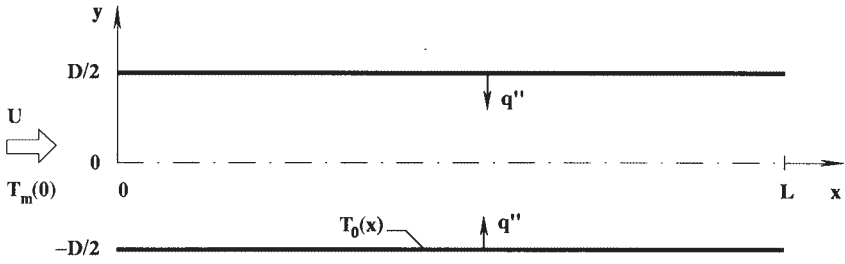
Figure 3.17   Heatlines in a parallel-plate duct with hydrodynamically and thermally fully developed flow. (From Ref. 55.)

at the inlet; therefore, we set $T_{\text{ref}} = T_m(x = 0)$ in eq. (3.125). The heatfunction obtained by integrating eqs. (3.125) and (3.126) can be written as

$$\tilde{H}(\tilde{x}, \tilde{y}) = \tilde{x}\left(\frac{3}{4}\tilde{y} - \frac{1}{4}\tilde{y}^3\right)$$

$$+ \frac{1}{128}\frac{D}{L}\text{Pe}_D\left(-\frac{117}{35}\tilde{y} + \frac{249}{35}\tilde{y}^3 - \frac{21}{5}\tilde{y}^5 + \frac{3}{7}\tilde{y}^7\right) \qquad (3.127)$$

where $\text{Pe}_D = UD/\alpha$, and

$$\tilde{H} = \frac{H}{2Lq''}, \qquad \tilde{x} = \frac{x}{L}, \qquad \tilde{y} = \frac{y}{D/2} \qquad (3.128)$$

In the step prior to eq. (3.127), the constant of integration was determined by setting $\tilde{H} = 0$ at the start of each wall. Note also that the heatfunction scale $2Lq''$, which was used in the nondimensionalization of H, is the total (known) heat transfer rate released from both walls. Finally, eq. (3.80) shows that the group $(D/L)\text{Pe}_D$ in eq. (3.127) must be on the order of 1 or smaller because $X_T \ll L$ and

$$\frac{D}{L}\text{Pe}_D \sim 10\frac{X_T}{L} \qquad (3.129)$$

The solution (3.127) shows that the heatfunction varies linearly along the walls, increasing along the top and decreasing along the bottom, $\tilde{H}(\tilde{x}, \pm 1) = \pm\ \tilde{x}/2$. This linear variation accounts for the equidistant heatlines that are seen coming out of the walls in Fig. 3.17. The heatlines are perpendicular to the wall because right next to the wall the longitudinal velocity is zero, and the transfer of heat is by pure conduction. Close to the midplane of the channel, the flow bends the heatlines downstream.

The hot-wall frames of Fig. 3.17 show that the heatline pattern does not change much as the group $(D/L)\text{Pe}_D$ decreases from 1 to 0. In conclusion, when $(D/L)\text{Pe}_D < 1$, the heatfunction $\tilde{H}$ is approximated well by the first group on the right-hand side of eq. (3.127); in other words, $\tilde{H}$ is independent of $(D/L)\text{Pe}_D$.

The heatline pattern changes when the wall is colder than the fluid (i.e., when q'' has a negative value in the sketch at the top of Fig. 3.17). In this case, the mean temperature and the wall temperature decrease linearly as we follow the flow. The lowest temperature in the entire system occurs on the trailing edges of the walls; therefore, in eq. (3.125), we set $T_{\text{ref}} = T_0(x = L)$. The analysis consists of integrating eqs. (3.125) and (3.126) by using eqs. (3.124) and (3.19), and the result is

$$\tilde{H}(\tilde{x}, \tilde{y}) = (1 - \tilde{x})\left(\frac{3}{4}\tilde{y} - \frac{1}{4}\tilde{y}^3\right)$$

$$+ \frac{1}{128}\frac{D}{L}\text{Pe}_D\left(-15\tilde{y} + 11\tilde{y}^3 - \frac{21}{5}\tilde{y}^5 + \frac{3}{7}\tilde{y}^7\right) \qquad (3.130)$$

The last frame of Fig. 3.17 shows the heatline pattern when $(D/L)\mathrm{Pe}_D = 0$. The heatlines are equidistant and perpendicular as they enter the cold walls. Note also that this pattern is the mirror image of the one drawn immediately above it for the same $(D/L)\mathrm{Pe}_D$ value. The last two frames illustrate the significant reorientation of the paths of convection when the role of the walls switches from heat source to heat sink. The growing field of heatline visualization is described by the references at the end of Chapter 1.

3.8   DUCT SHAPE FOR MINIMUM FLOW RESISTANCE

Round pipes with constant diameter are not the best ducts. Here we consider the problem of the optimal geometry (shape) of a duct [56] that must carry a stream ($\dot{m}$) between two pressure levels (P_0 and $P_L = P_0 - \Delta P$) separated by a fixed distance (L). The objective is to minimize the overall flow resistance $\Delta P/\dot{m}$. The duct is straight, with the flow pointing in the x direction; however, the cross-sectional area $A(x)$ and wetted perimeter $p(x)$ may vary with the longitudinal position.

There are at least two constraints. One is the total duct volume constraint,

$$\int_0^L A(x)\, dx = V \qquad \text{(constant)} \tag{3.131}$$

in which $A(x)$ is the unknown duct shape. Another constraint is the amount of duct wall material,

$$\int_0^L P(x)\, dx = M \qquad \text{(constant)} \tag{3.132}$$

where $p(x)$ is the unknown wetted perimeter of the duct cross section. The material constraint is crucial in designs where the unit cost of the material is high, or where the weight of the overall heat exchanger is constrained, as in aerospace applications.

The overall flow resistance can be calculated by noting that regardless of whether the flow is laminar, turbulent, or fully developed, the pressure gradient is given by [cf. eq. (3.23)]

$$\frac{dP}{dx} = -\tau_w(x)\frac{p(x)}{A(x)} \tag{3.133}$$

In this expression we substitute $f = \tau_w/\left(\frac{1}{2}\rho U^2\right)$, $\mathrm{Re}_{D_h} = D_h U/\nu$, and $\dot{m} = \rho U A$, and integrate from the inlet to the outlet to obtain the flow resistance,

$$\frac{\Delta P}{\dot{m}} = \int_0^L f\ \mathrm{Re}_{Dh}\frac{p\nu}{2A^2 D_h}dx \tag{3.134}$$

Consider first the hydraulic entrance region of a duct with round cross section [diameter $D(x)$] through which the flow is sufficiently isothermal such that ν may be regarded as constant. Note further that since the cross section is circular, D_h is equal to D, while $p = \pi D$ and $A = \pi D^2/4$. It follows that the geometric group p/A^2D appearing in eq. (3.134) scales as D^{-4}.

In the developing entrance region of a tube of constant diameter, the group $f\,\mathrm{Re}_D$ decreases approximately as $x^{-1/2}$. This group is usually plotted in dimensionless terms versus $x/(D\,\mathrm{Re}_D)$ (see Fig. 3.3). In the present problem, D is not a constant—in fact, to find the optimal function $D(x)$ is the objective. Consequently, instead of $f\,\mathrm{Re}_D$, we write $\phi(x)$, where the function ϕ could be determined after the duct shape $D(x)$ is known. If the duct shape $D(x)$ turns out to be a weak function of x, that is, if the duct diameter is nearly constant throughout the $0 < x < L$ domain, it is reasonable to expect ϕ to decrease as $x^{-1/2}$. We return to this observation at the end of this section.

In sum, the integrand of eq. (3.134) behaves as ϕ/D^4. On the other hand, the integrand of the volume constraint (3.131) varies as D^2. The problem of finding the function $D(x)$ that minimizes the flow resistance (3.134) subject to the fixed volume (3.131) reduces to minimizing the integral

$$I_1 = \int_0^L \left(\frac{\phi}{D^4} + \lambda_1 D^2 \right) dx \tag{3.135}$$

where λ_1 is a Lagrange multiplier. The variational calculus solution has the form

$$D_{\mathrm{opt}}(x) = \left[\frac{2}{\lambda_1} \phi(x) \right]^{1/6} \tag{3.136}$$

where assuming that $\phi(x)$ is known, the constant λ_1 is determined by substituting (3.136) into the volume constraint (3.131). We develop a better feel for the optimal duct shape prescribed by (3.136) by *assuming* that D_{opt} is a sufficiently weak function of x so that we may take $x^{-1/2}$ as the x dependence of the function ϕ. Combining this assumption with (3.136), we conclude that the D_{opt} must vary approximately as $x^{-1/12}$, which is indeed a weak function of longitudinal position. It means that (3.136) reads approximately $D_{\mathrm{opt}}(x) \cong (\text{constant})x^{-1/12}$.

In conclusion, for minimum flow resistance, the entrance region to a pipe should be shaped like a trumpet. The constant listed in the $D_{\mathrm{opt}}(x)$ expression is determined from the volume constraint, so that the closed-form result of this first example is

$$D_{\mathrm{opt}}(x) \cong \left(\frac{10V}{3\,\pi L} \right)^{1/2} \left(\frac{L}{x} \right)^{1/12} \tag{3.137}$$

A similar conclusion is reached if the flow resistance of the same entrance region is minimized subject to the wall surface (material) constraint (3.132) [56]. The entrance regions of other duct geometries may be optimized in the same

way. If the duct cross section is a flat rectangle of height $D(x)$ and constant width W, such what $W \gg D(x)$, the group $p/A^2 D_h$ of eq. (3.134) varies as $1/D^3 W$. Assuming that the x dependence of D is sufficiently weak, the $f\, \mathrm{Re}_{D_h}$ product may be recognized again as a function proportional to $x^{-1/2}$. The optimal $D(x)$ function that minimizes the flow resistance integral subject to volume constraint is

$$D_{\mathrm{opt}}(x) \cong \frac{7V}{8WL}\left(\frac{L}{x}\right)^{1/8} \tag{3.138}$$

The optimal entrance shape is such that the plate-to-plate D tapers down very slowly as the flow develops downstream. If instead of the volume we keep the total duct wall surface fixed

$$\int_0^L 2W\,dx = M \tag{3.139}$$

we find that the M constraint does not depend on the narrow spacing of the duct cross section, D. This means that an optimal wall-to-wall spacing function $D(x)$ does not exist. Instead, we may consider D as constant and the cross-sectional width W variable, while D remains negligible with respect to $W(x)$. The optimal entrance width that minimizes the overall flow resistance subject to the constraint (3.139) is

$$W_{\mathrm{opt}}(x) \cong \frac{3M}{8L}\left(\frac{L}{x}\right)^{1/4} \tag{3.140}$$

This optimal entrance geometry is one in which the width of the flat cross section decreases gradually in the flow direction, while D remains constant.

3.9 TREE-SHAPED FLOW

A new research direction in convection is traced by flow architectures shaped as tree networks [8, 57, 58]. A tree-shaped flow is required in order to connect one point (source, or sink) with a very large number of points (volume, or area). When the flow proceeds from the point (root) to the volume (canopy), the tree flow serves as a distribution network: The tree distributes the single stream to every ''inhabitant'' of the volume. When the flow is oriented from the canopy to the root, the tree is a collection network. In such cases the tree structure generates (constitutes) a single stream out of a large number of mini-streams that emanate from every point of the volume.

According to constructal theory [8], tree-shaped flow structures are manifestations of a natural tendency to flow more easily by changing the configuration of the flow. This tendency is at work everywhere, and it is condensed in the constructal law. It is widely applicable in engineering, from urban design to the cooling of electronics and to heat exchanger design in general [8]. It

is particularly evident in the continuing march toward smaller scales, where increased ''density'' is achieved not only through smaller working elements but also through better constructs (geometry, structure, architecture, packing).

In this section we outline the method and main features and properties of tree-shaped constructs of ducts. Tree networks are special because they do not have loops—tree networks are not ''nets.'' The flow path between the root and one point in the canopy is unique. We start with the simplest tree, which is the T-shaped construct of round tubes shown in Fig. 3.18. The flow connects one point (source or sink) with two points. There are two constraints:

1. Total duct volume $(D_1^2 L_1 + 2D_2^2 L_2 = \text{constant})$
2. Total space allocated to the construct $(2L_2 L_1 = \text{constant})$

If the flow is laminar and fully developed, the minimization of the flow resistance subject to constraint 1 yields the ratio of tube diameters,

$$\frac{D_1}{D_2} = 2^{1/3} \tag{3.141}$$

This ratio is an old result, which in physiology is known as the Hess–Murray *law* [8, p. 115]. This result is remarkable for its robustness: The optimal D_1/D_2 ratio is independent of the assumed tube lengths and the relative position of
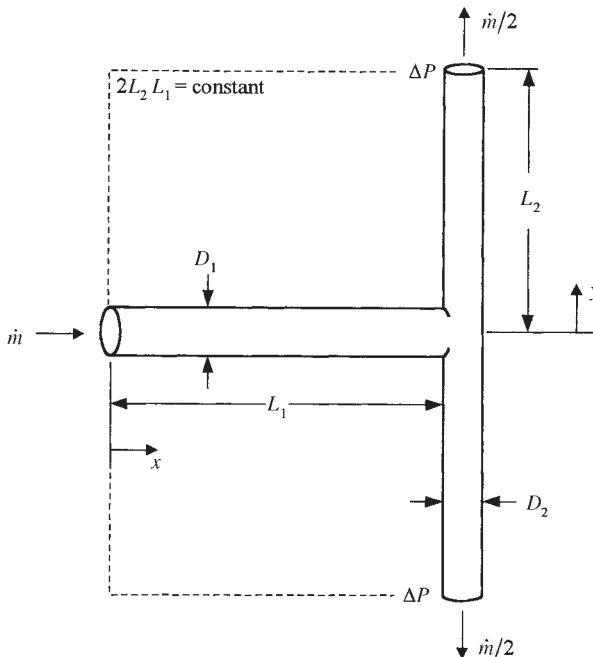
Figure 3.18   T-shaped construct of round tubes. (From Ref. 60.)

the three tubes. It is independent of layout. The result equivalent to eq. (3.141) for channels that are formed between parallel plates of spacings D_1 and D_2 is $D_1/D_2 = 2^{1/2}$ (see Problem 12.22).

New is the second level of optimization, which consists of selecting the ratio L_1/L_2 subject to space constraint 2. The result

$$\frac{L_1}{L_2} = 2^{1/3} \tag{3.142}$$

shows that at the junction the tube lengths must change in the same proportion as the tube diameters. Equations (3.141) and (3.142) are a condensed summary of the geometric proportions found more laboriously in the optimization of three-dimensional flow constructs [59], where the tube lengths increase by factors in the cyclical sequence 2, 1, 1, 2, 1, 1, ... The average of this factor for one step is $2^{1/3}$, which means that the optimization of the plane construct of Fig. 3.18 is an abbreviated substitute for the optimization of the three-dimensional construct.

If the flow in the T-shaped construct is fully developed and turbulent (see Section 8.2), eqs. (3.141) and (3.142) are replaced by [60]

$$\frac{D_1}{D_2} = 2^{3/7}, \qquad \frac{L_1}{L_2} = 2^{1/7} \tag{3.143}$$

Unlike in the laminar case, in which the ratio D/L was preserved in going from each tube to its stem or branch, in turbulent flow the geometric ratio that is preserved is D/L^3. Note that eqs. (3.143) yield $D_1/L_1^3 = D_2/L_2^3$. The assembly of three tubes can be optimized further by giving the morphing geometry more degrees of freedom. One example is to allow the angle of confluence to vary so that the T-shaped construct acquires an optimized Y shape.

In the designs of eqs. (3.141)–(3.143), the time of fluid residence in the small channels (D_2) is equal to the residence time in the large channel (D_1). This is true for laminar and turbulent flow, river basin design, and urban traffic [7].

Other simple flow constructs (e.g., open channels, gravity-driven flows) and other global constraints (e.g., tube wall material) lead to similar, compact conclusions. Another way to see the robustness of the results is to compare the minimized flow resistances for laminar and turbulent flow in the T-shaped arrangement (Fig. 3.18). It was found that the minimized resistance can be expressed in terms of the two constraints, the total tube volume (V) and the total area of the territory (A),

$$R_{\text{lam}} = 4\frac{A^{3/2}}{V^2}, \qquad R_{\text{turb}} = 4\frac{A^{7/4}}{V^{5/2}} \tag{3.144}$$

These expressions are surprisingly close even though their respective flow regimes are drastically different. Equations (3.144) indicate the role played by global constraints. Flow resistances are smaller when the served territories are smaller and when the tube volumes are larger.

More complex tree-shaped flow architectures are taught in Ref. 8. For illustration, consider the problem of distributing a stream from one central point

to many points situated on a circle. This flow configuration has applications in the cooling of electronics mounted on a disk [61–66]. A stream of coolant that enters the disk through its center bathes the disk and exits through ports located on the disk perimeter. There are two fundamental problems: the flow architecture for best cooling (minimal overall thermal resistance) and the architecture for minimal fluid flow resistance. In Figs. 3.19–3.21 we consider the fluid-flow problem by employing two methods, the minimization of flow resistance [63] and the much simpler and more direct method of minimizing flow path lengths [64].

The flow structure covers the disk shown in Fig. 3.19a. The disk radius is R. The mass flow rate and pressure drop from the center to the periphery are $\dot{m}$ and ΔP. The fluid flows in the Hagen–Poiseuille regime through round tubes of diameter D_i, length L_i, and flow rate $\dot{m}_i$, where i indicates the tube level ($i = 0$ near the center and increasing i values toward the periphery). The flow resistance posed by each tube is

$$\frac{\Delta P_i}{\dot{m}_i} = \frac{128\nu}{\pi}\frac{L_i}{D_i^4} \tag{3.145}$$

In the example of Fig. 3.19a, there are three levels of branching or pairing, such that the numbers of tubes of the same level increase from the center to the periphery: $n_0 = 3$, $n_1 = 6$, $n_2 = 12$, $n_3 = 24$. The number of outlets on the disk perimeter is N; in Fig. 3.19a, for example, N is equal to 24. The global flow resistance $\Delta P/\dot{m}$ can be minimized by selecting all the geometric features of the flow structure [63]. These include not only the lengths and angles, but also the ratios of tube diameters. When the total volume occupied by the tubes is constrained, the optimal tube diameters are sized relative to each other in accordance with eq. (3.141). When space is constrained, branchings with only two tributaries pose less resistance than branchings with more tributaries [60].

The flow architecture of Fig. 3.19a was optimized numerically for minimal global $\Delta P/\dot{m}$, by selecting the angles (α, β, γ) and tube lengths (L_0, L_1, L_2) subject to geometric constraints such as $L_0 + x_1 + x_2 = R$. See also Ref. 8. The flow architecture has two degrees of freedom. Figure 3.19a shows one example of optimized layout of tubes. The optimal bifurcation angle is almost uniform ($75°$) throughout the design, especially away from the center. The minimized flow resistance is reported as point 2 ($N = 12$) in Fig. 3.20, where f is a dimensionless flow resistance factor defined by

$$\frac{\Delta P}{\dot{m}} = 8\pi\nu\frac{R^3}{V^2}f \tag{3.146}$$

and V is the total volume occupied by the tubes. Point 2 is the start of the ''two pairings'' or two levels of branching curve, which was obtained by generating the optimized structures for cases with increasing numbers of outlets (N) on the perimeter. The number $N(= 4n_0)$ varies discretely as the number of central tubes n_0 increases, despite the impression given by the continuous curve shown in Fig. 3.20. Every flow structure on that curve has two levels of pairing or
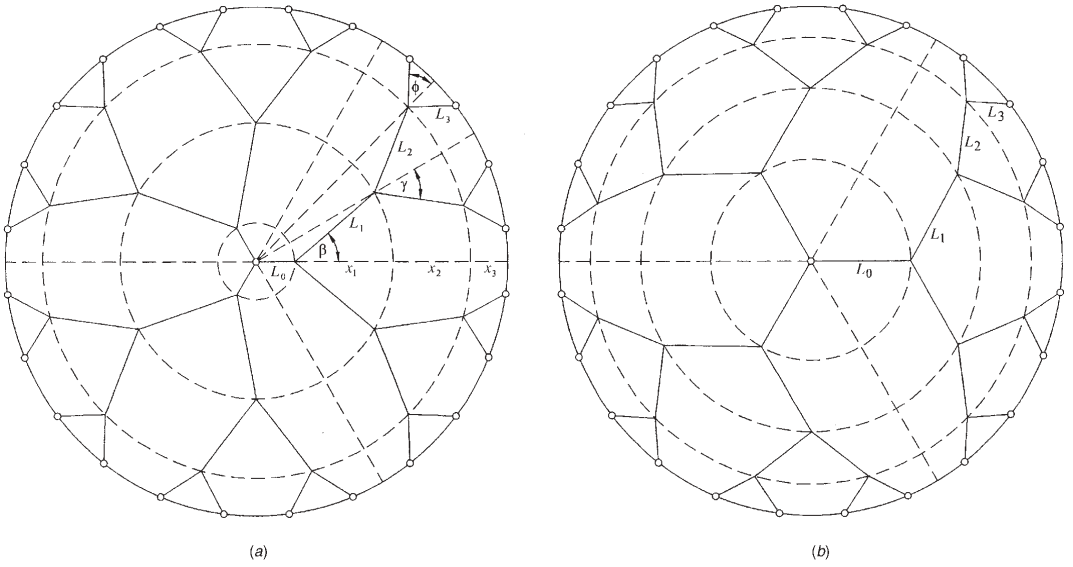
Figure 3.19 Tree flows between a circle and its center: (*a*) construct obtained by optimizing every geometric detail such that the global flow resistance is minimal; (*b*) construct generated by minimizing every flow path length. (From Ref. 64.)
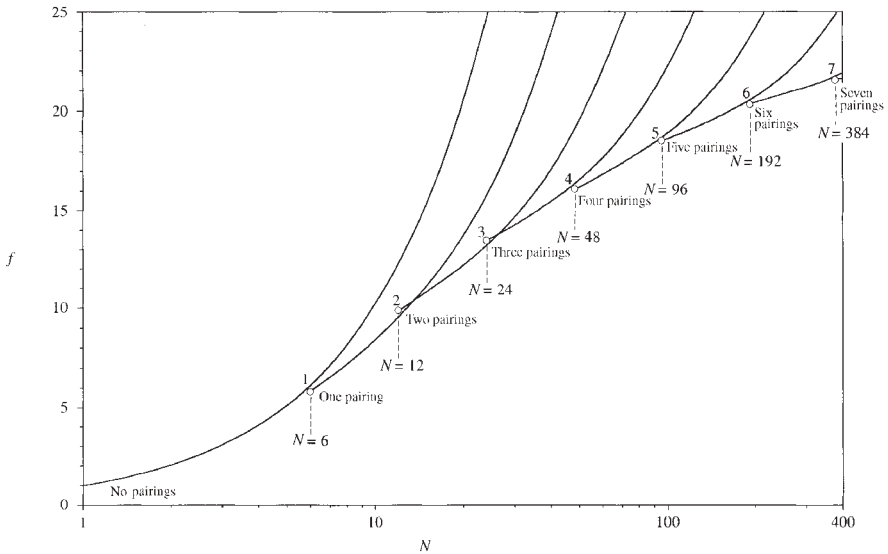
Figure 3.20   Effect of the number of levels of pairing on the global flow resistance (*f*) when the number of points on the periphery (*N*) is fixed and the disk radius and total tube volume are fixed. (From Ref. 63.)

bifurcation. Complexity increases when the number of pairing levels increases. For example, point 3 represents the simplest design with three pairings: This is drawn to scale in Fig. 3.19*a*.

All the tree-shaped flows developed so far represent *design*—geometric form with purpose. Which dendritic pattern is better? The answer depends on what is fixed. We rely on one of the first features in constructal theory: The smallest length scale of the flow pattern—the elemental scale—is known and fixed [8, 59]. This length scale is the distance (*d*) between two adjacent points on the circle. The radius of the circle (*R*) is also fixed. This means that the number of points on the circle (*N*) is fixed. Under these circumstances, formulas such as eq. (3.146) show that the global flow resistance of the tree construct ($\Delta P / \dot{m}$) varies proportionally with *f*, while the other factors are constant. The flow pattern with less global resistance is the one with the lower *f* value.

Figure 3.20 is instructive for several reasons. One conclusion is that pairing is a useful feature if *N* is sufficiently large (greater than 6). The larger the *N* value, the more likely the need to design more levels of pairings into the flow structure. If the number of points on the rim of the structure (*N*) increases, the flow structure with minimal flow resistance becomes more complex. Complexity increases because *N* increases and because the number of pairing levels increases. The right complexity, however, is finite (modest), not infinite or maximal. The right complexity is one of the features of the flow design uncovered with the constructal law [8].

If we take a fixed disk (R) with more and more points on the rim (N), the search for minimal flow resistance between the rim and the center requires discrete changes in the structure that covers the disk. To start with, N has to be large enough for an optimized structure with one or more pairings to exist. The starting N values (6, 12, 24, . . .) are indicated with circles in Fig. 3.20. As the structures become more complex, the circles describe a nearly smooth curve in the semilogarithmic field. When there are three or more levels of pairing, the circles indicate the *transition* from one type of structure to the next type with one more level of branching. This transition, or competition between two flow structures, is analogous to the transition and flow pattern selection in Bénard convection (see Section 5.5). In the vicinity of each circle in Fig. 3.20, the designer can choose between two structures, as both have nearly the same resistance.

It was shown by Lorente et al. [64] that it is much simpler to optimize the layout of the flow structure by minimizing the lengths of the tubes that inhabit every area element. The method is detailed in Refs. 8 and 64. Figure 3.19*b* shows one minimal-length tree next to the design based on the resistance minimization method. Visually, there is little difference between the two constructions. The same can be said about the f values of the competing designs. The squares plotted on Fig. 3.21 show that although consistently inferior, the performance of minimal-length structures resembles closely the performance of fully optimized structures. In conclusion, the length-minimization method proposed by Lorente
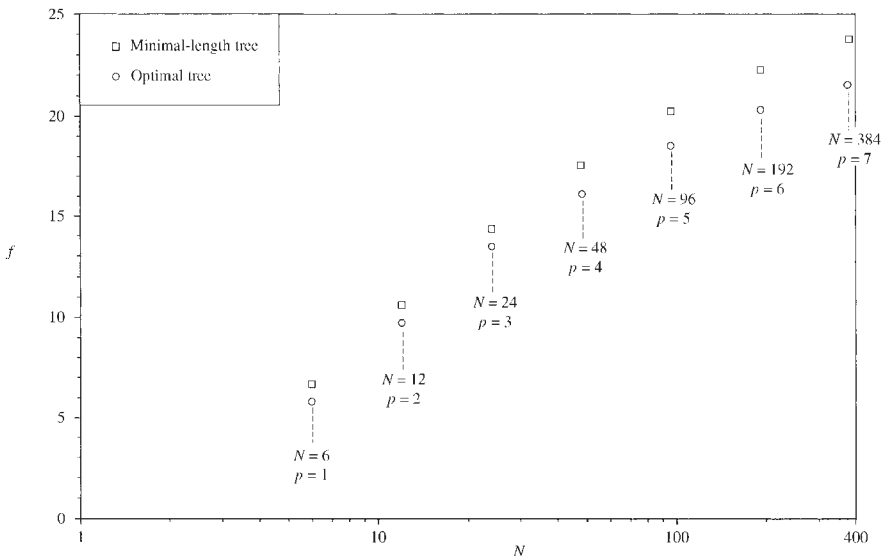
Figure 3.21   Minimal global flow resistance for (*a*) constructs obtained by optimizing every geometric detail and (*b*) constructs produced by minimizing every flow path length. (From Ref. 64.)

et al. [64] provides a very effective shortcut to designs that come close to the best designs. The minimal-length designs approach the optimal designs in terms of global performance, and architecturally as well. The closeness between designs (Figs. 3.19–3.21) shows again that optimized tree flow structures are robust.

The design features described in this section are important in general (i.e., regardless of what flows through the complex flow structure). For example, structures similar to those of Fig. 3.19 can be used in the conduction cooling of electronics. In such cases the disk generates heat at every point, and the ''ducts'' are blades or fibers with very high thermal conductivity, which are embedded in the heat-generating medium. The heat sink is the center of the disk. In the optimized design the inserts are arranged as a tree, which becomes larger, more complex, and more robust as the size of the disk increases [62].

In summary, the convection cooling of a heat-generating body is a design challenge with at least two objectives: minimal thermal resistance and minimal flow resistance (pumping power) [8, 65]. In this section we outlined the emergence of tree-shaped structures when only one objective is being pursued—minimal flow resistance. Unlike in thermodynamic optimization [7], where the search is for a unique balance (for minimal irreversibility) between heat transfer performance and fluid mechanics performance, in constructal design the search is for architectures in which both levels of performance are as high as possible. On a graph of thermal resistance versus fluid flow resistance (Fig. 3.22), there is one curve for each flow architecture. In forced-convection configurations, the thermal resistance decreases as the pumping power increases. The objective is to morph the flow configuration—to optimize the flow architecture so that it is represented by the curve that is situated as close as possible to the origin [8, 66].
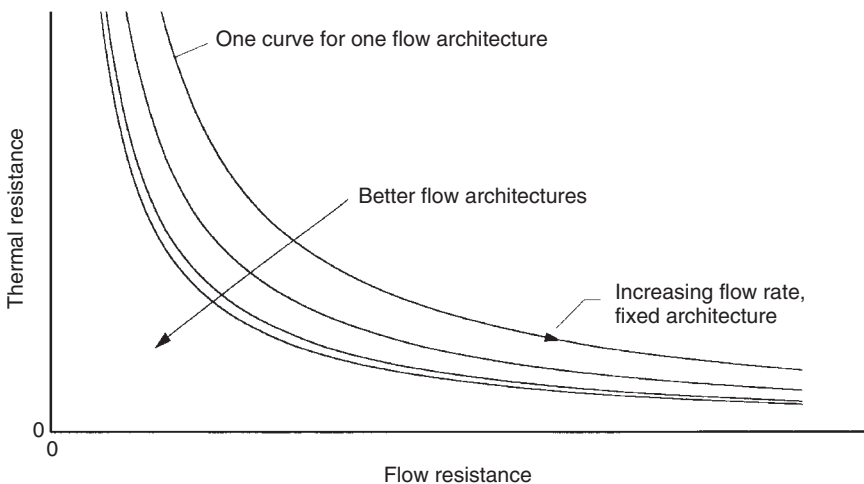
Figure 3.22   Search for flow architectures with two objectives: low thermal resistance and low fluid flow resistance. (From Ref. 66.)

Dendritic flow architectures were first reported in 1996 for minimal-time transportation and for the cooling of electronics, where they were used to optimize the insertion of high-conductivity blades and needles into the heat-generating packages [67–69]. Trees for heat convection, fin assemblies, fluid flow, traffic, economics, and business have also been optimized based on constructal theory and are reviewed in Refs. 8, 57, and 58. The interest in tree-shaped flow architectures is spreading to other sectors of heat and mass transfer, as illustrated by recent papers [70–106].

REFERENCES

1. A. Bejan and A. D. Kraus, eds., *Heat Transfer Handbook*, Wiley, Hoboken, 2003, Chapter 5.

2. E. M. Sparrow, Analysis of laminar forced convection heat transfer in the entrance region of flat rectangular ducts, NACA TN 3331, 1955.

3. H. Schlichting, *Boundary Layer Theory*, 4th ed., McGraw-Hill, New York, 1960, p. 169.

4. H. L. Langhaar, Steady flow in the transition length of a straight tube, *J. Appl. Mech.*, Vol. 9, 1942, pp. A55–A58.

5. G. Hagen, Über die Bewegung des Wassers in engen zylindrischen Röhren, *Pogg. Ann.*, Vol. 46, 1839, p. 423.

6. J. Poiseuille, Recherches expérimentales sur le mouvement des liquides dans les tubes de très petits diamètres, *Comptes Rendus*, *Vol.* 11, 1840, pp. 961, 1041.

7. A. Bejan, *Advanced Engineering Thermodynamics*, 3rd ed., Wiley, Hoboken, 2006.

8. A. Bejan and S. Lorente, *Design with Constructal Theory*, Wiley, Hoboken, 2008.

9. O. G. Tietjens, Preface, in L. Prandtl and O. G. Tietjens, *Fundamentals of Hydro and Aeromechanics*, Dover, New York, 1957, p. vii.

10. R. K. Shah and A. L. London, *Laminar Flow Forced Convection in Ducts,* Supplement 1 *to Advances in Heat Transfer*, Academic Press, New York, 1978.

11. S. W. Churchill, *Viscous Flows*: *The Practical Uses of Theory*, Butterworth, Boston, 1988, pp. 9, 40.

12. Y. Asako, H. Nakamura, and M. Faghri, Developing laminar flow and heat transfer in the entrance region of regular polygonal ducts, *Int. J. Heat Mass Transfer*, Vol. 31, 1988, pp. 2590–2593.

13. D. A. Nield and J. L. Lage, The role of longitudinal diffusion in fully developed forced convective slug flow in a channel, *Int. J. Heat Mass Transfer*, Vol. 41, 1998, pp. 4375–4377.

14. R. W. Hornbeck, An all-numerical method for heat transfer in the inlet of a tube, Paper 65-WA/HT-36, ASME, New York, 1965.

15. L. Graetz, Über die Warmeleitungsfähigkeit von Flüssigkeiten [On the thermal conductivity of liquids], Part 1, *Ann. Phys. Chem.*, Vol. 18, 1883, pp. 79–94; Part 2, *Ann. Phys. Chem.*, Vol. 25, 1885, pp. 337–357.

16. A. Lévêque, Les lois de la transmission de chaleur par convection, *Ann. Mines Mem. Ser.*, Vols. 12, 13, 1928, pp. 201–299, 305–362, 381–415.

17. R. K. Shah and M. S. Bhatti, Laminar convective heat transfer in ducts, in S. Kakac, R. K. Shah, and W. Aung, eds., *Handbook of Single-Phase Convective Heat Transfer*, Wiley, New York, 1987, Chapter 3.

18. K. Stephan, Wärmeübergang und Druckabfall bei nicht ausgebildeter Laminarströmung in Röhren und in ebenen Spalten, *Chem. Int. Tech.*, Vol. 31, 1959, pp. 773–778.

19. S. W. Churchill and H. Ozoe, Correlations for forced convection with uniform heating in flow over a plate and in developing and fully developed flow in a tube, *J. Heat Transfer*, Vol. 95, 1973, pp. 78–84.

20. A. Bejan, Dendritic constructal heat exchanger with small-scale crossflows and larger-scales counterflows, *Int. J. Heat Mass Transfer*, Vol. 45, 2002, pp. 4607–4620.

21. J. V. C. Vargas and L. Gavidia-Ceballos, Temperature distribution in expiratory speaking flow, and early detection of vocal fold pathology, *J. Med. Techn.*, Vol. 21, 1997, pp. 190–198.

22. Y. S. Muzychka, E. Walsh, and P. Walsh, Simple models for laminar thermally developing slug flow in noncircular ducts and channels, *J. Heat Transfer*, Vol. 132, 2010, 111702.

23. A. Bejan and E. Sciubba, The optimal spacing of parallel plates cooled by forced convection, *Int. J. Heat Mass Transfer*, Vol. 35, 1992, pp. 3259–3264.

24. A. Bejan, *Heat Transfer*, Wiley, New York, 1993, pp. 331–332.

25. A. Bejan, *Convection Heat Transfer*, 1st ed., Wiley, New York, 1984, problem 11, p. 157.

26. J. Lewins, Bejan's constructal theory of equal potential distribution, *Int. J. Heat Mass Transfer*, Vol. 46, 2003, pp. 1541–1543.

27. S. Bhattacharjee and W. L. Grosshandler, The formation of a wall jet near a high temperature wall under microgravity environment, *ASME HTD*, Vol. 96, 1988, pp. 711–716.

28. S. Petrescu, Comments on the optimal spacing of parallel plates cooled by forced convection, *Int. J. Heat Mass Transfer*, Vol. 37, 1994, p. 1283.

29. M. Favre-Marinet, S. Le Person, and A. Bejan, Maximum heat transfer rate density in two-dimensional minichannels and microchannels, in S. G. Kandlilkar, ed., *Proceedings of the First ASME International Conference on Microchannels and Minichannels*, 2003, pp. 765–772; to appear in *Microscale Thermophysical Engineering*, 2004.

30. T. Bello-Ochende and A. Bejan, Fitting the duct to the ''body'' of the convective flow, *Int. J. Heat Mass Transfer*, Vol. 46, 2003, pp. 1693–1701.

31. A. Bejan and Y. Fautrelle, Constructal multi-scale structure for maximal heat transfer density, *Acta Mech.*, Vol. 163, 2003, pp. 39–49.

32. A. Bejan, I. Dincer, S. Lorente, A. F. Miguel, and A. H. Reis, *Porous and Complex Flow Structures in Modern Technologies*, Springer-Verlag, New York, 2004.

33. G. Stanescu, A. J. Fowler, and A. Bejan, The optimal spacing of cylinders in free-stream cross-flow forced convection, *Int. J. Heat Mass Transfer*, Vol. 39, 1996, pp. 311–317.

34. A. J. Fowler, G. A. Ledezma, and A. Bejan, Optimal geometric arrangement of staggered plates in forced convection, *Int. J. Heat Mass Transfer*, Vol. 40, 1997, pp. 1795–1805.

35. T. Furukawa and W.-J. Yang, Thermal optimization of channel flows with discrete heating sections, *J. Non-Equilib. Thermodyn.*, Vol. 28, 2003, pp. 299–310.

36. A. Campo, Bounds for the optimal conditions of forced convective flows inside multiple channels whose plates are heated by a uniform flux, *Int. Comm. Heat Mass Transfer*, Vol. 26, 1999, pp. 105–114.

37. R. S. Matos, J. V. C. Vargas, T. A. Laursen, and F. E. M. Saboya, Optimization study and heat transfer comparison of staggered circular and elliptic tubes in forced convection, *Int. J. Heat Mass Transfer*, Vol. 44, 2001, pp. 3953–3961.

38. L. A. O. Rocha, F. E. M. Saboya, and J. V. C. Vargas, A comparative study of elliptical and circular sections in one- and two-row tubes and plate fin heat exchangers, *Int. J. Heat Fluid Flow*, Vol. 18, 1997, pp. 247–252.

39. G. Ledezma, A. M. Morega, and A. Bejan, Optimal spacings between pin fins with impinging flow, *J. Heat Transfer*, Vol. 118, 1996, pp. 570–577.

40. G. W. Recktenwald, *Numerical Methods with MATLAB: Implementations and Applications*, Prentice Hall, Upper Saddle River, NJ, 2000.

41. L. A. O. Rocha and A. Bejan, Geometric optimization of periodic flow and heat transfer in a volume cooled by parallel tubes, *J. Heat Transfer*, Vol. 123, 2001, pp. 233–239.

42. W.-J. Yang, T. Furukawa, and S. Torii, Optimal package design of stacks of convection-cooled printed circuit boards using entropy generation minimization method, *Int. J. Heat Mass Transfer*, Vol. 51, 2008, pp. 4038–4046.

43. L. Gosselin, Fitting the flow regime in the internal structure of heat transfer systems, *Int. Comm. Heat Mass Transfer*, Vol. 33, 2006, pp. 30–38.

44. S. Gheorghiu and M.-O. Coppens, Optimal bimodal pore networks for heterogeneous catalysis, *AIChE J.*, Vol. 50, 2004, pp. 812–820.

45. M. Yari, Entropy generation analysis for Couette–Poiseuille flow through parallel-plates microchannel, *Int. J. Exergy*, Vol. 6, 2009, pp. 809–825.

46. T. Bello-Ochende, J. P. Meyer, and J. Dirker, Three-dimensional multi-scale plate assembly for maximum heat transfer rate density, *Int. J. Heat Mass Transfer*, Vol. 53, 2010, pp. 586–593.

47. F. Wu, L. Chen, A. Shu, X. Kan, K. Wu, and Z. Yang, Constructal design of stack filled with parallel plates in standing-wave thermo-acoustic cooler, *Cryogenics*, Vol. 49, 2009, pp. 107–111.

48. Y.-T. Yang and H.-S. Peng, Numerical study of thermal and hydraulic performance of compound heat sink, *Numer. Heat Transfer Part A*, Vol. 55, 2009, pp. 432–447.

49. A. Andreozzi, B. Buonomo, and O. Manca, Transient natural convection in vertical channels symmetrically heated at uniform heat flux, *Numer. Heat Transfer Part A*, Vol. 55, 2009, pp. 409–431.

50. D.-K. Kim, S. J. Kim, and J.-K. Bae, Comparison of thermal performances of plate-fin and pin-fin heat sinks subject to an impinging flow, *Int. J. Heat Mass Transfer*, Vol. 52, 2009, pp. 3510–3517.

51. P. Bhave, A. Narasimhan, and D. A. S. Rees, Natural convection heat transfer enhancement using adiabatic block: Optimal block size and Prandtl number effect, *Int. J. Heat Mass Transfer*, Vol. 49, 2006, pp. 3807–3818.

52. A. Narasimhan and S. Karra, An inverse heat transfer method to provide near-isothermal surface for disc heaters used in microlithography, *Int. J. Heat Mass Transfer*, Vol. 49, 2006, pp. 4624–4632.

53. C. Zamfirescu and I. Dincer, Thermodynamic performance analysis and optimization of a SOFC-H$^+$ system, *Thermochim. Acta*, Vol. 486, 2009, pp. 32–40.

54. Y. S. Muzychka, Constructal design of forced convection cooled microchannel heat sinks and heat exchangers, *Int. J. Heat Mass Transfer*, Vol. 48, 2005, pp. 3119–3127.

55. A. M. Morega and A. Bejan, Heatline visualization of convective heat transfer in porous media, *Int. J. Heat Fluid Flow*, Vol. 15, 1994, pp. 42–47.

56. P. Jany and A. Bejan, Ernst Schmidt's approach to fin optimization: an extension to fins with variable conductivity and the design of ducts for fluid flow, *Int. J. Heat Mass Transfer*, Vol. 31, 1988, pp. 1635–1644.

57. A. Bejan and S. Lorente, The constructal law and the evolution of design in nature, *Physics of Life Reviews*, Vol. 8, 2011, pp. 209–240.

58. A. Bejan and J. P. Zane, *Design in Nature. How the Constructal Law Governs Evolution in Biology, Physics, Technology and Social Organization*, Doubleday, New York, 2012.

59. A. Bejan, *Shape and Structure, from Engineering to Nature*, Cambridge University Press, Cambridge, 2000.

60. A. Bejan, L. A. O. Rocha, and S. Lorente, Thermodynamic optimization of geometry: T- and Y-shaped constructs of fluid streams, *Int. J. Therm. Sci.*, Vol. 49, 2000, pp. 949–960.

61. D. V. Pence, Improved thermal efficiency and temperature uniformity using fractal-like branching channel networks, in G. P. Celata, V. P. Carey, M. Groll, I. Tanasawa, and G. Zummo, eds., *Heat Transfer and Transport Phenomena*, Begell House, New York, 2000, pp. 142–148.

62. L. A. O. Rocha, S. Lorente, and A. Bejan, Constructal design for cooling a disc-shaped area by conduction, *Int. J. Heat Mass Transfer*, Vol. 45, 2002, pp. 1643–1652.

63. W. Wechsatol, S. Lorente, and A. Bejan, Optimal tree-shaped networks for fluid flow in a disc-shaped body, *Int. J. Heat Mass Transfer*, Vol. 45, 2002, pp. 4911–4924.

64. S. Lorente, W. Wechsatol, and A. Bejan, Tree-shaped flow structures designed by minimizing path lengths, *Int. J. Heat Mass Transfer*, Vol. 45, 2002, pp. 3299–3312.

65. A. Bejan and M. R. Errera, Convective trees of fluid channels for volumetric cooling, *Int. J. Heat Mass Transfer*, Vol. 43, 2000, pp. 3105–3118.

66. W. Wechsatol, S. Lorente, and A. Bejan, Dendritic convection on a disc, *Int. J. Heat Mass Transfer*, Vol. 46, 2003, pp. 4381–4391.

67. A. Bejan, Street network theory of organization in nature, *J. Adv. Transp.*, Vol. 30, No. 1, June 1996, pp. 85–107.

68. A. Bejan, Constructal-theory network of conducting paths for cooling a heat generating volume, *Int. J. Heat Mass Transfer*, Vol. 40, 1997; pp. 799–816, issue published on Nov. 1, 1996.

69. A. Bejan, *Advanced Engineering Thermodynamics*, 2nd ed., Wiley, New York, 1997.

70. M. M. Fyrillas, Heat conduction in a solid slab embedded with a pipe of general cross-section: shape factor and shape optimization, *Int. J. Eng. Sci.*, Vol. 46, 2008, pp. 907–916.

71. T. Bello-Ochende, J. P. Meyer, and A. Bejan, Constructal ducts with wrinkled entrances, *Int. J. Heat Mass Transfer*, Vol. 52, 2009, pp. 3628–3633.

72. P. Xu, X. Q. Wang, A. S. Mujumdar, C. Yap, and B. M. Yu, Thermal characteristics of tree-shaped microchannel nets with/without loops, *Int. J. Therm. Sci.*, Vol. 48, 2009, pp. 2139–2147.

73. M. Gonzalez, N. Jelisavcic, R. J. Moral, D. Sahoo, G. S. Dulikravich, and T. J. Martin, Multi-objective design optimization of topology and performance of branching networks of cooling passages, *Int. J. Therm. Sci.*, Vol. 46, 2007, 1191–1202.

74. Y. Chen, C. Zhang, M. Shi, and Y. Yang, Thermal and hydrodynamic characteristics of constructal tree-shaped minichannel heat sink, *AIChE J.*, Vol. 56(8), 2010, pp. 2018–2029.

75. X.-Q. Wang, P. Xu, A. S. Mujumdar, and C. Yap, Flow and thermal characteristics of offset branching network, *Int. J. Therm. Sci.*, Vol. 49, 2010, pp. 272–280.

76. S. B. Zhou, L. G. Chen, and F. R. Sun, Constructal optimization for a solid-gas reactor based on triangular element, *Sci. China Ser. E-Tech. Sci.*, Vol. 51, 2008, pp. 1554–1562.

77. C. Amador, A. Gavriilidis, and P. Angeli, Flow distribution in different microreactor scale-out geometries and the effect of manufacturing tolerances and channel blockage, *Chem. Eng. J.*, Vol. 101, 2004, pp. 379–390.

78. V. A. P. Raja, T. Basak, and S. K. Das, Thermal performance of a multi-block heat exchanger designed on the basis of Bejan's constructal theory, *Int. J. Heat Mass Transfer*, Vol. 51, 2008, pp. 3582–3594.

79. J. Dallaire, L. Gosselin, and A. K. da Silva, Conceptual optimization of a rotary heat exchanger with a porous core, *Int. J. Therm. Sci.*, Vol. 49, 2010, pp. 454–462.

80. F. Rogiers and M. Baelmans, Towards maximal heat transfer rate densities for small-scale high effectiveness parallel-plate heat exchangers, *Int. J. Heat Mass Transfer*, Vol. 53, 2010, pp. 605–614.

81. J.-F. Cornet, Calculation of optimal design and ideal productivities of volumetrically lightened photobioreactors using the constructal approach, *Chem. Eng. Sci.*, Vol. 65, 2010, pp. 985–998.

82. C.-D. Ho, Jr-W. Tu, and C.-M. Yang, Conjugated heat transfer in double-pass laminar counterflow concentric-tube heat exchangers with sinusoidal wall fluxes, *Int. J. Heat Mass Transfer*, Vol. 52, 2009, pp. 45–55.

83. N. Mahir and Z. Altac, Numerical investigation of convective heat transfer in unsteady flow past two cylinders in tandem arrangements, *Int. J. Heat Fluid Flow*, Vol. 29, 2008, 1309–1318.

84. C. Bai and L. Wang, Constructal design of particle volume fraction in nanofluids, *J. Heat Transfer*, Vol. 131, 2009, 1.

85. D.-H. Kang, S. Lorente, and A. Bejan, Constructal architecture for heating a stream by convection, *Int. J. Heat Mass Transfer*, Vol. 53(9–10), 2010, pp. 2248–2256.

86. B. V. R. Reddy, P. V. Ramana, and A. Narasimhan, Steady and transient thermo-hydraulic performance of disc with tree-shaped micro-channel networks with and without radial inclination, *Int. J. Therm. Sci.*, Vol. 47, 2008, pp. 1482–1489.

87. R. Boichot, L. Luo, and Y. Fan, Tree-network structure generation for heat conduction by cellular automaton, *Energy Conver. Manage.*, Vol. 50, 2009, pp. 376–386.

88. S. Wei, L. Chen, and F. Sun, The area-point constructal optimization for discrete variable cross-section conducting path, *Appl. Energy*, Vol. 86, 2009, pp. 1111–1118.

89. X. Xianghua, L. Xingang, and R. Jianxun, Optimization of heat conduction using combinatorial optimization algorithms, *Int. J. Heat Mass Transfer*, Vol. 50, 2007, pp. 1675–1682.

90. G. H. Jones, P. Chanda, and S. Ghassemi, Thermal optimization of a composite heat spreader: finite volume fraction for high-conductivity blade.

91. A. Karakas, U. Camdali, and M. Tunc, Constructal optimisation of heat generating volumes, *Int. J. Exergy*, Vol. 6, 2009, pp. 637–654.

92. A. M. Aragón, J. K. Wayer, P. H. Geubelle, D. E. Goldberg, and S. R. White, Design of microvascular flow networks using multi-objective genetic algorithms, *Comput. Methods Appl. Mech. Eng.*, Vol. 197, 2008, pp. 4399–4410.

93. F. Huchet, J. Comiti, P. Legentilhomme, C. Solliec, J. Legrand, and A. Montillet, Multi-scale analysis of hydrodynamics inside a network of crossing minichannels using electrodiffusion method and PIV measurements, *Int. J. Heat Fluid Flow*, Vol. 29, 2008, pp. 1411–1421.

94. Y. Kwak, D. Pence, J. Liburdy, and V. Narayanan, Gas−liquid flows in a microscale fractal-like branching flow networks, *Int. J. Heat Fluid Flow*, Vol. 30, 2009, pp. 868–876.

95. H. Pedro, M. H. Kobayashi, C. F. M. Coimbra, and A. K. da Silva, Effectiveness of complex design through an evolutionary approach, *J. Thermophys. Heat Transfer.*, Vol. 22, 2008, pp. 115–118.

96. M. S. Sayeed, I. A. Ahmed, A. A. Syed, P. H. Raju, and M. S. Salman, Experimental study of tree networks for minimal pumping power, *Int. J. Design Nature Ecodynamics*, Vol. 3, 2008, pp. 135–149.

97. D. Haller, P. Woias, and N. Kockmann, Simulation and experimental investigation of pressure loss and heat transfer in microchannel networks containing bends and T-junctions, *Int. J. Heat Mass Transfer*, Vol. 52, 2009, pp. 2678–2689.

98. L. Gosselin, Optimization of tree-shaped fluid networks with size limitations, *Int. J. Therm. Sci.*, Vol. 46, 2007, pp. 434–443.

99. Z. Fan, X. Zhou, L. Luo, and W. Yuan, Experimental investigation of the flow distribution of a 2-dimensional constructal distributor, *Exp. Therm. Fluid Sci.*, Vol. 33, 2008, pp. 77–83.

100. F. Maddalena and S. Solimini, A variational model of irrigation patterns, *Interfaces Free Boundaries*, Vol. 5, 2003, pp. 391–415.

101. A. Majumdar, A. M. Alencar, S. V. Buldyrev, Z. Hantos, H. E. Stanley, and B. Suki, Fluid transport in branched structures with temporary closures: a model for quasistatic lung inflation, *Phys. Rev. E*, Vol. 67, 2003, 031912.

102. R. Godde and H. Kurz, Structural and biophysical simulation of angiogenesis and vascular remodeling, *Dev. Dyn.*, Vol. 220, 2001, pp. 387–401.

103. D. Tondeur, Y. Fan, and L. Luo, Constructal optimization of arborescent structures with flow singularities, *Chem. Eng. Sci.*, Vol. 64, 2009, pp. 3968–3982.

104. A. F. Miguel, Dendritic structures for fluid flow: laminar, turbulent and constructal design, *J. Fluids Struc.*, Vol. 26, 2010, pp. 330–335.

105. J. Yue, R. Boichot, L. Luo, Y. Gonthier, G. Chen, and Q. Yuan, Flow distribution and mass transfer in a parallel microchannel contactor integrated with constructal distributors, *AIChE J.*, Vol. 56, 2010, pp. 298–317.

106. J. C. Ordonez, A. Bejan, and R. S. Cherry, Designed porous media: optimally nonuniform flow architectures connecting one point with more points, *Int. J. Therm. Sci.*, Vol. 42, 2003, pp. 857–870.

107. A. Bejan, A. M. Morega, S. W. Lee, and S. J. Kim, The cooling of a heat generating board inside a parallel plate channel, *Int. J. Heat Fluid Flow*, Vol. 14, 1993, pp. 170–176.

108. D. B. Tuckerman and R. F. W. Pease, High-performance heat sinking for VLSI, *IEEE Electron Device Lett.*, Vol. EDL-2, 1981, pp. 126–129.

109. R. W. Knight, J. S. Goodling, and D. J. Hall, Optimal thermal design of forced convection heat sinks—analytical, *J. Electron. Packag.*, Vol. 113, 1991, pp. 313–321.

110. A. Bar-Cohen and A. D. Kraus, eds., *Advances in Thermal Modeling of Electronic Components and Systems*, Vol. 2, ASME Press, New York, 1990.

PROBLEMS

3.1. Determine the skin friction coefficient $C_{f,x}$ for hydrodynamically developing flow in a parallel-plate duct by using the integral solution for the velocity distribution shown in eqs. (3.5) and (3.6).

3.2. Determine the velocity distribution corresponding to fully developed (Hagen–Poiseuille) flow through the annular space formed between two concentric tubes. Let r_i and r_o be the inner and outer radii, respectively. Show that the inner wall shear stress τ_{w,r_i} differs from the value along the outer wall, τ_{w,r_o}. Calculate the friction factor for this flow by using instead of τ_w in eq. (3.24) the *average* τ_w value defined based on a force balance of type (3.23): $\pi(r_o^2 - r_i^2) \; \Delta P = \tau_{w,\mathrm{avg}} 2\pi(r_o + r_i)L = 2\pi L(r_o \tau_{w,r_o} + r_i \tau_{w,r_i})$.

3.3. Determine the velocity distribution and friction factor for Hagen–Poiseuille flow through a duct whose cross section has the shape of an extremely slender wedge (a triangle with tip angle $\epsilon \ll 1$ and long sides equal to b). Neglect the friction effect introduced by the short wall opposing the tip angle, whose length is ϵb. Start with eq. (3.30), where y is along b and z along ϵb. Check the relative order of magnitude of the two terms on the right-hand side of eq. (3.30), and neglect the insignificant one. To calculate the friction factor, use the *perimeter-averaged* wall shear stress $\tau_{w,\mathrm{avg}}$ defined in Problem 3.2.

3.4. Determine the Hagen–Poiseuille flow through a duct of rectangular cross section (Fig. 3.5) by solving eq. (3.30) for $u(y, z)$ as a Fourier series. This problem is analytically identical to determining the temperature distribution inside a rectangular object with internal heat generation and isothermal walls. With reference to Fig. 3.5, the problem statement is

$$\nabla^2 u = \frac{1}{\mu} \frac{dP}{dx} = \text{constant}$$

$$u = \begin{cases} 0 & \text{at } y = \pm a/2 \\ 0 & \text{at } z = \pm b/2 \end{cases} \tag{A}$$

To solve it, assume that

$$u(y, z) = u_1(y) + u_2(y, z)$$

where $u_1(y)$ is the Hagen–Poiseuille flow through the infinite parallel-plate channel of width $2a$,

$$\frac{d^2 u_1}{dy^2} = \frac{1}{\mu} \frac{dP}{dx}$$

$$u_1 = 0 \qquad \text{at } y \pm a/2 \tag{B}$$

and where u_2 is the necessary correction,

$$\nabla^2 u_2 = 0$$

$$u_2 = \begin{cases} 0 & \text{at } y = \pm a/2 \\ -u_1(y) & \text{at } z = \pm b/2 \end{cases} \tag{C}$$

Note that adding problems B and C equation by equation yields the original problem A. The advantage of decomposing the problem as A = B + C is that problem C can be solved by Fourier series expansion, whereas problem A cannot. Problem C is solvable because the equation $\nabla^2 u_2 = 0$ is homogeneous and one set of boundary conditions (y) is homogeneous (see Ref. 24, pp. 91–98).

3.5. Consider the approximate solution to Hagen–Poiseuille flow through a duct with rectangular cross section [eqs. (3.31)–(3.37)]. Retrace the analytical steps of this solution by starting with another velocity profile instead of eq. (3.31), for example,

$$u(y, z) = u_0 \cos \frac{\pi y}{a} \cos \frac{\pi z}{b}$$

3.6. Table 3.2 and Fig. 3.7 suggest that an approximation for f and Nu in fully developed duct flow is

$$f = \frac{16}{\text{Re}_{Dh}} \frac{\pi D_h^2/4}{A_{\text{duct}}}$$

$$\text{Nu} = \begin{cases} 3.66 \dfrac{\pi D_h^2/4}{A_{\text{duct}}}, & T_0 = \text{constant} \\[2ex] 4.36 \dfrac{\pi D_h^2/4}{A_{\text{duct}}}, & q'' = \text{constant} \end{cases}$$

Check the accuracy of these geometric correlations by completing Table P3.6 for friction and heat transfer through a duct with regular hexagonal cross section.

Table P3.6

	Numerical Results (Table 3.3)	Approximate Results
$f\,\text{Re}_{Dh}$	15.065	
$\text{Nu}(T_0 = \text{constant})$	3.353	
$\text{Nu}(q'' = \text{constant})$	4.021	

3.7. Determine the fully developed temperature profile in a tube with constant wall temperature by solving eqs. (3.72)–(3.74) using the method of successive approximations. The technique consists of guessing a particular polynomial for $\phi(r_*)$, substituting this guess into the left-hand side of eq. (3.72), and finally, integrating eq. (3.72) to obtain a better guess (approximation) for $\phi(r_*)$. The procedure can be repeated until the change in the Nu value from one approximation to the next is below a cost-determined percentage. To start the procedure, a reasonable initial guess is $\phi_0(r_*) = 1$.

3.8. The heat flux through the walls of the channel of Fig. 3.1 is uniform, q''. The flow regime is laminar. The velocity and temperature profiles are fully developed. Derive the expression for the fully developed temperature profile, and show that the Nusselt number based on hydraulic diameter is $\text{Nu} = 8.235$.

3.9. Solid food is heated by flowing through a parallel-plate channel of spacing D. The plates are isothermal at T_0, and the flow is thermally fully developed. The flow can be modeled as slug, with the longitudinal velocity U uniform across the channel. Attach a system of coordinates to the channel as in Fig. 3.1, and determine the fully developed temperature profile and the

longitudinal variation of the mean temperature. Show that the Nusselt number based on hydraulic diameter is $\mathrm{Nu} = \pi^2$.

3.10. Consider the thermal development in the entrance region X_T of a tube with uniform (slug) flow throughout the X_T length. This assumption amounts to imagining a $\mathrm{Pr} = 0$ fluid; in addition, the energy equation in eqs. (3.83) is simplified as $(1 - r_*^2)$ is being replaced by the constant $\frac{1}{2}$. Solve this simplified version of the problem using the separation of variables indicated in eq. (3.85). As a guide, use a conduction heat transfer textbook and the observation that the simplified problem is analytically identical to the problem of transient heat conduction in an initially isothermal $(\theta_* = 1)$ cylindrical object with isothermal boundary $(\theta_* = 0)$, where x_* assumes the role of dimensionless time.

3.11. Consider the Graetz series solution for Nu_x in a thermally developing Hagen–Poiseuille flow in a tube [Table 3.4 and eqs. (3.89)–(3.91)]. Show that in the range $x_* > O(1)$, the series expressions for Nu_x and Nu_{0-x} tend to the fully developed value of 3.66 (Table 3.2).

3.12. Evaluate the hydraulic diameter of a tube of internal diameter D, which has a slowly twisting tape insert (dividing wall) positioned right through the middle (see Fig. P3.12).
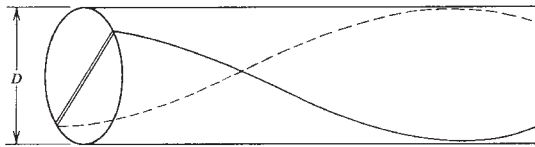
Figure P3.12

3.13. A water stream is heated in fully developed flow through a pipe with uniform heat flux at the wall. The flow rate is $\dot{m} = 10$ g/s, the heat flux $q'' = 0.1\,\mathrm{W/cm}^2$, and the pipe radius $r_0 = 1$ cm. The properties of water are $\mu = 0.01$ g/cm $\cdot$ s and $k = 0.006$ W/cm $\cdot$ K. Calculate (**a**) the Reynolds number based on pipe diameter and mean fluid velocity, (**b**) the heat transfer coefficient, and (**c**) the difference between the wall temperature and the mean (bulk) fluid temperature.

3.14. A water chiller passes a stream of 0.1 kg/s through a pipe immersed in a bath containing a mixture of crushed ice and water. Thus, the pipe wall temperature may be assumed to be $T_w = 0°\mathrm{C}$. The original (inlet) temperature of the stream is $T_1 = 40°\mathrm{C}$, and the specific heat of water is $c = 4.182$ J/g $\cdot$ K.

  (**a**) If the effectiveness of this heat exchanger is $\epsilon = 0.85$, calculate the final (outlet) temperature of the water stream.

  (**b**) Under the same conditions, what is the overall heat transfer rate between the stream and ice-water bath?

(c) Assume that the pipe length is L, the diameter D, and the flow regime fully developed laminar. If a new pipe is to be used ($D_1 = D/2$) and if the effectiveness is to remain unchanged, what should be the length of the new pipe (relative to the old length L), $L_1/L = ?$

3.15. Consider the Hagen-Poiseuille flow through a tube of radius r_0. The flow is extremely viscous, so that the energy equation reduces to

$$0 = k\frac{1}{r}\frac{d}{dr}\left(r\frac{dT}{dr}\right) + \mu\Phi$$

where Φ is the viscous dissipation term $\Phi = (du/dr)^2$. Determine the temperature distribution inside the pipe, subject to $T = T_0$ (constant) at $r = r_0$. Let Q be the total heat transfer rate through the pipe wall, over a pipe length L. Prove that $Q = (\dot{m}\,\Delta P)/\rho$, where $\dot{m}$ and ΔP are the mass flow rate and the pressure drop over the length L. Comment on the thermodynamic (lost-work) significance of this result; show that it is the same as eq. (1.48).

3.16. Water is heated as it flows through a stack of parallel metallic blades. The blade-to-blade spacing is $D = 1\,\text{cm}$ and the mean velocity through each channel is $U = 3.2\,\text{cm/s}$. Each blade is heated electrically so that the two sides of the blade together release $1600\,\text{W/m}^2$ into the water. Assuming that the water properties can be evaluated at $50°\text{C}$ and that the flow is thermally fully developed:

(a) Verify that the flow is laminar.

(b) Calculate the mean temperature difference between the blade and the water stream.

(c) Calculate the rate of temperature increase along the channel.

(d) Show how long the channel must be so that the assumption that the flow is thermally fully developed is valid.

3.17. The air flow through the gaps formed at the top and bottom of a closed door is driven by the local air pressure difference between the two sides of the door (Fig. P3.17). The door separates two isothermal rooms at different temperatures, T_c and T_h. In each room, the pressure distribution is purely hydrostatic, $P_c(y)$ and $P_h(y)$, and the height-averaged pressure is the same on both sides of the door.

(a) Assume that the air flow through each gap is laminar and fully developed. In terms of the geometric parameters indicated in the figure, show that the air flow rate through one gap is

$$\dot{m} = (\rho_c - \rho_h)\frac{gD^3WH}{24\nu L}$$

where W is the door width in the direction perpendicular to the plane of the figure. Show further that the net convection heat transfer rate from the warm room to the cold room, through the two gaps, is

$$q = \dot{m}c_P(T_h - T_c)$$

(b) Given are $T_c = 10°C$, $T_h = 30°C$, $D = 0.5$ mm, $L = 5$ cm, $H = 2.2$ m, and $W = 1.5$ m. Calculate $\dot{m}$ and q, and comment on how these quantities react to an increase in the gap thickness D.
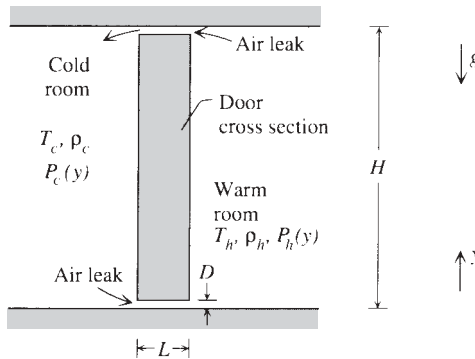
Figure P3.17

3.18. The metallic blade shown in Fig. P3.18 is an electric conductor that must be cooled by forced convection in a channel with insulated walls, with spacing D and length L [107]. The blade and the channel are sufficiently long in the direction perpendicular to the figure. The pressure difference across the arrangement is fixed, ΔP, and the flow on either side of the blade is laminar and fully developed. The inlet temperature is T_0.
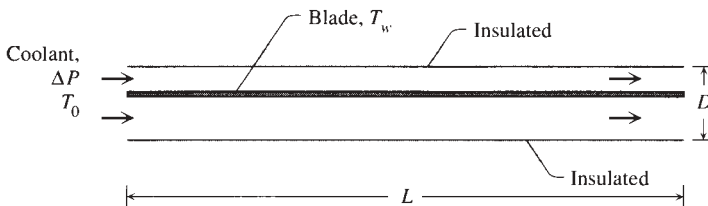
Figure P3.18

The objective is to lower the blade temperature as much as possible. The total heat transfer rate from the blade to the fluid, through both sides of the blade, is fixed by electrical design. What is the best position that the blade should occupy in the channel—right in the middle, or closer to one of the walls?

For simplicity, assume that the blade is isothermal (T_w). Assume that on either side of the blade (area A_w), the group $hA_w/\dot{m}c_P$ is sufficiently greater than 1 so that the outlet temperature of the stream is approximately equal to T_w. The blade thickness is negligible relative to D.

3.19. Figure P3.19 shows a simplified model of an electronic circuit board cooled by a laminar fully developed flow in a parallel-wall channel of fixed length L. The walls of the channel are insulated. The board substrate has a sufficiently high thermal conductivity so that the board temperature T_w may be assumed uniform in the longitudinal direction. The pressure difference that drives the flow is fixed, ΔP, and the fluid inlet temperature is T_0.
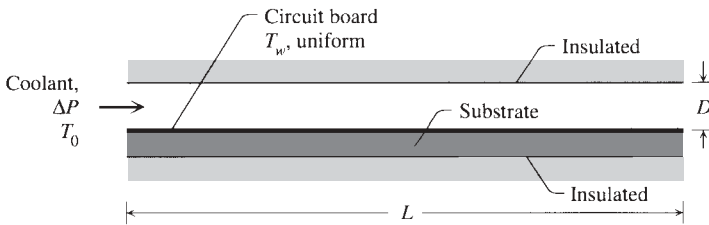
Figure P3.19

The channel spacing D must be selected such that the thermal conductance $q/(T_w - T_0)$ is maximum. In this ratio, q is the total heat transfer rate removed by the stream from the board. Show that the optimal spacing is given by

$$\frac{D_{\text{opt}}}{L} = 2.70 \ \text{Be}_L^{-1/4}$$

and that the corresponding maximum thermal conductance or average heat transfer coefficient is

$$\left(\frac{\bar{q}''}{T_w - T_0}\right)_{\text{max}} \frac{L}{k} = 0.693 \ \text{Be}_L^{1/4}$$

where $\text{Be}_L = (\Delta P \, L^2)/\mu\alpha$.

3.20. The electronic circuit board shown in Fig. P3.20 is thin and long enough to be modeled as a surface with uniform heat flux q''. The heat generated by circuitry is removed by fully developed laminar flow channeled by the board and a parallel wall above it. That wall and the underside of the board are insulated. The length L is specified, and the inlet temperature of the coolant is T_0.

The circuit board reaches its highest temperature (T_h) at the trailing edge, that is, in the plane of the outlet. That temperature ceiling is fixed by

electrical design; otherwise, the performance of the electronic components incorporated in the board will deteriorate. The objective is to build as much circuitry and as many components into the board as possible. This is equivalent to seeking a board and channel design that ensures the removal of the largest rate of heat generated by the board ($q''L$). The lone degree of freedom is the selection of the spacing D.
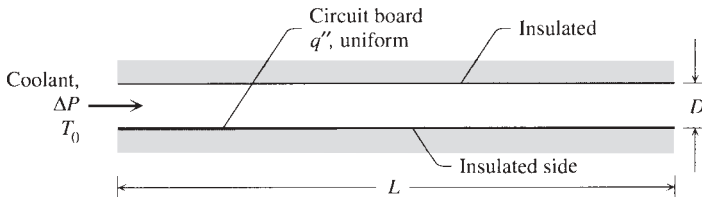
Figure P3.20

(a) Maximize the heat transfer rate removed by the stream, and show that the optimal design is characterized by

$$\frac{D_{opt}}{L} = 3.14 \ Be_L^{-1/4}$$

$$\left(\frac{q''}{T_h - T_0}\right)_{max} \frac{L}{k} = 0.644 \ Be_L^{1/4}$$

where $Be_L = \Delta P \, L^2/\mu\alpha$.

(b) Compare this optimal design with the results of Problem 3.19 (with $T_w = T_h$), in which the board was made isothermal by bonding it to a high-conductivity substrate. Why is the maximum heat transfer rate higher when the board is isothermal? Is the increase in heat transfer significant enough to justify the use of a high-conductivity substrate?

3.21. Figure P3.21 shows the cross section through a bundle of microscopic water channels that are intended to serve as a heat sink in the substrate of an integrated circuit. Their purpose is to remove the heat generated by the circuit. The channels are etched into the high-conductivity substrate (silicon) and are capped with a cover plate that is a relatively poor thermal conductor. Water is pumped through the channels, and the flow is laminar and fully developed. Several ways of optimizing the geometry of this compact heat sink are described in Refs. 108–110. In this problem, we consider only one question: What is the optimal fin thickness (t) that maximizes the heat transfer rate from the substrate (T_w) to the water flow (local bulk temperature T_f)? We conduct the optimization in the cross section, that is, at each location along the stream.

Assume that the heat transfer from T_w to T_f occurs primarily through the fins, in other words, that heat transfer through the unfinned portions of the substrate is negligible. For estimating the heat transfer coefficient only, assume that $L \gg D$ and that the wetted surfaces are almost isothermal along L. Assume further that the thermal resistance posed by the substrate of thickness S is negligible. Derive a formula for the total heat transfer rate removed by all the channel streams, q'. This quantity is expressed per unit length in the direction of flow. Arrange your results in the dimensionless form

$$Q = \text{function}\left(b, \ \frac{t}{D}\right)$$

where Q and b are two dimensionless groups

$$Q = \frac{q'}{k_w(T_w - T_f)B/L} \qquad b = \frac{L}{D}\left(\text{Nu}\frac{k_f}{k_w}\right)^{1/2}$$

In this notation k_f, k_w, and Nu are the fluid thermal conductivity, the fin thermal conductivity, and the Nusselt number (constant) for fully developed flow and heat transfer in the individual channel.
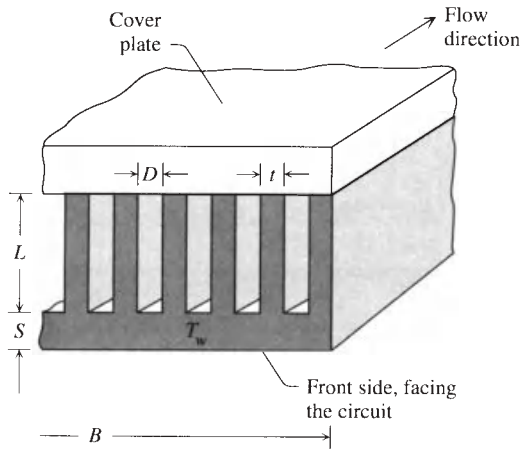
Figure P3.21

To find the optimal fin thickness for maximum q' when all the other parameters are fixed, you can maximize Q with respect to t/D for every b. In this way, you can show that the optimal fin thickness is approximately equal to the channel spacing when $b \gtrsim 2$. On the other hand, when $b \lesssim 1$, the optimal fin thickness is proportional to (i.e., a fraction of) the fin length L.

3.22. The electronic circuit board shown in Fig. P3.22 must be cooled by forced convection in a parallel-plate channel of spacing D, length L, and width W perpendicular to the plane of the figure [107]. The channel walls are insulated. The coolant (air) is forced to flow through the channel by the pressure difference ΔP, which is maintained by a fan. All the surfaces may be modeled as smooth. The channel is sufficiently slender so that the flow is laminar and fully developed in both subchannels, that is, on both sides of the board.
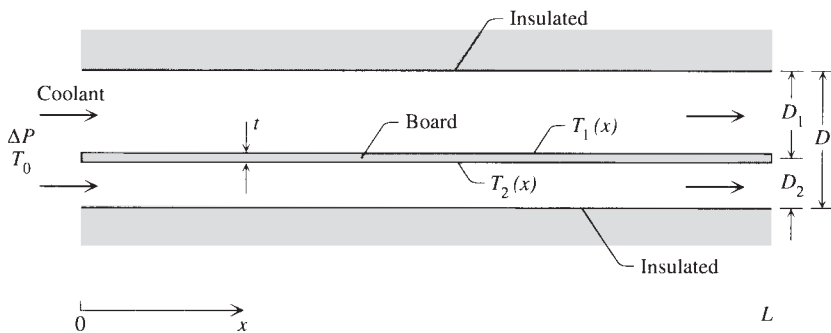
Figure P3.22

The board material has the thermal conductivity k_w and thickness t, which is negligible relative to D. The two surfaces of the board are loaded equally and uniformly with electronics; the constant heat generation rate per unit board surface is q''. It is important to note, however, that the heat fluxes removed by the two streams generally are not equal because of the conduction heat transfer across the board. The temperatures of the two board surfaces (T_1, T_2) increase in the downstream direction and reach their highest levels at the trailing edge, $x = L$.

How would you mount the board inside the channel to lower the highest board temperature as much as possible? Would you place it in the middle of the channel or closer to one of the sidewalls? You will discover that the correct answer depends on the degree to which the board substrate is a good thermal conductor in the transversal direction.

To simplify the analysis, assume that the local bulk temperature of each stream is nearly the same as the temperature of the neighboring spot on the board surface bathed by that stream. In other words, assume that the local temperature difference between the stream and the board surface is considerably smaller than the temperature rise from $x = 0$ to $x = L$ along the board surface. Derive expressions for the surface temperature distributions $T_1(x)$ and $T_2(x)$, and try to minimize the larger of the two trailing-edge temperatures, $T_1(L)$ or $T_2(L)$. Formulate the analysis in terms of the following dimensionless parameters:

$$\xi = \frac{x}{L}, \quad y = \frac{D_1}{D}, \quad 1 - y = \frac{D_2}{D}$$

$$\theta_1 = (T_1 - T_0)\frac{\rho c_P}{12\mu L^2 q''}\frac{\Delta P\ D^3}{}, \quad \theta_2 = (T_2 - T_0)\frac{\rho c_P}{12\mu L^2 q''}\frac{\Delta P\ D^3}{}$$

$$B = 12\frac{k_w}{k}\frac{\mu\alpha L^2}{\Delta P\ D^3 t}$$

The number B expresses the relative size of the thermal conductance of the board substrate. The optimal board location (y) will be a function of B.

3.23. In this problem you will determine the optimal spacing of cylinders in cross flow [33]. The fixed volume $H \times L \times W$ shown in Fig. P3.23 contains a bundle of parallel cylinders of diameter D and temperature T_w and is bathed by a cross flow of temperature T_∞ and velocity U_∞. Maximize the heat transfer q between the bundle and the surrounding fluid by selecting the cylinder-to-cylinder spacing S, or the number of cylinders in the bundle.

That an optimal number of cylinders must exist can be expected based on the following argument. If the volume $H \times L \times W$ contains only one
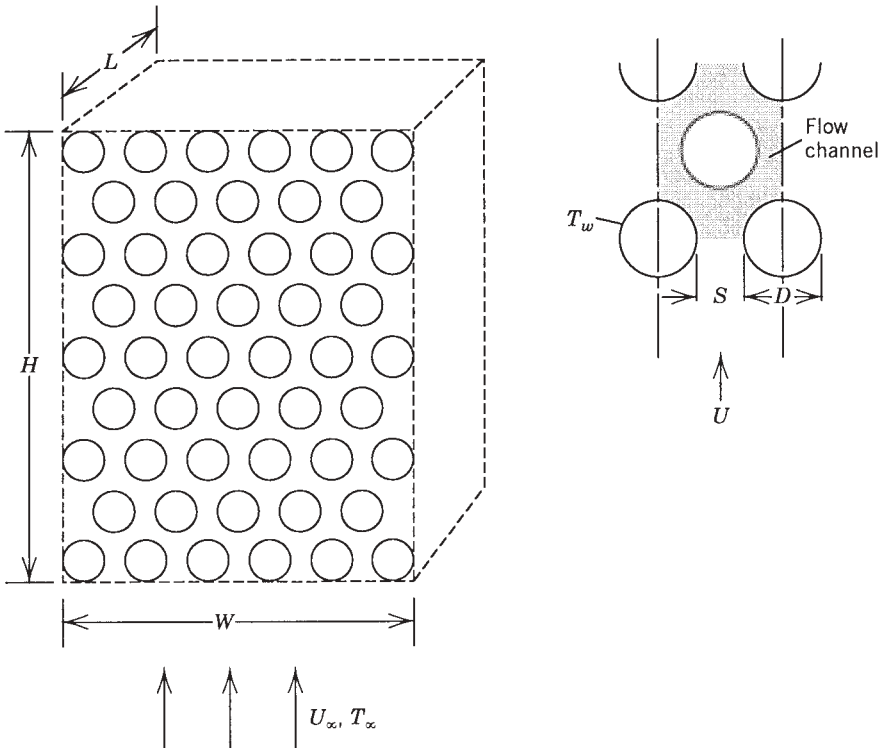
Figure P3.23

cylinder, then perhaps two or more cylinders will transfer more heat to the surrounding flow. This trend continues until the cylinders become so numerous that they almost touch, the bundle becomes impermeable to the free stream, and the flow stops. The optimal spacing S emerges as a trade-off between the limit of dense cylinders (large heat transfer area) and that of sparse cylinders (large flow cross-sectional area).

This argument also suggests the analysis that you should construct. Begin with the calculation of the heat transfer rate in the two asymptotic regimes noted above. For the large-S limit, assume that $Nu_D = c(U_\infty D/\nu)^{1/2}$, where c is an empirical constant that can be deduced from eq. (7.112). Finally, determine the optimal cylinder-to-cylinder spacing by intersecting the two asymptotic estimates obtained for the total heat transfer between the bundle and the free stream.

3.24. The optimal spacing derived in eq. (3.120) is valid for $Pr > 0.5$. Use the intersection-of-asymptotes method (Section 3.6), assume that the group is of low-Pr fluids ($Pr < 0.5$), and show that eqs. (3.120) and (3.121) are replaced by

$$\frac{D_{\text{opt}}}{L} \simeq 3.33 Be^{-1/4} \; Pr^{1/16}$$

$$q'_{\text{max}} \lesssim 0.92(\rho \, \Delta P)^{1/2} \; Pr^{-3/8} \; Hc_p(T_w - T_\infty)$$

3.25. The two-dimensional volume shown in Fig. P3.25 contains a solid of low thermal conductivity k_0. This solid generates heat volumetrically at the uniform rate $q'''(W/m^3)$. The overall size ($A = HL$) is fixed, but the geometric aspect ratio H/L may vary. The perimeter of the $H \times L$ rectangle is insulated. The heat current generated ($q'''A$) is removed by a stream of ideal gas (c_P), which flows through a thin channel of spacing D. The mass flow rate $\dot{m}'(kg/s \cdot m)$ is proportional to the frontal dimension (H), $\dot{m}' = \dot{m}''H$, where $\dot{m}''(kg/s \cdot m^2)$ is a constant. Assume that $D \ll H$
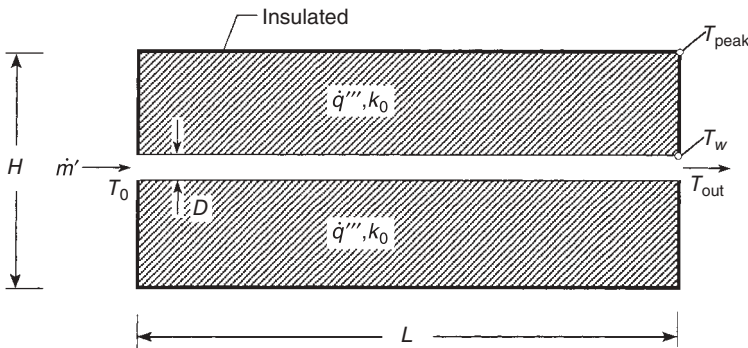
Figure P3.25

and $H \ll L$. In this limit the conduction through the k_0 material is oriented in the direction perpendicular to the channel.

The hot spots (T_{peak}) occur in the two corners that are situated farthest from the inlet. Derive an expression for the overall thermal conductance $\Delta \tilde{T} = (T_{peak} - T_0)/(q'''A/k_0)$, and minimize it with respect to the shape parameter H/L. Report analytically $(H/L)_{opt}$ and $\Delta \tilde{T}_{min}$. For simplicity in the derivation of $\Delta \tilde{T}$, neglect the difference between the channel wall temperature and the bulk temperature of the stream $(T_w - T_{out})$. How large must $\dot{m}''$ be so that your analytical results are valid?

3.26. Assume that in Fig. 3.16 the flow is not driven by an imposed pressure difference ΔP. Instead, the flow approaches the stack from the left with a uniform velocity U, and when the stack is sufficiently dense, it stagnates against the stack. The approach velocity U should not be confused with the free-stream velocity in the channels, U_∞. Approximate as $\Delta P \sim \frac{1}{2} \rho U^2$ the effective pressure rise that drives the flow through the stack, and derive expressions that replace eqs. (3.120) and (3.123).

3.27. Consider the scale X of the hydrodynamic and thermal entrance regions of a parallel-plate channel with spacing D and a fluid with $Pr \sim 1$. Show that this scale can also be written as

$$\frac{X}{D} \sim Be_D^{1/2}$$

where $Be_D = (\Delta P D^2)/\alpha \mu$, and ΔP is the pressure drop along X.

3.28. Consider a Y-shaped construct of three tubes. The stem has length L_1 and diameter D_1. The two branches are identical and have length L_2 and diameter D_2. The flow is fully developed and laminar (Hagen-Poiseuille), with negligible junction losses. The mass flow rate in the stem ($\dot{m}_1$) is twice the mass flow rate in one of the branches ($\dot{m}_2$). The total pressure drop (ΔP) along the Y-shaped construct is fixed. The total volume of the three tubes is also fixed.

Determine the ratio D_1/D_2 such that the total residence time in the Y-shaped construct is minimal. The residence time in one tube is $t = L/U$, where U is the average velocity. The total residence time is $t = t_1 + t_2$. Does the optimal ratio D_1/D_2 depend on L_1 and L_2? Comment on this optimal D_1/D_2 ratio and the $2^{1/3}$ value obtained by minimizing the flow resistance of the Y construct.

3.29. Consider the Y-shaped construct of three tubes described in the preceding problem. Assume that the tubes are sufficiently short, that all the pressure drops are dominated by losses at the junctions. Now the issue is the flow resistance of a ''tree of junctions,'' with pressure at the junctions, not along the tubes. The pressure drop at the junction between the stem (L_1, D_1) and the two branches (L_2, D_2) is $\Delta P_1 = K \frac{1}{2} \rho V_1^2$, where V_1 is the mean

velocity in the L_1 tube. The pressure drop in the subsequent junctions (downstream of the L_2 tubes) is $\Delta P_2 = K\frac{1}{2}\rho V_2^2$, where V_2 is the mean velocity in the L_2 tubes.

Minimize the overall pressure loss $(\Delta P_1 + \Delta P_2)$ subject to the total flow volume of the three-tube construct, and show that the ratio of tube diameters should be

$$\frac{D_1}{D_2} = 2^{1/2}\left(\frac{L_2}{L_1}\right)^{1/6}$$

Note that if $L_1 = 8L_2$, then $D_1 = D_2$, which means that all the tubes should have the same diameter.

Next, assume that the area A occupied by the layout of three tubes is fixed. The two L_2 tubes are collinear and perpendicular to the L_1 tube, in other words, the three-tube construct is shaped as a T. The area is $A = 2L_2L_1$, and its shape L_1/L_2 is free to vary. Minimize the overall pressure drop with respect to L_1/L_2 (i.e., after using the D_1/D_2 ratio determined above), and show that the T-shaped configuration with optimal D_1/D_2 and L_1/L_2 is represented by

$$\frac{D_1}{D_2} = 20^{1/4}, \qquad \frac{L_2}{L_1} = 5^{3/2}$$

3.30. In this problem we ask whether ducts with square cross sections (s) are better than parallel-plate channels (p) for achieving greater heat transfer densities in volumes packed with such channels. The comparison is shown in Fig. P3.30. The flow is from left to right, and the pressure difference is ΔP in both designs. Each channel is the best that it can be: Its boundary layers merge just as they exit the channel.

(p) Parallel plates   (s) Square ducts
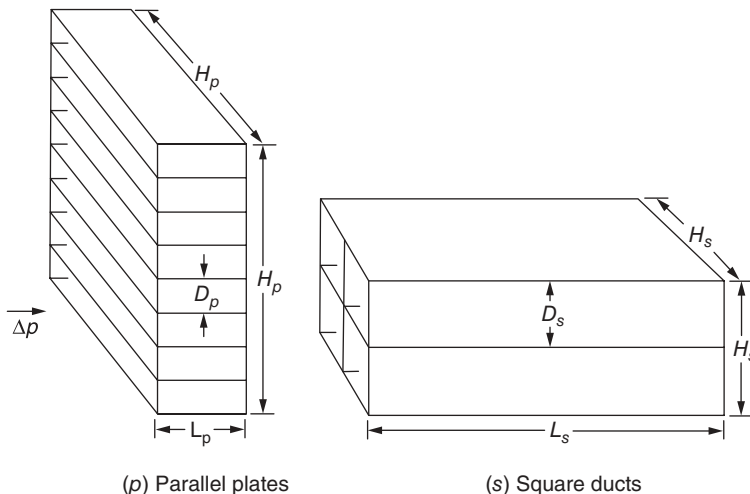
Figure P3.30

According to Section 3.6, the optimal spacing between parallel plates with fixed length (L_p) and pressure drop ΔP is $D_p/L_p = a_p \, Be_p^{-1/4}$. The corresponding maximum heat transfer rate (q_p) packed in a stack of thickness H_p and width H_p is $q_p L_p/(H_p^2 k \, \Delta T) = b_p \, Be_p^{1/2}$, where $Be_p = \Delta P L_p^2/(\mu\alpha)$. There are $n_p = H_p/D_p$ plates in the stack. Each plate has the area $H_p L_p$ and negligible thickness.

The numerical factors a_p and b_p are dimensionless and of order 1. We assume that these factors do not change much when the shape of the channel cross section changes. Thus, for a stack of channels with square cross sections (square side D_s, length L_s), we write similarly $D_s/L_s = a_s \, Be_s^{-1/4}$ and $q_s L_s/(H_s^2 k \Delta T) = b_s \, Be_s^{1/2}$, where $Be_s = \Delta P L_s^2/(\mu\alpha)$, $a_s \simeq a_p$ and $b_s \simeq b_p$. For simplicity, assume that $a_s = a_p$ and $b_s = b_p$.

Two global constraints apply to both configurations, parallel plates and squares. The total volume of the stack is the same, and so is the total amount of channel wall material. Show that the (p) and (s) configurations have the relative dimensions drawn in Fig. P3.30:

$$\frac{D_p}{D_s} = \frac{1}{2}\frac{L_p}{L_s} = \frac{1}{4}\frac{H_p}{H_s} = 2$$

3.31. Here we determine the optimal tapering of a slender tube with Hagen-Poiseuille flow and round cross section shown in Fig. P3.31. The tube length is L, and the axial coordinate is x. The tube diameter varies along the tube, $D(x)$. The tube volume is fixed. The stream with mass flow rate $\dot{m}_L$ enters the tube through its $x = L$ end. The mass flow rate $\dot{m}(x)$ varies along the tube because fluid leaks laterally (perpendicularly to x) at a uniform rate $d\dot{m}/dx$ that is proportional to x^p, where p is a known constant. The $x = 0$ end of the tube is closed. The pressure difference maintained between $x = L$ and $x = 0$ is ΔP. Determine the tube shape $D(x)$ for which the overall flow resistance $\Delta P/\dot{m}_L$ is minimal. *Hint*: Assume power law solutions, $\dot{m} = ax^{1+p}$ and $D = bx^n$, and determine the constants a, b, and n.

Figure P3.31

4
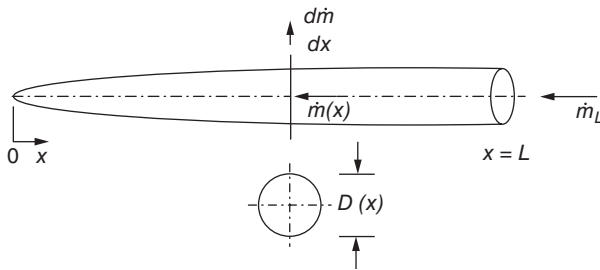
EXTERNAL NATURAL CONVECTION

The basic feature that unites the external flow problems of Chapter 2 with the internal flow problems of Chapter 3 is the presence of an additional entity (a mechanism) that in all cases is responsible for driving the flow. Fluid flow is not merely a body of fluid such as the stagnant water pool in a glass: It is the *relative motion* of one fluid layer past an adjacent fluid layer or solid surface. Since it is an intrinsic property of any flow (fluid, heat, mass) to destroy exergy [1,2], all flows require a driving mechanism in order to exist.

For example, in order to witness the boundary layer forming along a smooth wall in parallel uniform flow (Fig. 2.1), somebody must spend mechanical power to drag the solid wall through the fluid; in the case of motorized sea transport, that ''somebody'' is the ship's power plant. Similarly, in the duct flows of Chapter 3, the fluid must be pumped (forced to flow) through the duct: The operation of a pump always requires the expense of mechanical power.

For the thermodynamic reason outlined above, the convective heat transfer problems of Chapters 2 and 3 can be regarded as examples of *forced* convection. The creation and maintenance of the flow require a consistent sacrifice of mechanical power (exergy).

Mathematically, the fluid flow problem in forced convection is decoupled from the heat transfer problem. Historically, this has been the case, as the Blasius flow solution preceded the Pohlhausen heat transfer solution and as the Hagen–Poiseuille flow emerged almost 100 years before the fully developed heat transfer results summarized in Table 3.2. The flow field must be known, or at least assumed, before proceeding with an analysis of heat transfer in forced convection.

In this chapter we focus on a class of convective heat transfer problems that differ fundamentally from the forced convection class. The difference is that the flows of this chapter are not forced by a visible mechanism. They happen naturally, freely, as if pushed by buoyancy forces due to the presence of

gravitational acceleration and density variations from one fluid layer to another. Mathematically, the flow field is intimately coupled to the temperature field, as temperature variations within the fluid can induce density variations.

We will see that, although invisible, the driving mechanism for natural convection is present, and it is a work-producing engine like all the engines that drive the fans and pumps of forced convection. It is customary to refer to natural (or free) convection as ''buoyancy-driven'' flows. This is not correct, because buoyancy is a force, and a force does not drive. A force pushes or pulls. No work is produced unless there is displacement, that is, unless the force moves while being opposed. Displacement means movement (flow), and it can only be driven by the mechanisms that produce the work that is destroyed by the movement. The mechanisms are heat engines, and they drive everything that moves in nature. Natural convection flows are driven by natural engines.

4.1   NATURAL CONVECTION AS A HEAT ENGINE IN MOTION

A simple configuration with natural convection is in Fig. 4.1. Think of a body of temperature T_0 and height H immersed in a fluid of temperature T_∞. For a more meaningful discussion, think of a heat-generating body immersed in a cold
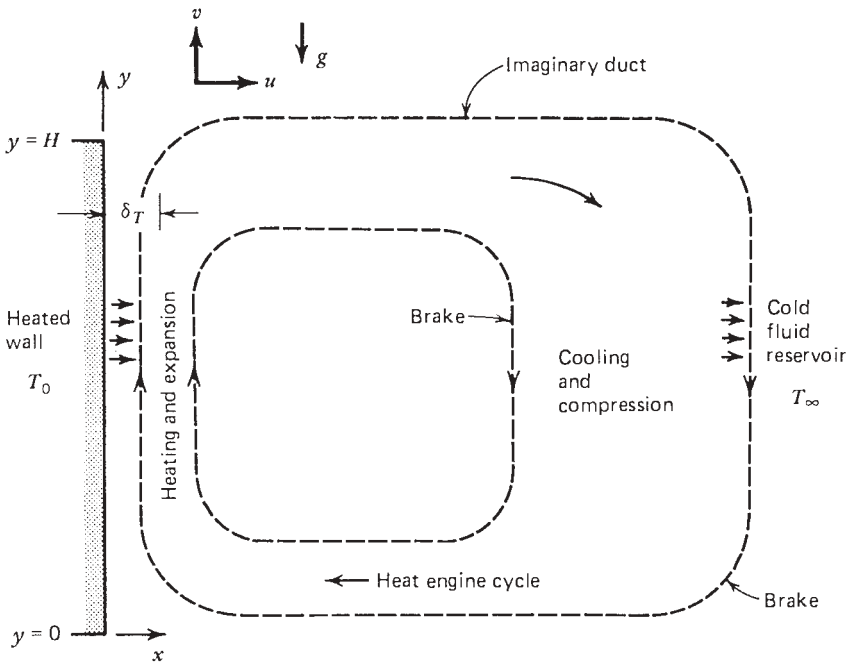

Figure 4.1   Heat engine responsible for driving natural convection.

fluid reservoir, such as an old-fashioned stove in the middle of a room. Since air at constant pressure expands upon being heated, the air layer adjacent to the wall expands (becomes lighter, less dense) and rises. At the same time, the cold reservoir fluid is displaced *en masse* downward. Thus, the wall–reservoir temperature difference induces the all-familiar ''natural circulation'' sketched in Fig. 4.1. In view of the thermodynamics discussed in the preceding segment, we ask the question: What power plant is responsible for the steady cyclic flow encountered in natural convection?

To answer this question, we follow the evolution of a fluid packet through the imaginary closed duct that guides the flow loop. Starting from the bottom of the heated wall, the packet is heated by the wall and expands as it rises to lower pressures in the hydrostatic pressure field maintained by the reservoir. Later, along the downflowing branch of the cycle, the fluid packet is cooled by the reservoir and compressed as it reaches the depths of the reservoir. From the circuit executed by every fluid packet, we learn that the loop-shaped flow is the succession of four processes,

$$\text{heating} \rightarrow \text{expansion} \rightarrow \text{cooling} \rightarrow \text{compression}$$

In conclusion, the fluid packet traveling along the flow loop of Fig. 4.1 is equivalent to the cycle executed by the working fluid in a heat engine modeled as a closed system. This heat engine cycle should be capable of delivering work if we insert a suitably designed propeller in the stream; this is the origin of the ''wind power'' discussed in connection with the harnessing of solar work indirectly from the atmospheric heat engine loop. In the absence of work-collecting devices (e.g., windmill wheels), the heat engine cycle drives its working fluid fast enough so that its entire work output is destroyed because of irreversibilities due to friction between adjacent fluid layers and heat transfer along finite temperature gradients. The entire circulation pattern (Fig. 4.1) is an infinity of nested heat engine loops with friction between them.

The thermodynamics of natural convection is new for a heat transfer course such as this. Yet, it illustrates with amazing simplicity and nakedness the principle that governs all movement in nature, animate and inanimate [3–5], and for this reason it has generated already a body of new research on the thermodynamics of natural convection [2, 6–9].

The legacy of inanimate flow systems on earth is the same as that of animate flow systems. They all move mass by destroying exergy that originates from the sun. Rivers and animals use and destroy exergy in proportion with the moved weight (Mg) times the horizontal displacement (L). The same holds for our vehicles, on land, in air, and in water. The spent fuel is proportional to the weight of the vehicle times the distance traveled.

River and animal designs have been morphed and perfected over millions of years. Engineered design is evolving right now, on design tables and in factories. The vehicle motor burns fuel in proportion to the high-temperature heating rate Q_H. This stream of heat is converted partially into mechanical power delivered to the wheels (W), while the remainder (Q_L, or $Q_H - W$) is dissipated into the
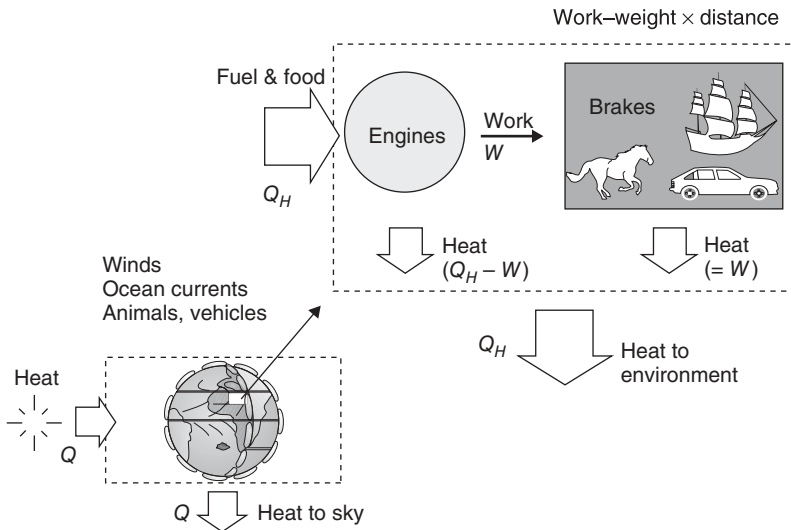
Figure 4.2   The whole Earth is an engine + brake system, containing innumerably smaller "engine + brake" systems (winds, ocean currents, animals, and human and machine species).

environment. Not mentioned in thermodynamics until recently [2−5] is the fact that W is itself dissipated into the ambient, because of the movement of vehicle weight (Mg) over the horizontal distance L (Fig. 4.2).

To summarize, all the high-temperature heating that comes from burning fuel (Q_H) is ultimately transmitted to lower temperature into the environment. This is evident in Fig. 4.2 and any other ''heat transfer'' configuration. The need for higher efficiencies in power generation (greater W/Q_H) is the same as the need to have more W, that is, the need to move more weight over larger distances on the surface of the earth, which is the natural phenomenon (tendency) summarized in the constructal law.

At the end of the day, when all the fuel has been burned, and all the food has been eaten, this is what animate flow systems have achieved. They have moved mass on the surface of the earth (they have ''mixed'' the earth's crust) more than in the absence of animate flow systems.

The moving animal or vehicle is the equivalent to an engine connected to a brake (Fig. 4.2), first proposed in 1976 [10] and later [2,11]. The power generated by muscles and motors is ultimately and necessarily dissipated by rubbing against the environment. There is no taker for the W produced by the animal and vehicle. This is why in Fig. 4.3 the GDP of a country is roughly proportional to the amount of fuel burned in that country [5].

Figure 4.2 holds also for the whole earth, as a closed thermodynamic system (note: closed does not mean isolated). Earth, with its solar heat input, heat rejection, and wheels of atmospheric and oceanic circulation, is a heat engine without shaft. Its mechanical power output cannot be delivered to an
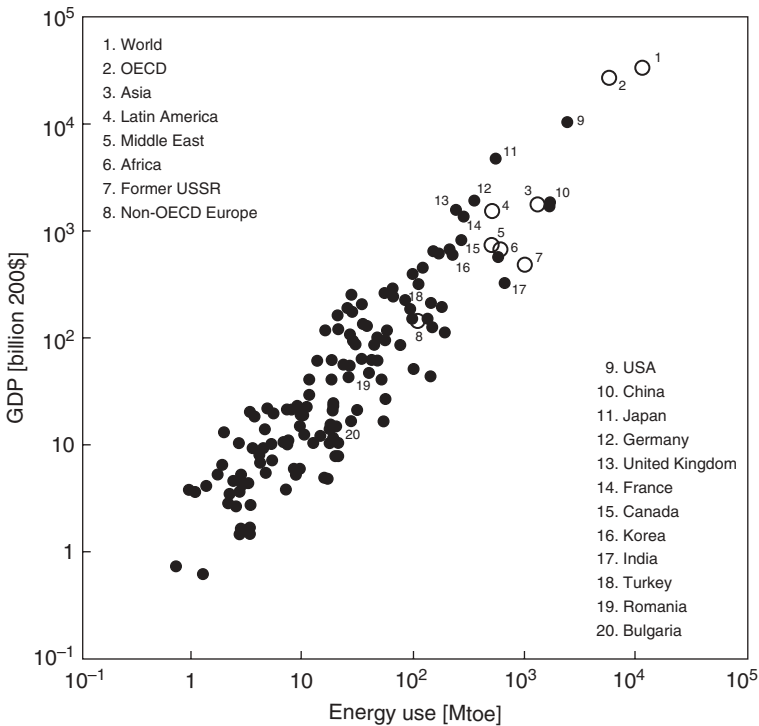
Figure 4.3   Economic activity means fuel that is being burned. The annual gross domestic product of regions and countries all over the globe versus their annual consumption of fuel.

extraterrestrial system. Instead, the earth engine must dissipate through air, water, and solid (rocks) friction and other irreversibilities (e.g., heat leaks, mass diffusion) all the mechanical power that it produces. It does so by ''spinning in its brake'' as fast as is necessary (and from this follow the winds and the ocean currents, which proceed along easier and easier routes, and flow at finite, characteristic speeds, never getting out of hand). This is the constructal-law basis of all natural convection phenomena.

In the human and nonhuman biosphere (power plants, animals, vegetation, water flow) the engines have shafts, rods, legs, and wings that deliver the mechanical power to external entities that use the power (e.g., vehicles and animal bodies needing propulsion). Because the engines of engineering and biology are constructal, they morph in time toward easier flowing configurations. They evolve toward producing more mechanical power (under finiteness constraints), which, for them, means a time evolution toward *less* dissipation or greater efficiency.

Outside the engineering or biology engine, all the mechanical power is destroyed through friction and other irreversibility mechanisms (e.g., transportation and manufacturing for humans, animal locomotion, and body heat loss to

ambient). The engine and its immediate environment (the ''brake''), as one thermodynamic system, are analogous to the entire earth. The flowing earth (with all its engine + brake components, rivers, fish, turbulent eddies, etc.) accomplishes as much as any other flow architecture, animate or inanimate: It mixes the earth's crust most effectively—more effectively than in the absence of constructal phenomena of generation of flow configuration.

The movement of animals—the flow of animal mass on earth—is analogous to other moving and mixing designs such as the turbulent eddies in rivers, oceans, and the atmosphere. It is not an exaggeration to regard animals as self-driven packs of water, that is, motorized vehicles of water mass, which spread and mix the earth like the eddies in the ocean and the atmosphere.

Irrefutable evidence in support of this unifying view is how all these moving packs of biological matter have morphed and spread over larger areas, depths and altitudes, in this remarkable sequence *in time*: fish in water, walking fish and other animals on land, flying animals in the atmosphere, human and machine species in the air, and human and machine species in the outer space. Not in the opposite time direction. The balanced and intertwined flows that generate our engineering, economics, and social organization are no different than the natural flow architectures of biology (animal design) and geophysics (river basins, global circulation) [12].

Returning to Fig. 4.1, we see the fundamental difference between forced convection and natural convection. In forced convection, the engine that drives the flow is external, whereas in natural convection the engine is built into the flow itself.

Natural convection will be analyzed by focusing on two extremes. In this chapter we discuss mainly the interaction between a vertical heated object and a much larger fluid reservoir, so large that the downward motion sketched in Fig. 4.1 is negligible. In Chapter 5 we study the circulation present in finite-size fluid layers heated from the side (Fig. 5.1); in that case, the downward portion of the natural convection loop of Fig. 4.1 is as strong as the upward portion because both portions are driven by two vertical walls maintained at different temperatures.

4.2 LAMINAR BOUNDARY LAYER EQUATIONS

The heat transfer problem in Fig. 4.1 is to predict the heat transfer rate Q when the wall–reservoir temperature difference is known,

$$Q = (HW)h_{0-H}(T_0 - T_\infty) \qquad (4.1)$$

In other words, the objective is to calculate the wall-averaged heat transfer coefficient h_{0-H}. Note that HW is the wall area and W the wall dimension in the direction perpendicular to the x–y plane. In this section we focus on the boundary layer regime, where the scale of h_{0-H} is k/δ_T and the thermal boundary layer thickness δ_T is negligibly small in comparison with H.

Proceeding as in Chapter 2, the complete Navier–Stokes equations for the steady constant-property two-dimensional flow of Fig. 4.1 are

$$\frac{\partial u}{\partial x} + \frac{\partial v}{\partial y} = 0 \tag{4.2}$$

$$\rho \left(u \frac{\partial u}{\partial x} + v \frac{\partial u}{\partial y} \right) = -\frac{\partial P}{\partial x} + \mu \, \nabla^2 u \tag{4.3}$$

$$\rho \left(u \frac{\partial v}{\partial x} + v \frac{\partial v}{\partial y} \right) = -\frac{\partial P}{\partial y} + \mu \, \nabla^2 v - \rho g \tag{4.4}$$

$$u \frac{\partial T}{\partial x} + v \frac{\partial T}{\partial y} = \alpha \, \nabla^2 T \tag{4.5}$$

Compare these with the equations of Chapter 2, and note the presence of the body force term $-\rho g$ in the vertical momentum equation (4.4). Equations (4.2)–(4.5) reduce to simpler forms if the focus is on the boundary layer region ($x \sim \delta_T$, $y \sim H$, and $\delta_T \ll H$). Thus, only the $\partial^2/\partial x^2$ term survives in the ∇^2 operator and, as demonstrated in Chapter 2, the transversal momentum equation (4.3) reduces to the statement that in the boundary layer, the pressure is a function of longitudinal position only,

$$\frac{\partial P}{\partial y} = \frac{dP}{dy} = \frac{dP_\infty}{dy} \tag{4.6}$$

The boundary layer equations for momentum and energy are then

$$\rho \left(u \frac{\partial v}{\partial x} + v \frac{\partial v}{\partial y} \right) = -\frac{dP_\infty}{dy} + \mu \frac{\partial^2 v}{\partial x^2} - \rho g \tag{4.7}$$

$$u \frac{\partial T}{\partial x} + v \frac{\partial T}{\partial y} = \alpha \frac{\partial^2 T}{\partial x^2} \tag{4.8}$$

Noting further that dP_∞/dy is the hydrostatic pressure gradient dictated by the reservoir fluid of density ρ_∞, $dP_\infty/dy = -\rho_\infty g$, the equation (4.7) becomes

$$\rho \left(u \frac{\partial v}{\partial x} + v \frac{\partial v}{\partial y} \right) = \mu \frac{\partial^2 v}{\partial x^2} + (\rho_\infty - \rho)g \tag{4.9}$$

Equations (4.2), (4.8), and (4.9) must be solved in order to determine u, v, and T in the boundary layer. Through the body force term $(\rho_\infty - \rho)g$ in the momentum equation (4.9), the flow is driven by the density field $\rho(x, y)$ generated by the temperature field $T(x, y)$. Equations (4.8) and (4.9) are coupled via the *equation of state* of the fluid; for example, if the fluid behaves according to the ideal gas model [2],

$$P = \rho R T \tag{4.10}$$

At a level y, we have

$$\rho = \frac{P_\infty/R}{T} \qquad \text{and} \qquad \rho_\infty = \frac{P_\infty/R}{T_\infty} \tag{4.11}$$

and

$$\rho - \rho_\infty = \rho\left(1 - \frac{T}{T_\infty}\right) \tag{4.12}$$

Expression (4.12) can be rearranged as

$$\frac{\rho_\infty - \rho}{\rho_\infty}\left(1 - \frac{\rho_\infty - \rho}{\rho_\infty}\right)^{-1} = \frac{T - T_\infty}{T_\infty} \tag{4.13}$$

which in the limit $(T - T_\infty) \ll T_\infty$ yields

$$\rho \simeq \rho_\infty\left[1 - \frac{1}{T_\infty}(T - T_\infty) + \cdots\right] \tag{4.14}$$

This result states that the density decreases slightly below ρ_∞ as the local *absolute* temperature increases slightly above the reservoir absolute temperature T_∞. In general, for fluids that are not necessarily ideal gases, expression (4.14) is written as

$$\rho \simeq \rho_\infty[1 - \beta(T - T_\infty) + \cdots] \tag{4.15}$$

where β is the volume expansion coefficient at constant pressure [2],

$$\beta = -\frac{1}{\rho}\left(\frac{\partial\rho}{\partial T}\right)_P \tag{4.16}$$

Implicit in the expansion (4.15) is the assumption that the dimensionless product $\beta(T - T_\infty)$ is considerably smaller than unity.

The *Boussinesq approximation* of the boundary layer equations amounts to substituting eq. (4.15) into eqs. (4.8) and (4.9) and, in each case, retaining the dominant term. For example, in the momentum equation (4.9), ρ appears in the inertia terms as well as in the body force term; using approximation (4.15), the inertia terms will be multiplied by the dominant term $\rho_\infty = $ constant, whereas the leading body force term becomes $\rho_\infty\beta g(T - T_\infty)$. Therefore, the momentum equation (4.9) becomes

$$u\frac{\partial v}{\partial x} + v\frac{\partial v}{\partial y} = \nu\frac{\partial^2 v}{\partial x^2} + g\beta(T - T_\infty) \tag{4.17}$$

where g, β, T_∞, and $\nu = \mu/\rho_\infty$ are constants. Similarly, the thermal diffusivity appearing in the energy equation (4.8), $\alpha = k/\rho_\infty c_P$ is assumed constant.

The Boussinesq-approximated momentum equation (4.17) effects the coupling between the temperature field and the flow field. If the fluid is isothermal $(T = T_\infty)$, the driving force is zero everywhere and eqs. (4.17) and (4.2) yield the ''no-flow'' solution $u = v = 0$. When the fluid is heated by the

wall, the body force term is finite $[\sim g\beta(T_0 - T_\infty)]$ and so are the velocity components u and v. In what follows we focus in more detail on the solution to the Boussinesq boundary layer equations (4.2), (4.8), and (4.17) subject to the following conditions:

Impermeable, no slip, isothermal wall:

$$u = v = 0 \quad \text{and} \quad T = T_0 \quad \text{at } x = 0 \tag{4.18a}$$

Stagnant, isothermal infinite reservoir:

$$v = 0 \quad \text{and} \quad T = T_\infty \quad \text{as } x \to \infty \tag{4.18b}$$

4.3 SCALE ANALYSIS

Consider the conservation of mass, momentum, and energy in the *thermal* boundary layer region $(x \sim \delta_T, y \sim H)$, where the heating effect of the wall is felt. In the steady state, the heat conducted from the wall into the fluid is swept and carried upwards as an enthalpy stream. The equation (4.8) expresses a balance between longitudinal convection and transverse conduction,

$$\underbrace{u \frac{\Delta T}{\delta_T}, \quad v \frac{\Delta T}{H}}_{\text{Convection}} \sim \underbrace{\alpha \frac{\Delta T}{\delta_T^2}}_{\text{Conduction}} \tag{4.19}$$

where $\Delta T = T_0 - T_\infty$ is the scale of the variable $T - T_\infty$. From mass conservation in the same layer, that is,

$$\frac{u}{\delta_T} \sim \frac{v}{H} \tag{4.20}$$

we learn that the two convection terms in eq. (4.19) are of order $(v\,\Delta T)/H$. Thus, the energy balance involves two scales,

$$v \frac{\Delta T}{H} \sim \alpha \frac{\Delta T}{\delta_T^2} \tag{4.21}$$

and it yields

$$v \sim \frac{\alpha H}{\delta_T^2} \tag{4.22}$$

where the thermal thickness δ_T is still unknown.

Turning our attention to the momentum equation (4.17) and still focusing on the $\delta_T \times H$ region, we recognize the interplay among three forces:

$$\underbrace{u \frac{v}{\delta_T}, \quad v \frac{v}{H}}_{\text{Inertia}} \quad \underbrace{v \frac{v}{\delta_T^2}}_{\text{Friction}} \quad \underbrace{g\beta\,\Delta T}_{\text{Buoyancy}} \tag{4.23}$$

The mass conservation scaling (4.20) indicates that the two inertia terms are of order v^2/H. It remains to establish under what conditions the δ_T layer is ruled by the inertia $\sim$ buoyancy balance, as opposed to the friction $\sim$ buoyancy balance. The buoyancy force is not negligible because, without it, there would be no flow. Dividing expression (4.23) through the buoyancy scale $g\beta \, \Delta T$ and using eq. (4.22) to eliminate the vertical velocity scale v, we obtain

$$\underbrace{\left(\frac{H}{\delta_T}\right)^4 \text{Ra}_H^{-1} \text{Pr}^{-1}}_{\text{Inertia}} \qquad \underbrace{\left(\frac{H}{\delta_T}\right)^4 \text{Ra}_H^{-1}}_{\text{Friction}} \qquad \underbrace{1}_{\text{Buoyancy}} \tag{4.24}$$

where the *Rayleigh number* is defined as

$$\text{Ra}_H = \frac{g\beta \, \Delta T \, H^3}{\alpha v} \tag{4.25}$$

Expression (4.24) shows that the competition between inertia and friction is decided by a *fluid property*, the Prandtl number: High-Pr fluids will form a δ_T layer ruled by the friction–buoyancy balance, while low-Pr fluids will form a δ_T layer with buoyancy balanced by inertia. Below, we examine these two possibilities in detail.

4.3.1 High-Pr Fluids

When $\text{Pr} \gg 1$, the friction–buoyancy balance of eq. (4.24) yields

$$\delta_T \sim H \, \text{Ra}_H^{-1/4} \tag{4.26}$$

and using eq. (4.22),

$$v \sim \frac{\alpha}{H} \text{Ra}_H^{1/2} \tag{4.27}$$

Since the heat transfer coefficient scales as k/δ_T, the Nusselt number scale is

$$\text{Nu} = \frac{hH}{k} \sim \text{Ra}_H^{1/4} \tag{4.28}$$

It will be shown later that the $\text{Nu} \sim \text{Ra}_H^{1/4}$ proportionality for $\text{Pr} \gg 1$ fluids is confirmed by more precise analyses and numerous laboratory measurements; therefore, the δ_T and v scales derived above are the correct scales for the thermal boundary layer region.

Figure 4.4*a* shows qualitatively the conclusions reached so far: the δ_T-thick layer effects the transition from T_0 to T_∞ and at the same time drives fluid upward with a velocity given by eq. (4.27). The fluid motion is not restricted to a layer of thickness δ_T. It is possible for the heated δ_T layer to entrain viscously a layer of outer (unheated) fluid. Let δ be the thickness of this outer layer and let us also assume that $\delta \gg \delta_T$. Consider now the conservation of momentum in the boundary layer of thickness δ [eq. (4.17)]. Since the outer fluid is isothermal,
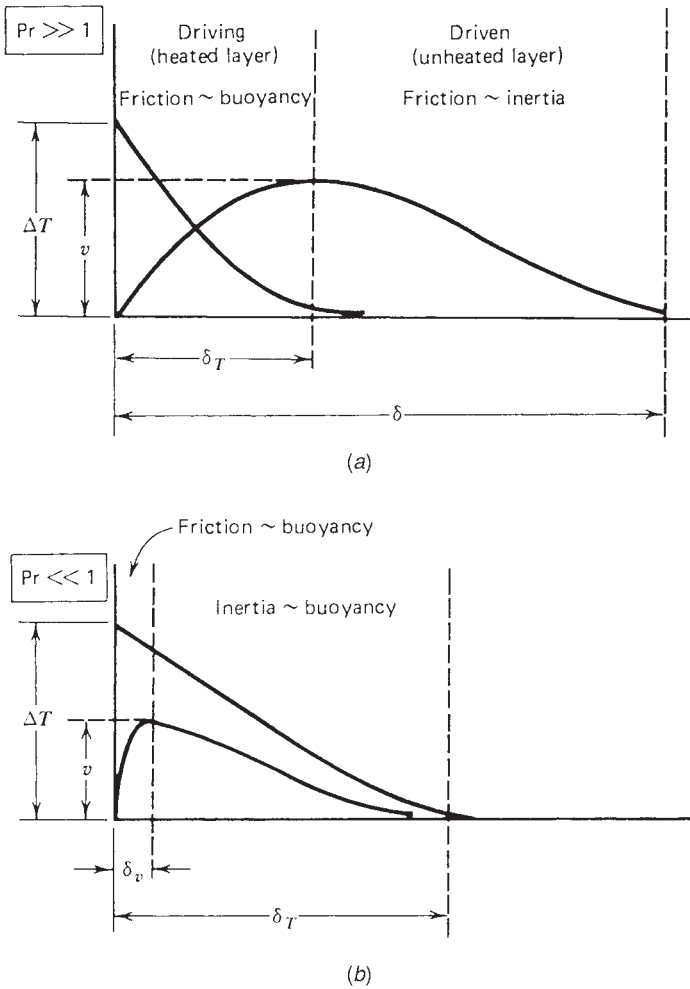
Figure 4.4 Two length scales of the boundary layer flow along a heated vertical wall.

the buoyancy effect is absent. The δ layer is driven viscously by the much thinner δ_T layer, and it is restrained by its own inertia. Thus, eq. (4.17) dictates an inertia $\sim$ friction balance in a layer of thickness δ,

$$v \frac{v}{H} \sim \nu \frac{v}{\delta^2} \tag{4.29}$$

where the vertical velocity scale v is imposed by the driving instrument (the δ_T layer); eliminating v between eqs. (4.29) and (4.27) yields

$$\delta \sim H \, \mathrm{Ra}_H^{-1/4} \, \mathrm{Pr}^{1/2} \tag{4.30}$$

In other words,

$$\frac{\delta}{\delta_T} \sim \mathrm{Pr}^{1/2} > 1 \tag{4.31}$$

In conclusion, the higher the Prandtl number, the thicker the layer of unheated fluid driven upward by the heated layer. Influenced by the language of forced convection (Chapter 2), we call δ the *velocity boundary layer thickness*. This terminology is conceptually inappropriate because it obscures the fundamental difference between forced convection boundary layers and natural convection boundary layers. This fundamental difference is illustrated in Fig. 4.4, where the *velocity profile* is described by *two length scales* (δ_T and δ), not by a single length scale (δ) as in forced convection. The velocity scale [eq. (4.27)] is reached within a thin layer δ_T, while the velocity decays to zero within a thick layer δ.

4.3.2   Low-Pr Fluids

Looking back at eq. (4.24), when $\mathrm{Pr} \ll 1$, we see a balance between inertia and buoyancy in a layer of thickness δ_T. Combining this balance with the v scale of eq. (4.22) yields, in order,

$$\delta_T \sim H(\mathrm{Ra}_H\ \mathrm{Pr})^{-1/4} \tag{4.32}$$

$$v \sim \frac{\alpha}{H}(\mathrm{Ra}_H\ \mathrm{Pr})^{1/2} \tag{4.33}$$

$$\mathrm{Nu} = \frac{hH}{k} \sim (\mathrm{Ra}_H\ \mathrm{Pr})^{1/4} \tag{4.34}$$

Correct scale analysis reveals the correct (new) dimensionless group, $\mathrm{Ra}_H\ \mathrm{Pr}$, which plays the same role for low-Pr fluids as Ra_H plays for high-Pr fluids. The name *Boussinesq number* is used for this group:

$$\mathrm{Bo}_H = \mathrm{Ra}_H\ \mathrm{Pr} = \frac{g\beta\ \Delta T\ H^3}{\alpha^2} \tag{4.35}$$

Figure 4.4*b* shows the meaning of scales (4.32) and (4.33): The δ_T layer is driven upward by buoyancy and restrained by inertia. This means that outside the δ_T layer, where the fluid is isothermal and the buoyancy effect is absent, the fluid is motionless. The velocity profile must then be as wide as the temperature profile. However, since the no-slip condition still applies at the wall, the location of the velocity peak is an important second-length scale in the description of the velocity profile. Let δ_v be the thickness of a very thin layer right near the wall, a layer in which the buoyancy-driven fluid is restrained viscously by the wall. The buoyancy $\sim$ friction balance in the layer of thickness δ_v yields

$$\nu\frac{v}{\delta_v^2} \sim g\beta\ \Delta T \tag{4.36}$$

where the v scale is dictated by the δ_T layer scale [eq. (4.33)]. Combining, we find that

$$\delta_v \sim H \, \mathrm{Gr}_H^{-1/4} \qquad (4.37)$$

where the *Grashof number* is defined as

$$\mathrm{Gr}_H = \frac{g\beta \, \Delta T \, H^3}{v^2} = \frac{\mathrm{Ra}_H}{\mathrm{Pr}} \qquad (4.38)$$

Dividing eqs. (4.37) and (4.32) side by side yields

$$\frac{\delta_v}{\delta_T} \sim \mathrm{Pr}^{1/2} < 1 \qquad (4.39)$$

This relationship is shown qualitatively in Fig. 4.4; however, it should not be confused with eq. (4.31), as δ_v should not be confused with δ.

As we saw in Chapter 2, the boundary layer thickness is the transversal distance to which the effect of thermal diffusion spreads during the time needed by the flow to sweep the wall. In the present case, the transversal diffusion time is $t_{\delta_T} \sim \delta_T^2/\alpha$ and the longitudinal convection time is $t_H \sim H/v$. If we substitute the δ_T and v scales for $\mathrm{Pr} > 1$ fluids, eqs. (4.26) and (4.27), we find that these two time scales are the same time scale, $t_{\delta_T} \sim t_H$. The same conclusion holds if we use the δ_T and v scales for $\mathrm{Pr} < 1$ fluids, eqs. (4.32) and (4.33).

4.3.3 Observations

Table 4.1 provides a bird's-eye view of the conclusions reached based on scale analysis. The first three columns contain the length scales governing the thermal layer and the buoyancy-driven wall jet. It is apparent that the length scale $H \, \mathrm{Ra}_H^{-1/4}$ plays the role of primary length unit and that the remaining length scales follow from $H \, \mathrm{Ra}_H^{-1/4}$ through an appropriate stretching/compression factor depending solely on Pr. The relative order of magnitude of all length scales is shown in Fig. 4.5 using $H \, \mathrm{Ra}_H^{-1/4}$ as the length unit on the ordinate; it is clear that the boundary layer geometry of $\mathrm{Pr} < 1$ fluids differs from the geometry of $\mathrm{Pr} > 1$ fluids.

Table 4.1 Summary of flow and heat transfer scales in a natural convection boundary layer along a vertical wall

Prandtl Number Range	Thermal Boundary Layer Thickness	Wall Jet Velocity Profile			Nusselt Number $\mathrm{Nu} = \dfrac{hH}{k}$
		Distance from Wall to Velocity Peak	Thickness of Wall Jet	Velocity Scale	
$\mathrm{Pr} > 1$	$H \, \mathrm{Ra}_H^{-1/4}$	$H \, \mathrm{Ra}_H^{-1/4}$	$\mathrm{Pr}^{1/2}(H \, \mathrm{Ra}_H^{-1/4})$	$\dfrac{\alpha}{H}\mathrm{Ra}_H^{1/2}$	$\mathrm{Ra}_H^{1/4}$
$\mathrm{Pr} < 1$	$\mathrm{Pr}^{-1/4}(H \, \mathrm{Ra}_H^{-1/4})$	$\mathrm{Pr}^{1/4}(H \, \mathrm{Ra}_H^{-1/4})$	$\mathrm{Pr}^{-1/4}(H \, \mathrm{Ra}_H^{-1/4})$	$\dfrac{\alpha}{H}(\mathrm{Pr} \, \mathrm{Ra}_H)^{1/2}$	$(\mathrm{Pr} \, \mathrm{Ra}_H)^{1/4}$
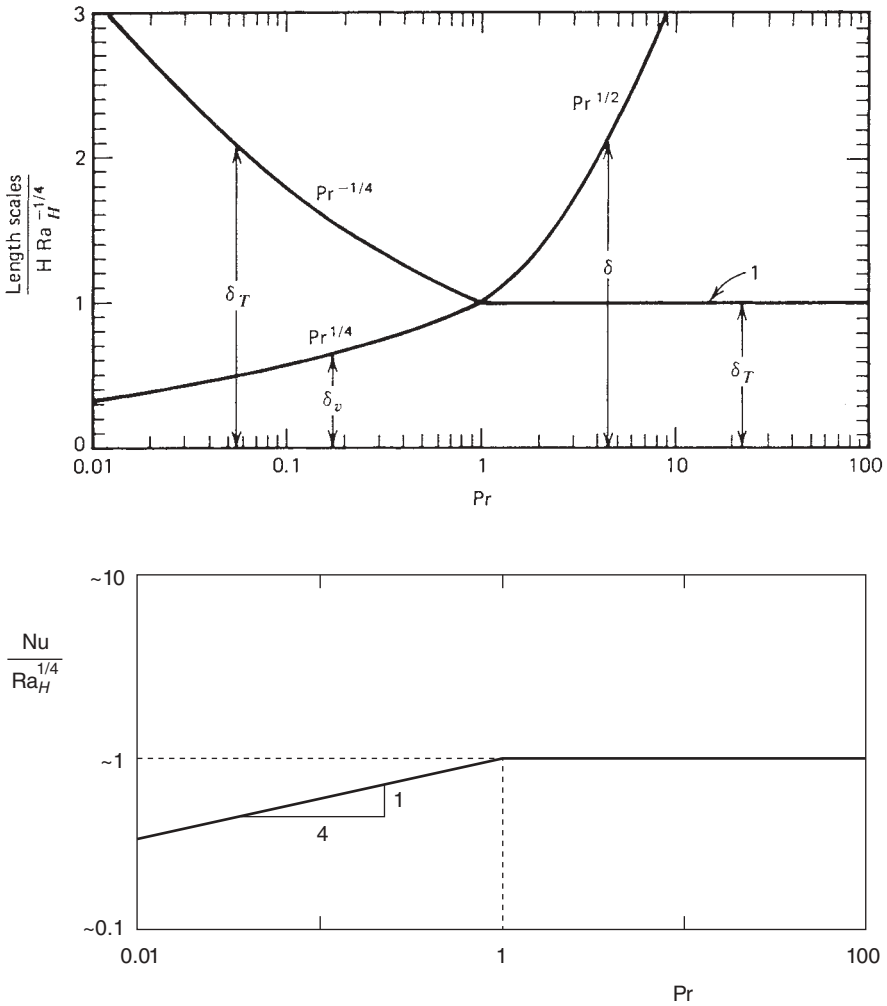
Figure 4.5 Length scales (thicknesses) and the Nu scaling of natural convection boundary layers.

I developed the double-layer structure and scale analysis based on Fig. 4.4 while writing the first (1984) edition of this book. Subsequently, I found that Kuiken [13,14] had recognized the same double-layer structure earlier. Although the scales of Table 4.1 are the result of remarkably simple and brief analysis, they are still unknown or misused in contemporary natural convection research. Most common is the erroneous view that for Pr > 1 fluids, the wall jet thickness varies as $Gr_H^{-1/4}$. This is responsible for the widespread and incorrect use of the Grashof number in the nondimensional presentation of natural convection results in external (boundary layer) flow. The scales derived in this section demonstrate

that Gr_H appears as a relevant dimensionless group only in the δ_v scale for $Pr < 1$ fluids [eq. (4.37)]: As such, Gr_H would be relevant to estimating the shear force along a vertical wall immersed in a liquid metal—not a pressing engineering problem! From a *heat transfer* standpoint, the important groups in external natural convection are the Rayleigh number for $Pr > 1$ fluids and the Boussinesq number for $Pr < 1$ fluids.

An important observation concerns the very *meaning* of dimensionless numbers such as Ra_H, Bo_H, and Gr_H. We often hear that the Grashof number can be interpreted as the parameter describing the ratio of buoyancy to viscous forces in the natural convection boundary layer. To see the error in this interpretation, consider the natural convection of air along the cold vertical wall in a room, where $Gr_H \sim 10^8 - 10^{10}$: According to the traditional interpretation, the viscous forces must be negligible in comparison with the body force because the Grashof number is enormous vis-à-vis unity. This is certainly not true, because for air ($Pr \sim 1$) there always exists a balance between friction and buoyancy (or between inertia and buoyancy): Without a *balance* of forces, the wall jet cannot exist in the *steady state*. As shown in Problem 4.18, the notion that the inertia/friction ratio scales as Gr_H comes from incorrect scale analysis performed in a flow region distinct from the boundary layer region.

By themselves, dimensionless numbers such as Ra_H, Bo_H, and Gr_H have no meaning. What has meaning is the one-fourth power of these numbers:

$$Ra_H^{1/4} \sim \frac{\text{wall height}}{\text{thermal boundary layer thickness}} \qquad (Pr > 1)$$

$$Bo_H^{1/4} \sim \frac{\text{wall height}}{\text{thermal boundary layer thickness}} \qquad (Pr < 1)$$

$$Gr_H^{1/4} \sim \frac{\text{wall height}}{\text{wall shear layer thickness}} \qquad (Pr < 1)$$

The meaning of $Ra_H^{1/4}$, $Bo_H^{1/4}$, and $Gr_H^{1/4}$ is purely *geometric*; these numerical values account for the *slenderness* of the boundary layer region occupied by the buoyancy-induced flow. When in an actual problem the calculated value of Ra_H or Gr_H is enormous compared with unity, Nature is telling us that the real-life slenderness ratio $Ra_H^{1/4}$ (already a number much greater than 1, because boundary layers are present) was unnecessarily raised to the fourth power!

4.4   INTEGRAL SOLUTION

As a step beyond scale analysis, an integral solution to the governing equations may be used to determine the actual y variation of features such as local heat flux (q''), thermal boundary layer thickness (δ_T), and wall jet velocity profiles. So far, we know only the order of magnitude of the relevant flow and heat transfer parameters (Table 4.1). Integrating the momentum equation (4.17) and

the energy equation (4.8) from the wall ($x = 0$) to a far enough plane $x = X$ in the motionless isothermal cold reservoir, we obtain the integral boundary layer equations for momentum and energy,

$$\frac{d}{dy} \int_0^X v^2 \, dx = -\nu \left(\frac{\partial v}{\partial x} \right)_{x=0} + g\beta \int_0^X (T - T_\infty) \, dx \qquad (4.40)$$

$$\frac{d}{dy} \int_0^X v(T_\infty - T) \, dx = \alpha \left(\frac{\partial T}{\partial x} \right)_{x=0} \qquad (4.41)$$

The length scales of Table 4.1 and Fig. 4.3 are very useful in selecting the proper shapes of v and T profiles to be substituted into the integral equations (4.40) and (4.41). We must carry out the integral analysis in two parts, for Pr > 1 and Pr < 1, as the boundary layer constitution changes dramatically across Pr $\sim$ 1. The other lesson learned from Fig. 4.5 is that the velocity profile shape is governed by two length scales, one for the wall shear layer and another for the overall thickness of the moving layer of fluid.

4.4.1   High-Pr Fluids

A suitable set of profiles for Pr > 1 fluids compatible with Fig. 4.4a is

$$T - T_\infty = \Delta T e^{-x/\delta_T} \qquad (4.42)$$

$$v = V e^{-x/\delta} (1 - e^{-x/\delta_T}) \qquad (4.43)$$

where V, δ_T, and δ are unknown functions of altitude (y), and $\Delta T = T_0 - T_\infty = $ constant. Substituting profiles (4.42) and (4.43) into the momentum and energy integrals and setting $X \rightarrow \infty$ yield

$$\frac{d}{dy} \left[\frac{V^2 \delta q^2}{2(2+q)(1+q)} \right] = -\frac{\nu V q}{\delta} + g\beta \, \Delta T \frac{\delta}{q} \qquad (4.44)$$

$$\frac{d}{dy} \left[\frac{V\delta}{(1+q)(1+2q)} \right] = \frac{\alpha}{\delta} \qquad (4.45)$$

where q is the Pr function (Fig. 4.3):

$$q(\text{Pr}) = \frac{\delta}{\delta_T} \qquad (4.46)$$

In eqs. (4.44) and (4.45), we have two equations for three unknowns: $V(y)$, $\delta(y)$, and $q(\text{Pr})$. The third equation, necessary for determining V, δ, and q uniquely, is a challenging proposition. Historically, older integral analyses such as Squire's [15] avoided this problem by assuming that $\delta_T = \delta$ from the outset (i.e., $q = 1$). However, since a great deal of the information relating to boundary layer geometry is buried in the δ/δ_T function (Table 4.1, Fig. 4.5), it is instructive

to meet the challenge of an integral analysis with $\delta \neq \delta_T$. It is up to the individual researcher to come up with a third equation that, next to eqs. (4.44) and (4.45), determines V, δ, and q uniquely. First, we must keep in mind that eqs. (4.44) and (4.45) are approximate substitutes for the real equations to be satisfied [eqs. (4.17) and (4.8)]. So we have the freedom to bring into the analysis any other condition (equation) that accounts approximately for conservation of momentum or conservation of energy. Since the energy equation is, in a scaling sense, less ambiguous than the momentum equation,[*] it makes sense to select as a third equation a force balance: One that is both clear and analytically brief is the statement that in the no-slip layer $0 < x < 0^+$, the inertia terms of eq. (4.17) are zero:

$$0 = \nu \frac{\partial^2 v}{\partial x^2} + g\beta(T_0 - T_\infty) \tag{4.47}$$

This is to say that right next to the wall, there is no ambiguity associated with whether inertia is negligible compared with both friction and buoyancy, regardless of the Prandtl number.

Equations (4.44), (4.45), and (4.47) are then solved for V, δ, and q by first noting that $\delta \sim y^{1/4}$ and $V \sim y^{1/2}$. The main results are the function $q(\text{Pr})$

$$\text{Pr} = \frac{5}{6}q^2 \frac{q + \frac{1}{2}}{q + 2} \tag{4.48}$$

and the local Nusselt number

$$\text{Nu} = \frac{q''}{T_0 - T_\infty} \frac{y}{k} = \left[\frac{3}{8} \frac{q^3}{(q + 1)\left(q + \frac{1}{2}\right)(q + 2)} \right]^{1/4} \text{Ra}_y^{1/4} \tag{4.49}$$

In the limit $\text{Pr} \to \infty$, this solution reduces to

$$\frac{\delta}{\delta_T} = \left(\frac{6}{5} \text{Pr} \right)^{1/2} \quad \text{and} \quad \text{Nu} = 0.783 \text{Ra}_y^{1/4} \tag{4.50}$$

thus confirming the scaling laws summarized in Table 4.1.

4.4.2 Low-Pr Fluids

According to Fig. 4.4b, for a $\text{Pr} < 1$ fluid, we combine the temperature profile (4.42) with a new velocity profile:

$$v = V_1 e^{-x/\delta_T}(1 - e^{-x/\delta_v}) \tag{4.51}$$

---

[*]Because in natural boundary layer flow, the energy equation spells conduction $\sim$ convection, whereas the momentum equation spells either friction $\sim$ buoyancy or inertia $\sim$ buoyancy.

where V_1, δ_T, and δ_v are unknown functions of y. Again using eqs. (4.40), (4.41), and (4.47), and noticing from Table 4.1 that $\delta_T \sim y^{1/4}$, $\delta_v \sim y^{1/4}$, and $V_1 \sim y^{1/2}$, the solution reduces to

$$\text{Pr} = \frac{5}{3}\left(\frac{q_1}{1+q_1}\right)^2, \qquad q_1 = \frac{\delta_v}{\delta_T} \tag{4.52}$$

$$\text{Nu} = \frac{q''}{T_0 - T_\infty}\frac{y}{k} = \left(\frac{3}{8}\right)^{1/4}\left(\frac{q_1}{2q_1+1}\right)^{1/2}\text{Ra}_y^{1/4} \tag{4.53}$$

In the limit $\text{Pr} \to 0$, these results become

$$\frac{\delta_v}{\delta_T} = \left(\frac{3}{5}\text{Pr}\right)^{1/2} \qquad \text{and} \qquad \text{Nu} = 0.689\,(\text{Pr Ra}_y)^{1/4} \tag{4.54}$$

Once again, this limiting behavior confirms within a numerical factor of order 1 the scaling laws discovered in the preceding section.

The integral heat transfer results are summarized in Fig. 4.6 next to the similarity solution outlined in Section 4.5. The Nu expressions (4.49) and (4.53) match at $\text{Pr} = 5/12$, where the assumed velocity profiles are identical ($q = 1$, $q_1 = 1$).

As shown in Table 2.1, the Nusselt number calculations depend to some extent on the choice of analytical expressions for velocity and temperature
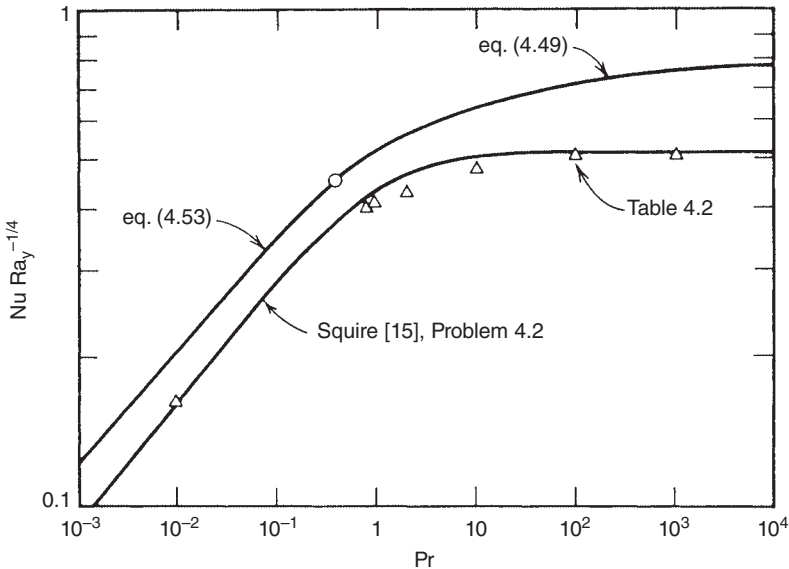

Figure 4.6 Local Nusselt number for laminar natural convection on a vertical wall: integral versus similarity results.

profile. This choice is always a trade-off between what constitutes a reasonable profile shape and the function that leads to the fewest analytical complications. In the preceding example, the choice of exponentials in the makeup of temperature and velocity profiles led to a relatively simple analysis. Figure 4.6 also shows the Nusselt number predicted by Squire's integral analysis [15], which assumes polynomial temperature and velocity profiles with $\delta_T = \delta$; this analysis is outlined in Problem 4.2. Although the $\delta_T = \delta$ assumption is justified only for fluids with $\text{Pr} \sim 1$, the Squire analysis predicts the correct Nusselt number in a wide Pr range.

4.5   SIMILARITY SOLUTION

Following the argument centered around Fig. 2.5, we can think of temperature and wall jet profiles whose shape remains unchanged as both profiles occupy wider areas as y increases. From Table 4.1 and the integral solution, we know that any length scale of the boundary layer region is proportional to $y^{1/4}$. The dimensionless similarity variable $\eta(x, y)$ can then be constructed as x divided by any of the length scales summarized in Table 4.1; selecting the $\text{Pr} > 1$ thermal boundary layer thickness $y\,\text{Ra}_y^{-1/4}$ as the most appropriate length scale (Fig. 4.5), the similarity variable emerges as

$$\eta = \frac{x}{y}\,\text{Ra}_y^{1/4} \tag{4.55}$$

Introducing the streamfunction $u = \partial\psi/\partial y$, $v = -\partial\psi/\partial x$ in place of the continuity equation (4.2), the boundary layer equations (4.8) and (4.17) become

$$\frac{\partial\psi}{\partial y}\frac{\partial T}{\partial x} - \frac{\partial\psi}{\partial x}\frac{\partial T}{\partial y} = \alpha\frac{\partial^2 T}{\partial x^2} \tag{4.56}$$

$$-\frac{\partial\psi}{\partial y}\frac{\partial^2\psi}{\partial x^2} + \frac{\partial\psi}{\partial x}\frac{\partial^2\psi}{\partial x\partial y} = -v\frac{\partial^3\psi}{\partial x^3} + g\beta(T - T_\infty) \tag{4.57}$$

Now, from the first column of Table 4.1 we note that, in general, the dimensionless temperature profile will be a function of both $\eta(x, y)$ and Pr; let this unknown function be $\theta(\eta, \text{Pr})$, defined as

$$\frac{T - T_\infty}{T_0 - T_\infty} = \theta(\eta,\ \text{Pr}) \tag{4.58}$$

For the vertical velocity profile v, from the fourth column of Table 4.1 where $\text{Pr} > 1$, we select the expression

$$v = \frac{\alpha}{y}\,\text{Ra}_y^{1/2}\,G(\eta,\ \text{Pr}) \tag{4.59}$$

where $(\alpha/y)\, \mathrm{Ra}_y^{1/2}$ represents the scale of v, and $G(\eta, \mathrm{Pr})$ is the dimensionless similarity profile of the wall jet. From the definition $v = -\partial\psi/\partial x$, we conclude that the streamfunction expression must be

$$\psi = \alpha\, \mathrm{Ra}_y^{1/4}\, F(\eta,\ \mathrm{Pr}) \tag{4.60}$$

where $G = -\partial F/\partial\eta$. Substituting eqs. (4.58) and (4.60) into the boundary layer equations for energy and momentum [eqs. (4.56) and (4.57)], we obtain a system of dimensionless equations

$$\tfrac{3}{4}F\theta' = \theta'' \tag{4.61}$$

$$\frac{1}{\mathrm{Pr}}\left(\frac{1}{2}F'^2 - \frac{3}{4}FF''\right) = -F''' + \theta \tag{4.62}$$

where $(\cdot)'$ is shorthand notation for $\partial(\cdot)/\partial\eta$. These equations show once again the meaning of the $\mathrm{Pr} > 1$ scaling adopted in the definition of η and G (both of order 1) [eqs. (4.55) and (4.59)]. The energy equation (4.61) is a balance between convection and conduction, while the momentum equation (4.62) reduces to a balance between friction and buoyancy as $\mathrm{Pr} \to \infty$, that is, as the inertia effect vanishes.

Equations (4.61) and (4.62) must be solved subject to the similarity formulation of the appropriate boundary conditions [see eqs. (4.18)]:

$$
\begin{array}{lll}
\textbf{(i) At } x = 0, & u = 0 & F = 0 \\
(\eta = 0) & v = 0 & F' = 0 \\
& T = T_0 & \theta = 1 \\
\textbf{(ii) As } x \to \infty, & v = 0 & F' = 0 \\
(\eta \to \infty) & T = T_\infty & \theta = 0
\end{array} \tag{4.63}
$$

Figures 4.7a and b present the solution as temperature profiles and velocity profiles in the thermal boundary layer region $\eta = O(1)$. As anticipated by Fig. 4.4, in the limit $\mathrm{Pr} \to \infty$, the temperature profiles collapse onto a single curve. Also, in the same limit, the $\eta \sim 1$ portions of the velocity profiles approach a single curve, while the dimensionless velocity peak is consistently a number of order 1 (the velocity peak falls in the region occupied by the thermal boundary layer). As Pr increases, the velocity profile extends farther and farther into isothermal fluid. All these observations support the scale analysis whose results have been summarized in Table 4.1.

The numerical solution plotted in Fig. 4.7 was obtained by modifying the numerical results published by Ostrach as a solution to a different formulation of the same problem [16]. For the boundary layer length scale, Ostrach chose $y\ \mathrm{Gr}_y^{-1/4}$ which, as observed in Section 4.3.3, is an incorrect scale (this scale had
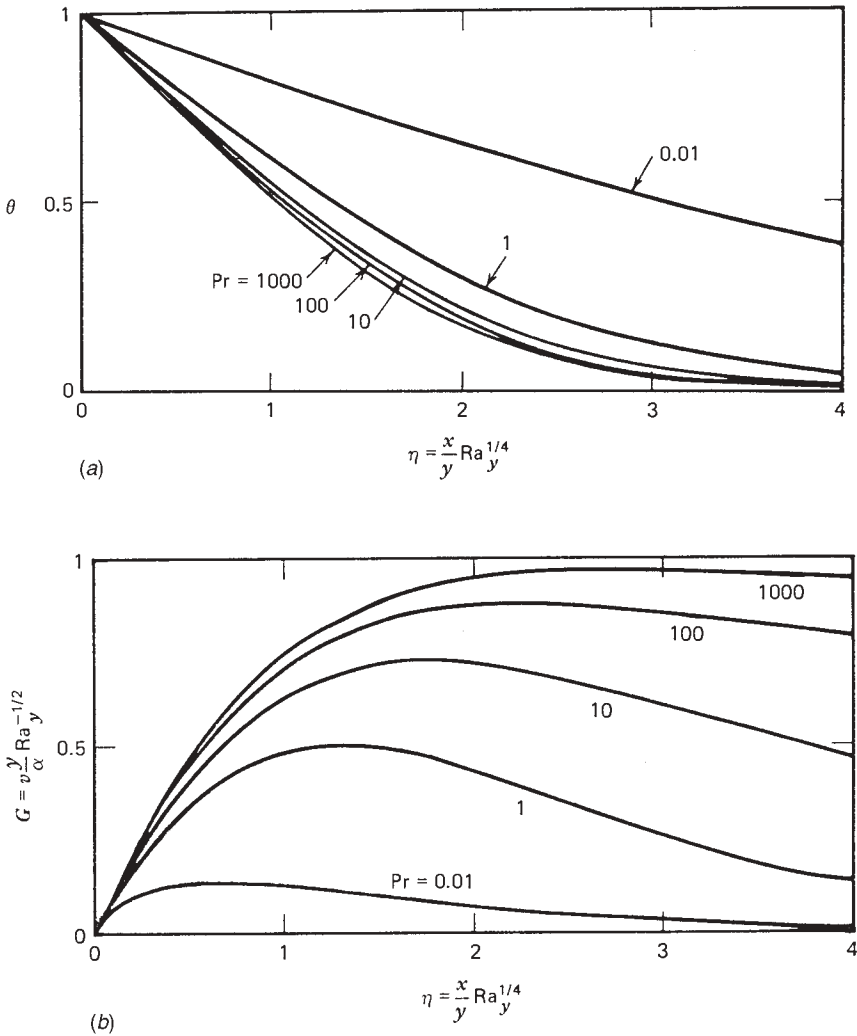
Figure 4.7 Similarity solution for laminar natural convection boundary layer flow: (a) temperature profiles; (b) vertical velocity profiles. These drawings are based on the correct scales of the δ_T-thick layer in a Pr > 1 fluid.

been used earlier by Schmidt and Beckmann [17], who were the first to apply boundary layer theory to solve the laminar natural convection problem).

The local heat transfer coefficient predicted by the similarity solution is

$$\mathrm{Nu} = \frac{hy}{k} = -(\theta')_{\eta=0}\ \mathrm{Ra}_y^{1/4} \tag{4.64}$$

which is the expected scaling law in the Pr ≫ 1 range (Table 4.1). The numerical coefficient $-(\theta')_{\eta=0}$ is, in general, a function of the Prandtl number, as shown

Table 4.2 Similarity solution heat transfer results for natural convection boundary layer along a vertical isothermal wall[a]

Pr	0.01	0.72	1	2	10	100	1000
$\text{Nu Ra}_y^{-1/4}$	0.162	0.387	0.401	0.426	0.465	0.490	0.499

[a]Numerical values calculated from Ostrach's solution [16].

in Table 4.2 and Fig. 4.6. In the two Pr limits of interest, the Nusselt number approaches the following asymptotes [18]:

$$\text{Nu} = 0.503\,\text{Ra}_y^{1/4} \qquad \text{as } \text{Pr} \to \infty \qquad (4.65)$$

$$\text{Nu} = 0.6(\text{Ra}_y\ \text{Pr})^{1/4} \quad \text{as } \text{Pr} \to 0 \qquad (4.66)$$

Noting that since $h \sim y^{-1/4}$ the average heat transfer coefficient for a wall of height H is $h_{0-H} = (4/3)h(y = H)$, the average Nusselt number $\text{Nu}_{0-H} = h_{0-H}H/k$ is equal to $(4/3)\,\text{Nu}(y = H)$. Therefore, the wall-averaged heat transfer results corresponding to the two Pr limits are

$$\text{Nu}_{0-H} = 0.671\,\text{Ra}_H^{1/4} \qquad \text{as } \text{Pr} \to \infty \qquad (4.65')$$

$$\text{Nu}_{0-H} = 0.8(\text{Ra}_H\ \text{Pr})^{1/4} \quad \text{as } \text{Pr} \to 0 \qquad (4.66')$$

These conclusions are anticipated within 30 percent by the scaling laws of Table 4.1: Such good agreement is common when the scale analysis is correct.

Figure 4.6 shows that despite the factor of 10 increase in the Prandtl number from air (Pr = 0.72) to water (Pr $\simeq$ 5–7), the Nusselt number varies by only 15 percent if the Rayleigh number is held constant. This observation is why the natural convection of air in room-size systems is often simulated in small-scale laboratory systems using water as working fluid (see Problem 4.4).

4.6 UNIFORM WALL HEAT FLUX

The analyses presented so far are based on the assumption that the vertical wall is isothermal. This would be a good approximation in cases where the vertical wall is massive and highly conducting in the vertical y direction: Indeed, the object of Problem 4.5 is to estimate the needed vertical conductance through the wall so that the $T_0 = \text{constant}$ description is valid.

From a practical standpoint, however, an equally important wall model is the uniform heat flux condition $q'' = \text{constant}$. In many applications, the wall heating effect is the result of radiation heating from the other side or, as in the case of electronic components, the result of resistive heating. The constant heat flux condition applies to nuclear radiation heating, and only under special conditions to thermal radiation heating (in general, in thermal radiation heat transfer, the wall heat flux depends on the wall temperature). The heat transfer problem in such cases consists of predicting the wall—ambient temperature

difference $T_0(y) - T_\infty$ when the uniform heat flux q'' is given. The solution can be pursued step by step according to the methodology outlined in the preceding three sections. To avoid repetition, however, we outline only the scale analysis, leaving the integral and similarity solutions as journal-assisted homework for the reader (Problems 4.6 and 4.7).

Regardless of how q'', ΔT, and δ_T vary with altitude y, the definition of wall heat flux requires that

$$q'' \sim k\frac{\Delta T}{\delta_T} \tag{4.67}$$

Figure 4.8a illustrates this scaling law in the case of an isothermal wall, where both ΔT and the product $q''\delta_T$ are independent of y. Figure 4.8b shows what
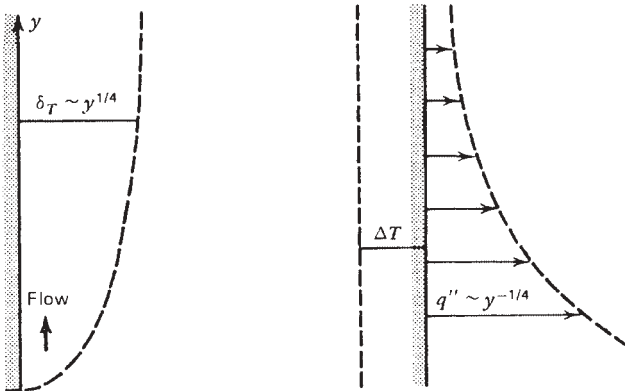
(a) Isothermal wall
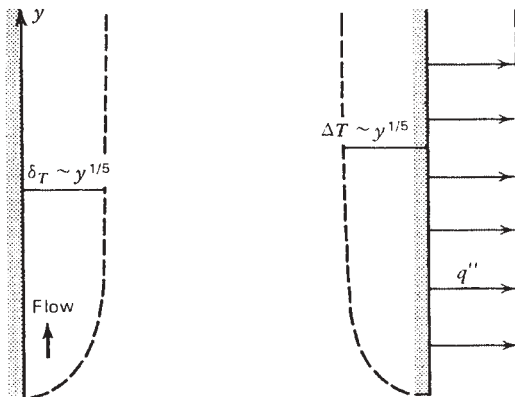
(b) Uniform wall heat flux

Figure 4.8   Effect of the thermal boundary condition on the natural convection boundary layer along a vertical wall.

to expect in the case of constant q'', namely, identical ΔT and δ_T functions of y. To determine these y functions, we make the observation that the scaling analysis starting with eq. (4.19) is general; in other words, in that analysis, δ_T and ΔT represent the correct order of magnitudes of thermal layer thickness and wall–ambient temperature difference along a wall of height H.

For $\Pr \gg 1$ fluids, eq. (4.26) recommends

$$\delta_T \sim H\left(\frac{g\beta\,\Delta T\,H^3}{\alpha\nu}\right)^{-1/4} \tag{4.68}$$

Recognizing that in the present problem ΔT is not given (q'' is), we use eq. (4.67) to eliminate ΔT and solve for δ_T,

$$\delta_T \sim H\,\mathrm{Ra}_{*_H}^{-1/5} \tag{4.69}$$

where Ra_* is a Rayleigh number based on heat flux q'',

$$\mathrm{Ra}_{*_H} = \frac{g\beta H^4 q''}{\alpha\nu k} \tag{4.70}$$

From eq. (4.67), the corresponding ($\Pr \gg 1$) scale of the wall–ambient temperature difference is

$$\Delta T \sim \frac{q''}{k}\,H\,\mathrm{Ra}_{*_H}^{-1/5} \tag{4.71}$$

Note that both δ_T and ΔT are proportional to $H^{1/5}$; because the H-averaged quantities are proportional to $H^{1/5}$, the local values of δ_T and ΔT are proportional to $y^{1/5}$. This conclusion is illustrated in Fig. 4.8b. The local Nusselt number for a constant heat flux wall is defined as

$$\mathrm{Nu} = \frac{q''}{T_0(y) - T_\infty}\frac{y}{k} \tag{4.72}$$

Therefore, in the range $\Pr \gtrsim 1$, the Nusselt number must scale as

$$\mathrm{Nu} \sim \frac{H}{\delta_T} \sim \mathrm{Ra}_{*_H}^{1/5} \tag{4.73}$$

For the low–Prandtl number fluids, we start with eq. (4.32) and, using the same analysis as above, obtain

$$\delta_T \sim H(\mathrm{Ra}_{*_H}\,\Pr)^{-1/5}$$

$$\Delta T \sim \frac{q''}{k}\,H(\mathrm{Ra}_{*_H}\,\Pr)^{-1/5} \tag{4.74}$$

$$\mathrm{Nu} \sim (\mathrm{Ra}_{*_H}\,\Pr)^{1/5}$$

The validity of these scaling results can be tested by referring to more exact analyses published on the same topic. Sparrow [19] carried out an integral analysis of the same type as Squire's [15] (i.e., assuming only one length scale δ_T for the velocity profile) and arrived at the local Nusselt number

$$\mathrm{Nu} = \frac{2}{360^{1/5}} \left(\frac{\mathrm{Pr}}{\frac{4}{5} + \mathrm{Pr}} \right)^{1/5} \mathrm{Ra}_{*y}^{1/5} \qquad (4.75)$$

The similarity solution was reported by Sparrow and Gregg [20], who found that eq. (4.75) is, in fact, an adequate curve fit for the similarity Nu results in the range $0.01 < \mathrm{Pr} < 100$. Thus, in the two Pr limits, eq. (4.75) yields the following local Nusselt numbers:

$$\mathrm{Nu} = \begin{cases} 0.616\mathrm{Ra}_{*y}^{1/5} & (\mathrm{Pr} \to \infty) \\ 0.644\mathrm{Ra}_{*y}^{1/5}\,\mathrm{Pr}^{1/5} & (\mathrm{Pr} \to 0) \end{cases} \qquad (4.76)$$

Note that these limiting expressions are anticipated correctly by the scale laws [eqs. (4.73) and (4.74)].

Similarity solutions can be developed for an infinity of wall temperature conditions, provided that they obey either the power law $T_0 - T_\infty = Ay^m$ [21], the exponential law $T_0 - T_\infty = Ae^{my}$ [21], or the line $T_0 - T_\infty = A + By$ [22], where A, B, and m are all constants. Thus, the $T_0 = $ constant and $q'' = $ constant problems discussed so far are only two special cases of the vast analytically accessible class of problems. From an engineering standpoint, however, the $T_0 = $ constant and $q'' = $ constant results are by far the most useful.

4.7   EFFECT OF THERMAL STRATIFICATION

To discover the basics of natural convection, so far we considered the simplest model possible, that is, the heat transfer interaction between a vertical wall and an isothermal semi-infinite fluid reservoir (Fig. 4.1). Now, we take a closer look at a real situation involving natural convection. Vertical walls are rarely in communication with semi-infinite isothermal pools of fluid: More often, their height is finite and the heated boundary layer eventually hits the ceiling. At that point, the heated stream has no choice but to discharge horizontally into the fluid reservoir (to the right in Fig. 4.1): The direction of this discharge is horizontal because the discharge contains fluid warmer than the rest of the reservoir. The long-time effect of this discharge is thermal stratification, or warm fluid layers floating on top of colder layers. Indeed, thermal stratification is a characteristic of all fluid bodies surrounded by differentially heated sidewalls lined by boundary layers, as demonstrated in Chapter 5. At this point it is sufficient to recognize that the air in any room with the doors closed is thermally stratified in such a way that the lowest layers assume the temperature of the coldest wall, and the layers near the ceiling approach the temperature of the warmest wall.

In view of this discussion, the inset in Fig. 4.9 is a more general model for the buoyancy-driven flow near a vertical wall. The fluid reservoir is now linearly stratified,

$$T_\infty(y) = T_{\infty,0} + \gamma y \qquad (4.77)$$

$T_{\infty,0}$ being the lowest temperature in the arrangement and γ the constant temperature gradient (assumed known). The dashed line in Fig. 4.9 shows the location of the isothermal reservoir model employed so far ($\gamma = 0°$C/m). If the bottom temperature difference $T_0 - T_{\infty,0}$ remains constant, we expect the overall heat transfer rate to *decrease* as γ increases: The reason for this expectation is that the effective (mean) temperature difference between wall and fluid decreases as γ increases.
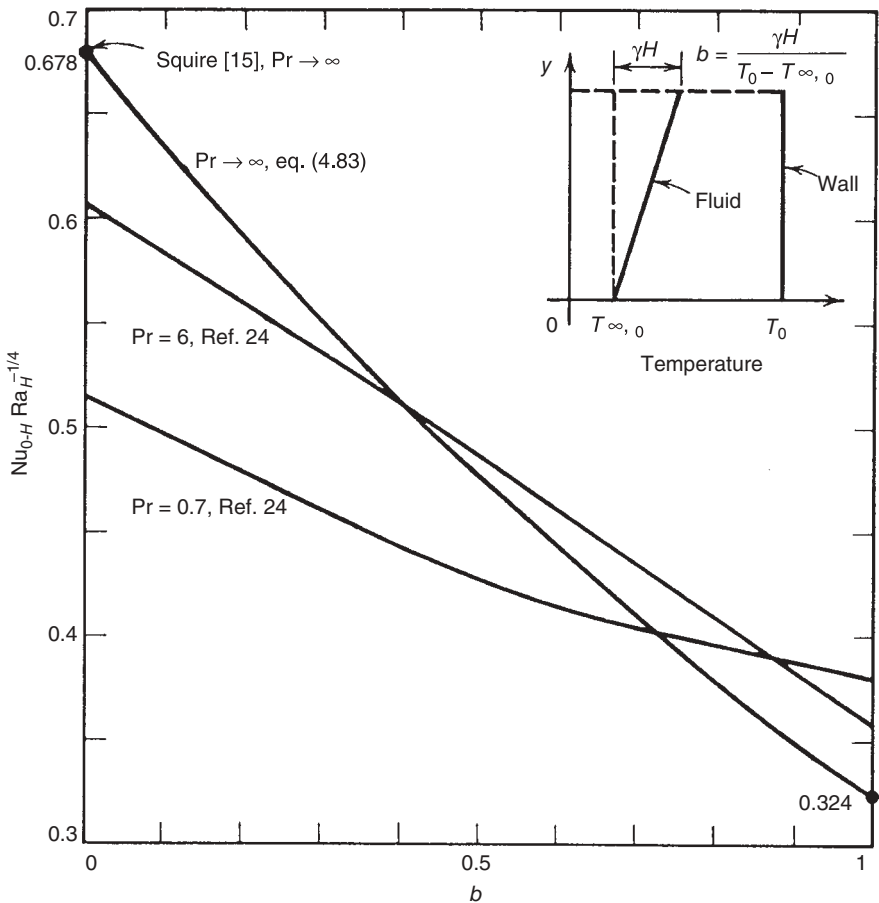

Figure 4.9 Effect of reservoir thermal stratification on the heat transfer from an isothermal vertical wall.

An integral solution can be constructed in a relatively straightforward manner by combining the integral equations (4.40) and (4.41) with polynomial temperature and velocity profiles:

$$T - T_\infty = (T_0 - T_\infty)\left(1 - \frac{x}{\delta_T}\right)^2$$

$$v = V\frac{x}{\delta}\left(1 - \frac{x}{\delta}\right)^2 \tag{4.78}$$

where $\delta_T = \delta$ and, according to eq. (4.77), $T_0 - T_\infty(y) = T_0 - T_{\infty,0} - \gamma y$. In the dimensionless form required by numerical integration, the momentum and energy equations reduce to

$$\frac{1}{(105)\,\mathrm{Pr}}\frac{d}{dy_*}(V_*^2\delta_*) = -\frac{V_*}{\delta_*} + \frac{\delta_*}{3}(1 - by_*) \tag{4.79}$$

$$\frac{d}{dy_*}[V_*\delta_*(1 - by_*)] = \frac{60}{\delta_*}(1 - by_*) \tag{4.80}$$

with the nondimensional notation suggested by Table 4.1, and the definition of a new dimensionless stratification parameter (b):

$$y_* = \frac{y}{H}, \qquad \delta_* = \frac{\delta}{H\,\mathrm{Ra}_H^{-1/4}}$$

$$V_* = \frac{V}{(\alpha/H)\mathrm{Ra}_H^{1/2}}, \qquad \mathrm{Ra}_H = \frac{\delta\beta H^3(T_0 - T_{\infty,0})}{\alpha\nu} \tag{4.81}$$

$$b = \frac{\gamma H}{T_0 - T_{\infty,0}} = 1 - \frac{\Delta T_{\min}}{\Delta T_{\max}}, \qquad \Delta T = T_0 - T_\infty(y)$$

Equations (4.79) and (4.80) can be integrated numerically from $y_* = 0$ to $y_* = 1$ to determine $\delta_*(y_*, b)$ and $V_*(y_*, b)$. The local heat flux is then

$$q'' = -k\left(\frac{\partial T}{\partial x}\right)_{x=0} = \frac{k(T_0 - T_{\infty,0})}{H\,\mathrm{Ra}_H^{-1/4}}\frac{2}{\delta_*}(1 - by_*) \tag{4.82}$$

Integrating q'' over the wall height H yields q' and the overall Nusselt number

$$\mathrm{Nu}_{0-H} = \frac{q'}{k(T_0 - T_{\infty,0})} = \mathrm{Ra}_H^{1/4}\int_0^1 \frac{2}{\delta_*}(1 - by_*)\,dy_* \tag{4.83}$$

The result of this calculation for $\mathrm{Pr} \to \infty$ is shown in Fig. 4.9 as $\mathrm{Nu}_{0-H}\,\mathrm{Ra}_H^{-1/4}$ versus the new dimensionless group b, where it should be kept in mind that both Nu_{0-H} and Ra_H are based on the *maximum* temperature difference $T_0 - T_{\infty,0}$. Of special interest is the heat transfer rate in the fully stratified limit ($b = 1$),

$$\mathrm{Nu}_{0-H} = 0.324\mathrm{Ra}_H^{1/4} \qquad (\mathrm{Pr} \to \infty) \tag{4.84}$$

that matches within 11 percent the conclusion of an Oseen-linearized analysis of boundary layer convection in a stratified enclosure [23]. (The details of this analysis are given in Chapter 5.)

Figure 4.8 also shows the Pr = 6 and Pr = 0.7 results predicted for the same problem by Chen and Eichhorn [24], based on the *local nonsimilarity technique* [25]. The general trend is the same as in the integral solution, namely, a gradual decrease in Nu_{0-H} as the stratification degree b increases. In the isothermal reservoir limit, the Chen and Eichhorn results match the similarity solution (Table 4.2); hence, they fall slightly below the corresponding results based on the Squire type of integral analysis (Fig. 4.6).

4.8   CONJUGATE BOUNDARY LAYERS

There are many engineering situations in which the vertical wall that heats a buoyant boundary layer is itself heated on the back side by a sinking boundary layer. Such is the case in walls, partitions, and baffles encountered regularly in the thermal design of living quarters and insulation systems. As shown in Fig. 4.10, this heat transfer arrangement describes the common *single-pane window* where an insulating impermeable wall of finite thickness separates two fluid reservoirs at different temperatures.

Boundary layers form on both sides of the wall; however, the wall temperature or heat flux are not known a priori as in the simpler models considered earlier; the condition of the wall is the result of the heat transfer interaction between the two boundary layers. It is said that depending on the layer-to-layer interaction, the wall temperature ''floats'' to an equilibrium distribution between the two extreme temperatures maintained by the two reservoirs. Since one boundary drives the other, the boundary layers are termed *conjugate* (as two oxen engaged in the same yoke; note the Latin verb *conjungĕre* = to yoke).

Figure 4.10 shows the Nusselt number predicted analytically in the $Pr \rightarrow \infty$ limit based on the Oseen-linearization method (Chapter 5) [26]. This approach consists of writing integral conservation equations analogous to eqs. (4.40) and (4.41) for both sides of the wall, with the additional complication that the wall temperature $T_0(y)$ is unknown. The additional equation necessary for determining T_0 is the condition of heat flux continuity in the x direction, from one face of the wall to the other. In Fig. 4.10, both the overall Nusselt number and the Rayleigh number are based on the overall temperature difference imposed by the two fluid reservoirs. The heat transfer rate (hence, the ratio $Nu_{0-H}/Ra_H^{1/4}$) decreases as the wall thickness resistance parameter ω increases. The dimensionless *wall number* proposed in Ref. 26 is

$$\omega = \frac{t}{H}\frac{k}{k_w}Ra_H^{1/4} \tag{4.85}$$

where *t, H, k,* and k_w are the wall thickness, wall height, fluid conductivity, and wall conductivity, respectively. Note that ω is the ratio of wall thermal
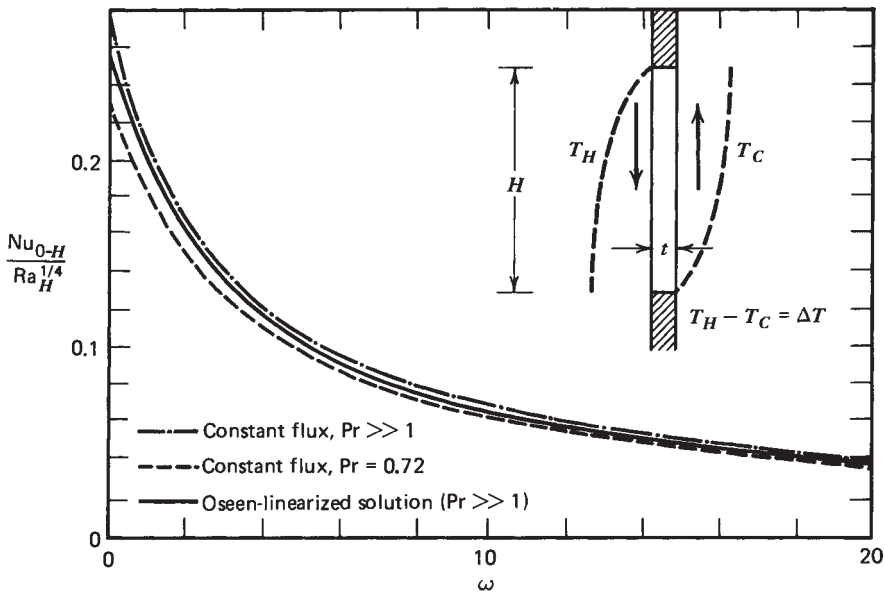
Figure 4.10 Heat transfer between two fluid reservoirs separated by a vertical wall with natural convection boundary layers on both sides. Note that both Nu_{0-H} and Ra_H are based on the overall temperature difference $\Delta T = T_H - T_C$. (From Ref. 26.)

resistance t/Hk_w divided by the thermal resistance of one boundary layer $(H\,Ra_H^{-1/4})/Hk$.

One of the contributions of the analysis described in Ref. 26 is to show that the wall heat flux distribution negotiated between two conjugate natural convection boundary layers is approximated satisfactorily by the $q'' = $ constant model discussed earlier. Therefore, as shown in Problem 4.9 and in Ref. 26, an estimate of the $Nu_{0-H}(\omega, Ra_H)$ relationship can be obtained by adding in series the three resistances constituted by the two $q'' = $ constant boundary layers sandwiching the wall. Figure 4.10 shows good agreement between this more direct approach and the Oseen-linearized analysis.

The effect of thermal stratification on the conjugate boundary layer configuration has been documented in Ref. 27. Figure 4.11 shows that the coefficient in the $Nu_{0-H} \sim Ra_H^{1/4}$ proportionality increases as the degree of thermal stratification on either side increases (the dimensionless temperature gradients a and b are defined graphically in Fig. 4.11). This behavior appears to contradict the effect shown in Fig. 4.9 for a single isothermal wall. The contradiction is explained by the fact that in Fig. 4.9, both Nu_{0-H} and Ra_H are based on the maximum temperature difference, whereas in Fig. 4.11 (and in Fig. 4.10), the same numbers are based on the reservoir-to-reservoir temperature difference evaluated at mid-height. Thus, the ΔT sketched in Fig. 4.11 is the average temperature difference between the two stratified reservoirs.
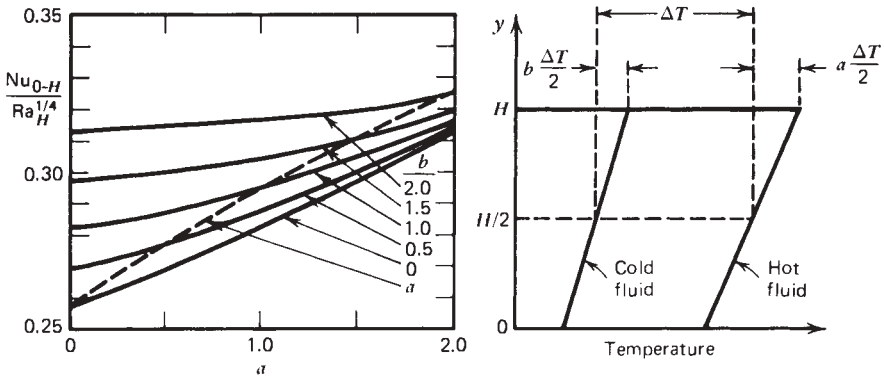
Figure 4.11   Effect of thermal stratification on heat transfer between two fluid reservoirs separated by a vertical wall ($\omega = 0$, $Pr \geq 1$). (From Ref. 27.)

4.9   VERTICAL CHANNEL FLOW

Consider now the interaction between the boundary layers formed along two parallel walls facing each other (Fig. 4.12). If the boundary layer thickness scales are much smaller than the wall-to-wall spacing D, the flow along one wall may be regarded (approximately) as a wall jet unaffected by the presence of another wall. On the other hand, if the boundary layer grows to the point that its thickness becomes comparable to D, the two wall jets merge into a single buoyant stream rising through the chimney formed by the two walls.
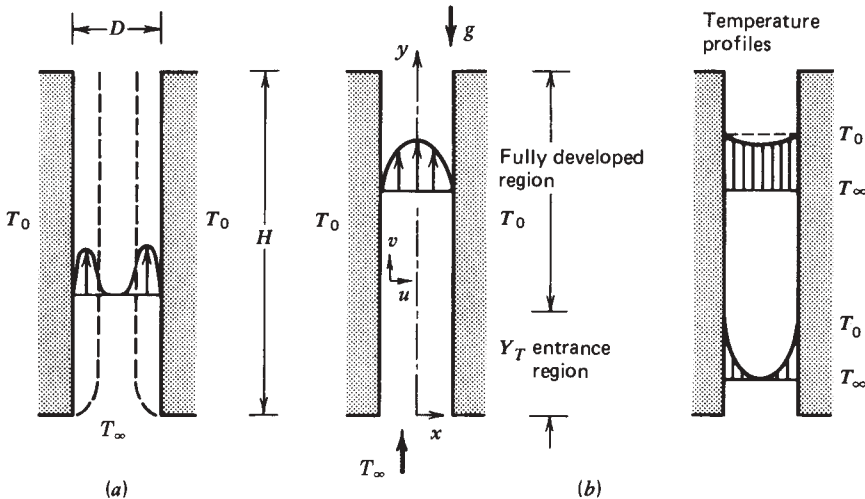
Figure 4.12   Natural convection in the channel formed between two vertical hot plates.

It is clear from Fig. 4.12 that the channel flow departs from the wall jet description in the same way that the duct flows of Chapter 3 depart from the pure boundary layer flows of Chapter 2. Here we focus on the simplest analysis of the channel flow, with the final objective of predicting the capability of this flow to cool or heat the walls of the channel. The flow part of the problem may be solved by considering the momentum equation in the y direction (for notation, see Fig. 4.12):

$$\rho \left(u \frac{\partial v}{\partial x} + v \frac{\partial v}{\partial y} \right) = -\frac{\partial P}{\partial y} + \mu \, \nabla^2 v - \rho g \tag{4.86}$$

The mass continuity equation, in conjunction with the assumption that the channel is long enough so that the u scale becomes sufficiently small, leads to the concept of *fully developed flow*, for which we have

$$u = 0 \quad \text{and} \quad \frac{\partial v}{\partial y} = 0 \tag{4.87}$$

The momentum equation in the lateral direction x can be used to show that the pressure in the fully developed region is a function of y only, and, because both ends of the channel are open to the ambient of density ρ_∞,

$$\frac{\partial P}{\partial y} = \frac{dP}{dy} = -\rho_\infty g \tag{4.88}$$

Combining eqs. (4.86)–(4.88) and again using the Boussinesq approximation yields the much simpler momentum equation

$$\frac{d^2 v}{dx^2} = -\frac{g\beta}{v}(T - T_\infty) \tag{4.89}$$

which is the natural convection equivalent of the Hagen–Poiseuille equation encountered in Chapter 3.

To solve eq. (4.89), it is necessary to derive the temperature profile $T - T_\infty$; the reader can verify that in order to derive the temperature profile from the energy equation, one must know the velocity profile. The two profiles, velocity and temperature, are coupled; hence, eq. (4.89) and the energy equation must be solved simultaneously. A much simpler solution approach is possible if we observe that in the fully developed region between two *isothermal* walls, the temperature difference can be approximated by $T_0 - T_\infty$; in other words,

$$T_0 - T \ll T_0 - T_\infty \tag{4.90}$$

The range of validity of this approximation will be determined later in this section. Based on this approximation, the right-hand side of eq. (4.89) becomes

a constant, and the heat transfer solution follows without difficulty in a few algebraic steps. The main features of this solution are:

Velocity profile:

$$v = \frac{g\beta D^2 (T_0 - T_\infty)}{8\nu} \left[1 - \left(\frac{x}{D/2} \right)^2 \right]$$

Mass flow rate per unit length normal to the plane of Fig. 4.12:

$$\dot{m} = \frac{\rho g \beta D^3 (T_0 - T_\infty)}{(12)\nu} \tag{4.91}$$

Total heat transfer rate between stream and channel walls:

$$q' = \dot{m}(\text{outlet enthalpy} - \text{inlet enthalpy})$$

$$= \dot{m}c_P(T_0 - T_\infty)$$

Average heat flux:

$$q''_{0-H} = q'/(2H)$$

Overall Nusselt number:

$$\frac{q''_{0-H}H}{(T_0 - T_\infty)k} = \frac{\text{Ra}_D}{24}$$

Note that the dimensionless group emerging from this analysis is the Rayleigh number based on wall-to-wall spacing,

$$\text{Ra}_D = \frac{g\beta D^3 (T_0 - T_\infty)}{\alpha\nu} \tag{4.92}$$

and that the Grashof number is once again absent from the discussion. This conclusion answers again the question of whether the Grashof number is a relevant dimensionless group in natural convection. It is not.

The fully developed flow and heat transfer solution (4.91) is valid for all Prandtl numbers. The Rayleigh number range of its validity follows from the requirement that the thermal entrance length Y_T be much smaller than the channel height H,

$$Y_T < H \tag{4.93}$$

The order of magnitude of Y_T follows from the observation that the thermal boundary layer thickness δ_T becomes of order $D/2$ when y is of order Y_T, that is,

$$Y_T \text{Ra}_{Y_T}^{-1/4} \sim \frac{D}{2} \qquad (\text{Pr} > 1)$$

$$Y_T \text{Bo}_{Y_T}^{-1/4} \sim \frac{D}{2} \qquad (\text{Pr} < 1) \tag{4.94}$$

Evaluating Y_T from above, criterion (4.93) becomes

$$\text{Ra}_D^{1/4} < 2\left(\frac{H}{D}\right)^{1/4} \qquad (\text{Pr} > 1)$$

$$\text{Bo}_D^{1/4} < 2\left(\frac{H}{D}\right)^{1/4} \qquad (\text{Pr} < 1)$$

(4.95)

In conclusion, the fully developed flow and temperature profile assumptions break down if the Rayleigh number exceeds an order of magnitude dictated by the geometric aspect ratio of the channel, *H/D* (see also Problem 4.13).

The chimney flow is being contemplated in the design of ''solar chimney'' power plants [28].

4.10   COMBINED NATURAL AND FORCED CONVECTION (MIXED CONVECTION)

If we think of the configuration examined in this chapter (Figs. 4.1 and 4.4) as a model of the flow near a wall in a room, a major limitation of this model is the assumption that the fluid reservoir is motionless. Look around any modern building and you will see that the air inventory of each room is replenished continuously or intermittently by, in most cases, a central air-conditioning system. This means that in the vicinity of every heated wall or cooled window, the room air reservoir is actually in motion: The reservoir is *forced* into and out of the room by an external agent (the fan in the ventilation system). Depending on the strength of this forced circulation, the heat transfer from the wall to the room air may be ruled by either natural convection or forced convection or a combination of natural and forced convection.

There are many ways in which these two mechanisms can interact, as there are many ways in which the reservoir fluid may move relative to the direction of buoyant flow near the wall. Think of the heated wall jet rising on the outer surface of a flat solar collector in wintertime and how this wall jet will be affected by the changing wind direction and velocity. Due to the diversity of the natural–forced convection interaction, it is impossible to treat this subject fully; however, it is instructive to study one simple configuration and to experience the power and cost-effectiveness of pure scaling arguments.

As is shown in the inset of Fig. 4.13, let us consider the heat transfer from a vertical heated wall (T_0) to an isothermal fluid reservoir moving upward (T_∞, U_∞), that is, in the same direction as the natural wall jet present when $U_\infty = 0$. From a heat transfer standpoint, the key question is: Under what conditions is the combined natural–forced phenomenon characterized (approximately) by the scales of pure natural convection, and conversely, under what conditions is it characterized by the scales of pure forced convection? In other words, what is the criterion for the *transition* from one convection mechanism to another?
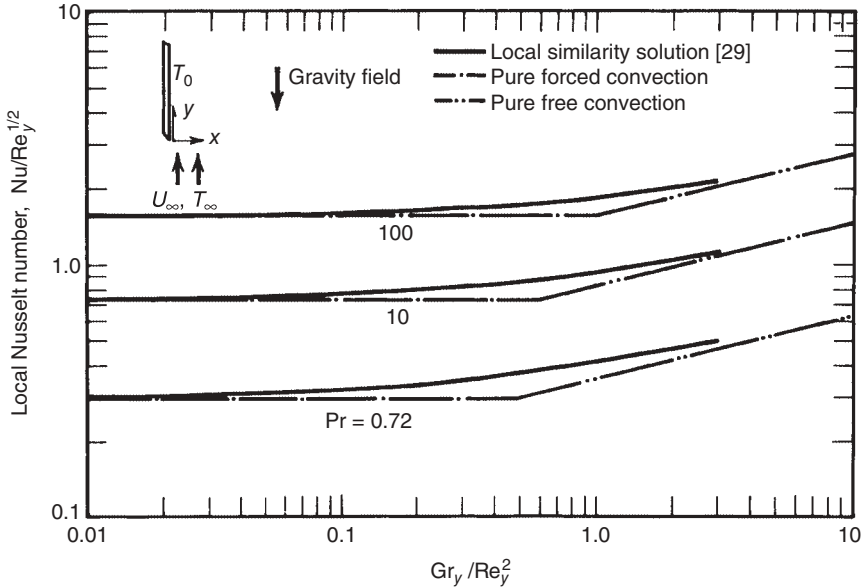
Figure 4.13   Heat transfer by natural and forced convection along a vertical wall. (After Ref. 29.)

If the mechanism is natural convection, the thermal distance between the heat-exchanging entities is of order

$$(\delta_T)_{NC} \sim y \, Ra_y^{-1/4} \qquad (Pr > 1) \qquad (4.96)$$

as reservoir fluid supplies the buoyant wall jet of thermal boundary layer thickness $(\delta_T)_{NC}$. On the other hand, if the mechanism is forced convection, the wall and the reservoir are separated by a thermal length of order (cf. Chapter 2)

$$(\delta_T)_{FC} \sim y \, Re_y^{-1/2} Pr^{-1/3} \qquad (Pr > 1) \qquad (4.97)$$

According to the constructal law [2–5], the type of convection mechanism is decided by the *smaller* of the two distances, $(\delta_T)_{NC}$ or $(\delta_T)_{FC}$, because the wall will leak heat to the nearest heat sink (or because currents seek and construct paths of greater access, or faster mixing). Thus, the scale criterion for transition from natural to forced convection is

$$
\begin{aligned}
(\delta_T)_{NC} < (\delta_T)_{FC} & \qquad \text{natural convection} \\
(\delta_T)_{NC} > (\delta_T)_{FC} & \qquad \text{forced convection}
\end{aligned}
\qquad (4.98)
$$

In other words, for $Pr > 1$ fluids,

$$\frac{Ra_y^{1/4}}{Re_y^{1/2} \, Pr^{1/3}} \begin{cases} > O(1) & \text{natural convection} \\ < O(1) & \text{forced convection} \end{cases} \qquad (4.99)$$

To verify the validity of this criterion, we examine the local similarity solution to the combined heat transfer problem (Fig. 4.13). This solution shows that forced convection dominates at small values of the group Gr_y/Re_y^2, while natural convection takes over at large values of the same parameter. Note, however, that the knee in each Nusselt number curve shifts to the right as Pr increases: This effect is due to the fact that the abscissa parameter used, Gr_y/Re_y^2, is not the same as the dimensionless group that serves as transition parameter in eq. (4.99):

$$\frac{Gr_y}{Re_y^2} = \left(\frac{Ra_y^{1/4}}{Re_y^{1/2} \, Pr^{1/3}} \right)^4 Pr^{1/3} \qquad (4.100)$$

Figure 4.14 shows the replotting of the similarity solution [29] using the transition parameter on the abscissa and the forced convection Nusselt number scaling on the ordinate. The sign of correct scaling [hence the validity of criterion
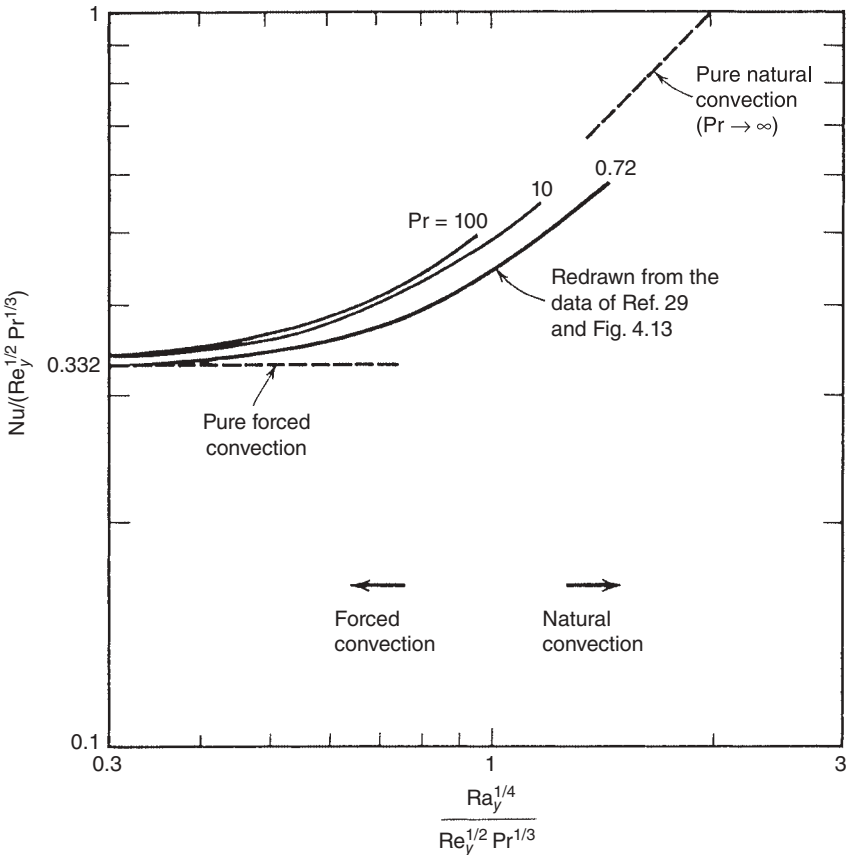

Figure 4.14 Correct transition between natural and forced convection on a vertical wall when Pr ≥ 1.

(4.99)] is that the $Pr > 1$ curves fall on top of each other, and the knee of all the curves is at $O(1)$ on the abscissa. Figure 4.14 shows that we can estimate the Nusselt number with sufficient accuracy and efficiency by first using criterion (4.99) and by relying on the appropriate asymptotic scaling (i.e., either pure natural convection or pure forced convection).

In conclusion, mixed convection can be understood and predicted by intersecting its asymptotes, natural convection and forced convection. This is one of the earliest applications of the *intersection-of-asymptotes method* (cf. the 1984 edition of this book, pp. 142–146).

Repeating the geometric argument of eq. (4.98), this time for $Pr < 1$ fluids, we find the following transition criterion:

$$\frac{Bo_y^{1/4}}{Pe_y^{1/2}} \begin{cases} > O(1) & \text{natural convection} \\ < O(1) & \text{forced convection} \end{cases} \tag{4.101}$$

Note that the dimensionless group $Bo_y^{1/4}\ Pe_y^{-1/2}$ is equal to Lloyd and Sparrow's [29] abscissa parameter Gr_y/Re_y^2 raised to the one-fourth power (Fig. 4.13).

The progress on mixed natural and forced convection was reviewed in Refs. 30 and 31.

4.11 HEAT TRANSFER RESULTS INCLUDING THE EFFECT OF TURBULENCE

4.11.1 Vertical Walls

Consider again the vertical walls sketched in Figs. 4.1 and 4.8. The boundary layer flow remains laminar if y is small enough so that the Rayleigh number Ra_y does not exceed a critical value. Until recently, it was thought that the transition to turbulent flow occurs at the y position where $Ra_y \sim 10^9$, regardless of the value of the Prandtl number. The established view was questioned by Bejan and Lage [32], who showed that it is the *Grashof number of order* 10^9 (i.e., not the Rayleigh number of order 10^9) that marks the transition in all fluids:

$$Gr_y \sim 10^9 \qquad (10^{-3} \le Pr \le 10^3) \tag{4.102}$$

This universal transition criterion is a manifestation of the constructal law [3] and is derived in Section 6.6. It can also be expressed in terms of the Rayleigh number by recalling that $Ra_y = Gr_y\, Pr$,

$$Ra_y \sim 10^9\, Pr \qquad (10^{-3} \le Pr \le 10^3) \tag{4.103}$$

The heat transfer rate from a vertical wall in the presence of turbulence in the boundary layer has been measured experimentally and correlated as a function $\overline{Nu}_y(Ra_y, Pr)$, where $\overline{Nu}_y$ is an alternative notation for the overall Nusselt number Nu_{0-y}. It was found that in the turbulent regime, $\overline{Nu}_y$ is

approximately proportional to $Ra_y^{1/3}$; this dependence differs from the $\overline{Nu}_y \sim Ra_y^{1/4}$ proportionality that characterizes laminar flow in high-Pr fluids.

An empirical isothermal-wall correlation that reports the wall-averaged Nusselt number $\overline{Nu}_y$ for the entire Rayleigh number range—laminar, transition, turbulent—was constructed by Churchill and Chu [33]:

$$\overline{Nu}_y = \left\{ 0.825 + \frac{0.387 Ra_y^{1/6}}{\left[1 + (0.492/Pr)^{9/16} \right]^{8/27}} \right\}^2 \tag{4.104}$$

This correlation holds for $10^{-1} < Ra_y < 10^{12}$ and for all Prandtl numbers. The physical properties used in the definition of $\overline{Nu}_y$, Ra_y, and Pr are evaluated at the film temperature $(T_w + T_\infty)/2$. In the case of air, eq. (4.104) yields

$$\overline{Nu}_y = (0.825 + 0.325 Ra_y^{1/6})^2 \qquad (Pr = 0.72) \tag{4.105}$$

In the *laminar range*, $Gr_y < 10^9$, a correlation that represents the experimental data more accurately than eq. (4.104) is [33]

$$\overline{Nu}_y = 0.68 + \frac{0.67 Ra_y^{1/4}}{[1 + (0.492/Pr)^{9/16}]^{4/9}} \tag{4.106}$$

$$\overline{Nu}_y = 0.68 + 0.515 Ra_y^{1/4} \qquad (Pr = 0.72) \tag{4.107}$$

These correlations are an alternative to eq. (4.65′), especially in the low–Rayleigh number limit, where the boundary layer (slender flow) approximation loses its validity.

When the vertical wall is heated uniformly, $q_w'' = $ constant, the wall temperature T_w increases monotonically in the y direction. In the laminar regime, the temperature difference $(T_w - T_\infty)$ increases as $y^{1/5}$ (e.g., Fig. 4.8b). In fluids of the air–water Prandtl number range, the transition to turbulence occurs in the vicinity of $Ra_{*y} \sim 10^{13}$. Vliet and Liu [34] recommend the formulas

$$\left. \begin{array}{l} Nu_y = 0.6 Ra_{*y}^{1/5} \\[4pt] \overline{Nu}_y = 0.75 Ra_{*y}^{1/5} \end{array} \right\} \qquad \begin{array}{l} \text{laminar,} \\[4pt] 10^5 < Ra_{*y} < 10^{13} \end{array} \tag{4.108}$$

$$\left. \begin{array}{l} Nu_y = 0.568 Ra_{*y}^{0.22} \\[4pt] \overline{Nu}_y = 0.645 Ra_{*y}^{0.22} \end{array} \right\} \qquad \begin{array}{l} \text{turbulent,} \\[4pt] 10^{13} < Ra_{*y} < 10^{16} \end{array} \tag{4.109}$$

The average Nusselt number $\overline{Nu}_y$ is based on the wall-averaged temperature difference $(\overline{T}_w - T_\infty)$. In particular, for heat transfer to air, Ref. 35, recommends

$$Nu_y = 0.55 Ra_{*y}^{1/5} \qquad \text{laminar} \tag{4.110}$$

$$Nu_y = 0.17 Ra_{*y}^{1/4} \qquad \text{turbulent} \tag{4.111}$$

A correlation that is valid for all Rayleigh and Prandtl numbers is [33]

$$\overline{Nu}_y = \left\{0.825 + \frac{0.387 Ra_y^{1/6}}{\left[1 + (0.437/\,Pr)^{9/16}\right]^{8/27}}\right\}^2 \tag{4.112}$$

In this expression, Ra_y is based on the y-averaged temperature difference $(\overline{T}_w - T_\infty)$. This correlation is almost identical to the one recommended for isothermal walls, eq. (4.104). For air at normal (room) conditions, eq. (4.112) reduces to

$$\overline{Nu}_y = (0.825 + 0.328 Ra_y^{1/6})^2 \qquad (Pr = 0.72) \tag{4.113}$$

The high–Rayleigh number asymptote of this last formula is

$$\overline{Nu}_y \cong 0.107 Ra_y^{1/3} \qquad (Pr = 0.72 \text{ and } Ra_y > 10^{10}) \tag{4.114}$$

Equations (4.112)–(4.114) can be restated in terms of the flux Rayleigh number Ra_{*y} by noting the substitution $Ra_y = Ra_{*y}/\overline{Nu}_y$. For example, the high–Rayleigh number asymptote for air (4.114) becomes

$$\overline{Nu}_y \cong 0.187 Ra_{*y}^{1/4} \qquad (Pr = 0.72 \text{ and } Ra_{*y} > 10^{12}) \tag{4.115}$$

4.11.2 Inclined Walls

Figure 4.15 shows four possible configurations in which a plane wall is inclined relative to the vertical direction. The angle between the plane and the vertical direction ϕ is restricted to the range $-60° < \phi < 60°$ (horizontal walls are discussed in Section 4.11.3). In cases a and d—heated wall tilted upward and cooled wall tilted downward—the effect of the angle ϕ is to thicken the tail end of the boundary layer and to give the wall jet a tendency to separate from the wall. The opposite effect is illustrated in cases b and c, where the wall jet is pinched as it flows over the trailing edge.

In the boundary layer analysis of the flows of Fig. 4.15, it is found that the momentum equation is analogous to eq. (4.17), except that $g \cos\phi$ replaces g in the buoyancy term. The group $g \cos\phi$ is the gravitational acceleration component oriented parallel to the wall. For this reason, the heat transfer rate in the *laminar regime* along an isothermal wall can be calculated with eq. (4.106), provided that the Rayleigh number is based on $g \cos\phi$:

$$Ra_y = \frac{g \cos\phi \, \beta(T_w - T_\infty)y^3}{\alpha \nu} \tag{4.116}$$

Similarly, for laminar flow over a plate with uniform heat flux, the Nusselt number can be calculated with eqs. (4.108) and (4.110), in which

$$Ra_{*y} = \frac{g \cos\phi \, \beta q_w'' y^4}{\alpha \nu k} \tag{4.117}$$
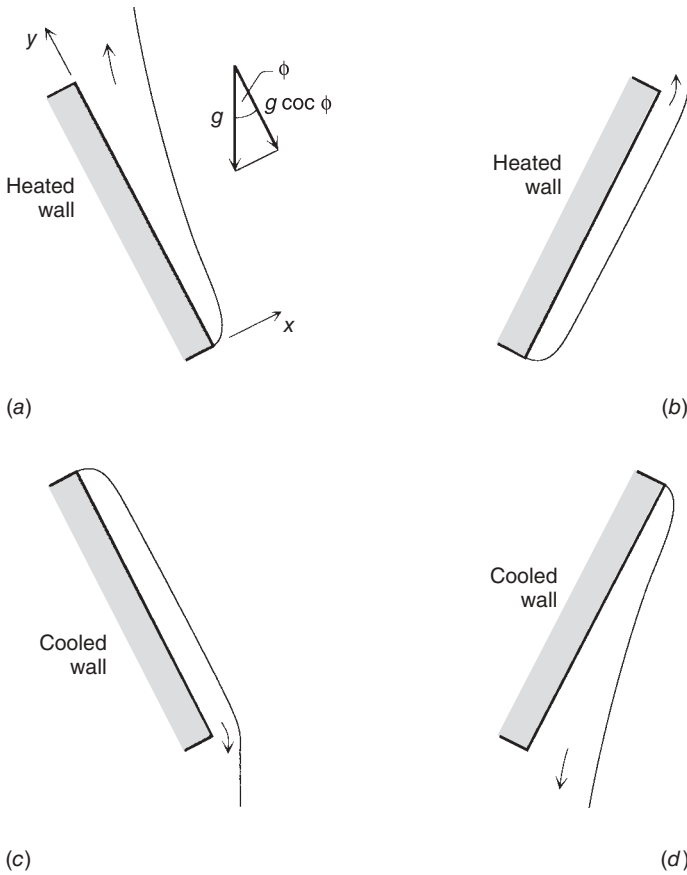
Figure 4.15   Plane walls inclined relative to the vertical direction.

In the *turbulent regime*, it was found that the heat transfer measurements are correlated better using g instead of $g \cos\phi$ in the Rayleigh number [36]. Therefore, eq. (4.104) is recommended for isothermal plates. For inclined walls with uniform heat flux, the Nusselt number is given by eqs. (4.109) and (4.111).

The angle ϕ has a noticeable effect on the location of the laminar–turbulent transition, when the uniform-flux wall is oriented as in cases a and d of Fig. 4.15. The flux Rayleigh numbers tabulated below mark the beginning and the end of the transition region in water experiments (Pr $\cong$ 6.5):

ϕ	Ra_{*y}
$0°$	$5 \times 10^{12} - 10^{14}$
$30°$	$3 \times 10^{10} - 10^{12}$
$60°$	$6 \times 10^7 - 6 \times 10^9$

The Ra_{*y} spread between the beginning and end of transition covers almost two orders of magnitude. This observation reinforces the approximate character of the threshold value $Ra_{*y} \sim 10^{13}$ used in eqs. (4.108)–(4.109). See also the transition criterion derived in Section 6.4. The effect of wall inclination on transition along an *isothermal* wall in water (Pr $\sim$ 6) is [37]:

ϕ	Ra_y
$0°$	8.7×10^8
$20°$	2.5×10^8
$45°$	1.7×10^7
$60°$	7.7×10^5

Once again, the transition Rayleigh number $[Ra_y = (g\beta y^3 \Delta T)/\alpha\nu]$ decreases as the angle ϕ increases.

4.11.3   Horizontal Walls

The flow changes its character as the tilt angle ϕ increases beyond the moderate values considered in Fig. 4.15. Two flow types are encountered in the extreme where the plane wall becomes horizontal (Fig. 4.16). When the wall is heated and faces upward, or when it is cooled and faces downward, the flow leaves the boundary layer as a vertical plume rooted in the central region of the wall. When the temperature difference is sufficiently large, the heated fluid rises from all over the surface. As illustrated in Fig. 4.17, this flow is intermittent and consists of balls of heated fluid (called *thermals*) that rise in buckling fashion through the colder fluid [38].

In cases where the surface is hot and faces downward, or when it is cold and faces upward, the boundary layer covers the entire surface, and the flow spills
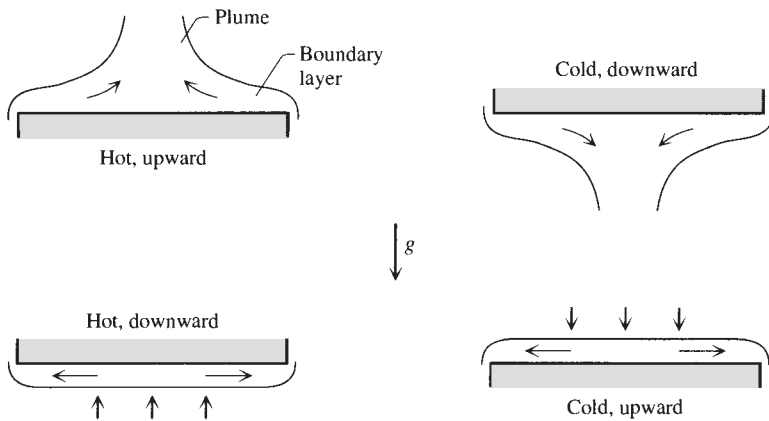
Figure 4.16   Horizontal surfaces with plume (top row) and without plume (bottom row).
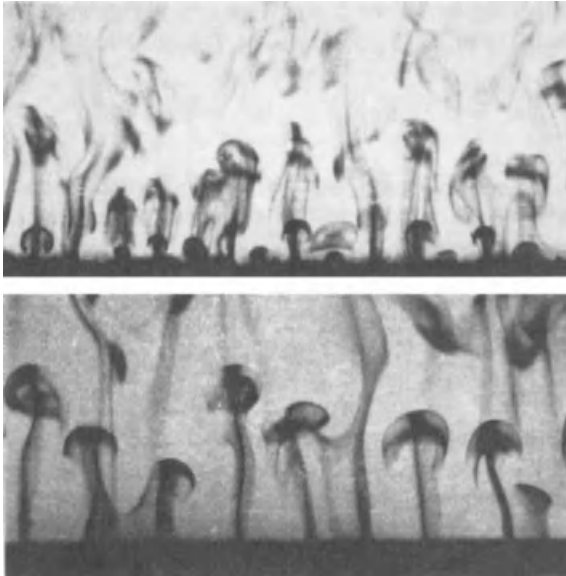
Figure 4.17   Intermittent rise of heated fluid (thermals) from a horizontal surface facing upward in a colder pool of water. (Reprinted with permission from E. M. Sparrow et al., *Journal of Fluid Mechanics*, Vol. 41, pp. 793–800, 1970. Copyright © 1970 Cambridge University Press.)

over the edges. This situation is illustrated in the lower half of Fig. 4.16. A two-sided plate, hot or cold, will have flow of one type on the top side and flow of the other type on the bottom side.

Average Nusselt number measurements for several horizontal-plate configurations have been correlated by defining the *characteristic length* of the plane surface [39]:

$$L = \frac{A}{p} \tag{4.118}$$

In this definition, A is the area of the plane surface and p is the perimeter of A. If A is a disk of diameter D, then $L = D/4$. The $\overline{\mathrm{Nu}}_L$ formulas listed below are valid for Prandtl numbers greater than 0.5. The average Nusselt number $\overline{\mathrm{Nu}}_L$ and the Rayleigh number Ra_L are both based on L.

In the case of hot surfaces facing upward or cold surfaces facing downward (Fig. 4.16, top), the Nusselt number varies as [40]

$$\overline{\mathrm{Nu}}_L = \begin{cases} 0.54\mathrm{Ra}_L^{1/4} & (10^4 < \mathrm{Ra}_L < 10^7) \quad (4.119) \\ 0.15\mathrm{Ra}_L^{1/3} & (10^7 < \mathrm{Ra}_L < 10^9) \quad (4.120) \end{cases}$$

The corresponding correlation for hot surfaces facing downward or cold surfaces facing upward (Fig. 4.16, bottom) is (cf. Ref. 41, p. 548)

$$\overline{\mathrm{Nu}}_L = 0.27\mathrm{Ra}_L^{1/4} \qquad (10^5 < \mathrm{Ra}_L < 10^{10}) \tag{4.121}$$

Equations (4.119)–(4.121) are for isothermal surfaces. The same correlations can be used for uniform-flux surfaces, noting that in those cases, $\overline{\mathrm{Nu}}_L$ and Ra_L would be based on the *L-averaged* temperature difference between the surface and the surrounding fluid. The flux Rayleigh number Ra_{*L} can be made to appear on the right side by noting that $\mathrm{Ra}_L = \mathrm{Ra}_{*L}/\overline{\mathrm{Nu}}_L$.

4.11.4 Horizontal Cylinder

The natural convection around an isothermal cylinder positioned horizontally in a fluid reservoir (Fig. 4.18) is similar to the flow along a vertical surface. The difference is that now the wall is curved, and instead of the wall height y (or H), the vertical dimension is the cylinder diameter D. These similarities explain why the heat transfer correlation for horizontal cylinders [33],

$$\overline{\mathrm{Nu}}_D = \left\{ 0.6 + \frac{0.387 \mathrm{Ra}_D^{1/6}}{\left[1 + (0.559/\mathrm{Pr})^{9/16}\right]^{8/27}} \right\}^2 \tag{4.122}$$

has the same form as the vertical wall correlation (4.104). Equation (4.122) is valid for $10^{-5} < \mathrm{Ra}_D < 10^{12}$ and the entire Prandtl number range. The average Nusselt number and the Rayleigh number are based on diameter,

$$\overline{\mathrm{Nu}}_D = \frac{\overline{q''_{w,D}}}{\Delta T} \frac{D}{k}, \qquad \mathrm{Ra}_D = \frac{g\beta\,\Delta T\,D^3}{\alpha\nu} \tag{4.123}$$

4.11.5 Sphere

The flow around a sphere suspended in a pool at a different temperature has the general features outlined in Fig. 4.18. The vertical dimension of the spherical
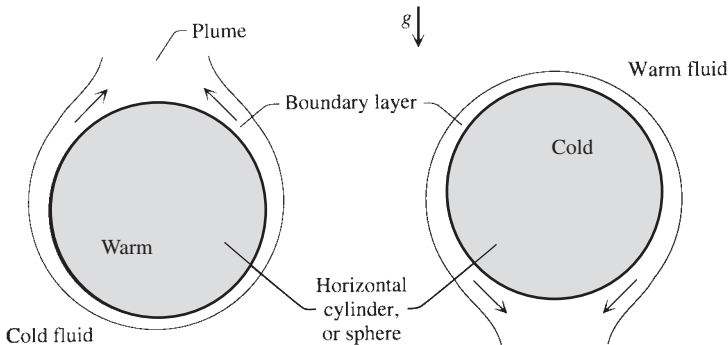
Figure 4.18 Horizontal cylinder, or sphere, immersed in a fluid at a different temperature.

body is its diameter D, on which both $\overline{\mathrm{Nu}}_D$ and Ra_D are based [cf. eqs. (4.123)]. Heat transfer data are correlated well by the formula [42]

$$\overline{\mathrm{Nu}}_D = 2 + \frac{0.589 \mathrm{Ra}_D^{1/4}}{[1 + (0.469/\mathrm{Pr})^{9/16}]^{4/9}} \tag{4.124}$$

in which the appropriate ranges are $\mathrm{Pr} \gtrsim 0.7$ and $\mathrm{Ra}_D < 10^{11}$.

4.11.6   Vertical Cylinder

There are three surfaces in the vertical-cylinder geometry: the top and bottom disks, which can be treated as in Section 4.11.3, and the lateral surface. The boundary layer flow that develops over the lateral surface is illustrated in Fig. 4.19. When the boundary layer thickness δ_T is much smaller than the cylinder diameter D, the curvature of the lateral surface does not play a role, and the Nusselt number can be calculated with the vertical-wall formulas (4.104)–(4.107). Note that if H is the height of the cylinder, and if $\mathrm{Pr} \gtrsim 1$, the δ_T criterion requires that

$$\frac{D}{H} > \mathrm{Ra}_H^{-1/4} \tag{4.125}$$

The inequality above and the simplified heat transfer calculation recommended by it represent the ''thick cylinder'' limit. The opposite limit is illustrated on the right side of Fig. 4.19. An integral heat transfer solution that accounts for the effect of wall curvature in the laminar regime is [43]

$$\overline{\mathrm{Nu}}_H = \frac{4}{3}\left[\frac{7\mathrm{Ra}_H\ \mathrm{Pr}}{5\,(20 + 21\,\mathrm{Pr})}\right]^{1/4} + \frac{4(272 + 315\,\mathrm{Pr})H}{35(64 + 63\,\mathrm{Pr})D} \tag{4.126}$$

Figure 4.19   Vertical cylinders with natural convection boundary layers on the lateral surfaces.

where $\overline{\mathrm{Nu}}_H = \overline{h}H/k$, $\mathrm{Ra}_H = (g\beta\,\Delta T\,H^3)/\alpha\nu$, $\overline{h}$ is the wall-averaged heat transfer coefficient, and ΔT is the temperature difference between the surface and the fluid reservoir.
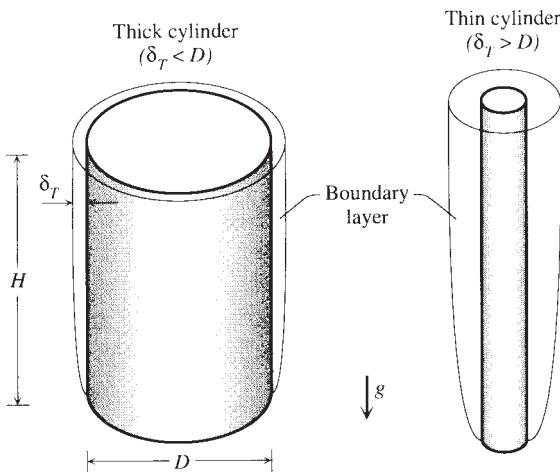
4.11.7   Other Immersed Bodies

So far, we have reviewed the simplest and most common body shapes that are encountered in calculations of external natural convection. It turns out that the heat transfer from bodies of other, less regular shapes follows $\overline{\mathrm{Nu}}$–Ra relations that are similar to what we have seen so far. This similarity and the general need for fewer and simpler formulas continue to stimulate research on a universal heat transfer correlation for immersed bodies of various shapes. The simplest formula of this kind was proposed by Lienhard [44],

$$\overline{\mathrm{Nu}}_l \cong 0.52\mathrm{Ra}_l^{1/4} \tag{4.127}$$

in which $\overline{\mathrm{Nu}}_l = hl/k$, $\mathrm{Ra}_l = (g\beta\,\Delta T\,l^3)/\alpha\nu$, and $\overline{h}$ is the heat transfer coefficient averaged over the entire surface of the body. Lienhard's length l, on which both Nu_l and Ra_l are based, is the distance traveled by the boundary layer fluid while in contact with the body. In the case of a horizontal cylinder, for example, $l = \pi D/2$. Equation (4.127) should be accurate within 10 percent provided that $\mathrm{Pr} \gtrsim 0.7$ and the Rayleigh number is sufficiently large so that the boundary layer is thin.

Yovanovich [45] developed a correlation that covers the entire laminar range, $0 < \mathrm{Ra}_{\mathscr{L}} < 10^8$ that includes the limit of pure conduction $\mathrm{Ra}_{\mathscr{L}} \to 0$. As length scale, he used the square root of the entire surface of the immersed body,

$$\mathscr{L} = A^{1/2} \tag{4.128}$$

and defined $\overline{\mathrm{Nu}}_{\mathscr{L}} = \overline{h}\mathscr{L}/k$ and $\mathrm{Ra}_{\mathscr{L}} = (g\beta\,\Delta T\,\mathscr{L}^3)/\alpha\nu$. The correlation contains two constants,

$$\overline{\mathrm{Nu}}_{\mathscr{L}} = \overline{\mathrm{Nu}}_{\mathscr{L}}^0 + \frac{0.67G_{\mathscr{L}}\,\mathrm{Ra}_{\mathscr{L}}^{1/4}}{[1+(0.492/\,\mathrm{Pr})^{9/16}]^{4/9}} \tag{4.129}$$

namely, the conduction-limit Nusselt number $\overline{\mathrm{Nu}}_{\mathscr{L}}^0$ and the geometric parameter $G_{\mathscr{L}}$. The latter is a weak function of body shape, aspect ratio, and orientation in the gravitational field. Table 4.3 lists the values of these two constants for the bodies and orientations shown in Fig. 4.20. These values do not vary appreciably; therefore, a general expression based on the average values of $\overline{\mathrm{Nu}}_{\mathscr{L}}^0$ and $G_{\mathscr{L}}$ and valid for $\mathrm{Pr} \gtrsim 0.7$ is [45]

$$\overline{\mathrm{Nu}}_{\mathscr{L}} \cong 3.47 + 0.51\mathrm{Ra}_{\mathscr{L}}^{1/4} \tag{4.130}$$

A more extensive correlation that covers the conduction, laminar, and turbulent regimes was developed by Hassani and Hollands [46]. This correlation employs two length scales, one of which is $\mathscr{L}$, eq. (4.128). It covers the Rayleigh number range 0–10^{14}.

Table 4.3   Constants for Yovanovich's correlation [45] for laminar natural convection heat transfer from immersed bodies (Fig. 4.20)

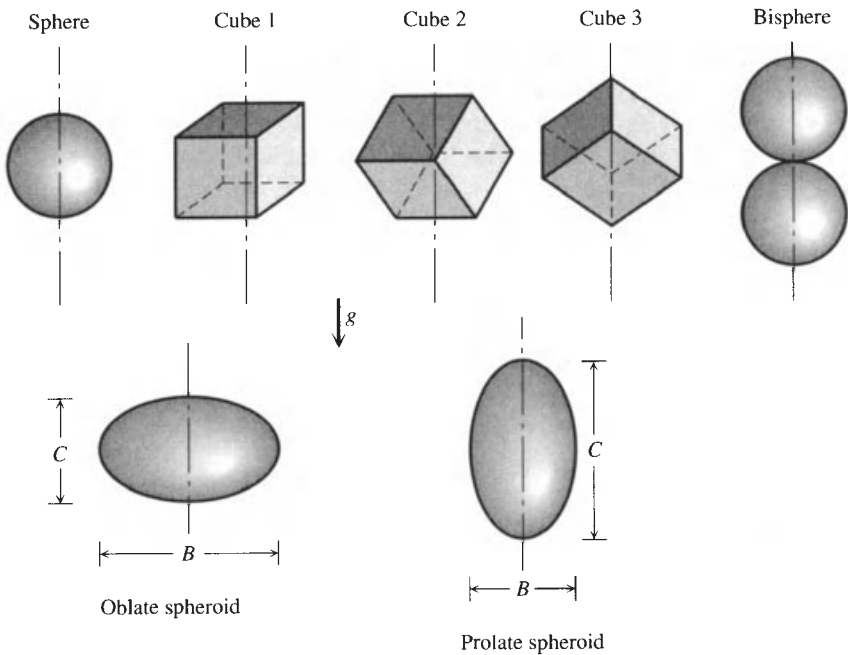| Body Shape	$\overline{Nu}_{\mathcal{L}}^{0}$	$G_{\mathcal{L}}$
Sphere	3.545	1.023
Bisphere	3.475	0.928
Cube 1	3.388	0.951
Cube 2	3.388	0.990
Cube 3	3.388	1.014
Vertical cylinder[a]	3.444	0.967
Horizontal cylinder[a]	3.444	1.019
Cylinder[a] at $45°$	3.444	1.004
Prolate spheroid ($C/B = 1.93$)	3.566	1.012
Oblate spheroid ($C/B = 0.5$)	3.529	0.973
Oblate spheroid ($C/B = 0.1$)	3.342	0.768

[a]Short cylinder, $H = D$.

Figure 4.20   Shapes and orientations of bodies immersed in a fluid (Table 4.3).

4.12 STACK OF VERTICAL HEAT-GENERATING PLATES

Here we consider the natural convection analog of the forced convection question posed in Section 3.6. The optimization of spacings for natural convection was the first theoretical step toward optimal internal structure (cf. the 1984 edition, p. 157, problem 11) and the philosophy of *design with constructal theory* [47]. This step also marked the beginning of *the method of intersecting the asymptotes*. For a current generalization and use of the method, see Lewins [48].

   With reference to Fig. 4.21, we seek the optimal spacing D so that the heat transfer rate from the vertical stack to the ambient (T_∞) is maximized. This problem is fundamental in the cooling of electronic packages, where the objective is to maximize the density of heat-generating electronics that can be fitted in a package of specified volume. In Fig. 4.21, the package volume is LHW, where W is the width perpendicular to the plane of the figure.

   The simplest way to solve this problem is by recognizing the limiting regimes ($D \to 0$ versus $D \to \infty$) of the stack cooling mechanism. For this analysis it is sufficient to assume that the surface of each board is smooth and isothermal at T_0 and that the board thickness t is negligible with respect to D. The number of boards is $n \cong L/D$, and the parameters H, W, T_0, T_∞, and L are assumed given.

(a) Small Spacings Limit. Consider first the limit of vanishingly small plate-to-plate spacing, $D \to 0$. In this limit we can use with confidence eq. (4.91) for the overall heat transfer rate extracted from the two surfaces of one channel,

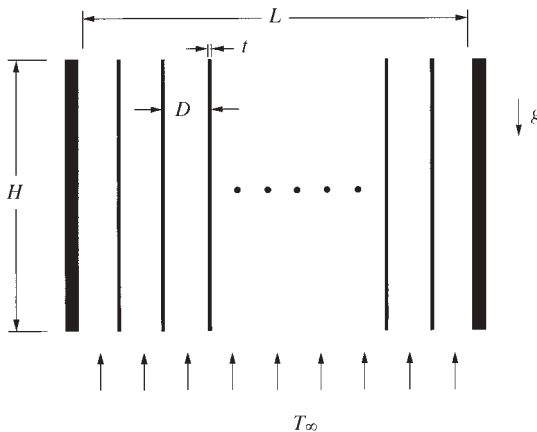$$q_1 = \frac{\rho g \beta c_p (\Delta T)^2 D^3}{12\nu} W \tag{4.131}$$

Figure 4.21   Vertical stack of heat-generating plates cooled by natural convection.
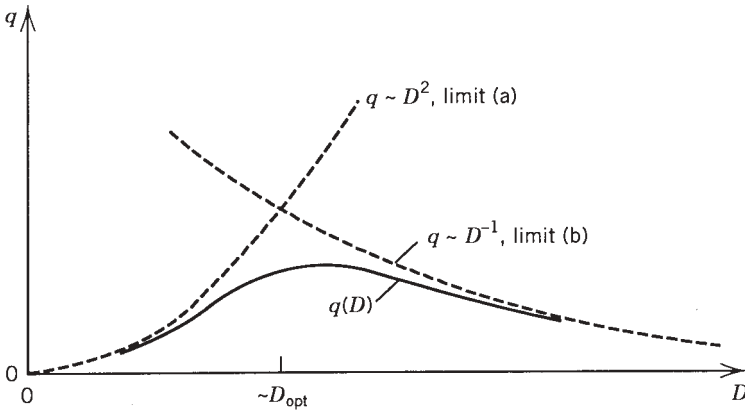
Figure 4.22   Optimal plate-to-plate spacing as the intersection of (a) the small-D asymptote with (b) the large-D asymptote.

where $\Delta T = T_0 - T_\infty$. The total number of channels is L/D; therefore, the total heat transfer rate from the assembly is

$$q_a = q_1 \frac{L}{D} = \frac{\rho g \beta c_p (\Delta T)^2 D^3}{12\nu} W \frac{L}{D} \tag{4.132}$$

This shows that in the $D \to 0$ limit, the total heat transfer rate decreases as D^2. This trend is shown in Fig. 4.22.

(b) Large Spacings Limit. Consider now the limit in which the spacing D is sufficiently large, that is, larger than the thickness of the air boundary layer formed on one of the vertical surfaces, $D > H \, \mathrm{Ra}_H^{-1/4}$, where $\mathrm{Ra}_H = (g\beta H^3 \Delta T)/\alpha\nu$ and $\Delta T = T_0 - T_\infty$. The boundary layers are distinct (thin compared with D), and the center of the plate-to-plate spacing is occupied by T_∞-air. The number of air boundary layers is $2(L/D)$ because there are two for each D spacing. The corresponding formula for the total heat transfer rate is

$$q_b = 2 \frac{L}{D} q_{BL} \tag{4.133}$$

where q_{BL} is the heat transfer through one boundary layer (one surface $W \times H$):

$$q_{BL} = \bar{h}_H WH \, \Delta T \tag{4.134}$$

We set $\mathrm{Pr} = 0.72$ and calculate the average heat transfer coefficient based on Table 4.2, where $\overline{\mathrm{Nu}} = (4/3)\mathrm{Nu} = (4/3)0.387 = 0.516$,

$$\bar{h}_H = \frac{k}{H} 0.516 \mathrm{Ra}_H^{1/4} \tag{4.135}$$

In conclusion, in the large-D limit, the total heat transfer rate is proportional to $1/D$:

$$q_b = 2\frac{L}{D} WH \,\Delta T \frac{k}{H} 0.516\mathrm{Ra}_H^{1/4} \tag{4.136}$$

Intersection of Asymptotes. We have determined the two asymptotes of the real (unknown) curve of q versus D. Figure 4.22 shows that the asymptotes intersect above what would be the q maximum of the actual curve. The optimum spacing (D_{opt}) can be estimated (approximately) as the D value where the two asymptotes intersect,

$$q_a \cong q_b \tag{4.137}$$

By using eqs. (4.132) and (4.136) and setting $D = D_{opt}$, we obtain, in order,

$$\mathrm{Ra}_{D_{opt}} \sim 12.4\mathrm{Ra}_H^{1/4} \tag{4.138}$$

$$D_{opt} \sim 2.3H\mathrm{Ra}_H^{-1/4} \tag{4.139}$$

The maximum heat transfer rate that corresponds to this optimal spacing is obtained by placing $D = D_{opt}$ in eq. (4.136) or (4.132):

$$q_{max} \lesssim 0.45k \,\Delta T\frac{LW}{H}\mathrm{Ra}_H^{1/2} \tag{4.140}$$

The inequality sign is a reminder that the peak of the actual curve q versus D is located under the intersection of the two asymptotes, as shown in Fig. 4.22. Despite this inequality, the right side of eq. (4.140) represents the correct order of magnitude of q_{max}. The maximum heat-generation (or electronics) density q_{max}/HLW is proportional to $H^{-1/2}\Delta T^{3/2}$ because Ra_H is proportional to $H^3\Delta T$.

I first proposed this problem and method of solution in the 1984 edition of this book, specifically, as Problem 11 on p. 157. The same problem was analyzed simultaneously by a much lengthier method by Bar-Cohen and Rohsenow [49]. In fact, both versions, my 1984 book and Ref. 49, appeared in print at exactly the same time, in August 1984, displayed side by side in the book exhibit at the 1984 National Heat Transfer Conference in Niagara Falls, New York. I remember my first reaction to this amazing coincidence. Warren Rohsenow had been my heat transfer professor at MIT. I thought that if a full-length article in a top journal was needed to determine what my students could derive on the back of an envelope by solving a homework problem, then my method of intersecting the asymptotes is novel and extremely powerful.

History has proven this to be true. The identification of spacings for the internal structures of volumes cooled by natural, forced and mixed convection, laminar and turbulent, has become a very active and distinct research direction in heat transfer and constructal design. This growing field is reviewed in a recent book [47].

4.13 DISTRIBUTION OF HEAT SOURCES ON A VERTICAL WALL

Consider a vertical wall of height H in contact with a fluid reservoir of temperature T_∞ (Fig. 4.23) [50]. The wall is heated by horizontal line heat sources. Each source has the strength q'(W/m). To start, assume that the heat sources appear as points on the wall sketched in Fig. 4.23. Each line heat source extends in the direction perpendicular to the figure. The flow is two-dimensional and by natural convection in the boundary layer regime. The number of sources per unit of wall height is unknown, $N'(y)$,

$$N' = \frac{\text{number of sources}}{\text{unit length}} \tag{4.141}$$

According to constructal design (the optimal distribution of imperfection), the global system (the wall and the fluid that bathes it) will perform best when all its elements work as hard as the hardest working elements [47]. This means that if T_{max} is the maximal temperature that must not be exceeded at the hot spots that occur on the wall, then the entire wall should operate at T_{max}. The problem is to determine the distribution of heat sources on the wall, $N'(y)$, such that the wall temperature is near the allowed limit,

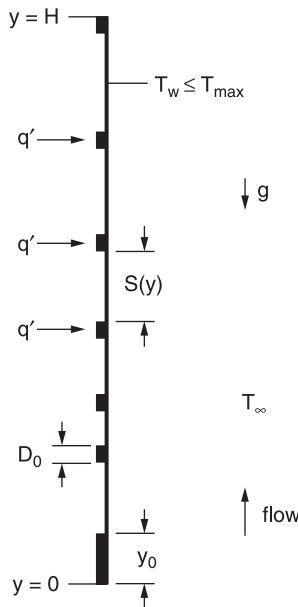$$T_w(y) \cong T_{max}, \qquad \text{constant} \tag{4.142}$$

Figure 4.23   The multiple length scales of the nonuniform distribution of finite-size heat sources on a vertical wall.

Assume that the density of line sources is sufficiently high so that we may regard the distribution of discrete q' sources as a nearly continuous distribution of nonuniform heat flux,

$$q''(y) = q'N' \qquad (4.143)$$

The heat flux distribution that corresponds to eqs. (4.142) and (4.143) and $\Pr \gtrsim 1$ is approximately

$$\mathrm{Nu} \cong 0.5\,\mathrm{Ra}_y^{1/4} \qquad (4.144)$$

or, more explicitly,

$$\frac{q''}{T_{\max} - T_\infty}\frac{y}{k} \cong 0.5 \left[\frac{g\beta\,(T_{\max} - T_\infty)\,y^3}{\alpha\nu} \right]^{1/4} \qquad (4.145)$$

By eliminating $q''(y)$ between eqs. (4.143) and (4.145), we obtain the required distribution of heat sources:

$$N'(y) \cong 0.5\frac{k}{q'}(T_{\max} - T_\infty)^{5/4}\left(\frac{g\beta}{\alpha\nu}\right)^{1/4} y^{-1/4} \qquad (4.146)$$

This function shows that the heat sources must be positioned closer when they are near the start of the boundary layer. They must be farther apart on sections of the wall near $y = H$. The total number of q' sources that must be installed on the wall of height H is

$$N = \int_0^H N'\,dy \cong \frac{2}{3}\frac{k}{q'}(T_{\max} - T_\infty)\,\mathrm{Ra}^{1/4} \qquad (4.147)$$

where $\mathrm{Ra} = g\beta H^3\,(T_{\max} - T_\infty)/(\alpha\nu)$. The Rayleigh number is a dimensionless parameter that accounts for two global constraints, the wall height H and the maximal allowable excess temperature at the hot spots. The total heat transfer rate from the q' sources to the T_∞ fluid is

$$Q' = q'N \cong \tfrac{2}{3}k(T_{\max} - T_\infty)\mathrm{Ra}^{1/4} \qquad (4.148)$$

This represents the global performance level to which any of the nonuniform distributions of concentrated heat sources will aspire.

The physical implementation of the preceding results begins with the observation that the smallest scale that can be manufactured in the heating scheme of Fig. 4.23 is the D_0 height of the line heat source. The local spacing between two adjacent lines is $S(y)$. This spacing varies with altitude in accordance with the N' distribution function (4.146). The wall height interval that corresponds to a single line heat source is $D_0 + S(y)$. This means that the local number of heat sources per unit of wall height is

$$N'(y) = \frac{1}{D_0 + S(y)} \qquad (4.149)$$

The heat strength of one source (q') is spread uniformly over the finite height of the source, $q_0'' = q'/D_0$. The heat flux q_0'' is a known constant, unlike the function $q''(y)$ of eq. (4.145), which will be the result of design. By eliminating $N'(y)$ between eqs. (4.146) and (4.149), we obtain the rule for how the wall heating scheme should be constructed:

$$\frac{S(y)}{H} \cong \frac{2q'\,\mathrm{Ra}^{-1/4}}{k\,(T_{\max} - T_\infty)} \left(\frac{y}{H}\right)^{1/4} - \frac{D_0}{H} \tag{4.150}$$

The function $S(y)$ of eq. (4.150) has negative values in the vicinity of the start of the boundary layer. The smallest value that S can have is zero. This means that there is a starting wall section ($0 < y < y_0$) over which the line sources should be mounted flush against each other. The height of this section (y_0) is obtained by setting $S = 0$ and $y = y_0$ in eq. (4.150).

$$\frac{y_0}{H} \cong \mathrm{Ra} \left(\frac{D_0}{H}\right)^4 \left[\frac{k\,(T_{\max} - T_\infty)}{2q'}\right]^4 \tag{4.151}$$

From $y = 0$ to $y = y_0$ the wall is heated with uniform flux of strength $q_0'' = q'/D_0$. The number of sources that cover the height y_0 is $N_0 = y_0/D_0$. Above $y = y_0$ the wall is heated on discrete patches of height D_0, and the spacing between patches increases with height.

These basic features of the design are illustrated in Fig. 4.23. The design has multiple length scales: H, D_0, y_0, and $S(y)$. The first two are constraints. The last two are interrelated and are results of global maximization of performance subject to the constraints. Taken together, the lengths represent the constructal design—the flow architecture that out of an infinity of possible architectures brings the entire wall to the highest performance level possible.

This fundamental problem of constructal design for natural convection [47, 50] is driving a new research domain (e.g., Refs. 51–53), which is reviewed in Ref. 47.

REFERENCES

1. A. Bejan, *Entropy Generation through Heat and Fluid Flow*, Wiley, New York, 1982, Chapter 3.

2. A. Bejan, *Advanced Engineering Thermodynamics*, 3rd ed., Wiley, Hoboken, 2006.

3. A. Bejan and S. Lorente, The constructal law of design and evolution in nature, *Phil. Trans. R. Soc. B.*, Vol. 365, 2010, pp. 1335–1347.

4. A. Bejan and S. Lorente, Constructal theory of generation of configuration in nature and engineering, *J. Appl. Phys.*, Vol. 100, 2006, 041301.

5. A. Bejan and S. Lorente, The constructal law and the evolution of design in nature, *Phys. Life Rev.*, Vol. 8, 2011, pp. 209–240.

6. V. A. F. Costa, Thermodynamics of natural convection with viscous dissipation, *Int. J. Heat Mass Transfer*, Vol. 48, 2005, pp. 2333–2341.

7. M. Pons and P. Le Quéré, An example of entropy balance in natural convection, 1: The *usual* Boussinesq equations; 2: The *thermodynamic* Boussinesq equations, *C. R. Mec.* (formerly *C. R. Acad. Sci. Mec*), Vol. 333, 2005, pp. 127–138.

8. A. H. Reis and A. Bejan, Constructal theory of global circulation and climate, *Int. J. Heat Mass Transfer*, Vol. 49, 2006, pp. 1857–1975.

9. M. Clausse, F. Meunier, A. H. Reis, and A. Bejan, Climate change, in the framework of the Constructal Law, *Int. J. Global Warming*, Vol. 4, Nos. 3/4, 2012, pp. 242–260.

10. A. Bejan and H. M. Paynter, *Solved Problems in Thermodynamics*, Massachusetts Institute of Technology, Department of Mechanical Engineering, Cambridge, MA, 1976, Problem VII-A.

11. A. Bejan, *Entropy Generation through Heat and Fluid Flow*, Wiley, New York, 1982.

12. A. Bejan and J. P. Zane, *Design in Nature. How the Constructal Law Governs Evolution in Biology, Physics, Technology and Social Organization*, Doubleday, New York, 2012.

13. H. K. Kuiken, An asymptotic solution for large Prandtl number free convection, *J. Eng. Math.*, Vol. 2, 1968, pp. 355–371.

14. H. K. Kuiken, Free convection at low Prandtl numbers, *J. Fluid Mech.*, Vol. 37, 1969, pp. 785–798.

15. H. B. Squire, in S. Goldstein, ed., *Modern Developments in Fluid Dynamics*, Vol. II, Dover, New York, 1965, pp. 641–643.

16. S. Ostrach, An analysis of laminar-free-convection flow and heat transfer about a flat plate parallel to the direction of the generating body force, NACA TN 2635, 1952.

17. E. Schmidt and W. Beckmann, Das Temperatur und Geschwindigkeitsfeld von einer wärme abgebenden senkrechten Platte bei natürlicher Konvektion, *Forsch. Ingenieurwes.*, Vol. 1, 1930, p. 391.

18. E. J. LeFevre, Laminar free convection from a vertical plane surface, Paper 1-168 presented at the 9th International Congress on Applied Mechanics, Brussels, 1956.

19. E. M. Sparrow, Laminar free convection on a vertical plate with prescribed nonuniform wall heat flux or prescribed nonuniform wall temperature, NACA TN 3508, July 1955.

20. E. M. Sparrow and J. L. Gregg, Laminar free convection from a vertical plate with uniform surface heat flux, *Trans. ASME*, Vol. 78, 1956, pp. 435–440.

21. E. M. Sparrow and J. L. Gregg, Similar solutions for free convection from a non-isothermal vertical plate, *Trans. ASME*, Vol. 80, 1958, pp. 379–386.

22. K. T. Yang, Possible similarity solutions for laminar free convection on vertical plates and cylinders, *J. Appl. Mech.*, Vol. 27, 1960, pp. 230–236.

23. A. Bejan, Note on Gill's solution for free convection in a vertical enclosure, *J. Fluid Mech.*, Vol. 90, 1979, pp. 561–568.

24. C. C. Chen and R. Eichhorn, Natural convection from a vertical surface to a thermally stratified medium, *J. Heat Transfer*, Vol. 98, 1976, pp. 446–451.

25. W. J. Minkowycz and E. M. Sparrow, Local nonsimilar solution for natural convection on a vertical cylinder, *J. Heat Transfer*, Vol. 96, 1974, pp. 1778–1783.

26. R. Anderson and A. Bejan, Natural convection on both sides of a vertical wall separating fluids at different temperatures, *J. Heat Transfer*, Vol. 102, 1980, pp. 630–635.

27. R. Anderson and A. Bejan, Heat transfer through single and double vertical walls in natural convection: theory and experiment, *Int. J. Heat Mass Transfer*, Vol. 24, 1981, pp. 1161–1620.

28. A. Koonsrisuk, S. Lorente, and A. Bejan, Constructal solar chimney configuration, *Int. J. Heat Mass Transfer*, Vol. 53, 2010, pp. 327–333.

29. J. R. Lloyd and E. M. Sparrow, Combined forced and free convection flow on vertical surfaces, *Int. J. Heat Mass Transfer*, Vol. 13, 1970, pp. 434–438.

30. Y. Jaluria, Natural convection, in A. Bejan and A. D. Kraus, eds., *Heat Transfer Handbook*, Wiley, New York, 2003.

31. T. de Lorenzo and J. Padet, Parametric study of transient free convection heat transfer, *Int. J. Heat Mass Transfer*, Vol. 45, 2002, pp. 2629–2632.

32. A. Bejan and J. L. Lage, The Prandtl number effect on the transition in natural convection along a vertical surface, *J. Heat Transfer*, Vol. 112, 1990, pp. 787–790.

33. S. W. Churchill and H. H. S. Chu, Correlating equations for laminar and turbulent free convection from a vertical plate, *Int. J. Heat Mass Transfer*, Vol. 18, 1975, pp. 1323–1329.

34. G. C. Vliet and C. K. Liu, An experimental study of turbulent natural convection boundary layers, *J. Heat Transfer*, Vol. 91, 1969, pp. 517–531.

35. G. C. Vliet and D. C. Ross, Turbulent natural convection on upward and downward facing inclined heat flux surfaces, *J. Heat Transfer*, Vol. 97, 1975, pp. 549–555.

36. G. C. Vliet, Natural convection local heat transfer on constant-heat-flux inclined surfaces, *J. Heat Transfer*, Vol. 91, 1969, pp. 511–516.

37. J. R. Lloyd and E. M. Sparrow, On the instability of natural convection flow on inclined plates, *J. Fluid Mech.*, Vol. 42, 1970, pp. 465–470.

38. E. M. Sparrow, R. B. Husar, and R. J. Goldstein, Observations and other characteristics of thermals, *J. Fluid Mech.*, Vol. 41, 1970, pp. 793–800.

39. R. J. Goldstein, E. M. Sparrow, and D. C. Jones, Natural convection mass transfer adjacent to horizontal plates, *Int. J. Heat Mass Transfer*, Vol. 16, 1973, pp. 1025–1035.

40. J. R. Lloyd and W. R. Moran, Natural convection adjacent to horizontal surfaces of various planforms, Paper 74-WA/HT-66, ASME, New York, 1974.

41. F. P. Incropera and D. P. DeWitt, *Fundamentals of Heat and Mass Transfer*, 3rd ed., Wiley, New York, 1990, pp. 539–540.

42. S. W. Churchill, Free convection around immersed bodies, in E. U. Schünder, ed., *Heat Exchanger Design Handbook*, Hemisphere, New York, 1983, Section 2.5.7.

43. E. J. LeFevre and A. J. Ede, Laminar free convection from the outer surface of a vertical circular cylinder, in *Proceedings of the 9th International Congress on Applied Mechanics*, *Brussels*, Vol. 4, 1956, pp. 175–183.

44. J. H. Lienhard, On the commonality of equations for natural convection from immersed bodies, *Int. J. Heat Mass Transfer*, Vol. 16, 1973, pp. 2121–2123.

45. M. M. Yovanovich, On the effect of shape, aspect ratio and orientation upon natural convection from isothermal bodies of complex shape, ASME HTD-Vol. 82, 1987, pp. 121–129.

46. A. V. Hassani and K. G. T. Hollands, On natural convection heat transfer from three-dimensional bodies of arbitrary shape, *J. Heat Transfer*, Vol. 111, 1989, pp. 363–371.

47. A. Bejan and S. Lorente, *Design with Constructal Theory*, Wiley, Hoboken, 2008.

48. J. Lewins, Bejan's constructal theory of equal potential distribution, *Int. J. Heat Mass Transfer*, Vol. 46, 2003, pp. 1541–1543.

49. A. Bar-Cohen and W. M. Rohsenow, Thermally optimum spacing of vertical, natural convection cooled, parallel plates, *J. Heat Transfer*, Vol. 106, 1984, pp. 116–123.

50. A. K. da Silva, S. Lorente, and A. Bejan, Optimal distribution of discrete heat sources on a wall with natural convection, *Int. J. Heat Mass Transfer*, Vol. 47, 2004, pp. 203–214.

51. T. Dias, Jr. and L. F. Milanez, Optimal location of heat sources on a vertical wall with natural convection through genetic algorithms, *Int. J. Heat Mass Transfer*, Vol. 49, 2006, pp. 2090–2096.

52. T. V. V. Sudhakar, C. Balaji, and S. P. Venkateshan, A heuristic approach to optimal arrangement of multiple heat sources under conjugate natural convection, *Int. Heat Mass Transfer*, Vol. 53, 2010, pp. 431–444.

53. Q.-H. Deng, Fluid flow and heat transfer characteristics of natural convection in square cavities due to discrete source–sink pairs, *Int. J. Heat Mass Transfer*, Vol. 51, 2008, pp. 5949–5957.

54. J. S. Lim, A. Bejan, and J. H. Kim, The optimal thickness of a wall with convection on one side, *Int. J. Heat Mass Transfer*, Vol. 35, 1992, pp. 1673–1679.

PROBLEMS

4.1. Derive the integral forms of the momentum and energy equations [eqs. (4.40) and (4.41)] by integrating eqs. (4.17) and (4.8) from the wall ($x = 0$) to a plane $x = X$ outside the vertical boundary layer.

4.2. Perform an integral analysis of the natural convection boundary layer by assuming the following temperature and velocity profiles [15]:

$$T - T_\infty = \Delta T \left(1 - \frac{x}{\delta_T} \right)^2, \quad v = V \frac{x}{\delta} \left(1 - \frac{x}{\delta} \right)^2$$

For simplicity, assume that $\delta = \delta_T$. Follow the steps between eqs. (4.42) and (4.49) to show that the local Nusselt number is given by

$$\text{Nu} = \frac{q''}{T_0 - T_\infty} \frac{y}{k} = 0.508 \left(1 + \frac{20}{(21)\,\text{Pr}} \right)^{-1/4} \text{Ra}_y^{1/4}$$

Note that since $\delta_T = \delta$, eq. (4.47) cannot be satisfied by the solution. Comment on the Pr range of validity of this $\delta_T = \delta$ integral solution, and explain why the Nusselt number predicted agrees with more exact calculations over a surprisingly wide range (Fig. 4.6).

4.3. Derive the equations for energy and momentum in the similarity solution formulation [eqs. (4.61) and (4.62)]; start with eqs. (4.56) and (4.57) and exploit the similarity variable transformation (4.55) and (4.58)–(4.60).

4.4. Consider the natural convection heat leak from a life-size room with one 3-m-tall wall exposed to the cold ambient. The room-air temperature is 25°C, while the room-side surface of the cold wall has an average

temperature of $10°C$. If the room circulation is to be simulated in a small laboratory apparatus filled with water, how tall should the water cavity of the apparatus be? In the laboratory water experiment, the temperature difference between the water body and the inner surface of the cooled wall is $10°C$.

4.5. In many analyses of natural convection heat transfer problems, the vertical wall heating a fluid or dividing two differentially heated fluids is modeled as isothermal. This is an approximation valid in some cases and invalid in others. To be isothermal, while bathed by natural convection in boundary layer flow, a vertical solid wall must be thick enough. Comparing the thermal conductance to vertical conduction through the wall ($k_w W/H$) with the thermal conductance to lateral heat transfer through the same wall (and the fluid boundary layer, kH/δ_T), determine below what range of wall widths W the ''isothermal wall'' assumption becomes inadequate (k_W, H, k, and δ_T are the wall thermal conductivity, wall height, fluid thermal conductivity, and thermal boundary layer thickness, respectively). For a wall of fixed geometry (W, H), is the isothermal wall assumption getting better or worse as Ra_H increases?

4.6. Determine the local Nusselt number for the boundary layer natural convection along a $q'' = $ constant vertical wall by performing an integral analysis using the profiles [19]

$$T - T_\infty = \Delta T\left(1 - \frac{x}{\delta_T}\right)^2, \quad v = V\frac{x}{\delta}\left(1 - \frac{x}{\delta}\right)^2$$

and taking $\delta_T = \delta$. Show that the wall temperature distribution is

$$T_0(y) - T_\infty = 1.622\frac{q''y}{k}\left(\frac{\frac{4}{5} + \mathrm{Pr}}{\mathrm{Pr}}\right)^{1/5}\mathrm{Ra}_{*y}^{-1/5}$$

and that the local Nusselt number is given by eq. (4.75).

4.7. Construct the similarity formulation of the boundary layer flow problem along a vertical wall with uniform heat flux. Start with eqs. (4.56) and (4.57) and obtain the equivalent of eqs. (4.61) and (4.62) by first noting the similarity variable dictated by the scaling law (4.69), $\eta = (x/y)\mathrm{Ra}_{*y}^{1/5}$. Compare your final expressions for momentum and energy conservation with the equations of Ref. 20; keep in mind that Ref. 20 uses $(x/y)(\mathrm{Ra}_{*y}/\mathrm{Pr})^{1/5}$ as the similarity variable, not $(x/y)\mathrm{Ra}_{*y}^{1/5}$.

4.8. Consider the integral analysis of laminar natural convection along a vertical wall bathed by a linearly stratified fluid (Fig. 4.9). Starting with eqs. (4.78), show that the integral momentum and energy equations can be expressed as in eqs. (4.79)–(4.81). Solve these equations in the limit of

negligible inertia, $\text{Pr} \to \infty$; show that in this limit the differential equation of $\delta_*(y_*)$ is

$$\frac{d\Delta}{dy_*} = \frac{240 + \frac{8}{3}b\Delta}{1 - by_*}$$

where $\Delta = \delta_*^4$. Approximate this equation via finite differences and integrate it setting $b = 1$. Compare your estimate of the average Nusselt number [eq. (4.83)] with Fig. 4.9 and eq. (4.84).

4.9. Estimate the $\text{Nu}_{0-H}(\omega, \text{Ra}_H)$ function displayed in Fig. 4.10 by matching in series the thermal resistance of one $q'' = \text{constant}$ boundary layer [eq. (4.75)], the thermal resistance of the wall, and finally, the resistance of another $q'' = \text{constant}$ boundary layer. Assume that the temperature along each face of the wall is y-independent and equal to the actual temperature averaged over the wall height. Keep in mind that eq. (4.75) describes the *local* heat transfer (hence, the local temperature difference) and that the end result of this analysis, Nu_{0-H}, describes the *overall* heat transfer. For more details on how to approach this solution, consult Ref. 26.

4.10. An electrical conductor in a piece of electronic equipment may be modeled as an isothermal plate (T_0) oriented vertically. The heat transfer rate generated in the plate and released via laminar natural convection to the ambient (T_∞) is *fixed* and equal to Q. The height of the plate (H) may vary.

(a) Neglecting numerical factors of order 1, what is the relationship between the Nusselt number and the Rayleigh number for this arrangement?

(b) How will the temperature difference $(T_0 - T_\infty)$ vary with the height of the system? In other words, if H increases by a factor of 2, what happens to $(T_0 - T_\infty)$?

4.11. One way to visualize the $y^{1/4}$ dependence of the thickness of the laminar natural convection boundary layer is to execute the experiment shown in Fig. P4.11. The vertical isothermal wall, $T_w = 20°\text{C}$, is placed in contact with an isothermal pool of paraffin, $T_\infty = 35°\text{C}$. Since the solidification point of this paraffin is $T_m = 27.5°\text{C}$, the wall becomes covered with a thin layer of solidified paraffin.

Show that under steady-state conditions, the thickness of the solidified layer, L, is proportional to the laminar boundary layer thickness; that is, it increases in the downward direction as $y^{1/4}$. Calculate L numerically and plot to scale the $L(y)$ shape of the solidified layer. The relevant properties of liquid paraffin are $k_f = 0.15 \text{ W/m} \cdot \text{K}$, $\beta = 8.5 \times 10^{-4} \text{ K}^{-1}$, $\alpha = 9 \times 10^{-4} \text{ cm}^2/\text{s}$, and $\text{Pr} = 55.9$. The thermal conductivity of solid paraffin is $k_s = 0.36 \text{ W/m} \cdot \text{K}$. The overall height of the isothermal wall is $H = 10 \text{ cm}$.
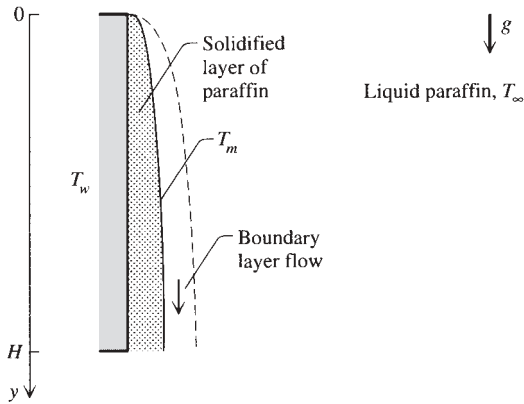
Figure P4.11

4.12. The fully developed natural convection channel flow analysis presented in Section 4.9 refers to only one simple geometry (the parallel-plate channel). Using this analysis as a guideline, develop the corresponding Nusselt number formula for other vertical channel cross sections, for example, **(a)** circular, **(b)** square, and **(c)** equilateral triangle. Express your result in the form

$$\frac{q''_{0-H}H}{(T_0 - T_\infty)k} = (?)\mathrm{Ra}_{D_h}$$

where (?) is a numerical coefficient to be determined for each channel cross-sectional shape and Ra_{D_h} is the Rayleigh number based on hydraulic diameter. [*Hint*: Note that, in general, eq. (4.89) is replaced by

$$\nabla^2 v = -\frac{g\beta}{\nu}(T_0 - T_\infty)$$

which is of the same type as eq. (3.20). The mean velocity solution to this equation may be deduced from the friction factor data assembled in Table 3.2.]

4.13. Find the Rayleigh number range in which the fully developed regime formulas (4.91) are valid by translating the inequality (4.90) in the language of Ra_D and H/D. Demonstrate that the $\mathrm{Ra}_D(H/D)$ criterion determined in this manner is essentially the same as criterion (4.95).

4.14. Prove that for $\mathrm{Pr} < 1$ fluids, the scale criterion for transition from natural convection to forced convection in boundary layer flow along a vertical wall (Fig. 4.13) is given by eq. (4.101).

4.15. One $0.5\,\mathrm{m} \times 0.5\,\mathrm{m}$ vertical wall of parallelepiped water container is heated uniformly by an array of electrical strip heaters mounted on its back. The total heat transfer rate furnished by these heaters is $1000\,\mathrm{W}$. The water

temperature is 25°C. Calculate the height-averaged temperature of the heated surface. Later, verify that most of the boundary layer that rises along this surface is turbulent.

4.16. The air in a room is thermally stratified so that its temperature increases by 5°C for each 1-m rise in altitude. Facing the room air is a 10°C vertical window which is 1 m tall and 0.8 m wide. The room-air temperature at the same level as the window midheight is 20°C. Assume that the natural convection boundary layer that falls along the window is laminar, and calculate the heat transfer rate through the window.

4.17. You have a bottle of beer at room temperature, and you would like to drink it cold as soon as possible. The beer bottle has a height/diameter ratio of about 5. You place the bottle in the refrigerator; however, you have the option of positioning the bottle (1) vertically or (2) horizontally. The refrigerator cools by natural convection (it does not employ forced circulation). Which way should you position the bottle? Describe the goodness of your decision by calculating the ratio t_1/t_2, where t represents the order of magnitude of the time needed for the bottle to reach thermal equilibrium with the refrigeration chamber (base this calculation on scale analysis).

4.18. Consider a vertical wall of height H in contact with an isothermal fluid reservoir, as shown in Fig. 4.1. For the purpose of scale analysis, select the square flow region of height H and horizontal thickness H. Show that if in the momentum equation (4.17) you invoke a balance between friction and buoyancy, the inertia/friction ratio comes out to be of order $Gr_H = (g\beta \, \Delta T \, H^3)/\nu^2$ (note that the $H \times H$ region is not the boundary layer region; hence, the conclusion "inertia/friction $\sim Gr_H$" does not apply to the boundary layer region). Is the vertical velocity scale derived above compatible with the v scale recommended by the energy equation (4.8) for the $H \times H$ region? In other words, is the invoked balance friction $\sim$ buoyancy in the $H \times H$ region realistic?

4.19. The downward trend exhibited versus b by the $\overline{Nu}_H/Ra_H$ curves of Fig. 4.9 can be anticipated by means of a very simple analysis. Let ΔT_{avg} be the average temperature difference between the isothermal wall and the stratified reservoir. Assume a large Prandtl number (Pr $\to \infty$), and estimate the Nusselt number by using eq. (4.65′), in which both $\overline{Nu}_y$ and Ra_y are based on ΔT_{avg} (note also that $y = H$). Multiply and divide this relationship by ΔT_{max} to reshape it in terms of the $\overline{Nu}_H$ and Ra_H groups defined in eqs. (4.83) and (4.81). Show that this relationship becomes

$$\overline{Nu}_H = 0.671\left(1 - \frac{b}{2}\right)^{5/4} Ra_H^{1/4}$$

and that it approximates within 13 percent the values suggested by the Pr $\to \infty$ curve of Fig. 4.9.

4.20. A long, rectangular metallic blade has width $H = 4$ cm and temperature $T_w = 40°$C. It is surrounded on both sides by atmospheric air at $T_\infty = 20°$C. The long side of the blade is always horizontal. Calculate the total heat transfer rate per unit of blade length when the short side of its rectangular shape (H) is **(a)** vertical, **(b)** inclined at $45°$ relative to the vertical, and **(c)** horizontal. Comment on the effect that blade orientation has on the total heat transfer rate.

4.21. The external surface of a spherical container with the diameter $D = 3$ m has a temperature of $10°$C. The container is surrounded by $30°$C air, which is motionless except in the immediate vicinity of the container.

  (a) Calculate the total heat transfer rate absorbed by the spherical container.

  (b) It is proposed to replace the spherical container with one shaped as a horizontal cylinder with the diameter $d = 1.5$ m. This new container would have the same volume as the old one. Calculate the total heat transfer rate absorbed by the cylindrical container.

  (c) Which container design would you choose if your objective is to prevent the warming of the liquid stored inside the container?

4.22. A cubic block of metal is immersed in a pool of $20°$C water and is oriented as ''Cube 1'' in Fig. 4.20. The cube has a 2-cm side and an instantaneous temperature of $80°$C. Calculate the average heat transfer coefficient between the cube and the water by using **(a)** Lienhard's method, eq. (4.127); **(b)** Yovanovich's method, eq. (4.129); and **(c)** Yovanovich's simplified formula (4.130). Comment on the agreement among these three estimates.

4.23. A block of ice has the shape of a parallelepiped with the dimensions indicated in Fig. P4.23. The block is oriented in such a way that two of its long surfaces are horizontal. It is surrounded by $20°$C air from all sides.
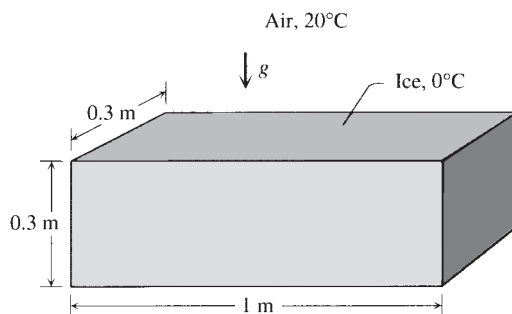

Figure P4.23

Calculate the total heat transfer rate between the ambient air and the ice block, $q(W)$, by estimating the heat transfer through each face. Also calculate the ice melting rate that corresponds to the total heat transfer rate. The ice latent heat of melting is $h_{sf} = 333.4 \, \text{kJ/kg}$.

4.24. Consider again the natural convection heat transfer from air to the ice block described in Problem 4.23. Obtain a ''quick'' estimate of the total heat transfer rate $q(W)$ by using Lienhard's formula (4.127). The length l on which $\overline{\text{Nu}}_l$ and Ra_l are based can be approximated as the half-perimeter of the smaller ($0.3 \, \text{m} \times 0.3 \, \text{m}$) cross section of the ice block (see Fig. P4.23).

4.25. An electrical wire of diameter $D = 1 \, \text{mm}$ is suspended horizontally in air of temperature $20°C$. The Joule heating of the wire is responsible for the heat generation rate $q' = 0.01 \, \text{W/cm}$ per unit length in the axial direction. The wire can be modeled as a cylinder with isothermal surface. Sufficiently far from the wire, the ambient air is motionless. Calculate the temperature difference that is established between the wire and the ambient air. [*Note*: This calculation requires a trial-and-error procedure; expect a relatively small Rayleigh number.]

4.26. The single-pane window problem consists of estimating the heat transfer rate through the vertical glass layer shown in Fig. P4.26. The window separates two air reservoirs of temperatures T_h and T_c. Assuming constant properties, laminar boundary layers on both sides of the glass, and a uniform glass temperature T_w, show that the average heat flux $\overline{q}''$ from T_h to T_c obeys the relationship
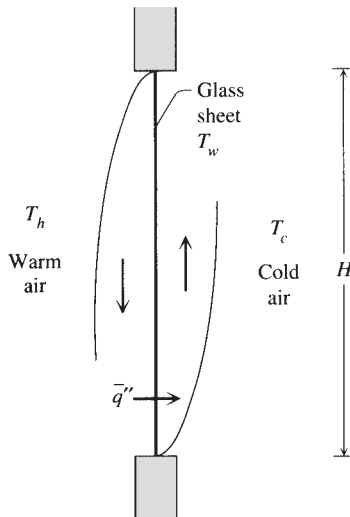

Figure P4.26

$$\frac{\overline{q}''}{T_h - T_c}\frac{H}{k} = 0.217\left[\frac{g\beta\left(T_h - T_c\right)H^3}{\alpha\nu}\right]^{1/4}$$

Use Table 4.2 as a starting point in this analysis, and neglect the thermal resistance due to pure conduction across the glass layer itself.

4.27. Consider again the single-pane window described in Problem 4.26, and model the heat flux through the glass layer as uniform, q''. Starting with the height-averaged version of eq. (4.75) for air, show that the relationship between q'' and the overall temperature difference $T_h - T_c$ is

$$\frac{q''}{T_h - T_c}\frac{H}{k} = 0.252\left[\frac{g\beta\left(T_h - T_c\right)H^3}{\alpha\nu}\right]^{1/4}$$

Compare this result with the formula recommended by the uniform-T_w model in Problem 4.26, and you will get a feel for the certainty with which you can calculate the total heat transfer rate through the window.

4.28. Evaluate the proposal to install windows with glass panes of nonuniform thickness as a means of minimizing the heat leak from a room to the cold outside air. This proposal was stimulated by the thought that since the room-side heat transfer coefficient is higher near the top of the window (at the start of the descending boundary layer), it is there that a thicker glass layer can have the greatest effect on reducing the local heat flux [54]. This thought points toward the tapered glass design illustrated on the left side of Fig. P4.28. The thickness of the glass layer has been exaggerated to make the notation clearer.
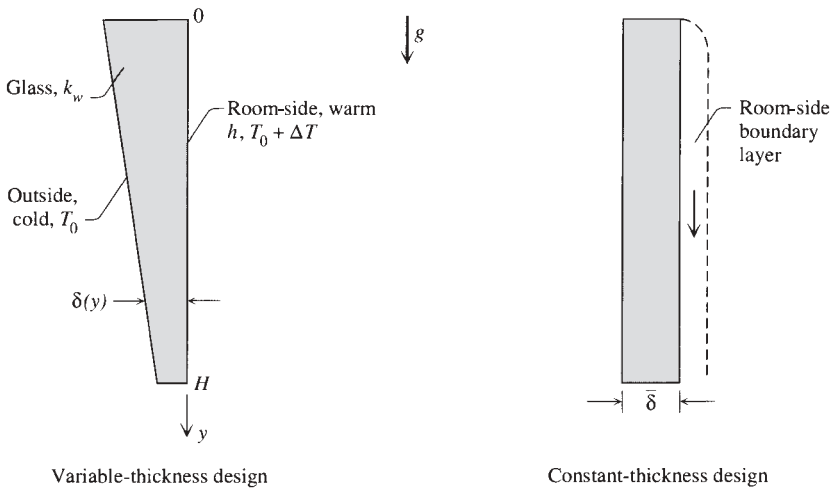

Figure P4.28

One way to evaluate the merit of the proposed design is to compare the total heat leak through the window, q' (W/m), with the corresponding heat leak through a constant-thickness glass window. The amount of glass used in the variable-thickness design is the same as in the constant-thickness (or reference) design. For the tapered glass window, assume that the glass thickness decreases linearly in the downward direction:

$$\delta = \overline{\delta} + b\left(\tfrac{1}{2} - \xi\right)$$

In this expression, $\xi = y/H$, and the taper parameter $b = -\,d\delta/d\xi$ is a design variable that must be determined optimally. The H-averaged thickness $\overline{\delta}$ is fixed because the window height H and the glass volume are fixed.

For the heat transfer coefficient on the room-air side, assume a y dependence consistent with that found in laminar natural convection boundary layers,

$$h = h_{\min}\xi^{-1/4}$$

where $h_{\min}$ is the smallest h value that occurs at the bottom of the window, where the room-side boundary layer is the thickest. The heat transfer coefficient on the outside of the glass layer is sufficiently large so that the temperature of that surface is equal to the atmospheric temperature.

To have access to a bird's-eye view of the merit of the proposed design relative to the reference design, determine numerically the ratio q'/q'_{ref} as a function of two dimensionless groups, the taper parameter

$$S = \frac{H}{\overline{\delta}}\left(-\frac{d\delta}{dy}\right)$$

and the bottom-end Biot number $\mathrm{Bi} = h_{\min}\overline{\delta}/k_w$. Determine the best taper parameter S for the smallest q'/q'_{ref} ratio for a fixed Bi. By means of a numerical example, determine the Bi range in which a common window is likely to operate. Comment on the practicality of the heat leak reduction promised by the tapered glass design.

4.29. The optimal spacing between horizontal tubes in a fixed volume cooled by natural convection can be determined based on the method of Section 4.12. Consider the bundle of horizontal cylinders shown in Fig. P4.29. The overall dimensions of the bundle (H, L, W) and the cylinder diameter (D) are fixed. Natural convection heat transfer (q) occurs between the cylinder surfaces (T_w) and the surrounding fluid reservoir (T_∞). The objective is to select the number of cylinders in the bundle, or the cylinder-to-cylinder spacing (S) such that the overall thermal conductance between the bundle and the ambient $q/(T_w - T_\infty)$ is maximized.
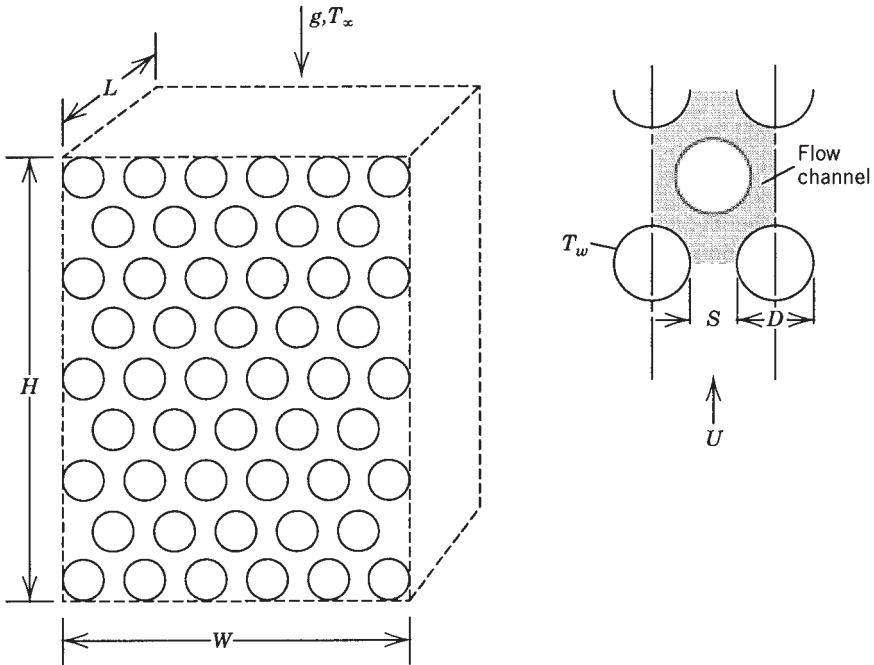
Figure P4.29

For the sake of concreteness, assume that the cylinders are staggered and that their centers form equilateral triangles. Other arrays can be treated similarly. The analysis consists of estimating the overall thermal conductance in the two asymptotic regimes (large S, small S) and intersecting the two asymptotes to locate the optimal spacing for maximum conductance.

4.30. This problem is about the thermodynamics fundamentals of the natural convection engine described at the start of Section 4.1. We explore the fundamentals in two parts, in accordance with Fig. P4.30.

(a) Consider a stream of ideal gas with the flow rate $\dot{m}$, which flows isothermally and reversibly through the system shown in Fig. P4.30a. The temperature T is constant throughout the system. The inlet and outlet pressures are P_{in} and P_{out}. Invoke the first law and the second law, the ideal gas model, and the isothermal and reversible model, and show that the heat input rate $\dot{Q}$ and work output rate $\dot{W}$ are equal and given by

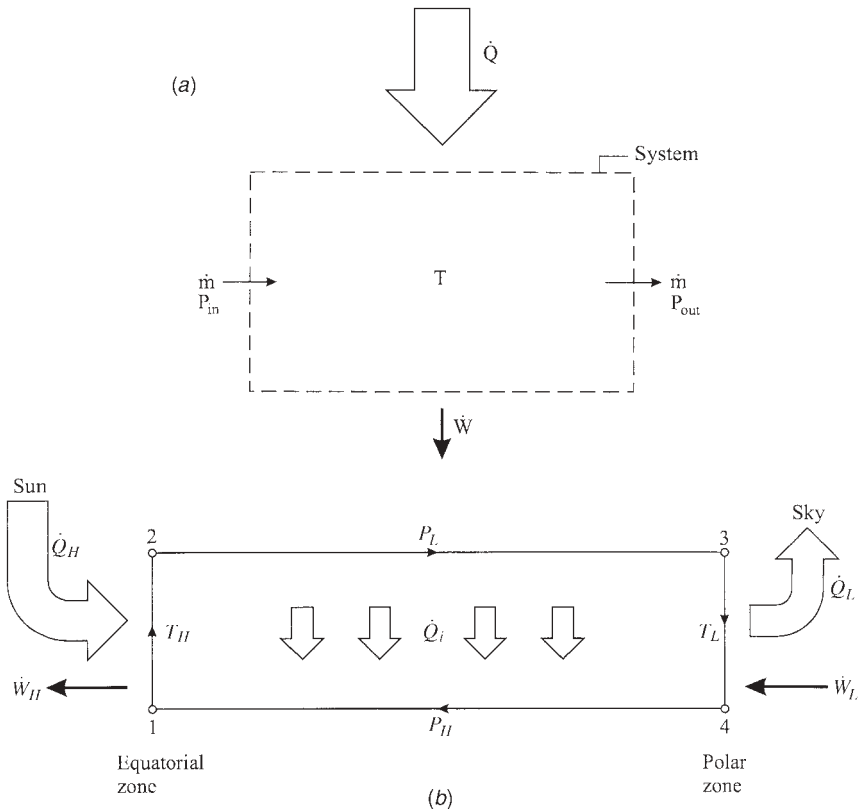$$\dot{Q} = \dot{W} = \dot{m}RT \ln \frac{P_{in}}{P_{out}}$$

Figure P4.30

(b) Next, the circulation of the atmosphere can be modeled as a heat engine that functions in a cycle of four processes (Fig. P4.30*b*): 1–2, isothermal heating and expansion at T_H, 2–3, isobaric cooling at P_L, 3–4, isothermal cooling and compression at T_L, and 4–1, isobaric heating at P_H. The cycle is executed reversibly: There are no pressure drops from 2 to 3, and from 4 to 1, and locally, there is no temperature difference between the 2–3 and 4–1 streams. The internal (regenerative) heat transfer $\dot{Q}_i$ occurs across a zero temperature difference. The heating and expansion process is a model for how the air warms up and rises to higher altitudes (lower pressures) over the equatorial zone (T_H). The cooling and compression make of a model for the sinking of the same airstream over the polar zones (T_L). The counterflow formed by the 4–1 and 2–3 streams is a model for the circulation of the atmosphere in the meridional direction.

Use the results of part (a) to calculate the net power output of the atmospheric heat engine ($\dot{W}_{net} = \dot{W}_H - \dot{W}_L$) and the energy conversion

efficiency $\eta = \dot{W}_{net}/\dot{Q}_H$. Does your resulting expression for η look familiar? Why?

4.31. A cylindrical cup of height H and radius R is filled completely with hot tea and leaks heat to the ambient. See Fig. P4.31. Assume that the temperature difference between tea and ambient is constant, ΔT. Neglect the thermal insulation effect of the wall of the cup. The heat flux (W/m^2) from the cup to the ambient is equal to ΔT times the water–ambient heat transfer coefficient. Assume that the heat transfer coefficient between the tea free surface and the ambient is constant, h_1. The heat transfer coefficient between the remaining surfaces (lateral an bottom) and the ambient is also constant, h_2. The cup volume is fixed. Show that the total heat leak from tea to ambient is minimal when the cup shape is $R/H = (h_1/h_2 + 1)^{-1}$. Sketch and describe the cup with optimal shape for the case where $h_1 = h_2$.
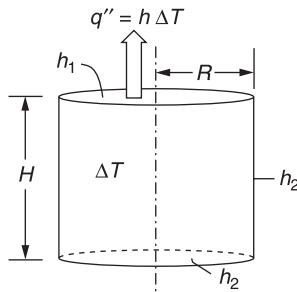

Figure P4.31

5

INTERNAL NATURAL CONVECTION

Enclosures filled with fluid are central components in a long list of engineering and geophysical systems. The flow induced in the inner airspace of a double-pane window system differs fundamentally from the external natural convection boundary layer considered earlier. In this chapter we focus on natural convection as an *internal flow*; convection in an enclosure is the result of the complex interaction between a finite-size fluid system in thermal communication with all the walls that confine it.

The phenomenon of natural convection in an enclosure is as varied as the geometry and orientation of the enclosure. Judging from the number of potential engineering applications, the enclosure phenomena can be organized into two classes: (1) enclosures heated from the side and (2) enclosures heated from below. The first class is representative of applications such as solar collectors, double-wall insulations, and air circulation through the rooms in a building. In addition, we find enclosures heated from the side in the cooling systems of industrial-scale rotating electric machinery. The second class refers to the functioning of thermal insulations oriented horizontally, for example, the heat transfer through a flat-roof attic space. The study of both flow classes is also relevant to our understanding of natural circulation in the atmosphere, the hydrosphere, and the molten core of the earth.

5.1 TRANSIENT HEATING FROM THE SIDE

5.1.1 Scale Analysis

Consider a two-dimensional enclosure of height H and horizontal length L, as is shown in Fig. 5.1. The enclosure is filled with a Newtonian fluid such as air or water. We are interested in the transient behavior of the cavity
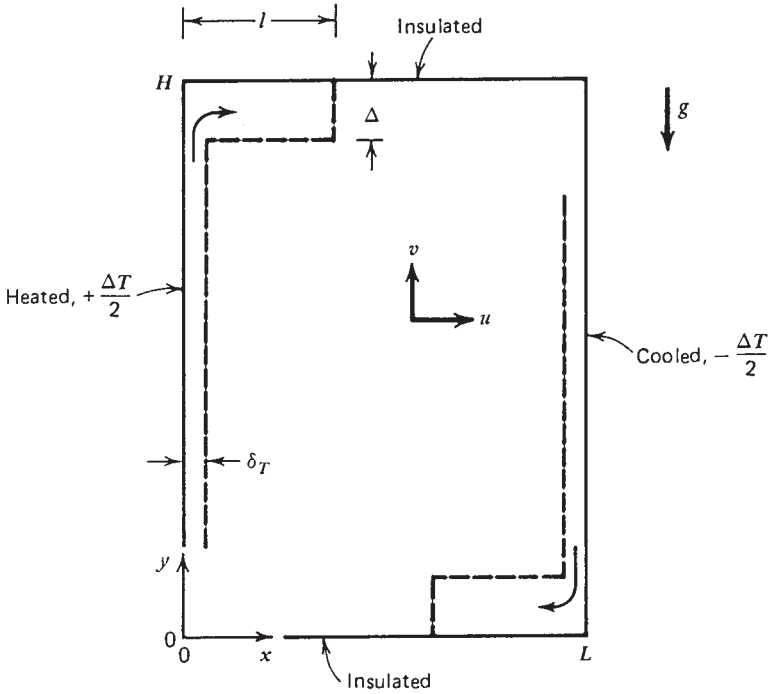
Figure 5.1   Two-dimensional rectangular enclosure with isothermal sidewalls.

fluid as the sidewalls are instantaneously heated and, respectively, cooled to temperatures $+\Delta T/2$ and $-\Delta T/2$. The top and bottom walls ($y = 0, H$) remain insulated throughout this experiment. Initially, the fluid is isothermal ($T = 0$) and motionless ($u = v = 0$) everywhere inside the cavity.

    The equations governing the conservation of mass, momentum, and energy at every point in the cavity are

$$\frac{\partial u}{\partial x} + \frac{\partial v}{\partial y} = 0 \tag{5.1}$$

$$\frac{\partial u}{\partial t} + u\frac{\partial u}{\partial x} + v\frac{\partial u}{\partial y} = -\frac{1}{\rho}\frac{\partial P}{\partial x} + \nu\left(\frac{\partial^2 u}{\partial x^2} + \frac{\partial^2 u}{\partial y^2}\right) \tag{5.2}$$

$$\frac{\partial v}{\partial t} + u\frac{\partial v}{\partial x} + v\frac{\partial v}{\partial y} = -\frac{1}{\rho}\frac{\partial P}{\partial y} + \nu\left(\frac{\partial^2 v}{\partial x^2} + \frac{\partial^2 v}{\partial y^2}\right) - g[1 - \beta(T - T_0)] \tag{5.3}$$

$$\frac{\partial T}{\partial t} + u\frac{\partial T}{\partial x} + v\frac{\partial T}{\partial y} = \alpha\left(\frac{\partial^2 T}{\partial x^2} + \frac{\partial^2 T}{\partial y^2}\right) \tag{5.4}$$

The symbols appearing in eqs. (5.1)–(5.4) are defined in Fig. 5.1. Note that in writing these equations, we modeled the fluid as Boussinesq-incompressible, in other words, ρ = constant everywhere except in the body force term of the y momentum equation, where it is replaced by $\rho[1-\beta(T-T_0)]$.

   Instead of solving eqs. (5.1)–(5.4) numerically, we rely on pure scale analysis to predict theoretically the types of flow and heat transfer patterns that can develop in the enclosure [1]. Immediately after $t = 0$, the fluid bordering each sidewall is motionless: This means that near the sidewall, the energy equation (5.4) expresses a balance between thermal inertia and conduction normal to the wall,

$$\frac{\Delta T}{t} \sim \alpha \frac{\Delta T}{\delta_T^2} \tag{5.5}$$

This equality of scales follows from recognizing ΔT, t, and δ_T as the scales of changes in T, t, and x in eq. (5.4). In the same equation, we took $u = v = 0$; we also recognized that $\partial^2 T/\partial y^2 \ll \partial^2 T/\partial x^2$ because near $t = 0^+$, the thermal boundary layer thickness δ_T is much smaller than the enclosure height (note that $y \sim H$ and $x \sim \delta_T$). Equation (5.5) dictates that immediately following $t = 0$, each sidewall is coated with a conduction layer the thickness of which increases as

$$\delta_T \sim (\alpha t)^{1/2} \tag{5.6}$$

   The layer δ_T rises along the heated wall. The velocity scale of this motion v is easier to see if we first eliminate the pressure P between the two momentum equations (5.2) and (5.3):

$$\frac{\partial}{\partial x}\left(\frac{\partial v}{\partial t} + u\frac{\partial v}{\partial x} + v\frac{\partial v}{\partial y}\right) - \frac{\partial}{\partial y}\left(\frac{\partial u}{\partial t} + u\frac{\partial u}{\partial x} + v\frac{\partial u}{\partial y}\right)$$
$$= v\left[\frac{\partial}{\partial x}\left(\frac{\partial^2 v}{\partial x^2} + \frac{\partial^2 v}{\partial y^2}\right) - \frac{\partial}{\partial y}\left(\frac{\partial^2 u}{\partial x^2} + \frac{\partial^2 u}{\partial y^2}\right)\right] + g\beta\frac{\partial T}{\partial x} \tag{5.7}$$

This new equation contains three basic groups of terms: inertia terms on the left-hand side and four viscous diffusion terms plus the buoyancy term on the right-hand side. It is easy to show that the three terms that dominate each basic group are (Problem 5.1)

$$\begin{array}{ccc} \text{Inertia} & \text{Friction} & \text{Buoyancy} \end{array}$$
$$\frac{\partial^2 v}{\partial x\,\partial t}, \qquad v\frac{\partial^3 v}{\partial x^3}, \qquad g\beta\frac{\partial T}{\partial x} \tag{5.8}$$

In terms of representative scales, the momentum balance (5.8) reads

$$\frac{v}{\delta_T t}, \qquad v\frac{v}{\delta_T^3} \qquad \sim \qquad \frac{g\beta\,\Delta T}{\delta_T} \tag{5.9}$$

The driving force in this balance is the buoyancy effect $(g\beta\ \Delta T)/\delta_T$, which is not zero. It is important to determine whether the buoyancy effect is balanced by friction *or* inertia. Dividing eq. (5.9) through the friction scale and recalling that $\delta_T^2 \sim \alpha t$ yields

$$\underset{\text{Inertia}}{\frac{1}{\text{Pr}},} \quad \underset{\text{Friction}}{1} \quad \sim \quad \underset{\text{Buoyancy}}{\frac{g\beta\ \Delta T\ \delta_T^2}{\nu\ \nu}} \tag{5.10}$$

Therefore, for fluids with Prandtl number of order 1 or greater, the correct momentum balance at $t = 0^+$ is between buoyancy and friction,

$$1 \sim \frac{g\beta\ \Delta T\ \delta_T^2}{\nu\ \nu} \tag{5.11}$$

We conclude that the initial vertical velocity scale is

$$v \sim \frac{g\beta\ \Delta T\ \alpha t}{\nu} \tag{5.11'}$$

This velocity scale is valid for fluids such as water and oils (Pr > 1) and is marginally valid for gases (Pr $\sim$ 1).

Next, we turn our attention back to the energy equation. The heat conducted from the sidewall into the fluid layer δ_T is no longer spent solely on thickening the layer: Part of this heat input is carried away by the layer δ_T rising with velocity v. Thus, in the energy equation, we see a competition among three distinct effects:

$$\underset{\text{Inertia}}{\frac{\Delta T}{t},} \quad \underset{\text{Convection}}{v\frac{\Delta T}{H}} \quad \sim \quad \underset{\text{Conduction}}{\alpha\frac{\Delta T}{\delta_T^2}} \tag{5.12}$$

As t increases, the convection effect increases [$v \sim t$, eq. (5.11')], while the effect of inertia decreases in importance. There comes a time t_f when the energy equation expresses a balance between the heat conducted from the wall and the enthalpy carried away vertically by the buoyant layer,

$$v\frac{\Delta T}{H} \sim \alpha\frac{\Delta T}{\delta_T^2} \tag{5.13}$$

which yields

$$t_f \sim \left(\frac{\nu H}{g\beta\ \Delta T\ \alpha}\right)^{1/2} \tag{5.13'}$$

At such a time, the layer thickness is

$$\delta_{T,f} \sim (\alpha t_f)^{1/2} \sim H\ \text{Ra}_H^{-1/4} \tag{5.14}$$

where Ra_H is the Rayleigh number based on the enclosure height,[*]

$$Ra_H = \frac{g\beta \, \Delta T \, H^3}{\alpha \nu} \tag{5.15}$$

The time t_f when the δ_T layer becomes convective could have also been determined by setting inertia $\sim$ convection in eq. (5.12). Note further that beyond the time t_f, the convection $\sim$ conduction balance in eq. (5.12) is preserved *only* if both ν and δ_T no longer increase in time. Therefore, beyond $t \sim t_f$, the thermal layers along each sidewall reach a *steady state* characterized by an energy balance between conduction and convection and a momentum balance between buoyancy and viscous diffusion (see Chapter 4).

In addition to thermal layers of thickness $\delta_{T,f}$, the sidewalls develop viscous (velocity) wall jets. The thickness of these jets δ_ν from the momentum balance (5.7) for the region of thickness $x \sim \delta_\nu$ *outside* the thermal layer. In this region, the buoyancy effect is minor, and we have a balance between inertia and viscous diffusion,

$$\frac{\nu}{\delta_\nu t} \sim \nu \frac{\nu}{\delta_\nu^3} \tag{5.16}$$

Hence,

$$\delta_\nu \sim (\nu t)^{1/2} \sim Pr^{1/2} \, \delta_T \tag{5.17}$$

In the steady state, $t > t_f$, the fluid near each sidewall is characterized by a *two-layer structure*: a thermal boundary layer of thickness $\delta_{T,f}$ and a thicker wall jet $\delta_{\nu,f} \sim Pr^{1/2}\delta_{T,f}$. The development of this structure is shown in Fig. 5.2.

5.1.2   Criterion for Distinct Vertical Layers

If the final thermal boundary layer thickness $\delta_{T,f}$ is smaller than the transversal extent of the enclosure (L), the thermal layers will be *distinct*; using eq. (5.14), this criterion reads

$$\frac{H}{L} < Ra_H^{1/4} \tag{5.18}$$

We could have arrived at the same inequality by stating that the vertical layers become convective in a time shorter than the thermal diffusion time between the two vertical walls ($t_f < L^2/\alpha$). The $H/L - Ra_H$ subdomain in which we should expect distinct wall layers in the horizontal temperature

*Note that the majority of the experimental studies on natural convection in enclosures, particularly those on tall enclosures, report their results in terms of a Rayleigh number based on the horizontal dimension L; from a theoretical scaling viewpoint, this choice is without foundation.
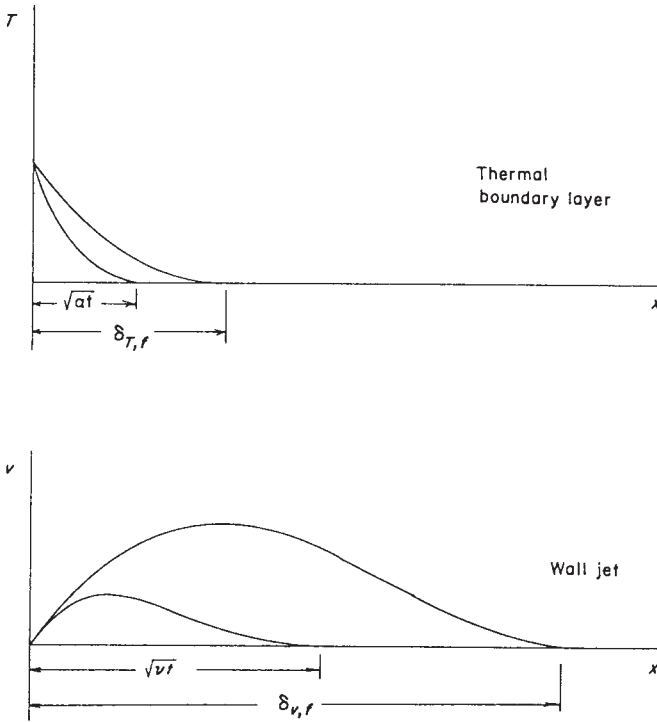
Figure 5.2 Development of two-layer structure near the warm wall.

profile is shown in Fig. 5.3. This subdomain is bounded on the left by the conduction heat transfer regime (the proof that $Ra_H < 1$ is the criterion for conduction-dominated heat transfer is proposed as Problem 5.3). Note further that the corresponding criterion for distinct velocity boundary layers (wall jets) is $\delta_{v,f} < L$; hence,

$$\frac{H}{L} < Ra_H^{1/4} \, Pr^{-1/2} \tag{5.19}$$

5.1.3 Criterion for Distinct Horizontal Jets

The scale analysis presented so far can be extended to cover events near the two horizontal adiabatic walls in an attempt to predict the shape of the temperature and velocity profiles vertically across the cavity [1]. A more direct approach to predicting the presence of distinct wall layers in the steady state is to regard the circulation loop as a counterflow heat exchanger in which the horizontal branches can communicate thermally over a horizontal distance of order L [2].
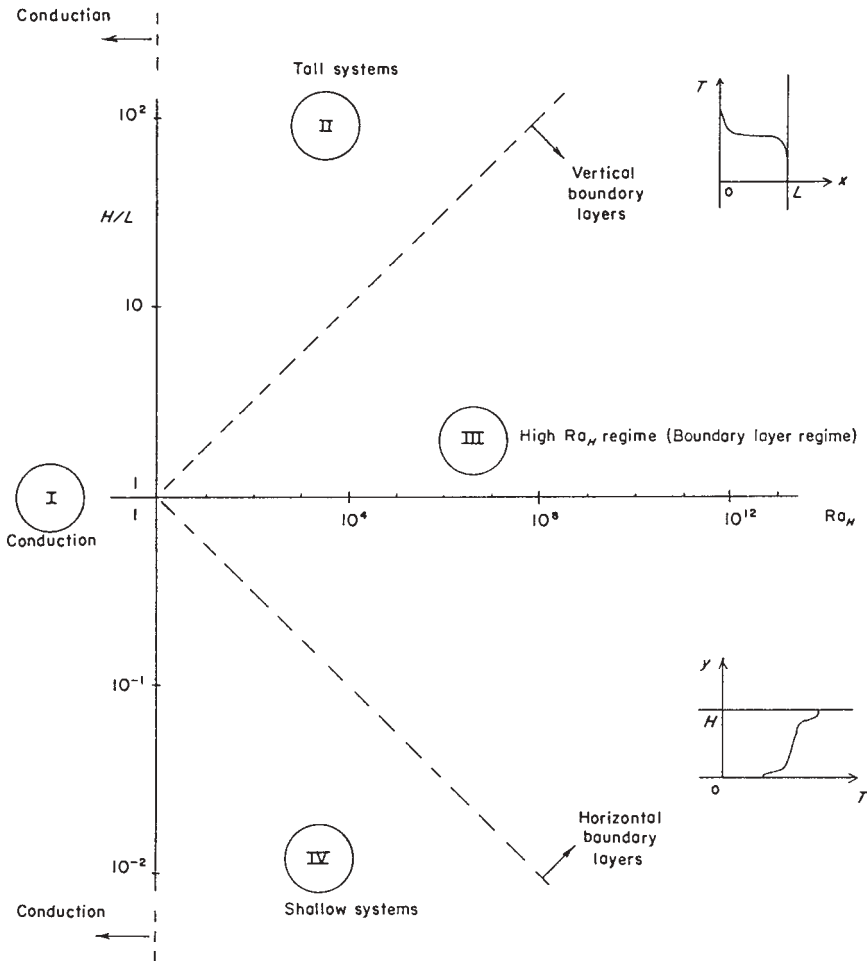
Figure 5.3 Four heat transfer regimes for natural convection in an enclosure heated from the side.

The enthalpy flow between the two vertical ends is

$$q'_{\text{convection}} \sim (\rho v \, \delta_T)_f \, c_P \, \Delta T$$
$$\text{left} \rightarrow \text{right}$$
$$(\text{Fig. 5.1})$$

$$\sim k \, \Delta T \, \text{Ra}_H^{1/4} \qquad (5.20)$$

This estimate is the same as the heat transfer rate through each of the vertical walls, $(k/\delta_{T,f})H \, \Delta T$. Heat diffuses vertically from the warm upper branch of the

counterflow to the lower branch at a rate

$$q'_{\substack{\text{conduction} \\ \text{top}\to\text{bottom} \\ \text{(Fig. 5.1)}}} \sim kL\frac{\Delta T}{H} \tag{5.21}$$

The enthalpy carried by the stream $(\rho v \delta_T)_f$ reaches the opposite end intact when the vertical diffusion is negligible,

$$kL\frac{\Delta T}{H} < k \ \Delta T \ \mathrm{Ra}_H^{1/4}$$

in other words, when

$$\frac{H}{L} > \mathrm{Ra}_H^{-1/4} \tag{5.22}$$

When condition (5.22) is met, the horizontal streams along the adiabatic walls retain their temperature identity, as shown in the sketch accompanying the $H/L = \mathrm{Ra}_H^{-1/4}$ line in Fig. 5.3.

The two criteria for distinct thermal layers [eqs. (5.18) and (5.22)] and the convective heat transfer requirement [$\mathrm{Ra}_H > 1$] divide the $H/L - \mathrm{Ra}_H$ field into four sectors. Each sector corresponds to a distinct regime in the steady state:

- *Regime I: conduction limit*. The temperature varies linearly across the cavity; hence, the heat transfer rate between the two sidewalls is of order $(kH \ \Delta T)/L$. The horizontal temperature gradient $\Delta T/L$ gives rise to a slow clockwise circulation; however, the heat transfer contribution of this flow is insignificant.

- *Regime II: tall enclosure limit*. For most of the enclosure height, the temperature varies linearly between the two sidewalls. The heat transfer rate is of order $(kH \ \Delta T)/L$, as in the preceding case. The clockwise circulation pattern is characterized by distinct layers in the vicinity of the top and bottom walls.

- *Regime III: high-Ra_H limit (boundary layer regime)*. Vertical thermal boundary layers form distinctly along the differentially heated sidewalls. The heat transfer rate across the cavity scales as $(k/\delta_{T,f})H \ \Delta T$. The adiabatic horizontal walls are lined by distinct thermal layers. Most of the cavity fluid (the core) is relatively stagnant and thermally stratified.

- *Regime IV: shallow enclosure limit*. The heat transfer mechanism is dominated by the presence of vertical thermal layers; hence, it scales again as $(k/\delta_{T,f})H \ \Delta T$. This scale represents an upper bound because an additional insulation effect is provided by the long horizontal core of the cavity. In this region, the two branches of the horizontal counterflow make good thermal contact, rendering the counterflow an effective insulation in the left–right direction [3].
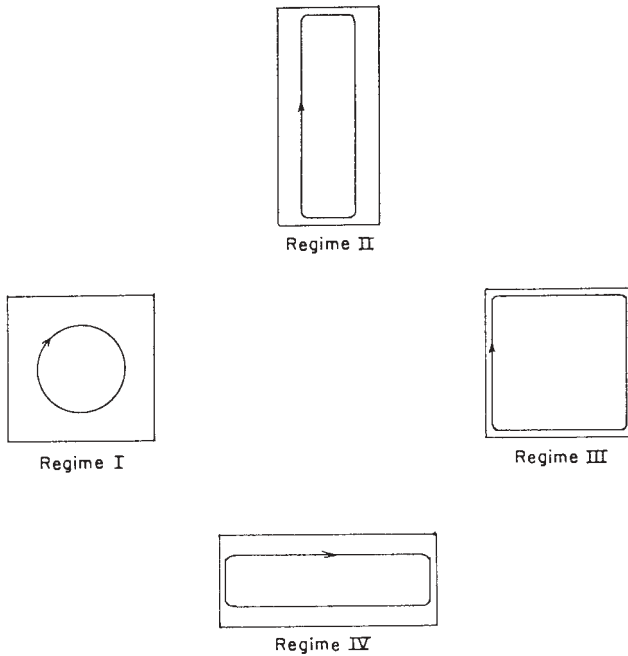
Figure 5.4   Circulation patterns associated with regimes I–IV shown in Fig. 5.3.

The flow patterns in regimes I–IV are sketched in Fig. 5.4. These patterns have been confirmed by numerous experimental studies involving Pr > 1 fluids. The scales and regimes of natural convection in shallow enclosures were investigated by Boehrer [4]. The identification of the time scale of the rotation of the fluid inside a cavity with periodic heating from the side led to the discovery of a phenomenon of resonance for the global heat transfer across the cavity [5]. This development generated a new direction in heat transfer research [6–14].

5.2   BOUNDARY LAYER REGIME

In the next two sections we focus on two classes of analytical advances in the direction of predicting the heat transfer rate under regimes III and IV. The first major theoretical work on natural convection in enclosures [15] considered regimes (I), (II), and (III). Although it served as a stimulus for the theoretical work that followed, it is not as critical to heat transfer engineering because under regimes I and II, the heat transfer rate is practically equal to the pure conduction estimate.

When vertical thermal boundary layers are present, the heat transfer rate is controlled by the thermal resistance of order $\delta_{T,f}/k$, which coats each sidewall.

To calculate this thermal resistance we must determine the *temperature field* in the vertical region of thickness $\delta_{T,f}$. This justifies the following nondimensionalization of the governing equations (5.1), (5.4), and (5.7):

$$x_* = \frac{x}{\delta_{T,f}}, \qquad\qquad y_* = \frac{y}{H}$$

$$T_* = \frac{T}{\Delta T} \qquad\qquad\qquad (5.23)$$

$$u_* = \frac{u}{(\delta_{T,f}/H)v_f}, \qquad\qquad v_* = \frac{v}{v_f}$$

In these definitions, $\delta_{T,f}$ is the final thermal boundary layer thickness [eq. (5.14)] and v_f is the velocity scale (5.11′) evaluated at $t = t_f$. Substituting the new dimensionless variables (5.23) into the steady-state conservation equations yields

$$\frac{\partial u_*}{\partial x_*} + \frac{\partial v_*}{\partial y_*} = 0 \qquad\qquad (5.24)$$

$$u_*\frac{\partial T_*}{\partial x_*} + v_*\frac{\partial T_*}{\partial y_*} = \frac{\partial^2 T_*}{\partial x_*^2} + \mathrm{Ra}_H^{-1/2}\frac{\partial^2 T_*}{\partial y_*^2} \qquad\qquad (5.25)$$

$$\frac{1}{\mathrm{Pr}}\left[\frac{\partial}{\partial x_*}\left(u_*\frac{\partial v_*}{\partial x_*} + v_*\frac{\partial v_*}{\partial y_*}\right) - \mathrm{Ra}_H^{-1/2}\frac{\partial}{\partial y_*}\left(u_*\frac{\partial u_*}{\partial x_*} + v_*\frac{\partial u_*}{\partial y_*}\right)\right]$$

$$= \frac{\partial}{\partial x_*}\left(\frac{\partial^2 v_*}{\partial x_*^2} + \mathrm{Ra}_H^{-1/2}\frac{\partial^2 v_*}{\partial y_*^2}\right) - \mathrm{Ra}_H^{-1/2}\frac{\partial}{\partial y_*}\left(\frac{\partial^2 u_*}{\partial x_*^2} + \mathrm{Ra}_H^{-1/2}\frac{\partial^2 u_*}{\partial y_*^2}\right)$$

$$+ \frac{\partial T_*}{\partial x_*} \qquad\qquad (5.26)$$

In the high-Ra_H limit and for $\mathrm{Pr} > 1$ fluids, eqs. (5.24)–(5.26) reduce to

$$\frac{\partial u_*}{\partial x_*} + \frac{\partial v_*}{\partial y_*} = 0 \qquad\qquad (5.24')$$

$$u_*\frac{\partial T_*}{\partial x_*} + v_*\frac{\partial T_*}{\partial y_*} = \frac{\partial^2 T_*}{\partial x_*^2} \qquad\qquad (5.25')$$

$$0 = \frac{\partial^3 v_*}{\partial x_*^3} + \frac{\partial T_*}{\partial x_*} \qquad\qquad (5.26')$$

Gill [16] solved these equations approximately subject to the sidewall conditions

$$u_* = v_* = 0, \quad T_* = \frac{1}{2} \qquad \text{at } x_* = 0 \qquad\qquad (5.27)$$

and the outer (far from the wall) conditions

$$u_* \to u_{*\infty}(y_*), \quad v_* \to 0 \qquad\qquad \text{as } x_* \to \infty \qquad\qquad (5.28)$$

$$T_* \to T_{*\infty}(y_*) \qquad\qquad\qquad \text{as } x_* \to \infty \qquad\qquad (5.29)$$

where $u_{*\infty}$ and $T_{*\infty}$ are the unknown flow and temperature stratification of the core. To circumvent the nonlinearity of the energy equation (5.25′), Gill [16] used the Oseen-linearization technique and replaced the u_* and $\partial T_*/\partial y_*$ factors appearing on the convective side of eq. (5.25′) with two unknown functions of altitude, $u_A(y_*)$ and $T'_A(y_*)$,

$$(u_A)\frac{\partial T_*}{\partial x_*} + (T'_A)v_* = \frac{\partial^2 T_*}{\partial x_*^2} \qquad\qquad (5.25'')$$

Eliminating T_* between this equation and the momentum equation (5.26′) yields

$$\frac{\partial^4 v_*}{\partial x_*^4} - (u_A)\frac{\partial^3 v_*}{\partial x_*^3} + (T'_A)v_* = 0 \qquad\qquad (5.30)$$

This equation can be integrated in x_*. The general solution has the form

$$v_* = \sum_{i=1}^{4} a_i(y_*)e^{-\lambda_i(y_*)x_*} \qquad\qquad (5.31)$$

where the λ_i's are the four roots of the characteristic equation

$$\lambda^4 + u_A\lambda^3 + T'_A = 0 \qquad\qquad (5.31')$$

Applying the boundary conditions (5.27)–(5.29), the solution takes the form

$$v_* = \frac{\frac{1}{2} - T_{*\infty}}{\lambda_2^2 - \lambda_1^2}\ (-e^{-\lambda_2 x_*} + e^{-\lambda_1 x_*}) \qquad\qquad (5.32)$$

$$T_* = \frac{\frac{1}{2} - T_{*\infty}}{\lambda_2^2 - \lambda_1^2}\ (\lambda_2^2 e^{-\lambda_2 x_*} - \lambda_1^2 e^{-\lambda_1 x_*}) + T_{*\infty} \qquad\qquad (5.33)$$

where λ_1 and λ_2 are the two roots with positive real parts of eq. (5.31′).

The solution expressed by eqs. (5.32) and (5.33) depends on four unknown functions of altitude, $\lambda_1, \lambda_2, u_{*\infty}$, and $T_{*\infty}$. The fourth unknown, $u_{*\infty}$, appears in the expression for u_*, which is obtained by combining eqs. (5.32) and (5.24). Gill determined these functions uniquely by invoking the energy integral condition

$$\int_0^\infty \left(u_*\frac{\partial T_*}{\partial x_*} + v_*\frac{\partial T_*}{\partial y_*}\right)dx_* = -\left(\frac{\partial T_*}{\partial x_*}\right)_{x_*=0} \qquad\qquad (5.34)$$

plus two centrosymmetry conditions, meaning that the cold-side boundary layer solution must approach the *same* core solution (5.28) and (5.29). The integral condition (5.34) must be an energy condition because the inexact character of solution (5.32, 5.33) stems from the Oseen-linearization (approximation) of the energy equation (5.25′). Gill's results are

$$\lambda_{1,2} = \tfrac{1}{4}p(1-q)[1 \pm i(1+2q)^{1/2}] \qquad (5.35)$$

$$T*_{\infty} = \frac{q}{1+q^2} \qquad (5.36)$$

where $p(y_*)$ is an even function and $q(y_*)$ is an odd function resulting from the system:

$$p = \frac{2(1+3q^2)^{11/9}}{C(1+q^2)^{2/3}(1-q^2)} \qquad (5.37)$$

$$\frac{dq}{dy_*} = \frac{2(1+3q^2)^{53/9}}{C^4(7-q^2)(1-q^2)^3(1+q^2)^{2/3}} \qquad (5.38)$$

For this formulation, the origin of y_* was taken at the midheight of the enclosure, so that y_* varies from $-\tfrac{1}{2}$ to $\tfrac{1}{2}$. Gill integrated eqs. (5.37) and (5.38) numerically and determined the constant C from the *arbitrary* condition that the vertical velocity in the boundary layers (v_*) is zero at the two corners ($y_* = \pm\tfrac{1}{2}$). Representative boundary layer isotherms and streamlines based on this solution are reproduced in Fig. 5.5 (note the different notation; in Fig. 5.5, z is y_*, T is T_*, and ψ is the streamfunction defined as $u_* = -\partial\psi/\partial y_*$, $v_* = \partial\psi/\partial x_*$). The complete solution was compared with the temperature and velocity profiles reported experimentally by Elder [17]. The agreement between theory and experiment proved adequate, although questions have persisted in connection with the arbitrary choice of impermeable top and bottom walls made to determine the constant C. The basis for these equations is the fact that the solution for v_* is valid in the *boundary layer* only; therefore, it is improper to use it in the corners, where the boundary layer scaling (5.23) breaks down.

The important heat transfer result of the preceding analysis, not reported by Gill [16], is the *overall* heat transfer rate across the enclosure [18],

$$q' = k \int_{-H/2}^{H/2} \left(-\frac{\partial T}{\partial x}\right)_{x=0} dy$$

$$= 0.364k\,\Delta T\,\mathrm{Ra}_H^{1/4} \qquad (5.39)$$

Noting that the majority of experimental and numerical studies have reported their findings as overall $\overline{\mathrm{Nu}}$ correlations where

$$\overline{\mathrm{Nu}} = \frac{q'}{q'_{\text{pure conduction}}}$$
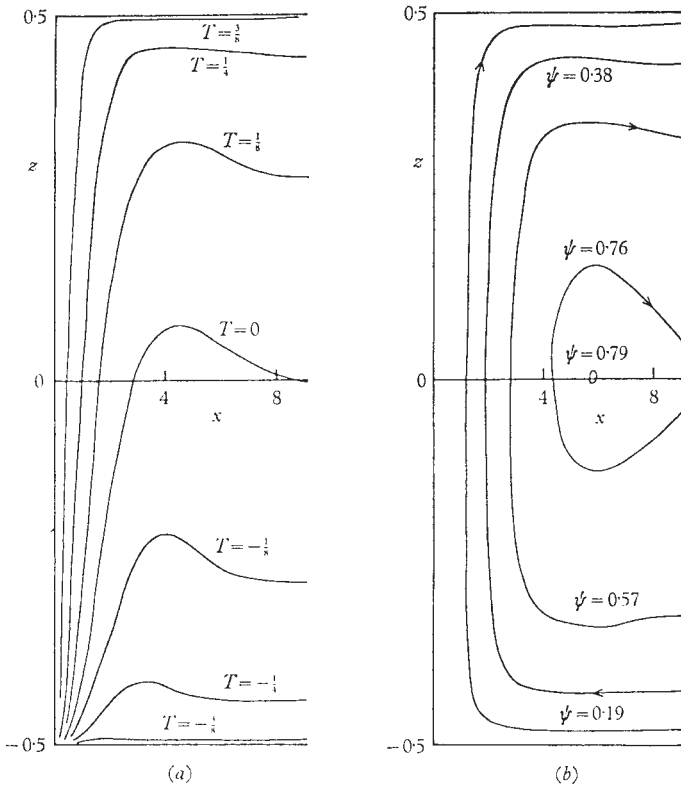
Figure 5.5   Streamlines and isotherms near the vertical wall in the boundary layer regime. (Reprinted with permission from A. E. Gill, *Journal of Fluid Mechanics*, Vol. 26, pp. 515–536, 1966. Copyright © 1966 Cambridge University Press.)

the present result can be rewritten as

$$\overline{\mathrm{Nu}} = \frac{q'}{(kH\ \Delta T)/L} = 0.364\frac{L}{H}\ \mathrm{Ra}_H^{1/4} \tag{5.40}$$

The analytical heat transfer result developed above was improved and extended. As a substitute for Gill's choice of impermeable wall conditions at $y_* = \pm\frac{1}{2}$, Bejan [18] proposed the condition of zero net energy flow (by convection and conduction) through the top and bottom walls,

$$q'_y = \int_0^L \left(\rho c_P v T - k\frac{\partial T}{\partial y} \right)\ dx = 0 \qquad \text{at } y = \pm H/2 \tag{5.41}$$

This statement takes into account, in an integral sense, the conditions of both impermeable *and* adiabatic horizontal walls. The heat transfer result based on
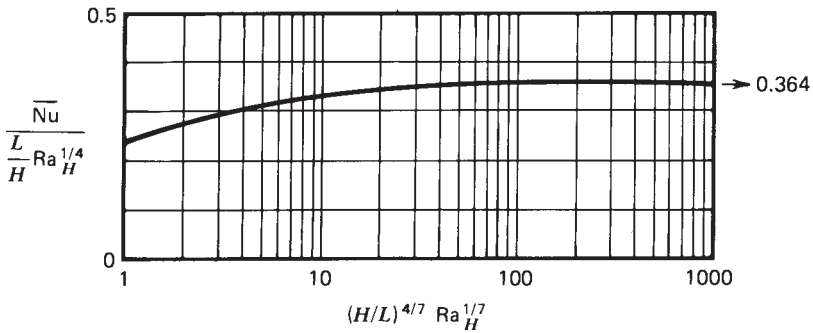
Figure 5.6   Overall Nusselt number for the boundary layer regime in an enclosure heated from the side. (From Ref. 18.)

this approach is shown in Fig. 5.6: The numerical factor in the $\overline{Nu} \sim (L/H)$ $Ra_H^{1/4}$ relation (5.40) is a function of the new group $Ra_H^{1/7}(H/L)^{4/7}$. Equation (5.40) emerges as a limiting result, valid for the boundary layer regime in the high-Ra_H limit. The general result of Fig. 5.6 shows that the $\overline{Nu}$ $(H/L, Ra_H)$
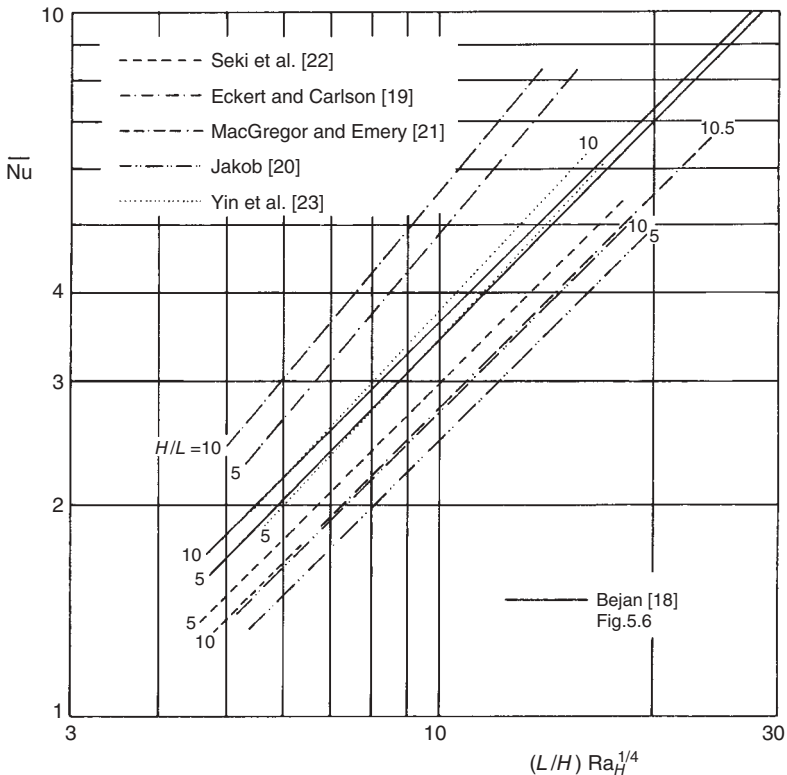
Figure 5.7   Comparison of the theoretical Nusselt number (Fig. 5.6) with experimental correlations. (From Ref. 18.)

relationship is more complicated than the one suggested by eq. (5.40). As shown by the solid curves of Figs. 5.7 and 5.8, this relationship cannot be expressed as a power law of the type $\overline{Nu} = a(L/H)^b \, Ra_H^c$, with constant a, b, and c (note that, in general, $c > \frac{1}{4}$ and $b < 1$).

We end this section with a survey of the overall $\overline{Nu}$ correlations found in the literature. Figures 5.7 and 5.8 show a selection of experimental [19–23] and numerical [24–27] correlations vis-à-vis the theoretical result of Fig. 5.6. As should be expected, the numerical correlations of Fig. 5.8 are in superior mutual agreement compared with the experimental results in Fig. 5.7. The analytical results for the overall Nusselt number (the solid lines) split the field covered by these correlations right through the middle.

The agreement between theory and correlations based on numerical correlations is excellent, particularly near $(L/H)Ra^{1/4} \sim 10$, which is the range where the boundary layer model $(L/\delta_{T,f} > 1)$ is an acceptable approximation. Below this range, the heat transfer mechanism is slowly replaced by direct conduction in the horizontal direction (see Fig. 5.3). Above this range, the boundary layer picture becomes considerably more complicated due to the transition to turbulent flow. The theoretical Nusselt number of Fig. 5.6 and eq. (5.40) can be used with
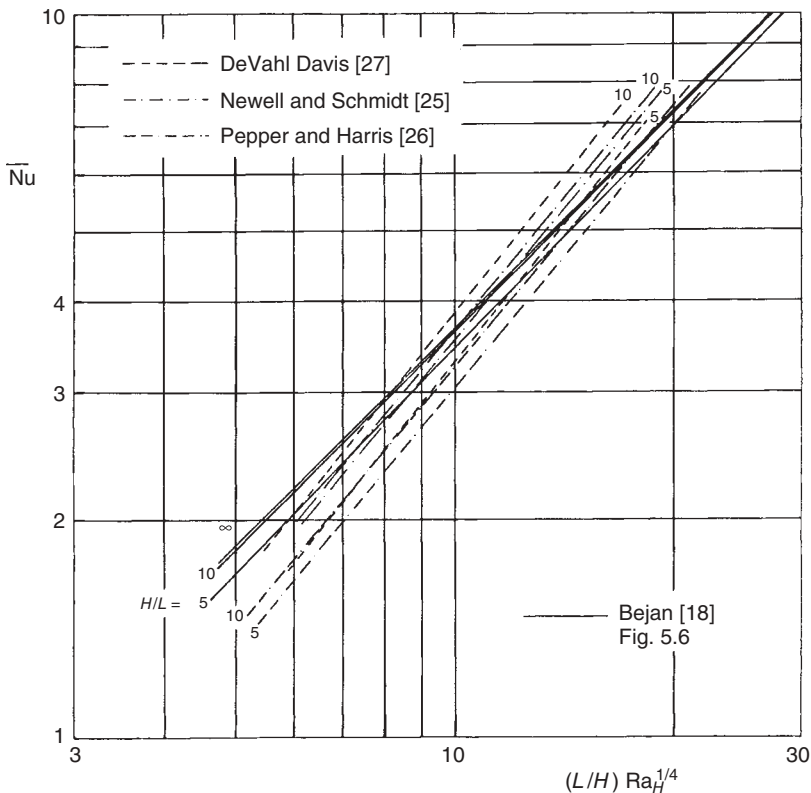

Figure 5.8 Comparison of the theoretical Nusselt number (Fig. 5.6) with numerical correlations. (From Ref. 18.)

the same if not a higher degree of confidence than the heat transfer correlations available today.

In this section we focused on the boundary layer regime in enclosures filled with Pr > 1 fluids such as water, oils, and as a limiting case, gases (air).

5.3   SHALLOW ENCLOSURE LIMIT

Another convection-dominated regime is regime IV: According to Figs. 5.3 and 5.4, if H/L decreases and Ra_H and Pr remain fixed, the cavity becomes dominated by a horizontal counterflow in which the two branches are in very good thermal contact. Of interest is the end-to-end insulation effect produced by the horizontal counterflow sandwiched by the two adiabatic walls of the enclosure. For this reason, we focus on the core region—that is, the region sufficiently far from both vertical walls—where the proper scales for x and y are L and H, respectively (see Fig. 5.9).

In the shallow enclosure limit $H/L \rightarrow 0$, the scales of the terms that dominate the steady-state mass, energy, and momentum conservation statements [eqs. (5.1), (5.4), and (5.7)] are

$$\frac{u}{L} \sim \frac{v}{H} \tag{5.42}$$

$$\underbrace{u\frac{\Delta T}{L}}_{\text{Convection}} \sim \underbrace{\alpha\frac{\Delta T}{H^2}}_{\substack{\text{Vertical} \\ \text{conduction}}} \tag{5.43}$$

$$\underbrace{\frac{u^2}{HL}}_{\text{Inertia}} \quad \text{or} \quad \underbrace{v\frac{u}{H^3}}_{\text{Friction}} \quad \sim \quad \underbrace{g\beta\frac{\Delta T}{L}}_{\text{Buoyancy}} \tag{5.44}$$
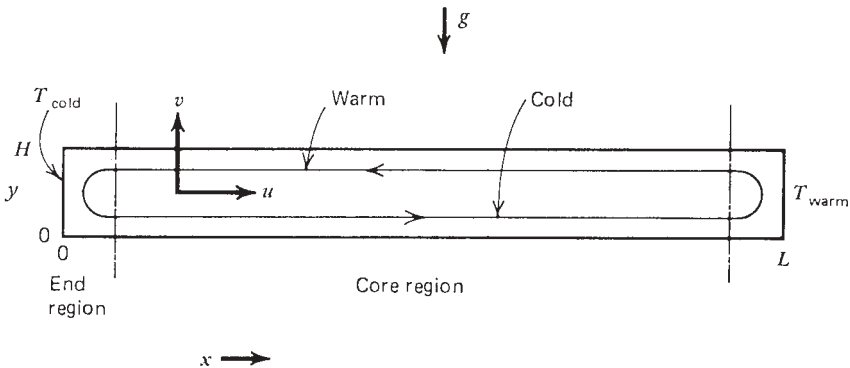

Figure 5.9   Shallow enclosure heated in the horizontal direction.

This display is instructive because it unmasks the potential for erroneously evaluating the scales of u and v: We have three apparent balances [eqs. (5.42)–(5.44)] for determining only two unknowns, u and v. The correct way to proceed is to recognize that, physically, the velocity scale is the result of a *force* balance. This means that the u scale follows from eq. (5.44), not from eq. (5.43). Now, in the momentum equation (5.44), we distinguish two possibilities:

1. Friction $\sim$ buoyancy
2. Inertia $\sim$ buoyancy

In both cases, the buoyancy effect is present because it is the driving effect (without it, i.e., when $g = 0$, there is no flow). The second choice, inertia $\sim$ buoyancy, is incompatible with the $H/L \to 0$ limit (see Problem 5.5). Assuming the first possibility, friction $\sim$ buoyancy, we find that

$$u \sim \frac{g\beta H^3\,\Delta T}{\nu L} \tag{5.45}$$

and from eq. (5.42),

$$v \sim \frac{g\beta H^4\,\Delta T}{\nu L^2} \tag{5.46}$$

Using these scales, the relative order of magnitude of the terms appearing in the energy and momentum equations is

$$\underbrace{\left(\frac{H}{L}\right)^2 \mathrm{Ra}_H}_{\substack{\text{Convection} \\ (\to\ 0)}} \sim \underbrace{1}_{\substack{\text{Vertical} \\ \text{conduction}}} \tag{5.43'}$$

$$\underbrace{\left(\frac{H}{L}\right)^2 \frac{\mathrm{Ra}_H}{\mathrm{Pr}}}_{\substack{\text{Inertia} \\ (\to\ 0)}},\ \underbrace{1}_{\text{Friction}} \sim \underbrace{1}_{\text{Buoyancy}} \tag{5.44'}$$

Examining eq. (5.44'), we conclude that the assumed balance between friction and buoyancy is the correct choice for the flow regime of interest ($H/L \to 0$). Second, expression (5.43') states that in this regime, the heat transfer by thermal diffusion in the vertical direction is far greater than the enthalpy flow in the horizontal (end-to-end) direction. Indeed, the sharp imbalance revealed by expression (5.43') is the meaning of ''good thermal contact in the vertical direction,'' the distinguishing feature of regime IV (Fig. 5.3).

Scales (5.45) and (5.46) recommend the following dimensionless variables for the core region:

$$u_c = \frac{u}{(g\beta H^3 \ \Delta T)/\nu L}, \qquad v_c = \frac{v}{(g\beta H^4 \ \Delta T)/\nu L^2}$$

$$x_c = \frac{x}{L}, \qquad y_c = \frac{y}{H}, \qquad T_c = \frac{T - T_{\text{cold}}}{\Delta T} \qquad (5.47)$$

where T_{cold} is the cold-end temperature and $\Delta T = T_{\text{warm}} - T_{\text{cold}}$ is the end-to-end temperature difference. Expressions (5.43′) and (5.44′) indicate that in the $H/L \to 0$ limit, the governing equations reduce to the following:

Mass:
$$\frac{\partial u_c}{\partial x_c} + \frac{\partial v_c}{\partial y_c} = 0$$

Momentum:
$$\epsilon \frac{\text{Ra}_H}{\text{Pr}} \left[\epsilon \frac{\partial}{\partial x_c} \left(u_c \frac{\partial v_c}{\partial x_c} + v_c \frac{\partial v_c}{\partial y_c} \right) - \frac{\partial}{\partial y_c} \left(u_c \frac{\partial u_c}{\partial x_c} + v_c \frac{\partial u_c}{\partial y_c} \right) \right] \qquad (5.48)$$

$$= \epsilon \frac{\partial}{\partial x_c} \left(\epsilon \frac{\partial^2 v_c}{\partial x_c^2} + \frac{\partial^2 v_c}{\partial y_c^2} \right) - \frac{\partial}{\partial y_c} \left(\epsilon \frac{\partial^2 u_c}{\partial x_c^2} + \frac{\partial^2 u_c}{\partial y_c^2} \right) + \frac{\partial T_c}{\partial x_c} \qquad (5.49)$$

Energy:
$$\epsilon \, \text{Ra}_H \left(u_c \frac{\partial T_c}{\partial x_c} + v_c \frac{\partial T_c}{\partial y_c} \right) = \epsilon \frac{\partial^2 T_c}{\partial x_c^2} + \frac{\partial^2 T_c}{\partial y_c^2} \qquad (5.50)$$

where $\epsilon = (H/L)^2$ is a number considerably smaller than unity. We seek solutions of the type

$$u_c, \ v_c, \ T_c = \underbrace{(u_c, v_c, T_c)_0}_{\sim 1} + \underbrace{\epsilon (u_c, v_c, T_c)_1}_{\sim \epsilon} + \underbrace{\epsilon^2 (u_c, v_c, T_c)_2}_{\sim \epsilon^2} + \cdots \qquad (5.51)$$

The solution for u_c, v_c, and T_c is developed systematically by substituting the series expansions (5.51) into the three governing equations (5.48)–(5.50). Next, the terms multiplied by the same power of ϵ are grouped together and, as a group, set equal to zero. Corresponding to each power of ϵ, say, ϵ^k, we must solve a system of three equations, subject to solid adiabatic wall conditions, yielding as a solution $(u_c, v_c, T_c)_k$. For this procedure to work, we must start with the $k = 0$ solution and *sequentially* work our way down the right-hand side of the series expansion (5.51). This asymptotic expansion procedure is described in some detail in Ref. 28, which shows that except for $(u_c, v_c, T_c)_0$, all the functions

$(u_c, v_c, T_c)_k$ have the same analytical form, regardless of order k. The core solution emerges as

$$u_c(y_c) = K_1 \left(\frac{y_c^3}{6} - \frac{y_c^2}{4} + \frac{y_c}{12} \right), \qquad v_c = 0 \tag{5.52}$$

$$T_c(x_c, y_c) = K_1 x_c + K_2 + K_1^2 \left(\frac{H}{L} \right)^2 \mathrm{Ra}_H \left(\frac{y_c^5}{120} - \frac{y_c^4}{48} + \frac{y_c^3}{72} \right) \tag{5.53}$$

Parameters K_1 and K_2 must be determined from end conditions in the x direction to account for the flow and temperature patterns prevailing in the two end regions (Fig. 5.9). The velocity and temperature profiles across the core region are plotted in Fig. 5.10; the core flow consists of a thermally stratified counterflow whose velocity profile and degree of thermal stratification are independent of longitudinal position x.

The net heat transfer rate from T_warm to T_cold (Fig. 5.9) follows from the energy flux integral at any x across the core counterflow:

$$q' = \int_0^H \left(k \frac{\partial T}{\partial x} - \rho c_p u T \right) dy \tag{5.54}$$
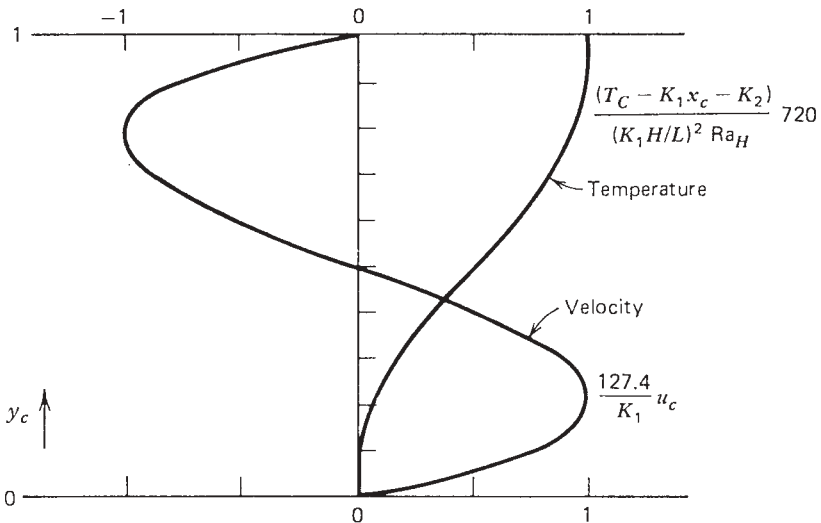

Figure 5.10 Velocity and temperature profiles in the core region of a shallow enclosure. (From Ref. 29.)

Combining this statement with the core solution [eqs. (5.52) and (5.53)] and using the conduction-referenced Nusselt number (5.40), we obtain [29]

$$\overline{Nu} = K_1 + \frac{K_1^3}{362{,}880} \left(\frac{H}{L} \, Ra_H \right)^2 \tag{5.55}$$

The heat transfer rate depends on the core axial gradient K_1. To determine K_1, we reason that as $(H/L)^2 \, Ra_H$ decreases, the core temperature distribution (5.53) becomes independent of y_c; hence, the core temperature must decrease linearly between the extreme ends of the cavity [29]. Writing

$$T_c = 0 \quad \text{at } x_c = 0 \quad \text{and} \quad T_c = 1 \quad \text{at } x_c = 1 \tag{5.56}$$

in the limit $(H/L)^2 \, Ra_H \to 0$, we find that

$$K_1 = 1 \quad \text{and} \quad K_2 = 0 \tag{5.57}$$

Therefore,

$$\overline{Nu} = 1 + \frac{1}{362{,}880} \left(\frac{H}{L} Ra_H \right)^2 \quad \text{as} \quad \left(\frac{H}{L} \right)^2 Ra_H \to 0 \tag{5.55'}$$

The asymptotic heat transfer result (5.55′) is of limited applicability; the real challenge lies in evaluating parameters $K_{1,\,2}$ for the general $\overline{Nu}$ expression (5.55) when $(H/L)^2 \, Ra_H$ is finite, that is, when the longitudinal temperature drop across the core region is *less* than the overall end-to-end temperature difference $T_{warm} - T_{cold}$. The general situation is shown schematically in Fig. 5.11
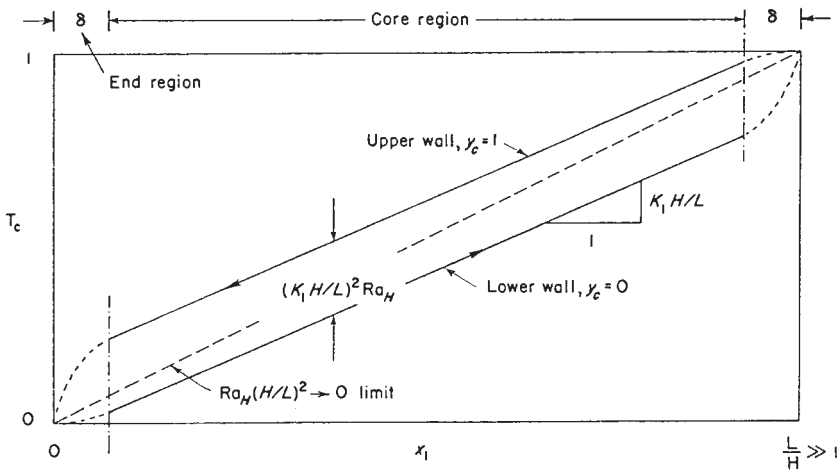

Figure 5.11 Temperature distribution along the top and bottom walls of a shallow enclosure. (From Ref. 29.)

where, in order to make the end regions visible, the horizontal coordinate is defined as

$$x_1 = \frac{x}{H} \tag{5.58}$$

Figure 5.11 shows that as $(H/L)^2 \, \mathrm{Ra}_H$ increases, the thermal stratification of the core must be taken into account. One way of treating this general case analytically is to match the core solution [eqs. (5.52) and (5.53)] to integral solutions for flow and temperature in the end regions [29].

We define the *end region* as that portion of the horizontal enclosure in which the core solution [eqs. (5.52) and (5.53)] breaks down. Inside the end region, $0 < x_1 < \delta$, the flow is turned around and cooled as it comes in contact with the vertical wall at $x_1 = 0$. We seek two equations for the unknown K_1 and K_2. The first follows from integrating the steady-state energy equation (5.4) twice, from $y_c = 0$ to $y_c = 1$, and from $x_1 = 0$ to $x_1 = \delta$. To obtain the second equation, we also integrate the momentum equation (5.7) twice:

$$\int_0^1 \left. \frac{\partial T_e}{\partial x_1} \right|_{x_1=0} dy_c = \frac{H}{L} \, K_1 - \int_0^1 |u_e T_e|_{x_1=\delta} \; dy_c \tag{5.59}$$

$$\left| \int_0^1 T_e \, dy_c \right|_{x_1=0}^{x_1=\delta} = \int_0^\delta \left. \frac{\partial^2 u_e}{\partial y_c^2} \right|_{y_c=0}^{y_c=1} dx_c - \frac{d^2}{dx_1^2} \int_0^1 v_e \, dy_c \Big|_{x_1=0}^{x_1=\delta} \tag{5.60}$$

The next step is the selection of reasonable profiles for the velocity and temperature distributions inside the end region (these functions are denoted by subscript e). The recommendation is to select profiles that satisfy the boundary conditions along the solid walls ($y_c = 0$, 1 and $x_1 = 0$) and match the value and slope of the core profiles at $x_1 = \delta$, as shown in Fig. 5.12. Thus, using

$$u_e = \frac{H}{L} \, K_1 \left(\frac{x_1}{\delta} \right)^2 \left[6 - 8\frac{x_1}{\delta} + 3 \left(\frac{x_1}{\delta} \right)^2 \right] \left(\frac{y_c^3}{6} - \frac{y_c^2}{4} + \frac{y_c}{12} \right)$$

$$v_e = -\frac{H}{L} \frac{K_1}{\delta} \left(\frac{x_1}{\delta} \right) \left(1 - \frac{x_1}{\delta} \right)^2 \left(\frac{y_c^4}{2} - y_c^3 + \frac{y_c^2}{2} \right) \tag{5.61}$$

$$T_e = \left(T_c - \delta K_1 \frac{H}{L} \right) \left[2\frac{x_1}{\delta} - \left(\frac{x_1}{\delta} \right)^2 \right] + \frac{H}{L} \, K_1 x_1$$

the energy and momentum integrals (5.59) and (5.60) yield

$$\left(\frac{H}{L} \, K_1 \right)^3 \frac{\delta \; \mathrm{Ra}_H^2}{725{,}760} = K_2 + \left(\frac{H}{L} \, K_1 \right)^2 \frac{\mathrm{Ra}_H}{1440} \tag{5.59'}$$

$$\frac{2}{5} \frac{H}{L} \, K_1 \delta \left(\frac{1}{4\delta^4} - 1 \right) = K_2 + \left(\frac{H}{L} \, K_1 \right)^2 \frac{\mathrm{Ra}_H}{1440} \tag{5.60'}$$
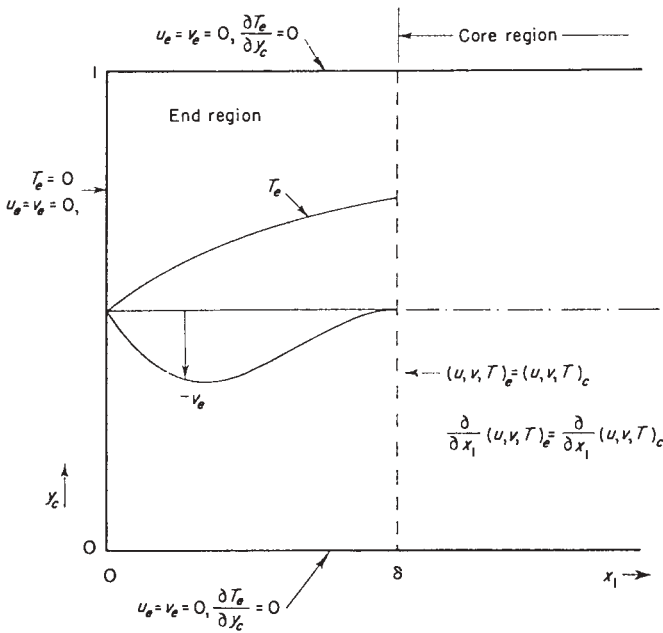
Figure 5.12   Boundary conditions for the end region. (From Ref. 29.)

The third equation necessary for uniquely determining K_1, K_2, and δ must come from the equivalent integral analysis of the warm-end region, $(L/H - \delta) < x_1 < L/H$. This procedure is equivalent to noticing that the flow in the entire cavity is symmetric about the geometric center of the cavity; the centrosymmetry condition can be expressed as

$$T_c = \frac{1}{2} \qquad \text{at } x_c = y_c = \frac{1}{2} \tag{5.62}$$

or, substituting into the core temperature expression (5.53),

$$\frac{K_1}{2} + K_2 + \left(\frac{H}{L} K_1\right)^2 \frac{\text{Ra}_H}{1440} = \frac{1}{2} \tag{5.62'}$$

Equations (5.59'), (5.60'), and (5.62') constitute a parametric solution for the result of interest, the function $K_1(H/L, \text{Ra}_H)$. Substituting this result into the general $\overline{\text{Nu}}$ expression (5.55) leads to the relationship $\overline{\text{Nu}}(H/L, \text{Ra}_H)$, which is displayed in Fig. 5.13. The presentation is made on a $\overline{\text{Nu}} - (H/L) \, \text{Ra}_H$ field, so that the asymptote (5.55') is plotted as a single line. Figure 5.13 also shows that the Nusselt number predicted by the integral analysis of the end regions [29] is in excellent agreement with experimental and numerical results [30, 31] for a wide variety of shallow enclosures, including the square geometry ($H/L = 1$).
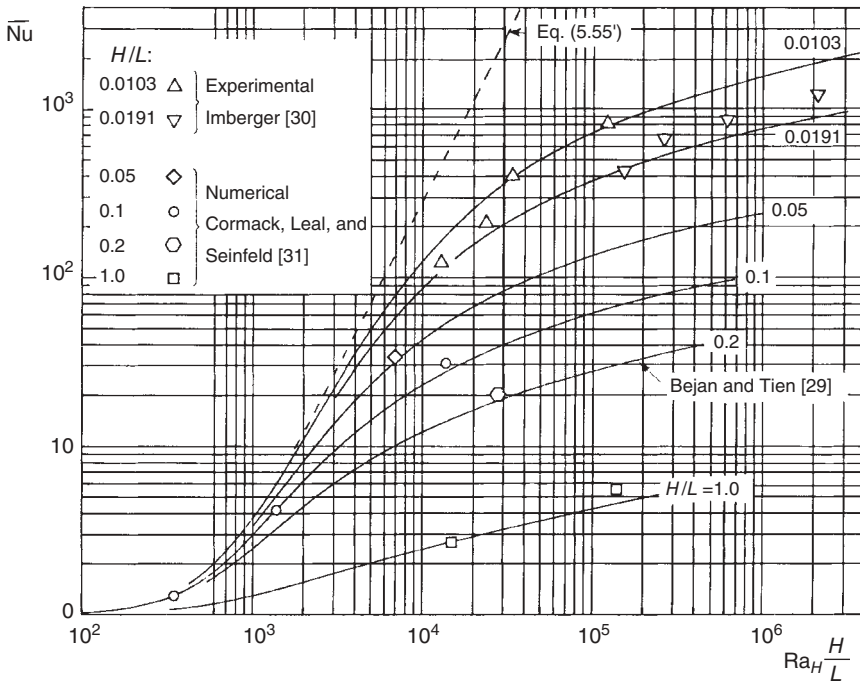
Figure 5.13   Natural convection in a shallow enclosure heated from the side. (From Ref. 29.)

The usefulness of Fig. 5.13 is stressed further by the fact that the theoretical curves agree with the empirical data not only in domain IV (Fig. 5.3), but also well into domain (III): This would be easy to see if the III–IV frontier $Ra_H \sim (H/L)^{-4}$ were plotted on Fig. 5.13 (the frontier is not shown because it would interfere with the reading of the $\overline{Nu}$ information). The success of the theoretical curves in domain III is explained by the fact that the theory takes into account the thermal resistances associated with the vertical end walls: Earlier in this chapter, we concluded that regime III is one where the vertical boundary layers dominate the overall $T_{warm} \to T_{cold}$ thermal resistance.

5.4   SUMMARY OF RESULTS FOR HEATING FROM THE SIDE

5.4.1   Isothermal Sidewalls

In Sections 5.2 and 5.3, we stressed the method behind two theoretical results that predict the heat transfer through a two-dimensional rectangular space heated from the side. A good way to use these results is to think of three classes of possible applications:

1. *Tall enclosures* ($H/L > 1$). The Nusselt number formula recommended for this class is eq. (5.40) or Fig. 5.6. As shown by the experimental and

numerical data cited in Figs. 5.7 and 5.8, this calculation is applicable when $(L/H)\,\mathrm{Ra}_H^{1/4} \gtrsim 5$, that is, when the convective heat transfer effect is significant (Nu > 1).

2. *Shallow enclosures* (*H/L < 1*). For this class of applications, the theoretical curves shown in Fig. 5.13 are adequate. For cases not plotted in Fig. 5.13, the Nusselt number can be calculated using eqs. (5.55), (5.59′), (5.60′), and (5.62′).

3. *Square enclosures* (*H/L = 1*). Figure 5.13 showed that the integral matching analysis of Ref. 29 predicts the Nusselt number correctly, provided that $(H/L)\,\mathrm{Ra}_H$ does not exceed 10^5. A better way is to use the formula recommended for tall cavities [eq. (5.40)]; Figure 5.14 shows that eq. (5.40) agrees very well with numerical and experimental data [32] gathered from eight independent sources.

Figure 5.15 presents an alternative summary of the heat transfer methodology discussed in this chapter. Plotting the conduction-referenced Nusselt number $\overline{\mathrm{Nu}}$ versus the geometric ratio *H/L*, we learn that the convective heat transfer effect reaches a maximum in the vicinity of *H/L* ∼ 1, that is, when the enclosure geometry does not suppress the fluid circulation. Conversely, the convective heat transfer contribution vanishes ($\overline{\mathrm{Nu}} \to 1$) as the buoyancy-driven loop is snuffed out (flattened) into a counterflow whose two branches are in excellent thermal contact (*H/L*→0 or *H/L* → ∞).

One way to see why $\overline{\mathrm{Nu}}$ can reach a maximum is to think of a double-wall structure, as shown in the upper part of Fig. 5.15. The fluid layer is heated from the side ($\Delta T = T_h - T_c$), and its thickness—the horizontal dimension—is fixed. The ensuing flow is segmented into rolls by the insertion of horizontal partitions, which are impermeable and adiabatic. The partitions are equidistant, but their vertical spacing *H* may vary. The changes occur at constant *L*, that is, at the constant Rayleigh number based on *L*, $\mathrm{Ra}_L = (g\beta\,\Delta T\,L^3)/\alpha\nu$. The thermal conductance reaches a maximum when each roll has a certain, intermediate
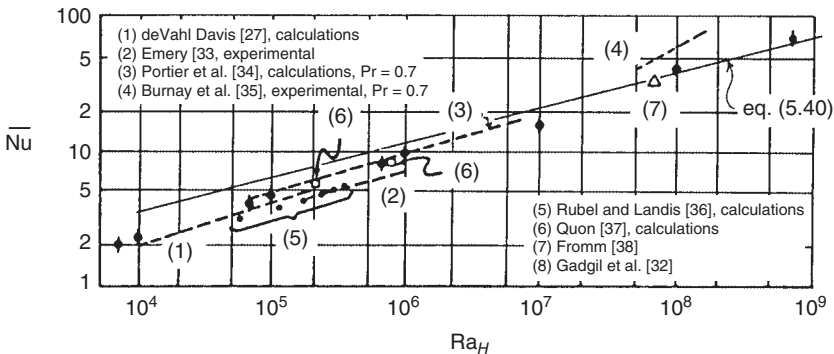

Figure 5.14 Experimental and numerical convection in a square enclosure. (From Ref. 32.)
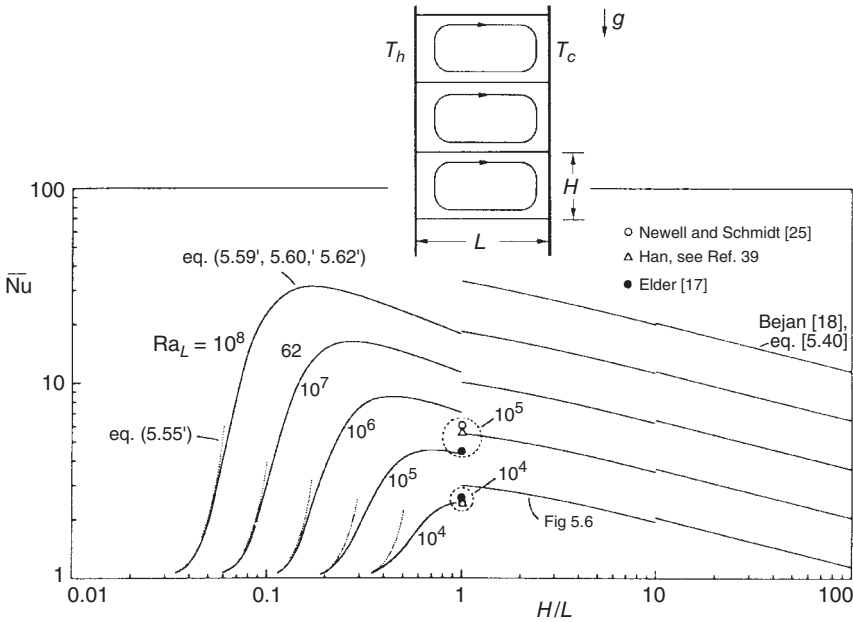
Figure 5.15   Effect of cavity shape on heat transfer through an enclosure heated from the side. (From Ref. 39.)

shape (not too tall, not too shallow). The evidence that supports the maxima exhibited in Fig. 5.15 is strong and comes from seven independent studies, which are indicated in the figure. The optimal roll shape becomes more slender as the convection becomes more intense (i.e., as Ra_L increases).

The analogy between the geometric optimization of segmented vertical layers (Fig. 5.15) and the geometric maximization of thermal conductance in layers heated from below (Section 5.5.3) was not noted until Refs. 40 and 41. An analogous geometric principle governs the maximization of thermal conductance across a segmented vertical layer filled with a fluid-saturated porous medium [39]. The maximum of Fig. 5.15 was confirmed more recently by Frederick [42]. Costa et al. [43] showed that further improvements are possible if the corners of the two-dimensional cavity are rounded. Noteworthy is the research direction started in Refs. 44–47, in which the cavity walls are deformable and the effect of deformation on global heat transfer is documented.

The enclosure flows discussed so far are all laminar. As shown in Chapter 6, the transition to turbulence occurs when the wall jet Reynolds number based on the vertical velocity scale and the local thickness of the jet exceeds $O(10^2)$.

The heatline visualization of natural convection in a square cavity with isothermal sidewalls is presented in Fig. 5.16. This was in fact the first heatline illustration of convection. The Rayleigh number is high enough so that the side-to-side heat transfer rate is dominated by convection. The heatlines show
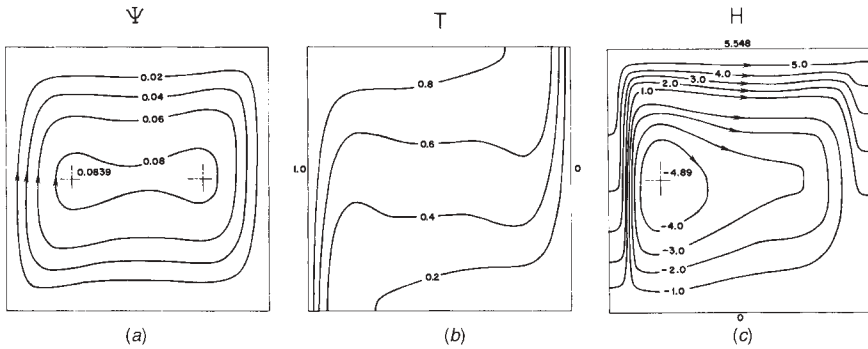
Figure 5.16   Heatlines in natural convection (square enclosure, Pr $= 7$, $Ra_H = 1.4 \times 10^5$): (a) streamlines; (b) isotherms; (c) heatlines. (From Ref. 48.)

vividly that "heat rises" and that the true energy corridor consists of two vertical boundary layers connected through an energy tube positioned along the upper wall. The heatlines are parallel to the top and bottom walls, which are adiabatic. Along the two isothermal vertical walls, the heat-lines are normal to the wall because the near-wall regions are dominated by conduction (both u and v vanish at the wall). One contribution of the heatline pattern is that it shows graphically the magnitude of the Nusselt number: The conduction-referenced Nusselt number appears in Fig. 5.16c as the value of maximum H on the top heatline of the heatfunction plot. Note further that the heatline pattern shows graphically the flow of energy downward through the core.

A comprehensive correlation for laminar natural convection in a rectangular enclosure heated and cooled from the side is due to Berkovsky and Polevikov [49]:

$$\overline{Nu}_H = 0.22\left(\frac{Pr}{0.2 + Pr}\ Ra_H\right)^{0.28}\left(\frac{L}{H}\right)^{0.09}$$

$$2 < \frac{H}{L} < 10, \quad Pr < 10^5, \quad Ra_H < 10^{13} \qquad (5.63)$$

$$\overline{Nu}_H = 0.18\left(\frac{Pr}{0.2 + Pr}\ Ra_H\right)^{0.29}\left(\frac{L}{H}\right)^{-0.13}$$

$$1 < \frac{H}{L} < 2, \quad 10^{-3} < Pr < 10^5$$

$$10^3 < \frac{Pr}{0.2 + Pr}\ Ra_H\left(\frac{L}{H}\right)^3 \qquad (5.64)$$

where $\overline{Nu}_H = \overline{q''}H/(k\ \Delta T)$. These correlations are valid in the domain indicated $(H/L, Pr, Ra_H)$ and in the "wide" cavity limit, eq. (5.18). In Ref. 49, the

Berkovsky–Polevikov correlations show a deceptively strong L/H effect because the Nusselt and Rayleigh numbers in that paper were based on L as length scale, namely, $\overline{\mathrm{Nu}}_L$ and Ra_L.

5.4.2   Sidewalls with Uniform Heat Flux

A fully analytical solution for the flow and temperature field is possible [50] when the sidewalls are heated and, respectively, cooled with uniform heat flux, q''. In the boundary layer regime, the temperature increases linearly in the vertical direction along the heated wall and the cooled wall and in the core region,

$$\frac{\partial T}{\partial y} = 0.0425 \frac{\alpha \nu}{g \beta H^4} \left(\frac{H}{L}\right)^{4/9} \mathrm{Ra}_{*H}^{8/9} \quad \text{(constant)} \tag{5.65}$$

Because the temperature increases at the same rate in the vertical direction along both walls, the wall-to-wall temperature difference is a constant at every level, $T_h(y) - T_c(y) = \Delta T$. The solution for the average Nusselt number $\overline{\mathrm{Nu}}_H = q'' H/(\Delta T \ k)$ in the boundary layer regime in $\mathrm{Pr} \gtrsim 1$ fluids is

$$\overline{\mathrm{Nu}}_H = 0.34 \mathrm{Ra}_{*H}^{2/9} \left(\frac{H}{L}\right)^{1/9} \tag{5.66}$$

where $\mathrm{Ra}_{*H} = g\beta H^4 q''/(\alpha \nu k)$. If, instead of the flux Rayleigh number Ra_{*H}, we use the ΔT-based Rayleigh number $\mathrm{Ra}_H = \mathrm{Ra}_{*H}/\overline{\mathrm{Nu}}_H = (g\beta \ \Delta T \ H^3)/\alpha \nu$, then eq. (5.66) becomes

$$\overline{\mathrm{Nu}}_H = 0.25 \mathrm{Ra}_H^{2/7} \left(\frac{H}{L}\right)^{1/7} \tag{5.67}$$

Note that since $\mathrm{Ra}_H^{2/7} = \mathrm{Ra}_H^{0.286}$, this theoretical alternative reproduces almost all the features of the empirical correlations (5.63) and (5.64) recommended for enclosures with isothermal sidewalls. This reinforces the observation that the heat transfer correlations developed for a system with isothermal walls apply reasonably well to the uniform-flux configuration, provided that the Ra_H number is then based on the wall-averaged temperature difference, $\mathrm{Ra}_H = \mathrm{Ra}_{*H}/\overline{\mathrm{Nu}}_H$. The analytical solution for the rectangular enclosure with uniform flux on the sidewalls was validated through numerical simulations of the flow and temperature fields [50], Fig. 5.17. Natural convection in enclosures with discrete heat sources arranged in an array was documented numerically by Tou et al. [51].

5.4.3   Partially Divided Enclosures

Real-life systems such as buildings, lakes, and solar collectors rarely conform to the single-enclosure model used in much of the natural convection literature. A very basic model for the study of natural convection in such systems is
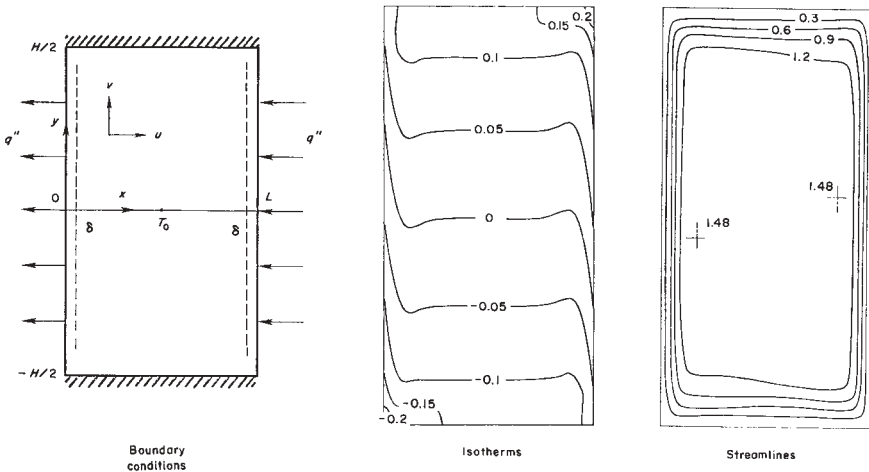
Figure 5.17   Natural convection in an enclosure with uniform heat flux (Pr = 7, Ra_H = 3.5 × 10^6, H/L = 2). (From Ref. 50.)

the association of two enclosures communicating laterally through a doorway, window, or corridor or over an incomplete dividing wall. The partially divided enclosure model was studied [52–57] in the form of basic experiments involving the two-dimensional geometries sketched in Fig. 5.18.

The new flow feature caused by the presence of a vertical obstacle inside the cavity is the *trapping* of the fluid on one side of the obstacle. For example, if the partial wall is mounted on the floor of the cavity, the fluid on the cold side of the obstacle becomes trapped and inactive with respect to convection heat transport. Relative to convection in a box without internal flow obstructions, where the flow fills the entire cavity, the presence of sizable pools of inactive
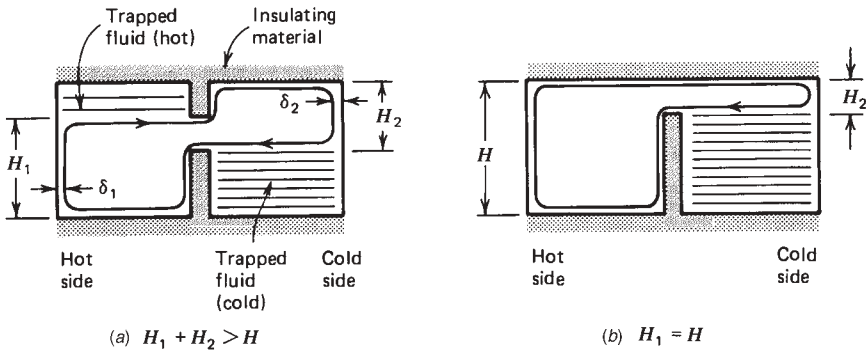
Figure 5.18   Natural convection patterns in enclosures communicating through a side opening.

fluid in Fig. 5.18 has a significant effect on the overall heat transfer rate between the far ends of the cavity.

The reduction in the end-to-end heat transfer rate can be predicted based on scale analysis, as shown in Refs. 52 and 55. Assuming that no heat transfer takes place through the incomplete partition, the end-to-end heat transfer is impeded by the two thermal resistances associated with the two vertical boundary layers driven by the differentially heated end walls. Let (δ_1, H_1) and (δ_2, H_2) be the length scales of the two boundary layers, as shown in Fig. 5.18. The two heights, H_1 and H_2, are known from the geometry of the internal partition. The thermal boundary layer thickness scales are known from arguments presented earlier in this chapter and in Chapter 4 for $\mathrm{Pr} > 1$,

$$\delta_1 \sim H_1 \; \mathrm{Ra}_{H_1}^{-1/4}, \qquad \delta_2 \sim H_2 \; \mathrm{Ra}_{H_2}^{-1/4} \tag{5.68}$$

where the subscripts H_1 and H_2 indicate that in each case, the Rayleigh number is based on the actual height of the boundary layer, not on the height of the enclosure, H. Noting that the thermal resistances of the two boundary layers scale as

$$\frac{\delta_1}{kH_1} \quad \text{and} \quad \frac{\delta_2}{kH_2} \tag{5.69}$$

the end-to-end heat transfer rate q' may be calculated as

$$q' = \frac{\Delta T}{C_1 \, \delta_1/kH_1 + C_2 \, \delta_2/kH_2} \tag{5.70}$$

where C_1 and C_2 are by definition numerical coefficients of order $O(1)$. This heat transfer result may be cast in dimensionless form to show the effect of obstacle geometry:

$$\frac{q'}{k \, \Delta T} = \frac{\mathrm{Ra}_H^{1/4}}{C_1 (H/H_1)^{3/4} + C_2 (H/H_2)^{3/4}} \tag{5.71}$$

Looking at Fig. 5.18b and at eq. (5.71), we see that as the opening left above the partition decreases, the ratio H/H_2 becomes very large and the heat transfer rate drops sharply. Setting $C_1 = 1.5$ and $C_2 = 3$, eq. (5.71) correlates the heat transfer rates measured in a box with a single internal partition [55] (as in Fig. 5.18b, where $H = H_1$) in the Ra_H range $10^9 – 10^{10}$.

The ''fluid trap'' phenomenon created by the partitions considered above is capable of totally shutting off the natural circulation in the enclosure. Figure 5.19 shows the two ways in which one could install two incomplete internal walls whose heights add to more than H. If the floor obstacle is on the hot side of the enclosure, the fluid sandwiched between the two obstacles is stably stratified and natural convection is prohibited. If the floor obstacle is on the cold side, Fig. 5.19 shows that natural convection is possible as a single cell strangled by the two obstacles. The effect of a venetian blind inserted in a double-walled enclosure and modeled as a vertical permeable screen was studied by Zhang et al. [58].
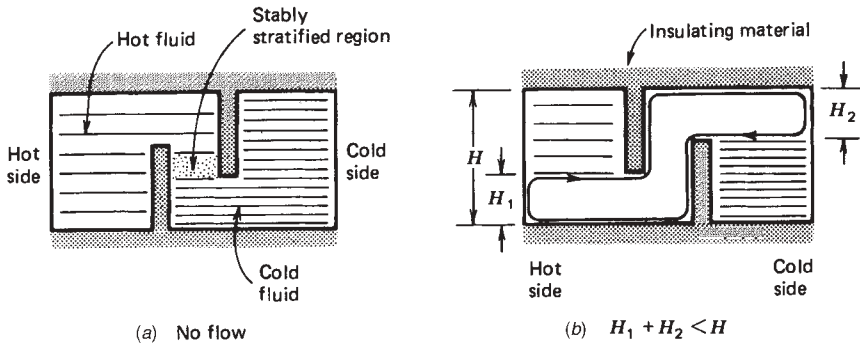
Figure 5.19   Incomplete partitions in an enclosure.

5.4.4   Triangular Enclosures

Another basic enclosure geometry that has important applications is the triangular enclosure with different temperatures maintained along the horizontal wall and the sloped wall. The interest in this geometry stems from problems involving the natural circulation in shallow waters with sloping bottoms heated by solar radiation, and energy conservation in solar collectors and attics. Experiments in triangular enclosures were reported in Refs. 59 and 60. Numerical simulations for $1 < \mathrm{Ra}_H < 10^6$ and an asymptotic analytical solution valid for very shallow attic spaces are also available [61]. Attic spaces were simulated more recently by Haese and Teubner [62].

Natural convection in triangular enclosures is an interesting interaction between the two basic configurations identified in the introduction to this chapter: enclosures heated from the side and enclosures heated from below. If the sloped wall is situated above the horizontal wall, and if the sloped wall is heated and the bottom wall is cooled, the downward heat transfer through the enclosure is ruled by pure conduction. If the sloped wall is cooled and the bottom wall is heated, the enclosure is ruled by a single-cell flow driven by the sloped wall. The single-cell circulation persists (in a time-averaged sense) even at high Rayleigh numbers, where the flow is turbulent [60]. The interesting aspect of this conclusion is that whereas the enclosure is cooled from above *and* from the side (along the sloped wall), the natural circulation observed is of the type associated with enclosures heated from the side (i.e., single-cell).

5.5   ENCLOSURES HEATED FROM BELOW

The fundamental difference between enclosures heated from the side (Fig. 5.1) and enclosures heated from below (Fig. 5.20) is that in enclosures heated from the side, a buoyancy-driven flow is present as soon as a very small temperature difference $(T_h - T_c)$ is imposed between the two sidewalls. By contrast, in
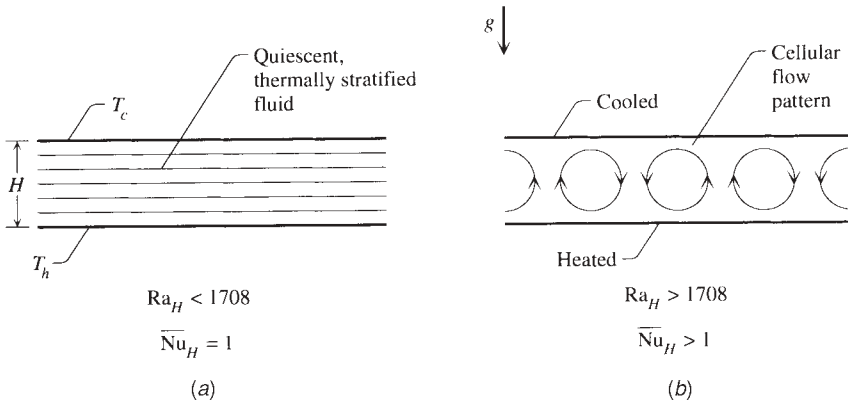
Figure 5.20   Horizontal fluid layer heated from below.

enclosures heated from below, the imposed temperature difference must exceed a finite *critical* value before the first signs of fluid motion and convective heat transfer are detected. In this section we start with a review of the experimental evidence on enclosures heated from below and continue with a series of new and purely theoretical attempts to predict the experimental results.

5.5.1   Heat Transfer Results

When the enclosure is sufficiently long and wide in the horizontal direction, the condition for the onset of convection is expressed by the critical Rayleigh number [63]

$$\text{Ra}_H \gtrsim 1708 \tag{5.72}$$

where $\text{Ra}_H = g\beta(T_h - T_c)H^3/\alpha\nu$. As suggested in Fig. 5.20, immediately above $\text{Ra}_H \cong 1708$, the flow consists of counterrotating two-dimensional rolls, the cross sections of which are almost square. This flow pattern is commonly recognized as *Bénard cells*, or *Bénard convection*, in honor of H. Bénard who reported the first investigation of this phenomenon in 1900. The cellular flow becomes considerably more complicated as Ra_H exceeds by one or more orders of magnitude the convection-onset value. The two-dimensional rolls break up into three-dimensional cells, which appear hexagonal in shape when viewed from above (Fig. 5.21). At even higher Rayleigh numbers, the cells multiply (become narrower), and eventually, the flow becomes oscillatory and turbulent. The hierarchy of flow regimes and various transitions in Bénard convection has been reviewed by Busse [64].

   The generation of Bénard-like cells is visible in the process of filling a glass with dark beer, while pouring as closely as possible to the center of the glass (Fig. 5.22). The bubbles present in the beer are the flow visualization device: They collect along the surface only in those regions that correspond to downward
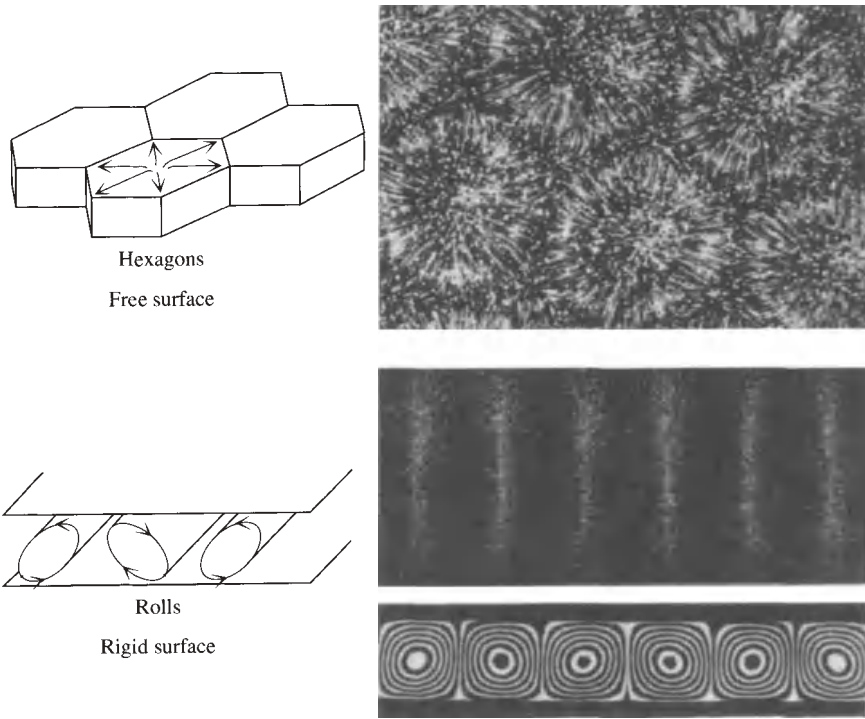
Figure 5.21 Rolls and hexagonal cells in a fluid layer heated from below. (Reprinted with permission from J. Zierep and H. Oertel, Jr., eds., *Convective Transport and Instability Phenomena*, 1982, p. 10. Copyright © 1982 G. Braun, Karlsruhe, Germany).

flow. The photographs show clearly the formation of surprisingly regular cells, as each downflow zone is sandwiched between upflow zones (dark areas). After some practice, it becomes possible to vary the pouring rate and to discover that the cell number decreases as the pouring is done more gently. The flow has the natural property to select its own length scales.

The heat transfer effect of the cellular flow is to augment the net heat transfer rate in the vertical direction (i.e., to increase it above the pure-condition rate that would prevail in the absence of fluid motion). The dimensionless number that measures this augmentation effect is the average Nusselt number based on the vertical dimension H, namely, $\overline{Nu}_H = \overline{q''} H / (k\,\Delta T)$. Experimental heat transfer measurements in the range $3 \times 10^5 < Ra_H < 7 \times 10^9$ support the correlation [65]

$$\overline{Nu}_H = 0.069 Ra_H^{1/3}\ Pr^{0.074} \tag{5.73}$$

The physical properties needed for calculating $\overline{Nu}_H$, Ra_H, and Pr are evaluated at the average fluid temperature $(T_h + T_c)/2$. Equation (5.73) holds when the horizontal layer is sufficiently wide so that the effect of the short vertical sides is minimal.

Figure 5.22 Constructal design of turbulence in a glass of dark beer. The momentum from the falling jet is transferred more effectively to the body of stationary liquid by a design of eddies regularly spaced around the rim. The bubbles present in the beer are the visualization secret. They gather on the surface only above the regions that correspond to downward flow.

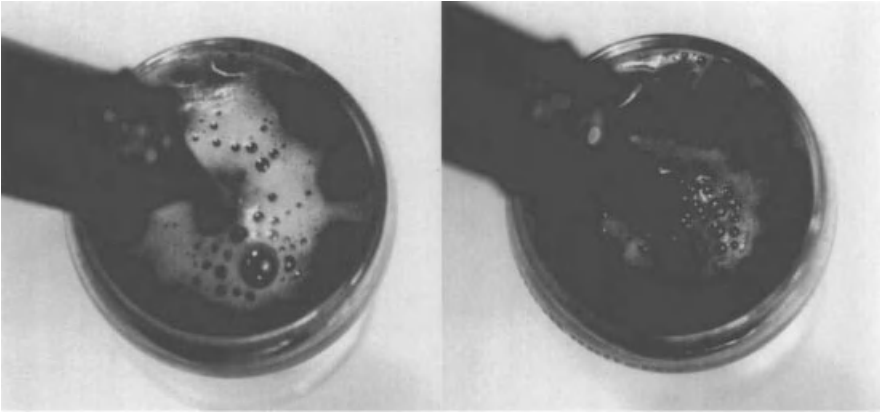The experimental data correlated by eq. (5.73) line up in such a way that the exponent of Ra_H increases slightly as Ra_H increases. The exponent is closer to 0.29 at the low-Ra_H end of the correlation (roughly, when $Ra_H < 10^8$). Its value becomes practically equal to $\frac{1}{3}$ when Ra_H exceeds approximately 10^8. The proportionality $\overline{Nu}_H \sim Ra_H^{1/3}$ persists as Ra_H increases above the range covered by eq. (5.73).

I pointed out that the proportionality $\overline{Nu}_H \sim Ra_H^{1/3}$ means that the actual heat transfer rate $(\overline{q''})$ from T_h to T_c is independent of the layer thickness H. In the 1984 edition of this book, I showed that the $\overline{Nu}_H \sim Ra_H^{1/3}$ proportionality can be predicted theoretically by performing the scale analysis of a single roll (cell) of the Bénard convection pattern. Two alternative theories are presented later in this section.

At subcritical Rayleigh numbers, $Ra_H \lesssim 1708$, the fluid is quiescent, and the temperature decreases linearly from T_h to T_c. The heat transfer rate across the fluid layer is by pure conduction; therefore, $\overline{Nu}_H = 1$.

The convection onset criterion (5.72)—the value 1708 on the right side— refers strictly to an infinite horizontal layer with rigid (no-slip) and isothermal top and bottom boundaries. Similar criteria, all with critical Rayleigh numbers on the order of 10^3, hold for other horizontal layer configurations (i.e., combinations of top and bottom boundary conditions).

5.5.2 Scale Theory of the Turbulent Regime

When the Rayleigh number Ra_H is orders of magnitude greater than the critical value, convection in the bottom-heated fluid layer is turbulent. The core of the fluid layer is practically at the average temperature $(T_h + T_c)/2$, while temperature drops of size $(T_h - T_c)/2$ occur across thin fluid layers that line the two horizontal
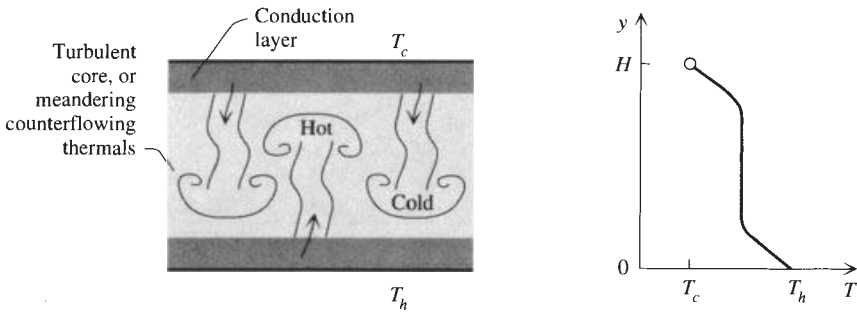
Figure 5.23   Flow structure of a layer heated from below in the high-Ra$_H$ regime.

walls (Fig. 5.23). The turbulence over most of the horizontal layer of thickness H is caused by the buckling thermals that rise from the heated bottom and those that fall from the cooled top. The turbulent core of the layer is sandwiched between two δ-thin conduction layers. Each δ layer becomes unstable when its Rayleigh number based on height (δ) exceeds the order 10^3:

$$\text{Ra}_\delta \sim 10^3 \qquad (5.74)$$

This is equivalent to writing

$$\text{Ra}_H \sim 10^3 \left(\frac{H}{\delta}\right)^3 \qquad (5.75)$$

in which Ra$_H$ is the usual Rayleigh number, $\text{Ra}_H = (g\beta\ \Delta T\ H^3)/\alpha\nu$, and $\Delta T = T_h - T_c$. The heat transfer from T_h to T_c is impeded by layers of thickness δ (not H); therefore,

$$\overline{q''} \sim k\frac{\Delta T}{\delta} \qquad (5.76)$$

and

$$\overline{\text{Nu}}_H = \frac{\overline{q''}}{(k\ \Delta T)/H} \sim \frac{H}{\delta} \qquad (5.77)$$

By eliminating H/δ between eqs. (5.75) and (5.77), we obtain

$$\overline{\text{Nu}}_H \sim 10^{-1}\text{Ra}_H^{1/3} \qquad (5.78)$$

This simple theoretical result reproduces almost all the features of the empirical correlation recommended for turbulent (high-Ra$_H$) Benard convection calculations, eq. (5.73). This back-of-the-envelope derivation is also a reminder that the heat transfer rate does not depend on H [see eq. (5.76)].

5.5.3 Constructal Theory of Bénard Convection

Considerably more theoretical progress was made recently based on the constructal law [41,66–68]. First is the transition between the two heat transfer regimes shown in Fig. 5.20. Why should a disorganized motion and heat transfer mechanism (chaotic, molecular thermal diffusion) change abruptly such that the disorganized entities ride together in a macroscopic motion visible as streams? Why should shapelessness (diffusion) coexist with shape and structure (streams)?

The single-phase fluid layer is characterized by the thickness H and the bottom excess temperature $\Delta T = T_h - T_c$. In line with the access-facilitating principle of the constructal law, we search for the most direct route for heat transfer across the fluid layer. In other words, we subject heat transfer to the same principle of facilitating momentum transfer that in Chapter 6 is used to predict turbulence. The classical solution for time-dependent thermal diffusion near a wall with a sudden jump in temperature (ΔT) is

$$\frac{T - T_c}{\Delta T} = \mathrm{erfc}\left[\frac{y}{2(\alpha t)^{1/2}}\right] \tag{5.79}$$

where T_c is the far-field temperature in the fluid. The effect of the wall temperature jump is felt to the distance

$$\frac{y}{2(\alpha t)^{1/2}} \sim 1 \tag{5.80}$$

which represents the knee in the temperature profile of eq. (5.79). The time needed by the heating effect to travel by thermal diffusion the distance H is

$$t_0 \sim \frac{H^2}{4\alpha} \tag{5.81}$$

The time t_0 corresponds to the heating of the entire layer ($y \sim H$). The factor 4 in the denominator arises from the shape of the time-dependent temperature profile in eq. (5.79).

Pure conduction continues to be the preferred heat transfer mechanism, and the fluid layer remains macroscopically motionless as long as H is small enough that t_0 is the shortest time of transporting heat across the layer. The alternative to conduction is convection, or the *channeling* of energy transport on the back of fluid streams, which act as conveyor belts (rolls, Fig. 5.21b). The question is whether the convection time (t_1) around the convection cell is shorter than t_0: This is the constructal law of greater flow access in time [66–68]. The convection time is $t_1 \sim 4H/v$, where v is the vertical velocity of the fluid (the peripheral velocity of the roll).

To evaluate the v and t_1 scales, we rely on scale analysis. The effective diameter of each roll is on the order of H, but smaller, for example, $H/2$. When the roll turns, an excess temperature on the order on $\Delta T/2$ is created between the moving stream and the average temperature of the fluid layer. This excess

temperature induces buoyancy on the order of $(g\beta \ \Delta T)/2$. The total buoyancy force that drives the roll is on the order of $[g\beta \ \Delta T/2]\rho(H/2)^2$. When the Prandtl number is on the order of 1 or greater, the driving force is balanced by the viscous shearing force $\tau H/2$, where the shear stress scale is $\tau \sim \mu v/(H/4)$. The force balance buoyancy $\sim$ friction yields the velocity scale $v \sim (g\beta \ \Delta T H^2)16v$ and the corresponding convection time scale

$$t_1 \sim \frac{64v}{g\beta \ \Delta T \ H} \tag{5.82}$$

To see the emergence of an opportunity to greater flow access, imagine that H increases. The thermal diffusion time t_0 increases with H, whereas the convection time t_1 (a *property* of the H-tall system, even if quiescent) decreases monotonically. Setting $t_1 \lesssim t_0$ and using eqs. (5.81) and (5.82), we find that the first streams should occur when $Ra_H = 256$, where $Ra_H = (g\beta \ \Delta T H^3)/\alpha v$ is the Rayleigh number.

The exact solution for this critical condition is $Ra_H = 1708$, in other words, $Ra_H = O(10^3)$. The error in the result of scale analysis is understandable (and not important) because it can be attributed to the imprecise geometric ratios (factors on the order of 1) introduced along the argument made above eq. (5.82). A more exact estimate can be achieved in an analysis that estimates better the scales of the flow, as we demonstrate next. What is important is that the critical Ra_H predicted is a *constant* considerably greater than 1. This constant expresses the compounded effect of all the geometric ratios of the roll-between-plates configuration. Had we neglected the geometric reality of how the rolls must fit, e.g., the geometric fact that the factor 4 belongs in the denominator of approximation (5.81), we would have obtained only $Ra_H \sim 1$ [i.e., the correct dimensionless group Ra_H but not the important result that the critical Ra_H is a *geometric* (structural) constant]. All the transition (critical) numbers of fluid mechanics are constants that reflect the geometry (shape) of the "elemental system" of constructal theory—the first roll or the first eddy (e.g., Table 6.1), where stream flow is balanced by diffusion.

When convection is present there are two heat transfer mechanisms, not one. Each roll characterized by $t_0 \sim t_1$ is an elemental system in the sense of constructal theory. The equipartition of time $t_0 \sim t_1$ is the analog of the equipartition of temperature difference and pressure drop in other constructal multiscale flow structures [41,66–68]. Conduction, or thermal diffusion, is present and does its job at every point inside the elemental volume $H \times 2L_r$, shown in Figs. 5.24 and 5.25. Superimposed on this volumetric heat flow is an optimal pattern of convection streets that guide the imposed heat current *faster* across H.

The decrease of the temperature difference across H continues to manifest itself as H (or Ra_H) increases, and convection becomes more intense. This is achieved through the selection of the number of rolls that fill a layer of horizontal dimension L, or the selection of the roll aspect ratio H/L_r. We can describe
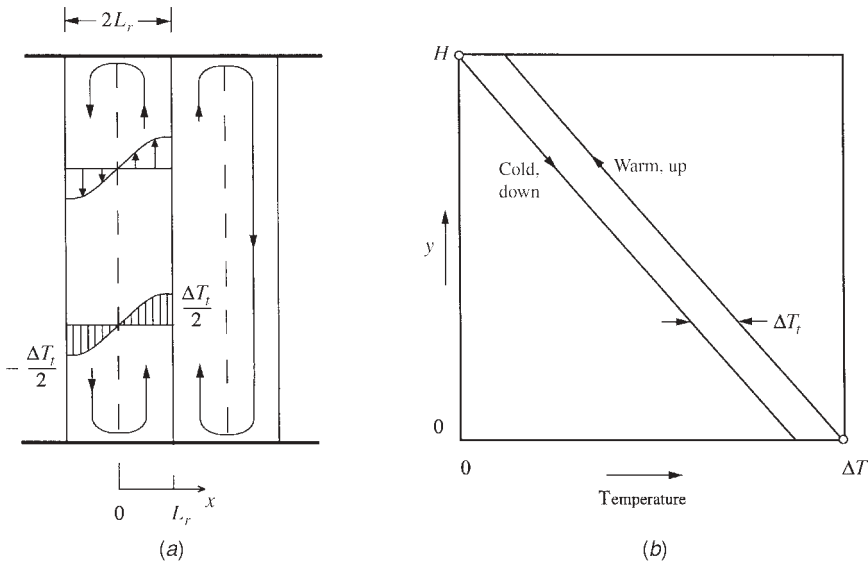
Figure 5.24   Flow geometry in the many-cells limit. (From Ref. 41.)

this process analytically by intersecting the two asymptotes of the geometric configuration: many cells versus few cells.

All of the physical parameters of the system of Fig. 5.20 are fixed except for the half-thickness of the cell L_r, or the number of cells. For simplicity, we assume that the flow is two-dimensional; however, a strongly three-dimensional flow can be discovered by use of the same intersection-of-asymptotes method [69]. Because we are free to vary L_r, we can imagine the many-cells limit shown in Fig. 5.24. Each cell is a very slender counterflow, which has the important property that it can sustain a longitudinal (i.e., vertical) temperature gradient of the same order as the imposed gradient $\Delta T/H$. The longitudinal temperature gradient occurs because one branch of the counterflow loses heat to (or gains heat from) the other branch.

We are interested in more than just the orders of magnitude of the flow variables: This is why in addition to using scale analysis we assume a reasonable shape for the laminar temperature profile. If the temperature profile is parabolic across each branch (Fig. 5.24), and if the maximum temperature difference across one branch is $\Delta T_t/2$, the average temperature difference between the two branches is $\frac{2}{3}\Delta T_t$. We can estimate the mass flow rate of one branch, $\dot{m}'$, by writing the momentum equation for fully developed flow in the upflowing branch:

$$\frac{d^2v}{dx^2} = -\frac{g\beta}{\nu}\ (\overline{T}_{\text{up}} - \overline{T}_{\text{down}}) \qquad (5.83)$$
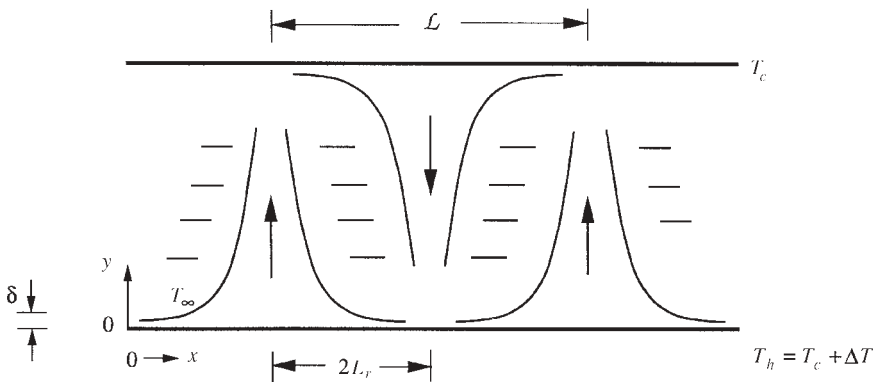
Figure 5.25   Flow geometry in the few-cells limit. (From Ref. 41.)

where $\overline{T}_{\text{up}}$ and $\overline{T}_{\text{down}}$ are the average temperatures of the upflowing and down-flowing branches. Noting that $(\overline{T}_{\text{up}} - \overline{T}_{\text{down}}) \cong \frac{2}{3}\Delta T_t$ and integrating eq. (5.83) subject to the conditions of no-slip at $x = 0$ and zero shear at $x = L_r$, we obtain $v(x)$ and the mass flow rate,

$$\dot{m}' = \frac{2\rho g \beta L_r^3 \, \Delta T_t}{9\nu} \tag{5.84}$$

The enthalpy lost by the upflowing branch is $\dot{m}' c_P (T_{\text{in}} - T_{\text{out}})$, where T_{in} and T_{out} are the start and the finish bulk temperatures of the branch. Figure 5.24b shows that $T_{\text{in}} - T_{\text{out}} = \Delta T - \Delta T_t$. This enthalpy loss is being conducted horizontally to the downflowing branch. The horizontal temperature gradient across the interface between the two branches ($x = 0$; dashed line in Fig. 5.24a) is $2\left(\frac{1}{2}\Delta T_t / L_r\right)$, where the leading factor of 2 is the mark of the assumed parabolic temperature profile. Finally, the first law of thermodynamics written for the upflowing branch as a flow system of size $H \times L_r$ is

$$\dot{m}' c_P (\Delta T - \Delta T_t) = kH \frac{\Delta T_t}{L_r} \tag{5.85}$$

Combining eqs. (5.84) and (5.85), we find the relation between the transversal temperature difference ΔT_t and the difference imposed vertically (ΔT):

$$\frac{\Delta T_t}{\Delta T} = 1 - \frac{9}{2\text{Ra}_H} \left(\frac{H}{L_r}\right)^4 \tag{5.86}$$

Another property of the counterflow is that it convects energy longitudinally (upward) at the rate $\dot{m}' c_P (\overline{T}_{\text{up,b}} - \overline{T}_{\text{down,b}})$. The present analysis is sufficiently approximate so that we may replace the bulk temperature difference with the

mean temperature difference $\frac{2}{3}\Delta T_t$. The counterflow carries this energy current upward through a space of thickness $2L_r$. Consequently, the average heat flux removed by the counterflow from the bottom wall is

$$q'' = \frac{\dot{m}'c_p\ \frac{2}{3}\Delta T_t}{2L_r} \tag{5.87}$$

or, after eqs. (5.84)–(5.86) are used,

$$q'' = \frac{2kg\beta L_r^2}{27\alpha v}(\Delta T)^2\left[1 - \frac{9}{2\mathrm{Ra}_H}\left(\frac{H}{L_r}\right)^4\right]^2 \tag{5.88}$$

This result has been sketched in Fig. 5.26. The heat flux decreases approximately as L_r^2 in the limit $L_r \to 0$ (i.e., as the cells become more numerous).

In the opposite limit, the flow is spread out and consists of a small number of upflows and downflows (Fig. 5.25). Each vertical flow is a plume formed over a long portion of horizontal wall of length $L = 4L_r$. The thermal resistance is due to the horizontal boundary layers that line each section of length $2L_r$. Although it is possible to obtain a purely theoretical estimate for the heat transfer rate across such a boundary layer, we may use an estimate derived from an experimental correlation. The plume rises or sinks in a quiescent and thermally stratified fluid of average temperature difference $\Delta T/2$. This means that the effective temperature difference between the horizontal base of each plume and the fluid reservoir that surrounds it is $\theta = \Delta T/2$. The average heat flux removed by the plume is known from measurements [70]:

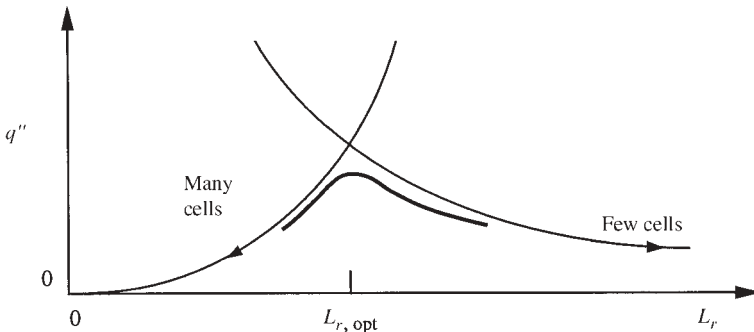$$\frac{q''L}{\theta k} = 0.54\mathrm{Ra}_{L,\theta}^{1/4} \tag{5.89}$$

Figure 5.26   Intersection of asymptotes yields Bénard convection: many cells versus few cells. (From Ref. 41.)

where $\mathrm{Ra}_{L,\theta}$ is the Rayleigh number based on L and θ and $\mathrm{Ra}_{L,\theta} < 10^7$. Note in eq. (5.89) the heat flux is independent of the vertical dimension of the system, H. Expressed in terms of L_r and ΔT, eq. (5.89) reads as

$$q'' = 0.161 \frac{k\,\Delta T}{H}\left(\frac{H}{L_r}\right)^{1/4}\mathrm{Ra}_H^{1/4} \tag{5.90}$$

In conclusion, when the horizontal surfaces are covered sparsely with isolated plumes, the wall-averaged heat flux decreases monotonically as the spacing L_r increases. This asymptotic trend has been added to Fig. 5.26 to show that a flow geometry with maximal heat flux exists. We can locate the constructal flow structure (L_r) by intersecting asymptotes (5.88) and (5.90):

$$\mathrm{Ra}_H^{1/3}\left(\frac{L_{r,\mathrm{opt}}}{H}\right)\left[1 - \frac{9}{2\mathrm{Ra}_H}\left(\frac{H}{L_{r,\mathrm{opt}}}\right)^4\right]^{8/9} = 1.41 \tag{5.91}$$

It is convenient to define the dimensionless factor f as

$$f = \frac{L_{r,\mathrm{opt}}}{H\,\mathrm{Ra}_H^{-1/3}} \tag{5.92}$$

such that eq. (5.91) provides implicitly the function $f(\mathrm{Ra}_H)$:

$$f^4 - 1.474\,f^{23/8} = \tfrac{9}{2}\,\mathrm{Ra}_H^{1/3} \tag{5.93}$$

Equations (5.92) and (5.93) pinpoint the value of the flow slenderness ratio $L_{r,\mathrm{opt}}/H$ as a function of Ra_H. The heat flux that corresponds to this geometry is obtained by substitution of $L_r = L_{r,\mathrm{opt}}$ into eq. (5.88) or (5.90):

$$\mathrm{Nu}_{\max} \le 0.161 f^{-1/4}\mathrm{Ra}_H^{1/3} \tag{5.94}$$

The inequality sign is a reminder that the actual peak of the $q''_{\max}(L_r)$ curve falls under the intersection of the two asymptotes (Fig. 5.26). Electronics cooling applications of the intersection-of-asymptotes method have shown repeatedly that the inequality sign accounts for a factor of approximately $\frac{1}{2}$ between the height of the point of intersection and the peak of the actual curve. Finally, at the intersection, eq. (5.86) reads as

$$\frac{\Delta T_t}{\Delta T} = 1.47 f^{-9/8} \tag{5.95}$$

Figure 5.27 shows the main features of the geometry derived based on this theory. The plotted $\mathrm{Nu}_{\max}$ curve is based on relation (5.94) with the equal sign,

$$(a)$$

$$(b)$$
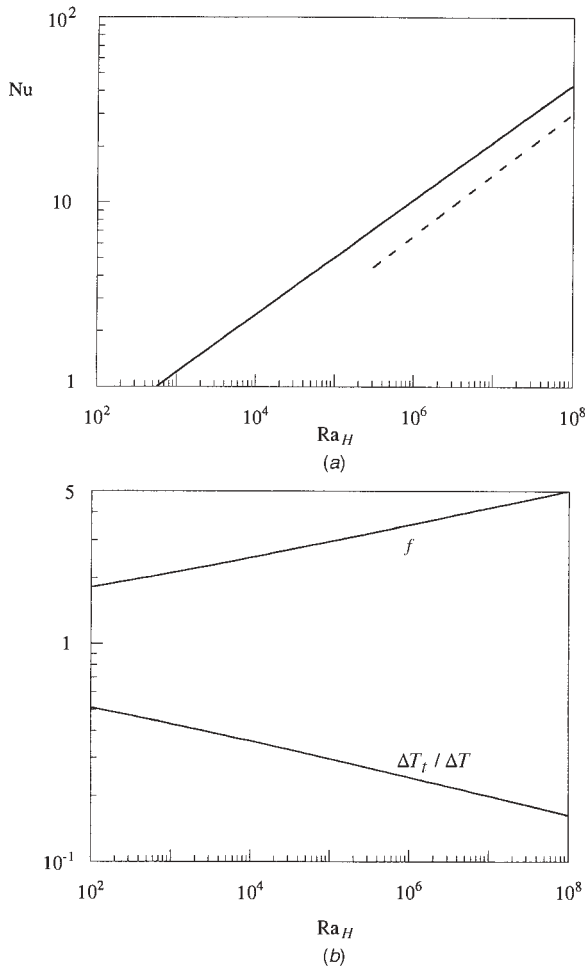
Figure 5.27   Heat transfer in the cellular flow design defined by the intersection of asymptotes in Fig. 5.26. (From Ref. 41.)

which means that the actual $\mathrm{Nu_{max}}$ should be lower by a factor of the order of $\frac{1}{2}$. Several features of this solution are worth nothing:

1. The $\mathrm{Nu_{max}}(\mathrm{Ra}_H)$ curve comes close to the experimental data [e.g., the $\mathrm{Pr} \sim 1$ range of the widely accepted correlation (5.73)]. If the expected factor on the order of $\frac{1}{2}$ is applied, the $\mathrm{Nu_{max}}$ curve falls right on top of the correlation, which is shown by a dashed line in Fig. 5.27a. Furthermore, $L_{r,\,\mathrm{opt}}/H \cong 0.35$, which agrees with the linear stability solution $L_{r,\,\mathrm{opt}}/H \sim 0.5$.

2. The $Nu_{max}(Ra_H)$ curve cuts the $Nu_{max} = 1$ line at an $Ra_H \cong 526$, which is a value of order 10^3. The predicted transition between pure diffusion and stream flow is in agreement with the constructal law. This improved estimate of the critical Ra_H for the onset of convection validates the comments made in the second paragraph under eq. (5.87).

3. The $Nu_{max}(Ra_H)$ curve is described approximately by $Nu_{max} \sim Ra_H^n$, where the exponent n decreases from 0.333 to 0.313 as Ra_H increases. Over most of the Ra_H range of Fig. 5.27, the n value is close to 0.313 as the f factor approaches $1.033 \, Ra_H^{1/12}$. This behavior also agrees with observations. The minor and gradual decrease of the Ra_H exponent is well known and is one point of controversy in the field of Bénard convection. In this section we predicted this trend from pure theory.

4. The transversal temperature difference between the vertical branches of the roll (ΔT_t) decreases as Ra_H increases (i.e., as convection intensifies). Although this trend may seem counterintuitive, it is explained by the fact that the rolls become more slender as Ra_H increases. In this limit the vertical streams find themselves in a more intimate thermal contact.

5. The slenderness ratio is $L_{r, \, opt} = Hf \, Ra_H^{1/3}$ and approaches $L_{r, \, opt} \cong 1.033H$ $Ra_H^{-1/4}$ as Ra_H increases (i.e., when $f \cong 1.033 \, Ra_H^{1/12}$).

5.6 INCLINED ENCLOSURES

In the tilted configuration (Fig. 5.28), L is the distance measured in the direction of the imposed temperature difference $(T_h - T_c)$. The angle made with the horizontal direction, τ, is defined such that in the range $0° < \tau < 90°$, the heated surface is positioned *below* the cooled surface. The enclosure heated from the side is the $\tau = 90°$ case of the inclined enclosure. The $\tau = 0°$ case represents the rectangular enclosure heated from below (Fig. 5.20), except that now the distance between the differentially heated walls is labeled L.

The angle τ has a dramatic effect on the heat and flow characteristics of the enclosure. As τ decreases from $180°$ to $0°$, the heat transfer mechanism switches from pure conduction at $\tau = 180°$, to single-cell convection at $\tau = 90°$, and finally, to Bénard convection at $\tau = 0°$. The conduction-referenced Nusselt number $\overline{Nu}_L = \overline{q''}L/(k \, \Delta T)$ rises from the pure conduction level $\overline{Nu}_L \, (180°) = 1$ to a maximum $\overline{Nu}_L$ value near $\tau = 90°$. As τ decreases below $90°$, the Nusselt number decreases and passes through a local minimum at a special tilt angle $\tau = \tau*$, which is a function of the geometric aspect ratio of the enclosure [71]:

H/L	1	3	6	12	>12
τ^*	$25°$	$53°$	$60°$	$67°$	$70°$
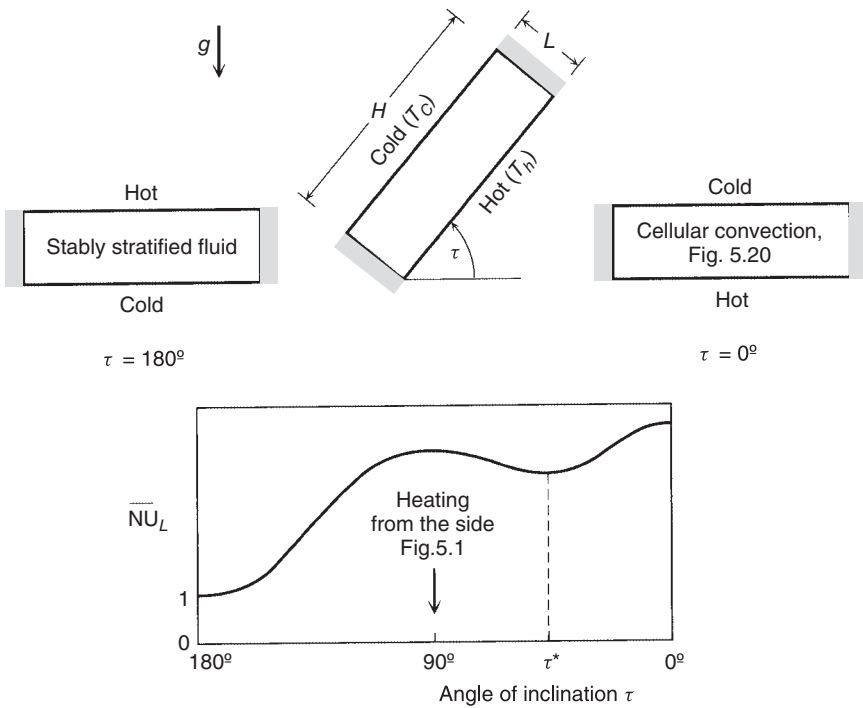
Figure 5.28 Effect of inclination on natural convection in enclosures.

As τ continues to decrease below $\tau = \tau^*$, the heat transfer rate rises toward another maximum associated with the Bénard convection regime, $\overline{\mathrm{Nu}}_L(0°)$. The $\overline{\mathrm{Nu}}_L(\tau)$ curve is illustrated qualitatively in the lower part of Fig. 5.28. According to Ref. 49, the various portions of the curve are represented well by

$$180° > \tau > 90°: \qquad \overline{\mathrm{Nu}}_L(\tau) = 1 + [\overline{\mathrm{Nu}}_L(90°) - 1] \ \sin \tau \qquad (5.96)$$

$$90° > \tau > \tau^*: \qquad \overline{\mathrm{Nu}}_L(\tau) = \overline{\mathrm{Nu}}_L(90°)(\sin \tau)^{1/4} \qquad (5.97)$$

$$\tau^* > \tau > 0° \text{ and } H/L < 10: \qquad \overline{\mathrm{Nu}}_L(\tau) = \overline{\mathrm{Nu}}_L(0°)$$

$$\times \left[\frac{\overline{\mathrm{Nu}}_L(90°)}{\overline{\mathrm{Nu}}_L(0°)} \ (\sin \tau^*)^{1/4} \right]^{\tau/\tau^*} \qquad (5.98)$$

$\tau^* > \tau > 0°$ and $H/L > 10$:

$$\overline{\mathrm{Nu}}_L(\tau) = 1 + 1.44\left(1 - \frac{1708}{\mathrm{Ra}_L \ \cos\ \tau}\right)^*$$

$$\times \left[1 - \frac{(\sin\ 1.8\tau)^{1.6}1708}{\mathrm{Ra}_L\ \cos\ \tau}\right]^*$$

$$+ \left[\left(\frac{\mathrm{Ra}_L\ \cos\ \tau}{5830}\right)^{1/3} - 1\right]^* \qquad (5.99)$$

The quantities in parentheses with an asterisk, $(\cdot)^*$, must be set equal to zero if they become negative. The Rayleigh number is based on the distance between the differentially heated walls, $\mathrm{Ra}_L = g\beta(T_h - T_c)L^3/\alpha\nu$.

5.7   ANNULAR SPACE BETWEEN HORIZONTAL CYLINDERS

The flow generated between concentric horizontal cylinders at different temperatures (T_i, T_o) has features similar to the circulation in an enclosure heated from the side. As illustrated in Fig. 5.29, in the laminar regime, two counterrotating kidney-shaped cells are positioned symmetrically about the vertical plane drawn through the cylinder centerline. Because the two cells are heated and cooled from the side, the overall heat transfer correlation should have the features of eqs. (5.63)–(5.64). The role of vertical dimension in this case can be played by either of the two diameters (D_i, D_o): When D_i is sensibly smaller than D_o, the overall heat transfer rate is determined ("throttled") by the smallness of D_i rather than D_o. These expectations are confirmed
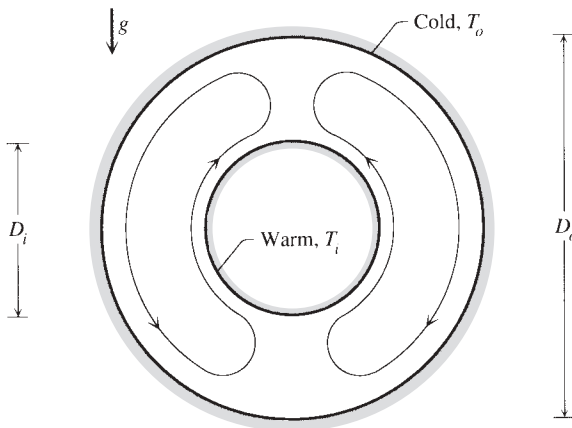

Figure 5.29   Natural convection in the space between concentric cylinders or spheres.

by the present interpretation* of a correlation developed by Raithby and Hollands [72],

$$q' \cong \frac{2.425k(T_i - T_o)}{[1 + (D_i/D_o)^{3/5}]^{5/4}} \left(\frac{\text{Pr } \text{Ra}_{D_i}}{0.861 + \text{Pr}}\right)^{1/4} \tag{5.100}$$

This q' (W/m) expression refers to the total heat transfer rate between the two cylinders per unit length in the direction normal to the plane of Fig. 5.29. The Rayleigh number is based on the cylinder-to-cylinder temperature difference and on the *inner* diameter, $\text{Ra}_{D_i} = g\beta(T_i - T_o)D_i^3/\alpha\nu$.

Equation (5.100) agrees within $\pm$ 10 percent with experimental data at moderate (laminar regime) Rayleigh numbers as high as 10^7. The low–Rayleigh number limit of the validity of eq. (5.100) occurs where the thickest free-convection boundary layer would become larger than the transversal dimension of the annular cavity

$$D_o \text{ Ra}_{D_o}^{-1/4} > D_o - D_i \tag{5.101}$$

The left side of this inequality shows the thermal boundary layer thickness along the outer cylinder, which—it is easy to see†—is greater than the corresponding thickness associated with the inner cylinder, $D_i \text{ Ra}_{D_i}^{-1/4}$. When the Rayleigh number is small enough that the inequality (5.101) is satisfied, the heat transfer mechanism approaches the pure conduction regime. Another way of making sure that the Rayleigh number is large enough for eq. (5.100) to apply is to calculate q' twice, using eq. (5.100) and the pure conduction formula, and to retain the larger of the two q' values. This alternative is based on the *constructal law* of increase of flow access [66–68]: The true heat transfer rate q' cannot be smaller than the pure-conduction estimate.

Equation (5.100) has been tested extensively in the range $\text{Pr} > 0.7$. It should hold also in the low-Prandtl number range because the function $[\text{Pr}/(0.861 + \text{Pr})]^{1/4}$ is known to account properly for the Pr effect at both ends of the Pr spectrum. Compare, for example, eq. (5.100) with eq. (4.106). All the physical properties that appear on the right side of eq. (5.100) are evaluated at the average temperature $(T_i + T_o)/2$. A lengthier correlation that covers a wider Rayleigh number range, including the turbulent regime, was developed by Kuehn and Goldstein [73].

---

*The writing and use of the original correlation [72] are more complicated because its Rayleigh number was based on the thickness of the annular space, $(D_o - D_i)/2$.

†Recall that in laminar boundary layer natural convection along (or around) a surface (flat, or curved) of a certain height, the boundary layer thickness increases as the height raised to the power $\frac{1}{4}$. The boundary layer thickness scale is equal to the height divided by the Rayleigh number (based on height) raised to the power $\frac{1}{4}$.

5.8 ANNULAR SPACE BETWEEN CONCENTRIC SPHERES

The natural circulation in the annulus between two concentric spheres has the approximate shape of a doughnut. At small enough Rayleigh numbers in the laminar regime, a vertical cut through the center of the two spheres reveals two kidney-shaped flow patterns similar to what we saw in Fig. 5.29. A compact expression for the total heat transfer rate q (W) between the two spherical surfaces can be deduced from a correlation due to Raithby and Hollands [72],

$$q \cong \frac{2.325kD_i(T_i - T_o)}{[1 + (D_i/D_o)^{7/5}]^{5/4}} \left(\frac{\text{Pr } \text{Ra}_{D_i}}{0.861 + \text{Pr}}\right)^{1/4} \qquad (5.102)$$

where $\text{Ra}_{D_i} = g\beta(T_i - T_o)D_i^3/\alpha\nu$. The argument for basing the Rayleigh number on D_i is the same as in the opening paragraph of Section 5.7. Equation (5.102) holds over the entire Prandtl number range, and the physical properties are evaluated at the average temperature $(T_i + T_o)/2$. The similarities between eq. (5.102) and eq. (5.100) are worth noting.

Equation (5.102) is accurate within ± 10 percent in the laminar range, at Rayleigh numbers as high as 10^7. When the Rayleigh number is so low that the inequality (5.101) applies, eq. (5.102) is no longer valid and the heat transfer must be evaluated based on the pure conduction model. As a safety check, it is a good idea to calculate q based on both formulas, eq. (5.102) and pure conduction and to retain the larger of the two values, in accordance with the constructal law.

5.9 ENCLOSURES FOR THERMAL INSULATION AND MECHANICAL STRENGTH

The internal structure of a cavernous wall can be derived from the competition between the thermal insulation and mechanical strength functions of the wall [74]. This combination of two functions, thermal and mechanical, is new in a design at such a simple and fundamental level. The classical literature on walls with air enclosures deals primarily with the thermal insulation characteristics of various wall structures.

Here is why we expect to find an optimal cavity size when we design a cavernous wall as an insulation system. The two-dimensional wall configuration shown in Fig. 5.30 has the thickness L, height H, and width W, which is perpendicular to the plane of the figure. There are n vertical air-filled cavities of thickness t_a, which are distributed equidistantly over the wall thickness L. This means that there are $(n + 1)$ slabs of solid wall material (e.g., brick) of individual thickness t_b, which are also distributed equidistantly. We characterize the air and brick (terra-cotta) composite by using the air volume fraction ϕ, which along
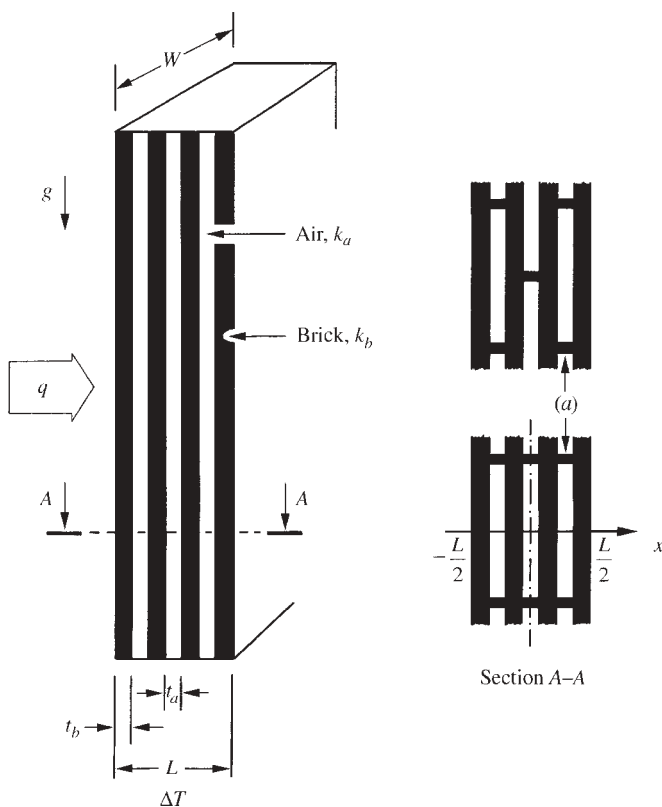
Figure 5.30 Vertical insulating wall with alternating layers of solid material (brick) and air. (From Ref. 74.)

with the wall volume HLW is a global design parameter,

$$\phi = nt_a/L \tag{5.103}$$

$$1 - \phi = (n+1)t_b/L \tag{5.104}$$

The overall thermal resistance of this composite is the sum of the resistances of air and brick layers. If the heat transfer across each airspace is by pure conduction, the thermal resistance posed by each airspace is $t_a/k_a HW$, where k_a is the thermal conductivity of air. Similarly, the resistance of each layer of brick material is $t_b/k_b HW$. The overall resistance is

$$R = \frac{nt_a}{k_a HW} + \frac{(n+1)t_b}{k_b HW} \tag{5.105}$$

or, after using eqs. (5.103) and (5.104),

$$R = \frac{\phi L}{k_a HW} + \frac{(1-\phi)L}{k_b HW} \tag{5.106}$$

Equation (5.106) states that the thermal performance of the composite does not depend on how many airspaces and slabs of brick we use. This is correct only when the airspace is ruled by pure conduction, that is, when the thickness t_a is smaller than the thickness of the laminar natural convection boundary layers that would line the vertical walls of each cavity,

$$t_a \lesssim H \; \mathrm{Ra}_{H,\theta}^{-1/4} \tag{5.107}$$

The Rayleigh number $\mathrm{Ra}_{H,\theta}$ is based on the height (H) and temperature difference (θ) across one air cavity,

$$\mathrm{Ra}_{H,\theta} = g\beta H^3 \theta / \alpha \nu \tag{5.108}$$

The temperature difference θ is smaller than the overall temperature difference ΔT that is maintained across the entire system. In the case of air and brick material, the two thermal conductivities are markedly different ($k_b/k_a \approx 20 \gg 1$), and the overall ΔT is essentially the sum of the temperature differences across all the air cavities,

$$\Delta T \cong n\theta \tag{5.109}$$

Putting eqs. (5.107)–(5.109) together, we see that the insensitivity of R to varying the internal structure (n) [eq. (5.106)] can be expected only when the number of airspaces is sufficiently large so that

$$n^{5/4} \gtrsim \phi \frac{L}{H} \; \mathrm{Ra}_{H,\Delta T}^{1/4} \tag{5.110}$$

In this inequality, $\mathrm{Ra}_{H,\,\Delta T}$ is based on the overall temperature difference, $\mathrm{Ra}_{H,\,\Delta T} = (g\beta H^3 \Delta T)/\alpha \nu$, and is a known constant because H and ΔT are specified global parameters.

   If the number of airspaces is smaller than in eq. (5.110), the natural convection effect decreases the resistance posed by each airspace, and the overall R value is greater than in eq. (5.105). This is why a large enough n, or a small enough t_a, is desirable from a thermal insulation standpoint. On the other hand, the effect of a large n is detrimental to the mechanical stiffness of the wall assembly. When ϕ is prescribed, the stiffest wall is the one where all the solid material is placed in the outermost planes (i.e., the wall where two t_b-thin slabs sandwich a single airspace). The stiffest wall is the worst thermal insulator, because it contains the thickest airspace, which is penetrated by the largest natural convection heat transfer current.

The optimal internal structure of the wall (n) results from the competition between thermal performance and mechanical performance. If the mechanical performance is specified, the wall stiffness serves as a constraint in the process of maximizing thermal performance, from which the optimal geometric form emerges. The mechanical strength of the wall, or its resistance to bending and buckling in the plane of Fig. 5.29 is controlled by the area moment of inertia of the horizontal wall cross section:

$$I_n = \int_{-L/2}^{L/2} x^2 W \, dx \tag{5.111}$$

The cross section over which this integral is performed is shown in Fig. 5.30b. The area element $W \, dx$ counts only the solid parts of the cross section, namely, the t_b-thick slabs of brick material. For the sake of simplicity, this calculation neglected the transversal ribs [detail (a), Fig. 5.30] that connect the t_b slabs so that the wall cross section rotates as a plane during pure bending. It is assumed that the transversal ribs use considerably less material than do the t_b slabs. Their role is the same as that of the web of the profile of an I-beam. In fact, the cross section of the cavernous wall structure is a conglomerate of I-beam profiles that have been fused solidly over the top and bottom surfaces of the I shape. In practice, the ribs (a) are more commonly arranged in a staggered pattern, as shown in the upper-right corner of Fig. 5.30.

In the case of a wall with no cavities ($\phi = 0$), the area moment of inertia is maximum and equal to $L^3 W/12$. We use this value as reference in the nondimensionalization of I_n,

$$\tilde{I}_n = \frac{I_n}{L^3 W/12} \tag{5.112}$$

where the subscript n indicates the number of air gaps. The integral (5.111) can be evaluated case by case [74], assuming that the cross section is symmetric about $x = 0$, for example, $\tilde{I}_1 = 1 - \phi^3$ and $\tilde{I}_\infty = 1 - \phi$. The stiffness is larger when n and ϕ are smaller. Alternatively, when the stiffness is constrained, $\tilde{I}_n$ is constant, and for each geometry (n) that the designer might contemplate, there is one value of ϕ that the wall composite must have. In such cases the ϕ value is larger when the number of air gaps is smaller. Less structural (solid) material is needed when there are fewer air gaps.

When the effect of natural convection cannot be neglected, the overall thermal resistance formula (5.105) has the form

$$R = \frac{n t_a}{k_a HW \; \mathrm{Nu}} + \frac{(n+1) t_b}{k_b HW} \tag{5.113}$$

In the denominator of the first term (the contribution of all the air gaps), Nu is the overall Nusselt number that expresses the relative heat transfer augmentation

effect due to natural convection in a single airspace, $\text{Nu} = q_{\text{actual}}/q_{\text{conduction}}$. The geometric maximization of R was performed numerically by using a Nu function that covers smoothly the entire range of possibilities, from conduction (small t_a) to convection (large t_a). The convection asymptote (5.40),

$$\text{Nu} = 0.364\frac{t_a}{H}\ \text{Ra}_{H,\theta}^{1/4} \qquad (\text{when } \text{Nu} \gtrsim 2) \qquad (5.114)$$

was joined with the pure conduction asymptote ($\text{Nu} = 1$) by using the technique of Churchill and Usagi [75],

$$\text{Nu} = \left[1 + \left(0.364\frac{t_a}{H}\ \text{Ra}_{H,\theta}^{1/4}\right)^m\right]^{1/m} \qquad (5.115)$$

with $m = 3$. The overall resistance formula (5.113) can be nondimensionalized by using as reference scale the resistance across a completely solid wall (L/k_bHW), and converting $\text{Ra}_{H,\theta}$ into $\text{Ra}_{H,\Delta T}$ via eqs. (5.108) and (5.109):

$$\tilde{R} = \frac{R}{L/k_bHW}$$

$$= \frac{k_b}{k_a}\ \phi\left[1 + \left(0.364n^{-5/4}\phi\frac{L}{H}\ \text{Ra}_{H,\Delta T}^{1/4}\right)^m\right]^{-1/m} + 1 - \phi \qquad (5.116)$$

The overall resistance $\tilde{R}$ emerges as a function of the geometric parameters n and ϕ, the fixed ratio k_b/k_a and the natural convection parameter

$$b = \frac{L}{H}\ \text{Ra}_{H,\Delta T}^{1/4} \qquad (5.117)$$

The geometric parameters n and ϕ are related through the global stiffness constraint. When the stiffness constraint is invoked, the global resistance $\tilde{R}$ depends on only one geometric parameter, ϕ or n. This effect is illustrated in Fig. 5.31, which shows that $\tilde{R}$ can be maximized with respect to the number of air cavities. The $\tilde{R}$ maximum shifts toward larger n values (more numerous and narrower air gaps) as b increases. The $\tilde{R}$ maximization illustrated in Fig. 5.31 was repeated for other $\tilde{I}$ values in the range 0.7–0.95. Let $\tilde{R}_{\text{max}}$ and n_{opt} denote the coordinates of the peak of one of the $b = $ constant curves. Larger b values represent stronger natural convection, and this is reflected in smaller $\tilde{R}_{\text{max}}$ values. Larger $\tilde{I}$ values represent stiffer walls that use more solid material, and consequently, $\tilde{R}_{\text{max}}$ decreases as $\tilde{I}$ increases. The optimal number of air gaps (n_{opt}) that corresponds to $\tilde{R}_{\text{max}}$ is reported in Fig. 5.32. Fewer air gaps are better when the natural convection effect is weak (small b) and when the required stiffness approaches that of the solid wall ($\tilde{I} = 1$).

In sum, simultaneous consideration of the thermal and mechanical functions of the complex structure is the defining feature of the idea pursued in this
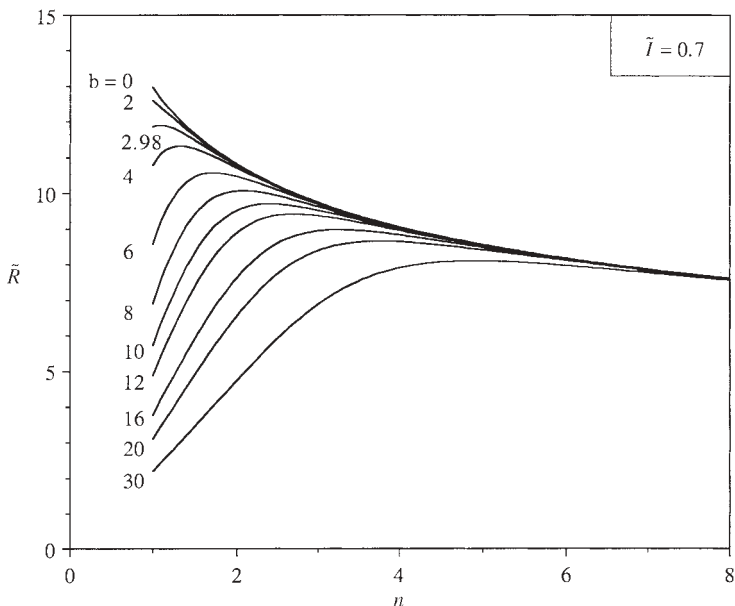
Figure 5.31 Overall thermal resistance as a function of the number of air gaps when the natural convection parameter b and stiffness parameter $\tilde{l}$ are fixed. (From Ref. 74.)
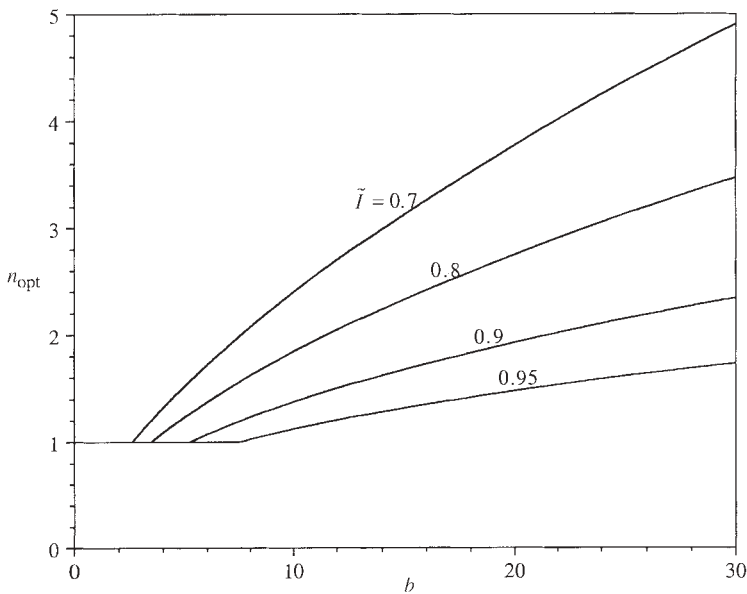

Figure 5.32 Optimal number of air gaps as a function of the natural convection parameter b and the stiffness parameter $\tilde{l}$. (From Ref. 74.)

section. The chief conclusion is that the number of air gaps built into the wall can be optimized when the overall stiffness is specified. The optimal number of air gaps increases when the effect of natural convection increases and when the specified wall stiffness decreases. The maximized wall thermal resistance is larger when the effect of natural convection in the air gaps is weaker and when the wall stiffness is smaller. The optimal volume fraction occupied by air in the cavernous structure decreases when the natural convection effect becomes stronger and when the wall stiffness increases.

The interplay between air conduction and natural convection in bricks with cavities depends, among other things, on how the bricks are assembled in the wall. A brick is usually 20–25 cm tall, while a wall has a height of roughly 250 cm (the height of a floor). This means that the aspect ratio of one continuous (vertical) airspace formed by stacking the bricks is 10 times greater than the aspect ratio of the airspace of a single brick. Consequently, the global heat transfer across the airspace changes. Lorente [46] reported calculations based on a combined model of conduction, radiation, and natural convection [76]. The results show that the behavior of the global thermal resistance changes when the height of the airspace changes. In the model, the total thickness of the bricks remains constant but the number of enclosures (and thus their thickness) could vary. The cavity width was always greater than the airspace thickness, so that the natural convection pattern was essentially two-dimensional.

Another effect is that of radiation in the airspaces, which can be modeled through the use of surface radiosities [77]. The shapes of air cavities in terra-cotta walls and the type of thermal boundary conditions on such cavities also play important roles in the model [76, 78]. Furthermore, terra-cotta is a porous material in which thermal diffusion is accompanied by the diffusion of moisture. The latter has an important effect on heat transfer, as shown by Vasile et al. [79].

The work outlined in this section is fundamental and exploratory. Its principal objective is to show that the ''combined heat flow and strength'' method advanced in Ref. 74 can be used in a wide domain of great contemporary importance: structures that combine mechanical strength with thermal resistance. An important contemporary application is the optimization of the architecture of mechanical structures that must serve two functions, mechanical strength and resistance (survival) in the presence of sudden intense heating (terrorist attack, explosion, fire) [80–82]. This is unlike traditional approaches, where structures are optimized for mechanical strength alone, and for heat resistance alone.

On the background of the constructal architectures that have been developed so far [66–68], this section outlined the first steps toward the constructal design of multiobjective (multidisciplinary) architectures.

REFERENCES

1. J. Patterson and J. Imberger, Unsteady natural convection in a rectangular cavity, *J. Fluid Mech.*, Vol. 100, 1980, pp. 65–86.

2. A. Bejan, A. A. Al-Homoud, and J. Imberger, Experimental study of high Rayleigh number convection in a horizontal cavity with different end temperatures, *J. Fluid Mech.*, Vol. 109, 1981, pp. 283–299.

3. A. Bejan, A general variational principle for thermal insulation system design, *Int. J. Heat Mass Transfer*, Vol. 22, 1979, pp. 219–228.

4. B. Boehrer, Convection in a long cavity with differentially heated end walls, *Int. J. Heat Mass Transfer*, Vol. 40, 1997, pp. 4105–4114.

5. J. L. Lage and A. Bejan, The resonance of natural convection in an enclosure heated periodically from the side, *Int. J. Heat Mass Transfer*, Vol. 36, 1993, pp. 2027–2038.

6. B. V. Antohe and J. L. Lage, A dynamic thermal insulator: inducing resonance within a fluid saturated porous medium enclosure heated periodically from the side, *Int. J. Heat Mass Transfer*, Vol. 37, 1994, pp. 771–782.

7. B. V. Antohe and J. L. Lage, Amplitude effect on convection induced by time-periodic horizontal heating, *Int. J. Heat Mass Transfer*, Vol. 39, 1996, pp. 1121–1133.

8. B. V. Antohe and J. L. Lage, Experimental investigation on pulsating horizontal heating of a water-filled enclosure, *J. Heat Transfer*, Vol. 118, 1996, pp. 889–896.

9. B. V. Antohe and J. L. Lage, The Prandtl number effect on the optimum heating frequency of an enclosure filled with fluid or with a saturated porous medium, *Int. J. Heat Mass Transfer*, Vol. 40, 1997, pp. 1313–1323.

10. H. S. Kwak and J. M. Hyun, Natural convection in an enclosure having a vertical sidewall with time-varying temperature, *J. Fluid Mech.*, Vol. 329, 1996, pp. 65–88.

11. H. S. Kwak, K. Kuwahara, and J. M. Hyun, Resonant enhancement of natural convection heat transfer in a square enclosure, *Int. J. Heat Mass Transfer*, Vol. 41, 1998, pp. 2837–2846.

12. H. S. Kwak, K. Kuwahara, and J. M. Hyun, Prediction of natural convection in an enclosure heated periodically from the side, *Int. J. Heat Mass Transfer*, Vol. 41, 1998, pp. 3157–3160.

13. G. B. Kim, J. M. Hyun, and H. S. Kwak, Enclosed buoyant convection of a variable-viscosity fluid under time-periodic thermal forcing, *Numer. Heat Transfer, Part A*, Vol. 43, 2003, pp. 137–154.

14. S. K. Kim, S. Y. Kim, and Y. D. Choi, Resonance of natural convection in a side heated enclosure with mechanically oscillating bottom wall, *Int. J. Heat Mass Transfer*, Vol. 45, 2002, pp. 3155–3162.

15. G. K. Batchelor, Heat transfer by free convection across a closed cavity between vertical boundaries at different temperature, *Q. Appl. Math.*, Vol. 12, 1954, pp. 209–233.

16. A. E. Gill, The boundary layer regime for convection in a rectangular cavity, *J. Fluid Mech.*, Vol. 26, 1966, pp. 515–536.

17. J. W. Elder, Laminar convection in a vertical slot, *J. Fluid Mech.*, Vol. 23, 1965, pp. 77–98.

18. A. Bejan, Note on Gill's solution for free convection in a vertical enclosure, *J. Fluid Mech.*, Vol. 90, 1979, pp. 561–568.

19. E. R. G. Eckert and W. O. Carlson, Natural convection in an air layer enclosed between two vertical plates with different temperatures, *Int. J. Heat Mass Transfer*, Vol. 2, 1961, pp. 106–120.

20. M. Jakob, *Heat Transfer*, Wiley, New York, 1957.

21. R. K. MacGregor and A. F. Emery, Paper 68-WA HT-4, ASME, New York, 1968.

22. N. Seki, S. Fukusako, and H. Inaba, Visual observation of natural convective flow in a narrow vertical cavity, *J. Fluid Mech.*, Vol. 84, 1978, pp. 695–704.

23. S. H. Yin, T. Y. Wung, and K. Chen, Natural convection in an air layer enclosed within rectangular cavities, *Int. J. Heat Mass Transfer*, Vol. 21, 1978, pp. 307–315.

24. F. Landis and A. Rubel, discussion of Ref. 25, *J. Heat Transfer*, Vol. 92, 1970, pp. 167–168.

25. M. E. Newell and F. W. Schmidt, Heat transfer by natural convection within rectangular enclosures, *J. Heat Transfer*, Vol. 92, 1970, pp. 159–167.

26. D. W. Pepper and S. D. Harris, Numerical simulation of natural convection in closed containers by a fully implicit method, *J. Fluids Eng.*, Vol. 99, 1977, pp. 649–656.

27. G. de Vahl Davis, Laminar natural convection in an enclosed rectangular cavity, *Int. J. Heat Mass Transfer*, Vol. 11, 1968, pp. 1675–1693.

28. D. E. Cormack, L. G. Leal, and J. Imberger, Natural convection in a shallow cavity with differentially heated end walls. Part 1: Asymptotic theory, *J. Fluid Mech.*, Vol. 65, 1974, pp. 209–229.

29. A. Bejan and C. L. Tien, Laminar natural convection heat transfer in a horizontal cavity with different end temperatures, *J. Heat Transfer*, Vol. 100, 1978, pp. 641–647.

30. J. Imberger, Natural convection in a shallow cavity with differentially heated end walls. Part 3. Experimental results, *J. Fluid Mech.*, Vol. 65, 1973, pp. 247–260.

31. D. E. Cormack, L. G. Leal, and J. H. Seinfeld, Natural convection in a shallow cavity with differentially heated end walls: Part 2. Numerical solutions, *J. Fluid Mech.*, Vol. 65, 1974, pp. 231–246.

32. A. Gadgil, F. Bauman, and R. Kammerud, Natural convection in passive solar buildings: experiments, analysis, and results, *Passive Solar J.*, Vol. 1, 1982, pp. 28–40.

33. A. F. Emery, The effect of a magnetic field upon the free convection in a conducting fluid, *Trans. ASME*, *J. Heat Transfer*, Vol. 85, No. 2, 1963, pp. 119–124.

34. J. J. Portier and O. A. Arnas, *Heat Transfer and Turbulent Buoyant Convection*, Vol. II, Hemisphere, Washington, DC, 1977.

35. G. Burnay, J. Hannay, and J. Portier, *Heat Transfer and Turbulent Buoyant Convection*, Vol. II, Hemisphere, Washington, DC, 1977.

36. A. Rubel and R. Landis, Numerical study of natural convection in a vertical rectangular enclosure, *Phys. Fluids, Suppl*. II, Vol. 12-II, 1969, pp. 208–213.

37. C. Quon, High Rayleigh number convection in an enclosure: a numerical study, *Phys. Fluids*, Vol. 15-I, 1972, pp. 12–19.

38. J. E. Fromm, A numerical method for computing the nonlinear, time dependent, buoyant circulation of air in rooms*, Building Science Series 39*, National Bureau of Standards, Washington, DC, 1971.

39. A. Bejan, A synthesis of analytical results for natural convection heat transfer across rectangular enclosures, *Int. J. Heat Mass Transfer*, Vol. 23, 1980, pp. 723–726.

40. R. A. Nelson, Jr. and A. Bejan, Constructal optimization of internal flow geometry in convection, *J. Heat Transfer*, Vol. 120, 1998, pp. 357–365.

41. A. Bejan, *Shape and Structure, from Engineering to Nature*, Cambridge University Press, Cambridge, 2000.

42. R. L. Frederick, On the aspect ratio for which heat transfer in differentially heated cavities is maximum, *Int. Commun. Heat Mass Transfer*, Vol. 26, 1999, pp. 549–558.

43. V. A. F. Costa, M. S. A. Oliveira, and A. C. M. Sousa, Control of laminar natural convection in differentially heated square enclosures using solid inserts at the corners, *Int. J. Heat Mass Transfer*, Vol. 46, 2003, pp. 3529–3537.

44. B. Lartigue, S. Lorente, and B. Bourret, Multicellular natural convection in a high aspect ratio cavity: experimental and numerical results, *Int. J. Heat Mass Transfer*, Vol. 43, 2000, pp. 3159–3170.

45. B. Lartigue, S. Lorente, B. Bourret, and R. Escudié, PIV investigation of multicellular laminar natural flow in vertical bent cavities, *Exp. Heat Transfer*, Vol. 14, 2001, pp. 89–106.

46. S. Lorente, Heat losses through building walls with closed, open and deformable cavities, *Int. J. Energy Res.*, Vol. 26, 2002, pp. 611–632.

47. S. Lorente and B. Lartigue, Maximization of heat flow through a cavity with natural convection and deformable boundaries, *Int. Commun. Heat Mass Transfer*, Vol. 29, 2002, pp. 633–642.

48. S. Kimura and A. Bejan, The ''heatline'' visualization of convective heat transfer, *J. Heat Transfer*, Vol. 105, 1983, pp. 916–919.

49. I. Catton, Natural convection in enclosures, in *Proceedings of the 6th International Heat Transfer Conference*, *Toronto*, *1978*, Vol. 6, pp. 13–43.

50. S. Kimura and A. Bejan, The boundary layer natural convection regime in a rectangular cavity with uniform heat flux from the side, *J. Heat Transfer*, Vol. 106, 1984, pp. 98–103.

51. S. K. W. Tou and X. F. Zhang, Three-dimensional numerical simulation of natural convection in an inclined liquid-filled enclosure with an array of discrete heaters, *Int. J. Heat Mass Transfer*, Vol. 46, 2003, pp. 127–138.

52. A. Bejan and A. N. Rossie, Natural convection in horizontal duct connecting two fluid reservoirs, *J. Heat Transfer*, Vol. 103, 1981, pp. 108–113.

53. M. W. Nansteel and R. Grief, Natural convection in undivided and partially divided rectangular enclosures, *J. Heat Transfer*, Vol. 103, 1981, pp. 623–629.

54. S. M. Bajorek and J. R. Lloyd, Experimental investigation of natural convection in partitioned enclosures, *J. Heat Transfer*, Vol. 104, 1982, pp. 527–532.

55. N. N. Lin and A. Bejan, Natural convection in a partially divided enclosure, *Int. J. Heat Mass Transfer*, Vol. 26, 1983, pp. 1867–1878.

56. R. Jetli, S. Acharya, and E. Zimmerman, Influence of baffle location on natural convection in a partially divided enclosure, *Numer. Heat Transfer*, Vol. 10, 1986, pp. 521–536.

57. J. Neymark, C. R. Boardman III, A. T. Kirkpatrick, and R. Anderson, High Rayleigh number natural convection in partially divided air and water filled enclosures, *Int. J. Heat Mass Transfer*, Vol. 32, 1989, pp. 1671–1679.

58. Z. Zhang, A. Bejan, and J. L. Lage, Natural convection in a vertical enclosure with internal permeable screen, *J. Heat Transfer*, Vol. 113, 1991, pp. 377–383.

59. R. D. Flack, T. T. Konopnicki, and J. H. Rooke, The measurement of natural convective heat transfer in triangular enclosures, *J. Heat Transfer*, Vol. 101, 1979, pp. 648–654.

60. D. Poulikakos and A. Bejan, Natural convection experiments in a triangular enclosure, *J. Heat Transfer*, Vol. 105, 1983, pp. 652–655.

61. D. Poulikakos and A. Bejan, The fluid dynamics of an attic space, *J. Fluid Mech.*, Vol. 131, 1983, pp. 251–269.

62. P. M. Haese and M. D. Teubner, Heat exchange in an attic space, *Int. J. Heat Mass Transfer*, Vol. 45, 2002, pp. 4925–4936.

63. A. Pellew and R. V. Southwell, On maintained convective motion in a fluid heated from below, *Proc. R. Soc.*, Vol. A176, 1940, pp. 312–343.

64. F. H. Busse, Non-linear properties of thermal convection, *Rep. Prog. Phys.*, Vol. 41, 1978, pp. 1929–1967.

65. S. Globe and D. Dropkin, Natural convection heat transfer in liquids confined by two horizontal plates and heated from below, *J. Heat Transfer*, Vol. 81, 1959, pp. 24–28.

66. A. Bejan and S. Lorente, The constructal law of design and evolution in nature, *Phil. Trans. R. Soc. B.*, Vol. 365, 2010, pp. 1335–1347.

67. A. Bejan and S. Lorente, Constructal theory of generation of configuration in nature and engineering, *J. Appl. Phys.*, Vol. 100, 2006, 041301.

68. A. Bejan and S. Lorente, The constructal law and the evolution of design in nature, *Phys. of Life Rev.*, Vol. 8, 2011, pp. 209–240.

69. G. Ledezma, A. M. Morega, and A. Bejan, Optimal spacing between fins with impinging flow, *J. Heat Transfer*, Vol. 118, 1996, pp. 570–577.

70. J. R. Lloyd and W. R. Moran, Natural convection adjacent to horizontal surfaces of various platforms, Paper 74-WA/HT-66, ASME, New York, 1974.

71. J. N. Arnold, I. Catton, and D. K. Edwards, Experimental investigation of natural convection in inclined rectangular regions of differing aspect ratios, *J. Heat Transfer*, Vol. 98, 1976, pp. 67–71.

72. G. D. Raithby and K. G. T. Hollands, A general method of obtaining approximate solutions to laminar and turbulent free convection problems, *Adv. Heat Transfer*, Vol. 11, 1975, pp. 265–315.

73. T. H. Kuehn and R. J. Goldstein, Correlating equations for natural convection heat transfer between horizontal circular cylinders, *Int. J. Heat Mass Transfer*, Vol. 19, 1976, pp. 1127–1134.

74. S. Lorente and A. Bejan, Combined ''flow and strength'' geometric optimization: internal structure in a vertical insulating wall with air cavities and prescribed strength, *Int. J. Heat Mass Transfer*, Vol. 45, 2002, pp. 3313–3320.

75. S. W. Churchill and R. Usagi, A standardized procedure for the production of correlations in the form of a common empirical equation, *Ind. Eng. Chem. Fundam.*, Vol. 13, 1974, pp. 39–46.

76. S. Lorente, M. Petit, and R. Javelas, Simplified analytical model for thermal transfer in a vertical hollow brick, *Energy Build.*, Vol. 24, 1996, pp. 95–103.

77. S. Lorente, R. Javelas, M. Petit, and K. N'Guessan, Modélisation simplifiée des écoulements dans une cavité verticale de petites dimensions, *Rev. Gén. Therm.*, Vol. 388, 1994, pp. 273–279.

78. S. Lorente, M. Petit, and R. Javelas, The effects of temperature conditions on the thermal resistance of walls made with different shapes vertical hollow bricks, *Energy Build.*, Vol. 28, 1998, pp. 237–240.

79. C. Vasile, S. Lorente, and B. Perrin, Study of convective phenomena inside cavities coupled with heat and mass transfers through porous media—application to vertical hollow bricks—a first approach, *Energy Build.*, Vol. 28, 1998, pp. 229–235.

80. L. Gosselin, A. Bejan, and S. Lorente, Combined 'heat flow and strength' optimization of geometry: mechanical structures most resistant to thermal attack, *Int. J. Heat Mass Transfer*, Vol. 47, 2004, pp. 3477–3489.

81. K-M. Wang, S. Lorente, and A. Bejan, Vascular structures for volumetric cooling and mechanical strength, *J. Appl. Phys.*, Vol. 107, 2010, 044901.

82. E. Cetkin, S. Lorente, and A. Bejan, Vascularization for cooling and mechanical strength, *Int. J. Heat Mass Transfer*, Vol. 54, 2011, pp. 2774–2781.

83. A. Bejan and S. Kimura, Penetration of free convection into a lateral cavity, *J. Fluid Mech.*, Vol. 103, 1981, pp. 465–478.

PROBLEMS

5.1. Employing the proper scales for the development of a thermal boundary layer along the heated vertical walls of a rectangular enclosure, show that the momentum equation (5.7) is dominated by the three terms the scales of which are listed as expression (5.9).

5.2. Derive the criterion for distinct vertical thermal boundary layers [expression (5.18)] by comparing the time of convective layer development (t_f) with the time of penetration by pure conduction over the entire length of the enclosure L.

5.3. Rely on pure scaling arguments to prove that $Ra_H < 1$ denotes the domain in which the overall heat transfer rate across a square enclosure is dominated by pure conduction.

5.4. Derive an expression for the horizontal velocity u_* in the vertical boundary layer in the high-Ra_H regime. Recognizing $u_{*\infty} = \lim_{x* \to \infty} u_*$ as the horizontal velocity through the core region, show that $u_{*\infty}$ is an odd function of altitude. What is the scale of the horizontal velocity in the core region?

5.5. Prove that inertia $\sim$ buoyancy in eq. (5.44) is inadmissible as a momentum balance in the shallow enclosure limit ($H/L \to 0$). In view of this finding, is the stratified counterflow core solution (5.52) and (5.53) valid for all values of Pr?

5.6. Machined into a solid wall of temperature T is a slender two-dimensional cavity of height H and length L ($H \ll L$). The cavity communicates laterally with an infinitely large fluid reservoir of temperature $T + \Delta T$. The situation is shown schematically in Fig. 12.17a. Show that if the cavity is slender enough, the buoyancy-driven flow will penetrate the cavity only to a certain depth whose order of magnitude is

$$L_x \sim H \ Ra_H^{1/2}$$

Determine the order of magnitude of the total heat transfer rate between the fluid reservoir and the walls of the cavity. Compare your scale analysis result with the similarity solution to the same problem [83].

5.7. Consider the penetration of natural convection into a vertical slender cavity of height H and gap thickness L ($H \gg L$). As is shown in Fig. 12.17b, one end of the cavity is closed and the other communicates with a very large fluid reservoir. Rely on scaling arguments to show that when a temperature difference ΔT is established between the fluid reservoir and the walls of the cavity, the flow penetrates vertically to a depth that scales as

$$L_y \sim L \ \mathrm{Ra}_L$$

Estimate the order of magnitude of the heat transfer rate between the fluid reservoir and the walls of the cavity, assuming that $L_y < H$.

5.8. Predict the time interval between the formation of two successive balls of heated fluid (thermals) that rise from the same spot on the hot surface photographed in Fig. 4.16. The bottom surface and water pool temperatures are 43.1 and 23.6°C. Use an order-of-magnitude calculation based on the view that the surface heats by conduction a thin layer of water. As shown in Fig. P5.8, the thickness of this layer increases in time until its thickness-based Rayleigh number reaches the critical level for the onset of convection. Thermals are the aftermath of the onset of convection in the conduction layer that grew over the surface.

Figure P5.8
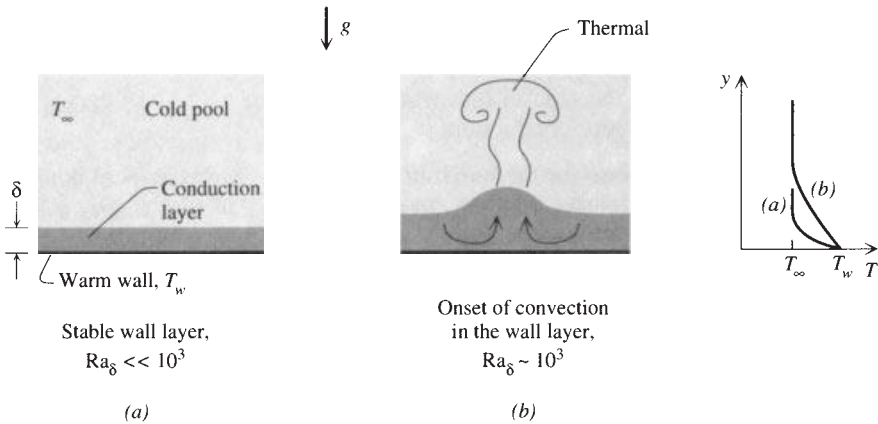
5.9. The large-diameter cylindrical reservoir shown in Fig. P5.9 is perfectly insulated and filled with water. Two horizontal tubes with an outer diameter of 4 cm are positioned at the same level in the vicinity of the reservoir centerline. The temperatures of the tube walls are maintained at $T_1 = 30°$C and $T_2 = 20°$C by internal water streams of appropriate (controlled) temperature.
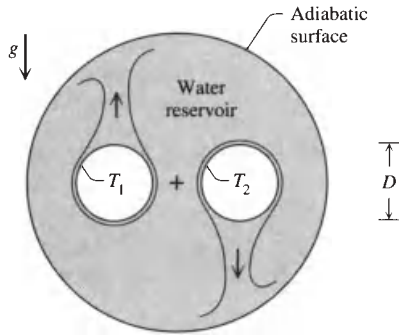
Figure P5.9

Calculate the heat transfer rate from the hot tube to the cold tube via the water reservoir by assuming that the tube-to-tube spacing is wide enough so that the boundary layers that coat the tubes do not touch (this case is illustrated in the figure). Assume further that the film–temperature properties of the two boundary layers are equal to the properties evaluated at the average temperature of the water reservoir, T_∞. Begin with the calculation of T_∞, and recognize the centrosymmetry of the flow pattern, that is, the symmetry about the centerline of the large reservoir.

5.10. The *double-pane window problem* consists of determining the H-averaged heat flux through the system when the overall temperature difference $T_h - T_c$ is specified (see Fig. P5.10). If the glass-to-glass spacing is wide enough to house distinct laminar boundary layers, it is possible to approximate the double-pane system as a sandwich of two of the single-pane windows. Use the formula listed in Problem 4.26 for the single-pane window with uniform heat flux, and show that the average heat flux through the double-pane window system is given approximately by

Figure P5.10

$$\frac{q''}{T_h - T_c} \cong 0.106 \left[\frac{g\beta \left(T_h - T_c\right) H^3}{\alpha \gamma} \right]^{1/4}$$

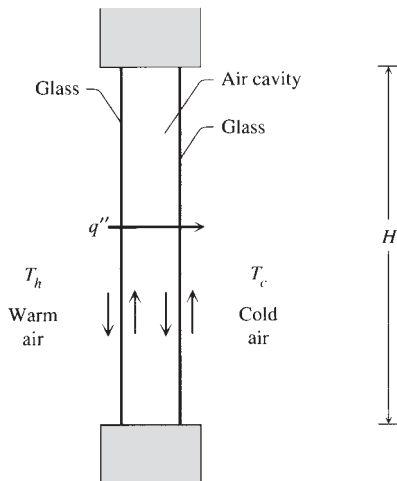**5.11.** The thermal insulation capability of a horizontal layer of fluid is impaired if natural convection currents are present. As shown in Fig. 5.20, the heat transfer coefficient is lower when convection is absent, and the transfer of heat from the bottom wall to the top wall is by pure conduction. Consider the design of a thermal insulation that consists of a horizontal layer of fluid of thickness H and bottom-to-top temperature difference $T_h - T_c = \Delta T$. These two parameters, H and ΔT, happen to be large enough so that convection currents would form in the fluid. To suppress the formation of these currents, it is proposed to install a horizontal partition at some level between the bottom wall and the top wall (Fig. P5.11). What is the optimal level at which the partition should be installed?
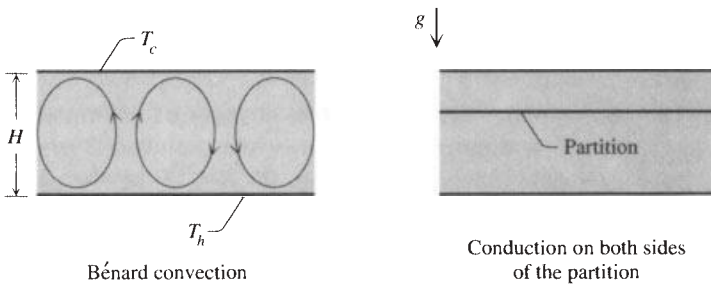
Figure P5.11

To simplify your analysis, assume that the partition can be modeled as an isothermal wall with a temperature between the bottom wall temperature and the top wall temperature. Assume further that convection currents are absent above and below the partition. Find the optimal partition level by maximizing the overall temperature difference ΔT for which this state of pure conduction can be preserved.

5.12. The steam generator of a modern power plant uses the siphon circulation scheme shown in Fig. P5.12. There are two vertical columns of height H. The downcomer (D_1) contains dense fluid (liquid) with density ρ_1. The riser (D_2) contains a mixture of liquid and vapor with density ρ_2. The flow along each column is fully developed turbulent in the fully rough limit, meaning that the friction coefficients f_1 and f_2 are two constants independent of flow rate. The total volume of the two columns is specified. Determine the optimal allocation of volume (D_1/D_2) so that the global flow resistance encountered by the circulation is minimal or the flow rate $\dot{m}$ is maximal. Show that the result is $(D_1/D_2)_{opt} = (f_1/f_2)^{1/7} (\rho_2/\rho_1)^{1/7}$.
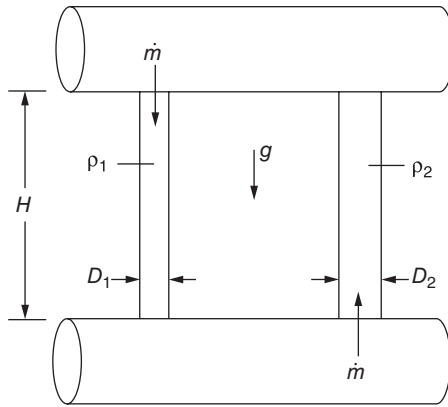
Figure P5.12

5.13. A panel of tubes in a steam superheater consists of three parallel tubes which are supplied with T_0 steam from a bottom plenum, Fig. P5.13. The heated streams are collected in the upper plenum and discharged at the temperature T_{out}. The total heating rate $(q = 2q_1 + q_2)$ is fixed: It is provided by flames from a burner. The total mass flow rate $(\dot{m} = 2\dot{m}_1 + \dot{m}_2)$ is also fixed. Because the burner is not as wide as the three-tube assembly, the inner tube receives a greater share of the heat transfer rate, $q_2/q_1 > 1$. Close inspection of the design shows that a system of bottom valves is used in order to adjust the tube flow rates $(\dot{m}_2/\dot{m}_1)$ such that all the tube outlets have the same temperature $(T_1 = T_2)$.
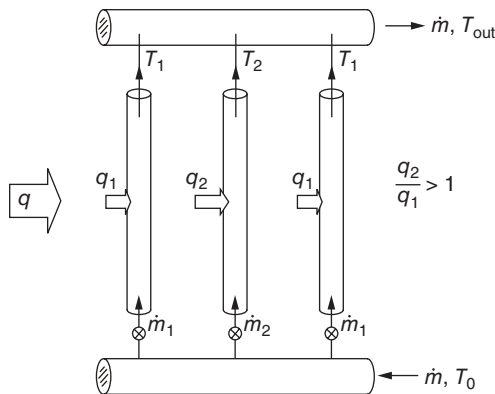
Figure P5.13

(a) Is the maintenance of $T_1 = T_2$ beneficial for the purpose of improving (i) thermodynamic performance, (ii) mechanical integrity, or (i) and (ii)?

(b) If the heat transfer rate imbalance is $q_2/q_1 = \alpha$, what is the required mass flow rate $\dot{m}_2/\dot{m}_1$ as a function of α?

(c) It is proposed to eliminate the system of valves and to maintain the required flow imbalance $\dot{m}_2/\dot{m}_1$ by using an inner tube with a diameter larger than the diameter of the outer tubes. Note that without the valves the plenum-to-plenum pressure drop is the same for all the tubes. Assume that the flow through each tube is in the fully developed fully rough turbulent regime. Determine the required ratio D_2/D_1 as a function of α.

6

TRANSITION TO TURBULENCE

Most of the flows treated in the preceding chapters are laminar and, as such, are destined to exist only under special circumstances. It is common knowledge—a fact reinforced daily by direct observations—that laminar flows can come undone and break down to a seemingly more complicated flow called *turbulence*. It is also observed that turbulent flows that slow down become laminar. Yet there is absolutely nothing in the laminar flow solutions of Chapters 2–5 to suggest that these laminar flows do not exist for all Reynolds and Rayleigh numbers imaginable. The special circumstances necessary for the transition from analytically predictable laminar flows to analytically unpredictable turbulent flows (as shown in Chapter 7) form one of the most active fields in fluid mechanics research today. In convective heat transfer research, however, the study of *transition* is important because the heat transfer potential of a turbulent flow differs vastly from that of its laminar counterpart.

The traditional presentation of the phenomenon of transition in convective heat transfer is empirical—a collection of observations recorded as ''critical'' dimensionless groups (Reynolds numbers, Rayleigh numbers, etc.). In this chapter we review this body of information, and in addition, we develop a theory to predict transition in every flow configuration imaginable. The theory is based on the constructal law [1, 2] (also Section 5.5.3), according to which the flow opts for configurations that offer greater access to its currents. We shall see that the natural choice between the laminar and turbulent regimes is the one that facilitates the transfer of momentum (mixing) between the fast and slow layers of fluid.

6.1 EMPIRICAL TRANSITION DATA

The available observations of transition are summarized in Table 6.1. There are important reasons for doing this up front. First, there is little interesting in

Table 6.1 Summary of physical observations concerning the beginning of transition from laminar to turbulent flow

Flow Configuration	Condition[a] Necessary for the Existence of Laminar Flow	Source	Observations
Boundary layer flow (without longitudinal pressure gradient)	$\mathrm{Re} < 3.5 \times 10^5$ $\mathrm{Re} < 2 \times 10^4 - 10^6$	[3][b]	Re is the Reynolds number based on wall length and free-stream velocity
Duct flow	$\mathrm{Re} < 2000$		Re is based on hydraulic diameter and duct-averaged velocity
Free-jet flow (axisymmetric)	$\mathrm{Re} < 10 - 30$	[4]	Re is based on nozzle diameter and mean velocity through the nozzle
Wake flow (two-dimensional)	$\mathrm{Re} < 32$	[5]	Re is based on the cylinder diameter and free-stream velocity
Natural convection boundary layer flow			
Isothermal wall	$\mathrm{Gr} < 1.5 \times 10^9$ (Pr = 0.71) $\mathrm{Gr} < 1.3 \times 10^9$ (Pr = 6.7)	[6][c] [6, 7]	The Grashof number Gr is based on wall height and wall–ambient temperature difference
Constant-heat-flux wall	$\mathrm{Gr}_* < 1.6 \times 10^{10}$ (Pr = 0.71) $\mathrm{Gr}_* < 6.6 \times 10^{10}$ (Pr = 6.7)	[6] [8]	Gr_* is the Grashof number based on heat flux and wall height [see eq. (4.70), where $\mathrm{Gr}_* = \mathrm{Ra}_*/\mathrm{Pr}$]
Plume flow (axisymmetric)	$\mathrm{Ra}_q < 10^{10}$ (Pr = 0.71)	[9]	Ra_q is the Rayleigh number based on heat source strength and plume height [see eq. (6.6)]
Film condensation on a vertical plate	$\dfrac{4\Gamma}{\mu} < 1800$	[10]	Γ is the condensate mass flow rate per unit of film width

[a]All numerical values are order-of-magnitude approximate and vary from one experimental report to another.
[b]The transition is triggered by velocity disturbances in excess of 18 percent of the free-stream velocity.
[c]Averaged from the data compiled in Ref. 6.

repeating after so many others that particular laminar flows break down at certain (critical) Reynolds and Grashof numbers when, as demonstrated in the earlier chapters, the conceptual basis for even speaking about numbers such as Re and Gr is not at all clear. That laminar flows break down according to Table 6.1 is of practical interest, of course (this is why the table is shown). But an important

story lies beneath the type of physical observations we usually associate with transition. The goal in this chapter is to stimulate the reader to search for the meaning behind the numbers of Table 6.1: why they exist, why each is a constant, and why each constant is much greater than 1.

6.2 SCALING LAWS OF TRANSITION

Nature offers us clear signs that the phenomenon of transition is associated with a fundamental property of fluid flow. Table 6.1 shows that any special class of laminar flows is characterized by a *critical number* that serves as a landmark for the laminar–turbulent transition. One century of research on transition has shown that these critical numbers are *universal*, despite the sometimes sizable numerical variations from one experimental reporting of transition observations to another. The concept of critical number of transition is empirical in origin. The real challenge is to predict these numbers.

Another important clue emphasized in some textbooks (e.g., Ref. 11) is that although the critical transition numbers differ in orders of magnitude from one flow class to another, they all seem to suggest that an appropriate Reynolds number based on the relevant velocity and *transversal* dimension of the flow has in all cases the same order of magnitude, $O(10^2)$. This observation is true not only for forced boundary layer flow, as shown in Ref. 11, but for wall jet flows and free-jet flows encountered in natural convection phenomena, as well as for jet and wake flows (Table 6.1). It is important to keep in mind that this seemingly universal transition Reynolds number is a number *considerably greater than $O(1)$*.

We can identify the most important features of the laminar–turbulent transition by taking a close look at one of the most common occurrences of the phenomenon, namely, the cigarette-smoke plume shown in Fig. 6.1. The air plume was generated by a concentrated heat source of known strength q (W) and where the smoke was introduced separately only to visualize the flow [9]. One feature is that the laminar plume prevails below a certain characteristic plume height y_{tr}. Another feature is that the transition is marked by the meandering or *buckling* of the plume into a sinusoidal shape of characteristic wavelength λ_B. One can take many photographs of the type shown in Fig. 6.1; one can cough or not cough while taking each picture, but the buckling or meandering wavelength λ_B always turns out to be proportional to the transition height y_{tr} [9]. By varying the heat source strength q, one has the opportunity to observe many cigarette-smoke plumes; as summarized in Fig. 6.2a, although λ_B and y_{tr} decrease as q increases, the $\lambda_B \sim y_{tr}$ proportionality is preserved. The line

$$y_{tr} \sim 10\lambda_B \tag{6.1}$$

is an order-of-magnitude curve fit for the observations reported in Ref. 9. We will return to this observation in Fig. 6.8.
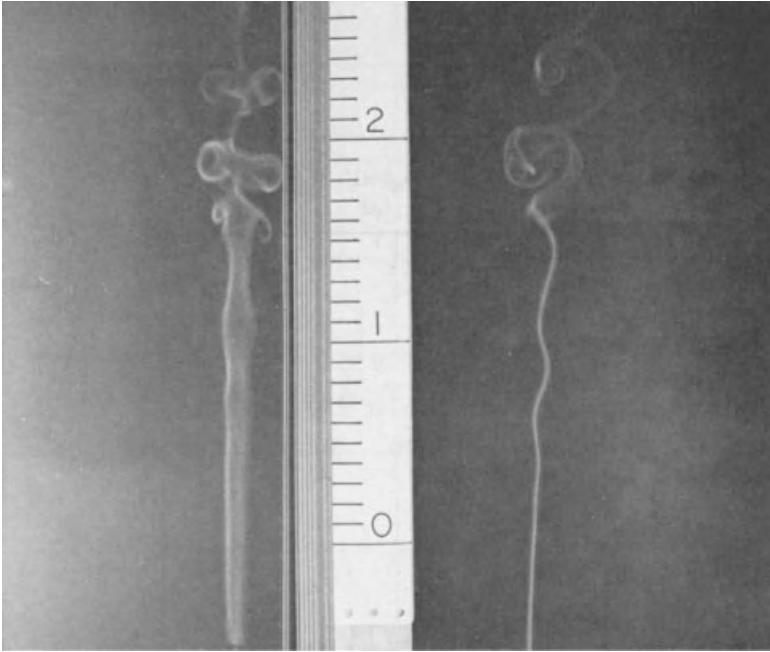
Figure 6.1   Smoke visualization of transition in air plume flow above a concentrated heat source: left side, side view; right side, direct view ($q = 5.1$ W; one division on the vertical scale equals 1 cm). (From Ref. 9.)
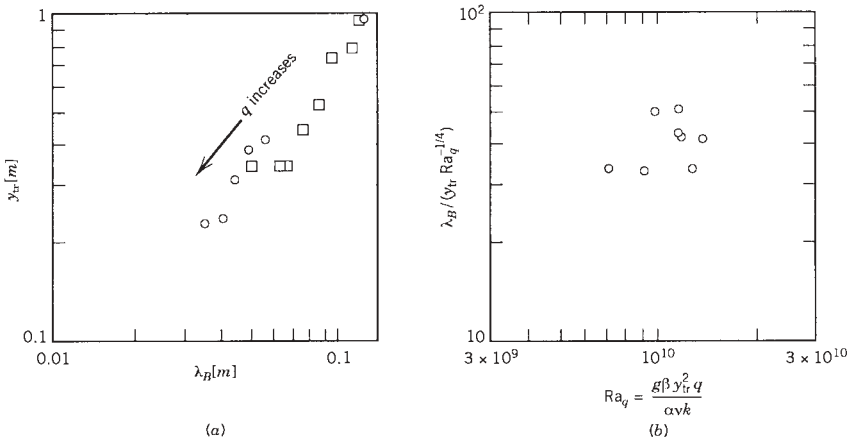
Figure 6.2   Observations on transition in air plume flow: (*a*) transition height versus buckling wavelength; (*b*) constancy of the transition Rayleigh number and local proportionality between buckling wavelength and stream thickness scale. (From Ref. 9.)

Another interesting aspect of these observations is that the buckled shape of the transition section of the plume is in one plane. By photographing the plume simultaneously from the front and the side, one learns that the meander is most visible from the special viewing direction that happens to be perpendicular to the plane of the meander. This observation is important because it contradicts the belief that the transitional shape of the buoyant jet is spiral (helical), hence three-dimensional. This belief is a good example of how an existing theory (hydrodynamic stability) influences the written record of experimental observations: In the first analytical treatment of the instability of an inviscid axisymmetric jet, Batchelor and Gill [12] *postulated* the existence of helical, not plane-sinusoidal, disturbances. This postulate was adopted by subsequent theoretical studies (e.g., Refs. 13 and 14) and it soon became fashionable to talk about observed helical and corkscrew deformations based on a purely two-dimensional photographic record (e.g., Refs. 15 and 16).

In the case of the cigarette-smoke plume of Fig. 6.1, the disturbances were unknown (random), yet the observed shape was plane–sinusoidal and the wavelength was basically the same from one photograph to another. It seems that the flow has the natural property to, as Gebhart and Mahajan [17] put it, ''sharply filter disturbances for essentially a single frequency'' out of an entire spectrum of unspecified disturbances. The flow has the natural property to meander with a characteristic wavelength during transition, *regardless* of the nature of the disturbing agent. This observation is important because it illustrates the conflict between hydrodynamic stability thinking, to which the postulate of *disturbances* is a necessity, and the natural meandering* tendency of real-life flows during transition.

The characteristic wavelength chosen by the flow during transition is proportional to the local thickness of the flow (the stream). For the air plumes documented in Fig. 6.2a, we know from the scale analysis presented in Chapter 4 that (see Table 4.1, and set Pr $\sim$ 1)

$$D \sim y_{tr} \left(\frac{g\beta \; \Delta T \; y_{tr}^3}{\alpha \nu} \right)^{-1/4} \tag{6.2}$$

where D is the transversal length scale of the plume and ΔT is the plume–ambient temperature difference scale. We also know the vertical velocity scale

$$\nu \sim \frac{\alpha}{y_{tr}} \left(\frac{g\beta \; \Delta T \; y_{tr}^3}{\alpha \nu} \right)^{1/2} \tag{6.3}$$

and from the argument that the plume carries all the energy released by the heat source,

$$q \sim \rho c_P D^2 \nu \; \Delta T \tag{6.4}$$

---

*In the present context, *meandering* or *buckling* means a naturally sinusoidal flow with a universal proportionality (scaling) between longitudinal wavelength and stream thickness.

Combining eqs. (6.2)–(6.4) to eliminate v and ΔT, we find that

$$D \sim y_{\text{tr}} \text{Ra}_q^{-1/4} \tag{6.5}$$

where Ra_q is the Rayleigh number based on heat source strength,

$$\text{Ra}_q = \frac{g\beta q \, y_{\text{tr}}^2}{\alpha v k} \tag{6.6}$$

Figure 6.2*b* shows the replotting of the transition data of Fig. 6.2*a* as λ_B/D versus Ra_q. It is clear that regardless of the source strength q, the meander wavelength λ_B always scales with the local plume thickness scale D. In addition, the value of Ra_q at transition oscillates about 10^{10} as q varies: It is easy to show that the local Reynolds number (vD/v) based on the scales (6.3) and (6.5) is of order 10^2 at transition [see Problem 6.3 and eq. (6.15)].

To summarize, cigarette-smoke observations suggest that the transition from laminar flow to turbulent flow is characterized by two scaling laws:

1. A universal proportionality between longitudinal wavelength and stream thickness, that is, by a meander or buckling phenomenon
2. A local Reynolds number of order 10^2, where the Reynolds number is based on the local stream velocity scale and the local stream thickness scale

These features can be seen in many other flows that undergo transition in nature; an extensive compilation of such observations is provided in Refs. 18 and 19. Perhaps, the most striking transition phenomenon that confirms conclusions 1 and 2 is the highly regular (buckled) vortex street formed in the wake of a solid obstacle. There, the universal proportionality between wake wavelength and wake thickness is obvious, and the local Reynolds number is certainly of order 10^2 (see Table 6.1). Deep down, the rule for being able to see these common characteristics in other naturally behaving flows appears to be Leonardo da Vinci's advice, ''*O miseri mortali aprite li occhi*!'' [20].*

6.3   BUCKLING OF INVISCID STREAMS

If the transition phenomenon is characterized by *scaling laws* 1 and 2, then to *predict* the transition is to account for these scaling laws *theoretically*. The remainder of this chapter is devoted to the presentation of two alternative theoretical arguments, both capable of predicting the transition laws 1 and 2. The first argument is the most direct and is based on the buckling property of inviscid flow [18]. The second approach is based on reviewing the scaling implications of classical results known from the hydrodynamic stability analysis of inviscid flows [9].

---

*O, wretched mortals, open your eyes!
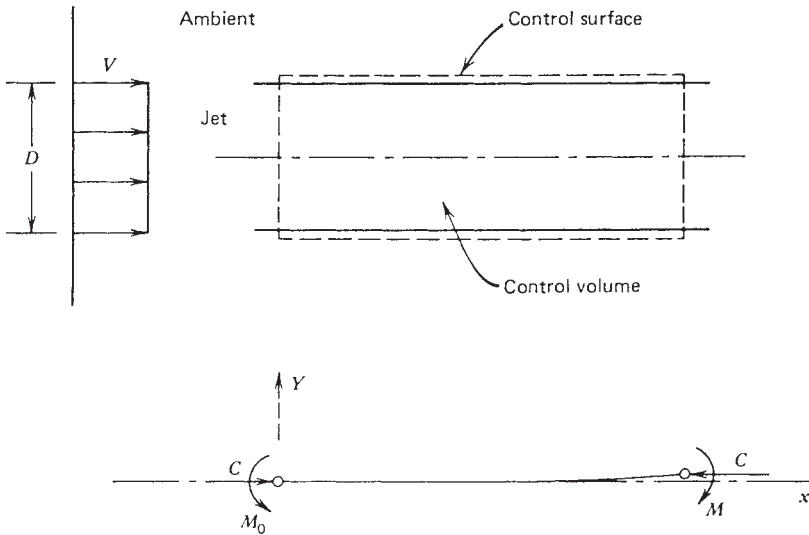
Figure 6.3   Translational and rotational equilibrium of a finite-size stream. (From Ref. 18.)

An interesting analogy between the buckling of elastic solid columns and the meandering of inviscid streams results from considering the static equilibrium of a *finite-size control volume* drawn around the stream. If, as shown in Fig. 6.3, the stream and control volume thickness is of order D and if the stream cross section is A, the control volume (or the thin-walled hose surrounding the stream) satisfies the two conditions necessary for sinusoidal infinitesimal buckling in elastic systems:

1. The control volume is in a state of axial compression subject to the impulse and reaction forces (see the force balance discussed also in connection with Fig. 2.3*b*)

$$C = \rho V^2 A \tag{6.7}$$

2. If subjected to a *separate* bending test, the control volume develops in its cross section a resistive bending moment that is directly proportional to the induced curvature (see Problem 6.4)

$$M = -\rho V^2 I \frac{d^2 Y}{dx^2} \tag{6.8}$$

In eq. (6.8), I is the area moment of inertia of the stream cross section, $I = \int\int_A z^2 \, dA$, and $(-Y'')$ is the local curvature of the infinitesimally deformed control volume. Note also that eq. (6.8) is analogous to the equation $M = -EIY''$ derived from applying the same bending test of prescribed curvature to a slender elastic beam. This means that in inviscid streams, the product ρV^2 plays the role

of *modulus of elasticity*, a fact confirmed easily by trying to bend a thin-walled hose containing a high-Reynolds-number stream. The stream control volume possesses *elasticity*, that is, conservative mechanical properties, because in the inviscid flow limit, the material and flow that fill the control volume are incapable of generating entropy [18].

Conditions 1 and 2 are essential to the *static equilibrium* of the control volume. The translational equilibrium is evident, as the two forces C balance each other. However, as in Euler's buckling theory of solid columns, the rotational equilibrium must be preserved even when the two forces C are not perfectly collinear; hence,

$$-M(x) + CY + M_0 = 0 \tag{6.9}$$

or, substituting expressions (6.7) and (6.8),

$$(\rho V^2 I)Y'' + (\rho V^2 A)Y + M_0 = 0 \tag{6.10}$$

This static rotational equilibrium condition indicates that the equilibrium shape of the nearly straight stream column is a *sinusoid* of vanishingly small amplitude and characteristic (*unique*) wavelength,

$$\lambda_B = 2\pi \left(\frac{I}{A}\right)^{1/2} = \begin{cases} \dfrac{\pi}{2}D & \text{circular cross section} \\[2mm] \dfrac{\pi}{3^{1/2}}D & \text{rectangular cross section} \end{cases} \tag{6.11}$$

which means that in an order-of-magnitude sense,

$$\lambda_B \sim 2D \tag{6.11'}$$

The buckling *wavelength* λ_B is a geometric property of the finite-size control volume, a length about twice the transversal dimension D. The $\lambda_B \sim D$ scaling predicted by the buckling theory of inviscid streams accounts for the empirical scaling law 1 detected during transition (see Section 6.2). Before showing how the buckling property also accounts for the transition scaling law 2, it is worth making the following observations:

1. The buckling wavelength of an inviscid stream is unique (and of order D) because the compressive load $\rho V^2 A$ is always proportional to the elasticity modulus ρV^2. This feature sharply distinguishes the buckling of inviscid streams from that of elastic solid columns where C and E are independent. This is why in solid columns we encounter an infinity of λ_B's (an additional degree of freedom) and out of these we must determine a discrete sequence of special λ_B's that satisfy end-clamping conditions. In the case of inviscid streams, the buckling wavelength is unique, and end-boundary conditions are not an issue (*where* along the jet the first meander appears depends on the transition scaling law 2, as is shown later in this section and in Fig. 6.7).

2. The buckling theory of inviscid streams invokes the equilibrium of a *finite-size* region of the flow field and, as such, represents a dramatic departure from the methodology that prevails in contemporary fluid mechanics. Routine fluid mechanics analysis has as its starting point the Navier–Stokes equations, which account for mechanical equilibrium among infinitesimally small fluid packets (see Chapter 1).

3. Although the proportionality $\lambda_B \sim D$ is universal, the control volume of transversal dimension D has been selected arbitrarily. Any fluid fiber, that is, any control volume of thickness $D' \neq D$, satisfies conditions 1 and 2 for infinitesimal buckling. Out of this infinity of fibers, however, only a special class is in a state of *unstable* equilibrium. The instability of inviscid flow, the discovery that certain fluid fibers are unstable, is an entirely different flow property and the contribution of an entirely different theory (hydrodynamic stability). As shown in Section 6.4, it is only the fibers thicker than the stream that are unstable, that *resonate* when shaken with a prescribed frequency (wavelength) by the mathematician, or the loudspeaker in a laboratory flow experiment.

4. The buckling property or the scaling law $\lambda_B \sim D$ is widely observed in natural flows and can also be visualized in the laboratory. An extensive photographic record of such observations is presented in Refs. 18 and 19; among these, we note the river meandering phenomenon [21], the waving of flags and the meandering fall of paper ribbons [22], the buckling of fast liquid jets shot through the air [23], the wrinkling of two-dimensional fluid layers being pushed from one end [24], and the sinuous structure of all turbulent plumes [25].

   Anyone can visualize the buckling scaling (6.11′) by placing an obstacle under the capillary water column falling from a faucet. Figure 6.4
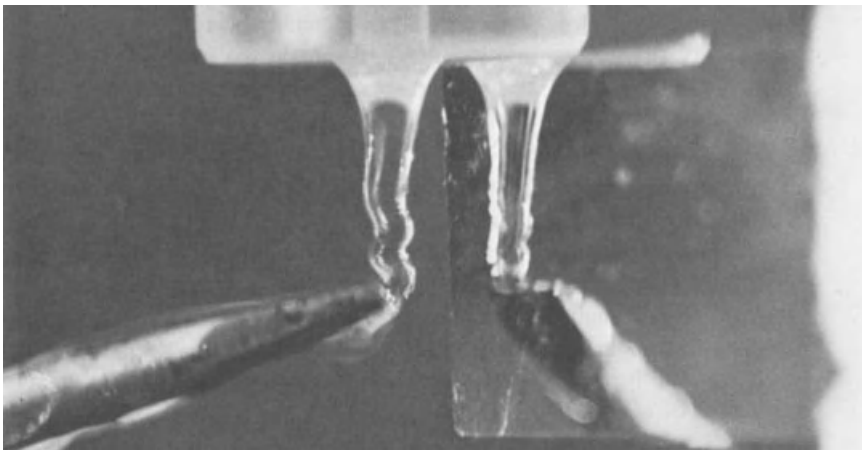

Figure 6.4   Plane buckled shape of a water column impinging on the flat end of a screwdriver: left side, direct view; right side, view through the side mirror. (From Ref. 26.)

shows the front and side views of the buckled stream: The sinuous defor-
mation is mainly in one plane, like the cigarette-smoke plume of Fig. 6.1,
and the locally measured λ_B/D ratio is consistently on the order of 2,
as in eq. (6.11′).

6.4   LOCAL REYNOLDS NUMBER CRITERION FOR TRANSITION

We now return to transition scaling law 2 armed with the idea that a stream has
the $\lambda_B \sim D$ property *if it is inviscid*. The inviscidity (or viscidity) of the stream
is a *flow property*, not a fluid property. It is inappropriate to refer to fluids such
as honey and lava as viscous when if the respective streams are wide and fast
enough, they buckle (meander) just as rivers do.

Consider the transition from the state of *viscid stream* to that of *inviscid
stream*, in the flow sketched in Fig. 6.3. In time, viscous diffusion penetrates in
the direction normal to the stream–ambient interface, so that in a time of order

$$t_v \sim \frac{D^2}{16\nu} \tag{6.12}$$

the stream is fully viscous. The time scale above follows from the error-function
solution to the problem of viscous diffusion normal to an impulsively started
wall (see Problem 6.5); according to this solution, the knee of the error function
is such that the time of viscous penetration to the stream centerline (to a depth
$D/2$) is given by

$$\frac{D/2}{2(\nu t_v)^{1/2}} \sim 1 \tag{6.12′}$$

Whether or not the stream has time to become viscous depends on how fast it
can buckle as an inviscid stream. The result of the incipient buckling analyzed
early in this section is the birth of eddies, as the crests of the λ_B waves roll at
the stream–ambient interface. From symmetry, the λ_B wave moves along the
stream with a velocity of order $V/2$; hence, the *buckling time* or the time of eddy
formation is

$$t_B \sim \frac{\lambda_B}{V/2} \tag{6.13}$$

The stream can buckle only if $t_B < t_v$, in other words, if the *buckling frequency
number* $N_B = t_v/t_B$ is greater than 1. The same comparison of time scales and the
same transition criterion are recommended by the constructal law of facilitating
the flow of momentum transversally, from the stream to the surrounding fluid,
that is, by facilitating a greater growth rate for the transversal flow, $D(t)$ [1,27].

In conclusion, the time-scale argument presented above recommends the
following criterion for transition:

$$N_B = \frac{t_v}{t_B} \begin{cases} < 1 & \text{laminar flow} \\ \sim 1 & \text{transition} \\ > 1 & \text{buckling or turbulent flow} \end{cases} \tag{6.14}$$

After replacing t_v and t_B with $D^2/16\nu$ and $2\lambda_B/V$, respectively, this criterion becomes

$$\text{Re}_l = \frac{VD}{\nu} \begin{cases} < 10^2 & \text{laminar flow} \\ \sim 10^2 & \text{transition} \\ > 10^2 & \text{buckling or turbulent flow} \end{cases} \quad (6.15)$$

The group VD/ν is the *local Reynolds number* Re_l, which is based on the local longitudinal velocity scale (V) and the local transverse dimension of the stream (D). The local Reynolds number criterion (6.15) correctly predicts transition scaling law 2, discovered empirically in Section 6.3.

Examine now the empirical critical numbers associated with the transition (Table 6.1) by first recognizing the correct V and D scales and then calculating the associated local Reynolds number. This bird's-eye view of the transition phenomenon is provided by Table 6.2 and Fig. 6.5. For example, the critical local Reynolds number of laminar boundary layer flow over a flat plate is nearly the same as that of the buoyancy-driven jet along a heated vertical wall. It can be argued that the Re_l range for transition in round jet flow is actually higher than the nozzle Reynolds number listed because the laminar jet expands rapidly outside the nozzle (i.e., the D scale of the jet is larger than the nozzle diameter). The same observation applies to the transition in the wake behind a long cylinder, where the Reynolds number listed is based on the diameter of the cylinder, not on the transversal length scale of the wake.

On the high side of the transition criterion $\text{Re}_l \sim 10^2$, we note that the transition in pipe flow occurs at diameter-based Reynolds numbers of order 2000. The actual thickness of the centerline flow ''fiber'' that exhibits the sinuous motion is considerably smaller than the pipe diameter; therefore, the *local* Reynolds number is correspondingly smaller than 2000. This is why a smaller value ($\text{Ra}_l \sim 500$) is listed in the second column of the table.

Table 6.2 Traditional critical numbers for transition in several key flows and the corresponding local Reynolds number scale

| Flow	Traditional Critical Number	Local Reynolds Number
Boundary layer flow over flat plate	$\text{Re}_x \sim 2 \times 10^4 - 10^6$	$\text{Re}_l \sim 94 - 660$
Natural convection boundary layer along vertical wall with uniform temperature ($\text{Pr} \sim 1$)	$\text{Ra}_y \sim 10^9$	$\text{Re}_l \sim 178$
Natural convection boundary layer along vertical wall with constant heat flux ($\text{Pr} \sim 1$)	$\text{Ra}_{*y} \sim 4 \times 10^{12}$	$\text{Re}_l \sim 330$
Round jet	$\text{Re}_{\text{nozzle}} \sim 30$	$\text{Re}_l \gtrsim 30$
Wake behind long cylinder in cross-flow	$\text{Re} \sim 40$	$\text{Re}_l \gtrsim 40$
Pipe flow	$\text{Re} \sim 2000$	$\text{Re}_l \sim 500$
Film condensation on a vertical wall	$\text{Re} \sim 450$	$\text{Re}_l \sim 450$
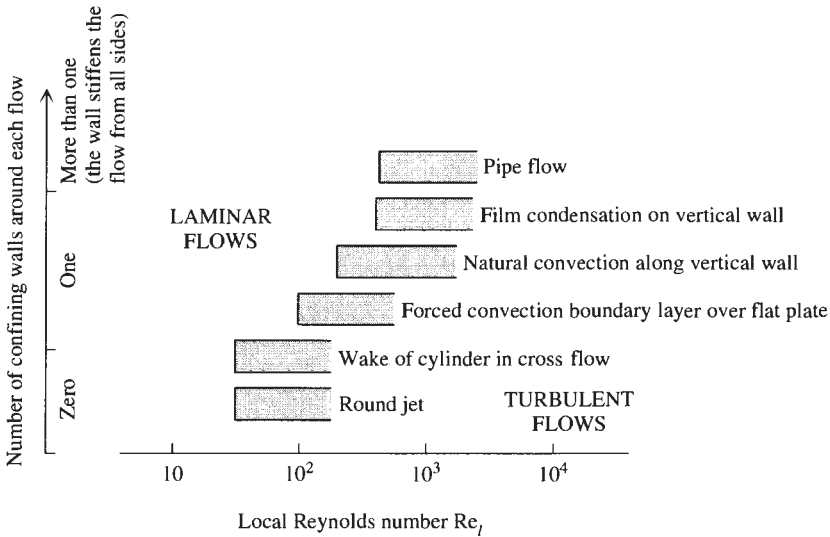
Figure 6.5   Universal transition criterion: local Reynolds number of order 10^2.

Figure 6.5 reviews the local Reynolds numbers that correspond to the transitions considered in Table 6.2. One remarkable aspect of this figure is that it condenses the transition observations to a relatively narrow band of values centered around $Re_l \sim 10^2$: Compare this narrow band with the $10–10^{12}$ range covered by the traditional critical numbers.

Another interesting aspect of Fig. 6.5 is that it unveils the flow-straightening effect that solid walls have on transition. Flows without solid walls (jets, wakes, plumes) exhibit Re_l values that are on the low side of 10^2. Flows stiffened by one solid wall have somewhat higher local Reynolds numbers at transition. The pipe flow is straightened by solid surfaces from all sides, and consequently, its transition Re_l value is on the high side of 10^2.

To summarize, the buckling property and the constructal law provide a theoretical basis for the transition scaling laws 1 and 2, or the proportionality between wavelength and stream thickness, and the local Reynolds number of order 10^2 during transition. In the next section we learn that the predicted scales are *consistent* with scales also recommended by the hydrodynamic stability theory of inviscid flow. This does not mean that the two theories, buckling and hydrodynamic stability, are equivalent. The purpose of a theory is to explain known physical observations and to forecast future observations. Since no theory is perfect (capable of explaining everything), it is possible that the domains covered by two theories overlap. The next section is about such an overlap, namely, the explanation of scaling laws 1 and 2. However, the discovery of this overlap and even stating in English scaling laws 1 and 2 are contributions of the newer theory.

6.5 INSTABILITY OF INVISCID FLOW

The issue of whether a parallel inviscid flow is stable or unstable is a century-old problem in modern fluid mechanics, a problem so traveled that it is one of the most voluminous chapters in the field. The analytical treatment of this problem originated with Helmholtz [28], Kelvin [29], and Rayleigh [30], who focused on the inertial instability of a homogeneous incompressible fluid. In this section we take another look at Rayleigh's analysis of an inviscid jet [30] in order to identify the proper length and time scales that govern the transition phenomenon.

Consider the parallel flow of homogeneous incompressible fluid shown in Fig. 6.6. Modeling the flow as inviscid and two-dimensional, the continuity and momentum equations become

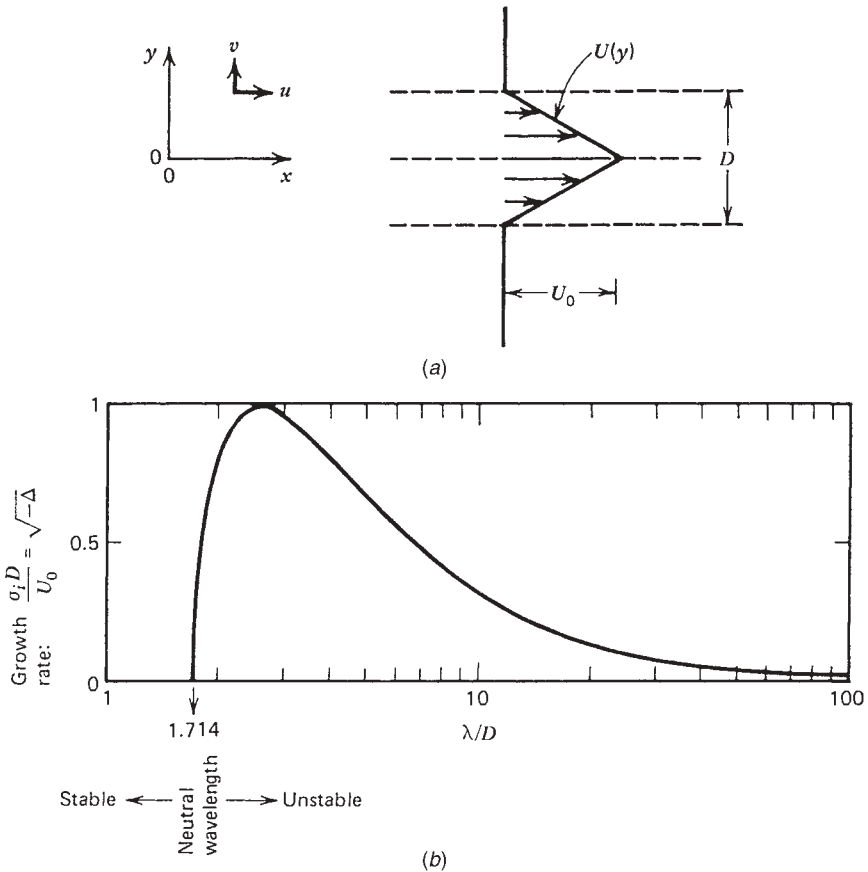$$\frac{\partial u}{\partial x} + \frac{\partial v}{\partial y} = 0 \tag{6.16}$$

Figure 6.6 Stability characteristics of an inviscid jet of triangular profile.

$$\frac{\partial \zeta}{\partial t} + u\frac{\partial \zeta}{\partial x} + v\frac{\partial \zeta}{\partial y} = 0 \tag{6.17}$$

$$\zeta = \frac{\partial v}{\partial x} - \frac{\partial u}{\partial y} \tag{6.18}$$

where ζ is the vorticity function. Equations (6.17) and (6.18) are obtained by eliminating the pressure gradient terms between eqs. (1.19a) and (1.19b). Next, we assume that the parallel flow $U(y)$ is disturbed slightly, such that

$$u = U(y) + u' \tag{6.19}$$
$$v = 0 + v'$$

where the disturbance components (u',v') are regarded as small compared with the base flow $U(y)$. Finally, we seek to find out whether the disturbance amplitude grows with time, that is, whether the flow is unstable *relative* to the postulated disturbance.

Substituting the (base flow) + (disturbance) decomposition (6.19) into the governing equations and linearizing the result (i.e., neglecting the terms of second order in u',v') yields

$$\frac{\partial u'}{\partial x} + \frac{\partial v'}{\partial y} = 0$$

$$\left(\frac{\partial}{\partial t} + U\frac{\partial}{\partial x}\right)\left(\frac{\partial v'}{\partial x} - \frac{\partial u'}{\partial y}\right) - \frac{d^2 U}{dy^2}v' = 0 \tag{6.20}$$

Having observed *sinusoidal* disturbances that grow or decay in time (i.e., using empiricism), Rayleigh replaced u' and v' by the real parts of

$$\hat{u}e^{i(kx+\sigma t)} \quad \text{and} \quad \hat{v}e^{i(kx+\sigma t)} \tag{6.21}$$

where k is the wave number $2\pi/\lambda$ describing the disturbance periodicity in the x direction. Substituting these expressions into eqs. (6.20) and solving for $\hat{v}(y)$ yielded what is recognized in the literature as the *Rayleigh equation*,

$$\left(\frac{\sigma}{k} + U\right)(\hat{v}'' - k^2\hat{v}) - U''\hat{v} = 0 \tag{6.22}$$

Think about the step between eqs. (6.20) and (6.22). The postulate of *sinusoidal* disturbances is now made routinely and without explanation in stability analyses of all kinds. Rayleigh, however, had a very good reason to be curious about the growth of *sinusoidal* disturbances. He lived and created in a period when rooms were lit by gaslight and candlelight and when the university club did not display a ''No Smoking'' sign; his mind was stimulated by images similar to Fig. 6.1, that is, by the flickering of cigarette smoke and candle flames. Rayleigh referred

to such flows as *sensitive jets* because they all appeared to resonate and meander most visibly when exposed to a *particular* sound frequency (musical tone).

From the preceding discussion and Fig. 6.2, it is already clear that this natural *sensitivity* is the same as the buckling property of the jet manifested for the first time during transition. For Rayleigh and his epigones, the postulate of *sinusoidal* disturbances is pure empiricism, the result of unexplained physical observations. In sharp contrast with stability analysis, the buckling theory predicts the *mathematically* sinusoidal shape of the deformed stream in the earliest stages of transition. Herein lies the aggregate contribution of the two theories: In time, the hydrodynamic stability analysis begins where the buckling theory leaves off.

To solve eq. (6.22), most insight per unit effort is achieved by modeling the base flow as a dashed-line profile (Fig. 6.6). Thus, U'' vanishes in any region of the base flow; hence,

$$\hat{v}'' - k^2 \hat{v} = 0 \tag{6.23}$$

with the general solution

$$\hat{v} = C_1 e^{ky} + C_2 e^{-ky} \tag{6.24}$$

For the four-line jet profile of Fig. 6.6, we write

$$
\begin{aligned}
\hat{v} &= C_1 e^{ky} + C_2 e^{-ky}, & y &> D/2 \\
\hat{v} &= C_3 e^{ky} + C_4 e^{-ky}, & D/2 &> y > 0 \\
\hat{v} &= C_5 e^{ky} + C_6 e^{-ky}, & 0 &> y > -D/2 \\
\hat{v} &= C_7 e^{ky} + C_8 e^{-ky}, & -D/2 &> y
\end{aligned}
\tag{6.25}
$$

where from the condition that $\hat{v}$ does not blow up as $y \to \pm\infty$, we have $C_1 = C_8 = 0$. The remaining six unknowns, C_2–C_7, are determined from the six conditions that account for the continuity of $\hat{v}$ and pressure across the three interfaces, $y = -D/2, 0, D/2$. For example, the condition that $\hat{v}$ is continuous across $y = 0$ yields $C_3 + C_4 = C_5 + C_6$. The three pressure continuity conditions are obtained by integrating the Rayleigh equation (6.22) across each interface,

$$\left(\frac{\sigma}{k} + U\right)(\hat{v}'_+ - \hat{v}'_-) - \hat{v}(U'_+ - U'_-) = 0 \tag{6.26}$$

where the (+) and (−) subscripts indicate values calculated at the interface, while approaching the interface from above and below. It is easy to see that these six continuity conditions form a system of homogeneous equations; setting the determinant equal to zero yields the condition necessary for nontrivial solutions

$$(m - \gamma^2)[m^2 + (kD - 3 + \gamma^2)m + \gamma^2(1 + kD)] = 0 \tag{6.27}$$

where

$$\gamma = e^{-kD/2} \quad \text{and} \quad m = 1 + \frac{\sigma D}{U_0}$$

Equation (6.27) contains the information sought by the stability analysis: namely, the growth rate σ compatible with the postulated wave number k. From the exponential forms chosen for u' and v' [eqs. (6.21)], it is clear that only if σ is complex will the disturbance grow exponentially in time, indicating *instability*. Complex σ's are possible if the discriminant is negative in the quadratic formed by setting the brackets of eq. (6.27) equal to zero,

$$\Delta = (kD - 3 + \gamma^2)^2 - 4\gamma^2(1 + kD) < 0 \tag{6.28}$$

Solving this for kD, we find that the instability condition means that

$$kD < 3.666 \quad \text{or} \quad \lambda > 1.714D \tag{6.29}$$

In conclusion, the disturbance wavelength must exceed a certain multiple of the jet diameter D for the flow to be unstable relative to the postulated disturbance. Consulting eqs. (6.21), we discover that during instability, the time rate of growth of the disturbance (the imaginary part of σ) is proportional to $(-\Delta)^{1/2}$:

$$\frac{\sigma_i D}{U_0} = (-\Delta)^{1/2} \tag{6.30}$$

The growth rate has been plotted in Fig. 6.6*b*, showing once again that the neutral wavelength scales with the jet transversal scale D. Beginning with Rayleigh's paper [30], much has been made in the literature of the maximum exhibited by the growth rate curve $\sigma_i D/U_0$. More important, however, is the ''coincidence'' that the neutral wavelength $1.714D$ is only 5 percent smaller than the buckling wavelength scale of a two-dimensional stream $[(\pi/3^{1/2})D = 1.81D$, eq. (6.11)]. This coincidence seems to be insensitive to the actual shape of the $U(y)$ profile chosen for analysis. For example, in a stack of D-thick counterflow jets of sinusoidal profile ($u = U_0 \sin \pi y/D$), the neutral wavelength is $2D$, which is only 10 percent greater than the buckling length scale $(\pi/3^{1/2})D$. The same scaling between flow thickness and neutral wavelength is revealed by the stability analysis of many other finite-thickness flows [19].

What does this scaling tell us about the laminar–turbulent transition? It says that during transition, the stream can fluctuate relative to its ambient with a period on the order of $\lambda/(U_0/2)$, where λ is the assumed disturbance wavelength. Because λ is greater than a length nearly identical to λ_B, the fluctuation time scale can only be greater than the buckling time scale t_B [eq. (6.13)]. Therefore, the fluctuation period exceeds a minimum time scale that is proportional to the transversal length scale D. The domain of inviscid instability appears to the right of the t_B–D line sketch in Fig. 6.7. However, as was argued in the preceding section and in Ref. 18, any stream of finite thickness becomes viscid at times greater than the viscous penetration scale t_v given by eq. (6.12); the viscid flow domain belongs to the right of the $t_v \sim D^2$ curve sketched in Fig. 6.7.

To read Fig. 6.7, imagine the upward development of a plume like the cigarette smoke shown in Fig. 6.1. The stream thickness increases monotonically with
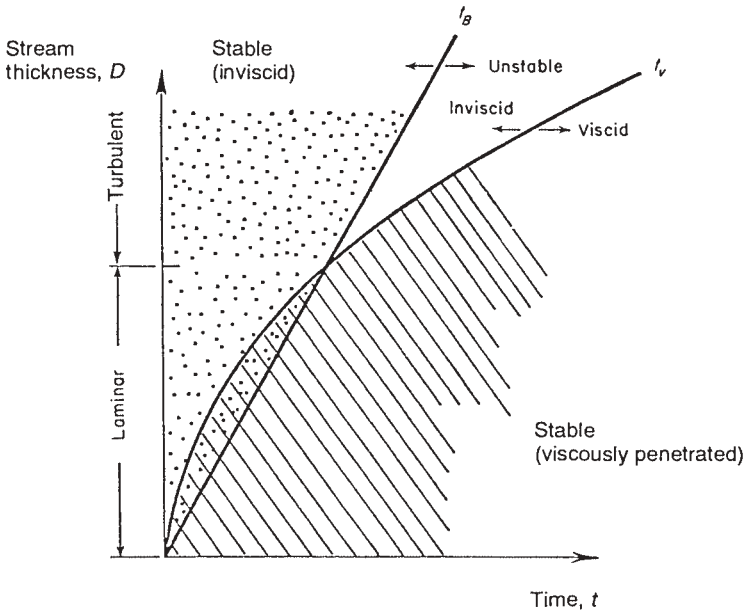
Figure 6.7 Transition as the competition between the viscous penetration time (t_v) and the time of buckling and rollup (t_B).

altitude (this is why D is plotted on the ordinate in Fig. 6.7) and remains laminar as long as $t_v < t_B$. Transition becomes possible beyond a critical plume diameter (or plume height) marked by $t_v \sim t_B$ or by criterion (6.15) established earlier. The first wave during transition has a length about twice the local stream thickness.

In conclusion, the scaling revealed by the stability analysis of an inviscid jet (Fig. 6.6) leads back to the local Reynolds number criterion for transition (6.15). In this way, the inviscid stability scaling accounts for transition laws 1 and 2 stated in Section 6.2.

The existence of a semi-infinity of wavelengths for which the D-thick jet is unstable (Fig. 6.6) would seem to contradict the uniqueness of the wavelength scale predicted by the buckling theory. In fact, there is no contradiction. The scale analysis of the Rayleigh equation (6.22) or (6.23) indicates that the disturbance amplitude is always felt to a y thickness of order $k^{-1} \sim \lambda$. This means that the thickness of the fluid layer that resonates to the imposed disturbance wavelength λ always scales with λ, regardless of the actual thickness of the base flow region [31].

It was shown [32,33] that the transition scaling laws 1 and 2 mean that the laminar sections of all slender (i.e., boundary layer type) flows are geometrically similar. For example, the proportionality between the laminar length and the first buckling wavelength, which in eq. (6.1) was identified empirically, is universal and can be derived from the local Reynolds number criterion of eq. (6.15). Figure 6.8 reproduces Gore et al.'s [33] compilation of the transition
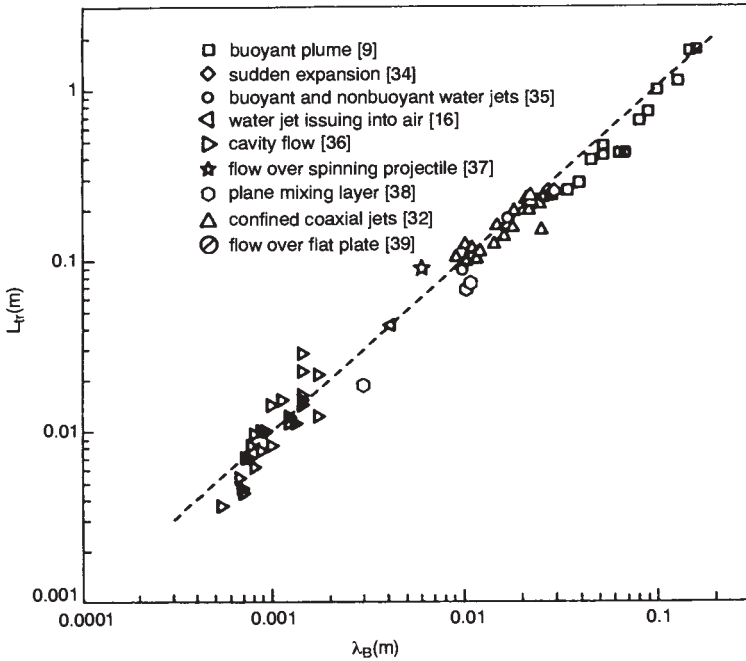
Figure 6.8 Proportionality between the length of the laminar section and the buckling wavelength. (From Ref. 33.)

observations furnished by experiments with several flow types, which show that the proportionality (6.1) is valid universally:

$$L_{tr} \sim 10\lambda_B \tag{6.31}$$

In this proportionality, L_{tr} represents the length to transition [i.e., the length of the laminar section of the slender flow (boundary layer, jet, plume, shear layer)].

The scaling law (6.31) can be predicted based on the two scaling laws recognized at the start of this chapter,

$$\lambda_B \sim 2D \tag{6.32}$$

$$\frac{VD}{\nu} \sim 10^2 \tag{6.33}$$

where V and D are the local velocity scale and the local thickness of the flow. For example, if the flow is a laminar boundary layer on a flat plate, the thickness at transition is

$$D \sim \delta \sim cL\left(\frac{VL}{\nu}\right)^{-1/2} \tag{6.34}$$

where L is the length of the laminar section and c is a factor of order 2 or 3, depending on how the boundary layer thickness δ is calculated (see Chapter 2).

By eliminating V and D between eqs. (6.32)–(6.34), we obtain

$$L \sim \frac{50}{c^2} \ \lambda_B \sim 10\lambda_B \tag{6.35}$$

which anticipates fully the empirical correlation (6.31).

6.6 TRANSITION IN NATURAL CONVECTION ON A VERTICAL WALL

A principle is powerful when it predicts observations and when it corrects and simplifies older beliefs that are based on empirical evidence. The competition of time scales on which this chapter is based, is the action of the constructal law toward facilitating access for the flow of momentum and heat transfer [1]. In this chapter, this principle accounted for many transition phenomena across the board, and the literature continues to show that this principle is universally applicable [40]. We close with one more example—natural convection on a vertical wall (Fig. 6.9)—and show how the theory unveils the effect that the Prandtl number has on transition.

Turbulent region

T_w

Reservoir fluid entrained by large eddy

The shaded fluid has been penetrated by viscous diffusion

T_∞

Transition region

Wavelength proportional to thickness of the wall jet

The transition Gr_y corresponding to this band of y values is shown in Fig. **6.10**
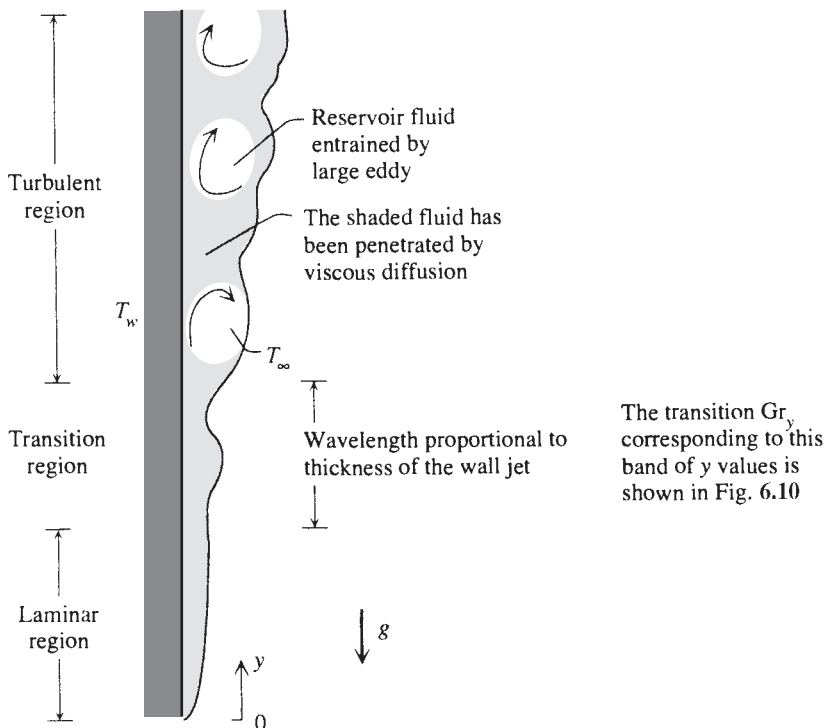
Laminar region

g

y

0

Figure 6.9 Laminar, transition, and turbulent sections of a natural convection boundary layer along a vertical wall. (From Ref. 41.)

For a long time it was thought that the transition from laminar to turbulent flow occurs at the y position where $Ra_y \sim 10^9$, regardless of the value of the Prandtl number. The established view was questioned by Bejan and Lage [42], who showed that it is the Grashof number of order 10^9, not the Rayleigh number, that marks the transition in all fluids:

$$Gr_y \sim 10^9 \qquad (10^{-3} \leq Pr \leq 10^3) \tag{6.36}$$

This universal transition criterion can be expressed in terms of the Rayleigh number, by recalling that $Ra_y = Gr_y\,Pr$:

$$Ra_y \sim 10^9\,Pr \qquad (10^{-3} \leq Pr \leq 10^3) \tag{6.37}$$

It is supported very well by the experimental observations [43–51] reviewed in Fig. 6.10 and in great detail in Ref. 42. The $Gr_y \sim 10^9$ transition criterion coincides with the traditional criterion $Ra_y \sim 10^9$ in the case of fluids with Prandtl numbers of order 1 (e.g., air). In the liquid-metal range $Pr \sim 10^{-3}$–10^{-2}, the Grashof number criterion (6.32) means that the actual transition Rayleigh number is of order 10^6–10^7, which is well below the often-mentioned threshold of 10^9.

The Pr range of the transition observations assembled in Fig. 6.10 can be extended by adding the observations reported by Lloyd et al. [52]. In the current context, Lloyd et al.'s experiments indicated that the laminar boundary layer regime expires somewhere above $Ra_y \sim 3 \times 10^{11}$ when $Pr = 2000$. This agrees very well with the transition criterion (6.32), as $Gr_y = Ra_y/Pr \sim (3 \times 10^{11})/2000 = 1.5 \times 10^8$.

Correlations of transition for natural convection were reported more recently by Yang [53]. Buckling of plumes and salt fingers during solidification was described by Wirtz et al. [54]. Universality and correlation of transition observations were developed by Levi [55], Cervantes et al. [56], and Gharib et al. [57] for vortex rings. Oscillating buckling jets were analyzed by Cervantes and Solorio [58]. The Pr effect on transition in an enclosure with natural convection was documented numerically by Lage and Bejan [59].
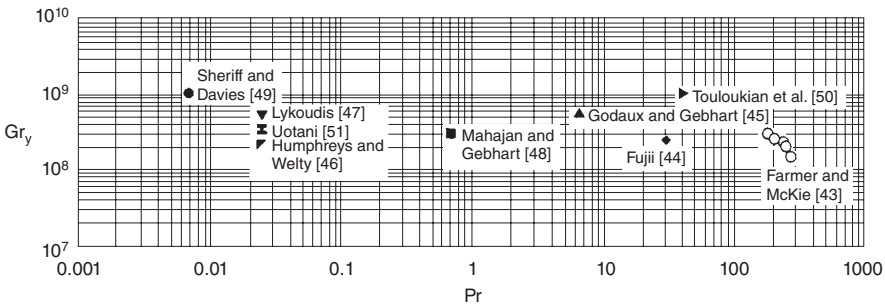

Figure 6.10 Universal criterion for transition to turbulence along a vertical wall with natural convection boundary layer flow. (From Ref. 42.)

REFERENCES

1. A. Bejan and S. Lorente, The constructal law and the evolution of design in nature, *Phys. Life Rev.*, Vol. 8, 2011, pp. 209–240.

2. A. Bejan and S. Lorente, *Philos. Trans. Roy. Soc. B*, Vol. 365, 2010, pp. 1335–1347.

3. R. A. Granger, *Fluid Mechanics*, Holt, Rinehart and Winston, New York, 1984.

4. A. J. Reynolds, Observations of a liquid-into-liquid jet, *J. Fluid Mech.*, Vol. 14, 1962, pp. 552–556.

5. F. Homann, Einfluss grosser Zähigkeit bei Strömung um Zylinder, *Forsch. Ingenieurwes.*, Vol. 7, 1936, pp. 1–10.

6. R. L. Mahajan and B. Gebhart, An experimental determination of transition limits in a vertical natural convection flow adjacent to a surface, *J. Fluid Mech.*, Vol. 91, 1979, pp. 131–154.

7. A. A. Szewczyk, Stability and transition of the free convection layer along a vertical flat plate, *Int. J. Heat Mass Transfer*, Vol. 5, 1962, pp. 903–914.

8. R. Godaux and B. Gebhart, An experimental study of the transition of natural convection flow adjacent to a vertical surface, *Int. J. Heat Mass Transfer*, Vol. 17, 1974, pp. 93–107.

9. S. Kimura and A. Bejan, Mechanism for transition to turbulence in buoyant plume flow, *Int. J. Heat Mass Transfer*, Vol. 26, 1983, pp. 1515–1532.

10. W. M. Rohsenow and H. Y. Choi, *Heat, Mass and Momentum Transfer*, Prentice-Hall, Englewood Cliffs, NJ, 1961, p. 243.

11. W. M. Kays and M. E. Crawford, *Convective Heat and Mass Transfer*, 2nd ed., McGraw-Hill, New York, 1980, p. 163.

12. G. K. Batchelor and A. E. Gill, Analysis of the stability of axisymmetric jets, *J. Fluid Mech.*, Vol. 14, 1962, pp. 529–551.

13. P. G. Drazin and L. N. Howard, Hydrodynamic stability of parallel flow of inviscid fluid, *Adv. Appl. Mech.*, Vol. 9, 1966, pp. 1–89.

14. J. L. Lopez and U. H. Kurzweg, Amplification of helical disturbances in a round jet, *Phys. Fluids*, Vol. 20, 1977, pp. 860–861.

15. S. C. Crow and F. H. Champagne, Orderly structure in jet turbulence, *J. Fluid Mech.*, Vol. 48, 1971, pp. 547–593.

16. J. W. Hoyt and J. J. Taylor, Waves on water jets, *J. Fluid Mech.*, Vol. 83, 1977, pp. 119–127.

17. B. Gebhart and R. Mahajan, Characteristic disturbance frequency in vertical natural convection, *Int. J. Heat Mass Transfer*, Vol. 18, 1975, pp. 1143–1148.

18. A. Bejan, *Entropy Generation through Heat and Fluid Flow*, Wiley, New York, Chapter 4.

19. A. Bejan, Buckling flows: A new frontier in fluid mechanics, in T. C. Chawla, ed., *Annual Review of Numerical Fluid Mechanics and Heat Transfer*, Vol. 1, Hemisphere, Washington, DC, 1987, pp. 262–304.

20. J. P. Richter, *The Notebooks of Leonardo da Vinci*, Vol. II, Dover, New York, 1970, p. 295.

21. A. Bejan, Theoretical explanation for the incipient formation of meanders in straight rivers, *Geophys. Res. Lett.*, Vol. 9, 1982, pp. 831–834.

22. A. Bejan, The meandering fall of paper ribbons, *Phys. Fluids*, Vol. 25, 1982, pp. 741–742.

23. M. G. Stockman and A. Bejan, The nonaxisymmetric (buckling) flow regime of fast capillary jets, *Phys. Fluids*, Vol. 25, 1982, pp. 1506–1511.

24. K. R. Blake and A. Bejan, Experiments on the buckling of thin fluid layers undergoing end-compression, *J. Fluids Eng.*, Vol. 106, 1984, pp. 74–78.

25. A. Bejan, Theory of instantaneous sinuous structure in turbulent buoyant plumes, *Wärme Stoffübertrag.*, Vol. 16, 1982, pp. 237–242.

26. S. Kimura and A. Bejan, The buckling of a vertical liquid column, *J. Fluids Eng.*, Vol. 105, 1983, pp. 469–473.

27. A. F. Miguel and A. Bejan, The principle that generates dissimilar patterns inside aggregates of organisms, *Physica*, Vol. 388, 2009, pp. 727–731.

28. H. Helmholtz, Über diskontinuierliche Flüssigkeitsbewegungen, *Monatsber. Königl. Preuss. Akad. Wiss. Berlin*, 1868, pp. 215–228; translation by F. Guthrie, On discontinuous movements of fluids, *Philos. Mag.*, Vol. 4, No. 36, 1868, pp. 337–346.

29. W. Kelvin, The influence of wind on waves in water supposed frictionless, *Philos. Mag.*, Vol. 4, No. 42, 1871, pp. 368–374.

30. J. W. S. Rayleigh, On the stability, or instability of certain fluid motions, *Proc. London Math. Soc.*, Vol. XI, 1880, pp. 57–70.

31. R. Anderson and A. Bejan, The instability of a round jet surrounded by an annular shear layer, *J. Fluids Eng.*, Vol. 107, 1985, pp. 258–263.

32. R. A. Gore, C. T. Crowe, and A. Bejan, Experimental observations on transition to turbulence in confined coaxial jets and other boundary layer flows, *ASME FED*, Vol. 94, 1990, pp. 79–83.

33. R. A. Gore, C. T. Crowe, and A. Bejan, The geometric similarity of the laminar sections of boundary layer-type flows, *Int. Commun. Heat Mass Transfer*, Vol. 17, 1990, pp. 465–475.

34. K. J. McNaughton and C. G. Sinclair, Submerged jets in short cylindrical vessels, *J. Fluid Mech.*, Vol. 25, 1966, pp. 367–375.

35. C. D. Ungate, D. R. F. Harleman, and G. H. Jirka, Mixing of submerged turbulent jets at low Reynolds numbers, Report 197, Ralph M. Parsons Laboratory for Water Resources and Hydrodynamics, Department of Civil Engineering, Massachusetts Institute of Technology, Cambridge, MA, Feb. 1975.

36. C. Brennen, Cavity surface wave patterns and general appearance, *J. Fluid Mech.*, Vol. 44, 1970, pp. 33–49.

37. T. J. Mueller, R. C. Nelson, J. T. Kegelman, and M. V. Morkovin, Visualization of boundary layer transition on a spinning axisymmetric body, *AIAA J.*, Vol. 19, 1981, pp. 1607–1608.

38. G. L. Brown and A. Roshko, On density effects and large structures in turbulent mixing layers, *J. Fluid Mech.*, Vol. 64, 1974, pp. 775–816.

39. H. Werle, Transition and separation: visualization in the ONERA water tunnel, *Rech. Aerosp.*, 1980–5, pp. 35–49.

40. A. Bejan and S. Lorente, Constructal theory of generation of configuration in nature and engineering, *J. Appl. Phys.*, Vol. 100, 2006, 041301.

41. A. Bejan, *Heat Transfer*, Wiley, New York, 1993.

42. A. Bejan and J. L. Lage, The Prandtl number effect on the transition in natural convection along a vertical surface, *J. Heat Transfer*, Vol. 112, 1990, pp. 787–790.

43. W. P. Farmer and W. T. McKie, Natural convection from a vertical isothermal surface in oil, Paper 64-WA/HT-12, ASME, New York, 1964.

44. T. Fujii, Experimental studies of free convection heat transfer, *Bull. JSME*, Vol. 2, No. 8, 1959, pp. 555–558.

45. R. Godaux and B. Gebhart, An experimental study of the transition of natural convection flow adjacent to a vertical surface, *Int. J. Heat Mass Transfer*, Vol. 17, 1974, pp. 93–107.

46. W. W. Humphreys and J. R. Welty, Natural convection with mercury in a uniformly heated vertical channel during unstable laminar and transitional flow, *AIChE J.*, Vol. 21, 1975, pp. 268–274.

47. P. S. Lykoudis, private communication, 1989.

48. R. L. Mahajan and B. Gebhart, An experimental determination of transition limits in a vertical natural convection flow adjacent to a surface, *J. Fluid Mech.*, Vol. 91, 1979, pp. 131–154.

49. N. Sheriff and N. W. Davies, Sodium natural convection from a vertical plate*, Heat Transfer 1978*, Vol. 5, Hemisphere, Washington, DC, 1978, pp. 131–136.

50. Y. S. Touloukian, G. A. Hawkins, and M. Jakob, Heat transfer by free convection from heated vertical surfaces to liquids, *Trans. ASME*, Vol. 70, 1948, pp. 13–23.

51. M. Uotani, Natural convection heat transfer in thermally stratified liquid metal, *J. Nucl. Sci. Technol.*, Vol. 24, No. 6, 1987, pp. 442–451.

52. J. R. Lloyd, E. M. Sparrow, and E. R. G. Eckert, Laminar, transition and turbulent natural convection adjacent to inclined and vertical surfaces, *Int. J. Heat Mass Transfer*, Vol. 15, 1972, pp. 457–473.

53. S.-M. Yang, Improvement of the basic correlating equations and transition criteria of natural convection heat transfer, *Heat Transfer—Asian Res.*, Vol. 30, 2001, pp. 293–300.

54. K. Wirtz, M. Koochesfahani, J. J. McGrath, and A. Benard, Molecular tagging velocimetry applied to buoyancy-driven convective phenomena during solidification, ASME HTD-Vol. 361–4, 1998, pp. 103–110.

55. E. Levi, A universal Strouhal law, *ASCE J. Eng. Mech.*, Vol. 109, 1983, pp. 718–727.

56. J. G. Cervantes, F. J. Solorio, and F. Mendez, On the buckling and the Strouhal law of fluid columns: the case of turbulent jets and wakes, *J. Fluids Struct.*, Vol. 17, No. 8, pp. 1203–1211, 2003.

57. M. Gharib, E. Rambod, and K. Shariff, A universal time scale for vortex ring formation, *J. Fluid Mech.*, Vol. 360, 1998, pp. 121–140.

58. J. G. Cervantes and F. J. Solorio, Entropy generation in a plane turbulent oscillating jet, *Int. J. Heat Mass Transfer*, Vol. 45, 2002, pp. 3125–3129.

59. J. L. Lage and A. Bejan, The Ra–Pr domain of laminar natural convection in an enclosure heated from the side, *Numer. Heat Transfer, Part A: Appl.*, Vol. 19, 1991, pp. 21–41.

60. A. Bejan and G. R. Cunnington, Theoretical considerations of transition to turbulence in natural convection near a vertical wall, *Int. J. Heat Fluid Flow*, Vol. 4, 1983, pp. 131–139.

PROBLEMS

6.1. Show that the transition condition listed for boundary layer flow in Table 6.1 corresponds to a critical Reynolds number of order 10^2 if this critical Reynolds number is based on either the displacement or momentum thickness of the boundary layer.

6.2. Show that for the vertical natural convection boundary layer flow, the local Reynolds number based on vertical velocity scale and velocity boundary layer thickness (Table 4.1) is of order $\Pr^{-1/2} \operatorname{Ra}_y^{1/4}$ if $\Pr > 1$. By examining Table 6.1, prove that during transition, this local Reynolds number is of order 10^2.

6.3. Prove that in the case of the cigarette-smoke plume of Figs. 6.1 and 6.2, the local Reynolds number based on the scales (6.3) and (6.5) is of the same order as $\operatorname{Ra}_q^{1/4}$ during transition. Based on the physical observations compiled in Fig. 6.2, show that this locally defined Reynolds number is of order 10^2.

6.4. Consider the straight inviscid stream (ρ, V, P_0, D, A) shown in Fig. 6.3. Subject this stream to a bending test of prescribed radius of curvature R_∞. Show that in the limit of vanishingly small curvature, $D/R_\infty \to 0$, the resistive bending moment integrated over the stream cross section is

$$M = \iint_A [\rho v(z)^2 + P(z)]z \, dA = \frac{\rho V^2 I}{R_\infty}$$

where z is measured radially away from the stream centerline and toward the center of curvature. [*Hint:* Invoke the Bernoulli equation along a streamline and a force balance in the radial direction to derive analytical expressions for the velocity and pressure profiles $v(z)$ and $P(z)$ in the stream cross section.]

6.5. Consider the transient flow generated in the vicinity of a flat wall: At times $t < 0$, both the fluid and the wall are motionless, whereas for $t > 0$, the wall moves along itself with a constant velocity U. Recognizing that the wall is infinitely long (compared with the thickness of the viscous boundary layer forming along the wall), show that the fluid is entrained in laminar flow according to

$$u = U \operatorname{erfc}\left(\frac{y}{2(\nu t)^{1/2}}\right)$$

where u is the fluid velocity in the direction parallel to the wall and y is the distance measured away from the wall. Show that the knee in the above velocity profile resides at $y/2(\nu t)^{1/2} \sim 1$.

6.6. Verify that the local Reynolds number of a stream VD/ν is of order 10^2 during transition, that is, when the buckling frequency number N_B is of order 1. [*Hint:* Use eqs. (6.11)–(6.14).]

6.7. Determine the range of disturbance wavelengths for which the following inviscid flows are unstable:

(a) Shear flow: $U = U_0$ for $y > h$

$U = U_0 y/h$ for $h > y > -h$

$U = -U_0$ for $-h > y$

(b) Wall jet [60]: $U = 0$ for $y > D$

$U = U_0 \left(2 - \dfrac{y}{D/2}\right)$ for $D > y > D/2$

$U = U_0 \dfrac{y}{D/2}$ for $\dfrac{D}{2} > y > 0$

In each case, verify that the neutral wavelength scales with the transversal length scale of the flow. [*Hint:* Follow the analytical course traced between eqs. (6.22) and (6.30).]

6.8. A two-dimensional jet discharges freely into a reservoir that contains the same fluid as the jet. The jet nozzle is a two-dimensional slit of gap D_0. The Reynolds number based on nozzle size (D_0) and mean velocity through the nozzle (U_0) is $Re_0 = 1$. Consulting Table 6.1 and the scaling laws of transition discussed in this chapter, decide whether the jet is laminar over its entire length, or turbulent, or something else (review the scaling laws revealed by the solution to Problem 2.22).

6.9. One of the most fundamental problems of convection in lubrication by sliding contact is the ''lid-driven cavity'' problem (see Fig. P6.9). A groove with square cross section of side D is machined into one of the solid parts and is filled with a fluid of kinematic viscosity ν. The other solid part slides over the top of the square cavity with the velocity U and drives a clockwise circulation of fluid inside the cavity. Predict the value of the cavity Reynolds number ($Re_D = UD/\nu \sim 400$) that marks the transition between laminar flow and turbulent flow. Rely on the local Reynolds number criterion (6.15) and the thickness of the laminar boundary layer that lines the sliding wall.
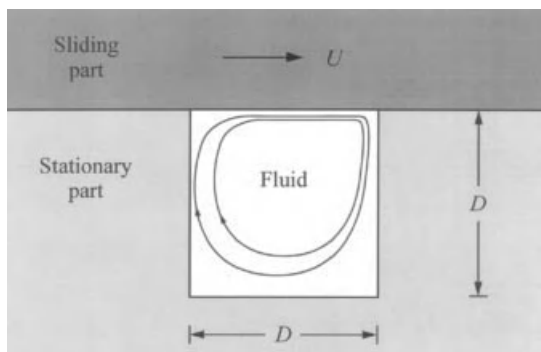

Figure P6.9

<div align="right">

7

</div>

TURBULENT BOUNDARY LAYER FLOW

7.1 LARGE-SCALE STRUCTURE

Looking back at the ground covered so far, we formulated the fundamental principles that govern all convection phenomena (Chapter 1) and then used these principles to predict friction and heat transfer in laminar flow (Chapters 2–5). The limitations of the laminar flow description formed the subject of Chapter 6, in which we relied on the constructal law to predict the transition to turbulent flow. It is natural to continue here with momentum and heat transfer in turbulent flow.

The objective of the present treatment is to review the basic ideas behind the contemporary treatment of turbulent heat transfer. This objective is both interesting and feasible because most of the turbulent heat transfer language in use today was coined almost a century ago by Reynolds, Boussinesq, and Prandtl, and because during all this time, relatively little has been done to question the ideas that produced this language.

It goes without saying that a turbulent flow is complicated,* as witnessed by the irregularity in the electrical output from velocity and temperature probes inserted in the flow. It is not difficult to relate this irregularity to the *eddy* motion exhibited so clearly by many flows that surround us (cumulus clouds, muddy rivers, or the post-transition upper section of the cigarette-smoke plume of Fig. 6.1). Thus, there is a great temptation to define turbulence as an irregular and random fluid motion, but to do this would mean disregarding the fact that turbulent flows possess *orderly structure* [1, 2]. For this reason, we

---

*After all, this is why this type of flow was even named *turbulent* (note the original Latin meaning of this terminology: the words *turba, turbidus, turbulentus*, etc., were used to describe tumult, uproar, commotion in a crowd of people, confusion, the mentally deranged, muddy waters).

Figure 7.1   Turbulent boundary layer in boiling water flowing from left to right over a flat surface; $U_\infty = 0.52$ m/s, $q_0'' = 4.8 \times 10^5$ W/m^2. (Reprinted with permission from J. H. Lienhard, *A Heat Transfer Textbook*, 1981, p. 417. Copyright © 1981 Prentice-Hall, Inc.)

begin with Figs. 7.1 and 7.2, which show two strikingly similar turbulent flows photographed under strikingly different circumstances by two strikingly different people.

Figure 7.1 shows the turbulent boundary layer downstream from the leading edge of a flat plate; the flow is visualized by boiling, that is, by the entrainment of vapor bubbles formed near the solid surface. Figure 7.2 offers a glimpse of the turbulent boundary layer over the surface of the South Atlantic; the visualization in this case is made possible by flames (fed by an oil slick) and thick black smoke. Of course, one may argue that in both photographs, the flow visualization agents are buoyant and interfere with the actual boundary layer flow. This
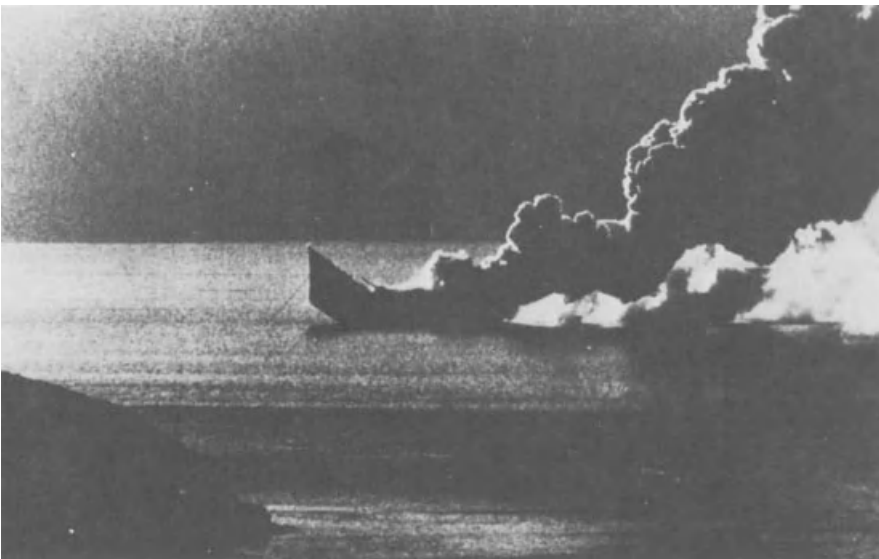

Figure 7.2   Smoke showing the large-sale structure of the turbulent boundary layer over the South Atlantic. (From Wide World Photos.)

interpretation is correct only for regions situated sufficiently far downstream, where buoyancy has had enough time to accelerate the marked fluid to a vertical velocity comparable with the horizontal velocity of unmarked fluid.

The visualization method is closest to revealing the truth near the leading edge of each flow. It is near the leading edge that both flows exhibit the same *large-scale structure*. Note the sharpness of the interface between boundary layer and free stream, and note the waviness of this interface. Large eddies protrude through the interface, and their diameters appear to scale with both the local thickness of the boundary layer and the local distance between two consecutive large eddies. This scaling is consistent with the $\lambda_B/D = $ constant scaling law recommended by the buckling theory of inviscid flow in Chapter 6. In fact, the theoretical λ_B/D can be used to predict that the angle between the wavy interface and the solid surface is roughly $20°$ [3], which is the angle visible in Figs. 7.1 and 7.2. We return to this theoretical prediction in Fig. 9.9.

In this chapter we focus on the mechanism by which turbulent flows transport energy between a stream and a solid wall. The presentation is constructed along the same lines as classical turbulent heat transfer methodology, which is based on the time-averaged description of the convection phenomenon and must rely heavily on empirical information in order to solve the *closure problem* (i.e., the fact that the time-averaged governing equations are fewer than the number of unknowns). However, wherever possible, we shall invoke the constructal law [4, 5] to minimize the empirical content of the time-averaged analysis.

7.2   TIME-AVERAGED EQUATIONS

It has been impossible to determine the turbulent flow solution at any point in space and time by applying the mass, momentum, and energy conservation equations in the form reported in Chapter 1. Mathematically, it has been difficult enough to determine the smooth and time-independent velocity and temperature profiles of simple laminar flows (Chapters 2–5); imagine, then, trying to determine analytically a turbulent profile, for example, the longitudinal velocity profile in turbulent boundary layer flow (when visualized, this wiggly profile fluctuates in time in much the same way as an electric arc).

Confronted with this difficulty, Reynolds [6] thought that some of the complications of instantaneous turbulent flow could be removed if one considers not the instantaneous behavior, but the mean behavior averaged over a long enough period. In terms of mean velocities, pressure, and temperature, the time-averaged flow field is a simpler one, a field without fluctuations (eddies).

The time-averaged flow behavior is not a simpler *flow* (because only the real turbulent flow exists); rather, it is a simpler *way to think* about turbulent flows. Unfortunately, this is also an effective method of simplifying the reader's mind, inviting it to see smoothness in turbulence rather than coarseness, orderly structure, and ''design.''

The derivation of the conservation laws for time-averaged flow begins with the transformation

$$u = \bar{u} + u', \qquad P = \bar{P} + P'$$
$$v = \bar{v} + v', \qquad T = \bar{T} + T' \tag{7.1}$$
$$w = \bar{w} + w'$$

where the quantities denoted with an overbar $(\bar{\cdot})$ represent the mean values obtained by time averaging over a long enough period,

$$\bar{u} = \frac{1}{\text{period}} \int_0^{\text{period}} u \, d(\text{time}) \tag{7.2}$$

Combining eqs. (7.1) and (7.2), we recognize that, by definition, the fluctuating components denoted with a prime $(\cdot)'$ average to zero over time,

$$\int_0^{\text{period}} u' \, d(\text{time}) = 0 \tag{7.3}$$

Definitions (7.2) and (7.3) are the foundation of a special kind of algebra that emerges in the process of substituting the $(\bar{\cdot}) + (\cdot)'$ decomposition (7.1) into the mass, momentum, and energy equations and then time averaging these equations according to definition (7.2). The rules (theorems) of this algebra are

$$\overline{u + v} = \bar{u} + \bar{v} \tag{7.4}$$

$$\overline{\bar{u}u'} = 0 \tag{7.5}$$

$$\overline{uv} = \bar{u}\bar{v} + \overline{u'v'} \tag{7.6}$$

$$\overline{u^2} = \bar{u}^2 + \overline{u'^2} \tag{7.7}$$

$$\overline{\frac{\partial u}{\partial x}} = \frac{\partial \bar{u}}{\partial x} \tag{7.8}$$

$$\frac{\partial \bar{u}}{\partial t} = 0 \tag{7.9}$$

$$\overline{\frac{\partial u}{\partial t}} = 0 \tag{7.10}$$

Consider first the transformation of the mass conservation equation (1.8),

$$\frac{\partial \bar{u}}{\partial x} + \frac{\partial u'}{\partial x} + \frac{\partial \bar{v}}{\partial y} + \frac{\partial v'}{\partial y} + \frac{\partial \bar{w}}{\partial z} + \frac{\partial w'}{\partial z} = 0 \tag{7.11}$$

Integrating this equation term by term over time and applying rules (7.3) and (7.8) yields

$$\frac{\partial \bar{u}}{\partial x} + \frac{\partial \bar{v}}{\partial y} + \frac{\partial \bar{w}}{\partial z} = 0 \tag{7.12}$$

which is analytically identical to the original equation [eq. (1.8)]. Equation (7.12) represents the condition for conservation of mass in time-averaged flow.

Consider next the x momentum equation listed as eq. (1.19a); this equation may be rewritten as

$$\frac{\partial u}{\partial t} + \frac{\partial}{\partial x}(u^2) + \frac{\partial}{\partial y}(uv) + \frac{\partial}{\partial z}(uw) = -\frac{1}{\rho}\frac{\partial P}{\partial x} + \nu \nabla^2 u \tag{7.13}$$

Averaging each term over time and applying rules (7.8)–(7.10) yields

$$\frac{\partial}{\partial x}(\overline{u^2}) + \frac{\partial}{\partial y}(\overline{uv}) + \frac{\partial}{\partial z}(\overline{uw}) = -\frac{1}{\rho}\frac{\partial \overline{P}}{\partial x} + \nu \nabla^2 \bar{u} \tag{7.14}$$

Now applying the product averaging rules (7.6) and (7.7), we obtain

$$\frac{\partial}{\partial x}(\overline{u}^2) + \frac{\partial}{\partial y}(\bar{u}\bar{v}) + \frac{\partial}{\partial z}(\bar{u}\bar{w})$$

$$= -\frac{1}{\rho}\frac{\partial \overline{P}}{\partial x} + \nu \nabla^2 \bar{u} - \frac{\partial}{\partial x}(\overline{u'^2}) - \frac{\partial}{\partial y}(\overline{u'v'}) - \frac{\partial}{\partial z}(\overline{u'w'}) \tag{7.15}$$

Making use of the mass continuity equation (7.12), the left-hand side of eq. (7.15) can be simplified to read

$$\bar{u}\frac{\partial \bar{u}}{\partial x} + \bar{v}\frac{\partial \bar{u}}{\partial y} + \bar{w}\frac{\partial \bar{u}}{\partial z} = -\frac{1}{\rho}\frac{\partial \overline{P}}{\partial x} + \nu \nabla^2 \bar{u} - \frac{\partial}{\partial x}(\overline{u'^2})$$

$$-\frac{\partial}{\partial y}(\overline{u'v'}) - \frac{\partial}{\partial z}(\overline{u'w'}) \tag{7.16a}$$

The corresponding time-averaged forms of the momentum equations in the y and z directions are

$$\bar{u}\frac{\partial \bar{v}}{\partial x} + \bar{v}\frac{\partial \bar{v}}{\partial y} + \bar{w}\frac{\partial \bar{v}}{\partial z} = -\frac{1}{\rho}\frac{\partial \overline{P}}{\partial y} + \nu \nabla^2 \bar{v} - \frac{\partial}{\partial x}(\overline{u'v'})$$

$$-\frac{\partial}{\partial y}(\overline{v'^2}) - \frac{\partial}{\partial z}(\overline{v'w'}) \tag{7.16b}$$

$$\bar{u}\frac{\partial \bar{w}}{\partial x} + \bar{v}\frac{\partial \bar{w}}{\partial y} + \bar{w}\frac{\partial \bar{w}}{\partial z} = -\frac{1}{\rho}\frac{\partial \overline{P}}{\partial z} + \nu \nabla^2 \bar{w} - \frac{\partial}{\partial x}(\overline{u'w'})$$

$$-\frac{\partial}{\partial y}(\overline{v'w'}) - \frac{\partial}{\partial z}(\overline{w'^2}) \tag{7.16c}$$

Finally, the energy equation expressed as eq. (1.42) yields, after a similar time-averaging procedure,

$$\bar{u}\frac{\partial\overline{T}}{\partial x} + \bar{v}\frac{\partial\overline{T}}{\partial y} + \bar{w}\frac{\partial\overline{T}}{\partial z} = \alpha\,\nabla^2\overline{T} - \frac{\partial}{\partial x}\,(\overline{u'T'}) - \frac{\partial}{\partial y}\,(\overline{v'T'}) - \frac{\partial}{\partial z}\,(\overline{w'T'}) \quad (7.17)$$

The derivation of eq. (7.17) follows in the steps contained between eqs. (7.13) and (7.16a) in the derivation of the time-averaged x momentum equation.

To summarize, the time-averaged conservation laws for constant-property flow are represented by eqs. (7.12), (7.16a-c), and (7.17). These are five equations for 17 unknowns [the unknowns are $\bar{u}$, $\bar{v}$, $\bar{w}$, $\overline{P}$, $\overline{T}$, and the 12 terms of type $\partial\,(\overline{u'v'})/\partial y$ appearing in eqs. (7.16a-c) and (7.17)]: hence, the *closure problem*. The difference between the number of equations and the number of unknowns has its origin in the original transformation [eqs. (7.1)], which doubled the number of unknowns; the final number of unknowns ballooned to 17 due to the various product combinations of fluctuating quantities that survive the time-averaging process. Fortunately, the gap between equations and unknowns is not nearly as menacing if we consider especially simple flow configurations such as boundary layers and fully developed flows through straight ducts.

7.3   BOUNDARY LAYER EQUATIONS

Consider turbulent flow near a wall parallel to a free stream U_∞, T_∞ oriented in the positive x direction, as in Fig. 2.1 Although the actual turbulent flow is *three-dimensional* regardless of how simple the flow boundaries, from symmetry, the terms representing the $\partial/\partial z$ derivative of time-averaged quantities in eqs. (7.16a) and (7.17) must vanish. Furthermore, if we think of u' and v' as the velocity fluctuations caused by an eddy (a rotating fluid blob; a wheel) as it rides along with the mean flow, then u' and v' are of comparable orders of magnitude. This means that in the boundary layer, we can neglect $(\partial/\partial x)(\overline{u'^2})$ relative to $(\partial/\partial y)(\overline{u'v'})$ in eq. (7.16a), and $(\partial/\partial x)(\overline{u'T'})$ relative to $(\partial/\partial y)(\overline{v'T'})$ in eq. (7.17). Applying the other simplifications that result from boundary layer theory (Chapter 2), the x momentum and energy equations reduce to

$$\bar{u}\frac{\partial\bar{u}}{\partial x} + \bar{v}\frac{\partial\bar{u}}{\partial y} = -\frac{1}{\rho}\frac{d\overline{P}}{dx} + \nu\frac{\partial^2\bar{u}}{\partial y^2} - \frac{\partial}{\partial y}\,(\overline{u'v'}) \quad (7.18)$$

$$\bar{u}\frac{\partial\overline{T}}{\partial x} + \bar{v}\frac{\partial\overline{T}}{\partial y} = \alpha\frac{\partial^2\overline{T}}{\partial y^2} - \frac{\partial}{\partial y}\,(\overline{v'T'}) \quad (7.19)$$

Note that the use of $d\overline{P}/dx$ instead of $\partial\overline{P}/\partial x$ in eq. (7.18) is the result of having taken into account the boundary layer momentum equation in the y direction (which says that $\overline{P}$ in the boundary layer is a function of x only; see

Chapter 2). Equations (7.18) and (7.19), in conjunction with the two-dimensional mass continuity equation

$$\frac{\partial \bar{u}}{\partial x} + \frac{\partial \bar{v}}{\partial y} = 0 \tag{7.20}$$

represent the time-averaged conservation laws inside the boundary layer region. These equations look very much like their counterparts in laminar flow [eqs. (2.26), (2.27), and (2.7)] with one important difference: the $(\partial/\partial y)\overline{(u'v')}$ and $(\partial/\partial y)\overline{(v'T')}$ terms appearing in eqs. (7.18) and (7.19). These terms represent two additional unknowns and account for the closure problem in the two-dimensional boundary layer geometry.

It is instructive to rewrite eqs. (7.18) and (7.19) as

$$\bar{u}\frac{\partial \bar{u}}{\partial x} + \bar{v}\frac{\partial \bar{u}}{\partial y} = -\frac{1}{\rho}\frac{d\bar{P}}{dx} + \frac{1}{\rho}\frac{\partial}{\partial y}\left(\mu\frac{\partial \bar{u}}{\partial y} - \rho\overline{u'v'}\right) \tag{7.21}$$

$$\bar{u}\frac{\partial \bar{T}}{\partial x} + \bar{v}\frac{\partial \bar{T}}{\partial y} = \frac{1}{\rho c_P}\frac{\partial}{\partial y}\left(k\frac{\partial \bar{T}}{\partial y} - \rho c_P\overline{v'T'}\right) \tag{7.22}$$

and to ask this question: If the products $\overline{u'v'}$ and $\overline{v'T'}$ survive the time-averaging process, that is, if they are nonzero, are they negative or positive? The answer is visible in Fig. 7.3, which shows two possibilities in the evolution of the instantaneous u velocity at some point N in the boundary layer. Figure 7.3a presumes the existence of an eddy that causes a downward velocity fluctuation through point N, $v' < 0$; if the instantaneous u profile is such that the fluid moves faster if situated farther from the wall, the short-time effect of $v' < 0$ is to increase the longitudinal velocity at point N, in other words, to induce a positive fluctuation $u' > 0$.

The reverse of this scenario is illustrated in Fig. 7.3b, and what is most interesting, the product $u'v'$ emerges as a negative quantity regardless of the sign of u' and v'. Based on this argument (which applies unchanged to figuring out the sign of $v'T'$), we expect that the time-averaged products $\overline{u'v'}$ and $\overline{v'T'}$ are negative. Since the size of the u' and T' fluctuations with which the flow responds to the postulated v' depends on the steepness of the average $\bar{u}$ and $\bar{T}$ profiles (Fig. 7.3), it makes sense to introduce the notation [7]

$$-\rho\overline{u'v'} = \rho\epsilon_M\frac{\partial \bar{u}}{\partial y} \qquad \text{eddy shear stress}$$

$$-\rho c_P\overline{v'T'} = \rho c_P\epsilon_H\frac{\partial \bar{T}}{\partial y} \qquad \text{eddy heat flux} \tag{7.23}$$

That $-\rho\overline{u'v'}$ and $-\rho c_P\overline{v'T'}$ represent shear stress and heat flux can be seen from the last terms of eqs. (7.21) and (7.22): For example, in the momentum equation (7.21), the molecular diffusion shear stress $\mu(\partial \bar{u}/\partial y)$ is augmented by
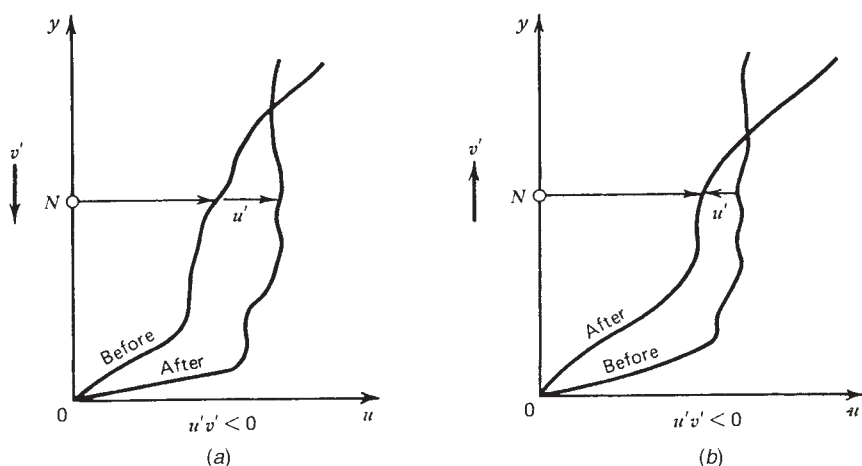
Figure 7.3   Behavior of the instantaneous longitudinal velocity profile, showing how the product $u'v'$ survives the time averaging of the x momentum equation.

the time-averaged eddy shear stress $(-\rho\overline{u'v'})$. Comparing the momentum and energy equations for turbulent boundary layer flow [eqs. (7.21) and (7.22)] with the laminar boundary layer equations (2.26) and (2.27), we see that the role played by shear stress and heat flux in turbulent flow is played by augmented expressions*

$$\tau_{\text{app}} = \mu\frac{\partial\overline{u}}{\partial y} - \rho\overline{u'v'} = \rho(\nu + \epsilon_M)\frac{\partial\overline{u}}{\partial y} \qquad \text{apparent shear stress}$$

$$-q''_{\text{app}} = k\frac{\partial\overline{T}}{\partial y} - \rho c_P\overline{v'T'} = \rho c_P(\alpha + \epsilon_H)\frac{\partial\overline{T}}{\partial y} \qquad \text{apparent heat flux} \qquad (7.24)$$

Substituting the new notation (7.23) into the boundary layer equations (7.21) and (7.22) yields

$$\overline{u}\frac{\partial\overline{u}}{\partial x} + \overline{v}\frac{\partial\overline{u}}{\partial y} = -\frac{1}{\rho}\frac{d\overline{P}}{dx} + \frac{\partial}{\partial y}\left[(\nu + \epsilon_M)\frac{\partial\overline{u}}{\partial y}\right] \qquad (7.25)$$

$$\overline{u}\frac{\partial\overline{T}}{\partial x} + \overline{v}\frac{\partial\overline{T}}{\partial y} = \frac{\partial}{\partial y}\left[(\alpha + \epsilon_H)\frac{\partial\overline{T}}{\partial y}\right] \qquad (7.26)$$

*Note that as in Chapter 2, q'' is defined as positive when heat is transferred from the wall to the fluid.

where ϵ_M and ϵ_H are two empirical functions known as *momentum eddy diffusivity* and *thermal eddy diffusivity*, respectively. Note that ϵ_M and ϵ_H are *flow parameters*, not fluid properties. Although eqs. (7.25) and (7.26) look even more like their correspondents in laminar flow, no real improvement has taken place in solving the problem theoretically, that is, without relying on experiment. The problem consists of three equations [eqs. (7.20), (7.25), and (7.26)] outnumbered by five unknowns ($\bar{u}, \bar{v}, \bar{T}, \epsilon_M$, and ϵ_H).

The search for additional information to close the problem is the objective of the activity known as *turbulence modeling*. This empirical activity consists of scrutinizing the available body of experimental data in order to identify possible trends that might lead to generally applicable expressions (models) for ϵ_M and ϵ_H. In the present treatment, we discuss first the simplest and oldest models that lead to concise formulas for wall friction and heat transfer.

7.4 MIXING LENGTH MODEL

The order of magnitude of ϵ_M can be determined based on the following scaling argument due to Prandtl [8]. In the boundary layer of Fig. 7.3, imagine a ball of fluid that at some point in time is situated at a distance y where the mean longitudinal velocity is $\bar{u}(y)$. This ball migrates toward the wall to the new location $y - l$, where the mean velocity is $\bar{u}(y - l)$; the distance l is the *mixing length* along which the ball of fluid *maintains its identity*. Assuming that from (y) to $(y - l)$ the ball does not lose its longitudinal momentum, the u' fluctuation produced by it at the new level $(y - l)$ is on the order of $\bar{u}(y) - \bar{u}(y - l)$; in other words,

$$O(u') = l\frac{\partial \bar{u}}{\partial y} \tag{7.27}$$

As argued earlier, in the motion of an eddy superimposed on the time-averaged motion, v' is of the same order of magnitude as u'; hence,

$$O(v') = l\frac{\partial \bar{u}}{\partial y} \tag{7.28}$$

Recalling the message of Fig. 7.3, namely, the negative sign of $\overline{u'v'}$, we write

$$-\overline{u'v'} = l^2\left(\frac{\partial \bar{u}}{\partial y}\right)^2 \tag{7.29}$$

where l is the length scale associated with travel normal to the wall. Therefore, from the definition of momentum eddy diffusivity [eqs. (7.23)], we conclude

$$\epsilon_M = l^2\left|\frac{\partial \bar{u}}{\partial y}\right| \tag{7.30}$$

There is no general rule for estimating the mixing length l since it varies from one type of flow to another. In a turbulent boundary layer, however, an upper bound for l must be the distance to the wall,

$$l = \kappa y \tag{7.31}$$

where κ is an empirical constant of order $O(1)$. As is shown later, a suitable value for von Kármán's constant κ turns out to be 0.4, thus reconfirming the view that y is an upper bound for the mixing length of individual eddies. Combining eqs. (7.30) and (7.31), we conclude that Prandtl's mixing length model for momentum eddy diffusivity is

$$\epsilon_M = \kappa^2 y^2 \left| \frac{\partial \bar{u}}{\partial y} \right| \tag{7.32}$$

with the value of κ and the goodness of this model to be decided based on experiment.

Using eq. (7.32) or an equivalent model for ϵ_M, the mass and momentum conservation equations (7.20) and (7.25) could be integrated numerically to determine the flow field $\bar{u}$, $\bar{v}$. However, as shown below, some analytical progress can be made based on additional scaling arguments.

7.5 VELOCITY DISTRIBUTION

If we are interested primarily in how the turbulent boundary layer rubs against the wall and how it carries heat away from the wall, we can imagine an *inner region* situated close enough to the wall that the left-hand side of eq. (7.25) is sufficiently small. If the longitudinal pressure gradient dP/dx is zero, as in the case of uniform flow parallel to a flat wall, the inner region is also characterized by an apparent shear stress $(\nu + \epsilon_M)(\partial \bar{u}/\partial y)$ that does not vary with y [see eq. (7.25)]. Therefore, we can write after Prandtl [9]

$$(\nu + \epsilon_M)\frac{\partial \bar{u}}{\partial y} = \frac{\tau_0}{\rho} \tag{7.33}$$

in which τ_0 is the actual wall shear stress, that is, the value of τ_{app} at $y = 0$ where the Reynolds stress $-\rho\overline{u'v'}$ vanishes. Keep in mind that τ_0 is the objective of the entire analysis; however, since the dimensions of $(\tau_0/\rho)^{1/2}$ are those of velocity, the group $(\tau_0/\rho)^{1/2}$ is recognized in the turbulence literature as the *friction velocity**

$$u_* = \left(\frac{\tau_0}{\rho} \right)^{1/2} \tag{7.34}$$

---

*The fact that u_* has the dimensions m/s does not mean that u_* is the appropriate scale of $\bar{u}$ in the boundary layer (the appropriate scale of $\bar{u}$ is U_∞). That the friction velocity is not the appropriate velocity scale is illustrated by the numerical values of u^+, which are very much different from $O(1)$ (see Fig. 7.4).

and is used in the *wall coordinate* nondimensionalization of the flow problem,

$$u^+ = \frac{\overline{u}}{u_*}, \qquad v^+ = \frac{\overline{v}}{u_*}$$

$$x^+ = \frac{xu_*}{\nu}, \qquad y^+ = \frac{yu_*}{\nu} \tag{7.35}$$

The constant τ_{app} assumption (7.33) becomes

$$\left(1 + \frac{\epsilon_M}{\nu}\right) \frac{du^+}{dy^+} = 1 \tag{7.36}$$

where it should be noted that u^+ is a function of y^+ only (hence, the d/dy^+ derivative sign) and that the x dependence is accounted for in the friction velocity u_* used in definitions (7.35).

The velocity distribution near the wall $u^+(y^+)$ results from integrating eq. (7.36) in conjunction with a suitable ϵ_M model such as eq. (7.32). The integration is considerably simpler and more instructive if we recognize that the $u^+(y^+)$ function produced by eq. (7.36) must have two distinct limiting behaviors, depending on the relative size of ϵ_M and ν. That the ratio ϵ_M/ν must vary with the distance measured away from the wall is argued by the mixing length model outlined in Section 7.4. In the inner layer defined by the constant τ_{app} assumption (7.33), we can visualize two *sublayers*:

1. The *viscous sublayer* (VSL), where $\nu \gg \epsilon_M$
2. The *fully turbulent sublayer* (or the *turbulent core*), where $\epsilon_M \gg \nu$

These two sublayers mesh at some value of y^+, say, y^+_{VSL}, where ν and ϵ_M are of the same order of magnitude. Neglecting the term ϵ_M/ν in eq. (7.36) and integrating from the wall condition $u^+(0) = 0$, we find that in the viscous sublayer the velocity profile is linear,

$$u^+ = y^+ \tag{7.37}$$

In the fully turbulent sublayer, the eddy diffusivity dominates, and eq. (7.36) reduces to

$$\frac{\epsilon_M}{\nu} \frac{du^+}{dy^+} = 1 \tag{7.38}$$

or, using Prandtl's mixing length model (7.32),

$$\kappa^2 (y^+)^2 \left(\frac{du^+}{dy^+}\right)^2 = 1 \tag{7.39}$$

Integrating this equation from the sublayer interface y^+_{VSL} [where, according to eq. (7.37), $u^+ = y^+_{VSL}$] to any y^+ in the fully turbulent sublayer yields

$$u^+ = \frac{1}{\kappa} \ln y^+ + y^+_{VSL} - \frac{1}{\kappa} \ln y^+_{VSL} \tag{7.40}$$

In other words,

$$u^+ = A \ln y^+ + B \tag{7.41}$$

where A and B are two empirical constants. Equation (7.41) is referred to as the *law of the wall* and is attributed to both Prandtl and Taylor [10]. Fitting the logarithmic expression (7.41) to experimental measurements, it is found that the constants are approximately

$$A \cong 2.5 \quad \text{and} \quad B \cong 5.5 \tag{7.42}$$

By examining eq. (7.40), note that A and B are equivalent to

$$\kappa \cong 0.4 \quad \text{and} \quad y^+_{VSL} \cong 11.6 \tag{7.43}$$

Equations (7.37) and (7.41) are one way (perhaps, the simplest) to empirically fit the $u^+(y^+)$ measurements that pertain to the inner region. The success of fitting the data with the law of the wall (7.41) (see Fig. 8 in Ref. 10) demonstrates the goodness of Prandtl's constant τ_{app} assumption (7.33) and mixing length model (7.32). In fact, experimental measurements indicate that the law of the wall holds even in situations with finite pressure gradient [note the dP/dx assumption that preceded eq. (7.33)].

As expected, eqs. (7.37) and (7.41) fail to agree with experiment in the vicinity of $y^+ = y^+_{VSL}$, where neither ν nor ϵ_M can be neglected (see Fig. 7.4). A number of improved models have been proposed to smooth out the transition between the two limiting behaviors; these have been reviewed in Ref. 10 and are summarized in Table 7.1. It is not difficult to verify that the analytical expressions for $u^+(y^+)$ listed in Table 7.1 fall in the area covered by experimental measurements in the Purtell et al. [11] data reproduced in Fig. 7.4.

The experimental observation that the transition from the viscous sublayer to the fully turbulent sublayer takes place around $y^+_{VSL} = O(10)$ is an interesting example of the general applicability of the constructal theory of transition advanced in Chapter 6. The nature and very existence of a viscous sublayer free of eddy motion have been the subject of debate because for a long time it was impossible to probe the velocity field so close to the wall. The development of techniques (e.g., laser–Doppler anemometers) has made it possible to observe the evolution of the instantaneous velocity near the wall. The viscous sublayer maintains the same thickness $y^+_{VSL} = O(10)$, regardless of the overall thickness of the boundary layer. As shown in Fig. 7.4, as the overall boundary layer
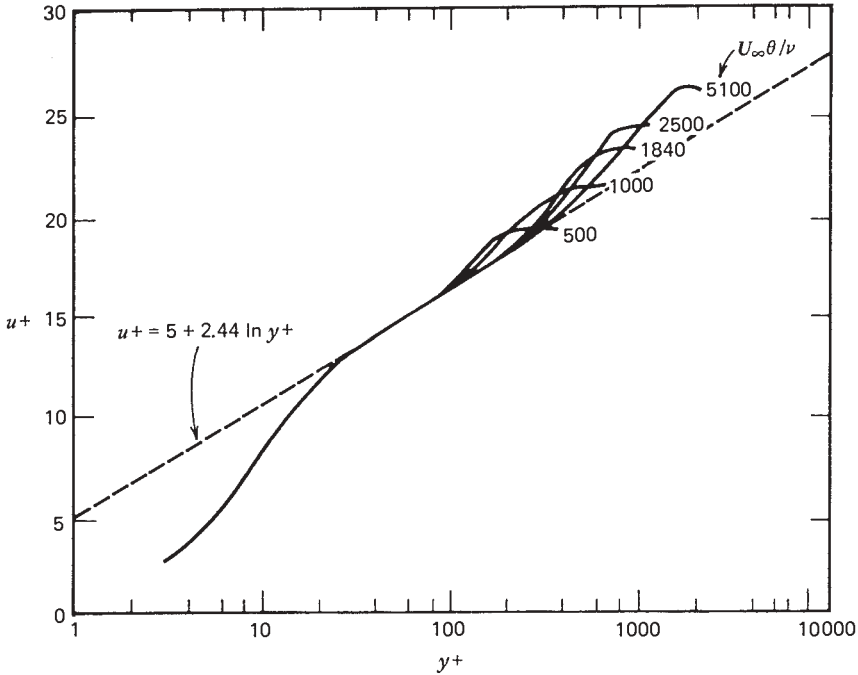
Figure 7.4   Example of $u^+(y^+)$ velocity measurements in turbulent boundary layer flow without longitudinal pressure gradient. Note the use of $A \cong 2.44$ and $B \cong 5$ to fit the data. (Reprinted with permission from L. P. Purtell et al., *Physics of Fluids*, Vol. 24, pp. 802–811, May 1981. Copyright © 1981 American Institute of Physics.)

thickness increases, the viscous sublayer occupies a smaller fraction of the boundary layer.

To predict the viscous sublayer based on the theory of Chapter 6, consider one event that repeats itself many times near the solid wall. Imagine the high-momentum fluid ball envisioned in the mixing length argument that led to eq. (7.32). When this fluid packet slams into the wall, due to its high longitudinal momentum, it gives birth to a sheer layer adjacent to the wall (Fig. 7.5). Initially, the shear layer will be *laminar* because it is very thin and its transversal viscous communication time is very short. The laminar shear layer grows until the local Reynolds number based on local thickness becomes of order 10^2, of. eq. (6.15),

$$\frac{y_{\text{VSL}} U_\infty}{\nu} \sim 10^2 \tag{7.44}$$

The velocity scale outside the laminar shear layer is U_∞, which is a reasonable upper bound for the longitudinal velocity of the fluid ball that ran into the wall. Under the same conditions, the wall shear stress scales as $\mu U_\infty / y_{\text{VSL}}$. The scale

Table 7.1 Summary of longitudinal velocity expressions for the inner region of a turbulent boundary layer

$u^+(y^+)$	Range	Reference
$u^+ = y^+$	$0 < y^+ < 11.6$	Prandtl and
$u^+ = 2.5 \ln y^+ + 5.5$	$y^+ > 11.6$	Taylor [9]
$u^+ = y^+$	$0 < y^+ < 5$	von Kármán [12]
$u^+ = 5 \ln y^+ - 3.05$	$5 < y^+ < 30$	
$u^+ = 2.5 \ln y^+ + 5.5$	$y^+ > 30$	
$u^+ = 14.53 \tanh(y^+/14.53)$	$0 < y^+ < 27.5$	Rannie [13]
$u^+ = 2.5 \ln y^+ + 5.5$	$y^+ > 27.5$	
$\dfrac{du^+}{dy^+} = \dfrac{2}{1 + \{1 + 4\kappa^2 y^{+2}[1 - \exp(-y^+/A^+)]^2\}^{1/2}}$	All y^+	van Driest [14]
$\kappa = 0.4 \qquad A^+ = 26$		
$u^+ = 2.5 \ln(1 + 0.4y^+)$	All y^+	Reichardt [15]
$\quad + 7.8[1 - \exp(-y^+/11)$		
$\quad - (y^+/11)\ \exp(-0.33y^+)]$		
$\dfrac{du^+}{dy^+} = \dfrac{1}{1 + n^2 u^+ y^+[1 - \exp(-n^2 u^+ y^+)]}$	$0 < y^+ < 26$	Deissler [16]
$\quad n = 0.124$		
$\quad u^+ = 2.78 \ln y^+ + 3.8$		
$y^+ = u^+ + A[\exp Bu^+ - 1 - Bu^+ - \dfrac{1}{2}(Bu^+)^2$		
$\quad - \dfrac{1}{6}(Bu^+)^3 - \dfrac{1}{24}(Bu^+)^4]$	All y^+ $A = 0.1108$	Spalding [17]
(last term in u^{+4} may be omitted)	$B = 0.4$	

Source: After Ref. 10.

of y_{VSL}^+ at transition can be calculated from eq. (7.35),

$$y_{VSL}^+ = \frac{y_{VSL}}{\nu}\left(\frac{\tau_0}{\rho}\right)^{1/2} = \left(\frac{y_{VSL}U_\infty}{\nu}\right)^{1/2} \tag{7.45}$$

or using the transition criterion (7.44),

$$y_{VSL}^+ \sim 10 \tag{7.46}$$

Since $O(10)$ is the measured scale of y_{VSL}^+, the derivation of eq. (7.46) implies that the time-averaged viscous sublayer is the superposition of many laminar shear layers terminated by buckling when $N_B = O(1)$ [3].
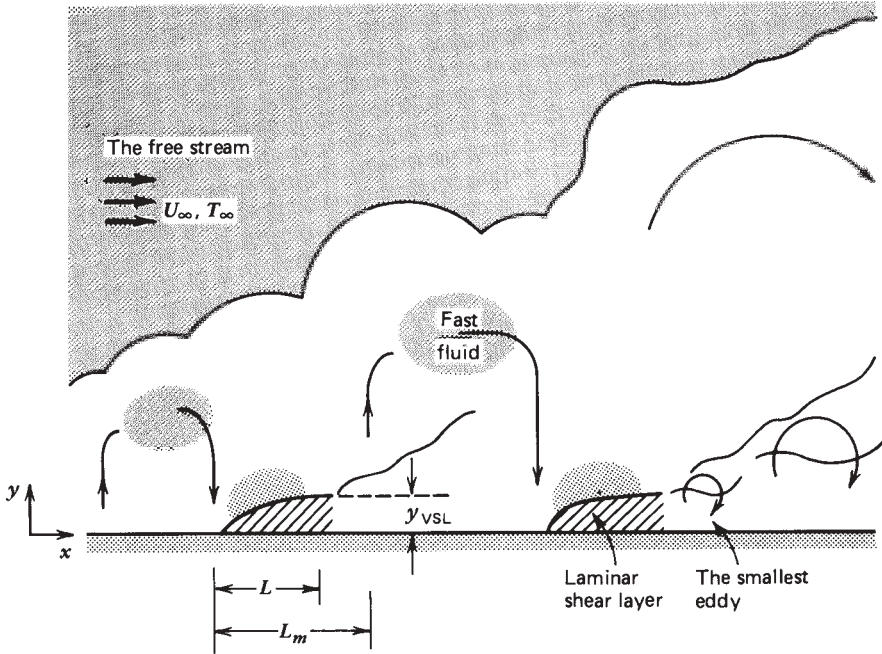
Figure 7.5 Formation of the viscous sublayer as the time-averaged superposition of laminar shear layers with *local Reynolds numbers* no greater than ~10^2.

In conclusion, the constructal law of Chapter 6 provides a purely theoretical basis for the existence of a viscous sublayer and for predicting the thickness of such a sublayer. It also provides a means for estimating the B constant in eq. (7.41) *without* relying on experiment [note the definition of B in terms of y_{VSL}^+ and κ in eq. (7.40)].

An important implication of the $y_{VSL}^+ \sim 10$ theory presented above is that the *first eddy* that forms immediately after the laminar shear layer reaches a local Reynolds number value of order 10^2 is also characterized by a local Reynolds number of order 10^2. According to the scenario sketched in Fig. 7.5, the first eddy is also the smallest eddy in the eddy population resulting from the repeated buckling and rolling-up of the shear layer. Thus, the smallest eddy Reynolds number (based on peripheral velocity and eddy diameter) is of order 10^2 [3]; this conclusion contradicts the often-quoted statement that the small-scale eddy motion is characterized by a Reynolds number equal to 1.

Why does the mixing-length-generated velocity profile (7.41) depend on *two* empirical constants (A and B, or κ and y_{VSL}^+) when, in fact, the mixing length model (7.32) introduces only one such constant (κ)? It is always important, I believe, to question the origin of empirical constants in any analysis. To find the answer to this question, let us derive the $u^+(y^+)$ profile as if we were unaware of the derivation taught in eqs. (7.37)–(7.41). Combining the

mixing length model (7.32) with the near-wall momentum equation (7.36) yields

$$\left[1 + \kappa^2 (y^+)^2 \frac{du^+}{dy^+}\right] \frac{du^+}{dy^+} = 1 \tag{7.47}$$

Note that this equation was integrated earlier in two extremes, each time by neglecting one of the terms appearing in brackets. But since this time we are "unbiased," we proceed with eq. (7.47) alone and find that it can be integrated in closed form. Integrating away from the wall, where the boundary condition is $u^+(0) = 0$, we obtain

$$\kappa u^+ = \frac{\cos \alpha - 1}{\sin \alpha} + \ln \left[\tan \left(\frac{\pi}{4} + \frac{\alpha}{2}\right)\right] \tag{7.48}$$

where

$$\alpha = \arctan(2\kappa y^+) \tag{7.49}$$

The reader can easily verify that regardless of the value of κ, the solution above is not a good curve fit for the data presented in Fig. 7.4. For example, in the two limits discussed earlier in this section, the κ-dependent solution (7.48) and (7.49) yields

$$u^+ \to y^+ \quad \text{as} \quad y^+ \to 0$$

$$u^+ \to \frac{1}{\kappa} \ln y^+ + \frac{2 \ln 2 + \ln \kappa - 1}{\kappa} \quad \text{as} \quad y^+ \to \infty \tag{7.50}$$

Furthermore, if $\kappa \cong 0.4$, the law of the wall recommended by this solution is

$$u^+ = 2.5 \ \ln \ y^+ - 1.325 \tag{7.51}$$

Comparing this result with the curve that agrees with the data [eqs. (7.41) and (7.42)], we conclude that the single-constant profile (7.48) fails in the high-y^+ limit. To ensure a reasonable curve fit in the high-y^+ limit is the function of an *additional* constant, B [eq. (7.41)]. The additional constant is the result of a sleight of hand, namely, the breaking up of the integration of eq. (7.47) into cases 1 and 2. The additional constant B represents the newly created degree of freedom associated with joining the two solutions at a certain intermediate y^+, which was determined later.

As shown in Fig. 7.4, the two-constant curve fitting of the velocity data works for sufficiently low values of y^+, say $y^+ < 100$. This means that the constant τ_{app} assumption that led to the law of the wall (7.41) breaks down as we leave the wall region. The departure of $u^+(y^+)$ measurement away from the law of the wall is demonstrated by the right side of Fig. 7.4. The turbulent boundary layer region emerges as the sandwiching of two distinct zones: an inner zone*

---

*The inner zone divided earlier into a viscous sublayer and a fully turbulent sublayer, in the discussion immediately preceding eq. (7.37).

where the τ_{app} = constant assumption is fairly good and an outer zone where that assumption fails. Recognizing the logarithmic scale employed on the abscissa of Fig. 7.4, we note that the outer zone is generally much thicker than the constant τ_{app} layer. Furthermore, the thickness of the outer zone increases relative to that of the inner zone as the momentum thickness Reynolds number $U_\infty \theta / \nu$ increases (in other words, the outer zone becomes relatively thicker in the downstream x direction, as θ is expected to increase monotonically in x).

If the outer zone is a region where the τ_{app} = constant assumption fails, then according to the complete momentum boundary layer equation (7.25), the outer zone is ruled by a balance between inertia and changes in τ_{app}. It is shown in Chapter 9 that such a balance is characteristic of all turbulent shear flows in regions situated sufficiently far from solid walls (jets, wakes, plumes). For this reason and due to the similar appearance of turbulent wakes and the outer regions of turbulent boundary layers, the literature refers to the outer region of a boundary layer as *the wake region*. The outer region is visible in Figs. 7.1 and 7.2. Note also the similarity between the large-scale buckling of this region and the meanders displayed by turbulent jets, wakes, and plumes (Chapter 9).

7.6 WALL FRICTION IN BOUNDARY LAYER FLOW

Of interest is the time-averaged friction force exerted by the turbulent boundary layer on the wall. The wall shear stress τ_0 or, in dimensionless form, the local skin friction coefficient

$$C_{f,x} = \frac{\tau_0}{\frac{1}{2}\rho U_\infty^2} \tag{7.52}$$

can be derived from the longitudinal velocity measurements plotted in Fig. 7.4. Recall that τ_0 was used to nondimensionalize the abscissa and the ordinate in Fig. 7.4. Let the function $f_u(y^+)$ be an appropriate curve fit for the velocity data of Fig. 7.4,

$$u^+ \cong f_u(y^+) \tag{7.53}$$

Examples of f_u expressions can be found in the left column of Table 7.1. Now, assuming that f_u fits the measurements sufficiently well near the high-y^+ extremity of the profile (i.e., in the wake region), we can use the curve fit (7.53) to define an outer boundary layer thickness δ such that the time-averaged velocity $\bar{u}$ calculated with eq. (7.53) equals U_∞ when y equals δ. This definition amounts to applying eq. (7.53) at the point of $\bar{u} = U_\infty$ and $y = \delta$:

$$\frac{U_\infty}{(\tau_0/\rho)^{1/2}} \cong f_u\left[\frac{\delta}{\nu}\left(\frac{\tau_0}{\rho}\right)^{1/2}\right] \tag{7.54}$$

Equation (7.54) is the source of a particular formula for τ_0 or $C_{f,x}$, a formula that depends on the particular expression chosen for f_u. However, to derive this

formula, we must determine the outer boundary layer thickness δ. To do this, we first recognize that the thickness δ and its x variation are intimately tied to the behavior of the wake region. In other words, the thickening of the boundary layer must be due to the progressive slowing down of outer layers of the free stream as the flow proceeds in the x direction. To account for this phenomenon, we must consider the complete form of the momentum equation for the boundary layer [eq. (7.25)]. Integrating this equation across the boundary layer and keeping in mind that in the present case $d\overline{P}/dx = 0$ yields

$$\frac{d}{dx}\int_0^\infty \overline{u}(U_\infty - \overline{u})\ dy = \frac{\tau_0}{\rho} \tag{7.55}$$

The derivation of the more general momentum integral, for finite $d\overline{P}/dx$, is the object of Problem 7.6.

Equations (7.54) and (7.55) are sufficient for determining $\delta(x)$ and $\tau_0(x)$. For example, using Prandtl's one-seventh power law as the fit for the $u^+(y^+)$ data,

$$f_u = 8.7(y^+)^{1/7} \tag{7.56}$$

we obtain

$$\frac{\tau_0}{\rho U_\infty^2} = 0.0225\left(\frac{U_\infty\delta}{\nu}\right)^{-1/4} \tag{7.57}$$

$$\frac{\delta}{x} = 0.37\left(\frac{U_\infty x}{\nu}\right)^{-1/5} \tag{7.58}$$

$$\delta = 8\delta^* = \tfrac{72}{7}\ \theta \tag{7.59}$$

Combining eqs. (7.57) and (7.58) yields the local and average skin friction coefficients

$$\frac{\tau_0}{\rho U_\infty^2} = \tfrac{1}{2}C_{f,\,x} = 0.0296\left(\frac{U_\infty x}{\nu}\right)^{-1/5} \tag{7.60}$$

$$\frac{\tau_{0-x}}{\rho U_\infty^2} = \tfrac{1}{2}C_{f,0-x} = 0.037\left(\frac{U_\infty x}{\nu}\right)^{-1/5} \tag{7.60'}$$

Equation (7.60) is shown plotted in Fig. 7.6 next to Schultz-Grunow's empirical correlation [18]

$$C_{f,\,x} = 0.37\left[\log_{10}\left(\frac{U_\infty x}{\nu}\right)\right]^{-2.584} \tag{7.61}$$

The figure shows that the agreement between formula (7.60) and measurements deteriorates above $U_\infty x/\nu$ of order 10^7–10^8. The imperfect character of expression (7.60) can be traced back to the approximate character of the velocity profile
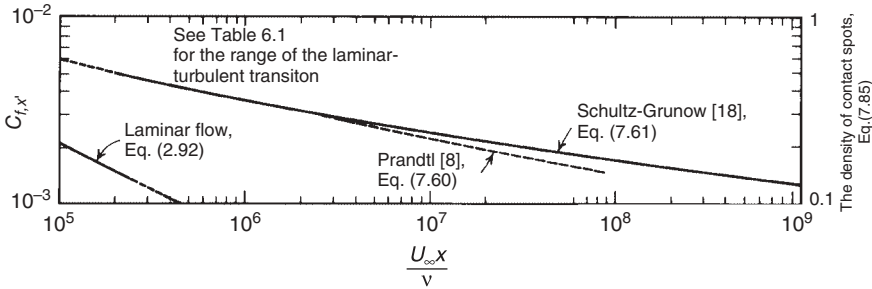
Figure 7.6 Local skin friction coefficient for turbulent boundary layer flow over a plane wall.

curve fit f_u chosen for the analysis that produced eq. (7.60). Other curve fits f_u will lead to friction formulas that differ from eq. (7.60) and to boundary layer thickness formulas that differ from eq. (7.58).

This last observation is particularly relevant to understanding the not-so-fundamental character of the notion that the turbulent boundary layer thickness δ varies as $x^{4/5}$, as might be memorized from eq. (7.58) or Ref. 9. What varies as $x^{4/5}$ is the distance normal to the wall, calculated by intersecting $\bar{u} = U_\infty$ with an *arbitrarily* chosen curve fit of the velocity profile [eq. (7.56)]. The distance defined in such an arbitrary manner is certainly not the distance from the wall to the stepped interface so evident in the turbulent boundary layer photographs shown as Figs. 7.1 and 7.2.

7.7 HEAT TRANSFER IN BOUNDARY LAYER FLOW

For the heat transfer part of the turbulent boundary layer problem, we use the time-averaged energy equation (7.26) and make the assumption that sufficiently close to the solid wall the left-hand side of eq. (7.26) becomes negligible. This move is analogous to the constant τ_{app} assumption made earlier in connection with the velocity profile. The energy equation reduces to the statement that sufficiently close to the wall the apparent heat flux q''_{app} does not depend on y,

$$(\alpha + \epsilon_H)\frac{\partial \overline{T}}{\partial y} = \left[(\alpha + \epsilon_H)\frac{\partial \overline{T}}{\partial y} \right]_{y=0} \tag{7.62}$$

In other words,

$$(\alpha + \epsilon_H)\frac{\partial \overline{T}}{\partial y} = \frac{-q''_0}{\rho c_P} \tag{7.63}$$

As we shall demonstrate shortly, the assumed constancy of q''_{app} leads in relatively few steps to an analytical expression for temperature distribution in the

close vicinity of the wall. Introducing the wall coordinates (7.35), the constant q''_{app} statement (7.63) becomes

$$\frac{\rho c_p u_*}{-q''_0} \frac{\partial}{\partial y^+} (\overline{T} - T_0) = \frac{1}{\alpha/\nu + \epsilon_H/\nu} \tag{7.64}$$

This form is the basis for defining the temperature in wall coordinates:

$$T^+(x^+, \ y^+) = (T_0 - \overline{T})\frac{\rho c_p u_*}{q''_0} \tag{7.65}$$

In this notation, the integral of eq. (7.64) reads

$$T^+ = \int_0^{y^+} \frac{dy^+}{1/\text{Pr} + (1/\text{Pr}_t)(\epsilon_M/\nu)} \tag{7.66}$$

We see that the temperature profile in the $q''_{app} = $ constant region is governed by the Prandtl number, the *turbulent Prandtl number* ($\text{Pr}_t = \epsilon_M/\epsilon_H$), and, via ϵ_M/ν, the velocity distribution in the same region [see eq. (7.36)]. The integral appearing on the right-hand side of eq. (7.66) can be evaluated in closed form based on further assumptions regarding Pr, Pr_t, and ϵ_M/ν. To begin with, we note that in the fully turbulent region of the constant τ_{app} layer, eqs. (7.36) and (7.41) yield

$$\frac{\epsilon_M}{\nu} = \frac{dy^+}{du^+} = \kappa y^+ \tag{7.67}$$

Therefore, according to the mixing length model, the second term in the denominator of the integrand in (7.66) increases steadily as y^+ increases. Considering the range of values taken by y^+ (Fig. 7.4) and assuming that both Pr and Pr_t do not depart too drastically from $O(1)$, chances are good that in the integrand of eq. (7.66), the term $(\epsilon_M/\nu)/\text{Pr}_t$ will outweigh the term $1/\text{Pr}$ if y^+ is sufficiently large. This suggests the two-part integration of (7.66):

$$T^+ = \int_0^{y^+_{\text{CSL}}} \frac{dy^+}{\dfrac{1}{\text{Pr}} + \left(\begin{array}{c}\text{negligible}\\ \text{term}\end{array}\right)} + \int_{y^+_{\text{CSL}}}^{y^+} \frac{dy^+}{\left(\begin{array}{c}\text{negligible}\\ \text{term}\end{array}\right) + \dfrac{1}{\text{Pr}_t} \dfrac{\epsilon_M}{\nu}} \tag{7.68}$$

where y^+_{CSL} is the dimensionless thickness of a *conduction sublayer* (CSL) in which the molecular mechanism outweighs the eddy transport of heat. Combining eqs. (7.68) and (7.67) and regarding Pr_t as y independent, we obtain a broken line expression for the temperature profile

$$T^+ = \begin{cases} \text{Pr } y^+, & y^+ < y^+_{\text{CSL}} \\[2mm] \text{Pr } y^+_{\text{CSL}} + \dfrac{\text{Pr}_t}{\kappa} \ln \dfrac{y^+}{y^+_{\text{CSL}}}, & y^+ > y^+_{\text{CSL}} \end{cases} \tag{7.69}$$

This result depends on three empirical constants, Pr_t, κ, and y_{CSL}^+. Agreement with temperature measurements is achieved if [19]

$$Pr_t \cong 0.9, \qquad \kappa \cong 0.41, \qquad y_{CSL}^+ \cong 13.2 \tag{7.70}$$

provided that the Prandtl number of the fluid is in the range 0.5–5. Substituting these values into the $y^+ > y_{CSL}^+$ portion of the T^+ profile (7.69) yields

$$T^+ = 2.195 \ \ln y^+ + 13.2 Pr - 5.66 \tag{7.71}$$

In the fully turbulent region where q''_{app} is constant, the temperature profile T^+ is analytically the same as the law of the wall [eq. (7.41)].

A wall heat flux formula consistent with the temperature distribution developed above can be derived by assuming that eq. (7.69) holds well enough near the outer edge of the boundary layer (i.e., at the edge of the wake region). This assumption is made for analytical convenience because the wake region is neither one of constant q''_{app} nor one of constant τ_{app}. However, this assumption turns out to be a fairly good one, and the heat transfer coefficient formula facilitated by it turns out to be instructive. Setting $\overline{T} = T_\infty$ at $y = \delta$ in eq. (7.69), we obtain

$$\rho c_P u_* \frac{T_0 - T_\infty}{q''_0} = Pr \ y_{CSL}^+ + \frac{Pr_t}{\kappa} \ln \frac{\delta u_*/\nu}{y_{CSL}^+} \tag{7.72}$$

The heat transfer coefficient $h = q''_0/(T_0 - T_\infty)$ appears explicitly and δ is an unknown. To determine δ, we might be tempted to rely on eq. (7.58), but this would be inappropriate because Prandtl's formula for $\delta(x)$ is based on the one-seventh power law velocity profile, whereas the temperature profile (7.69) is based on the law of the wall. Therefore, to be consistent, we apply the law of the wall (7.41) at the outermost edge of the boundary layer,

$$\frac{U_\infty}{u_*} = \frac{1}{\kappa} \ln \frac{\delta u_*}{\nu} + B \tag{7.73}$$

Eliminating $\delta u_*/\nu$ between eqs. (7.72) and (7.73) and keeping in mind that

$$\frac{U_\infty}{u_*} = \left(\frac{2}{C_{f,x}}\right)^{1/2} \tag{7.74}$$

we obtain the desired heat transfer result,

$$\frac{h}{\rho c_P U_\infty} = \frac{\frac{1}{2}C_{f,x}}{Pr_t + \left(\frac{1}{2}C_{f,x}\right)^{1/2}[Pr \ y_{CSL}^+ - B \ Pr_t - (Pr_t/\kappa) \ln y_{CSL}^+]} \tag{7.75}$$

The left-hand side of this equation is a dimensionless way of expressing the heat transfer coefficient in turbulent flow, namely, the local *Stanton number*:

$$\text{St}_x = \frac{h}{\rho c_P U_\infty} = \frac{\text{Nu}_x}{\text{Pe}_x} = \frac{\text{Nu}_x}{\text{Re}_x \, \text{Pr}} \tag{7.76}$$

The right-hand side of eq. (7.75) can be refined by using appropriate values for the empirical constants; for example, using the constants listed as eq. (7.70) and taking $B \cong 5.1$, the heat transfer rate formula becomes [19]

$$\text{St}_x = \frac{\frac{1}{2}C_{f,x}}{0.9 + \left(\frac{1}{2}C_{f,x}\right)^{1/2}(13.2\text{Pr} - 10.25)} \tag{7.77}$$

This result is worth thinking about before proceeding. Looking at the already weak relationship between $C_{f,x}$ and Re_x displayed by Fig. 7.6, we get the idea that the denominator in expression (7.77) is not very sensitive to changes in the Reynolds number. Also, the Prandtl number Pr was already assumed to be in the range 0.5–5, which means that the denominator is of order $O(1)$ and Pr-dependent. We reach the conclusion that at any x along the wall, the Stanton number and the skin friction coefficient are proportional and of the same order of magnitude and that the proportionality factor is a function of the Prandtl number. Indeed, heat transfer measurements over a wider Pr range ($0.6 < \text{Pr} < 60$) satisfy an *empirical formula* suggested by Colburn [20]:

$$\text{St}_x \, \text{Pr}^{2/3} = \tfrac{1}{2}C_{f,x} \tag{7.78}$$

The analysis outlined here between eqs. (7.63) and (7.77) is a simplified version of what von Kármán obtained based on a smoother, three-region integration of eq. (7.66) [14]. The three y^+ regions are listed in Table 7.1. If $\text{Pr}_t = 1$, the local Stanton number expression produced by this analysis is

$$\text{St}_x = \frac{\frac{1}{2}C_{f,x}}{1 + 5\left(\frac{1}{2}C_{f,x}\right)^{1/2}\left\{\text{Pr} - 1 + \ln\left[1 + \frac{5}{6}(\text{Pr} - 1)\right]\right\}} \tag{7.79}$$

The Colburn analogy (7.78) can be restated in terms of Nu_x and Re_x, in accordance with eqs. (7.60) and (7.76):

$$\text{Nu}_x = \tfrac{1}{2}C_{f,x} \, \text{Re}_x \, \text{Pr}^{1/3}$$

$$= 0.0296 \text{Re}_x^{4/5} \, \text{Pr}^{1/3} \quad (\text{Pr} \gtrsim 0.5) \tag{7.78'}$$

$$\overline{\text{Nu}}_L = 0.037 \text{Re}_L^{4/5} \, \text{Pr}^{1/3} \quad (\text{Pr} \gtrsim 0.5) \tag{7.78''}$$

Although eq. (7.78′) was developed for an isothermal wall, it works satisfactorily when the wall heat flux is uniform. The Nu_x value for a wall with uniform heat

flux is only 4 percent greater than the value furnished by eq. (7.78′). Note further that when the wall heat flux is uniform, the local Nusselt number is defined by $\mathrm{Nu}_x = q_0'' x/k[T_0(x) - T_\infty]$. Regardless of the thermal boundary condition that may exist at the wall, the reference temperature for evaluating the properties in eqs. (7.78) and (7.78′) is the average film temperature $(\overline{T}_0 + T_\infty)/2$, where $\overline{T}_0$ is the x-averaged wall temperature.

7.8   THEORY OF HEAT TRANSFER IN TURBULENT BOUNDARY LAYER FLOW

It is instructive to substitute numerical values for Re_x and Pr into formulas (7.77) and (7.79) to discover that they predict practically the same heat transfer rate as Colburn's empirical correlation (7.78). The success of an extremely compact analytical expression to convey the same message as fancier formulas produced by increasingly fancier analyses suggests that Colburn's formula is the carrier of fundamental information regarding the nature (the physics) of turbulent heat transfer near a solid wall in both boundary layer flow and duct flow. I use this opportunity to present a theory that predicts Colburn's empirical formula (7.78) and its Pr range of validity*.

The Pr = 1 equivalent of Colburn's formula can be derived rather easily based on an argument recognized as the *Reynolds analogy* between heat transfer and wall friction in turbulent flow [21],

$$\mathrm{St}_x = \frac{1}{2}C_{fx} \qquad (\mathrm{Pr} = 1) \tag{7.80}$$

The same result follows from setting Pr = 1 in von Kármán's expression (7.79). To derive the Reynolds analogy from the basic premises of this chapter, recall that the near-wall region is characterized by constant τ_{app} and constant q''_{app},

$$\tau_0 = (\mu + \rho\epsilon_M)\frac{d\overline{u}}{dy} \tag{7.81}$$

$$-q_0'' = (k + \rho c_P \epsilon_H)\frac{d\overline{T}}{dy} \tag{7.82}$$

Setting Pr = 1 and $\epsilon_M = \epsilon_H$ and dividing eqs. (7.81) and (7.82) yields

$$\frac{\tau_0}{-q_0''} = \frac{1}{c_P}\frac{d\overline{u}}{d\overline{T}} \tag{7.83}$$

*Colburn did not offer any theoretical basis for the $\mathrm{Pr}^{2/3}$ factor appearing in eq. (7.78). A number of authors before him proposed similar empirical formulas, with the Pr exponent ranging from 0.6 to 0.7: Colburn chose the $0.66 = \frac{2}{3}$ exponent ''because it is more or less an average value'' [20].

Integrating this from the wall ($\bar{u} = 0$, $\bar{T} = T_0$) all the way to the free stream ($\bar{u} = U_\infty$, $\bar{T} = T_\infty$; note the reality-bending character of this move) leads to

$$\frac{\tau_0}{-q_0''} = \frac{U_\infty}{c_P(T_\infty - T_0)} \tag{7.84}$$

Recalling the definitions of the skin friction coefficient [eq. (7.52)] and the Stanton number [eq. (7.76)], we conclude that eq. (7.84) is the same as eq. (7.80). Considering the $\Pr_t = 1$ assumption that led to eqs. (7.80) and (7.84), the Reynolds analogy is nothing but shorthand for the view that each eddy has the same propensity to convect heat as it has to transfer momentum in the direction normal to the wall. Although the Reynolds analogy works for $\Pr \cong 1$ fluids such as the common gases, it must be distinguished from Colburn's formula (7.78) because any time we try to relax the $\Pr = \Pr_t = 1$ assumptions in time-averaged analysis, we end up with St_x expressions that *never* reproduce the Prandtl number dependence envisioned by Colburn [e.g., eqs. (7.77) and (7.79)].

The observation above is, in fact, a very good clue for the path to follow toward predicting the Colburn formula on a *purely theoretical basis*. If time-averaged analysis never leads to Colburn's correlation of so many experimental results, perhaps the opposite sort of analysis does. To try the opposite analysis (in this case, an analysis based on the view that the turbulent boundary layer is a coarse structure pulsating in time, not a smooth picture that does not change in time) is to proceed *against method*, against the march of the crowd.

By recognizing the fluctuating character of the boundary layer, we have already been able to predict the existence of a viscous sublayer as well as its time-averaged thickness [see Fig. 7.5 and eqs. (7.44)–(7.46)]. Now we rely on the same point of view and conclude that the instantaneous distribution of shear stress $\tau_0(t)$ and heat flux $q_0''(t)$ along the wall of Fig. 7.5 must be as shown in Fig. 7.7. Each spot on the wall that is instantaneously in contact with U_∞-fast and T_∞-cold fluid is instantaneously characterized by maximum shear stress and heat flux. The in-between regions, being covered by slow and already hot fluid that is ejected from the wall, are regions of substantially lower shear stress and heat flux.

Pictures of $\tau_0(t)$ and $q_0''(t)$ (of the type sketched in Fig. 7.7) dance along the x–x' wall section as time passes. The time-averaged quantities $\tau_0(x)$ and $q_0''(x)$ are related to the local *density of contact spots*, defined as

$$\eta(x) = \frac{\text{cumulative length of direct contact spots}}{\text{total length of sample wall section } (x - x')} \tag{7.85}$$

That relationship is

$$\frac{\tau_0}{\tau_{0,\,\text{max}}} \sim \eta \sim \frac{q_0''}{q_{0,\,\text{max}}''} \tag{7.86}$$
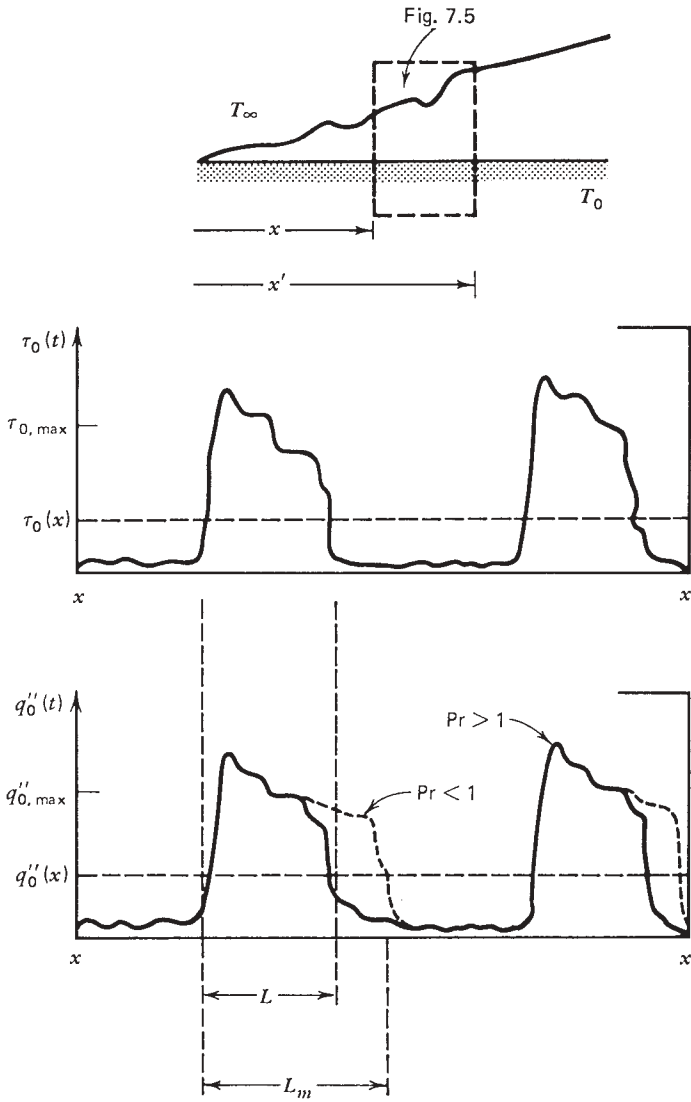
Figure 7.7   Analogy between skin friction and wall heat flux in turbulent boundary layer flow.

Focusing on only the extreme ends of this relation and writing the time-averaged τ_0 and q_0'' in terms of the local coefficients $C_{f,x}$ and St_x, we obtain

$$\frac{St_x}{\frac{1}{2}C_{f,x}} \sim \frac{q_{0,\,max}''}{T_0 - T_\infty} \frac{U_\infty}{c_P \tau_{0,\,max}} \tag{7.87}$$

Finally, since the direct contact spots are covered with laminar shear flow, and since outside these laminar layers the flow temperature conditions are described by U_∞ and T_∞, the scales of $\tau_{0,\,\text{max}}$ and $q''_{0,\,\text{max}}$ are (see Chapter 2)

$$\tau_{0,\,\text{max}} \sim \rho U_\infty^2 \left(\frac{U_\infty L}{\nu}\right)^{-1/2} \tag{7.88}$$

$$\frac{q''_{0,\,\text{max}}}{T_0 - T_\infty} \sim \frac{k}{L} \text{Pr}^{1/3} \left(\frac{U_\infty L}{\nu}\right)^{1/2} \qquad (\text{Pr} > 1) \tag{7.89}$$

In eqs. (7.88) and (7.89), L is the longitudinal length scale of each laminar shear layer. Combining eqs. (7.87)–(7.89), we obtain the following expression:

$$\frac{\text{St}_x}{\frac{1}{2} C_{f,\,x}} \sim \text{Pr}^{-2/3} \qquad (\text{Pr} > 1) \tag{7.90}$$

This is the same as Colburn's formula (7.78). Therefore, experimental measurements of both wall friction and wall heat flux support the constructal theory of Chapter 6, which, after all, is the basis for the intermittent-contact scenario illustrated in Figs. 7.5 and 7.7.

There is more to this theory than the ability to predict Colburn's formula. Regarding the new geometric concept of *density of contact spots* [eq. (7.85)], we can easily estimate the order of magnitude of η,

$$\eta \sim \frac{\tau_0}{\tau_{0,\,\text{max}}} \sim \frac{C_{f,\,x}}{(U_\infty L / \nu)^{-1/2}} \tag{7.91}$$

Recalling that the growth of each laminar layer is terminated when the thickness-referenced Reynolds number is of order 10^2, eq. (6.15), and that in laminar shear flow the thickness varies as $L^{1/2}$, we conclude that the Reynolds number based on spot length scale L has a characteristic order of magnitude

$$\frac{U_\infty L}{\nu} \sim 10^4 \tag{7.92}$$

Substituting this result into the density formula (7.91), we find that

$$\eta \sim 10^2 C_{f,\,x} \tag{7.93}$$

This prediction is worth thinking about. Looking at Fig. 7.6, which shows that $C_{f,\,x}$ is consistently of order 10^{-3}–10^{-2}, we predict that the density of contact spots is of order $0.1 - 1$; in other words, the laminar contact regions cover a significant percentage of the wall. This is why the laminar shear layer thickness alone accounts successfully for the time-averaged viscous sublayer thickness [eqs. (7.44)–(7.46)]. Most important, however, is the proportionality between η

and $C_{f,x}$: This proportionality gives us a geometric interpretation for the meaning of the skin friction coefficient in turbulent boundary layer flow. In addition, eq. (7.93) explains why the $C_{f,x}$ values are so much smaller than 1.

Geometrically, the turbulent boundary layer emerges as a sequence of laminar spots terminated when their buckling number N_B exceeds $O(1)$ (Chapter 6), a population the density of which decreases very gradually as the outer thickness of the boundary layer increases in the downstream direction.

The theory that led to eq. (7.90) predicts that the Colburn analogy (7.78) should be valid in the $Pr > 1$ range. What, then, is the corresponding theory for liquid-metal near-wall turbulence? To answer this question, we recall that in $Pr < 1$ fluids the thermal diffusivity is such that given the same fluid layer thickness, the thermal communication time across the layer is shorter than the viscous communication time. Thus, although the laminar spot breaks down when it reaches a length L, the direct thermal contact between wall (T_0) and outer fluid (T_∞) persists over a longer length L_m (Fig. 7.5). In other words, if the Prandtl number is sufficiently small, the wall will communicate via thermal diffusion even across the first (smallest) eddies formed in the wake of laminar spot breakdown.

As in the case of transition to turbulence (Chapter 6), the eddy diameter D_T across which the thermal diffusion effect will still have time to travel can be estimated by equating the thermal diffusion time $D_T^2/16\alpha$ with the rolling period $D_T/(U_\infty/2)$; hence,

$$\frac{D_T U_\infty}{\alpha} \sim 10^2 \tag{7.94}$$

From the study of laminar thermal boundary layers in liquid metals (Chapter 2), we recall that

$$\frac{D_T}{L_m} \sim Pr^{-1/2} \left(\frac{U_\infty L_m}{\nu} \right)^{-1/2} \tag{7.95}$$

Combining eqs. (7.94) and (7.95), we find that

$$\frac{L_m U_\infty}{\nu} \sim 10^4 Pr^{-1} \tag{7.96}$$

or, using eq. (7.92),

$$\frac{L_m}{L} \sim \frac{1}{Pr} > 1 \tag{7.97}$$

We conclude that for liquid metals, which occupy the Pr range 10^{-1}–10^{-3}, the ratio L_m/L evaluated above would be of order 10–10^3. However, since L_m cannot be greater than L/η [Fig. 7.7 and eq. (7.85)], and since η is of order 10^{-1} (Fig. 7.6), we learn that the ratio L_m/L cannot exceed $O(10)$. This means that in liquid metals, the intermittent thermal contact between free stream and wall is not terminated by criterion (7.94) but by the next inrush of free-stream fluid (note that the longitudinal length scale between two consecutive inrush events

is of order L/η). The thermal contact between wall and free stream is therefore characterized by the front portion of a thermal boundary layer of length L/η in the $\mathrm{Pr} \to 0$ limit (Chapter 2):

$$q_0'' \sim \frac{k(T_0 - T_\infty)}{L/\eta} \mathrm{Pr}^{1/2} \left(\frac{U_\infty L/\eta}{\nu} \right)^{1/2} \tag{7.98}$$

Combining this estimate with eqs. (7.92) and (7.93), we predict the following relation between St_x and $C_{f,x}$ for liquid metals:

$$\frac{\mathrm{St}}{\left(\frac{1}{2} C_{f,x} \right)^{1/2}} \sim 10^{-1} \mathrm{Pr}^{-1/2} \tag{7.99}$$

The validity of eq. (7.99) is confirmed by experimental results available for turbulent pipe flow; see the discussion of eq. (8.39).

7.9   OTHER EXTERNAL FLOWS

7.9.1   Single Cylinder in Cross Flow

In the preceding sections we uncovered the most basic aspects of turbulent convection by focusing on the simplest wall geometry—the flat plate. The same fundamentals govern the more complicated configurations and account for the largest portion of the external-convection literature and handbooks. This section is a problem solving–oriented review of some of the simplest external convection results that have been obtained for nonplane walls.

Consider the heat transfer between a long cylinder oriented across a fluid stream of uniform velocity (U_∞) and temperature (T_∞) (Fig. 7.8). The temperature of the cylindrical surface is uniform (T_w). There are many heat transfer correlations for this configuration, but generally speaking, they are not in very good agreement with the experimental data. For example, one correlation that is based on data from many independent sources was developed by Churchill and Bernstein [22],

$$\overline{\mathrm{Nu}}_D = 0.3 + \frac{0.62 \mathrm{Re}_D^{1/2} \mathrm{Pr}^{1/3}}{[1 + (0.4/\mathrm{Pr})^{2/3}]^{1/4}} \left[1 + \left(\frac{\mathrm{Re}_D}{282{,}000} \right)^{5/8} \right]^{4/5} \tag{7.100}$$

where $\overline{\mathrm{Nu}}_D = \bar{h}D/k$. This formula holds for all values of Re_D and Pr, provided that the Péclet number $\mathrm{Pe}_D = \mathrm{Re}_D \mathrm{Pr}$ is greater than 0.2. In the intermediate range $7 \times 10^4 < \mathrm{Re}_D < 4 \times 10^5$, eq. (7.100) predicts $\overline{\mathrm{Nu}}_D$ values that can be 20 percent smaller than those furnished by direct measurement. The physical properties needed for calculating Nu_D, Pr, and Re_D are evaluated at the film temperature $(T_\infty + T_w)/2$. Equation (7.100) also applies to a cylinder with
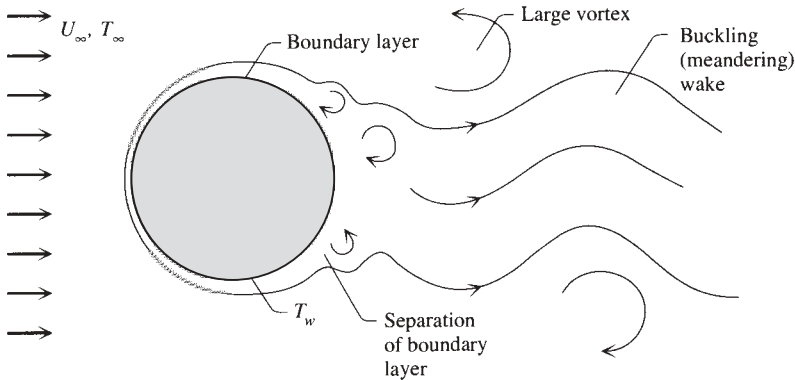
Figure 7.8   Single cylinder or sphere in turbulent cross flow.

uniform heat flux, in which case the average heat transfer coefficient $\overline{h}$ is based on the perimeter-averaged temperature difference between the cylindrical surface and the free stream.

In flows slow enough so that $\mathrm{Pe}_D < 0.2$, a formula due to Nakai and Okazaki [23] is more accurate than eq. (7.100):

$$\overline{\mathrm{Nu}}_D = \frac{1}{0.8237 - 0.5 \ \ln(\mathrm{Pe}_D)} \tag{7.101}$$

This agrees well with experimental measurements conducted in air; however, it has not been tested for a wide range of Prandtl numbers.

The single cylinder in cross flow also has been studied extensively from a fluid mechanics standpoint. The first portion of the surrounding flow that becomes turbulent as the Reynolds number $\mathrm{Re}_D = U_\infty D/\nu$ increases is the wake. When the Reynolds number is of order 10 or smaller, the flow is nearly symmetric about the transversal diameter of the cylinder. Eddies of size comparable with the cylinder itself begin to shed periodically when $\mathrm{Re}_D \sim 40–70$: This is another manifestation of the local Reynolds number criterion of transition to turbulence (Table 6.1). The wake becomes increasingly turbulent as Re_D increases; however, the shedding of vortices of diameter comparable with D remains a feature of the wake over most of the $10^2 < \mathrm{Re}_D < 10^7$ range. The frequency $f_v[\mathrm{s}^{-1}]$ with which the vortices shed is roughly proportional to the flow velocity [24]:

$$f_v \sim 0.21 \frac{U_\infty}{D} \tag{7.102}$$

The total, time-averaged drag force F_D exerted by the flow on the cylinder can be calculated with the help of Fig. 7.9. Plotted on the ordinate is the *drag*
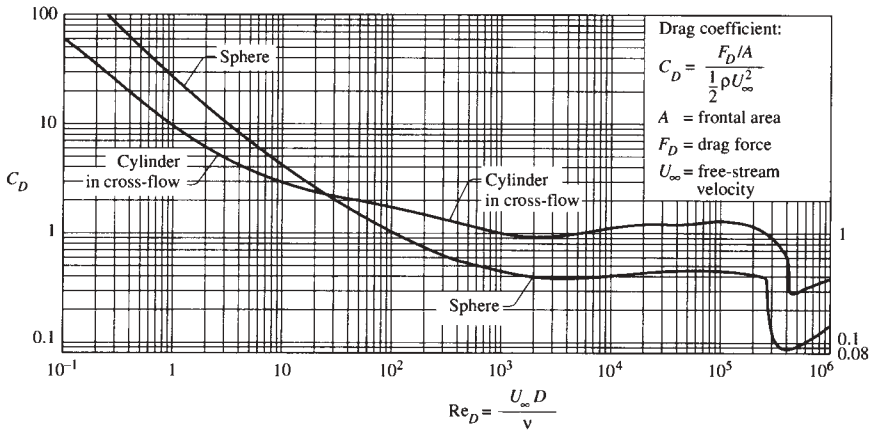
Figure 7.9   Drag coefficients of smooth sphere and a single smooth cylinder in cross flow. (Drawn based on data from Ref. 9, p. 16.)

coefficient C_D, which is a dimensionless way of expressing the drag force:

$$C_D = \frac{F_D/A}{\frac{1}{2}\rho U_\infty^2} \tag{7.103}$$

The area A is the *frontal* area of the cylinder (as seen by the approaching stream), namely, $A = LD$, if L is the length of the cylinder. The drag coefficients of several other body shapes have been compiled by Simiu and Scanlan [25].

7.9.2   Sphere

For the average heat transfer coefficient between an isothermal spherical surface (T_w) and an isothermal free stream (U_∞, T_∞) (Fig. 7.8), Whitaker [26] proposed the correlation

$$\overline{\mathrm{Nu}}_D = 2 + (0.4\mathrm{Re}_D^{1/2} + 0.06\mathrm{Re}_D^{2/3})\mathrm{Pr}^{0.4}\left(\frac{\mu_\infty}{\mu_w}\right)^{1/4} \tag{7.104}$$

This relation has been tested for $0.71 < \mathrm{Pr} < 380$, $3.5 < \mathrm{Re}_D < 7.6 \times 10^4$, and $1 < \mu_\infty/\mu_w < 3.2$. All the physical properties in eq. (7.104) are evaluated at the free-stream temperature T_∞, except the viscosity at the surface temperature, $\mu_w = \mu(T_w)$. It is worth noting that the no-flow limit of this formula, $\overline{\mathrm{Nu}}_D = 2$, represents the pure-conduction estimate for steady radial conduction between the spherical surface and the motionless, infinite conducting medium that surrounds it. Equation (7.104) also applies to spherical surfaces with uniform heat flux, with the understanding that in such cases, $\overline{\mathrm{Nu}}_D$ is based on the

surface-averaged temperature difference between the sphere and the surrounding stream, $\overline{\mathrm{Nu}}_D = \bar{h}D/k = q_w''D/k(\overline{T}_w - T_\infty)$.

Figure 7.9 shows the dimensionless drag coefficient for a sphere suspended in a uniform stream. The total time-averaged drag force F_D experienced by the holder of the sphere can be calculated with eq. (7.103), in which the frontal area this time is $A = (\pi/4)D^2$. The regimes that are exhibited by the flow around the sphere are analogous to those encountered in the case of a cylinder in cross flow.

Correlations for turbulent heat transfer from spherical and cylindrical objects immersed in air flow have been developed by Dincer and Genceli [27] and Dincer [28–30], with application to the cooling and drying of food products. Additional results are reviewed in a heat transfer handbook [31].

7.9.3 Other Body Shapes

The single cylinder and sphere discussed in Sections 7.9.1 and 7.9.2 are the simplest geometries of bodies immersed in a uniform flow of different temperature. The heat transfer literature contains a wealth of analogous results for bodies of other shapes. Some of these formulas have been reviewed critically by Yovanovich [32], who also proposed a universal correlation for *spheroids*, bodies of nearly spherical shape.

As illustrated in the lower part of Fig. 4.19, a spheroid can be obtained by rotating an ellipse about one of the semiaxes. The spheroid geometry is characterized by two dimensions (C, B), where C is the semiaxis aligned with the free stream U_∞. As length scale for the definition of the Reynolds and Nusselt numbers, Yovanovich chose the square root of the spheroid surface (A),

$$\pounds = A^{1/2} \tag{7.105}$$

Therefore,

$$\mathrm{Re}_\pounds = \frac{U_\infty \pounds}{\nu} \quad \text{and} \quad \overline{\mathrm{Nu}}_\pounds = \frac{\bar{h}\pounds}{k} \tag{7.106}$$

The universal correlation developed by Yovanovich [32] is

$$\overline{\mathrm{Nu}}_\pounds = \overline{\mathrm{Nu}}_\pounds^0 + \left[0.15 \left(\frac{p}{\pounds} \right)^{1/2} \mathrm{Re}_\pounds^{1/2} + 0.35 \mathrm{Re}_\pounds^{0.566} \right] \mathrm{Pr}^{1/3} \tag{7.107}$$

where p is the maximum (equatorial) perimeter of the spheroid, perpendicular to the flow direction U_∞. The constant $\overline{\mathrm{Nu}}_\pounds^0$ is the overall Nusselt number in the no-flow limit (pure conduction). Representative values of this constant are listed in Table 4.3, which is to be read in conjunction with Fig. 4.19. Equation (7.107) is recommended for $0 < \mathrm{Re}_\pounds < 2 \times 10^5$, $\mathrm{Pr} > 0.7$, and $0 < C/B < 5$. The physical properties involved in the definitions of $\overline{\mathrm{Nu}}_\pounds$ and $\mathrm{Re}_\pounds$ are evaluated at the film temperature.

7.9.4   Arrays of Cylinders in Cross Flow

A considerably more complicated geometry is that of a large number of regularly spaced (parallel) cylinders in cross flow (Fig. 7.10). This geometry is characterized by the cylinder diameter (D), the longitudinal spacing of two consecutive rows (longitudinal pitch, X_l), and the transversal spacing between cylinders (transversal pitch, X_t). It is assumed that the array is wide enough; that is, enough cylinders exist in each row, so that the top and bottom boundaries (the shroud) do not affect the overall flow and heat transfer characteristics of the array.

In the field of heat exchanger design, arrays such as those of Fig. 7.10 form when *tube banks* or *tube bundles* are placed perpendicular to a stream of fluid. Assume, for example, that the stream is warm. A second stream of cold fluid flows inside the many tubes of the bundle, and because of the heat transfer interaction between each tube and the external cross flow, it absorbs the energy lost by the warm stream.

The two most common types of arrays have cylinders that are *aligned* one behind the other in the direction of flow (Fig. 7.10*a*) and cylinders that are *staggered* (Fig. 7.10*b*). Aligned cylinders form rectangles with the centers of their cross sections, whereas staggered cylinders form isosceles triangles.

The work published on the heat transfer performance of banks of cylinders in cross flow was reviewed by Zukauskas [33]. The overall Nusselt number formulas presented below are based on Zukauskas's recommendations, in which

$$\overline{\mathrm{Nu}}_D = \frac{\overline{h}D}{k} \tag{7.108}$$

and $\overline{h}$ is the heat transfer coefficient averaged over all the cylindrical surfaces in the array. The total area of these surfaces is $nm\pi DL$, where n is the number of
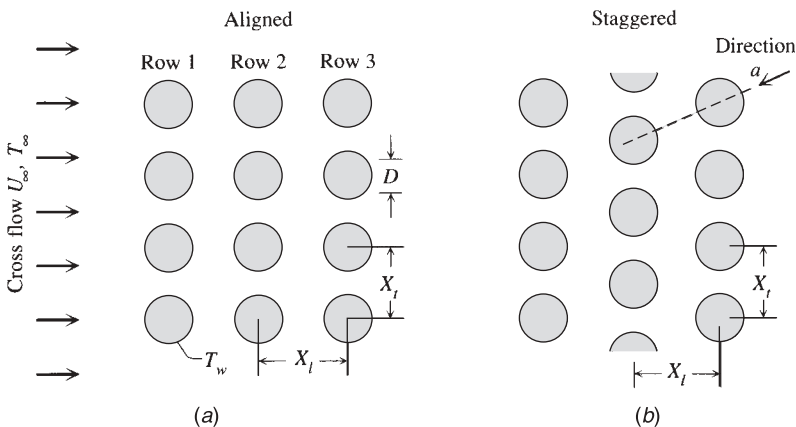

Figure 7.10   Cylinders in cross flow: (*a*) aligned array versus (*b*) staggered array.

rows, m the number of cylinders in each row (across the flow direction), and L the length of the array in the direction perpendicular to the plane of Fig. 7.10.

For *aligned arrays* of cylinders, the array-averaged Nusselt number is anticipated within ± 15 percent by

$$
\overline{Nu}_D =
\begin{cases}
0.9C_n \, Re_D^{0.4} \, Pr^{0.36} \left(\dfrac{Pr}{Pr_w} \right)^{1/4} & (Re_D = 1 - 10^2 \\[2ex]
0.52C_n \, Re_D^{0.5} \, Pr^{0.36} \left(\dfrac{Pr}{Pr_w} \right)^{1/4} & = 10^2 - 10^3 \\[2ex]
0.27C_n \, Re_D^{0.63} \, Pr^{0.36} \left(\dfrac{Pr}{Pr_w} \right)^{1/4} & = 10^3 - 2 \times 10^5 \\[2ex]
0.033C_n \, Re_D^{0.8} \, Pr^{0.4} \left(\dfrac{Pr}{Pr_w} \right)^{1/4} & = 2 \times 10^5 - 2 \times 10^6)
\end{cases}
\tag{7.109}
$$

where C_n is a function of the total number of rows in the array (Fig. 7.11). The Reynolds number Re_D is based on the average velocity through the narrowest cross section formed by the array, that is, the *maximum* average velocity $U_{\max}$,

$$
Re_D = \frac{U_{\max}D}{\nu}
\tag{7.110}
$$

In the case of aligned cylinders, the narrowest flow cross section forms in the plane that contains the centers of the cylinders of one row. The conservation of
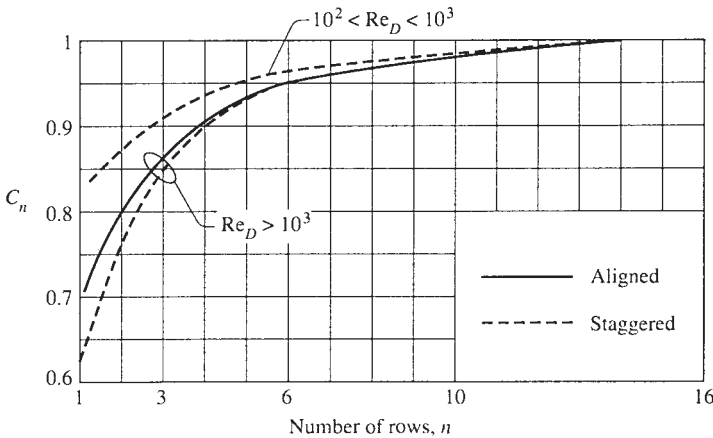
Figure 7.11   Effect of the number of rows on the array-averaged Nusselt number for banks of cylinders in cross flow. (After Ref. 33.)

mass through such a plane requires that (see Fig. 7.10*a*)

$$U_\infty X_t = U_{\max}(X_t - D) \tag{7.111}$$

All the physical properties except Pr_w in eqs. (7.109) are evaluated at the *mean* temperature of the fluid that flows through the spaces formed between the cylinders. The mean (or ''bulk'') temperature is a concept defined in eq. (3.42), in which the cross flow of Fig. 7.10 can be viewed as a stream that flows through the ''duct'' constituted by all the spaces between cylinders. The denominator Pr_w is the Prandtl number evaluated at the temperature of the cylindrical surface, $Pr_w = Pr(T_w)$.

Figure 7.11 shows that the number of rows has an effect on the array-averaged Nusselt number only when n is less than approximately 16. In the $n < 16$ range, C_n and $\overline{\mathrm{Nu}}_D$ increase as more rows are added to the array. This effect is analogous to the observation that the individual $\overline{h}$ value of a cylinder positioned in the front row is lower than that of the cylinder situated behind it. The front-row cylinder is coated by a relatively smooth boundary layer formed by the undisturbed incoming stream U_∞, whereas a downstream cylinder benefits from the heat transfer augmentation effect provided by the eddies of the turbulent wake created by the preceding cylinder.

For *staggered arrays*, the following relations approximate $\overline{\mathrm{Nu}}_D$ within ± 15 percent [33]:

$$\overline{\mathrm{Nu}}_D = \begin{cases} 1.04 C_n \, \mathrm{Re}_D^{0.4} \, \mathrm{Pr}^{0.36} \left(\dfrac{\mathrm{Pr}}{\mathrm{Pr}_w}\right)^{1/4} & (\mathrm{Re}_D = 1 - 500 \\[2.5ex] 0.71 C_n \, \mathrm{Re}_D^{0.5} \, \mathrm{Pr}^{0.36} \left(\dfrac{\mathrm{Pr}}{\mathrm{Pr}_w}\right)^{1/4} & = 500 - 10^3 \\[2.5ex] 0.35 C_n \, \mathrm{Re}_D^{0.6} \, \mathrm{Pr}^{0.36} \left(\dfrac{\mathrm{Pr}}{\mathrm{Pr}_w}\right)^{1/4} \left(\dfrac{X_t}{X_l}\right)^{0.2} & = 10^3 - 2 \times 10^5 \\[2.5ex] 0.031 C_n \, \mathrm{Re}_D^{0.8} \, \mathrm{Pr}^{0.36} \left(\dfrac{\mathrm{Pr}}{\mathrm{Pr}_w}\right)^{1/4} \left(\dfrac{X_t}{X_l}\right)^{0.2} & = 2 \times 10^5 - 2 \times 10^6) \end{cases} \tag{7.112}$$

The observations made in connection with eqs. (7.109) apply here as well. A new effect is the role played by the aspect ratio of the isosceles triangle, X_t/X_l, which is felt at relatively large Reynolds numbers. The Reynolds number continues to be based on $U_{\max}$, eq. (7.110); however, which flow cross section is the narrowest depends on the slenderness of the isosceles triangle. For example, in the staggered array shown in Fig. 7.10*b*, the narrowest flow area occurs in the vertical plane drawn through the centers of one row of cylinders. In the other extreme, where X_l is considerably smaller than X_t, the strangling of the flow may occur through the area aligned with the direction labeled ''*a*.''

The pressure drop experienced by the cross flow is proportional to the number of tube rows counted in the flow direction, n_l:

$$\Delta P = n_l f \chi \cdot \frac{1}{2}\rho V_{max}^2 \tag{7.113}$$

The dimensionless factors f and χ are presented in Fig. 7.12 for aligned arrays. Each array is described by the longitudinal pitch X_l and the transversal pitch X_t, or by their dimensionless counterparts,

$$X_l^* = \frac{X_l}{D}, \qquad X_t^* = \frac{X_t}{D} \tag{7.114}$$

in which D is the tube outside diameter. The f curves in Fig. 7.12 correspond to a square array ($X_l = X_t$), while the χ correction factor accounts for arrangements in which $X_l \neq X_t$. Note that $\chi = 1$ for the square arrangement.

Figure 7.13 contains the corresponding f and χ information for staggered arrays. The f curves have been drawn for the equilateral triangle arrangement [$X_t = X_d$ or $X_l = (3^{1/2}/2)X_t$]. The upper-right inset shows that the χ value plays the role of correction factor in cases where the tube centers do not form equilateral triangles.

Zukauskas' eq. (7.113) and Figs. 7.12 and 7.13 are valid when $n_l > 9$. They were constructed based on extensive experiments in which the test fluid was air, water, and several oils [33].
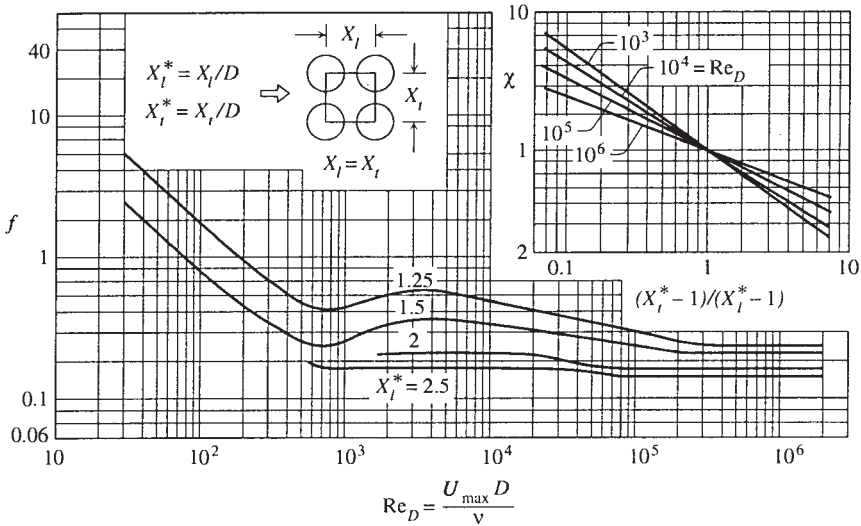
Figure 7.12 Arrays of aligned cylinders: coefficients f and χ for the pressure drop formula (7.113). (Reprinted with permission from A. A. Zukauskas, in S. Kakac et al., eds., *Handbook of Single-Phase Convective Heat Transfer*, 1987, Chapter 6. Copyright © 1987 John Wiley & Sons, Inc.)
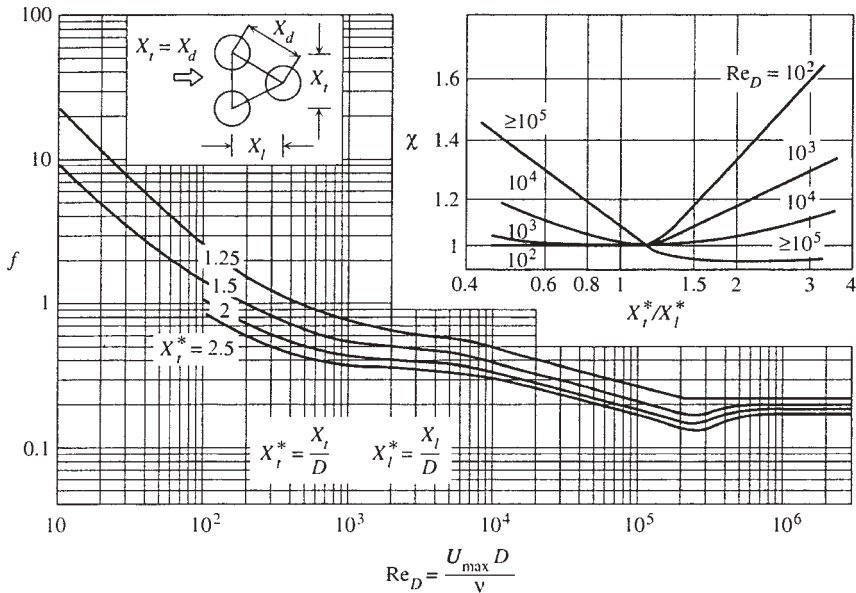
Figure 7.13   Arrays of staggered cylinders: coefficients f and χ for the pressure drop formula (7.113). (Reprinted with permission from A. A. Zukauskas, in S. Kakac et al., eds., *Handbook of Single-Phase Convective Heat Transfer*, 1987, Chapter 6. Copyright © 1987 John Wiley & Sons, Inc.)

Zukauskas' curves are numerous and complicated but are in fact collapsible onto a single curve, as shown in Fig. 7.14 [34,35]. They represent a single phenomenon: fluid friction through compact porous structures in the transition regime between coarse and dense porous structures. The dense porous media are described well by the Darcy flow model (Chapter 12). The departure from the Darcy flow model is covered by Fig. 7.14, and it is valid for all porous structures, arrays of cylinders in cross flow, wire meshes, cloth, textiles, gauze, and so on. The flow friction results or all these ''complicated'' structures obey the simple representation presented in Fig. 7.14.

The four curves drawn as one tight bundle for staggered cylinders in Fig. 7.14 are for the curves with transverse pitch/cylinder diameter ratios 1.25, 1.5, 2, and 2.5 in Fig. 7.13. The technique consists of treating the bundle as a fluid-saturated porous medium and using the volume-averaged velocity U, the pore Reynolds number $UK^{1/2}/\nu$ on the abscissa, and the dimensionless pressure gradient group $(\Delta P/L)K^{1/2}/(\rho U^2)$ on the ordinate. This formulation forms the subject of Section 12.2. The effective permeability of the bundle of cylinders (K) is estimated based on the Carman–Kozeny model, $K \cong D^2\phi^3/[k_z(1 - \phi)^2]$, where ϕ is the porosity of the assembly, D is the cylinder diameter, and the empirical constant is $k_z = 100$.
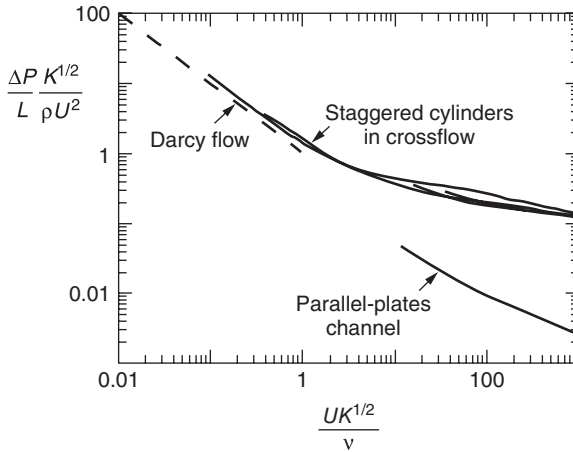
Figure 7.14 Porous medium representation of the classical pressure drop data for flow through staggered cylinders and stacks of parallel plates. (From Refs. 34 and 35.)

Figure 7.14 shows very clearly the transition between Darcy flow (slope -1) and Forchheimer flow (slope 0). The porous medium presentation of the array of cylinders leads to a very tight collapse of the curves taken from Zukauskas' chart. The figure also shows the pressure drop curve for turbulent flow through a heat exchanger core formed by a stack of parallel plates. Figure 7.14 extends the curves (Zukauskas' data) reliably into the low–Reynolds number limit (Darcy flow), where classical heat exchanger data are not available.

The method of Fig. 7.14 deserves to be applied to other configurations to test the prediction that the single curve discovered for staggered cylinders is generally applicable to flows through packings, weaves, meshes, and arrays of objects of many shapes.

7.10   NATURAL CONVECTION ALONG VERTICAL WALLS

We studied laminar boundary layers in natural convection in Chapters 4 and 5 and then featured this phenomenon in order to identify the scaling laws of transition to turbulence (Chapter 6). Key correlations for laminar and *turbulent* natural convection heat transfer have been assembled in Section 4.11.

In this section we focus on the vertical wall with turbulent natural convection (Fig. 7.15) in light of what we learned from the time-averaged treatment of the forced convection boundary layer (Section 7.3). Consider the Churchill–Chu correlation (4.104), which for an isothermal wall (T_0) of height H reads

$$\frac{h_{0-H}H}{k} \cong \left\{ 0.825 + \frac{0.387 \mathrm{Ra}_H^{1/6}}{\left[1 + (0.492/\mathrm{Pr})^{9/16}\right]^{8/27}} \right\}^2 \qquad (7.115)$$
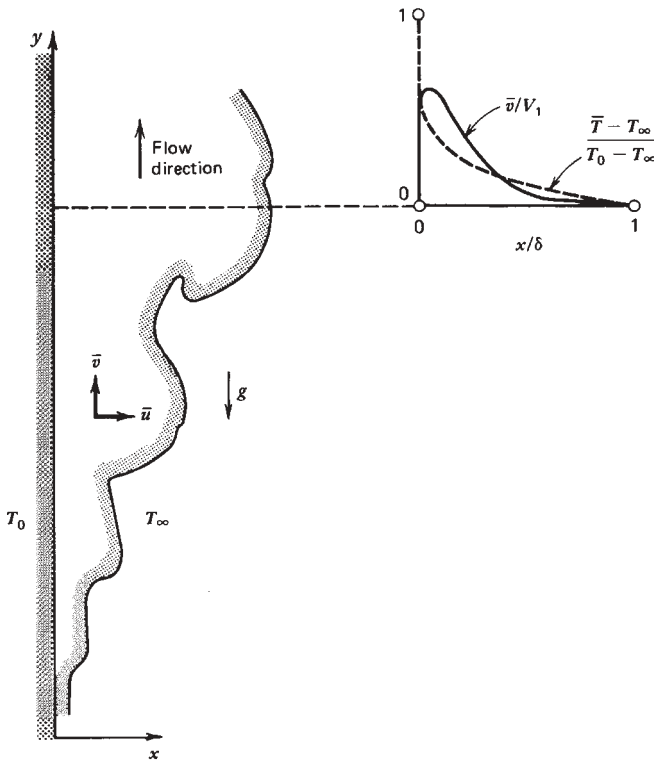
Figure 7.15 Coordinates for turbulent natural convection along a vertical wall and the velocity and temperature profiles used by Eckert and Jackson. (From Ref. 36.)

In this expression, h_{0-H} is the heat transfer coefficient averaged over the wall height H and Ra_H is the Rayleigh number based on H and $(T_0 - T_\infty)$. Of special interest are the asymptotes suggested by the Churchill–Chu correlation in the turbulent flow limit (large Ra_H),

$$\frac{h_{0-H}H}{k} \cong \begin{cases} 0.15\mathrm{Ra}_H^{1/3} & (\mathrm{Pr} \gg 1) \\ 0.19(\mathrm{Ra}_H\mathrm{Pr})^{1/3} & (\mathrm{Pr} \ll 1) \end{cases} \tag{7.116}$$

In the lower expression, the 0.19 coefficient is replaced by 0.198 if the wall condition is of uniform heat flux. Equations (7.116) should not be seen as exact or definitive answers to the heat transfer question; nevertheless, they do offer a bird's-eye view of the trends followed by heat transfer data.

On the analytical side, the continuing effort of explaining the foregoing trends has been influenced by the first analysis reported by Eckert and Jackson [36]. Here I outline an *abbreviated version* of the Eckert–Jackson analysis, a version

that is better suited for the classroom because it accomplishes as much as Eckert and Jackson's analysis with less algebra. Relative to the time-averaged turbulent flow analysis presented earlier in this chapter, the new element in vertical boundary layer convection is the momentum equation with the body force term. For the frame of Fig. 7.15, the time-averaged boundary layer momentum equation is

$$\bar{u}\frac{\partial \bar{v}}{\partial x} + \bar{v}\frac{\partial \bar{v}}{\partial y} = \frac{\partial}{\partial x}\left[(\nu + \epsilon_M)\frac{\partial \bar{v}}{\partial x}\right] + g\beta(\bar{T} - T_\infty) \tag{7.117}$$

Note the use of the Boussinesq incompressible flow model already seen in the treatment of laminar flow (Chapter 4). Integrating eq. (7.117) across the boundary layer region yields

$$\frac{d}{dy}\int_0^\infty \bar{v}^2 \ dx = -\frac{\tau_0}{\rho} + g\beta\int_0^\infty (\bar{T} - T_\infty)\ dx \tag{7.118}$$

Eckert and Jackson used this momentum integral in conjunction with the following velocity and temperature profiles:

$$\bar{v} = V_1\left(1 - \frac{x}{\delta}\right)^4 \left(\frac{x}{\delta}\right)^{1/7}$$
$$\bar{T} - T_\infty = (T_0 - T_\infty)\left[1 - \left(\frac{x}{\delta}\right)^{1/7}\right] \tag{7.119}$$

which have been sketched in Fig. 7.15. Here we depart from Eckert and Jackson's analysis and *neglect the inertia term* in eq. (7.118):

$$\frac{\tau_0}{\rho} = \frac{\delta}{8}g\beta(T_0 - T_\infty) \tag{7.120}$$

The energy equation for the boundary layer flow of Fig. 7.15 is

$$\bar{u}\frac{\partial \bar{T}}{\partial x} + \bar{v}\frac{\partial \bar{T}}{\partial y} = \frac{\partial}{\partial x}\left[(\alpha + \epsilon_H)\frac{\partial \bar{T}}{\partial x}\right] \tag{7.121}$$

Integrating this equation across the boundary layer,

$$\frac{d}{dy}\int_0^\infty \bar{v}(\bar{T} - T_\infty)\ dx = \frac{q_0''}{\rho c_P} \tag{7.122}$$

and making use of the assumed profiles [eqs. (7.119)] yields

$$0.0366 \ (T_0 - T_\infty)\frac{d}{dy}(V_1\delta) = \frac{q_0''}{\rho c_P} \tag{7.123}$$

At this stage we have two equations for four unknowns (τ_0, q_0'', δ, V_1) [eqs. (7.120) and (7.123)]. To close the problem, Eckert and Jackson made two additional assumptions:

1. The wall shear stress τ_0 depends on the velocity scale V_1 and on the outer boundary layer thickness δ in the same manner as in *forced convection*,

$$\tau_0 \cong 0.0225 \rho V_1^2 \left(\frac{V_1 \delta}{\nu} \right)^{-1/4} \tag{7.124}$$

2. The local shear stress and heat flux are related through a scaling law of the Colburn type,

$$\frac{q_0''}{(T_0 - T_\infty)\rho c_P V_1} \mathrm{Pr}^{2/3} = \frac{\tau_0}{\rho V_1^2} \tag{7.125}$$

By solving the problem represented in this book by eqs. (7.120) and (7.123)–(7.125), we obtain the local Nusselt number (see Problem 7.25),

$$\mathrm{Nu}_y = \frac{q_0'' y}{(T_0 - T_\infty)k} = 0.039 \mathrm{Pr}^{-1/5} \mathrm{Ra}_y^{2/5} \tag{7.126}$$

If the inertia term of eq. (7.118) is not neglected (i.e., unlike in the analysis sketched above), the local Nusselt number takes the seemingly more general form derived by Eckert and Jackson [36].

$$\mathrm{Nu}_y = \frac{0.0295 \ \mathrm{Pr}^{1/15}}{(1 + 0.494 \mathrm{Pr}^{2/3})^{2/5}} \mathrm{Ra}_y^{2/5} \tag{7.127}$$

Equation (7.127) becomes the same as eq. (7.126) as $\mathrm{Pr} \to \infty$ but leaves the impression that by taking the inertia term into account, it is valid for low Prandtl numbers as well. In reality, the Eckert and Jackson formula (7.127) can only refer to fluids with Pr of order $O(1)$ or greater* because the $\mathrm{Pr} \to 1$ range is a constraint brought into the analysis through adoption of the scaling law (7.125) (see the theory based on Fig. 7.7). Therefore, the retention of the inertia term in eq. (7.118) only complicates the analysis because it is inconsistent with a simplifying assumption inserted later. This inconsistency is corrected in Problem 7.26, where the retention of the inertia term is combined with a more appropriate assumption for $\mathrm{Pr} < 1$, that is, with eq. (7.99) in place of the Colburn form (7.125).

REFERENCES

1. A. Roshko, Structure of turbulent shear flows: a new look. Dryden Research Lecture, *AIAA J.*, Vol. 14, 1976, pp. 1349–1357.

---

*As eq. (7.126) does after considerably less algebra.

 2. B. J. Cantwell, Organized motion in turbulent flow, *Annu. Rev. Fluid Mech.*, Vol. 13, 1981, pp. 457–515.

 3. A. Bejan, *Entropy Generation through Heat and Fluid Flow*, Wiley, New York, 1982, pp. 88, 89.

 4. A. Bejan, *Shape and Structure, from Engineering to Nature*, Cambridge University Press, Cambridge, 2000.

 5. A. Bejan and J. P. Zane, *Design in Nature*, Doubleday, New York, 2012.

 6. O. Reynolds, On the dynamical theory of incompressible viscous fluids and the determination of the criterion, *Philos. Trans. R. Soc. London, Ser. A*, Vol. 186, 1895, pp. 123–164.

 7. J. Boussinesq, Théorie de l'écoulement tourbillonant, *Mémoire présenté par divers savants à l'Académie des Sciences*, Vol. XXIII, pp. 46–51, Paris, 1897.

 8. L. Prandtl, *Essentials of Fluid Dynamics*, Blackie & Son, London, 1969, p. 117; in German, *Führer durch die Strömungslehre*, Vieweg, Braunschweig, Germany, 1949.

 9. H. Schlichting, *Boundary Layer Theory*, 4th ed., McGraw-Hill, New York, 1960, p. 489.

10. J. Kestin and P. D. Richardson, Heat transfer across turbulent, incompressible boundary layers, *Int. J. Heat Mass Transfer*, Vol. 6, 1963, pp. 147–189.

11. L. P. Purtell, P. S. Klebanoff, and F. T. Buckley, Turbulent boundary layer at low Reynolds number, *Phys. Fluids*, Vol. 24, May 1981, pp. 802–811.

12. T. von Kármán, The analogy between fluid friction and heat transfer, *Trans. ASME*, Vol. 61, 1939, pp. 705–710.

13. W. D. Rannie, Heat transfer in turbulent shear flow, *J. Aero Sci.*, Vol. 23, 1956, pp. 485–489.

14. E. R. van Driest, On turbulent flow near a wall, *J. Aero Sci.*, Vol. 23, 1956, pp. 1007–1011.

15. H. Reichardt, Die Grundlagen des turbulenten Wärmeüberganges, *Arch. Gesamte Waermetech.*, Vol. 2, 1951, pp. 129–142.

16. R. G. Deissler, Analysis of turbulent heat transfer, mass transfer and friction in smooth tubes at high Prandtl and Schmidt number, NACA TN 3145, 1954.

17. D. B. Spalding, A single formula for the ''law of the wall,'' *J. Appl. Mech.*, Vol. 28, 1961, pp. 455–457.

18. F. Schultz-Grunow, Neues Widerstandsgesetz für glatte Platten, *Luftfahrtforschung*, Vol. 17, 1940, p. 239; also NACA TM-986, 1941.

19. W. M. Kays and M. E. Crawford, *Convective Heat and Mass Transfer*, McGraw-Hill, New York, 1980.

20. A. P. Colburn, A method of correlating forced convection heat transfer data and a comparison with fluid friction, *Trans. Am. Inst. Chem. Eng.*, Vol. 29, 1933, pp. 174–210.

21. O. Reynolds, On the extent and action of the heating surface for steam boilers, *Proc. Manchester Lit. Philos. Soc.*, Vol. 14, 1874, pp. 7–12.

22. S. W. Churchill and M. Bernstein, A correlating equation for forced convection from gases and liquids to a circular cylinder in crossflow, *J. Heat Transfer*, Vol. 99, 1977, pp. 300–306.

23. S. Nakai and T. Okazaki, Heat transfer from horizontal circular wire at small Reynolds and Grashof numbers: I. Pure convection, *Int. J. Heat Mass Transfer*, Vol. 18, 1975, pp. 387–396.

24. J. H. Lienhard, *A Heat Transfer Textbook*, 2nd ed., Prentice-Hall, Englewood Cliffs, NJ, 1987, p. 346.

25. E. Simiu and R. H. Scanlan, *Wind Effects on Structures*, 2nd ed., Wiley, New York, 1986, pp. 143–152.

26. S. Whitaker, Forced convection heat transfer correlations for flow in pipes, past flat plates, single cylinders, single spheres, and flow in packed beds and tube bundles, *AIChE J.*, Vol. 18, 1972, pp. 361–371.

27. I. Dincer and O. F. Genceli, Cooling process and heat transfer parameters of cylindrical products cooled both in water and in air, *Int. J. Heat Mass Transfer*, Vol. 37, 1994, pp. 625–633.

28. I. Dincer, Development of new effective Nusselt–Reynolds correlations for air-cooling of spherical and cylindrical products, *Int. J. Heat Mass Transfer*, Vol. 37, 1994, pp. 2781–2787.

29. I. Dincer, Surface heat transfer coefficients of cylindrical food products cooled with water, *J. Heat Transfer*, Vol. 116, 1994, pp. 764–767.

30. I. Dincer, Heat transfer models for practical cooling applications, *Int. J. Transport Phenomena*, Vol. 3, 2001, pp. 283–290.

31. A. Bejan and A. D. Kraus, *Heat Transfer Handbook*, Wiley, New York, 2003.

32. M. M. Yovanovich, General expression for forced convection heat and mass transfer from isopotential spheroids, Paper AIAA 88–0743, presented at the AIAA 26th Aerospace Sciences Meeting, Reno, NV, January 11–14, 1988.

33. A. A. Zukauskas, Convective heat transfer in cross flow, in S. Kakac, R. K. Shah, and W. Aung, eds., *Handbook of Single-Phase Convective Heat Transfer*, Wiley, New York, 1987, Chapter 6.

34. A. Bejan and A. M. Morega, Optimal arrays of pin fins and plate fins in laminar forced convection, *J. Heat Transfer*, Vol. 115, 1993, pp. 75–81.

35. A Bejan, I. Dincer, S. Lorente, A. F. Miguel, and A. H. Reis, *Porous and Complex Flow Structures in Modern Technologies*, Springer, New York, 2004.

36. E. R. G. Eckert and T. W. Jackson, Analysis of turbulent free convection boundary layer on a flat plate, NACA Report 1015, 1951.

PROBLEMS

7.1. Prove the validity of the time-averaging rules of eqs. (7.4)–(7.10).

7.2. Derive the time-averaged form of the energy equation [eq. (7.17)] by starting with eq. (1.42) and applying the rules of time averaging [eqs. (7.4)–(7.10)]. Use the derivation of eq. (7.16a) as a guide.

7.3. One way to improve the mixing length model, that is, to achieve a smoother overlap between measurements and the empirically adjusted curves suggested by the mixing length model (Fig. 7.4), is to do away with the assumption that the eddy diffusivity ϵ_M is zero in a layer of finite

thickness y_{VSL}. Instead, as proposed by van Driest [14], assume that ϵ_M decays rapidly as y decreases and becomes zero strictly at the wall. Starting with the new mixing length model,

$$l = \kappa y (1 - e^{-y^+/A^+})$$

and assuming that it is valid throughout the inner region defined by the constant shear stress postulate (7.33), develop the analytical means for calculating u^+ as a function of y^+, κ, and A^+. Setting $\kappa = 0.4$, show that the new u^+ calculation fits the data of Fig. 7.4 smoothly if the new empirical constant A^+ is approximately 25.

7.4. Integrate the constant τ_{app} equation (7.47), using the wall condition $u^+(0) = 0$. A hint for performing the integration is hidden in eq. (7.49). Show graphically that in the $y^+ \to \infty$ limit, the $u^+(\kappa, y^+)$ formula (7.48) does not agree with the data plotted in Fig. 7.4. Show that the disagreement persists even if the value of κ is lowered below 0.4.

7.5. Prove that in a time-averaged turbulent boundary layer, the total flow rate through the viscous sublayer, $\int_0^{y_{VSL}} \bar{u}\, dy$, is independent of the longitudinal position x.

7.6. Derive the integral momentum equation for a boundary layer with a finite longitudinal pressure gradient. Start with eq. (7.25) and integrate it across the boundary layer; show that the resulting momentum equation is

$$\frac{d\theta}{dx} + (H + 2) \frac{\theta}{U_\infty} \frac{dU_\infty}{dx} = \frac{\tau_0}{\rho U_\infty^2}$$

where θ is the momentum thickness [see eq. (2.87)]. Parameter H is the *shape factor*,

$$H = \frac{\delta^*}{\theta}$$

where δ^* is the displacement thickness [see eq. (2.86)]. Is the momentum integral above valid only for time-averaged turbulent flow?

7.7. Derive the skin friction coefficient formula recommended by Prandtl's one-seventh power law velocity profile [eq. (7.56)]. Note that in this case, eq. (7.54) means that $\bar{u}/U_\infty = (y/\delta)^{1/7}$. Step by step, compare your findings with those listed as eqs. (7.57)–(7.60).

7.8. The x variation of the boundary layer thickness δ [eq. (7.58)] depends on the choice of the analytical curve fit for the $u^+(y^+)$ data. Prove this statement by deriving general formulas for $\tau_0(x)$ and $\delta(x)$ based on the general curve fit

$$f_u = C(y^+)^{1/m}$$

where C and m are constants. Note that the expression above is a generalization of eq. (7.56) and that the present problem is a generalization of Problem 7.7.

7.9. Consider the classical view that there exists an inner (near-wall) region in turbulent boundary layer flow where the apparent shear stress τ_{app} and the apparent heat flux q''_{app} are constant, that is, independent of the distance to the wall y. What is then the constant (q''_{app}/τ_{app}) according to the Colburn correlation $St_x Pr^{2/3} = \frac{1}{2} C_{f,x}$?

7.10. Consider the heat transfer in boundary layer flow from an isothermal wall T_0 to a constant temperature stream (U_∞, T_∞). The leading laminar section of the boundary layer has a length comparable with the length of the trailing turbulent section; consequently, the heat flux averaged over the entire wall length L is influenced by both sections. Derive a formula for the L-averaged Nusselt number, assuming that the laminar–turbulent transition is located at a point x (between $x = 0$ and $x = L$) where $xU_\infty/\nu = 3.5 \times 10^5$.

7.11. (a) Show that these relationships exist among the Stanton, Nusselt, Reynolds, Péclet, and Prandtl numbers in boundary layer flow:

$$St_x = \frac{Nu_x}{Re_x \, Pr} = \frac{Nu_x}{Pe_x}$$

(b) Show that the Colburn analogy (7.78) also applies to the *laminar* section of the boundary layer near an isothermal wall if the fluid has a Prandtl number in the range $Pr \gtrsim 0.5$.

7.12. Water flows with the velocity $U_\infty = 0.2$ m/s parallel to a plane wall. The following calculations refer to the position $x = 6$ m measured downstream from the leading edge. The water properties can be evaluated at $20°C$.

(a) A probe is to be inserted in the viscous sublayer to the position represented by $y^+ = 2.7$. Calculate the actual spacing y (mm) between the probe and the wall.

(b) Calculate the boundary layer thickness δ, and compare this value with the estimate based on the assumption that the length x is covered by turbulent boundary layer flow.

(c) Calculate the heat transfer coefficient averaged over the length x.

7.13. In this book it was proposed to reduce the drag experienced by the hull of a ship by heating the hull to a high enough temperature so that the viscosity of the water in the boundary layer decreases. Evaluate the merit of this proposal in the following steps:

(a) Model the hull as a flat wall of length L that is swept by turbulent boundary layer flow. Show that the power spent on dragging the wall through the water is proportional to $\nu^{1/5}$.

    (b) Assume that the hull temperature is raised to 90°C, while the water free-stream temperature is 10°C. Calculate the relative decrease in the drag power, a decrease that is caused by the heating of the wall.

    (c) Compare the savings in drag power with the electrical power that would be needed to maintain a wall temperature of 90°C. Show that when the ship speed is of order 10 m/s, the savings in drag power are much smaller than the power used for heating the wall.

7.14. A flat sheet (tabular) iceberg drifts over the ocean as it is driven by the wind that blows over the top. The temperature of the surrounding seawater is 10°C, and the relative velocity between it and the iceberg is 10 cm/s. The length of the iceberg in the direction of drift is L. Calculate the corresponding wind velocity when the atmospheric air temperature is 40°C.

7.15. Air flows with velocity 3.24 m/s over the top surface of the flat iceberg discussed in Problem 7.14. The air temperature outside the boundary layer is 40°C, and the ice surface temperature is 0°C. The length of the iceberg in the direction of air flow is $L = 100$ m. The ice latent heat of melting is $h_{sf} = 333.4$ kJ/kg.

    Calculate the L-averaged heat flux deposited by the air flow into the upper surface of the iceberg (model this surface as flat). Calculate, in millimeters per hour, the rate of melting caused by this heat flux, that is, the erosion (thinning) of the ice slab.

7.16. The large faces of the tall building shown in Fig. P7.16 are swept by a parallel wind with $U_\infty = 15$ m/s and $T_\infty = 0°$C. Calculate the heat transfer coefficient for the outer surface of a window situated on a large face at $x = 60$ m downstream from the leading surface of the building. Evaluate all the air properties at 0°C. Do you expect the calculated heat transfer coefficient to be smaller or larger than the true value?
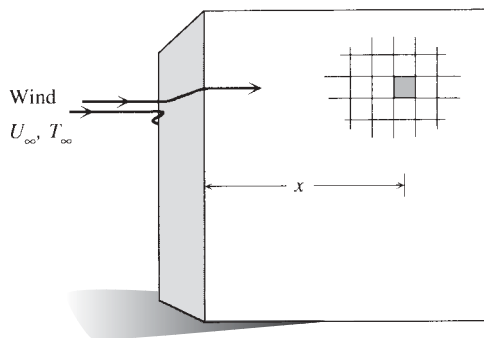

Wind

U_∞, T_∞

x

Figure P7.16

7.17. You are fishing while wading in a 75-cm-deep river that flows at 1 m/s. The immersed portion of each bare leg can be approximated as a vertical cylinder with a diameter of 15 cm. The river velocity is approximately uniform, and the water temperature is 10°C.

   (a) Calculate the horizontal drag force experienced by one leg.

   (b) Compare the drag force with the weight (in air) of the immersed portion of one leg.

   (c) Determine the average heat transfer coefficient between the wetted skin and the river water.

   (d) After a long-enough wait, the temperature of the wetted skin drops to 11°C. Calculate the instantaneous heat transfer rate that escapes into the river through one leg.

7.18. The baseballs used in the major leagues have an average diameter of 7.4 cm and an average weight of 145 g. The distance between the pitcher's mound and home plate is 18.5 m. The pitcher throws an 80-mile/h fast-ball. The rotation of the ball and its motion in the vertical direction are negligible.

   (a) Calculate the drag force experienced by the fastball.

   (b) Show that the drag force calculated is comparable with the weight of the ball.

   (c) Estimate the final horizontal velocity of the baseball as it reaches the catcher's mitt.

7.19. By holding and rubbing the ball in his hand, the pitcher warms the leather cover of the baseball to 30°C. The outside air temperature is 20°C and the ball diameter is 7 cm. The pitcher throws the ball at 50 miles/h to the catcher, who is stationed 18.5 m away.

   (a) Assume that the ball surface temperature remains constant, and calculate the heat transferred from the ball to the surrounding air during the throw.

   (b) Calculate the temperature drop experienced by the leather cover to account for the heat transfer calculated in part (a). Assume that the thickness of the layer of leather that experiences the air cooling effect is comparable to the conduction penetration depth $\delta \sim (\alpha t)^{1/2}$, where α is the thermal diffusivity of leather. Validate the correctness of the constant surface temperature assumption made in part (a).

7.20. An electrical light bulb for the outdoors is approximated well by a sphere with a diameter of 6 cm. It is being swept by a 2-m/s wind and its surface temperature is 60°C. The air temperature is 10°C. Calculate the rate of forced convection heat transfer from the outer surface of the light bulb to the atmosphere.

7.21. During the cooling and hardening phase of its manufacturing process, a glass bead with a diameter of 0.5 mm is dropped from a height of 10 m. The bead falls through still air of temperature 20°C. The properties of the bead material are the same as those listed for window glass in Appendix B.

(a) Calculate the "terminal" velocity of the free-falling bead, that is, the velocity when its weight is balanced by the air drag force. Also, calculate the approximate time that is needed by the bead to achieve this velocity, and show that the bead travels most of the 10-m height at terminal velocity.

(b) Calculate the average heat transfer coefficient between the bead surface and the surrounding air when the bead travels at terminal velocity and when its surface temperature is 500°C. Treat the bead as a lumped capacitance and estimate its temperature at the end of the 10-m fall. Assume that its initial temperature was 500°C.

7.22. Hot air with the average velocity $U_\infty = 2$ m/s flows across a bank of 4-cm-diameter cylinders in an array with $X_l = X_t = 7$ cm. Assume that the air bulk temperature is 300°C and that the cylinder wall temperature is 30°C. The array has 20 rows in the direction of flow. Calculate the average heat transfer coefficient when the cylinders are (a) aligned and (b) staggered. Comment on the relative heat transfer augmentation effect associated with staggering the cylinders.

7.23. The core of a cross-flow heat exchanger employs a bank of staggered *bare* tubes with a longitudinal pitch of 20.3 mm and transverse pitch of 24.8 mm (Fig. P7.23). The outer diameter of each tube is 10.7 mm. Air flows perpendicular to the bare tubes. The frontal area seen by the air-stream is a 0.5 m × 0.5 m square. The length of the heat exchanger core is 0.5 m. The air mass flow rate is 1500 kg/h, and the air properties may be evaluated at 200°C and 1 atm. Calculate the air pressure drop across the core of the heat exchanger.
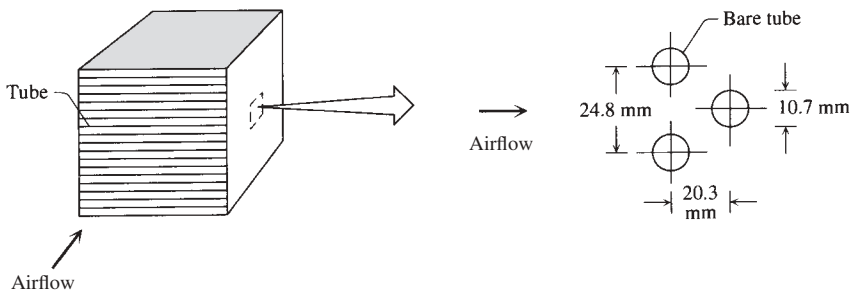

Figure P7.23

7.24. In a cross-flow heat exchanger, air flows across a bundle of tubes with dimensions $D = 5$ cm and $X_t = X_l = 9$ cm. The air velocity averaged over the frontal area of the bundle is 3 m/s. There are 21 rows of tubes counted in the direction of air flow. The average air temperature inside the heat exchanger is $100°$C. Calculate the air pressure drop caused by the tubes by assuming that the tubes are (**a**) aligned and (**b**) staggered. Compare the two pressure drops, and comment on the effect of staggering the tubes in the array.

7.25. Consider the turbulent natural convection boundary layer shown in Fig. 7.14. Derive the local Nusselt number formula (7.126) by combining the momentum and energy integrals (7.120) and (7.123) with Eckert and Jackson's assumptions (7.124) and (7.125). [*Hint:* Assume power law expressions for velocity and boundary layer thickness, $V_1 = Ay^m$, $\delta = By^n$.] Derive the corresponding formula for the wall shear stress τ_0, and sketch qualitatively the variation of τ_0 with altitude y.

7.26. As noted in the text, Eckert and Jackson's formula (7.127) cannot be applied to Pr < 1 fluids. Construct an abbreviated analysis of the type shown in the text between eqs. (7.119)–(7.126), this time for the Pr < 1 limit. In the integral momentum equation (7.118), retain only the buoyancy and inertia terms, and instead of the Colburn analogy (7.125), use the scaling law for Pr < 1 fluids [eq. (7.99)]. Compare your result with eqs. (7.116) and (7.127) for Pr $\ll 1$ fluids.

7.27. In the cases of air and water, numerically compare the abbreviated analysis result (7.126) with the Pr > 1 asymptote followed by measurements [eq. (7.116)]. Determine the Ra_H range in which the agreement between these two formulas is better than 5 percent. [Note that eq. (7.126) refers to the local Nusselt number.]

7.28. Consider the round turbulent jet analyzed in Section 9.2.2. The nozzle is horizontal, and the nozzle conditions are diameter D_0, mean velocity U_0, and temperature T_0. The fluid reservoir is motionless and at a lower temperature T_∞. Buoyancy acts and bends the jet upward. Far enough from the nozzle, the initially horizontal jet becomes a vertical plume.

(**a**) Let $y(x)$ be the curve that describes the centerline of the time-averaged jet plume. The virtual origin is located at $x = y = 0$. Determine $y(x)$ based on the following simplified approach. Assume that in the vicinity of the bend the horizontal and vertical components of the centerline velocity $(\bar{u}_c, \bar{v}_c)$ are represented adequately by the pure-jet and pure-plume solutions listed in the text: namely, $\bar{u}_c = c_1 x^n$ and $\bar{v}_c = c_2 y^m$. Identify the appropriate constants C_1, C_2, n, and m.

(**b**) Let (x_1, y_1) be the point on the centerline where the trajectory reaches the $45°$ angle. This point may be regarded as the location where the flow makes the transition from horizontal jet to vertical plume.

Show that y_1/x_1 is a constant independent of the initial momentum and energy strengths of the nozzle flow.

(c) The round plume of Section 9.3.1 is driven by a concentrated heat source of strength q. What quantity plays the role of q in the present jet–plume problem?

7.29. In this problem we explore the idea to replace the two-dimensional design of a wind mill blade or airplane wing with a three-dimensional design that has bulbous features on the front of the wing (Fig. P7.29). If the frontal portion of the wing is approximated by a long cylinder of diameter D_c, the proposal is qualitatively the same as replacing this material with several equidistant spheres of diameter D_s and spacing S. The approach air velocity is V. In the Reynolds number range $10^3 < VD_{c,\,s}/\nu < 10^5$, the sphere and cylinder drag coefficients are $C_s \cong 0.4$ and $C_c \cong 1$ (cf. Fig. 7.9). Evaluate the merit of this proposal by comparing the drag forces experienced by the spheres and cylinder segment alone (i.e., by neglecting the rest of the wing).

Figure P7.29

<div style="text-align: right; font-size: 3em; font-weight: bold;">8</div>
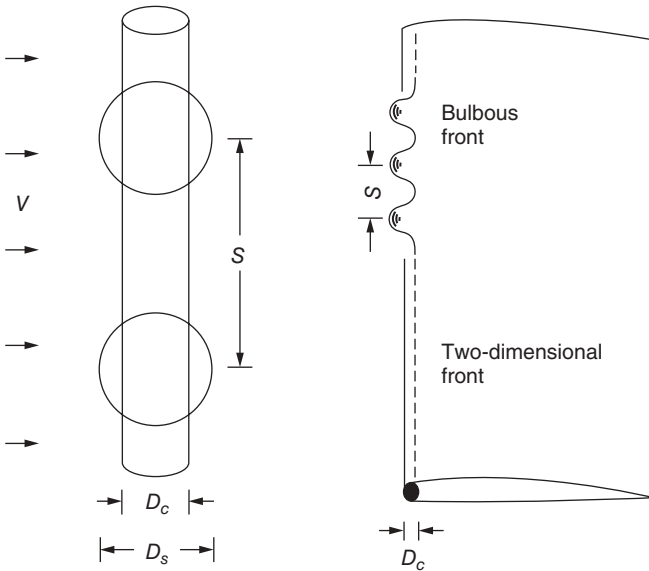
TURBULENT DUCT FLOW

In this chapter we turn our attention to the effect of turbulence on the duct heat transfer configurations considered in Chapter 3 for laminar flow. The time-averaged analysis of friction and heat transfer in turbulent duct flow involves many of the assumptions made in the presentation of the turbulent boundary layer problem (Chapter 7). To avoid repetition, we highlight only the differences.

8.1 VELOCITY DISTRIBUTION

Consider turbulent flow through the round tube sketched in Fig. 8.1. The time-averaged equations for mass, momentum, and energy are

$$\frac{\partial \overline{u}}{\partial x} + \frac{1}{r}\frac{\partial}{\partial r}(r\overline{v}) = 0 \tag{8.1}$$

$$\overline{u}\frac{\partial \overline{u}}{\partial x} + \overline{v}\frac{\partial \overline{u}}{\partial r} = -\frac{1}{\rho}\frac{\overline{dP}}{dx} + \frac{1}{r}\frac{\partial}{\partial r}\left[r\left(\nu + \epsilon_M\right)\frac{\partial \overline{u}}{\partial r}\right] \tag{8.2}$$

$$\overline{u}\frac{\partial \overline{T}}{\partial x} + \overline{v}\frac{\partial \overline{T}}{\partial r} = \frac{1}{r}\frac{\partial}{\partial r}\left[r\left(\alpha + \epsilon_H\right)\frac{\partial \overline{T}}{\partial r}\right] \tag{8.3}$$

Equations (8.1) and (8.2) have already been simplified based on boundary layer arguments of the type employed in Chapter 7 [see eqs. (7.25) and (7.26)]. It is observed that the turbulent flow becomes hydrodynamically and thermally *fully developed* after a relatively short distance from the entrance to the tube,

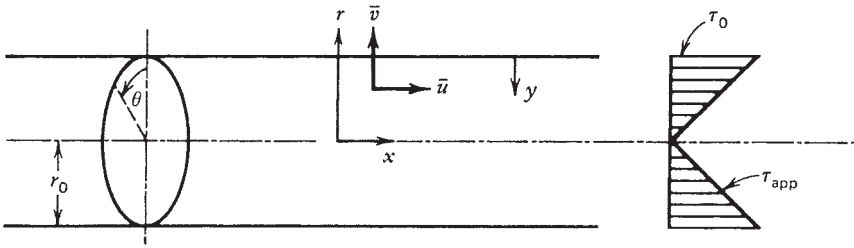$$\frac{X}{D} \cong 10 \cong \frac{X_T}{D} \tag{8.4}$$

Figure 8.1   Distribution of apparent shear stress in fully developed turbulent flow in a pipe.

This full development criterion is particularly applicable to fluids with Prandtl numbers of order 1. The turbulent entrance length (8.4) is much shorter than the would-be laminar estimate (3.90) when $Re_D > 2000$. It is easy to verify that eq. (8.4) is a consequence of the linear growth of turbulent shear layers (also, the wake region of turbulent boundary layers), as illustrated in Figs. 7.5, 7.7, 9.3, and 9.4. In other words, the observations summarized by eq. (8.4) offer additional support for the constructal theory presented in Chapter 6 and Ref. 1, because theory was the basis for drawing instantaneous turbulent-flow images such as Figs. 7.5, 7.7, 9.3, and 9.4.

Review the beginning of Chapter 3 for the scaling implications of the concept of fully developed flow. The first feature that distinguishes the pipe flow from the boundary layer flow is that if the pipe flow is fully developed, the inertia terms vanish from the left-hand side of eq. (8.2). This means that in pipe flow there is no room for a wake region, not even in the close vicinity of the centerline. The momentum equation (8.2) becomes

$$0 = -\frac{1}{\rho}\frac{d\bar{P}}{dx} + \frac{1}{r}\frac{\partial}{\partial r}\left[r\left(\nu + \epsilon_M\right)\frac{\partial \bar{u}}{\partial r}\right] \tag{8.5}$$

where $d\bar{P}/dx$ is a function of x only. Next, we integrate eq. (8.5) from the centerline ($r = 0$) to any r,

$$\frac{1}{\rho}\frac{d\bar{P}}{dx}\frac{r}{2} = \left(\nu + \epsilon_M\right)\frac{\partial \bar{u}}{\partial r} \tag{8.6}$$

which at the wall ($r = r_0$, $\epsilon_M \ll \nu$) reads

$$\frac{1}{\rho}\frac{d\bar{P}}{dx}\frac{r_0}{2} = \nu\left(\frac{\partial \bar{u}}{\partial r}\right)_{r_0} \tag{8.6'}$$

From eq. (7.24) we recall that

$$\tau_{\text{app}} = \rho(\nu + \epsilon_M)\frac{\partial \bar{u}}{\partial y} \quad \text{and} \quad \tau_0 = \rho\nu\left(\frac{\partial \bar{u}}{\partial y}\right)_{y=0} \tag{8.6''}$$

where $y = r_0 - r$ is the distance measured away from the wall. Finally, by dividing eqs. (8.6) and (8.6′) we reach the conclusion that the apparent shear stress decreases linearly away from the wall,

$$\frac{\tau_{app}}{\tau_0} = 1 - \frac{y}{r_0} \tag{8.7}$$

According to the fully developed flow momentum equation (8.7), close enough to the wall (i.e., such that $y \ll r_0$), the turbulent flow is one of constant τ_{app}. For this reason, the mixing length analysis that produced the law of the wall (7.41) for boundary layer flow could be applied here as well, with the understanding that it breaks down near the pipe centerline, where τ_{app} is no longer approximately equal to τ_0. It is found that the broken-line velocity distribution represented by eqs. (7.37) and (7.41) (with $A \cong 2.5$ and $B \cong 5.5$) fits measurements sufficiently well. One drawback of the $\tau_{app} \cong \tau_0$ approximation of eq. (8.7) is that it produces a velocity profile with a finite slope at the pipe centerline,

$$\left(\frac{du^+}{dy^+}\right)_{y=r_0} = 2.5 \frac{\nu}{r_0(\tau_0/\rho)^{1/2}} \tag{8.8}$$

An empirical velocity profile with zero slope at the centerline is [2]

$$u^+ = 2.5 \ln\left[\frac{3(1 + r/r_0)}{2[1 + 2(r/r_0)^2]}y^+\right] + 5.5 \tag{8.9}$$

This profile is identical to the law of the wall (7.41) in the limit $y^+ \rightarrow 0$. Evidence that supports a power law profile, rather than the logarithmic law, has been reviewed by Barenblatt et al. [3].

8.2   FRICTION FACTOR AND PRESSURE DROP

To each analytical expression that fits the measured velocity distribution corresponds a certain formula for τ_0, the friction factor

$$f = \frac{\tau_0}{\frac{1}{2}\rho U^2} \tag{8.10}$$

As in all duct flow problems, the role of velocity scale U is played by the velocity averaged over the duct cross section; in the geometry of Fig. 8.1, the average velocity is

$$U = \frac{1}{\pi r_0^2}\int_0^{2\pi}\int_0^{r_0} \bar{u}r\,dr\,d\theta \tag{8.11}$$

To illustrate the analytical derivation of a friction factor formula, consider Prandtl's one-seventh power law (7.56) under the assumption that it holds all the way to the pipe centerline ($\bar{u} = U_c$, $y = r_0$):

$$\frac{U_c}{(\tau_0/\rho)^{1/2}} \cong 8.7 \left[\frac{r_0(\tau_0/\rho)^{1/2}}{\nu} \right]^{1/7} \tag{8.12}$$

Noting that the f definition (8.10) implies that $(\tau_0/\rho)^{1/2} = U(f/2)^{1/2}$ and that eq. (8.11) provides the needed relationship between the centerline velocity U_c and the average velocity U (namely, $U_c/U = 120/98$), the friction factor formula derived from eq. (8.12) is

$$f \cong 0.078\mathrm{Re}_D^{-1/4} \tag{8.13}$$

In this notation, Re_D is the Reynolds number based on average velocity and pipe diameter, $D = 2r_0$. Formula (8.13) agrees well with measurements for Re_D values up to 80,000 [4]; this formula is nearly identical to the one proposed by Blasius in 1913, $f \cong 0.0791\mathrm{Re}_D^{-1/4}$ [5]. An empirical relation that holds at higher Reynolds numbers in smooth tubes (Fig. 8.2) is

$$f \cong 0.046\mathrm{Re}_D^{-1/5}, \qquad 2 \times 10^4 < \mathrm{Re}_D < 10^6 \tag{8.14}$$

An alternative formula that has wider applicability is obtained working with the law of the wall, $u^+ = 2.5 \ln y^+ + 5.5$ [eq. (7.41)] instead of the one-seventh power law. The result is [4]

$$\frac{1}{f^{1/2}} = 1.737 \ln[\mathrm{Re}_D f^{1/2}] - 0.396 \tag{8.15}$$

which agrees with measurements for Re_D values of up to $O(10^6)$. The heat transfer literature refers to eq. (8.15) as the Kármán–Nikuradse relation; this relation is displayed as the lowest curve in Fig. 8.2. The figure shows that regardless of the Reynolds number, the friction factor in turbulent flow is considerably greater than that in laminar flow in the *hypothetical case* that the laminar regime can exist at such large Reynolds numbers. The same observation can be made in connection with the local skin friction coefficient $C_{f,x}$ displayed in Fig. 7.6.

The fact that for the same Reynolds number, the values of f and $C_{f,x}$ in turbulent flow are greater than their counterparts in imaginary laminar flow might tempt the student to think that turbulent flows are more viscid than laminar flows. This thought would be in grave error: As pointed out in Chapter 6, if there exists a ''viscid'' flow, that can only be the laminar flow (i.e., the flow that is thoroughly penetrated by the viscous shear forces emitted by its confining walls). The friction factor is greater in turbulent flow than in the imaginary laminar case because in turbulent flow, the shear flow is a sequence of laminar shear layers (tips of laminar boundary layers, Fig. 7.5) the thicknesses of which are much

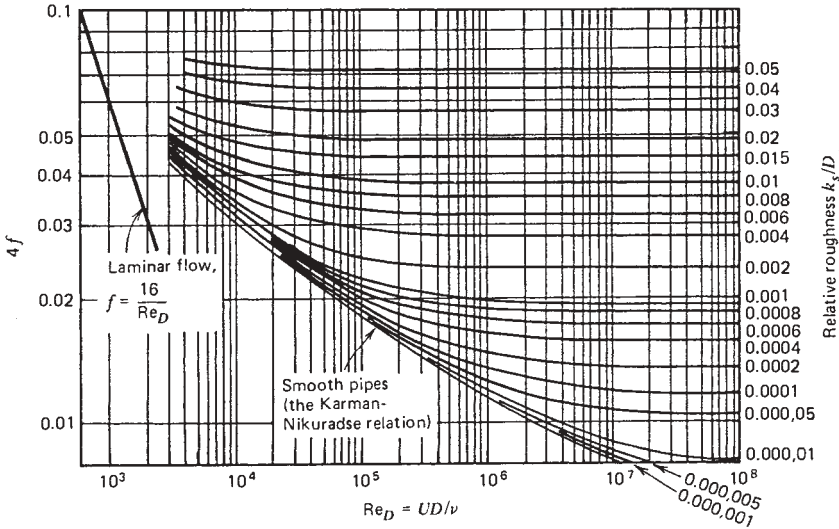| Surface condition	k_s [mm]		
Riveted steel	0.9-9	Asphalted cast iron	0.12
Concrete	0.3-3	Commercial steel or	
Wood stave	0.18-0.9	Wrought iron	0.05
Cast iron	0.26	Drawn tubing	0.0015
Galvanized iron	0.15		

Figure 8.2   Friction factor for duct flow. (After Ref. 6.)

smaller than the pipe radius (i.e., much smaller than the shear layer thickness in the imagined laminar flow).

The jump exhibited by both f and $C_{f,x}$ across the laminar–turbulent transition (Figs. 7.6 and 8.2) says something about the nature of the turbulent flow in the vicinity of each laminar contact region. If the duct flow is in the Re_D range that makes the transition possible and if turbulence occurs in one isolated region on the wall, the flow has the tendency to redistribute itself so as to go around the turbulent spot. This effect is due to a greater resistance to flow through the turbulent region than through the remaining laminar region, as both regions are subjected to the same driving pressure gradient. This ''tendency'' is the constructal law of design for flow access, or optimal distribution of imperfection, where *imperfection* is a thermodynamics term that in this case means resistance to flow.

The same flow redistribution effect is a well-known problem that causes the clogging of parallel heat exchanger tubes (the more fouled a tube, the slower the flow through it, hence the greater its fouling tendency; the opposite feedback mechanism works in the parallel tube that has to make up the flow rate lost in the fouled tube). Closer to home, the imbalance of flow through two parallel ducts is why we breathe through one nostril most of the time! This phenomenon

was studied for flows between one point and a large number of points, with the conclusion that the ''maldistribution'' of channels gives birth to dendritic flow structures [7]. The role of nonuniformly distributed (dendritic) flow arrangements for heat exchanger design, as opposed to uniformly distributed arrangements (e.g., parallel tubes), is discussed in Ref. 8.

Each spot of direct contact between wall and outer fluid (Fig. 7.5) is a region of *three-dimensional flow*, as the surrounding fluid must go around what it perceives as a region of relatively higher resistance. This is illustrated with greater clarity by the photograph of the transition to turbulence in a water rivulet sandwiched between two glass plates [9] (Fig. 8.3). The laminar straight portion is a strand of the Hagen–Poiseuille flow that would have filled the entire parallel-plate channel; this strand shows that whenever a turbulent region develops, the flow seeks ways to go around this region (note that the Reynolds number based on gap thickness is about 2000, in agreement with Table 6.1).

For fully developed flow through ducts with cross sections other than round, the Kármán–Nikuradse relation (8.15) still holds if Re_D is replaced by the Reynolds

(a)   (b)   (c)
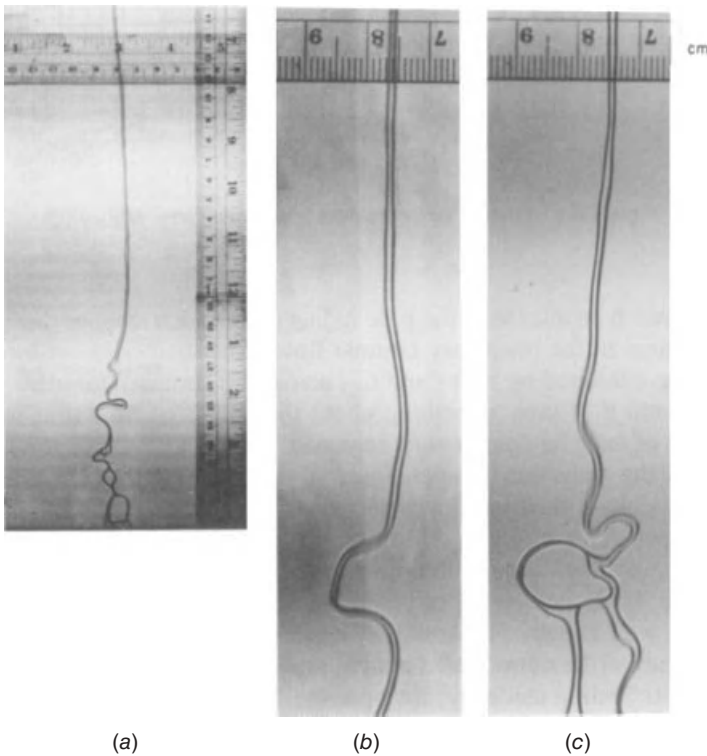
Figure 8.3 Transition to turbulence in Hagen-Poiseuille water rivulet flow between two transparent plates: (a) overall view; (b, c) closeups of the transition zone. Plate-to-plate spacing $= 1.45$ mm, volumetric flow rate $= 1.35$ ml/s, transition Reynolds number based on mean velocity and spacing $= 1950$. (From Ref. 9.)

number based on hydraulic diameter, Re_{D_h}. Note that for a duct of noncircular cross section, the time-averaged τ_0 is not uniform around the periphery of the cross section; hence, in definition (8.10), τ_0 is the perimeter-averaged wall shear stress.

An important feature that must be taken into account in the calculation of pressure drop in turbulent flow through a straight duct is the wall roughness. Experimentally, it is found that the performance of commercial surfaces that do not feel rough to the touch departs from the performance of well-polished surfaces. This effect is due to the very small thickness acquired by the laminar sublayer in many applications [e.g., since $U_\infty y_{VSL}/\nu$ is of order 10^2, i.e., $y_{VSL}^+ = O(10)$, in water flow through a pipe with $U \sim 10$ m/s and $\nu \sim 0.01$ cm^2/s, y_{VSL} is approximately 0.01 mm!]. Consequently, even slight imperfections of the surface interfere with the natural formation of the laminar shear flow contact spots sketched in Figs. 7.5 and 7.7. If the surface irregularities are taller than y_{VSL}, these ''mountains'' alone will rule the friction process by which, on the one hand, the flow exerts a force on the wall and, on the other, the wall generates eddies that slow the flow in a boundary layer.

Nikuradse [10] measured the effect of surface roughness on the friction factor by coating the inside surface of pipes with sand of definite grain size glued as tightly as possible to the wall. If k_s is the grain size in Nikuradse's sand roughness, the friction factor *fully rough limit* is given by

$$f \cong \left(1.74 \ln \frac{D}{k_s} + 2.28 \right)^{-2} \tag{8.16}$$

The fully rough limit is the regime where the roughness size exceeds the order of magnitude of what would have been the laminar sublayer in time-averaged turbulent flow over a smooth surface,

$$k_s^+ = \frac{k_s(\tau_0/\rho)^{1/2}}{\nu} > O(10) \tag{8.17}$$

The roughness effect described by Nikuradse is illustrated by the upper curves on the Moody chart (Fig. 8.2).

Moody's chart [6] is reproduced in Fig. 8.2 for two reasons. First, it represents a very useful tool for calculating pressure drop in many applications involving diverse flow regimes, duct cross sections, and roughness conditions. Second, Moody's chart shines as an example of the importance of investing creativity into the *graphic reporting of technical information*. Moody is not the one who discovered the duct friction information projected on the chart that bears his name; these discoveries are mainly the work of Nikuradse. Moody compiled what was known in the 1940s (e.g., Nikuradse's experiments [10] and the analyses triggered by it [11,12]) and displayed this information on a single chart in terms of easy-to-use dimensionless groups. The graphic presentation of this information eliminated much of the difficulty associated with handling

implicit friction factor formulas on the slide rule. In addition to being very useful, Moody's original chart is also a high-quality drawing: this, I feel, is responsible for the so-frequent reproduction of this drawing in its original form (without even mentioning Nikuradse, unfortunately).

Roughness can be useful: Skin friction can be reduced by using a random arrangement of protuberances [13].

8.3   HEAT TRANSFER COEFFICIENT

The heat transfer potential of turbulent pipe flow may be deduced from the friction factor information discussed above by adopting further simplifying assumptions. Rewrite the energy equation (8.3) for fully developed flow:

$$\rho c_P \bar{u} \frac{\partial \overline{T}}{\partial x} = \frac{1}{r} \frac{\partial}{\partial r}(r q''_{\text{app}}) \tag{8.18}$$

and then integrate it from 0 to r and from 0 to r_0:

$$\int_0^r \rho c_P \bar{u} \frac{\partial \overline{T}}{\partial x} r\, dr = r q''_{\text{app}} \tag{8.19}$$

$$\int_0^{r_0} \rho c_P \bar{u} \frac{\partial \overline{T}}{\partial x} r\, dr = r_0 q''_0 \tag{8.20}$$

Dividing eqs. (8.19) and (8.20) side by side and using the distribution of τ_{app} (8.7) as a guide, we obtain [14]

$$\frac{q''_{\text{app}}}{q''_0} = M\left(1 - \frac{y}{r_0}\right) \tag{8.21}$$

where

$$M = \frac{\frac{2}{r^2} \int_0^r \bar{u} \frac{\partial \overline{T}}{\partial x} r\, dr}{\frac{2}{r_0^2} \int_0^{r_0} \bar{u} \frac{\partial \overline{T}}{\partial x} r\, dr} \tag{8.22}$$

In particular, if the pipe is heated with x-independent heat flux, the longitudinal temperature gradient $\partial \overline{T}/\partial x$ is independent of r; hence,

$$M = \frac{\frac{2}{r^2} \int_0^r \bar{u} r\, dr}{\frac{2}{r_0^2} \int_0^{r_0} \bar{u} r\, dr} \tag{8.23}$$

Function M is the ratio of $\bar{u}$ averaged over a round cross section of radius r divided by $\bar{u}$ averaged over the entire pipe cross section. Because the pipe velocity profile $\bar{u}$ resembles the slug profile (the laminar sublayer is one or two orders of magnitude thinner than the pipe radius), in many practical cases, M is approximately equal to 1, while not a strong function of r. Therefore, an acceptable approximation for the distribution of apparent heat flux over the pipe cross section is

$$\frac{q''_{\text{app}}}{q''_0} \cong 1 - \frac{y}{r_0} \tag{8.24}$$

In conclusion, the apparent heat flux follows a distribution that is practically the same as the one followed by the apparent shear stress. This observation is the starting point in an analysis that ties the Stanton number to the friction factor information presented earlier in this section. The following analysis was first reported by Prandtl in 1910 (more detailed accounts of this analysis may be found in Ref. 4, pp. 403–407, and Ref. 15, pp. 494–496). Dividing eqs. (8.6) and (8.24) and recognizing the definitions of q''_{app} and τ_{app} yields

$$\frac{\nu + \epsilon_M}{\tau_0} d\bar{u} = \frac{c_P(\alpha + \epsilon_H)}{-q''_0} d\bar{T} \tag{8.25}$$

Now, imagine that the pipe cross section is composed of two distinct regions: an annular region near the wall ($0 < y < y_1$) where $\nu \gg \epsilon_M$ and $\alpha \gg \epsilon_H$ and a disk-shaped region in the center ($y_1 < y < r_0$) where $\nu \ll \epsilon_M$ and $\alpha \ll \epsilon_H$. Integrating eq. (8.25) from $y = 0$ to $y = y_1$, neglecting both ϵ_M and ϵ_H, we obtain

$$\frac{\nu}{\tau_0}\bar{u}_1 = \frac{c_P\alpha}{-q''_0}(\bar{T}_1 - T_0) \tag{8.26}$$

where $\bar{u}_1$ and $\bar{T}_1$ are the time-averaged quantities at $y = y_1$. Next, we integrate eq. (8.25) from $y = y_1$ to $y = y_2$, where y_2 is chosen in such a way that $\bar{T}(y_2)$ is equal to the *mean* temperature T_m and $\bar{u}(y_2)$ is *approximately* the same as the mean velocity U; the result of this second integration is

$$\frac{\epsilon_M}{\tau_0}(U - \bar{u}_1) = \frac{c_P\epsilon_H}{-q''_0}(\bar{T}_m - \bar{T}_1) \tag{8.27}$$

Eliminating $\bar{T}_1$ between eqs. (8.26) and (8.27) and using the definitions of friction factor $\tau_0 / \left(\frac{1}{2}\rho U^2\right)$ and Stanton number $h/(\rho c_P U)$, we find that

$$\text{St} = \frac{f/2}{\text{Pr}_t + (\bar{u}_1/U)(\text{Pr} - \text{Pr}_t)} \tag{8.28}$$

As in the case of turbulent boundary layers, the Stanton numbers turn out to be proportional to the dimensionless wall shear stress, $f/2$ in this case. The

proportionality factor in this relation is a function of the Prandtl number and two more parameters (Pr_t, $\bar{u}_1/U$) that have to be adjusted empirically. Prandtl's formula (8.28) agrees with the measurements involving fluids with Prandtl numbers greater than 0.5 if $Pr_t = \epsilon_M/\epsilon_H$ is taken as unity and $\bar{u}_1/U$ is replaced by Hofmann's empirical correlation $\bar{u}_1/U \cong 1.5Re_D^{-1/8} Pr^{-1/6}$ [16].

More consistent agreement with measurements is registered by Colburn's [17] empirical correlation:

$$St\, Pr^{2/3} \cong \frac{f}{2} \tag{8.29}$$

This formula is analytically the same as the one encountered in boundary layer flow, eq. (7.78). Its success further supports the validity of the theoretical argument used to deduce eqs. (7.85)–(7.90).

The Colburn analogy (8.29) holds for $Pr \gtrsim 0.5$ and is to be used in conjunction with the Moody chart (Fig. 8.2), which supplies the value of the friction factor. It applies to ducts of various cross-sectional shapes, with wall surfaces having various degrees of roughness. For example, in the special case of a pipe with smooth internal surface, we can combine eq. (8.29) with eq. (8.14) to derive the Nusselt number formula

$$Nu_D = \frac{hD}{k} = 0.023Re_D^{4/5}\, Pr^{1/3} \tag{8.30}$$

which, in accordance with eq. (8.14), holds for $2 \times 10^4 < Re_D < 10^6$.

There are many formulas that in one way or another improve on the accuracy with which eq. (8.30) predicts actual measurements. A review of these formulas has been published by Bhatti and Shah [18]. The most popular formula is a correlation due to Dittus and Boelter [19],

$$Nu_D = 0.023Re_D^{4/5}\, Pr^n \tag{8.31}$$

which was developed for $0.7 \le Pr \le 120$, $2500 \le Re_D \le 1.24 \times 10^5$, and $L/D > 60$. The Prandtl number exponent is $n = 0.4$ when the fluid is being heated ($T_0 > T_m$), and $n = 0.3$ when the fluid is being cooled ($T_0 < T_m$). All the physical properties needed for the calculation of Nu_D, Re_D, and Pr are to be evaluated at the bulk temperature T_m. The maximum deviation between experimental data and values predicted using eq. (8.31) is on the order of 40 percent.

For applications in which temperature influence on properties is significant, recommended is Sieder and Tate's [20] modification of eq. (8.30),

$$Nu_D = 0.027Re_D^{4/5}\, Pr^{1/3}\left(\frac{\mu}{\mu_0}\right)^{0.14} \tag{8.32}$$

which is valid for $0.7 < Pr < 16{,}700$ and $Re_D > 10^4$. The effect of temperature-dependent properties is taken into account by evaluating all the properties

(except μ_0) at the mean temperature of the stream, T_m. The viscosity μ_0 is evaluated at the wall temperature, $\mu_0 = \mu(T_0)$.

The most accurate of the correlations of type (8.30)–(8.32) is a formula due to Gnielinski [21]:

$$Nu_D = \frac{(f/2)(Re_D - 10^3)Pr}{1 + 12.7\,(f/2)^{1/2}(Pr^{2/3} - 1)} \tag{8.33}$$

in which the friction factor is supplied by Fig. 8.2. It is accurate within $\pm 10\%$ in the range $0.5 < Pr < 10^6$ and $2300 < Re_D < 5 \times 10^6$. Like eqs. (8.30)–(8.32), the Gnielinski correlation (8.33) can be used in both constant-q_0'' and constant-T_0 applications. Two simpler alternatives to eq. (8.33) are [21]

$$Nu_D = \begin{cases} 0.0214\left(Re_D^{0.8} - 100\right)Pr^{0.4} & \begin{aligned}&(0.5 \le Pr \le 1.5, \\ &10^4 \le Re_D \le 5 \times 10^6)\end{aligned} & (8.34) \\[2ex] 0.012(Re_D^{0.87} - 280)Pr^{0.4} & \begin{aligned}&(1.5 \le Pr \le 500, \\ &3 \times 10^3 \le Re_D \le 10^6)\end{aligned} & (8.35) \end{cases}$$

The preceding results refer to gases and liquids, that is, to the range $Pr \gtrsim 0.5$. For liquid metals, the most accurate formulas are those of Notter and Sleicher [22]:

$$Nu_D = \begin{cases} 6.3 + 0.0167Re_D^{0.85}\,Pr^{0.93} & (q_0'' = \text{constant}) & (8.36) \\[1ex] 4.8 + 0.0156Re_D^{0.85}\,Pr^{0.93} & (T_0 = \text{constant}) & (8.37) \end{cases}$$

These are valid for $0.004 < Pr < 0.1$ and $10^4 < Re_D < 10^6$ and are based on both computational and experimental data. All the properties used in eqs. (8.36)–(8.37) are evaluated at the mean temperature T_m.

One peculiarity of the mean temperature of the stream is that it varies with the position along the duct, $T_m(x)$. This variation is linear in the case of constant-q_0'' and exponential when the duct wall is isothermal (review Figs. 3.9 and 3.10). In order to simplify the recommended evaluation of the physical properties at the T_m temperature, it is convenient to choose as representative mean temperature the average value

$$T_m = \tfrac{1}{2}(T_{in} + T_{out}) \tag{8.38}$$

In this definition, T_{in} and T_{out} are the bulk temperatures of the stream at the duct inlet and outlet, respectively (Fig. 8.4).

In closing, note that the high-Re_D limit of the liquid metals correlation (8.36) can be combined with eq. (8.14) to yield

$$\frac{St}{(f/2)^{1/2}} \cong (0.11Re_D^{-0.05})Pr^{-0.07} \tag{8.39}$$

In the Re_D range 10^4–10^6, the right-hand side of this equation is equal to a number of order 10^{-1} times a function that decreases with increasing Pr. This
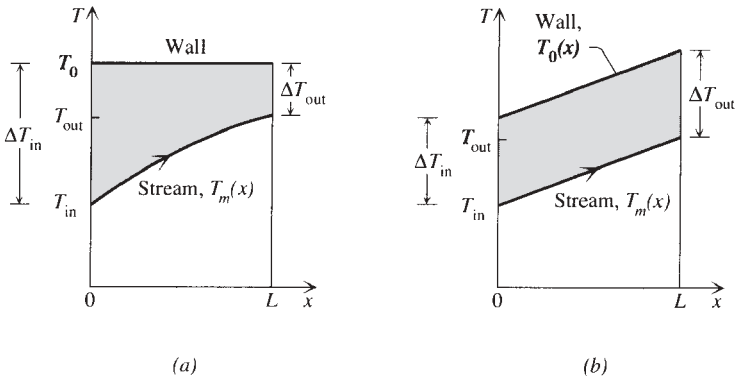
Figure 8.4   Temperature distributions along the duct: (*a*) isothermal wall; (*b*) wall with uniform heat flux.

result confirms the scaling law proposed on purely theoretical grounds in eq. (7.99). The fact that the Pr exponent in eq. (8.39) is not as large as in eq. (7.99) does not necessarily spell disagreement, considering the narrow Pr range on which the experimental correlation (8.36) is based.

8.4   TOTAL HEAT TRANSFER RATE

A primary objective of Chapter 3 and Section 8.3 has been the evaluation of the heat transfer coefficient between the duct wall and the stream. We learned, for example, that in *fully developed* laminar and turbulent duct flows, h is independent of longitudinal position. The heat transfer coefficient is essential in calculation of the *total* heat transfer rate $q(W)$ that is received by the stream as it travels the entire length of the duct, L. The heat transfer rate q is proportional to the h constant, the total duct surface swept by the stream ($A_w = pL$), and an effective temperature difference that is labeled ΔT_{lm} which is determined next:

$$q = hA_w \, \Delta T_{lm} \tag{8.40}$$

8.4.1   Isothermal Wall

The magnitude of the effective temperature difference ΔT_{lm} depends on how the actual wall–stream temperature difference varies along the duct, $T_0(x) - T_m(x)$. Consider first the case where the wall temperature T_0 is constant, as shown in Fig. 8.4*a*. In fully developed laminar or turbulent flow, the temperature difference

$$\Delta T = T_0 - T_m \tag{8.41}$$

decreases exponentially in the downstream direction, from a value at the duct inlet to a value at the outlet,

$$\Delta T_{\text{in}} = T_0 - T_{\text{in}}, \qquad \Delta T_{\text{out}} = T_0 - T_{\text{out}} \qquad (8.42)$$

The effective temperature difference ΔT_{lm} falls somewhere between the extremes ΔT_{in} and ΔT_{out}. Its value can be determined by deriving the q formula (8.40) based on thermodynamic analysis. For the stream viewed as an elongated control volume, the total heat transfer rate through the duct wall is

$$q = \dot{m}c_P(T_{\text{out}} - T_{\text{in}}) \qquad (8.43)$$

Figure 8.4a shows that the bulk temperature excursion $(T_{\text{out}} - T_{\text{in}})$ is the same as the difference $(\Delta T_{\text{in}} - \Delta T_{\text{out}})$; therefore, an alternative to eq. (8.43) is

$$q = \dot{m}c_P(\Delta T_{\text{in}} - \Delta T_{\text{out}}) \qquad (8.44)$$

It remains to determine the relationship between the heat capacity flow rate $\dot{m}c_P$ and the group hA_w that appears on the right side of eq. (8.40). For this, we use eq. (3.39), in which $p = 2\pi r_0, A = \pi r_0^2$, and $q_0'' = h(T_0 - T_m)$; therefore,

$$\frac{dT_m}{T_0 - T_m} = \frac{hp}{A\rho c_P U}dx \qquad (8.45)$$

Assuming constant A, p, and c_P, we integrate eq. (8.45) from the inlet ($T_m = T_{\text{in}}$ at $x = 0$) all the way to the outlet ($T_m = T_{\text{out}}$ at $x = L$) and obtain

$$\ln\frac{T_0 - T_{\text{in}}}{T_0 - T_{\text{out}}} = \frac{hpL}{\rho AUc_P} \qquad (8.46)$$

In this equation we recognize the inlet and outlet temperature differences (8.42), the mass flow rate $\rho AU = \dot{m}$, and the total duct wall area $pL = A_w$; therefore, an alternative form of eq. (8.46) is

$$\ln\frac{\Delta T_{\text{in}}}{\Delta T_{\text{out}}} = \frac{hA_w}{\dot{m}c_P} \qquad (8.47)$$

The proper definition of the ΔT_{lm} factor adopted in eq. (8.40) emerges as we eliminate $\dot{m}c_P$ between eqs. (8.47) and (8.44),

$$q = hA_w\frac{\Delta T_{\text{in}} - \Delta T_{\text{out}}}{\ln(\Delta T_{\text{in}}/\Delta T_{\text{out}})} \qquad (8.48)$$

In other words,

$$\Delta T_{lm} = \frac{\Delta T_{\text{in}} - \Delta T_{\text{out}}}{\ln(\Delta T_{\text{in}}/\Delta T_{\text{out}})} \qquad (8.49)$$

The ΔT_{lm} factor is recognized as the *log-mean temperature difference* between the wall and the stream. When the wall and inlet temperatures are specified, eq. (8.48) expresses the relationships among the total heat transfer rate q, the total duct surface conductance hA_w, and the outlet temperature of the stream. Alternatively, eqs. (8.47)–(8.49) can be combined to express the total heat transfer rate in terms of the inlet temperatures, mass flow rate, and duct surface conductance,

$$q = \dot{m}c_P \, \Delta T_{in} \left[1 - \exp\left(-\frac{hA_w}{\dot{m}c_P}\right) \right] \qquad (8.50)$$

In cases where the heat transfer coefficient varies longitudinally, $h(x)$, the h factor on the right side of eqs. (8.46) and (8.47), represents the L-averaged heat transfer coefficient, namely,

$$\bar{h} = \frac{1}{L} \int_0^L h(x) \, dx \qquad (8.51)$$

8.4.2   Uniform Wall Heating

In the analysis of heat exchangers [23], it can be shown that the applicability of eq. (8.48) is considerably more general than what is suggested by Fig. 8.4a. For example, when the heat transfer rate q is distributed uniformly along the duct, the temperature difference ΔT does not vary with the longitudinal position. This case is illustrated in Fig. 8.4b, where it was again assumed that A, p, h, and c_P are independent of x. The effective value ΔT_{lm} is the same as the constant ΔT all along the duct,

$$\Delta T_{lm} = \Delta T_{in} = \Delta T_{out} \qquad (8.52)$$

Equation (8.52) is a special case of eq. (8.49): the limit $\Delta T_{in}/\Delta T_{out} \to 1$.

8.4.3   Time-Dependent Heat Transfer

When the heat transfer is between a single-phase stream ($\dot{m}c_P, T_{in}$) and a wall that belongs to a body with finite heat capacity (liquid or solid, mass m, specific heat c), the stream and wall temperatures vary in time as they approach T_{in}. This scenario is expressible analytically for a model where the wall and the finite-size body are isothermal at a temperature $T_0(t)$ that varies in time from an initial level $T_0(0)$. The wall temperature and fluid outlet temperature histories are

$$\frac{T_0(t) - T_0(0)}{T_{in} - T_0(0)} = 1 - e^{-y\theta} \qquad (8.53)$$

$$\frac{T_{out}(t) - T_0(0)}{T_{in} - T_0(0)} = 1 - y e^{-y\theta} \qquad (8.54)$$

where θ is the dimensionless time

$$\theta = \frac{\dot{m}c_P}{mc}t \tag{8.55}$$

and

$$y = 1 - e^{-N_{tu}}, \quad N_{tu} = \frac{hA_w}{\dot{m}c_P} \tag{8.56}$$

Both T_{out} and T_0 approach T_{in} as t increases. The mechanism captured by eqs. (8.53) – (8.56) rules the processes of sensible-heat energy storage and retrieval when the storage material (m) can be modeled as having a single temperature at a given time.

8.5   MORE REFINED TURBULENCE MODELS

The fundamental feature that distinguishes the analysis of time-averaged turbulent flow from other analyses (laminar flow, Chapters 2–5, 10, 11; porous media, Chapter 12) is the closure problem. Even in relatively simple time-averaged turbulent flows such as the boundary layer near a flat wall or the fully developed flow through a round tube, the number of unknowns exceeded the number of equations.

To proceed with the analysis, the difference between these numbers was made up by introducing additional equations whose validity is supported by a combination of intuitive reasoning and laboratory measurements. Thus, in the case of the flow part of the turbulent convection problem, we relied on Prandtl's mixing length model [eq. (7.32)] to evaluate the unknown called *momentum eddy diffusivity* ϵ_M. Similarly, for the heat transfer part of the convection problem, we assumed a constant value for the turbulent Prandtl number [eq. (7.70)] in order to evaluate the thermal eddy diffusivity ϵ_H. In both cases, ϵ_M and ϵ_H resulted from the assumed algebraic expressions, that is, from *algebraic models* of turbulence. Alternatives to the mixing length model as an algebraic model for ϵ_M are summarized in Table 7.1. Alternatives to writing $\text{Pr}_t \cong 0.9$, constant, as a means of evaluating ϵ_H are reviewed by Reynolds [24].

The main shortcoming of these simple models is their proven lack of universal applicability. For example, a model that works near the wall in turbulent pipe flow breaks down near the pipe centerline [eq. (8.8)]. Also, as shown in Chapter 9, turbulent flow regions situated sufficiently far from solid walls demand eddy diffusivity models that differ from eq. (7.32). The need for a universally applicable turbulence model is obvious; however, the idea that such a model could be invented has been met with varying degrees of difficulty by proponents and users of turbulence models. Due to technological advances in computers during recent decades, the field of heat transfer has witnessed the emergence of a new generation of more powerful turbulence models. The progress in this area

of research has been reviewed in monographs [25, 26]. Below, we illustrate this approach to turbulence modeling by means of the $k - \epsilon$ *model* [27].

The starting point in the $k-\epsilon$ model and other nonalgebraic (one- and two-equation) models is the analogy that can be drawn between the motion of a fluid packet in turbulent flow and the random motion of a molecule in an ideal gas. A classical result in the kinetic theory of gases (a result derived first by Maxwell in 1860 [28]) is that the kinematic viscosity of a gaseous substance may be calculated with the formula $\nu = \frac{1}{3}a\lambda$, where a is the mean speed of the molecule and λ is the mean free-path length. In the case of a fluid packet in turbulent flow, the mean speed scale is $k^{1/2}$, where k is the *turbulence energy*,

$$k = \tfrac{1}{2}[\overline{(u')^2} + \overline{(v')^2} + \overline{(w')^2}] \tag{8.57}$$

Therefore, the momentum eddy diffusivity ϵ_M may be modeled as

$$\epsilon_M = C_\mu k^{1/2} L \tag{8.58}$$

where C_μ is a dimensionless empirical constant, and for the time being, L is an unknown length scale that plays the same role for the fluid packet as the mean free-path length plays for the molecule of a gas. The eddy diffusivity model represented by eq. (8.58) was proposed independently by Kolmogorov [29] and Prandtl [30]. This model says that in order to calculate ϵ_M, that is, in order to close the flow part of the problem, we must determine two more local quantities, k and L. As shown below, these two quantities follow from two more equations: the k-equation and the ϵ-equation.

The k-equation may be derived from the complete momentum equations. The procedure consists of multiplying the x momentum equation (7.13) by u', the y momentum equation by v', and the z momentum equation by w'; time averaging the three equations; and then adding them term by term. From the resulting equation, we subtract the equation obtained by first multiplying the x momentum equation by $\overline{u}$, the y momentum equation by $\overline{v}$, and the z momentum equation by $\overline{w}$, and then time averaging and adding these equations term by term.

A more direct approach is to imagine a control volume in a *slender flow region* [e.g., boundary layer (Fig. 7.5)] and to argue that the convection of k into the control volume (Dk/Dt) equals the eddy diffusion of k in the transversal (y) direction plus the rate of k generation minus the rate of k destruction [31]. Assuming that $\epsilon_M \gg \nu$, the rate of k diffusion in the transversal direction may be written as

$$\frac{\partial}{\partial y}\left(\frac{\epsilon_M}{\sigma_k}\frac{\partial k}{\partial y}\right)$$

where σ_k is a dimensionless empirical constant. The rate of k production can be evaluated by multiplying the eddy shear stress ($\epsilon_M \, \partial\overline{u}/\partial y$) by the time-averaged

velocity gradient $(\partial \bar{u}/\partial y)$,

$$\epsilon_M \left(\frac{\partial \bar{u}}{\partial y} \right)^2 = C_\mu k^{1/2} L \left(\frac{\partial \bar{u}}{\partial y} \right)^2 \tag{8.59}$$

Finally, the rate of k destruction or the *dissipation rate* ϵ may be evaluated by imagining a fluid packet of diameter L oscillating with velocity $k^{1/2}$ in a turbulent flow field. The drag force on this fluid packet is of order $C_D \, \rho L^2 (k^{1/2})^2$, where C_D is a *drag coefficient* approximately equal to 1; the mechanical power dissipated per unit mass is $k^{1/2} C_D \, \rho L^2 (k^{1/2})^2 / \rho L^3 \sim C_D (k^{1/2})^3 / L$; in other words, $\epsilon = C_D k^{3/2}/L$. In conclusion, the k-equation for a boundary layer type of flow region is

$$\underbrace{\frac{Dk}{Dt}}_{\text{Convection}} = \underbrace{\frac{\partial}{\partial y} \left(\frac{\epsilon_M}{\sigma_k} \frac{\partial k}{\partial y} \right)}_{\text{Diffusion}} + \underbrace{\epsilon_M \left(\frac{\partial \bar{u}}{\partial y} \right)^2}_{\text{Generaton}} - \underbrace{\epsilon}_{\text{Destruction}} \tag{8.60}$$

where the dissipation rate ϵ should not be confused with the momentum eddy diffusivity ϵ_M.

The ϵ-equation for a boundary layer type of region may be constructed in a similar manner:

$$\frac{D\epsilon}{Dt} = \frac{\partial}{\partial y} \left(\frac{\epsilon_M}{\sigma_\epsilon} \frac{\partial \epsilon}{\partial y} \right) + C_1 \epsilon_M \left(\frac{\partial \bar{u}}{\partial y} \right)^2 \frac{\epsilon}{k} - C_2 \frac{\epsilon^2}{k} \tag{8.61}$$

where σ_ϵ, C_1, and C_2 are three more dimensionless empirical constants. Finally, setting $C_D = 1$ and eliminating the unknown length scale L between eqs. (8.58) and $\epsilon = C_D k^{3/2}/L$ yield

$$\epsilon_M = C_\mu \frac{k^2}{\epsilon} \tag{8.62}$$

The three equations (8.60)–(8.62) are sufficient for determining the three unknowns (k, ϵ, and ϵ_M). The recommended values for the five empirical constants appearing in these equations are [32] $C_\mu = 0.09, C_1 = 1.44, C_2 = 1.92, \sigma_k = 1$, and $\sigma_\epsilon = 1.3$. These values have been found to be appropriate for the plane jets and plane shear layers discussed in Chapter 9. A nearly identical set of constants works for turbulent boundary layers; hence, it is reasonable to expect the foregoing constants to adequately serve the numerical simulation of boundary layers as well.

To solve the heat transfer part of the problem, the most common approach is to combine the ϵ_M calculation above with the statement that the turbulent Prandtl number ϵ_M/ϵ_H is equal to 0.9.

It is instructive to look back at the mixing length model used throughout Chapters 7 and 8 and to see if there is any overlap between that model and

the $k-\epsilon$ model of eqs. (8.60)–(8.62). According to the mixing length model [eq. (7.30)], we can write

$$\left(\frac{\partial \bar{u}}{\partial y}\right)^2 = \frac{\epsilon_M^2}{l^4} \tag{8.63}$$

where l is the mixing length. This means that the k-generation term in the k-equation (8.58) assumes the form

$$\epsilon_M \left(\frac{\partial \bar{u}}{\partial y}\right)^2 = \frac{\epsilon_M^3}{l^4} = C_\mu^3 k^{3/2} \frac{L^3}{l^4} = \frac{C_\mu^3}{C_D}\left(\frac{L}{l}\right)^4 \epsilon \tag{8.64}$$

which shows that the k-generation term equals the k-destruction term ϵ if the length scale L is taken as

$$L = l\left(\frac{C_D}{C_\mu^3}\right)^{1/4} \tag{8.65}$$

We conclude that in the inner region of a turbulent boundary layer (i.e., in the layer where the mixing length model works), the generation of k is balanced by the dissipation of k. For this reason, the inner layer is referred to as the *equilibrium layer*. In general, a given turbulent flow region is the space for competition among four effects: convection, diffusion, generation, and destruction, as indicated by eq. (8.60).

The $k-\epsilon$ model outlined above is valid only in flow regions that are strongly turbulent, that is, in regions where the eddy diffusivity ϵ_M overwhelms the molecular diffusivity ν. This limitation is illustrated by the construction of the diffusion terms in eqs. (8.60) and (8.61). In the case of turbulent boundary layer flow or fully developed turbulent flow through a duct, eqs. (8.60)–(8.61) do not apply in the viscous sublayer.

One way to bridge the viscous sublayer and to impose the solid-wall boundary condition on the $k-\epsilon$ simulation of the strongly turbulent regions is the *wall-function method*. Let y_c be the physical distance to the solid wall from a point situated just outside the viscous sublayer, where the logarithmic law of the wall holds (Fig. 7.4). The wall-function approach consists of the assumption that at $y = y_c$, the velocity component parallel to the wall obeys the logarithmic law of the wall [eq. (7.40)],

$$\frac{\bar{u}_c}{u_*} = \frac{1}{\kappa}\ln\left(\frac{u_* y_c}{\nu}\right) + B \tag{8.66}$$

and that at the same location, the generation of k is in equilibrium with the destruction of k. If k_c and ϵ_c are the turbulence energy and dissipation rate at $y = y_c$, it can be shown [33] that the conditions imposed on eqs. (8.60) and (8.61) in lieu of solid-wall boundary conditions are $k_c = u_*^2/C_\mu^{1/2}$ and $\epsilon_c = u_*^3/(\kappa y_c)$. For further instructions on the numerical implementation of the $k-\epsilon$ model, the reader is directed to Refs. 25, 26, 32, and 33.

8.6 HEATLINES IN TURBULENT FLOW NEAR A WALL

In the second edition of this book it was reported that the time-averaged solution for heat transfer from a plane wall with turbulent flow can also be visualized by using heatlines. With reference to the coordinates shown in Fig. 2.1, the boundary layer–approximated energy equation is

$$\bar{u}\frac{\partial \bar{T}}{\partial x} + \bar{v}\frac{\partial \bar{T}}{\partial y} = \frac{\partial}{\partial y}\left[(\alpha + \epsilon_H)\frac{\partial \bar{T}}{\partial y}\right] \tag{8.67}$$

The heatfunction $\bar{H}(x, y)$ that satisfies eq. (8.67) identically is defined by

$$\frac{\partial \bar{H}}{\partial y} = \rho c_P \bar{u}(\bar{T} - T_{\text{ref}}) \tag{8.68}$$

$$-\frac{\partial \bar{H}}{\partial x} = \rho c_P \bar{v}(\bar{T} - T_{\text{ref}}) - (k + \rho c_P \epsilon_H)\frac{\partial \bar{T}}{\partial y} \tag{8.69}$$

with the observation that in eq. (8.69), the apparent heat flux $q''_{\text{app}} = -(k + \rho c_P \epsilon_H)\partial \bar{T}/\partial y$ can be replaced with the wall heat flux, $q''_{\text{app}} = q''_0(x)$. The heatfunction is obtained by integrating eqs. (8.68) and (8.69), for which we need $\bar{u}, \bar{v}, \bar{T}$, and q''_0. Analytical expressions for $\bar{u}(x, y)$ and $\bar{v}(x, y)$ are obtained by assuming that Prandtl's one-seventh power curve fit, eq. (7.56), is a good approximation:

$$\frac{\bar{u}}{u_*} = 8.7\left(\frac{u_* y}{\nu}\right)^{1/7} \tag{8.70}$$

where $u_* = (\tau_0/\rho)^{1/2}$ and $\tau_0(x)$ is the wall shear stress based on eq. (8.70), namely, eq. (7.60). Combining u_* with eq. (8.70), we obtain

$$\frac{\bar{u}}{U_\infty} = 1.164\left(\frac{U_\infty x}{\nu}\right)^{-8/70}\left(\frac{U_\infty y}{\nu}\right)^{1/7} \tag{8.71}$$

The corresponding $\bar{v}(x, y)$ expression follows from integrating the mass conservation equation (7.20),

$$\frac{\bar{v}}{U_\infty} = 0.116\left(\frac{U_\infty x}{\nu}\right)^{-78/70}\left(\frac{U_\infty y}{\nu}\right)^{8/7} \tag{8.72}$$

To obtain a simple analytical expression for $\bar{T}(x, y)$, we make the classical assumption that $\epsilon_M = \epsilon_H$ or $\text{Pr}_t = 1$. If, in addition, the fluid has a Prandtl number of order 1, we may write $\text{Pr} = 1$ such that in wall coordinates, we have $T^+(y^+) = u^+(y^+)$, or after using eq. (8.70),

$$[T_0(x) - \bar{T}]\frac{\rho c_P u_*}{q''_0(x)} = 8.7\left(\frac{u_* y}{\nu}\right)^{1/7} \tag{8.73}$$

Combining eq. (7.60) and the Colburn analogy [eq. (7.78) for Pr $= 1$], we obtain an estimate for the local heat transfer coefficient,

$$\frac{q_0''/(T_0 - T_\infty)}{\rho c_P U_\infty} = 0.0296 \left(\frac{U_\infty x}{\nu} \right)^{-1/5} \tag{8.74}$$

When the wall is isothermal ($T_0 = $ constant) and warmer than the free stream ($T_{ref} = T_\infty$), the integration of eqs. (8.68)–(8.69) by using eqs. (8.71)–(8.74) yields

$$\frac{\overline{H}}{k(T_0 - T_\infty)Re_L^{4/5}} = 1.015 \, \widetilde{x}^{-8/70} \, \widetilde{y}^{8/7} - 1.054 \, \widetilde{x}^{-16/70} \, \widetilde{y}^{9/7} - 0.037 \, \widetilde{x}^{4/5} \tag{8.75}$$

where $\widetilde{x} = x/L$ and $\widetilde{y} = (y/L)Re_L^{1/5}$. Equation (8.75) is obtained if eq. (8.68) is integrated first and eq. (8.69) second. If the order of integration is reversed, the coefficient 1.054 on the right side of eq. (8.75) is replaced by 0.591. This small discrepancy is due to the fact that the assumed $\overline{u}$ profile (8.70) is an approximation. Figure 8.5 shows the heatlines based on eq. (8.75). This figure can be compared with Fig. 2.16 to see the differences between the heatlines of the turbulent flow and the laminar flow. That the heatlines are inclined as they come out of the wall in Fig. 8.5 illustrates the high velocity ($\overline{u} \sim U_\infty$) that occurs close to the wall when the flow is turbulent.
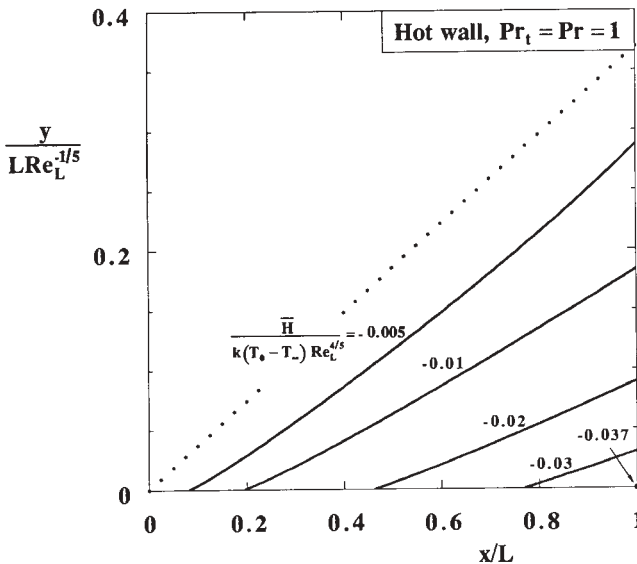
Figure 8.5   Heatlines near a hot isothermal wall with turbulent flow. (Drawn by A. M. Morega.)
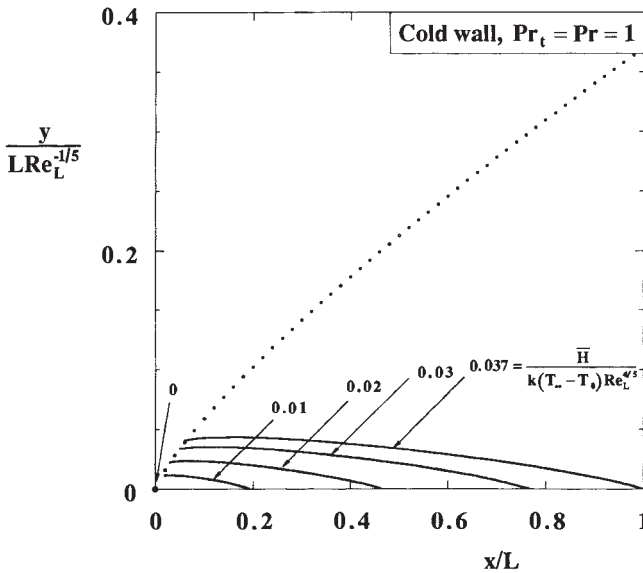
Figure 8.6 Heatlines near a cold isothermal wall with turbulent flow. (Drawn by A. M. Morega.)

The corresponding heatline pattern for the cold isothermal wall with turbulent boundary layer flow is shown in Fig. 8.6. This is based on setting $T_{\mathrm{ref}} = T_0$ and integrating eq. (8.68) before eq. (8.69), which yields

$$\frac{\overline{H}}{k(T_\infty - T_0)\mathrm{Re}_L^{4/5}} = 1.054\,\tilde{x}^{-16/70}\,\tilde{y}^{9/7} + 0.037\,\tilde{x}^{4/5} \qquad (8.76)$$

If eq. (8.69) is integrated before eq. (8.68), the coefficient 1.054 is again replaced by 0.591. The heatline pattern of Fig. 8.6 has some of the features seen in laminar flow (Fig. 2.15), except that the heatlines are straighter and enter the cold wall at an angle. The dotted lines in Figs. 8.5 and 8.6 show the thickness of the boundary layer according to eq. (7.58).

8.7 CHANNEL SPACINGS FOR TURBULENT FLOW

The packing of channels into a fixed volume, which in Section 3.14 was outlined for laminar duct flow, can be pursued based on the same method when the flow is turbulent [34]. With reference to the notation defined in Fig. 3.17, where the dimension perpendicular to the figure is W, the analysis consists of intersecting the two asymptotes of the design: a few wide spaces with turbulent boundary layers and many narrow channels with fully developed turbulent flow. The plate

thickness (t) is not negligible with respect to the spacing D. When $Pr \geq 0.5$, the optimal spacing and maximal global conductance of the *HWL* package are

$$\frac{D_{opt}/L}{(1 + t/D_{opt})^{4/11}} = 0.071 \, Pr^{-5/11} \, Be^{-1/11} \tag{8.77}$$

and

$$\left[\frac{q'L}{kH\left(T_{max} - T_\infty\right)}\right]_{max} \leq 0.57 Pr^{4/99}\left(1 + \frac{t}{D_{opt}}\right)^{-67/99} Be^{47/99} \tag{8.78}$$

where $Be = (\Delta P \, L^2)/\mu\alpha$. These results are valid in the range $10^4 \leq Re_{D_h} \leq 10^6$ and $10^6 \leq Re_L \leq 10^8$, which can be shown to correspond to the pressure drop number range $10^{11} \leq Be \leq 10^{16}$.

The literature on turbulent heat transfer in ducts and other enclosed spaces is vast [35–37]. For example, in the electronics cooling field, turbulent flows have been studied numerically and experimentally with application to the cooling of walls with discrete heat sources [38–40]. Noteworthy also is the progress toward small dimensions and low Reynolds numbers. Muzychka and Yovanovich [41, 42] have developed models for predicting the thermohydraulic characteristics of offset strip fin arrays at low Reynolds numbers. Chen and Cheng [43] have constructed a fractal description of the effect of wall roughness on pressure drop in microchannels.

REFERENCES

1. A. Bejan, *Advanced Engineering Thermodynamics*, 2nd ed., Wiley, New York, 1997, chapter 13.

2. H. Reichardt, Die Grundlagen des turbulenten Wärmeüberganges, *Arch. Gesamte Waermetech.*, Vol. 2, 1951, pp. 129–142.

3. G. I. Barenblatt, A. J. Chorin, and V. M. Prostokishin, Scaling laws for fully developed turbulent flow in pipes, *Appl. Mech. Rev.*, Vol. 50, 1997, pp. 413–429.

4. L. Prandtl, *Essentials of Fluid Dynamics*, Blackie & Son, London, 1969, p. 117; in German, *Führer durch die Strömungslehre*, Vieweg, Braunschweig, Germany, 1949.

5. H. Blasius, *Forschungsarb. Ver. Deutsch. Ing.*, No. 131, 1913; see also Ref. 4, p. 163.

6. L. F. Moody, Friction factors for pipe flow, *Trans. ASME*, Vol. 66, 1944, pp. 671–684.

7. J. C. Ordonez, A. Bejan, and R. S. Cherry, Designed porous media: optimally nonuniform flow structures connecting one point with more points, *Int. J. Therm. Sci.*, Vol. 42, 2003, pp. 857–870.

8. A. Bejan, Dendritic constructal heat exchanger with small-scale crossflows and larger-scales counterflows, *Int. J. Heat Mass Transfer*, Vol. 45, 2002, pp. 4607–4620.

9. A. Anand and A. Bejan, Transition to meandering rivulet flow in vertical parallel-plate channels, *J. Fluids Eng.*, Vol. 108, 1986, pp. 269–272.

10. J. Nikuradse, Strömungsgesetze in rauhen Rohren, *VDI-Forschungsh.*, Vol. 361, 1933, pp. 1–22.

11. T. von Kármán, Mechanische Ähnlichkeit und Turbulenz, *Nachr. Ges. Wiss. Göttingen Math. Phys. Kl. Fachgruppe 1*, 1930, No. 5, pp. 58–76; also, Mechanical similitude and turbulence, NACA TM 611, 1931.

12. L. Prandtl, Neuere Ergebnisse der Turbulenzforschung, *Z. Ver. Dtsch. Ing.*, Vol. 77, 1933, pp. 105–114.

13. P. Carpenter, The right sort of roughness, *Nature*, Vol. 388, Aug. 21, 1997, pp. 713–714.

14. W. M. Rohsenow and H. Y. Choi, *Heat, Mass and Momentum Transfer*, Prentice-Hall, Englewood Cliffs, NJ, 1961, p. 183.

15. H. Schlichting, *Boundary Layer Theory*, 4th ed., McGraw-Hill, New York, 1960, p. 489.

16. E. Hofmann, Die Wämeübertragung bei der Strömung im Rohr, *Z. Gesamte Kälte-Ind.*, Vol. 44, 1937, pp. 99–107.

17. A. P. Colburn, A method of correlating forced convection heat transfer data and a comparison with fluid friction, *Trans. Am. Inst. Chem. Eng.*, Vol. 29, 1933, pp. 174–210.

18. M. S. Bhatti and R. K. Shah, Turbulent and transition flow convective heat transfer in ducts, in S. Kakac, R. K. Shah, and W. Aung, eds., *Handbook of Single-Phase Convective Heat Transfer*, Wiley, New York, 1987, Chapter 4.

19. P. W. Dittus and L. M. K. Boelter, Heat transfer in automobile radiators of the tubular type, *Univ. Calif. Publ. Eng.*, Vol. 2, No. 13, Oct. 17, 1930, pp. 443–461; reprinted in *Int. Commun. Heat Mass Transfer*, Vol. 12, 1985, pp. 3–22.

20. E. N. Sieder and G. E. Tate, Heat transfer and presure drop of liquids in tubes, *Ind. Eng. Chem.*, Vol. 28, 1936, pp. 1429–1436.

21. V. Gnielinski, New equations for heat and mass transfer in turbulent pipe and channel flow, *Int. Chem. Eng.*, Vol. 16, 1976, pp. 359–368.

22. R. H. Notter and C. A. Sleicher, A solution to the turbulent Graetz problem: III. Fully developed and entry region heat transfer rates, *Chem. Eng. Sci.*, Vol. 27, 1972, pp. 2073–2093.

23. A. Bejan, *Heat Transfer*, Wiley, New York, 1993, Chapter 9.

24. A. J. Reynolds, The prediction of turbulent Prandtl and Schmidt numbers, *Int. J. Heat Mass Transfer*, Vol. 18, 1975, pp. 1055–1069.

25. B. E. Launder and D. B. Spalding, *Mathematical Models of Turbulence*, Academic Press, New York, 1972.

26. D. Anderson, J. C. Tannehill, and R. H. Pletcher, *Computational Fluid Mechanics and Heat Transfer*, Hemisphere, Washington, DC, 1984.

27. F. H. Harlow and P. Nakayama, Transport of turbulence energy decay rate, Report LA-3854, Los Alamos Science Laboratory, University of California, 1968.

28. R. D. Present, *Kinetic Theory of Gases*, McGraw-Hill, New York, 1958, p. 41.

29. A. N. Kolmogorov, Equations of turbulent motion of an incompressible turbulent fluid, *Izv. Akad. Nauk SSSR, Ser. Fiz.*, Vol. VI, No. 1–2, 1942, pp. 56–58.

30. L. Prandtl, Über ein neues Formelsystem für die ausgebildete Turbulenz, *Nachr. Akad. Wiss. Göttingen*, 1945.

31. E. R. G. Eckert and R. M. Drake, Jr., *Analysis of Heat and Mass Transfer*, McGraw-Hill, New York, 1972, pp. 364–368.

32. B. E. Launder and D. B. Spalding, The numerical computation of turbulent flows, *Comput. Methods Appl. Mech. Eng.*, Vol. 3, 1974, pp. 269–289.

33. W. Rodi, Examples of turbulence models of incompressible flows, *AIAA J.*, Vol. 20, 1982, pp. 872–879.

34. A. Bejan and A. M. Morega, The optimal spacing of a stack of plates cooled by turbulent forced convection, *Int. J. Heat Mass Transfer*, Vol. 37, 1994, pp. 1045–1048.

35. A. E. Bergles, Techniques to augment heat transfer, in W. M. Rohsenow, J. P. Hartnett, and E. N. Ganic, eds., *Handbook of Heat Transfer Applications*, McGraw-Hill, New York, 1985, Chapter 3.

36. R. L. Webb, *Principles of Enhanced Heat Transfer*, Wiley, New York, 1994.

37. A. Bejan and A. D. Kraus, *Heat Transfer Handbook*, Wiley, New York, 2003.

38. G. P. Xu, K. W. Tou, and C. P. Tso, Numerical modelling of turbulent heat transfer from discrete heat sources in a liquid-cooled channel, *Int. J. Heat Mass Transfer*, Vol. 41, 1998, pp. 1157–1166.

39. K. W. Tou, G. P. Xu, and C. P. Tso, Direct liquid cooling of electronic chips by single-phase forced convection of FC-72, *Exp. Heat Transfer*, Vol. 11, 1998, pp. 121–134.

40. C. P. Tso, G. P. Xu, and K. W. Tou, An experimental study on forced convection heat transfer from flush-mounted discrete heat sources, *J. Heat Transfer*, Vol. 121, 1999, pp. 326–332.

41. Y. S. Muzychka and M. M. Yovanovich, Modeling *f* and *j* characteristics of the offset strip fin array, *J. Enhanced Heat Transfer*, Vol. 8, 2001, pp. 243–259.

42. Y. S. Muzychka and M. M. Yovanovich, Modeling *f* and *j* characteristics for transverse flow through an offset strip fin at low Reynolds number, *J. Enhanced Heat Transfer*, Vol. 8, 2001, pp. 261–277.

43. Y. Chen and P. Cheng, Fractal characterization of wall roughness on pressure drop in microchannels, *Int. Commun. Heat Mass Transfer*, Vol. 30, 2003, pp. 1–11.

PROBLEMS

8.1. Derive the friction factor formula (8.13) recommended by Prandtl's one-seventh power velocity distribution (7.56). In the course of this derivation, show that the average velocity is only slightly smaller than the centerline velocity, $U = 0.817 U_c$.

8.2. Use the scaling laws of transition discussed in Chapter 6 to explain the jump in the value of *f* as the laminar flow breaks down (Fig. 8.2).

8.3. Determine the function M [eq. (8.23)] for Hagen–Poiseuille flow through a pipe, and compare it with the M function that corresponds to the time-averaged turbulent profile fitted with the one-seventh power law, $\overline{u}/U_c = (y/r_0)^{1/7}$. Comment on the validity of the linear distribution of apparent heat flux shown as eq. (8.24).

8.4. Consider the fully developed turbulent flow through a parallel-plate channel with uniform heat flux. Following the procedure outlined in the text for turbulent pipe flow, show that τ_{app} decreases linearly from τ_0 at the wall to zero along the centerline. Derive the equivalent of eq. (8.21) and show that the apparent heat flux follows approximately the same linear distribution.

8.5. Consider the case of uniform heat flux to fully developed turbulent flow in a pipe, and derive a relationship among St, $f/2$, and Pr [i.e., an equivalent of eq. (8.28)] in the following manner. Start with the energy equation (8.18) and assume that $\bar{u}$ is practically independent of r and equal to U. Show that in wall coordinates, the integral of the energy equation reads

$$T^+ = \int_0^{y^+} \frac{1 - y/r_0}{(1/\text{Pr}) + (\epsilon_H/\nu)} dy^+$$

Integrate this result by breaking the $0 < y^+ < r_0^+$ interval into a conduction sublayer $0 < y^+ < y_{CSL}^+$ where $\epsilon_H/\nu \ll 1/\text{Pr}$ and a core region in which $1/\text{Pr}$ is negligible relative to ϵ_H/ν. Make the additional assumptions that Pr_t is a constant and that ϵ_M/ν is adequately represented by the mixing length model [see eq. (7.38)]. Derive the relationship St($f/2$, Pr, Pr_t, κ, y_{CSL}^+) by writing $T^+(r_0^+) = T_c^+$ and noting the difference between centerline temperature $\overline{T}_c$ and mean temperature $\overline{T}_m$ in the definition of heat transfer coefficient. Assume the one-seventh power law for the distribution of both $\bar{u}(r)$ and $(T_0 - \overline{T})/(T_0 - \overline{T}_c)$ in order to calculate the ratios $U/\bar{u}_c$ and $(T_0 - \overline{T}_m)/(T_0 - \overline{T}_c)$.

8.6. Consider the flow of a fluid through a tube of fixed diameter D and length L. The mass flow rate $\dot{m}$ is also fixed. The only change that may occur is the switch from laminar to turbulent flow because the Reynolds number Re_D happens to be in the vicinity of 2000. In either regime, the flow is fully developed. Calculate the change in the pumping power required as the laminar flow is replaced by turbulent flow.

8.7. A stream of air ($\text{Pr} = 0.72$) is heated in fully developed flow through a pipe of diameter D (fixed) and uniform heat flux q''_w (fixed). Since the Reynolds number Re_D happens to be equal to 2500, there is some uncertainty with regard to the flow regime that prevails in the airstream. Calculate the relative change experienced by the local temperature difference $T_w - T_m$ as the flow regime switches from laminar to turbulent.

8.8. Water flows at the rate of 0.5 kg/s through a 10-m-long pipe with an inside diameter of 2 cm. It is being heated with uniform wall heat flux at the rate of 5×10^4 W/m². Evaluate the water properties at 20°C, assume that the flow and temperature fields are fully developed, and calculate **(a)** the pressure drop over the entire pipe length, **(b)** the heat transfer coefficient based on the Colburn analogy (8.29), **(c)** the heat transfer coefficient

based on the Dittus–Boelter correlation (8.31), **(d)** the difference between the wall temperature and the local mean water temperature, and **(e)** the temperature increase experienced by the mean water temperature in the longitudinal direction from the inlet to the outlet.

8.9. Steam condenses at atmospheric pressure on the outside of a metallic tube and maintains the tube wall temperature uniform at $100°C$. The interior of the tube is cooled by a stream of 1-atm air with a mean velocity of 5 m/s and an inlet temperature of $30°C$. The tube inside diameter is 4 cm. Assume that the flow and temperature distributions across the tube are fully developed, and calculate **(a)** the heat transfer coefficient, **(b)** the length of the tube if the outlet mean temperature of the airstream is $90°C$, and **(c)** the flow and thermal entrance lengths. Is the assumption of fully developed flow and heat transfer justified?

8.10. Water is being heated in a straight pipe with an inside diameter of 2.5 cm. The heat flux is uniform, $q''_w = 10^4$ W/m², and the flow and temperature fields are fully developed. The local difference between the wall temperature and the mean temperature of the stream is $4°C$. Calculate the mass flow rate of the water stream, and verify that the flow is turbulent. Evaluate the properties of water at $20°C$.

8.11. Tap water of temperature $20°C$ flows through a straight pipe 1 cm in diameter, with a mean velocity of 1 m/s. Verify that the flow regime is turbulent, and calculate the friction factor f for fully developed flow. If the dimensionless thickness of the viscous sublayer of the constant-τ_{app} region of the flow is equal to $y^+ \cong 11.6$, what is the actual thickness y (mm) of the viscous sublayer?

8.12. One method of extracting the energy contained in a geothermal reservoir consists of using the ''downhole coaxial heat exchanger'' shown in Fig. P8.12. The underground temperature increases almost linearly with depth. The stream $\dot{m} = 100$ tons/h of cold water is pumped downward through the annular space of outer diameter $D_o = 22$ cm and inner diameter $D_i = 16$ cm. In this portion of its circuit, the stream is heated by contact with the increasingly warmer rock material, across the wall of diameter D_o.

After reaching the lower extremity of the well, the heated stream returns to the surface by flowing through the inner pipe. A very effective layer of insulation is built into the wall of diameter D_i, which separates the downflowing cold stream from the upflowing hot stream.

(a) Consider only the downflow through the annular space, and assume that the depth (x) to which your calculations apply is such that the mean temperature of the stream is $80°C$. The wetted surfaces of the annular space are made of commercial steel. Calculate the frictional pressure drop per unit length experienced by the stream at that depth.
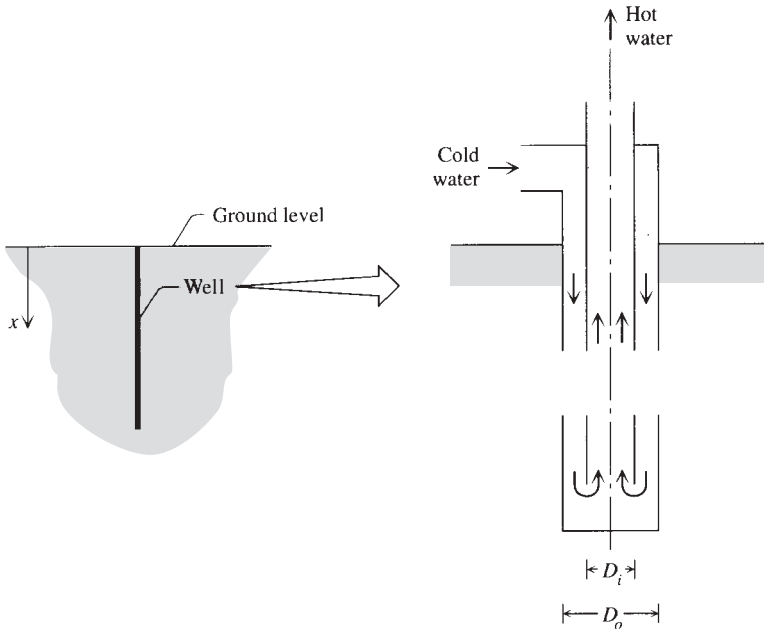
Figure P8.12

(b) Calculate the temperature difference ΔT between the outer wall of the annulus and the mean temperature of the stream. Again, the depth x is such that the mean temperature of the stream is $80°$C. Known also is the mean temperature gradient $dT_m/dx = 200°$C/km, that is, the rate of temperature increase with depth.

8.13. The single-stream coaxial heat exchanger described in Problem 8.12 brings up a fundamental design question regarding the diameter of the inner pipe, D_i. The thickness of the wall of diameter D_i is assumed negligible. If D_i is much smaller than D_o, the stream is "strangled" as it flows upward through the inner pipe. Conversely, when D_i is nearly the same as D_o, the flow is impeded by the narrowness of the annular space. In both extremes, the overall pressure drop that must be overcome by the pump is excessive. Clearly, when D_o is fixed, there exists an optimal inner diameter D_i (or an optimal ratio D_i/D_o) such that the total pressure drop experienced by the stream is minimum.

(a) Determine this optimal D_i/D_o ratio in the large–Reynolds number limit of the turbulent regime (Fig. 8.2) where the friction factors for the annular space (f_a) and for the upflow through the inner pipe (f_i) are both constant. For simplicity, assume that $f_a = f_i$.

(b) Consider next the regime in which the flow is laminar both through the annular space and through the inner pipe. Assume that the friction factor for the annular space is approximately equal to the friction factor for flow between two parallel plates positioned $(D_o - D_i)/2$ apart. Calculate the optimal D_i/D_o ratio for minimum total pressure drop, and show that this result is almost the same as the result obtained in part (a).

8.14. Air at $300°C$ and $2\,m/s$ approaches a bundle of 4-cm-diameter tubes arranged in a staggered array ($X_t = X_l = 7\,cm$), with 21 rows and six or five tubes per row (i.e., across the flow) (see Fig. P8.14). Each tube is $3\,m$ long, and its wall temperature is maintained at $30°C$ by water flowing in the tube. The bundle-averaged heat transfer coefficient between tubes and airstream is $62\,W/m^2 \cdot K$. The parallel sidewalls of the air duct are insulated. Calculate the outlet temperature of the airstream and the total heat transfer rate absorbed by the tube bundle.
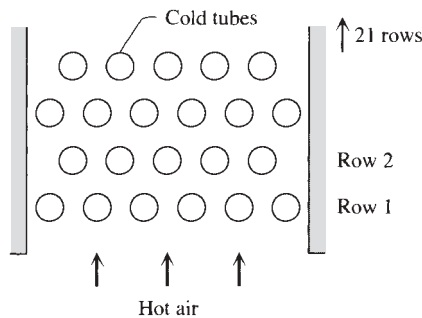
Figure P8.14

8.15. Consider the turbulent flow near a solid wall, and let y_c be the distance to the wall from a point situated in the layer where the logarithmic law of the wall (8.66) holds. Prove that according to the $k-\epsilon$ model, the turbulence energy k_c and the dissipation rate ϵ_c at $y = y_c$ are related to the friction velocity u_* by the k_c and ϵ_c expressions listed under eq. (8.66).

8.16. Consider again the stack of parallel boards cooled by forced convection (Fig. 3.17), and this time, assume that the flow is turbulent [34]. The total heat transfer rate removed from the $H \times L$ stack is q'. Assume that the board surfaces are isothermal at T_{max}, while the coolant supply temperature is T_∞. The pressure difference across the stack is fixed, ΔP. The board thickness t is not necessarily negligible when compared with the board-to-board spacing D. In other words, the number of boards in the stack of thickness H is $n = H/(D + t)$, where we assume that $n \gg 1$. Assume further that $Pr \gtrsim 0.5$ and that the board surfaces are smooth.

Determine the optimal spacing or the optimal n such that the overall thermal conductance $q'/(T_{max} - T_\infty)$ is maximized. Do this by applying step by step the method used in Section 3.6 for laminar flow. Show that in turbulent flow, the optimal spacing and maximum conductance are generally given by

$$\frac{D_{opt}/L}{(1 + t/D_{opt})^{1/2}} = (fC_f)^{1/2} Pr^{-2/3}$$

$$\left[\frac{q'L}{kH(T_{max} - T_\infty)}\right]_{max} \lesssim \left(\frac{C_f}{f}\right)^{1/4} Pr^{1/6} \left(1 + \frac{t}{D_{opt}}\right)^{-3/4} \left(\frac{\Delta P L^2}{\mu\alpha}\right)^{1/2}$$

Finally, substitute appropriate expressions for C_f and f, and show that the optimal spacing and maximum conductance are given by eqs. (8.77) and (8.78).

8.17. Consider the equivalent of Problem 3.28 for a parallel-plate channel that bifurcates into two parallel-plate channels. The stem channel has length L_1 and plate-to-plate spacing D_1. Each branch has length L_2 and spacing D_2. The stem mass flow rate $\dot{m}'_1$ (kg/s · m) splits into two equal streams of size $\dot{m}'_2$. Assume that the flow in every channel is in the Poiseuille regime.

(a) Show that the overall flow resistance of the construct of three channels depends on geometry in this way:

$$R = \frac{L_1}{D_1^3} + \frac{L_2}{2D_2^3}$$

(b) Assume that the volume of the flow space is fixed. This constraint is the same as constraining the area A of the profile of the construct of three channels. Minimize R subject to $A = $ constant and show that

$$\frac{D_1}{D_2} = 2^{1/2}$$

(c) If the flow regime in a parallel-plate channel $(L, D)_{1,2}$ is fully developed turbulent in the fully rough regime, one can show that the pressure drop along each channel scales as $\Delta P \sim (\dot{m}')^2 L/(\rho D^3)$. Show that the total pressure drop along the stem and one of the two branches depend on geometry in accordance with the function $L_1/D_1^3 + L_2/(4D_2^3)$. Minimize this function subject to the fixed total flow volume and show that the optimal ratio of spacings is $D_1/D_2 = 2^{3/4}$.

9

FREE TURBULENT FLOWS

The tradition in the field of convection is to discuss turbulent transport only in the context of the wall friction and wall heat transfer problems stated in Chapter 2. Wall problems are very important because they constitute the backbone of many applied activities (e.g., heat exchanger development). In the present chapter we depart from tradition and add a different class of turbulent transport problems to the field, ''free'' turbulent flow through regions that are situated sufficiently far from solid walls that the effect of the walls is not important.

To include free-stream turbulent flows in a course on convection is to recognize the emphasis placed by *affluent* societies on coexisting with and protecting the environment. Almost without exception, the interactions between our lifestyle and the environment are turbulent transport processes. The smoke plume swept by the wind in the wake of an industrial area and the water jets discharged by a city into the river are how our presence affects what surrounds us.

These flows rely on *turbulent mixing* to diminish the effect that high concentrations of our refuse have on the biosphere. Our reliance on turbulent jets and plumes to disperse pollutants (thermal as well as chemical) is due to the fact that turbulent mixing is the most effective transport mechanism known. Turbulent flow is a manifestation of the natural tendency to increase the access for momentum transfer, or mixing. This is achieved through the generation of design: macroscopic flow architecture (streams, eddies), as opposed to viscous diffusion, in accord with the constructal law [1].

9.1 FREE SHEAR LAYERS

9.1.1 Free Turbulent Flow Model

The simplest turbulent mixing problems concerning regions far away from solid surfaces is sketched in Fig. 9.1. Consider the time-averaged growth (swelling) of
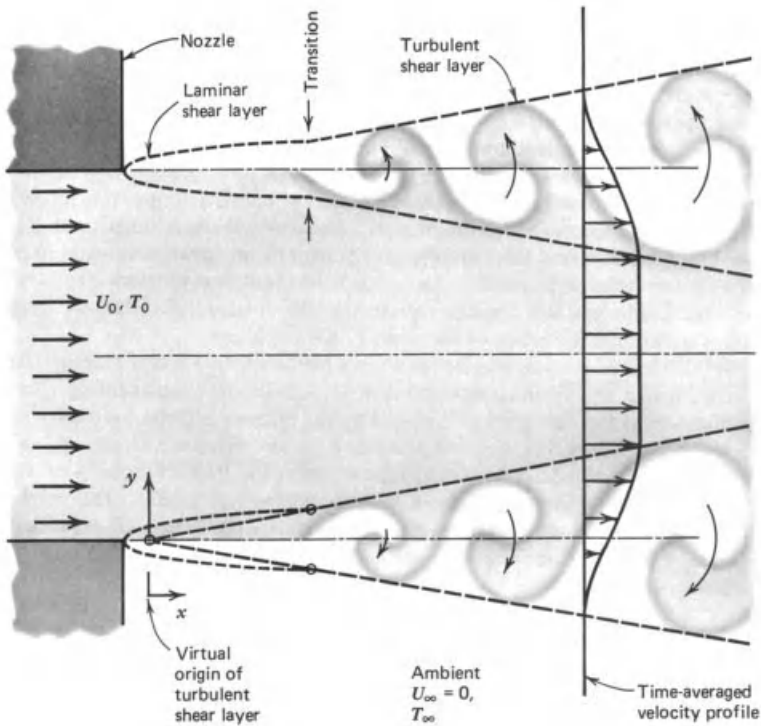
Figure 9.1   Development of the free shear layers on the two sides of a two-dimensional jet.

the turbulent interface between a stream and a stagnant fluid reservoir, and keep in mind that the instantaneous picture of the interface (the *shear layer*) is, in fact, dominated by a chain of large eddies—so large that their diameters define the visual thickness of the shear layer. The instantaneous large-scale structure of a two-dimensional shear layer is shown in Fig. 9.2: Two shear layers of this type form on both sides of a two-dimensional jet discharging from a slit into a reservoir, as shown in Fig. 9.1.

How thick will the shear layer be a certain distance x downstream from the edge of the nozzle? The answer to this question is relevant to predicting the mixing of (U_0, T_0) fluid with stagnant reservoir fluid (U_∞, T_∞). Considering the flow part of the mixing problem first, we begin with the time-averaged continuity and momentum equations for the (x, y) frame drawn in Fig. 9.1,

$$\frac{\partial \overline{u}}{\partial x} + \frac{\partial \overline{v}}{\partial y} = 0 \tag{9.1}$$

$$\overline{u}\frac{\partial \overline{u}}{\partial x} + \overline{v}\frac{\partial \overline{u}}{\partial y} = -\frac{1}{\rho}\frac{d\overline{P}}{dx} + \frac{\partial}{\partial y}\left[\left(\nu + \epsilon_M\right)\frac{\partial \overline{u}}{\partial y}\right] \tag{9.2}$$
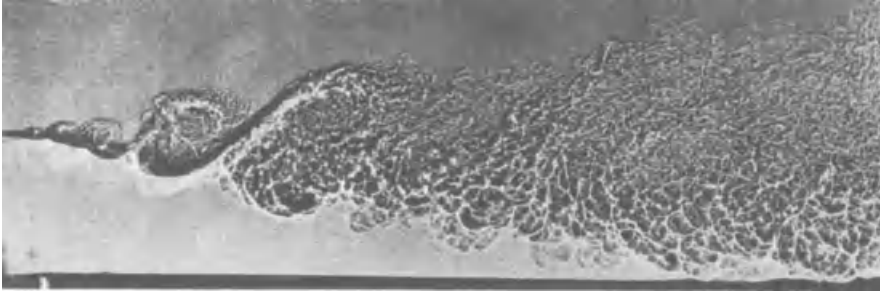
Figure 9.2 Discrete, stepwise growth of a turbulent shear layer (upper side: helium, $U_0 = 9.15$ m/s; lower side: nitrogen, $U_\infty = 0.33$ m/s; pressure $= 7$ atm) [5]. (Reprinted with permission from G. L. Brown and A. Roshko, *J. Fluid Mechanics*, Vol. 64, pp. 775−816. Copyright © 1974 Cambridge University Press.)

The momentum equation (9.2) is of the boundary layer type; hence, it applies to the space occupied by the shear layer *only if the shear layer is slender*. The two unknowns to be determined from eqs. (9.1) and (9.2) are $\bar{u}$ and $\bar{v}$; however, in order to proceed with an analytical solution, it is necessary to invoke additional simplifying assumptions:

1. The longitudinal pressure gradient in the shear layer ($d\bar{P}/dx$) is zero, as the static pressure is uniform on both sides of the shear layer. This assumption is fairly good for most turbulent free shear layer flows, including the two-dimensional jet development sketched in Fig. 9.1. The pressure inside a developing jet is practically the same as that of the ambient fluid at rest [2].

2. The momentum eddy diffusivity ϵ_M is much greater than the kinematic viscosity ν, so that ν can be omitted on the right-hand side of eq. (9.2). This assumption is made without much hesitation in classical treatments of the free shear layer problem (e.g., Refs. 2–4), because the flow region is already assumed to be situated sufficiently far from solid surfaces. However, if we look at the tip section of the shear layer of Fig. 9.2, we see that near its origin the shear layer must be laminar; in other words, sufficiently close to $x = 0$ the $\nu \ll \epsilon_M$ assumption must break down. The fact that the $\nu \ll \epsilon_M$ assumption is valid only beyond a certain value of x (hence, beyond a certain shear layer thickness) should be expected based on the constructal theory of transition presented in Chapter 6.

    The governing equations (9.1) and (9.2) could be solved for laminar flow by setting $\epsilon_M = 0$ and applying the boundary layer methods of Chapter 2. Since there is nothing in the steady-state laminar shear layer solution to suggest that it does not hold for all values of x, and since the transition criterion (6.15) has universal applicability, the laminar shear layer is destined to break down when it exceeds a certain thickness: in other words, when x exceeds a certain order of magnitude (see Problem 9.1).

The $\nu \ll \epsilon_M$ assumption is valid only in the turbulent section of the shear layer, sufficiently far downstream from the laminar–turbulent transition region that the largest eddies are much bigger than the critical thickness of the shear layer during transition (i.e., much bigger than the *smallest eddies* discussed in Chapter 7).

3. The third assumption concerns the eddy diffusivity ϵ_M: This assumption is necessary for closing the $(\bar{u}, \bar{v})$ problem described by eqs. (9.1) and (9.2). What is usually assumed as an expression for ϵ_M [namely, eq. (9.4)] is purely *empirical* in origin: This ϵ_M model is the result of observing that *the shear layer thickness D appears to be proportional to x* (cf. Fig. 9.2). Based on this observation and subject to assumptions 1 and 2 above, the momentum equation (9.2) represents the following balance of scales:

$$\frac{U_0^2}{x} \sim \epsilon_M \frac{U_0}{D^2} \tag{9.3}$$

Since the eye sees $D \sim x$, the scaling law (9.3) requires that

$$\epsilon_M \sim U_0 x \tag{9.4}$$

The ϵ_M scale derived above can also be derived by invoking the mixing length model (Chapter 7) coupled with the $D \sim x$ observation, as done originally by Prandtl [2]. Thus, writing

$$\epsilon_M = l^2 \left| \frac{\partial \bar{u}}{\partial y} \right| \tag{9.5}$$

and by taking in an order-of-magnitude sense

$$\frac{\partial \bar{u}}{\partial y} \sim \frac{U_0}{D} \quad \text{and} \quad l \sim D \tag{9.6}$$

the mixing length model (9.5) becomes identical to the scaling law (9.4). In conclusion, physical observations suggest that ϵ_M is proportional to x and that ϵ_M is not a function of y. The conclusion that ϵ_M is independent of y may seem paradoxical considering that regardless of how large ϵ_M is inside the shear layer, ϵ_M must decrease to zero outside the shear layer, where, as Fig. 9.2 shows clearly, there are no eddies. In fact, no paradox exists, simply because eq. (9.4) is the result of scale analysis that is valid only *inside* the slender shear layer region.

9.1.2 Velocity Distribution

According to assumptions 1 and 2, the boundary layer momentum equation (9.2) reduces to

$$\bar{u} \frac{\partial \bar{u}}{\partial x} + \bar{v} \frac{\partial \bar{u}}{\partial y} = \epsilon_M \frac{\partial^2 \bar{u}}{\partial y^2} \tag{9.7}$$

The $D \sim x$ observation that led to the ϵ_M model (9.4) suggests the following formulation for seeking a similarity solution to the turbulent free shear layer problem,

$$\eta = \sigma \frac{y}{x} \qquad \epsilon_M = \frac{1}{4\sigma^2} U_0 x$$

$$\bar{u} = \frac{\sigma}{2} U_0 F'(\eta) \qquad \overline{\psi} = \frac{x}{2} U_0 F(\eta) \tag{9.8}$$

where σ is an empirical constant, η is the similarity variable, and $\overline{\psi}$ is the time-averaged streamfunction defined as $\bar{u} = \partial\overline{\psi}/\partial y$, $\bar{v} = -\partial\overline{\psi}/\partial x$. Function $F'(\eta)$ represents the shape of the dimensionless velocity profile in the shear layer region. In the notation of eqs. (9.8), the mass and momentum equations (9.1) and (9.7) collapse into

$$F''' + 2\sigma F F'' = 0 \tag{9.9}$$

subject to the following boundary conditions:

$$
\begin{array}{llll}
\bar{u} = U_0 & \text{as } y \to \infty & \text{or} \quad F' = \dfrac{2}{\sigma} & \text{as } \eta \to \infty \\[2mm]
\bar{u} = 0 & \text{as } y \to -\infty & \text{or} \quad F' = 0 & \text{as } \eta \to -\infty \\[2mm]
\bar{v} = 0 & \text{as } y \to -\infty & \text{or} \quad F = 0 & \text{as } \eta \to -\infty
\end{array}
\tag{9.10}
$$

The similarity problem (9.9)–(9.10) can be solved numerically, and the resulting velocity profile resembles the shape sketched in Fig. 9.1. A closed-form curve fit to the numerical solution is [6]

$$\bar{u} \cong \frac{U_0}{2} \left[1 + \mathrm{erf}\left(\sigma \frac{y}{x} \right) \right] \tag{9.11}$$

Comparison with measurements indicates that

$$\sigma \cong 13.5 \tag{9.12}$$

is the approximate value for the empirical constant that accounts for the linear growth of the shear layer.

9.1.3 Structure of Free Turbulent Flows

The large-scale structure observed for the shear layer (Fig. 9.2) is responsible for the closed-form solution, (9.11) and (9.12). Geometrically, this solution implies that the shear layer thickness grows linearly in x, the actual growth rate depending on the *definition* of shear layer thickness: for example, if the effective thickness is defined as the knee-to-knee distance D_{k-k} sketched in Fig. 9.3, where the two knees are the intersections of the line $\bar{u}/y = (d\bar{u}/dy)_{y=0}$ with the two vertical lines $\bar{u} = U_0$ and $\bar{u} = 0$. The knee-to-knee growth angle α_{k-k} is

$$\alpha_{k-k} = \arctan \frac{\pi^{1/2}}{\sigma} \cong 7.5° \tag{9.13}$$

Half-angle of visual growth: $\arctan\left(\dfrac{\frac{1}{2}D}{\frac{3}{2}\lambda_B}\right)$

U_0

Local thickness

Knee

y

D_{k-k} α_{k-k} x or $\bar{u}$

Virtual origin

D

Knee

Knee-to-knee angle

λ_B

Local wavelength

Time-averaged velocity profile
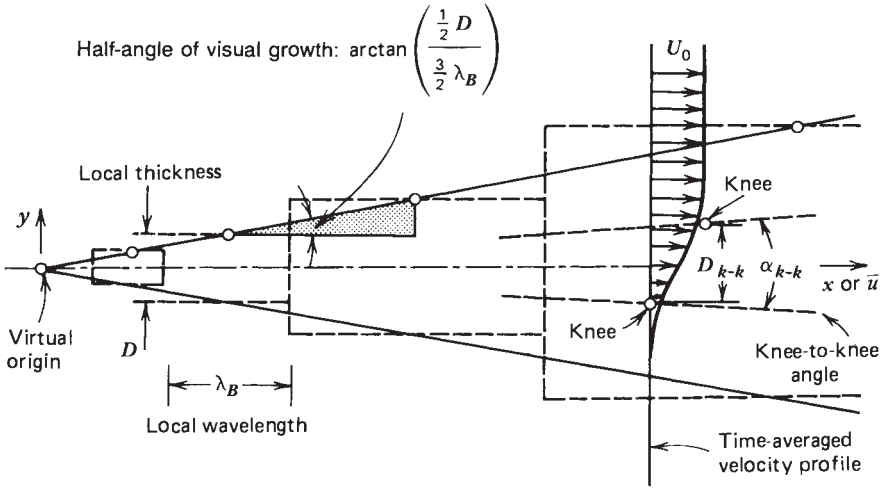
Figure 9.3   Constant-angle growth of a turbulent shear layer, as the repeated manifestation of the $\lambda_\mathrm{B} \sim D$ buckling law of Chapter 6.

The numerical value of $\alpha_{k-k} = 7.5°$ is intimately connected to the definition of knee-to-knee thickness. Figure 9.2, for example, shows that the visual growth angle is considerably greater (on the order of $20°$ [5]); a purely theoretical explanation for the growth rate illustrated was reported in Ref. 7 based on the $\lambda_B \sim D$ scaling law discussed in Chapter 6 and is presented below. The same scaling law provides a theoretical basis for the time-averaged *linear* growth rate of the shear layer, a fact that until recently was accepted empirically in the development of the ϵ_M model given by eq. (9.4) (see Ref. 7, pp. 84, 89).

The scaling argument that predicts the constant-angle shape of the shear layer is the following: If the $\lambda_B \sim D$ proportionality is a *property* of the shear layer as a finite-size region, the λ_B wave will be rolled into a large eddy in time of order $t_B \sim \lambda_B/(U_0/2)$. Note that from symmetry, $U_0/2$ is the scale of the relative velocity between the shear layer fluid and the fluid situated on either side of the shear layer. During the same period, the formation of the eddy leads to the stepwise thickening of the shear layer into a new region of thickness $D_{\mathrm{new}} > D_{\mathrm{old}}$ (scale analysis of the lateral growth of each elbow of the λ_B wave indicates that $D_{\mathrm{new}} \sim 2D_{\mathrm{old}}$ [7, p. 75]). Also during a time of order t_B, the shear layer fluid travels downstream to a distance of order λ_B because the shear layer fluid velocity relative to one of the fluid reservoirs at rest is $U_0/2$.

In summary, the shear layer region thickens stepwise in the downstream direction, and as shown schematically in Fig. 9.3, each building block is D thick and λ_B long. Furthermore, if the $\lambda_B \sim D$ proportionality is universal, that is, if it applies anywhere along the shear layer, all the steps are geometrically similar. Averaging in time the parade of large eddies through this sequence of steps, we anticipate that the time-averaged shear layer region must grow linearly with a constant half-angle of order $\arctan[(D/2)/(3\lambda_B/2)] = \arctan[1/(\pi 3^{1/2})] \sim 10°$.

The linear growth of turbulent free shear layers (and turbulent jets and plumes) is amply documented, and through the eddy diffusivity model (9.4), it forms the backbone of the classical time-averaged analytical description exhibited in this chapter. Because of this ample documentation, the scaling argument developed in the preceding two paragraphs could be reversed to conclude that the universally observed constant-angle geometry of turbulent shear flow validates the theory—the view that the $\lambda_B \sim D$ scaling is a fundamental property of the flow. Additional evidence that supports this view has been compiled in Chapter 6 and in Refs. 7–9.

An important consequence of the stepped (repeated buckling) structure of the shear layer (Fig. 9.3) is that, in time, the birth of the small eddy precedes the birth of the next (larger) eddy. At every position x, the flow is a conglomerate of eddies, small ones rolled up inside larger ones. In this conglomerate, the smallest eddy is the oldest, and the largest is the youngest. This structure and distribution of ages are shared by all the turbulent flows treated in this chapter, not just the two-dimensional shear layer. They are shared by all flow designs in nature, e.g., trees.

I stressed these features in my 1982 review of the buckling theory of turbulent flow [7, p. 83] as well as in the 1984 edition of this book and Refs. 8 and 9. The idea that the small eddy is older than the next size (larger) eddy was restated a decade later by Gibson [10] in the annual forum entitled *Some Unanswered Questions in Fluid Mechanics*. Gibson pointed out that present-day turbulence theory is built on exactly the opposite view that, in time, large eddies break down into smaller eddies. He traced the classical view to a Richardson's [11] poem, which influenced the early days of thinking about turbulence:

> *Big whorls have little whorls,*
> *Which feed on their velocity;*
> *And little whorls have lesser whorls,*
> *And so on to viscosity*
> *(in the molecular sense).*

9.1.4   Temperature Distribution

Turning our attention to the thermal mixing between T_∞ and T_0 fluids in the shear layer region, we note that assumptions 2 and 3 in Section 9.1.1 can also be applied to the eddy thermal diffusivity. Based on the assumptions that ϵ_H is much greater than α and that ϵ_H is not a function of y inside the shear layer region, the time-averaged energy equation assumes the simpler form

$$\overline{u}\, \frac{\partial \overline{T}}{\partial x} + \overline{v}\, \frac{\partial \overline{T}}{\partial y} = \epsilon_H \frac{\partial^2 \overline{T}}{\partial y^2} \tag{9.14}$$

Making the additional assumption that the turbulent Prandtl number is a constant equal to 1,

$$\mathrm{Pr}_t = \frac{\epsilon_M}{\epsilon_H} \cong 1 \tag{9.15}$$

the eddy thermal diffusivity ϵ_H is given by the same expression as that for ϵ_M in eqs. (9.8). Finally, comparing the $y \to \pm\infty$ boundary conditions for temperature $\overline{T}$ with those for longitudinal velocity $\overline{u}$, and noting the identical form of the simplified momentum and energy equations [eqs. (9.7) and (9.14)], the temperature field problem $\overline{T}(x, y)$ becomes identical to the flow problem $\overline{u}(x, y)$ already discussed (see also Problem 9.5):

$$\frac{\overline{T} - T_\infty}{T_0 - T_\infty} = \frac{\overline{u}}{U_0} \cong \frac{1}{2}\left[1 + \operatorname{erf}\left(\sigma\frac{y}{x}\right)\right] \tag{9.16}$$

According to this solution, the temperature gradient $\partial\overline{T}/\partial y$ is maximum at $y = 0$; in other words, the heat transfer rate between the two semi-infinite fluid reservoirs is maximum across the plane of original velocity discontinuity. If we are asked to evaluate the time-averaged heat flux across the $y = 0$ plane, we might be tempted to write $q''_{y=0} = k(\partial\overline{T}/\partial y)_{y=0}$, as in the early chapters of this book; this would be wrong because the temperature field solution (9.16) was developed based on the assumption that the eddy heat transport mechanism is much more effective than the molecular mechanism (assumption 2). Therefore, the proper way to evaluate the midplane heat flux is by writing

$$q''_{y=0} = \rho c_P \epsilon_H \left(\frac{\partial\overline{T}}{\partial y}\right)_{y=0} \tag{9.17}$$

which combined with the eddy diffusivity model [eq. (9.8)] and with the Pr_t assumption (9.15) yields [4]

$$\frac{q''_{y=0}}{T_0 - T_\infty} = \frac{1}{4\sigma\pi^{1/2}}\rho c_P U_0 \tag{9.18}$$

We reach the interesting conclusion that the midplane heat transfer coefficient is x-independent or that the midplane Stanton number is a constant equal to $(4\sigma\pi^{1/2})^{-1} \cong 0.01$.

9.2 JETS

Jets are similar to rivers, except that they are fluid-in-fluid streams. Rivers are fluid-in-solid streams or, more precisely, fluid in an erodible solid that stabilizes the tendency of every turbulent stream to buckle, with bulging elbows that become eddies. In rivers, the stabilized tendency to develop elbows is visible as meanders, which are not static but morph and move along the stream very slowly. Turned around, this analogy means that the turbulent jet domain (Fig. 9.4) is like a river delta in which all the river channels have become so unstable that they broke up into a hierarchy of eddies (few large and many small [12]) similar to the hierarchy of the river channels themselves [13].
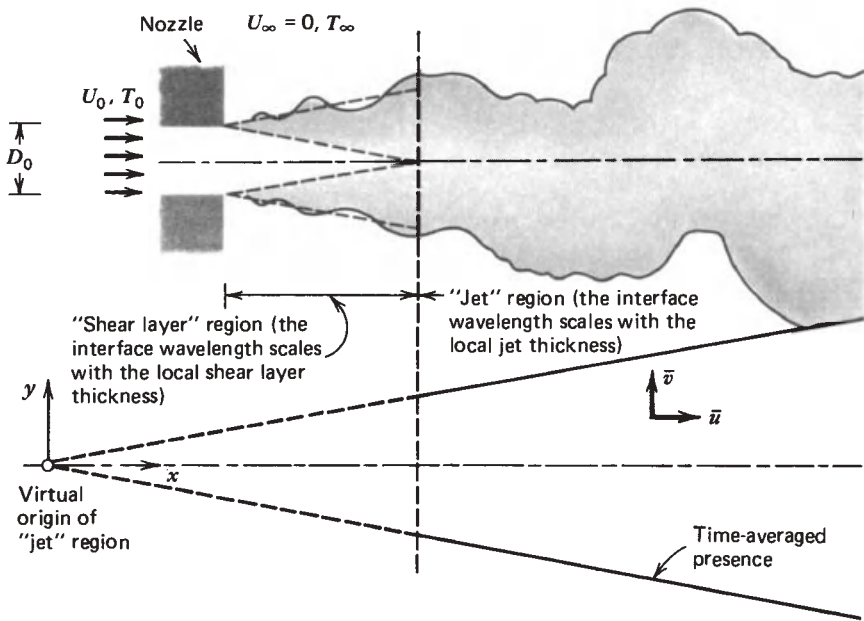
Figure 9.4   Large-scale buckled structure of a two-dimensional turbulent jet and constant angle of the time-averaged flow region.

9.2.1   Two-Dimensional Jets

An example of free-stream turbulent mixing is the jet discussed in connection with Fig. 9.1. In the case of a two-dimensional jet (U_0, T_0) injected through a slit of width D_0 into a stagnant isothermal fluid reservoir (T_∞), the initial mixing between the two fluids is ruled by the free shear layer phenomenon. Since the two shear layers grow linearly in the direction of the flow, they are destined to merge downstream from the nozzle at a characteristic distance that scales with the nozzle dimension D_0. In the shear layer section of the flow (Fig. 9.4), the centerline velocity is very close to U_0 and practically independent of x. Beyond the point where the two shear layers merge, the stream proceeds as a *jet* and the centerline velocity $\bar{u}_c$ decreases monotonically with x. The following analysis applies only to the jet region of the flow, again, based on the boundary layer theory assumption that this region is *slender*.

   An analytical description of the time-averaged jet profile is possible [6] if the mass and momentum equations (9.1) and (9.2) are coupled with assumptions 1–3 in Section 9.1.1. In particular, assumption 3 is justified by the empirical fact (the observation) that the jet region flares out linearly in the x direction. As shown in the bottom half of Fig. 9.4, if the jet thickness D is proportional to x, the point of $x = 0$ represents a fictitious, point-size origin of the jet flow. After assumptions 1–3, the momentum equation assumes the simpler form (9.7), with

the eddy diffusivity obeying the model

$$\epsilon_M = \frac{1}{4\gamma^2} \bar{u}_c x \tag{9.19}$$

where γ is the empirical constant accounting for the growth rate of the jet region.

Before proceeding with the similarity solution to eqs. (9.1), (9.7), and (9.19), it is instructive first to deduce the relationship between $\bar{u}_c$ and x. As shown in Problem 2.22, by integrating the x momentum equation from $y = -\infty$ all the way to $y = \infty$, we find that

$$\int_{-\infty}^{\infty} \bar{u}^2 \, dy = U_0^2 D_0 \quad \text{(constant)} \tag{9.20}$$

In an order-of-magnitude sense, eq. (9.20) states

$$\bar{u}_c^2 D \sim U_0^2 D_0 \tag{9.21}$$

or defining x_0 such that $D/D_0 = x/x_0$, we can now write

$$\frac{\bar{u}_c}{U_0} = \left(\frac{x}{x_0}\right)^{-1/2} \tag{9.22}$$

In conclusion, in a two-dimensional turbulent jet, the centerline velocity decays as $x^{-1/2}$. This scaling is the basis for the following construction of the similarity solution:

$$\eta(x, y) = \gamma \frac{y}{x}, \qquad \bar{u} = U_0 \left(\frac{x}{x_0}\right)^{-1/2} F'(\eta) \tag{9.23}$$

In terms of the time-averaged streamfunction,

$$\overline{\psi} = \frac{1}{\gamma} U_0 x_0^{1/2} x^{1/2} F(\eta) \tag{9.24}$$

where $\bar{u} = \partial \overline{\psi}/\partial y, \bar{v} = -\partial \overline{\psi}/\partial x$, the momentum equation (9.7) reduces to

$$(F')^2 + FF'' + \tfrac{1}{2}F''' = 0 \tag{9.25}$$

The boundary conditions on the dimensionless streamfunction profile F are

$$\begin{aligned} F &= 0 \quad \text{and} \quad F'' = 1 \quad \text{at } \eta = 0 \\ F' &= 0 \qquad\qquad\qquad\;\, \text{at } \eta = \infty \end{aligned} \tag{9.26}$$

The problem of eqs. (9.25) and (9.26) can be solved in closed form (see Ref. 3),

$$\bar{u} = U_0 \left(\frac{x}{x_0}\right)^{-1/2} (1 - \tanh^2 \eta) \tag{9.27}$$

To use the velocity solution (9.27), we have to determine the value of x_0 in terms of the *jet strength* $U_0^2 D_0$, which is assumed known. Substituting eq. (9.27) into the jet strength constraint (9.20) yields

$$\frac{\gamma D_0}{x_0} = \int_{-\infty}^{\infty} (1 - \tanh^2 \eta)^2 \, d\eta = \frac{4}{3} \tag{9.28}$$

Finally, it is found that the linear growth parameter γ that produces the best agreement between experimental measurements and the similarity profile is [14]

$$\gamma \cong 7.67 \tag{9.29}$$

This empirical constant is comparable with the one determined for shear layers, stressing once more the universality of constant-angle growth in free-stream turbulent flow. We return to this observation in Fig. 9.9.

The temperature distribution in the jet region is closely related to the velocity distribution. The close connection between the two fields is to be expected in view of the large-scale eddy formation process that, as in shear layers (Fig. 9.3), is responsible for the lateral growth of the jet. Indeed, starting with the assumption that ϵ_H is equal to ϵ_M, it is not difficult to show that the temperature excess function $(\bar{T} - T_\infty)$ is given by an expression analogous to eq. (9.27) as the boundary layer momentum and energy equations become identical and the jet strength constraint (9.20) is replaced by an enthalpy flow constraint (see Problem 2.23). However, experimentally, it is found that the temperature field data are fitted better by [15]

$$\frac{\bar{T} - T_\infty}{\bar{T}_c - T_\infty} \cong \left(\frac{\bar{u}}{\bar{u}_c}\right)^{\text{Pr}_t} \tag{9.30}$$

where $\text{Pr}_t \cong 0.5$ and $(\bar{T}_c - T_\infty)$ is the time-averaged temperature difference between jet centerline and stagnant ambient. The temperature difference $(\bar{T}_c - T_\infty)$ decreases in the downstream direction as $x^{-1/2}$, that is, in the same manner as the centerline velocity $\bar{u}_c$. The curve fit (9.30) shows that at a fixed longitudinal position x, the temperature profile is *broader* than the velocity profile because the ratio $\bar{u}/\bar{u}_c$ is always less than 1 and the exponent Pr_t is also less than 1.

The jet analysis reviewed in this section was based on the equations of motion and the energy equation (the first law of thermodynamics). The complete thermodynamic analysis of the two-dimensional turbulent jet must also account for the second law of thermodynamics (i.e., for the irreversibility of the heat and fluid flow in the jet region). This analysis has been performed [16,17], and one

of its results is that the *natural* shape of the velocity and temperature profiles of the turbulent jet is the one that minimizes the total rate of entropy generation. The analysis of entropy generation in a two-dimensional turbulent jet with quasiperiodic lateral oscillations was reported by Cervantes and Solorio [18].

9.2.2 Round Jets

Another common free turbulent flow is the round jet formed by discharge from a nozzle into a fluid reservoir. The initial section of this type of jet is also governed by the free shear layer flow sketched in Fig. 9.1; this time, the shear layer fills an annular region that surrounds the fluid issuing from the nozzle. The jet section of the flow begins at a distance of approximately $5D_0$ downstream from the nozzle [19], D_0 being the nozzle diameter.

An analytical solution for the time-averaged flow in the jet section is again possible based on assumptions $1-3$ [20]. In a cylindrical coordinate system (r, x) drawn as in the lower half of Fig. 9.4 (where r replaces y), the mass continuity and the simplified momentum equations are

$$\frac{\partial \bar{u}}{\partial x} + \frac{1}{r} \frac{\partial}{\partial r} (r\bar{v}) = 0 \tag{9.31}$$

$$\bar{u} \frac{\partial \bar{u}}{\partial x} + \bar{v} \frac{\partial \bar{u}}{\partial r} = \frac{1}{r} \frac{\partial}{\partial r} \left(\epsilon_M r \frac{\partial \bar{u}}{\partial r} \right) \tag{9.32}$$

Because ϵ_M is modeled as proportional to the product $x\bar{u}_c$, it is independent of r, and eq. (9.32) becomes

$$\bar{u} \frac{\partial \bar{u}}{\partial x} + \bar{v} \frac{\partial \bar{u}}{\partial r} = \epsilon_M \frac{1}{r} \frac{\partial}{\partial r} \left(r \frac{\partial \bar{u}}{\partial r} \right) \tag{9.32'}$$

The jet strength defined as

$$K = 2\pi \int_0^\infty \bar{u}^2 r \, dr = \frac{\pi}{4} U_0^2 D_0^2 \tag{9.33}$$

must have the same value at any distance x downstream from the fictitious point-size origin of the jet (Fig. 9.4). The jet strength constraint (9.33) implies that

$$\bar{u}_c^2 D^2 \sim K \qquad \text{(not a function of } x) \tag{9.34}$$

In other words,

$$\bar{u}_c \sim \frac{K^{1/2}}{x} \tag{9.35}$$

because, visually, the jet thickness D is proportional to x. Recognizing once more the eddy diffusivity model, we conclude that

$$\epsilon_M \sim x\bar{u}_c \sim K^{1/2} \qquad \text{(constant)} \tag{9.36}$$

The conclusion that in turbulent round jets the eddy diffusivity can be modeled as a constant independent of x or y is important. Its immediate implication is that, analytically, the turbulent round jet problem is identical to the laminar round jet problem [21] as the constant eddy diffusivity ϵ_M replaces the kinematic viscosity ν in the boundary layer formulation of the momentum equation [eq. (9.32)]. Therefore, the solution for the velocity profile can be written by inspection as

$$\bar{u} = \frac{\gamma_0}{2}\left(\frac{3}{\pi}\right)^{1/2}\frac{K^{1/2}}{x}\left(1 + \frac{\eta^2}{4}\right)^{-2} \tag{9.37}$$

where η is the similarity variable,

$$\eta = \gamma_0 \frac{r}{x} \tag{9.38}$$

and γ_0 is the empirical constant related to the angle of the cone filled by the time-averaged round jet. Reichardt's experiments indicate that the value

$$\gamma_0 \cong 15.2 \tag{9.39}$$

is adequate for matching expression (9.37) to longitudinal velocity measurements [3, p. 608]. An alternative way to curve-fit the time-averaged velocity profile is to use the Gaussian form

$$\bar{u} = \bar{u}_c \exp\left[-\left(\frac{r}{b}\right)^2\right] \tag{9.40}$$

where b is a characteristic radial dimension proportional to the transversal length scale D. Fischer et al. [22] surveyed the $\bar{u}$ data produced by 15 independent experiments with water and concluded that

$$b = (0.107 \pm 0.003)x \tag{9.41}$$

In other words, the Gaussian profile used more often as a substitute for expression (9.37) is

$$\bar{u} = \bar{u}_c \exp\left[-\left(9.35\frac{r}{x}\right)^2\right] \tag{9.42}$$

The reader can easily verify that expressions (9.37) and (9.42) are essentially equivalent if $\eta < 2$. Furthermore, substituting eq. (9.42) into the jet strength constraint (9.33) yields $\bar{u}_c = 7.46K^{1/2}/x$, which is only 0.4 percent higher than the corresponding $\bar{u}_c$ value deduced from the right-hand side of eq. (9.37).

The temperature distribution is again closely related to the velocity field. It is found that the transversal scale of the flow region heated by the turbulent

jet is proportional to x. Using Gaussian forms to curve-fit the temperature profile,

$$\overline{T} - T_\infty = (\overline{T}_c - T_\infty) \exp\left[-\left(\frac{r}{b_T}\right)^2\right] \tag{9.43}$$

the 15 experiments compared by Fischer et al. [22] showed that the transversal length scale b_T varies little from one report to another,

$$b_T = (0.127 \pm 0.004)x \tag{9.44}$$

The variation of the centerline temperature can be determined by invoking the conservation of the flow of energy in a constant-x cut,

$$2\pi \int_0^\infty \rho c_P \overline{u}(\overline{T} - T_\infty)r\, dr = \text{constant} = \rho c_P U_0(T_0 - T_\infty)\frac{\pi}{4}D_0^2 \tag{9.45}$$

The constant shown on the right side was determined by performing the integral in the plane of the nozzle, where $\overline{u} = U_0$ and $\overline{T} = T_0$. Using eqs. (9.40) and (9.43) in the integral of eq. (9.45), we obtain the expression for the temperature difference between the centerline and the reservoir,

$$\overline{T}_c - T_\infty \cong 5.65\, \frac{(T_0 - T_\infty)D_0}{x} \tag{9.46}$$

The excess centerline temperature decreases as x^{-1} in the downstream direction. Together, eqs. (9.43) and (9.46) describe the extent to which the hotness or coldness of the jet has spread into the isothermal reservoir. Formulas (9.41) and (9.44) indicate that at a given axial location x, the temperature profile is slightly broader than the velocity profile,

$$\frac{b_T}{b} \cong 1.19 \tag{9.47}$$

The consistency of this observation, not only here but also in two-dimensional jets and free shear layers, is worthy of our curiosity (Problem 9.5).

9.2.3 Jet in Density-Stratified Reservoir

When a jet is injected horizontally into a stratified fluid reservoir, it becomes turbulent only if the density stratification is sufficiently weak. I use this opportunity to show that the $\lambda_B \sim D$ scaling law of Chapter 6 can be used to predict the critical stratification for the transition to the turbulent jet flows described so far in this section.

Consider the inviscid jet of transversal length scale D and longitudinal velocity scale V sketched in Fig. 9.5. The inviscid stream has the property to buckle with
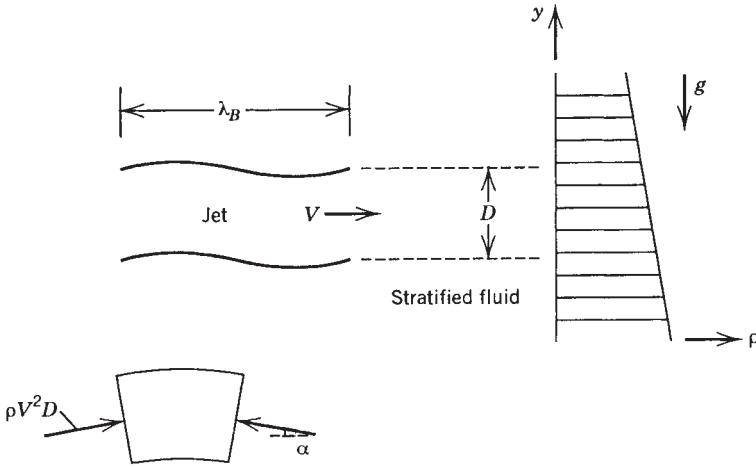
Figure 9.5   Horizontal jet flowing through a density-stratified reservoir. (From Ref. 9.)

a longitudinal wavelength scale λ_B that is fixed by the stream thickness D, eq. (6.11). The subsequent instability of the infinitesimally buckled stream can be viewed as the result of the net lateral force (F_{up}) that acts on a control volume (an elbow) of thickness D and length $\lambda_B/2$,

$$F_{up} \sim \rho V^2 D \alpha \tag{9.48}$$

where the angle α is assumed infinitesimally small. The lateral instability and eventual roll-up (eddy formation) may be inhibited if the stream flow through a stably stratified medium,

$$\rho(y) = \rho_0 - by \tag{9.49}$$

where $b = -d\rho/dy > 0$ is the degree of stratification (density gradient). Note that the displaced finite-size control volume is pulled down by a restoring body force of order

$$F_{down} \sim \lambda_B D g \, \Delta\rho \tag{9.50}$$

where $\Delta\rho$ is the density defect scale of the control volume ($\Delta\rho \sim b\alpha\lambda_B$).
   The condition for transition to buckling (turbulent flow) can be written sequentially as

$$F_{down} < F_{up} \tag{9.51}$$

$$\lambda_B D g b \alpha \lambda_B < \rho V^2 D \alpha \tag{9.52}$$

$$\frac{gb}{\rho(V/D)^2} < \left(\frac{D}{\lambda_B}\right)^2 \tag{9.53}$$

The left-hand side in inequality (9.53) is known as the *Richardson number*,

$$\text{Ri} = \frac{gb}{\rho(V/D)^2} \tag{9.54}$$

On the right-hand side of eq. (9.53), λ_B is roughly equal to $2D$ [cf. eq. (6.11)], so that the (9.53) criterion for transition to turbulent jet flow is simply [9]

$$\text{Ri} \lesssim \tfrac{1}{4} \tag{9.55}$$

The same criterion describes the transition to turbulence in a two-dimensional shear flow, where *V/D* represents the scale of the velocity gradient of the shear flow.

It is important to note that eq. (9.55) is the same as one of the classical results of hydrodynamic stability theory [23]; however, the analysis presented above is much shorter and more direct (and transparent) than the classical stability analysis. By reading eqs. (9.48)–(9.55) in the reverse order, we conclude that if eq. (9.55) is classical and acceptable, then also acceptable is the $\lambda_B \sim D$ scaling law of the buckling theory, eq. (6.11). The same kind of reverse-reading argument can be used in connection with the success of the local Reynolds number criterion for the laminar–turbulent transition (Table 6.2 and Fig. 6.5), the prediction of the viscous sublayer thickness (Section 7.5), and the derivation of the Colburn formula, eq. (7.90).

9.3 PLUMES

9.3.1 Round Plume and the Entrainment Hypothesis

In this section we analyze the mixing in turbulent jet flows driven not by the strength given to them by the nozzle, but by the effect of buoyancy. Consider the vertical flow of heated fluid above a point heat source or above a round nozzle discharging upward, and attach to this flow a cylindrical coordinate system (y,r) such that the axial point $y = 0$ coincides with the virtual origin of the time-averaged plume. As suggested by Fig. 9.6, it is widely observed that at sufficiently large values of y, the plume thickness D is proportional to y. The time-averaged plume fills a cone.

In the case of free shear layers and jets, we saw that the observed constant-angle growth of the flow region leads in relatively few steps to similarity solutions that represent the time-averaged flow quite adequately. In this section we conduct an integral analysis of the round plume: The chief conceptual focus of this analysis is to highlight the relationship between the universally observed $D \sim y$ proportionality and a technique known as the *entrainment hypothesis* [24].
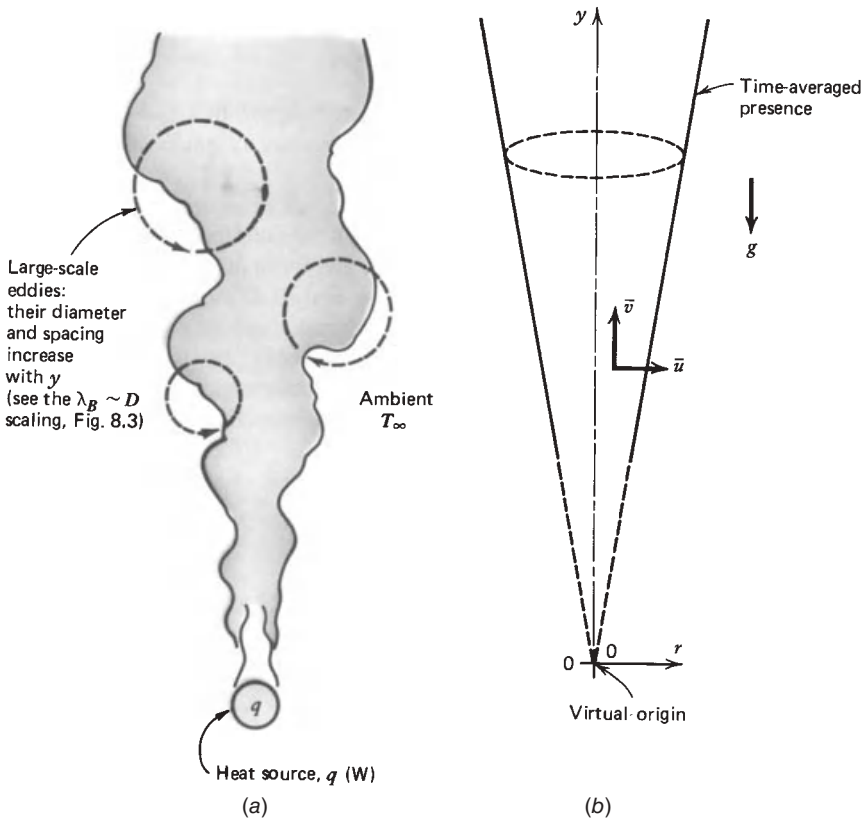
Figure 9.6 (a) Buckled shape of a turbulent plume above a concentrated heat source; (b) funnel shape of the time-averaged flow region.

The mass, momentum, and energy equations applicable to the plume as a *slender* flow region are

$$\frac{1}{r}\frac{\partial}{\partial r}(r\bar{u}) + \frac{\partial \bar{v}}{\partial y} = 0 \tag{9.56}$$

$$\frac{\partial}{\partial y}(\bar{v}^2) + \frac{1}{r}\frac{\partial}{\partial r}(r\bar{u}\,\bar{v}) = \frac{1}{r}\frac{\partial}{\partial r}\left[r\left(v + \epsilon_M\right)\frac{\partial \bar{v}}{\partial r}\right] + g\beta(\bar{T} - T_\infty) \tag{9.57}$$

$$\frac{\partial}{\partial y}(\bar{v}\bar{T}) + \frac{1}{r}\frac{\partial}{\partial r}(r\bar{u}\bar{T}) = \frac{1}{r}\frac{\partial}{\partial r}\left[r\left(\alpha + \epsilon_H\right)\frac{\partial \bar{T}}{\partial r}\right] \tag{9.58}$$

The integral analysis begins with integrating eqs. (9.56)–(9.58) over the flow cross section defined by the plane $y = $ constant. Integrating the mass

continuity equation (9.56) yields

$$(r\bar{u})_\infty - (r\bar{u})_0 + \frac{d}{dy}\int_0^\infty \bar{v}r\,dr = 0 \qquad (9.59)$$

In this equation, the second term is zero because of symmetry. The first term requires special attention because it is tempting to see a vanishing $\bar{u}$ as r becomes large. We must keep in mind, however, that in this boundary layer-type analysis, "large r" means "sufficiently larger than the transversal length scale of the plume." Therefore, as we look at the instantaneous picture of the plume edge (in Fig. 9.6 or in an actual industrial smoke discharge), we conclude that $(r\bar{u})_\infty$ must be *finite* because at the edge both r and $\bar{u}$ are finite. The actual scale of $(r\bar{u})_\infty$ will become evident later in this section. In conclusion, eq. (9.59) reduces to

$$\frac{d}{dy}\int_0^\infty \bar{v}r\,dr = -(r\bar{u})_\infty \qquad (9.60)$$

The integral form of the momentum equation (9.57) is

$$\frac{d}{dy}\int_0^\infty \bar{v}^2r\,dr + (r\bar{u}\,\bar{v})_\infty - (r\bar{u}\,\bar{v})_0$$

$$= \left[r\left(\nu + \epsilon_M\right)\frac{\partial\bar{v}}{\partial r}\right]_\infty - \left[r\left(\nu + \epsilon_M\right)\frac{\partial\bar{v}}{\partial r}\right]_0 + g\beta\int_0^\infty (\bar{T} - T_\infty)r\,dr \quad (9.61)$$

Although $(r\bar{u})_\infty$ is finite, the second term, $(r\bar{u}\,\bar{v})_\infty$, vanishes because $\bar{v}$ vanishes as we approach the T_∞ reservoir. The third term, $(r\bar{u}\,\bar{v})_0$, is zero due to symmetry. On the right-hand side of eq. (9.61), the first term vanishes because $\bar{v} = 0$ and the second term is zero, again due to symmetry. Thus, the momentum equation (9.57) reduces to

$$\frac{d}{dy}\int_0^\infty \bar{v}^2r\,dr = g\beta\int_0^\infty (\bar{T} - T_\infty)r\,dr \qquad (9.62)$$

Finally, the energy equation (9.58) can be integrated over the plume cross section to yield

$$\frac{d}{dy}\int_0^\infty \bar{v}\bar{T}r\,dr + (r\bar{u}\bar{T})_\infty - (r\bar{u}\bar{T})_0$$

$$= \left[r\left(\alpha + \epsilon_H\right)\frac{\partial\bar{T}}{\partial r}\right]_\infty - \left[r\left(\alpha + \epsilon_H\right)\frac{\partial\bar{T}}{\partial r}\right]_0 \qquad (9.63)$$

The last three terms in this equation drop out based on arguments similar to those preceding eq. (9.62). The second term $(r\bar{u}\bar{T})_\infty$ is, in fact, $(r\bar{u})_\infty T_\infty$, where $(r\bar{u})_\infty$ is given by the mass conservation equation (9.60). Therefore, combining

eqs. (9.60) and (9.63), we conclude that the enthalpy flow rate is conserved in any cross section,

$$\frac{d}{dy} \int_0^\infty \overline{v}(\overline{T} - T_\infty)r\, dr = 0 \qquad (9.64)$$

A more useful version of eq. (9.64) is to write that the integral alone is y-independent and proportional to the strength of the heat source q: Setting q equal to the enthalpy flow rate through each cross section yields

$$\int_0^\infty \overline{v}(\overline{T} - T_\infty)r\, dr = \frac{q}{2\pi\rho c_P} \qquad (9.65)$$

The second phase of any integral analysis is to assume known the actual variation of the unknowns in the direction in which the governing equations were integrated. Assuming the Gaussian profiles recommended by the survey of round water jet data [22]

$$\overline{v} = \overline{v}_c \exp\left[-\left(\frac{r}{b}\right)^2\right] \qquad (9.66)$$

$$\overline{T} - T_\infty = (\overline{T}_c - T_\infty) \exp\left[-\left(\frac{r}{b_T}\right)^2\right] \qquad (9.67)$$

and keeping in mind that the ratio b_T/b is a constant of order 1 [eq. (9.47)], the integral equations (9.60), (9.62), and (9.65) reduce to

$$\frac{d}{dy}(\overline{v}_c b^2) = -2(r\overline{u})_\infty \qquad (9.68)$$

$$\frac{d}{dy}(\overline{v}_c^2 b^2) = 2g\beta(\overline{T}_c - T_\infty)b_T^2 \qquad (9.69)$$

$$\overline{v}_c(\overline{T}_c - T_\infty) = \frac{q}{\pi\rho c_P}\frac{1 + (b/b_T)^2}{b^2} \qquad (9.70)$$

These three equations are sufficient for determining $\overline{v}_c(y)$, $\overline{T}_c(y)$, and $b(y)$ provided that the entrainment term $(r\overline{u})_\infty$ is known. The scale of $(r\overline{u})_\infty$ is the direct consequence of *observing* that the time-averaged thickness of the plume is proportional to the plume height,

$$b \sim y \qquad (9.71)$$

From this observation and eq. (9.68), we deduce the following scaling law:

$$\overline{v}_c b \sim (r\overline{u})_\infty \qquad (9.72)$$

In other words, near the sharp interface between the plume stream and the ambient, the entrainment velocity must scale with the longitudinal (vertical) velocity. This conclusion is consistent with the eddy formation mechanism recommended by the $\lambda_B \sim D$ property of any inviscid stream: The growth of the stream thickness is affected by D-wide eddies, which, rotating like bicycle wheels on a track (on the ambient), bring ambient fluid into the stream with a velocity proportional to the peripheral velocity of the eddy. Noting that in the case of a plume $\overline{v}_c > 0$ and $(r\overline{u})_\infty < 0$, we write

$$(r\overline{u})_\infty = -\hat{\alpha} b \overline{v}_c \tag{9.73}$$

where $\hat{\alpha}$ is an empirical constant tied to the measured cone angle of the plume. This linear growth feature—either accepted empirically or derived theoretically based on the $\lambda_B \sim D$ property—is the source of eq. (9.73).

The entrainment model (9.73) becomes the necessary substitute for the similarity variable $\eta = \gamma_0 r/x$ [eq. (9.38)] if the similarity formulation of the earlier sections is replaced by the integral formulation presented in this section. The same entrainment hypothesis was used by Morton et al. [25] in the analysis of buoyant turbulent jets in stratified media. Thus, combining the entrainment assumption (9.73) with the integral equations (9.68)–(9.70) and appropriate starting conditions (at $y = 0$), we have the means to derive the y dependence of $\overline{v}_c$ and $\overline{T}_c$.

The starting conditions for integrating eqs. (9.68)–(9.70) require special attention. We can focus on the simplest case—the *simple plume*—in which we assume that the strength of the jet $\overline{v}_c^2 b^2$ is zero at $y = 0$. In addition, we take the flow rate $\overline{v}_c b^2$ to be zero at $y = 0$. These assumptions make the simple plume one that originates from a fictitious point, as shown on the right-hand side of Fig. 9.6. The integral solution subjected to these starting conditions is [24]

$$b = \tfrac{6}{5}\hat{\alpha} y \tag{9.74}$$

$$\overline{v}_c = \left[\frac{25}{24\pi\hat{\alpha}^2} \frac{qg\beta}{\rho c_P y} \left(1 + \frac{b_T^2}{b^2} \right) \right]^{1/3} \tag{9.75}$$

$$\overline{T}_c - T_\infty = 0.685 \left(1 + \frac{b^2}{b_T^2} \right) \left(1 + \frac{b_T^2}{b^2} \right)^{-1/3} \left(\frac{q}{\pi\rho c_P} \right)^{2/3} \hat{\alpha}^{-4/3} y^{-5/3} (g\beta)^{-1/3} \tag{9.76}$$

The value of the empirical constant is $\alpha = 0.12$ [24].

Historically, the turbulent simple-plume problem was first solved and published in 1941 by Wilhelm Schmidt [26], who used a similarity formulation of the type presented earlier in the chapter (in other words, he used the mixing length eddy diffusivity model instead of the entrainment hypothesis of integral analysis). Fifteen years later, Morton et al. [25] published an integral solution for the more general problem involving ambient stratification and pointed out that the integral solution for zero stratification [eqs. (9.74)–(9.76)] ''is of the same

form as that of Schmidt [26].'' They also pointed out that the agreement between Schmidt's solution and the integral solution for zero stratification ''illustrates the fact that the entrainment assumption is consistent with Schmidt's mixture length assumptions.''

The integral equations (9.68)–(9.70) can be solved for the more general case where the initial section of the plume is, in fact, a forced jet, one defined by a nozzle producing a jet of known flow rate $(\overline{v}_c b^2)_{y=0}$ and known strength $(\overline{v}_c^2 b^2)_{y=0}$. Given enough time, that is, above a certain height, the strength of the buoyant jet becomes dominated by the effect of buoyancy [eq. (9.69)] and the behavior of the buoyant jet becomes similar to that of the simple plume. The height above which the initial jet becomes a plume can be evaluated by comparing the local strength of the simple plume [$\overline{v}_c^2 b^2$, eqs. (9.74) and (9.75)] with the imposed jet strength $(\overline{v}_c^2 b^2)_{y=0}$.

9.3.2   Pulsating Frequency of Pool Fires

The time-averaged turbulent plume description provided by eqs. (9.74)–(9.76) in conjunction with the assumed Gaussian profiles (9.66)–(9.67) is adequate only for sufficiently large values of y, depending on the particular device that acts as a heat source. For example, in the case of the smoke plume shown in Fig. 6.1, the section immediately above the heat source is laminar; hence, the $y = 0$ point of Fig. 9.6 does not coincide with the heat source. Another example is the plume generated by a very large heat source (e.g., a barbecue or a campfire). In its initial stages, this flow accelerates upward as an inviscid stream, and over a height of a few diameters, its thickness decreases. Eventually, the formation of large eddies takes over as a plume-thickening mechanism, and the upper section of the plume falls in line with eqs. (9.74)–(9.76). However, even near the base, the stream exhibits the $\lambda_B \sim D$ scaling law; Fig. 9.7 compares the sinuous shape predicted by buckling theory [27] with the photographed base section of a natural gas well on fire [7].

The known buckled structure of the turbulent plume is the key to predicting the natural pulsating frequency of pool fires [28]. To predict this frequency was the problem proposed by Pagni [29] to the 1989 forum on *Some Unanswered Questions in Fluid Mechanics*. With reference to the empirical frequency data of Fig. 9.8, he pointed out that ''it has been known for twenty years that fires pulsate with a regular frequency, releasing large annular vortices (coherent structures) from their bases. What is not known is why the formula

$$f_v^2 \cong \frac{2.3 \text{ m/s}^2}{D} \tag{9.77}$$

describes the shedding frequency of pool-flame oscillation over more than three orders of magnitude of the flame base diameter, from 0.03 to 60 m?''

The data displayed in Fig. 9.8 represent a wide variety of fuels and fire pool (base) shapes, from circular to rectangular. These data were produced by six
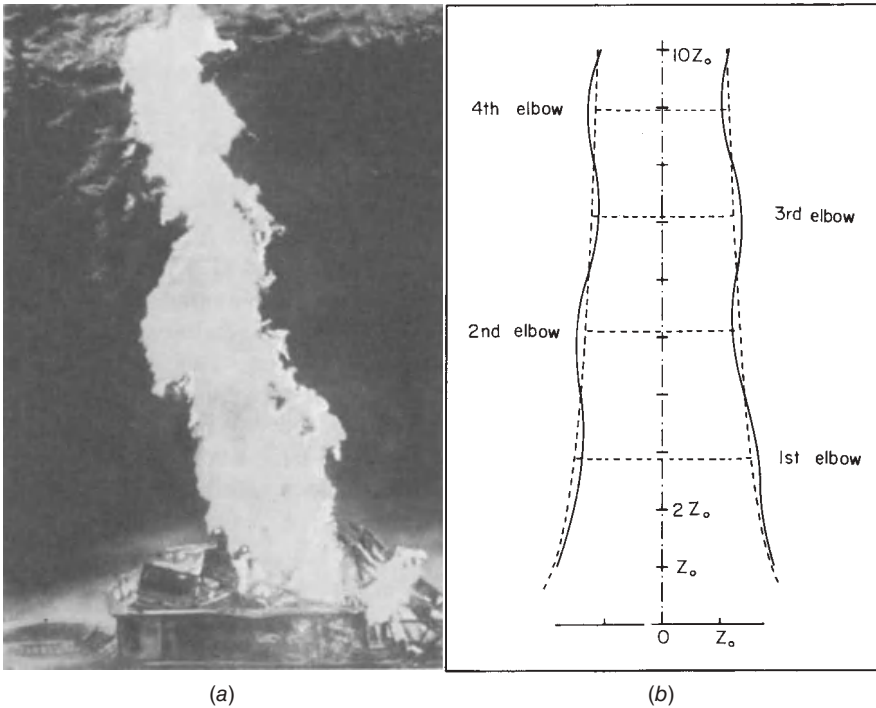
Figure 9.7 Buckled shape of a turbulent plume rising from rest: (*a*) night photograph of a natural gas well on fire; (*b*) large-scale sinuous structure predicted by buckling theory. [(*a*) From Ref. 7, courtesy of World Wide Photos; (*b*) from Ref. 27.]

independent studies. The alignment of the (f_v, D) data along the line represented by eq. (9.77) is remarkable. The alignment calls for theory. It demands to be predicted.

In this section, I show that eq. (9.77) can be derived in only a few steps from eq. (6.11), which says that

$$\frac{\lambda_B}{D} \cong C \qquad (9.78)$$

with $C \cong 1.6$ for a stream with round cross section and $C \cong 1.8$ for one with a two-dimensional (flat) cross section. Consider now the fire plume rising above the base of width D in Fig. 9.8 and assume that the plume thickness (of order D itself) is large enough so that the stream is not penetrated horizontally by viscous diffusion (i.e., it is "inviscid"). We validate this assumption at the end of this section. In an inviscid plume, the vertical flow is ruled by the balance between buoyancy and inertia. At a height corresponding to the wavelength of the buckled shape, the vertical velocity scale is the same as the Galilean velocity

$$v \cong (2g'\lambda_B)^{1/2} \qquad (9.79)$$
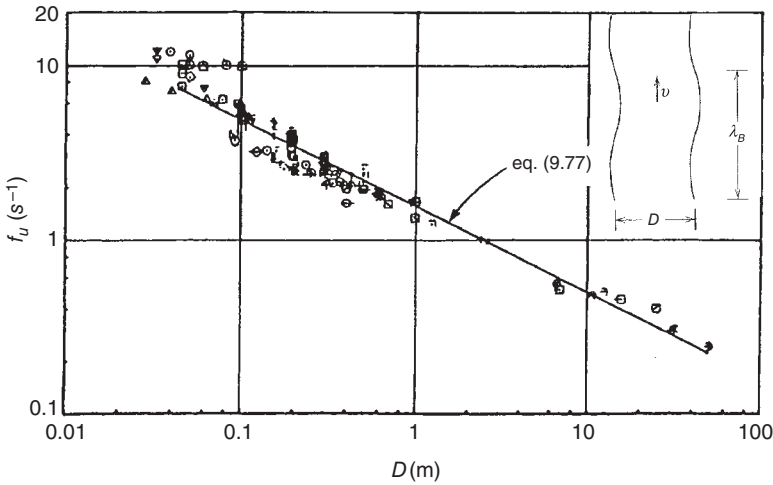
Figure 9.8 Natural pulsating frequency of fires: measurements collected from six independent studies (from Ref. 29.) and basic scales of a pulsating fire plume (from Ref. 28).

where

$$g' = \frac{\rho_\infty - \rho_{\text{fire}}}{\rho_\infty} g \tag{9.80}$$

and ρ_∞ is the density of the surrounding atmosphere. The effective gravitational acceleration g' is nearly the same as g because $\rho_\infty \gg \rho_{\text{fire}}$ (recall that $\rho = P/RT$, $P = \text{constant}$, $T_\infty \sim 300$ K, and $T_{\text{fire}} \sim 1000\text{--}2000$ K); therefore, $g' \cong g$.

The symmetry of the shear flow about the fire–ambient interface suggests that if the plume velocity is v and the ambient velocity is zero, the interface (meander) velocity is approximately $v/2$. This means that the meander of the length λ_B rises along the plume with the velocity $v/2$. The period of the swaying motion of the λ_B-tall section of the fire plume is

$$t \cong \frac{\lambda_B}{v/2} \tag{9.81}$$

From the point of view of the observer on the ground, t is also the period of the fire vortex shedding process. The frequency of this pulsating motion is

$$f_v = \frac{1}{t} \cong \frac{v/2}{\lambda_B} \tag{9.82}$$

or, after using eqs. (9.78) and (9.79) and $g' \cong g$,

$$f_v^2 \cong \frac{g/2C}{D} \tag{9.83}$$

This theoretical trend already agrees with the trend of the empirical correlation (9.77). It also agrees *quantitatively*, because if we substitute $g = 9.81$ m/s^2, we obtain

$$f_v^2 \cong \begin{cases} \dfrac{3.1 \text{ m/s}^2}{D} & \text{(round plume)} \quad\quad\quad\quad\quad\quad (9.84) \\[4mm] \dfrac{2.7 \text{ m/s}^2}{D} & \text{(two-dimensional plume)} \quad (9.85) \end{cases}$$

The better than 16 percent agreement between these theoretical f_v values and the empirical f_v value provided by eq. (9.77) is remarkable in view of the simplicity of the scale analysis on which eqs. (9.84)–(9.85) are based. Furthermore, the 7 percent discrepancy between the f_v values calculated with eqs. (9.84) and (9.85) explains some of the scatter that is visible in the data of Fig. 9.8. This scatter can be attributed in part to the different shapes of the pool fires whose pulsating frequencies have been plotted in that figure.

It remains to clarify when the fire plume is thick enough to be modeled as inviscid. According to the constructal theory of Chapter 6, the plume is not penetrated by viscous diffusion when the order of magnitude of the local Reynolds number is greater than 10^2 [cf. eq. (6.15)],

$$\frac{vD}{\nu} > 10^2 \quad\quad\quad\quad\quad\quad (9.86)$$

When this inequality holds, the plume buckles and becomes turbulent. The vertical velocity scale can be calculated by using eqs. (9.78) and (9.79). The kinematic viscosity ν can be approximated as the viscosity of air at atmospheric pressure and a temperature of order 1000°C. And if we use $C \cong 1.7$ as an average value of the geometric constant of the buckled plume, the inequality (9.86) assumes the dimensional form

$$D > 0.02 \text{ m} \quad\quad\quad\quad\quad\quad (9.87)$$

This order-of-magnitude threshold for the size of the flame base agrees very well with Pagni's observation that vortex shedding occurs when D exceeds 0.03 m [see the quotation following eq. (9.77) and the leftmost data in Fig. 9.8]. It also suggests that vortex shedding should be observed in pool fires with base diameters even larger than 60 m (i.e., to the right of the data of Fig. 9.8).

9.3.3 Geometric Similarity of Free Turbulent Flows

Based on the foregoing treatment of turbulent free shear layers, jets, and plumes, we draw the very important conclusion that in a time-averaging sense, all these flows and their associated temperature fields are *geometrically similar*. Figure 9.9 shows a drawn-to-scale summary of the mean velocity profiles discussed earlier in this chapter. This drawing is a restatement of the observation that the transversal
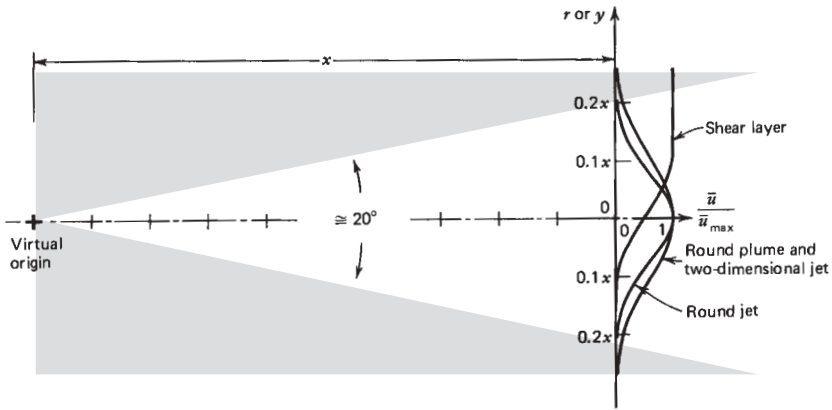
Figure 9.9 Constant-angle mixing regions of turbulent shear layers, jets, and plumes.

Table 9.1 Effect of the longitudinal length x on the time-averaged scales of free turbulent flows

Flow Configuration	D	$\bar{v}_c$	$\bar{T}_c - T_\infty$
Shear layers			
Two-dimensional	x	x^0	x^0
Jets			
Axisymmetric	x	x^{-1}	x^{-1}
Two-dimensional	x	$x^{-1/2}$	$x^{-1/2}$
Plumes			
Axisymmetric	x	$x^{-1/3}$	$x^{-5/3}$
Two-dimensional	x	x^0	x^{-1}

length scale of shear layers, jets, and plumes is proportional to the distance x measured from a fictitious origin. This observation was the basis for the similarity treatment of shear layers and jets, and for the entrainment hypothesis used in the integral analysis of the simple plume. The constant-angle growth is a consequence of the $\lambda_B \sim D$ scaling law of inviscid flow (Fig. 9.3).

Table 9.1 summarizes the results that we have obtained for the effect of the longitudinal distance x on the flow thickness scale (D), centerline velocity ($\bar{v}_c$), and centerline excess temperature ($\bar{T}_c - T_\infty$). The two-dimensional plume forms the subject of Problem 9.3. The table shows that the proportionality between D and x is a feature that characterizes all these flows.

9.4 THERMAL WAKES BEHIND CONCENTRATED SOURCES

A relatively simple way to model the spreading of thermal pollution in the wake of a concentrated heat source is shown in Fig. 9.10. Consider a line heat source
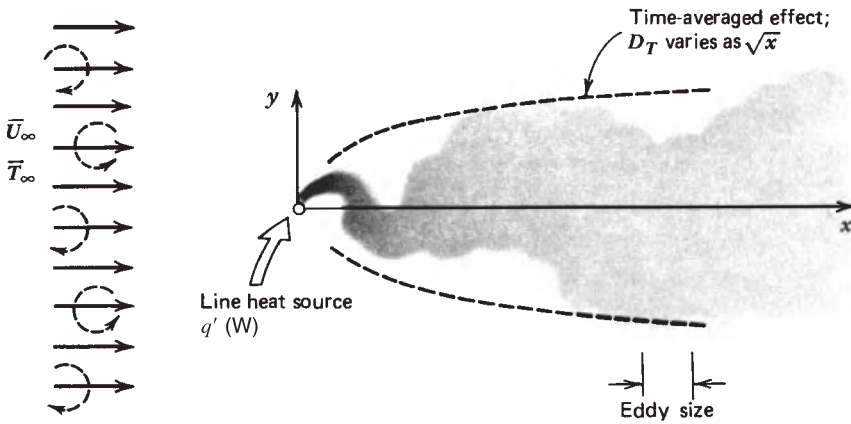
Figure 9.10 Development of a thermal wake behind a line heat source perpendicular to a uniform stream with grid-generated turbulence.

of strength q' (W/m), positioned normal to a time-averaged uniform stream $(\overline{U}_\infty, \overline{T}_\infty)$ populated throughout by eddies that have the same characteristic size and peripheral speed. This sort of turbulence can be created in the laboratory, immediately behind a turbulence-generating grid installed normal to the flow in a wind tunnel. In nature, *grid-generated turbulence* is no more than an approximate model for the eddy transport capability of *large* streams that bathe concentrated sources of heat or mass (e.g., the atmospheric boundary layer and the mainstream section of a river). The eddy population in such streams is the result of earlier stream–wall and stream–stream interactions of the type discussed in Chapters 7 and 8 and the preceding sections of this chapter.

To determine the time-averaged temperature field in the wake of the line source of Fig. 9.10, consider the energy equation applicable to that situation:

$$\overline{U}_\infty \frac{\partial \overline{T}}{\partial x} = \epsilon_H \frac{\partial^2 \overline{T}}{\partial y^2} \tag{9.88}$$

Equation (9.88) has been simplified based on the following assumptions:

1. The thermal eddy diffusivity is much greater than the molecular diffusivity, $\epsilon_H \gg \alpha$.
2. The thermal wake region is slender; hence, eq. (9.88) is of the boundary layer type.
3. The eddy diffusivity ϵ_H is not a function of either y or x; the value of this constant, assumed known, is controlled by the mechanism that generates turbulence in the $\overline{U}_\infty$ stream.

With these assumptions in mind, the scale analysis of the energy equation shows that the thermal wake thickness scales as $(\epsilon_H x/\overline{U}_\infty)^{1/2}$. Also, the scale analysis of the enthalpy conservation constraint

$$q' = \rho c_P \int_{-\infty}^{\infty} \overline{U}_\infty (\overline{T} - \overline{T}_\infty) \, dy \tag{9.89}$$

shows that the centerline-to-ambient temperature difference $(\overline{T}_c - \overline{T}_\infty)$ scales as $(q'/\rho c_P)(\overline{U}_\infty \epsilon_H x)^{-1/2}$. The similarity solution recommended by these scales is

$$\overline{T}(x, y) - \overline{T}_\infty = \frac{q'/\rho c_P}{(\overline{U}_\infty \epsilon_H x)^{1/2}} \, \theta(\eta) \tag{9.90}$$

$$\eta = y \left(\frac{\overline{U}_\infty}{\epsilon_H x} \right)^{1/2} \tag{9.91}$$

where the similarity profile θ is given by the solution to the following problem:

$$-\tfrac{1}{2}(\theta + \eta\theta') = \theta'', \quad \theta \to 0 \text{ as } \eta \to \pm\infty, \quad \text{and} \quad \int_{-\infty}^{\infty} \theta \, d\eta = 1 \tag{9.92}$$

The result is

$$\theta = \frac{1}{2\pi^{1/2}} \exp\left(-\frac{\eta^2}{4} \right) \tag{9.93}$$

In conclusion, the time-averaged temperature field behind the line source has a Gaussian profile the span of which increases as $x^{1/2}$. The centerline temperature difference $\overline{T}(x, 0) - \overline{T}_\infty$ decreases as $1/x^{1/2}$ in the flow direction [eq. (9.90)]. The temperature field is known if the eddy diffusivity ϵ_H associated with the uniform turbulence is known; in fact, the solution above can be combined with actual measurements of $\overline{T}(x, y)$ in order to calculate the ϵ_H value of the population of eddies produced by a laboratory technique.

The thermal wake behind a point source immersed in grid-generated turbulence can be analyzed according to the same model. The temperature field is given by (see Problem 9.4)

$$\overline{T}(x, r) - \overline{T}_\infty = \frac{q}{4\pi\rho c_P \epsilon_H x} \exp\left(-\frac{\overline{U}_\infty r^2}{4\epsilon_H x} \right) \tag{9.94}$$

where $q(\text{W})$ is the strength of the point source and r is the radial distance measured away from the wake centerline.

Free turbulent flows and their effect on the dispersal of heat and mass in environmental configurations are treated in Ref. 30, which focuses on the interface between energy engineering and environmental and civil engineering.

REFERENCES

1. A. Bejan and J.P. Zane, *Design in Nature*, Doubleday, New York, 2012.

2. L. Prandtl, *Essentials of Fluid Dynamics*, Blackie & Son, London, 1969, p. 122.

3. H. Schlichting, *Boundary Layer Theory*, 4th ed., McGraw-Hill, New York, 1960, p. 596.

4. E. R. G. Eckert and R. M. Drake, Jr., *Analysis of Heat and Mass Transfer*, McGraw-Hill, New York, 1972, p. 386.

5. G. L. Brown and A. Roshko, On density effects and large scale structures in turbulent mixing layers, *J. Fluid Mech.*, Vol. 64, 1974, pp. 775–816.

6. H. Görtler, Berechnung von Aufgaben der freien Turbulenz auf Grund eines neuen Näherungsansatzes, *Z. Angew. Math. Mech.*, Vol. 22, 1942, pp. 244–254.

7. A. Bejan, *Entropy Generation through Heat and Fluid Flow*, Wiley, New York, 1982.

8. A. Bejan, Buckling flows: a new frontier in fluid mechanics, in T. C. Chawla, ed., *Annual Review of Numerical Fluid Mechanics and Heat Transfer*, Vol. 1, Hemisphere, Washington, DC, 1987, pp. 262–304.

9. A. Bejan, Buckling flows: a new frontier in convection heat transfer, *Lat. Am. J. Heat Mass Transfer*, Vol. 10, 1986, pp. 83–103.

10. C. H. Gibson, The direction of the turbulence cascade, in L. M. Trefethen, R. L. Panton, and J. A. C. Humphrey, eds., *Some Unanswered Questions in Fluid Mechanics*, 1991, Paper 91-WA-FE-1, ASME, New York.

11. L. F. Richardson, Atmospheric diffusion shown on a distance–neighbour graph, *Proc. R. Soc.*, Vol. A110, No. 756, 1926, pp. 709–737.

12. S. Lorente and A. Bejan, Few large and many small: hierarchy in movement on earth, *Int. J. Design Nature Ecodynam.*, Vol. 5, No. 3, 2010, pp. 254–267.

13. A. Bejan, S. Lorente, A. F. Miguel, and A. H. Reis, Constructal theory of distribution of river sizes, in A. Bejan, *Advanced Engineering Thermodynamics*, 3rd ed., Wiley, Hoboken, 2006, pp. 779–782.

14. H. Reichardt, Gesetzmässigkeiten der freien Turbulenz, *VDI-Foschungsch.*, 1942, p. 414, 2nd ed., 1951; also, Ref. 3, p. 607.

15. H. Reichardt, Impuls und Wärmeaustausch in freier Turbulenz, *Z. Angew. Math. Mech.*, Vol. 24, 1944, p. 268.

16. A. Bejan, Thermodynamics of an ''isothermal'' flow: the two-dimensional turbulent jet, *Int. J. Heat Mass Transfer*, Vol. 34, 1991, pp. 407–413.

17. A. Bejan, *Entropy Generation Minimization*, CRC Press, Boca Raton, FL, 1996.

18. J. Cervantes and F. Solorio, Entropy generation in a plane turbulent oscillating jet, *Int. J. Heat Mass Transfer*, Vol. 45, 2002, pp. 3125–3129.

19. S. C. Crow and F. H. Champagne, Orderly structure in jet turbulence, *J. Fluid Mech.*, Vol. 48, 1971, pp. 547–592.

20. W. Tollmien, Berechnung turbulenter Ausbreitungsvorgänge, *Z. Angew. Math. Mech.*, Vol. 6, 1926, pp. 468–479; also, NACA TM 1085, 1945.

21. H. Schlichting, Laminare Strahlausbreitung, *Z. Angew. Math. Mech.*, Vol. 13, 1933, p. 260; also, Ref. 3, p. 181.

22. H. B. Fischer, E. J. List, R. C. Y. Koh, J. Imberger, and N. H. Brooks, *Mixing in Inland and Coastal Waters*, Academic Press, New York, 1979, Chapter 9.

23. Y. Jaluria, *Natural Convection Heat and Mass Transfer*, Pergamon, Oxford, 1980, p. 198.

24. J. S. Turner, *Buoyancy Effects in Fluids*, Cambridge University Press, Cambridge, 1973.

25. B. Morton, G. I. Taylor, and J. S. Turner, Turbulent gravitational convection from maintained and instantaneous sources, *Proc. R. Soc. London*, *Ser. A*, Vol. 234, 1956, pp. 1–23.

26. W. Schmidt, Turbulente Ausbreitung eines Stromes erhitzter Luft, *Z. Angew. Math. Mech.*, Vol. 21, 1941, pp. 265–278, 351–363.

27. A. Bejan, Theory of instantaneous sinuous structure in turbulent buoyant plumes, *Wärme Stoffübertrag.*, Vol. 16, 1982, pp. 237–242.

28. A. Bejan, Predicting the pool fire vortex shedding frequency, *J. Heat Transfer*, Vol. 113, 1991, pp. 261–263.

29. P. J. Pagni, Pool vortex shedding frequencies, in L. M. Trefethen and R. L. Panton, eds., *Some Unanswered Questions in Fluid Mechanics*, 1989, Paper 89-WA/FE-5, ASME, New York.

30. A. Bejan, I. Dincer, S. Lorente, A. F. Miguel, and A. H. Reis, *Porous and Complex Flow Structures in Modern Technologies*, Springer-Verlag, New York, 2004.

31. A. Bejan, *Heat Transfer*, Wiley, New York, 1993, p. 179.

PROBLEMS

9.1. Study the slender shear layer region of Fig. 9.1 as a laminar flow problem. Rely on scale analysis to show that the thickness of this laminar region must increase as $(\nu x/U_0)^{1/2}$. Note the difference between the nonlinear growth of the laminar layer and the linear growth of the turbulent case treated in the text. Apply the local Reynolds number criterion for the laminar–turbulent transition [eq. (6.15)], and determine the laminar tip length of the shear layer. Sketch to scale the structure of the shear layer, showing the laminar and turbulent sections for cases (a) and (b) such that $(U_0)_a = 2(U_0)_b$. Comment on the change in this structure as U_0 increases.

9.2. Repeat the scaling argument of Fig. 9.3 for the more general case where both U_0 and U_∞ are finite (note that Fig. 9.2 corresponds to such a case). Show that relative to the observer at rest, the constant angle of the mixing region must scale as

$$\arctan \frac{D(U_0 - U_\infty)}{3\lambda_B(U_0 + U_\infty)}$$

where λ_B/D is a constant comparable with 2. The implication of this result is that the angle photographed in Fig. 9.2 stands to decrease as U_∞ approaches U_0. Test this conclusion against the comprehensive set of photographs published in Ref. 5 and against Fig. 7 of Ref. 5.

9.3. Consider the time-averaged development of a two-dimensional turbulent plume above a horizontal line heat source of strength q' (W/m). In the usual Cartesian system (x, y) and $(\bar{u}, \bar{v})$, with y and $\bar{v}$ pointing upward, derive the integral equations for mass, momentum, and energy in each horizontal cut through the plume. Combining the mass continuity equation with the lateral entrainment hypothesis (discussed in the text in conjunction with round plumes), and assuming that the velocity profile thickness D is of the same order as the temperature profile thickness D_T, use scale analysis to derive the scales of $D_T, \bar{v}$, and $\bar{T}_c - T_\infty$. In this notation, $\bar{T}_c - T_\infty$ is the temperature between a point on the centerplane and the ambient fluid reservoir. Sketch qualitatively the variation of $D_T, \bar{v}$, and $\bar{T}_c - T_\infty$ with the altitude y. Assuming Gaussian profiles for both $\bar{v}$ and $\bar{T}_c - T_\infty$, derive expressions for the centerline velocity and temperature difference, $\bar{v}_c$ and $\bar{T}_c - T_\infty$. Compare your results with the bottom line of Table 9.1.

9.4. Consider the development of a thermal wake behind a point source of strength q (W) situated in a uniform stream $\bar{U}_\infty$ that contains grid-generated eddies. The eddy thermal diffusivity of this stream ϵ_H is constant and assumed known. Develop a similarity solution for the time-averaged temperature field behind the point source. Express your result as

$$\bar{T}(r, x) - \bar{T}_\infty = \text{function}(q, \epsilon_H, U_\infty, r, x)$$

where (r, x) is the cylindrical coordinate system attached to the point source, with the x axis pointing downstream, in the same direction as U_∞. Note the analogy between the energy equation simplified for this problem and the transient equation for pure radial conduction away from a line source. Show that your solution for the thermal wake behind a point source is analytically the same as that for transient conduction around a line source instantly releasing a finite amount of energy per unit length [31].

9.5. Consider the free shear layer formed between two streams at different temperatures (Fig. 9.1). Show that in Pr > 1 fluids, the thickness of the velocity profile, D, must be of the same order as the thickness of the temperature profile, D_T. [*Hint*: Based on scale analysis, estimate the thermal penetration distance by which the D-size eddy swells as a temperature field during one rotation. What is the scale of D_T/D in Pr < 1 fluids?]

10

CONVECTION WITH CHANGE OF PHASE

When the temperature difference between the fluid and the wetted solid surface is sufficiently large, the fluid or the surface may experience a change of phase. The circumstances where convection heat transfer is accompanied by phase change are extremely diverse, and to cover them all is not the objective of this book. The objective is to show how the basic principles and analytical tools of single-phase convection can be extended to problems of convection with phase change. We accomplish this in two steps. In the first part of the chapter we review the main results of the classical phase-change topics of condensation and boiling. In the second part we discuss two basic phenomena of melting with fluid flow: contact melting and lubrication and melting in the presence of natural convection. These phenomena have generated considerable interest in contemporary research.

10.1   CONDENSATION

10.1.1   Laminar Film on a Vertical Surface

A simple configuration for phase change is the condensation of a vapor on a cold vertical surface (Fig. 10.1). The film of condensate that forms on the surface can have three distinct regions. The *laminar section* is near the top, where the film is relatively thin. The film thickness increases in the downward direction as more and more of the surrounding vapor condenses on the exposed surface of the film. There comes a region where the film becomes thick enough to show the first signs of transition to a nonlaminar flow regime, cf. eq. (6.15). In this *wavy flow region*, the visible surface of the film shows a sequence of regular ripples: The film buckles (cf. Chapter 6 and Refs. 2–5). Finally, if the wall extends sufficiently far downward, the film enters and remains in the *turbulent region*, where the ripples appear irregular in both space and time.
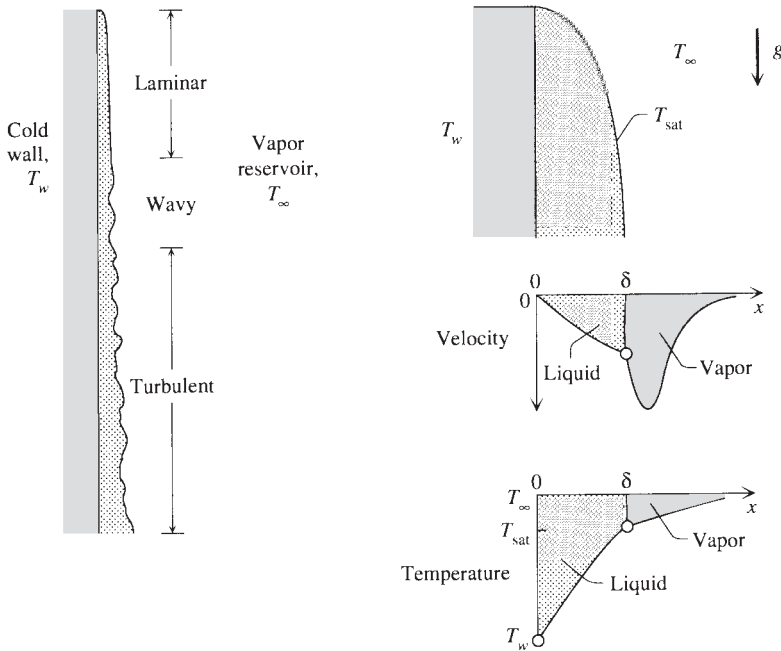
Figure 10.1   Flow regimes of the film of condensate on a cooled vertical surface. (From Ref. 1.)

The right side of Fig. 10.1 shows that even in the laminar film region, which is the simplest of the three regions, the flow of the liquid film interacts with the descending boundary layer of cooled vapor. The temperature of the liquid–vapor interface is the saturation temperature that corresponds to the local pressure along the wall, T_{sat}. The saturation temperature is sandwiched between the temperature of the isothermal vapor reservoir, T_{∞}, and the wall temperature, T_w.

Through the shear stress at the liquid–vapor interface, the falling jet of vapor aids the downward flow of the liquid film. The vapor in the falling jet is colder than the vapor reservoir and warmer than the liquid in the film attached to the wall.

This two-phase flow is considerably more complicated in the wavy and turbulent sections of the wall. To make matters even more complicated, when the film is sufficiently long to exhibit all three regimes, the overall heat transfer rate from the vapor reservoir to the wall is dominated by the contributions from the wavy and turbulent sections. The same can be said about the total rate of condensation, which, as we will learn in eq. (10.21), is proportional to the total heat transfer rate from the vapor to the vertical wall.

Consider the two-dimensional laminar film sketched in Fig. 10.2, in which the distance y measures downward the length of the film. This flow is considerably simpler than the one shown in Fig. 10.1, because here the entire reservoir of vapor is assumed isothermal at the saturation pressure T_{sat}. The merit of this
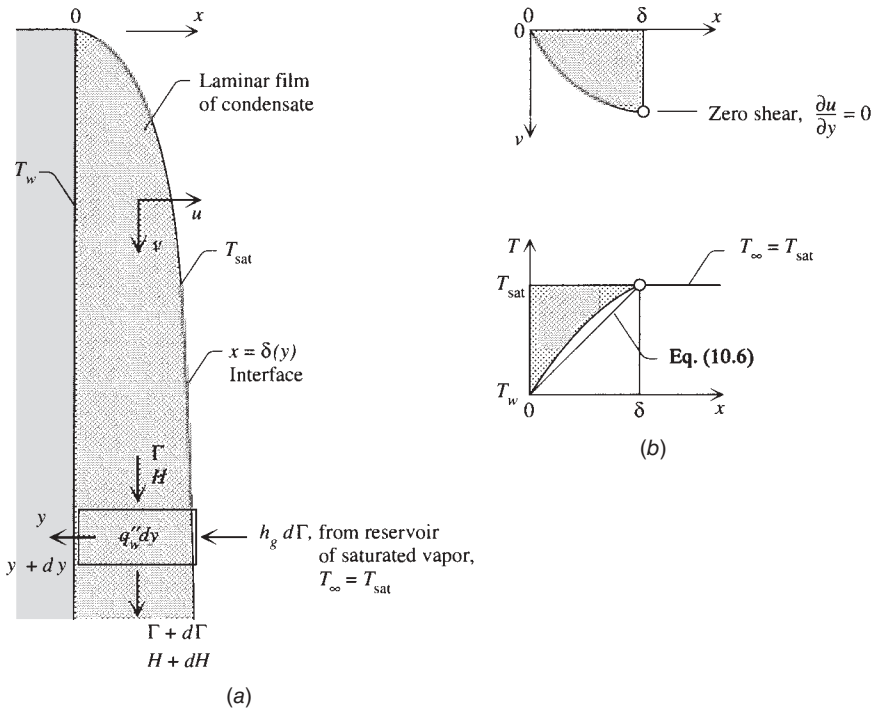
Figure 10.2 Laminar liquid film supplied by a reservoir of saturated vapor. (From Ref. 1.)

simplification is that it allows us to focus exclusively on the flow of the liquid film and to neglect the movement of the nearest layers of vapor.

The analysis of the flow of liquid begins with the steady-state version of the momentum equations (1.19), which in the case of a *slender film* (i.e., in boundary layer flow) reduce to the single equation

$$\rho_l \left(u\frac{\partial v}{\partial x} + v\frac{\partial v}{\partial y} \right) = -\frac{dP}{dy} + \mu_l \frac{\partial^2 v}{\partial x^2} + \rho_l g \tag{10.1}$$

The last term on the right side represents the body force experienced by each small packet of liquid. Because of the slenderness of the film, the vertical pressure gradient in the liquid is the same as the hydrostatic pressure gradient in the external vapor, $dP/dy = \rho_v g$. Review the second simplification of the boundary layer momentum equations in Chapter 2, namely eq. (2.25). Equation (10.1) can now be rewritten to show that the net sinking force felt by the liquid is, in general, resisted by a combination of the effects of friction and inertia:

$$\underbrace{\rho_l \left(u\frac{\partial v}{\partial x} + v\frac{\partial v}{\partial y} \right)}_{\text{Inertia}} = \underbrace{\mu_l \frac{\partial^2 v}{\partial x^2}}_{\text{Friction}} + \underbrace{g(\rho_l - \rho_v)}_{\text{Sinking effect}} \tag{10.2}$$

We continue the analysis by assuming that the inertia effect is small compared with the effect of friction and set the left side of eq. (10.2) equal to zero. The domain of validity of this assumption is discussed at the end of this section. Without the inertia terms, eq. (10.2) can be integrated twice in x and subjected to the no-slip conditions at the wall ($v = 0$ at $x = 0$) and zero shear at the liquid–vapor interface ($\partial v/\partial x = 0$ at $x = \delta$). The solution for the vertical liquid velocity profile is

$$v(x, y) = \frac{g}{\mu_l}(\rho_l - \rho_v)\delta^2 \left[\frac{x}{\delta} - \frac{1}{2}\left(\frac{x}{\delta}\right)^2 \right] \tag{10.3}$$

in which the film thickness is an unknown function of longitudinal position, $\delta(y)$. The local mass flow rate through a cross section of the film is

$$\Gamma(y) = \int_0^\delta \rho_l v \, dx = \frac{g\rho_l}{3\mu_l}(\rho_l - \rho_v)\delta^3 \tag{10.4}$$

The mass flow rate Γ (kg/s · m) is expressed per unit length in the direction normal to the plane of Fig. 10.2. The downward velocity and the flow rate are proportional to the sinking effect $g(\rho_l - \rho_v)$; they are also inversely proportional to the liquid viscosity.

The film thickness $\delta(y)$ can be determined by invoking the first law of thermodynamics for the control volume $\delta \times dy$ shown in the lower part of Fig. 10.2a. Entering this control volume from the right is the saturated vapor stream $d\Gamma$, the enthalpy flow rate of which is $h_g \, d\Gamma$. The vertical enthalpy inflow associated with the mass flow rate Γ (W/m) is

$$H = \int_0^\delta \rho_l v[h_f - c_{P,l}(T_{\text{stat}} - T)] \, dx \tag{10.5}$$

The quantity in brackets is the local specific enthalpy (kJ/kg) of the liquid at the point (x, y). Since the liquid is slightly subcooled ($T < T_{\text{sat}}$), its specific enthalpy is smaller than the specific enthalpy of saturated liquid (h_f). Next, we assume [6] that the local temperature T is distributed approximately linearly across the film,

$$\frac{T_{\text{sat}} - T}{T_{\text{sat}} - T_w} \cong 1 - \frac{x}{\delta} \tag{10.6}$$

and after using eqs. (10.3) and (10.6) in the integral (10.5), we obtain

$$H = \left[h_f - \tfrac{3}{8}c_{P,l}\left(T_{\text{sat}} - T_w\right) \right]\Gamma \tag{10.7}$$

Finally, in accordance with the linear temperature profile assumption (10.6), the heat flux absorbed by the wall is

$$q_w'' \cong k_l \frac{T_{\text{sat}} - T_w}{\delta} \tag{10.8}$$

The first law of thermodynamics for the $\delta \times dy$ system requires that in the steady state

$$0 = H - (H + dH) + h_g \, d\Gamma - q_w'' \, dy \tag{10.9}$$

or, after using eqs. (10.7) and (10.8),

$$\frac{k_l}{\delta}(T_{\text{sat}} - T_w) \, dy = \underbrace{[h_{fg} + \tfrac{3}{8}c_{P,l}(T_{\text{sat}} - T_w)]}_{h'_{fg}} \, d\Gamma \tag{10.10}$$

The group h'_{fg} represents the *augmented* latent heat of condensation, which includes the actual latent heat (h_{fg}) and a sensible-heat contribution accounting for the cooling of the fresh condensate to temperatures below T_{sat}. Combined with the Γ expression (10.4), eq. (10.10) becomes

$$\frac{k_l \nu_l (T_{\text{sat}} - T_w)}{h'_{fg} g (\rho_l - \rho_v)} \, dy = \delta^3 \, d\delta \tag{10.11}$$

and after integrating from $y = 0$ where $\delta = 0$,

$$\delta(y) = \left[y \, \frac{4 k_l \nu_l \left(T_{\text{sat}} - T_w\right)}{h'_{fg} g (\rho_l - \rho_v)} \right]^{1/4} \tag{10.12}$$

In conclusion, the thickness of the laminar film increases as the film length raised to the power $\frac{1}{4}$, that is, in the same way as the thickness (thermal, or velocity) of the vertical laminar boundary layer in a single-phase fluid, eq. (4.26). Knowing $\delta(y)$, we can calculate in order the local heat transfer coefficient

$$h_y = \frac{q_w''}{T_{\text{sat}} - T_w} = \frac{k_l}{\delta} = \left[\frac{k_l^3 h'_{fg} g \left(\rho_l - \rho_v\right)}{4 y \nu_l (T_{\text{sat}} - T_w)} \right]^{1/4} \tag{10.13}$$

the average heat transfer coefficient for a film of height L,

$$\overline{h}_L = \tfrac{4}{3} h_{y=L} \tag{10.14}$$

and the overall Nusselt number based on the L-averaged heat transfer coefficient,

$$\overline{\text{Nu}}_L = \frac{\overline{h}_L L}{k_l} = 0.943 \left[\frac{L^3 h'_{fg} g \left(\rho_l - \rho_v\right)}{k_l \nu_l (T_{\text{sat}} - T_w)} \right]^{1/4} \tag{10.15}$$

Regarding the physical meaning of the dimensionless group formed on the right side of eq. (10.15), we note that it is nearly equal to the geometric slenderness ratio of the liquid film [cf. eq. (10.12)]:

$$\frac{L}{\delta(L)} = 0.707 \left[\frac{L^3 h'_{fg} g \left(\rho_l - \rho_v\right)}{k_l \nu_l (T_{\text{sat}} - T_w)} \right]^{1/4} \tag{10.16}$$

The results reported in eqs. (10.12)–(10.16) can also be obtained based on scale analysis, as we showed for laminar boundary layer natural convection in Section 4.3. The resulting formulas are the same as in eqs. (10.12)–(10.16), but without factors of order 1 such as 0.943 and 0.707 in eqs. (10.15) and (10.16).

In numerical calculations with these formulas, the liquid properties are best evaluated at the average film temperature $(T_w + T_{sat})/2$. The latent heat of condensation h_{fg} is found in thermodynamic tables of saturated-state properties and takes the value that corresponds to the phase-change temperature T_{sat}. Rohsenow [7] refined the preceding analysis by discarding the linear profile assumption (10.6) and by performing an integral analysis of the temperature distribution across the film. He found a temperature profile whose curvature increases with the degree of liquid subcooling, $c_{P,l}(T_{sat} - T_w)$. In place of the modified latent heat h'_{fg} defined under eq. (10.10), Rohsenow recommended

$$h'_{fg} = h_{fg} + 0.68 c_{P,l}(T_{sat} - T_w) \tag{10.17}$$

This expression is also recommended for calculations involving the wavy and turbulent flow regimes. It can be rewritten as

$$h'_{fg} = h_{fg}(1 + 0.68\text{Ja}) \tag{10.18}$$

in which the *Jakob number* Ja is a relative measure of the degree of subcooling experienced by the liquid film,

$$\text{Ja} = \frac{c_{P,l}(T_{sat} - T_w)}{h_{fg}} \tag{10.19}$$

To summarize, the total heat transfer rate absorbed by the wall per unit length in the direction normal to the plane of Fig. 10.2 is

$$q' = \overline{h}_L L(T_{sat} - T_w) = k_l(T_{sat} - T_w)\overline{\text{Nu}}_L \tag{10.20}$$

The total flow rate collected at the bottom end $\Gamma(L)$ can be calculated by substituting $y = L$ in what results from combining eqs. (10.4) and (10.12). It is easy to show that the total condensation rate $\Gamma(L)$ is proportional to the total cooling rate provided by the vertical wall,

$$\Gamma(L) = \frac{q'}{h'_{fg}} = \frac{k_l}{h'_{fg}}(T_{sat} - T_w)\overline{\text{Nu}}_L \tag{10.21}$$

Equations (10.20) and (10.21) are global: They hold for the entire film, not just for the laminar section. Rewritten as $q' = \Gamma(L)h_{fg}(1 + 0.68\,\text{Ja})$, eq. (10.21) also shows that the cooling rate q' increases with the latent heat h_{fg} and the degree of liquid subcooling Ja. This trend is expected because the cooling provided by the wall causes condensation of vapor at the $x = \delta$ interface and cooling of the newly formed liquid to temperatures below T_{sat}.

The laminar-film results discussed until now were derived by Nusselt [6] based on the assumption that the effect of inertia is negligible in the momentum equation (10.2). The complete momentum equation was used by Sparrow and Gregg [8] in a similarity formulation of the same problem. Their solution for $\overline{\mathrm{Nu}}_L$ falls below Nusselt's eq. (10.15) when the Prandtl number is smaller than 0.03 and the Jakob number is greater than 0.01.

In a subsequent analysis, Chen [9] abandoned the assumption of zero shear at the liquid–vapor interface (Fig. 10.2b), while retaining the effect of inertia in the momentum equation. The vapor was assumed saturated and stagnant sufficiently far from the interface. Next to the interface, the vapor is dragged downward by the falling film of condensate and forms a velocity boundary layer that bridges the gap between the downward velocity of the interface and the zero velocity of the outer vapor (see the small detail above Fig. 10.3). Chen's chart for calculating the overall Nusselt number $\overline{\mathrm{Nu}}_L$ is reproduced in Fig. 10.3. Especially at low Prandtl numbers, the $\overline{\mathrm{Nu}}_L$ values read off Fig. 10.3 are smaller than those furnished by Sparrow and Gregg's solution [8] and agree better with experimental data. The lower $\overline{\mathrm{Nu}}_L$ values are due to the additional restraining effect that the vapor drag has on the downward acceleration of the liquid film.

The scale analysis of the laminar film condensation problem [mentioned after eq. (10.16)] was reported in the first edition of this book (see Ref. 10, pp. 146–151). It showed that the fall of the liquid film is restrained by friction when $\mathrm{Pr}_l > \mathrm{Ja}$ and by inertia when $\mathrm{Pr}_l < \mathrm{Ja}$. The group that marks the transition from one type of flow to the other is the ratio $\mathrm{Pr}_l/\mathrm{Ja}$. Indeed, if we use the group $\mathrm{Pr}_l/\mathrm{Ja}$ on the abscissa of Fig. 10.4, the low-Pr_l information of Fig. 10.3 is correlated well by the single curve shown in Fig. 10.4.

$$\frac{\overline{\mathrm{Nu}}_L}{0.943\left[\dfrac{L^3 h'_{fg}\, g(\rho_l - \rho_v)}{k_l \nu_l (T_{\mathrm{sat}} - T_w)}\right]^{1/4}}$$

and

$$\frac{\overline{\mathrm{Nu}}_D}{0.729\left[\dfrac{D^3 h'_{fg}\, g(\rho_l - \rho_v)}{k_l \nu_l (T_{\mathrm{sat}} - T_w)}\right]^{1/4}}$$

$$\mathrm{Ja} = \frac{c_l (T_{\mathrm{sat}} - T_w)}{h'_{fg}}$$
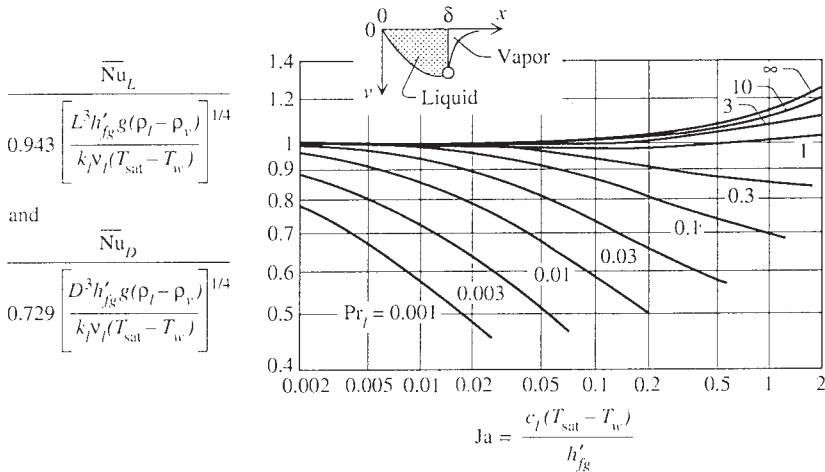
Figure 10.3 Prandtl number and wall subcooling (Ja) effects on laminar film condensation on a vertical wall and on a single horizontal cylinder. (From Refs. 1 and 9.)

$$\frac{\overline{Nu}_L}{0.943\left[\dfrac{L^3 h'_{fg} g(\rho_l - \rho_v)}{k_l \nu_l (T_{sat} - T_w)}\right]^{1/4}}$$

and

$$\frac{\overline{Nu}_D}{0.729\left[\dfrac{D^3 h'_{fg} g(\rho_l - \rho_v)}{k_l \nu_l (T_{sat} - T_w)}\right]^{1/4}}$$
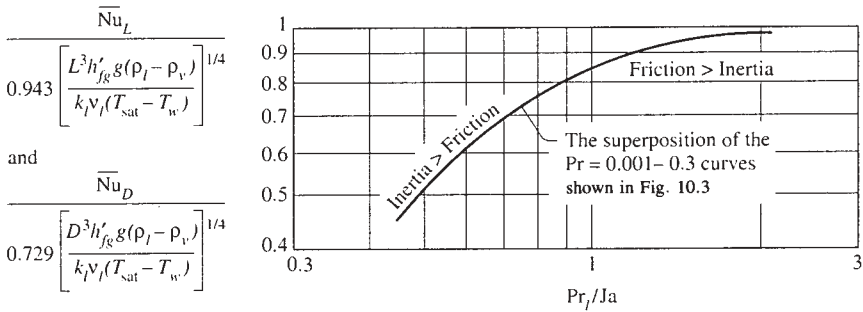
Figure 10.4 Transition from inertia-restrained film to friction-restrained film condensation on a vertical wall and on a single horizontal cylinder. (After Ref. 10.)

10.1.2 Turbulent Film on a Vertical Surface

The liquid film becomes wavy and, farther downstream, turbulent when the order of magnitude of its local Reynolds number is greater than 10^2 (see Chapter 6). The *local* Reynolds number of the liquid film [eq. (6.15)] is the group $\rho_l \overline{u} \delta / \mu_l$, in which δ is the local thickness and $\overline{u}$ is the representative scale of the local downward velocity. Because the product $\rho_l \overline{u} \delta$ is of the same order of magnitude as the local liquid mass flow rate Γ, the local Reynolds number can also be expressed as the ratio Γ / μ_l. This is why in the field of condensation heat transfer, the local Reynolds number of the liquid film has historically been defined as

$$\text{Re}_y = \frac{4}{\mu_l} \Gamma(y) \tag{10.22}$$

The flow rate $\Gamma(y)$ and the Reynolds number Re_y increase in the downstream direction. Experimental observations of the condensate indicate that the laminar section of the film expires in the general vicinity of $\text{Re}_y \sim 30$. The film can be described as wavy in the segment corresponding approximately to $30 \lesssim \text{Re}_y \lesssim 1800$. Farther downstream, the film appears turbulent. The succession of these flow regimes is illustrated on the abscissa of Fig. 10.5.

Experiments also revealed that the heat transfer rate in the wavy and turbulent sections is considerably larger than the estimate based on the laminar film analysis, eq. (10.15) and Fig. 10.3. The sizable record of experimental data and correlations on condensation heat transfer in the wavy and turbulent regimes was reviewed by Chen et al. [11], who developed the following correlation for the *average* heat transfer coefficient for an L-tall film that may have wavy and turbulent regions:

$$\frac{\overline{h}_L}{k_l}\left(\frac{\nu_l^2}{g}\right)^{1/3} = (\text{Re}_L^{-0.44} + 5.82 \times 10^{-6} \text{Re}_L^{0.8} \, \text{Pr}_l^{1.3})^{1/2} \tag{10.23}$$
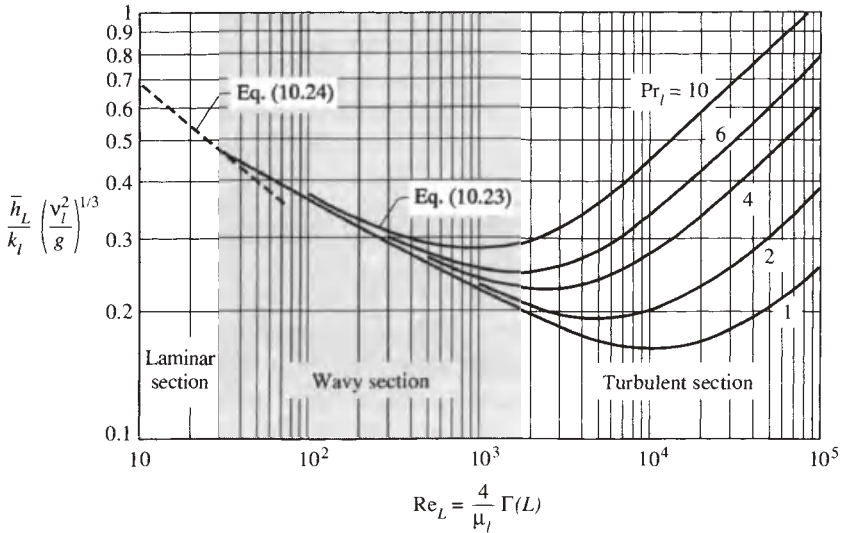
Figure 10.5   *L*-averaged heat transfer coefficient for laminar, wavy, and turbulent film condensation on a vertical surface. (From Ref. 1.)

Figure 10.5 shows that this correlation applies only above $\text{Re}_L \sim 30$. Equation (10.23) agrees within ± 10 percent with measurements where the vapor was stagnant (or slow enough) so that the effect of shear at the interface was negligible. Below $\text{Re}_L \sim 30$, the average heat transfer formula recommended is eq. (10.15), which when $\rho_l \gg \rho_v$ can be projected on Fig. 10.5 as the line

$$\frac{\bar{h}_L}{k_l}\left(\frac{v_l^2}{g}\right)^{1/3} = 1.468\text{Re}_L^{-1/3} \tag{10.24}$$

The usual unknown in the vertical-film condensation problem is the total condensation rate $\Gamma(L)$, or alternatively, Re_L. This unknown influences both sides of eq. (10.23), i.e., the ordinate and abscissa parameters of Fig. 10.5. Instead of the trial-and-error procedure required by eq. (10.23) or Fig. 10.5, it is more convenient to rewrite the ordinate parameter of Fig. 10.5 as [1]

$$\frac{\bar{h}_L}{k_l}\left(\frac{v_l^2}{g}\right)^{1/3} = \frac{\text{Re}_L}{B} \tag{10.25}$$

in which B is a new dimensionless group that is proportional to the physical quantities [L and $(T_{\text{sat}} - T_w)$] that, when increasing, tend to augment the condensation rate,

$$B = L(T_{\text{sat}} - T_w)\frac{4k_l}{\mu_l h'_{fg}}\left(\frac{g}{v_l^2}\right)^{1/3} \tag{10.26}$$

The B group is the *driving parameter for film condensation* [1]. Equation (5) is a consequence of the global statements (10.20)–(10.21) and allows us to rewrite eqs. (10.23) and (10.24) as

$$B = \text{Re}_L (\text{Re}_L^{-0.44} + 5.82 \times 10^{-6}\text{Re}_L^{0.8}\, \text{Pr}_l^{1.3})^{-1/2} \tag{10.27}$$

$$= 0.681\text{Re}_L^{4/3} \tag{10.28}$$

Figure 10.6 displays this information by using the unknown Re_L on the abscissa and the driving parameter B on the ordinate. We see at a glance how the condensation rate and the bottom-end Reynolds number increase monotonically as the driving parameter increases. The condensation rate increases faster when the film length is dominated by the turbulent regime.
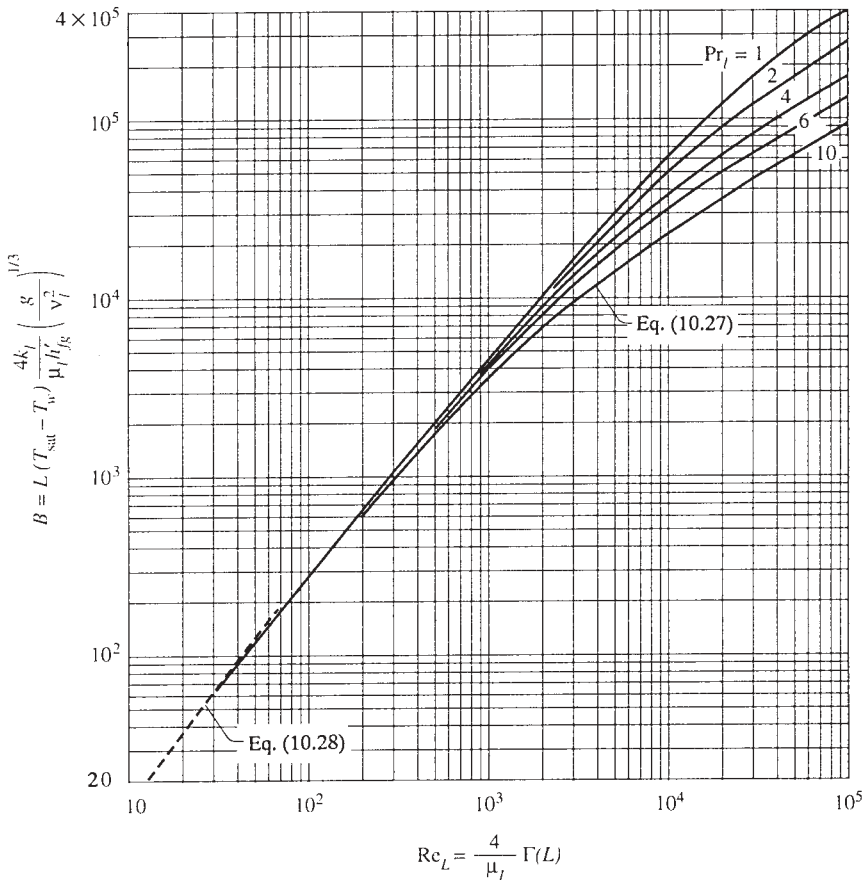
Figure 10.6   Film condensation on a vertical surface: the total condensation rate (or Re_L) as a function of the condensation driving parameter B. (From Ref. 1.)

10.1.3 Film Condensation in Other Configurations

The vertical-wall results described until now hold not only for flat surfaces (Fig. 10.7a) but also for curved vertical surfaces on which the film of condensate is sufficiently thin. In the case of the vertical cylindrical surface (internal or external) shown in Fig. 10.7b, the film is "thin" when the order of magnitude of its thickness is smaller than the cylinder diameter.

In the case of a plane wall inclined at an angle θ with respect to the vertical direction (Fig. 10.8a), the gravitational acceleration component along the surface is $g \cos \theta$. Condensation heat transfer results for the inclined wall can be obtained by replacing g with $g \cos \theta$ in the results reported until now for a vertical plane wall.
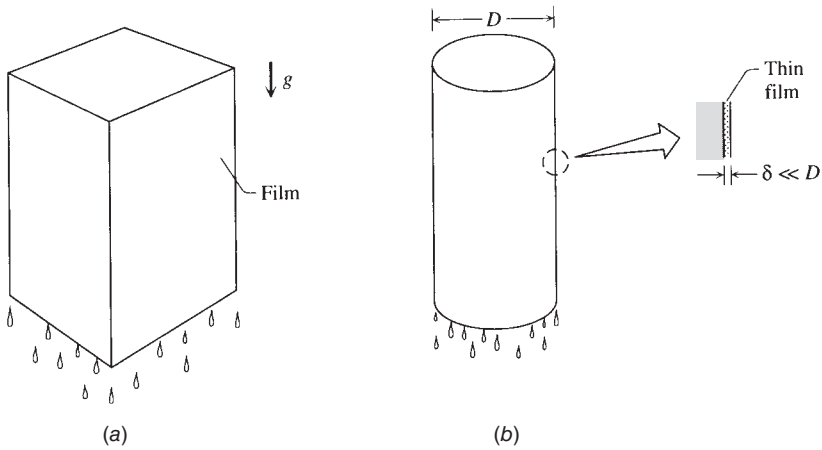
Figure 10.7 Vertical surfaces whose films of condensate can be modeled as a plane. (From Ref. 1.)
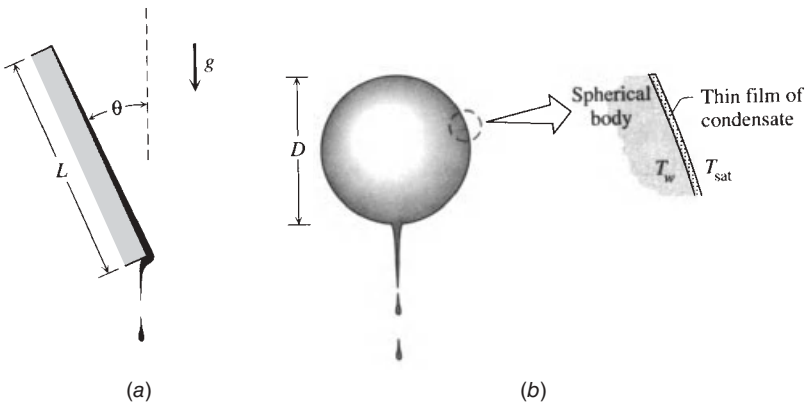
Figure 10.8 Film condensation on (a) inclined plane surface and (b) spherical surface. (From Ref. 1.)

More complicated surface shapes are those that are curved in such a way that the tangential component of gravity varies along the flowing film of condensate. One example is the spherical surface shown in Fig. 10.8b. If the film is laminar all around, the diameter-averaged heat transfer coefficient is given by [12]

$$\overline{\mathrm{Nu}}_D = \frac{\overline{h}_D D}{k_l} = 0.815 \left[\frac{D^3 h'_{fg} g \left(\rho_l - \rho_v \right)}{k_l \nu_l (T_{\mathrm{sat}} - T_w)} \right]^{1/4} \tag{10.29}$$

The laminar-film condensation on the surface of a single horizontal cylinder of diameter D (Fig. 10.9a) was first analyzed by Nusselt [6], who relied on the same simplifying assumptions as in the vertical-wall analysis detailed in Section 10.1.1. The formula for the average heat transfer coefficient under a condensate film that is laminar all around the cylinder is [12]

$$\overline{\mathrm{Nu}}_D = \frac{\overline{h}_D D}{k_l} = 0.729 \left[\frac{D^3 h'_{fg} g \left(\rho_l - \rho_v \right)}{k_l \nu_l (T_{\mathrm{sat}} - T_w)} \right]^{1/4} \tag{10.30}$$
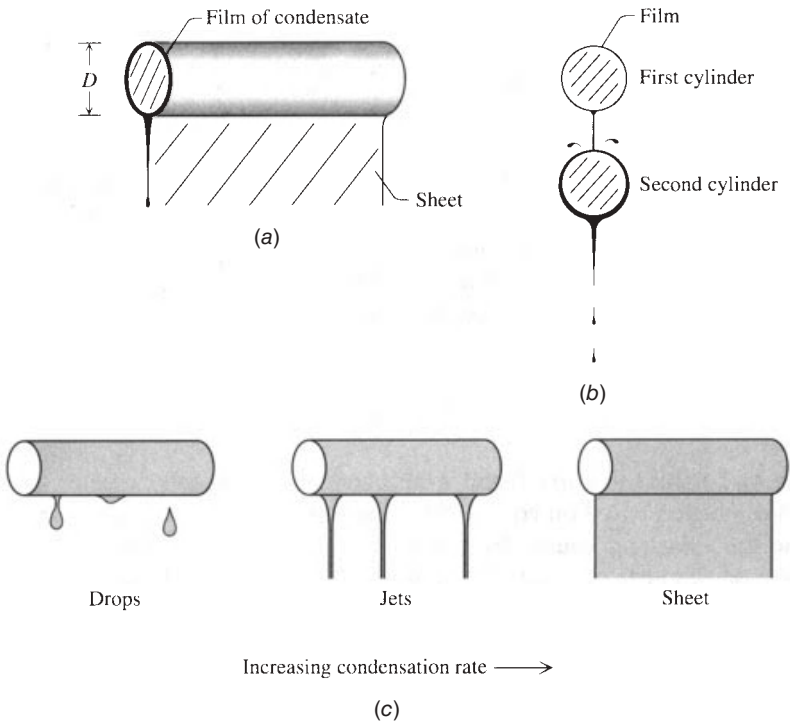
Figure 10.9 Film condensation on (a) single horizontal cylinder and (b) vertical column (e.g., $n = 2$) of horizontal cylinders. (c) Effect of the condensation rate on the type of flow that impinges on the next cylinder. (From Ref. 1.)

This expression is similar to the laminar-film relations for the sphere, eq. (10.29), and the vertical wall, eq. (10.15). For the horizontal cylinder and the sphere, the diameter D plays the role of vertical dimension in the same sense that L measures the height of the vertical plane wall in eq. (10.15). The physical properties needed in eqs. (10.29), (10.30), and other formulas presented in this subsection are to be evaluated at the film temperature $(T_w + T_{\text{sat}})/2$.

The Prandtl number effect on laminar-film condensation on a single horizontal cylinder was documented by Sparrow and Gregg [13] and Chen [14]. The latter also took into account the effect of interfacial shear and found that the Pr_l effect is described fairly well by the curves plotted in Fig. 10.3. Note the alternative $\overline{\text{Nu}}_D$ meaning of the ordinates of Figs. 10.3 and 10.4.

Analogous to the analysis that yields the single-cylinder formula (10.30), the laminar-film analysis of a vertical column of n horizontal cylinders (Fig. 10.9b) leads to

$$\overline{\text{Nu}}_{D,n} = \frac{\overline{h}_{D,n}D}{k_l} = 0.729\left[\frac{D^3 h'_{fg}g\left(\rho_l - \rho_v\right)}{nk_l\nu_l(T_{\text{sat}} - T_w)}\right]^{1/4} \qquad (10.31)$$

The heat transfer coefficient $\overline{h}_{D,n}$ has been averaged over all the cylindrical surfaces, so that the total heat transfer rate per unit of cylinder length is $q' = \overline{h}_{D,n}n\pi D(T_{\text{sat}} - T_w)$. By comparing the right sides of eqs. (10.30) and (10.31), we note that the average heat transfer coefficient of the n-tall column is smaller than that of the single cylinder,

$$\overline{h}_{D,n} = \frac{\overline{h}_D}{n^{1/4}} \qquad (10.32)$$

The $\overline{h}_{D,n}$ values that are found experimentally are usually greater than the values calculated based on eq. (10.31). This augmentation effect can be attributed to the splashing caused by the sheet or droplets of condensate, as they impinge on the next cylinder. Figure 10.9c shows that the condensation rate depends on the type of flow (i.e., drops, jets, or sheet) that falls on the next cylinder as the condensation rate increases. An additional factor is the condensation that takes place on the sheet (or droplets) between two consecutive cylinders [14] because the falling sheet is at an average temperature below T_{sat}. Finally, if each tube is tilted or bowed slightly (due to its weight, or a defect in the assembly), the condensate runs longitudinally along the tube and drips only from its lowest region. In such cases, most of the length of the next cylinder is not affected by the condensate generated by the preceding cylinder.

When the cooled surface is perfectly horizontal and faces upward (Fig. 10.10a), the condensate flows away from the central region and spills over the edges [15]. In the case of a long horizontal strip of width L, the average heat transfer coefficient is given by a formula similar to eq. (10.15) except that the exponent of the dimensionless group on the right side is $\frac{1}{5}$:

$$\overline{\text{Nu}}_L = \frac{\overline{h}_L L}{k_l} = 1.079\left[\frac{L^3 h'_{fg}g\left(\rho_l - \rho_v\right)}{k_l\nu_l(T_{\text{sat}} - T_w)}\right]^{1/5} \qquad (10.33)$$

$$\Pi_H = \frac{H^3 h'_{fg} g(\rho_l - \rho_v)}{k_l \nu_l (T_{sat} - T_w)}$$

(a)

$$\left(\frac{L}{H}\right)^{4/5} \Pi_H^{-1/15} \quad \text{or} \quad \left(\frac{D}{H}\right)^{4/5} \Pi_H^{-1/15}$$

(b)
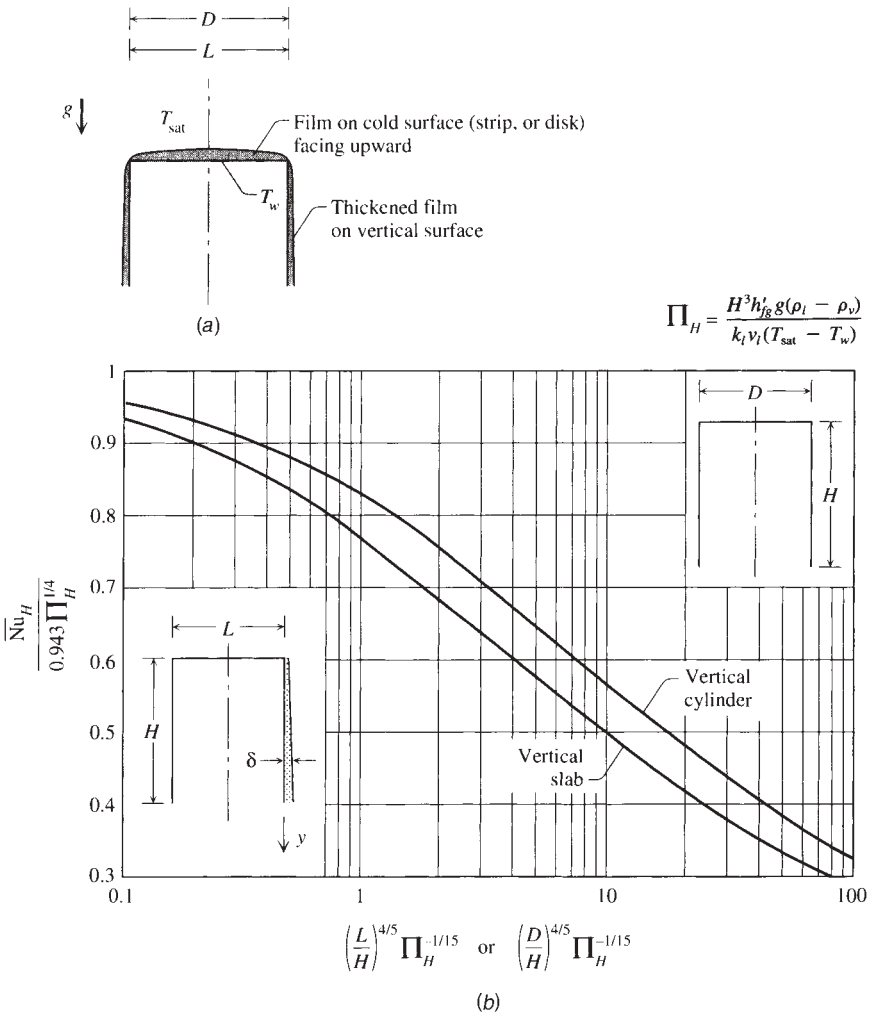
Figure 10.10 Film of condensate on a horizontal strip of width L and on a horizontal disk of diameter D. (From Refs. 1 and 15.)

The average heat transfer coefficient for an upward-facing disk with free edges is similar [15]:

$$\overline{Nu}_D = \frac{\overline{h}_D D}{k_l} = 1.368 \left[\frac{D^3 h'_{fg} g (\rho_l - \rho_v)}{k_l \nu_l (T_{sat} - T_w)}\right]^{1/5} \tag{10.34}$$

The corresponding formula for any other surface whose shape is somewhere between the very long shape of the strip and the round shape of the disk can be deduced from eqs. (10.33)–(10.34) by using the concept of *characteristic length*

of eq. (4.118). Equations (10.33) and (10.34) are based on an analysis and set of assumptions of the same type as those outlined in Section 10.1.1.

These results may be used to estimate the contribution made by the horizontal ''roof'' surface to the total condensation rate on a three-dimensional body. The horizontal surface contributes to the total condensation rate in two ways: directly, through the flow rate estimated based on eqs. (10.33) and (10.34), and indirectly, by thickening the film that coats the vertical lateral surface [15]. When the condensate collected on the top surface spills over the edge, the vertical-surface heat transfer coefficient is smaller than the value that would be calculated based on eq. (10.15). This effect is documented in Fig. 10.10b, in which [unlike in eq. (10.15)] the height of the vertical surfaces is labeled H. The symbol Π_H is defined on the figure and represents the dimensionless group that emerged on the right side of eq. (10.15). Figure 10.10 shows that the roof condensate inhibits condensation on the vertical surfaces when the abscissa parameters exceed the order of magnitude 1.

The film condensation processes described until now are examples of natural convection because the flow is being driven by gravity. Considerably more complicated are condensation processes where the vapor is forced to flow over the cooled surface. In these processes the vapor and the condensate film interact across their mutual interface. The forced flow of vapor tends to drag the liquid in its direction, and the overall condensation heat transfer process is one of natural convection mixed with forced convection.

One example of this type is the film condensation on the outside of a horizontal cylinder in cross flow (Fig. 10.11a). The surface heat transfer coefficient depends on the free-stream velocity of the vapor, U_∞, as well as on gravity [16]:

$$\frac{\bar{h}_D D}{k_l} = 0.64 \mathrm{Re}_D^{1/2} \left[1 + \left(1 + 1.69 \frac{g h'_{fg} \mu_l D}{U_\infty^2 k_l \left(T_\mathrm{sat} - T_w \right)} \right)^{1/2} \right]^{1/2} \qquad (10.35)$$

(a)

(b)
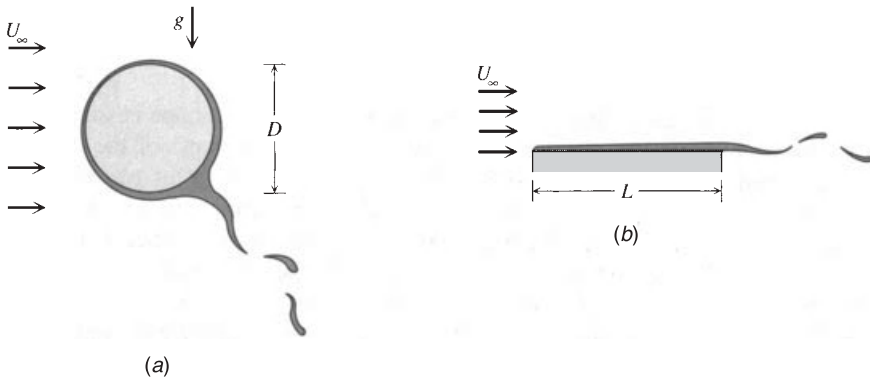
Figure 10.11 Film condensation on (a) horizontal cylinder in cross flow and (b) flat plate parallel to flow. (From Ref. 1.)

The Reynolds number is based on the kinematic viscosity of the liquid, $\text{Re}_D = U_\infty D/\nu_l$. Equation (10.35) holds for Reynolds numbers up to 10^6. In the limit of negligible gravitational effect, the right side of (10.35) approaches $0.64\text{Re}_D^{1/2}$. In the opposite extreme, when the vapor stream slows to a halt, eq. (10.35) becomes identical to eq. (10.30), which represents the pure natural convection limit of the process of Fig. 10.11.

The results for laminar film condensation on a flat plate in a parallel stream of saturated vapor (Fig. 10.11b) are represented by [17]

$$\frac{\overline{h}_L L}{k_l} = 0.872\text{Re}_L^{1/2}\left[\frac{1.508}{\left(1 + \text{Ja}/\text{Pr}_l\right)^{3/2}} + \frac{\text{Pr}_l}{\text{Ja}}\left(\frac{\rho_v \mu_v}{\rho_l \mu_l}\right)^{1/2}\right]^{1/3} \tag{10.36}$$

The Reynolds number is again based on the liquid viscosity, $\text{Re}_L = U_\infty L/\nu_l$, and the Jakob number is the same as the one defined in eq. (10.19). Equation (10.36) has the proper asymptotic behavior and has been tested in the range $(\rho_l \mu_l/\rho_v \mu_v)^{1/2} \sim 10\text{--}500$ and $\text{Ja}/\text{Pr}_l \sim 0.01\text{--}1$.

Inside a vertical cylinder with cocurrent vapor flow (Fig. 10.12), the downward progress of the liquid is aided by the vapor that flows through the core of the cross section. The liquid film is therefore thinner than in the absence of downward vapor flow, and the L-averaged heat transfer coefficient $(\overline{h}_L)$ and the condensation rate are greater. Chen et al. [11] reviewed the experimental information available on this configuration and proposed a correlation that can be rearranged in the following way:

$$\frac{\overline{h}_L}{k_l}\left(\frac{\nu_l^2}{g}\right)^{1/3} = \left[\text{Re}_L^{-0.44} + 5.82 \times 10^{-6}\text{Re}_L^{0.8}\text{Pr}_l^{1/3}\right.$$

$$+ 3.27 \times 10^{-4}\frac{\text{Pr}_l^{1.3}}{D^2}\left(\frac{\nu_l^2}{g}\right)^{2/3}\left(\frac{\mu_v}{\mu_l}\right)^{0.156}$$

$$\left.\times\left(\frac{\rho_l}{\rho_v}\right)^{0.78}\frac{\text{Re}_L^{0.4}\,\text{Re}_t^{1.4}}{(1.25 + 0.39\text{Re}_L/\text{Re}_t)^2}\right]^{1/2} \tag{10.37}$$

This formula is similar to eq. (10.23) because the only difference between the present configuration (Fig. 10.12) and those of Fig. 10.7 is the presence of the core flow of vapor. Indeed, the third group on the right side of eq. (10.37) accounts for the increase in $\overline{h}_L$ that is due to the interfacial shear between the vapor and the liquid film. The Reynolds number Re_L is defined according to eq. (10.22). The terminal Reynolds number Re_t is based not on the actual flow rate $\Gamma(L)$, but on $\dot{m}_v/\pi D$, in which $\dot{m}_v$ is the total flow rate of the vapor that enters through the top of the tube. In other words, the *terminal* Reynolds number Re_t is the maximum value approached by Re_L as a greater and greater fraction of the original vapor stream is converted into liquid at the bottom of the tube (note that $\text{Re}_L < \text{Re}_t$).
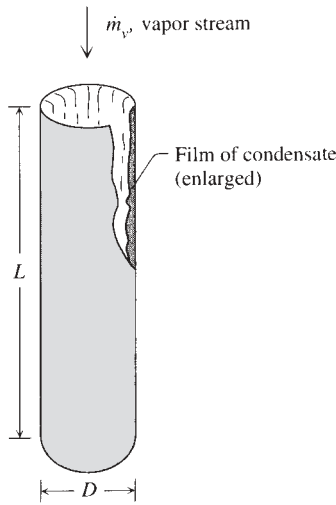
Figure 10.12   Condensation in a vertical tube with cocurrent flow of vapor. (From Ref. 1.)

The tube orientation is no longer a factor when the vapor stream is fast enough so that the last term overwhelms the others on the right side of eq. (10.37). In this limit, the gravitational effect is negligible, and the average heat transfer coefficient can be calculated with the simpler formula

$$\frac{\overline{h}_L D}{k_l} = 0.0181 \mathrm{Pr}_l^{0.65} \left(\frac{\mu_v}{\mu_l}\right)^{0.078} \left(\frac{\rho_l}{\rho_v}\right)^{0.39} \frac{\mathrm{Re}_L^{0.2}\, \mathrm{Re}_t^{0.7}}{1.25 + 0.39 \mathrm{Re}_L/\mathrm{Re}_t} \tag{10.38}$$

The rate of condensation inside a horizontal tube with fast vapor flow (Fig. 10.13a) can be calculated based on eq. (10.37). In this limit, the liquid film coats the perimeter of the cross section uniformly. When the vapor flow is slow,
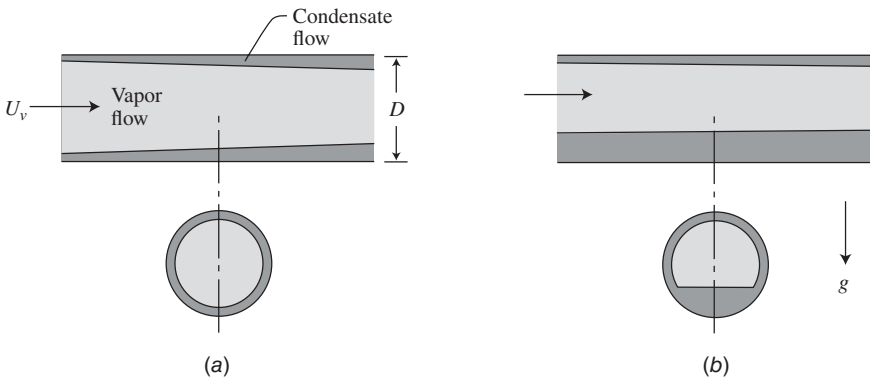
Figure 10.13   (a) Condensation as annular film in a tube with fast vapor flow; (b) accumulation of condensate in a horizontal tube with slow vapor flow. (From Ref. 1.)

the liquid flow favors the lower region of the tube cross section (Fig. 10.13b). Chato [18] found that when the vapor flow Reynolds number is small,

$$\frac{\rho_v U_v D}{\mu_v} < 3.5 \times 10^4 \tag{10.39}$$

the condensation process is dominated by natural convection and that $\bar{h}_D$ is given by an expression similar to eq. (10.30):

$$\frac{\bar{h}_D D}{k_l} = 0.555 \left[\frac{D^3 h'_{fg} g \left(\rho_l - \rho_v \right)}{k_l \nu_l (T_{\text{sat}} - T_w)} \right]^{1/4} \tag{10.40}$$

In eq. (10.40) the effect of the buildup of condensate in the longitudinal direction has not been taken into account.

Procedures for calculating the heat transfer and condensation rates in several other configurations are described in Refs. 19 and 20. For example, in cases where the vapor is superheated, $T_\infty > T_{\text{sat}}$, Rohsenow [20] recommended replacing h'_{fg} with a slightly larger quantity, h''_{fg}, which also accounts for the cooling experienced by the vapor en route to its saturation temperature at the interface,

$$h''_{fg} = h'_{fg} + c_{P,v}(T_\infty - T_{\text{sat}}) \tag{10.41}$$

A common feature of all the configurations discussed until now is that the vapor is pure (i.e., it contains nothing but the substance that eventually condenses into the liquid film). When the gas is a mixture containing not only the condensing species but also one or more noncondensable gases, the heat transfer coefficient is significantly lower than when the noncondensable gases are absent. The condensation rate is lower because the condensing species must first diffuse through the concentration boundary layer that coats the gas side of the interface. The condensing species must first overcome the mass transfer resistance posed by the concentration boundary layer. This process and its effect on the condensation rate are described in Refs. 21 and 22.

10.1.4 Drop Condensation

The condensate distributes itself as a continuous thin film on the cooled surface only when the liquid wets the solid. This happens when the surface tension between the liquid and the solid material is sufficiently small: for example, when the solid surface is clean (grease-free), as in the condensation of steam on a clean metallic surface.

When the surface tension is large, the condensate coalesces into a multitude of droplets of many sizes. In time, each droplet grows as more vapor condenses on its exposed surface. The formation of each droplet is initiated at a point of surface imperfection (pit, scratch) called a *nucleation site*. There comes a time when the tangential pull of gravity, or shear force exerted by the vapor stream, dislodges the droplet and carries it downstream. The moving droplet devours

the smaller droplets found in its path, creating in this way a clean trail ready for the initiation of a new generation of droplets of the smallest size. Since the condensation rate is the highest in the absence of condensate on the surface (film or droplets), the periodic cleaning performed by the large drops renews finite-size regions of the surface for restart of the time-dependent condensation process. This *surface renewal* process is the main reason why dropwise condensation is a highly effective mechanism, which can be designed *constructally* to promote condensation [23]. The heat transfer coefficient for dropwise condensation is approximately 10 times greater than the corresponding coefficient estimated based on the assumption that the condensate forms a continuous film. To be conservative, it is recommended that the heat transfer coefficient be estimated based on the continuous film model.

In the design of condensers, the function of which is to cool a vapor stream and to convert it into liquid, there is a great incentive to promote the breakup of the condensate film into drops. This can be accomplished by (1) coating the solid surface with an organic substance (e.g., oil, wax, kerosene, oleic acid), (2) injecting nonwetting chemicals into the vapor so that they would be deposited on the condenser surface, and (3) coating the surface with a polymer with low surface energy (e.g., Teflon, silicone), or with a noble metal (e.g., gold, silver) [24]. In methods 1 and 2, unfortunately, the ''promoter'' material wears off, as it is gradually removed by the scraping action of the droplet movement. In method 3, fluorocarbon coatings such as Teflon have good surface characteristics but a relatively low thermal conductivity. If the coating is thicker than about 20 μm, its conduction resistance tends to offset the heat transfer augmentation effect due to dropwise condensation on the vapor side of the coating.

As a fundamental mechanism of convection with change of phase, the phenomenon of dropwise condensation is complicated by its intermittent time-dependent character, the dominant effect of surface tension (drop size and shape), and the uncertainty associated with the location of nucleation sites and the time when the largest droplet would start its movement downstream. For all these reasons, a unifying theory of dropwise condensation has not been developed. Reviews of the experimental information on the performance of surfaces with promoters of dropwise condensation can be found in Ref. 25.

The film and drop condensation mechanisms are two examples of what is generally referred to as *surface condensation*. In both cases, the condensate adheres to a solid surface that is being cooled by an external entity (from the back side). A different mechanism is *direct-contact condensation*, in which the solid surface is absent and the cooling effect is provided by the large pool of subcooled liquid through which bubbles of condensing vapor rise. Surface tension plays an important role in determining the size, shape, and life of each vapor bubble. The progress on direct-contact condensation has been reviewed in Ref. 26. The field of convection was reviewed most recently in Ref. 27. A novel augmentation technique is Belghazi et al.'s [28] use of dendritic (cross-shaped) fins with laminar film condensation. This is an application of dendritic fins [3, 29] to condensation heat transfer.

10.2   BOILING

10.2.1   Pool Boiling Regimes

Boiling heat transfer occurs when the temperature of a solid surface is sufficiently higher than the saturation temperature of the liquid with which it comes in contact. The solid–liquid heat transfer is accompanied by the transformation of some of the heated liquid into vapor and by the formation of vapor bubbles, jets, and films. The vapor and surrounding packets of heated liquid are carried away by buoyancy (natural convection or pool boiling) or by a combination of buoyancy and the forced flow of liquid that may be sweeping the solid heater (mixed convection, or flow boiling).

  We begin with the configuration of Fig. 10.14, in which the heater surface (T_w) is immersed in a pool of initially stagnant liquid (T_l). The fundamental physics problem is to determine the relationship between the surface heat flux (q'_w) and the temperature difference ($T_w - T_{sat}$), where T_{sat} is the saturation temperature of the liquid. When, as shown in Fig. 10.14a, the liquid mass is at a temperature below saturation (i.e., subcooled, $T_l < T_{sat}$), boiling is confined to a layer in the immediate vicinity of the heater surface. The vapor bubbles collapse (they recondense) as they rise through the subcooled liquid. When the liquid pool is at the saturation temperature (Fig. 10.14b), the vapor generated at the heater surface reaches the free surface of the pool. In what follows it is assumed that the liquid in the pool is all saturated ($T_l = T_{sat}$).

  Figure 10.15 shows the main features of the *boiling curve*, the relationship between q''_w and the excess temperature ($T_w - T_{sat}$). This particular curve corresponds to the pool boiling of water at atmosphere pressure; however, its roller coaster shape is a characteristic of the curves describing the pool boiling of other liquids. The nonmonotonic relationship between heat flux and excess
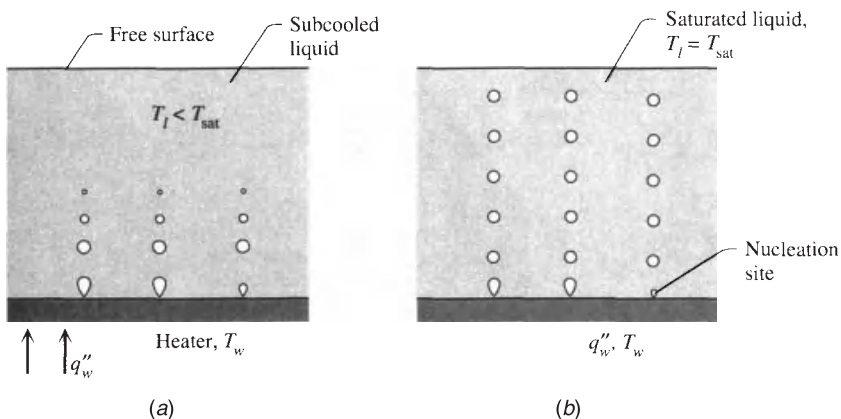
Figure 10.14   Nucleate pool boiling in (a) subcooled liquid and (b) saturated liquid. (From Ref. 1.)
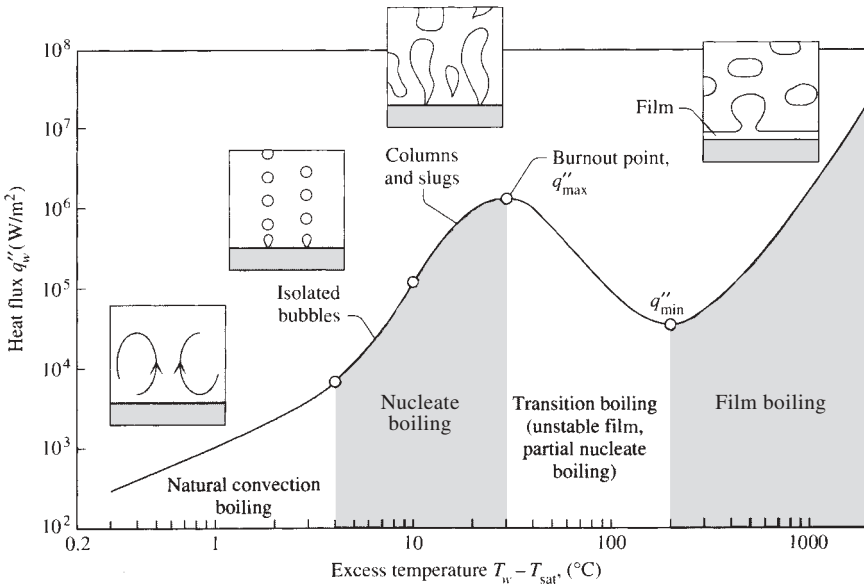
Figure 10.15   Regimes of pool boiling in water at atmospheric pressure. (From Ref. 1.)

temperature is due to the various configurations (bubbles, film) that the newly generated vapor takes in the vicinity of the heater surface. The shape of the boiling curve is the basis for distinguishing among several pool boiling regimes. The transition from one regime to the next can be seen by reading Fig. 10.15 from left to right. This corresponds to a boiling experiment in which the heater surface temperature is increased monotonically and the resulting heat flux is measured. At the end of this section we return to the experiment setups that can be used to trace the boiling curve.

The first interesting aspect of the curve is that at very low excess temperatures (in water, at $T_w - T_{sat} \lesssim 4°C$), the heat transfer occurs without the appearance of bubbles on the heater surface. In this regime, the near-surface liquid becomes superheated and rises in the form of *natural convection* currents to the free surface of the pool. If the heater surface is horizontal and large, and if the liquid pool is shallow, the convection currents are similar to the cellular (Bénard) flow shown in Fig. 5.20b. The relationship between q''_w and $T_w - T_{sat}$ depends on the shape and orientation of the immersed heater and can be determined by employing the formulas assembled in Chapters 4 and 5.

Proceeding toward larger excess temperatures, the next regime is that of *nucleate boiling*. This is characterized by the generation of vapor at a number of spots on the surface (nucleation sites). A probable nucleation site is a tiny crack in the surface, in which the trapped liquid is surrounded by a relatively large heater area per unit of liquid volume. At the low end of the nucleate boiling curve, the boiling process consists of isolated bubbles. At higher temperatures,

the bubble frequency increases, the nucleation sites multiply, and the isolated bubbles interact and are replaced by slugs and columns of vapor.

The formation of more and more vapor in the vicinity of the surface has the effect of gradually insulating the surface against the T_{sat}-cold liquid. This effect is responsible for the gradual decrease in the slope of the nucleate boiling part of the curve and for its expiration at the point of maximum (peak) heat flux, q''_{max}. The latter is also called *critical heat flux* (CHF), and in water it is on the order of 10^6 W/m². The excess temperature at this point is approximately 30°C.

The next regime is the most peculiar because the heat flux actually decreases as the excess temperature $(T_w - T_{sat})$ continues to increase. This trend is a reflection of the fact that increasingly greater portions of the heater surface become coated with a continuous film of vapor. The vapor is unstable and is replaced intermittently by nucleate boiling. This regime is called *transition boiling*: It expires at the point of minimum heat flux (q''_{min}), where the excess temperature (the Leidenfrost temperature [30]) has become just large enough to sustain a stable vapor film on the heater surface. In water at 1 atm, the minimum heat flux is in the range $10^4 - 10^5$ W/m² and occurs at an excess temperature in the range 100–200°C.

At even larger excess temperatures, the vapor film covers the entire surface and the heat flux q''_w resumes its monotonic increase with $T_w - T_{sat}$. Radiation heat transfer across the film plays a progressively greater role as the excess temperature increases. This high-temperature mode is known as the *film boiling regime*. It persists until T_w reaches the melting point of the surface material [i.e., until the meltdown (burnout) of the heater surface]. If, as in the case of a platinum surface, the melting point is very high (e.g., 2042 K), the film boiling portion of the boiling curve can extend to heat fluxes above the critical q''_{max} of the nucleate boiling regime.

The tracing of the boiling curve from left to right in Fig. 10.15 was based on the assumption that the excess temperature $(T_w - T_{sat})$ can be controlled and increased monotonically. An experiment in which the heater temperature control is possible is shown in Fig. 10.16a. The heater is a horizontal tube immersed in a pool of liquid. The heater surface temperature is controlled by a preheated stream that flows through the tube. In this temperature-controlled experiment, the boiling curve can be traced in either direction by increasing or decreasing the excess temperature gradually.

An alternative setup is the power-controlled experiment shown in Fig. 10.16b. The heater is a horizontal cylinder (wire) stretched in a pool of liquid. The heat flux q''_w is controlled by the experimentalist, who measures the power dissipated in the electrical resistance posed by the wire. In this experiment, the shape of the emerging boiling curve depends on whether the power is increased or decreased.

When the power increases monotonically, the experimentalist observes the transition from the natural convection regime to the several forms of the nucleate boiling regime. As the imposed heat flux increases slightly above the critical value q''_{max}, the wire temperature increases abruptly to the value associated with the film boiling portion of the boiling curve. In most cases, this new temperature
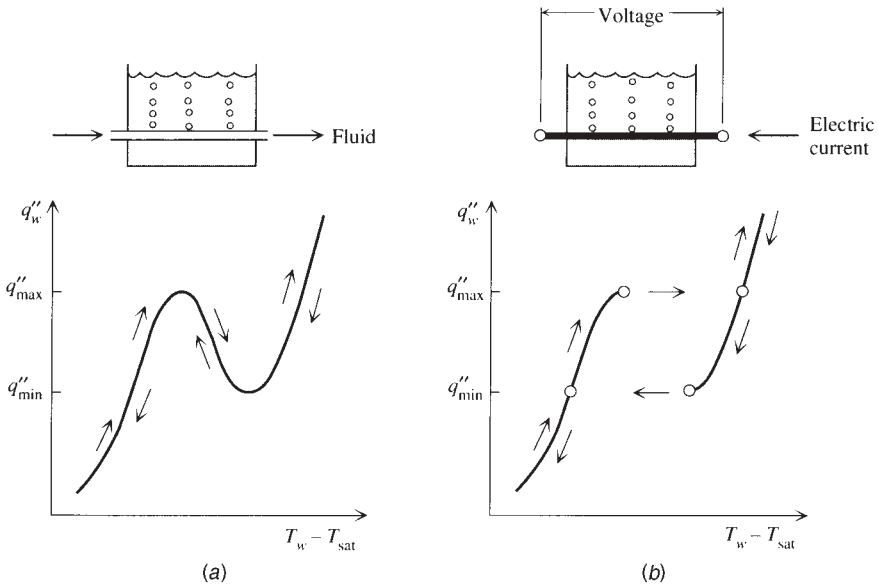
Figure 10.16 Pool boiling curve in (a) temperature-controlled experiment and (b) power-controlled experiment. (From Ref. 1.)

would be above the melting point of the surface material, and the wire burns up. This is why the peak of the nucleate boiling portion of the curve is often called the *burnout point*. The catastrophic event that can occur at heat fluxes comparable with and greater than q''_{max} is why in power-controlled applications of boiling heat transfer (e.g., nuclear reactors, electrical resistance heaters), it is advisable to operate at heat fluxes safely smaller than q''_{max}.

The power-controlled pool boiling experiment can be run in reverse by decreasing the heat flux. In that case, the excess temperature decreases along the film boiling portion of the curve all the way down to the Leidenfrost temperature. As the heat flux is lowered slightly below the minimum heat flux of film boiling, q''_{min}, the vapor film collapses, isolated bubbles form, and the wire temperature drops to the low level associated with the nucleate boiling regime.

To summarize, during heat flux-controlled boiling, the transition boiling regime is inaccessible, and certain portions of the boiling curve can be reached while varying q''_{w} in only one direction. For example, the nucleate boiling regime in the vicinity of the point of maximum heat flux can be established only by increasing the heat flux, starting from a sufficiently low level. Although much less important in practice, the film boiling regime in the vicinity of q''_{min} can be achieved only by decreasing the heat flux, by starting from a sufficiently high level. It is said that q''_{w}-controlled boiling is an example of *hysteresis*,* a

*This term has its origin in the Greek words *hysteresis* (a deficiency) and *hysterein* (to lag, to be behind, to come short).

phenomenon that depends not only on the imposed condition (q_w''), but also on its previous history: in this case, the previous value of q_w''.

The boiling curve was discovered by S. Nukiyama [31] of Tohoku University (Sendai, Japan), who employed the q_w''-controlled method illustrated in Fig. 10.16b. The existence of the missing transition-boiling portion of the curve was demonstrated based on T_w-controlled experiments by Drew and Mueller [32].

10.2.2 Nucleate Boiling and Peak Heat Flux

In practice, the important regime of the curve displayed in Fig. 10.15 is nucleate boiling, because here the boiling heat transfer coefficient

$$h = \frac{q_w''}{T_w - T_{\text{sat}}} \tag{10.42}$$

reaches characteristically large values. These cover the range $10^3 - 10^5$ W/m$^2 \cdot$ K. An enormous volume of research has been devoted to the measurement and correlation of the nucleate-boiling heat transfer coefficient. One of the earliest and most successful correlations, which has withstood the test of time, was proposed by Rohsenow [33]:

$$T_w - T_{\text{sat}} = \frac{h_{fg}}{c_{P,l}} \text{Pr}_l^s \, C_{sf} \left[\frac{q_w''}{\mu_l h_{fg}} \left(\frac{\sigma}{g \left(\rho_l - \rho_v \right)} \right)^{1/2} \right]^{1/3} \tag{10.43}$$

This correlation applies to clean surfaces and is insensitive to the shape and orientation of the surface. It depends on two empirical constants, C_{sf} and s, which are listed in Table 10.1. The dimensionless factor C_{sf} accounts for the particular combination of liquid and surface material, while the Prandtl number exponent s differentiates only between water and other liquids. The subscripts l and v denote saturated liquid and saturated vapor and indicate the temperature (T_{sat}) at which the properties are evaluated.

Representative values of the surface tension σ (N/m) have been collected in Table 10.2 along with other data needed for boiling heat transfer calculations. The surface tension plays an important role in the growth of vapor bubbles, and this role is being recognized in the theories aimed at predicting the nucleate boiling curve. For example, in Problem 10.8, it is shown that the radius of a spherical vapor bubble in mechanical equilibrium is $2\sigma/(P_v - P_l)$, where P_v and P_l are the pressures inside and outside the bubble.

Written as eq. (10.43), Rohsenow's nucleate boiling correlation can be used to calculate the excess temperature ($T_w - T_{\text{sat}}$) when the heat flux q_w'' is known. The calculated excess temperature agrees with experimental data within ±25 percent. In the reverse case, in which the excess temperature is specified, eq. (10.43) can be rewritten as

$$q_w'' = \mu_l h_{fg} \left[\frac{g \left(\rho_l - \rho_v \right)}{\sigma} \right]^{1/2} \left[\frac{c_{P,l} \left(T_w - T_{\text{sat}} \right)}{\text{Pr}_l^s \, C_{sf} H_{fg}} \right]^3 \tag{10.44}$$

Table 10.1   Empirical constants for Rohsenow's nucleate pool boiling correlation (10.43)–(10.44)

Liquid–Surface Combination	C_{sf}	s
Water–copper		
Polished	0.013	1.0
Scored	0.068	1.0
Emery polished, paraffin treated	0.015	1.0
Water–stainless steel		
Ground and polished	0.008	1.0
Chemically etched	0.013	1.0
Mechanically polished	0.013	1.0
Teflon pitted	0.0058	1.0
Water–brass	0.006	1.0
Water–nickel	0.006	1.0
Water–platinum	0.013	1.0
$CC1_4$–copper	0.013	1.7
Benzene–chromium	0.010	1.7
n-Pentane–chromium	0.015	1.7
n-Pentane–copper		
Emery polished	0.0154	1.7
Emery rubbed	0.0074	1.7
Lapped	0.0049	1.7
n-Pentane–nickel		
Emery polished	0.013	1.7
Ethyl alcohol–chromium	0.0027	1.7
Isopropyl alcohol–copper	0.0025	1.7
35% K_2CO_3–copper	0.0054	1.7
50% K_2CO_3–copper	0.0027	1.7
n-Butyl alcohol–copper	0.0030	1.7

Source: Refs. 33 and 34.

in order to calculate the unknown heat flux. In this case, the q_w'' calculated agrees with actual heat flux measurements within ± 100 percent.

In conclusion, eqs. (10.43) and (10.44) provide only an approximate estimate of the true position of the nucleate boiling curve. One reason for this is the S shape taken by the nucleate boiling curve on the logarithmic grid of Fig. 10.15: This shape departs from the straight line that would correspond to eq. (10.44). Another reason is the potential effect of surface roughness, which tends to increase the number of active nucleation sites. In artificially roughened surfaces, for example, the heat flux can be one order of magnitude greater than the q_w'' value furnished by eq. (10.44).

For calculations involving the critical or peak heat flux on a large horizontal surface, the recommended relation is [39]

$$q_{max}'' = 0.149 h_{fg} \rho_v^{1/2} [\sigma g(\rho_l - \rho_v)]^{1/4} \tag{10.45}$$

Table 10.2   Surface tension and other physical properties needed for calculating boiling and condensation heat transfer rates

Fluid	T_{sat} K	T_{sat} °C	P (10⁵ N/m²)[a]	ρ_l (kg/m³)	ρ_v (kg/m³)	h_{fg} (kJ/kg)	σ (N/m)
Ammonia	223	−50	0.409	702	0.38	1417	0.038
	300	27	10.66	600	8.39	1158	0.020
Ethanol	351	78	1.013	757	1.44	846	0.018
Helium	4.2	−269	1.013	125	16.9	20.42	10^{-4}
Hydrogen	20.3	−253	1.013	70.8		442	0.002
Lithium	600	327	4.2×10^{-9}	503		22,340	0.375
	800	527	9.6×10^{-6}	483	10^{-6}	21,988	0.348
Mercury	630	357	1.013	12,740	3.90	301	0.417
Nitrogen	77.3	−196	1.013	809	4.61	198.4	0.0089
Oxygen	90.2	−183	1.013	1134		213.1	0.013
Potassium	400	127	1.84×10^{-7}	814	2.2×10^{-7}	2196	0.110
	800	527	0.0612	720	0.037	2042	0.083
Refrigerant 12	243	−30	1.004	1488	6.27	165.3	0.016
Refrigerant 22	200	−73	0.166	1497	0.87	252.8	0.024
	250	−23	2.174	1360	9.64	221.9	0.016
	300	27	10.96	1187	46.55	180.1	0.007
Sodium	500	227	7.64×10^{-7}	898	4.3×10^{-7}	4438	0.175
	1000	727	0.1955	776	0.059	4022	0.130
Water	323	50	0.1235	988	0.08	2383	0.068
	373	100	1.0133	958	0.60	2257	0.059
	423	150	4.758	917	2.55	2114	0.048
	473	200	15.54	865	7.85	1941	0.037
	523	250	39.73	799	19.95	1716	0.026
	573	300	85.81	712	46.15	1405	0.014

Source: Adapted from Refs. 35–38.
[a]Note that the standard atmospheric pressure is nearly the same as the pressure of 10^5 N/m² (i.e., 1 bar); specifically, 1 atm $= 1.0133 \times 10^5$ N/m².

This analytical expression has a theoretical foundation, having first been proposed based on dimensional analysis by Kutateladze [40] and based on the hydrodynamic stability of vapor columns by Zuber [41].

The peak heat flux formula (10.45) is independent of the surface material. It applies to a sufficiently large surface whose linear length is considerably greater than the characteristic size of the vapor bubble. Equation (10.45) can also be used for a sufficiently large horizontal cylinder by replacing the factor 0.149 with 0.116 [42]. When the size of the heater is comparable with or smaller than the bubble size, the peak heat flux also depends on the size and geometry of the heater. The peak heat flux can be calculated with a formula similar to eq. (10.45), which contains an additional geometric correction factor [39]. Overall, the peak heat flux is relatively insensitive to the shape and orientation of the heater surface; therefore, eq. (10.45) provides an adequate order-of-magnitude estimate of q''_{max} when more specific correlations are not available.

The maximum heat flux of eq. (10.45) depends strongly on the pressure that prevails in the liquid pool. The pressure effect is brought into this relation through both h_{fg} and σ. Near the critical pressure, for example, the peak heat flux approaches zero because both h_{fg} and $\rho_l - \rho_v$ approach zero. The relationship between $q''_{\max}$ and pressure is not monotonic; in the case of water, $q''_{\max}$ increases as the pressure rises to about 70 atm and then decreases to zero as the pressure approaches the critical-point pressure of 218.2 atm.

Regarding the effect of the gravitational acceleration, the nucleate boiling correlations presented in this and the next section are valid in the range $10-1$ m/s^2. Despite the proportionality between q''_w and $g^{1/2}$ indicated by eq. (10.44), it has been found that the gravitational effect has a considerably weaker effect on the nucleate boiling heat flux.

10.2.3   Film Boiling and Minimum Heat Flux

The outstanding feature of the film boiling regime is the continuous layer of vapor (typically, $0.2-0.5$ mm thick) that separates the heater surface from the rest of the liquid pool. The minimum heat flux $q''_{\min}$ is registered at the lowest heater temperature where the film is still continuous and stable (Fig. 10.15). The recommended correlation for the minimum heat flux on a sufficiently large horizontal plane surface is

$$q''_{\min} = 0.09 h_{fg} \rho_v \left[\frac{\sigma g \left(\rho_l - \rho_v \right)}{(\rho_l + \rho_v)^2} \right]^{1/4} \tag{10.46}$$

An interesting feature of this correlation is that $q''_{\min}$ does not depend on the excess temperature $T_w - T_{\mathrm{sat}}$. The analytical form of eq. (10.46) was discovered by Zuber [41], who analyzed the Taylor instability of the horizontal vapor–liquid interface of the film. The 0.09 numerical coefficient in eq. (10.46) was determined by Berenson [43] based on experimental data.

The minimum heat flux calculated with eq. (10.46) agrees within 50 percent with laboratory measurements at low and moderate pressures. The accuracy deteriorates as the pressure increases. The surface roughness has a negligible effect on the minimum heat flux (on the order of 10 percent) because the surface asperities are cushioned by the film against the liquid.

For the rising portion of the film boiling curve, the correlations that have been developed have the same analytical form as the formulas encountered in our study of film condensation. For example, the formula for the average heat transfer coefficient on a horizontal cylinder [44],

$$\frac{\bar{h}_D D}{k_v} = 0.62 \left[\frac{D^3 h'_{fg} g \left(\rho_l - \rho_v \right)}{k_v \nu_v (T_w - T_{\mathrm{sat}})} \right]^{1/4} \tag{10.47}$$

is similar to the film condensation formula (10.30). One important difference is that in eq. (10.47) the transport properties are those of vapor (k_v, ν_v) because
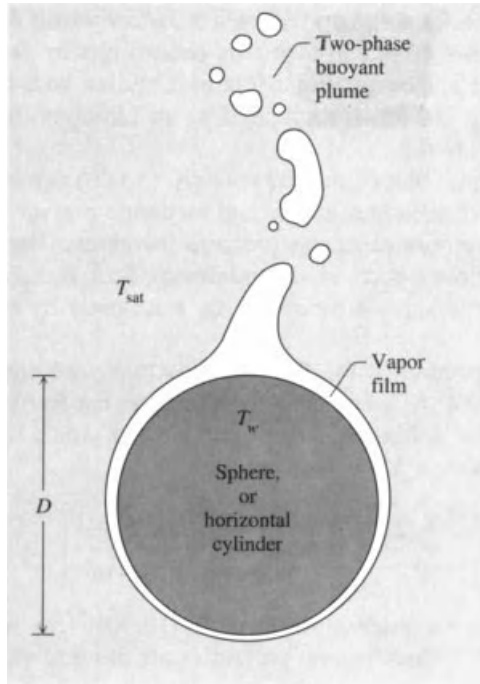
Figure 10.17   Film boiling regime on a sphere or horizontal cylinder. (From Ref. 1.)

the film is occupied by vapor. The similarity between film boiling and film condensation is also geometric, as can be seen by comparing Fig. 10.17 with Fig. 10.9a. The corresponding formula for film boiling on a sphere is [39]

$$\frac{\bar{h}_D D}{k_v} = 0.67 \left[\frac{D^3 h'_{fg} g \left(\rho_l - \rho_v \right)}{k_v \nu_v (T_w - T_{sat})} \right]^{1/4} \tag{10.48}$$

In eqs. (10.47) and (10.48), the augmented latent heat of vaporization h'_{fg} also accounts for the superheating of the fresh vapor to temperatures above the saturation temperature [44]

$$h'_{fg} = h_{fg} + 0.4 c_{P,v}(T_w - T_{sat}) \tag{10.49}$$

The vapor properties k_v, ν_v, ρ_v, and $c_{P,v}$ are best evaluated at the average film temperature $(T_w + T_{sat})/2$. Equations (10.47)–(10.48) state further that the heat transfer coefficient $\bar{h}_D$ is proportional to $(T_w - T_{sat})^{-1/4}$, which means that during film boiling the heat flux q''_w is proportional to $(T_w - T_{sat})^{3/4}$.

As the heater temperature increases, the effect of thermal radiation across the film contributes more and more to the overall heat transfer rate from the heater

to the liquid pool. Bromley [44] showed that the thermal radiation effect can be incorporated into an effective heat transfer coefficient $\bar{h}$,

$$\bar{h} \cong \bar{h}_D + \tfrac{3}{4}\bar{h}_{\mathrm{rad}} \qquad (\text{when } \bar{h}_D > \bar{h}_{\mathrm{rad}}) \qquad (10.50)$$

for which $\bar{h}_D$ is furnished by eqs. (10.47)–(10.48) and $\bar{h}_{\mathrm{rad}}$ is the radiation heat transfer coefficient

$$\bar{h}_{\mathrm{rad}} = \frac{\sigma \epsilon_w (T_w^4 - T_{\mathrm{sat}}^4)}{T_w - T_{\mathrm{sat}}} \qquad (10.51)$$

The σ factor is the Stefan–Boltzmann constant, $\sigma = 5.669 \times 10^{-8} \text{ W/m}^2 \cdot \text{K}^4$, which should not be confused with the symbol used for surface tension. In the same equation, ϵ_w is the emissivity of the heater surface, and numerically, the temperatures (T_w, T_{sat}) must be expressed in kelvin. Equation (10.51) can be derived from the more general formula for the net radiation heat transfer across a narrow gap [1] by assuming that the emissivity of the liquid surface is equal to 1.

In water, the effect of thermal radiation begins to be felt as $T_w - T_{\mathrm{sat}}$ increases above the range 550–660°C [45]. When $\bar{h}_{\mathrm{rad}}$ is comparable with or greater than $\bar{h}_D$, the recommended rule for the effective heat transfer coefficient $\bar{h}$ is [44]

$$\bar{h} = \bar{h}_D \left(\frac{\bar{h}_D}{\bar{h}} \right)^{1/3} + \bar{h}_{\mathrm{rad}} \qquad (\text{when } \bar{h}_D \lesssim \bar{h}_{\mathrm{rad}}) \qquad (10.52)$$

Sparrow [46] showed that a rigorous analysis of combined convection and radiation in the vapor film leads to results that match within a few percentage points the values calculated based on eq. (10.52). It can be shown that the simpler eq. (10.50) follows from eq. (10.52) as $\bar{h}_{\mathrm{rad}}/\bar{h}_D \to 0$.

All the pool boiling heat transfer correlations described until now apply when the pool contains saturated liquid. In cases where the bulk of the liquid is subcooled (e.g., Fig. 10.14a), the degree of liquid subcooling ($T_{\mathrm{sat}} - T_l$) constitutes an additional parameter that further complicates the relationship between the actual heat flux q_w'' and the excess temperature ($T_w - T_{\mathrm{sat}}$). On the natural convection portion of the boiling curve, where the liquid flow is single phase, the heat flux increases if the degree of liquid subcooling increases. For example, when the heater is small enough so that the natural convection flow is laminar, the heat flux increases as $(T_w - T_l)^{5/4}$, or in terms of the degree of subcooling as $[(T_w - T_{\mathrm{sat}}) + (T_{\mathrm{sat}} - T_l)]^{5/4}$. The subcooling parameter ($T_{\mathrm{sat}} - T_l$) has a relatively negligible effect on q_w'' in the nucleate boiling regime, while both q_{max}'' and q_{min}'' increase linearly with $T_{\mathrm{sat}} - T_l$. The effect of liquid subcooling is most pronounced in the film boiling regime.

New directions of inquiry are emerging in the current literature. One is the use of constructal theory [3–5, 29, 47, 48] to account for the emergence of hierarchical multiscale flows in the presence of phase change. The effect of the interaction between neighboring nucleation sites was documented by Golobic and Gjerkes [49]. The constructal design of tree-shaped networks with evaporating

flow, which are used for cooling a surface (e.g., skating rink), was developed by Zamfirescu and Bejan [50]. Another direction is study of metastable explosive evaporation, which may occur when the formation of bubbles is delayed and the liquid that comes in contact with a wall with high superheat is metastable. In such a liquid, the formation of vapor may occur en masse, causing a sudden and explosive expansion of the mixture. This process is important in the design of work-producing devices at very small scales. It is also relevant to predicting the effect of vapor explosions at large scales, for example, in hypothetical nuclear reactor accidents [51–54].

10.2.4 Flow Boiling

Boiling heat transfer is considerably more complicated and difficult to correlate in situations where the liquid is forced to flow past the heater. In nucleate flow boiling (e.g., Fig. 7.1), the heat transfer rate is due to a combination of two closely interrelated effects: (1) the bubble formation and motion near the surface and (2) the direct sweeping of the heater surface by the liquid itself. The heat transfer mechanism is a combination of two basic ones: the nucleate pool boiling of Section 10.2.2 and a forced convection phenomenon of the type treated in Chapters 2, 3, 7, 8, and 9.

There is no general, definitive method of correlating flow boiling data. The progress in this direction has been reviewed in Ref. 55. Rohsenow showed that the experimental data on nucleate boiling with convection are represented adequately by the additive formula [56]

$$q'' = q''_w + q''_c \qquad (10.53)$$

In this expression, q''_w is the nucleate pool boiling heat flux calculated based on eq. (10.44) and the assumption that the bulk of the liquid is stationary. The second term, q''_c, is the single-phase convection heat flux to the liquid, $q''_c = h_c(T_w - T_l)$, for which the convection heat transfer coefficient h_c can be estimated by employing the results listed in the single-phase convection chapters. For nucleate boiling in duct flow, Rohsenow recommended calculating h_c by replacing the coefficient 0.023 with 0.019 in the Dittus–Boelter correlation (8.31). The superposition formula (10.53) works best when the flowing liquid is subcooled and the generation of vapor near the heater surface is not excessive.

10.3 CONTACT MELTING AND LUBRICATION

In this section we turn our attention to close-contact melting, which is a relatively new subfield in phase-change heat transfer. Melting and lubrication can occur between two mating solid parts, one of which is at the melting point. It is a phenomenon complicated by the fact that the phase-change heat transfer is tied intimately to the fluid mechanics of the thin film of melt and to the mechanics of

the two solid bodies. The research progress on contact melting and lubrication is reviewed in Ref. 57.

The classical example of contact melting and lubrication is the friction on ice and snow [58, 59]. Among the more modern applications is the coating of a metallic part with another metal whose melting point is considerably lower. The function of the latter is to melt and serve as a lubricant in the manufacturing process to which the former may be subjected. Another application is in the field of interior ballistics, where a projectile (e.g., brass bullet) melts superficially as it travels along the gun barrel. Other applications include the storage of energy as latent heat inside capsules and the burial of heat-generating objects.

10.3.1   Plane Surfaces with Relative Motion

The principles of contact melting and lubrication become evident if we analyze the simplest geometric configuration possible [60], which is shown in Fig. 10.18. A block of a substance at the melting point (T_m) is pushed with the force F_n (N/m) against another solid that moves to the right with the velocity U. The sliding solid is relatively warmer ($T_m + \Delta T$) and causes steady melting at the lower surface of the T_m block. The liquid that is generated by this melting process fills the gap δ and lubricates the relative motion between the two solids. The tangential (friction) force is F_t (N/m).

The energy equation for the liquid film δ can be written with reference to the (x, y) frame shown in Fig. 10.18, in which (u, v) are the corresponding liquid velocity components,

$$\underbrace{u\frac{\partial T}{\partial x} + v\frac{\partial T}{\partial y}}_{\dfrac{U\,\Delta T}{L}} = \underbrace{\alpha\frac{\partial^2 T}{\partial y^2}}_{\alpha\dfrac{\Delta T}{\delta^2}} + \underbrace{\frac{\mu}{\rho\,c_P}\Phi}_{\dfrac{\mu}{\rho c_P}\left(\dfrac{U}{\delta}\right)^2} \tag{10.54}$$
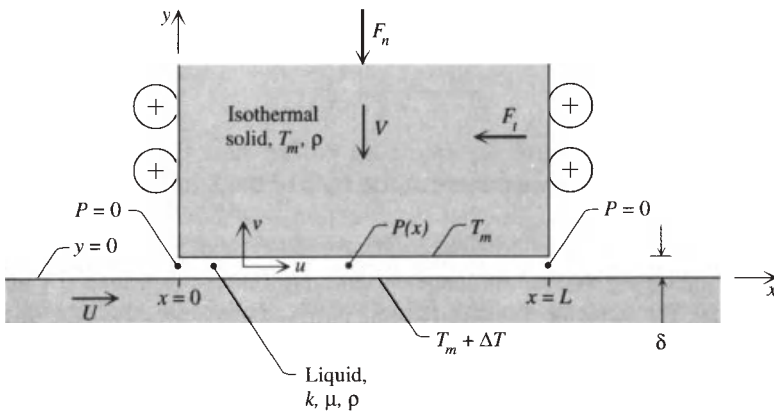
Figure 10.18   Block of melting material pressed against a plane slider. (From Ref. 1.)

Equation (10.54) is based on the ''boundary layer'' assumption that the film is thin, $\delta \ll L$. Listed underneath are the representative scales of the three effects that compete in the energy balance, convection, conduction, and internal heat generation. The transversal conduction effect is always important because, without it, there is no melting at the $y = \delta$ interface. Convection is negligible relative to conduction if $(U \Delta T)/L \ll (\alpha \Delta T)/\delta^2$, which means that

$$\left(\frac{\delta}{L}\right)^2 \frac{UL}{\alpha} \ll 1 \tag{10.55}$$

This holds true in most film lubrication problems because the film is very thin, $\delta/L \ll 1$, and the Péclet number UL/α is finite. The viscous heating effect is negligible with respect to transversal conduction when $(\mu/\rho c_P)(U/\delta)^2 \ll (\alpha \Delta T)/\delta^2$, which means that

$$\frac{\mu U^2}{k \, \Delta T} \ll 1 \tag{10.56}$$

where the scale of the temperature difference is $\Delta T = T_w - T_m$. Note that the viscous dissipation criterion (10.56) does not depend on the film thickness δ.

When conditions (10.55) and (10.56) are satisfied simultaneously, the heat transfer in the liquid film is by pure conduction across the film. The energy equation for the liquid in the relative-motion gap reduces to

$$\frac{\partial^2 T}{\partial y^2} = 0 \tag{10.57}$$

with the general solution $T = f_1 y + f_2$, where f_1 and f_2 are at most functions of x. They are determined from the boundary conditions

$$T = \begin{cases} T_m + \Delta T & \text{at } y = 0 & (10.58) \\ T_m & \text{at } y = \delta & (10.59) \end{cases}$$

so that the temperature distribution emerges as a function of y only:

$$T = T_m + \left(1 - \frac{y}{\delta}\right) \Delta T \tag{10.60}$$

The energy balance for a control volume of infinitesimal thickness drawn around the melting front requires that

$$\underbrace{L\rho V h_s}_{\substack{\text{Enthalpy} \\ \text{inflow from} \\ \text{above}}} + \underbrace{Lk\frac{\Delta T}{\delta}}_{\substack{\text{Conduction} \\ \text{heat transfer} \\ \text{from below}}} = \underbrace{L\rho V h_f}_{\substack{\text{Enthalpy} \\ \text{outflow,} \\ \text{downward}}} \tag{10.61}$$

The second term on the left side comes from using eq. (10.60) in the definition of the heat transfer rate oriented in the y direction,

$$q' = Lk\left(-\frac{\partial T}{\partial y}\right)_{y=\delta} \tag{10.62}$$

Equation (10.61) is one relationship between the chief unknowns of this problem, the melting speed V and the liquid gap thickness δ:

$$V\delta = \frac{k\,\Delta T}{\rho\,h_{sf}} \tag{10.63}$$

The second relationship between V and δ is provided by the fluid mechanics of the liquid flow. The momentum equation reduces to

$$\frac{dP}{dx} = \mu\frac{\partial^2 u}{\partial y^2} \tag{10.64}$$

and this yields

$$u = \frac{1}{2\mu}\left(\frac{dP}{dx}\right)y^2 + f_3 y + f_4 \tag{10.65}$$

The functions $f_3(x)$ and $f_4(x)$ are determined by invoking the boundary conditions

$$u = \begin{cases} U & \text{at } y = 0 \\ 0 & \text{at } y = \delta \end{cases} \qquad\begin{matrix}(10.66)\\(10.67)\end{matrix}$$

and the resulting expression for $u(x, y)$ is

$$u = \frac{1}{2\mu}\left(\frac{dP}{dx}\right)(y^2 - y\delta) + U\left(1 - \frac{y}{\delta}\right) \tag{10.68}$$

This solution cannot be used yet because it involves the unknown excess pressure gradient dP/dx. The excess pressure must be related to the normal force with which the melting block is pushed downward and to the fact that $P = 0$ at both ends of the liquid channel, $x = 0$ and $x = L$. We determine the excess pressure distribution by first calculating the liquid flow rate

$$Q = \int_0^\delta u\,dy \tag{10.69}$$

which, after using eq. (10.68), becomes

$$Q = \frac{1}{12\mu}\left(-\frac{dP}{dx}\right)\delta^3 + \frac{1}{2}U\delta \tag{10.70}$$

Next, we recognize the mass conservation statement

$$\frac{\partial u}{\partial x} + \frac{\partial v}{\partial y} = 0 \tag{10.71}$$

which can be integrated across the liquid gap to yield

$$\frac{d}{dx}\underbrace{\int_0^\delta u\,dy}_{Q} + \underbrace{(v)_{y=\delta}}_{-V} - \underbrace{(v)_{y=0}}_{zero} = 0 \tag{10.72}$$

or $dQ/dx = V$, where V is the downward velocity of the solid block (Fig. 10.18). By eliminating Q from eq. (10.70), we obtain an equation for $P(x)$,

$$\frac{1}{12\mu}\left(-\frac{d^2P}{dx^2}\right)\delta^3 = V \tag{10.73}$$

which can be integrated subject to the end conditions ($P = 0$ at $x = 0$ and $x = L$)

$$P(x) = \frac{6\mu V}{\delta^3}(Lx - x^2) \tag{10.74}$$

Integrated along the liquid gap, this yields a second relationship between V and δ,

$$F_n = \int_0^L P\,dx = \mu V\left(\frac{L}{\delta}\right)^3 \tag{10.75}$$

The melting speed is obtained by eliminating δ between eqs. (10.63) and (10.75):

$$V = \left(\frac{F_n}{\mu}\right)^{1/4}\left(\frac{k\,\Delta T}{\rho h_{sf}L}\right)^{3/4} \tag{10.76}$$

An alternative form of this result, which will be compared later with the general correlation (10.89), is

$$\frac{VL}{\alpha} = \left(\frac{c_P\,\Delta T}{h_{sf}}\right)^{3/4}\mathrm{Be}_L^{1/4} \tag{10.76'}$$

where Be_L is the dimensionless pressure-difference number defined in eq. (3.120'), $\mathrm{Be}_L = (F_n/L) \cdot L^2/\mu\alpha$, and F_n/L is the scale of the pressure difference. The tangential force experienced by the melting block is equal to the negative of the shear force felt by the hot slider:

$$F_t = -\int_0^L \mu\left(\frac{\partial u}{\partial y}\right)_{y=0}dx = L\mu\frac{U}{\delta} \tag{10.77}$$

The coefficient of friction is [60]

$$\mu_f = \frac{F_t}{F_n} = U\left(\frac{\mu}{F_n}\right)^{3/4}\left(\frac{\rho h_{sf}L}{k\,\Delta T}\right)^{1/4} \tag{10.78}$$

which shows that the coefficient of friction decreases as the normal force increases. All the results developed in this section can also be derived based on scale analysis, for example, eqs. (10.76) and (10.78). See Section 10.3.3.

10.3.2   Other Contact Melting Configurations

To review the diversity of the contact melting field [57], it is sufficient to list the theoretical results that have been reported. The melting of a phase-change material inside a horizontal cylinder (Fig. 10.19) was analyzed by Bareiss and Beer [62]. The solid is at the melting point (T_m) and fills the cylinder. The wall temperature is raised to T_w at time $t = 0$. The time t_f needed to melt all the solid is given by the dimensionless expression

$$\frac{\alpha t_f}{R^2} = 2.49\left(\frac{\rho}{\rho_s}\text{Ste}\right)^{-3/4}(\text{Pr Ar})^{-1/4}(1 + C)^{-1} \tag{10.79}$$

where the Stefan number and Archimedes number are defined by

$$\text{Ste} = \frac{c_P(T_w - T_m)}{h_{sf}}, \qquad \text{Ar} = \left(1 - \frac{\rho}{\rho_s}\right)\frac{gR^3}{\nu^2} \tag{10.80}$$

The term C is an empirical correction that accounts for additional melting (a minor effect) associated with natural convection over the upper surface of the solid,

$$C = 0.25\left(\frac{\rho}{\rho_s}\text{Ste}\frac{\text{Ra}}{\text{Pr Ar}}\right)^{1/4} \tag{10.81}$$
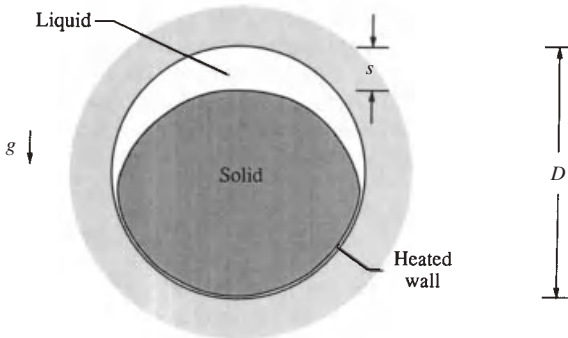
Figure 10.19   Contact melting inside a capsule shaped as a sphere or horizontal cylinder. (From Ref. 61.)

in which $Ra = g\beta(T_w - T_m)D^3/\alpha\nu$. Labeled s in Fig. 10.19 is the distance traveled by the geometric center of the original solid in the downward direction. This distance is the same as the largest liquid gap $s(t)$ at the top of the solid when melting over the upper surface of the solid is negligible. Bareiss and Beer [62] found that the solid falls with the nearly uniform speed $\overline{V} = D/t_f$ because $s(t)$ increases almost linearly from $s(0) = 0$ to $s(t_f) = D$.

Roy and Sengupta [63] and Bahrami and Wang [64] reported thin-film analyses for contact melting in a spherical enclosure. Roy and Sengupta's results are presented as a family of curves with Ste/Pr and Ar(ρ/ρ_s) as independent parameters. The predicted melting rate agrees with Moore and Bayazitoglu's [65] experiments with n-octadecane. In addition, analysis shows that the contact melting film is thinner at the lowest point of the spherical surface, and the melting rate decreases as Ar/(ρ/ρ_s) decreases. Bahrami and Wang [64] developed a closed-form expression for the time interval needed to melt all the solid. If we use the dimensionless formulation of the present treatment, Bahrami and Wang's expression can be rewritten as

$$\frac{\alpha t_f}{R^2} = 2.03\left(\frac{\rho}{\rho_s}\text{Ste}\right)^{-3/4}(\text{Pr Ar})^{-1/4} \qquad (10.82)$$

If we turn the geometry of Fig. 10.19 inside out, we arrive at Fig. 10.20, which shows how a hot object sinks into a larger body of solid phase-change material. Contact melting occurs over the leading portion of the hot object: The pressure built in the liquid film supports the weight of the object during its quasisteady sinking motion. If the solid phase-change material is subcooled, the liquid wake generated behind the object refreezes at some distance downstream.
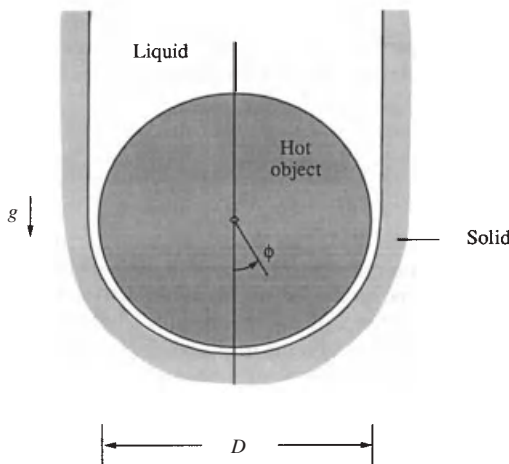
Figure 10.20 Hot sphere or horizontal cylinder sinking in a solid phase-change material. (From Ref. 61.)

Emerman and Turcotte [66] studied the motion of a heated sphere (T_w) through a solid phase-change material whose temperature T_∞ is below its melting point (T_m). They found that the liquid film thickness $\delta(\phi)$ increases dramatically in the direction away from the nose of the sphere ($\phi = 0$),

$$\delta(\phi) = \frac{\alpha \, \text{Ste}}{V \cos \phi} \qquad (\text{Ste} \ll 1) \qquad (10.83)$$

where the Stefan number $\text{Ste} = c_P (T_w - T_m)/h'_{sf}$ is based on the augmented latent heat of melting $h'_{sf} = h_{sf} + c_s (T_m - T_\infty)$. The vertical velocity of the sphere, V, is proportional to the imposed temperature difference $(T_w - T_m)$ raised to the power $\frac{3}{4}$. If the Stefan number is much smaller than 1, the velocity is given by

$$\frac{VR}{\alpha} = \text{Ste}^{3/4} \left(\frac{8g \, \Delta\rho \, R^3}{3\mu\alpha} \right)^{1/4} \qquad (\text{Ste} \ll 1) \qquad (10.84)$$

in which $\Delta\rho = \rho_0 - \rho$ is the difference between the density of the object (sphere) and the density of the surrounding melt.

The sinking of a horizontal cylinder embedded in a solid phase-change medium was studied experimentally and analytically by Moallemi and Viskanta [67]. Their analytical results are valid for any Stefan number. In the $\text{Ste} \ll 1$ limit, the film thickness varies according to eq. (10.83) over the leading surface of the cylinder, while the vertical velocity V is given by

$$\frac{VR}{\alpha} = \text{Ste}^{3/4} \left(\frac{5\pi}{16} \frac{g \, \Delta\rho \, R^3}{\mu\alpha} \right)^{1/4} \qquad (\text{Ste} \ll 1) \qquad (10.85)$$

10.3.3 Scale Analysis and Correlation

All the contact melting results reviewed in Sections 10.3.1 and 10.3.2 can be anticipated based on a very simple analysis [61]. We write ℓ for the longitudinal length scale of liquid flow through the film and further assume that the contact surface is not necessarily plane (Fig. 10.21). The conservation of mass in the liquid film requires that

$$u\delta \sim V\ell \qquad (10.86)$$

The momentum balance is simply

$$\frac{\Delta P}{\ell} \sim \mu \frac{u}{\delta^2} \qquad (10.87)$$

because, if present, the shearing caused by relative motion does not contribute to the longitudinal pressure gradient $\Delta P/\ell$. Finally, the conservation of energy at the melting front requires that

$$k \frac{\Delta T}{\delta} \sim \rho_s h_{sf} V \qquad (10.88)$$
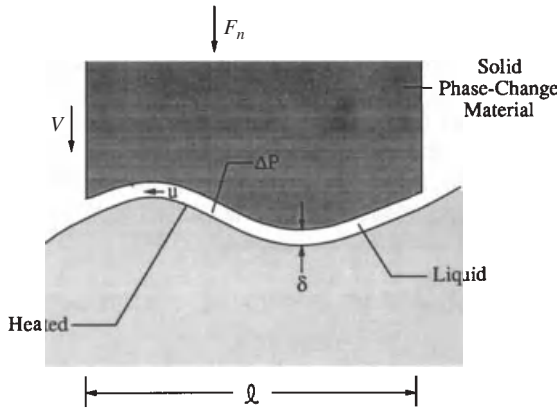
Figure 10.21 General shape of mating surfaces with close-contact melting. (From Ref. 61.)

If we eliminate u and δ between eqs. (10.86)–(10.88), we obtain a melting speed that can be nondimensionalized in the form of the Péclet number based on ℓ,

$$\frac{V\ell}{\alpha} \sim \left(\frac{\rho}{\rho_s} \text{Ste}\right)^{3/4} \text{Be}_\ell^{1/4} \tag{10.89}$$

The pressure difference number is also based on ℓ, $\text{Be}_\ell = (\Delta P\ell^2)/\mu\alpha$.

The scaling law (10.89) reproduces exactly the plane contact melting result (10.76) if we set $\ell = L$ and $\Delta P = F_n/L$. More important is that eq. (10.89) also correlates the results for contact melting inside capsules and around embedded hot objects. First, we must recognize that the excess pressure scale ΔP is, in general,

$$\Delta P = \frac{\text{net weight of the object surrounded by liquid}}{\text{horizontal projected area of that object}} \tag{10.90}$$

In the case of melting inside capsules, the numerator in this definition represents the net *initial* weight of the solid phase-change material. The definition (10.90) yields $\Delta P = g\,\Delta\rho(\pi D/4)$ for a horizontal cylinder, and $\Delta P = g\,\Delta\rho(2D/3)$ for a sphere. The excess density of the sinking object is $\Delta\rho = \rho_s - \rho$ for melting inside a capsule (Fig. 10.19) and $\Delta\rho = \rho_0 - \rho$ for objects embedded in a solid phase-change material (Fig. 10.20). The contact melting results reviewed in Section 10.3.2 can now be rediscovered as follows:

Cylindrical capsule, horizontal [Fig. 10.19, eq. (10.79) with $(1 + C) \cong 1$ and $\overline{V} = D/t_f$]:

$$\frac{\overline{V}D}{\alpha} = 1.015\frac{\rho}{\rho_s}\text{Ste}^{3/4}\,\text{Be}_D^{1/4} \qquad (\ell = 0.971D) \tag{10.91}$$

Spherical capsule [Fig. 10.19, eq. (10.82) with $\overline{V} = D/t_f$]:

$$\frac{\overline{V}D}{\alpha} = 1.297 \frac{\rho}{\rho_s} \mathrm{Ste}^{3/4} \, \mathrm{Be}_D^{1/4} \qquad (\ell = 0.595D) \qquad (10.92)$$

Embedded horizontal cylinder [Fig. 10.20, eq. (10.85)]:

$$\frac{VD}{\alpha} = 1.257 \mathrm{Ste}^{3/4} \, \mathrm{Be}_D^{1/4} \qquad (\ell = 0.633D) \qquad (10.93)$$

Embedded sphere [Fig. 10.20, eq. (10.84)]:

$$\frac{VD}{\alpha} = 1.682 \mathrm{Ste}^{3/4} \, \mathrm{Be}_D^{1/4} \qquad (\ell = 0.353D) \qquad (10.94)$$

The Bejan number is based on D as length scale, $\mathrm{Be}_D = (\Delta P D^2)/\mu\alpha$.

Equations (10.76) and (10.91)–(10.94) show that the scaling law (10.89) anticipates within percentage points the melting speed in all geometries if the length scale ℓ is interpreted as the actual dimension of the projected area of contact, namely, $\ell = D$, in Figs. 10.19 and 10.20. There is some disagreement with regard to the role played by the density ratio ρ/ρ_s. Note that this ratio enters as $(\rho/\rho_s)^{3/4}$ in the scaling law (10.89), as ρ/ρ_s in the formulas (10.91) and (10.92) for melting inside capsules, while being absent from the results (10.93) and (10.94) for melting around embedded hot objects. Numerically, however, the effect of ρ/ρ_s is very small because this ratio is a number close to 1.

Listed in parentheses to the right of eqs. (10.91)–(10.94) are the ℓ values that would make these equations agree exactly with eq. (10.89), again, if we discount the small ρ/ρ_s effect. In this case, exact agreement means that the leading numerical factor on the right-hand side of eqs. (10.91)–(10.94) becomes equal to 1. Contact melting in various configurations was analyzed subsequently in Refs. 68–72.

10.3.4 Melting Due to Viscous Heating in the Liquid Film

In the configurations covered in Sections 10.3.1–10.3.3 melting is caused by a temperature difference maintained between the solid surface and the melting front. Consider now the case where the plane slider of Fig. 10.18 is not heated externally and where the viscous heating of the liquid film is responsible for the steady melting of the phase-change material. This happens at sufficiently high slider velocities U. In this limit the conduction heat transfer absorbed by the melting front is balanced by the viscous heating effect, as shown by the last two scales of eq. (10.54),

$$\alpha \frac{\Delta T}{\delta^2} \sim \frac{\mu}{\rho c_P} \left(\frac{U}{\delta} \right)^2 \qquad (10.95)$$

so that the temperature difference scale becomes

$$\Delta T \sim \frac{\mu}{k} U^2 \tag{10.96}$$

The ΔT scale is independent of the film thickness δ. The order-of-magnitude conservation statements for mass, momentum, and energy continue to be represented by eqs. (10.86)−(10.88), for which $\ell \sim L$, and the ΔT scale is now furnished by eq. (10.96). By solving these equations, we obtain the melting speed V,

$$\frac{VL}{\alpha} \sim \left(\frac{\rho}{\rho_s} \mathrm{Ste}_\mu \right)^{3/4} \mathrm{Be}_L^{1/4} \tag{10.97}$$

where $\mathrm{Be}_L = (\Delta P L^2)/\mu\alpha$. Equation (10.97) looks like eq. (10.89) except that Ste_μ is a new dimensionless group: the Stefan number based on the viscous heating temperature rise (10.96),

$$\mathrm{Ste}_\mu = \frac{c_P}{h_{sf}} \left(\frac{\mu}{k} U^2 \right) = \mathrm{Pr} \frac{U^2}{h_{sf}} \tag{10.98}$$

Equation (10.97) shows that when the contact melting is due to viscous heating, the melting speed V is proportional to $U^{3/2}$. We saw earlier that when viscous heating is negligible [eq. (10.76)], V is independent of U. The film thickness scale is

$$\frac{\delta}{L} \sim \left(\frac{\rho}{\rho_s} \mathrm{Ste}_\mu \right)^{1/4} \mathrm{Be}_L^{-1/4} \tag{10.99}$$

which shows that the film thickness increases as $U^{1/2}$ (i.e., as the viscous heating effect intensifies). The δ scale is also proportional to $L^{1/2}$ and $\Delta P^{-1/4}$. Finally, the friction coefficient is obtained by dividing the total friction force $F_t \sim \mu(U/\delta)L$ by the total normal force $F_n = \Delta PL$,

$$\mu_f \sim \frac{UL}{\alpha} \left(\frac{\rho}{\rho_s} \mathrm{Ste}_\mu \right)^{-1/4} \mathrm{Be}_L^{-3/4} \tag{10.100}$$

This can be compared with eq. (10.78) to see the difference that the viscous heating effect makes in the behavior of the friction coefficient. In eq. (10.100), the friction coefficient is proportional to $U^{1/2}$, whereas in eq. (10.78), it is proportional to U. The dependence of μ_f on L and ΔP is the same in eqs. (10.78) and (10.100); in other words, the impact of parameters L and ΔP is insensitive to the degree to which viscous heating sustains the melting and lubrication process.

The scaling trends outlined in this section agree with the more exact results delivered by complete thin-film analyses of the viscous melting and lubrication process [57]. In addition to the scale shown in eq. (10.99), the film thickness has the peculiar feature illustrated in Fig. 10.22. The relative motion gap is a converging–diverging channel with liquid squirting out through both ends. The slider moves to the right, so that $x = 0$ represents the upstream end and $x = L$
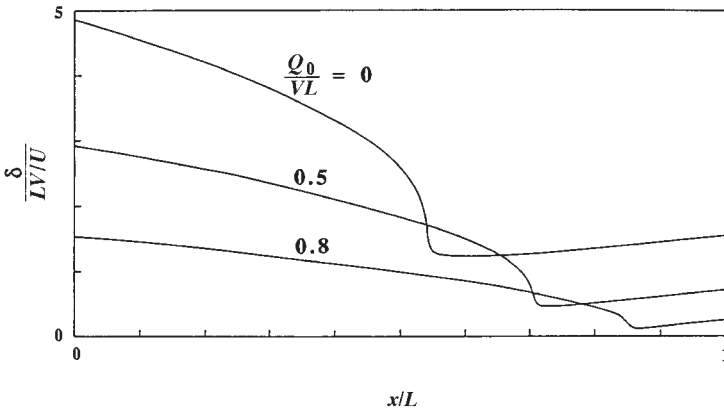
Figure 10.22 Shape of the relative motion gap when melting is driven by viscous heating in the liquid film. (From Ref. 60.)

the downstream end. The curves are labeled according to the liquid flow rate Q_0 forced to the left through the $x = 0$ opening. This flow rate increases with the normal force (or $\Delta P = F_n/L$) in a manner that is reported parametrically in Ref. 60. The excess temperature between the slider (T_w) and the melting front (T_m) varies longitudinally as shown in Fig. 10.23. The hot spot is always on the
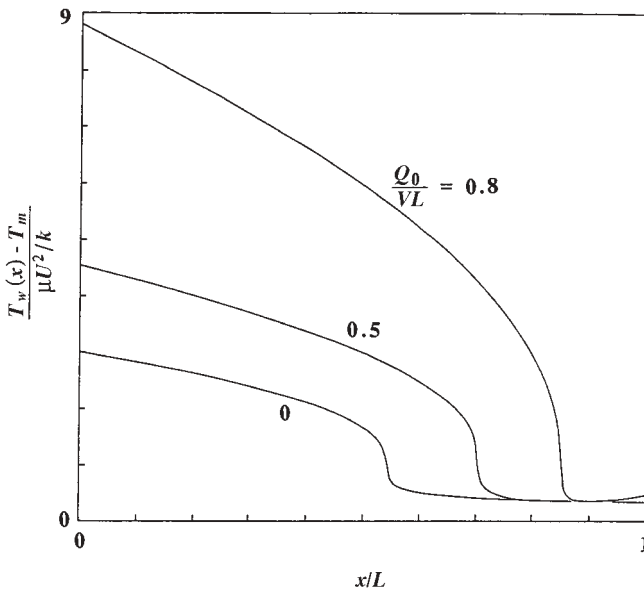
Figure 10.23 Temperature of the slider in Fig. 10.18 when melting is driven by viscous heating in the liquid film. (From Ref. 60.)

slider and in the plane of its entrance to the contact region ($x = 0$). The slider temperature increases as Q_0 and the normal force increase.

Contact melting and lubrication can occur in several other circumstances. One example is when the phase-change material is subcooled (below the melting point) and the slider is not isothermal [73]. Melting can occur when a shaft rotates inside a bearing [74] and when a cylinder rolls on a plane surface [75]. A topic that attracts constant attention is the sliding friction on ice [58], which is complicated further by the asperities of the melting surface and the effect of *pressure melting*, or the decrease experienced by the ice melting point as the applied pressure increases [59,76]. Finally, glasslike substances can provide a contact-heating lubrication effect similar to that of melting phase-change materials [77].

10.4   MELTING BY NATURAL CONVECTION

Melting in the presence of significant natural convection is an important phenomenon in the field of materials processing, thermal energy storage in phase-change materials, waste heat utilization as latent heat, the loss of heat from building foundations to frozen ground, deicing, and the melting of the ice that builds up on transmission lines. Considerable empirical and theoretical work has been devoted already to this phenomenon, and one 1985 conclusion was that this phenomenon is quite complicated, to the point that ''no unified theoretical treatment . . . is within our grasp'' [78]. The complications stem from the strong coupling that exists between the flow of the liquid phase and the melting rate of the solid. It is this coupling that determines the instantaneous shape of the two-phase interface, which constitutes one of the unknowns in each problem.

10.4.1   Transition from the Conduction Regime to the Convection Regime

The key to the correct correlation of complicated trends of natural convection melting is the identification of the correct scales of the phenomenon. Consider the two-dimensional configuration shown in Fig. 10.24, in which the solid phase-change material is at the melting point ($T_s = T_m$). Beginning with a certain point in time ($t = 0$), the left wall of the enclosure is heated and maintained at the constant temperature level T_w. This heating induces melting at the liquid–solid interface and natural convection in the region carved out by the liquid phase.

The natural convection melting process can be analyzed as a sequence of four regimes [79]: These are labeled (a)–(d) in Fig. 10.24. The first regime is the conduction limit, when the heat flux across the incipient vertical liquid film is balanced entirely by the enthalpy absorbed at the two-phase interface,

$$k\frac{T_w - T_s}{s} \sim \rho h_{sf}\frac{ds}{dt} \qquad (10.101)$$
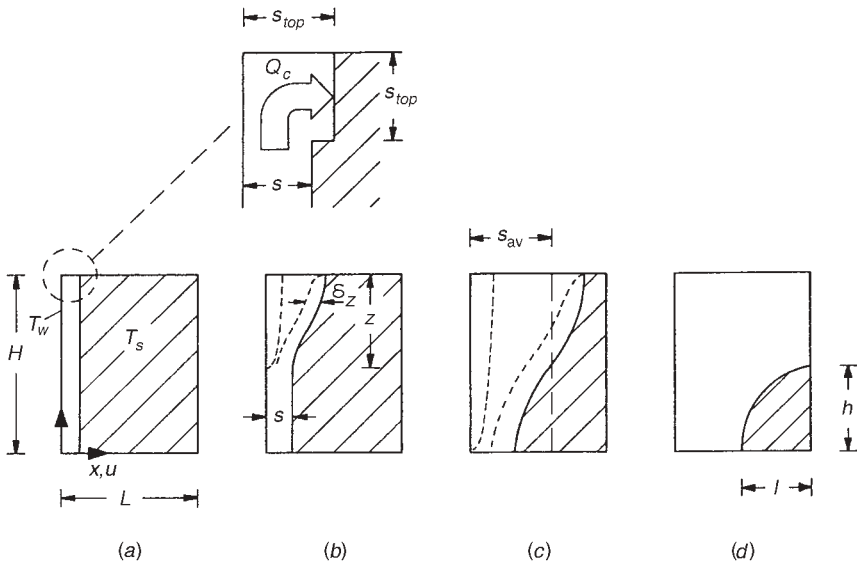
Figure 10.24 Regimes for melting in the presence of significant natural convection when the phase-change material is being heated from the side. (From Ref. 79.)

In dimensionless terms, this yields

$$\frac{s}{H} \sim \theta^{1/2} \tag{10.102}$$

where θ is the dimensionless time group

$$\theta = \frac{k(T_w - T_s)}{\rho h_{sf} H^2} t = \text{Ste Fo} \tag{10.103}$$

and Ste and Fo are the Stefan and Fourier numbers,

$$\text{Ste} = \frac{c(T_w - T_s)}{h_{sf}}, \qquad \text{Fo} = \frac{\alpha t}{H^2} \tag{10.104}$$

The Nusselt number that corresponds to this conduction limit is

$$\text{Nu} = \frac{Q}{k(T_w - T_s)} \sim \frac{H}{s} \sim \theta^{-1/2} \tag{10.105}$$

where Q is the total heat transfer rate through the left wall of the enclosure, per unit length in the direction perpendicular to the plane of Fig. 10.24.

In the second regime, the conduction process is gradually replaced by convection. This has been named the *mixed regime* (conduction + convection) and is characterized by an upper liquid region that has become wide enough so that its lateral surfaces are lined by distinct boundary layers (Fig. 10.24*b*). Let the

unknown dimension z be the height of this upper region. Heat transfer across the remainder of the liquid space (height $H - z$) continues to be ruled by conduction.

Convection in the upper zone means that the thermal boundary layer thickness in this zone, δ_z, is smaller than the horizontal dimension of the carved-out upper zone. The convective zone expires at its lower extremity, where δ_z is of the same order as the gap thickness of the lower (conduction) zone:

$$\delta_z \sim s \qquad \text{at the convection–conduction transition level} \qquad (10.106)$$

Assuming that the liquid has a Prandtl number of order 1 or greater, we write [cf. eq. (4.26)]

$$\delta_z \sim z \ \text{Ra}_z^{-1/4} \qquad (10.107)$$

where Ra_z is the Rayleigh number based on z, namely, $\text{Ra}_z = g\beta z^3(T_w - T_s)/\alpha\nu$ or $\text{Ra}_z = (z/H)^3 \text{Ra}$. Combining eqs. (10.106) and (10.107) with eq. (10.102) for the conduction gap s yields

$$z \sim H \ \text{Ra} \ \theta^2 \qquad (10.108)$$

In conclusion, the convection zone expands downward as the time increases. The expansion is faster at higher Rayleigh numbers.

With regard to the total heat transfer rate through the heated wall, Q, we note that the heat transfer mechanism is convection over the height z and conduction over $H - z$. The total heat transfer rate is therefore the sum

$$Q \sim kz \frac{T_w - T_s}{\delta_z} + k(H - z)\frac{T_w - T_s}{s} \qquad (10.109)$$

which in view of eqs. (10.102), (10.105), (10.107), and (10.108) translates into

$$\text{Nu} = K_1 \ \theta^{-1/2} + K_2 \ \text{Ra} \ \theta^{3/2} \qquad (10.110)$$

where K_1 and K_2 are constants of order 1. The Nusselt number is made up of two contributions, one due to conduction and the other to convection. One rewarding feature of eq. (10.110) is that it meshes perfectly with the scaling law that holds in the $\theta \to 0$ limit, eq. (10.105). This time, however, the convection contribution ($\text{Ra} \ \theta^{3/2}$) is not necessarily negligible compared with the conduction contribution ($\theta^{-1/2}$).

In conclusion, the heat transfer scaling law (10.110) holds starting with $\theta = 0$ until the assumed convection zone (height z) extends all the way to the bottom of the liquid space, that is, until $z \sim H$. If we label θ_1 the time scale that corresponds to $z \sim H$, eq. (10.108) suggests that the mixed regime ends at a time of order

$$\theta_1 \sim \text{Ra}^{-1/2} \qquad (10.111)$$

in which the factor of order 1 on the right side is neglected. The Nusselt number scaling law (10.110) distinguishes itself through the theoretical prediction of an Nu minimum of order

$$\text{Nu}_{\min} \sim \text{Ra}^{1/4} \qquad \text{at } \theta_{\min} \sim \text{Ra}^{-1/2} \qquad (10.112)$$

(i.e., at the end of the mixed heat transfer regime, $\theta_{min} \sim \theta_1$). These scales follow from applying $\partial Nu/\partial \theta = 0$ to eq. (10.110). The Nu minimum is confirmed by many experiments and is one of the reasons for the statement quoted from Ref. 78 at the start of this section.

10.4.2 Quasisteady Convection Regime

In the convection regime (Fig. 10.24c), convection fills the entire liquid space of height H. According to eq. (4.28), the overall Nusselt number scale is

$$Nu \sim Ra^{1/4} \tag{10.113}$$

This scaling law holds even though the phase-change interface is deformed and continues to deviate from the vertical plane shape. It is known that the boundary layer convection scaling law (10.113) also works very well for curved surfaces, provided that Ra is based on a length scale of the same order as the vertical dimension of the surface. The same is true in single-phase natural convection (Chapter 4). The height-averaged melting front location that corresponds to eq. (10.113) is

$$s_{av} \sim H\, Ra^{1/4}\, \theta \tag{10.114}$$

In a system of finite horizontal extent L, this scenario holds until the liquid—solid interface reaches the right wall, $s_{av} \sim L$. Let θ_2 represent the time scale associated with this event. Equation (10.114) yields immediately

$$\theta_2 \sim \frac{L}{H}\, Ra^{-1/4} \tag{10.115}$$

The convection regime exists only if $\theta_2 > \theta_1$, that is, if

$$Ra^{1/4} > \frac{H}{L} \tag{10.116}$$

When this criterion is not satisfied (i.e., when $\theta_2 < \theta_1$), the mixed conduction plus convection regime of Fig. 10.24b ends at a time of order θ_2, that is, before the Nu (θ) curve has had time to reveal its minimum. Criterion (10.116) and the Nu minimum are threatened as Ra decreases: This is illustrated by the numerical Nu (θ) curves plotted in Fig. 10.25. What happens after the melting front reaches the right wall, $\theta > \theta_2$, constitutes a distinct heat transfer regime, the main features of which are sketched in Fig. 10.24d. The scales of this regime are described in Ref. 79.

The scaling trends reviewed above have been verified numerically, as shown in Figs. 10.25 and 10.26. The numerical simulations are based on the quasi-steady natural convection approximation [79] and are valid in the limit of negligible liquid thermal inertia, Ste $\ll$ 1. Figure 10.25 shows how the Rayleigh number affects the shape and position of the Nusselt number versus time curve. Each Nu (θ) curve has the features anticipated by the scale analysis: first, the pure conduction decay of order $\theta^{-1/2}$, followed by the mixed regime with its Nu minimum, and finally, the pure convection Nu plateau of order $Ra^{1/4}$.
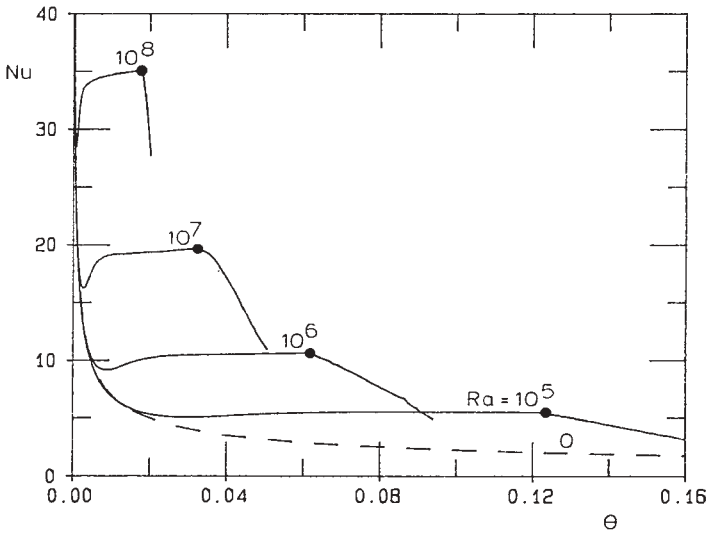
Figure 10.25   Numerical solutions for the average Nusselt number as a function of time and Rayleigh number. (From Ref. 79.)
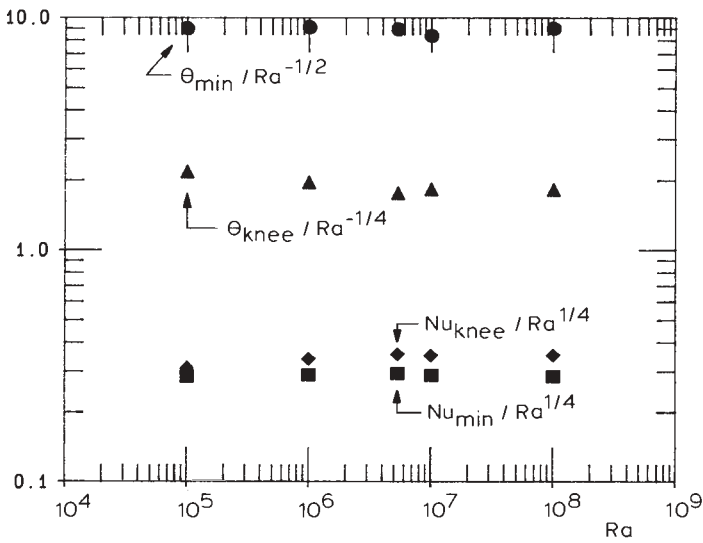
Figure 10.26   Numerical verification of the theoretical scales predicted for θ_{min}, θ_{knee}, Nu_{min}, and Nu_{knee}. (From Ref. 79.)

The Nusselt number curve changes slope as it passes through the "knee" point where the melting front first touches the right-hand-side adiabatic boundary. The time associated with this event is θ_{knee}. At times greater than θ_{knee}, the Nusselt number decreases relatively fast and almost linearly in time.

Figure 10.26 tests the correctness of some of the scaling laws reviewed earlier in this section. The top row of points shows that the time of the Nusselt number minimum, θ_{min}, is indeed on the order of θ_1. The second row of points shows that the time θ when the melting front reaches the right wall is of order $Ra^{-1/2}$. The third row of points uses the knee-point Nusselt number to show that in the pure convection limit the Nusselt number scales as $Ra^{1/4}$. The bottom row shows that Nu_{min} scales as $Ra^{1/4}$, as anticipated in eq. (10.113).

The tested Nusselt number and time scales provide the necessary backbone on which to construct a heat transfer correlation that spans the conduction, mixed, and convection regimes. In the conduction regime ($\theta \ll \theta_1$), the Nusselt number must approach the pure-conduction asymptote $(2\theta)^{-1/2}$. In the mixed regime ($\theta \sim \theta_1$), the $Nu(\theta)$ passes through a minimum of order $Ra^{1/4}$. In the pure convection regime ($\theta_1 < \theta < \theta_2$), the Nusselt number is time independent and of order $Ra^{1/4}$. These three behaviors are evident in the single correlation [79]

$$Nu = (2\theta)^{-1/2} + [c_1\, Ra^{1/4} - (2\theta)^{-1/2}][1 + (c_2\, Ra^{3/4}\, \theta^{3/2})^n]^{1/n} \quad (10.117)$$

for which the recommended empirical constants are $c_1 = 0.35$, $c_2 = 0.0175$, and $n = -2$.

The numerical results obtained for the average melting-front location versus time can be correlated similarly,

$$\frac{s_{av}}{H} = \{[(2\theta)^{1/2}]^m + [c_1\, Ra^{1/4}\, \theta]^m\}^{1/m} \quad (10.118)$$

by using the numerical constants $c_1 = 0.35$ and $m = 5$. It was shown that the correlations (10.117) and (10.118) agree very well with numerical and experimental data [79]. It is possible to go significantly beyond scale analysis and to produce an entirely analytical description of the heat transfer and melting process [80–82].

10.4.3   Horizontal Spreading of the Melt Layer

In this final section we consider the effect of the severe deformation undergone by the upper end of the melting front [83]. The preceding analysis was based on the assumption that the melting front is relatively smooth and nearly vertical. In reality, even during the earliest stages (conduction-dominated melting), the freshly formed liquid erodes the upper end of the melting front much faster, creating a shallow pool near the upper surface (Fig. 10.24a detail). This pool continues to grow horizontally and after some time becomes a distinct layer of shallow liquid. Its development is evident in Fig. 10.27, which is based on experimental observations at high Rayleigh numbers ($Ra_H \sim 10^{10}$ [81]). The horizontal liquid layer is labeled A_1 on the left side of Fig. 10.28.
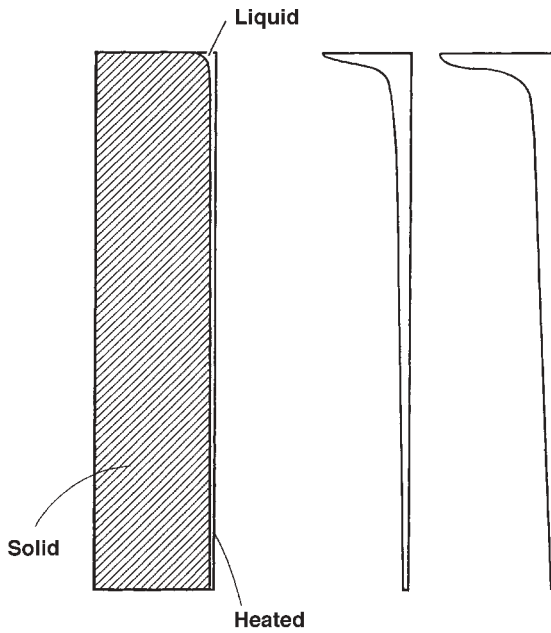
Figure 10.27   Development of a shallow intrusion layer of liquid on top of a block of *n*-octadecane heated from the right. (From Ref. 83; drawn to scale after Ref. 81.)
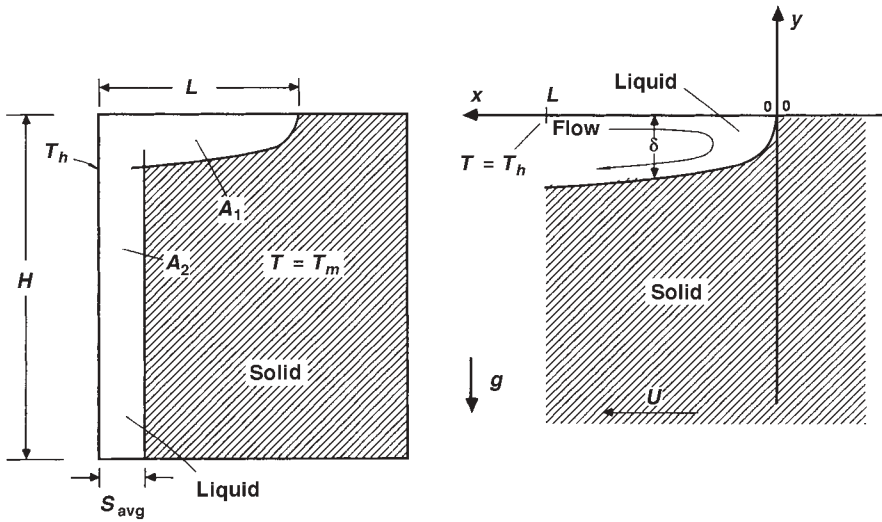
Figure 10.28   Liquid zone as a vertical slot (A_2) added to a horizontal intrusion layer (A_1) (the heating is from the left). (From Ref. 83.)

The behavior of the horizontal intrusion layer can be anticipated based on scale analysis, as shown in Ref. 83. Consider the two-dimensional layer enlarged on the right side of Fig. 10.28. The coordinate system $x-y$ is attached to the tip of the liquid layer, which advances to the right with the velocity $U = dL/dt$, where $L(t)$ is the instantaneous length of the layer. The solid moves to the left with the velocity U. The solid is isothermal and at the melting point T_m.

The analysis is based on two key assumptions. First, the natural convection velocities in the liquid layer are greater than the melting speed, $u \gg U$. The domain of validity of this assumption will be established later in eq. (10.128). When this assumption is valid, the natural convection in the horizontal layer is quasisteady; that is, it proceeds as if the liquid blowing velocity across the melting front (the melting effect) is negligible. The second assumption is that the horizontal liquid intrusion layer is slender, $\delta \ll L$. Later, in eq. (10.129), we will see that this assumption is justified when the Rayleigh number is large. Based on these assumptions, the equations that govern the conservation of mass, momentum, and energy in the horizontal liquid layer are

$$\frac{\partial u}{\partial x} + \frac{\partial v}{\partial y} = 0 \tag{10.119}$$

$$v\frac{\partial^3 u}{\partial y^3} - g\beta\frac{\partial T}{\partial x} = 0 \tag{10.120}$$

$$u\frac{\partial T}{\partial x} + v\frac{\partial T}{\partial y} = \alpha\frac{\partial^2 T}{\partial y^2} \tag{10.121}$$

The inertia terms have been neglected in the momentum equation (10.120) because the Prandtl number is considerably greater than 1 (for n-octadecane, Pr $\cong 50$). The liquid is being modeled as Newtonian with constant properties (α, β, v); the use of the Boussinesq approximation is evident in eq. (10.120).

An additional equation is provided by the melting-front energy continuity condition. According to this, the conduction heat flux arriving from the liquid side of the interface is balanced by the new solid that crosses the $\partial\delta/\partial x$-sloped interface with the horizontal velocity U,

$$k\left(\frac{\partial T}{\partial y}\right)_{y=-\delta} = \rho h_{sf} U \frac{\partial\delta}{\partial x} \tag{10.122}$$

It is assumed that the solid density ρ is equal to the liquid density. Properties k and h_{sf} are the liquid thermal conductivity and the latent heat of melting.

The system selected for scale analysis is the liquid layer of length L and depth of order δ. The scale of the liquid excess temperature above the melting point is $\Delta T = T_h - T_m$, where T_h is the temperature of the left wall in Fig. 10.28. With this notation, and if we write u and v for the horizontal and vertical velocity scales, we can replace eqs. (10.119)–(10.122) by the following order-of-magnitude statements:

$$\frac{u}{L} \sim \frac{v}{\delta} \tag{10.123}$$

$$\nu \frac{u}{\delta^3} \sim g\beta \frac{\Delta T}{L} \tag{10.124}$$

$$u \frac{\Delta T}{L}, \ v \frac{\Delta T}{\delta} \sim \alpha \frac{\Delta T}{\delta^2} \tag{10.125}$$

$$k \frac{\Delta T}{\delta} \sim \rho h_{sf} U \frac{\delta}{L} \tag{10.126}$$

The mass conservation equation (10.123) implies that the two scales listed on the left side of eq. (10.125) are both of order $(u\Delta T)/L$. The system (10.123)–(10.126) can be combined with $U \sim L/t$ in order to solve for L,

$$L \sim (\Delta T)^{7/4} \left(\frac{g\beta}{\alpha\nu}\right)^{1/2} \left(\frac{kt}{\rho h_{sf}}\right)^{5/4} \tag{10.127}$$

or in dimensionless form,

$$\frac{L}{H} \sim \text{Ra}_H^{1/2} (\text{Ste Fo})^{5/4} \tag{10.127'}$$

where $\text{Ra}_H = (g\beta H^3 \Delta T)/\alpha\nu$, while Ste Fo is the dimensionless time θ of eq. (10.103). By solving the same system, it can be shown that the assumption that the melting front moves slowly, $U \ll u$, is equivalent to the statement that the degree of liquid superheat is small,

$$\text{Ste} \ll 1 \tag{10.128}$$

Similarly, the shallow-layer assumption $\delta \ll L$ holds when

$$\text{Ra}_H (\text{Ste Fo})^{3/2} \gg 1 \tag{10.129}$$

Equation (10.127′) agrees in an order-of-magnitude sense with the $L(t)$ measurements [84–86] that covered a relatively wide domain in Rayleigh number (10^6–10^9) and in Ste Fo time number (10^{-4}–10^{-1}). The data are fitted within 30 percent by the correlation [83],

$$\frac{L}{H} \cong 0.11 \text{Ra}_H^{1/3} \text{ Ste Fo} \tag{10.130}$$

Note that in eq. (10.130) the effect of H cancels out, leaving a penetration distance L that increases as

$$L \cong 0.11(\Delta T)^{4/3} \left(\frac{g\beta}{\alpha\nu}\right)^{1/3} \frac{kt}{\rho h_{sf}} \tag{10.131}$$

This correlation is qualitatively similar to the form anticipated analytically in eq. (10.127). The solidification counterpart of the melting phenomenon of Section 10.4 was analyzed in Ref. 87.

REFERENCES

1. A. Bejan, *Heat Transfer*, Wiley, New York, 1993.

2. A. Bejan, *Entropy Generation through Heat and Fluid Flow*, Wiley, New York, 1982, Chapter 4.

3. A. Bejan, *Shape and Structure, from Engineering to Nature*, Cambridge University Press, Cambridge, 2000, Chapter 6.

4. A. Bejan and S. Lorente, The constructal law of design and evolution in nature, *Philos. Trans. Roy. Soc. B*, Vol. 365, 2010, pp. 1335–1347.

5. A. Bejan and P. J. Zane, *Design in Nature*, Doubleday, New York, 2012.

6. W. Nusselt, Die Oberflächenkondensation der Wasserdampfes, *Z. Ver. Dtsch. Ing.*, Vol. 60, 1916, pp. 541–569.

7. W. M. Rohsenow, Heat transfer and temperature distribution in laminar-film condensation, *Trans. ASME*, Vol. 78, 1956, pp. 1645–1648.

8. E. M. Sparrow and J. L. Gregg, A boundary-layer treatment of laminar-film condensation, *J. Heat Transfer*, Vol. 81, 1959, pp. 13–18.

9. M. M. Chen, An analytical study of laminar film condensation: 1. Flat plates, *J. Heat Transfer*, Vol. 83, 1961, pp. 48–54.

10. A. Bejan, *Convection Heat Transfer*, Wiley, New York, 1984.

11. S. L. Chen, F. M. Gerner, and C. L. Tien, General film condensation correlations, *Exp. Heat Transfer*, Vol. 1, 1987, pp. 93–107.

12. V. K. Dhir and J. H. Lienhard, Laminar film condensation on plane and axisymmetric bodies in non-uniform gravity, *J. Heat Transfer*, Vol. 93, 1971, pp. 97–100.

13. E. M. Sparrow and J. L. Gregg, Laminar condensation heat transfer on a horizontal cylinder, *J. Heat Transfer*, Vol. 81, 1959, pp. 291–296.

14. M. M. Chen, An analytical study of laminar film condensation: Part 2. Single and multiple horizontal tubes, *J. Heat Transfer*, Vol. 83, 1961, pp. 55–60.

15. A. Bejan, Film condensation on an upward facing plate with free edges, *Int. J. Heat Mass Transfer*, Vol. 34, 1991, pp. 578–582.

16. I. G. Shekriladze and V. I. Gomelauri, Theoretical study of laminar film condensation of flowing vapour, *Int. J. Heat Mass Transfer*, Vol. 9, 1966, pp. 581–591.

17. J. W. Rose, A new interpolation formula for forced-convection condensation on a horizontal surface, *J. Heat Transfer*, Vol. 111, 1989, pp. 818–819.

18. J. C. Chato, Laminar condensation inside horizontal and inclined tubes, *J. ASHRAE*, Vol. 4, Feb. 1962, pp. 52–60.

19. J. G. Collier, *Convective Boiling and Condensation*, 2nd ed., McGraw-Hill, New York, 1981.

20. W. M. Rohsenow, Film condensation, in W. M. Rohsenow and J. P. Hartnett, eds., *Handbook of Heat Transfer*, McGraw-Hill, New York, 1973, Section 12A.

21. E. M. Sparrow and S. H. Lin, Condensation in the presence of a non-condensible gas, *J. Heat Transfer*, Vol. 86, 1963, pp. 430–436.

22. W. J. Minkowycz and E. M. Sparrow, Condensation heat transfer in the presence of noncondensibles, interfacial resistance, superheating, variable properties, and diffusion, *Int. J. Heat Mass Transfer*, Vol. 9, 1966, pp. 1125–1144.

23. J. V. C. Vargas and A. Bejan, Optimization of film condensation with periodic wall cleaning, *Int. J. Thermal Sci.*, Vol. 38, 1999, pp. 113–120.

24. K. M. Holden, A. S. Wanniarachchi, P. J. Marto, D. H. Boone, and J. W. Rose, The use of organic coatings to promote dropwise condensation of steam, *J. Heat Transfer*, Vol. 109, 1987, pp. 768–774.

25. I. Tanasawa, Advances in condensation heat transfer, *Adv. Heat Transfer*, Vol. 21, 1991, pp. 55–139.

26. F. Kreith and R. Boehm, eds., *Direct Contact Heat Transfer*, Hemisphere, Washington, DC, 1988.

27. M. A. Kedzierski, J. C. Chato, and T. J. Rabas, Condensation, in A. Bejan and A. D. Kraus, eds., *Heat Transfer Handbook*, Wiley, New York, 2003, Chapter 10.

28. M. Belghazi, A. Bontemps, and C. Marvillet, Condensation heat transfer on enhanced surface tubes: experimental results and predictive theory, *J. Heat Transfer*, Vol. 124, 2002, pp. 754–761.

29. A. Bejan and S. Lorente, *Design with Constructal Theory*, Wiley, Hoboken, 2008.

30. C. Wares, On the fixation of water in diverse fire, *Int. J. Heat Mass Transfer*, Vol. 9, 1966, pp. 1153–1166.

31. S. Nukiyama, The maximum and minimum values of the heat Q transmitted from metal to boiling water under atmospheric pressure, *J. Jpn. Soc. Mech. Eng.*, Vol. 37, 1934, pp. 367–374; English translation in *Int. J. Heat Mass Transfer*, Vol. 9, 1966, pp. 1419–1433.

32. T. B. Drew and C. Mueller, Boiling, *Trans. AIChE*, Vol. 33, 1937, pp. 449–473.

33. W. M. Rohsenow, A method for correlating heat transfer data for surface boiling of liquids, *Trans. ASME*, Vol. 74, 1952, pp. 969–976.

34. R. I. Vachon, G. H. Nix, and G. E. Tanger, Evaluation of constants for the Rohsenow pool-boiling correlation, *J. Heat Transfer*, Vol. 90, 1968, pp. 239–247.

35. P. E. Liley, Thermophysical properties, in S. Kakac, R. K. Shah, and W. Aung, eds., *Handbook of Single-Phase Convective Heat Transfer*, Wiley, New York, 1987, Chapter 22.

36. *ASHRAE Handbook of Fundamentals*, ASHRAE, New York, 1981.

37. R. H. Kropschot, B. W. Birmingham, and D. B. Mann, eds., *Technology of Liquid Helium*, Monograph 111, National Bureau of Standards, Washington, DC, October 1968.

38. D. K. Edwards, V. E. Denny, and A. F. Mills, *Transfer Processes*, 2nd ed., Hemisphere, Washington, DC, 1979.

39. J. H. Lienhard and V. K. Dhir, Extended hydrodynamic theory of the peak and minimum pool boiling heat fluxes, NASA CR-2270, July 1973.

40. S. S. Kutateladze, On the transition to film boiling under natural convection, *Kotloturbostroenie*, *No. 3*, 1948, p. 10.

41. N. Zuber, On the stability of boiling heat transfer, *Trans. ASME*, Vol. 80, 1958, pp. 711–720.

42. K. H. Sun and J. H. Lienhard, The peak pool boiling heat flux on horizontal cylinders, *Int. J. Heat Mass Transfer*, Vol. 13, 1970, pp. 1425–1439.

43. P. J. Berenson, Film boiling heat transfer for a horizontal surface, *J. Heat Transfer*, Vol. 83, 1961, pp. 351–358.

44. A. L. Bromley, Heat transfer in stable film boiling, *Chem. Eng. Prog.*, Vol. 46, 1950, pp. 221–227.

45. M. R. Duignan, G. A. Greene, and T. F. Irvine, Jr., Film boiling heat transfer to large superheats from a horizontal flat surface, *J. Heat Transfer*, Vol. 113, 1991, pp. 266–268.

46. E. M. Sparrow, The effect of radiation on film-boiling heat transfer, *Int. J. Heat Mass Transfer*, Vol. 7, 1964, pp. 229–238.

47. R. A. Nelson, Jr. and A. Bejan, Constructal optimization of internal flow geometry in convection, *J. Heat Transfer*, Vol. 120, 1998, pp. 357–364.

48. R. A. Nelson, Jr. and A. Bejan, Self-organization of the internal flow geometry in convective heat transfer, ASME HTD-Vol. 357-3, 1998, pp. 149–161.

49. I. Golobic and H. Gjerkes, Interactions between laser-activated nucleation sites in pool boiling, *Int. J. Heat Mass Transfer*, Vol. 44, 2001, pp. 143–153.

50. C. Zamfirescu and A. Bejan, Constructal tree-shaped two-phase flow for cooling a surface, *Int. J. Heat Mass Transfer*, Vol. 46, 2003, pp. 2785–2797.

51. O. Craciunescu, A. Bejan, D. G. Cacuci, and W. Schütz, Time-dependent interaction between water at supercritical pressures and a hot surface, *Numer. Heat Transfer, Part A; Appl.*, Vol. 30, 1996, pp. 535–554.

52. A. Bejan, N. Dan, D. G. Cacuci, and W. Schütz, On the thermodynamic efficiency of energy conversion during the expansion of a mixture of hot particles, steam and liquid water, *Energy*, Vol. 22, 1997, pp. 1119–1133.

53. N. Dan, A. Bejan, D. G. Cacuci, and W. Schütz, Evolution of a mixture of hot particles, steam, and water immersed in a water pool, *Numer. Heat Transfer, Part A; Appl.*, Vol. 34, 1998, pp. 463–478.

54. A. Bejan, N. Dan, D. G. Cacuci, and W. Schütz, Exergy analysis of energy conversion during the thermal interaction between hot particles and water, *Energy*, Vol. 23, 1998, pp. 913–928.

55. J. R. Thome, Boiling, in A. Bejan and A. D. Kraus, eds., *Heat Transfer Handbook*, Wiley, New York, 2003, Chapter 9.

56. W. M. Rohsenow, Boiling, in W. M. Rohsenow and J. P. Hartnett, eds., *Handbook of Heat Transfer*, McGraw-Hill, New York, 1973, Section 13.

57. A. Bejan, Contact melting heat transfer and lubrication, *Adv. Heat Transfer*, Vol. 24, 1994, pp. 1–38.

58. A. J. Fowler and A. Bejan, Contact melting during sliding on ice, *Int. J. Heat Mass Transfer*, Vol. 36, 1993, pp. 1171–1179.

59. A. Bejan and P. A. Tyvand, The pressure melting of ice under a body with flat base, *J. Heat Transfer*, Vol. 114, 1992, pp. 529–531.

60. A. Bejan, The fundamentals of sliding contact melting and friction, *J. Heat Transfer*, Vol. 111, 1989, pp. 13–20.

61. A. Bejan, Single correlation for theoretical contact melting results in various geometries, *Int. Commun. Heat Mass Transfer*, Vol. 19, 1992, pp. 473–483.

62. M. Bareiss and H. Beer, An analytical solution of the heat transfer process during melting of an unfixed solid phase change material inside a horizontal tube, *Int. J. Heat Mass Transfer*, Vol. 27, 1984, pp. 739–746.

63. S. K. Roy and S. Sengupta, An analysis of the melting process within a spherical enclosure, *ASME SED—Vol.* 1, 1985, pp. 27–32.

64. P. A. Bahrami and T. G. Wang, Analysis of gravity and conduction-driven melting in a sphere, *J. Heat Transfer*, Vol. 109, 1987, pp. 806–809.

65. F. E. Moore and Y. Bayazitoglu, Melting within a spherical enclosure, *J. Heat Transfer*, Vol. 104, 1982, pp. 19–23.

66. S. H. Emerman and D. L. Turcotte, Stokes' problem with melting, *Int. J. Heat Mass Transfer*, Vol. 26, 1983, pp. 1625–1630.

67. M. K. Moallemi and R. Viskanta, Melting around a migrating heat source, *J. Heat Transfer*, Vol. 107, 1985, pp. 451–458.

68. M. Oka and V. P. Carey, A unified treatment of the direct contact melting processes in several geometric cases, *Int. Commun. Heat Mass Transfer*, Vol. 23, 1996, pp. 187–202.

69. S. A. Fomin, P. S. Wei, and V. A. Chugunov, Contact melting by a non-isothermal heating surface of arbitrary shape, *Int. J. Heat Mass Transfer*, Vol. 38, 1995, pp. 3275–3284.

70. M. Lacroix, Contact melting of a phase change material inside a heated parallel-epipedic capsule, *Energy Convers. Manage.*, Vol. 42, 2001, pp. 35–47.

71. S. A. Fomin and A. V. Wilchinsky, Shape-factor effect on melting in an elliptic capsule, *Int. J. Heat Mass Transfer*, Vol. 45, 2002, pp. 3045–3054.

72. D. Groulx and M. Lacroix, Study of close contact melting of ice from a sliding heated flat plate, *Int. J. Heat Mass Transfer*, Vol. 49, 2006, pp. 4407–4416.

73. P. A. Litsek and A. Bejan, Sliding contact melting: the effect of heat transfer in the solid parts, *J. Heat Transfer*, Vol. 112, 1990, pp. 808–812.

74. A. M. Morega, A. M. Filip, A. Bejan, and P. A. Tyvand, Melting around a shaft rotating in a phase-change material, *Int. J. Heat Mass Transfer*, Vol. 36, 1993, pp. 2499–2509.

75. A. Bejan, The process of melting by rolling contact, *Int. J. Heat Mass Transfer*, Vol. 31, 1988, pp. 2273–2283.

76. P. A. Tyvand and A. Bejan, The pressure melting of ice due to an embedded cylinder, *J. Heat Transfer*, Vol. 114, 1992, pp. 532–535.

77. A. Bejan and P. A. Litsek, The contact heating and lubricating flow of a body of glass, *Int. J. Heat Mass Transfer*, Vol. 32, 1989, pp. 751–760.

78. R. Viskanta, Natural convection melting and solidification, in S. Kakac, W. Aung, and R. Viskanta, eds., *Natural Convection: Fundamentals and Applications*, Hemisphere, Washington, DC, 1985.

79. P. Jany and A. Bejan, Scaling theory of melting with natural convection in an enclosure, *Int. J. Heat Mass Transfer*, Vol. 31, 1988, pp. 1221–1235.

80. A. Bejan, Analysis of melting by natural convection in an enclosure, *Int. J. Heat Fluid Flow*, Vol. 10, 1989, pp. 245–252.

81. Z. Zhang and A. Bejan, Melting in an enclosure heated at constant rate, *Int. J. Heat Mass Transfer*, Vol. 32, 1989, pp. 1063–1076.

82. Z. Zhang and A. Bejan, The problem of time-dependent natural convection melting with conduction in the solid, *Int. J. Heat Mass Transfer*, Vol. 32, 1989, pp. 2447–2457.

83. A. Bejan, Z. Zhang, and J. H. Kim, Analytical advances on melting by natural convection, keynote paper presented at the 22nd ICHMT International Symposium on Manufacturing and Materials Processing, Dubrovnik, Yugoslavia, Aug. 27–31, 1990.

84. M. Bareiss and H. Beer, Experimental investigation of melting heat transfer with regard to different geometric arrangement, *Int. Commun. Heat Mass Transfer*, Vol. 11, 1984, pp. 323–333.

85. C. Bénard, D. Gobin, and A. Zanoli, Moving boundary problem: heat convection in the solid phase of a phase-change material during melting driven by natural convection in the liquid, *Int. J. Heat Mass Transfer*, Vol. 29, 1986, pp. 1669–1681.

86. N. W. Hale and R. Viskanta, Photographic observation of the solid–liquid interface motion during melting of a solid heated from an isothermal vertical wall, *Lett. Heat Mass Transfer*, Vol. 5, 1978, pp. 329–337.

87. Z. Zhang and A. Bejan, Solidification in the presence of high Rayleigh number convection in an enclosure cooled from the side, *Int. J. Heat Mass Transfer*, Vol. 33, 1990, pp. 661–671.

PROBLEMS

10.1. Consider the control volume drawn around the entire film of height L shown in Fig. P10.1, and make no assumption concerning the flow regimes that may be present inside the control volume. The vertical wall is isothermal, T_w. To the right of the film of condensate, the vapor is stagnant and saturated. Show that in this general configuration, the total wall cooling rate is proportional to the condensate mass flow rate, $q' = h'_{fg} \Gamma(L)$.
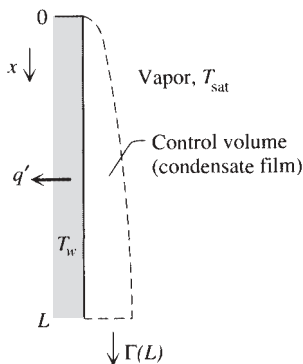
Figure P10.1

10.2. Show that regardless of the flow regime, the length of a vertical film of condensate L is related to the average heat transfer coefficient $\bar{h}_L$ and the total condensation rate $\Gamma(L)$ by the general formula

$$L = \frac{h'_{fg} \Gamma(L)}{(T_{sat} - T_w)\bar{h}_L}$$

Use this formula to derive eq. (10.24), which holds only for a *laminar* vertical film, when $\rho_l \gg \rho_v$.

10.3. Saturated vapor condenses on a cold vertical slab of height L. Both sides of the slab are covered by laminar films of condensate. A single horizontal cylinder of diameter D and at the same temperature as the slab is immersed in the same saturated vapor. For what special diameter D will the total condensation rate on the cylinder equal the total condensation rate produced by the slab?

10.4. The horizontal thin-walled tube shown in Fig. P10.4 is cooled by an internal fluid of temperature T_w. The tube is immersed in a stagnant atmosphere of saturated vapor, which condenses in laminar-film fashion on the outer cylindrical surface. It is proposed to increase the total condensation rate by flattening the tube cross section into the shape shown on the right side of the figure. Calculate the percent increase in condensation flow rate associated with this design change.

Round-tube design   Flat-tube design
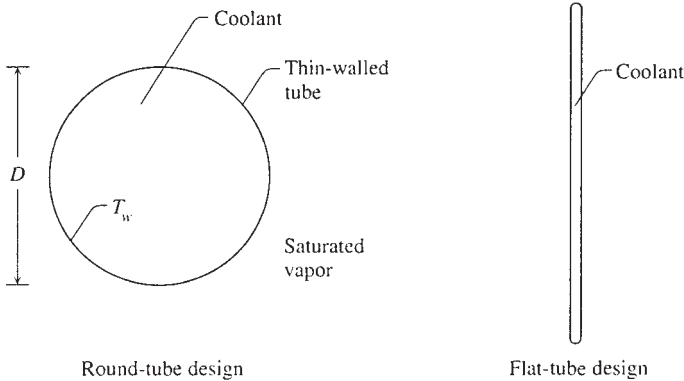
Figure P10.4

10.5. A plane rectangular surface of width $L = 1\,\mathrm{m}$, length $Z \gg L$, and temperature $T_w = 80°C$ is suspended in saturated steam of temperature $100°C$. When this surface is oriented such that L is aligned with the vertical, the steam condenses on it at the rate $0.063\,\mathrm{kg/s} \cdot \mathrm{m}$. The purpose of this exercise is to show how the condensation rate decreases when the surface becomes tilted relative to the vertical direction (Fig. P10.5).

(a) Calculate the condensation rate when the L width makes a $45°$ angle with the vertical and the Z length is aligned with the horizontal. Determine also the film Reynolds number and the flow regime.

(b) Assume that the surface is perfectly horizontal facing upward (as the top surface in Fig. 10.10) and that the film of condensate is laminar. Calculate the condensation rate and the Reynolds number of

the liquid film spilling over one edge, and verify the validity of the laminar film assumption.

(a)   (b)
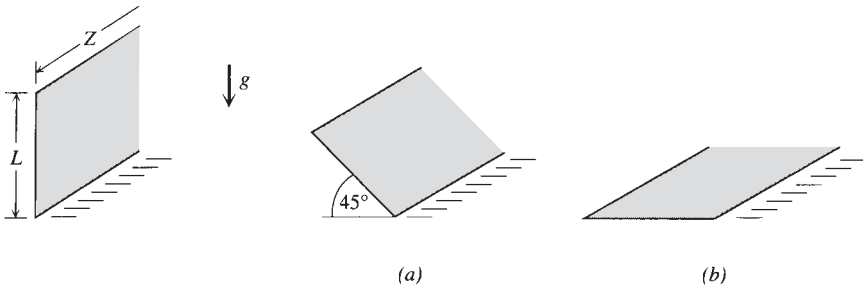
Figure P10.5

10.6. The bank of horizontal tubes shown in Fig. P10.6a is surrounded by 100°C saturated steam, which condenses on the outside of each tube. The tube surface is maintained at 60°C by a cold fluid that flows through each tube in the direction perpendicular to the plane of the figure. Assuming that the condensate film is laminar, calculate the total mass flow rate of condensate per unit length of tube bank. In a competing design, the same bundle of tubes appears rotated by 90°, as shown in Fig. P10.6b. Calculate the total condensate mass flow rate in this new design, and comment on the effect of the 90° rotation.

(a)   (b)
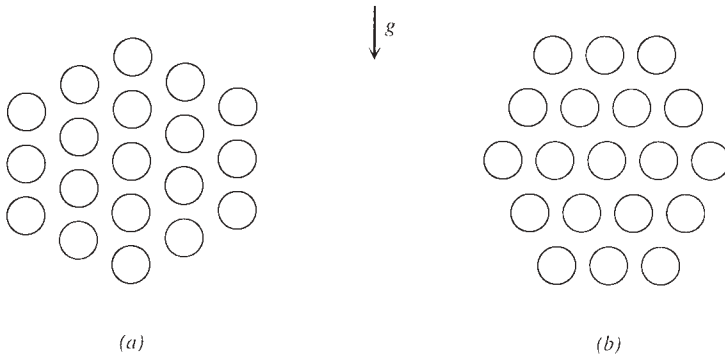
Figure P10.6

10.7. The average heat transfer coefficients for film condensation on an upward-facing strip and disk (Fig. 10.10) are listed in eqs. (10.33)–(10.34). Rewrite each of these formulas by using as a length scale the characteristic length of the surface, $L_c = A/p$, where A and p are the area and perimeter

of the surface. Show that the average heat transfer coefficient of any other surface whose shape is somewhere between the ''very long'' limit (the strip) and the ''round'' limit (the disk) is given by the approximate formula

$$\overline{Nu}_{L_c} = \frac{\overline{h}L_c}{k_l} \cong 0.8 \left[\frac{L_c^3 h'_{fg} g \left(\rho_l - \rho_v \right)}{k_l v_l (T_{\text{sat}} - T_w)} \right]^{1/5}$$

10.8. Consider the spherical vapor bubble of radius r shown in Fig. P10.8. The pressure and temperature inside the bubble (P_v, T_v) are slightly above the pressure and temperature in the liquid (P_l, T_l). The liquid is saturated, $T_l = T_{\text{sat}}$.

(a) Invoke the mechanical equilibrium of one hemispherical control volume and show that the bubble radius varies inversely with the pressure difference, $r = 2\sigma/(P_v - P_l)$.

(b) Rely on the Clausius–Clapeyron thermodynamics relation $dP/dT = h_{fg}/Tv_{fg}$ in order to show that the bubble radius also varies inversely with the temperature difference, $r = 2\sigma T_{\text{sat}}/h_{fg} \rho_v(T_v - T_{\text{sat}})$.

(c) Calculate the radius of a steam bubble with $T_v - T_{\text{sat}} = 2$ K in water at $T_{\text{sat}} = 100°C$.
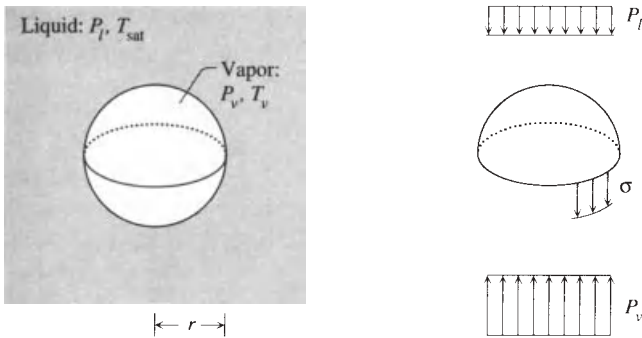
Figure P10.8

10.9. The vacuum insulation around a spherical liquid helium vessel develops an air leak and allows the heat transfer rate of $q''_w = 10^3$ W/m² to land on the external surface of the vessel (Fig. P10.9). An amount of saturated liquid helium at atmospheric pressure boils at the bottom of the vessel. Calculate the excess temperature ($T_w - T_{\text{sat}}$) by assuming nucleate boiling with $C_{sf} = 0.02$ and $s = 1.7$. Compare the heat leak q''_w with the peak heat flux for nucleate boiling in the pool of liquid helium.
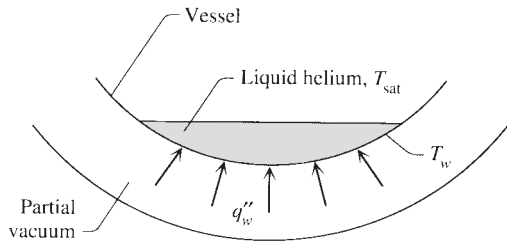
Figure P10.9

10.10. Water boils in the pressurized cylindrical vessel shown in Fig. P10.10. The steam relief valve is set in such a way that the pressure inside the vessel is 4.76×10^5 N/m^2. The bottom surface is made out of copper (polished), and its temperature is maintained at $T_w = 160°$C. Assume nucleate boiling, and calculate the total heat transfer rate from the bottom surface to the boiling water. Later, verify the correctness of the nucleate boiling assumption.
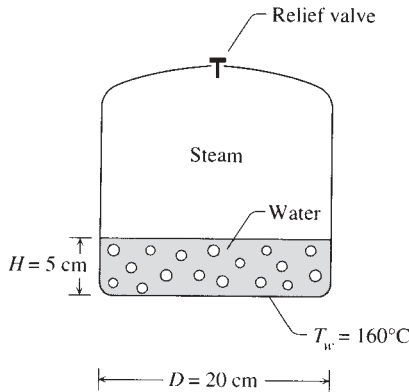
Figure P10.10

10.11. The cylindrical vessel described in Problem 10.10 has an inner diameter of 20 cm. The depth of the original amount of liquid is 5 cm, and the pressure is maintained at 4.76×10^5 N/m^2 (Fig. P10.11). The nucleate boiling heat transfer rate to the liquid (calculated in Problem 10.10) is $q_w = 12.44$ kW.

(a) Estimate the time needed to evaporate all the liquid. Base your estimate on the relation $q_w = \dot{m}h_{fg}$, which is used routinely.

(b) The $q_w = \dot{m}h_{fg}$ relation is valid only approximately and is incorrect from a thermodynamic standpoint. With reference to the control

volume defined by the pressurized vessel, show that the correct proportionality between q_w and $\dot{m}$ is $q_w = \dot{m}[h_g - (u_f v_g - u_g v_f)/(v_g - v_f)]$ where u, v, $(\cdot)_g$, and $(\cdot)_f$ are the usual thermodynamics symbols for specific internal energy, specific volume, saturated vapor, and saturated liquid. Note that the pressure (or temperature) and the total volume (V) remain constant. Numerically, show that the quantity arrived at in parentheses deviates from h_{fg} [assumed in part (a)] as the saturated liquid–vapor mixture approaches the critical point.
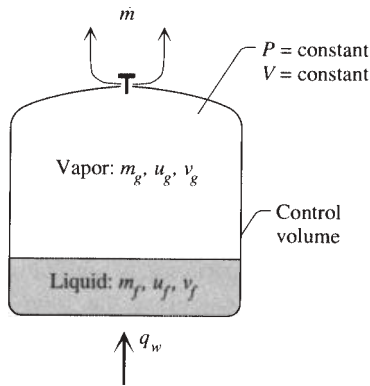
Figure P10.11

10.12. In a power-controlled pool boiling experiment, a horizontal cylindrical heater is immersed in saturated water at atmospheric pressure. The peak heat flux is 10^6 W/m². The power is increased slightly above this level, and the nucleate boiling regime is replaced abruptly by film boiling (Fig. 10.16b). Estimate the excess temperature in this new regime by assuming that radiation is the only mode of heat transfer across the film. Also assume that $\epsilon_w = 1$. Compare your estimate with the value read off Fig. 10.15. Will the actual excess temperature be larger or smaller than this pure-radiation estimate?

10.13. Film boiling occurs on the surface of a sphere of temperature $T_w = 354°C$ and diameter $D = 2$ cm which is plunged in a bath of saturated water at atmospheric pressure. The sphere is made out of polished copper.

(a) Calculate the heat transfer coefficient due to convection, $\bar{h}_D$, the correction due to radiation, $\bar{h}_{rad}$, and the total heat transfer rate from the copper ball to the water pool. For the emissivity of the copper surface, assume that $\epsilon_w = 0.05$.

(b) Model the copper sphere as a lumped capacitance, and calculate its new temperature 10 s after the start of film boiling.

10.14. Solar energy is stored by heating from above a large pool of molten
salt (Fig. P10.14). The heated liquid is drawn slowly horizontally. Cold
salt at the temperature T_∞ is injected slowly and horizontally along the
bottom of the pool. As a very good approximation, the motion of the
salt is purely vertical with the uniform velocity V. The temperature field
is unidimensional, $T(y)$. The temperature gradient at the free surface
$(y = 0)$ is fixed by the solar heat flux q'', which is a known constant.
The temperature of the molten salt sufficiently far from the surface
approaches T_∞. Determine analytically the temperature distribution $T(y)$
and the surface temperature $T(0)$. What is the order of magnitude of the
thickness of the salt layer that is heated by the solar effect?

Figure P10.14

11
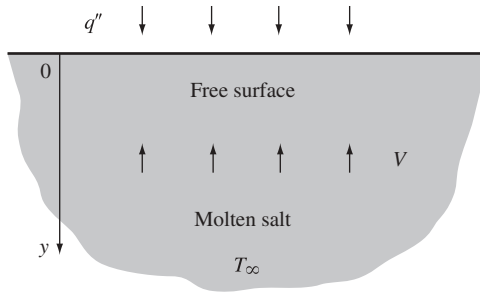
MASS TRANSFER

Convective phenomena in nature are often accompanied by *mass transfer*, that is, by the transport of substances that act as components (constituents, species) in the fluid mixture. The circulation of atmospheric air is driven by differential heating; however, in an industrial area, atmospheric circulation also acts as a carrier for the many exhaust streams put out by factories into the atmosphere. Ocean currents driven by differential heating also act as freight trains for salt (in the form of saline water).

Convection mass transfer alone (in the absence of heat transfer) constitutes the backbone of many operations in the chemical industry. This seems enough reason to include mass transfer in this convection course. An additional reason is the *analogy* that exists between convective mass transfer and convective heat transfer. I highlight this analogy with a review of the principles outlined in this book, including the application of constructal design to the maximization of mass transfer density in mass exchangers [1] and fuel cells [2], and an extension to topics of natural convection mass transfer and mass convection through porous media.

11.1 PROPERTIES OF MIXTURES

The study of convective heat transfer—the object of the first 10 chapters of this book—began with a review of the thermodynamics of pure substances. That review was demanded, first, by the role of mutual relative played by thermodynamics to both heat transfer and fluid mechanics [3] and, second, by the fact that the student is likely to have been exposed first to thermodynamics. For the same reasons, we begin the discussion of mass convection with a review of the thermodynamics and nomenclature of mixtures of substances.

Consider a batch of fluid of volume V and mass m. Like the air surrounding a fin in natural convection or like the river water sweeping away the discharge from a chemical plant, this fluid batch is a mixture of identifiable *components* (e.g., in the case of air, the components are nitrogen, oxygen, carbon dioxide, inert gases, and impurities). Let m_i be the individual masses of the components that constitute the mixture. Then, by definition, the concentration of component i in the mixture (m, V) is

$$C_i = \frac{m_i}{V} \qquad (11.1)$$

with units of kg/m^3. Concentration is another word for the component density ρ_i demanded by the viewpoint that each component (m_i) fills the entire volume V,

$$\rho_i = \frac{m_i}{V} \qquad (11.2)$$

Because all the components contribute to the total mass of the batch, $\Sigma\, m_i = m$, the aggregate density of the mixture ρ is the sum of all concentrations,

$$\rho = \sum C_i \qquad (11.3)$$

The aggregate density ρ is the density used in the preceding chapters to describe the mixture's ability to act as a conveyer belt for energy.

The size of the fluid batch can be described in terms of its extensive properties mass (m) and volume (V). An alternative description, preferred by chemical engineers, involves the concept of *mole*: A 2-mole batch of a certain substance is bigger than a 1-mole batch of the same substance. By definition, a *mole* is the amount of substance in a batch (in a thermodynamic system) that contains as many elementary entities (e.g., molecules) as there are in 0.012 kg of carbon-12 [3]. That special number of entities is *Avogadro's constant*, 6.022×10^{23}.

The mole is not a mass unit, simply because the mass of 1 mole is not the same for all substances (five basketballs together weigh more than five tennis balls taken together; note that in this example, the group of five entities plays the role of 1 mole). The *molar mass M* of a mixture or a component (a molecular species) in a mixture is the mass of 1 mole of that mixture or component. The units of molar mass M are g/mol or kg/kmol, where kmol represents 1000 moles. The total number of moles n found in a batch is obtained by dividing the total mass of the batch by the mass of 1 mole,

$$n = \frac{m}{M} \qquad (11.4)$$

The number of moles of a component (n_i) found in a mixture is equal to the mass of that component (m_i) divided by its molar mass (M_i),

$$n_i = \frac{m_i}{M_i} \qquad (11.5)$$

A dimensionless way to describe the composition of a mixture is by use of the *mass fraction* of each constituent,

$$\Phi_i = \frac{m_i}{m} \tag{11.6}$$

where $\Sigma \Phi_i = 1$. The concept of mass fraction is the same as that of quality encountered in the study of liquid and vapor mixtures. (When the quality of wet steam is 0.9, the mass fraction of saturated steam in the two-phase mixture is 0.9.) Another dimensionless alternative to describing composition is by comparing the number of moles of each component (n_i) with the total number of moles found in the mixture (n),

$$x_i = \frac{n_i}{n}, \quad \sum x_i = 1 \tag{11.7}$$

The ratio x_i is the *mole fraction* of component i. To summarize, we have seen three alternative ways to discuss composition: a dimensional concept (concentration) and two dimensionless ratios (mass fraction and mole fraction). The conversion formulas relating these three properties are

$$C_i = \rho \Phi_i = \rho \frac{M_i}{M} x_i \tag{11.8}$$

where the equivalent molar mass of the mixture (M) is related to the molar masses of all the constituents by

$$M = \sum M_i x_i \tag{11.9}$$

If the mixture can be modeled as an *ideal gas*, one of its equations of state is

$$PV = mRT \quad \text{or} \quad PV = n\overline{R}T \tag{11.10}$$

where the mixture's ideal gas constant (R) and the universal gas constant ($\overline{R} = 8.314\,\text{J/mol} \cdot \text{K}$) are related via

$$R = \frac{\overline{R}}{M} \tag{11.11}$$

The partial pressure P_i of constituent i is the pressure that one would measure if constituent i alone were to fill the mixture volume (V) at the same temperature as the mixture (T):

$$P_i V = m_i RT \quad \text{or} \quad P_i V = n_i \overline{R}T \tag{11.12}$$

Summing the foregoing equations over i, we obtain Dalton's law,

$$P = \sum P_i \tag{11.13}$$

which states that the pressure of a mixture of gases at a specified volume and temperature is equal to the sum of the partial pressures of constituents. Of use in the calculation of concentrations is the relationship between partial pressure and mole fraction,

$$\frac{P_i}{P} = x_i \tag{11.14}$$

which is obtained by dividing eqs. (11.12) and (11.10). The concentration of a gaseous species (C_i) is related to the partial pressure of that gas via eq. (11.8).

   The nomenclature reviewed in this section applies to a mixture in *equilibrium*, that is, to a fluid batch whose composition, pressure, and temperature do not vary from point to point. Beginning in the next section, we focus on a fundamental departure from the equilibrium mixture description: a mixture whose composition, pressure, and temperature may vary from one point to another. We view this nonequilibrium mixture as a patchwork of small equilibrium batches of the type described in the field of entropy generation minimization [3]; the equilibrium state of each of these batches varies slightly as one shifts from one small batch to the next.

11.2   MASS CONSERVATION

The centerpiece of convective mass transfer analysis is the principle of mass conservation in (or *continuity* through) the control volume sketched in Fig. 11.1. In Chapter 1 we invoked the same principle for a fluid of density ρ whose composition was not questioned: that fluid might very well have been a mixture of two or more fluids. In this section we apply the principle of mass conservation to each component or constituent in the mixture. Relative to Fig. 11.1, we argue that the net flow of constituent i into the control volume is equal to the rate of accumulation of constituent i inside the control volume,

$$\frac{\partial \rho_i}{\partial t} \, \Delta x \, \Delta y = \rho_i u_i \, \Delta y - \left[\rho_i u_i + \frac{\partial}{\partial x} \left(\rho_i u_i \right) \Delta x \right] \Delta y$$

$$+ \rho_i v_i \, \Delta x - \left[\rho_i v_i + \frac{\partial}{\partial y} \left(\rho_i v_i \right) \Delta y \right] \Delta x + \dot{m}_i''' \, \Delta x \, \Delta y \tag{11.15}$$

   In the balance above, ρ_i is the number of kilograms of constituent i per cubic meter found locally in the mixture at point (x, y). The velocity components (u_i, v_i) account for the motion of constituent i relative to the control volume. The use of the (u_i, v_i) notation at this stage should not be taken as a suggestion that a motion with such velocity components can actually be seen or measured. These velocity components do have a physical meaning: The group $\rho_i u_i$ represents the net mass flux of constituent i (measured in kg/s · m^2) in the x direction. Concluding eq. (11.15) is the term containing $\dot{m}_i'''$, which is the volumetric rate of constituent i generation (the units of $\dot{m}_i'''$ are kg/s · m^3). This last term must
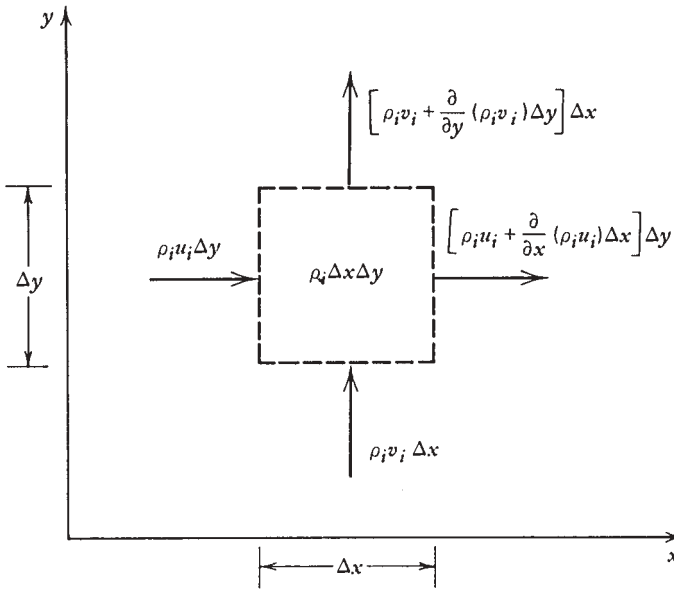
Figure 11.1 Conservation of the mass of component i during the flow of a mixture.

be taken into account in reactive flows that generate constituent i locally, as a product of reaction. If constituent i is consumed by the reaction, the species generation rate $\dot{m}_i'''$ is negative.

The mass conservation statement (11.15) reduces to

$$\frac{\partial \rho_i}{\partial t} + \frac{\partial}{\partial x}(\rho_i u_i) + \frac{\partial}{\partial y}(\rho_i v_i) = \dot{m}_i''' \qquad (11.16)$$

which in the absence of constituent generation ($\dot{m}_i''' = 0$) has the same form as the mass conservation statement for mixture flow, eq. (1.3). Indeed, the mass conservation equation for mixture flow can be derived as in Fig. 11.1 by viewing the mixture flow as the superposition of all the flows involving one constituent at a time. Superposing the constituent flows, that is, summing eq. (11.16) over i and letting $\dot{m}_i''' = 0$, we obtain

$$\frac{\partial \rho}{\partial t} + \frac{\partial}{\partial x}\sum \rho_i u_i + \frac{\partial}{\partial y}\sum \rho_i v_i = 0 \qquad (11.17)$$

This mass conservation statement must be the same as the statement derived in Chapter 1,

$$\frac{\partial \rho}{\partial t} + \frac{\partial}{\partial x}(\rho u) + \frac{\partial}{\partial y}(\rho v) = 0 \qquad (11.18)$$

A term-by-term comparison of eqs. (11.17) and (11.18) brings us to a very important concept in mass convection—the concept of *mass-averaged velocity* components (u, v),

$$u = \frac{1}{\rho}\sum \rho_i u_i, \qquad v = \frac{1}{\rho}\sum \rho_i v_i, \tag{11.19}$$

What in the heat transfer part of this convection book was called the *velocity component* emerges in mass transfer as a weighted average of all the constituent velocities.

In general, the mass-averaged velocity differs from the velocity of each constituent. To see this, take a glass with some water in it and inject a layer of grenadine syrup in the lower portion of the glass. What happens is shown in Fig. 11.2: In time, the syrup *diffuses* upward, its place being taken by clear water diffusing downward. In any horizontal cross section, the vertical velocity of each constituent is finite (one positive and the other negative), while the mass-averaged velocity—the velocity of the mixture as a whole—is zero (to the reader of Chapter 1, the water in the glass is stagnant). Clearly, each constituent moves relative to the mixture as a whole.

The velocity difference $(u_i - u)$ is the *diffusion velocity* of constituent i in the x direction. The product $\rho_i(u_i - u)$ is the flow rate of constituent i per unit area in the x direction relative to the bulk motion of the mixture; a shorter name for this quantity is *diffusion flux*, $j_{x,i}$. Combining the diffusion flux definitions

$$j_{x,i} = \rho_i(u_i - u) \tag{11.20}$$

$$j_{y,i} = \rho_i(v_i - v)$$

0 h   7 h   15 h   25 h   38 h
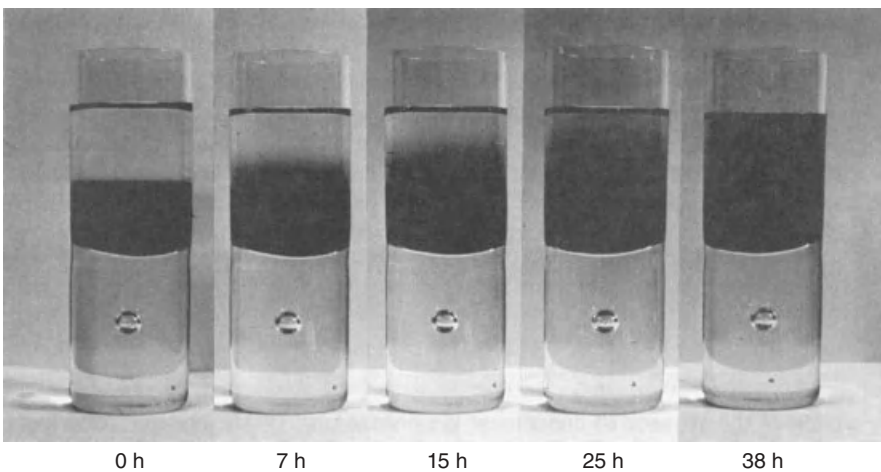
Figure 11.2   Vertical diffusion of grenadine syrup in water.

with the mass continuity equation for constituent i [eq. (11.16)] yields

$$\frac{\partial \rho_i}{\partial t} + \frac{\partial}{\partial x}(\rho_i u) + \frac{\partial}{\partial y}(\rho_i v) = -\frac{\partial j_{x,i}}{\partial x} - \frac{\partial j_{y,i}}{\partial y} + \dot{m}_i''' \qquad (11.21)$$

Reverting now to the concentration notation [$C_i = \rho_i$, eqs. (11.1) and (11.2)] and assuming that the mixture flow may be treated as one with $\rho = $ constant, the conservation of constituent i requires that

$$\frac{\partial C_i}{\partial t} + u\frac{\partial C_i}{\partial x} + v\frac{\partial C_i}{\partial y} = -\frac{\partial j_{x,i}}{\partial x} - \frac{\partial j_{y,i}}{\partial y} + \dot{m}_i''' \qquad (11.22)$$

The three-dimensional counterpart of this conclusion is

$$\frac{DC_i}{Dt} = -\nabla \cdot \mathbf{j}_i + \dot{m}_i''' \qquad (11.23)$$

The diffusion flux vector $\mathbf{j}_i$ is driven by the concentration gradient ∇C_i in the same manner that the conduction heat flux is driven by the local temperature gradient. This idea was put forth by the German physiologist Adolph Fick in 1855 [4]: It has the merit of having triggered the modern analytical development of the field of mass transfer in the same way that Fourier's ideas on conduction made heat transfer a modern science. For a two-component mixture, Fick's law of mass diffusion is

$$\mathbf{j}_1 = -D_{12}\,\nabla C_1 \qquad (11.24)$$

where $D_{12} = D_{21} = D$ is the mass diffusivity of component 1 into component 2, and vice versa. The diffusivity D, whose units are m^2/s, is a transport property whose numerical value depends, in general, on the mixture pressure, temperature, and composition. In view of the thermodynamics of irreversible processes, the diffusion flux is caused solely by the concentration gradient [as in eq. (11.24)] strictly in a fluid with uniform pressure and temperature [3]; nevertheless, eq. (11.24) is a useful approximation even in combined mass and heat transfer problems. Substituting eq. (11.24) in the mass conservation statement (11.23) and dropping the subscript i yields

$$\frac{DC}{Dt} = D\,\nabla^2 C + \dot{m}''' \qquad (11.25)$$

Throughout the remainder of this chapter, the concentration C refers to the component whose migration by mixture flow is of interest.

The mass transfer problem consists of solving eq. (11.25) for the concentration field $C(x, y, z)$, and determining the mass fluxes associated with the concentration field from Fick's law (11.24). From the outset, we note the similarities between the mass convection problem and the energy convection problem formulated in

Chapter 1. The latter consists of determining the temperature field $T(x, y, z)$ from the energy equation

$$\frac{DT}{Dt} = \alpha \ \nabla^2 T + \frac{q'''}{\rho c_P} \tag{11.26}$$

and the heat fluxes from Fourier's law of thermal diffusion, $\mathbf{q}'' = -k \ \nabla T$ [recall that eq. (11.26) holds under special circumstances outlined in Chapter 1]. Equations (11.25) and (11.26) show that the concentration C occupies the place of temperature, while the mass diffusivity D replaces the thermal diffusivity α. To streamline the presentation and to avoid repetition, the correspondence between mass transfer and heat transfer will be exploited throughout this chapter.

The mass conservation or *concentration equation* (11.25) has the following forms in three dimensions (Fig. 1.1):

Cartesian (x, y, z):

$$\frac{\partial C}{\partial t} + u\frac{\partial C}{\partial x} + v\frac{\partial C}{\partial y} + w\frac{\partial C}{\partial z} = D\left(\frac{\partial^2 C}{\partial x^2} + \frac{\partial^2 C}{\partial y^2} + \frac{\partial^2 C}{\partial z^2}\right) + \dot{m}''' \tag{11.27a}$$

Cylindrical (r, θ, z):

$$\frac{\partial C}{\partial t} + v_r\frac{\partial C}{\partial r} + \frac{v_\theta}{r}\frac{\partial C}{\partial \theta} + v_z\frac{\partial C}{\partial z}$$

$$= D\left[\frac{1}{r}\frac{\partial}{\partial r}\left(r\frac{\partial C}{\partial r}\right) + \frac{1}{r^2}\frac{\partial^2 C}{\partial \theta^2} + \frac{\partial^2 C}{\partial z^2}\right] + \dot{m}''' \tag{11.27b}$$

Spherical (r, φ, θ):

$$\frac{\partial C}{\partial t} + v_r\frac{\partial C}{\partial r} + \frac{v_\phi}{r}\frac{\partial C}{\partial \phi} + \frac{v_\theta}{r \ \sin \ \phi}\frac{\partial C}{\partial \theta}$$

$$= D\left[\frac{1}{r^2}\frac{\partial}{\partial r}\left(r^2\frac{\partial C}{\partial r}\right) + \frac{1}{r^2 \ \sin \ \phi}\frac{\partial}{\partial \phi}\left(\sin \ \phi\frac{\partial C}{\partial \phi}\right)\right.$$

$$\left. + \frac{1}{r^2 \ \sin^2\phi}\frac{\partial^2 C}{\partial \theta^2}\right] + \dot{m}''' \tag{11.27c}$$

Given the proportionality that links concentration, mass fraction, and mole fraction as a means of quantizing composition [eq. (11.8)], the concentration equations formulated above can be replaced with equations written in terms of mass fraction (Φ),

$$\frac{D\Phi}{Dt} = D\nabla^2\Phi + \frac{\dot{m}'''}{\rho} \tag{11.28}$$

$$\mathbf{j} = -\rho D \ \nabla\Phi \tag{11.29}$$

or in terms of mole fraction (x),

$$\frac{Dx}{Dt} = D\,\nabla^2 x + \frac{M}{M_1}\frac{\dot{m}'''}{\rho} \tag{11.30}$$

$$\mathbf{j} = -\rho\frac{M_1}{M}\,D\,\nabla x \tag{11.31}$$

where M_1 is the molar mass of the constituent of interest (whose mole fraction is x). To be consistent, the material that follows refers to only one formulation, the concentration-type equations (11.24), (11.25), and (11.27).

11.3 MASS DIFFUSIVITIES

To solve the concentration equation (11.27), we need information on the mass diffusivity of the species of interest, D, and the species conservation at the two surfaces that define the mass transfer medium. The second item—the specification of boundary conditions—forms the subject of the next section. Here, we review the contents of Tables 11.1 and 11.2 and the ways in which these mass diffusivity data can be extrapolated to temperatures and pressures that differ from those specified in the tables.

Consider first the case of a *binary gaseous mixture* such as hydrogen and nitrogen at atmospheric pressure and room temperature. Let subscripts 1 and 2 represent the two components in the mixture. Table 11.1 shows the value of the mass diffusivity D, which is the mass diffusivity of species 1 into 2 [namely, D_{12}, eq. (11.24)], and the mass diffusivity of species 2 into 1 (labeled D_{21}); in other words, $D \equiv D_{12} = D_{21}$. For this reason, the D values listed in Table 11.1 are also known as *mutual* diffusion coefficients.

The theoretical work of predicting the mass diffusivity in binary gaseous mixtures has been reviewed in Refs. 6 and 8. Recommended is a semiempirical correlation developed by Fuller et al. [9], according to whom D is proportional to the group $T^{1.75}/P$, where T and P are the mixture absolute temperature and pressure. This functional dependence can be used to extend the applicability of the mass diffusivity data of Table 11.1. If T_0 and P_0 are the mixture temperature and pressure specified in the table, the diffusivity at different values of T and P can be evaluated by writing

$$\frac{D(T,P)}{D(T_0,P_0)} \cong \left(\frac{T}{T_0}\right)^{1.75}\frac{P_0}{P} \tag{11.32}$$

The effect of temperature on mass diffusivity deviates somewhat from this simple formula if the ratio T/T_0 is significantly greater than 1. Worth keeping in mind is that the mass diffusivity of a binary gaseous mixture does not depend on the concentration.

Table 11.1   Mass diffusivities of binary gaseous mixtures at atmospheric pressure

Gaseous Mixture	D (m²/s)	T (K)
Air-acetone	1.09×10^{-5}	273
Air-ammonia	2.80×10^{-5}	298
Air-benzene	0.77×10^{-5}	273
Air-carbon dioxide	1.42×10^{-5}	276
	1.77×10^{-5}	317
Air-ethanol	1.45×10^{-5}	313
Air-helium	7.65×10^{-5}	317
Air-*n*-hexane	0.80×10^{-5}	294
Air-methanol	1.32×10^{-5}	273
Air-naphthalene	5.13×10^{-6}	273
Air-water vapor	2.60×10^{-5}	298
	2.88×10^{-5}	313
Ammonia-hydrogen	5.70×10^{-5}	263
	1.10×10^{-4}	358
Argon-carbon dioxide	1.33×10^{-5}	276
Argon-hydrogen	8.29×10^{-5}	295
Benzene-hydrogen	4.04×10^{-5}	311
Benzene-nitrogen	1.02×10^{-5}	311
Carbon dioxide-nitrogen	1.67×10^{-5}	298
Carbon dioxide-oxygen	1.53×10^{-5}	293
Carbon dioxide-water vapor	1.98×10^{-5}	307
Cyclohexane-nitrogen	0.73×10^{-5}	288
Helium-methane	6.76×10^{-5}	298
Hydrogen-nitrogen	7.84×10^{-5}	298
Hydrogen-water vapor	9.15×10^{-5}	307
Methane-water vapor	3.56×10^{-5}	352
Nitrogen-water vapor	3.59×10^{-5}	352
Oxygen-water vapor	3.52×10^{-5}	352

Source: Data from Refs. 5–7.

The evaluation of mass diffusivities is considerably more complicated for a multicomponent gaseous mixture because the mixture composition plays an important role (see, e.g., Ref. 7). Nevertheless, Fick's law of diffusion and eq. (11.27) continue to hold, provided that D is an appropriately chosen (calculated, or measured) coefficient. The method for making this selection is outlined in Refs. 6 and 9–12.

The mass diffusivities of liquid mixtures are generally $10^4 - 10^5$ times smaller than the diffusivities exhibited by gaseous mixtures. In binary liquid mixtures, the mass diffusivity is a function of composition (i.e., unlike in binary gaseous mixtures). The effect of mixture composition on D becomes negligible in the limit of infinite dilution, where only small amounts of the diffusing species of interest (the solute) are mixed with a second species (the solvent).

Table 11.2   Mass diffusivities of gases and organic solutes at low concentrations in water (dilute aqueous solutions)

Solute	Solvent	D (m^2/s)	T (K)
Acetone	Water	1.16×10^{-9}	293
Air	Water	2.5×10^{-9}	293
Aniline	Water	0.92×10^{-9}	293
Benzene	Water	1.02×10^{-9}	293
Carbon dioxide	Water	1.92×10^{-9}	298
Chlorine	Water	1.25×10^{-9}	298
Ethanol	Water	0.84×10^{-9}	298
Ethylene glycol	Water	1.04×10^{-9}	293
Glycerol	Water	0.72×10^{-9}	288
Hydrogen	Water	4.5×10^{-9}	298
Nitrogen	Water	2.6×10^{-9}	293
Oxygen	Water	2.1×10^{-9}	298
Propane	Water	0.97×10^{-9}	293
Urea	Water	1.2×10^{-9}	293
Vinyl chloride	Water	1.34×10^{-9}	298

Source: Data from Refs. 5 and 6.

Table 11.2 shows a collection of mass diffusivity data for dilute binary liquid mixtures, in which the solvent is always liquid water. More data for other dilute binary liquid mixtures can be found in Refs. 5 and 6. *Dilute* means that the solute mole fraction does not exceed approximately 5 percent.

The D values of Table 11.2 refer strictly to the mixture temperature listed in the rightmost column. Let subscript 1 represent the solute and subscript 2 represent the solvent in the dilute binary liquid mixture. It has been shown [13] that the diffusion coefficient of interest (D_{12}, or D in Table 11.2) increases with the temperature as the group T/μ_2, where the viscosity of the solvent (μ_2) is, in general, a function of temperature. If T_0 is the absolute temperature that corresponds to the D value listed in Table 11.2, the temperature domain covered by that table can be extended by using the relation

$$\frac{D(T)}{D(T_0)} \cong \frac{T}{T_0} \frac{\mu_2(T_0)}{\mu_2(T)} \tag{11.33}$$

11.4   BOUNDARY CONDITIONS

An important feature of the boundary conditions to be specified in connection with the concentration equation is that each condition applies to the *inner side* of the boundary. The inner side is the side that faces the medium through which the species of interest diffuses. This feature has been stressed in the drawing of Fig. 11.3, where the boundary conditions have been attached to

(a)

(b)

(c)
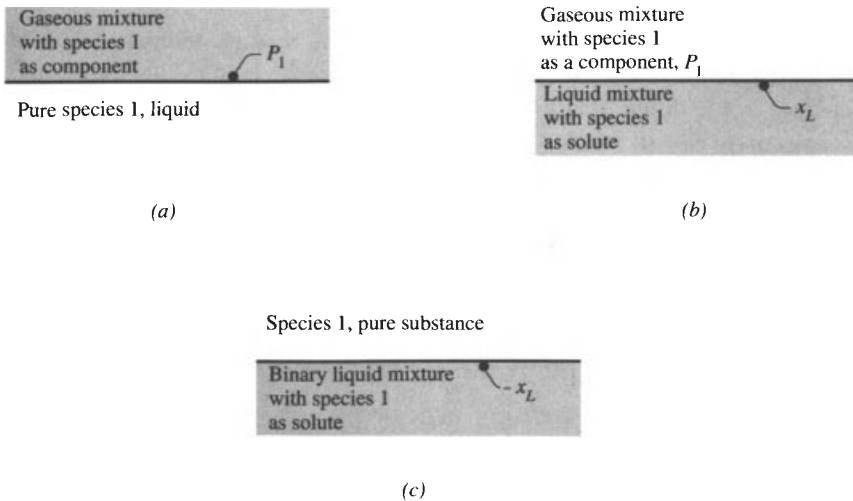
Figure 11.3   Boundary types and ways of specifying boundary conditions. (From Ref. 14.)

the inner sides of the boundary (i.e., in the shaded domain). It is an important feature because—unlike the temperature—the species concentration does not vary continuously across the interface. The exception is the case of the single-component system (pure substance), in which the mole fraction is equal to 1 on both sides of the interface. Figure 11.3 shows three examples of interfaces that may confine a certain diffusive domain. The diffusive domain of interest is indicated by the shaded area and forms the subject of the mass transfer analysis.

Figure 11.3*a* shows the interface between an ideal-gas mixture and the liquid phase of one of its components. For example, if 1 is a pure substance in the liquid phase (e.g., water), 1 is also a component in the gaseous mixture above the interface (i.e., water vapor in air). The proper boundary condition on the gas side of the interface states that the vapor pressure of the component of interest (P_1) is equal to its own saturation pressure at the temperature of interface liquid (T),

$$P_1 = P_{1,\text{sat}}(T) \tag{11.34}$$

The second example (Fig. 11.3*b*) is the interface between a liquid medium and a gaseous mixture. The species of interest—species 1—diffuses through the liquid and is also present as a component in the gaseous mixture. The boundary condition of interest is the mole fraction of species 1 on the liquid side of the interface: namely, x_L. The boundary mole fraction x_L will be greater when larger quantities of species 1 are present in the mixture on the gaseous side of the interface, that is, when the partial pressure P_1 is higher. In the case of a dilute

Table 11.3 Henry's constant H for several gases in water at moderate pressures

T (K)	H (bar)					
	Air	N_2	O_2	H_2	CO_2	CO
290	6.2×10^4	7.6×10^4	3.8×10^4	6.7×10^4	1.3×10^3	5.1×10^4
300	7.4×10^4	8.9×10^4	4.5×10^4	7.2×10^4	1.7×10^3	6×10^4
320	9.2×10^4	1.1×10^5	5.7×10^4	7.6×10^4	2.7×10^3	7.4×10^4
340	1.04×10^5	1.24×10^5	6.5×10^4	7.6×10^4	3.7×10^3	8.4×10^4

Source: Data from Ref. 15.

solution, where only small amounts of the solvent 1 are found in the liquid, x_L and P_1 are linked through the proportionality known as Henry's law,

$$x_L = \frac{P_1}{H} \qquad (11.35)$$

Table 11.3 shows a collection of values of Henry's constant H, the units of which are those of pressure. In addition to the dilute-solution requirement mentioned already, it should be noted that Henry's law applies only at low and moderate pressures, for example, when the partial pressure P_1 does not exceed 1 atm in the gaseous mixture [5]. At higher partial pressures, Henry's constant is a function of the partial pressure itself, and the use of a certain H value in eq. (11.35) is restricted to a limited range of partial pressures P_1.

The third example (Fig. 11.3c) refers to a binary liquid mixture in which species 1 is the solute. The other side of the interface is occupied by pure 1, as a pure substance at the temperature and pressure of the liquid mixture. For example, this type of boundary condition occurs between a block of salt (NaCl), which would be situated on the upper side of the interface in Fig. 11.3c, and a pool of saline water (NaCl and H_2O). The concentration of NaCl on the liquid side of the interface can be determined by claiming thermodynamic equilibrium at the interface and consulting the solubility data available in the chemical engineering literature [5, 15–17]. For the example above, Ref. 5 indicates that the solubility of NaCl in H_2O is 35.7 at $0°C$, which means that 35.7 g of NaCl will coexist with 100 g of H_2O in the solution. The mass fraction of NaCl on the liquid side of the interface is therefore $35.7/(35.7 + 100) = 0.263$ if the interface temperature is $0°C$.

11.5 LAMINAR FORCED CONVECTION

The analogy between mass transfer and heat transfer is clear in laminar boundary layer flow (Fig. 11.4). A uniform stream U_∞ flows parallel to a solid surface coated or made out of a substance that is soluble in the stream. An example is the forced convection drying of a porous solid wall saturated with water. The
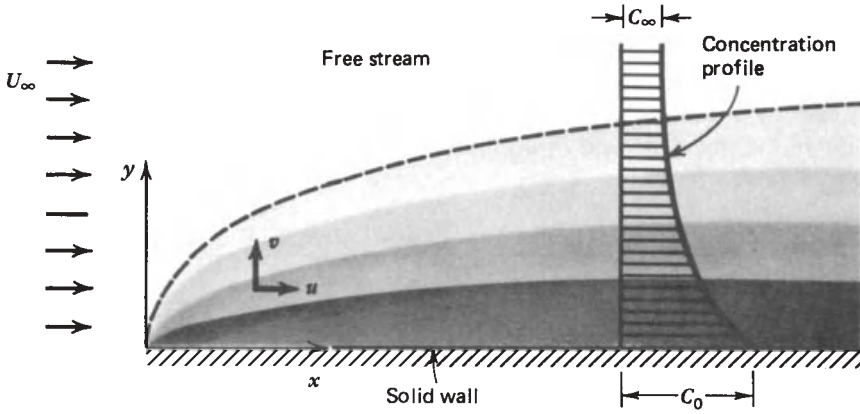
Figure 11.4   Concentration boundary layer near a flat surface.

airstream U_∞ is humid, its water vapor content far away from the wall described by the free-stream concentration C_∞. Following the boundary layer method of Chapter 2, we can expect a concentration boundary layer in the vicinity of the wall, that is, a concentration distribution that smoothes out the discrepancy between the relatively dry free stream C_∞ and the relatively wet flow *lamina* situated close to the wall C_0. The concentration gradient between the wall and the free stream sucks the soluble substance away from the wall: To predict the rate of such mass transfer is the objective of this chapter.

The wall concentration C_0 is the concentration of a fluid batch adjacent to the wall, not the concentration of soluble substance inside the wall. The concentration C_0 is the concentration on the $y = 0^+$ side of the wall (Fig. 11.4). Returning to the wall-drying example of the preceding paragraph, the concentration of H_2O can differ vastly from $y = 0^-$ to $y = 0^+$. The concentration inside the wall $(y = 0^-)$ depends on the porosity of the wall and the degree to which the pores are filled with water. The concentration on the fluid side of the wall–stream interface is dictated by the equilibrium vapor pressure of water at the free-stream pressure and temperature (assuming that $dP_\infty/dx = 0$ and there is no wall–stream temperature difference) [18].

The mass flux from the wall into the stream is, by Fick's law,

$$j_0 = -D\left(\frac{\partial C}{\partial y}\right)_{y=0} \tag{11.36}$$

The concentration field $C(x, y)$ is obtained by solving the boundary layer concentration equation

$$u\frac{\partial C}{\partial x} + v\frac{\partial C}{\partial y} = D\frac{\partial^2 C}{\partial y^2} \tag{11.37}$$

subject to the following boundary conditions:

$$C = C_0 \quad \text{at } y = 0, \quad C \to C_\infty \quad \text{as } y \to \infty \tag{11.38}$$

where both C_0 and C_∞ are constants. The mixture flow field (u, v) is known from Blasius's solution for laminar boundary layer flow (Chapter 2). The mass transfer problem [(11.37) and (11.38)] is identical to that solved by Pohlhausen for heat transfer [see eqs. (2.93)–(2.96)]; hence, the wall concentration gradient can be written by noting the $T \to C$, $\alpha \to D$ transformation:

$$\left(\frac{\partial C}{\partial y}\right)_{y=0} = (C_\infty - C_0)\left(\frac{U_\infty}{\nu x}\right)^{1/2}\left\{\int_0^\infty \exp\left[-\frac{\nu/D}{2}\int_0^\gamma f(\beta)\, d\beta\right] d\gamma\right\}^{-1} \tag{11.39}$$

In this solution we see the emergence of a new dimensionless group, the *Schmidt number*,

$$\text{Sc} = \frac{\nu}{D} \tag{11.40}$$

in place of the Prandtl number ν/α of the original Pohlhausen solution. Recalling the two asymptotes of the nested integral of eq. (11.39), we conclude that

$$\frac{(\partial C/\partial y)_{y=0}}{(C_\infty - C_0)(U_\infty/\nu x)^{1/2}} = \begin{cases} 0.332\text{Sc}^{1/3} & (\text{Sc} > 1) \\ 0.564\text{Sc}^{1/2} & (\text{Sc} < 1) \end{cases} \tag{11.41}$$

Mimicking the Nusselt number nondimensionalization of temperature gradient (or wall heat flux) employed in convective heat transfer, the conclusion above can be put in dimensionless form as a *local Sherwood number*,

$$\text{Sh} = \left(\frac{\partial C}{\partial y}\right)_{y=0}\frac{x}{C_\infty - C_0} = \frac{j_0}{C_0 - C_\infty}\frac{x}{D} \tag{11.42}$$

namely,

$$\text{Sh} = \begin{cases} 0.332\text{Sc}^{1/3}\,\text{Re}_x^{1/2} & (\text{Sc} \gtrsim 0.5) & (11.43) \\ 0.564\text{Sc}^{1/2}\,\text{Re}_x^{1/2} & (\text{Sc} \lesssim 0.5) & (11.44) \end{cases}$$

Carrying the analogy between mass transfer and heat transfer one step further, the ratio

$$h_m = \frac{j_0}{C_0 - C_\infty} \tag{11.45}$$

may be called the *mass transfer coefficient h_m*, so that the Sherwood number can also be defined as

$$\text{Sh} = \frac{h_m x}{D} \tag{11.46}$$

The symmetry between the mass transfer scaling laws (11.43) and (11.44) and their heat transfer correspondents [eqs. (2.102) and (2.107)] implies that if the bulk (mixture) flow configuration is the same in both problems and if the wall boundary condition is the same (e.g., $T_0 = $ constant versus $C_0 = $ constant), the mass transfer result is obtained directly from the heat transfer result through the transformation

$$\text{Nu} \to \text{Sh}, \qquad \text{Pr} \to \text{Sc}, \qquad \text{Re}_x \to \text{Re}_x \qquad (11.47)$$

The local mass transfer coefficient h_m can be calculated with eqs. (11.43) and (11.44), in which $h_m = (\text{Sh }D)/x$. This coefficient can be averaged over the total length L of the swept surface,

$$\bar{h}_m = \frac{1}{L} \int_0^L h_m \, dx \qquad (11.48)$$

The overall Sherwood number based on this L-averaged mass transfer coefficient is

$$\overline{\text{Sh}} = \frac{\bar{h}_m L}{D} \qquad (11.49)$$

and, after using eqs. (11.43) and (11.44), can be calculated with the formulas

$$\overline{\text{Sh}} = \begin{cases} 0.664 \text{Sc}^{1/3} \, \text{Re}_L^{1/2} & (\text{Sc} \gtrsim 0.5) & (11.50) \\ 1.128 \text{Sc}^{1/2} \, \text{Re}_L^{1/2} & (\text{Sc} \lesssim 0.5) & (11.51) \end{cases}$$

In summary, the mass transfer coefficient is needed to calculate the rate at which the species leaves the surface swept by the flow:

$$\dot{m}' = \bar{h}_m L (C_0 - C_\infty) \qquad (11.52)$$

The mass transfer rate $\dot{m}'$ (kilograms of species per second per meter) is expressed per unit length in the direction perpendicular to Fig. 11.4. More general is the relation

$$\dot{m} = \bar{h}_m A (C_0 - C_\infty) \qquad (11.53)$$

in which A is the area of the swept surface and $\dot{m}$ (kilograms of species per second) is the total mass transfer rate.

11.6   IMPERMEABLE SURFACE MODEL

The mass transfer–heat transfer analogy described in Section 11.5 rests on the important assumption that the transversal velocity of the flow (v, in Fig. 11.4)

is zero at the wall. Only then is the flow distribution [u, v, assumed known in eq. (11.37)] the same as in the velocity boundary layer studied in Section 2.5. In a mass transfer problem, this assumption is an approximation because the transfer of mass through the surface amounts to a flow perpendicular to the surface. The $v = 0$ approximation is justified when the concentration of the species of interest is ''low'' (i.e., lower than a critical level).

To see this, consider the laminar boundary layer mass transfer configuration studied in relation to Fig. 11.4. The mass transfer conclusions (11.50)–(11.51) mean that the mass flux (kg/s · m^2) through the $y = 0$ surface has the scale:

$$j_0 \sim (C_0 - C_\infty)\frac{D}{x}\mathrm{Re}_x^{1/2}\,\mathrm{Sc}^n \qquad (11.54)$$

The exponent n is $\frac{1}{3}$ when $\mathrm{Sc} \gtrsim 0.5$ and $\frac{1}{2}$ when $\mathrm{Sc} \lesssim 0.5$.

The next challenge is to determine when the transversal mass flow (or surface blowing effect) is negligible. The analysis presented in the second edition was based on a comparison of two transversal velocity scales, which was first reported in Ref. 14. One scale is the transversal velocity associated with the addition of the mass flux j_0 from the wall side of the concentration boundary layer,

$$v_0 \sim \frac{j_0}{\rho} \qquad (11.55)$$

The other scale is the transversal velocity of the laminar boundary layer, which according to eq. (2.81) is

$$v_\infty \sim U_\infty \mathrm{Re}_x^{-1/2} \qquad (11.56)$$

Weber [19] pointed out that this comparison is valid only for $\mathrm{Sc} \lesssim 0.5$, when the velocity boundary layer is thinner than the concentration boundary layer. The following alternative is valid for all Schmidt numbers. The comparison now is not between v_0 and v_∞, but between v_0 and the transversal velocity at the outer edge of the concentration boundary layer, v_c. The wall mass transfer is negligible, and the wall may be regarded as impermeable, when $v_0 < v_c$.

When $\mathrm{Sc} \lesssim 0.5$, the concentration boundary layer thickness δ_c is greater than the velocity boundary layer thickness δ, and consequently, $v_c \sim v_\infty$. The impermeable wall condition v_0/v_c becomes $v_0 < v_\infty$, which after using eqs. (11.54)–(11.56) and $n = \frac{1}{2}$ yields

$$\frac{C_0 - C_\infty}{\rho} < \mathrm{Sc}^{1/2} < 1 \qquad (11.57)$$

When $\mathrm{Sc} \gtrsim 0.5$, the concentration thickness δ_c is smaller than the velocity thickness δ,

$$\frac{\delta_c}{\delta} \sim \mathrm{Sc}^{-1/3} < 1 \qquad (11.58)$$

This can be deduced by comparing eq. (11.43), in which $\text{Sh} \sim x/\delta_c$, with eqs. (2.31) and (2.33), where $C_f \sim x/\delta$. Next, at the edge of the concentration boundary layer, the longitudinal velocity scale is

$$u_c \sim U_\infty \frac{\delta_c}{\delta} \tag{11.59}$$

Mass conservation in the δ_c layer requires that [cf. eq. (2.7)]

$$v_c \sim \frac{u_c \delta_c}{x} \tag{11.60}$$

Combining eqs. (11.59)–(11.60) with $\delta \sim x\,\text{Re}_x^{-1/2}$ leads to

$$\frac{v_c}{v_\infty} \sim \left(\frac{\delta_c}{\delta}\right)^2 \sim \text{Sc}^{-2/3} \tag{11.61}$$

Finally, the impermeable wall condition $v_0 < v_\infty$ can be written by using eqs. (11.54)–(11.56) with $n = \frac{1}{3}$ and eq. (11.60). The result is

$$\frac{C_0 - C_\infty}{\rho} < 1 \tag{11.62}$$

In summary, eqs. (11.57) and (11.62) show that the impermeable-surface assumption is valid at sufficiently low concentrations. Table 11.4 lists the Sc values of several common substances that diffuse through air or water.

11.7 OTHER EXTERNAL FORCED CONVECTION CONFIGURATIONS

Analogous mass transfer rate formulas can be deduced for the other external forced convection configurations treated in this book. For example, in the case of a turbulent boundary layer flow over a flat surface, we begin with the overall Nusselt number relation (7.78''):

$$\overline{\text{Nu}}_L = 0.037\text{Pr}^{1/3}\,\text{Re}_L^{4/5} \qquad (\text{Pr} \gtrsim 0.5, \quad 10^6 < \text{Re}_L < 10^8) \tag{11.63}$$

and substitute $\overline{\text{Sh}}_L$ in place of $\overline{\text{Nu}}_L$ and Sc in place of Pr. We arrive at the overall Sherwood number, or the L-averaged mass transfer coefficient $\overline{h}_m$,

$$\overline{\text{Sh}}_L = \frac{\overline{h}_m L}{D} = 0.037\text{Sc}^{1/3}\,\text{Re}_L^{4/5} \qquad (\text{Sc} \gtrsim 0.5, \quad 10^6 < \text{Re}_L < 10^8) \tag{11.63'}$$

Table 11.4 Schmidt number, Lewis number, and composition buoyancy coefficient at low concentration, 1 atm, and approximately 25°C

Main Fluid	Species at Low Concentrations	$Sc = \nu/D$	$Le = Sc/Pr$	$\rho\beta_c = -(\partial\rho/\partial\rho_i)_{T,P}$
Air ($Pr = 0.7$)	Ammonia	0.78	1.11	+1.07
	Carbon dioxide	0.94	1.34	−0.34
	Hydrogen	0.22	0.314	+13.4
	Oxygen	0.75	1.07	−0.094
	Water vapor	0.60	0.86	+0.61
	Benzene	1.76	2.51	−0.63
	Ether	1.66	2.37	−0.61
	Methanol	0.97	1.39	−0.095
	Ethyl alcohol	1.30	1.86	−0.37
	Ethylbenzene	2.01	2.87	−0.73
Water ($Pr = 7$)	Ammonia	445	63.57	−0.5
	Carbon dioxide	453	64.71	
	Hydrogen	152	21.71	
	Oxygen	356	50.86	
	Nitrogen	468	66.86	
	Chlorine	617	88.14	
	Sulfur dioxide	523	74.71	
	Calcium chloride	750	107.14	+0.8
	Sodium chloride	580	82.86	+0.7
	Methanol	556	79.43	−0.17
	Sucrose	1700	242.86	

Source: After Ref. 20.

An alternative expression for the high-Re_L range can be obtained by recognizing the Colburn relation for the local heat transfer coefficient,

$$St_x = \tfrac{1}{2}C_{f,x}\, Pr^{-2/3} \qquad (Pr \gtrsim 0.5) \qquad (11.64)$$

and the corresponding local skin friction coefficient expression

$$\frac{1}{2}C_{f,x} = 0.0296\left(\frac{U_\infty x}{\nu}\right)^{-1/5} \qquad (11.64')$$

Combined, eqs. (11.64) and (11.64') yield

$$St_x = 0.0296 Pr^{-2/3}\, Re_x^{-1/5} \qquad (Pr \gtrsim 0.5) \qquad (11.65)$$

The next challenge is to find the mass transfer analog of the local Stanton number that appears on the left side of eq. (11.65): namely,

$$St_x = \frac{h_x}{\rho c_P U_\infty} = \frac{h_x \alpha}{k U_\infty} = \frac{q_0'' \alpha}{(T_0 - T_\infty) k U_\infty} \tag{11.65'}$$

The mass transfer analog of St_x is obtained by replacing q_0'' with j_0, $T_0 - T_\infty$ with $C_0 - C_\infty$, α with D, and k again with D:

$$\frac{q_0'' \alpha}{(T_0 - T_\infty) k U_\infty} \rightarrow \frac{j_0 D}{(C_0 - C_\infty) D U_\infty} \tag{11.66}$$

What emerges on the right side of (11.66) is simply the ratio h_m/U_∞, which is called the *local mass transfer Stanton number*,

$$St_m = \frac{h_m}{U_\infty} \tag{11.66'}$$

In the end, the mass transfer analog of eq. (11.65) becomes

$$St_m = 0.0296 Sc^{-2/3} Re_x^{-1/5} \qquad (Sc \gtrsim 0.5) \tag{11.67}$$

or in terms of the *L*-averaged mass transfer coefficient,

$$\overline{St_m} = \frac{\overline{h}_m}{U_\infty} = 0.037 Sc^{-2/3} Re_L^{-1/5} \qquad (Sc \gtrsim 0.5) \tag{11.67'}$$

For a single *cylinder in cross flow*, the expression for the surface-averaged Sherwood number can be derived from the heat transfer correlation listed in eq. (7.100), where $\overline{Nu}_D$ is replaced by

$$\overline{Sh}_{D_0} = \frac{\overline{h}_m D_0}{D} \tag{11.68}$$

in which the outer diameter of the cylinder (D_o, Fig. 11.5) must not be confused with the mass diffusivity coefficient D. As usual, on the right side of eq. (7.100), the Reynolds number retains its position and becomes Re_{D_o}, while Pr is replaced by Sc:

$$\overline{Sh}_{D_0} = 0.3 + \frac{0.62 Re_{D_0}^{1/2} Sc^{1/3}}{[1 + (0.4/Sc)^{2/3}]^{1/4}} \left[1 + \left(\frac{Re_{D_0}}{282,000} \right)^{5/8} \right]^{4/5} \qquad (Re_{D_0} Sc > 0.2) \tag{11.69}$$

The surface-averaged Sherwood number for mass transfer from a *sphere* of diameter D_0 to a uniform flow (U_∞, C_∞, Fig. 11.5) can be deduced from
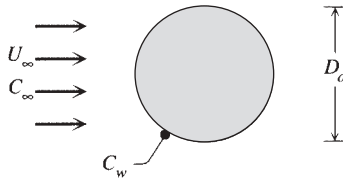
Figure 11.5   Uniform flow past a perpendicular cylinder or a sphere.

eq. (7.104). The operation consists of replacing Pr with Sc and $\overline{\text{Nu}}_D$ with the average Sherwood number defined in eq. (11.68):

$$\overline{\text{Sh}}_{D_0} = 2 + (0.4\text{Re}_{D_0}^{1/2} + 0.06\text{Re}_{D_0}^{2/3})\text{Sc}^{0.4} \qquad (3.5 < \text{Re}_{D_0} < 7.6 \times 10^4) \tag{11.70}$$

11.8   INTERNAL FORCED CONVECTION

In configurations of internal forced convection, or duct flow, the local mass transfer coefficient is based on the difference between the species concentration of the exposed side of the wall (C_w) and the bulk concentration of the stream (C_b),

$$h_m = \frac{j_w}{C_w - C_b} \tag{11.71}$$

In a way that parallels the definition of bulk temperature at the start of Chapter 3, the bulk concentration of the stream is defined by

$$C_b = \frac{1}{UA} \int_A uC \, dA \tag{11.72}$$

In this averaging process, u is the longitudinal velocity of the stream (Fig. 11.6), U is the cross-sectional averaged velocity, and A is the cross-sectional area.
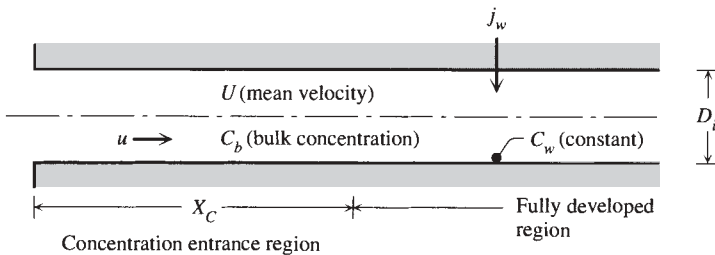
Figure 11.6   Flow through a round tube with constant species concentrations at the wall.

The flow begins with an entrance region, followed by a fully developed region. In the entrance region, the concentration profile changes shape from one longitudinal location to the next. In accordance with eqs. (3.8) and (3.91) and the mass transfer—heat transfer analogy discussed in the preceding sections, the concentration entrance length X_C for laminar flow is

$$\frac{X_C}{D_h} \cong 0.04 \mathrm{Re}_{D_h} \, \mathrm{Sc} \tag{11.73}$$

The Reynolds number is based on the mean velocity U and the hydraulic diameter D_h; in other words, $\mathrm{Re}_{D_h} = U D_h / \nu$. The X_C estimate provided by eq. (11.73) is valid for all Schmidt numbers.

In the case of laminar flow through a round tube with constant species concentration at the wall (C_w, Fig. 11.6), the local mass transfer coefficient h_m can be estimated with the help of Fig. 3.14. On the ordinate of that figure, Nu_x is replaced by the local Sherwood number based on the tube inner diameter D_i,

$$\mathrm{Sh}_{D_i} = \frac{h_m D_i}{D} \tag{11.74}$$

In this definition, the tube inner diameter D_i should not be confused with the mass diffusivity D. The subscript i means that the diameter D_i is internal. In other words, i does not refer to the species i mentioned in many parts of this chapter.

The new dimensionless group for the abscissa of Fig. 3.14 is $(x/D_i)/(\mathrm{Re}_{D_i}\mathrm{Sc})$, while the new parameter that distinguishes between the curves is Sc instead of Pr. This modified version of Fig. 3.14 shows that in the fully developed region the mass transfer coefficient becomes independent of longitudinal position, approaching the value

$$\frac{h_m D_i}{D} = 3.66 \tag{11.75}$$

In the turbulent regime, the concentration entrance length is about 10 times the tube diameter [i.e., approximately the same as the hydrodynamic entrance length X of eq. (8.4)]. The heat transfer correlations of Chapter 8 can be converted into their mass transfer equivalents through the substitutions $\mathrm{Nu}_D \rightarrow \mathrm{Sh}_{D_i}$, $\mathrm{Pr} \rightarrow \mathrm{Sc}$, and $\mathrm{Re}_D \rightarrow \mathrm{Re}_{D_i}$. For example, the heat transfer correlation (8.30) leads to the following estimate for the Sherwood number in fully developed turbulent flow:

$$\mathrm{Sh}_{D_i} = 0.023 \mathrm{Re}_{D_i}^{4/5} \, \mathrm{Sc}^{1/3} \qquad (\mathrm{Sc} \gtrsim 0.5, \quad 2 \times 10^4 < \mathrm{Re}_{D_i} < 10^6) \tag{11.76}$$

Forced convection mass transfer plays an important role in modern technologies [21]. One example is the constructal design of the flow architecture of desalination units [22].

11.9   NATURAL CONVECTION

Consider the vertical wall with heat and mass transfer sketched in Fig. 11.7, where T_0, T_∞, C_0, and C_∞ are constants. The vertical boundary layer flow is due to the buoyancy effect due to the density difference between boundary layer fluid and unaffected (reservoir) fluid. As was shown in Chapter 4, the boundary layer momentum equation for this flow is

$$u\frac{\partial v}{\partial x} + v\frac{\partial v}{\partial y} = v\frac{\partial^2 v}{\partial x^2} + \frac{1}{\rho}(\rho_\infty - \rho)g \qquad (11.77)$$

In the case of heat transfer, we saw that the density difference $(\rho_\infty - \rho)$ is approximately proportional to the temperature difference $(T - T_\infty)$, in accordance with the Boussinesq approximation. In the presence of mass transfer, the driving density difference $(\rho_\infty - \rho)$ may also be due to the concentration difference (Fig. 11.7); a vertical buoyant layer forms if the wall releases a substance less dense than the reservoir fluid mixture. The thermodynamic state of the fluid mixture depends on pressure, temperature, and composition. In the limit of small
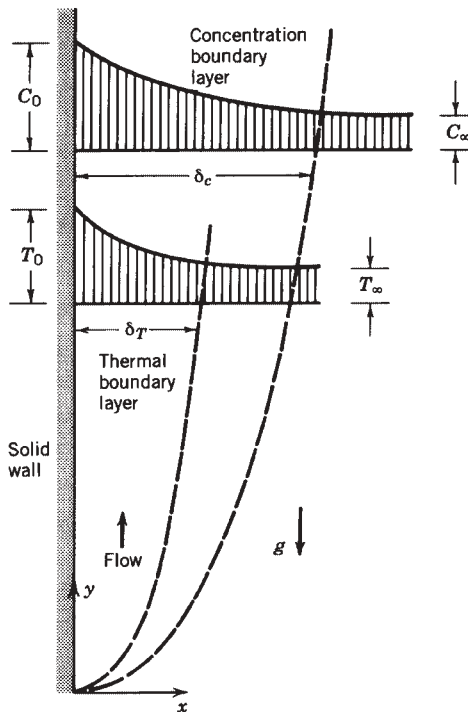
Figure 11.7   Combined mass and heat transfer effected by a buoyant boundary layer flow.

density variations at constant pressure, we can write

$$\rho \cong \rho_\infty + \left(\frac{\partial \rho}{\partial T}\right)_P (T - T_\infty) + \left(\frac{\partial \rho}{\partial C}\right)_P (C - C_\infty) + \cdots \tag{11.78}$$

Recalling the definition of thermal expansion coefficient,

$$\beta = -\frac{1}{\rho}\left(\frac{\partial \rho}{\partial T}\right)_P \tag{11.79}$$

we introduce the *concentration expansion coefficient*,

$$\beta_c = -\frac{1}{\rho}\left(\frac{\partial \rho}{\partial C}\right)_P \tag{11.80}$$

to obtain the equivalent of the Boussinesq approximation for the combined heat and mass transfer problem. Coefficients β and β_c can be positive or negative; hence, in the scale analysis of this section, $\beta(T_0-T_\infty)$ means the absolute value of $\beta(T_0-T_\infty)$. Based on the approximation (11.78), the boundary layer momentum equation (11.77) becomes

$$\underbrace{u\frac{\partial v}{\partial x} + v\frac{\partial v}{\partial y}}_{\text{inertia}} = \underbrace{\nu\frac{\partial^2 v}{\partial x^2}}_{\text{Friction}} + \underbrace{g\beta(T - T_\infty)}_{\substack{\text{Body force}\\\text{due to}\\\text{nonuniform}\\\text{temperature}}} + \underbrace{g\beta_c(C - C_\infty)}_{\substack{\text{Body force}\\\text{due to}\\\text{nonuniform}\\\text{concentration}}} \tag{11.81}$$

The flow field is coupled to the temperature and concentration fields obtained by solving the boundary layer energy and concentration equations

$$u\frac{\partial T}{\partial x} + v\frac{\partial T}{\partial y} = \alpha\frac{\partial^2 T}{\partial x^2} \tag{11.82}$$

$$u\frac{\partial C}{\partial x} + v\frac{\partial C}{\partial y} = D\frac{\partial^2 C}{\partial x^2} \tag{11.83}$$

11.9.1 Mass-Transfer-Driven Flow

To determine the mass transfer rate between wall and fluid reservoir, we focus on two limiting situations. Consider first the limit of no heat transfer, that is, the case of a boundary layer driven solely by the concentration gradient. The problem reduces to solving eqs. (11.81) and (11.83), subject to the velocity and concentration boundary conditions sketched in Fig. 11.7. This problem is analytically identical to the heat transfer problem solved in Chapter 4; the local

Sherwood number is obtained by subjecting the heat transfer results to the transformation Nu $\rightarrow$ Sh, $\alpha \rightarrow D$, Pr $\rightarrow$ Sc, $\beta(T_0-T_\infty) \rightarrow \beta_c(C_0-C_\infty)$. The mass transfer results are

$$\text{Sh} = \begin{cases} 0.503\text{Ra}_{m,y}^{1/4} & (\text{Sc} > 1) & (11.84) \\ 0.6(\text{Ra}_{m,y} \text{ Sc})^{1/4} & (\text{Sc} < 1) & (11.85) \end{cases}$$

where $\text{Ra}_{m,\,y}$ is the local ''mass transfer Rayleigh number'' of a vertical boundary layer the buoyancy of which is caused by mass transfer

$$\text{Ra}_{m,y} = \frac{g\beta_c(C_0 - C_\infty)y^3}{\nu D} \qquad (11.86)$$

11.9.2   Heat-Transfer-Driven Flow

The second limit is the mass transfer to a vertical boundary layer driven by the wall–reservoir temperature difference. The length and velocity scales of such a layer have been summarized in Table 4.1. Below we rely on scale analysis to derive the mass transfer rate, or the Sherwood number.

Let δ_c be the boundary layer thickness scale of the concentration profile. In the flow region of thickness δ_c and height H, the concentration equation (11.83) requires that

$$\frac{v}{H} \sim \frac{D}{\delta_c^2} \qquad (11.87)$$

Note that v is the vertical velocity scale in the region of thickness δ_c: Naturally, v will depend on the relative size of δ_c and the other (two) length scales of the ΔT-driven boundary layer flow. Four possibilities exist, as is shown in Fig. 11.8. We examine in some detail the first possibility (Pr > 1, $\delta_c < \delta_T$), and for the remaining three, we list only the conclusions (Table 11.5).

Table 4.1 shows that in a heat-transfer-driven boundary layer, the vertical velocity reaches the order of magnitude $(\alpha/H)\text{Ra}_H^{1/2}$ at a distance of order $H\,\text{Ra}_H^{-1/4}$ away from the wall (if Pr > 1). From the first sketch of Fig. 11.8, we conclude that the velocity scale in the δ_c-thin layer is

$$v \sim \frac{\delta_c}{\delta_T} \frac{\alpha}{H}\text{Ra}_H^{1/2}, \qquad \delta_c < \delta_T \qquad (11.88)$$

where $\delta_T \sim H\text{Ra}_H^{-1/4}$ is the thermal boundary layer thickness. Combining eqs. (11.87) and (11.88), we obtain the δ_c scale,

$$\delta_c \sim H\left(\frac{D}{\alpha}\right)^{1/3} \text{Ra}_H^{-1/4} \qquad (11.89)$$
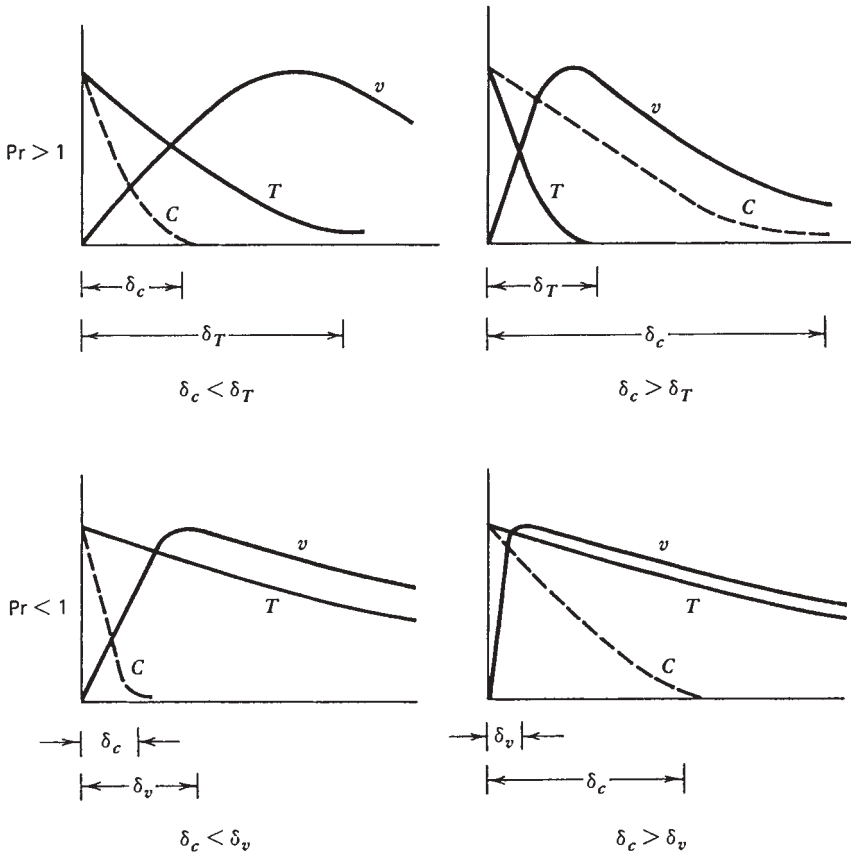
Figure 11.8 Relative size of the boundary layer thicknesses in natural convection mass and heat transfer.

Table 11.5   Mass transfer rate scales for a vertical boundary layer driven by heat transfer

Fluid	Overall Sherwood Number or Concentration Layer Slenderness Ratio H/δ_c	
$Pr > 1$, $\delta_c < \delta_T$ (or Le > 1)	$Le^{1/3}Ra_H^{1/4}$	
$Pr > 1$, $\delta_c > \delta_T$ (or Le < 1)	$Le^{1/2}Ra_H^{1/4}$	(Sc > 1)
	$Le\,Pr^{1/2}Ra_H^{1/4}$	(Sc < 1)
$Pr < 1$, $\delta_c < \delta_v$ (or Sc > 1)	$Le^{1/3}Pr^{1/12}Ra_H^{1/4}$	
$Pr < 1$, $\delta_c > \delta_v$ (or Sc < 1)	$Le^{1/2}Pr^{1/4}Ra_H^{1/4}$	(Le > 1)
	$Le\,Pr^{1/4}Ra_H^{1/4}$	(Le < 1)

The order of magnitude of the overall Sherwood number is inversely proportional to δ_c,

$$\overline{Sh} = \frac{\bar{j}_0}{C_0 - C_\infty} \frac{H}{D} \sim \frac{H}{\delta_c} \tag{11.90}$$

Hence,

$$\overline{Sh} \sim \left(\frac{\alpha}{D}\right)^{1/3} Ra_H^{1/4} \tag{11.91}$$

More exact analyses could be carried out to refine this mass transfer result [23–25]. However, based on the extensive comparison of scaling results with integral and similarity results (Chapters 2–5), it is reasonable to expect eq. (11.91) to be correct within 25 percent.

It is known that dimensional analysis reveals all the dimensionless groups that could be formed by combining the dimensional parameters of the problem algebraically. Scale analysis, on the other hand, leads (1) to quantitative *results* and (2) to only those dimensionless groups that have a physical meaning. In this way, eqs. (11.90) and (11.91) teach us that the slenderness ratio of the concentration boundary layer is governed by a new dimensionless group,

$$\left(\frac{\alpha}{D}\right)^{1/3} Ra_H^{1/4} \sim \frac{\text{height of boundary layer}}{\text{thickness of concentration layer}} \tag{11.92}$$

The dimensionless ratio α/D has been identified already by dimensional analysis and is called the *Lewis number*,

$$Le = \frac{\alpha}{D} \quad \text{or} \quad Le = \frac{Sc}{Pr} \tag{11.93}$$

Finally, the $\delta_c < \delta_T$ assumption made in the beginning of this analysis means that

$$H \, Le^{-1/3} \, Ra_H^{-1/4} < H \, Ra_H^{-1/4} \tag{11.94}$$

or

$$Le > 1 \tag{11.95}$$

In conclusion, the first case of Fig. 11.8 corresponds to fluid mixtures with both Prandtl number and Lewis number greater than 1. The remaining three possibilities are sketched in Fig. 11.8, and their corresponding mass transfer scaling laws are listed in Table 11.5. The student is invited to derive these results based on scale analysis (see Problem 11.11). Note that in the case of low-Prandtl number fluids, the concentration thickness δ_c is compared with the viscous layer thickness δ_v (Chapter 4).

To summarize, we analyzed the combined heat and mass transfer problem in natural convection first by calculating mass transfer in a mass-transfer-driven

flow [eqs. (11.84) and (11.85)] and later by deriving the mass transfer scales in boundary layers driven by heat transfer (Table 11.5). It remains to decide whether a given layer is actually driven by mass transfer or heat transfer; in other words, is the Sherwood number given by eqs. (11.84) and (11.85) or Table 11.5?

One way to decide is to think of the wall surface, whose concentration is C_0, as being coated with two mass-insulating blankets, one $(\delta_c)_{MT}$ thick when the layer is driven by mass transfer, and the other with a thickness $(\delta_c)_{HT}$ when heat transfer is the driving mechanism [one blanket extends from $x = 0$ to $x = (\delta_c)_{MT}$ and the other from $x = 0$ to $x = (\delta_c)_{HT}$]. According to the constructal law [3, 26, 27], the mass flux released by the wall will select the flow design that provides easier flow access, which means the shorter path to the mass sink (the reservoir); hence, the scales of Table 11.5 hold when their corresponding δ_c's are smaller than the concentration profile thickness in a mass-transfer-driven layer,

$$(\delta_c)_{HT} < (\delta_c)_{MT} \tag{11.96}$$

For example, for fluids with Pr > 1 and Le > 1 (the top line in Table 11.5), criterion (11.96) implies that

$$\frac{\beta(T_0 - T_\infty)}{\beta_c(C_0 - C_\infty)} > Le^{-1/3} \tag{11.97}$$

is the condition for heat-transfer-driven natural convection mass transfer. This criterion is not the same as the direct comparison of the scales of the last two terms in the boundary layer momentum equation (11.81).

In the scale analysis above, the competition between the temperature and concentration layers of Fig. 11.7 was illustrated by calculating the mass transfer rate from the wall to the fluid reservoir. The transition from concentration-driven to temperature-driven natural convection also has an interesting effect on the heat transfer rate calculation. This aspect is examined in Problem 11.13.

Similarity and integral solutions for vertical boundary layer natural convection driven by the combined effect of mass and heat transfer have been reported by Gebhart and Pera [20], Somers [28], and Khair and Bejan [23]. The problem formulated in Ref. 23 was extended to natural convection along a wavy wall [29] and in a fluid-saturated porous medium [30].

11.10   TURBULENT FLOW

11.10.1   Time-Averaged Concentration Equation

The analogy between mass transfer and heat transfer also rules turbulent convection again under conditions of low-wall-mass transfer rates. The time-fluctuating concentration field can be smoothed out through the process of time averaging of Chapter 7, which begins with the decomposition

$$C = \overline{C} + C' \tag{11.98}$$

where $\overline{C}(x, y, z)$ is the time-averaged concentration field. Substituting eq. (11.98) into the concentration equation (11.27a) with $\dot{m}''' = 0$ and observing the rules of time-averaging algebra yields

$$\overline{u}\frac{\partial \overline{C}}{\partial x} + \overline{v}\frac{\partial \overline{C}}{\partial y} + \overline{w}\frac{\partial \overline{C}}{\partial z} = D\,\nabla^2\overline{C} - \frac{\partial}{\partial x}(\overline{u'C'}) - \frac{\partial}{\partial y}(\overline{v'C'}) - \frac{\partial}{\partial z}(\overline{w'C'}) \quad (11.99)$$

The time-averaged products of type $(\overline{v'C'})$ are the additional unknowns that are responsible for the closure problem in turbulent convective mass transfer.

In a two-dimensional slender flow region such as the forced boundary layer sketched in Fig. 11.4, the time-averaged concentration equation (11.99) assumes the simpler form

$$\overline{u}\frac{\partial \overline{C}}{\partial x} + \overline{v}\frac{\partial \overline{C}}{\partial y} = D\frac{\partial^2 \overline{C}}{\partial y^2} - \frac{\partial}{\partial y}(\overline{v'C'}) \quad (11.100)$$

To bring into view the eddy mass transfer across the boundary layer, we write eq. (11.100) as

$$\overline{u}\frac{\partial \overline{C}}{\partial x} + \overline{v}\frac{\partial \overline{C}}{\partial y} = -\frac{\partial j_{\mathrm{app}}}{\partial y} \quad (11.101)$$

where the apparent mass flux $j_{\mathrm{app}}(x, y)$ is due to molecular and eddy transport,

$$j_{\mathrm{app}} = -D\frac{\partial \overline{C}}{\partial y} + \overline{v'C'} \quad (11.102)$$

Based on an argument similar to the one presented in Fig. 7.3 for heat transfer, the eddy mass flux term $\overline{v'C'}$ is related to the mean concentration gradient

$$-\overline{v'C'} = \epsilon_m\frac{\partial \overline{C}}{\partial y} \qquad \text{eddy mass flux} \quad (11.103)$$

This equation is the definition for the *mass eddy diffusivity* $\epsilon_m(x, y)$, an empirical function that is not to be confused with the momentum eddy diffusivity ϵ_M of Chapter 7. In sum, we can write the boundary layer concentration equation (11.100) as

$$\overline{u}\frac{\partial \overline{C}}{\partial x} + \overline{v}\frac{\partial \overline{C}}{\partial y} = \frac{\partial}{\partial y}\left[(D + \epsilon_m)\frac{\partial \overline{C}}{\partial y}\right] \quad (11.104)$$

11.10.2 Forced Convection Results

The similarity between eq. (11.104) and the boundary layer energy equation (7.26) makes many of the turbulent heat transfer results convertible into mass transfer results. Thus, in the case of mass transfer in turbulent boundary layer

flow from a wall surface of concentration C_0 to a free stream of concentration C_∞, we can combine the $\tau_{app} = \tau_0$ analysis of the momentum boundary layer with a similar assumption for the concentration layer,

$$j_{app} = j_0 \quad \text{independent of } y \tag{11.105}$$

to obtain the equivalent of eq. (7.77),

$$\frac{h_m}{U_\infty} = \frac{\frac{1}{2}C_{f,x}}{0.9 + \left(\frac{1}{2}C_{f,x}\right)^{1/2}(13.2\text{Sc} - 10.25)} \tag{11.106}$$

Here $C_{f,x}$ is the local skin friction coefficient (Fig. 7.6). Experimental measurements of the mass transfer coefficient h_m are correlated very well by formulas like eq. (11.106), or the Colburn relation,

$$\frac{h_m}{U_\infty}\text{Sc}^{2/3} = \frac{1}{2} \, C_{f,x} \tag{11.107}$$

In conclusion, experiment-aided formulas for the mass transfer coefficient in turbulent boundary layer flow can be obtained by subjecting the heat transfer correlations to the transformation

$$\frac{h}{\rho c_P U_\infty} \rightarrow \frac{h_m}{U_\infty} \tag{11.108}$$

$$\text{Pr} \rightarrow \text{Sc} \tag{11.109}$$

For fully developed turbulent mass transfer inside a duct, we can derive the mass transfer equivalent of eq. (8.28). Simpler experimental correlations are the formulas obtained by changing the notation in the Colburn and Dittus-Boelter relations, eqs. (8.29) and (8.31),

$$\frac{h_m}{U}\text{Sc}^{2/3} \cong \frac{f}{2} \tag{11.110}$$

$$\frac{h_m D_h}{D} \cong 0.024\text{Sc}^{0.4} \, \text{Re}_{D_h}^{0.8} \tag{11.111}$$

In these formulas D_h is the hydraulic diameter of the duct, D the mass diffusivity, and U the cross-section-averaged velocity.

The turbulent mixing of a flow region surrounded by a region of different concentration is a phenomenon of great interest in environmental engineering. The mass transfer by free-stream turbulence can be analyzed based on the methodology constructed in Chapter 9. The first idea in this methodology is that free-stream mixing regions such as shear layers, jets, and plumes are *slender*, so that the boundary layer approximation applies. In addition, recognizing the

overwhelming contribution of large eddies to turbulent transport across the stream, it is assumed that the eddy diffusivity is independent of the coordinate normal to the stream. Finally, based on empirical observations or the $\lambda_B/D = $ constant property of inviscid flow (Chapter 6), it is recognized that all these mixing regions grow linearly in the flow direction (Fig. 9.9).

For a two-dimensional flow proceeding in the x direction, the boundary layer concentration equation (11.104) reduces to

$$\bar{u}\frac{\partial \bar{C}}{\partial x} + \bar{v}\frac{\partial \bar{C}}{\partial y} = \epsilon_m \frac{\partial^2 \bar{C}}{\partial y^2} \tag{11.112}$$

because in the free-stream region, ϵ_m can be regarded as much greater than D. The identical form of eq. (11.112) for mass transfer and eq. (9.14) for heat transfer suggests that the time-averaged temperature fields derived in Chapter 9 can be converted to concentration fields via the transformation

$$\bar{T} \rightarrow \bar{C} \tag{11.113}$$

$$\epsilon_H \rightarrow \epsilon_m \tag{11.114}$$

For example, the time-averaged concentration in a two-dimensional shear layer may be condensed in the expression

$$\frac{\bar{C} - C_\infty}{C_0 - C_\infty} \cong \frac{1}{2}\left[1 + \mathrm{erf}\left(\sigma\frac{y}{x}\right)\right] \tag{11.115}$$

where C_0 and C_∞ are the constant concentrations found on either side of the shear layer and where σ is an empirical constant accounting for the angle of the mixing region ($\sigma = 13.5$). Note that expression (11.115) also rests on the assumption that the *turbulent Schmidt number* Sc_t is approximately equal to 1,

$$\mathrm{Sc}_t = \frac{\epsilon_M}{\epsilon_m} \cong 1 \tag{11.116}$$

As a second example, the turbulent mixing zone created by the discharge of a round jet of concentration C_0 into a reservoir of concentration C_∞ has a concentration field described by [eq. (9.43)]

$$\frac{\bar{C} - C_\infty}{\bar{C}_c - C_\infty} \cong \exp\left[-\left(\frac{r}{0.127x}\right)^2\right] \tag{11.117}$$

The centerline concentration $\bar{C}_c$ is related to the nozzle concentration C_0 by invoking the conservation of the constituent of concentration $\bar{C}$,

$$u_0(C_0 - C_\infty)\frac{r_0^2}{2} = \int_0^\infty \bar{u}(\bar{C} - C_\infty)r\,dr \tag{11.118}$$

where u_0 is the cross-section-averaged velocity through the nozzle and $\bar{u}$ is the time-averaged velocity distribution in the conical mixing region, eq. (9.40).

As a third example, the concentration downstream from a point mass source bathed by a turbulent stream with uniform time-averaged velocity $\overline{U}_\infty$ and uniform eddy diffusivity ϵ_m (grid-generated turbulence, Chapter 9) is distributed according to

$$\overline{C} - C_\infty = \frac{\dot{m}}{4\pi\epsilon_m x} \exp\left(-\frac{r^2\overline{U}_\infty}{4\epsilon_m x}\right) \tag{11.119}$$

In this expression, $\dot{m}$ is the strength of the point mass source measured in kilograms (of the constituent whose concentration is C) per second. The concentration field downstream from a line source of strength $\dot{m}$ (kg/m · s) is analogous to the temperature field behind a line heat source in a uniform turbulent stream, eqs. (9.90) and (9.93),

$$\overline{C} - C_\infty = \frac{\dot{m}'}{(4\pi\overline{U}_\infty\epsilon_m x)^{1/2}} \exp\left(-\frac{y^2\overline{U}_\infty}{4\epsilon_m x}\right) \tag{11.120}$$

11.10.3 Contaminant Removal from a Ventilated Enclosure

We close this section with an example of numerical results of turbulent mass transfer, with emphasis on correlating the results by relying on a simple theory. The example is the time-dependent removal of contaminated air from a two-dimensional enclosure with one inlet and one outlet [31] (Fig. 11.9 inserts). It is a very important application, stimulated by concern over the quality of indoor air and that office workers may be exposed to the sick building syndrome. A healthy building must supply an adequate amount of outside air and control indoor contaminants in addition to saving energy. This mass transfer phenomenon is also relevant to the problem of providing adequate forced convection cooling to enclosures containing electronic components.

In the two-dimensional model of Fig. 11.9, the chamber is initially filled with contaminated air in which the contaminant concentration is C_0. Clean air starts flowing through the inlet at $t = 0$, while an equal flow rate of contaminated air exits through the outlet. In time, the amount of contaminant held in the enclosure decreases. Its evolution is described by the *ventilation* or *displacement efficiency*

$$\eta_d = \frac{C_0 - \overline{C}}{C_0 - C_{\text{in}}} \tag{11.121}$$

where $\overline{C}(t)$ is the instantaneous contaminant concentration averaged over the enclosure volume and C_{in} is the concentration in the inlet stream ($C_{\text{in}} = 0$). The dimensionless time is

$$\tau^* = \frac{tU_{\text{in}}h}{LH} \tag{11.122}$$
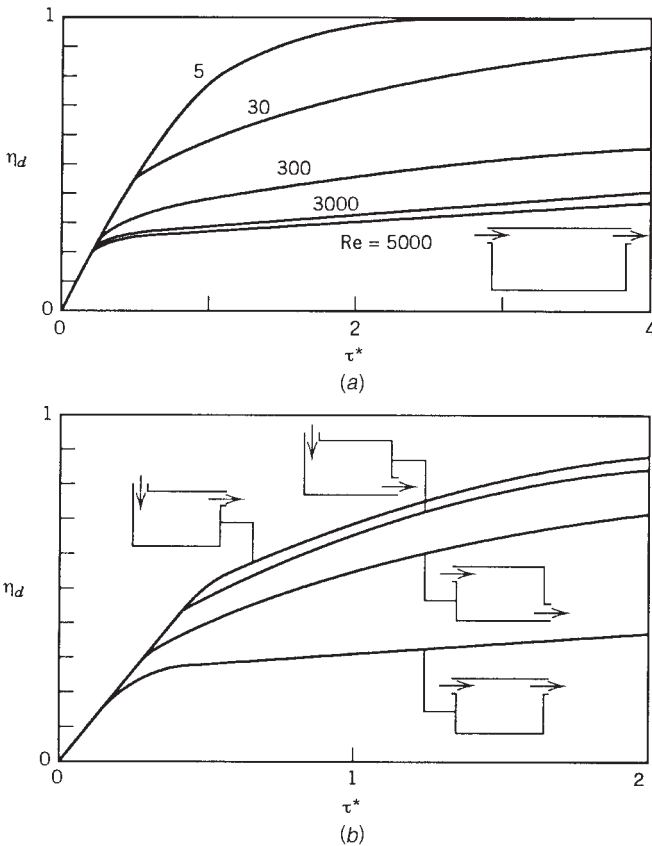
Figure 11.9 Effect of (a) Reynolds number and (b) flow configuration on the ventilation displacement efficiency (Re = 1000). (From Ref. 31.)

where L and H are the length and height of the enclosure, U_{in} is the mean velocity through the inlet, and h is the inlet width (the dimension transversal to the flow). The enclosure becomes clean ($\eta_d \to 1$) as $t \to \infty$.

The numerical results sampled in Fig. 11.9 were obtained for Sc = 1, $Sc_t = 0.7$, $L/H = 2$, and $h/H = 0.1$ by solving eq. (11.99) in combination with the turbulence model of Jones and Launder [32]. The details of the model, numerical formulation, and execution can be found in Ref. 31. The evolution of the flow and concentration patterns is illustrated in Fig. 11.10, where Ψ is defined by writing $U = \partial\Psi/\partial Y$, $V = -\partial\Psi/\partial X$, $(X, Y) = (x, y)/h$, and $(U, V) = (u, v)/U_{in}$. The local instantaneous dimensionless concentration is $\tilde{C} = (C_0 - C)/(C_0 - C_{in})$.

The important feature revealed by the numerical results is that the ventilation efficiency depends very strongly on the position and orientation of the inlet and
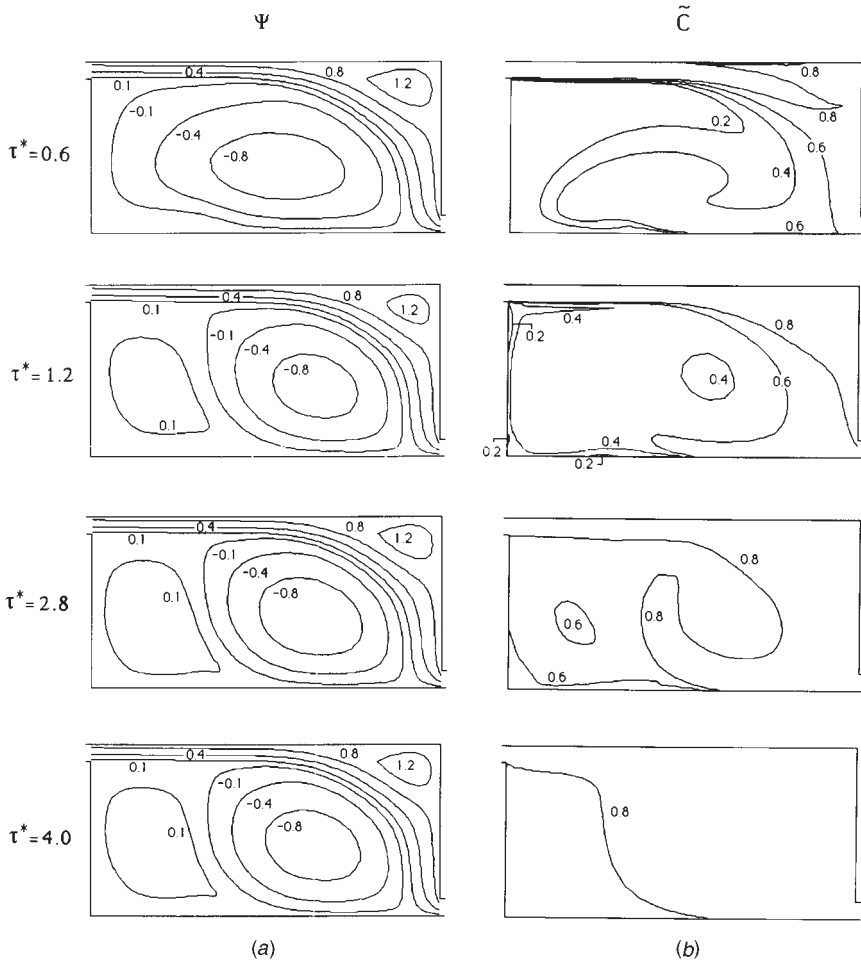
Figure 11.10   Evolution of the flow and concentration patterns when the inlet and outlet ports are located in diametrically opposite corners (Re = 5000). (From Ref. 31.)

outlet and on the Reynolds number based on inlet quantities,

$$
\mathrm{Re} = \frac{U_{\mathrm{in}} h}{\nu}
\tag{11.123}
$$

Many charts like Fig. 11.9 can be produced numerically; however, the challenge is to explain the emerging trends and to try to anticipate them. Let us not forget that the objective is to predict and, later, minimize by design the characteristic time associated with the removal of the original contaminant. This can be done only if the trends are understood and if the results can be predicted without having to simulate numerically every single possible design configuration.

For environmental design calculations, it is useful to condense the numerical ventilation efficiency curves into simple analytical expressions of the type η_d (τ^*, Re, flow configuration). The analytical form of these expressions can be anticipated theoretically. Three possible models are sketched in Fig. 11.11.

In the first model (Fig. 11.11a), it is assumed that the new fluid ($\tilde{C} = 0$) displaces the contaminated fluid in pistonlike fashion. This is equivalent to assuming that (1) the new and old fluids do not mix and (2) the new fluid arrives at the outlet only after all the old fluid has vacated the enclosure. Under these circumstances, the ventilation efficiency is given by

$$\eta_d = \begin{cases} \tau^*, & 0 \le \tau^* \le 1 \\ 1, & \tau^* > 1 \end{cases} \qquad (11.124)$$

In the second model (Fig. 11.11b), the instantaneous fluid inventory of the enclosure is assumed perfectly mixed, so that the concentration at the outlet is
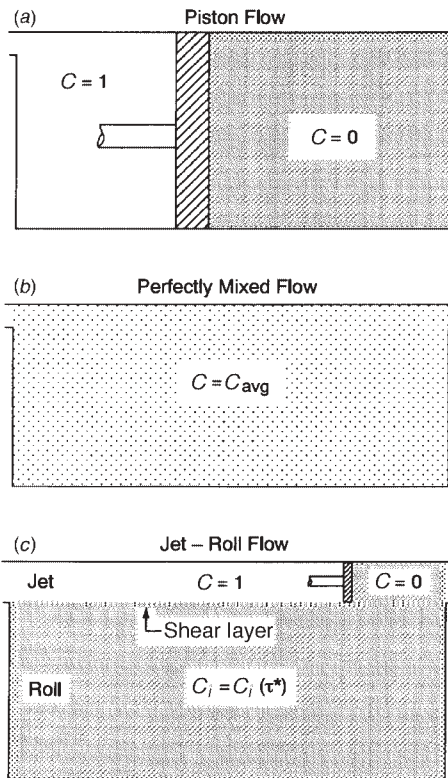
Figure 11.11   Three models for predicting the ventilation efficiency function. (From Ref. 31.)

equal to the concentration at a point inside the enclosure. The analysis is the same as in the classical problem of batch mixing (Ref. 14, p. 499). The result is that the concentration of the mixed fluid rises exponentially to the concentration of the inlet stream

$$\eta_d = 1 - \exp(-\tau^*) \tag{11.125}$$

One would think that these two simple models—no mixing and perfect mixing—would recommend formulas that act as upper and lower bounds for the actual η_d value revealed by numerical simulations. Figure 11.12 shows that, surprisingly, both models overpredict the displacement efficiency for all times $\tau^* > h/H$. The overprediction is dramatic at high Reynolds numbers, while the simple models do relatively well in the low-Re range of 5–30. The piston-flow model is successful only in the very beginning of the through-flow process, when the new fluid travels directly from the inlet to the outlet.

A third model is outlined in Fig. 11.11c. The enclosure volume is viewed as a sandwich of two regions. The upper region—the ''jet''—connects the inlet to the outlet and has a width on the order of h. Only in this region does the new fluid displace the contaminated fluid in pistonlike fashion. The jet region becomes filled completely with new fluid at a time t on the order of L/U_{in}, which corresponds to the dimensionless time $\tau^* \sim h/H$. At times τ^* shorter than h/H, this new model is equivalent to the piston-flow model discussed first; therefore, the displacement efficiency is

$$\eta_d = \tau^*, \qquad \tau^* \le h/H \tag{11.126}$$
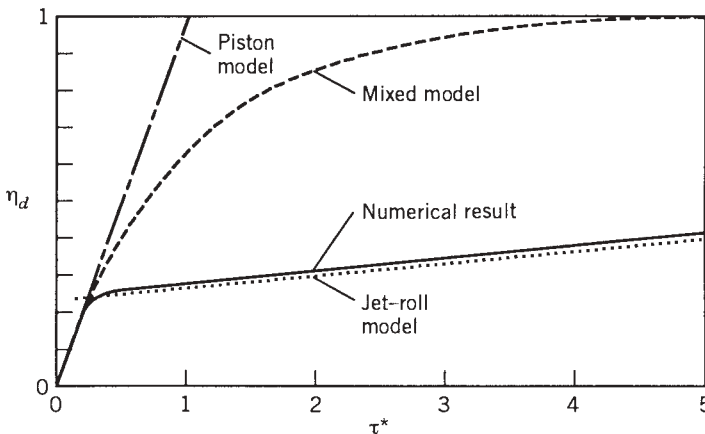
Figure 11.12 Ventilation efficiency: comparison between numerical results and predictions based on the models of Fig. 11.11 (Re = 5000; inlet and outlet oriented as in Fig. 11.9a). (From Ref. 31.)

At times $\tau^* > h/H$, the jet region is inhabited by new fluid ($\widetilde{C} = 1$). It is assumed that the remaining (lower) volume of the enclosure—the "roll" (Fig. 11.10, left)—contains fluid that is well mixed by the recirculating flow. The instantaneous dimensionless concentration in this lower region is time-dependent $\widetilde{C}_i(\tau^*)$. This concentration increases in time because of the mass transfer that takes place across the turbulent shear layer that separates the jet region from the roll region (Fig. 11.11c). The existence of this turbulent shear layer was already noted while examining Fig. 11.10b, which shows a thin concentration boundary layer between the jet and the roll.

It is assumed finally that the mass transfer rate across the jet-roll concentration boundary layer is proportional to the instantaneous jet-roll concentration difference $(1 - \widetilde{C}_i)$. Taking into account the geometry of the enclosure, we write that the conservation of contaminant in the roll region of height $(H-h)$ and length L requires that

$$L(H - h)\frac{d\widetilde{C}_1}{dt} = b_1 L(1 - \widetilde{C}_i) \tag{11.127}$$

in which the factor b_1 accounts for the effective mass eddy diffusivity in the boundary layer region. This factor will be determined empirically.

In the search for the η_d expression in the limit $\tau^* \to \infty$, we integrate eq. (11.127) from the beginning ($\widetilde{C}_i = 0$ at $\tau^* = 0$),

$$\widetilde{C}_i = 1 - \exp\left[-\frac{LH}{h(H - h)}\widetilde{b}_1 \tau^*\right] \tag{11.128}$$

by writing $\widetilde{b}_1$ for the dimensionless empirical factor that corresponds to b. Next, we note that the ventilation efficiency η_d is equal to the concentration averaged over the entire volume (jet + roll),

$$\eta_d = \frac{h}{H} + \frac{H - h}{H}\widetilde{C}_i \tag{11.129}$$

and arrive in this way at the expression

$$\eta_d = 1 - \left(1 - \frac{h}{H}\right)\exp\left[-\frac{LH}{h(H - h)}\widetilde{b}_1 \tau^*\right] \tag{11.130}$$

Finally, we note that in the volume-averaging operation executed in eq. (11.129), the geometric factors h/H and $(H-h)/H$ are correct in an order-of-magnitude sense. This means that a more accurate alternative to eq. (11.130) is

$$\eta_d = 1 - \left(1 - \frac{h}{H}\right)\widetilde{b}_2 \exp\left(-\frac{L/h}{1 - h/H}\widetilde{b}_1 \tau^*\right) \tag{11.131}$$
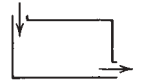
where $\widetilde{b}_2$ is a second empirical factor whose expected order of magnitude is 1.

The contribution of the jet-roll model is that it predicts the exponential form (11.131), in which $\tilde{b}_1$ and $\tilde{b}_2$ are independent of time. The constancy of $\tilde{b}_1$ in time stems from the observation that the flow pattern (in particular, the turbulent shear layer) is in steady state during most of the long-time interval ($\tau^* \geq h/H$) in which eq. (11.131) applies. This prediction is equivalent to saying that the numerical η_d results must appear as a straight line when plotted as log $(1-\eta_d)$ versus τ^*. It has been shown that this is indeed the case [31]. Such figures were drawn for each flow configuration to determine the $\tilde{b}_1$ and $\tilde{b}_2$ factors that lead to the best agreement between eq. (11.131) and the numerical η_d data. The $\tilde{b}_1$ and $\tilde{b}_2$ values were themselves curve fitted as functions of Reynolds number in the range 5–5000, as shown in Table 11.6. Equation (11.131) reproduces the calculation η_d values with an accuracy better than 4.3 percent. This correlation also includes the effect of the geometry (*L/H, h/H*), which was fixed during the numerical simulations.

In conclusion, significant gains in ventilation efficiency can be achieved by properly positioning and orienting the inlet and outlet ports. Figure 11.9 (bottom) showed that the highest efficiency belongs to geometric arrangements where the path of the jet that transverses the enclosure is the longest. Important is the demonstration that it is possible to invent a simple theory to correlate numerical results into formulas that have wider applicability. It is not sufficient to produce volumes of empirical results (numerical or experimental) aimlessly and to blindly accept these results as "facts." Theory and empiricism must be given equal rights.

Another key problem in the design of healthy buildings is the removal of contaminated air from an enclosure in which the contaminant is produced by a discrete source. This problem was investigated similarly in Ref. 33, where it was shown that superior ventilation is achieved when the inlet and outlet ports are arranged in relation to the position of the source of contaminant. The

Table 11.6 Empirical factors $\tilde{b}_1$ and $\tilde{b}_2$ needed for the ventilation efficiency correlation (11.131)

	$\tilde{b}_1$	$\tilde{b}_2$
	$\tilde{b}_1 = 0.08\mathrm{Re}^{-0.43}$	$\tilde{b}_2 = 0.8$
	$\tilde{b}_1 = 0.11\mathrm{Re}^{-0.36}$	$\tilde{b}_2 = 4.38\mathrm{Re}^{-0.30}$
	$\tilde{b}_1 = 0.20\mathrm{Re}^{-0.28}$	$\tilde{b}_2 = 9.12\mathrm{Re}^{-0.40}$
	$\tilde{b}_1 = 0.16\mathrm{Re}^{-0.30}$	$\tilde{b}_2 = 7.06\mathrm{Re}^{-0.38}$

Source: Ref. 31.

time-dependent migration of contaminant from one region of a room to the remainder (initially clean region) of the same room is documented in Ref. 34.

11.11   MASSFUNCTION AND MASSLINES

The transport of mass by convection can be visualized by using the concepts of *massfunction* and *masslines* [35]. These are the mass transfer analogs of the heatfunction and heatlines discussed beginning in Section 1.6. With reference to the concentration equation (11.27a) for steady two-dimensional convection without chemical reaction,

$$u\frac{\partial C}{\partial x} + v\frac{\partial C}{\partial y} = D\left(\frac{\partial^2 C}{\partial x^2} + \frac{\partial^2 C}{\partial y^2}\right) \tag{11.132}$$

the massfunction $M(x, y)$ is defined by

$$\frac{\partial M}{\partial y} = u(C - C_{\text{ref}}) - D\frac{\partial C}{\partial x} \tag{11.133}$$

$$-\frac{\partial M}{\partial x} = v(C - C_{\text{ref}}) - D\frac{\partial C}{\partial y} \tag{11.134}$$

such that M satisfies eq. (11.132) identically. The pattern of masslines (the $M = $ constant curves) is most instructive when the reference concentration C_{ref} is set equal to the lowest concentration that occurs in the space of interest. Masslines are exhibited in Ref. 35 for mass transfer by natural convection in an enclosure with sidewalls at different temperatures and concentrations. Massline visualizations are reviewed in Section 1.6.

11.12   EFFECT OF CHEMICAL REACTION

In the laminar and turbulent mass transfer examples discussed so far, the mixture was not reacting chemically. Of interest in chemical engineering is the case when a chemical reaction is present and the constituent generation term $\dot{m}'''$ in eq. (11.25) is finite. In some reactions, the species of interest is a product of reaction ($\dot{m}''' > 0$); in others, the species is being consumed ($\dot{m}''' < 0$). In the case of homogeneous reactions, the volumetric mass rate of production of a species can be expressed as [8]

$$\dot{m}''' = k_n''' C^n \tag{11.135}$$

where n is the order of the reaction and k_n''' is the rate constant. In the case of a first-order reaction $n = 1$, and units of k_1''' are s^{-1}. In homogeneous reactions the production or consumption of the species takes place in the fluid, that is,

wherever the species exists. In heterogeneous reactions, the reaction takes place on the surface of a catalyst; the rate of species production in this case is

$$\dot{m}''' = k_n'' C_0^n \tag{11.136}$$

where C_0 is the concentration at the surface, n is the order of the reaction, and k_n'' is the reaction rate.

Because a reaction can either generate or consume a species, it influences the distribution of that species in the flow of the mixture. One way to illustrate the effect of chemical reaction on mass convection is to focus on a very basic problem for which we already know the solution for the case when the chemical reaction is absent. We will then solve the problem, allowing for the presence of a chemical reaction, and comparing the two solutions, we will develop a feeling for the effect of chemical reaction.

Consider the laminar boundary layer flow sketched in Fig. 11.4: Mass is being swept away from a wall surface of concentration C_0 by a uniform stream containing none of the species released by the wall, $C_\infty = 0$. The concentration field for this flow configuration is known [see the Pohlhausen solution leading to eq. (11.39)]. With homogeneous reaction present, the problem assumes a slightly different statement,

$$u\frac{\partial C}{\partial x} + v\frac{\partial C}{\partial y} = D\frac{\partial^2 C}{\partial y^2} - k_n''' C^n \tag{11.137}$$

$$C(x, 0) = C_0, \qquad C(x, \infty) = 0 \tag{11.138}$$

where the flow (u, v) is known from Chapter 2. Note the minus sign of the last term in eq. (11.137), which implies that in this example the chemical reaction consumes the species of interest. This homogeneous reaction problem was solved by Chambré and Young [36], and its counterpart with catalytic surface reaction by Chambré and Acrivos [37]. Below, we outline and extend the integral solution reported by Bird et al. [8]. The integral version of the concentration equation (11.137) is

$$\frac{d}{dx}\int_0^\infty uC\, dy = -D\left(\frac{\partial C}{\partial y}\right)_{y=0} - k_n'''\int_0^\infty C^n\, dy \tag{11.139}$$

Assuming the simplest shape for the velocity and concentration profiles

$$U = U_\infty \frac{y}{\delta(x)}, \qquad\qquad 0 \le y \le \delta \tag{11.140}$$

$$C = C_0\left[1 - \frac{y}{\delta_c(x)}\right], \qquad 0 \le y \le \delta_c \tag{11.141}$$

eq. (11.139) reduces to

$$\frac{1}{\text{Sc}} = \frac{4}{3}x\frac{d(\Delta^3)}{dx} + \Delta^3 + \frac{12k_n'''C_0^{n-1}}{(n+1)U_\infty}x\Delta^2 \tag{11.142}$$

where

$$\Delta = \frac{\delta_c}{\delta} \le 1 \tag{11.143}$$

Note that δ_c is the unknown thickness of the concentration profile, while the velocity boundary layer thickness δ is listed in Table 2.1,

$$\delta = 3.46x\,\text{Re}_x^{-1/2} \tag{11.144}$$

In the absence of chemical reaction ($k_n''' = 0$), the solution of eq. (11.142) is $\Delta = \text{Sc}^{-1/3}$, as is known already from eq. (2.61). With chemical reaction, the thickness ratio Δ emerges as a function of two parameters,

$$\Delta = \Delta(\text{Sc}, X) \tag{11.145}$$

where X is a dimensionless longitudinal variable

$$X = \frac{12k_n'''C_0^{n-1}}{(n+1)U_\infty}x \tag{11.146}$$

such that $X = 0$ represents the case of no chemical reaction. The local Sherwood number or the local wall mass flux can be expressed as

$$\text{Sh} = \frac{j_0}{C_0}\frac{x}{D} = \frac{x}{\delta_c} = \frac{0.289}{\Delta}\text{Re}_x^{1/2} \tag{11.147}$$

In the absence of chemical reaction, the local Sherwood number reduces to

$$\text{Sh} = 0.289\text{Sc}^{1/3}\,\text{Re}_x^{1/2} \qquad (\text{Sc} > 1) \tag{11.148}$$

which is only 13 percent below the similarity solution (11.43). Now the effect of chemical reaction on mass transfer can be presented as the ratio

$$\phi_r = \frac{\text{Sh(with chemical reaction)}}{\text{Sh(without chemical reaction)}} \tag{11.149}$$

which, dividing eq. (11.147) by eq. (11.148), means that

$$\phi_r = \frac{1}{\text{Sc}^{1/3}\,\Delta} \quad \text{or} \quad \phi_r = \frac{\Delta(\text{Sc}, 0)}{\Delta(\text{Sc}, X)} \tag{11.150}$$

Function ϕ_r has been plotted in Fig. 11.13 after integrating eq. (11.142) numerically from the initial condition $\Delta = Sc^{-1/3}$ at $X = 0$. It is evident that, depending on the values of Sc and X, the effect of chemical reaction on the mass transfer rate can be significant. For a given fluid (Sc = constant), the mass transfer rate with chemical reaction is greater than the mass transfer rate in the absence of chemical reaction, and the discrepancy between the two rates increases in the downstream direction. This effect is due to the decrease in δ_c caused by the chemical reaction (i.e., by the consumption of the species of concentration C). The reverse effect would be observed if the homogeneous reaction were generating the species in the boundary layer.

In conclusion, the local Sherwood number in Sc > 1 laminar boundary layer flow with homogeneous reaction that consumes the species can be calculated as

$$Sh = 0.289\phi_r \ Sc^{1/3} \ Re_x^{1/2} \tag{11.151}$$

where ϕ_r is given by Fig. 11.13. Sufficiently far downstream ($X > 10$), the correction factor ϕ_r approaches $Sc^{1/6}X^{1/2}$, the local Sherwood number becomes [8]

$$Sh = 0.289 \ Sc^{1/2} \left[\frac{12k_n''' C_0^{n-1} x^2}{(n+1) \nu} \right]^{1/2} \tag{11.152}$$

and the mass transfer rate j_0 (or δ_c) becomes independent of longitudinal position.
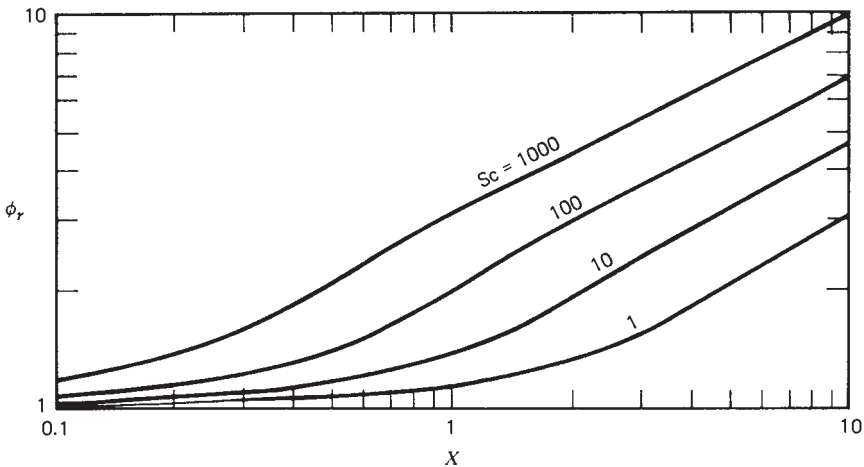
Figure 11.13   Effect of species-depleting chemical reaction on forced convection mass transfer to laminar boundary layer flow on a plane surface.

REFERENCES

1. A. Rivera-Alvarez and A. Bejan, Constructal geometry and operation of adsorption processes, *Int. J. Therm. Sci.*, Vol. 42, 2003, pp. 983–994.

2. J. V. C. Vargas, J. Ordonez, and A. Bejan, Constructal flow structure for a PEM fuel cell, *Int. J. Heat Mass Transfer*, Vol. 47, 2004, pp. 4177–4193.

3. A. Bejan, *Advanced Engineering Thermodynamics*, 3rd ed., Wiley, Hoboken, 2006.

4. A. Fick, *On liquid diffusion*, *Philos. Mag.*, Vol. 4, No. 10, 1855, pp. 30–39; reprinted in *J. Membrane Science*, Vol. 100, 1995, pp. 33–38.

5. H. R. Perry and C. H. Chilton, *Chemical Engineers' Handbook*, 5th ed., McGraw-Hill, New York, 1973.

6. R. C. Reid, J. M. Prausnitz, and T. K. Sherwood, *The Properties of Gases and Liquids*, 3rd ed., McGraw-Hill, New York, 1977.

7. T. R. Marrero and E. A. Mason, Gaseous diffusion coefficients, *J. Phys. Chem. Ref. Data*, Vol. 1, 1972, pp. 3–118.

8. R. B. Bird, W. E. Stewart, and E. N. Lightfoot, *Transport Phenomena*, Wiley, New York, 1960.

9. E. N. Fuller, P. D. Schettler, and J. C. Giddins, A new method for prediction of binary gas-phase diffusion coefficients, *Ind. Eng. Chem.*, Vol. 58, No. 5, 1966, pp. 19–27.

10. J. O. Hirschfelder, C. F. Curtiss, and R. B. Bird, *Molecular Theory of Gases and Liquids*, Wiley, New York, 1954.

11. R. Krishna and G. L. Standart, Mass and energy transfer in multicomponent systems, *Chem. Eng. Commun.*, Vol. 3, 1979, pp. 201–275.

12. E. Obermeier and A. Schaber, A simple formula for multicomponent gaseous diffusion coefficients derived from mean free path theory, *Int. J. Heat Mass Transfer*, Vol. 20, 1977, pp. 1301–1306.

13. C. R. Wilke and P. Chang, Correlation of diffusion coefficients in dilute solutions, *AIChE J.*, Vol. 1, 1955, pp. 264–270.

14. A. Bejan, *Heat Transfer*, Wiley, New York, 1993.

15. J. H. Perry, ed., *Chemical Engineers' Handbook*, McGraw-Hill, New York, 1950.

16. A. E. Markham and K. A. Kobe, The solubility of gases in liquids, *Chem. Rev.*, Vol. 28, 1941, pp. 519–588.

17. R. Battino and H. L. Clever, The solubility of gases in liquids, *Chem. Rev.*, Vol. 66, 1966, pp. 395–463.

18. D. K. Edwards, V. E. Denny, and A. F. Mills, Transfer Processes, 2nd ed., *Hemisphere*, Washington, DC, 1979, Chapter 3.

19. M. E. Weber, private communication, *McGill University, Montreal*, July 23, 1998.

20. B. Gebhart and L. Pera, The nature of vertical natural convection flows resulting from the combined buoyancy effects of thermal and mass diffusion, *Int. J. Heat Mass Transfer*, Vol. 14, 1971, pp. 2025–2050.

21. A. Bejan, I. Dincer, S. Lorente, A. F. Miguel, and A. H. Reis, *Porous and Complex Structures in Modern Technologies*, Springer-Verlag, New York, 2004.

22. M. Mehrgoo and M. Amidpour, Derivation of optimal geometry of a multi-effect humidification-dehumidification desalination unit: A constructal design, *Desalination*, Vol. 281, 2011 pp. 234–242.

23. K. R. Khair and A. Bejan, Mass transfer to natural convection boundary layer flow driven by heat transfer, *J. Heat Transfer*, Vol. 107, 1985, pp. 979–981.

24. A. Bejan, Mass and heat transfer by natural convection in a vertical cavity, *Int. J. Heat Fluid Flow*, Vol. 6, 1985, pp. 149–160.

25. A. Bejan, The basic scales of natural convection heat and mass transfer in fluids and fluid-saturated porous media, *Int. Commun. Heat Mass Transfer*, Vol. 14, 1987, pp. 107–123.

26. A. Bejan and S. Lorente, *Design with Constructal Theory*, Wiley, Hoboken, 2008.

27. A. Bejan and P. J. Zane, *Design in Nature*, Doubleday, New York, 2012.

28. E. V. Somers, Theoretical considerations of combined thermal and mass transfer from a vertical flat plate, *J. Appl. Mech.*, Vol. 23, 1956, pp. 295–301.

29. J.-H. Jang, W.-M. Yan, and H.-C. Liu, Natural convection heat and mass transfer along a vertical wavy surface, *Int. J. Heat Mass Transfer*, Vol. 46, 2003, pp. 1075–1083.

30. A. Bejan and K. R. Khair, Heat and mass transfer by natural convection in a porous medium, *Int. J. Heat Mass Transfer*, Vol. 28, 1985, pp. 909–918.

31. J. L. Lage, A. Bejan, and R. Anderson, Efficiency of transient contaminant removal from a slot ventilated enclosure, *Int. J. Heat Mass Transfer*, Vol. 34, 1991, pp. 2603–2615.

32. W. P. Jones and B. E. Launder, The prediction of laminarization with a two-equation model of turbulence, *Int. J. Heat Mass Transfer*, Vol. 15, 1972, pp. 301–314.

33. J. L. Lage, A. Bejan, and R. Anderson, Removal of contaminant generated by a discrete source in a slot ventilated enclosure, *Int. J. Heat Mass Transfer*, Vol. 35, 1992, pp. 1169–1180.

34. P. A. Litsek and A. Bejan, Transient natural convection between two zones in an insulated enclosure, *J. Heat Transfer*, Vol. 110, 1988, pp116. –125.

35. O. V. Trevisan and A. Bejan, Combined heat and mass transfer by natural convection in a vertical enclosure, *J. Heat Transfer*, Vol. 109, 1987, pp. 104–112.

36. P. L. Chambré and J. D. Young, On the diffusion of a chemically reacting species in a laminar boundary layer flow, *Phys. Fluids*, Vol. 1, 1958, pp. 48–54.

37. P. L. Chambré and A. Acrivos, On chemical surface reactions in laminar boundary layer flows, *J. Appl. Phys.*, Vol. 2, 1956, pp. 1322–1328.

PROBLEMS

11.1. Show that concentration (C_i), mass fraction (Φ_i), and mole fraction (x_i) are proportional to one another and that these proportionalities are given by eqs. (11.8) and (11.9).

11.2. Consider the configuration of Fig. 11.4, in which air passes in laminar boundary layer flow past a porous wall saturated with water. The wall contains 25 percent water on a volume basis. The airstream is at atmospheric pressure and temperature ($T_\infty = 310K$). Calculate the stream-side water concentration C_0, and compare the result with the water concentration immediately below the wall—stream interface.

11.3. A shallow pool is filled with water at 25°C. The pool surface is 3 m × 3 m square. The wind blows at 30 km/h parallel to the water surface and parallel to one side of the square. The atmospheric air has a temperature of 25°C and a relative humidity of 30 percent. Assume that relative to this air flow, the pool water surface behaves as a plane stationary wall.

    (a) Calculate the instantaneous flow rate of the water that is being removed by the wind.

    (b) How long does the wind have to blow for the pool level to drop by 2 mm?

11.4. Consider the straight duct with fully developed mixture flow sketched in Fig. P11.4. The mixture average velocity is U, the duct cross-sectional area is A_c, and the duct length is L. The cross-sectional perimeter is $p = A/L$, where A is the total surface of the duct wall. The bulk density of the species of interest is denoted by ρ (kg/m³) (the symbol C was used in the text). The ρ value at the duct inlet is known, ρ_{in}. Specified also is the ρ value on the duct wall, $\rho_w =$ constant. Show that the rate of mass transfer from the entire duct to the mixture stream is

$$\dot{m} = UA_c(\rho_w - \rho_{\text{in}})\left[1 - \exp\left(-\frac{h_m}{U}\frac{A}{A_c}\right)\right]$$
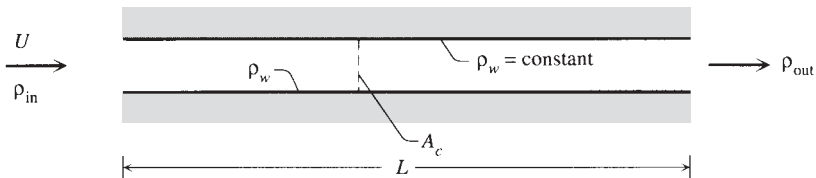
Figure P11.4

11.5. The double-pane window system shown in Fig. P11.5 is plagued by the deposition of liquid water (fogging) on the inner surfaces of the glass panes. On each surface, the liquid is approximated by a film with the constant thickness $\delta = 10^{-5}$ m. It is proposed to defog the window by blowing dry air through the parallel-plate channel. The mean velocity of the channel airstream is 0.1 m/s. The temperature in the entire system is uniform and equal to 25°C. The pressure is atmospheric. Neglecting natural convection effects, determine (a) the flow regime over most of the length L, **(b)** the mass transfer coefficient between the liquid films and the channel flow, **(c)** the rate at which the airstream removes water from

the wetted surfaces (using the formula listed in the preceding problem statement), and **(d)** the time needed to defog the double-pane window system completely.
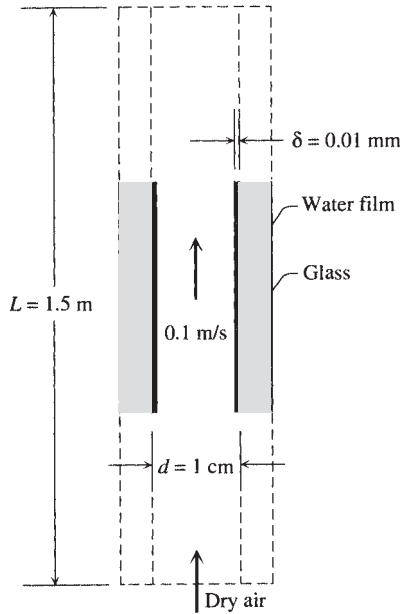
Figure P11.5

11.6. Determine the mass flux of a gas i that diffuses into a liquid film that falls along a vertical solid wall. Assume that the liquid film flow is laminar and that it has reached terminal velocity. Let $v_{max} = $ constant and $\delta = $ constant be the film velocity at the liquid—gas interface and the film thickness, respectively. Take a two-dimensional Cartesian system of coordinates with the y axis pointing downward and $x = 0$ on the liquid—gas interface. The concentration of i at the interface (on the liquid side) is $C_0 = $ constant, and the solid surface is impermeable to i, $\partial C/\partial x = 0$ at $x = \delta$. State the complete mathematical problem that would allow you to determine the mass flux $j_0 = - D(\partial C/\partial x)_{x=0}$ as a function of altitude. Solve this problem in the limit of ''small contact length y,'' that is, in the limit where the concentration boundary layer thickness (or penetration distance) δ_c is much smaller than the film thickness δ.

11.7. Use scale analysis or the order-of-magnitude conclusions of Problem 11.6 to estimate the rate of gas absorption from a gas bubble into the

liquid pool through which the gas bubble rises. The gas concentration on the liquid side of the gas—liquid interface is C_0 and the mass diffusivity is D. The bubble has a diameter D_b and rises through the liquid pool with the terminal velocity v_{max}. State clearly all the assumptions on which your scale analysis is based.

11.8. A film of liquid solvent flows downward along a vertical wall and in the process dissolves the layer of paint with which the wall is coated. The liquid film falls at terminal velocity in fully developed laminar flow; hence, its velocity distribution and thickness δ are independent of vertical position. Attach a two-dimensional Cartesian system to the wall such that the y axis points downward and the plane $x = 0$ coincides with the wall surface. The liquid film extends from $x = 0$ to $x = \delta$. The concentration of paint in the film is $C_0 = $ constant at $x = 0$. Determine the local mass flux $-D(\partial C/\partial x)_{x=0}$, assuming that the concentration layer is much thinner than the layer of liquid solvent. Is the coat of paint being eroded evenly?

11.9. Water wets as a thin film a vertical wall 1 m high and 1 m wide. The temperature of the wall and the surrounding air is $25°C$. The surrounding air is still and has a relative humidity of 40 percent. Calculate the mass transfer Rayleigh number based on height and the water mass transfer rate removed by the natural convection of humid air. Is the humid air rising or descending along the wall?

11.10. Consider the laminar natural convection boundary layer driven by mass transfer along a vertical wall of height H. The wall and the surrounding fluid mixture (density ρ) are at the same temperature, while the species mass concentration difference between the vertical surface and the mixture reservoir is $(\rho_{i, w} - \rho_{i, \infty})$.

(a) Invoke the analogy between natural convection mass transfer and natural convection heat transfer, and obtain an order-of-magnitude expression for the horizontal (or ''entrainment'') velocity component of the mixture.

(b) Rely on the same analogy to estimate the order of magnitude of the mass flux of species i through the wall.

(c) Compare the horizontal mass fluxes estimated in parts (a) and (b), and show that the vertical surface may be modeled as an impermeable surface when $|\rho_{i, w} - \rho_{i, \infty}| \ll \rho$. In other words, show that the analogy with the heat transfer phenomena of Chapter 4 holds when the species of interest is present in small quantities in the mixture.

11.11. Determine the overall Sherwood number scales for the last three configurations sketched in Fig. 11.8. In each case, determine the condition necessary for heat-transfer-driven natural convection mass transfer. [Note that for $Pr > 1$ and $Le > 1$, this condition is expressed by eq. (11.97).]

11.12. A vertical wall of height H heats a liquid pool in such a way that the local heat flux through the wall surface q'' is independent of position along the wall. This arrangement generates a natural convection boundary layer flow along the wall. The liquid has the property to dissolve the wall material; the concentration of wall material is C_0 at the wall surface and $C_\infty = 0$ sufficiently far from the surface. Assuming the mass diffusivity of wall material known, D, determine the order of magnitude of the mass transfer rate from the wall to the boundary layer flow. Assume that the boundary layer is driven by heat transfer.

11.13. Consider the concentration and temperature boundary layers sketched in Fig. 11.7. If the flow is driven by mass transfer (i.e., not by heat transfer), what is the wall-reservoir heat transfer rate?

11.14. Consider the mass transfer with chemical reaction in laminar boundary layer flow in the limit $Sc \to 0$. Construct an integral analysis based on eq. (11.137) and the assumption that the concentration layer is much thicker than the velocity boundary layer; hence, $u = U_\infty$ and $v = 0$. Determine the local Sherwood number, and explain how this parameter is influenced by the presence of chemical reaction.

11.15. Illustrate the effect of a first-order chemical reaction on the mass transfer rate in forced convection to a uniform flow ($U_\infty = $ constant, $C_\infty = 0$) adjacent to a surface of concentration C_0. Show that the concentration equation in this case reduces to

$$U_\infty \frac{\partial C}{\partial x} = D\frac{\partial^2 C}{\partial y^2} \pm k_1''' C$$

12

CONVECTION IN POROUS MEDIA

Convection in porous media was used for the first time as a heat transfer classroom topic in the first edition of this book. In this chapter we outline the basic principles of fluid mechanics and heat transfer through a fluid-saturated porous structure, in the same manner in which we developed the foundations of convective heat transfer in Chapter 1.

The fluid mechanics of flow through a porous medium is a relatively old topic because of the management of the underground water table and irrigation systems. The conceptual centerpiece in this branch of fluid mechanics—the Darcy flow model—originated in the nineteenth century in connection with the engineering of public fountains [1]. The convective heat transfer potential of flows through porous media is a relatively new topic, as the technologies of porous insulation, gas-cooled electric machinery, and nuclear reactors grew out of the contemporary concern with the cost of energy and the miniaturization of cooling schemes. This body of work was reviewed in Refs. 2 and 3.

12.1 MASS CONSERVATION

The heat and fluid flow through a porous medium is complicated: Figure 12.1 shows a porous structure with flow through the pores. The flow geometry differs unpredictably from one region of the material to another. It is tempting to disregard the local complication and unpredictability of the phenomenon and instead to concentrate on the overall capability of this system to transport fluid and energy. This decision is analogous to the idea of time averaging a turbulent flow field (Chapter 7) in order to smooth away the flow complications called *eddies*. These decisions do not simplify the respective flows—as smooth (laminarlike) porous media and turbulent flows do not exist—instead, they simplify the description of such phenomena.
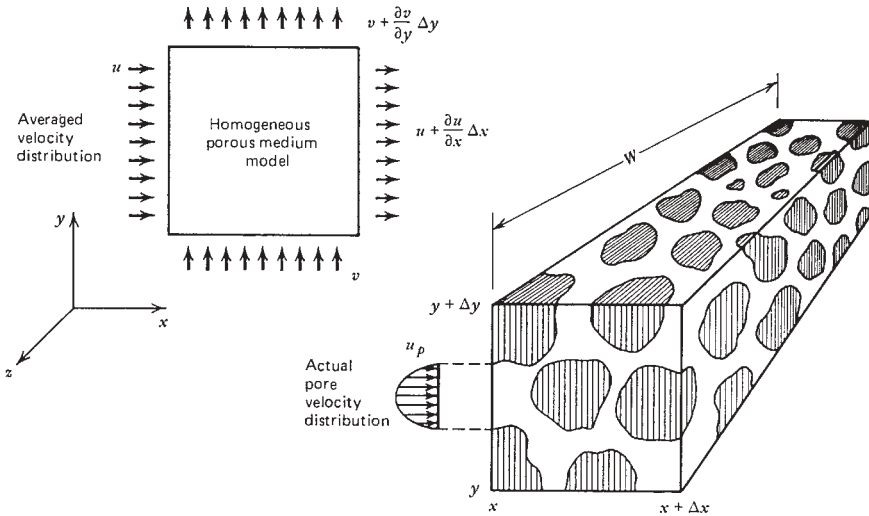
Figure 12.1   Averaging of the pore velocity distribution as a basis for the homogeneous porous medium model.

For these reasons, the analysis of convection through porous media is largely an empirical exercise. The method consists of applying the conservation principles of Chapter 1 to a ''gray'' medium visualized by holding the porous structure sufficiently far away so that the grain become indistinguishable [3]. A two-dimensional version of such a medium is sketched in Fig. 12.1, which shows that a small enough control volume $\Delta x \, \Delta y$ retains the irregular features of the grainy structure. Although the flow and heat transfer through the gray medium may be regarded as two-dimensional, the picture in the small control volume $\Delta x \, \Delta y$ differs from one $z =$ constant plane to another. Locally, in regions of size comparable with the channel size and solid grain size, the flow is always three-dimensional. This is another similarity between porous medium flow and turbulent flow.

From the two-dimensional flow we isolate a volume element ($\Delta x \, \Delta y \, W$) with W so much larger than either Δx or Δy so that for the purpose of mass-flow accounting the important flow rates are in the x and y directions only (the flow cross sections in the x and y directions are $W \, \Delta y$ and $W \, \Delta x$, and both are much larger than the flow cross section in the z direction, $\Delta x \, \Delta y$). Consider the mass flow rate entering the $\Delta x \, \Delta y \, W$ chunk of porous material from the left through the $x =$ constant plane,

$$\dot{m}_x = \rho \int_y^{y+\Delta y} \int_0^W u_p \, dz \, dy \tag{12.1}$$

where $u_p(y, z)$ is the uneven x-velocity distribution over the void patches of the $x =$ constant plane. Imagining a control surface $W \, \Delta y$ sufficiently larger than the

pore and solid grain cross sections, we define the area-averaged velocity in the x direction,

$$u = \frac{1}{W \, \Delta y} \int_y^{y+\Delta y} \int_0^W u_p \, (y, z) \, dz \, dy \qquad (12.2)$$

In other words,

$$\dot{m}_x = \rho u \, (W \, \Delta y) \qquad (12.3)$$

The area-averaged velocity in the y direction is defined in the same way,

$$v = \frac{1}{W \, \Delta x} \int_x^{x+\Delta x} \int_0^W v_p(x, z) \, dz \, dx \qquad (12.4)$$

so that the mass flow rate in the y direction can be expressed as in Chapter 1,

$$\dot{m}_y = \rho v (W \, \Delta x) \qquad (12.5)$$

In deriving eqs. (12.3) and (12.5), we treated the density ρ as constant in the $\Delta x \, \Delta y$ element of the two-dimensional flow. This does not mean that ρ is constant throughout the $x{-}y$ field.

The reward for smoothing out the complications of the channel flow and introducing the area-averaged velocities u and v is that, with expressions such as (12.3) and (12.5), the averaged flow looks like any other homogeneous fluid flow. Therefore, applying the mass conservation principle [eq. (1.1)] to the $\Delta x \, \Delta y \, W$ element yields

$$\frac{\partial}{\partial t}(\rho \phi W \, \Delta x \, \Delta y) + \frac{\partial \dot{m}_x}{\partial x} \, \Delta x + \frac{\partial \dot{m}_y}{\partial y} \, \Delta y = 0 \qquad (12.6)$$

where ϕ is the *porosity* or void fraction of the medium, $\phi = $ (void volume)/(total volume) [see also eq. (12.22)]. Note that $\phi W \, \Delta x \, \Delta y$ is the volume occupied by fluid in the $W \, \Delta x \, \Delta y$ element, and $\rho \phi W \, \Delta x \, \Delta y$ is the instantaneous fluid mass inventory of the element. Combining eqs. (12.3), (12.5), and (12.6), we obtain

$$\phi \frac{\partial \rho}{\partial t} + \frac{\partial(\rho u)}{\partial x} + \frac{\partial(\rho v)}{\partial y} = 0 \qquad (12.7)$$

In general, the mass conservation equation for three-dimensional flow is

$$\phi \frac{\partial \rho}{\partial t} + \nabla(\rho \mathbf{v}) = 0 \qquad (12.8)$$

where $\mathbf{v}$ is the volume-averaged velocity vector (u, v, w). Note that eq. (12.8) with $\phi = 1$ (pure fluid) is the same as eq. (1.6): This coincidence is not accidental because the concept of area-averaged velocity was introduced precisely to be able to apply the pure-fluids mathematical apparatus (Chapter 1) to flows through porous media.

12.2   DARCY FLOW MODEL AND THE FORCHHEIMER MODIFICATION

In the fluid mechanics of porous media, the place of momentum equations or force balances is occupied by the experimental observations summarized mathematically as the *Darcy law*. These observations were first reported by Darcy [1], who, based on measurement alone, discovered that the area-averaged fluid velocity through a column of porous material is proportional to the pressure gradient established along the column. Subsequent experiments proved that the area-averaged velocity is, in addition, inversely proportional to the viscosity (μ) of the fluid seeping through the porous material. For the history of these developments, the reader is directed to Lage [4].

With reference to Fig. 12.2a, the Darcy observations amount to writing

$$u = \frac{K}{\mu}\left(-\frac{dP}{dx}\right) \tag{12.9}$$

where K is an empirical constant called *permeability*. From eq. (12.9), which is the definition of permeability (in the same way as the Fourier law of heat
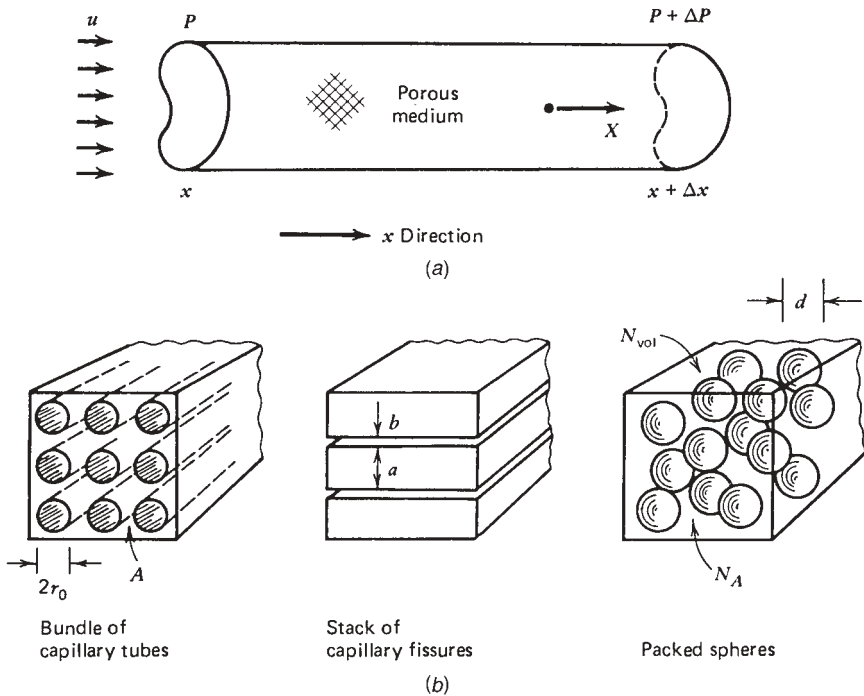
Figure 12.2   Darcy experiment and three possible models for estimating the permeability.

conduction is the definition of thermal conductivity), we learn that the dimensions of K must be

$$[K] = \frac{[\mu][u]}{[-dP/dx]} = (\text{length})^2 \tag{12.10}$$

There is a similarity between eq. (12.9) and the formula for average velocity in Hagen–Poiseuille flow [eq. (3.22)]; this similarity suggests that the Darcy flow is the macroscopic manifestation of a highly viscous flow through the pores of the permeable structure and that $K^{1/2}$ is a length-scale representative of the effective pore diameter. In fact, by assuming a small-scale bundle of channels of known geometry (e.g., Fig. 12.2), and assuming Hagen–Poiseuille flow through each channel, it is possible to derive eq. (12.9), where K emerges as a function of geometry. Analyses of this kind are proposed in Problems 12.2–12.4. Ergun [5] proposed that $K = d^2\phi^3/[150(1 - \phi)^2]$ as a correlation for the measured permeabilities of columns of packed spheres of diameter d and porosity ϕ.

Using $K^{1/2}$ as a length scale to define the Reynolds number

$$\text{Re} = \frac{uK^{1/2}}{\nu} \tag{12.11}$$

and the friction factor

$$f = \frac{\left(-\dfrac{dP}{dx}\right)K^{1/2}}{\rho u^2} \tag{12.12}$$

the Darcy law (12.9) can be rewritten as

$$f = \frac{1}{\text{Re}} \tag{12.13}$$

Experiments [6] have shown that eqs. (12.9) and (12.13) are valid as long as $O(\text{Re}) < 1$. There is a transition in the Re range 1–10, and if the Reynolds number based on $K^{1/2}$ exceeds $O(10)$, inertial effects flatten the $f(\text{Re})$ curve in a manner reminiscent of the friction factor curve in turbulent flow over a rough surface (Fig. 8.2):

$$f = \frac{1}{\text{Re}} + C \tag{12.14}$$

where C is an empirical constant approximately equal to 0.55 and discussed in Ref. 2. The more general friction factor expression (12.14) follows from Forchheimer's [7] modification of the Darcy law,

$$-\frac{dP}{dx} = \frac{\mu}{K}u + b\rho|u|u \tag{12.15}$$

where b is another empirical constant. Ergun's [5] correlation for a column of packed spheres is $b = 1.75(1 - \phi)/\phi^3 d$.

If a body force per unit volume ρg_x is present, the Darcy law (12.9) is

$$u = \frac{K}{\mu}\left(-\frac{\partial P}{\partial x} + \rho g_x\right) \tag{12.16}$$

acknowledging the fact that the flow through the porous column of Fig. 12.2 stops when the externally controlled pressure gradient dP/dx matches the hydrostatic gradient ρg_x. In vectorial notation, the three-dimensional generalization of eq. (12.16) is

$$\mathbf{v} = \frac{K}{\mu}(-\nabla P + \rho \mathbf{g}) \tag{12.17}$$

where $\mathbf{v}$ is the vector (u, v, w) and $\mathbf{g}$ the acceleration vector (g_x, g_y, g_z).

In many problems involving only the seepage flow of water through soil, ρ and μ may be regarded as constant. With the y axis oriented against the gravitational acceleration g, the acceleration vector is $(0, -g, 0)$, and eq. (12.17) becomes

$$\mathbf{v} = -\frac{K}{\mu}\nabla\phi \tag{12.18}$$

where the new function $\phi(x, y, z)$,

$$\phi = P + \rho g y \tag{12.19}$$

should not be confused with the porosity. Under the same conditions ($\rho = $ constant), the mass conservation statement (12.8) reduces to

$$\nabla \cdot \mathbf{v} = 0 \tag{12.20}$$

Combining eqs. (12.18) and (12.20), we find that seepage flows are governed by the Laplace equation

$$\nabla^2\phi = 0 \tag{12.21}$$

which in the absence of free surfaces can be solved in the (x, y, z) space with the classical methods of steady-state conduction heat transfer [8].

12.3 FIRST LAW OF THERMODYNAMICS

A simple way to derive the energy equation for a porous medium is to consider the one-dimensional heat and fluid flow model of Fig. 12.3. The figure shows the elementary building block suggested by models such as the capillary tube bundle and the capillary fissures of Fig. 12.2. The void space contained in the volume element $A \, \Delta x$ is $A_p \, \Delta x$; the volume element is defined such that the ratio
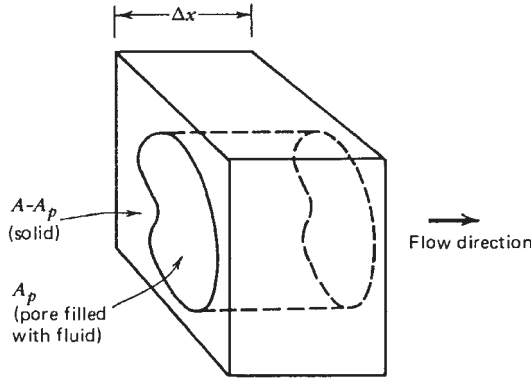
Figure 12.3 Unidirectional flow elements for formulating the first law of thermodynamics for a homogeneous porous medium.

$(A_p \, \Delta x)/(A \, \Delta x)$ matches the porosity ratio of the porous medium from which the elementary volume has been isolated,

$$\phi = \frac{A_p \, \Delta x}{A \, \Delta x} \tag{12.22}$$

To derive the energy equation for a homogeneous porous medium, we start with the energy equations for the solid and fluid parts and average these equations over the elementary volume $A \, \Delta x$. For the solid part, we have

$$\rho_s c_s \frac{\partial T}{\partial t} = k_s \frac{\partial^2 T}{\partial x^2} + q_s''' \tag{12.23}$$

where $(\rho, c, k)_s$ are the properties of the solid matrix and q_s''' is the rate of internal heat generation per unit volume of solid material. If the temperature T does not vary within the solid volume, the integral of eq. (12.23) over the solid is

$$\Delta x (A - A_p) \rho_s c_s \frac{\partial T}{\partial t} = \Delta x (A - A_p) k_s \frac{\partial^2 T}{\partial x^2} + \Delta x (A - A_p) q_s''' \tag{12.24}$$

The energy conservation equation in the space occupied by fluid is [eq. (1.39)]

$$\rho_f c_{Pf} \left(\frac{\partial T}{\partial t} + u_p \frac{\partial T}{\partial x} \right) = k_f \frac{\partial^2 T}{\partial x^2} + \mu \Phi \tag{12.25}$$

where $(\rho, c_P, k)_f$ are fluid properties. The subscript $(\cdot)_f$ is used to distinguish the fluid properties only in the energy equation; thus, ρ_f is the same as the fluid density ρ used in the mass conservation equation (12.8) and in the Darcy law

(12.17). It is assumed that the compressibility term $\beta T\, DP/Dt$ is negligible in eq. (1.39). It is also assumed that $(c, k)_s$ and $(c_P, k)_f$ are known constants.

Note further that T is the temperature of *both* parts, solid and fluid; in other words, the fluid and the porous structure are assumed to be in *local thermal equilibrium*. This assumption, although adequate for small-pore media such as geothermal reservoirs and fibrous insulation, must be relaxed in the study of nuclear reactor cores, electronic packages, and electrical windings where the temperature difference between solid and fluid (coolant) is a very important safety parameter. When the solid and fluid are not in thermal equilibrium locally, every point of the volume-averaged medium has two temperatures, one for the solid and the other for the fluid. Two-temperature models for the forced convection cooling of electronic microstructures are illustrated in Refs. 9 and 10.

Integrating eq. (12.25) over the pore volume $A_p\, \Delta x$ yields

$$\Delta x\, A_p \rho_f c_{Pf} \frac{\partial T}{\partial t} + \Delta x\, A \rho_f c_{Pf} u \frac{\partial T}{\partial x} = \Delta x\, A_p k_f \frac{\partial^2 T}{\partial x^2} + \Delta x\, \mu \iint_{A_p} \Phi\, dA_p \quad (12.26)$$

In the second term on the left-hand side we used the definition of average velocity [eq. (12.2)]: $Au = \iint_{A_p} u_p\, dA_p$. The last term on the right-hand side represents the internal heating associated with viscous dissipation or entropy generation. The dissipation term in eq. (12.26) equals the mechanical power needed to extrude the viscous fluid through the pore. This power requirement is equal to the mass flow rate times the externally maintained pressure drop divided by the fluid density,

$$\Delta x\, \mu \iint_{A_p} \Phi\, dA_p = Au \left(-\frac{\partial P}{\partial x} + \rho_f g_x \right) \Delta x \quad (12.27)$$

It is easy to prove this identity in the case of known Hagen–Poiseuille flows through pores with simple cross sections (Problem 12.6); however, eq. (12.27) holds for any unspecified pore geometry.

Volumetric averaging of the energy conservation statement is achieved by adding eqs. (12.24) and (12.26) side by side and dividing by the volume element $A\, \Delta x$ of the porous structure regarded as a homogeneous medium:

$$[\phi \rho_f c_{Pf} + (1 - \phi)\rho_s c_s] \frac{\partial T}{\partial t} + \rho_f c_{Pf} u \frac{\partial T}{\partial x}$$

$$= [\phi k_f + (1 - \phi)k_s] \frac{\partial^2 T}{\partial x^2} + (1 - \phi)q_s''' + u \left(-\frac{\partial P}{\partial x} + \rho_f g_x \right) \quad (12.28)$$

The thermal conductivity of the porous medium k emerges as a combination of the conductivities of the two constituents,

$$k = \phi k_f + (1 - \phi)k_s \quad (12.29)$$

This simple expression, however, is the result of the one-dimensional model of Fig. 12.3 which corresponds to a *parallel conduction model*. In general, k must be measured experimentally, as the thermal conductivity of the porous matrix filled with fluid.

Other models for approximating k when k_f and k_s are known are discussed in Refs. 2 and 3. The optimization of the configuration of the high-conductivity material (k_s in this case) is an opportunity to maximize the global thermal conductance of the two-material medium [11] and to minimize the thermal contact resistance at the boundary between this medium and another body [11,12]. The optimization of the fluid space configuration is pursued in Ref. 13, where it is shown that minimal global flow resistance is achieved when the flow is distributed non-uniformly or optimally ''maldistributed'' as a multiscale flow structure of small and large nonparallel channels (e.g., tree-shaped heat exchangers) [14,15]. When scales are small enough, the complex flow structures constructed in this manner may be viewed as *designed porous media*. This new direction is charted in Ref. 3.

The thermal inertia of the medium depends on the inertias of the solid and the fluid. This is accounted for by introducing the *capacity ratio*:

$$\sigma = \frac{\phi \rho_f c_{P_f} + (1 - \phi)\rho_s c_s}{\rho_f c_{P_f}} \tag{12.30}$$

The internal heat generation rate per unit volume of porous medium q''' decreases as the porosity increases,

$$q''' = (1 - \phi)q'''_s \tag{12.31}$$

With the new notation of eqs. (12.29)–(12.31), the energy equation for the *homogeneous* porous medium reads

$$\rho_f c_{P_f}\left(\sigma\frac{\partial T}{\partial t} + u\frac{\partial T}{\partial x}\right) = k\frac{\partial^2 T}{\partial x^2} + q''' + \frac{\mu}{K}u^2 \tag{12.32}$$

A similar derivation performed for a three-dimensional flow model yields

$$\rho_f c_{P_f}\left(\sigma\frac{\partial T}{\partial t} + \mathbf{v}\cdot\nabla T\right) = k\,\nabla^2 T + q''' + \frac{\mu}{K}(\mathbf{v})^2 \tag{12.33}$$

where $\mathbf{v}$ is the volume-averaged velocity vector (u, v, w). In situations without internal heat generation q''' and negligible viscous dissipation effect $(\mu/K)(\mathbf{v})^2$, the first law of thermodynamics reduces to

$$\sigma\frac{\partial T}{\partial t} + u\frac{\partial T}{\partial x} + v\frac{\partial T}{\partial y} + w\frac{\partial T}{\partial z} = \alpha\left(\frac{\partial^2 T}{\partial x^2} + \frac{\partial^2 T}{\partial y^2} + \frac{\partial^2 T}{\partial z^2}\right) \tag{12.34}$$

The thermal diffusivity of the homogeneous porous medium α is defined as

$$\alpha = \frac{k}{\rho_f c_{P_f}} \tag{12.35}$$

Note that k and α are aggregate properties of the fluid-saturated porous medium, whereas $\rho_f c_{P_f}$ is a property of the fluid alone.

In the present treatment, we rely on eqs. (12.8), (12.17), and (12.34) as governing equations for convection through a homogeneous porous medium. The assumptions made in deriving these equations are:

1. The medium is homogeneous; in other words, the solid material and the fluid permeating through the pores are distributed evenly throughout the porous medium.
2. The medium is isotropic, meaning that transport properties such as K and k do not depend on the direction of the experiment from which they are measured. When the medium is anisotropic, the permeability, conductivity, and thermal diffusivity depend on the direction of the measurement: namely, (K_x, K_y, K_z), (k_x, k_y, k_z), and $(\alpha_x, \alpha_y, \alpha_z) = (k_x, k_y, k_z)/\rho_f c_{Pf}$. When the principal directions of the anisotropic medium [16] coincide with the axes x, y, and z, the Darcy law (12.17) assumes the form

$$u = \frac{K_x}{\mu}\left(-\frac{\partial P}{\partial x} + \rho g_x\right)$$

$$v = \frac{K_y}{\mu}\left(-\frac{\partial P}{\partial y} + \rho g_y\right) \tag{12.36}$$

$$w = \frac{K_z}{\mu}\left(-\frac{\partial P}{\partial z} + \rho g_z\right)$$

and the energy equation (12.34) is replaced by

$$\sigma\frac{\partial T}{\partial t} + u\frac{\partial T}{\partial x} + v\frac{\partial T}{\partial y} + w\frac{\partial T}{\partial z} = \alpha_x\frac{\partial^2 T}{\partial x^2} + \alpha_y\frac{\partial^2 T}{\partial y^2} + \alpha_z\frac{\partial^2 T}{\partial z^2} \tag{12.37}$$

3. At any point in the porous medium, the solid matrix is in thermal equilibrium with the fluid filling the pores.
4. The local Reynolds number based on averaged velocity and $K^{1/2}$ does not exceed the range $1-10$, meaning that the Darcy law applies in its original form (12.17).

12.4 SECOND LAW OF THERMODYNAMICS

Convection processes through fluid-saturated porous media are inherently irreversible, due to the transfer of heat in the direction of finite temperature gradients and to the viscous flow through the pores. The second law of thermodynamics

[eq. (1.47)] may be applied to the one-dimensional flow model discussed in the preceding section (Fig. 12.3) to yield the entropy generation rate per unit volume of homogeneous porous medium,

$$S'''_{\text{gen}} = \frac{k}{T^2}\left(\frac{\partial T}{\partial x}\right)^2 + \frac{\mu u^2}{KT} \geq 0 \tag{12.38}$$

where it was assumed that $q''' = 0$. The analysis leading to eq. (12.38) is proposed as an exercise using Ref. 17 as a guide (Problem 12.7). For a general three-dimensional convection process, the local rate of entropy generation becomes

$$S'''_{\text{gen}} = \underbrace{\frac{k}{T^2}(\nabla T)^2}_{\geq 0} + \underbrace{\frac{\mu}{KT}(\mathbf{v})^2}_{\geq 0} \geq 0 \tag{12.39}$$

where, it must be stressed, T represents *absolute* temperature. Important to note is that the viscous irreversibility term in eq. (12.39) may not be negligible, even in cases when the viscous dissipation term can be neglected in the energy equation (12.33) (see Ref. 17, p. 102).

12.5   FORCED CONVECTION

12.5.1   Boundary Layers

The basic problem in heat convection through porous media consists of predicting the heat transfer rate between a differentially heated, solid impermeable surface and a fluid-saturated porous medium. We begin with the simplest *wall heat transfer* problem, namely, the interaction between a solid wall and the parallel flow permeating through the porous material confined by the wall.

Constant Wall Temperature. Relative to the two-dimensional coordinate system of Fig. 12.4, the steady-state governing equations are

$$\frac{\partial u}{\partial x} + \frac{\partial v}{\partial y} = 0 \tag{12.40}$$

$$u = -\frac{K}{\mu}\frac{\partial P}{\partial x} \qquad v = -\frac{K}{\mu}\frac{\partial P}{\partial y} \tag{12.41}$$

$$u\frac{\partial T}{\partial x} + v\frac{\partial T}{\partial y} = \alpha\frac{\partial^2 T}{\partial y^2} \tag{12.42}$$

where it has been assumed that ρ is constant, the boundary layer is slender, and the gravity effect is negligible. Consider now the uniform parallel flow

$$u = U_\infty, \qquad v = 0, \qquad P(x) = -\frac{\mu}{K}U_\infty x + \text{constant} \tag{12.43}$$
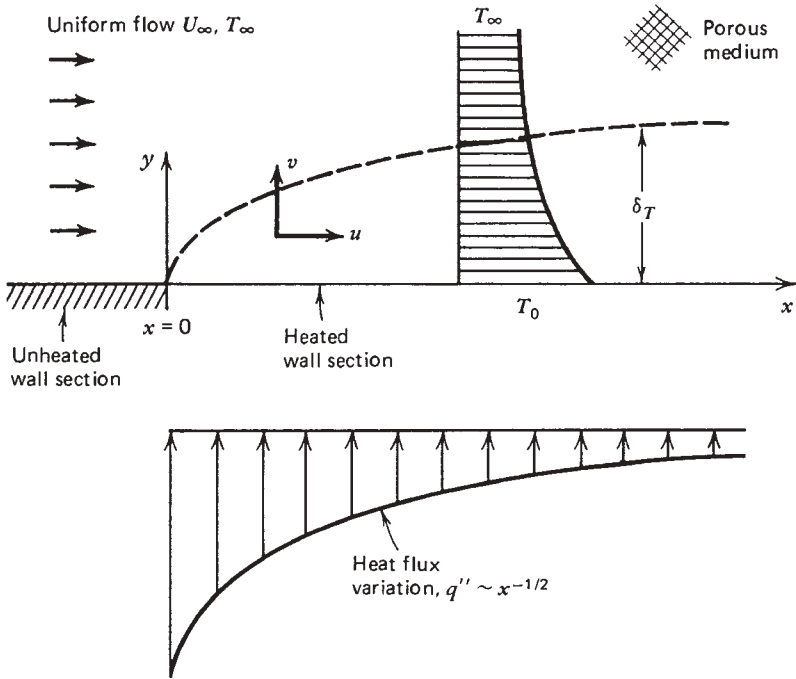
Figure 12.4   Thermal boundary layer near an isothermal wall with parallel flow.

which satisfies the fluid mechanics part of the problem [eqs. (12.40) and (12.41)]. If the temperature of the fluid-saturated medium is T_∞ and the wall temperature downstream of some point $x = 0$ is T_0, what is the heat transfer rate between the $x > 0$ wall and the porous medium? We answer this question based on scale analysis.

Let δ_T be the thickness of the slender layer of length x that affects the temperature transition from T_0 to T_∞. We refer to δ_T as the thermal boundary layer thickness, keeping in mind the analogy between the present problem and the Blasius–Pohlhausen problem of Chapter 2. However, unlike in Chapter 2, this time we do not encounter a velocity boundary layer thickness. Writing $\Delta T = T_0 - T_\infty$, the energy equation (12.42) reveals a balance between enthalpy flow in the x direction and thermal diffusion in the y direction,

$$U_\infty \frac{\Delta T}{x} \sim \alpha \frac{\Delta T}{\delta_T^2} \tag{12.44}$$

where it has been assumed that the thermal boundary layer region is *slender*, $\delta_T \ll x$. The heat transfer implications of eq. (12.44) are

$$\frac{\delta_T}{x} \sim \mathrm{Pe}_x^{-1/2} \tag{12.45}$$

$$\text{Nu}_x = h\frac{x}{k} \sim \frac{x}{\delta_T} \sim \text{Pe}_x^{1/2} \tag{12.46}$$

The *Péclet number* is based on the thermal diffusivity of the porous medium,

$$\text{Pe}_x = \frac{U_\infty x}{\alpha} \tag{12.47}$$

In conclusion, the thermal boundary layer thickness δ_T increases as $x^{1/2}$ downstream from the point where wall heating begins. The local heat transfer coefficient (or the local heat flux q'') decreases as $x^{-1/2}$. Since results (12.45) and (12.46) are based on the slender thermal boundary layer assumptions, they are valid only when $\text{Pe}_x^{1/2} > O(1)$, that is, sufficiently far downstream from $x = 0$.

The similarity solution to the heat transfer problem defined by eqs. (12.40)–(12.42) and the boundary conditions of Fig. 12.4 is developed by introducing the similarity variable suggested by the scaling law (12.45),

$$\eta = \frac{y}{x}\text{Pe}_x^{1/2} \tag{12.48}$$

The similarity temperature profile is

$$\frac{T - T_0}{T_\infty - T_0} = \theta(\eta) \tag{12.49}$$

With this notation, the energy equation and its boundary conditions become

$$\theta'' + \tfrac{1}{2}\eta\theta' = 0 \tag{12.50}$$

$$\theta(0) = 0, \qquad \theta(\infty) = 1 \tag{12.51}$$

Solving eqs. (12.50) and (12.51) by separation of variables, we find that

$$\theta = \text{erf}\left(\frac{\eta}{2}\right) \tag{12.52}$$

$$\left(\frac{d\theta}{d\eta}\right)_{\eta=0} = \pi^{-1/2} = 0.564 \tag{12.53}$$

According to this similarity solution, the local Nusselt number is

$$\text{Nu}_x = \frac{q''}{T_0 - T_\infty}\frac{x}{k} = \left(\frac{d\theta}{d\eta}\right)_{\eta=0}\text{Pe}_x^{1/2} = 0.564\text{Pe}_x^{1/2} \tag{12.54}$$

which agrees within a factor of order 1 with the scale law (12.46). Averaging the heat transfer coefficient over the wall length L, we obtain

$$\overline{\text{Nu}} = \bar{h}\frac{L}{k} = 1.128\text{Pe}_L^{1/2} \tag{12.55}$$

Constant Wall Heat Flux. If the impermeable wall is subjected to the uniform heat flux condition $q'' = $ constant, the temperature difference $T_0(x) - T_\infty$ varies as $x^{1/2}$ downstream from $x = 0$. This problem was first solved numerically in the first edition of this book, where the method was based on finite differences (Problem 12.10). Morega and Bejan [18] reported that the problem can be solved analytically in closed form; this compact approach is shown next.

The energy equation to solve is (12.42) with $u = U_\infty$ and $v = 0$, subject to the boundary conditions

$$\frac{\partial T}{\partial y} = -\frac{q''}{k} \quad \text{at } y = 0 \tag{12.56}$$

$$T \to T_\infty \quad \text{as } y \to \infty \tag{12.57}$$

We select the similarity variables by keeping in mind the proportionality between thermal boundary layer thickness and $x^{1/2}$, eq. (12.45), and the proportionality between $[T_0(x) - T_\infty]$ and $x^{1/2}$:

$$\zeta = y \left(\frac{U_\infty}{\alpha x} \right)^{1/2} \tag{12.58}$$

$$\tau(\zeta) = \frac{T(x, y) - T_\infty}{(q''/k)(\alpha x/U_\infty)^{1/2}} \tag{12.59}$$

The similarity version of eqs. (12.42), (12.56), and (12.57) is

$$\tau'' + \tfrac{1}{2}(\zeta \tau' - \tau) = 0 \tag{12.60}$$

$$\tau'(0) = -1 \tag{12.61}$$

$$\tau(\infty) = 0 \tag{12.62}$$

Separation of variables is achieved by differentiating eq. (12.60) once,

$$\frac{\tau'''}{\tau''} = -\tfrac{1}{2}\zeta \tag{12.63}$$

The equation is then integrated sequentially three times, and after using eqs. (12.60)–(12.62), the analytical expression for the similarity temperature profile becomes

$$\tau(\zeta) = \frac{2}{\pi^{1/2}} \exp\left(-\frac{\zeta^2}{4} \right) - \zeta \operatorname{erfc}\left(\frac{\zeta}{2} \right) \tag{12.64}$$

This expression shows that the value at the wall is $\tau(0) = 2/\pi^{1/2} = 1/0.886$. The local Nusselt number is therefore

$$\mathrm{Nu}_x = \frac{q'' x}{k[T_0(x) - T_\infty]} = 0.886 \mathrm{Pe}_x^{1/2} \tag{12.65}$$
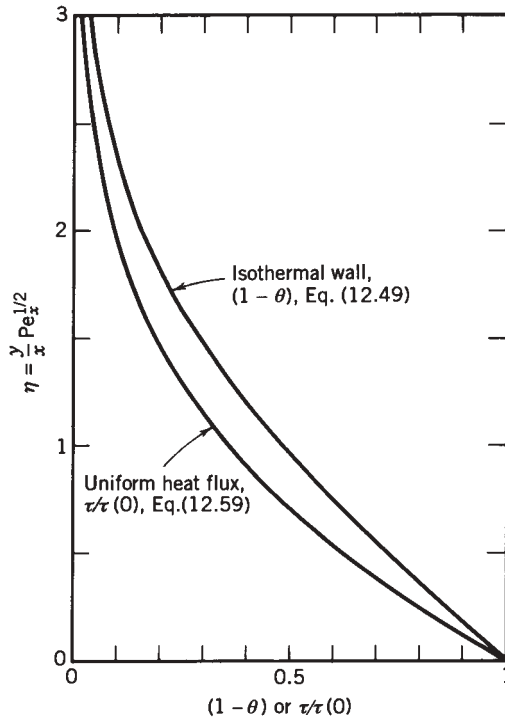
Figure 12.5 Similarity temperature profiles of the forced convection boundary layers in a porous medium with uniform flow.

with the corresponding overall Nusselt number

$$\overline{Nu} = \frac{q''L}{k(\overline{T}_0 - T_\infty)} = 1.329 Pe_L^{1/2} \tag{12.66}$$

where 1.329 stands for $3\pi^{1/2}/4$. The similarity temperature profile has been superimposed on Fig. 12.5 because ζ of eq. (12.58) is the same as η of eq. (12.48). This new curve was drawn as $\tau/\tau(0)$ such that its ends coincide with the ends of the $\theta(\eta)$ profile. In this way, Fig. 12.5 shows that the τ profile is steeper than the θ profile. The heatlines of these boundary layers are presented in Ref. 19. The analytical solution (12.64) also represents the $Pr \to 0$ limit of the thermal boundary layer on a flat plate with uniform heat flux (Section 2.6.3).

Other Conditions. In the preceding two examples, the flow was uniform and parallel to the impermeable wall. A more general class of problems emerges if we consider the uniform flow (U_∞, T_∞) incident to a wedge-shaped impermeable obstacle of included angle $m\pi$. As in the classical Falkner–Skan flows of

Section 2.7, potential flow theory reveals that the velocity along each side of the wedge varies as $u = Cx^n$, where $n = m/(2 - m)$. Cheng [20] showed that in such cases, a similarity solution exists for the heat transfer problem if the wall temperature varies as $T_0(x) = T_\infty + Ax^n$, with x measured downstream from the tip. The isothermal wall problem considered earlier in this section is the $n = 0$ special case of the class of wedge flows. The time-dependent heat transfer and thermal boundary layer near a wall heated suddenly in a porous medium are described in Ref. 21.

12.5.2 Concentrated Heat Sources

With reference to Fig. 12.6a, the temperature field $T(x,r)$ downstream from a *point heat source* of strength q buried in a fluid-saturated porous medium is [cf. eq. (9.94)]

$$T - T_\infty = \frac{q}{4\pi kx} \exp\left(-\frac{ur^2}{4\alpha x}\right) \tag{12.67}$$
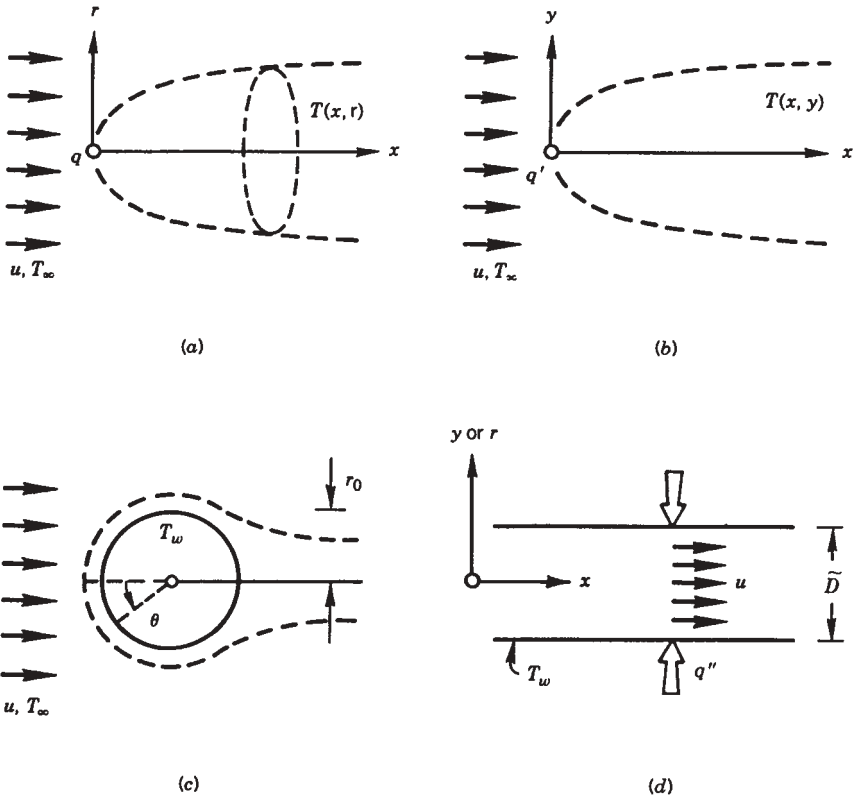
Figure 12.6 Forced convection configurations: (*a*) point heat source; (*b*) line heat source in cross flow; (*c*) sphere or cylinder in cross flow; (*d*) long duct filled with a porous medium.

This result is valid where convection overwhelms diffusion as a longitudinal heat transfer mechanism in the wake (i.e., where $ux/\alpha \gg 1$).

The thermal wake behind a *line heat source* perpendicular to a uniform volume-averaged flow (u, T_∞) is sketched in Fig. 12.6b. If the source strength is q', the two-dimensional temperature field $T(x, y)$ is analogous to what we derived in eqs. (9.90)–(9.93):

$$T - T_\infty = \frac{q'}{(\rho c_P)_f (4\pi u \alpha x)^{1/2}} \exp\left(-\frac{uy^2}{4\alpha x}\right) \tag{12.68}$$

Equation (12.68) holds in the convection-dominated regime, $ux/\alpha \gg 1$. When this criterion fails, the T field is governed by pure diffusion, and its analytical form may be derived by classical heat conduction methods (e.g., Ref. 8, pp. 177–184).

12.5.3   Sphere and Cylinder in Cross Flow

The distributions of heat flux around the sphere and cylinder in cross flow were determined by Cheng [22], who assumed that the flow is in the Darcy regime. With reference to the angular coordinate θ defined in Fig. 12.6c, Cheng obtained the following expressions for the local peripheral Nusselt number:

Sphere:

$$\mathrm{Nu}_\theta = 0.564 \left(\frac{ur_0\theta}{\alpha}\right)^{1/2} \left(\frac{3}{2}\,\theta\right)^{1/2} \sin^2\theta \left(\frac{1}{3}\cos^3\theta - \cos\theta + \frac{2}{3}\right)^{-1/2}$$
$$\tag{12.69}$$

Cylinder:

$$\mathrm{Nu}_\theta = 0.564 \left(\frac{ur_0\theta}{\alpha}\right)^{1/2} (2\theta)^{1/2} \, \sin\theta\,(1 - \cos\theta)^{-1/2} \tag{12.70}$$

Worth noting in these expressions is the Péclet number based on the swept arc $r_0\theta$: namely, $\mathrm{Pe}_\theta = ur_0\theta/\alpha$. The local Nusselt number is defined as $\mathrm{Nu}_\theta = q''r_0\theta/[k(T_w - T_\infty)]$. Equations (12.69) and (12.70) are valid when the boundary layers are distinct (thin) (i.e., when the boundary layer thickness $r_0 \mathrm{Pe}_\theta^{-1/2}$ is smaller than the radius r_0). This requirement can also be written as $\mathrm{Pe}_\theta^{1/2} \gg 1$ or $\mathrm{Nu}_\theta \gg 1$.

The heat flux averaged over the area of the cylinder and sphere, $\overline{q''}$, is calculated by averaging the local heat flux q'' of eqs. (12.69) and (12.70). This was done by Nield and Bejan [2], and the results are

$$\textit{Sphere}: \quad \overline{\mathrm{Nu}}_D = 1.128\mathrm{Pe}_D^{1/2} \tag{12.71}$$

$$\textit{Cylinder}: \quad \overline{\mathrm{Nu}}_D = 1.015\mathrm{Pe}_D^{1/2} \tag{12.72}$$

In these expressions, the Nusselt and Péclet numbers are based on the diameter $D = 2r_0$: namely, $\overline{\mathrm{Nu}}_D = \overline{q''}D/k(T_w - T_\infty)$ and $\mathrm{Pe}_D = uD/\alpha$.

12.5.4 Channel Filled with Porous Medium

Consider a flow of volume-averaged velocity u through a porous medium that fills a long channel (Fig. 12.6d). In the Darcy flow regime, the velocity u is uniform over the channel cross section. When the temperature field is fully developed, the relationship between wall heat flux q'' and local temperature difference $(T_w - T_m)$ is analogous to the formula for fully developed heat transfer to ''slug flow'' through a channel without a porous matrix (Chapter 3). The temperature T_m is the mean temperature of the stream that flows through the channel (Section 3.4.1), which for slug flow reduces to

$$T_m = \frac{1}{A} \int_A T \, dA \qquad (12.73)$$

in which A is the area of the channel cross section.

In cases where the confining wall is a tube with the internal diameter D, the relation for fully developed heat transfer can be expressed as a constant Nusselt number,

$$\mathrm{Nu}_D = \frac{q''(x)}{T_w - T_m(x)} \frac{D}{k} = 5.78 \quad (\text{tube, } T_w = \text{constant}) \qquad (12.74)$$

$$\mathrm{Nu}_D = \frac{q''}{T_w(x) - T_m(x)} \frac{D}{k} = 8 \quad (\text{tube, } q'' = \text{constant}) \qquad (12.75)$$

When the porous matrix is sandwiched between two parallel plates with the spacing D, the corresponding Nusselt numbers are

$$\mathrm{Nu}_D = \frac{q''(x)}{T_w - T_m(x)} \frac{D}{k}$$
$$= 4.93 \quad (\text{parallel plates, } T_w = \text{constant}) \qquad (12.76)$$

$$\mathrm{Nu}_D = \frac{q''}{T_w(x) - T_m(x)} \frac{D}{k}$$
$$= 6 \quad (\text{parallel plates, } q'' = \text{constant}) \qquad (12.77)$$

The forced correction results (12.74)–(12.77) are valid when the temperature profile across the channel is fully developed [i.e., sufficiently far from the channel entrance ($x = 0$ in Fig. 12.6d)]. The length needed for the temperature profile to become fully developed can be estimated by recalling from eq. (12.45) that the thermal boundary layer thickness scales as $(\alpha x/u)^{1/2}$. By setting $x \sim X_T$ in $(\alpha x/u)^{1/2} \sim D$, we obtain the thermal entrance length $X_T \sim D^2 u/\alpha$. Inside the entrance region $0 < x < X_T$, the heat transfer is impeded by the forced convection thermal boundary layers that line the channel walls and can be calculated approximately with the formulas derived in Section 12.5.1.

12.6 NATURAL CONVECTION BOUNDARY LAYERS

12.6.1 Boundary Layer Equations: Vertical Wall

In this section we consider the heat transfer between a vertical heated surface and a fluid-saturated semi-infinite porous reservoir (Fig. 12.7). This, the simplest boundary layer model for natural convection in porous media, was published in a classical paper by Cheng and Minkowycz [23]. Because the gravitational acceleration g is oriented in the negative y direction, the Darcy flow satisfies

$$u = -\frac{K}{\mu}\frac{\partial P}{\partial x} \qquad v = -\frac{K}{\mu}\left(\frac{\partial P}{\partial y} + \rho g\right) \tag{12.78}$$

or by eliminating P,

$$\frac{\partial u}{\partial y} - \frac{\partial v}{\partial x} = \frac{Kg}{\mu}\frac{\partial \rho}{\partial x} \tag{12.79}$$

Defining the streamfunction ψ

$$u = \frac{\partial \psi}{\partial y}, \qquad v = -\frac{\partial \psi}{\partial x} \tag{12.80}$$
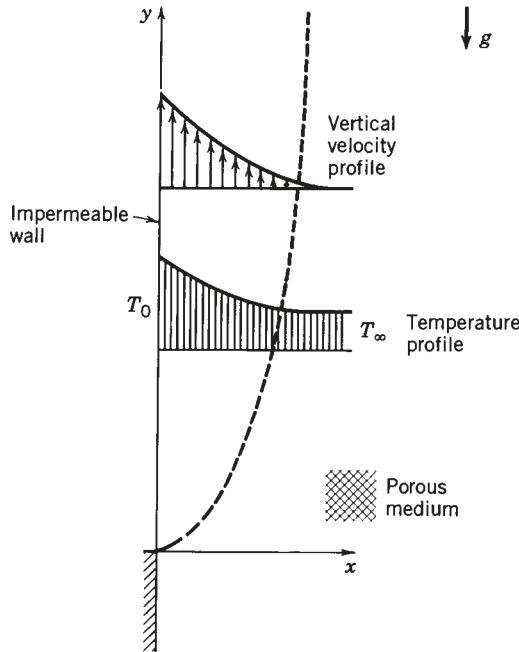
Figure 12.7 Natural convection boundary layer flow through a porous medium placed near a hot vertical wall.

so that the mass continuity equation (12.40) is satisfied identically, the Darcy law (12.79) becomes

$$\frac{\partial^2 \psi}{\partial x^2} + \frac{\partial^2 \psi}{\partial y^2} = \frac{Kg}{\mu} \frac{\partial \rho}{\partial x} \tag{12.81}$$

If the boundary layer of Fig. 12.7 is slender, the governing balances [force (12.81) and energy (12.34)] reduce to

$$\frac{\partial^2 \psi}{\partial x^2} = -\frac{Kg\beta}{\nu} \frac{\partial T}{\partial x} \tag{12.82}$$

$$\frac{\partial \psi}{\partial y} \frac{\partial T}{\partial x} - \frac{\partial \psi}{\partial x} \frac{\partial T}{\partial y} = \alpha \frac{\partial^2 T}{\partial x^2} \tag{12.83}$$

In writing eq. (12.82), we used the Boussinesq approximation of Chapter 4, $\rho = \rho_0[1 - \beta(T - T_0)]$, to effect the *coupling* between the flow field $\psi(x, y)$ and the temperature field $T(x, y)$.

12.6.2   Uniform Wall Temperature

Consider first the case where the temperature of the vertical impermeable wall is uniform, T_0; the boundary conditions are

$$T = T_0, \qquad \psi = 0 \qquad\quad \text{at } x = 0$$

$$T \to T_\infty, \qquad \partial \psi / \partial x \to 0 \quad \text{as } x \to \infty \tag{12.84}$$

The scale analysis of problem (12.82)–(12.84) reveals the order of magnitude of the heat transfer rate between the wall and the semi-infinite porous reservoir. From eqs. (12.82) and (12.83), we obtain

$$\frac{\psi}{\delta_T^2} \sim \frac{Kg\beta}{\nu} \frac{\Delta T}{\delta_T} \tag{12.85}$$

$$\frac{\psi \Delta T}{y \delta_T} \sim \alpha \frac{\Delta T}{\delta_T^2} \tag{12.86}$$

where δ_T is the boundary layer thickness (the x scale) and $\Delta T = T_0 - T_\infty$. Combining expressions (12.85) and (12.86), we conclude that

$$\frac{\delta_T}{y} \sim \mathrm{Ra}_y^{-1/2}, \qquad \psi \sim \alpha \, \mathrm{Ra}_y^{1/2} \tag{12.87}$$

$$\mathrm{Nu}_y = h\frac{y}{k} \sim \frac{y}{\delta_T} \sim \mathrm{Ra}_y^{1/2} \tag{12.88}$$

where the heat transfer coefficient scales as $h \sim q''/\Delta T \sim k/\delta_T$, and Ra_y is the *Darcy-modified Rayleigh number*

$$\mathrm{Ra}_y = \frac{Kg\beta y \, \Delta T}{\alpha \nu} \tag{12.89}$$

Natural boundary layers in Darcy flow porous media have a single length scale δ_T [eq. (12.87)]. This feature distinguishes them from their counterparts in pure fluids (Chapter 4), which are characterized by two length scales (see Fig. 4.3 and Table 4.1).

The similarity formulation of the isothermal wall problem starts with recognizing from the first of eqs. (12.87) the similarity variable

$$\eta = \frac{x}{y}\text{Ra}_y^{1/2} \tag{12.90}$$

Introducing the similarity profiles

$$\frac{\psi}{\alpha\,\text{Ra}_y^{1/2}} = f(\eta), \qquad \frac{T - T_\infty}{T_0 - T_\infty} = \theta(\eta) \tag{12.91}$$

the problem statement (12.82)–(12.84) becomes

$$f'' = -\theta' \tag{12.92}$$

$$f\theta' = 2\theta'' \tag{12.93}$$

$$\theta(0) = 1, \qquad f(0) = 0$$

$$\theta(\infty) \to 0, \qquad f'(\infty) \to 0 \tag{12.94}$$

The numerical integration performed by Cheng and Minkowycz [23] yielded

$$\text{Nu}_y = \frac{q''}{T_0 - T_\infty}\frac{y}{k} = 0.444\text{Ra}_y^{1/2} \tag{12.95}$$

or, averaged over a wall of height H,

$$\overline{\text{Nu}} = \bar{h}\frac{H}{k} = 0.888\text{Ra}_H^{1/2} \tag{12.96}$$

These exact heat transfer results confirm the validity of the scaling law (12.88).

Mixed convection is the heat transfer mechanism that occurs when, superimposed on the buoyancy effect shown in Fig. 12.7, there is also a forced stream such as the one shown in Fig. 12.4. The latter is pushed from the bottom in Fig. 12.7 and flows with the uniform velocity V_∞ in the y direction. According to eq. (12.45), the thermal boundary layer thickness in the limit of pure forced convection is $\delta_{FC} \sim y\,\text{Pe}_y^{-1/2}$, where $\text{Pe}_y = V_\infty y/\alpha$ and α is the thermal diffusivity of the saturated porous medium. In the limit of pure natural convection, eq. (12.87) indicates the thermal boundary layer thickness $\delta_{NC} \sim y\,\text{Ra}_y^{-1/2}$.

Note that both δ_{FC} and δ_{NC} increase as $y^{1/2}$. This is important because it means that the ratio δ_{FC}/δ_{NC} is a constant of order $(\text{Ra}_y/\text{Pe}_y)^{1/2}$. Invoking once again

the *constructal law* [16,24–26], we expect the flow field to acquire the smaller of δ_{FC} and δ_{NC} [27]. Accordingly, when $(\mathrm{Ra}_y/\mathrm{Pe}_y)^{1/2} < 1$, the forced convection thickness is the smaller thickness, and the mixed convection flow is dominated by forced convection. When $(\mathrm{Ra}_y/\mathrm{Pe}_y)^{1/2} > 1$, the natural convection thickness is the smaller of the two thicknesses: It is selected by the flow, and the heat transfer rate resembles the result known for the natural convection limit.

12.6.3 Uniform Wall Heat Flux

If the vertical wall is characterized by a uniform heat flux q'', the local temperature difference $T_0(y) - T_\infty$ and the boundary layer thickness δ_T must vary such that

$$q'' \sim k\frac{T_0(y) - T_\infty}{\delta_T} = \text{constant} \tag{12.97}$$

Combining this with the scaling results (12.85)–(12.87), we find

$$\frac{\delta_T}{y} \sim \mathrm{Ra}_{*y}^{-1/3} \tag{12.98}$$

where Ra_{*y} is the *Darcy-modified Rayleigh number based on heat flux*,

$$\mathrm{Ra}_{*y} = \frac{Kg\beta y^2 q''}{\alpha v k} \tag{12.99}$$

The local heat transfer rate must therefore scale as

$$\mathrm{Nu}_y = \frac{q''}{T_0(y) - T_\infty}\frac{y}{k} \sim \mathrm{Ra}_{*y}^{1/3} \tag{12.100}$$

The numerical solution to the similarity for formulation of this problem was reported by Cheng and Minkowycz [23] and confirms this scaling result (see Problem 12.14),

$$\mathrm{Nu}_y = \frac{q''}{T_0(y) - T_\infty}\frac{y}{k} = 0.772\mathrm{Ra}_{*y}^{1/3} \tag{12.101}$$

$$\overline{\mathrm{Nu}} = \frac{q''}{\overline{T}_0 - T_\infty}\frac{H}{k} = 1.03\mathrm{Ra}_{*H}^{1/3} \tag{12.102}$$

The results presented above for a vertical wall apply, subject to a slight modification, to the more general case where the wall is inclined relative to the vertical direction. The gravitational acceleration acts in both x and y directions,

$$u = -\frac{K}{\mu}\left(\frac{\partial P}{\partial x} - \rho g_x\right), \qquad v = -\frac{K}{\mu}\left(\frac{\partial P}{\partial y} - \rho g_y\right) \tag{12.103}$$

where g_x and g_y are the respective components of gravitational acceleration. Introducing the Boussinesq approximation and eliminating P between eqs. (12.103) yields

$$\frac{\partial^2 \psi}{\partial x^2} + \frac{\partial^2 \psi}{\partial y^2} = \frac{K\beta}{\nu}\left(g_y\frac{\partial T}{\partial x} - g_x\frac{\partial T}{\partial y}\right)$$
(12.104)

which is a more general version of eq. (12.82). In the boundary layer regime, we have $x \sim \delta_T$ and $y \gg \delta_T$; therefore, the boundary layer approximation of eq. (12.104) is

$$\frac{\partial^2 \psi}{\partial x^2} = \frac{Kg_y\beta}{\nu}\frac{\partial T}{\partial x}$$
(12.105)

This approximation is valid as long as g_x is not order-of-magnitude greater than g_y. Note that eq. (12.105) is the same as eq. (12.82) employed earlier. In conclusion, if the impermeable wall makes an angle γ with the vertical direction, the results developed for vertical walls are applicable as long as g is replaced by $g \cos \gamma$ in the Rayleigh number calculations.

12.6.4 Spacings for Channels Filled with Porous Structures

The constructal design of spacings in the limit of decreasing length scales (Sections 3.6 and 4.12) leads to flow structures that look more and more like porous structures with ''designed'' pores. The development of such structures defines a field that may be regarded as *designed porous media* [3].

In this section we cover another fundamental configuration of designed porous media: spacings between plates that sandwich a porous medium. For example, the channels may be occupied by a metallic foam such that the saturated porous medium has a thermal conductivity (k) and a thermal diffusivity (α) that are much higher than their pure fluid properties (k_f, α_f), which were used in Chapters 2–4. We consider both natural convection and forced convection with Boussinesq incompressible fluid and assume that the structures are fine enough that Darcy flow prevails in all cases. The analysis is another application of the intersection-of-asymptotes method [28,29].

The natural convection configuration is shown in Fig. 12.8. Each D-thin space is filled with the assumed fluid-saturated porous structure. The width in the direction perpendicular to Fig. 12.8 is W. The effective pressure difference that drives the flow is due to buoyancy,

$$\Delta P = \rho H g \beta (T_w - T_0)$$
(12.106)

This ΔP estimate is valid in the limit where the spacing D is sufficiently small so that the temperature in the channel porous medium is essentially the same as the plate temperature T_w. In this limit, the heat current extracted by the flow from the $H \times L$ volume is $q = \dot{m}c_P(T_w - T_0)$, with $\dot{m} = \rho ULW$ and Darcy's law, $U = K$
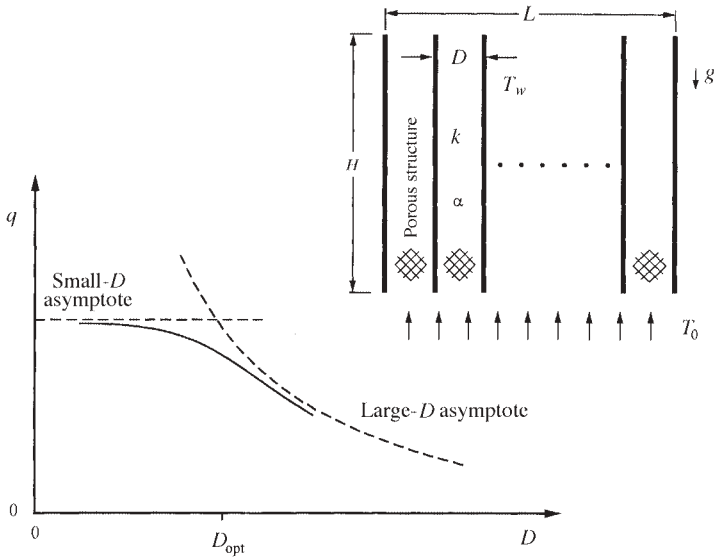
Figure 12.8   Volume filled with vertical heat-generating plates separated by a fluid-saturated porous medium and the effect of the channel spacing on the global thermal conductance.

$\Delta P / \mu H$, where K is the permeability of the structure. In conclusion, the total heat transfer rate in the small-D limit is independent of the spacing D (see Fig. 12.8),

$$q = \rho c_P (T_w - T_0)LW(K\,\Delta P)/\mu H \qquad (12.107)$$

In the opposite limit, D is large enough so that the natural convection boundary layers that line the H-tall plates are distinct. The heat transfer rate from one boundary layer is $\overline{h}HW(T_w - T_0)$, where eq. (12.96) yields $\overline{h}H/k = 0.888 \mathrm{Ra}_H^{-1/2}$, and Ra_H is the Rayleigh number for Darcy flow, $\mathrm{Ra}_H = Kg\beta H(T_w - T_0)/\alpha v$. The number of boundary layers in the $H \times L$ volume is $2L/D$. In conclusion, the total heat transfer rate decreases as D increases (see Fig. 12.8),

$$q = 1.78(L/D)Wk(T_w - T_0)\mathrm{Ra}_H^{1/2} \qquad (12.108)$$

The effect of the spacing requires discussion. For maximal thermal conductance $q/(T_w - T_0)$, the spacing D must be smaller than the estimate obtained by intersecting asymptotes (12.107) and (12.108),

$$D_{\mathrm{opt}}/H \lesssim 1.78\,\mathrm{Ra}_H^{-1/2} \qquad (12.109)$$

The simplest design that has the highest possible conductance is the design with the fewest plates (i.e., the one with the largest D_{opt}); hence $D_{\mathrm{opt}}/H \cong 1.78 \mathrm{Ra}_H^{-1/2}$ for the recommended design. Contrary to Fig. 12.8, however, q does not remain

constant if D decreases indefinitely. There exists a small enough D below which the passages are so tight (tighter than the pores) that the flow is snuffed out. An estimate for how large D should be so that eq. (12.109) is valid is obtained by requiring that the D_{opt} value for natural convection when the channels are filled only with fluid, $D_{opt}/H \cong 2.3\,[g\beta H^3(T_w - T_0)/\alpha_f \nu]^{-1/4}$ [cf. eq. (4.139)], must be smaller than the D_{opt} value of eq. (12.109). We find that this is true when

$$\frac{H^2}{K}\frac{\alpha}{\alpha_f} > \mathrm{Ra}_H \qquad (12.110)$$

in which, normally, $\alpha/\alpha_f \gg 1$ and $H^2/K \gg 1$.

The forced convection configuration can be optimized similarly. The flow is driven by the imposed ΔP through parallel-plates channels of length L and width W. The thermal conductance in the small-D limit is the same as in eq. (12.107). In the large-D limit there are $2H/D$ distinct boundary layers, and the heat transfer rate across one boundary layer is $\bar{h}LW(T_w - T_0)$, where $\bar{h}L/k = 1.128(UL/\alpha)^{1/2}$ [cf. eq. (12.55)]. Putting these formulas together, we find that in the large-D limit the global thermal conductance is

$$q = 2.26(H/D)Wk(T_w - T_0)(UL/\alpha)^{1/2} \qquad (12.111)$$

The forced convection asymptotes (12.107) and (12.111) behave as in Fig. 12.8. The highest conductance occurs to the left of the intersection of the two asymptotes, when

$$D_{opt}/L \lesssim 2.26\,\mathrm{Be}_p^{-1/2} \qquad (12.112)$$

and where Be_p is the *porous medium Bejan number*, $\mathrm{Be}_p = (\Delta P\,K)/\mu\alpha$. This forced convection optimization is valid when the D_{opt} estimate for the channel with pure fluid [eq. (3.133)] is smaller than the D_{opt} value provided by eq. (12.112), that is, when

$$\frac{L^2}{K}\frac{\alpha}{\alpha_f} > \mathrm{Be}_p \qquad (12.113)$$

In summary, eqs. (12.109) and (12.112) provide estimates for the constructal spacings when the channels between heat-generating plates are filled with a fluid-saturated porous structure. The relevant dimensionless groups are Ra_H, Be_p, K/H^2, K/L^2, and α/α_f. The symmetry between eqs. (12.109) and (12.112), and between eqs. (12.110) and (12.113), reinforces Petrescu's [30] argument that the role of the Bejan number in forced convection is analogous to that of the Rayleigh number in natural convection.

These results are most fundamental and are based on a simple model and a simple analysis: Darcy flow and the intersection-of-asymptotes method. The same idea of geometry *discovery* deserves to be pursued in future studies of ''designed porous media,'' based on more refined models and more accurate methods of flow simulation.

12.6.5 Conjugate Boundary Layers

Natural boundary layers are rarely driven by surfaces with *known* temperature or heat flux, as in Fig. 12.7; more often, they are the consequence of the thermal interaction between two fluid systems separated by a vertical (or inclined) impermeable wall. The wall may face fluid-saturated porous media on both sides (Fig. 12.9*a*) or on only one side (Fig. 12.9*b*). If a temperature difference exists between the two fluid systems, conjugate boundary layers form on both sides of the wall.

The problem of conjugate boundary layers on both sides of a solid wall inserted in a fluid-saturated porous medium was formulated and solved in Ref. 31. The problem was solved analytically based on the Oseen-linearization method described in Chapter 5: it was found that the coefficient in the (Nusselt number) $\sim$ (Rayleigh number)$^{1/2}$ proportionality decreases steadily as the wall thickness parameter ω increases,

$$\overline{\mathrm{Nu}} = 0.382(1 + 0.615\omega)^{-0.875}\, \mathrm{Ra}_H^{1/2} \qquad (12.114)$$

In this expression, $\overline{\mathrm{Nu}} = \overline{q''}H/[(T_{\infty,H} - T_{\infty,L})k]$ and $\overline{q''}$ is the heat flux averaged over the height H. In addition, $\mathrm{Ra}_H = Kg\beta H(T_{\infty,H} - T_{\infty,L})/\alpha\nu$; the wall thickness parameter ω is defined as $\omega = (Wk/Hk_w)\, \mathrm{Ra}_H^{1/2}$, where k_w is the thermal conductivity of wall material.

If one side of the wall faces a fluid reservoir (as the outer surface of a double wall filled with fiberglass insulation, in a house), the conjugate boundary layer
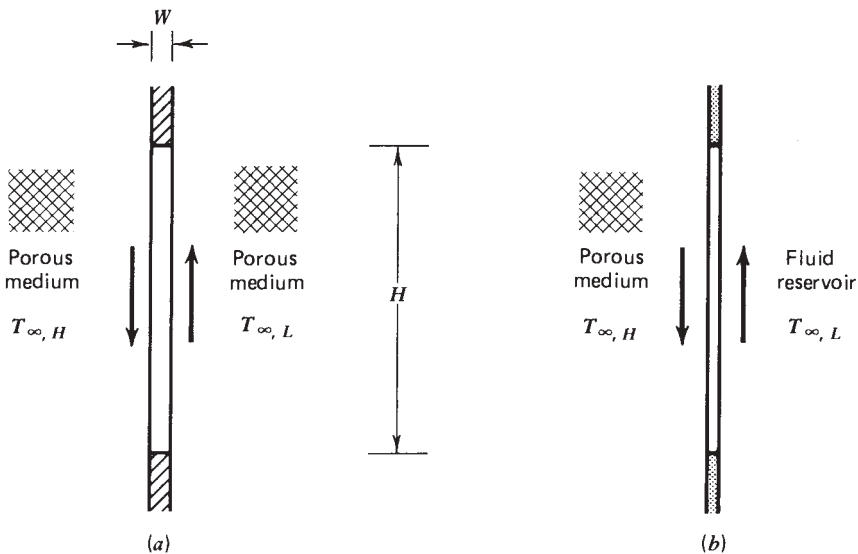
Figure 12.9 Conjugate boundary layers on the two sides of a vertical impermeable partition separating: (*a*) two porous media; (*b*) a porous medium and a fluid reservoir.

problem consists of the interaction of a porous medium layer with a wall jet (Fig. 12.9b). When both sides of the interface are lined by boundary layers, the overall Nusselt number may be estimated as [32]

$$\overline{Nu} = [(0.638)^{-1} + (0.888B)^{-1}]^{-1} \, Ra_{H,f}^{1/4} \tag{12.115}$$

where $\overline{Nu} = \overline{q''}H/[(T_{\infty,H} - T_{\infty,L})k]$ and $B = k \, Ra_H^{1/2}/k_f \, Ra_{H,f}^{1/4}$. The parameter k_f is the fluid-side thermal conductivity; the fluid-side Rayleigh number is $Ra_{H,f} = g(\beta/\alpha\nu)_f H^3(T_{\infty,H} - T_{\infty,L})$. Equation (12.115) is valid when both boundary layers are distinct, $Ra_H^{1/2} \gg 1$ and $Ra_{H,f}^{1/4} \gg 1$; it is also assumed that the fluid on the right side of the partition in Fig. 12.9b has a Prandtl number of order 1 or greater. Structures with solid walls separating cavities filled with porous media and spaces filled with air are being contemplated in the advanced design of bricks and buildings [33].

12.6.6 Thermal Stratification

Since the fluid-saturated porous medium of Fig. 12.7 is not infinite in the x and y directions, the discharge of the boundary layer into the medium leads, in time, to the thermal stratification of the $x > \delta_T$ region. According to Fig. 12.10, if the bottom (or *starting*) temperature difference $T_0 - T_{\infty,0}$ remains fixed, then as the positive temperature gradient $\gamma = dT_\infty/dy$ increases, the average temperature difference between the wall and the porous medium decreases. Therefore, we should expect a steady decrease in the total heat transfer rate as γ increases.

The effect of stable thermal stratification on natural convection in porous media was studied in the context of two conjugate boundary layers on both sides of an impermeable partition inserted vertically into a porous medium [31] (Fig. 12.9a). We focus on this case later. The simpler problem of a vertical or
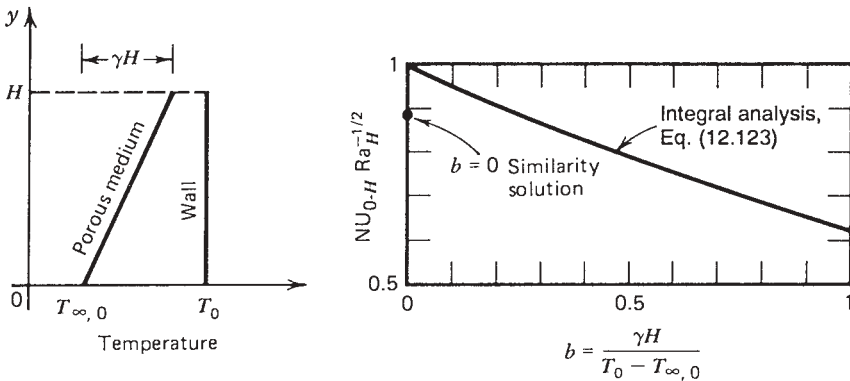
Figure 12.10 Heat transfer from a vertical isothermal wall to a linearly stratified porous medium saturated with fluid.

slightly inclined impermeable wall facing a linearly stratified porous medium was treated by integral analysis in the first edition of this book. This analysis is shown next.

In accordance with the previous notation and the new temperature conditions of Fig. 12.10, the Darcy law (12.82) integrated once requires

$$T = \frac{v}{Kg\beta}v + \text{function}(y) \tag{12.116}$$

Unlike in the Kármán–Pohlhausen integral procedure employed in Chapter 2, in the present case we have the freedom to choose only *one* profile shape (e.g., v), because the second profile follows from eq. (12.116). Let the vertical velocity profile be

$$v = v_0 \, \exp\left(-\frac{x}{\delta_T}\right) \tag{12.117}$$

where both v_0 ad δ_T are unknown functions of altitude. Then, using the Darcy law (12.116) and the temperature boundary conditions $T(0, y) = T_0$ and $T(\infty, y) = T_{\infty,0} + \gamma y$, the corresponding temperature profile is

$$T(x, y) = (T_0 - T_{\infty,0} - \gamma y) \, \exp\left(-\frac{x}{\delta_T}\right) + T_{\infty,0} + \gamma y \tag{12.118}$$

with the maximum (wall) vertical velocity $v_0 = (Kg\,\beta/v)(T_0 - T_{\infty,0} - \gamma y)$.

The integral form of the boundary layer energy equation is obtained by integrating eq. (12.83) across the boundary layer from $x = 0$ to $x \to \infty$,

$$(u)_{x\to\infty}(T)_{x\to\infty} + \frac{d}{dy}\int_0^\infty vT \, dx = -\alpha\left(\frac{\partial T}{\partial x}\right)_{x=0} \tag{12.119}$$

where $(T)_{x\to\infty} = T_{\infty,0} + \gamma y$ and, from the mass conservation equation,

$$(u)_{x\to\infty} = -\frac{d}{dy}\int_0^\infty v \, dx \tag{12.120}$$

Substituting the assumed v and T profiles into the energy integral equation (12.119) yields

$$\frac{d\delta_*}{dy_*} = \frac{2}{\delta_*(1 - by_*)} \tag{12.121}$$

with the following dimensionless notation:

$$b = \frac{\gamma H}{T_0 - T_{\infty,0}} \qquad \text{stratification parameter}$$

$$y_* = \frac{y}{H}, \qquad \delta_* = \frac{\delta_T}{H}\left[\frac{g\beta H\,(T_0 - T_{\infty,0})}{\alpha v}\right]^{1/2} \tag{12.122}$$

Integrating eq. (12.121) from $\delta_*(0) = 0$, we obtain $\delta_*(y_*) = [-(4/b) \ln (1 - by_*)]^{1/2}$, which yields the expected result $(\delta_* \sim y_*^{1/2})$ as b approaches zero. The total heat transfer rate can then be calculated by averaging the heat flux over the wall height H,

$$\frac{\text{Nu}_{0-H}}{\text{Ra}_H^{1/2}} = \int_0^1 \frac{(1 - by_*) \, dy_*}{[-(4/b) \ln (1 - by_*)]^{1/2}} \tag{12.123}$$

where both Nu_{0-H} and Ra_H are based on the maximum (starting) temperature difference

$$\text{Nu}_{0-H} = \frac{q_{0-H}'' H}{k(T_0 - T_{\infty,0})}, \qquad \text{Ra}_H = \frac{Kg\beta H}{\alpha v}(T_0 - T_{\infty,0}) \tag{12.124}$$

Equation (12.123) is plotted in Fig. 12.10: As expected, the coefficient in the $\text{Nu}_{0-H} \sim \text{Ra}_H^{1/2}$ proportionality decreases monotonically as b increases. The accuracy of the integral solution above can be assessed by comparing its $b = 0$ limit, $\text{Nu}_{0-H}/\text{Ra}_H^{1/2} = 1$, with the similarity average Nusselt number for an isothermal wall adjacent to an isothermal porous medium [eq. (12.96)]: The discrepancy between the two solutions is only 12.6 percent.

The effect of stable stratification on both sides of an impermeable wall was studied in Ref. 31 based on the Oseen-linearization method. The heat transfer result is reproduced in Fig. 12.11, along with the temperature conditions sufficiently far from the vertical wall (Fig. 12.9a). The stratification parameter
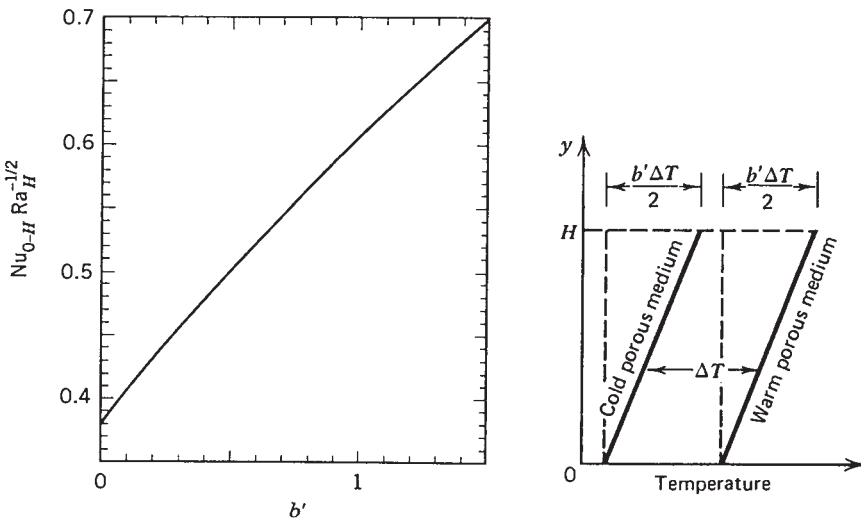
Figure 12.11 Effect of stable stratification on natural convection heat transfer through a vertical wall embedded in a porous medium. (From Ref. 31.)

b', defined in Fig. 12.11, is the same for both porous sides. The average Nusselt number Nu_{0-H} and the Rayleigh number are based on the temperature difference ΔT between the two fluid-saturated porous media (note that ΔT is a constant independent of y).

12.6.7 Sphere and Horizontal Cylinder

With reference to the coordinate system shown in Fig. 12.12a, the local Nusselt numbers for boundary layer convection around an impermeable sphere or a horizontal cylinder embedded in an infinite porous medium are:

Sphere:

$$\mathrm{Nu}_\theta = 0.444\mathrm{Ra}_\theta^{1/2}\left(\tfrac{3}{2}\theta\right)^{1/2}\sin^2\theta\left(\tfrac{1}{3}\cos^3\theta - \cos\theta + \tfrac{2}{3}\right)^{-1/2} \tag{12.125}$$

Horizontal cylinder:

$$\mathrm{Nu}_\theta = 0.444\mathrm{Ra}_\theta^{1/2}(2\theta)^{1/2}\sin\theta(1 - \cos\theta)^{-1/2} \tag{12.126}$$

where $\mathrm{Nu}_\theta = q''r_0\theta/k(T_w - T_\infty)$ and $\mathrm{Ra}_\theta = Kg\beta\theta r_0(T_w - T_\infty)/\alpha\nu$. These steady-state results have been reported by Cheng [22]; they are valid provided that the boundary layer region is slender (i.e., if $\mathrm{Nu}_\theta \gg 1$). The corresponding overall Nusselt numbers are (see Ref. 2):

Sphere:
$$\overline{\mathrm{Nu}}_D = 0.362\mathrm{Ra}_D^{1/2} \tag{12.125'}$$

Horizontal cylinder:
$$\overline{\mathrm{Nu}}_D = 0.565\mathrm{Ra}_D^{1/2} \tag{12.126'}$$

where $\overline{\mathrm{Nu}}_D = \overline{q''}D/k(T_w - T_\infty)$, $D = 2r_0$, and $\mathrm{Ra}_D = Kg\,\beta D\,(T_w - T_\infty)/\alpha\nu$.
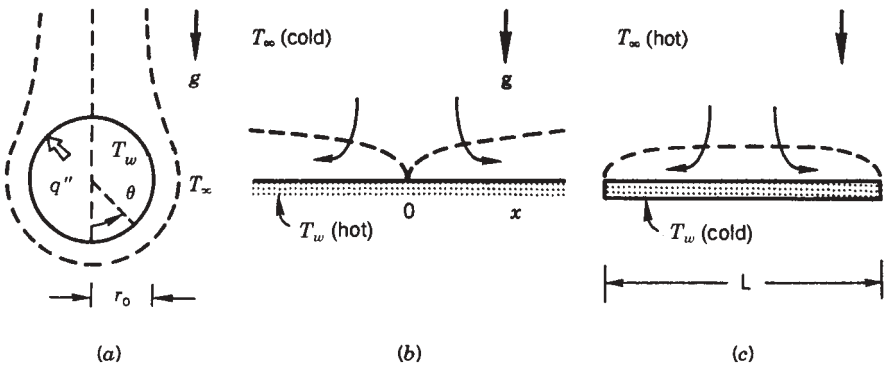
Figure 12.12 External natural convection in a porous medium: (*a*) impermeable sphere or horizontal cylinder; (*b*) hot surface facing upward; (*c*) cold surface facing upward.

12.6.8   Horizontal Walls

The boundary layer flow in the vicinity of a heated horizontal surface that faces upward (Fig. 12.12b) was studied by Cheng and Chang [34]. Measuring x horizontally away from the vertical plane of symmetry of the flow, the local Nusselt number for an isothermal wall is

$$\text{Nu}_x = 0.42\text{Ra}_x^{1/3} \tag{12.127}$$

where $\text{Nu}_x = q''x/k(T_w - T_\infty)$ and $\text{Ra}_x = Kg\,\beta x(T_w - T_\infty)/\alpha\nu$. The local Nusselt number for a horizontal wall heated with uniform flux is

$$\text{Nu}_x = 0.859\text{Ra}_{*x}^{1/4} \tag{12.128}$$

where $\text{Ra}_{*x} = Kg\beta x^2 q''/k\alpha\nu$. Equations (12.127) and (12.128) are valid in the boundary layer regime, $\text{Ra}_x^{1/3} \gg 1$ and $\text{Ra}_{*x}^{1/4} \gg 1$, respectively. They also apply to porous media bounded from above by a cold surface; this new configuration is obtained by rotating Fig. 12.12b by $180°$.

The other horizontal wall configuration, the upward-facing cold plate of Fig. 12.12c was studied by Kimura et al. [35]. The overall Nusselt number in this configuration is

$$\text{Nu} = 1.47\text{Ra}_L^{1/3} \tag{12.129}$$

where $\text{Nu} = q'/k(T_\infty - T_w)$ and $\text{Ra}_L = Kg\,\beta L(T_\infty - T_w)/\alpha\nu$, and where q' is the overall heat transfer rate through the upward-facing cold plate of length L. The result of eq. (12.129) holds if $\text{Ra}_L \gg 1$ and applies equally to hot horizontal plates facing downward in an isothermal porous medium.

12.6.9   Concentrated Heat Sources

The heat transfer from small heat sources buried inside conducting media is already a large and important chapter in conduction heat transfer (e.g., Ref. 8, Chap. 4). If the conducting medium is saturated with fluid, as, for example, the ground beneath us, the heat released by concentrated sources migrates in accord with the principles of natural convection through porous media. Applications of this class of convection problems are the cooling of underground electric cables and the environmental impact of underground explosions and buried nuclear (heat-generating) waste.

There are many heat source configurations that occur in real life: A review of the published work is available in Ref. 2. This work can be divided into two categories: (1) the low–Rayleigh number regime and (2) the high–Rayleigh number regime. Regime 1 is ruled by pure conduction, with a small contribution due to natural convection [36]. Regime 2 is dominated by convection: The thermal plume rising above the buried heat source is slender (i.e., of the boundary layer type), as shown in the following analysis.
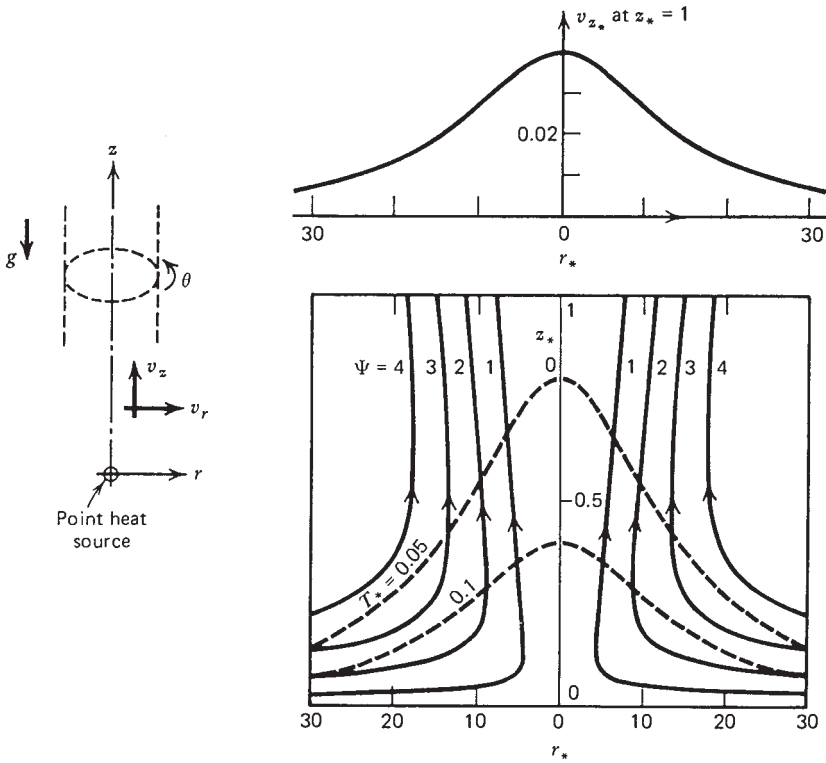
Figure 12.13   Natural convection above a point heat source in a porous medium.

Imagine a slender plume above the point heat source of Fig. 12.13 and attach a cylindrical system of coordinates (r, z) and (v_r, v_z) to the plume so that the z axis passes through the heat source and points against gravity. The governing equations for this θ-symmetric convection problem are

$$\frac{\partial v_r}{\partial r} + \frac{v_r}{r} + \frac{\partial v_z}{\partial z} = 0 \tag{12.130}$$

$$v_r = -\frac{K}{\mu}\frac{\partial P}{\partial r}, \qquad v_z = -\frac{K}{\mu}\left(\frac{\partial P}{\partial z} + \rho g\right) \tag{12.131}$$

$$v_r\frac{\partial T}{\partial r} + v_z\frac{\partial T}{\partial z} = \alpha\left[\frac{1}{r}\frac{\partial}{\partial r}\left(r\frac{\partial T}{\partial r}\right) + \frac{\partial^2 T}{\partial z^2}\right] \tag{12.132}$$

Inside the slender plume, we can write $r \sim \delta_T$ and $z \sim H \gg \delta_T$; therefore, after eliminating the pressure terms, eqs. (12.131) and (12.132) reduce to

$$\frac{\partial v_z}{\partial r} = \frac{Kg\,\beta}{\nu}\frac{\partial T}{\partial r} \tag{12.133}$$

$$v_r \frac{\partial T}{\partial r} + v_z \frac{\partial T}{\partial z} = \frac{\alpha}{r} \frac{\partial}{\partial r}\left(r \frac{\partial T}{\partial r}\right) \tag{12.134}$$

The scale analysis of these two equations dictates that

$$v_z \sim \frac{Kg\beta}{\nu} \Delta T \qquad \text{and} \qquad v_z \sim \frac{\alpha H}{\delta_T^2} \tag{12.135}$$

where ΔT is the plume–ambient temperature difference, $T - T_\infty = $ function (z). A third scaling law follows from the fact that energy released by the point source q (W) is convected upward through the plume flow,

$$q \sim \rho v_z \delta_T^2 c_P \, \Delta T \tag{12.136}$$

Combining relations (12.135) and (12.136) yields the plume scales

$$v_z \sim \frac{\alpha}{H} \text{Ra}, \qquad \delta_T \sim H \, \text{Ra}^{-1/2}, \qquad \Delta T \sim \frac{q}{kH} \tag{12.137}$$

where Ra is the Rayleigh number based on source strength, $\text{Ra} = Kg\,\beta q/\alpha\nu k$. The scale analysis above suggests the following dimensionless formulation:

Dimensionless variables:

$$z_* = \frac{z}{H}, \qquad r_* = \frac{r}{H}\text{Ra}^{1/2}$$

$$v_{z_*} = \frac{v_z}{(\alpha/H)\text{Ra}}, \qquad v_{r_*} = \frac{v_r}{(\alpha/H)\text{Ra}^{1/2}}, \qquad T_* = \frac{T - T_\infty}{q/kH} \tag{12.138}$$

Equations:

$$\frac{\partial v_{r_*}}{\partial r_*} + \frac{v_{r_*}}{r_*} + \frac{\partial v_{z_*}}{\partial z_*} = 0 \tag{12.139a}$$

$$\frac{\partial v_{z_*}}{\partial r_*} = \frac{\partial T_*}{\partial r_*} \tag{12.139b}$$

$$v_{r_*}\frac{\partial T_*}{\partial r_*} + v_{z_*}\frac{\partial T_*}{\partial z_*} = \frac{\partial^2 T_*}{\partial z_*^2} \tag{12.139c}$$

Boundary conditions:

$$v_{r_*} = 0, \qquad \frac{\partial T_*}{\partial r_*} = 0 \qquad \text{at } r_* = 0$$

$$v_{z_*} \to 0, \qquad T_* \to 0 \qquad \text{as } r_* \to \infty \tag{12.140}$$

Integrating eq. (12.139b) subject to the $r_* \to \infty$ boundary conditions, we find that $v_{z_*} = T_*$. Replacing T_* by v_{z_*} in eqs. (12.139c) and (12.140), we

obtain a problem identical to that of the laminar round jet discharging into a constant-pressure reservoir [see the discussion under eq. (9.36)]. We introduce the similarity variable η and streamfunction profile $F(\eta)$ such that

$$\eta = \frac{r_*}{z_*}, \qquad \psi = z_* F(\eta) \tag{12.141}$$

where ψ is the streamfunction

$$v_{r_*} = -\frac{1}{r_*}\frac{\partial \psi}{\partial z_*}, \qquad v_{z_*} = \frac{1}{r_*}\frac{\partial \psi}{\partial r_*} \tag{12.142}$$

Substituting eqs. (12.141) and (12.142) into eq. (12.139c) yields

$$\frac{d}{d\eta}\left(F'' - \frac{F'}{\eta} + \frac{FF'}{\eta}\right) = 0 \tag{12.143}$$

Integrating this result once and invoking the $\eta \to \infty$ condition, we obtain

$$FF' = F' - \eta F'' \tag{12.144}$$

The solution satisfying both eq. (12.144) and boundary conditions (12.140) is

$$F = \frac{(C\eta)^2}{1 + (C\eta/2)^2} \tag{12.145}$$

where constant C is determined from the energy conservation integral

$$q = \int_0^{2\pi}\int_0^\infty \rho c_P v_z (T - T_\infty) r\, dr\, d\theta \tag{12.146}$$

We find that $C = 1/(4\pi^{1/2}) = 0.141$; therefore, the solution is

$$T_* = v_{z_*} = \frac{2C^2}{z_*}\frac{1}{1 + (C\eta/2)^2}$$

$$v_{r_*} = \frac{C}{z_*}\frac{C\eta - \frac{1}{4}(C\eta)^3}{[1 + (C\eta/2)^2]^2}, \qquad \psi = 4z_* \ln\left[1 + \left(\frac{C\eta}{2}\right)^2\right] \tag{12.147}$$

Figure 12.13 shows the traces of the ψ, $T_* = $ constant surfaces in a $\theta = $ constant cut through the point source. The $T_* = $ constant trace has the same shape as the vertical velocity profile v_{z_*}, in accordance with the first of eqs. (12.147). Note further that the flow and temperature field is presented in dimensionless form (in the r_*, z_* domain). Whether or not the actual flow field is *slender* is determined by the slenderness condition $\delta_T/H < O(1)$, which, from eq. (12.137), translates

into $Ra^{1/2} > O(1)$. Therefore, the low-Ra steady-state solution of Ref. 36 coupled with the high-Ra solution presented as eqs. (12.147) and Fig. 12.13 covers the entire Ra range for convection around a point heat source in a saturated porous medium.

12.7   ENCLOSED POROUS MEDIA HEATED FROM THE SIDE

12.7.1   Four Heat Transfer Regimes

As in the study of natural convection in enclosed spaces filled with fluid (Chapter 5), we begin with the time and length scales of the flow in a porous layer heated from the side [37]. The system is shown in Fig. 12.14: A two-dimensional rectangular space of height H and horizontal dimension L is filled with a fluid-saturated porous medium of permeability K. In accordance with the homogeneous porous medium model, the equations governing the conservation of mass, momentum, and energy are

$$\frac{\partial u}{\partial x} + \frac{\partial v}{\partial y} = 0 \tag{12.148}$$

$$u = -\frac{K}{\mu}\frac{\partial P}{\partial x}, \qquad v = -\frac{K}{\mu}\left(\frac{\partial P}{\partial y} + \rho g\right) \tag{12.149}$$

$$\sigma\frac{\partial T}{\partial t} + u\frac{\partial T}{\partial x} + v\frac{\partial T}{\partial y} = \alpha\left(\frac{\partial^2 T}{\partial x^2} + \frac{\partial^2 T}{\partial y^2}\right) \tag{12.150}$$
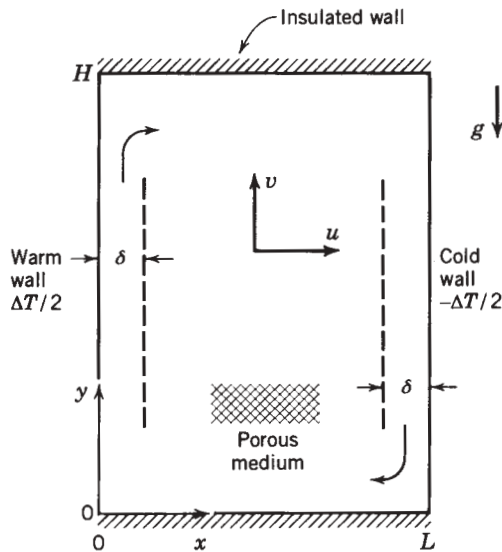
Figure 12.14   Enclosure filled with a porous medium and heated from the side.

It is convenient to eliminate the pressure P between eqs. (12.149) and to introduce the Boussinesq approximation $\rho = \rho_0[1 - \beta(T - T_0)]$ in the body force term. We obtain a single momentum conservation statement

$$\frac{\partial u}{\partial y} - \frac{\partial v}{\partial x} = -\frac{Kg\beta}{\nu}\frac{\partial T}{\partial x} \tag{12.151}$$

Initially, the porous layer is isothermal ($T = 0$) and the fluid is motionless ($u = v = 0$). At the time $t = 0$, the vertical wall temperatures are instantly changed to $+\Delta T/2$ and $-\Delta T/2$, respectively. We study the evolution of the flow through the porous layer, subject to the boundary conditions

$$
\begin{aligned}
u = 0, \quad & T = \Delta T/2 && \text{at } x = 0 \\
u = 0, \quad & T = -\Delta T/2 && \text{at } x = L \\
v = 0, \quad & \frac{\partial T}{\partial y} = 0 && \text{at } y = 0, H
\end{aligned}
\tag{12.152}
$$

These conditions account for the impermeability of the rectangular frame and for the fact that the two horizontal walls are insulated.

Since the fluid is initially motionless, the vertical wall effect first propagates into the porous space through pure conduction. Equation (12.150) dictates a balance between thermal inertia and heat conduction in the layer $\delta(t)$,

$$\sigma\frac{\Delta T}{t} \sim \alpha\frac{\Delta T}{\delta^2} \tag{12.153}$$

Hence

$$\delta \sim (\alpha t/\sigma)^{1/2} \tag{12.154}$$

The growth of the δ layer gives rise to a horizontal temperature gradient of order $\partial T/\partial x \sim \Delta T/\delta$. This development makes the buoyancy term in the momentum equation finite: The scales of the three terms in eq. (12.151) are

$$\frac{u}{H}, \qquad \frac{v}{\delta}, \qquad \frac{Kg\beta}{\nu}\frac{\Delta T}{\delta} \tag{12.155}$$

Noting that mass conservation requires $u/\delta \sim v/H$, we conclude that $(u/H)/(v/\delta) \sim (\delta/H)^2$. Therefore, if the vertical layer is slender ($\delta < H$), the momentum equation dictates a balance between the second and third terms in expression (12.155); the result of this balance is the vertical velocity scale in the vicinity of each vertical wall,

$$v \sim \frac{Kg\beta}{\nu}\Delta T \tag{12.156}$$

This scale is time independent. However, in view of the earlier result for $\delta(t)$ [eq. (12.154)], the flow rate driven by the heated wall ($v\delta$) increases in time as $t^{1/2}$.

Once fluid motion is initiated, the energy equation (12.150) is ruled by three different scales,

$$\underset{\substack{\text{Inertia} \\ t^{-1}}}{\sigma \frac{\Delta T}{t}}, \qquad \underset{\substack{\text{Convection} \\ t^0}}{v \frac{\Delta T}{H}}, \qquad \underset{\substack{\text{Conduction} \\ t^{-1}}}{\alpha \frac{\Delta T}{\delta^2}} \qquad (12.157)$$

Below each scale we see the evolution of each effect in time. Because conduction from the wall will always be present, the convection effect eventually takes the place of inertia in the energy balance. The time t_f when the vertical layer becomes convective is given by the balance $\sigma \Delta T/t_f \sim v \Delta T/H$, hence

$$t_f \sim \frac{\sigma H}{v} \qquad (12.158)$$

Beyond this point, the boundary layer thickness ceases to grow: its steady-state scale is

$$\delta_f \sim H \, \text{Ra}_H^{-1/2} \qquad (12.159)$$

where Ra_H is the Darcy-modified Rayleigh number based on height,

$$\text{Ra}_H = (Kg \, \beta H \, \Delta T)/\alpha v \qquad (12.160)$$

The necessary condition for the existence of distinct vertical boundary layers in the steady state is $\delta_f < L$; in other words,

$$\frac{L}{H} \, \text{Ra}_H^{1/2} > 1 \qquad (12.161)$$

This condition is plotted on the $H/L - \text{Ra}_H$ field of Fig. 12.15.

The flow scales reported as eqs. (12.156) and (12.159) can be used to predict the existence of distinct horizontal layers along the horizontal adiabatic walls (Fig. 12.14). The volumetric flow rate driven horizontally in counterflow is of order $v\delta_f$. This stream carries enthalpy between the two vertical walls at the rate

$$\underset{\substack{\text{left} \to \text{right} \\ (\text{Fig.12.14})}}{q'_{\text{convection}}} \sim v\delta_f(\rho c_P)_f \, \Delta T \qquad (12.162)$$

The two branches of this horizontal counterflow experience heat transfer by thermal diffusion at a rate

$$\underset{\substack{\text{top} \to \text{bottom} \\ (\text{Fig.12.14})}}{q'_{\text{conduction}}} \sim kL\frac{\Delta T}{H} \qquad (12.163)$$
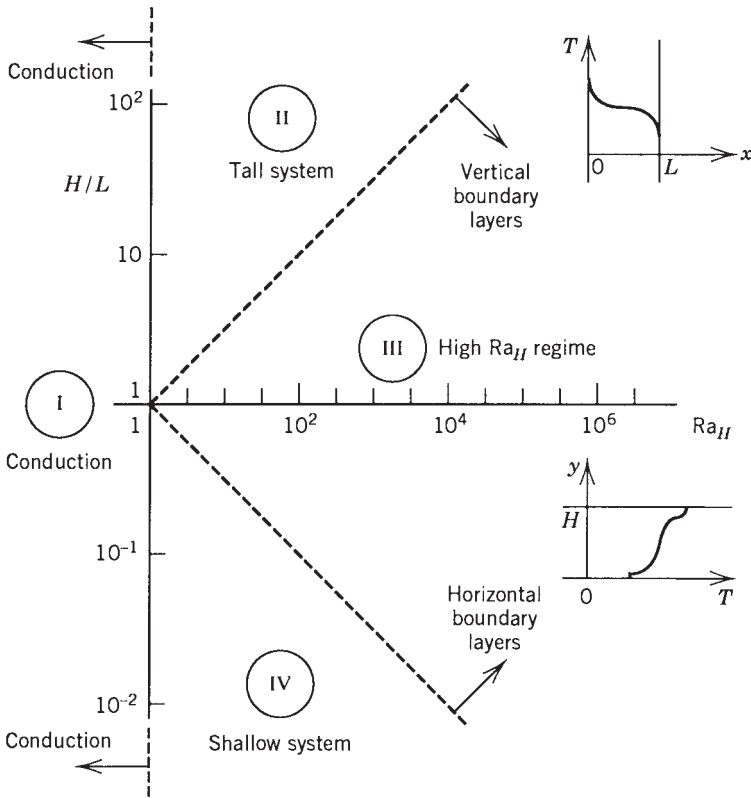
Figure 12.15   Heat transfer regimes for natural convection in a porous layer heated from the side. Compare with Fig. 5.3.

As in a poorly designed counterflow heat exchanger, one stream will travel the entire length of the porous layer (L) without a significant change in temperature when the vertical conduction rate (12.163) is negligible relative to the horizontal convection rate (12.162),

$$kL\frac{\Delta T}{H} < v\delta_f(\rho c_P)_f \, \Delta T \tag{12.164}$$

Therefore, the criterion for distinct horizontal layers is

$$\frac{H}{L}\mathrm{Ra}_H^{1/2} > 1 \tag{12.165}$$

Figure 12.15 shows the four natural convection regimes possible in a porous layer heated from the side. These regimes are analogous to regimes I–IV present in fluid-filled cavities heated from the side, Fig. 5.4. Of interest is the net heat

transfer rate q' across the overall ΔT. The results of this section reveal the following heat transfer rate scales:

$$\begin{array}{lll}
\text{(I) Pure conduction} & q' \sim (kH\,\Delta T)/L & \\
\text{(II) Tall layers} & q' \gtrsim (kH\,\Delta T)/L & \\
\text{(III) High-Ra}_H \text{ convection} & q' \sim (kH\,\Delta T)/\delta_f & \\
\text{(IV) Shallow layers} & q' \gtrsim (kH\,\Delta T)/\delta_f &
\end{array} \tag{12.166}$$

In the following section we focus on regimes III and IV, where the heat transfer rate is dominated by convection.

12.7.2 Convection Results

Considerable analytical, numerical, and experimental work has been done to estimate more accurately the overall heat transfer rate q', or the overall Nusselt number

$$\text{Nu} = \frac{q'}{kH(T_h - T_c)/L} \tag{12.167}$$

where $T_h - T_c = \Delta T$ is the side-to-side temperature difference. Unlike the single-wall configurations of Section 12.6, in confined layers of thickness L the Nusselt number is defined as the ratio (actual heat transfer rate)/(pure conduction heat transfer rate). An analytical solution that covers smoothly the four heat transfer regimes was developed by Bejan and Tien [38]:

$$\text{Nu} = K_1 + \frac{1}{120} K_1^3 \left(\text{Ra}_H \frac{H}{L} \right)^2 \tag{12.168}$$

where the function $K_1(H/L, \text{Ra}_H)$ is obtained by eliminating δ_e (i.e., the ratio end region thickness/H) from the system:

$$\frac{1}{120} \delta_e \, \text{Ra}_H^2 \, K_1^3 \left(\frac{H}{L} \right)^3 = 1 - K_1 = \frac{1}{2} K_1 \frac{H}{L} \left(\frac{1}{\delta_e} - \delta_e \right) \tag{12.169}$$

This result is displayed in Fig. 12.16, along with numerical results reported by Hickox and Gartling [39]. The two asymptotes of this solution are

$$\text{Nu} \sim 0.508 \frac{L}{H} \text{Ra}_H^{1/2} \qquad \text{as } \text{Ra}_H \to \infty \tag{12.170}$$

$$\text{Nu} \sim 1 + \frac{1}{120} \left(\text{Ra}_H \frac{H}{L} \right)^2 \qquad \text{as } \frac{H}{L} \to 0 \tag{12.171}$$
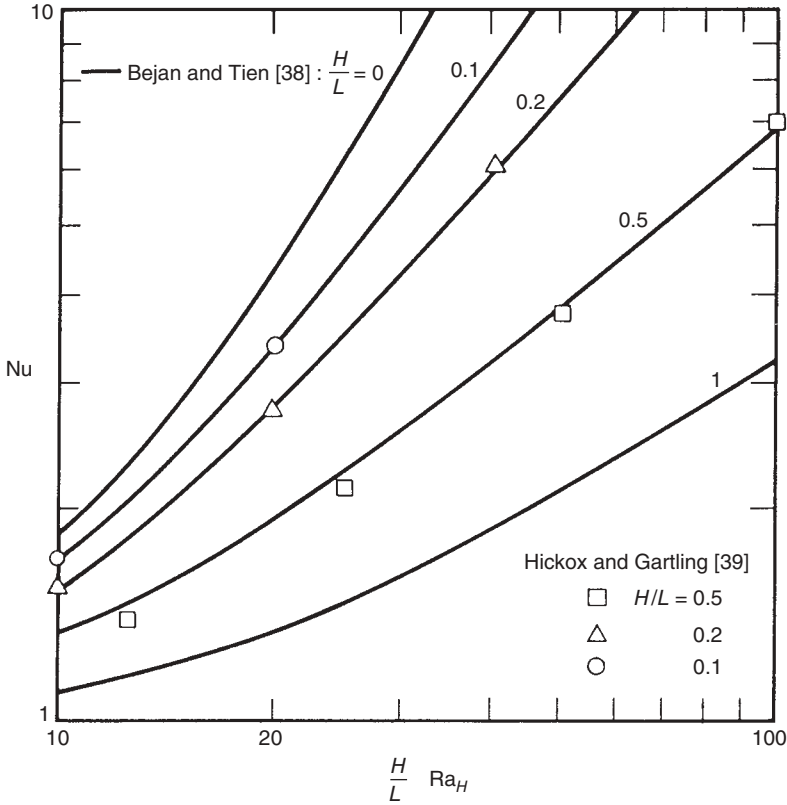
Figure 12.16   Rate of heat transfer through a porous layer heated from the side. (From Ref. 38.)

The heat transfer in the convection-dominated regime III is represented well by eq. (12.170) or by alternative results reported specifically for the high–Rayleigh number regime: Weber [40] obtained $Nu = 0.577(L/H)\,Ra_H^{1/2}$; this formula overestimates by roughly 14 percent experimental and numerical data from three sources (see the first edition of this book, p. 398). A more refined theory for regime III was proposed in Ref. 41, where the constant that appears in $Nu \sim (L/H)Ra_H^{1/2}$ is replaced by a weak function of both H/L and Ra_H. For calculations involving heat transfer dominated by convection, Fig. 12.16 is recommended for shallow layers and eq. (12.170) for regime III, $Ra_H^{-1/2} < H/L < Ra_H^{1/2}$.

Another model for heat transfer in the configuration of Fig. 12.14 is the case where the heat flux q'' is distributed uniformly along the two vertical sides of the porous layer. In the high–Rayleigh number regime (regime III), the overall heat transfer rate is given by [42]

$$Nu = \frac{1}{2}\left(\frac{L}{H}\right)^{4/5} Ra_{*H}^{2/5} \tag{12.172}$$

where $\mathrm{Ra}_{*H} = Kg\beta H^2 q''/\alpha vk$. The overall Nusselt number is defined as in eq. (12.167), where $T_h - T_c$ is now the height-averaged temperature difference between the two sides of the rectangular cross section. The result (12.172) holds in the high–Rayleigh number regime $\mathrm{Ra}_{*H}^{-1/3} < H/L < \mathrm{Ra}_{*H}^{1/3}$. Convection results for many other configurations of enclosed porous media can be found in Refs. 2 and 3.

12.8   PENETRATIVE CONVECTION

A separate class of buoyancy-driven flows through porous media is defined by the interaction of finite-size porous layers with neighboring heat reservoirs. This can be modeled as a two-dimensional layer of size $H \times L$, with three sides at one temperature. The fourth side is permeable and in communication with a reservoir (fluid, or porous, medium) of different temperature. We focus on two orientations of this configuration, a shallow layer with lateral heating (Fig. 12.17a) and a tall layer with heating from below or cooling from above (Fig. 12.17b). In both cases, natural convection penetrates the porous medium over a length dictated by the Rayleigh number alone and not by the geometric ratio H/L.

12.8.1   Lateral Penetration

To determine the scale of the lateral penetration length L_x, consider the governing equations (12.148), (12.150), and (12.151):

$$Mass: \quad \frac{u}{L_x} \sim \frac{v}{H} \qquad (12.173)$$
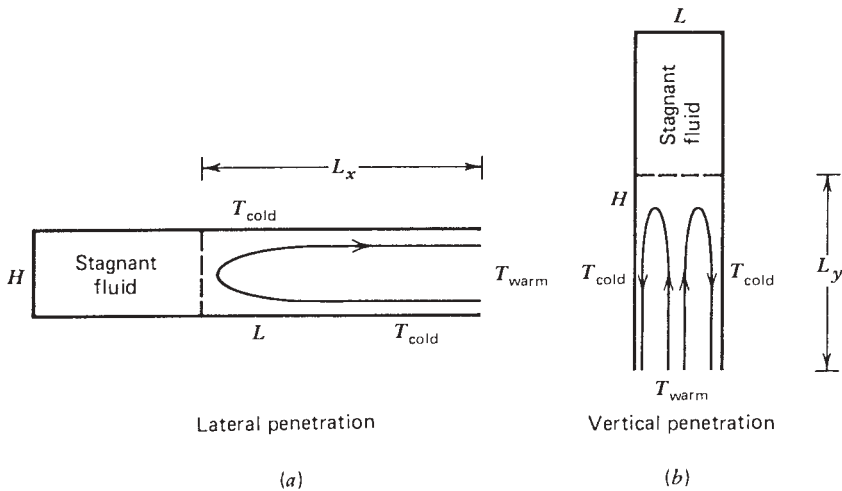
Figure 12.17   (a) Lateral and (b) vertical penetration of natural convection in a porous space heated from one end.

$$\textit{Energy}: \quad u\frac{\Delta T}{L_x} \sim \alpha\frac{\Delta T}{L_x^2}, \alpha\frac{\Delta T}{H^2} \qquad (12.174)$$

$$\textit{Momentum}: \quad \frac{u}{H}, \frac{v}{L_x} \sim \frac{kg\beta}{v}\frac{\Delta T}{L_x} \qquad (12.175)$$

Above, we have three equations for the three unknown scales u, v, and L_x. Assuming that the penetration is such that $L_x > H$, we obtain

$$L_x \sim H\,\mathrm{Ra}_H^{1/2} \qquad (12.176)$$

The convective heat transport between the isothermal porous layer and the heat reservoir positioned laterally scales as

$$q' \sim (\rho c_P)_f Hu\,\Delta T \sim k\,\Delta T\,\mathrm{Ra}_H^{1/2} \qquad (12.177)$$

This result shows that the actual length of the porous layer (L) does not influence the heat transfer rate; q' and L_x are set by the Rayleigh number Ra_H.

The flow and temperature patterns associated with the lateral penetration phenomenon have been determined analytically as a similarity solution [43]. The penetration length and heat transfer rate predicted by the similarity solution are $L_x = 0.158H\,\mathrm{Ra}_H^{1/2}$ and $q'/(k\Delta T) = 0.319\mathrm{Ra}_H^{1/2}$. Reference 43 also documents the effect of anisotropy in the medium and the effect of temperature variation along the horizontal walls of the porous layer.

12.8.2 Vertical Penetration

Consider the two-dimensional layer of Fig. 12.17b, where the bottom wall is permeable and in communication with a different reservoir. We learn in the next section that in porous layers heated from below (or cooled from above), fluid motion is possible only above a critical Rayleigh number. In Fig. 12.17b, however, fluid motion will set in as soon as a ΔT is imposed between the bottom surface and vertical walls. Fluid motion will be present because no matter how small the ΔT, the porous medium experiences a finite-temperature gradient of order $\Delta T/L$ in the *horizontal direction* near the heated wall [see eq. (12.151)].

Let L_y be the distance of vertical penetration. From eqs. (12.148), (12.150), and (12.151), we have the following balances:

$$\textit{Mass}: \quad \frac{u}{L} \sim \frac{v}{L_y} \qquad (12.178)$$

$$\textit{Energy}: \quad u\frac{\Delta T}{L} \sim \alpha\frac{\Delta T}{L^2}, \alpha\frac{\Delta T}{L_y^2} \qquad (12.179)$$

$$\textit{Momentum}: \quad \frac{u}{L_y}, \frac{v}{L} \sim \frac{kg\beta}{v}\frac{\Delta T}{L} \qquad (12.180)$$

Assuming vertical penetration over a distance L_y greater than L, we find

$$L_y \sim L\,\mathrm{Ra}_L \tag{12.181}$$

where Ra_L is the Rayleigh number based on L, $\mathrm{Ra}_L = (Kg\beta L\Delta T)/\alpha\nu$. The net heat transfer rate through the bottom wall of the system scales as

$$q_y' \sim (\rho c_P)_f\,Lv\,\Delta T \sim k\,\Delta T\,\mathrm{Ra}_L \tag{12.182}$$

Both L_y and q_y' are proportional to Ra_L, unlike the corresponding quantities in the case of lateral penetration, which are proportional to $\mathrm{Ra}_H^{1/2}$. Once again, the imposed temperature difference (ΔT) and the transversal dimension of the layer (L) determine the longitudinal extent (L_y) of the penetrative flow. The physical height of the porous layer (H) does not influence the phenomenon as long as it is greater than L_y.

The phenomenon of partial vertical penetration was also studied in the cylindrical geometry [44]. The vertical penetration length and net heat transfer rate are $L_y/r_0 = 0.0847\mathrm{Ra}_{r_0}$ and $q_y'/(r_0 k\,\Delta T) = 0.255\mathrm{Ra}_{r_0}$, where $\mathrm{Ra}_{r_0} = (Kg\beta r_0\,\Delta T)/\alpha\nu$ is the Rayleigh number based on the dimension perpendicular to the penetrative flow (the cylindrical well radius, r_0).

12.9 ENCLOSED POROUS MEDIA HEATED FROM BELOW

12.9.1 Onset of Convection

We now consider the Bénard-type flow, that is, the cellular convection that *may* take place through a porous layer heated from below and cooled from above, Fig. 12.18. We look at an infinite horizontal layer of thickness H with a warm bottom (T_0) and a cold top ($T_0 - \Delta T$). The steady-state version of the transient equations (12.148), (12.150), and (12.151) admits the no-flow (pure conduction) solution

$$u_b = v_b = 0$$

$$T_b = T_0 - \Delta T\frac{y}{H} \tag{12.183}$$
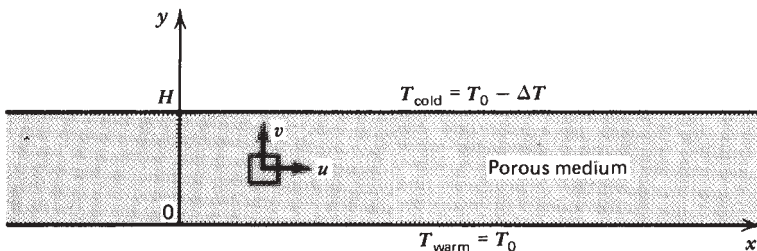
Figure 12.18 Two-dimensional porous layer heated from below.

The question is whether this no-flow solution will prevail forever, regardless of how high a ΔT we impose. We answer this question by running a stability experiment of the type described in Chapter 6 in connection with the laminar–turbulent flow transition. The stability experiment consists of disturbing the base solution (12.183) and observing under what conditions the imposed disturbance grows in amplitude. Thus, we substitute

$$
\begin{array}{rclcl}
T(x, y, t) & = & T_b(y) & + & T'\,(x, y, t) \\
u(x, y, t) & = & 0+ & & u'\,(x, y, t) \\
v(x, y, t) & = & 0+ & & v'\,(x, y, t)
\end{array}
\qquad (12.184)
$$

$$
\underbrace{\hphantom{T(x, y, t)}}_{\substack{\text{Transient} \\ \text{flow}}} \qquad \underbrace{\hphantom{0+}}_{\substack{\text{Base} \\ \text{solution}}} \qquad \underbrace{\hphantom{T'(x,y,t)}}_{\text{Disturbance}}
$$

into the transient governing equations. We obtain

$$
\frac{\partial u'}{\partial x} + \frac{\partial v'}{\partial y} = 0
\qquad (12.185)
$$

$$
\sigma \frac{\partial T'}{\partial t} + u' \frac{\partial T'}{\partial x} + v' \left(\frac{dT_b}{dy} + \frac{\partial T'}{\partial y} \right) = \alpha \left(\frac{\partial^2 T'}{\partial x^2} + \frac{\partial^2 T'}{\partial y^2} \right)
\qquad (12.186)
$$

$$
\frac{\partial u'}{\partial y} - \frac{\partial v'}{\partial x} = -\frac{Kg\beta}{\nu} \frac{\partial T'}{\partial x}
\qquad (12.187)
$$

In the energy equation (12.186), we eliminate the nonlinear terms $u'\partial T'/\partial x$ and $v'\partial T'/\partial y$ based on the assumption that in the very beginning, the flow and temperature disturbances are negligibly small. Thus, we retain only the first-order terms in primed (disturbance) quantities,

$$
\sigma \frac{\partial T'}{\partial t} - \frac{\Delta T}{H} v' = \alpha \left(\frac{\partial^2 T'}{\partial x^2} + \frac{\partial^2 T'}{\partial y^2} \right)
\qquad (12.188)
$$

To nondimensionalize the problem we introduce the variables

$$
\hat{x} = x/H, \quad \hat{y} = y/H
$$

$$
\hat{u} = \frac{u'}{\alpha/H}, \quad \hat{v} = \frac{v'}{\alpha/H}
\qquad (12.189)
$$

$$
\hat{T} = T'/\Delta T, \quad \hat{t} = \alpha t/H^2 \sigma
$$

The mass, momentum, and energy equations become

$$
\frac{\partial \hat{u}}{\partial \hat{x}} + \frac{\partial \hat{v}}{\partial \hat{y}} = 0
\qquad (12.190)
$$

$$
\frac{\partial \hat{u}}{\partial \hat{y}} - \frac{\partial \hat{v}}{\partial \hat{x}} = -\mathrm{Ra}_H \frac{\partial \hat{T}}{\partial \hat{x}}
\qquad (12.191)
$$

$$\frac{\partial \hat{T}}{\partial \hat{t}} - \hat{v} = \frac{\partial^2 \hat{T}}{\partial \hat{x}^2} + \frac{\partial^2 \hat{T}}{\partial \hat{y}^2} \tag{12.192}$$

The horizontal velocity $\hat{u}$ is eliminated by cross-differentiating between eqs. (12.190) and (12.191), leading to

$$\frac{\partial^2 \hat{v}}{\partial \hat{x}^2} + \frac{\partial^2 \hat{v}}{\partial \hat{y}^2} = \mathrm{Ra}_H \frac{\partial^2 \hat{T}}{\partial \hat{x}^2} \tag{12.193}$$

Equations (12.192) and (12.193) must be solved subject to the following isothermal impermeable wall conditions:

$$\hat{v} = \hat{T} = 0 \quad \text{at } \hat{y} = 0, 1 \tag{12.194}$$

The initial condition to this transient problem is arbitrary; however, inspired by visual observations of Bénard cells, i.e., based on empiricism, it makes sense to *assume* sinusoidal variation in $\hat{x}$ and exponential variation in $\hat{t}$,

$$\hat{T} = \theta(\hat{y})e^{p\hat{t}+i\alpha\hat{x}}, \qquad \hat{v} = V(\hat{y})e^{p\hat{t}+i\alpha\hat{x}} \tag{12.195}$$

This assumption transforms the $(\hat{T}, \hat{v})$ problem into one of determining the $\hat{y}$-profiles θ and V subject to

$$\textit{Momentum}: \quad -\alpha^2 V + V'' = -\alpha^2 \, \mathrm{Ra}_H \theta \tag{12.196}$$

$$\textit{Energy}: \quad p\theta - V = -\alpha^2 \theta + \theta'' \tag{12.197}$$

$$\textit{Boundary conditions}: \quad \theta = V = 0 \quad \text{at } \hat{y} = 0, 1 \tag{12.198}$$

Finally, we zero in on the condition of *neutral stability* ($p = 0$), and eliminating $V(y)$ between eqs. (12.196) and (12.197), we obtain

$$\theta^{\mathrm{IV}} - 2\alpha^2 \theta'' + \alpha^4 \theta = \alpha^2 \, \mathrm{Ra}_H \, \theta \tag{12.199}$$

This equation admits solutions of the form

$$\theta = C \, \sin(n\pi\hat{y}) \tag{12.200}$$

where C is an arbitrary constant and n is an integer so that the boundary conditions (12.198) are satisfied. Combining eqs. (12.200) and (12.199), we learn that the assumed flow is neutrally stable when

$$\mathrm{Ra}_H = \frac{(n^2\pi^2 + \alpha^2)^2}{\alpha^2} \tag{12.201}$$
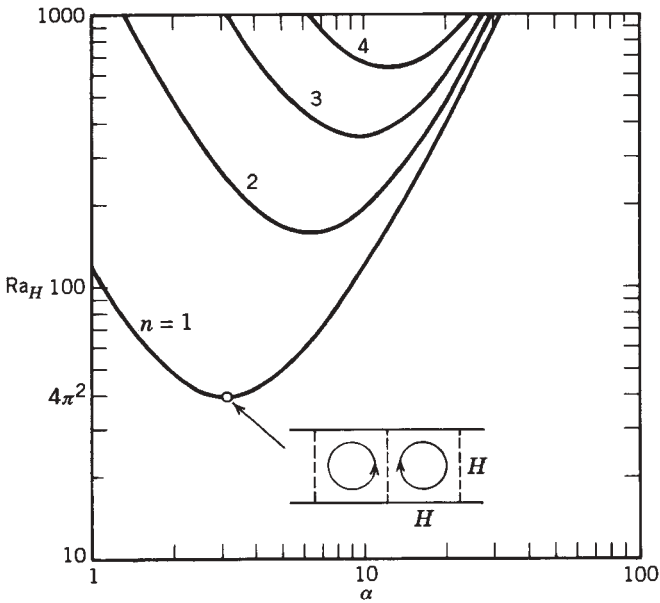
Figure 12.19   Rayleigh number for neutrally stable cellular convection in a porous layer heated from below.

This result says that the assumed disturbance (n, α) is likely to exist, neither growing nor decaying, if the Rayleigh number is as high as in eq. (12.201). Figure 12.19 shows the dependence of Ra_H on both α and n. As Ra_H increases above zero, the first chance of convective heat transfer materializes at $n = 1$ and $\partial Ra_H / \partial \alpha = 0$, that is, when

$$Ra_H = 4\pi^2 = 39.5 \qquad (n = 1, \ \alpha = \pi) \qquad (12.202)$$

As shown in Fig. 12.19, the disturbance $(n = 1, \ \alpha = \pi)$ represents rolls with square cross sections, that is, "square" rolls whose horizontal dimension is equal to the porous layer thickness H. In place of eq. (12.202), constructal theory and the intersection-of-asymptotes method [28,45,46] predict much more directly square rolls with the critical Rayleigh number $Ra_H = 12\pi = 37.7$.

Result (12.202) implies that only for Rayleigh numbers less than approximately 40 is the heat transfer rate accurately predicted by the pure conduction estimate. For Rayleigh numbers much larger than 40, we are forced to rely on experimental and numerical measurements. Figure 12.20 shows Cheng's [47] compilation of time-average Nusselt number measurements reported by nine independent investigators (the references are available in previous editions of this book). Figure 12.20 is perhaps the best tool to use in engineering calculations;
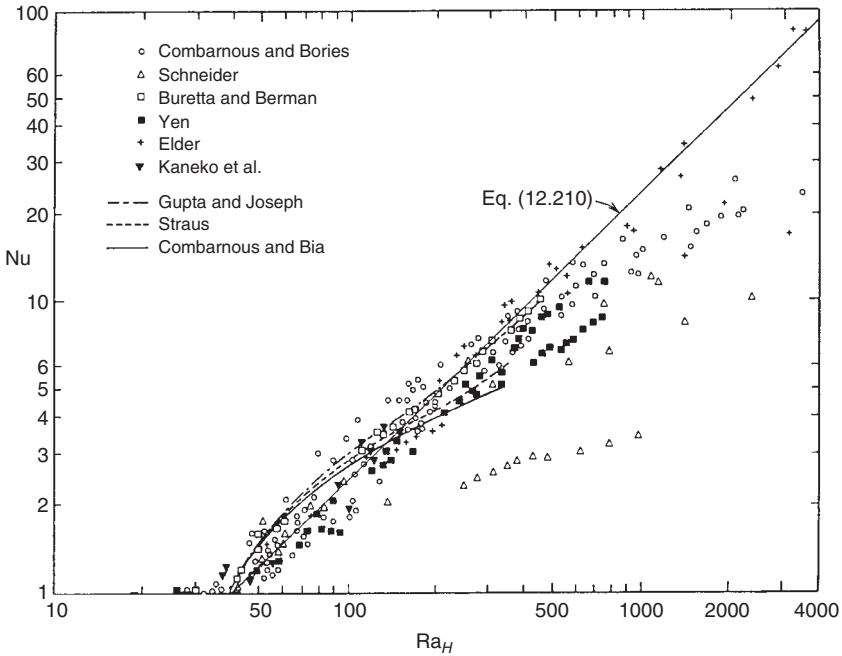
Figure 12.20   Heat transfer measurements in a porous layer heated from below. (Reprinted with permission from P. Cheng, *Adv. Heat Transfer*, Vol. 14, pp. 1–105, 1978. Copyright © 1978 Academic Press).

it shows that above $Ra_H \sim 40$, the conduction-referenced Nusselt number

$$Nu = \frac{q''}{(k\,\Delta T)/H} \tag{12.203}$$

is a strong function of the Rayleigh number and that there is considerable scatter in the data.

12.9.2   Darcy Flow

The slope of the log Nu–log Ra_H curve for $Ra_H > 40$ can be predicted on the basis of a pure scaling argument. Think of a convection-dominated regime made up of rising warm plumes coexisting with descending cold plumes. Let L (unknown) be the thickness of each plume, that is, the horizontal extent of an elementary cell (Fig. 12.21). Let δ_H be the thermal boundary layer thickness across which the bottom–top ΔT takes place. Note that in the convection-dominated regime, the scale of $\partial T/\partial y$ is not $\Delta T/H$; it is $\Delta T/\delta_H$, with δ_H unknown. The cellular flow model contains two building blocks:

1. *Core region*: a vertical counterflow of length H and thickness L
2. *End regions*: two identical boundary layers of length L and thickness δ_H
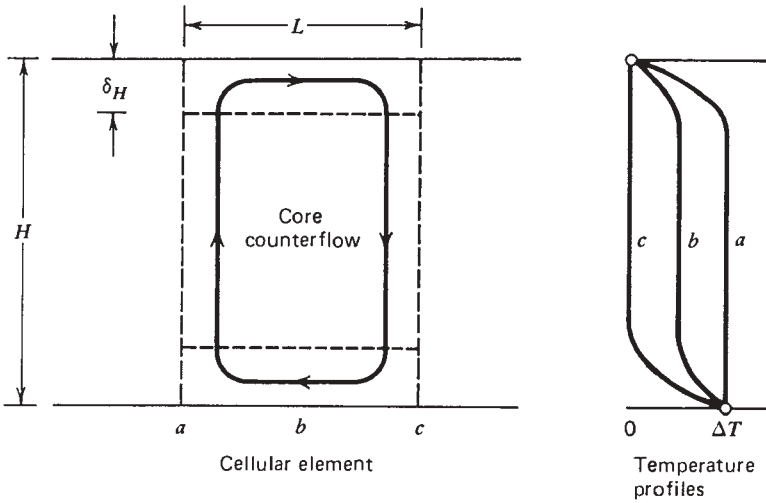
Figure 12.21 Cellular convection model for determining the scales of the convection regime in a porous layer heated from below.

Invoking the conservation principles in the core region, we write

$$\text{Momentum balance (Darcy)}: \quad \frac{v}{L} \sim \frac{Kg\beta}{v}\frac{\Delta T}{L} \tag{12.204}$$

$$\text{Energy balance}: \quad v\frac{\Delta T}{H} \sim \alpha\frac{\Delta T}{L^2} \tag{12.205}$$

$$\text{Results}: \quad L \sim H\,\text{Ra}_H^{-1/2} \tag{12.206}$$

$$v \sim (Kg\beta\,\Delta T)/v \tag{12.207}$$

A relationship for δ_H is obtained by stating that the enthalpy flow vertically through the core must match the heat conducted vertically through the end region, $\rho v L c_P\,\Delta T \sim (kL\,\Delta T)/\delta_H$, or

$$\delta_H \sim H\,\text{Ra}_H^{-1} \tag{12.208}$$

Therefore, in the convection-dominated regime with Darcy flow, the Nusselt number scales as

$$\text{Nu} = \frac{\text{actual heat transfer}}{\text{pure conductoin}} \sim \frac{(kL\,\Delta T)/\delta_H}{(kL\,\Delta T)/H} \sim \frac{H}{\delta_H} \sim \text{Ra}_H \tag{12.209}$$

This means that in Fig. 12.20, the initial slope of the log Nu–log Ra_H curve in the convective domain must be 1; this result is confirmed by the bulk of the heat

transfer measurements, and an adequate correlation is

$$
\text{Nu} = \begin{cases} 1 & \text{if } \text{Ra}_H < 40 \\ \frac{1}{40} \, \text{Ra}_H & \text{if } \text{Ra}_H > 40 \text{ (Darcy)} \end{cases} \tag{12.210}
$$

12.9.3 Forchheimer Flow

Wang and Bejan [48] showed that the deviation of experimental data from eq. (12.210) in Fig. 12.20 is due to inertial effects (i.e., the transition from Darcy flow to Forchheimer flow). They repeated the analysis based on the cellular model of Fig. 12.21 by using a momentum balance between inertia and buoyancy:

$$
\textit{Momentum balance (Forchheimer)}: \quad \frac{Kbv^2}{\nu L} \sim \frac{Kg\beta}{\nu} \frac{\Delta T}{L} \tag{12.211}
$$

The origin of the inertia scale on the left side of eq. (12.211) can be seen by comparing it with the Darcy scale of eq. (12.204) and with the two terms on the right side of eq. (12.15). Combining eqs. (12.211) and (12.205) yields

$$
L \sim H \left(\frac{\alpha^2 b}{g\beta \, \Delta T} \right)^{1/4} \tag{12.212}
$$

$$
v \sim \left(\frac{g\beta \, \Delta T}{b} \right)^{1/2} \tag{12.213}
$$

The continuity of energy from the core counterflow to the horizontal boundary layers, $\rho v L c_P \, \Delta T \sim (kL\Delta T)/\delta_H$, requires

$$
\delta_H \sim \alpha \left(\frac{b}{g\beta \, \Delta T} \right)^{1/2} \tag{12.214}
$$

The overall Nusselt number in Forchheimer flow must scale as (Fig. 12.22)

$$
\text{Nu} \sim \frac{H}{\delta_H} \sim (\text{Ra}_H \, \text{Pr}_p)^{1/2} \tag{12.215}
$$

where Pr_p is the new dimensionless group called *the porous medium Prandtl number* [49,50],

$$
\text{Pr}_p = \frac{\nu}{\alpha} \frac{H}{bK} \tag{12.216}
$$

The transition from Darcy flow to Forchheimer flow occurs at the intersection of eqs. (12.209) and (12.215),

$$
\text{Ra}_H \sim \text{Pr}_p \tag{12.217}
$$
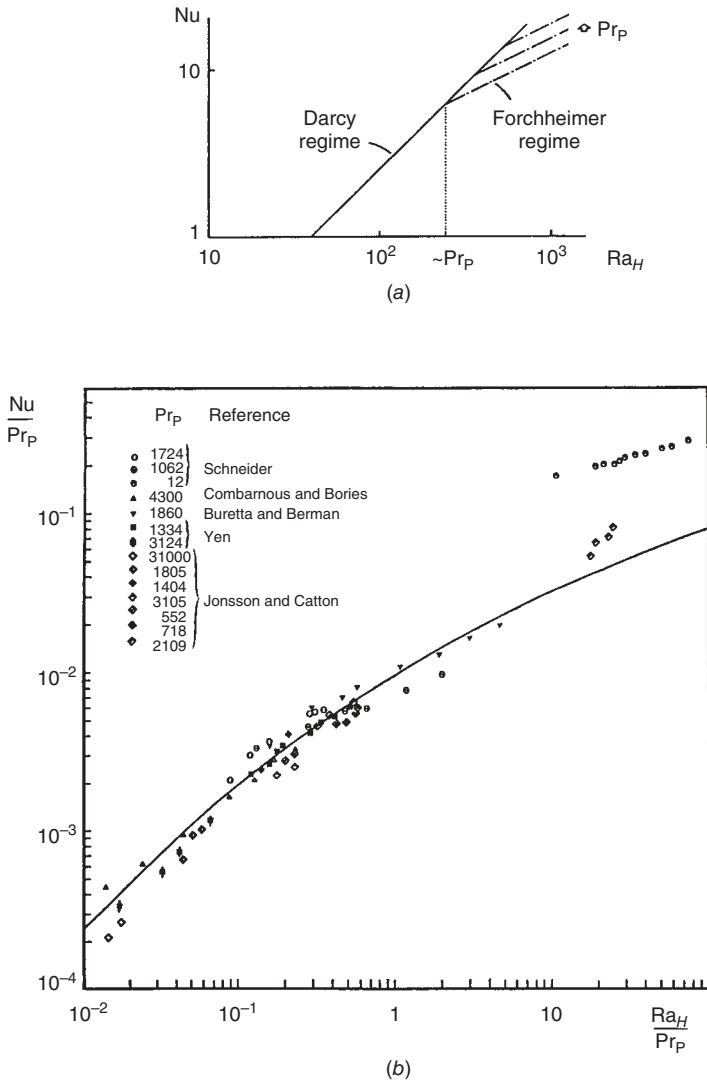
Figure 12.22 (a) Asymptotes of the function $\mathrm{Nu}(\mathrm{Ra}_H, \mathrm{Pr}_p)$ suggested by scale analysis; (b) heat transfer measurements in a horizontal layer heated from below. (From Ref. 48.)

from which we deduce

$$\frac{\mathrm{Nu}}{\mathrm{Pr}_p} \sim \frac{1}{40} \frac{\mathrm{Ra}_H}{\mathrm{Pr}_p}, \quad 40 < \mathrm{Ra}_H < \mathrm{Pr}_p \tag{12.218}$$

$$\frac{\mathrm{Nu}}{\mathrm{Pr}_p} \sim \left(\frac{\mathrm{Ra}_H}{\mathrm{Pr}_p}\right)^{1/2}, \quad \mathrm{Ra}_H > \mathrm{Pr}_p \tag{12.219}$$

An important feature of eqs. (12.218) and (12.219) is that they are both of the form $\mathrm{Nu}/\mathrm{Pr}_p = f(\mathrm{Ra}_H/\mathrm{Pr}_p)$. This motivates the plotting of $\mathrm{Nu}/\mathrm{Pr}_p$ against $\mathrm{Ra}_H/\mathrm{Pr}_p$ to produce the graph shown in Fig. 12.22b. The agreement is surprisingly good with the notable exception of Schneider's [51] data for $\mathrm{Pr}_p = 12$ in the top-right corner of the figure. A line through this subset of data has the correct slope but is clearly too high, and possibly the deduced Pr_p value of 12 is not correct [2]. With this subset ignored, Wang and Bejan [48] obtained the correlation

$$\mathrm{Nu} = \left\{ \left(\frac{\mathrm{Ra}}{40} \right)^n + [c(\mathrm{Ra}\,\mathrm{Pr}_p)^{1/2}]^n \right\}^{1/n} \tag{12.220}$$

where n and c are two empirical constants, $n = -1.65$ and $c = 1896$.

12.10   MULTIPLE FLOW SCALES DISTRIBUTED NONUNIFORMLY

In this section we bring together several of the main threads followed in this book: Convection in fluids vs. convection in porous media, constructal design of flow architecture, and the design of multiple scales and optimized complexity. We find that in the pursuit of greater heat transfer density, the design acquires multiple length scales that are distributed nonuniformly through the working volume. The flow and its length scales are intelligently *maldistributed* [3,50].

Smaller and smaller flow passages are placed in all the tiny spaces that can be forced to perform better, to contribute more to the global enterprise. As in the alveolus of the lung, when flow passages are small enough, the heat transfer mechanism of convection is replaced by conduction (diffusion) across the fluid. In the direction of decreasing scales, the flow structure becomes a *designed porous medium* [3].

The emergence of flow structures with multiple length scales that are distributed nonuniformly is well illustrated in the development of tree-shaped convective flows (cf. Section 3.9). Tree-shaped structures are unlike the classical structures of heat transfer and heat exchanger design. The classical structures have very small numbers of length scales (usually one or two), which are distributed uniformly through the flow system (e.g., parallel plates, bundles of cylinders in cross flow).

There we illustrate the development of multiscale structures for maximal heat transfer density by focusing on a constructal design: the existence of spacings in any convective heat transfer structure (cf. Sections 3.6 and 4.12). In Fig. 3.17, the optimal parallel-plate spacing has a single value. This length scale is distributed uniformly through the flow volume. Is the stack of Fig. 3.17 the best way to pack heat transfer into a fixed volume?

Bejan and Fautrelle [52] showed that structures such as Fig. 3.17 can be improved if more length scales $(D_0, D_1, D_2, \dots)$ are available. Improvement comes from more freedom. The technique consists of placing more heat transfer in regions of the volume HL_0 where the boundary layers are thinner (Fig. 12.23).
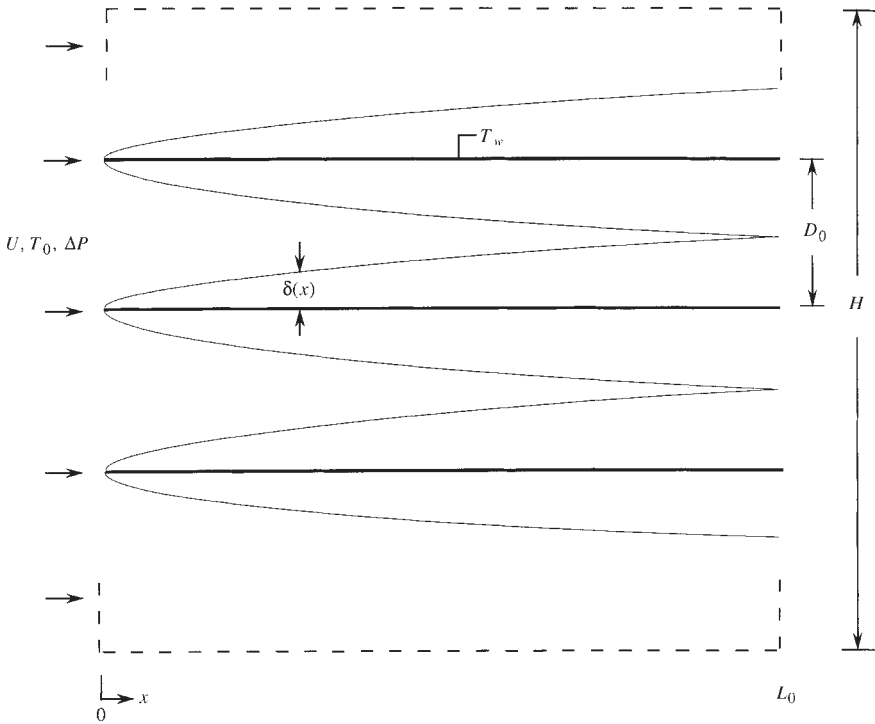
Figure 12.23   Optimal package of parallel plates with one spacing. (From Ref. 52.)

Those regions are situated immediately downstream of the entrance plane, $x = 0$. Regions that do not work in a heat transfer sense must either be put to work or eliminated. The key observation is that the wedges of flow contained between the tips of opposing boundary layers are not involved in transferring heat. They can be involved if heat-generating blades of shorter lengths (L_1) are installed on their planes of symmetry. This new design is shown in Fig. 12.24.

Each new L_1 blade is coated by Blasius boundary layers with the thickness $\delta(x) \cong 5x(Ux/\nu)^{-1/2}$ [cf. eq. (2.85)]. Because δ increases as $x^{1/2}$, the boundary layers of the L_1 blade merge with the boundary layers of the L_0 blades at a downstream position that is approximately equal to $L_0/4$. The approximation is due to the assumption that the presence of the L_1 boundary layers does not affect significantly the downstream development ($x > L_0/4$) of the L_0 boundary layers. By choosing L_1 such that the boundary layers that coat the L_1 blade merge with surrounding boundary layers at the downstream end of the L_1 blade, we invoke one more time the packing principle of Sections 3.6 and 4.12. We are being consistent as constructal designers, and because of this, every structure with merging boundary layers will be constructal and natural, no matter how complex.
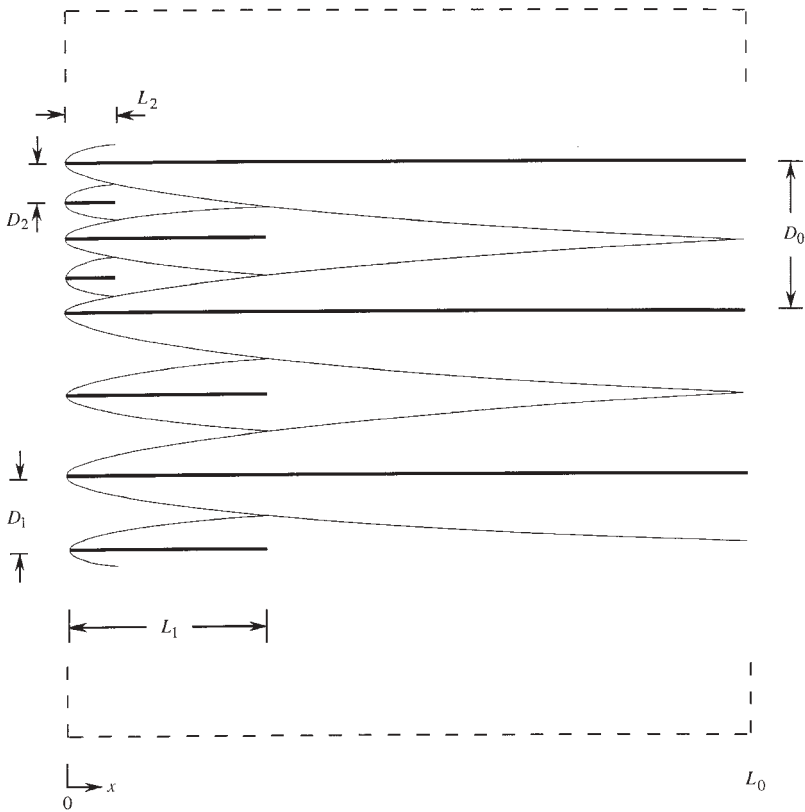
Figure 12.24   Optimal multiscale package of parallel plates. (From Ref. 52.)

The wedges of isothermal fluid (T_0) remaining between adjacent L_0 and L_1 blades can be populated with a new generation of even shorter blades, $L_2 \cong L_1/4$. Two such blades are shown in the upper-left corner of Fig. 12.24. The length scales become smaller (L_0, L_1, L_2), but the shape of the boundary layer region is the same for all the blades, because the blades are all swept by the same flow (U). The merging and expiring boundary layers are arranged according to the formulas

$$L_i \cong \tfrac{1}{4} L_{i-1}, \quad D_i \cong \tfrac{1}{2} D_{i-1} \quad (i = 1, 2, ..., m) \qquad (12.221)$$

where we shall see that m is finite, not infinite. In other words, as in all the constructal tree structures, the image generated by the algorithm (12.221) is not a fractal. It is a Euclidean image (cf. Ref. 53, p. 765). The sequence of decreasing length scales is finite, and the smallest size (D_m, L_m) is very important and known, as we will see in Section 12.10.3.

To complete the description of the discovery of the multiscale flow structure, we note that the number of blades of a certain size increases as the blade size decreases. Let $n_0 = H/D_0$ be the number of L_0 blades in the uniform structure of Fig. 12.23, where $D_0 \cong 2\delta(L_0) \cong 10(\nu L_0/U)^{1/2}$. The number of L_1 blades is $n_1 = n_0$, because there are as many L_1 blades as there are D_0 spacings. At scales smaller than L_1, the number of blades of one size doubles with every step,

$$n_i = 2n_{i-1} \quad (i = 2, 3, ..., m) \tag{12.222}$$

Two conflicting effects emerge as the structure grows in the sequence started in Fig. 12.24. One is attractive: The total surface of temperature T_w installed in the HL_0 volume increases. The other is detrimental: The flow resistance increases, the flow rate driven by the fixed ΔP decreases, and so does the heat transfer rate associated with a single boundary layer. The important question is how the volume is being used: What happens to the heat transfer rate *density* as complexity increases?

12.10.1   Heat Transfer

The total heat transfer rate from the T_w surfaces to the T_0 fluid can be estimated by summing up the contributions made by the individual blades. The heat transfer rate through one side of the L_0 blade is equal in an order of magnitude sense to the heat transfer rate associated with a laminar boundary layer [cf. eq. (2.110)], $\bar{q}_0'' L_0/(k\Delta T) \cong 0.664(UL_0/\nu)^{1/2}$. Here $\bar{q}_0''$ (W/m^2) is the L_0-averaged heat flux, $\Delta T = T_w - T_0$, and k is the fluid thermal conductivity. There are $2n_0$ such boundary layers, and their combined contribution to the total heat transfer rate of the package of Fig. 12.24 is $q_0' = 2n_0 \bar{q}_0'' L_0 \cong 1.328k \, \Delta T n_0 (UL_0/\nu)^{1/2}$.

The same calculation can be performed for any group of blades of one size, L_i. Their total heat transfer rate q_i' (W/m) is given by a formula similar to the q_0' formula above, in which n_0 and L_0 are replaced by n_i and L_i. The heat transfer rate of all the blades is the sum

$$q' = \sum_{i=0}^{m} q_i' \cong 1.328k \, \Delta T n_0 \left(\frac{UL_0}{\nu}\right)^{1/2} S \tag{12.223}$$

where S is the dimensionless parameter that accounts for geometry,

$$S = 1 + \frac{n_1}{n_0}\left(\frac{L_1}{L_0}\right)^{1/2} + \frac{n_2}{n_0}\left(\frac{L_2}{L_0}\right)^{1/2}$$

$$+ \cdots + \frac{n_m}{n_0}\left(\frac{L_m}{L_0}\right)^{1/2} = 1 + \frac{m}{2} \tag{12.224}$$

This analysis confirms the anticipated trend: The total heat transfer rate increases monotonically as the complexity of the structure (m) increases.

12.10.2 Fluid Friction

It is necessary to evaluate the flow resistance of the multiscale structure, because the velocity U that appears in eq. (12.223) is not specified. The pressure difference ΔP is specified, and it is related to all the friction forces felt by the blades. We estimate the friction force along one face of one blade by using the solution for the laminar boundary layer [cf. eq. (2.92′)], namely, $\tau_i \cong C_{fi}\rho U^2/2$ and $C_{fi} = 1.328/(UL_0/\nu)^{1/2}$. Here τ_i and C_{fi} are the averaged shear stress and skin friction coefficient, respectively. The total force felt by the blades of size L_i is $F_i = 2n_i\tau_i L_i \cong 1.328\rho(\nu L_i)^{1/2}n_i U^{3/2}$. The total force for the multiscale package is

$$F = \sum_{i=0}^{m} F_i \cong 1.328\ \rho(\nu L_0)^{1/2}n_0 U^{3/2}S \qquad (12.225)$$

This force is balanced by the longitudinal force imposed on the control volume, $\Delta P\, H = F$, which combined with eq. (12.225) and $D_0 \cong 10(\nu L_0/U)^{1/2}$ yields the order of magnitude of the average velocity of the fluid that permeates through the structure:

$$U \cong 2.7 \left(\frac{\Delta P}{\rho S}\right)^{1/2} \qquad (12.226)$$

This result confirms the second anticipated trend: The flow slows down as the complexity of the structure (S or m) increases.

12.10.3 Heat Transfer Rate Density: The Smallest Scale for Convection

Putting together the results of the heat transfer and fluid flow analyses, we find how the structure performs globally, when its constraints are specified ($\Delta P, \Delta T, H, L_0$). Eliminating U between eqs. (12.223) and (12.226) yields the dimensionless global thermal conductance,

$$\frac{q'}{k\Delta T} \cong 0.36\frac{H}{L_0}\mathrm{Be}^{1/2}S^{1/2} \qquad (12.227)$$

where the pressure drop number is based on ΔP and L_0: namely, $\mathrm{Be} = (\Delta P L_0^2)/\mu\alpha$. In this expression, μ and α are the viscosity and thermal diffusivity of the fluid. The alternative to using the global conductance is to use the heat transfer rate density, $q''' = q'/HL_0$. Both quantities increase with the applied pressure difference (Be) and the complexity of the flow structure (S).

In conclusion, despite the conflicting effects of S in eqs. (12.223) and (12.226), the effect of increasing S is beneficial from the point of view of packing more heat transfer in a given volume. Yet, we will see that the complexity must be finite. The constructal design of complexity should not be confused with the maximization of complexity.

How large can the factor S be? The answer follows from the observation that the geometry of Fig. 12.24 is valid when boundary layers exist (i.e., when they are distinct). To be distinct, boundary layers must be slender. Figure 12.24 makes it clear that boundary layers are less slender when their longitudinal scales (L_i) are shorter. The shortest blade length L_m below which the boundary layer heat transfer mechanism breaks down is $L_m \sim D_m$. At this scale, convection along the channel is as effective as diffusion across the channel. The channel becomes a pore. In view of eqs. (12.221), $L_m \sim D_m$ means that $L_0 \sim 2^m D_0$. The analysis concludes with the smallest scale, which occurs at the level m given by [52]: $2^m(1 + m/2)^{1/4} \sim 0.17\, \mathrm{Be}^{1/4}$. This establishes m as a slowly varying monotonic function of $\mathrm{Be}^{1/4}$, such that the complete effect of Be on the global heat transfer performance is

$$\frac{q'}{k\,\Delta T} \cong 0.36 \frac{H}{L_0} \mathrm{Be}^{1/2}\left(1 + \frac{1}{2}\,m\right)^{1/2} \tag{12.228}$$

In conclusion, the required complexity (m) increases monotonically with the imposed pressure difference (Be). More flow means more length scales and smaller smallest scales. The structure becomes not only more complex but also finer. The monotonic effect of m is accompanied by diminishing returns: Each new length scale (m) contributes to global performance less than the preceding length scale ($m - 1$).

Forced convection was used in Ref. 52 only for illustration (i.e., as a flow mechanism on which to build the multiscale structure). A completely analogous multiscale structure can be deduced for laminar natural convection. This is recommended by the complete analogy that exists between spacings in forced convection and natural convection [30].

12.11   NATURAL POROUS MEDIA: ALTERNATING TREES

Natural porous flow structures exhibit multiple scales and nonuniform distribution of length scales through the available space. Can such heterogeneous flow structures be derived from the constructal law of enhancing flow access? To answer this question, we explore the properties and performance of the dendritic flow architecture proposed in Ref. 54 and Fig. 12.25. The vision is to connect two parallel lines (or two parallel planes) with trees that alternate with upside-down
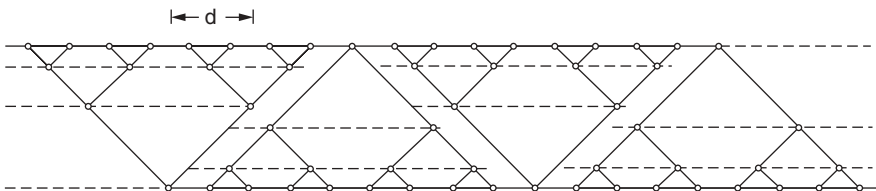
Figure 12.25   Tree architecture for connecting the points of one line with the points of another line [54].

trees. The resulting dendritic pattern connects the bottom boundary of the flow domain with the top boundary.

The flow access between the points of one line and the points of a parallel line can be viewed as a sequence of point-to-line flow access opportunities. The building block with which Fig. 12.25 is constructed was proposed in Lorente et al. [55], where it was based on optimally shaped rectangular area elements, which led to 90° angles between tributaries and to collinear ducts on the extremities of the V-shaped tree structure.

Consider the building blocks sketched in Fig. 12.26 and explore several ways in which to maximize line-to-line flow access. We assume a large number of bifurcation levels ($i = 1, 2, \ldots, n$). The tube lengths decrease by a factor of $\frac{1}{2}$, from the largest (L_0) to $L_1 = L_0/2$, $L_2 = L_1/2$, etc. The smallest length scale is the smallest tube length,

$$L_n = 2^{-n} L_0 \tag{12.229}$$

or the distance between the two ends of two neighboring L_n tubes,

$$d = 2L_n \sin \alpha \tag{12.230}$$

In this analysis [29], α is the half angle between the smallest branches, which according to the preceding discussion [55] is equal to 45°. We assume Hagen–Poiseuille flow in every tube. The pressure drop along one tube of length L_i and diameter D_i is

$$\Delta P_i = \dot{m}_i \frac{8}{\pi} \text{Po } \nu \frac{L_i}{D_i^4} \tag{12.231}$$

where Po is the Poiseuille constant (e.g., Po $= 16$ for round tubes), which appears in the formula for the friction factor (Table 3.2),

$$f_i = \frac{\text{Po}}{\text{Re}_{D_i}} \tag{12.232}$$
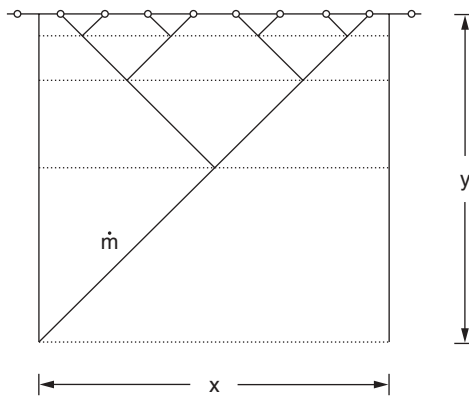
Figure 12.26   One of the point-to-line trees of Fig. 12.25. (From Ref. 54.)

and $\mathrm{Re}_{D_i} = U_i D_i / \nu$ with $U_i = \dot{m}_i / (\rho \, \pi D_i^2 / 4)$. Mass conservation at every junction requires that $\dot{m}_i = 2\dot{m}_{i+1}$, where it is again assumed that the tubes are sufficiently slender so that the asymmetry of the Y junction does not affect the splitting of $\dot{m}_i$ into two equal streams $\dot{m}_{i+1}$. After using the ratios for diameters, lengths, and mass flow rates indicated above, the total pressure drop from the open end of the L_0 tube to the open ends of the L_n tubes becomes

$$\Delta P = \sum_{i=1}^{n} \Delta P_i = \dot{m}_0 \, \frac{8}{\pi} \, \nu \, \mathrm{Po} \, \frac{L_0}{D_0^4} \, \sigma_1 \tag{12.233}$$

where $\sigma_1 = 1 + 2^{-2/3} + \cdots + 2^{-2n/3} = [1 - (2^{-2/3})^{n+1}]/(1 - 2^{-2/3})$. The total tube volume occupied by the tree flow is

$$V = \frac{\pi}{4} \, (D_0^2 L_0 + 2D_1^2 L_1 + \cdots + 2^n D_n^2 L_n) = \frac{\pi}{4} \, D_0^2 L_0 \sigma_1 \tag{12.234}$$

The largest length scale (L_0) is related to the vertical dimension of the tree (y) by

$$y = (L_0 + L_1 + \cdots + L_n) \cos \alpha = L_0 \sigma_2 \cos \alpha \tag{12.235}$$

where $\sigma_2 = 2 \, [1 - 2^{-(n+1)}]$. The horizontal dimension (x) of the area occupied by the tree projection is

$$x = 2^n d = 2 L_0 \sin \alpha = \frac{2}{\sigma_2} \, y \tan \alpha \tag{12.236}$$

where 2^n is the number of L_n tubes that reach the upper end of the construct. Eliminating L_0 and D_0 between eqs. (12.233) $-$ (12.235) we obtain

$$\Delta P = \dot{m}_0 \, \frac{\pi}{2} \, \mathrm{Po} \, \frac{\nu}{V^2} \left(\frac{\sigma_1 y}{\sigma_2 \cos \alpha} \right)^3 \tag{12.237}$$

We question how effective the tree structure of Fig. 12.26 is relative to a simpler reference architecture: an array of N equidistant parallel tubes each of length y and diameter D. This classical structure carries the same total flow rate $\dot{m}_0$ in the same total tube volume $[V = N \, (\pi/4) \, D^2 y]$ and over the same area $xy/2$. The structure has one degree of freedom, the tube diameter D, or the number of parallel tubes,

$$N = \frac{4V}{\pi D^2 y} \tag{12.238}$$

The pressure drop along this structure (ΔP_{ref}) is the same as the pressure drop along a single tube, cf. eq. (12.231), through which the flow rate now is $\dot{m}_0/N$,

$$\Delta P_{\mathrm{ref}} = \frac{\dot{m}_0}{N} \, \frac{8}{\pi} \, \mathrm{Po} \, \nu \, \frac{y}{D^4} \tag{12.239}$$

Eliminating D by using eq. (12.238), we obtain

$$\Delta P_{\text{ref}} = \dot{m}_0 \frac{\pi}{2} \text{Po} \frac{\nu}{V^2} N y^3 \tag{12.240}$$

The tree-shaped structure of Fig. 12.26 has a smaller flow resistance than the parallel channels when $\Delta P < \Delta P_{\text{ref}}$ or, using eqs. (12.237) and (12.240), when

$$N > \left(\frac{\sigma_1}{\sigma_2 \cos \alpha} \right)^3 \tag{12.241}$$

The right side of this inequality is a number on the order of 1. In conclusion, as the reference structure becomes finer (i.e., as N increases), the tree-shaped design of Fig. 12.26. becomes more attractive.

This conclusion can be read as a statement of how fine the tree structure must be such that it is preferable to the reference design. For a more practical comparison, assume that the smallest dimension (d) is the same in both architectures, that is, the d spacing of Fig. 12.26 is the same as the spacing between parallel tubes. This means that the number of parallel channels that occupy the area $y \times (x/2)$ is $N = 2^n/2$, and when $\alpha = 45°$, the inequality (12.241) becomes

$$\frac{\Delta P}{\Delta P_{\text{ref}}} \cong \frac{14}{2^n} < 1 \tag{12.242}$$

We conclude that when the number of branching levels is 4 or larger, the tree-shaped architecture offers greater access to the flow that permeates through the porous structure of thickness y. The superiority of the tree design increases fast as n increases: When $n = 7$, the ratio $\Delta P / \Delta P_{\text{ref}}$ is as low as $\frac{1}{10}$.

In closing, the flow architecture uncovered in this section is qualitatively the same as that of *natural porous materials*, for example, the soil of the hill slope in a river drainage basin, where two scales dominate: fine porous soil with seepage and larger pores (''pipes'') embedded in the fine structure. Very promising are the similarities that emerge between natural porous structures and the ones derived from the constructal law. They shed light on the natural process that *generates* multiple scales and heterogeneity in natural flow systems such as hill slope drainage and living tissues. The fact that natural flow structures (the champions of flow perfection) have features similar to those discovered in constructal design lends confidence in pursuit of better design with the constructal law [29,56].

REFERENCES

1. H. Darcy, *Les fontaines publiques de la ville de Dijon*, Victor Dalmont, Paris, 1856.
2. D. A. Nield and A. Bejan, *Convection in Porous Media*, 4th ed., Springer, New York, 2013.

3. A. Bejan, I. Dincer, S. Lorente, A. F. Miguel, and A. H. Reis, *Porous and Complex Flow Structures in Modern Technologies*, Springer, New York, 2004.

4. J. L. Lage, The fundamental theory of flow through permeable media from Darcy to turbulence, in D. B. Ingham and I. Pop, eds., *Transport Phenomena in Porous Media*, Pergamon, Oxford, 1998, pp. 1–30.

5. S. Ergun, Fluid flow through packed columns, *Chem. Eng. Prog.*, Vol. 48, No. 2, 1952, pp. 89–94.

6. J. C. Ward, Turbulent flow in porous media, *J. Hydraul. Div.*, ASCE, Vol. 90, No. HY5, 1964, pp. 1–2.

7. P. H. Forchheimer, *Z. Ver. Dtsch. Ing.*, Vol. 45, 1901, pp. 1782–1788.

8. A. Bejan, *Heat Transfer*, Wiley, New York, 1993, Chapter 3.

9. S. J. Kim and D. Kim, Forced convection in microstructures for electronic equipment cooling, *J. Heat Transfer*, Vol. 121, 1999, pp. 639–645.

10. S. J. Kim and S. P. Jang, Effects of the Darcy number, the Prandtl number and the Reynolds number on local thermal non-equilibrium, *Int. J. Heat Mass Transfer*, Vol. 45, 2002, pp. 3885–3896.

11. M. Neagu and A. Bejan, Constructal placement of high-conductivity inserts in a slab: optimal design of ''roughness,'' *J. Heat Transfer*, Vol. 123, 2001, pp. 1184–1189.

12. J. V. C. Vargas and A. Bejan, The optimal shape of the interface between two conductive bodies with minimal thermal resistance, *J. Heat Transfer*, Vol. 124, 2002, pp. 1218–1221.

13. J. C. Ordonez, A. Bejan, and R. S. Cherry, Designed porous media: optimally nonuniform flow structures for connecting one point with more points, *Int. J. Therm. Sci.*, Vol. 42, 2003, pp. 857–870.

14. A. Bejan, Dendritic constructal heat exchanger with small-scale cross flows and larger-scales counterflows, *Int. J. Heat Mass Transfer*, Vol. 45, 2002, pp. 4607–4620.

15. W. Wechsatol, S. Lorente, and A. Bejan, Dendritic convection on a disc, *Int. J. Heat Mass Transfer*, Vol. 46, 2003, pp. 4381–4391.

16. A. Bejan, *Advanced Engineering Thermodynamics*, 3rd ed., Wiley, Hoboken, 2006.

17. A. Bejan, *Entropy Generation through Heat and Fluid Flow*, Wiley, New York, 1982, Chapter 5.

18. A. M. Morega and A. Bejan, Heatline visualization of forced convection laminar boundary layers, *Int. J. Heat Mass Transfer*, Vol. 36, 1993, pp. 3957–3966.

19. A. M. Morega and A. Bejan, Heatline visualization of convective heat transfer in porous media, *Int. J. Heat Fluid Flow*, Vol. 15, 1994, pp. 42–47.

20. P. Cheng, Combined free and forced convection flow about inclined surfaces in porous media, *Int. J. Heat Mass Transfer*, Vol. 20, 1977, pp. 807–814.

21. A Bejan and D. A. Nield, Transient forced convection near a suddenly heated plate in a porous medium, *Int. Commun. Heat Mass Transfer*, Vol. 18, 1991, pp. 83–91.

22. P. Cheng, Mixed convection about a horizontal cylinder and a sphere in a fluid-saturated porous medium, *Int. J. Heat Mass Transfer*, Vol. 25, 1982, pp. 1245–1246.

23. P. Cheng and W. J. Minkowycz, Free convection about a vertical flat plate embedded in a saturated porous medium with application to heat transfer from a dike, *J. Geophys. Res.*, Vol. 82, 1977, pp. 2040–2044.

24. A. Bejan and S. Lorente, Constructal theory of generation of configuration in nature and engineering, *J. App. Phys.*, Vol. 100, 2006, 041301.

25. A. Bejan and S. Lorente, The constructal law of design and evolution in nature, *Philos. Trans. Roy. Soc. B*, Vol. 365, 2010, pp. 1335–1347.

26. A. Bejan and S. Lorente, The constructal law and the evolution of design in nature, *Phys. Life Rev.*, Vol. 8, 2011, pp. 209–240.

27. S. Lorente, Constructal view of electrokinetic transfer through porous media, *J. Phys. D Appl. Phys.*, Vol. 40, 2007, pp. 2941–2947.

28. A. Bejan, *Shape and Structure, from Engineering to Nature*, Cambridge University Press, Cambridge, 2000.

29. A. Bejan and S. Lorente, *Design with Constructal Theory*, Wiley, Hoboken, 2008.

30. S. Petrescu, Comments on the optimal spacing of parallel plates cooled by forced convection, *Int. J. Heat Mass Transfer*, Vol. 37, 1994, 1283.

31. A. Bejan and R. Anderson, Heat transfer across a vertical impermeable partition imbedded in a porous medium, *Int. J. Heat Mass Transfer*, Vol. 24, 1981, pp. 1237–1245.

32. A. Bejan and R. Anderson, Natural convection at the interface between a vertical porous layer and an open space, *J. Heat Transfer*, Vol. 105, 1983, pp. 124–129.

33. C. Vasile, S. Lorente, and B. Perrin, Study of convective phenomena inside cavities coupled with heat and mass transfers through porous media—application to vertical hollow bricks—a first approach, *Energy Build.*, Vol. 28, 1998, pp. 229–235.

34. P. Cheng and I. D. Chang, Buoyancy induced flows in a saturated porous medium adjacent to impermeable horizontal surfaces, *Int. J. Heat Mass Transfer*, Vol. 19, 1976, pp. 1267–1272.

35. S. Kimura, A. Bejan, and I. Pop, Natural convection near a cold plate facing upward in a porous medium, *J. Heat Transfer*, Vol. 107, 1985, pp. 819–815.

36. A. Bejan, Natural convection in an infinite porous medium with a concentrated heat source, *J. Fluid Mech.*, Vol. 89, 1978, pp. 97–107.

37. D. Poulilkakos and A. Bejan, Unsteady natural convection in a porous layer, *Phys. Fluids*, Vol. 26, 1983, pp. 1183–1191.

38. A. Bejan and C. L. Tien, Natural convection in a horizontal porous medium subjected to an end-to-end temperature difference, *J. Heat Transfer*, Vol. 100, 1978, pp. 191–198; also, Vol. 105, 1983, pp. 683, 684.

39. C. E. Hickox and D. K. Gartling, A numerical study of natural convection in a horizontal porous layer subjected to an end-to-end temperature difference, *J. Heat Transfer*, Vol. 103, 1981, pp. 797–802.

40. J. E. Weber, The boundary layer regime for convection in a vertical porous layer, *Int. J. Heat Mass Transfer*, Vol. 18, 1975, pp. 569–573.

41. A. Bejan, On the boundary layer regime in a vertical enclosure filled with a porous medium, *Lett. Heat Mass Transfer*, Vol. 6, 1979, pp. 93–102.

42. A. Bejan, The boundary layer regime in a porous layer with uniform heat flux from the side, *Int. J. Heat Mass Transfer*, Vol. 26, 1983, pp. 1339–1346.

43. A. Bejan, Lateral intrusion of natural convection into a horizontal porous structure, *J. Heat Transfer*, Vol. 103, 1981, pp. 237–241.

44. A. Bejan, Natural convection in a vertical cylindrical well filled with porous medium, *Int. J. Heat Mass Transfer*, Vol. 23, 1980, pp. 726–729.

45. R. A. Nelson, Jr. and A. Bejan, Constructal optimization of internal flow geometry in convection, *J. Heat Transfer*, Vol. 120, 1998, pp. 357–364.

46. R. A. Nelson, Jr. and A. Bejan, Self-organization and internal flow geometry in convective heat transfer, in *Proceedings of the 7th AIAA/ASME Joint Thermophysics and Heat Transfer Conference*, ASME HTD-Vol. 357-3, 1998, pp. 149–161.

47. P. Cheng, Heat transfer in geothermal systems, *Adv. Heat Transfer*, Vol. 14, 1978, pp. 1–105.

48. M. Wang and A. Bejan, Heat transfer correlation for Bénard convection in a fluid saturated porous layer, *Int. Commun. Heat Mass Transfer*, Vol. 14, 1987, pp. 617–626.

49. T. Jonsson and I. Catton, Prandtl number dependence of natural convection in porous media, *J. Heat Transfer*, Vol. 109, 1987, pp. 371–377.

50. J. C. Ordonez, A. Bejan, and R. S. Cherry, Designed porous media: optimally nonuniform flow structures connecting one point with more points, *Int. J. Therm. Sci.*, Vol. 42, 2003, pp. 857–870.

51. K. J. Schneider, in *Proceedings of the 11th International Congress on Refrigeration*, 1963, Paper 11-4.

52. A. Bejan and Y. Fautrelle, Constructal multi-scale structure for maximal heat transfer density, *Acta Mech.*, Vol. 163, 2003, pp. 39–49.

53. A. Bejan, *Advanced Engineering Thermodynamics*, 2nd ed., Wiley, New York, 1997.

54. S. Lorente and A. Bejan, Heterogeneous porous media as multiscale structures for maximum flow access, *Journal of Applied Physics*, Vol. 100, 2006, 114909.

55. S. Lorente, W. Wechsatol and A. Bejan, Tree-shaped flow structures designed by minimizing path lengths, *International Journal Heat and Mass Transfer*, Vol. 45, 2002, pp. 3299–3312.

56. H. Zhang, S. Lorente and A. Bejan, Vascularization with trees that alternate with upside-down trees, *Journal of Applied Physics*, Vol. 101, 2007, 094904.

57. A. Bejan, Designed porous media: maximal heat transfer density at decreasing length scales, *Int. J. Heat Mass Transfer*, Vol. 47, 2004, pp. 3073–3083.

PROBLEMS

12.1. Derive the two-dimensional mass conservation equation (12.7) by invoking the instantaneous conservation of mass in the $\Delta x\, \Delta y$ porous element of Fig. 12.1. [*Hint*: Start with eq. (1.1).]

12.2. The unidirectional flow through a porous medium can be modeled as the flow through a bundle of capillary tubes of diameter $2r_0$, as shown in Fig. 12.2. Assume that the density of such tubes per unit frontal area is N/A (tubes/m^2). Assume further that the flow through each tube can be modeled Hagen–Poiseuille (Chapter 3). Demonstrate that the Darcy law (12.9) can be derived analytically and that the effective permeability K

of the capillary tube bundle porous medium is

$$K = \frac{\pi r_0^4}{8} \frac{N}{A}$$

12.3. Another way of deriving the proportionality between mean velocity and pressure gradient, the Darcy law (12.9), is to employ the capillary fissure model of Fig. 12.2. Assume the existence of parallel cracks (fissures) separated by a distance a; the thickness of each crack is $b =$ constant. Assuming that in each crack the flow can be modeled as Hagen–Poiseuille through a parallel-plates channel, derive eq. (12.9) and show that the effective permeability of the medium is

$$K = \frac{b^3}{(12)(a + b)}$$

12.4. Model the porous column of Fig. 12.2 as a swarm of spherical particles of diameter d; the packing is such that the number of spheres per unit volume is N_{vol} (particles/m^3), and the number of spheres per unit frontal area is N_A (particles/m^2). For simplicity, assume that the fluid velocity u_p is uniform through the pores (void spaces) left between the N_A particles on the frontal area. If $u_p d/\nu$ is of order $O(1)$ or less, the drag force F_1 exerted by the flow on each particle is given by Stokes' solution

$$\frac{F_1/(\pi d^2/4)}{\frac{1}{2}\rho u_p^2} = C_D = \frac{24}{u_p d/\nu}$$

where C_D is the drag coefficient. Summing up these forces over the N_{vol} particles, derive the Darcy law (12.9) and the porosity function ϕ (d/L) and show that for this model the permeability is [57]

$$K = \frac{d^2 \phi}{18(1 - \phi)}$$

12.5. Derive the friction factor equation (12.14) from Forchheimer's modification of the Darcy law, eq. (12.15).

12.6. Model the elementary pore flow of Fig. 12.3 as Hagen–Poiseuille flow through a cylinder of radius r_0 and length Δx. Recalling that the volumetric dissipation rate anywhere in the fluid is (Chapter 1)

$$\mu \Phi = \mu \left(\frac{\partial u}{\partial r}\right)^2$$

demonstrate that eq. (12.27) is correct. Repeat this proof by modeling the pore flow as Hagen–Poiseuille through a fissure (parallel-plates channel) of thickness b.

12.7. Derive the local entropy generation rate formula (12.39) for a homogeneous porous medium. Start by applying eq. (1.47) to the one-dimensional convection model of Fig. 12.3; write eq. (1.47) for the solid part and the fluid part separately. Integrate each S'''_{gen} expression over their respective volumes, $(A - A_p)\,\Delta x$ and $A_p\,\Delta x$, and then average the sum of the two entropy generation integrals over the total volume $A\,\Delta x$. To obtain eqs. (12.38) and (12.39), make use of the appropriate mass and energy conservation statements and the canonical relation among entropy, enthalpy, and internal energy.

12.8. In the one-dimensional porous medium flow of Fig. 12.2a, top, the following scales are known: $x \sim L$, $\partial T/\partial x \sim \Delta T/L$, and $u \sim U$. In addition, the transport properties (k, K, μ) are known. Based on this information, it is found that the viscous dissipation term may be neglected in the energy equation (12.33); in other words,

$$k\frac{\Delta T}{L^2} > \frac{\mu U^2}{K}$$

Show that the scaling conclusion above does not imply that the viscous contribution to irreversibility can be neglected in the S'''_{gen} formula (12.39).

12.9. Develop the heat transfer results for uniform porous medium fluid flow along an isothermal wall [eqs. (12.54) and (12.55)]. Derive first the similarity form of the energy equation [eq. (12.50)] and integrate this equation, keeping in mind the error function notation reviewed in Appendix E.

12.10. Determine numerically the local heat transfer coefficient for uniform seepage flow parallel to a wall with uniform heat flux. Define the new similarity temperature profile $\theta_{q''}(\eta)$ by writing

$$T(x, y) - T_\infty = \frac{q''/k}{(-d\theta_{q''}/d\eta)_{\eta=0}}\left(\frac{\alpha x}{U_\infty}\right)^{1/2}\theta_{q''}(\eta)$$

where η is given by eq. (12.48). Show that the similarity energy equation is the same as eq. (12.60) with $\theta_{q''}$ in place of τ. Solve this equation numerically subject to $\theta_{q''} = 1$ at $\eta = 0$ and $\theta_{q''} = \theta'_{q''} = 0$ as $\eta \to \infty$. Divide the η domain into equal intervals of size $\Delta\eta$. At each level $\eta_i = i\,\Delta\eta$, approximate the $\theta_{q''}$ function and its derivatives by finite differences. Substituting these finite-difference approximations into the energy equation will yield a recurrence formula for calculating $\theta_{q''}$ at location i based on the $\theta_{q''}$ values at the preceding two locations ($i - 1$, $i - 2$). Determine the $\theta_{q''}(\eta)$ profile by marching from $\eta = 0$ to a sufficiently large η; this can be done by guessing the value of $(d\theta/d\eta)_{\eta=0}$ and ''shooting'' to satisfy the outer boundary conditions $\theta_{q''} = \theta'_{q''} = 0$

at as large a value of η as possible. Compare your result with the results summarized Table P12.10. Note that the accuracy of the numerical integration depends on the value chosen for $\Delta\eta$.

Table P12.10

Step Size $\Delta\eta$	$(-d\theta_{q''}/d\eta)_{\eta=0}$ or $\mathrm{Nu}_x\,\mathrm{Pe}_x^{-1/2}$	Value of η where $\theta_{q''} = \theta'_{q''} \simeq 0$
0.1	0.898	5.5
0.05	0.892	5.25
0.01	0.887	4.94
0.005	0.886	4.68
0.001	0.8863	5.722

12.11. Consider a fluid-saturated porous medium with $u = Cx^n$ near a solid impermeable wall of temperature $T_0 = T_\infty + Ax^\lambda$. The temperature T_∞ is the porous medium temperature sufficiently far away from the wall, outside the thermal boundary layer. Referring to eqs. (12.40)–(12.42), prove that a similarity temperature profile exists if $n = \lambda$. Derive the similarity form of the boundary layer energy equation (12.42), and show that this form matches eq. (12.50) if $n = 0$ (i.e., if the wall is isothermal).

12.12. Develop an integral solution for the natural boundary layer along the vertical isothermal wall of Fig. 12.7. Assume the vertical velocity profile

$$v = v_0\,\exp\left(-\frac{x}{\delta_T}\right)$$

where both v_0 and δ_T are unknown functions of altitude (y). Determine the temperature profile based on the assumption above and the boundary layer approximation of the Darcy law [eq. (12.82)]. Integrate the energy equation (12.83) across the boundary layer and determine $v_0(y)$ and $\delta_T(y)$. Verify that these results agree with the results of the scale analysis [eqs. (12.87)]. Calculate the local Nusselt number Nu_y, and estimate the percent departure of your result from the similarity result of eq. (12.95).

12.13. Develop the dimensionless similarity formulation of the problem of natural boundary layer convection along a vertical wall with uniform wall heat flux q''. Begin your analysis with the boundary layer equations (12.82) and (12.83) and use the scale analysis (12.97)–(12.100) in order to define the appropriate similarity variables.

12.14. For the local heat transfer coefficient in natural convection along a $q'' = $ constant wall, Cheng and Minkowycz [23] reported that

$$\mathrm{Nu}_y = 0.6788\mathrm{Ra}_y^{1/2}$$

where Nu_y and Ra_y are defined as in eqs. (12.89) and (12.95). Keeping in mind that $T_0 - T_\infty$ is a function of y and that the scales for uniform heat flux convection are given by eqs. (12.97)–(12.100), translate the expression above into the language of eq. (12.100); compare your result with the local Nusselt number given in eq. (12.101).

12.15. Consider the heat transfer between two isothermal porous media separated by an impermeable partition (Fig. 12.9a). Develop an approximate estimate for the overall heat transfer rate by modeling the partition as isothermal. Report your result in the dimensionless notation employed in eq. (12.114) with $\omega = 0$. Repeat this approximate calculation by modeling the partition as a surface with uniform heat flux. Comparing both results with eq. (12.114), which partition model is better—the constant temperature or the constant heat flux?

12.16. Consider the natural convection heat transfer between a porous medium and fluid reservoir separated by a vertical impermeable surface (Fig. 12.9b). Calculate the overall Nusselt number based on H and overall temperature difference $(T_{\infty, H} - T_{\infty, L})$ by first modeling the surface as isothermal. Show that the B number [eq. (12.115)] emerges from this calculation as the ratio of the thermal resistances for each side. Repeat the analysis by modeling the interface as a surface with uniform heat flux.

12.17. Repeat the integral analysis (12.116)–(12.124) for an isothermal wall facing a linearly stratified porous medium (Fig. 12.10) by assuming the parabolic velocity profile

$$v = v_0 \left(1 - \frac{x}{\delta_T} \right)^2$$

in place of the exponential profile (12.117). Based on this exercise, determine how susceptible the heat transfer results of Fig. 12.10 are to the selection of profile shapes for the integral analysis. Comparing your result with the similarity solution known for $b = 0$, decide which choice of profile shape yields more accurate predictions, the exponential or the parabolic.

12.18. A swarm of honeybees attached to a tree branch can be approximated as a ball of diameter $D \sim 10\,\mathrm{cm}$ containing packed spheres (the bees) of diameter $d \sim 1\,\mathrm{cm}$. The temperature inside the swarm is roughly $35°\mathrm{C}$, while the ambient temperature is $5°\mathrm{C}$. The swarm loses heat to the ambient in two ways: (1) internally, to the air that rises between the bees; and (2) externally, to the natural convection boundary layer that rises over the surface of the swarm. Rely on scale analysis to show that the ratio between the internal and external heat transfer rates is of order $(K/D^2)[(g\beta D^3 \Delta T)/\alpha\nu]^{3/4}$ and that the internal heat transfer rate is comparable with the external heat transfer rate.

12.19. Determine the boundary layer–type flow and temperature field above a horizontal line heat source of strength q' (W/m). Recognizing that this flow is two-dimensional, attach the coordinate system (x, y), (u, v) perpendicularly to the line source so that the y axis points upward. Proceeding in the same manner as in the analysis of high-Ra convection above a point source [eqs. (12.130)–(12.147)], show that the vertical velocity distribution is the same as in a plane incompressible momentum jet (Section 9.2.2).

12.20. Consider the heat transfer through a shallow porous layer with different end temperatures. Show that the heat transfer rate scale is $q' \gtrsim (kH\Delta T)/\delta_f$ and explain the basis for the "<" sign in this inequality [see eqs. (12.166), regime IV].

12.21. Show that in the $\mathrm{Ra}_H \to \infty$ limit, the Nusselt number of shallow layers [eq. (12.168)] acquires a form similar to that for the high-Ra_H regime [eq. (12.170)].

12.22. A fissured porous medium is dominated by features that can be modeled as bifurcated two-dimensional parallel-plate channels organized into Y-shaped constructs. As shown in Fig. P12.22, one channel of length L_1 and spacing D_1 branches into two identical channels of length L_2 and spacing D_2. One mechanism that generates such structures through natural porous media is the facilitating of flow access, or the *constructal* design of global resistance to fluid flow. Neglect local pressure losses associated with entrance and junction effects. Show that if the total fluid volume of the Y construct is fixed, the overall flow resistance of the construct is minimized when the ratio of channel spacings is $D_1/D_2 = 2^{1/2}$.
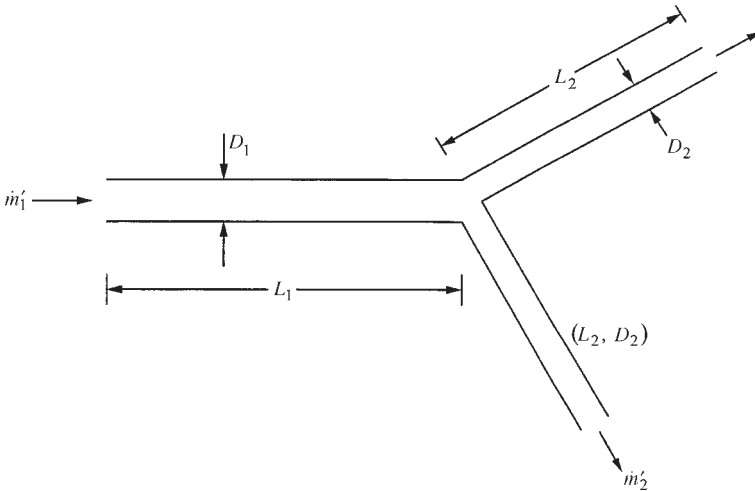
Figure P12.22

12.23. A fissured porous medium is used to enhance a chemical reaction between a gas and graphite. The porous structure shown in Fig. P12.23 is a stack of graphite blades of high thermal conductivity k_s and thickness D_s. The fissures are of size D_f and are filled with flowing gas of low thermal conductivity k_f. The structure is two-dimensional with the dimensions H, L, and W defined in the figure.
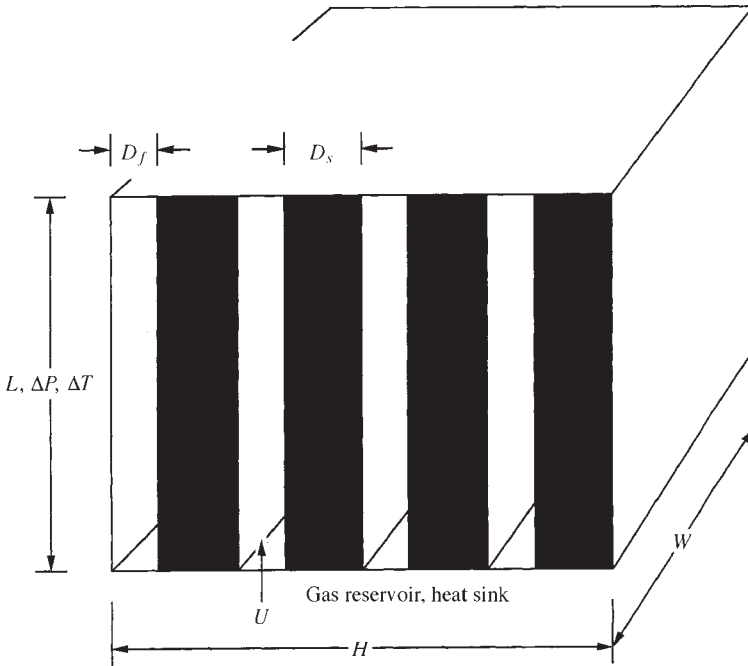
Figure P12.23

The gas is driven into the fissures by the pressure difference scale ΔP, which is measured between the entrance to the fissures (the bottom plane in the figure) and the pressure on each reacting adsorbing surface LW. The flow is in the Darcy regime, and the gas viscosity is μ. The chemical reaction is accompanied by heat generation: If $\dot{m}''$ is the scale of the mass flow rate of gas adsorption per unit area of adsorbing surface, then $q'' = C\dot{m}''$ is the rate of heat generation per unit area and C is a known constant factor. The heat current generated is conducted along the blades toward the gas reservoir, which acts as heat sink. The scale of the allowable excess temperature that drives the heat current is ΔT. The top

and lateral surfaces of the *HLW* volume shown in the figure are adiabatic and impermeable.

The objective is to maximize the use of the volume filled by the porous structure. The proposal is to select the flow structure that maximizes the volumetric rate of gas used ($\dot{m}''' = \dot{m}/HLW$), where $\dot{m}$ is the total gas flow rate. Of special interest is the optimal porosity of the structure, or the aspect ratio D_s/D_f.

APPENDIXES

A

CONSTANTS AND CONVERSION FACTORS

CONSTANTS

Universal ideal gas constant	$\overline{R} = 8.314 \text{ kJ/kmol} \cdot \text{K}$
	$= 1.9872 \text{ cal/mol} \cdot \text{K}$
	$= 1.9872 \text{ Btu/lbmol} \cdot {}^\circ\text{R}$
	$= 1545.33 \text{ ft} \cdot \text{lbf/lbmol} \cdot {}^\circ\text{R}$
Boltzmann's constant	$k = 1.38054 \times 10^{-23} \text{ J/K}$
Planck's constant	$h = 6.626 \times 10^{-34} \text{ J} \cdot \text{s}$
Speed of light in vacuum	$c = 2.998 \times 10^{8} \text{ m/s}$
Avogadro's number	$N = 6.022 \times 10^{23} \text{ molecules/mol}$
Stefan–Boltzmann constant	$\sigma = 5.669 \times 10^{-8} \text{ W/m}^2 \cdot \text{K}^4$
	$= 0.1714 \times 10^{-8} \text{ Btu/h} \cdot \text{ft}^2 \cdot {}^\circ\text{R}^4$
Atmospheric pressure	$P_{\text{atm}} = 0.101325 \text{ MPa}$
	$= 1.01325 \text{ bar}$
	$= 1.01325 \times 10^{5} \text{ N/m}^2$
Ice point at 1 atm	$T_{\text{ice}} = 0^\circ\text{C} = 273.15 \text{ K}$
Gravitational acceleration	$g = 9.807 \text{ m/s}^2$
	$= 32.17 \text{ ft/s}^2$
Calorie	$1 \text{ cal} = 4.187 \text{ J}$
Mole	$1 \text{ mol} = $ sample containing 6.022×10^{23} elementary entities (e.g., molecules); also abbreviated as 1 gmol, or

$$1 \, \text{mol} = 10^{-3} \, \text{kmol}$$
$$= 10^{-3} \, \text{kgmol}$$
$$= \frac{1}{453.6} \, \text{lbmol}$$

Natural logarithm	$\ln x = 2.30258 \log_{10} x$
	$\log_{10} x = 0.4343 \ln x$
Important numbers	$e = 2.71828$
	$\pi = 3.14159$
	$1° = 0.01745 \, \text{rad}$

CONVERSION FACTORS

Acceleration	$1 \, \text{m/s}^2 = 4.252 \times 10^7 \, \text{ft/h}^2$
Area	$1 \, \text{in}^2 = 6.452 \, \text{cm}^2$
	$1 \, \text{ft}^2 = 0.0929 \, \text{m}^2$
	$1 \, \text{yd}^2 = 0.8361 \, \text{m}^2$
	$1 \, \text{mi}^2 = 2.59 \, \text{km}^2$
	$1 \, \text{hectare} = (100 \, \text{m})^2$
	$1 \, \text{acre} = 4047 \, \text{m}^2$
Density	$1 \, \text{kg/m}^3 = 0.06243 \, \text{lbm/ft}^3$
	$1 \, \text{lbm/ft}^3 = 16.018 \, \text{kg/m}^3$
Energy	$1 \, \text{kJ} = 737.56 \, \text{ft} \cdot \text{lbf}$
	$= 0.9478 \, \text{Btu}$
	$= 3.725 \times 10^{-4} \, \text{hp} \cdot \text{h}$
	$= 2.778 \times 10^{-4} \, \text{kW} \cdot \text{h}$
	$1 \, \text{Btu} = 1055 \, \text{J}$
	$= 778.16 \, \text{ft} \cdot \text{lbf}$
	$= 3412.14 \, \text{kW} \cdot \text{h}$
	$= 2544.5 \, \text{hp} \cdot \text{h}$
	$1 \, \text{cal} = 4.187 \, \text{J}$
	$1 \, \text{erg} = 10^{-7} \, \text{J}$
Force	$1 \, \text{lbf} = 4.448 \, \text{N}$
	$= 0.4536 \, \text{kgf}$
	$1 \, \text{dyne} = 10^{-5} \, \text{N}$

Heat flux	$1 \, \text{W/m}^2 = 0.317 \, \text{Btu/h} \cdot \text{ft}^2$
	$1 \, \text{Btu/h} \cdot \text{ft}^2 = 3.154 \, \text{W/m}^2$
Heat transfer coefficient	$1 \, \text{W/m}^2 \cdot \text{K} = 0.1761 \, \text{Btu/h} \cdot \text{ft}^2 \cdot {}^\circ\text{F}$
	$= 0.8598 \, \text{kcal/h} \cdot \text{m}^2 \cdot {}^\circ\text{C}$
	$1 \, \text{Btu/h} \cdot \text{ft}^2 \cdot {}^\circ\text{F} = 5.6786 \, \text{W/m}^2 \cdot \text{K}$
Heat transfer rate	$1 \, \text{Btu/s} = 1055 \, \text{W}$
	$1 \, \text{Btu/h} = 0.2931 \, \text{W}$
	$1 \, \text{hp} = 745.7 \, \text{W}$
	$1 \, \text{ft} \cdot \text{lbf/s} = 1.3558 \, \text{W}$
Kinematic viscosity (ν), thermal diffusivity (α), mass diffusivity (D)	$1 \, \text{m}^2/\text{s} = 10^4 \, \text{cm}^2/\text{s}$
	$= 10^4 \, \text{stokes}$
	$= 3.875 \times 10^4 \, \text{ft}^2/\text{h}$
	$= 10.764 \, \text{ft}^2/\text{s}$
Latent heat, specific energy, specific enthalpy	$1 \, \text{kJ/kg} = 0.4299 \, \text{Btu/lbm}$
	$= 0.2388 \, \text{cal/g}$
	$1 \, \text{Btu/lbm} = 2.326 \, \text{kJ/kg}$
Length	$1 \, \text{in} = 2.54 \, \text{cm}$
	$1 \, \text{ft} = 0.3048 \, \text{m}$
	$1 \, \text{yd} = 0.9144 \, \text{m}$
	$1 \, \text{mile} = 1.609 \, \text{km}$
Mass	$1 \, \text{lbm} = 0.4536 \, \text{kg}$
	$1 \, \text{kg} = 2.2046 \, \text{lbm}$
	$= 1.1023 \times 10^{-3} \, \text{U.S. ton}$
	$= 10^{-3} \, \text{tonne}$
	$1 \, \text{oz} = 28.35 \, \text{g}$
Mass transfer coefficient	$1 \, \text{m/s} = 1.181 \times 10^4 \, \text{ft/h}$
	$1 \, \text{ft/h} = 8.467 \times 10^{-5} \, \text{m/s}$
Power	$1 \, \text{Btu/s} = 1055 \, \text{W} = 1.055 \, \text{kW}$
	$1 \, \text{Btu/h} = 0.293 \, \text{W}$
	$1 \, \text{W} = 3.412 \, \text{Btu/h}$
	$= 9.48 \times 10^{-4} \, \text{Btu/s}$
	$1 \, \text{HP} = 0.746 \, \text{kW}$
	$= 0.707 \, \text{Btu/s}$

Pressure, stress	$1 \, \text{Pa} = 1 \, \text{N/m}^2$
	$1 \, \text{psi} = 6895 \, \text{N/m}^2$
	$1 \, \text{atm} = 14.69 \, \text{psi}$
	$= 1.013 \times 10^5 \, \text{N/m}^2$
	$1 \, \text{bar} = 10^5 \, \text{N/m}^2$
	$1 \, \text{torr} = 1 \, \text{mmHg}$
	$= 133.32 \, \text{N/m}^2$
	$1 \, \text{psi} = 27.68 \, \text{in } H_2O$
	$1 \, \text{ft } H_2O = 0.4335 \, \text{psi}$
Specific heat, specific entropy	$1 \, \text{kJ/kg} \cdot \text{K} = 0.2388 \, \text{Btu/lbm} \cdot {}^{\circ}\text{F}$
	$= 0.2389 \, \text{cal/g} \cdot {}^{\circ}\text{C}$
	$1 \, \text{Btu/lbm} \cdot {}^{\circ}\text{F} = 4.187 \, \text{kJ/kg} \cdot \text{K}$
Speed	$1 \, \text{mi/h} = 0.447 \, \text{m/s}$
	$= 1.609 \, \text{km/h}$
	$1 \, \text{km/h} = 0.278 \, \text{m/s}$
	$= 0.622 \, \text{mi/h}$
	$1 \, \text{m/s} = 3.6 \, \text{km/h}$
	$= 2.237 \, \text{mi/h}$
Temperature	$1 \, \text{K} = 1 \, {}^{\circ}\text{C}$
	$1 \, (\text{K}) = (9/5) {}^{\circ}\text{F}$
	$T \, (\text{K}) = T({}^{\circ}\text{C}) + 273.15$
	$T \, ({}^{\circ}\text{C}) = 5/9 [T({}^{\circ}\text{F}) - 32]$
	$T \, ({}^{\circ}\text{F}) = T({}^{\circ}\text{R}) - 459.67$
Temperature difference	$\Delta T \, (\text{K}) = \Delta T \, ({}^{\circ}\text{C})$
	$= 5/9 \, \Delta T \, ({}^{\circ}\text{F})$
	$= 5/9 \, \Delta T \, ({}^{\circ}\text{R})$
Thermal conductivity	$1 \, \text{W/m} \cdot \text{K} = 0.5782 \, \text{Btu/h} \cdot \text{ft} \cdot {}^{\circ}\text{F}$
	$= 0.01 \, \text{W/cm} \cdot \text{K}$
	$= 2.39 \times 10^{-3} \, \text{cal/cm} \cdot \text{s} \cdot {}^{\circ}\text{C}$
	$1 \, \text{Btu/h} \cdot \text{ft} \cdot {}^{\circ}\text{F} = 1.7307 \, \text{W/m} \cdot \text{K}$
Thermal resistance	$1 \, \text{K/W} = 0.5275 \, {}^{\circ}\text{F/Btu} \cdot \text{h}$
	$1 \, {}^{\circ}\text{F/Btu} \cdot \text{h} = 1.896 \, \text{K/W}$
Viscosity (μ)	$1 \, \text{N} \cdot \text{s/m}^2 = 1 \, \text{kg/s} \cdot \text{m}$
	$= 2419.1 \, \text{lbm/ft} \cdot \text{h}$
	$= 5.802 \times 10^{-6} \, \text{lbf} \cdot \text{h/ft}^2$
	$1 \, \text{poise} = 1 \, \text{g/s} \cdot \text{cm}$

Volume	$1 \text{ L} = 10^{-3} \text{ m}^3 = 1 \text{ dm}^3$
	$1 \text{ in}^3 = 16.39 \text{ cm}^3$
	$1 \text{ ft}^3 = 0.02832 \text{ m}^3$
	$1 \text{ yd}^3 = 0.7646 \text{ m}^3$
	$1 \text{ gal (U.S.)} = 3.785 \text{ L}$
	$1 \text{ gal (imperial)} = 4.546 \text{ L}$
	$1 \text{ pint} = 0.5683 \text{ L}$
Volumetric heat generation	$1 \text{ Btu/h} \cdot \text{ft}^3 = 10.35 \text{ W/m}^3$
rate	$1 \text{ W/m}^3 = 0.0966 \text{ Btu/h} \cdot \text{ft}^3$

DIMENSIONLESS GROUPS USED IN THIS BOOK[a]

Bejan number	$\text{Be} = (\Delta P L^2)/\mu\alpha$
Biot number	$\text{Bi} = hL/k_s$
Boussinesq number	$\text{Bo} = (g\beta\,\Delta T\,H^3)/\alpha^2$
Eckert number	$\text{Ec} = U^2/(c_P\,\Delta T)$
Fourier number	$\text{Fo} = \alpha t/L^2$
Graetz number	$\text{Gz} = D^2 U/\alpha x = \text{Re}_D\,\text{Pr}\,(D/x)$
Grashof number	$\text{Gr} = (g\beta\,\Delta T\,H^3)/\nu^2$
Lewis number[b]	$\text{Le} = \alpha/D = \text{Sc/Pr}$
Mass transfer Rayleigh number[b]	$\text{Ra}_m = (g\beta_c\,\Delta\rho_i H^3)/\nu D$
Mass transfer Stanton number	$\text{St}_m = h_m/U$
Nusselt number	$\text{Nu} = hL/k_f$
Péclet number	$\text{Pe} = UL/\alpha = \text{Re Pr}$
Porous medium Bejan number[c]	$\text{Be} = (\Delta P\,K)/\mu\alpha$
Porous medium Péclet number[c]	$\text{Pe} = UL/\alpha$
Porous medium Prandtl number[c]	$\text{Pr} = (\nu/\alpha)(H/bK)$
Porous medium Rayleigh number, Darcy flow[c]	$\text{Ra} = (Kg\beta H\,\Delta T)/\alpha\nu$
Porous medium Rayleigh number based on heat flux, Darcy flow	$\text{Ra}_* = Kg\beta q'' H^2/\alpha\nu k$
Prandtl number	$\text{Pr} = \nu/\alpha = \text{Sc/Le}$

[a]Subscripts: $(\cdot)_s = $ solid, $(\cdot)_f = $ fluid.
[b]D is the mass diffusivity ($\text{m}^2\text{/s}$).
[c]k and α are properties of the fluid-saturated porous medium.

Rayleigh number	$\mathrm{Ra} = g\beta\,\Delta T H^3/\alpha\nu$
Rayleigh number based on heat flux	$\mathrm{Ra}_* = g\beta q'' H^4/\alpha\nu k$
Reynolds number	$\mathrm{Re} = UL/\nu$
Schmidt number[b]	$\mathrm{Sc} = \nu/D = \mathrm{Le}\,\mathrm{Pr}$
Sherwood number[b]	$\mathrm{Sh} = h_m L/D$
Stanton number	$\mathrm{St} = h/\rho c_P U = \mathrm{Nu}/\mathrm{Re}\,\mathrm{Pr}$
Stefan number	$\mathrm{Ste} = (c_f\,\Delta T)/h_{sf}$
Turbulent Prandtl number	$\mathrm{Pr}_t = \epsilon_M/\epsilon_H$

PROPERTIES OF SOLIDS

NONMETALLIC SOLIDS

Material	T (°C)	ρ (kg/m³)	c_P (kJ/kg · K)	k (W/m · K)	α (cm²/s)
Asbestos					
Cement board	20			0.6	
Felt (16	40			0.057	
laminations/cm)					
Fiber	50	470	0.82	0.11	0.0029
Sheet	20			0.74	
	50			0.17	
Asphalt	20	2120	0.92	0.70	0.0036
Bakelite	20	1270	1.59	0.230	0.0011
Bark	25	340	1.26	0.074	0.0017
Beef (see Meat)					
Brick					
Carborundum	1400			11.1	
Cement	10	720		0.34	
Chrome	100			1.9	
Common	20	1800	0.84	0.38–0.52	0.0028–0.0034
Facing	20			1.3	
Firebrick	300	2000	0.96	0.1	0.00054
Magnesite (50%	20	2000		2.68	
MgO)					
Masonry	20	1700	0.84	0.66	0.0046
Silica (95% SiO_2)	20	1900		1.07	
Zircon (62% ZrO_2)	20	3600		2.44	

NONMETALLIC SOLIDS (*Continued*)

Material	T (°C)	ρ (kg/m^3)	c_P (kJ/kg · K)	k (W/m · K)	α (cm^2/s)
Brickwork, dried in air	20	1400–1800	0.84	0.58–0.81	0.0049–0.0054
Carbon					
Diamond (type IIb)	20	3250	0.51	1350	8.1
Graphite (firm, natural)	20	2000–2500	0.61	155	1.02–1.27
Carborundum (SiC)	100	1500	0.62	58	0.62
Cardboard	0–20	~790		~0.14	
Celluloid	20	1380	1.67	0.23	0.001
Cement (Portland, fresh, dry)	20	3100	0.75	0.3	0.0013
Chalk (CaCO$_3$)	20	2000–3000	0.74	2.2	0.01–0.015
Clay	20	1450	0.88	1.28	0.01
Fireclay	100	1700–2000	0.84	0.5–1.2	0.35–0.71
Sandy clay	20	1780		0.9	
Coal	20	1200–1500	1.26	0.26	0.0014–0.0017
Anthracite	900	1500		0.2	
Brown coal	900			0.1	
Bituminous in situ		1300		0.5–0.7	0.003–0.004
Dust	30	730	1.3	0.12	0.0013
Concrete, made with	20	2200	0.88	1.28	0.0066
gravel, dry cinder	24			0.76	
Cork					
Board	20	150	1.88	0.042	0.0015
Expanded	20	120		0.036	
Cotton	30	81	1.15	0.059	0.0063
Earth					
Coarse-grained	20	2040	1.84	0.59	0.0016
Clayey (28% moisture)	20	1500		1.51	
Sandy (8% moisture)	20	1500		1.05	
Diatomaceous	20	466	0.88	0.126	0.0031
Fat	20	910	1.93	0.17	0.001
Felt, hair	−7	130–200		0.032–0.04	
	94	130–200		0.054–0.051	
Fiber insulating board	20	240		0.048	
Glass					
Borosilicate	30	2230		1.09	
Fiber	20	220		0.035	
Lead	20	2890	0.68	0.7–0.93	0.0036–0.0047
Mirror	20	2700	0.80	0.76	0.0035

NONMETALLIC SOLIDS (*Continued*)

Material	T (°C)	ρ (kg/m³)	c_P (kJ/kg · K)	k (W/m · K)	α (cm²/s)
Pyrex	60–100	2210	0.75	1.3	0.0078
Quartz	20	2210	0.73	1.4	0.0087
Window	20	2800	0.80	0.81	0.0034
Wool	0	200	0.66	0.037	0.0028
Granite	20	2750	0.89	2.9	0.012
Gypsum	20	1000	1.09	0.51	0.0047
Ice	0	917	2.04	2.25	0.012
Ivory	80			0.5	
Kapok	30			0.035	
Leather, dry	20	860	1.5	0.12–0.15	∼0.001
Limestone (Indiana)	100	2300	0.9	1.1	∼0.005
Linoleum	20	535		0.081	
Lunar surface dust, in high vacuum	250	1500 ± 300	∼0.6	∼0.0006	
Magnezia (85%)	38–204			0.067–0.08	
Marble	20	2600	0.81	2.8	0.013
Meat	25	∼1060		0.3–0.6	∼0.0014
Mica	20	2900		0.52	
Mortar	20	1900	0.8	0.93	0.0061
Paper	20	700	1.2	0.12	0.0014
Paraffin	30	870–925	2.9	0.24–0.27	∼0.001
Plaster	20	1690	0.8	0.79	0.0058
Plexiglas (acrylic glass)	20	1180	1.44	0.184	0.0011
Polyethylene	20	920	2.30	0.35	0.0017
Polystyrene	20	1050		0.157	
Polyurethane	20	1200	2.09	0.32	0.0013
Polyvinyl chloride (PVC)	20	1380	0.96	0.15	0.0011
Porcelain	95	2400	1.08	1.03	0.004
Quartz	20	2100–2500	0.78	1.40	∼0.008
Rubber					
Foam	20	500	1.67	0.09	0.0011
Hard (ebonite)	20	1150	2.01	0.16	0.0006
Soft	20	1100	1.67	∼0.2	∼0.001
Synthetic	20	1150	1.97	0.23	0.001
Salt (rock salt)	0	2100–2500	0.92	7	0.03–0.036
Sand					
Dry	20			0.58	
Moist	20	1640		1.13	
Sandstone	20	2150–2300	0.71	1.6–2.1	0.01–0.013
Sawdust, dry	20	215		0.07	

NONMETALLIC SOLIDS (*Continued*)

Material	T (°C)	ρ (kg/m³)	c_P (kJ/kg · K)	k (W/m · K)	α (cm²/s)
Silica aerogel	0	140		0.024	
Silica stone (85% SiC)	700	2720	1.05	1.56	0.055
Silicon	20	2330	0.703	153	0.94
Silk (artificial)	35	100	1.33	0.049	0.0037
Slag	20	2500–3000	0.84	0.57	0.0023–0.0027
Slate					
Parallel to lamination	20	2700	0.75	2.9	0.014
Perpendicular to lamination	20	2700	0.75	1.83	0.009
Snow, firm	0	560	2.1	0.46	0.0039
Soil (*see also* Earth)					
Dry	15	1500	1.84	1	0.004
Wet	15	1930		2	
Strawberries, dry	−18			0.59	
Sugar (fine)	0	1600	1.25	0.58	0.0029
Sulfur	20	2070	0.72	0.27	0.0018
Teflon (polytetrafluoroethylene)	20	2200	1.04	0.23	0.001
Wood, perpendicular to grain					
Ash	15	740		0.15–0.3	
Balsa	15	100		0.05	
Cedar	15	480		0.11	
Mahogany	20	700		0.16	
Oak	20	600–800	2.4	0.17–0.25	~0.0012
Pine, fir, spruce	20	416–421	2.72	0.15	0.0012
Plywood	20	590		0.11	
Wool					
Sheep	20	100	1.72	0.036	0.0021
Mineral	50	200	0.92	0.046	0.0025
Slag	25	200	0.8	0.05	0.0031

Source: Constructed based on data compiled in Refs. 1–9.

METALLIC SOLIDS

Metals, Alloys	Properties at 20°C (293 K)				Thermal Conductivity k (W/m · K)						
	ρ (kg/m³)	c_P (kJ/kg · K)	k (W/m · K)	α (cm²/s)	−100°C (173 K)	0°C (273 K)	100°C (373 K)	200°C (473 K)	400°C (673 K)	600°C (873 K)	1000°C (1273 K)
Aluminum											
Pure	2,707	0.896	204	0.842	215	202	206	215	249		
Duralumin (94–96% Al, 3–5% Cu, trace Mg)	2,787	0.883	164	0.667	126	159	182	194			
Silumin (87% Al, 13% Si)	2,659	0.871	164	0.710	149	163	175	185			
Antimony	6,690	0.208	17.4	0.125	19.2	17.7	16.3	16.0	17.2		
Beryllium	1,850	1.750	167	0.516	126	160	191	215			
Bismuth, polycrystalline	9,780	0.124	7.9	0.065	12.1	8.4	7.2	7.2			
Cadmium, polycrystalline	8,650	0.231	92.8	0.464	97	93	92	91			
Cesium	1,873	0.230	36	0.836							
Chromium	7190	0.453	90	0.276	120	95	88	85	77		
Cobalt (97.1% Co), polycrystalline	8,900	0.389	70	0.202							
Copper											
Pure	8,954	0.384	398	1.16	420	401	391	389	378	366	336
Commercial	8,300	0.419	372	1.07							
Aluminum bronze (95% Cu, 5% Al)	8,666	0.410	83	0.233							
Brass (70% Cu, 30% Zn)	8,522	0.385	111	0.341	88		128	144	147		
Brass (60% Cu, 40% Zn)	8,400	0.376	113	0.358							
Bronze (75% Cu, 25% Sn)	8,666	0.343	26	0.086							

METALLIC SOLIDS (Continued)

Metals, Alloys	Properties at 20°C (293 K)				Thermal Conductivity k (W/m·K)						
	ρ (kg/m³)	c_p (kJ/kg·K)	k (W/m·K)	α (cm²/s)	−100°C (173 K)	0°C (273 K)	100°C (373 K)	200°C (473 K)	400°C (673 K)	600°C (873 K)	1000°C (1273 K)
Bronze (85% Cu, 6% Sn, 9% Zn, 1% Pb)	8,800	0.377	61.7	0.186							
Constantan (60% Cu, 40% Ni)	8,922	0.410	22.7	0.061	21		22.2	26			
German silver (62% Cu, 15% Ni, 22% Zn)	8,618	0.394	24.9	0.073	19.2		31	40	48		
Gold	19,300	0.129	315	1.27		318		309			
Iron											
Pure	7,897	0.452	73	0.205	87	73	67	62	48	40	35
Cast (5% C)	7,272	0.420	52	0.170							
Carbon steel, 0.5% C	7,833	0.465	54	0.148		55	52	48	42	35	29
1.0% C	7,801	0.473	43	0.117		43	43	42	36	33	28
1.5% C	7,753	0.486	36	0.097		36	36	36	33	31	28
Chrome steel, 1% Cr	7,865	0.460	61	0.167		62	55	52	42	36	33
5% Cr	7,833	0.460	40	0.111		40	38	36	33	29	29
20% Cr	7,689	0.460	22	0.064		22	22	22	24	24	29
Chrome–nickel steel,											
15% Cr, 10% Ni	7,865	0.460	19	0.053							
20% Cr, 15% Ni	7,833	0.460	15.1	0.042							
Invar (36% Ni)	8,137	0.460	10.7	0.029							
Manganese steel, 1% Mn	7,865	0.460	50	0.139							
5% Mn	7,849	0.460	22	0.064							
Nickel–chrome steel											
80% Ni, 15% Cr	8,522	0.460	17	0.045			15.1	15.1	17	19	
20% Ni, 15% Cr	7,865	0.460	14	0.039	14						

Material											
Silicon steel, 1% Si	7,769	0.460	42	0.116			15	17	21	25	28
5% Si	7,417	0.460	19	0.056			16	18	20	23	
Stainless steel, type 304	7,817	0.460	13.8	0.040							
type 347	7,817	0.420	15	0.044							
Tungsten steel, 2% W	7,961	0.444	62	0.176	13	62	59	54	48	45	36
10% W	8,314	0.419	48	0.139							
Wrought (0.5% CH)	7,849	0.460	59	0.163		59	57	52	45	36	33
Lead	11,340	0.130	34.8	0.236	36.9	35.1	33.4	31.6	23.3		
Lithium	530	3.392	61	0.340		61	61				
Magnesium / Pure	1,746	1.013	171	0.970	178	171	168	163	109		
6–8% Al, 1–2% Zn, electrolytic	1,810	1.000	66	0.360		52	62	74	64		
2% Mn	1,778	1.000	114	0.640	93	111	125	130			
Manganese / Pure	7,300	0.486	7.8	0.022							
Manganin (85% Cu, 4% Ni, 12% Mn)	8,400	0.406	21.9	0.064							
Molybdenum	10,220	0.251	123	0.480	138	125	118	114		106	99
Monel 505 (at 60°C)	8,360	0.544	19.7	0.043							
Nickel / Pure	8,906	0.445	91	0.230	114	94	83	74		69	78
Nichrome (24% Fe, 16% Cr)	8,250	0.448	12.6	0.034							
90% Ni, 10% Cr	8,666	0.444	17	0.044		17.1	18.9	20.9	24.6		
Niobium	8,570	0.270	53	0.230							
Palladium	12,020	0.247	75.5	0.254		75.5	75.5	75.5	75.5		
Platinum	21,450	0.133	71.4	0.250	73	72	72	72	74	77	84

METALLIC SOLIDS (Continued)

Metals, Alloys	Properties at 20°C (293 K)				Thermal Conductivity k (W/m · K)						
	ρ (kg/m³)	c_P (kJ/kg · K)	k (W/m · K)	α (cm²/s)	−100°C (173 K)	0°C (273 K)	100°C (373 K)	200°C (473 K)	400°C (673 K)	600°C (873 K)	1000°C (1273 K)
Potassium	860	0.741	103	1.62							
Rhenium	21,100	0.137	48.1	0.166							
Rhodium	12,450	0.248	150	0.486							
Rubidium	1,530	0.348	58.2	1.09							
Silver, 99.99% Ag	10,524	0.236	427	1.72	431	428	422	417	401	386	
99.90% Ag	10,524	0.236	411	1.66	422	405		373	364		
Sodium	971	1.206	133	1.14							
Tantalum	16,600	0.138	57.5	0.251		57.4					
Tin, polycrystalline	7,304	0.220	67	0.417	76	68	63				
Titanium, polycrystalline	4,540	0.523	22	0.093	26	22	21	20	19	21	22
Tungsten, polycrystalline	19,300	0.134	179	0.692		182					
Uranium	18,700	0.116	28	0.129	24	27	29	31	36	41	
Vanadium	6,100	0.502	31.4	0.103		31.3					
Wood's metal (50% Bi, 25% Pb, 12.4% VCd, 12.5% Sn)	1,056	0.147	12.8	0.825							
Zinc	7,144	0.388	121	0.437	122	122	117	110	100		
Zirconium, polycrystalline	6,570	0.272	22.8	0.128		23.2					

Source: Constructed based on data compiled in Refs. 1–7.

ICE PROPERTIES

T (0°C)	ρ^b (g/cm^3)	h_{sf} (kJ/kg)	β (K^{-1})[a]
0	0.9164	333.4	
−5		308.5	
−10	0.9187	284.8	1.56×10^{-4}
−15		261.6	
−20	0.9203	241.4	1.38×10^{-4}
−40	0.9228		1.29×10^{-4}
−100	0.9273		1.24×10^{-4}
−200	0.9328		1.1×10^{-5}

Source: Constructed based on data compiled in Ref. 10.
[a]At atmospheric pressure.

POROUS MATERIALS

Material	Porosity φ	Permeability K (cm^2)	Contact Surface per Volume (cm^{-1})
Agar–agar		$2 \times 10^{-10} - 4.4 \times 10^{-9}$	
Black slate powder	0.57–0.66	$4.9 \times 10^{-10} - 1.2 \times 10^{-9}$	$7 \times 10^3 - 8.9 \times 10^3$
Brick	0.12–0.34	$4.8 \times 10^{-11} - 2.2 \times 10^{-9}$	
Catalyst (Fischer–Tropsch, granules only)	0.45		5.6×10^5
Cigarette		1.1×10^{-5}	
Cigarette filters	0.17–0.49		
Coal	0.02–0.12		
Concrete (ordinary mixes)	∼0.10		
Concrete (bituminous)		$1 \times 10^{-9} - 2.3 \times 10^{-7}$	
Copper powder (hot-compacted)	0.09–0.34	$3.3 \times 10^{-6} - 1.5 \times 10^{-5}$	
Cork board		$2.4 \times 10^{-7} - 5.1 \times 10^{-7}$	
Fiberglass	0.88–0.93		560–770
Granular crushed rock	0.45		
Hair (on mammals)	0.95–0.99		
Hair felt		$8.3 \times 10^{-6} - 1.2 \times 10^{-5}$	
Leather	0.56–0.59	$9.5 \times 10^{-10} - 1.2 \times 10^{-9}$	$1.2 \times 10^4 - 1.6 \times 10^4$
Limestone (dolomite)	0.04–0.10	$2 \times 10^{-11} - 4.5 \times 10^{-10}$	
Sand	0.37–0.50	$2 \times 10^{-7} - 1.8 \times 10^{-6}$	150–220
Sandstone (''oil sand'')	0.08–0.38	$5 \times 10^{-12} - 3 \times 10^{-8}$	
Silica grains	0.65		
Silica powder	0.37–0.49	$1.3 \times 10^{-10} - 5.1 \times 10^{-10}$	$6.8 \times 10^3 - 8.9 \times 10^3$
Soil	0.43–0.54	$2.9 \times 10^{-9} - 1.4 \times 10^{-7}$	
Spherical packings (well shaken)	0.36–0.43		
Wire crimps	0.68–0.76	$3.8 \times 10^{-5} - 1 \times 10^{-4}$	29–40

Source: Bejan et al. [11], based on data compiled in Refs. 12–14.

REFERENCES

1. E. R. G. Eckert and R. M. Drake, *Analysis of Heat and Mass Transfer*, McGraw-Hill, New York, 1972.

2. Y. S. Touloukian and C. Y. Ho, eds., *Thermophysical Properties of Matter*, Plenum, New York, 1972.

3. K. Raznjevic, *Handbook of Thermodynamic Tables and Charts*, Hemisphere, Washington, DC, 1976.

4. U. Grigull and H. Sandner, *Heat Conduction*, translated by J. Kestin, Hemisphere, Washington, DC, 1984, Appendix E.

5. F. Kreith and W. Z. Black, *Basic Heat Transfer*, Harper & Row, New York, 1980, Appendix E.

6. J. H. Lienhard, *A Heat Transfer Textbook*, 2nd ed., Prentice-Hall, Englewood Cliffs, NJ, 1987, Appendix A.

7. L. C. Witte, P. S. Schmidt, and D. R. Brown, *Industrial Energy Management and Utilization*, Hemisphere, New York, 1988.

8. M. S. Qashou, R. I. Vachon, and Y. S. Touloukian, Thermal conductivity of foods, *ASHRAE Trans.*, Vol. 78, pt. 1, 1972, pp. 165–183.

9. R. Dickerson, Jr. and R. B. Reed, Jr., Thermal diffusivity of meats, *ASHRAE Trans.*, Vol. 81, 1975, pp. 356–364.

10. P. V. Hobbs, *Ice Physics*, Oxford University Press, 1974, Chapter 5.

11. A. Bejan, I. Dincer, S. Lorente, A. F. Miguel and A. H. Reis, *Porous and Complex Flow Structures in Modern Technologies*, Springer-Verlag, New York, 2004.

12. D. A. Nield and A. Bejan, *Convection in Porous Media*, 2nd ed., Springer-Verlag, New York, 1999.

13. A. E. Scheidegger, *The Physics of Flow through Porous Media*, University of Toronto Press, Toronto, 1974.

14. A. Bejan and J. L. Lage, Heat transfer from a surface covered with hair, in S. Kakac, B. Kilkis, and F. A. Kulacki, eds., *Convective Heat and Mass Transfer in Porous Media*, Kluwer Academic, Dordrecht, The Netherlands, 1991.

C

PROPERTIES OF LIQUIDS

WATER AT ATMOSPHERIC PRESSURE

T (°C)	ρ (g/cm^3)	c_P (kJ/kg · K)	c_v (kJ/kg · K)	h_{fg} (kJ/kg)	β (K^{-1})
0	0.9999	4.217	4.215	2501	-0.6×10^{-4}
5	1	4.202	4.202	2489	$+0.1 \times 10^{-4}$
10	0.9997	4.192	4.187	2477	0.9×10^{-4}
15	0.9991	4.186	4.173	2465	1.5×10^{-4}
20	0.9982	4.182	4.158	2454	2.1×10^{-4}
25	0.9971	4.179	4.138	2442	2.6×10^{-4}
30	0.9957	4.178	4.118	2430	3.0×10^{-4}
35	0.9941	4.178	4.108	2418	3.4×10^{-4}
40	0.9923	4.178	4.088	2406	3.8×10^{-4}
50	0.9881	4.180	4.050	2382	4.5×10^{-4}
60	0.9832	4.184	4.004	2357	5.1×10^{-4}
70	0.9778	4.189	3.959	2333	5.7×10^{-4}
80	0.9718	4.196	3.906	2308	6.2×10^{-4}
90	0.9653	4.205	3.865	2283	6.7×10^{-4}
100[a]	0.9584	4.216	3.816	2257	7.1×10^{-4}

WATER AT ATMOSPHERIC PRESSURE (*Continued*)

T (°C)	μ (g/cm · s)	ν (cm²/s)	k (W/m · K)	α (cm²/s)	Pr	$\dfrac{g\beta}{\alpha\nu} = \dfrac{\text{Ra}_H}{H^3\ \Delta T}$ (K⁻¹ · cm⁻³)
0	0.01787	0.01787	0.56	0.00133	13.44	-2.48×10^3
5	0.01514	0.01514	0.57	0.00136	11.13	$+0.47 \times 10^3$
10	0.01304	0.01304	0.58	0.00138	9.45	4.91×10^3
15	0.01137	0.01138	0.59	0.00140	8.13	9.24×10^3
20	0.01002	0.01004	0.59	0.00142	7.07	14.45×10^3
25	0.00891	0.00894	0.60	0.00144	6.21	19.81×10^3
30	0.00798	0.00802	0.61	0.00146	5.49	25.13×10^3
35	0.00720	0.00725	0.62	0.00149	4.87	30.88×10^3
40	0.00654	0.00659	0.63	0.00152	4.34	37.21×10^3
50	0.00548	0.00554	0.64	0.00155	3.57	51.41×10^3
60	0.00467	0.00475	0.65	0.00158	3.01	66.66×10^3
70	0.00405	0.00414	0.66	0.00161	2.57	83.89×10^3
80	0.00355	0.00366	0.67	0.00164	2.23	101.3×10^3
90	0.00316	0.00327	0.67	0.00165	1.98	121.8×10^3
100	0.00283	0.00295	0.68	0.00166	1.78	142.2×10^3

Source: Data collected from Refs. 1–3.
[a]Saturated.

WATER AT SATURATION PRESSURE

T (°C)	ρ (g/cm³)	c_P (kJ/kg · K)	μ (g/cm · s)	ν (cm²/s)	k (W/m · K)	α (cm²/s)	Pr
0	0.9999	4.226	0.0179	0.0179	0.56	0.0013	13.7
10	0.9997	4.195	0.0130	0.0130	0.58	0.0014	9.5
20	0.9982	4.182	0.0099	0.0101	0.60	0.0014	7
40	0.9922	4.175	0.0066	0.0066	0.63	0.0015	4.3
60	0.9832	4.181	0.0047	0.0048	0.66	0.0016	3
80	0.9718	4.194	0.0035	0.0036	0.67	0.0017	2.25
100	0.9584	4.211	0.0028	0.0029	0.68	0.0017	1.75
150	0.9169	4.270	0.00185	0.0020	0.68	0.0017	1.17
200	0.8628	4.501	0.00139	0.0016	0.66	0.0017	0.95
250	0.7992	4.857	0.00110	0.00137	0.62	0.0016	0.86
300	0.7125	5.694	0.00092	0.00128	0.56	0.0013	0.98
340	0.6094	8.160	0.00077	0.00127	0.44	0.0009	1.45
370	0.4480	11.690	0.00057	0.00127	0.29	0.00058	2.18

Source: Data collected from Refs. 1 and 2.

AMMONIA, SATURATED LIQUID

T (°C)	ρ (g/cm^3)	c_P (kJ/kg · K)	μ (kg/s · m)	ν (cm^2/s)	k (W/m · K)	α (cm^2/s)	Pr
−50	0.704	4.46	3.06×10^{-4}	4.35×10^{-3}	0.547	1.74×10^{-3}	2.50
−25	0.673	4.49	2.58×10^{-4}	3.84×10^{-3}	0.548	1.81×10^{-3}	2.12
0	0.640	4.64	2.39×10^{-4}	3.73×10^{-3}	0.540	1.82×10^{-3}	2.05
25	0.604	4.84	2.14×10^{-4}	3.54×10^{-3}	0.514	1.76×10^{-3}	2.01
50	0.564	5.12	1.86×10^{-4}	3.30×10^{-3}	0.476	1.65×10^{-3}	2.00

Source: Constructed based on data compiled in Ref. 4.

CARBON DIOXIDE, SATURATED LIQUID

T (K)	P (bar)	ρ (g/cm^3)	c_P (kJ/kg · K)	μ (kg/s · m)	ν (cm^2/s)	k (W/m · K)	α (cm^2/s)	Pr
216.6	5.18	1.179	1.707	2.10×10^{-4}	1.78×10^{-3}	0.182	9.09×10^{-4}	1.96
220	6.00	1.167	1.761	1.86×10^{-4}	1.59×10^{-3}	0.178	8.26×10^{-4}	1.93
240	12.83	1.089	1.933	1.45×10^{-4}	1.33×10^{-3}	0.156	7.40×10^{-4}	1.80
260	24.19	1.000	2.125	1.14×10^{-4}	1.14×10^{-3}	0.128	6.03×10^{-4}	1.89
280	41.60	0.885	2.887	0.91×10^{-4}	1.03×10^{-3}	0.102	4.00×10^{-4}	2.57
300	67.10	0.680		0.71×10^{-4}	1.04×10^{-3}	0.081		
304.2	73.83	0.466		0.60×10^{-4}	1.29×10^{-3}	0.074		

Source: Constructed based on data compiled in Refs. 5 and 6.

FUELS, LIQUIDS AT P ≅ 1 atm

T (°C)	ρ (g/cm^3)	c_P (kJ/kg · K)	μ (kg/s · m)	ν (cm^2/s)	k (W/m · K)	α (cm^2/s)	Pr
			Gasoline				
20	0.751	2.06	5.29×10^{-4}	7.04×10^{-3}	0.1164	7.52×10^{-4}	9.4
50	0.721	2.20	3.70×10^{-4}	5.13×10^{-3}	0.1105	6.97×10^{-4}	7.4
100	0.681	2.46	2.25×10^{-4}	3.30×10^{-3}	0.1005	6.00×10^{-4}	5.5
150	0.628	2.74	1.56×10^{-4}	2.48×10^{-3}	0.0919	5.34×10^{-4}	4.6
200	0.570	3.04	1.11×10^{-4}	1.95×10^{-3}	0.0800	4.62×10^{-4}	4.2
			Kerosene				
20	0.819	2.00	1.49×10^{-3}	1.82×10^{-2}	0.1161	7.09×10^{-4}	25.7
50	0.801	2.14	9.56×10^{-4}	1.19×10^{-2}	0.1114	6.50×10^{-4}	18.3
100	0.766	2.38	5.45×10^{-4}	7.11×10^{-3}	0.1042	5.72×10^{-4}	12.4
150	0.728	2.63	3.64×10^{-4}	5.00×10^{-3}	0.0965	5.04×10^{-4}	9.9
200	0.685	2.89	2.62×10^{-4}	3.82×10^{-3}	0.0891	4.50×10^{-4}	8.5
250	0.638	3.16	2.01×10^{-4}	3.15×10^{-3}	0.0816	4.05×10^{-4}	7.8

Source: Constructed based on data compiled in Ref. 7.

HELIUM, LIQUID AT P = 1 atm

T (K)	ρ (g/cm^3)	c_P (kJ/kg · K)	μ (kg/s · m)	ν (cm^2/s)	k (W/m · K)	α (cm^2/s)	Pr
2.5	0.147	2.05	3.94×10^{-6}	2.68×10^{-4}	0.0167	5.58×10^{-4}	0.48
3	0.143	2.36	3.86×10^{-6}	2.69×10^{-4}	0.0182	5.38×10^{-4}	0.50
3.5	0.138	3.00	3.64×10^{-6}	2.64×10^{-4}	0.0191	4.62×10^{-4}	0.57
4	0.130	4.07	3.34×10^{-6}	2.57×10^{-4}	0.0196	3.71×10^{-4}	0.69
4.22[a]	0.125	4.98	3.17×10^{-6}	2.53×10^{-4}	0.0196	3.15×10^{-4}	0.80

Source: Data collected from Ref. 8.
[a]Saturated.

LITHIUM, SATURATED LIQUID

T (K)	P (bar)	ρ (g/cm^3)	c_P (kJ/kg · K)	μ (kg/s · m)	ν (cm^2/s)	k (W/m · K)	α (cm^2/s)	Pr
600	4.2×10^{-9}	0.503	4.23	4.26×10^{-4}	0.0085	47.6	0.223	0.038
800	9.6×10^{-6}	0.483	4.16	3.10×10^{-4}	0.0064	54.1	0.270	0.024
1000	9.6×10^{-4}	0.463	4.16	2.47×10^{-4}	0.0053	60.0	0.312	0.017
1200	0.0204	0.442	4.14	2.07×10^{-4}	0.0047	64.7	0.355	0.013
1400	0.1794	0.422	4.19	1.80×10^{-4}	0.0043	68.0	0.384	0.011

Source: Constructed based on data compiled in Refs. 5 and 6.

MERCURY, SATURATED LIQUID

T (K)	P (bar)	ρ (g/cm^3)	c_P (kJ/kg · K)	μ (kg/s · m)	ν (cm^2/s)	k (W/m · K)	α (cm^2/s)	Pr	β (K^{-1})
260	6.9×10^{-8}	13.63	0.141	1.79×10^{-3}	1.31×10^{-3}	8.00	0.042	0.0316	1.8×10^{-4}
300	3.1×10^{-6}	13.53	0.139	1.52×10^{-3}	1.12×10^{-3}	8.54	0.045	0.0248	1.8×10^{-4}
340	5.5×10^{-5}	13.43	0.138	1.34×10^{-3}	1.00×10^{-3}	9.06	0.049	0.0205	1.8×10^{-4}
400	1.4×10^{-3}	13.29	0.137	1.17×10^{-3}	8.83×10^{-4}	9.80	0.054	0.0163	1.8×10^{-4}
500	0.053	13.05	0.135	1.01×10^{-3}	7.72×10^{-4}	10.93	0.062	0.0125	1.8×10^{-4}
600	0.578	12.81	0.136	9.10×10^{-4}	7.10×10^{-4}	11.94	0.071	0.0100	1.9×10^{-4}
800	11.18	12.32	0.140	8.08×10^{-4}	6.56×10^{-4}	13.57	0.079	0.0083	1.9×10^{-4}
1000	65.74	11.79	0.149	7.54×10^{-4}	6.40×10^{-4}	14.69	0.084	0.0076	1.9×10^{-4}

Source: Constructed based on data compiled in Refs. 5 and 6.

NITROGEN, LIQUID AT P = 1 atm

T (K)	ρ (g/cm^3)	c_P (kJ/kg · K)	μ (kg/s · m)	ν (cm^2/s)	k (W/m · K)	α (cm^2/s)	Pr
65	0.861	1.988	2.77×10^{-5}	3.21×10^{-3}	0.161	9.39×10^{-4}	3.42
70	0.840	2.042	2.12×10^{-5}	2.53×10^{-3}	0.151	8.77×10^{-4}	2.88
75	0.819	2.059	1.77×10^{-5}	2.17×10^{-3}	0.141	8.36×10^{-4}	2.59
77.3[a]	0.809	2.065	1.64×10^{-5}	2.03×10^{-3}	0.136	8.15×10^{-4}	2.49

Source: Interpolated from data in Ref. 9.
[a]Saturated.

POTASSIUM, SATURATED LIQUID

T (K)	P (bar)	ρ (g/cm^3)	c_P (kJ/kg · K)	μ (kg/s · m)	ν (cm^2/s)	k (W/m · K)	α (cm^2/s)	Pr
400	1.84×10^{-7}	0.814	0.805	4.13×10^{-4}	0.0051	52.0	0.794	0.0064
600	9.26×10^{-4}	0.767	0.771	2.38×10^{-4}	0.0031	43.9	0.742	0.0042
800	0.0612	0.720	0.761	1.71×10^{-4}	0.0024	37.1	0.677	0.0035
1000	0.7322	0.672	0.792	1.35×10^{-4}	0.0020	31.3	0.589	0.0034
1200	3.963	0.623	0.846	1.14×10^{-4}	0.0018	26.3	0.499	0.0037
1400	12.44	0.574	0.899	0.98×10^{-4}	0.0017	21.5	0.416	0.0041

Source: Constructed based on data compiled in Refs. 5 and 6.

REFRIGERANT 12 (FREON 12, CCl$_2$F$_2$), SATURATED LIQUID

P (bar)	T (K)	ρ (g/cm^3)	c_P (kJ/kg · K)	μ (kg/s · m)	ν (cm^2/s)	k (W/m · K)	α (cm^2/s)	Pr
0.2	211.1	1.579	0.865	5.28×10^{-4}	3.34×10^{-3}	0.101	7.40×10^{-4}	4.52
0.4	223.5	1.554	0.876	4.48×10^{-4}	2.88×10^{-3}	0.097	7.12×10^{-4}	4.05
0.6	231.7	1.522	0.884	4.08×10^{-4}	2.68×10^{-3}	0.094	6.98×10^{-4}	3.84
1.0	243.0	1.488	0.894	3.59×10^{-4}	2.41×10^{-3}	0.089	6.68×10^{-4}	3.61
2.0	260.6	1.435	0.914	2.95×10^{-4}	2.06×10^{-3}	0.083	6.33×10^{-4}	3.25
3.0	272.3	1.392	0.930	2.62×10^{-4}	1.88×10^{-3}	0.079	6.11×10^{-4}	3.08
6.0	295.2	1.321	0.969	2.13×10^{-4}	1.61×10^{-3}	0.070	5.47×10^{-4}	2.95
10.0	314.9	1.247	1.023	1.88×10^{-4}	1.51×10^{-3}	0.063	4.94×10^{-4}	3.05
20.0	346.3	1.099	1.234	1.49×10^{-4}	1.36×10^{-3}	0.053	3.91×10^{-4}	3.47
30.0	367.2	0.955	1.520	1.16×10^{-4}	1.21×10^{-3}	0.042	2.89×10^{-4}	4.20

Source: Constructed based on data compiled in Refs. 5 and 6.

REFRIGERANT 22 (Freon 22, CHClF$_2$), Saturated Liquid

T (K)	P (bar)	ρ (g/cm^3)	c_p (kJ/kg · K)	μ (kg/s · m)	ν (cm^2/s)	k (W/m · K)	α (cm^2/s)	Pr
180	0.037	1.545	1.058	6.47×10^{-5}	4.19×10^{-4}	0.146	8.93×10^{-4}	0.47
200	0.166	1.497	1.065	4.81×10^{-5}	3.21×10^{-4}	0.136	8.53×10^{-4}	0.38
220	0.547	1.446	1.080	3.78×10^{-5}	2.61×10^{-4}	0.126	8.07×10^{-4}	0.32
240	1.435	1.390	1.105	3.09×10^{-5}	2.22×10^{-4}	0.117	7.62×10^{-4}	0.29
260	3.177	1.329	1.143	2.60×10^{-5}	1.96×10^{-4}	0.107	7.04×10^{-4}	0.28
280	6.192	1.262	1.193	2.25×10^{-5}	1.78×10^{-4}	0.097	6.44×10^{-4}	0.28
300	10.96	1.187	1.257	1.98×10^{-5}	1.67×10^{-4}	0.087	5.83×10^{-4}	0.29
320	18.02	1.099	1.372	1.76×10^{-5}	1.60×10^{-4}	0.077	5.11×10^{-4}	0.31
340	28.03	0.990	1.573	1.51×10^{-5}	1.53×10^{-4}	0.067	4.30×10^{-4}	0.36

Source: Constructed based on data compiled in Ref. 6.

SODIUM, SATURATED LIQUID

T (K)	P (bar)	ρ (g/cm^3)	c_P (kJ/kg · K)	μ (kg/s · m)	ν (cm^2/s)	k (W/m · K)	α (cm^2/s)	Pr
500	7.64×10^{-7}	0.898	1.330	4.24×10^{-4}	0.0047	80.0	0.67	0.0070
600	5.05×10^{-5}	0.873	1.299	3.28×10^{-4}	0.0038	75.4	0.66	0.0057
700	9.78×10^{-4}	0.850	1.278	2.69×10^{-4}	0.0032	70.7	0.65	0.0049
800	0.00904	0.826	1.264	2.30×10^{-4}	0.0028	65.9	0.63	0.0044
900	0.0501	0.802	1.258	2.02×10^{-4}	0.0025	61.4	0.61	0.0041
1000	0.1955	0.776	1.259	1.81×10^{-4}	0.0023	56.7	0.58	0.0040
1200	1.482	0.729	1.281	1.51×10^{-4}	0.0021	54.5	0.58	0.0036
1400	6.203	0.681	1.330	1.32×10^{-4}	0.0019	52.2	0.58	0.0034
1600	17.98	0.633	1.406	1.18×10^{-4}	0.0019	49.9	0.56	0.0033

Source: Constructed based on data compiled in Refs. 5 and 6.

UNUSED ENGINE OIL

T (K)	ρ (g/cm^3)	c_P (kJ/kg · K)	μ (kg/s · m)	ν (cm^2/s)	k (W/m · K)	α (cm^2/s)	Pr	β (K^{-1})
260	0.908	1.76	12.23	135	0.149	9.32×10^{-4}	144500	7×10^{-4}
280	0.896	1.83	2.17	24.2	0.146	8.90×10^{-4}	27200	7×10^{-4}
300	0.884	1.91	0.486	5.50	0.144	8.53×10^{-4}	6450	7×10^{-4}
320	0.872	1.99	0.141	1.62	0.141	8.13×10^{-4}	1990	7×10^{-4}
340	0.860	2.08	0.053	0.62	0.139	7.77×10^{-4}	795	7×10^{-4}
360	0.848	2.16	0.025	0.30	0.137	7.48×10^{-4}	395	7×10^{-4}
380	0.836	2.25	0.014	0.17	0.136	7.23×10^{-4}	230	7×10^{-4}
400	0.824	2.34	0.009	0.11	0.134	6.95×10^{-4}	155	7×10^{-4}

Source: Constructed based on data compiled in Refs. 5 and 6.

CRITICAL POINT DATA

Liquid	Critical Temperature		Critical Pressure		Critical Specific Volume (cm³/g)
	K	°C	MPa	atm	
Air	133.2	−140	3.77	37.2	2.9
Alcohol (ethyl)	516.5	243.3	6.39	63.1	3.6
Alcohol (methyl)	513.2	240	7.98	78.7	3.7
Ammonia	405.4	132.2	11.3	111.6	4.25
Argon	150.9	−122.2	4.86	48	1.88
Butane	425.9	152.8	3.65	36	4.4
Carbon dioxide	304.3	31.1	7.4	73	2.2
Carbon monoxide	134.3	−138.9	3.54	35	3.2
Carbon tetrachloride	555.9	282.8	4.56	45	1.81
Chlorine	417	143.9	7.72	76.14	1.75
Ethane	305.4	32.2	4.94	48.8	4.75
Ethylene	282.6	9.4	5.85	57.7	4.6
Helium	5.2	−268	0.228	2.25	14.4
Hexane	508.2	235	2.99	29.5	4.25
Hydrogen	33.2	−240	1.30	12.79	32.3
Methane	190.9	−82.2	4.64	45.8	6.2
Methyl chloride	416.5	143.3	6.67	65.8	2.7
Neon	44.2	−288.9	2.7	26.6	2.1
Nitric oxide	179.3	−93.9	6.58	65	1.94
Nitrogen	125.9	−147.2	3.39	33.5	3.25
Octane	569.3	296.1	2.5	24.63	4.25
Oxygen	154.3	−118.9	5.03	49.7	2.3
Propane	368.7	95.6	4.36	43	4.4
Sulfur dioxide	430.4	157.2	7.87	77.7	1.94
Water	647	373.9	22.1	218.2	3.1

Source: Based on a compilation from Ref. 10.

REFERENCES

1. A. Bejan, *Convection Heat Transfer*, Wiley, New York, 1984, pp. 462–465.
2. K. Raznjevic, *Handbook of Thermodynamic Tables and Charts*, Hemisphere, Washington, DC, 1976.
3. G. K. Batchelor, *An Introduction to Fluid Dynamics*, Cambridge University Press, Cambridge, 1967.
4. E. R. G. Eckert and R. M. Drake, *Analysis of Heat and Mass Transfer*, McGraw-Hill, New York, 1972.
5. D. W. Green and J. O. Maloney, eds., *Perry's Chemical Engineers' Handbook*, 6th ed., McGraw-Hill, New York, 1984, pp. 3–1 to 3–263.
6. P. E. Liley, Thermophysical properties, in S. Kakac, R. K. Shah, and W. Aung, eds., *Handbook of Single-Phase Convective Heat Transfer*, Wiley, New York, 1987, Chapter 22.

7. N. B. Vargaftik, *Tables on the Thermophysical Properties of Liquids and Gases*, 2nd ed., Hemisphere, Washington, DC, 1975.

8. R. D. McCarty, Thermophysical properties of Helium-4 from 2 to 1500 K with pressures to 1000 atmospheres, NBS TN 631, National Bureau of Standards, Washington, DC, November 1972.

9. R. T. Jacobsen, R.B. Stewart, R. D. McCarty, and H. J. M. Hanley, Thermophysical properties of nitrogen from the fusion line to 3500 R (1944 K) for pressures to 150,000 psia (10342 $\times$ 10^5 N/m^2), NBS TN 648, National Bureau of Standards, Washington, DC, December 1973.

10. A. Bejan, *Advanced Engineering Thermodynamics*, 3rd ed., Wiley, Hoboken, 2006.

D

PROPERTIES OF GASES

DRY AIR AT ATMOSPHERIC PRESSURE

T (°C)	ρ (kg/m^3)	c_P (kJ/kg · K)	μ (kg/s · m)	ν (cm^2/s)	k (W/m · K)	α (cm^2/s)	Pr	$\dfrac{g\beta}{\alpha\nu} = \dfrac{\mathrm{Ra}_H}{H^3\,\Delta T}$ (cm^{-3} · K^{-1})
−180	3.72	1.035	6.50×10^{-6}	0.0175	0.0076	0.019	0.92	3.2×10^4
−100	2.04	1.010	1.16×10^{-5}	0.057	0.016	0.076	0.75	1.3×10^3
−50	1.582	1.006	1.45×10^{-5}	0.092	0.020	0.130	0.72	367
0	1.293	1.006	1.71×10^{-5}	0.132	0.024	0.184	0.72	148
10	1.247	1.006	1.76×10^{-5}	0.141	0.025	0.196	0.72	125
20	1.205	1.006	1.81×10^{-5}	0.150	0.025	0.208	0.72	107
30	1.165	1.006	1.86×10^{-5}	0.160	0.026	0.223	0.72	90.7
60	1.060	1.008	2.00×10^{-5}	0.188	0.028	0.274	0.70	57.1
100	0.946	1.011	2.18×10^{-5}	0.230	0.032	0.328	0.70	34.8
200	0.746	1.025	2.58×10^{-5}	0.346	0.039	0.519	0.68	9.53
300	0.616	1.045	2.95×10^{-5}	0.481	0.045	0.717	0.68	4.96
500	0.456	1.093	3.58×10^{-5}	0.785	0.056	1.140	0.70	1.42
1000	0.277	1.185	4.82×10^{-5}	1.745	0.076	2.424	0.72	0.18

Source: Data collected from Refs. 1–3.

AMMONIA, GAS AT $P = 1$ atm

T ($^\circ$C)	ρ (kg/m^3)	c_P (kJ/kg · K)	μ (kg/s · m)	ν (cm^2/s)	k (W/m · K)	α (cm^2/s)	Pr
0	0.793	2.18	9.35×10^{-6}	0.118	0.0220	0.131	0.90
50	0.649	2.18	1.10×10^{-5}	0.170	0.0270	0.192	0.88
100	0.559	2.24	1.29×10^{-5}	0.230	0.0327	0.262	0.87
150	0.493	2.32	1.47×10^{-5}	0.297	0.0391	0.343	0.87
200	0.441	2.40	1.65×10^{-5}	0.374	0.0467	0.442	0.84

Source: Constructed based on data compiled in Ref. 4.

CARBON DIOXIDE, GAS AT $P = 1$ bar

T (K)	ρ (kg/m^3)	c_P (kJ/kg · K)	μ (kg/s · m)	ν (cm^2/s)	k (W/m · K)	α (cm^2/s)	Pr
300	1.773	0.852	1.51×10^{-5}	0.085	0.0166	0.109	0.78
350	1.516	0.898	1.75×10^{-5}	0.115	0.0204	0.150	0.77
400	1.326	0.941	1.98×10^{-5}	0.149	0.0243	0.195	0.77
500	1.059	1.014	2.42×10^{-5}	0.229	0.0325	0.303	0.76
600	0.883	1.075	2.81×10^{-5}	0.318	0.0407	0.429	0.74
700	0.751	1.126	3.17×10^{-5}	0.422	0.0481	0.569	0.74
800	0.661	1.168	3.50×10^{-5}	0.530	0.0551	0.714	0.74
900	0.588	1.205	3.81×10^{-5}	0.648	0.0618	0.873	0.74
1000	0.529	1.234	4.10×10^{-5}	0.775	0.0682	1.043	0.74

Source: Constructed based on data compiled in Refs. 5 and 6.

HELIUM, GAS AT $P = 1$ atm

T (K)	ρ (kg/m^3)	c_P (kJ/kg · K)	μ (kg/s · m)	ν (cm^2/s)	k (W/m · K)	α (cm^2/s)	Pr
4.22	16.9	9.78	1.25×10^{-6}	7.39×10^{-4}	0.011	6.43×10^{-4}	1.15
7	7.53	5.71	1.76×10^{-6}	2.34×10^{-3}	0.014	3.21×10^{-3}	0.73
10	5.02	5.41	2.26×10^{-6}	4.49×10^{-3}	0.018	6.42×10^{-3}	0.70
20	2.44	5.25	3.58×10^{-6}	0.0147	0.027	0.0209	0.70
30	1.62	5.22	4.63×10^{-6}	0.0286	0.034	0.0403	0.71
60	0.811	5.20	7.12×10^{-6}	0.088	0.053	0.125	0.70
100	0.487	5.20	9.78×10^{-6}	0.201	0.074	0.291	0.69
200	0.244	5.19	1.51×10^{-5}	0.622	0.118	0.932	0.67
300	0.162	5.19	1.99×10^{-5}	1.22	0.155	1.83	0.67
600	0.0818	5.19	3.22×10^{-5}	3.96	0.251	5.94	0.67
1000	0.0487	5.19	4.63×10^{-5}	9.46	0.360	14.2	0.67

Source: Data collected from Ref. 7.

n-HYDROGEN, GAS AT $P = 1$ atm

T (K)	ρ (kg/m^3)	c_P (kJ/kg $\cdot$ K)	μ (kg/s $\cdot$ m)	ν (cm^2/s)	k (W/m $\cdot$ K)	α (cm^2/s)	Pr
250	0.0982	14.04	7.9×10^{-6}	0.804	0.162	1.17	0.69
300	0.0818	14.31	8.9×10^{-6}	1.09	0.187	1.59	0.69
350	0.0702	14.43	9.9×10^{-6}	1.41	0.210	2.06	0.69
400	0.0614	14.48	1.09×10^{-5}	1.78	0.230	2.60	0.68
500	0.0491	14.51	1.27×10^{-5}	2.59	0.269	3.78	0.68
600	0.0408	14.55	1.43×10^{-5}	3.50	0.305	5.12	0.68
700	0.0351	14.60	1.59×10^{-5}	4.53	0.340	6.62	0.68

Source: Constructed based on the data compiled in Refs. 5 and 6.

NITROGEN, GAS AT $P = 1$ atm

T (K)	ρ (kg/m^3)	c_P (kJ/kg $\cdot$ K)	μ (kg/s $\cdot$ m)	ν (cm^2/s)	k (W/m $\cdot$ K)	α (cm^2/s)	Pr
77.33	4.612	1.123	5.39×10^{-6}	0.0117	0.0076	0.0147	0.80
100	3.483	1.073	6.83×10^{-6}	0.0197	0.0097	0.0261	0.76
200	1.711	1.044	1.29×10^{-5}	0.0754	0.0185	0.103	0.73
300	1.138	1.041	1.78×10^{-5}	0.156	0.0259	0.218	0.72
400	0.854	1.045	2.20×10^{-5}	0.258	0.0324	0.363	0.71
500	0.683	1.056	2.58×10^{-5}	0.378	0.0386	0.535	0.71
600	0.569	1.075	2.91×10^{-5}	0.511	0.0442	0.722	0.71
700	0.488	1.098	3.21×10^{-5}	0.658	0.0496	0.925	0.71

Source: Data collected from Ref. 8.

OXYGEN, GAS AT $P = 1$ atm

T (K)	ρ (kg/m^3)	c_P (kJ/kg $\cdot$ K)	μ (kg/s $\cdot$ m)	ν (cm^2/s)	k (W/m $\cdot$ K)	α (cm^2/s)	Pr
250	1.562	0.915	1.79×10^{-5}	0.115	0.0226	0.158	0.73
300	1.301	0.920	2.07×10^{-5}	0.159	0.0266	0.222	0.72
350	1.021	0.929	2.34×10^{-5}	0.229	0.0305	0.321	0.71
400	0.976	0.942	2.58×10^{-5}	0.264	0.0343	0.372	0.71
500	0.780	0.972	3.03×10^{-5}	0.388	0.0416	0.549	0.71
600	0.650	1.003	3.44×10^{-5}	0.529	0.0487	0.748	0.71
700	0.557	1.031	3.81×10^{-5}	0.684	0.0554	0.963	0.71

Source: Constructed based on the data compiled in Refs. 5 and 6.

REFRIGERANT 12 (FREON 12, CCl_2F_2), GAS AT $P = 1$ bar

T (K)	ρ (kg/m^3)	c_p (kJ/kg · K)	μ (kg/s · m)	ν (cm^2/s)	k (W/m · K)	α (cm^2/s)	Pr
300	4.941	0.614	1.26×10^{-5}	0.026	0.0097	0.032	0.80
350	4.203	0.654	1.46×10^{-5}	0.035	0.0124	0.045	0.77
400	3.663	0.684	1.62×10^{-5}	0.044	0.0151	0.061	0.73
450	3.248	0.711	1.75×10^{-5}	0.054	0.0179	0.077	0.70
500	2.918	0.739	1.90×10^{-5}	0.065	0.0208	0.097	0.67

Source: Constructed based on the data compiled in Refs. 5 and 6.

REFRIGERANT 22 (FREON 22, $CHClF_2$), GAS AT $P = 1$ atm

T (K)	ρ (kg/m^3)	c_P (kJ/kg · K)	μ (kg/s · m)	ν (cm^2/s)	k (W/m · K)	α (cm^2/s)	Pr
250	4.320	0.587	1.09×10^{-5}	0.025	0.008	0.032	0.80
300	3.569	0.647	1.30×10^{-5}	0.036	0.011	0.048	0.77
350	3.040	0.704	1.51×10^{-5}	0.050	0.014	0.065	0.76
400	2.650	0.757	1.71×10^{-5}	0.065	0.017	0.085	0.76
450	2.352	0.806	1.90×10^{-5}	0.081	0.020	0.105	0.77
500	2.117	0.848	2.09×10^{-5}	0.099	0.023	0.128	0.77

Source: Constructed based on the data compiled in Refs. 5 and 6.

STEAM AT $P = 1$ bar

T (K)	ρ (kg/m^3)	c_P (kJ/kg · K)	μ (kg/s · m)	ν (cm^2/s)	k (W/m · K)	α (cm^2/s)	Pr
373.15	0.596	2.029	1.20×10^{-5}	0.201	0.0248	0.205	0.98
400	0.547	1.996	1.32×10^{-5}	0.241	0.0268	0.246	0.98
450	0.485	1.981	1.52×10^{-5}	0.313	0.0311	0.324	0.97
500	0.435	1.983	1.73×10^{-5}	0.398	0.0358	0.415	0.96
600	0.362	2.024	2.15×10^{-5}	0.594	0.0464	0.633	0.94
700	0.310	2.085	2.57×10^{-5}	0.829	0.0581	0.899	0.92
800	0.271	2.151	2.98×10^{-5}	1.10	0.0710	1.22	0.90
900	0.241	2.219	3.39×10^{-5}	1.41	0.0843	1.58	0.89
1000	0.217	2.286	3.78×10^{-5}	1.74	0.0981	1.98	0.88
1200	0.181	2.43	4.48×10^{-5}	2.48	0.130	2.96	0.84
1400	0.155	2.58	5.06×10^{-5}	3.27	0.160	4.00	0.82
1600	0.135	2.73	5.65×10^{-5}	4.19	0.210	5.69	0.74
1800	0.120	3.02	6.19×10^{-5}	5.16	0.330	9.10	0.57
2000	0.108	3.79	6.70×10^{-5}	6.20	0.570	13.94	0.45

Source: Constructed based on data compiled in Refs. 5 and 6.

IDEAL GAS CONSTANTS AND SPECIFIC HEATS[a]

Gas		M (kg/kmol)	R (kJ/kg · K)	c_P (kJ/kg · K)	c_v (kJ/kg · K)
Air, dry	—	28.97	0.287	1.005	0.718
Argon	Ar	39.944	0.208	0.525	0.317
Carbon dioxide	CO_2	44.01	0.189	0.846	0.657
Carbon monoxide	CO	28.01	0.297	1.040	0.744
Helium	He	4.003	2.077	5.23	3.15
Hydrogen	H_2	2.016	4.124	14.31	10.18
Methane	CH_4	16.04	0.518	2.23	1.69
Nitrogen	N_2	28.016	0.297	1.039	0.743
Oxygen	O_2	32.000	0.260	0.918	0.658
Water vapor	H_2O	18.016	0.461	1.87	1.40

Source: After Ref. 9.
[a]The c_P and c_v values correspond to the temperature 300 K. This ideal gas model is valid at low and moderate pressures ($P \lesssim 1$ atm).

HUMID AIR AS AN IDEAL GAS MIXTURE OF DRY AIR AND WATER VAPOR

Mole fraction of water vapor:

$$x_v = \frac{P_v}{P}, \quad P_v = \text{partial pressure of water vapor}$$
$$P = \text{mixture pressure}$$

Relative humidity:

$$\phi = \frac{P_v}{P_{sat}(T)}, \quad P_{sat} = \text{pressure of saturated water vapor at the mixture temperature } T$$

$$\phi = \frac{x_v \text{ in the actual mixture, at } T \text{ and } P}{x_v \text{ in the saturated mixture, at the same } T \text{ and } P}$$

Specific humidity, or humidity ratio:

$$\omega = \frac{m_v \text{ (kg water vapor in the mixture)}}{m_a \text{ (kg dry air in the mixture)}}$$

$$\omega = \frac{0.622}{[P/\phi P_{sat}(T)] - 1}$$

Relations between relative humidity and specific humidity:

$$\phi = \frac{\omega}{\omega + 0.662} \frac{P}{P_{sat}(T)}$$

$$\phi = \frac{\omega P_a}{0.662 P_{sat}(T)}, \qquad P_a = P - P_v$$

Source: After Ref. 9.

REFERENCES

1. A. Bejan, *Convection Heat Transfer*, Wiley, New York, 1984, p. 465.
2. K. Raznjevic, *Handbook of Thermodynamic Tables and Charts*, Hemisphere, Washington, DC, 1976.
3. G. K. Batchelor, *An Introduction to Fluid Dynamics*, Cambridge University Press, Cambridge, 1967.
4. E. R. G. Eckert and R. M. Drake, *Analysis of Heat and Mass Transfer*, McGraw-Hill, New York, 1972.
5. D. W. Green and J. O. Maloney, eds., *Perry's Chemical Engineers' Handbook*, 6th ed., McGraw-Hill, New York, 1984, pp. 3.1 to 3–263.
6. P. E. Liley, Thermophysical properties, in S. Kakac, R. K. Shah, and W. Aung, eds., *Handbook of Single-Phase Convective Heat Transfer*, Wiley, New York, 1987, Chapter 22.
7. R. D. McCarty, Thermophysical properties of Helium-4 from 2 to 1500 K with pressures to 1000 atmospheres, NBS TN 631, National Bureau of Standards, Washington, DC, November 1972.
8. R. T. Jacobsen, R. B. Stewart, R. D. McCarty, and H. J. M. Hanley, Thermophysical properties of nitrogen from the fusion line to 3500°R (1944 K) for pressures to 150,000 psia ($10,342 \times 10^5$ N/m^2), NBS TN 648, National Bureau of Standards, Washington, DC, December 1973.
9. A. Bejan, *Advanced Engineering Thermodynamics*, 3rd ed., Wiley, Hoboken, 2006.

E

MATHEMATICAL FORMULAS

ERROR FUNCTION

Definition and properties:

$$\mathrm{erf}(x) = \frac{2}{\pi^{1/2}} \int_0^x e^{-m^2} \, dm$$

$$\mathrm{erf}(-x) = -\mathrm{erf}(x)$$

$$\mathrm{erfc}(x) = 1 - \mathrm{erf}(x) \qquad \text{(complementary error function)}$$

$$\frac{d}{dx}\,[\mathrm{erf}(x)]_{x=0} = \frac{2}{\pi^{1/2}} = 1.12838$$

The usual error-function table: finding $\mathrm{erf}(x)$ when x is specified.

x	$\mathrm{erf}(x)$	x	$\mathrm{erf}(x)$
0	0	0.9	0.79691
0.01	0.01128	1	0.8427
0.1	0.11246	1.2	0.91031
0.2	0.2227	1.4	0.95229
0.3	0.32863	1.6	0.97635
0.4	0.42839	1.8	0.98909
0.5	0.5205	2	0.99532
0.6	0.60386	2.5	0.99959
0.7	0.6778	3	0.99998
0.8	0.74210	∞	1

The inverted table: finding x when $\mathrm{erf}(x)$ is specified:

$\mathrm{erf}(x)$	x
0	0
0.1	0.08886
0.2	0.17914
0.25	0.22531
0.3	0.27246
0.4	0.37081
0.5	0.47694
0.6	0.59512
0.7	0.73287
0.75	0.81342
0.8	0.90619
0.9	1.16309
1	∞

Closed-form approximate expressions for $\mathrm{erf}(x)$ and $\mathrm{erfc}(c)$, accurate within 0.42 percent [1]:

$$\mathrm{erf}(x) \cong 1 - A\ \exp[-B(x+C)^2]$$

$$\mathrm{erfc}(x) \cong A\ \exp[-B(x+C)^2]$$

where A, B, and C are three constants,

$$A = 1.5577, \qquad B = 0.7182, \qquad C = 0.7856$$

LEIBNIZ'S FORMULA FOR DIFFERENTIATING AN INTEGRAL

$$\frac{d}{dx}\left[\int_{a(x)}^{b(x)} F(x,m)\ dm\right] = \int_{a(x)}^{b(x)} \frac{\partial F(x,m)}{\partial x}\ dm + F(x,b)\frac{db}{dx} - F(x,a)\frac{da}{dx}$$

REFERENCE

1. P. R. Greene, A useful approximation to the error function: applications to mass, momentum and energy transport in shear layers, *J. Fluids Eng.*, Vol. 111, 1989, pp. 224–226.

AUTHOR INDEX

SUBJECT INDEX